

# Lawrence Berkeley National Laboratory

## Recent Work

**Title**

NUCLEAR CHEMISTRY ANNUAL REPORT 1973

**Permalink**

<https://escholarship.org/uc/item/29s5v1p2>

**Author**

Lawrence Berkeley National Laboratory

**Publication Date**

1974-05-01

LBL-2366

2

RECEIVED  
LAWRENCE  
RADIATION LABORATORY

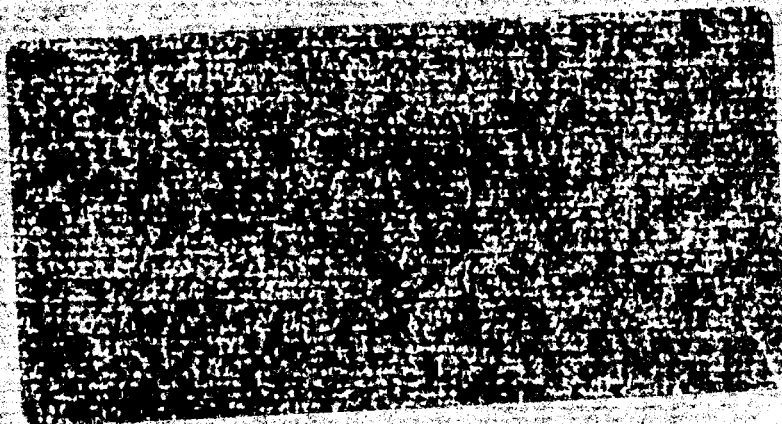
AUG 20 1974

LIBRARY AND  
DOCUMENTS SECTION

# NUCLEAR CHEMISTRY

## Annual Report

1973



Lawrence Berkeley Laboratory  
University of California  
Berkeley, California

LBL-2366

2

## **DISCLAIMER**

This document was prepared as an account of work sponsored by the United States Government. While this document is believed to contain correct information, neither the United States Government nor any agency thereof, nor the Regents of the University of California, nor any of their employees, makes any warranty, express or implied, or assumes any legal responsibility for the accuracy, completeness, or usefulness of any information, apparatus, product, or process disclosed, or represents that its use would not infringe privately owned rights. Reference herein to any specific commercial product, process, or service by its trade name, trademark, manufacturer, or otherwise, does not necessarily constitute or imply its endorsement, recommendation, or favoring by the United States Government or any agency thereof, or the Regents of the University of California. The views and opinions of authors expressed herein do not necessarily state or reflect those of the United States Government or any agency thereof or the Regents of the University of California.

# NUCLEAR CHEMISTRY

## Annual Report

### 1973

G. T. Seaborg, Director  
B. G. Harvey, Deputy Director  
Nuclear Chemistry Division

Editors: D. L. Hendrie  
C. F. Tsang  
A. Zalkin

**Lawrence Berkeley Laboratory**  
**University of California**  
**Berkeley, California**



Work done under  
U.S. Atomic Energy Commission  
Contract No. W-7405-eng-48

May 1974

Printed in the United States of America  
Available from  
National Technical Information Service  
U.S. Department of Commerce  
5285 Port Royal Road  
Springfield, Virginia 22151  
Price: Printed Copy \$13.60; Microfiche \$1.45

## FOREWORD

This Annual Report provides descriptions of significant research carried on in the Nuclear Chemistry Division of the Lawrence Berkeley Laboratory during the calendar year 1973. These brief accounts give an overview of this research and its interpretation; more complete descriptions are published in the relevant journals of scientific literature, and references to these journals available at the time of this publication are included.

The scope of the work of the Nuclear Chemistry Division has continually increased since the birth of the Division nearly 30 years ago, and recognition of this as well as the increasing diversity of its program led to the custom of issuing these more comprehensive annual reports. Under nuclear chemistry we include all areas to which chemists make contributions in the field of nuclear science and related fields. In our Division, nuclear chemistry includes within such a broad definition low energy nuclear physics (including nuclear reactions, nuclear structure physics, nuclear fission, and nuclear theory), the relatively new field of heavy ion interactions, chemical and atomic physics (including atomic and molecular spectroscopy and hyperfine interactions), physical, inorganic, and analytical chemistry (including the application of x-ray crystallography, photoelectron spectroscopy, atomic and molecular spectroscopy, magnetic susceptibility and magnetic resonance techniques), a program of actinide and lanthanide chemistry (including the preparation and characterization of organometallic compounds), radiation chemistry and radiochemistry, a program aimed toward the synthesis and identification of superheavy elements, archaeological research, the development of special instrumentation of many kinds, and a program of environmental research using the highly developed specialized techniques of the Division, such as neutron and  $^3\text{He}$  activation analysis, x-ray fluorescence analysis, photoelectron spectroscopy, and other applicable instrumentation.

A notable event during 1973 was the effective start-up of the rebuilt HILAC for regular research by both LBL and a substantial group of outside users. This essentially new machine, now referred to as the SuperHILAC, operated as a national facility, has consistently furnished krypton ions with energies of 7.5 MeV per nucleon and will have the ultimate capability of accelerating all ions in the periodic table to energies up to 8.5 MeV per nucleon. The SuperHILAC, the 88-Inch Cyclotron (now being used with increasing emphasis on heavy ions at the lower end of the mass scale), and the soon-to-be-available Bevalac (which should furnish heavy ions in the energy range of 2-3 GeV per nucleon) will all facilitate a future broad ranging program in heavy ion research.

Another new direction, just beginning to be reflected in this report, is an increasing effort in the general area of energy and environmental research.

## Contents

I. SCIENCE OF THE NUCLEUS

## NUCLEAR SPECTROSCOPY, RADIOACTIVITY, AND FISSION

Table of Isotopes Project (E. Browne, J. M. Dairiki, R. E. Doebler, J. M. Hollander, L. J. Jardine, C. M. Lederer, A. Shihab-Eldin, V. S. Shirley, and M. Whalley)	3
The Half-Life and the $\alpha$ -Decay Branching Ratio of $^{207}\text{Po}$ (B. Parsa and S. S. Markowitz)	5
High-Spin States in $^{155}\text{Dy}$ and $^{154}\text{Dy}$ from ( $^{12}\text{C}, \text{xn}, \gamma$ ) Studies (K. Krien, R. A. Naumann, J. O. Rasmussen, and I. Rezanka)	7
Levels in $^{165}\text{Tm}$ Excited by Decay of 10-Min $^{165}\text{Yb}$ and by the $^{158}\text{Gd}(^{11}\text{B}, 4\text{n})$ Reactions (T. Tamura, I. Rezanka, S. Iwata, J. O. Rasmussen, and J. Alonso)	10
An Isomeric State in $^{213}\text{Ra}$ (D. G. Raich, J. O. Rasmussen, and I. Rezanka)	16
A Test of Backbending Models Using Odd-A Nuclei (E. Grosse, F. S. Stephens, and R. M. Diamond)	18
Backbending in Odd-A Ho Isotopes (E. Grosse, F. S. Stephens, and R. M. Diamond)	20
Rotational Bands in the Light Odd-Mass Thallium Nuclei (J. O. Newton, F. S. Stephens, and R. M. Diamond)	22
Coulomb Excitation of $^{238}\text{U}$ with Kr Ions (E. Grosse, F. S. Stephens, B. Povh, P. Kienle, and R. M. Diamond)	24
Prolate Shape in Light Cerium and Neodymium Nuclei (J. Gizon, A. Gizon, M. R. Maier, E. Grosse, R. M. Diamond, and F. S. Stephens)	26
Shape Coexistence and Its Cause in $^{151}\text{Gd}$ (P. Kleinheinz, R. K. Sheline, M. R. Maier, R. M. Diamond, and F. S. Stephens)	27
Evidence for Deformed Shaped in $^{186}\text{Hg}$ (D. Proetel, R. M. Diamond, P. Kienle, J. R. Leigh, K. H. Maier, and F. S. Stephens)	29
Nuclear Deformations in $^{186}\text{Hg}$ from Lifetime Measurements (D. Proetel, R. M. Diamond, and F. S. Stephens)	31
Test of the Independence Postulate in the Bohr Theory of Compound-Nucleus Decay: $^{50}\text{Cr}^*$ System (M. K. Go and S. S. Markowitz)	33
Excitation Functions of $\text{La}(^{12}\text{C}, \text{xn})$ Eu Reactions (D. M. Lee and S. S. Markowitz)	34
Fission Probabilities in Lighter Nuclei: A Theoretical and Experimental Investigation of the Shell and Pairing Effects in Fissioning Nuclei (L. G. Moretto)	36

Fission Cross Section in $^4\text{He}$ Induced Fission of $^{204}\text{Pb}$ , $^{186}\text{W}$ , $^{165}\text{Ho}$ and of Some Hg Isotopes (L. G. Moretto, R. C. Gatti, and S. G. Thompson)	37
Measurement of Prompt Gamma Ray Lifetimes of Fission Fragments of $^{252}\text{Cf}$ (R. Jared, H. Nifenecker, and S. G. Thompson)	38
Core Polarization in $^{134}\text{Te}$ (R. A. Naumann, J. B. Wilhelmy, R. C. Jared, H. Nifenecker, and S. G. Thompson)	42
Simultaneous Emission of Two Light Charged Particles in Spontaneous Fission of $^{252}\text{Cf}$ (S. K. Kataria, E. Nardi, and S. G. Thompson)	45
Charge Distribution of the Fragments Emitted in the Reaction Between $^{63, 65}\text{Cu}$ and 606-MeV $^{84}\text{Kr}$ (S. G. Thompson, L. G. Moretto, R. C. Jared, R. P. Babinet, R. C. Gatti, and J. L. Levinson)	51
Study of the Charged Particles Produced in the Reaction Between $^{107, 109}\text{Ag}$ and 288 MeV $^{40}\text{Ar}$ (S. G. Thompson, L. G. Moretto, R. C. Jared, R. C. Gatti, R. P. Babinet, H. Gutbrod, D. Heunemann, J. C. Hunter, R. C. Schmitt, and J. L. Levinson)	52
Highly Inelastic Emission of Heavy Charged Particles in the Reaction Between $^{107, 109}\text{Ag}$ and $^{14}\text{N}$ (L. G. Moretto, R. C. Jared, S. G. Thompson, S. K. Kataria, D. Heunemann, R. P. Babinet, R. C. Schmitt, and J. L. Levinson)	54
Angular Distributions of Fragments Produced in the Bombardment of $^{107, 109}\text{Ag}$ and $^{159}\text{Tb}$ with $^{14}\text{N}$ (L. G. Moretto, R. C. Gatti, and S. G. Thompson)	57
X-Ray Analysis of Heavy Ion Reaction Products (R. C. Jared, R. P. Babinet, and S. G. Thompson)	59
Radiochemical Yield Determination of Various Reaction Products in the Reaction of $^{238}\text{U}$ with $^{40}\text{Ar}$ and $^{84}\text{Kr}$ Ions (I. Binder, J. V. Kratz, J. O. Liljenzin, A. E. Norris, and G. T. Seaborg)	61
NUCLEAR REACTIONS AND SCATTERING	
Deviations from Isospin-imposed Symmetry in the Reaction $^4\text{He}(\vec{d}, t)^3\text{He}$ (W. Dahme, H. E. Conzett, F. J. Arvieux, J. Birchall, and R. M. Larimer)	65
Depolarization in $\vec{p} - ^9\text{Be}$ Scattering and the Spin-Spin Interaction (J. Birchall, F. J. Arvieux, H. E. Conzett, W. Dahme, W. Haeberli, and R. M. Larimer)	66
The Depolarization Parameter in $\vec{p} - ^{10}\text{B}$ Elastic Scattering and the Spin-Spin Interaction (J. Birchall, H. E. Conzett, F. N. Rad, S. Chintalapudi, and R. M. Larimer)	68
Is the $^{12}\text{C}(d, d_0)$ Reaction a Good Polarization Standard? (J. Arvieux, J. Birchall, H. E. Conzett, W. Dahme, W. Haeberli, and R. M. Larimer)	69
The $j$ -Dependence of the Vector Analyzing Power for $(d, ^3\text{He})$ and $(d, t)$ Reactions (B. Mayer, H. E. Conzett, W. Dahme, D. G. Kovar, R. M. Larimer, and Ch. Leemann)	71
The Scattering of Polarized Protons from Si in the Giant Resonance Region of $^{29}\text{P}$ (C. R. Lamontagne, B. Frois, R. J. Slobodrian, H. E. Conzett, Ch. Leeman, and R. de Swiniarski)	74

The Scattering of Polarized Protons from $^{24}\text{Mg}$ , $^{27}\text{Al}$ , and $^{32}\text{S}$ in the Giant Resonance Regions of $^{25}\text{Al}$ , $^{28}\text{Si}$ , and $^{33}\text{Cl}$ (J. Birchall, H. E. Conzett, C. R. Lamontagne, R. M. Larimer, R. Roy, and R. J. Slobodrian)	78
A Study of the $(\alpha, \alpha'n)$ Reaction on Various Targets at 90 MeV (D. R. Brown, I. Halpern, D. L. Hendrie, and H. Homeyer)	79
Highly Inelastic Deuteron Scattering at 45 MeV (H. Wieman, M. Zisman, I. Halpern, and D. Hendrie)	80
The $^{12}\text{C}(^{14}\text{N}, ^{13}\text{N})^{13}\text{C}$ Reaction at 100 MeV (R. M. DeVries, M. S. Zisman, J. G. Cramer, K-L. Liu, F. D. Becchetti, B. G. Harvey, H. Homeyer, D. G. Kovar, J. Mahoney, and W. von Oertzen)	81
The $(^{16}\text{O}, ^{14}\text{C})$ Reaction and Spherical and Deformed Nuclei (W. von Oertzen, B. G. Harvey, D. L. Hendrie, H. Homeyer, D. G. Kovar, and J. Mahoney)	84
A Study of the $^{208}\text{Pb}(^{16}\text{O}, ^{15}\text{O})^{209}\text{Pb}$ Reaction and the Neutron Potential, $A > 200$ (F. Becchetti, D. Kovar, B. G. Harvey, H. Homeyer, J. Mahoney, C. Maguire, D. K. Scott, and W. von Oertzen)	86
A Study of the Two Proton Transfer Reactions $^{208}\text{Pb}(^{12}\text{C}, ^{10}\text{Be})^{210}\text{Po}$ and $^{208}\text{Po}(^{16}\text{O}, ^{14}\text{C})^{210}\text{Po}$ (F. D. Becchetti, D. G. Kovar, B. G. Harvey, D. L. Hendrie, H. Homeyer, J. Mahoney, W. von Oertzen, and N. K. Glendenning)	87
Analysis of Heavy Ion Induced Single Nucleon Transfer Reactions (D. G. Kovar, F. D. Becchetti, B. G. Harvey, D. L. Hendrie, H. Homeyer, J. Mahoney, and W. von Oertzen)	94
Indirect Processes in Heavy-Ion Transfer Reactions (D. K. Scott, N. D. Glendenning, B. G. Harvey, D. L. Hendrie, L. Kraus, C. Maguire, J. Mahoney, Y. Terrien, and K. Yagi)	96
Elastic and Inelastic Scattering of $^{16}\text{O}$ on $^{122}\text{Sn}$ at 104 MeV (Y. Terrien, N. K. Glendenning, B. G. Harvey, D. L. Hendrie, L. Kraus, C. Maguire, J. Mahoney, D. K. Scott, and K. Yagi)	99
Angular Distributions from the $^{122}\text{Sn}(^{16}\text{O}, ^{15}\text{N})^{123}\text{Sb}$ Reaction (C. Maguire, B. G. Harvey, D. L. Hendrie, L. Kraus, J. Mahoney, D. K. Scott, Y. Terrien, and K. Yagi)	100
The Reaction $^{208}\text{Pb}(^{20}\text{Ne}, \alpha)^{224}\text{Th}$ (B. G. Harvey, D. L. Hendrie, D. K. Scott, J. Mahoney, C. F. Maguire, Y. Terrien, L. Kraus, and K. Yagi)	101
Spectroscopy of Nuclei Far From Stability Using Heavy Ion Transfer Reactions (D. K. Scott, B. G. Harvey, D. L. Hendrie, L. Kraus, C. Maguire, J. Mahoney, Y. Terrien, and K. Yagi)	102
Feasibility of Alpha-Transfer Studies Via the $(\alpha, ^8\text{Be})$ Reaction at High Energies (G. J. Wozniak, N. A. Jelley, and J. Cerny)	103
Masses for $^{43}\text{Ar}$ and the New Isotopes $^{45}\text{Ar}$ and $^{46}\text{Ar}$ (N. A. Jelley, K. H. Wilcox, R. B. Weisenmiller, G. J. Wozniak, and J. Cerny)	105
Analyzing Powers in $^{208}\text{Pb}(\vec{p}, t)^{206}\text{Pb}$ Transitions (J. A. Macdonald, N. A. Jelley, and Joseph Cerny)	108

Analyzing Powers for ( $\vec{p}$ , $^3\text{He}$ ) Reactions in the 1p-Shell (J. A. Macdonald, Joseph Cerny, J. C. Hardy, H. L. Harney, A. D. Bacher, and G. R. Plattner) . . . . .	111
The Beta-Delayed Proton Decay of $^{25}\text{Si}$ (R. G. Sextro, R. A. Gough, and J. Cerny) . . . . .	114
High-Resolution Measurements of Beta-Delayed Protons from $^{37}\text{Ca}$ and $^{41}\text{Ti}$ (R. G. Sexto, R. A. Gough, and J. Cerny) . . . . .	118
The Discovery of Two Isotopes, $^{14}\text{Be}$ and $^{17}\text{B}$ , at the Limits of Particle Stability (J. D. Bowman, A. M. Poskanzer, R. G. Korteling, and G. W. Butler) . . . . .	122
Fragments from Uranium Irradiated by 2.1-GeV/Nucleon Deuterons and Alpha Particles (A. M. Poskanzer, J. D. Bowman, and A. M. Zebelman) . . . . .	125
On-Line Mass-Spectrometric Mass Measurements of Neutron Rich Isotopes of Li, Na, and K (R. Klapisch, C. Thibault, C. Rigaud, A. M. Poskanzer, L. Lessard, W. Reisdorf) . . . . .	126
High Energy Elastic Scattering by Recoil Detection (A. M. Poskanzer, A. M. Zebelman, and V. Viola) . . . . .	127
Free-Particle Collisions in Proton and Pion-Induced Nuclear Reactions (N. P. Jacob, Jr. and S. S. Markowitz) . . . . .	129
 NUCLEAR THEORY	
The Nuclear Droplet Model for Arbitrary Shapes (W. D. Myers and W. J. Swiatecki) . . . . .	131
The Dynamics of Charged Viscous Liquid Drops (C. T. Alonso) . . . . .	133
Macroscopic Nuclear Properties (J. Randrup) . . . . .	137
Quantization of the Seyler-Blanchard Model (J. Randrup) . . . . .	141
Proximity Forces (J. Randrup, W. J. Swiatecki, and C. F. Tsang) . . . . .	143
Compound Nucleus Formation in Heavy Ion Collisions (C. F. Tsang) . . . . .	146
Frictional Effects in Heavy Ion Collisions (C. F. Tsang) . . . . .	149
Total Reaction Cross Sections for Heavy Ions (J. R. Alonso and J. O. Rasmussen) . . . . .	150
On Subcoulomb Transfer Reactions (M. A. Nagarajan) . . . . .	153
On the Systematics of the Interference Between Direct and Indirect Modes in Two-Nucleon Pickup and Stripping Reactions Between Heavy Ions (N. K. Glendenning and R. J. Ascutto) . . . . .	154
The Effect of Indirect Transitions on Two Nucleon Transfer Between Heavy Ions (N. K. Glendenning and R. J. Ascutto) . . . . .	156
The Sensitivity of the Forward Cross Section in Transfer Reactions Between Heavy Ions to the Edge of the Nuclear Field (N. K. Glendenning and R. J. Ascutto) . . . . .	160
Abrasion and Ablation of Heavy Ions (J. D. Bowman, W. J. Swiatecki, and C. F. Tsang) . . . . .	163
Relativistic Heavy-Ion Elastic Scattering (W. L. Wang and R. G. Lipes) . . . . .	166
Differential $K_L \rightarrow K_S$ Regeneration in Coherent Production Model and Optical Model (W. L. Wang and F. Uchiyama) . . . . .	168

Angular Distribution and Polarization of $^{16}\text{O}(\gamma, n_0)^{15}\text{O}$ (W. L. Wang and C. M. Shakin) . . . . .	170
Coupled Channel Alpha Decay Theory for Odd-Mass Nuclei (A. J. Soinski, D. G. Raich, J. O. Rasmussen, and E. A. Rauscher) . . . . .	172
Extension of Alpha Decay Rate Theory to Spherical Odd-Odd Nuclei ( $^{210}\text{At}$ ) (A. Shihab-Eldin, L. J. Jardine, and J. O. Rasmussen) . . . . .	175
Backbending and Rotation Alignment (F. S. Stephens, P. Kleinheinz, R. K. Sheline, and R. S. Simon) . . . . .	178
Configuration Mixing of Two-Quasi-Particle States in Even-Even Deformed Nuclei (H. Massmann, J. O. Rasmussen, T. E. Ward, P. E. Hausteine, and F. M. Bernthal) . . . . .	181
Two Coriolis Mixed Rotational Band Expansion for Deformed Odd-Mass Nuclei (H. Massmann, J. O. Rasmussen, and W. Ribbe) . . . . .	183
Number-Displacement Degrees of Freedom in Nuclear Rotational Theory (J. O. Rasmussen and C. W. Ma) . . . . .	187
Exponential Dependence of the Nuclear Moment-of-Inertia on Pairing Correlation and the Pairing Stretch Model for Nuclear Rotation (C. W. Ma and J. O. Rasmussen) . . . . .	189
Cranking Model Calculation of $^{162}\text{Er}$ High-Spin Rotational States Including $i_{13/2}$ Recoupling (C. W. Ma and J. O. Rasmussen) . . . . .	192
Three-Dimensional Pairing Stretch Model Calculations (S. Y. Chu, J. O. Rasmussen and C. W. Ma) . . . . .	196
Microscopic Calculation of the Higher-Order Effects in Nuclear Quasi-Rotational Spectrum (C. W. Ma and C. F. Tsang) . . . . .	198
Statistical Properties of a Paired System with Fixed Quasi-Particle Number (L. G. Moretto and T. Clements) . . . . .	200
Finite Temperature Calculation of Angular Velocities and Moments of Inertia in Rotating Nuclei (L. G. Moretto) . . . . .	202
Pairing and Spin Distribution Effects on the Yrast Line (L. G. Moretto) . . . . .	205
Influence of Pairing and of the Spin Projection Distribution on the "Classical" Isothermal Rotations of a Nucleus (L. G. Moretto) . . . . .	207
Superfluid Properties of Excited Nuclei Arising from A $\delta$ -Force Residual Interaction (L. G. Moretto and S. K. Kataria) . . . . .	211
Studies on Statistically Excited Shell Model Nuclei: The Dependence of the Shell Structure and of the Pairing Correlation upon Angular Momentum (L. G. Moretto) . . . . .	214
Large Superfluidity Enhancement in the Penetration of the Fission Barrier (L. G. Moretto and R. P. Babinet) . . . . .	216
Theoretical Predictions of Fission Half-Lives of Elements with Z Between 92 and 106 (J. Randrup, C. F. Tsang, P. Möller, S. G. Nilsson, and S. E. Larsson) . . . . .	219
The Superheavy Elements: A Brief Review (C. F. Tsang) . . . . .	222
Nuclear Masses, Deformations, and Single-Particle Orbitals for Medium-Heavy and Heavy Nuclei (C. F. Tsang, I. Ragnarsson, S. G. Nilsson, P. Möller, and J. R. Randrup) . . . . .	223

II. CHEMICAL AND ATOMIC PHYSICS

## HEAVY ION INDUCED ATOMIC REACTIONS

Radiative Capture and Bremsstrahlung of Bound Electrons Induced by Heavy Ions* (P. Kienle, M. Kleber, B. Povh, R. M. Diamond, F. S. Stephens, E. H. Grosse, M. R. Maier, and D. Proetel)	227
Chemical Experiments Using Accelerated Heavy Ions at the Bevatron (M. E. Jayko and A. Chatterjee)	229
Lifetime of the $2^3S_1$ State of Helium-Like Argon ( $Z = 18$ ) and Helium-Like Titanium ( $Z = 22$ ) (H. Gould, R. Marrus, and R. W. Schmieder)	230
K-Vacancy Production in 150-MeV Kr + Kr Collisions (R. Anholt, W. E. Meyerhof, F. S. Stephens, Jr., R. M. Diamond, J. de Boer, D. Proetel, and P. O. Tjøm)	233
The Molecular Orbital X-ray Yield in Symmetric Collisions (R. Anholt and J. O. Rasmussen)	235
Theoretical X-ray Transition Probabilities for High-Z Superheavy Elements (R. Anholt and J. O. Rasmussen)	237

## ATOMIC AND MOLECULAR SPECTROSCOPY

Spectra and Energy Levels of V $\text{V}^*$ (C. H. H. Van Deurzen, J. G. Conway, and S. P. Davis)	239
The Prediction of Core-Level Binding-Energy Shifts from CNDO Molecular Orbitals* (D. W. Davis and D. A. Shirley)	244
Electron Paramagnetic Resonance of $^{239}\text{Pu}^{3+}$ and $^{234}\text{Am}^{4+}$ in $\text{CeO}_2$ and of $^{241}\text{Pu}^{3+}$ in $\text{ThO}_2$ (W. Kolbe, N. Edelstein, C. B. Finch, and M. M. Abraham)	247
Calculation of the Crystal Field Splittings of $\text{Sm}^{3+}$ Levels in $\text{LaCl}_3$ with Inclusion of J Mixing* (K. Rajnak, R. Mehlhorn, and N. Edelstein)	250
Geometries of the Methoxy Radical ( $X^2E$ and $A^2A_1$ States) and the Methoxide Ion* (D. R. Yarkony, H. F. Schaefer III, and S. Rothenberg)	252
Barrier Height for the Exchange Reaction $\text{F} + \text{HF} \rightarrow \text{FH} + \text{F}$ (S. V. O'Neil, H. F. Schaefer III, and C. F. Bender)	252
Theoretical Support for the Assignment of X-ogen to the $\text{HCO}^+$ Molecular Ion* (U. Wahlgren, B. Liu, P. K. Pearson, and H. F. Schaefer III)	254
HNC Molecule in Interstellar Space? Some Pertinent Theoretical Calculations* (P. K. Pearson, G. L. Blackman, H. F. Schaefer III, and U. Wahlgren)	257
Probable Nonexistence of Xenon Monofluoride as a Chemically Bound Species in the Gas Phase* (D. H. Liskow, H. F. Schaefer III, P. S. Bagus, and B. Liu)	259
Potential Energy Surfaces for Simple Chemical Reactions (H. F. Schaefer III)	261
Electronic Structure of Simple Inorganic Molecules (H. F. Schaefer III)	263



## PHOTOELECTRON SPECTROSCOPY AND HYPERFINE INTERACTIONS

ESCA* (D. A. Shirley)	267
X-ray Photoemission Study of Gd, Tb, and Dy 4f and Valence Bands (F. R. McFeely, S. P. Kowalczyk, L. Ley, and D. A. Shirley)	268
X-ray Photoemission from Sodium and Lithium* (S. P. Kowalczyk, L. Ley, F. R. McFeely, R. A. Pollak, and D. A. Shirley)	271
X-ray Photoemission Studies of Diamond, Graphite, and Glassy Carbon Valence Bands* (F. R. McFeely, S. P. Kowalczyk, L. Ley, R. G. Cavell, R. A. Pollak, and D. A. Shirley)	275
X-ray Photoemission from Zinc: Evidence for Extra-Atomic Relaxation Via Semilocalized Excitons (L. Ley, S. P. Kowalczyk, F. R. McFeely, R. A. Pollak, and D. A. Shirley)	277
X-ray Photoemission Studies of the Alkali Halides* (S. P. Kowalczyk, F. R. McFeely, L. Ley, R. A. Pollak, and D. A. Shirley)	281
Electronic Density of States and Bonding in Chalcopyrite-Type Semiconductors (Carmen Varea de Alvarez, Marvin L. Cohen, L. Ley, S. P. Kowalczyk, F. R. McFeely, D. A. Shirley, and R. W. Grant)	286
Total Valence Band Densities of States of III-V and II-VI Compounds from XPS (L. Ley, R. A. Pollak, F. R. McFeely, S. P. Kowalczyk, and D. A. Shirley)	289
Core-Level Binding Energy Shifts in Small Molecules* (D. W. Davis, M. S. Banna, and D. A. Shirley)	292
Anomalous Multiplet-Splitting Intensity Ratios in K-Level XPS Spectra of NO and O <sub>2</sub> (P. S. Bagus, M. Schrenk, D. W. Davis, and D. A. Shirley)	295
Multiplet Splitting in 1s Hole States of Molecules* (D. W. Davis, R. L. Martin, M. S. Banna, and D. A. Shirley)	298
Characteristic Energy Loss Structure of Solids* from X-ray Photoemission spectra (R. A. Pollak, L. Ley, F. R. McFeely, S. P. Kowalczyk, and D. A. Shirley)	303
The L <sub>2,3</sub> M <sub>45</sub> M <sub>45</sub> Auger Spectra of Metallic Copper and Zinc: Theory and Experiment* (S. P. Kowalczyk, R. A. Pollak, F. R. McFeely, L. Ley, and D. A. Shirley)	305
The Relative Effect of Extra-Atomic Relaxation on Auger and ESCA Shifts in Transition Metals and Salts* (S. P. Kowalczyk, L. Ley, F. R. McFeely, R. A. Pollak, and D. A. Shirley)	308
Theory of KLL Auger Energies Including Static Relaxation* (D. A. Shirley)	312
Theory of Auger Satellite Energy Shifts* (D. A. Shirley)	316
Quadrupole Coupling at <sup>193</sup> Ir Nuclei in Iron* (D. Salomon and D. A. Shirley)	319
Supertransferred Hyperfine Interaction: Perturbed Angular Correlation of <sup>111m</sup> Cd in KNiF <sub>3</sub> , KCoF <sub>3</sub> and RbMnF <sub>3</sub> (H. H. Rinneberg and D. A. Shirley)	321

III. PHYSICAL, INORGANIC, AND ANALYTICAL CHEMISTRY

## X-RAY CRYSTALLOGRAPHY

The Crystal and Molecular Structure of Triphenylmethylphosphonium 1, 1, 1-Tricarbonyl-4, 6-Dicar-1-Mangana-Closo-Nonaborate(1-) (F. J. Hollander, D. H. Templeton, and A. Zalkin)	325
Crystal Structure of $[\text{XeF}_5^+][\text{AsF}_6^-]$ (N. Bartlett, F. J. Hollander, D. H. Templeton, and A. Zalkin)	327
Crystal Structure of $[\text{XeF}_5^+]_2[\text{PdF}_6^{2-}]$ (K. Leary, D. H. Templeton, A. Zalkin, and N. Bartlett)	329
Structure of NdSBr and Isostructural Rare Earth Sulfo Bromides (N. Savigny, A. Zalkin, C. Adolphe, and D. H. Templeton)	331
Crystal Structures of the Fluosilicate Hexahydrates of Cobalt, Nickel, and Zinc (S. Ray, A. Zalkin, and D. H. Templeton)	332
Crystal Structure of Copper Fluosilicate Hexahydrate (S. Ray, A. Zalkin, and D. H. Templeton)	335
Sodium Chromate Tetrahydrate (H. Ruben, I. Olovsson, A. Zalkin, and D. H. Templeton)	337
The Crystal Structure of N, N' -BIS(2, 2, 6, 6-Tetramethylpiperidyl-4) Succinic Acid Diamide Dihydrate, $\text{C}_{22}\text{H}_{42}\text{O}_2\text{N}_4 \cdot 2\text{H}_2\text{O}$ (H. Ruben, A. Zalkin, and D. H. Templeton)	338
The Structure of the $10\pi$ Electron Cyclooctatetraene Dianion in Potassium Diglyme 1, 3, 5, 7-Tetramethylcyclooctatetraene Dianion, $[\text{K}(\text{CH}_3\text{OCH}_2\text{CH}_2)_2\text{O}]_2[\text{C}_8\text{H}_4(\text{CH}_3)_4]^{1-}$ (S. Z. Goldberg, K. N. Raymond, C. A. Harmon, and D. H. Templeton)	340
The Crystal and Molecular Structure of Melatonin (W. G. Quarles, D. H. Templeton, and A. Zalkin).	342
The Crystal and Molecular Structure of 5-Methoxytryptamine (W. G. Quarles, D. H. Templeton, and A. Zalkin)	344
Structure of 5-Hydroxy-2, 3-Norbornane Dicarboxylic Acid $\gamma$ -Lactone, $\text{C}_9\text{H}_{10}\text{O}_4$ (G. Chapuis, A. Zalkin, and D. H. Templeton)	347

## PHYSICAL AND INORGANIC CHEMISTRY

Chemical Processing of Superhilac Targets (J. V. Kratz, J. O. Liljenzin, and G. T. Seaborg)	349
Covalency Effects on the Ligand Field Splittings of Octahedral $5f^1$ Compounds (N. Edelstein, D. Brown, and B. Whittaker)	351
An Elementary Molecular Orbital Calculation on $\text{U}(\text{C}_8\text{H}_8)_2$ , and Its Application to the Electronic Structures of $\text{U}(\text{C}_8\text{H}_8)_2$ , $\text{Np}(\text{C}_8\text{H}_8)_2$ , and $\text{Pu}(\text{C}_8\text{H}_8)_2$ (R. G. Hayes and N. Edelstein)	356
Preparation of Di- $\pi$ -Cyclooctatetraene Complexes of Uranium, Thorium, and Plutonium by Direct Reaction of the Metals with Cyclooctatetraene (D. F. Starks and A. Streitwieser, Jr.)	358
DI- $\pi$ -Cyclooctatetraeneprotactinium (D. F. Starks, T. C. Parsons, A. Streitwieser, Jr., and N. Edelstein)	359

The Preparation, Crystallographic and Spectral Properties of the Octahedral Hexafluoroprotactinate (VI), $(\text{NET}_4)_2\text{PaF}_6$ (D. Brown, B. Whittaker, and N. Edelstein)	362
<b>RADIATION CHEMISTRY</b>	
Comparative Radiation Chemistry of Glycine and Its Oligopeptide Derivatives (W. M. Garrison)	369
Scavenger Effects in the Recoil Tritium Reactions of Cyclohexene (D. C. Fee and S. S. Markowitz)	370
Recoil Tritium Reactions with Methylcyclohexene: A Test of the Assumption of Energy Randomization Prior to Unimolecular Decomposition (D. C. Fee and S. S. Markowitz)	371
Recoil Tritium Reactions with Cyclohexene and Alkenes: Determination of Rate Parameters (D. C. Fee and S. S. Markowitz)	373
Recoil Tritium Reactions with Alkenes: Formation of "Polymer-T" (D. C. Fee and S. Markowitz)	376
Metastable Transitions in the Mass Spectra of Dimethylnitrosamine and Related Compounds (A. S. Newton)	378
<b>APPLICATIONS OF ACTIVATION ANALYSIS</b>	
On the Homogeneity of Columbia River Plateau Basalt and Its Relation to a Coastal Basalt Flow (H. R. Bowman, H. Schmincke, and A. Hebert)	381
Definitive Provenience Determinations on Mesoamerica Obsidian Artifacts (F. Asaro, H. R. Bowman, and F. Stross)	383
On the Reconstruction of the North Colossus of Memnon (H. R. Bowman, F. Asaro, F. H. Stross and R. F. Heizer)	385
Chemical Analysis of Ceramic Wares from Fustat, Egypt (H. V. Michel, F. Asaro, and J. D. Frierman)	387
A Lyons Branch of the Pottery-Making Firm of Ateius of Arezzo (F. Asaro, H. V. Michel, I. Perlman, F. Widemann, and M. Picon)	388
Neutron Activation, the Wheel, and Cypriote Pottery from Around 1600 B.C. (M. Artzy, F. Asaro, and I. Perlman)	396
The Bichrome Ware Krater from Tel Nagila (M. Artzy, F. Asaro, and I. Perlman)	399
The Late Bronze "Palestinian" Bichrome Ware in Its Cypriote Context (M. Artzy)	401
<b>ENVIRONMENTAL</b>	
Dispersion of Gaseous Emissions from a Ground-Level Line Source (K. D. Wings, E. A. Grens II, and T. Vermeulen)	406
Neutron Activation Analysis of Particulate Matter in Air (H. V. Michel and F. Asaro)	407
Characterization of Aerosols in California by X-Ray induced X-Ray Fluorescence Analysis (R. D. Giaque, L. Y. Goda, and N. E. Brown)	409
A Survey of the Occurrence of Dimethyl Mercury in the Atmosphere (A. F. Sciamanna and A. S. Newton)	410

Determination of Lead in Atmospheric Air and in Aluminum by $^3\text{He}$ -Induced Nuclear Reactions (B. Parsa and S. S. Markowitz)	413
Interlaboratory Lead Analysis of Standardized Samples of Sea Water (R. G. Clem and D. C. Girvin)	417
A Study of the Effects of Dredging and Spoiling Operation on the Uptake and Accumulation of Heavy Metals by Benthic Estuarine Species (V. Anderlini, J. Chapman, A. S. Newton, and R. W. Risebrough)	419
Enzymatic Utilization of Cellulosic Wastes (G. Mitra and C. R. Wilke)	422

#### IV. INSTRUMENTATION

88-Inch Cyclotron Operation, Development, and Studies (J. Bowen, R. Burleigh, D. J. Clark, W. Flood, P. E. Frazier, and D. Morris)	427
88-Inch Cyclotron Ion Source Development (S. Chintalapudi, D. J. Clark, P. E. Frazier, W. R. Holley, D. Morris, and M. Renkas)	429
A Simple and Efficient $^8\text{Be}$ Identifier (G. J. Wozniak, N. A. Jelley, and Joseph Cerny)	430
Superhilac Operations (R. M. Main)	433
Improvements to Resistive-Wire Focal Plane Detector (H. Homeyer, J. Mahoney, and B. G. Harvey)	434
Considerations of Beam Quality Requirements for Experiments with very Heavy Ions (J. R. Alonso)	435
The Temperature of Thin Foils in Ion Beams (J. O. Liljenzin)	439
Development of a Recoil Atom Mass Analyzer (RAMA) (R. A. Gough, D. Littlejohn, and J. Cerny)	443
F.A.K.E. — A Fast Automatic Chemistry Experiment (J. M. Nitschke)	446
Calibration of Si(Li) Electron Spectrometers with $^{180\text{m}}\text{Hf}$ , $^{207}\text{Bi}$ , and $^{210}\text{At}$ (L. J. Jardine and C. M. Lederer)	447
The Use of Glass Frits for Removal of Recoils from a Catcher Gas (J. V. Kratz, J. O. Liljenzin, and R. J. Silva)	450
Computer-Aided Analysis of $\gamma$ -Ray Spectra (I. Binder, M. DiCasa, J. V. Kratz, J. O. Liljenzin, and A. E. Norris)	451
IRATE (Interactive Retrieval and Text Editing) (E. Romascan, W. Greiman, C. M. Lederer, and A. Allen)	453
Four-Function Calculator Used to Automatically Compute Wavelength (M. Nakamura and G. V. Shalimoff)	454
On-Line Sparger for Voltammetric Studies (R. G. Clem and D. H. Anderberg)	455
Styrene-Impregnated $^{60}\text{Co}$ -Irradiated Graphite Electrode for Anodic Stripping Analysis (R. G. Clem and A. F. Sciamanna)	456
An Integral Instrument for Anodic Stripping Analysis (G. W. Kilian and R. G. Clem)	456
Studies on the Excitation of Spectra of Multiply-Ionized Atoms (C. H. H. Van Deurzen and J. G. Conway)	458

	Two-Chamber Furnace for Flameless Atomic Absorption Spectroscopy (D. A. Church, T. Hadeishi, L. Leong, R. D. McLaughlin, and B. D. Zok)	459
	Instrumentation for Air Pollution Monitoring (C. D. Hollowell and R. D. McLaughlin)	461
V.	<u>THESIS ABSTRACTS</u>	
	Core-Level Photoelectron Spectroscopy of Small Molecules (Donald William Davis)	467
	Recoil Tritium Reactions With Cyclohexene and Methylcyclohexene (Darrell Clark Fee)	467
	Structural Investigations of Transition Metal Pentacoordination (Frances Anne Jurnak)	468
	Two-Nucleon Transfer Reactions Induced by Polarized Protons (John Alan Macdonald)	470
	High-Resolution Studies of Beta-Delayed Proton Emission in Light Nuclei (Richard George Sextro)	470
	Systematics of the $(\alpha, 2\alpha)$ Reaction at $E_\alpha = 90$ MeV (Joseph Donald Sherman)	471
	Excitation Energies in an Electrically Pulsed Light-Emission Source Applied to the Separation of Higher Ionized Atomic States: Spectra and Energy Levels of Scandium 2+ and Vanadium 4+ (Cornelius H. H. Van Deurzen)	472
	Geometry of Some Metal Halides (Peter Alan Yarnell)	472
VI.	<u>1973 PUBLICATIONS</u>	477
VII.	<u>AUTHOR INDEX</u>	517

# I. Science of the Nucleus

*Nuclear Spectroscopy, Radioactivity, and Fission*

*Nuclear Reactions and Scattering*

*Nuclear Theory*







7th edition.

Many people have made use of these sources; in one instance, a scientist from EPA has made extended visits to abstract data from them.

The Table of Isotopes project also answers written requests for data. Many short requests have been answered, and several longer ones. The latter group includes a request for an evaluation of quantitative genetic relations for all fission-product isomers for use in a new fission-yield compilation. Another request was for the best decay data on the natural uranium and thorium decay chains for use in elemental analyses.

Computer programs and some data on magnetic tape have been supplied in response to several requests. (The project currently provides Hager and Seltzer internal conversion coefficients on magnetic tape upon request.) The utility teletype programs referred to above will soon be made available to people outside LBL via telephone lines and the ARPA net.

#### Reference

1. C.M. Lederer, LESAGE User's Manual, LBL-1996, October 1973.

## THE HALF-LIFE AND THE $\alpha$ -DECAY BRANCHING RATIO OF $^{207}\text{Po}$

Bahman Parsa\* and Samuel S. Markowitz

The  $\alpha$ -decay branching ratio of  $^{207}\text{Po}$  has not been experimentally determined yet. The only literature value available is the estimation made by Templeton et al.<sup>1</sup> in which an approximate value of 0.01% is predicted. Furthermore, the half-life of  $^{207}\text{Po}$  is not accurately known either. Templeton et al. observed its half-life to be  $5.7 \pm 0.1$  hr by counting its gamma radiation with a Geiger counter. Later, John<sup>2</sup> obtained a value of  $6.2 \pm 0.1$  hr by counting the gamma activities with a NaI scintillation counter. However, Bell and Skarsgard<sup>3</sup> observed a 5.7-hr activity by counting the K x-rays of  $^{207}\text{Po}$ . By measuring the  $\alpha$  activity of  $^{207}\text{Po}$ , Tielsch-Cassel<sup>4</sup> obtained a value of  $5.7 \pm 0.3$  hr for the  $^{207}\text{Po}$  half-life.

Our studies of the  $^3\text{He}$  reaction with lead has shown that  $^{207}\text{Po}$  is produced abundantly. Because of the need for an accurate value for the half-life of this nuclide in our activation analysis studies,<sup>5</sup> and due to the abundance of data available from the determination of the excitation function for the production of  $^{207}\text{Po}$  from irradiation of Pb by  $^3\text{He}$ , the evaluation of  $^{207}\text{Po}$  half-life and the  $\alpha$ -decay branching ratio was undertaken.

Recently the decay scheme of  $^{207}\text{Po}$  has been studied very accurately.<sup>6,7</sup> Using the results of the decay scheme work, we measured the half-life and the  $\alpha$ -decay branching ratio of  $^{207}\text{Po}$  with the techniques of  $\gamma$ - and  $\alpha$ -spectroscopy.

The  $^{207}\text{Po}$  activity was produced by bombarding foils of 2-mg/cm<sup>2</sup> thick metallic Pb evaporated onto a thin Al backing with  $^3\text{He}$  of

energy 34 - 38 MeV for a period of 1 hr. This energy range had been found to maximum for  $^{207}\text{Po}$  production.<sup>5</sup> The procedures for target preparation, irradiation, and chemical separation were similar to the ones described by Parsa and Markowitz.<sup>5</sup>

#### $\gamma$ -Ray Spectroscopy

Two trapezoidal Ge(Li) detectors of 30 cm<sup>3</sup> active volumes were used in conjunction with standard charge-sensitive preamplifiers, linear amplifiers, and biased amplifiers. With a Northern 1024-channel or a Victoreen 400-channel pulse-height analyzer, a system resolution of approximately 3 keV (FWHM) as measured at the  $^{60}\text{Co}$  1.33-MeV line was obtained. In every experiment the  $\gamma$ -ray photopeak efficiencies of the Ge(Li) detectors were measured with a set of International Atomic Energy Agency (IAEA) calibrated standards. In each half-life measurement the decay of the 922-keV  $\gamma$ -ray of  $^{207}\text{Po}$  (the most intense  $\gamma$ -ray of  $^{207}\text{Po}$ ) was followed continuously for a period of about two days.

#### $\alpha$ -Particle Spectroscopy

A surface-barrier silicon detector of 12-mm sensitive diameter together with associated electronics and a RIDL 400-channel pulse-height analyzer were used. Routinely, the  $\alpha$  spectra had peaks of approximately 20 keV FWHM. The energies of the peaks in the  $\alpha$  spectra were determined with  $^{210}\text{Po}$ ,  $^{241}\text{Am}$ , and  $^{243}\text{Am}$  sources. The efficiency of the  $\alpha$  detector was measured with a standard  $^{210}\text{Po}$  source. The alpha energy of the  $^{207}\text{Po}$  was

5.120 MeV.<sup>4</sup> For the  $\alpha$ -branching ratio experiments, the  $\alpha$  spectra were followed for a period of approximately one week. The counting commenced immediately after the chemical purification. In each experiment, the gamma-ray spectrum of the source was recorded prior to  $\alpha$  counting.

For each half-life determination experiment, the 922-keV photopeak areas from consecutive measurements of the  $^{207}\text{Po}$  decay together with the time datum were calculated. Then, the full set of data for each sample was analyzed by use of the laboratory's CDC 7600 computer and the CLSQ code.<sup>8</sup> A corresponding half-life was obtained. Figure 1 shows a typical decay curve of the 922-keV  $\gamma$ -ray of  $^{207}\text{Po}$ . The results of seven individual experiments for the determination of  $^{207}\text{Po}$  half-life are compiled in Table 1. From these results a mean half-life and standard deviation of  $350.3 \pm 4.1$  min (or  $5.84 \pm 0.07$  hr) is obtained for the  $^{207}\text{Po}$  half-life.

For the  $\alpha$ -decay branching experiments, the analysis of the  $\alpha$  spectra of  $^{207}\text{Po}$  was expected to be complicated due to the presence of 2.9-yr  $^{208}\text{Po}$  also produced in the  $\text{Pb} + ^3\text{He}$  bombardments. Polonium-208 has an  $\alpha$  branch (100%) at 5.118 MeV which is extremely close to the 5.120 MeV alpha energy of the  $^{207}\text{Po}$ .<sup>4</sup> However, the interference was not serious due to the much longer half-life and lower production cross section of  $^{208}\text{Po}$ . Here, the complex nature of the decay curve of such double lines were used for identifications and manipulations.

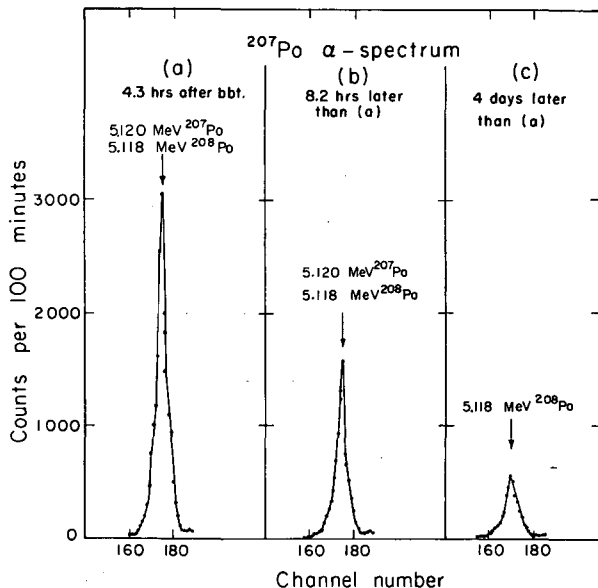


Fig. 1. Decay curve of the 922-keV  $\gamma$ -ray of  $^{207}\text{Po}$ . (XBL-735-2955)

Table 1. Results of the  $^{207}\text{Po}$  half-life determinations.

Experiment No.	Half-life (min)
1	346.5
2	357.0
3	344.7
4	352.8
5	349.9
6	349.0
7	352.2
Average	$350.3 \pm 4.1$

After the 5.12-MeV peak decays for several days, the shorter-lived  $^{207}\text{Po}$  completely diminished and  $^{208}\text{Po}$  was the sole contributor of the  $\alpha$  peak. Figure 2 presents a typical  $\alpha$ -decay plot of the 5.12 MeV lines as observed in different times. By following the decay of this peak for a period of about one week, the  $^{208}\text{Po}$  component was resolved and the remaining portion was observed to decay with a half-life corresponding to 5.8 hr. In each experiment, subsequent measurements of the  $^{208}\text{Po}$   $\alpha$  line from the two faces of the Po-plated Ag foil proved that the Po deposition was the same in both side of the foil. Finally, the two-side contribution of  $^{207}\text{Po}$  counting rate was corrected for the detection efficiency in order to obtain the total  $^{207}\text{Po}$   $\alpha$  activity of the source. Alpha self-absorption of the plated Po activity was negligible since the thickness of the carrier-free deposit was only in the order of  $0.1 \text{ ng/cm}^2$ . Subsequently, the total  $^{207}\text{Po}$  disintegration rate of the source was calculated from the results of the  $\gamma$ -spectroscopy data. The absolute

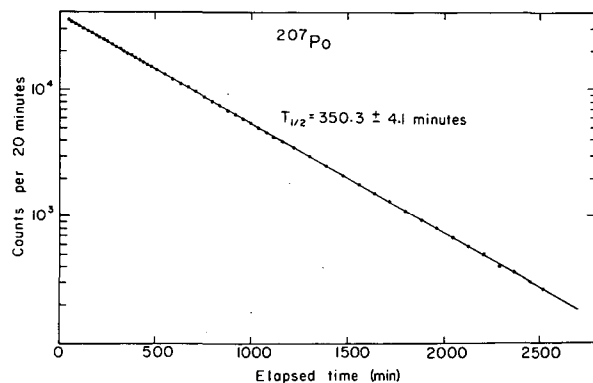


Fig. 2. Alpha spectrum of  $^{207}\text{Po}$  at various times. The 5.12-MeV alpha line is composed of alpha particles from  $^{207}\text{Po}$  and  $^{208}\text{Po}$ . (XBL-735-2954)

intensity of the 922-keV  $\gamma$ -ray of  $^{207}\text{Po}$  was calculated to be  $0.59 \pm 0.04 \gamma/\text{d}$  based on Astner and Alpsten's proposed decay scheme and their table of transition intensities.<sup>6</sup> Then the data were corrected for different times of analyses of  $\alpha$ - and  $\gamma$ -spectroscopy measurements and the subsequent  $^{207}\text{Po}$  decay. Table 2 shows the results of the analyses of the  $\alpha$ -decay branching experiments. The mean value and the standard deviation for the  $\alpha$ -decay branching of  $^{207}\text{Po}$  is found to be  $0.0210 \pm 0.002\%$ .

Table 2. Results of the  $^{207}\text{Po}$   $\alpha$ -branching experiments.

Experiment No.	$\alpha$ branching (%)
1	0.0229
2	0.0217
3	0.0215
4	0.0224
5	0.0192
6	0.0185
Average	$0.0210 \pm 0.002$

The authors wish to thank Mrs. Diana M. Lee for her assistance during this work. One of us (B. P.) would like to express his gratitude for a Senior Fulbright-Hays grant provided to him throughout this study.

### Footnotes and References

\* Accepted by J. Inorg. Nucl. Chem. 36, — 1974.

† Visiting Fulbright-Hays Grantee. Permanent address: Tehran University Nuclear Center, Tehran, Iran.

1. D. H. Templeton, J. J. Howland, and I. Perlman, Phys. Rev. 72, 758 (1947).
2. W. John, Jr., Phys. Rev. 103, 704 (1956).
3. R. E. Bell and H. M. Skarsgard, Can. J. Phys. 34, 745 (1956).
4. E. Tielsch-Cassel, Nucl. Phys. A100, 425 (1967).
5. B. Parsa and S. S. Markovitz, LBL-1901, Anal. Chem. 46, 186 (1974).
6. G. Astner and M. Alpsten, Nucl. Phys. A140, 643 (1970).
7. V. A. Shilin and V. R. Burmistrov, Izvest. Akad. Nauk SSSR, Ser. Fiz. 35, 1653 (1971).
8. J. B. Cumming, "Application of Computers to Nuclear and Radiochemistry", G. D. O'Kelly, Editor, Nat. Acad. Sci-Nat. Res. Council, Nucl. Sci. Ser. NAS-NS 3107, 25 (1963).

## HIGH-SPIN STATES IN $^{155}\text{Dy}$ AND $^{154}\text{Dy}$ FROM ( $^{12}\text{C}, \text{xn}, \gamma$ ) STUDIES

K. Krien,\*† R. A. Naumann,\*‡ J. O. Rasmussen,§ and I. Rezanka||

### Introduction

In-beam  $\gamma$ -spectroscopy enables the investigation of high-spin members of the rotational bands of deformed nuclei. For some odd-neutron rare-earth nuclei with neutron number  $N=89$  (i. e.,  $^{153}\text{Gd}$  and  $^{157}\text{Er}$ ) a positive-parity band has been identified<sup>1-3</sup> which is presumably related to Nilsson orbits originating in the  $N=6$   $i_{13/2}^+$  shell-model state. These rotational bands exhibit a structure which has been interpreted in terms of strong Coriolis coupling.

The nucleus  $^{155}\text{Dy}$  with 89 neutrons represents a missing member of the already studied deformed nuclei with 89 neutrons,  $^{153}\text{Gd}$  and  $^{157}\text{Er}$ . Levels in  $^{155}\text{Dy}$  have been investigated from the radioactive decay<sup>4,5</sup> of  $^{155}\text{Ho}$  and by (d, t) reaction studies.<sup>6</sup> Recently, low-energy

$\gamma$ -rays associated with a 6  $\mu\text{sec}$  isomeric state were reported<sup>7</sup> but no level assignment was attempted. None of these experiments revealed evidence for the high-spin members of a positive-parity band. We have therefore undertaken this study using the  $^{146}\text{Nd}(^{12}\text{C}, \text{xn}, \gamma)$  reactions at the Yale Heavy Ion Accelerator.

At a beam energy of 70 MeV a ( $\gamma\gamma$ ) coincidence experiment was performed. Two Ge(Li) detectors positioned at  $180^\circ$  to each other and  $90^\circ$  relative to the beam direction were used. Standard fast-slow electronics was employed resulting in a time resolution of about 3 nsec. All coincidence events were recorded serially on a magnetic tape. After completion of the experiment coincidence spectra were obtained by sorting the stored events with appropriate energy and time gates.

### The Level Scheme of $^{155}\text{Dy}$

The proposed level scheme for  $^{155}\text{Dy}$ , shown in Fig. 1, is based on all information now available for this nucleus. Borggreen and Sletten<sup>7</sup> have reported five strong  $\gamma$ -transitions in  $^{155}\text{Dy}$  associated with a 6  $\mu\text{sec}$  isomer. We also observe the five strong transitions. Guided by similarities in the level schemes proposed<sup>1,2</sup> for the neighboring isotone  $^{153}\text{Gd}$ , we associate this isomer with an  $11/2^-$  state at 233.4 keV. We place all delayed  $\gamma$ -lines observed by Borggreen and Sletten in the decay scheme except the 186 keV transition which was reported to have a different half-life. Our assignment is in agreement with the observed levels in  $^{155}\text{Dy}$  in the (d, p) reaction<sup>6</sup> and in the decay<sup>5</sup> of  $^{155}\text{Ho}$ . The measured multiplicities, particularly the E2 character of the 147.2 keV

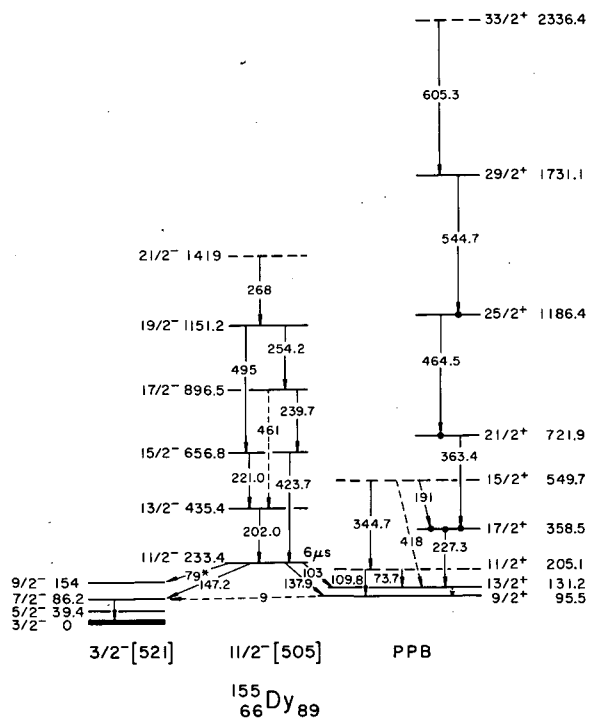


Fig. 1. Proposed  $^{155}\text{Dy}$  scheme of levels populated by the in-beam gamma experiments. Nilsson band assignments  $\Omega\pi [Nn_z\Lambda]$  are indicated for the two negative-parity bands. The positive-parity band (labeled PPB) is believed to be so strongly mixed by the Coriolis interaction that labeling by a single Nilsson band is inappropriate. Note that the in-beam work emphasizes higher spin levels.

(XBL-734-351)

and the M2(E1) character of the 137.9 keV transition, are in agreement with our spin-parity assignments. The hindrance of the E1 component of the 137.9 keV transition can be understood in terms of a K-forbiddenness, as the  $9/2^+$  level is composed primarily of the lower K-values,  $K=1/2, 3/2, 5/2$ . (See later discussion on Coriolis band mixing.)

In the nucleus  $^{155}\text{Dy}$ , the two well-developed rotational bands are quite different. The negative-parity band interpreted as an  $11/2^-$  [505] Nilsson orbital is very regular and can be well understood in terms of Bohr and Mottelson's scheme between the rotational and single-particle motions. This regular behavior occurs in spite of the fact that the nucleus  $^{155}\text{Dy}$  with 89 neutrons is in the transitional region between the deformed and spherical nuclei.

On the other hand, the level order in the positive-parity band, the lowest member of which has been assigned in this study as a  $9/2^+$  level, is of a different character resembling in its  $\gamma$ -decay pattern a spectrum of a doubly even nucleus. For nuclei in this mass region, such positive-parity levels originate in the  $i_{13/2}$  shell-model state. The Coriolis interaction among Nilsson states of this shell-model origin is usually so strong that the coupling scheme between particle motion and the deformed field is greatly altered. Although such deviations from the Bohr-Mottelson rotational strong coupling have been observed for a number of unique-parity bands, the 89-neutron systems seem to be the cases where this breakdown of the strong coupling between the single-particle and rotational motions is most prominent.

### The Level Scheme of $^{154}\text{Dy}$

The levels of  $^{154}\text{Dy}$  were studied before,<sup>8</sup> and a level scheme consisting of a ground-state quasi-rotational band up to  $10^+$  and a  $\beta$ -vibrational band was proposed. We do observe, however, additional transitions of the ground state band. The  $\beta$ -vibrational band is less intensely populated in the  $^{146}\text{Nd}(^{12}\text{C}, \text{xn}, \gamma)$  reaction. However, we were able to verify the previously proposed  $4^+$  and  $6^+$  members of this band by observing the transitions depopulating these levels. The observed coincidence relationships and the measured angular distributions are in agreement with proposed level scheme, Fig. 2.

The placement of transitions up to the  $14^+$  level is clear, but there are two extra transitions, 597 and 583 keV, which are in coincidence with lower cascade transitions and clearly belong to the band. In view of the common occurrence of "back-bending" behavior of

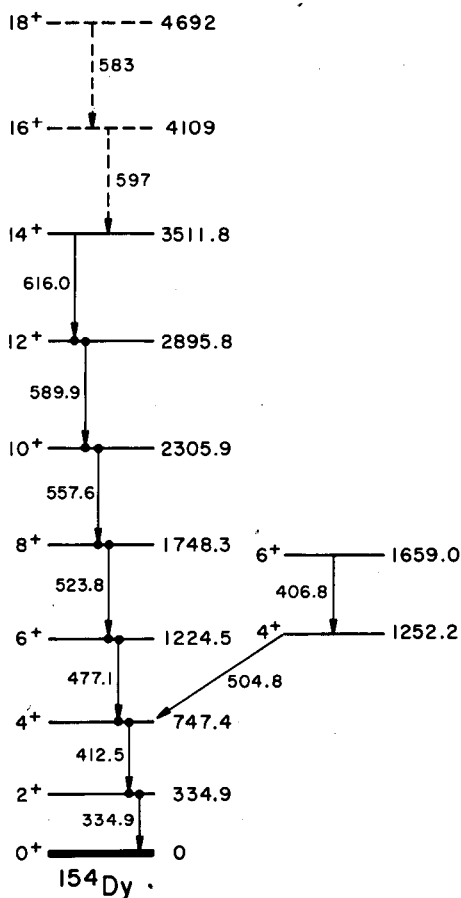


Fig. 2. Proposed level scheme of  $^{154}\text{Dy}$  from this work. Additional beta-band members were identified by Neiman and Ward.<sup>8</sup> The 16<sup>+</sup> and 18<sup>+</sup> levels are shown dashed, since the order of 597 and 583 keV transitions is not certain. (XBL-734-349)

rotational bands in this region, we believe the 597 and 583 keV transitions are just above the 14<sup>+</sup> level, probably in that order since the 597 is more intense in the singles. However, the intensities seem nearly equal in the coincidence spectrum, so the 583 keV transition could, alternatively, be assigned to 16<sup>+</sup> → 14<sup>+</sup>. There may also be a weak 579 keV transition in the coincidence spectrum. Thus, we have in Fig. 2 drawn the levels above 14<sup>+</sup> as dashed lines to indicate their tentative nature.

### Footnotes and References

# Report condensed from Nucl. Phys. A209, 72 (1973).

\* Princeton University, Princeton, NJ.

† Present address: Institut für Strahlen und Kern Physik, Universität Bonn, Bonn, Germany.

‡ On leave at Los Alamos Scientific Laboratory, Los Alamos, NM.

§ At Yale University during initial phase of this work.

|| Heavy Ion Accelerator Laboratory, Yale University, New Haven, CT.

1. I. Rezanka, F. M. Bernthal, J. O. Rasmussen, R. Stokstad, I. Fraser, J. Greenberg and D. A. Bromley, Nucl. Phys. A179, 51 (1972).

2. G. Løvholden, S. A. Hjorth, H. Ryde and L. Harms-Ringdahl, Nucl. Phys. A181, 589 (1972).

3. R. M. Diamond, Proc. of the Int. Conf. on the properties of nuclei far from the region of beta-stability, Leysin (CERN, Geneva, 1970), p. 56.

4. K. Ya. Gromov, F. N. Mukhtasimov and G. Ya. Umarov, Program and abstracts, 16th Conference on Nuclear Spectroscopy, Moscow (1966), p. 41.

5. J. P. Torres, P. Paris, D. Lecouturier and P. Kilcher, Nucl. Phys. A189, 609 (1972).

6. T. Grottdal, K. Nybø and B. Elbek, Mat. Fys. Medd. Dan. Vid. Selsk. 37 (1970) No. 12.

7. J. Borggreen and G. Sletten, Nucl. Phys. A143, 225 (1970).

8. M. Neiman and D. Ward, Nucl. Phys. A115, 529 (1968).

LEVELS IN  $^{165}\text{Tm}$  EXCITED BY DECAY OF 10-MIN  $^{165}\text{Yb}$   
AND BY THE  $^{158}\text{Gd}(^{11}\text{B}, 4n\gamma)$  REACTIONS

T. Tamura,\*† I. Rezanka,\* S. Iwata,+‡  
J. O. Rasmussen,§ and J. Alonso§

We initiated two-fold studies of  $^{165}\text{Tm}$  via radioactivity and heavy-ion in-beam gamma spectroscopy at the Yale Heavy Ion Accelerator Laboratory at a time when the information on this nucleus was limited. Before completion of our

work, the independent in-beam gamma studies of the Grenoble group of J. Gizon et al.<sup>1</sup> were published, nicely establishing four rotational band sequences up to high spin. Our in-beam studies confirm their assignments except for

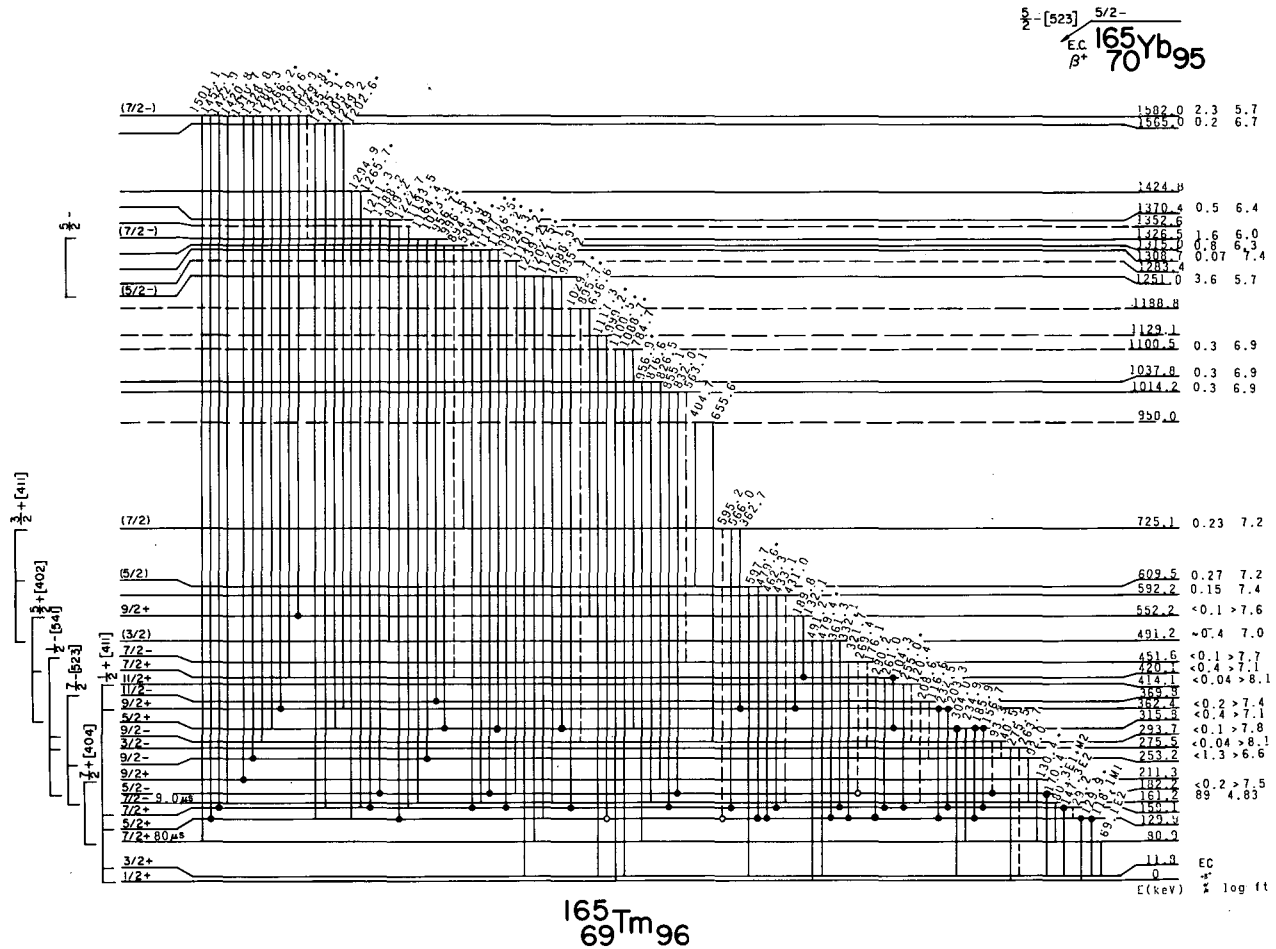


Fig. 1. Proposed radioactive decay scheme of  $^{165}\text{Yb}$ . Only those transitions and levels involved in the radioactive decay are shown. Dashed levels and transitions are placed with less certainty than others. All energies are in keV, and Nilsson quantum number assignments are the usual  $K\pi[Nn_z\Lambda]$ . The level energies are best values derived from experimental transition energies, but the gamma transition energies shown above each line are exact differences of the level energies and not the experimental values. Thus, the transition energies of the decay scheme may not always correspond exactly to the experimental energies of Table 1; the energy differences afford a ready test on consistency of the scheme. Multiply assigned transitions are indicated by asterisks. A solid dot at the upper (lower) end of a transition line means that transition has been measured to be in coincidence with some higher (lower) transition. Open circles indicate less certain coincidence observations.

(XBL-734-2805)

some changes above the  $7/2$  spin in the ground band, and our gamma angular distributions confirm multipolarity assignments. The complex radioactive decay populates many additional levels not observed by the in-beam work, thus providing a nice complementarity.

By repeated bombardments and decay curve counting it was possible to assign nearly a hundred gamma lines to the decay of  $^{165}\text{Yb}$ .

With the large number of gamma rays of  $^{165}\text{Yb}$  it was crucial to have extensive coincidence measurements. With three-dimensional (gamma-gamma-time) event-by-event tape recording of coincidences on the Yale HIA computer and using many source preparations, it was possible to accumulate sufficient events to be statistically significant for all the stronger transitions. Coincidence results can be read from the level scheme diagram (Fig. 1) where solid dots indicate the coincidence relationships.

Building on the framework of lower levels in the scheme of the Grenoble group, it is possible to take the radioactivity data to build up an expanded decay scheme. Insofar as possible we have relied on our coincidence data, but they are seriously limited by the microsecond isomerism of the  $7/2^+$  and  $7/2^-$  bandheads. Hence, energy sum and difference information had to be relied on also. With

the complexity of the decay we would concede that some of the transition placements and perhaps a level or two are accidental and incorrect. Dashed lines in the level scheme indicate uncertain features.

The proposed scheme of levels populated in radioactive decay of  $^{165}\text{Yb}$  is presented in Fig. 1. The gamma energies given in the scheme are exactly the differences of the proposed energy values of levels. These exact differences are frequently not the same as the experimental transition energies from spectral least squares analysis as given in Tables 1 and 2.

To avoid undue confusion, the radioactive decay scheme of Fig. 1 excludes levels seen only by in-beam work and does not show transitions seen in-beam. The complete level scheme is given in Fig. 2, including levels populated by radioactivity and in-beam by either our group or the Grenoble group. The transition lines are indicated only for gammas observed by us in-beam. Levels established by work of the Grenoble group but for which our statistics were insufficient to find the confirming gamma rays are also shown. In no case are these unconfirmed levels inconsistent with our data. We have recalculated all level energies using our own best values where possible and working up to higher levels with best Grenoble group energies.

Table 1. Level Energies in  $^{165}\text{Tm}$ .

Spin	$1/2^+ [411]$ Band		
	$E_{\text{exp}}$ (keV)		$E_{\text{calc}}$ (keV)
	This work	Grenoble	6-parameter power series <sup>c</sup>
1/2	0	0	- 0.17
3/2	11.8	11.9	12.11
5/2	129.9	130.2	129.80
7/2	159.1	159.2	159.54
9/2	362.4	367.0 <sup>b</sup>	362.92
11/2	414.1	414.2	413.62
13/2	689.7	703.4 <sup>b</sup>	689.87
15/2	769.2	769.5	769.70
17/2	1103.7	1128.2 <sup>b</sup>	1104.13
19/2	1216.8	1216.9	1229.40
21/2		1630.1 <sup>b</sup>	1609.58
23/2	1746.1 <sup>a</sup>	1746.2	1809.57
25/2		2184.7 <sup>b</sup>	2230.78
27/2		2333	2553.79
29/2			

(Continued)

Table 1. Continued

<u>7/2<sup>+</sup> [404] Band</u>			
7/2	80.9	81.1	81.09
9/2	211.3	211.3	211.29
11/2	366.9	366.9	366.88
13/2	546.1	546.1	546.28
15/2	747.4	747.2	747.04
17/2	968.4	969.0	968.97
19/2	1207.7	1207.0	1207.07
21/2	1468.5	1467.6	1467.60
23/2	1737.0 <sup>a</sup>	1736.3	<u>1736.29</u>
25/2	2030.3 <sup>a</sup>	2029.4	2038.16
27/2		2335.1	2334.17
29/2		2660	2690.83

<u>7/2<sup>-</sup> [523] Band</u>			
Spin	E <sub>exp</sub> (keV)		E <sub>calc</sub> (keV)
	This work	Grenoble	<u>6-parameter power series<sup>c</sup></u>
7/2	161.2	161.4	159.51
9/2	253.2	253.4	254.49
11/2	369.8	370.2	371.99
13/2	511.8	512.7	513.19
15/2	676.2	676.9	676.61
17/2	867.3	868.0	866.59
19/2	1073.5	1074.5	1073.25
21/2	1310.3	1311.0	1312.01
23/2	1552.5	1552.5	1553.34
25/2	1829.4	1830.2	1829.98
27/2	2099.5	2099.2	<u>2099.03</u>
29/2		2411.4	2365.18
31/2		2698.2	2690.94

(Continued)



Table 1. Continued

<u>1/2<sup>-</sup>[541] Band</u>			
1/2			156.55
3/2	275.0		276.11
5/2	182.2	182.2	180.99
7/2	451.1		450.44
9/2	293.7	293.9	294.30
11/2			690.77
13/2	497.8	498.4	499.37
15/2			986.74
17/2	796.3	796.9	797.06
19/2			1325.78
21/2	1186.0 <sup>a</sup>	1186.6	1185.79
23/2			1692.59
25/2	1661.0 <sup>a</sup>	1661.3	1660.91
27/2			2068.46
29/2	2212.9 <sup>a</sup>	2213.2	<u>2213.98</u>
31/2			2430.43
33/2		2832.5	2831.86

<u>5/2<sup>+</sup> [402] Band</u>			
Spin	<u>E<sub>exp</sub> (keV)</u>		<u>E<sub>calc</sub> (keV)</u>
	This work	Grenoble	6-parameter power series <sup>c</sup>
5/2	315.8		
7/2	420.1		
9/2	552.2		

<u>"Low K Band"</u>			
<u>(3/2<sup>+</sup> [411])</u>			
3/2	491.2		
5/2	609.5		
7/2	725.1		

<sup>a</sup>One or more transition energies from Grenoble work used to calculate level energy.

<sup>b</sup>These energy disagreements are due to our having assigned certain  $\gamma$ -rays differently than did the Grenoble group.

<sup>c</sup>Six-parameter energy expansion least-squares fit up through underlined level.

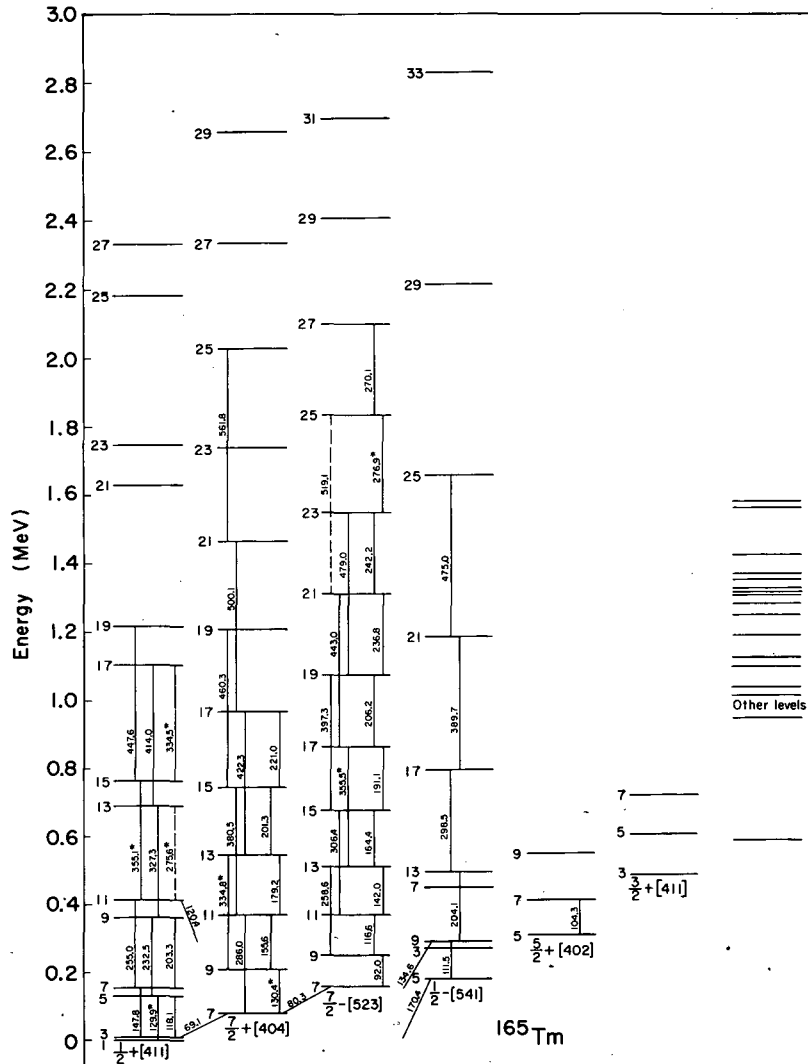


Fig. 2. Complete summary schematic of all levels observed in  $^{165}\text{Tm}$  by radioactivity and in-beam gamma spectroscopy. Spins are labeled by the integer that is twice the spin value. The only transition lines indicated are for transitions observed in our in-beam work. The higher levels seen by the Grenoble group with their spectra of better statistics are also included on the diagram. As in Fig. 1 the energies are differences of adopted level energy values, not experimental energies themselves. Asterisks indicate unresolved doublet assignments. The three slanted-line go between the  $1/2^+$  and  $1/2^-$  bands. There was not space to enter exact level energies, but they may be read from Fig. 1.

(XBL-734-2649)

Table 2. Parameters of the energy formula for bands in  $^{165}\text{Tm}$ .

Parameters	Band			
	1/2 [411]	1/2 [541]	7/2 [523]	7/2 [404]
A (keV)	14.02	10.19	10.20	15.17
B (eV)	-14.69	- 3.94	9.78	-18.19
C (eV $\times 10^{-3}$ )	55	- 3.25	- 35.7	30.04
A <sub>2k</sub>	- 9.98 keV	30.03 keV	603 $\mu\text{eV}$	164 $\mu\text{eV}$
B <sub>2k</sub>	42.3 eV	-127.9 eV	- 3.0 $\mu\text{eV}$	-0.35 $\mu\text{eV}$

The level energies have not been given on Fig. 2 because of space limitations but are summarized by band in Table 1 along with the values determined by the Grenoble group. Energies of levels not associated with bands can be read from Fig. 1 and are not repeated in Table 1.

#### Rotational Energy Parameters

We have applied the usual power series expansion to fit the rotational band energies by least squares, and one of these fits is presented in Table 1 for each band. Table 2 gives the parameter values for the particular fits given in Table 1.

#### Footnotes and References

This report condensed from Phys. Rev. C8, 2425 (1973).

\*Heavy Ion Accelerator Laboratory, Yale University, New Haven, CT.

†Present address: Division of Physics, Tokai Establishment, Japan Atomic Energy Research Institute, Tokai-mura Ibaraki-ken, Japan.

‡Present address: Research Reactor Institute, Kyoto University Kumatori-cho, Sennan-gun, Osaka, Japan.

§Yale Heavy Ion Accelerator Staff members during experimental work.

1. J. Gizon, A. Gizon, S.A. Hjorth, D. Barneoud, S. Andre, and J. Treherne, Nucl. Phys. A456, 654 (1972).

AN ISOMERIC STATE IN  $^{213}\text{Ra}^*$ D. G. Raich,<sup>†</sup> J. O. Rasmussen, and I. Rezanka<sup>‡</sup>

In a series of experiments on the Yale Heavy Ion Accelerator, particularly those involving bombardment of  $^{209}\text{Bi}$  targets with  $^{10}\text{B}$  ions at energies between 70 and 90 MeV, we have observed several  $\gamma$ -rays decaying with a half-life of 2.1 msec and having an excitation function peaked sharply at projectile energies of about 80 MeV. Comparison of our excitation function with those from similar bombardments in the  $\alpha$ -decay studies of Torgerson and Macfarlane<sup>1</sup> suggested that our activity was due to production of  $^{213}\text{Ra}$  [thus via the  $^{209}\text{Bi}(^{10}\text{B}, 6n)$  reaction], and additional experiments confirmed that assignment. Moreover, since we found coincidences between the stronger 2.1 msec  $\gamma$ -rays and Ra  $K_\alpha$  x-rays, and since  $^{213}\text{Ra}$  itself is known to decay with a much longer 2.74-min half-life, we concluded that our bombardments were populating a hitherto unobserved isomeric state in  $^{213}\text{Ra}$ . Table 1 lists the photon activity we believe is associated with de-excitation of  $^{213\text{m}}\text{Ra}$  to the ground state, along with tentative multipolarity assignments, and Fig. 1 illustrates the  $^{213}\text{Ra}$  level scheme we have derived on the basis of these assignments.

Although our level scheme explains our data quite well and is in good agreement with trends seen in the neighboring 125-neutron isotones  $^{207}\text{Pb}$ ,  $^{209}\text{Po}$ ,<sup>2</sup> and  $^{211}\text{Rn}$ ,<sup>1,3,4</sup> it can not yet be considered definitely established. Two significant problems remain to be resolved. First, our assignment of the isomeric state as a pure shell-model  $i_{13/2}$  neutron hole is open to some question. We have not yet fully excluded the possibility that the state involves coupling of a neutron hole to the  $h_{8/2}^+$   $8^+$  proton configuration analogous to the isomeric state in  $^{214}\text{Ra}$ .<sup>5</sup>

Second, evidently  $^{213\text{m}}\text{Ra}$  itself  $\alpha$ -decays to  $^{209}\text{Rn}$  to at least some extent, although we do not yet have good figures for the branching ratios or partial half-lives of the various decay modes. Preliminary calculations<sup>6</sup> suggest that a majority of such  $\alpha$ -decays could well go to an excited rather than ground state of  $^{209}\text{Rn}$ . Thus it is possible that some of the weaker  $\gamma$ -rays we had assigned to  $^{213}\text{Ra}$  (Table 1) actually are due to  $^{209}\text{Rn}$  de-excitations following  $\alpha$ -decay. In fact, closer examination of our original data shows a very weak 2.1-msec

Table 1. Gamma and x-ray activity of  $^{213\text{m}}\text{Ra}$  ( $T_{1/2} = 2.1 \pm 0.1$  msec). The three main  $\gamma$ -rays are observed in nanosecond coincidence with one another and with the Ra  $K_\alpha$  x-rays.

Transition energy (keV)	Relative photon intensity ( $I_{546} = 1.00$ )	Assigned multipolarity	Relative transition intensity ( $I_{546} = 1.00$ )	K-vacancies due to transition
49 (1)	0.006 (2)	E1—M2	0.011 (3)—7 (2)	Below K-edge
160.87 (5)	0.33 (1)	E2	0.76 (2)	0.078 (3)
210.45 (20)	0.022 (2)	M2—E3	0.21 (1)—0.13 (1)	0.130 (9)—0.0078 (5)
546.35 (5)	1.00 (2)	E2	1.00 (2)	0.0208 (4)
1062.5 (2)	0.94 (3)	E2	0.92 (3)	0.0058 (2)
				$\Sigma_{\text{K-vac}} = 0.23 (1) - 0.112 (3)$
85.5 (2) [ $K\alpha_2$ ]	0.037 (3)	}	0.123 (5)	
88.5 (2) [ $K\alpha_1$ ]	0.062 (4)			
99.9 (2) [ $K\beta'_1$ ]	0.019 (2)			
103.4 (2) [ $K\beta'_2$ ]	0.004 (1)			

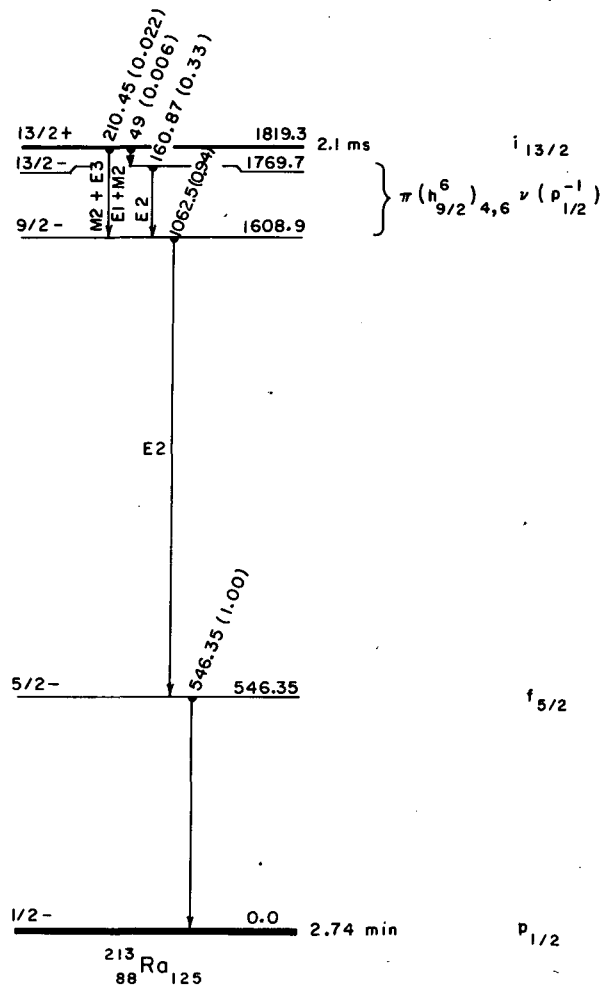


Fig. 1. Tentative level scheme deduced for  $^{213}\text{Ra}$ . Relative photon intensities are shown in parentheses.

(XBL739-4121)

component on a 109-keV line, which probably corresponds to the 109-keV  $^{209}\text{Rn}$  level of Valli and Hyde,<sup>4</sup> and we are concerned about the possibility that our 210.45-keV  $\gamma$ -ray arises likewise from the 214 ( $\pm 5$ ) keV level of  $^{209}\text{Rn}$  following  $\alpha$ -decay.

We are presently attempting to resolve these problems both through more refined  $\alpha$ -decay calculations and through additional experiments directed at refining the data in Table 1 while perhaps also elucidating a more detailed level scheme for  $^{209}\text{Rn}$ .

#### Footnotes and References

\* Final results will be submitted to Nucl. Phys. (1974).

† Yale University graduate student, presently resident at LBL.

‡ Heavy Ion Accelerator Laboratory, Yale University, New Haven, CT.

1. D. F. Torgerson and R. D. Macfarlane, Phys. Rev. C 2, 2309 (1970).

2. L. J. Jardine, S. G. Prussin, and J. M. Hollander, Lawrence Berkeley Laboratory Nuclear Chemistry 1972 Annual Report, LBL-1666, p. 9 (to be submitted to Nucl. Phys.).

3. T. Kempisty, A. Korman, T. Morek, L. K. Peker, Z. Haratym, and S. Chojnacki, Comm. of the Joint Inst. for Nucl. Research, Report P6-6723 (Dubna, 1972).

4. K. Valli and E. K. Hyde, Phys. Rev. 176, 1377 (1968).

5. K. H. Maier, J. R. Leigh, F. Pühlhofer, and R. M. Diamond, J. Phys. (Paris) 32 colloque C6, C6-221 (1974).

6. Based on a simplified variant of the formulation of J. O. Rasmussen, Nucl. Phys. 44, 93 (1963).

## A TEST OF BACKBENDING MODELS USING ODD-A NUCLEI

E. Grosse\*, F. S. Stephens and R. M. Diamond

A process known as "backbending" has recently been discovered<sup>1</sup> to occur at high spins in the ground-state rotational bands of some even-even rare-earth nuclei. The name refers to the fact that a plot of moment of inertia,  $\mathcal{J}$ , versus the square of the rotational frequency,  $(\hbar\omega)^2$ , for the various spin states of these nuclei has an s-shape form. That is,  $\hbar\omega$  becomes temporarily smaller around  $I \approx 16$ , while  $\mathcal{J}$  increases rather sharply with  $I$ . Since  $\hbar\omega$  is very nearly one-half the rotational transition energy, the above shape results from several transition energies around the critical spin value being lower than those for spins just below or above this value. It is by now quite clear that this occurs for many rare-earth nuclei, but it does not occur (at least in the same spin region) for others. The change in  $\mathcal{J}$  is typically from about half the rigid-rotor value to nearly the full value.

A number of explanations for backbending have been given. One of these is known as the Mottelson-Valatin effect.<sup>2</sup> This refers to a coherent collapse of the pairing correlations in the nucleus (probably only for the neutrons) due to the increasing Coriolis force as the system rotates more rapidly. An alternative explanation<sup>3</sup> was proposed shortly after the experiments in which it is suggested that only one

pair of  $i_{13/2}$  neutrons is broken by the Coriolis force. The angular momentum from this pair (up to  $12\hbar$ ) is then aligned with that of the rotating core to produce a band which crosses the ground-state band at the backbend and for larger spin values becomes the yrast band (rotation-alignment model). Other models involving centrifugal shape changes<sup>4</sup> or generalized "moment of inertia" changes<sup>5</sup> have been proposed, but the two types of Coriolis effects mentioned above have thus far received the most serious consideration. It is a challenge at the present time to find ways to distinguish between these models.

A new method is applied here to distinguish between these models. This test involves the properties of a particular type of band in odd-A nuclei. It has been shown<sup>6</sup> that under the proper conditions an odd nucleon in a high-j orbital "decouples". This term refers to the alignment by the Coriolis force of the particle angular momentum,  $j$ , with that of the rotor. The result is a band with spin values,  $j, j+2, j+4, \dots$ , and energy spacings like the levels having spins  $0, 2, 4, \dots$  in the adjacent even-even nuclei. Many odd-A nuclei have been shown to possess such decoupled bands. The decoupling described here is closely related to the rotation-alignment explanation of back-

Table I. Energies, intensities and  $A_2$ -coefficients of the transitions observed in  $^{157}\text{Er}$  and  $^{159}\text{Er}$ .

$I_i \rightarrow I_f$	$^{157}\text{Er}$			$^{159}\text{Er}$		
	$^{150}\text{Sm} + ^{12}\text{C}, 92 \text{ MeV}$			$^{152}\text{Sm} + ^{12}\text{C}, 88 \text{ MeV}$		
	$E_\gamma$ (keV)	$I_\gamma$	$A_2$	$E_\gamma$ (keV)	$I_\gamma$	$A_2$
17/2 $\rightarrow$ 13/2	266.1 $\pm$ 0.3	(100)	0.23 $\pm$ 0.02	208.3 $\pm$ 0.3	(100)	0.37 $\pm$ 0.02
21/2 $\rightarrow$ 17/2	415.1 $\pm$ 0.3	79 $\pm$ 4	0.24 $\pm$ 0.03	350.0 $\pm$ 0.3	83 $\pm$ 4	0.38 $\pm$ 0.03
25/2 $\rightarrow$ 21/2	527.2 $\pm$ 0.3	68 $\pm$ 4	0.35 $\pm$ 0.04	464.5 $\pm$ 0.3	77 $\pm$ 4	0.36 $\pm$ 0.04
29/2 $\rightarrow$ 25/2	622.4 $\pm$ 0.3	47 $\pm$ 3	0.31 $\pm$ 0.05	555.9 $\pm$ 0.3	56 $\pm$ 4	0.38 $\pm$ 0.05
33/2 $\rightarrow$ 29/2	702.2 $\pm$ 0.4	29 $\pm$ 3	0.39 $\pm$ 0.09	625.9 $\pm$ 0.3	49 $\pm$ 3	0.33 $\pm$ 0.08
37/2 $\rightarrow$ 33/2	765.0 $\pm$ 0.5	17 $\pm$ 2	0.34 $\pm$ 0.12	675.7 $\pm$ 0.4	25 $\pm$ 2	0.38 $\pm$ 0.09
41/2 $\rightarrow$ 37/2	802.9 $\pm$ 0.6	7 $\pm$ 1	0.5 $\pm$ 0.3	708.7 $\pm$ 0.5	12 $\pm$ 1	0.24 $\pm$ 0.11
(45/2 $\rightarrow$ 41/2)				(738.4 $\pm$ 0.8	8 $\pm$ 2	0.13 $\pm$ 0.20)

bending in the even-even nuclei; the band which intersects the ground band at the backbend is, in this model, essentially composed of two decoupled  $i_{13/2}$  neutrons. However, the Pauli principle prevents the second neutron from being fully aligned with the rotation axis.

Consideration of the above properties leads to the following proposed test of the backbending models. If one considers the effect on backbending of the presence of a decoupled  $i_{13/2}$  neutron, then opposite behavior is predicted by the two models. An odd neutron, due to blocking effects, will weaken the pairing correlations, so that they should collapse sooner (at lower  $\hbar\omega$  or  $I$ ) with rotation. On the other hand, such a decoupled  $i_{13/2}$  neutron interferes with the formation of the band which intersects the ground band in the rotation-alignment model, resulting in a later (higher  $\hbar\omega$  or  $I$ ) intersection. Provided the decoupled odd-A bands are correctly interpreted, a comparison of their properties in the backbending region with those of the adjacent even-even nuclei should indicate which explanation is correct.

We chose  $^{157}\text{Er}$  and  $^{159}\text{Er}$  as the odd-A nuclei to be studied for this test since the decoupled bands had previously been observed<sup>7</sup> in these nuclei and the backbends in  $^{156}, ^{158}, ^{160}\text{Er}$  were all known.<sup>8,9</sup> These isotopes were produced following  $^{12}\text{C}, 5n$  reactions on  $^{150}, ^{152}\text{Sm}$  at the LBL 88" Cyclotron. Table I contains a summary of the lines assigned to the decoupled bands in  $^{157}, ^{159}\text{Er}$ . In Fig. 1, the plot of  $2J/\hbar^2$  vs.  $(\hbar\omega)^2$  is shown for the ground band of  $^{156}, ^{158}\text{Er}$  and for the decoupled band of  $^{157}\text{Er}$  (beginning at  $I = j = 13/2$ ). The  $^{157}\text{Er}$  band appears to be completely decoupled in the beginning (lies midway between  $^{156}\text{Er}$  and  $^{158}\text{Er}$ ), but clearly does not backbend at the same  $\hbar\omega$  (or  $I$ ) as the adjacent even-even nuclei. The plot for  $^{158}, ^{159}, ^{160}\text{Er}$  is shown in Fig. 2, and is very similar, except that the  $^{159}\text{Er}$  band is not quite completely decoupled at the lowest spins. These plots show that the decoupled bands in both  $^{157}\text{Er}$  and  $^{159}\text{Er}$  backbend only at values of  $\hbar\omega$  (and  $I$ ) higher than the adjacent even-even nuclei, if they backbend at all. This is in accordance with the rotation-alignment model and in apparent contradiction to the expectations of the pairing-collapse model. A more complete report of this work has been published.<sup>10</sup>

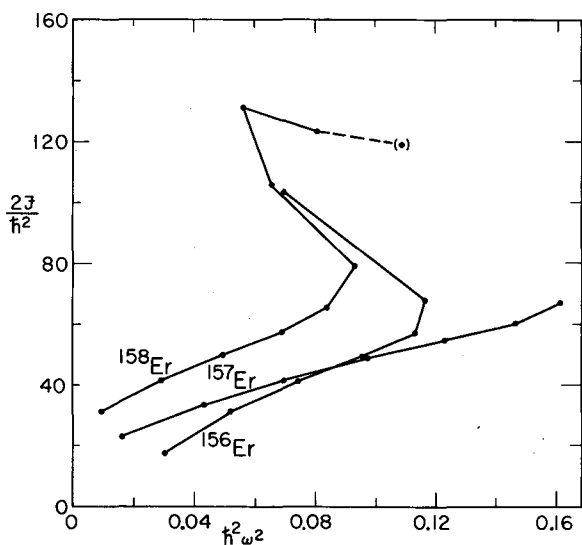


Fig. 1. Plot of  $2J/\hbar^2$  vs.  $(\hbar\omega)^2$  for  $^{156}, ^{157}, ^{158}\text{Er}$ . For the even-even nuclei,  $I' = I$ , and for the odd-A nuclei,  $I' = I - j$ .

(XBL736-3165)

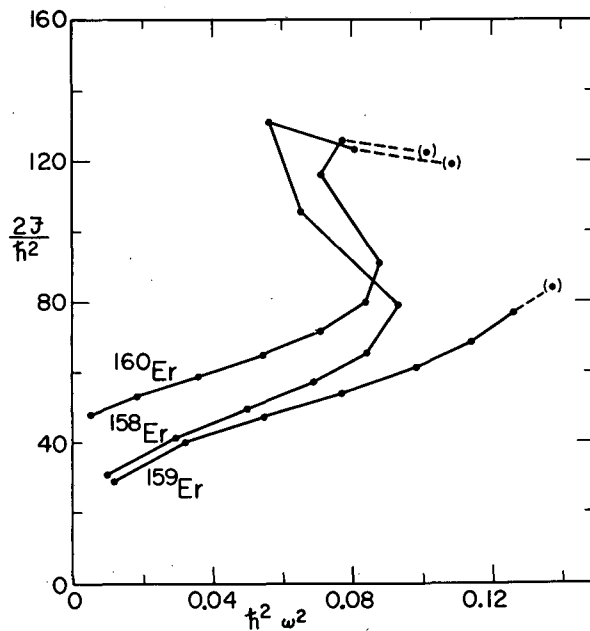


Fig. 2. Plot of  $2J/\hbar^2$  vs.  $(\hbar\omega)^2$  for  $^{158}, ^{159}, ^{160}\text{Er}$ .

(XBL736-3166)

### Footnote and References

\* On leave from MPI für Kernphysik, Heidelberg, Germany, under support from DAAD.

1. A. Johnson, H. Ryde and J. Sztarkier, Phys. Letters 34B, 605 (1971).
2. B. R. Mottelson and J. G. Valatin, Phys. Rev. Letters 5, 511 (1960).
3. F. S. Stephens and R. Simon, Nucl. Phys. A183, 257 (1972).
4. P. Thieberger, Preprint (1972).
5. C. K. Ross and Y. Nogami, Preprint (1973).
6. F. S. Stephens, R. M. Diamond, J. R. Leigh, T. Kammuri, and K. Nakai, Phys. Rev. Letters 29, 438 (1972).
7. F. S. Stephens, Proceedings of the Intern. Conf. on Properties of Nuclear States, Montreal (1969), p. 141; J. R. Leigh, R. M. Diamond, K. H. Maier, R. Nordhagen, and F. S. Stephens, UCRL-20426, p. 18.
8. H. Ryde, S. A. Hjorth, D. Barnéoud, A. Johnson, G. B. Hagemann, and B. Herskind, Nucl. Phys. A207, 513 (1973).
9. R. M. Lieder, H. Beuscher, W. F. Davidson, P. Jahn, H. J. Probst and C. Mayer-Böricke, Phys. Letters 39B, 196 (1972).
10. E. Grosse, F. S. Stephens, and R. M. Diamond, Phys. Rev. Letters 31, 840 (1973).

### BACKBENDING IN ODD-A Ho ISOTOPES

E. Grosse\*, F. S. Stephens, and R. M. Diamond

Since the discovery<sup>1</sup> of "backbending" in the ground-state rotational bands of  $^{160}\text{Dy}$  and  $^{162}\text{Er}$ , this effect has been extensively studied in many even-even nuclei.<sup>2</sup> The sudden decrease of the rotational frequency (transition energy) with increasing spin and moment of inertia has been found to occur in many deformed nuclei of the rare-earth region at spins of about 12 or 14  $\hbar$ . It has also been observed in other regions of the nuclide chart, though one cannot always be sure that the same process is involved. On the other hand, it does not seem to occur in some other strongly deformed rare-earth nuclei, especially in neutron-richer isotopes. Data are presented here which show for the first time that backbending can also occur in rotational bands of odd-A nuclei. The occurrence of backbending in certain bands of odd-A nuclei can give rather detailed information about the causes of backbending in the neighboring even-even nuclei.

We used the  $(^{11}\text{B}, 4n)$  reaction on  $^{150}\text{Sm}$ ,  $^{152}\text{Sm}$ , and  $^{154}\text{Sm}$  to study the  $\gamma$ -decay of high angular momentum states in  $^{157}\text{Ho}$ ,  $^{159}\text{Ho}$ , and  $^{161}\text{Ho}$ . This work was done at the LBL 88 inch Cyclotron. A typical spectrum is shown in Fig. 1. The strongest lines observed are transitions in the ground-state rotational band of  $^{157}\text{Ho}$ , which is based on the  $7/2$  [523] member of the  $h_{11/2}$  orbit. The Coriolis inter-

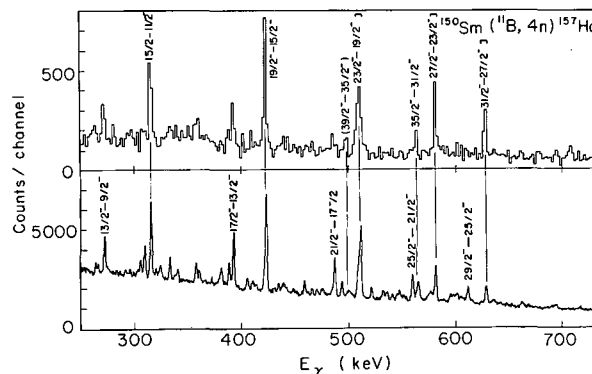


Fig. 1. Partial gamma-ray spectra following the  $^{150}\text{Sm}(^{11}\text{B}, 4n)^{157}\text{Ho}$  reaction. The lower spectrum is the sum of all coincidences recorded by one detector in a multi-dimensional coincidence measurement. The upper spectrum comes from the same data with gates set in the other detector on the three transitions with brackets above them. (XBL7310-4151)

action mixes this band with the other  $h_{11/2}$  bands, compressing the band and lowering the energy of the  $j + R'$  (where  $R'$  is even) levels relative to the others. This causes an oscillation in the level energies, so that in order to see the relative moment-of-inertia changes only every other level should be considered.



Thus, the band divides into two groups of levels, the favored ones ( $I = j + R'$ ) and the unfavored ones ( $I = j + R' - 1$ ). It has been shown previously that in the limit of large Coriolis interaction (e. g., at high angular momentum) the favored levels form a band which has the particle decoupled from the symmetry axis of the core and aligned along the rotation axis.<sup>3</sup> Although we believe the unfavored levels behave similarly, this letter is focussed on the behavior of the favored levels because they could be traced to higher angular momentum and because, as members of the developing decoupled band, they are somewhat simpler to understand.

Data on the favored levels in the three nuclei are compiled in Table I, and the backbending of these levels in the three nuclei can be seen in Fig. 2 which shows the dependence

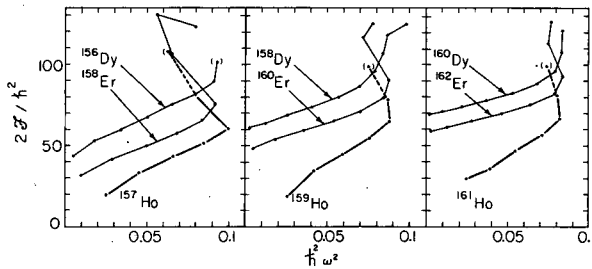


Fig. 2. A comparison of backbending in  $^{157}$ ,  $^{159}$ ,  $^{161}\text{Ho}$  with their even-even neighbors. The even-even curves are the usual ones of this type, and the odd-A bands are treated as described in the text. (XBL7310-4146)

of the moment of inertia on the rotational frequency. The moments of inertia were calculated from the formula:

$$\frac{2 \mathcal{F}(I, \omega)}{\hbar^2} = \frac{4R' + 6}{\Delta E}, \quad (1)$$

where  $R' = I - j$ ,  $\Delta E = E_{I+2} - E_I$ , and  $\hbar\omega = \Delta E/2$ . Equation (1) is valid only when the extra particle is completely decoupled.<sup>3</sup> Since this is not the case here, these  $\mathcal{F}(I, \omega)$  values for the odd nuclei do not represent moments of inertia of the core, but only lower limits, and they should be raised by increasing amounts as one goes to lower  $I$  values. However, it can be seen that this cannot change the conclusion that the band backbends. That property is determined only by the  $\hbar\omega$  values and follows immediately from the lower transition energies at higher spin values. The neighboring even-even nuclei<sup>2, 4</sup> are also shown in Fig. 2, and lie above the odd-A nuclei for the reasons just discussed; nevertheless, the similarity in the backbending of the odd-A and even-even nuclei is apparent.

This conclusion is in contrast to the situation recently found in the odd Er isotopes,<sup>5</sup> where no backbending was observed, even though the data extended well beyond the region (of spin or  $\hbar\omega$ ) where the even-even nuclei backbend. It seems likely that this difference in behavior can be related to the underlying cause of backbending. Since the occupation of the  $h_{11/2}$  orbital by the odd particle does not significantly change the backbending properties, it seems that this orbital cannot be closely involved in the mechanism (or cause) of the

Table I. Energies, intensities, and  $A_2$  coefficients for the favored levels of the ground-state band in  $^{157}\text{Ho}$ ,  $^{159}\text{Ho}$ , and  $^{161}\text{Ho}$ . The energies and the  $A_2$  coefficients are given for the crossover transitions, whereas the intensities are the sum of crossover and cascade transitions depopulating the level.

I	$^{157}\text{Ho}$ $^{150}\text{Sm} + ^{11}\text{B}, 58 \text{ MeV}$			$^{159}\text{Ho}$ $^{152}\text{Sm} + ^{11}\text{B}, 58 \text{ MeV}$			$^{161}\text{Ho}$ $^{154}\text{Sm} + ^{11}\text{B}, 51 \text{ MeV}$		
	$E_I - E_{I-2}$ (keV)	Int.	$A_2$	$E_I - E_{I-2}$ (keV)	Int.	$A_2$	$E_I - E_{I-2}$ (keV)	Int.	$A_2$
$15/2^-$	315.9±0.3	(100±16)	0.25±0.09	317.8±0.3	(100±15)	0.20±0.09	312.2±0.3	(100±15)	0.21±0.08
$19/2^-$	424.3±0.3	70±4	0.24±0.07	408.4±0.3	69±4	0.20±0.07	397.0±0.3	85±5	0.26±0.06
$23/2^-$	513.0±0.3	49±7	0.19±0.09	486.4±0.3	47±3	0.20±0.08	472.4±0.3	69±4	0.25±0.06
$27/2^-$	583.2±0.3	21±2	0.23±0.08	550.7±0.3	31±3	0.24±0.08	534.5±0.3	48±3	0.24±0.06
$31/2^-$	630.9±0.5	13±2	0.24±0.08	592.5±0.4	17±2	0.18±0.09	573.3±0.6	24±2	0.26±0.07
$35/2^-$	565.9±0.9	8±2	0.15±0.10	587.1±0.6	11±2	0.15±0.09	568.9±0.8	11±2	0.21±0.13
$(39/2^-)$	(500.1±0.9)	2±1	0.23±0.18	(547.3±1.0)	5±2	0.30±0.20	(544.8±1.0)	6±3	0.20±0.20

backbending behavior. On the other hand, the fact that occupation of the  $i_{13/2}$  orbital in the odd Er nuclei does affect the backbending properties, specifies this orbital as (the) one that is closely involved. The direction in which backbending is affected (enhanced or diminished, hastened or delayed) in the Er nuclei has given information for comparison with specific models.<sup>5</sup> The point we want to emphasize here, however, is that the odd particle can, in general, serve as a probe to tell if a particular orbital is or is not closely related to the cause of the backbending. A more complete report of this work has been published.<sup>6</sup>

### References

\* Present address: Max Plank Institut für Kernphysik, D69 Heidelberg, Germany.

1. A. Johnson, H. Ryde, and J. Sztarkier, Phys. Letters 34B, 605 (1971).
2. A. Johnson and Z. Szymanski, Phys. Rev. 7C, 181 (1973).
3. F. S. Stephens, R. M. Diamond, and S. G. Nilsson, Phys. Letters 44B, 429 (1973).
4.  $\phi$ . Saethre, S. A. Hjorth, A. Johnson, S. Jagere, H. Ryde, and Z. Szymanski, Nucl. Phys. A207, 486 (1973).
5. E. Grosse, F. S. Stephens, and R. M. Diamond, Phys. Rev. Letters 31, 840 (1973). (previous article).
6. E. Grosse, F. S. Stephens, and R. M. Diamond, Phys. Rev. Letters 32, 74 (1974).

## ROTATIONAL BANDS IN THE LIGHT ODD-MASS THALLIUM NUCLEI\*

J. O. Newton, F. S. Stephens, and R. M. Diamond

In the light odd-mass thallium nuclei, Diamond and Stephens<sup>1</sup> identified low-lying  $9/2^-$  isomeric states having excitation energies varying systematically with mass number. The interpretation of these states was a puzzle for some years, since the only low-lying state of high spin predicted by the simple spherical shell model is the  $11/2^-$  hole state arising from the  $h_{11/2}$  orbit. More recently Newton et al.<sup>2</sup> reported an in-beam study of  $^{199}\text{Tl}$  using the  $^{197}\text{Au}(\alpha, 2n\gamma)^{199}\text{Tl}$  reaction, and also included a preliminary report of some of the present work. They found the systematic occurrence of  $11/2^-$ ,  $13/2^-$  and  $15/2^-$  states above the  $9/2^-$  isomers. The proposed interpretation was that these states formed a rotational band based on the  $K = 9/2^- [505]$  state arising from the  $h_{9/2}$  orbital. Reasons were given why the thallium nuclei might be expected to have oblate deformation in this band, as required by this interpretation, and why the  $K = 9/2^-$  state should be low-lying. More recently, evidence has accumulated that rotational bands, based on states arising from high spin orbitals, are more commonly seen in supposedly spherical nuclei than previously thought.<sup>3</sup>

In the present report, we give level schemes for the nuclei  $^{191-197}\text{Tl}$ , (Figs. 1-4). A variety of heavy-ion, xn reactions was used to form the thallium isotopes, and the decay of the excited states was studied mainly through the  $\gamma$ -ray transitions, but also by means of the conversion electrons. Level schemes were deduced from coincidence relationships, energy

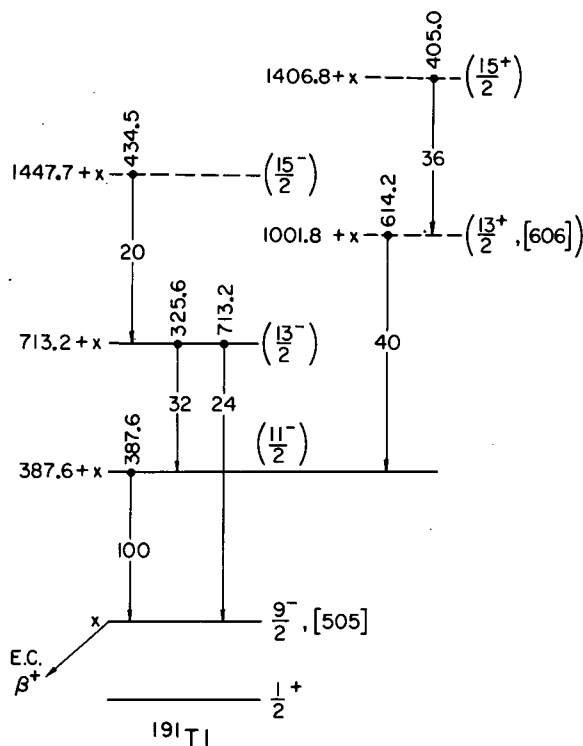


Fig. 1. Level scheme of  $^{191}\text{Tl}$ . Gamma-ray intensities ( $90^\circ$ ) and most probable assignments are shown. The levels indicated by broken lines were assigned only on the basis of intensities, systematics and theoretical considerations. (XBL741-2007)



E2/M1 amplitude mixing ratio  $\delta$  is negative in all cases. Nakai<sup>6</sup> has pointed out that the sign of  $\delta$  supports the hypothesis of oblate deformation in this band. Recently Stephens, et al.<sup>7</sup> have carried out computer calculations in which they have diagonalized the matrix of the Coriolis interaction operating on all the states arising from the  $h_9/2$  orbit. These calculations show more quantitatively that the above proposed explanation for this band in the odd-mass thallium nuclei appears to be correct. These are probably the best-developed rotational bands known to occur in nuclei with oblate deformation.

In addition, an analogous oblate band derived from the  $13/2^+$  [606] Nilsson state has most likely been identified in <sup>191,193,195</sup>Tl. This type of behavior could be expected to occur as a general feature just below closed shells if the potential energy as a function of deformation for the even-even core nucleus is sufficiently flat in the region of zero deformation. Whether this happens in other regions is at present an open and interesting question.

#### Acknowledgments

We would like to thank Dr. S. D. Cirilov for help with many aspects of this work, and also the operating crew of the HILAC for furnishing so patiently the variety of heavy-ion

beams of different energies required.

#### References

\* Condensed from LBL-2333.

1. R. M. Diamond and F. S. Stephens, Nucl. Phys. 45 (1963) 632.
2. J. O. Newton, S. D. Cirilov, F. S. Stephens and R. M. Diamond, Nucl. Phys. A 148 (1970) 593.
3. F. S. Stephens, Proceedings of the International Conference on Nuclear Physics, Munich, Vol. II, edited by J. de Boer and H. J. Mang, North-Holland, American Elsevier (1973).
4. K. Kumar and M. Baranger, Nucl. Phys. A 110 (1968) 529.
5. J. E. Blomqvist, Nuclear Theory Group Progress Report, State Univ. of New York at Stony Brook, p. 29, April (1969), and private communication, June, 1969.
6. K. Nakai, Phys. Letters 34 B (1971) 269.
7. F. S. Stephens, R. M. Diamond, D. Benson, and M. R. Maier, Phys. Rev. C 7 (1973) 2163.

### COULOMB EXCITATION OF <sup>238</sup>U WITH Kr IONS

E. Grosse,\* F. S. Stephens, B. Povh,<sup>†</sup> P. Kienle,<sup>‡</sup> and R. M. Diamond

Multiple Coulomb excitation using heavy ions has been shown to be an excellent method to investigate collective nuclear properties, especially the ground-state rotational band of deformed nuclei. The use of beams of medium and heavy nuclei make possible the excitation of high-spin levels, where deviations from simple rotational models have been found. These include "backbending" of the moment of inertia with increasing rotational frequency and variations of the quadrupole moment with spin. That is, Coulomb excitation not only allows one to observe high spins, but also gives information about the electromagnetic transition probabilities.

We used Kr-beams delivered by the Super HILAC to study the excitation of <sup>238</sup>U. De-excitation  $\gamma$ -rays were observed in Ge-detectors; singles spectra as well as those in coincidence with backscattered particles were taken, and examples are shown in Fig. 1.

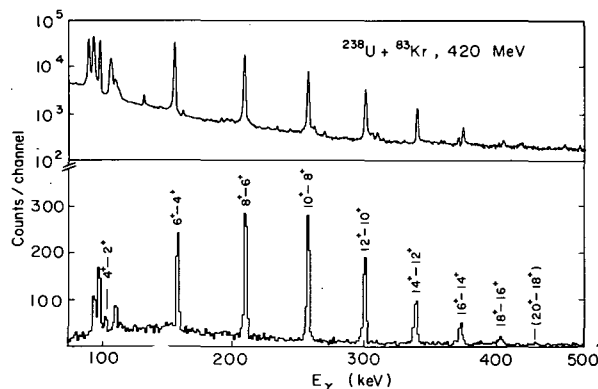


Fig. 1. Singles spectrum (above) and coincidences with backscattered <sup>83</sup>Kr particles (below) for 420 MeV <sup>83</sup>Kr on <sup>238</sup>U.

(XBL7310-4150)

With Kr projectiles of 420 MeV the ground-state rotational band of  $^{238}\text{U}$  could be observed up to spin  $18^+$  (tentatively  $20^+$ ). The deduced moments of inertia are plotted as a function of the square of the rotational frequency in Fig. 2. Up to spin 12 this dependence is quite linear; at higher spins an additional increase of the moment of inertia is observed, amounting to about 5% at spin 20. No real indication is yet seen of backbending effects, such as observed in many rare-earth nuclei at lower spin values.

The excitation probabilities were compared to calculations made in the semiclassical approximation using the de Boer-Winther computer code<sup>1</sup> and published E2-moments.<sup>2</sup> As calculations showed, the inclusion of E4-moments increases the excitation probabilities of the highest spin states by as much as 20%, whereas they are decreased by 5-10% when account is taken of dipole polarization effects and by roughly another 5-10% when excitation

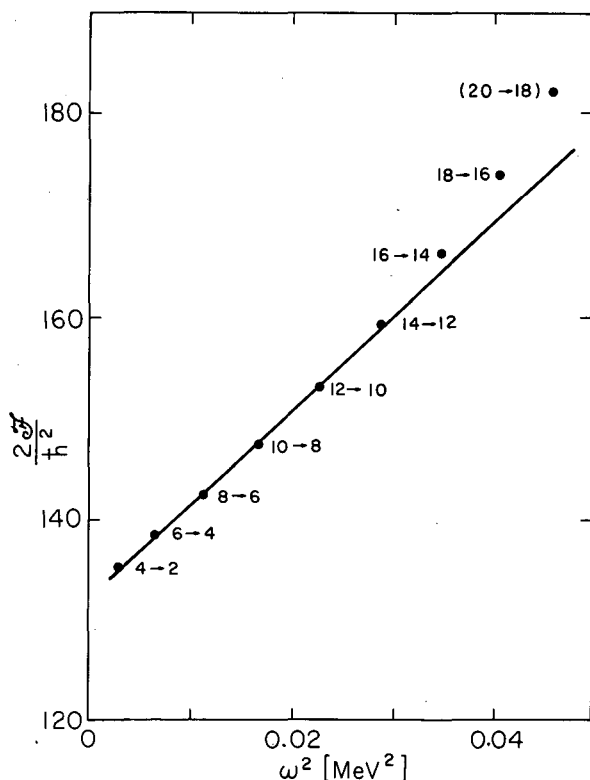


Fig. 2. The quantity,  $2I/\hbar^2$ , where  $I$  is the moment of inertia, vs  $(\hbar\omega)^2$ , with  $\hbar\omega$  equal to one-half the transition energy, is shown for the ground-state band of  $^{238}\text{U}$ . (XBL 736-3178)

of other collective bands is included. It has also been shown<sup>3</sup> that a proper quantal treatment further reduces the cross section for two-step excitations, but no calculations exist for higher than four-step excitation. We are left with the qualitative expectation that for the highest multiple excitations, quantal corrections could be as large as (or even larger than) 25%. Since so many of the corrections are uncertain, and the two largest (for E4 moments and for quantal effects) are of opposite sign in this case, we decided to compare the experimental yields with calculations using only the ground-state E2 matrix elements. This choice seems to us to be the best we can make at the present time.

In an experiment using an Ar beam we found that up to a laboratory energy of 185 MeV, corresponding to a distance of closest approach of  $1.16(A_1^{1/3} + A_2^{1/3}) + 4.0$  fermis, the calculated cross sections were in essential agreement with experiment. (The experimental errors being 10-20% for the  $12^+$  and  $14^+$  states.) A run using  $^{84}\text{Kr}$  of 385 MeV, 10 MeV lower than the energy corresponding to the distance between nuclei given above, yielded good agreement with the calculations up to spin 12, whereas the  $14^+$  and  $16^+$  states were excited too weakly by about 20%. This deviation is not far outside our present limits of error, determined mainly by uncertainties in the beam energy, and cannot be considered significant in view of the magnitudes of the corrections ignored as mentioned in the previous paragraph. Our results do show that large changes ( $\pm 50\%$ ) in the ground-band  $B(E2)$  values do not occur in  $^{238}\text{U}$  up to the  $16^+$  state, and they point up the urgent need for better Coulomb-excitation calculations.

#### Footnotes and References

\* On leave from MPI Kernphysik, Heidelberg; supported by DAAD.

† On leave from Universität Heidelberg.

‡ On leave from Technische Universität München.

1. A. Winther and J. de Boer, in *Coulomb Excitation*, edited by K. Alder and A. Winther (Academic Press, New York, 1966) p. 303.

2. F. K. McGowan, C. E. Bemis, Jr., J. L. C. Ford, Jr., W. T. Milner, R. L. Robinson, and P. H. Stelson, *Phys. Rev. Letters* **27**, 1741 (1971).

3. K. Alder, R. Morf, and F. Roesel, *Phys. Letters* **32B**, 645 (1970).

## PROLATE SHAPE IN LIGHT CERIUM AND NEODYMIUM NUCLEI

J. Gizon,\* A. Gizon,<sup>†</sup> M. R. Maier,<sup>‡</sup> E. Grosse,<sup>§</sup>  
R. M. Diamond, and F. S. Stephens

High spin levels in  $^{133,135}\text{Ce}$  and  $^{135,137}\text{Nd}$  have been populated by means of ( $^{16}\text{O}, 3n$ ) and ( $^{16}\text{O}, 5n$ ) reactions on  $^{120,122}\text{Sn}$  and  $^{122,124}\text{Te}$  targets at the Berkeley 88-inch cyclotron. The level structure of these odd-neutron nuclei has been studied by in-beam  $\gamma$ -ray spectroscopic techniques (excitation functions, prompt and delayed  $\gamma$ -ray spectra,  $\gamma$ -ray angular distributions and  $\gamma$ - $\gamma$  coincidences). Bands built on the  $11/2^-$  isomeric state in  $^{135}\text{Ce}$  and  $^{137}\text{Nd}$  and on the  $9/2^-$  ground state in  $^{133}\text{Ce}$  and  $^{135}\text{Nd}$  are found as shown in Figs. 1 and 2. These are not like the decoupled bands found in the odd-mass lanthanum nuclei<sup>1</sup> but are more like rotational bands heavily perturbed by the Coriolis interaction. The ratio of the transition energy  $E_{15/2^-} - E_{11/2^-}$  to that of the mean value of the  $2^+ \rightarrow 0^+$  transitions of the neighboring doubly even nuclei is of the order of 1.5 rather than 1. The level spacings become more rotational as the mass number decreases, but for a given number of neutrons (75 or 77) we find a very similar band structure.

The M1 + E2  $\gamma$ -transitions in these bands have very sharp angular distributions peaked at  $90^\circ$ , giving large negative values for the  $A_2$  coefficients ( $\sim -1.0$ ). In order to get such large negative  $A_2$  values, the sign of the mixing ratio,  $\delta$ , must be negative. Alder et al.<sup>2</sup> have shown that the sign of  $\delta$  equals the sign of  $g-g_R/Q_0$ , and Nakai<sup>3</sup> has pointed out that for  $I \geq 7/2$ ,  $(g-g_R) < 0$  for odd-neutron nuclei and  $(g-g_R) > 0$  for odd-proton nuclei. Using these relations we deduce that  $^{133,135}\text{Ce}$  and

$^{135,137}\text{Nd}$  are prolate.

The  $17/2^-$  levels in  $^{135}\text{Ce}$  and  $^{137}\text{Nd}$  appear to be fed principally from states at 2126 and 2122 keV, respectively, that are in the same energy range as a  $5^-$  state in neighboring, but heavier, even-even nuclei. The structure of these  $5^-$  states is unknown. For such a prolate shape it is possible to reproduce the order of the levels in the main band by calculations using a particle-plus-rotor model, as has been done previously in the  $A = 200$  and  $A = 130$  region of the periodic table.<sup>4</sup> The difference between the present schemes and those of the La nuclei is that the  $h_{11/2}$  shell is nearly full for these neutron states, but nearly empty in the proton case. One can also understand the existence of the  $9/2^-$  level in  $^{133}\text{Ce}$  and  $^{135}\text{Nd}$ , as the lowest level for the Fermi surface has dropped to the  $\Omega = 9/2^-$  orbit at this deformation. However, quantitative calculations of the level spacings in this model are not very good, due probably to asymmetric shape effects ( $\gamma$  distortion or softness). The very low-lying second  $2^+$  states in the doubly-even nuclei in this region indicate that such an effect must be large and the deviations of the experimental level spacings from those of the axially-symmetric particle-plus-rotor model are in the direction that could be explained by such distortion or softness. Thus the level schemes of these nuclei, though quite different from those of the La nuclei, are consistent with both the model and with a prolate (triaxial) shape.

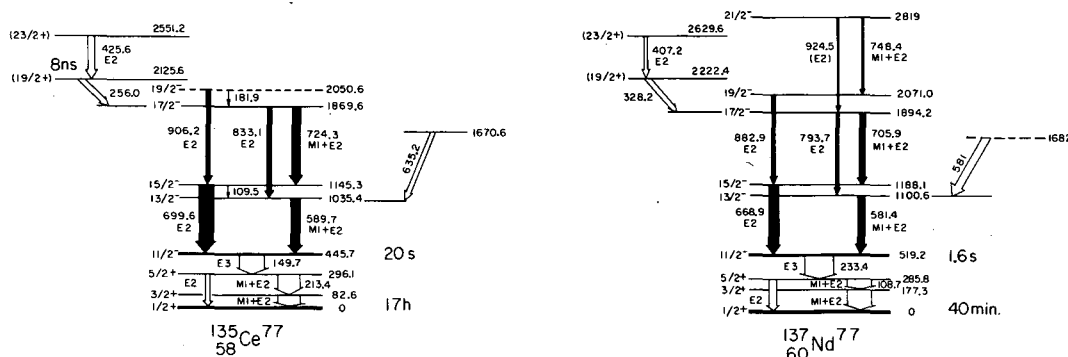


Fig. 1. Level schemes of  $^{137}\text{Nd}$  and  $^{135}\text{Ce}$ . The widths of the arrows are proportional to the intensities of the transitions. The transitions within the  $11/2^-$  band are solid.

(XBL 736-3107)

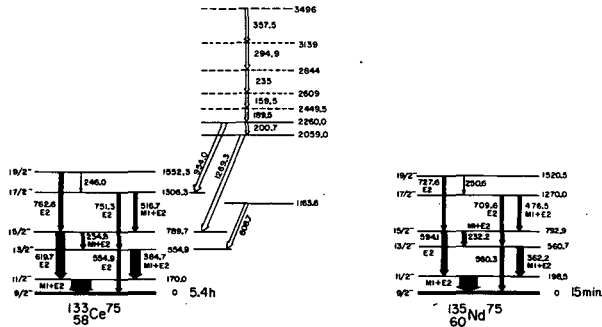


Fig. 2. Level schemes of  $^{135}\text{Nd}$  and  $^{133}\text{Ce}$ . The widths of the arrows are proportional to the intensities of the transitions. The transitions of the  $9/2^-$  bands are solid.

(XBL736-3108)

#### Footnotes and References

\* Nato fellow.

† On leave from Institut des Sciences Nucléaires,

Grenoble, France.

‡ On leave from Physik Department der TU Munchen, Garching, Germany.

§ On leave from Max-Planck-Institut fur Kernphysik, Heidelberg, Germany.

1. F. S. Stephens, R. M. Diamond, J. R. Leigh, T. Kammuri, and K. Nakai, *Phys. Rev. Letters* **29**, 438 (1972); J. R. Leigh, K. Nakai, K. H. Maier, F. Puhlhofer, R. M. Diamond, and F. S. Stephens, *Nucl. Phys. A* **213**, 1 (1973).

2. K. Alder, A. Bohr, T. Huus, B. Mottelson, and A. Winther, *Rev. Mod. Phys.* **28**, 432 (1956).

3. K. Nakai, *Phys. Letters* **34B**, 269 (1971).

4. F. S. Stephens, R. M. Diamond, D. Benson, Jr., and M. R. Maier, *Phys. Rev. C* **7**, 2163 (1973).

### SHAPE COEXISTENCE AND ITS CAUSE IN $^{151}\text{Gd}$

P. Kleinheinz, R. K. Sheline, M. R. Maier,\*  
R. M. Diamond, and F. S. Stephens

In order to obtain information about the moment of inertia of a nucleus from energy level spacings, the structure of the levels must be clear and reasonably simple. It has been pointed out that under certain conditions a system consisting of a single particle (or hole) with pure  $j$  coupled to an axially symmetric rotor gives rise to a particularly simple spectrum.<sup>1-3</sup> Specifically, for prolate deformations of intermediate size, a single-particle-plus-rotor system develops a band with spin sequence  $j, j+2, j+4, \dots$ , and energy spacings equal to those in the ground-state band of the even-even core; whereas, a single hole coupled to such a rotor gives rise to a normal rotational band built on the state with  $I=j$ , having members with  $\Delta I=1$  and energy spacings approaching  $I(I+1)$  at moderately large deformations. An odd- $A$  nucleus with the Fermi surface below (or above) the entire group of Nilsson orbitals that originate in a high- $j$  unique parity spherical state very nearly constitutes such a particle- (or hole-) plus-rotor system, and thus the energy spacings of the lowest-lying band associated with the particular high- $j$  shell can

provide rather unambiguous information on the moment of inertia of that odd- $A$  nucleus. In  $^{151}\text{Gd}$ , which has five neutrons beyond the  $N=82$  closed shell, the Fermi surface lies well outside both the  $i_{13/2}$  and  $h_{11/2}$  unique parity shells, which makes the interpretation of the bands associated with these excitations particularly unambiguous. From a study of these bands we determined the moments of inertia of  $^{151}\text{Gd}$  in these two configurations, and the results suggest a marked difference in deformation between the two bands.

The experiments consisted of in-beam  $\gamma$ -ray measurements following the  $^{150}\text{Sm}(\alpha, 3n)$  reaction at the LBL 88-inch cyclotron. Coincidence and angular distribution data identified a strongly populated cascade of stretched E2 transitions based on a level at 851 keV, establishing a band with states having  $\Delta I=2$ . A second, weakly populated band based on a level at 1210 keV was also identified. This latter band has very recently been seen in an independent  $(\alpha, xn\gamma)$  experiment.<sup>4</sup> Observation of crossover as well as cascade transitions clearly

establishes the  $\Delta I = 1$  sequence for these band members, and their approximate  $I(I+1)$  energy spacings suggest a normal rotational character. The remaining de-excitation intensity proceeds through a series of negative parity levels probably associated with the  $f_{7/2}$  and  $h_{9/2}$  shells. A partial level scheme for  $^{151}\text{Gd}$  showing the bands and their prominent modes of decay is given in Fig. 1. The ground-state spin of  $^{151}\text{Gd}$  has recently been measured<sup>5</sup> to be  $7/2$ , and the band-head spins assigned in Fig. 1 are in accord with the  $\gamma$ -ray data. They are independently supported by the results from an earlier  $^{152}\text{Gd}(d,t)^{151}\text{Gd}$  experiment.<sup>6</sup>

The band based on the level at 851 keV is analogous to similar decoupled bands recently identified in the odd-A lanthanum nuclei,<sup>7</sup> in that the level spacings very closely resemble those of the neighboring even isotopes. Using the very general empirical relationship between the  $2^+$  energies and the E2 transition lifetimes, which essentially all even-even nuclei follow, we can estimate<sup>1</sup> the deformation  $\beta$  as:

$$\beta \approx \sqrt{\frac{1225}{A^{7/3} \cdot 6(\hbar^2/2\mathcal{J})}}, \quad (1)$$

where  $\hbar^2/2\mathcal{J}$  is in MeV. For the  $13/2^+$  decoupled band in  $^{151}\text{Gd}$  we have

$$E_{17/2 \rightarrow 13/2} = 6(\hbar^2/2\mathcal{J}) = 0.493 \text{ MeV},$$

which gives  $\beta_{13/2} = +0.14$ .

The negative-parity band based on the 1210 keV  $11/2^-$  hole state is analogous to similar

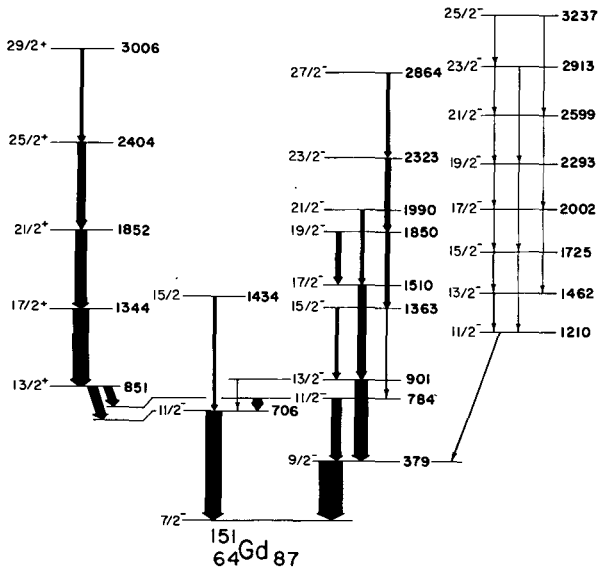


Fig. 1. The level scheme of  $^{151}\text{Gd}$ .  
(XBL738-3668)

bands observed in several odd-N rare-earth nuclei around  $N=91$ . The level energies for this band, based on a single hole in the high- $j$  shell, are predicted to approach  $\hbar^2/2\mathcal{J}$  times  $I(I+1)$ , as mentioned above. The absence in the observed energies of an oscillating term suggests that the  $11/2^-$  band in  $^{151}\text{Gd}$  is rather close to that limit. From the first level spacing

$$E_{13/2 \rightarrow 11/2} = 13(\hbar^2/2\mathcal{J}) = 0.252 \text{ MeV}$$

we calculate, with Eq. (1),  $\beta_{11/2} = +0.29$ . This value would be lowered by 5-10% if the Coriolis mixing were taken into account.

The occurrence of the two different deformations derived from the  $11/2^-$  and  $13/2^+$  bands is a very unusual result. Our conclusions so far are based on the moment-of-inertia parameters extracted from rotational energy spacings, which we expect to be especially reliable in these particular bands as discussed above. Independent support for these deformations comes from the single-neutron pickup cross sections<sup>6</sup> for the two band heads, and from energy systematics in this region, and has been given in a more complete report of this work.<sup>9</sup>

The very different deformations in  $^{151}\text{Gd}$  resulting from a single neutron in the  $i_{13/2}$  shell or a single hole in the  $h_{11/2}$  shell may be qualitatively understood in terms of the Nilsson diagram. Figure 2 shows the portion

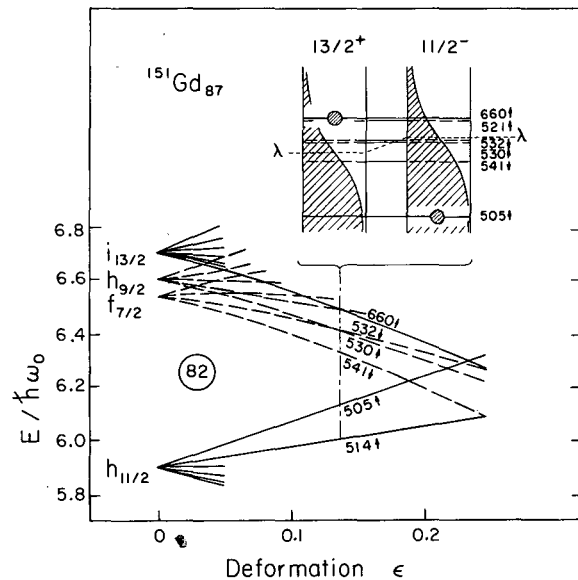


Fig. 2. Nilsson diagram for the  $N=82$  region. The inserts show the intrinsic configurations of the  $13/2^+$  and  $11/2^-$  band heads at  $\beta \approx 0.14$ , where the Fermi levels,  $\lambda$ , are estimated to be those calculated for  $N=86$  and  $N=88$ , respectively.  
(XBL739-4106)



of the diagram around the N=82 closed shell. Occupation of the  $11/2^- |505|$  orbital with its strong upward slope will favor a spherical nuclear equilibrium shape, whereas the orbitals immediately above N=82 generally slope downwards and thus favor deformation. In its ground state  $^{151}\text{Gd}$  has two pairs and the odd particle occupying the down-sloping orbitals above N=82. Promotion of the odd neutron from the ground-state orbital to the lowest  $i_{13/2}$  orbital represents a promotion from a moderately down-sloping orbital to a similar down-sloping orbital. Such a change in occupation should leave the nuclear deformation relatively unaffected. In the  $11/2^-$  configuration, however, a neutron has been lifted above the N=82 gap. The nucleus now has three pairs in the down-sloping orbitals and the  $11/2^- |505|$  orbital has become 50% unoccupied. Both consequences of this rearrangement produce a very strong tendency towards deformation.

This more detailed picture of the origin of shape coexistence in an odd-A nucleus might provide the means to identify similar phenomena in other regions of the nuclear chart. Bands similar to those in  $^{151}\text{Gd}$  should generally appear whenever the nuclear potential is soft towards  $\beta$ -deformation and the Fermi surface lies between two spherical j-shells, and recently identified<sup>10, 11</sup> bands in  $^{45}\text{Sc}$  and  $^{75}\text{Se}$  might be interpreted in this way.

#### Footnotes and References

\* On leave from Physik Department, Technische Universität, München, Germany.

1. F. S. Stephens, R. M. Diamond, J. R. Leigh,

T. Kammuri, and K. Nakai, *Phys. Rev. Letters* **29**, 438 (1972).

2. P. Kleinheinz, S. M. Harris, G. Løvnhøiden, and K. Nakai, *Bull. Am. Phys. Soc. II* **17**, 898 (1972), and to be published.

3. F. S. Stephens, R. M. Diamond, and S. G. Nilsson, *Phys. Letters* **44B**, 429 (1973).

4. G. Løvnhøiden and J. Waddington, private communication, and to be published.

5. C. Ekström, S. Ingelman, M. Olsmats, and B. Wannberg, *Physica Scripta* **6**, 181 (1972).

6. P. O. Tjøm and B. Elbek, *Mat. Fys. Medd. Dan. Vid. Selsk.* **36** (8) (1967).

7. K. Nakai, P. Kleinheinz, J. R. Leigh, K. H. Maier, F. S. Stephens, and R. M. Diamond, *Phys. Letters* **44B**, 443 (1973).

8. L. Grodzins, *Phys. Letters* **2**, 88 (1962).

9. P. Kleinheinz, R. K. Sheline, M. R. Maier, R. M. Diamond, and F. S. Stephens, Lawrence Berkeley Laboratory, Report LBL-1994, to be published in *Phys. Rev. Letters*.

10. P. G. Bizetti, A. M. Bizetti-Sona, M. Bucciolini, R. Huber, W. Kutschera, H. Morinaga, R. A. Ricci, and C. Signorini, *Proceedings of the International Conference on Nuclear Physics*, Munich (1973), edited J. de Boer and H. J. Mang, p. 173.

11. C. Protop, K. O. Zell, H. G. Friederichs, B. Heits, and P. von Brentano, *ibid.*, p. 216.

### EVIDENCE FOR DEFORMED SHAPED IN $^{186}\text{Hg}$

D. Proetel, R. M. Diamond, P. Kienle, J. R. Leigh, K. H. Maier, and F. S. Stephens

The discovery<sup>1</sup> of a sudden increase of the rms radius of the ground state of  $^{185}\text{Hg}$  compared to  $^{187}\text{Hg}$  has raised the question as to whether this is due to the onset of deformation in the former nucleus. Although larger deformation for the light Hg isotopes is expected from the systematics of the light Pt- and Os- nuclei which show rotational ground bands,  $\alpha$ -decay measurements of light Pb nuclei did not seem to support this hypothesis.<sup>2</sup>

In this contribution we report on (HI, xn $\gamma$ )

measurements leading to  $^{186}\text{Hg}$  performed at the HILAC in Berkeley. Excitation function measurements show that the lines in Table I are associated with the mass 186 chain, and particle- $\gamma$  coincidence experiments established that they are not due to the evaporation of  $\alpha$ -particles or protons. Gamma-gamma coincidence measurements showed them to be all in cascade with each other, and their angular distributions indicated that they have stretched E2 multipolarity. The level ordering, which is the crucial point, has been established by

Table I. Properties of transitions in  $^{186}\text{Hg}$ 

Transition	Energy	$A_2$	Relative Intensities			$\frac{\hbar^2}{2\mathcal{I}}$	Energies in	
			a	b	c		$^{184}\text{Pt}$	$^{190}\text{Hg}$
$2^+ \rightarrow 0^+$	405.3	0.17	100	100	100	67.5	162.1	416.4
$4^+ \rightarrow 2^+$	402.6	0.18	84	79	50	28.8	272.7	625.1
$6^+ \rightarrow 4^+$	356.7	0.22	76	48	30	16.2	362.5	730.2
$8^+ \rightarrow 6^+$	424.2	0.23	63	21	20	14.1	431.6	
$10^+ \rightarrow 8^+$	488.9	0.26	41			12.9	475.8	
$12^+ \rightarrow 10^+$	542.0	0.17	27			11.8		
$14^+ \rightarrow 12^+$	581.6	0.38	16			10.8		

a = In beam ( $^{162}\text{Dy} + ^{22}\text{Si}$ , 135 MeV).

b = Decay of an isomeric state with  $t_{1/2} = 100 \pm 10 \mu\text{sec}$ .

c =  $\beta$ -decay of  $^{186}\text{Tl}$ .

measuring the relative intensities of the transitions from in-beam spectra, from a 100  $\mu\text{sec}$  isomeric state in  $^{186}\text{Hg}$ , and from  $\beta$  decay of  $^{186}\text{Tl}$  (which was produced in the reaction  $^{159}\text{Tb} + ^{32}\text{S}$  at 164.5 MeV, and 191 MeV). The relative intensities of the transitions in  $^{186}\text{Hg}$  for these three different modes of population are listed in Table I, column a, b, and c, respectively. They leave little doubt about the level ordering for the states in  $^{186}\text{Hg}$ . (It must be noted that the nature of the isomeric state and its mode of decay in  $^{186}\text{Hg}$  is not clear at this time.) See Fig. 1.

The spectrum of the yrast states in  $^{186}\text{Hg}$  is very peculiar. The 405 keV energy of the  $2^+$  state is reduced by only a few keV from the  $2^+$  energies of the heavier even-even Hg nuclei which scatter around  $420 \pm 10$  keV in the Hg isotopes with  $188 \leq A \leq 198$ . But whereas the  $4^+ \rightarrow 2^+$  and  $6^+ \rightarrow 4^+$  transition energies increase significantly and about equally in the heavier Hg isotopes, one observes a drop to 403 keV and 357 keV, respectively, in the case of  $^{186}\text{Hg}$ . The transition energies connecting the states with higher spins then increase monotonically as can be seen in Table I. This suggests that in the ground state and the first excited  $2^+$  state,  $^{186}\text{Hg}$  is not much different from the heavier Hg isotopes with a deformation of  $|\beta| \approx 0.1$ . At higher angular momenta it makes a rather sudden change toward larger deformation which it then keeps approximately constant up to the  $14^+$  state. This assumption gets support from the similarity of the  $6^+ \rightarrow 4^+$ ,

$8^+ \rightarrow 6^+$  and  $10^+ \rightarrow 8^+$  transition energies in  $^{186}\text{Hg}$  with those of the nucleus  $^{184}\text{Pt}$  which has two protons less and is a reasonably good

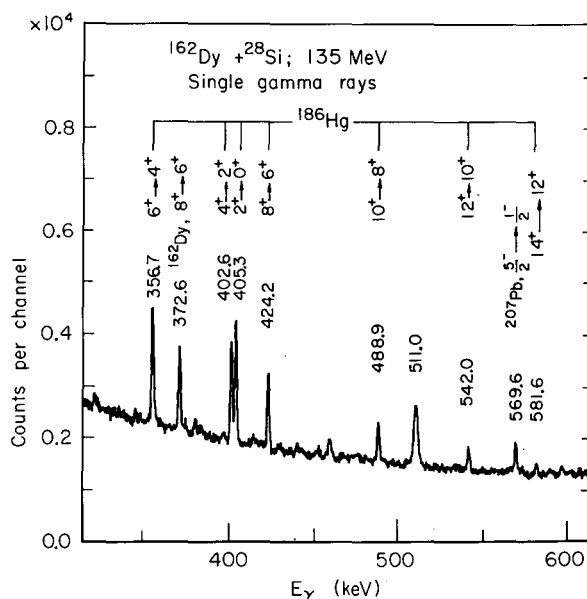


Fig. 1. Part of the  $\gamma$ -spectrum obtained by bombarding a  $1 \text{ mg/cm}^2$  thick lead-backed target of  $^{162}\text{Dy}$  with  $^{28}\text{Si}$  ions of 135 MeV. The arguments which led to the assignments of the lines are given in the text.

(XBL736-3222)

rotational nucleus. An estimate of the magnitude of the deformation based on the  $6^+ \rightarrow 4^+$  transition yields  $|\beta| \approx 0.25$ .

The conclusion seems to be that the bottom of this band in  $^{186}\text{Hg}$  is not very deformed but the upper parts are. This could be explained if the potential energy as a function of deformation widens significantly in some direction (or even forms a second minimum) at energies somewhat above the nearly spherical minimum. This widening (or second minimum), which is

apparently dropping with mass number, can provide a basis for the larger rms radius observed by Otten for lighter Hg nuclei.

#### References

1. J. Bonn, G. Huber, H. J. Kluge, L. Kugler, and E. W. Otten, Phys. Letters **38B**, 308 (1972).
2. P. Hornshøj, P. G. Hansen, B. Jonson, A. Lindahl, and O. B. Nielsen, Phys. Letters **43B**, 377 (1973).

### NUCLEAR DEFORMATIONS IN $^{186}\text{Hg}$ FROM LIFETIME MEASUREMENTS

D. Proetel,\* R. M. Diamond, and F. S. Stephens

In an earlier publication<sup>1</sup> we noted a very peculiar discontinuity in the spectrum of the yrast states of the nucleus  $^{186}\text{Hg}$ . The energy of the  $2^+$  state is 405.3 keV, and very similar to those of the vibrational heavier mercury isotopes, but above the  $4^+$  state we observed a rotation-like band up to the  $14^+$  state. Our interpretation was that  $^{186}\text{Hg}$  makes an angular-momentum-induced shape transition from small (perhaps oblate) deformation at low spins towards a larger prolate deformation at higher spins. This is also suggested by various potential-energy surface calculations.

In order to confirm such a shape transition, we measured the lifetimes of the  $2^+$ ,  $4^+$ ,  $6^+$  and  $8^+$  states in  $^{186}\text{Hg}$  using the Doppler-shift recoil-distance method. In this experiment a stretched, self-supporting  $^{170}\text{Yb}$  foil, 0.8 mg/cm<sup>2</sup> thick, was bombarded with a  $^{20}\text{Ne}$  beam of 108 MeV from the 88-inch cyclotron at the Lawrence Berkeley Laboratory. The recoiling  $^{186}\text{Hg}$  nuclei were stopped in a Bi stopper; the resulting gamma-ray spectra at various target stopper distances are shown in Fig. 1. A recoil velocity of  $v/c = 1.00\%$  was determined. The determination of the shifted and stopped intensities involved a fit of the respective peaks to the lineshapes obtained in the runs at "infinite" (2.1 mm) and zero (Pb-backed) distances.

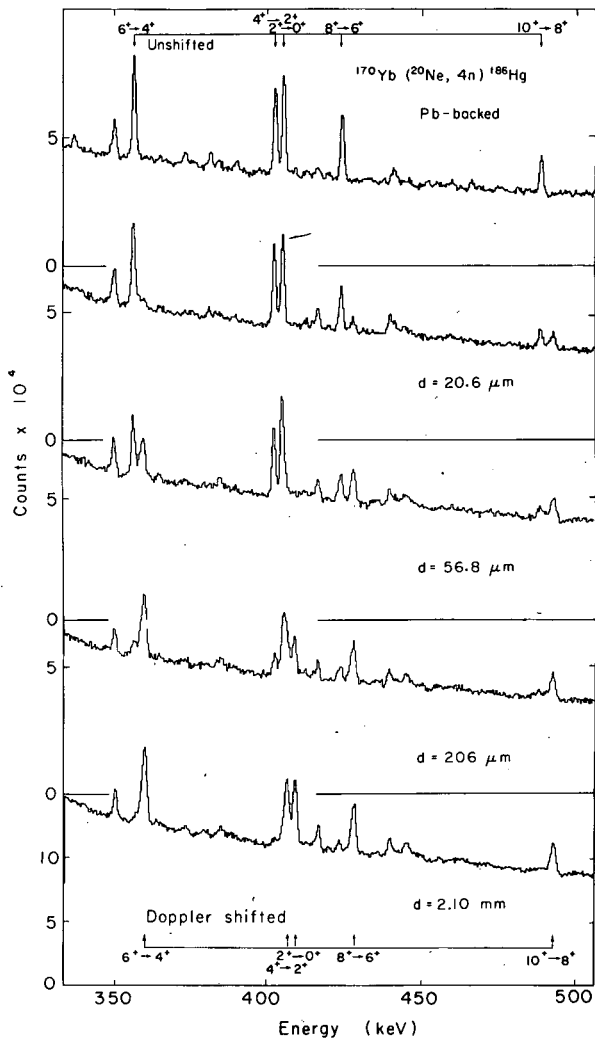


Fig. 1. Partial  $\gamma$ -ray spectra from  $^{170}\text{Yb}$  ( $^{20}\text{Ne}$ ,  $4n$ ) $^{186}\text{Hg}$  at 108 MeV incident energy for various target-stopper distances.

(XBL 7310-4144)

Figure 2 shows, on a semi-logarithmic plot, the ratios of the stopped intensity over the total intensity for the decay of all the states from  $2^+$  to  $10^+$ . It is apparent from these decay curves, especially for the short-lived  $8^+$  and  $10^+$  states, that we are dealing with two components, the longer one having a half-life of approximately 37 psec and corresponding to about 30% of the intensity. This contribution—shown as dashed lines in Fig. 2 for the decay curves of the  $2^+$  and  $6^+$  states—was subtracted from the data prior to further analysis. The corrected data were fitted simultaneously as the decay of a three-step cascade with a computer code which also allowed for delayed feeding of the whole cascade.

The results of our measurement are summarized in Table 1, which shows the transitions, their energies, half-lives,  $B(E2, I \rightarrow I-2)$  values and deformations, calculated on the basis of the rotor model. Our results show very convincingly that  $^{186}\text{Hg}$  is almost spherical,  $|\beta| \approx 0.13$ , near its ground state, but changes to a strongly deformed shape by the  $6^+$  state,  $|\beta(6^+)| = 0.27 \pm 0.05$ . The simplest explanation for this behavior would be centrifugal stretching, if the potential energy forms a minimum at small deformation and develops a shoulder or a second shallow minimum at larger deformation and somewhat higher energy. The lower yrast states are then confined in the first well at small deformation, but the centrifugal potential, which has to be added to the static potential, eventually produces a lower relative energy in the second well for the higher spin values.

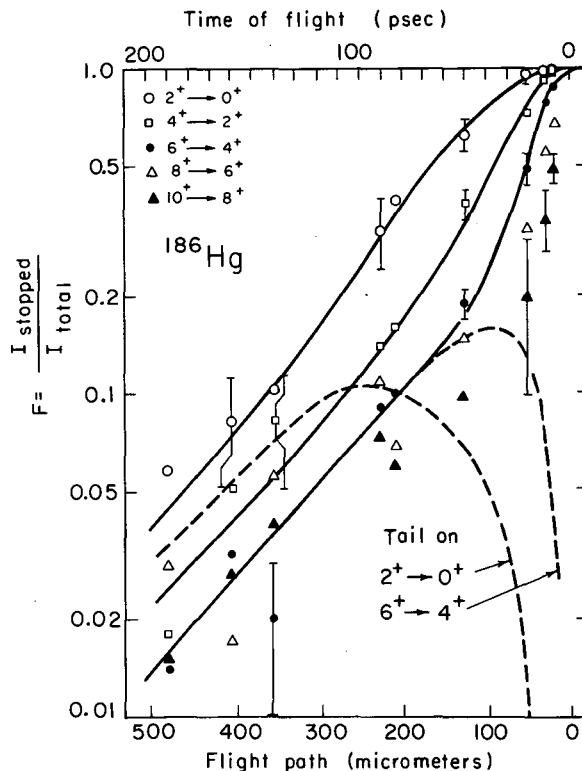


Fig. 2. Recoil-distance decay curves for the  $2^+$ ,  $4^+$ ,  $6^+$ ,  $8^+$ , and  $10^+$  states in  $^{186}\text{Hg}$ , as obtained in the reaction  $^{170}\text{Yb}(^{20}\text{Ne}, 4n)$ . The solid lines are the counter fits to the corrected data points (for details see text) with the long-lived tails, shown as dashed lines, added back in. (XBL 7310-4249)

Table 1. Half-lives and deformations of states in  $^{186}\text{Hg}$ .

Transition	Energy (keV)	$t_{1/2}$ (psec)	$B(E2)$ $e^2 b^2$	Deformation $ \beta $
$2^+ \rightarrow 0^+$	405.3	$18 \pm 3$	$0.28 \pm 0.05$	$0.13 \pm 0.01$
$4^+ \rightarrow 2^+$	402.6	$9 \pm 3$	$0.6 \pm 0.2$	$0.16 \pm 0.03$
$6^+ \rightarrow 4^+$	356.7	$5 \pm 2$	$1.9 \pm 0.8$	$0.27 \pm 0.05$
$8^+ \rightarrow 6^+$	424.2	$\approx 3$	$\approx 1.4$	$\approx 0.22$

### References

\* D. P. would like to thank the West German BMBW and the Kultusministerium of Bavaria for support.

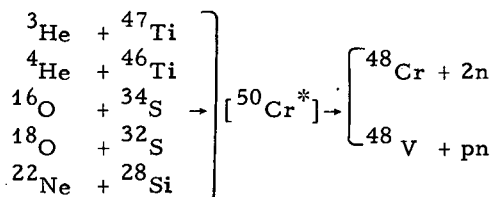
1. D. Proetel, R. M. Diamond, P. Kienle, J. R. Leigh, K. H. Maier, and F. S. Stephens, Phys. Rev. Letters **31**, 896 (1973).

TEST OF THE INDEPENDENCE POSTULATE IN THE BOHR THEORY  
OF COMPOUND-NUCLEUS DECAY:  $^{50}\text{Cr}^*$  SYSTEM

M. K. Go\* and S. S. Markowitz

One of the important theories concerning nuclear reactions in the intermediate energy region (<10 MeV per incident nucleon) is the compound-nucleus model.<sup>1</sup> In this model, the decay of the compound nucleus is independent of its mode of formation. Since the work by Ghoshal<sup>2</sup> in which the decay of the  $^{64}\text{Zn}^*$  compound nucleus formed with protons was compared with that formed with a particle, many investigations<sup>3</sup> have been performed along the same line. In most cases, the independence postulate is upheld roughly. More recently, when comparing the reaction excitation functions, care has been taken to match not only the excitation energy of the compound nucleus, but also its angular momentum.<sup>4</sup> However, very few investigations have compared heavy-ion induced reactions with those induced by light projectiles (such as p, n,  $^3\text{He}$ ,  $\alpha$ ). It is felt that the independence postulate can be subjected to a more severe test when comparing reactions involving vastly different reactants.

In this work, the compound nucleus  $^{50}\text{Cr}^*$  is formed by different entrance channels and the decay of this compound nucleus is observed through products from pn and 2n emissions. The reactions are given below:



In all the reactions studied, the excitation energy of the compound nucleus is less than 60 MeV.

Excitation functions for the production of  $^{48}\text{V}$  and  $^{48}\text{Cr}$  from incident ions  $^3\text{He}$ ,  $\alpha$ ,

$^{16}\text{O}$ ,  $^{18}\text{O}$ , and  $^{22}\text{Ne}$  involving the compound system  $^{50}\text{Cr}^*$  have been measured. Test of the independence postulate was performed in a Ghoshal type of experiment. Effects of the nuclear Coulomb barrier and high reaction Q value upon the two-nucleon evaporation excitation functions were noted. For all the reaction pairs, the  $^{48}\text{V}$  production is more than a factor of 10 bigger than the corresponding  $^{48}\text{Cr}$  cross section. This phenomenon can be explained by the effect of odd-even nucleon number of the product nucleus. Simple calculations of the angular momentum and rotational energy of the product nucleus. Simple calculations of the angular momentum and rotational energy of the compound nucleus were performed. The energy shift of the excitation function can be explained by the effect of angular momentum. The reactions involved were found to be generally consistent with the compound-nucleus model.

Footnotes and References

\* Submitted in partial fulfillment of the Ph.D. requirements of the Dept. of Chemistry, University of California, Berkeley. Thesis reference UCRL-20483. Condensation of Phys. Rev. C 7, 1464 (1973); excitation functions and details of calculations are presented there. Present address: Western Regional Research Laboratory, Albany, California.

1. N. Bohr, Nature 137, 344 (1936).
2. S. N. Ghoshal, Phys. Rev. 80, 939 (1950).
3. C. F. Smith, Jr., Lawrence Radiation Laboratory Report UCRL-11862, (1950).
4. M. J. Fluss, J. M. Miller, J. M. D'Avria, N. Dudey, B. M. Foreman, Jr., L. Kowalski, and R. C. Reedy, Phys. Rev. 187, 1449 (1969).

EXCITATION FUNCTIONS OF  $\text{La}(^{12}\text{C}, x\text{n}\gamma)$  Eu REACTIONS

D. M. Lee and S. S. Markowitz

Measurements of excitation functions constitute an important source of information concerning some properties of reaction mechanism, and various nuclear parameters. In particular, excitation function in compound-nucleus reactions have been used to investigate the statistical properties of nuclei at high excitation energies, and the nuclear evaporation model provides a test of the validity of the statistical model calculations.

In regions where fission can be ignored, the use of Jackson's neutron-emission formula<sup>1</sup> as modified to include angular-momentum effects has been successful in fitting the experimental functions.<sup>2</sup> Our present experiment is to measure the excitation functions in the rare-earth region using heavy-ions as projectiles. The measured excitation functions are then compared to evaporation calculations based on Jackson's formula.

The first compound nuclei we have chosen to study is  $^{151}\text{Eu}$  which is produced by bombarding  $^{139}\text{La}$  with  $^{12}\text{C}$ . Four excitation functions of the reactions  $^{139}\text{La}(^{12}\text{C}, x\text{n}\gamma)^{151-x}\text{Eu}$ , where  $x = 3, 4, 5, 6$ , were measured, spanning a region of incident energy of projectiles from 35 MeV to 101 MeV. There are several advantages in this system. The decay scheme of the product nuclides is well studied and all products decay to stable nuclides so there are no interfering activities from daughter products or from nuclides produced directly in  $(^{12}\text{C}, x\text{n}, y\text{p})$  reactions. The half lives and gamma-rays are well separated to permit direct measurement of the radioactivities from

product nuclides simultaneously by using gamma-spectroscopy without chemical separation. The  $^{139}\text{La}$  target can be prepared as pure metal or as oxide with nearly 100% isotopic abundant in natural lanthanum compound.

The experimental procedure consisted of assembling several thin targets on thin aluminum cover foils in a water cooled holder and irradiating the stack with a  $^{12}\text{C}$  beam from the Berkeley 88-inch cyclotron. The beam intensity was measured with a Faraday cup connected to an integrating electrometer. The initial 105-MeV  $^{12}\text{C}$  beam was degraded to an appropriate energy by Al foils, and the energies at various positions in the stack were calculated with the computer code by Steward.<sup>3</sup> The thin targets were prepared by vacuum evaporation of La metal or  $\text{La}_2\text{O}_3$ . After bombardment, absolute yield of the radioactivities was determined by gamma-ray spectrum with a high-resolution Ge(Li) detector. The radioactivities of  $^{145}\text{Eu}$ ,  $^{146}\text{Eu}$ ,  $^{147}\text{Eu}$ ,  $^{148}\text{Eu}$  were determined with the 894 keV (69%), 747 keV (100), 197 keV (24%) and 550 keV (120%) gamma-rays respectively.

The results of experimental and calculated maximum cross sections are given in Table I. The absolute values of the cross sections are subject to the uncertainties in absolute counter calibration, decay branching ratios, variation of target of thickness, absolute accuracy of the beam current measurements. We estimate that the systematic error introduced from these sources may be as large as 25%. The

Table I. Experimental and calculated maximum cross sections for  $^{139}\text{La}(^{12}\text{C}, x\text{n})^{151-x}\text{Eu}$  reactions.

Reactions	Experimental peak energies (MeV)	Calculated peak energies MeV	Experimental $\sigma$ (mb)	Calculated $\sigma$ (mb)
$(^{12}\text{C}, 3\text{n})$	56.2	56.6	240	772
$(^{12}\text{C}, 4\text{n})$	69.5	68.5	520	1273
$(^{12}\text{C}, 5\text{n})$	82.5	80.5	550	1350
$(^{12}\text{C}, 6\text{n})$	99.1	96.8	385	1830

relative cross sections however, contain only random errors, estimated to be about 10%.

Figure 1 shows the experimental excitation functions and the threshold energies for the reactions  $^{139}\text{La}(^{12}\text{C}, xn)^{151-xn}\text{Eu}$ , where  $x = 3, 4, 5, 6$ . Several significant features are apparent from Fig. 1. The excitation functions are of the general shape characteristic of compound nucleus reactions, the cross sections rising rapidly to a maximum and then decrease rapidly. Cross sections of this system ( $^{12}\text{C} + ^{139}\text{La}$ ) has not been measured previously; however, measurements of this similar type in the rare-earth region had been done.<sup>4,5</sup> The results of this Eu system is similar to Kaplan's Sm compound system; in general, both show the same shape of the excitation functions, and similar magnitude of maximum cross sections.

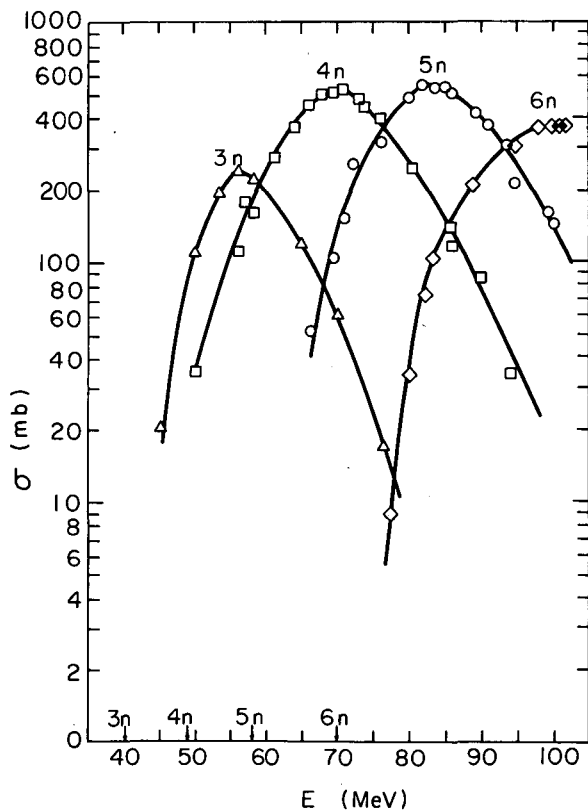


Fig. 1. Experimental excitation functions for the reactions  $^{139}\text{La}(^{12}\text{C}, xn)^{151-xn}\text{Eu}$  ( $x = 3, 4, 5, 6$ ). Product cross sections are plotted as functions of  $^{12}\text{C}$  ion energy in the laboratory system. The triangles, squares, circles and diamonds correspond to  $x = 3, x = 4, x = 5, x = 6$  respectively. The labeled arrows indicate the threshold energies for the respective xn reactions. (XBL 742-2454)

For the comparisons between experimental and calculated excitation functions,<sup>6</sup> we were concerned with agreement of shapes, thresholds and peak energies. The Jackson model of nuclear evaporation is assuming constant temperature and neutron emission alone is considered. Since this model predicts that the energy of maximum cross section in the excitation function is a function of nuclear temperature, this parameter was used as free parameter to obtain a reasonable good fit for all peak energies. Figure 2 shows a comparison between experimental and calculated excitation functions ( $T = 2$  MeV) for the reactions  $^{139}\text{La}(^{12}\text{C}, xn)^{151-xn}\text{Eu}$  ( $x = 3, 4, 5, 6$ ). A reasonable good fit for all peak energies was obtained by setting  $T = 2$  MeV. But the calculated shape is still narrower than the experimental shape. Experimental threshold energies in Fig. 1 seem to be in agreement with calculated threshold energies in Fig. 2. A large discrepancy

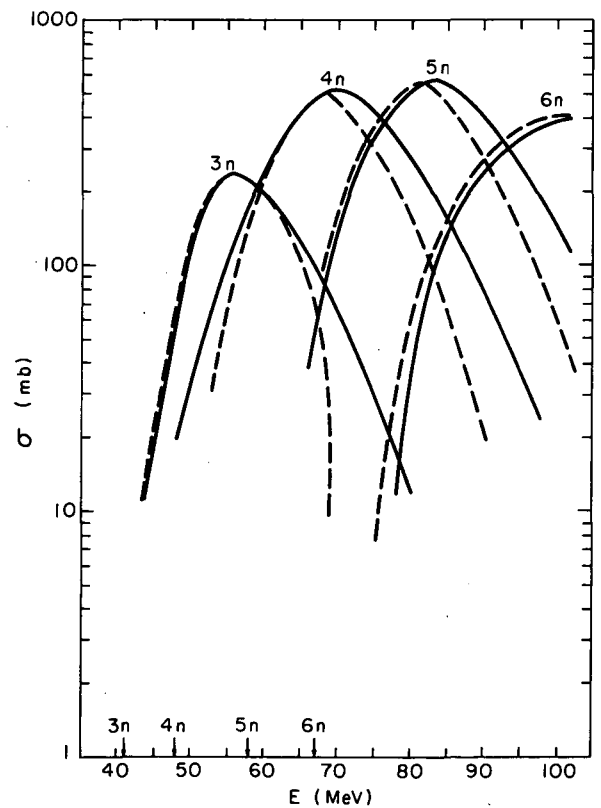


Fig. 2. Experimental and calculated results for the reactions  $^{139}\text{La}(^{12}\text{C}, xn)^{151-xn}\text{Eu}$  ( $x = 3, 4, 5, 6$ ). The labeled arrows indicate the calculated threshold energies for the respective xn reactions. Solid lines denote experimental results; dashed lines denote calculated values which have been normalized at the peak to the experimental points. See Table I for the un-normalized calculated maximum cross sections. (XBL 742-2459)

of absolute cross sections between experimental and calculated values was observed. Jackson's simplified model fails to predict the absolute cross section in the rare-earth region. Further study is underway to obtain more experimental data in this region, and to compare it to another scheme of calculation suggested by Gilat, etc.

#### Footnotes and References

1. J. D. Jackson, Can. J. Phys. 34, 767 (1956).
2. T. Sikkeland, Arkiv. Fysik 36, 539 (1967).
3. P. G. Steward, Lawrence Radiation Laboratory Report UCRL-18127 (1968) (Ph.D. thesis).
4. M. Kaplan, Phys. Rev. 143, 894 (1966).
5. J. M. Alexander and G. N. Simonoff, Phys. Rev. 133, B93 (1964).
6. Computer Code used for this calculation was supplied by Dr. Jose Alonso.
7. J. Gilat, E. R. Jones, III, and J. M. Alexander, Phys. Rev. C 7, 1973 (1973).

### FISSION PROBABILITIES IN LIGHTER NUCLEI: A THEORETICAL AND EXPERIMENTAL INVESTIGATION OF THE SHELL AND PAIRING EFFECTS IN FISSIONING NUCLEI\*

L. G. Moretto

The general features of the fission probabilities are reviewed in the light of the modern developments on the statistical properties of nuclei. The general thermodynamical aspects of the fission probabilities are first discussed without relying on any specific nuclear model. The effects of the shell structure and of the collective degrees of freedom on the saddle-point and ground state phase space volume are then considered. A general method to include the effect of shells and pairing in the fission probability calculation is illustrated. The disappearance of the shell and pairing effects with increasing excitation energy and its influence on the fission probabilities is exemplified by means of a calculation performed on superheavy elements. The experimental data available in nuclei in the Pb region and lighter nuclei are discussed in detail and an analysis based upon the present knowledge of shell and

pairing effects is performed. It is found that the experimental evidence on shell effects in these data are accounted for satisfactorily by including the Nilsson model and the BCS Hamiltonian in the calculation. A reliable set of fission barriers is obtained and the liquid drop model predictions are tested. The saddle point single particle level densities which are also obtained in the analysis show the expected A dependence and their magnitude, about 8% larger than the corresponding ground state quantity, seems to be due to an increase in the nuclear surface at the saddle point.

#### Footnote

\*Invited paper presented at the Third Symposium on the Physics and Chemistry of Fission, Rochester, New York, August 13-17, 1973.



FISSION CROSS SECTION IN  $^4\text{He}$  INDUCED FISSION OF  $^{204}\text{Pb}$ ,  $^{186}\text{W}$ ,  $^{165}\text{Ho}$   
AND OF SOME Hg ISOTOPES

L. G. Moretto, R. C. Gatti, and S. G. Thompson

The analysis of the fission excitation-functions has been shown to be a most powerful method of determining the fission barrier heights in medium-heavy nuclei.<sup>1,2</sup> The fission barrier heights constitute valuable information in the investigation of the smooth nuclear properties such as the parameters of the liquid drop and droplet models.

At present very large gaps in the available data exist in the region of  $^{208}\text{Pb}$  and in that region immediately preceding it as well as in the rare earths region. The new measurements, to be completed for  $^4\text{He}$  projectiles and to be extended to  $^1\text{H}$  projectiles, have the purpose of contributing to the closure of these gaps. These measurements are made possible, in the case of the Hg isotopes, by a new method of preparing the targets. The separated Hg isotope, in metallic form, is evaporated onto a high purity Ag foil in such an amount that the formed amalgam remains solid. The amalgam foil, so prepared, is then clad between two thin evaporated layers of Pd metal, which does not form an amalgam and which serves the purpose of trapping the Hg inside the target.

The experimental setup, shown in Fig. 1, consists of a scattering chamber provided with a 3 mm diameter collimator and with a target holder that exposes the target at  $45^\circ$  to the beam. The beam is collected by a Faraday cup and integrated by an electrometer. The fission detectors consist of small mica sheets of  $\sim 1\text{ cm}^2$  areas; they are four in number and can be exposed to the fission fragments at  $135^\circ$  with respect to the beam in succession after each energy change without breaking the vacuum.

The changes in bombarding energy are obtained in two ways. When the energy change is large, it is achieved by changing the energy of the primary beam. When the change is small,

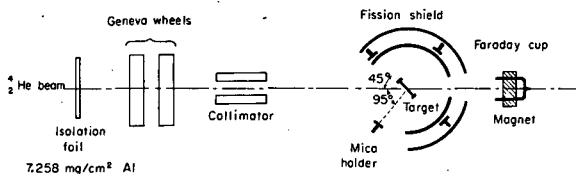


Fig. 1. Schematic drawing of the apparatus.  
(XBL 742-2460)

the beam is degraded by means of combinations of absorbers of various thicknesses mounted on two Geneva wheels preceding the collimator.

Since the geometry factor and the beam charge are measured, as well as the target thickness, the angular distribution remains to be known in order to calculate the total cross section. The angular distribution is expected to be proportional to  $[\sin\Theta]^{-1}$  for angles somewhat removed from  $0^\circ$  and  $180^\circ$  and lower than  $[\sin\Theta]^{-1}$  close to  $0^\circ$  and  $180^\circ$ . A  $[\sin\Theta]^{-1}$  distribution, after integration over the solid angle is equivalent to a constant angular distribution normalized to the cross section at  $\Theta = 140.5^\circ$  in the center of mass. We have chosen the angle  $\Theta = 135^\circ$  in the lab system in order to account both for the kinematical shift in angle and for the deviation of the angular distribution from  $[\sin\Theta]^{-1}$  close to  $0^\circ$  and  $180^\circ$ .

The experimental data are shown in Fig. 2.

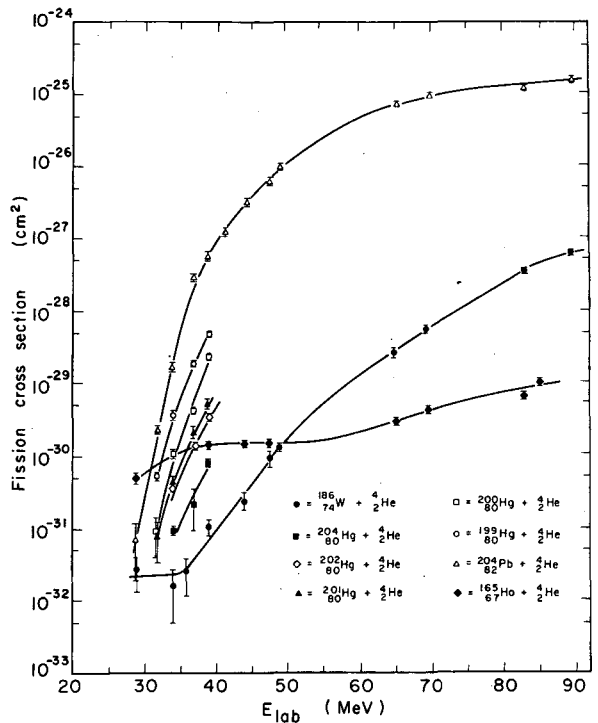


Fig. 2. Fission cross sections as a function of the  $^4\text{He}$  bombarding energy.  
(XBL 742-2461)

In all the excitation functions the rapid rise of the cross section with increasing energy is visible. Flattening of the cross section at the lowest energies for the  $^{186}\text{W}$  and the  $^{165}\text{Ho}$  targets is due to contaminants ( $^{232}\text{Th}$ ,  $^{238}\text{U}$ ).

Of particular interest are the cross sections for the five Hg isotopes ( $^{199}\text{Hg}$ ,  $^{200}\text{Hg}$ ,  $^{201}\text{Hg}$ ,  $^{202}\text{Hg}$ ,  $^{209}\text{Hg}$ ). These cross sections show the progressive onset of the  $N=126$  shell starting from  $^{199}\text{Hg} + ^4\text{He}$  corresponding to  $N=121$ , up to  $^{204}\text{Hg} + ^4\text{He}$  corresponding to  $N=126$ . The increase in the shell effect increases the fission barrier height which in turn decreases the cross section rather dramatically.

### MEASUREMENT OF PROMPT GAMMA RAY LIFETIMES OF FISSION FRAGMENTS OF $^{252}\text{Cf}^*$

R. C. Jared, H. Nifenecker, and S. G. Thompson

In the recent past, interest in the neutron rich isotopes near  $A = 100$  has been generated by the observation of rotational-like energy levels which suggested a new region of deformation. The fission of  $^{252}\text{Cf}$  produces isotopes in this region and thus is a convenient source for use in their study.

In this paper we report the results of a new series of experiments where the lifetimes of the high yield gamma lines in the spontaneous fission of  $^{252}\text{Cf}$  are measured by using their known velocities and defined flight paths. The length of the flight path is adjusted to six different positions. Each position corresponds to a well defined average flight-path from fission until the fragments are stopped and thus to a known flight time of the fission fragments. Due to the high velocity of the fission fragments, the gamma rays emitted during flight are Doppler shifted and easily separated from those of the stopped fragments. At each position approximately  $10^7$  events were collected and mass sorted to obtain gamma ray spectra as a function of the fragment mass. The intensities of the unshifted gamma lines are used along with the flight path length to obtain the lifetimes of the transitions. From the lifetimes and energies of the transitions, information on the deformation parameters of the even-even isotopes is obtained.

The experimental arrangement shown in Fig. 1 consists of five detectors. The fragment detector (F1) is fixed in position and is parallel to the  $^{252}\text{Cf}$  source and to the fission fragment detector (F2). The position of the

The analysis of a more complete set of data which should be available shortly will provide fission barrier heights precise within  $\sim 1$  MeV.

### References

1. L. G. Moretto, S. G. Thompson, J. Routti, and R. C. Gatti, Phys. Letters **38B**, 471 (1972).
2. L. G. Moretto, Invited Paper presented at the Third Symposium on the Physics and Chemistry of Fission, Rochester, New York, August 13-17, 1973; Lawrence Berkeley Laboratory Report LBL-1914.

in respect to fragment detector (F1) can be varied by means of a micrometer screw in order to obtain different flight distances for the fission fragments. Since the velocity of the fragments is known, each distance corresponds to a particular time between fission and the instant when the fragment is stopped in the

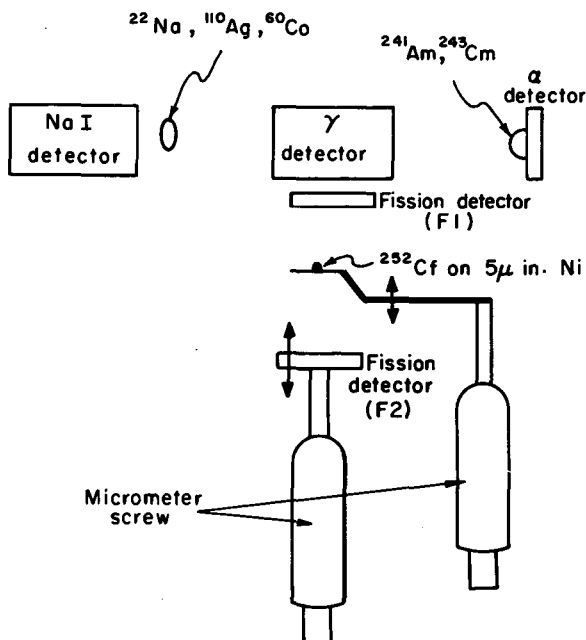


Fig. 1. The arrangement of the detectors. (XBL736-3163)

detector. The pulses produced by the gamma detector located behind the F2 detector are analyzed when they occur between 0 and 50 nsec after a fission event is detected. The gamma rays emitted while the fragments are moving are Doppler-shifted upwards by approximately 4%. This shift allows for an easy isolation of the gamma rays emitted after the fragment has stopped. Only the unshifted gamma rays from the stopped fragments are used to obtain the lifetimes. The gamma detector (3 cm<sup>3</sup> intrinsic germanium) is used to measure the intensities of the gamma lines from the stopped fragments. Fragment detector (F2) is adjusted so that the variation in flight path over the finite acceptance angle is less than 10%. The alpha and NaI detectors operated in coincidence with the gamma detectors are used to provide gamma lines for digital gain stabilization and zero intercept corrections.

The signals from the detectors were accepted in multidimensional formats by a PDP-9 computer. The computer monitored the experiment and performed an on-line mass calculation. This mass calculation is performed by means of a table look-up procedure. An array containing masses indexed by the two fragments pulse height F1, F2 is precalculated and used as the table. The mass calculation is similar to that described by Watson et al.<sup>1</sup> We differ

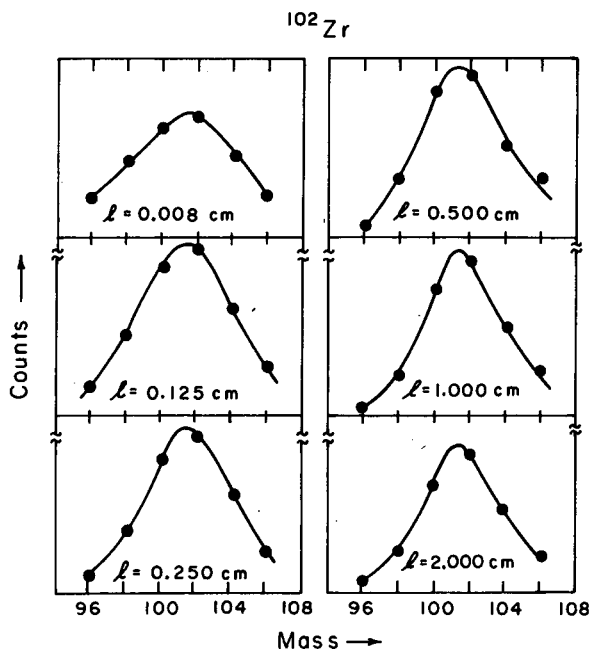


Fig. 2. A composite plot of the intensity of  $^{102}\text{Zr } 2^+ \rightarrow 0^+$  transition as a function of mass for each position. The counts are in arbitrary units and are not normalized to the number of fissions. (XBL737-3527)

in that we are using the neutron data from Nifenecker et al.<sup>2</sup> Possible grid effects were removed by recording fission fragment's pulse heights with 4096 channels. Windows were set on the calculated mass to obtain gamma distributions as a function of mass. There are 32 such distributions, 4096 channels long, corresponding to adjacent mass windows of 2 amu. The gamma distributions are analyzed in a larger computer at the end of the experiment to obtain the gamma-ray intensities.

The gamma-ray spectrum associated with each mass window is analyzed with the photopeak analysis code developed by Routti and Prussin<sup>3</sup> to obtain the gamma line intensities. Since the mass resolution ( $\sigma = 2-4$  amu) is much broader than our mass windows (2 amu) it is necessary to fit the intensities of a particular gamma line as a function of mass assuming the shape of a Gaussian in order (Fig. 2) to obtain the total yield at each position.

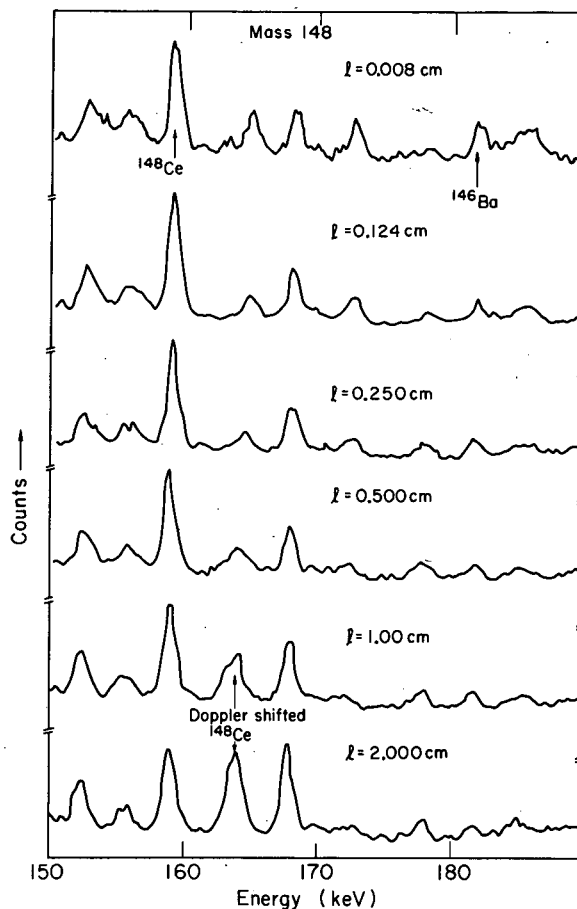


Fig. 3. Gamma spectra at different distances. The counts are in arbitrary units and are not normalized to the number of fissions. (XBL737-3425)

Table 1.

	Fragment Velocity cm/nsec	t <sub>1/2</sub> nsec	Energy keV	B(E <sub>2</sub> ) <sub>ex</sub> cm <sup>4</sup> × 10 <sup>-51</sup>	B(E <sub>2</sub> ) B(E <sub>2</sub> ) <sub>sp</sub>	β <sub>2</sub>	Q <sub>0</sub>   cm <sup>2</sup> × 10 <sup>-24</sup>	Q <sub>0</sub> Calculated <sup>a</sup>	
								Oblate	Prolate
<sup>100</sup> Zr 2 <sup>+</sup> → 0 <sup>+</sup>	1.39	0.714±0.03	212.7	845±40	62±3	0.32±0.02	2.9±0.2	-2.3	3.26
<sup>102</sup> Zr 2 <sup>+</sup> → 0 <sup>+</sup>	1.52	2.21±0.17	151.9	1825±120	110±10	0.45±0.03	4.3±0.3	-2.33	3.53
<sup>104</sup> Mo 2 <sup>+</sup> → 0 <sup>+</sup>	1.36	0.911±0.03	192.3	1060±40	74±3	0.32±0.02	3.26±0.2	-2.36	3.22
<sup>106</sup> Mo 2 <sup>+</sup> → 0 <sup>+</sup>	1.44	1.25±0.03	171.7	1300±40	88±3	0.35±0.02	3.61±0.2	-2.37	3.40
<sup>108</sup> Ru 2 <sup>+</sup> → 0 <sup>+</sup>	1.28	0.345±0.03	242.3	930±80	61±6	0.28±0.02	3.05±0.2	-2.42	2.88
<sup>110</sup> Ru 2 <sup>+</sup> → 0 <sup>+</sup>	1.38	0.34±0.04	240.8	970±120	62±7	0.28±0.02	3.12±0.2	-2.50	3.05
<sup>112</sup> Ru 2 <sup>+</sup> → 0 <sup>+</sup>	1.44	0.32±0.03	236.8	1120±110	70±7	0.32±0.02	3.35±0.2	-2.58	3.01
<sup>114</sup> Pd 2 <sup>+</sup> → 0 <sup>+</sup>	1.34	0.198±0.06	332.9	340±100	21±6	0.16±0.03	1.85±0.3	-2.42	2.73
<sup>116</sup> Pd 2 <sup>+</sup> → 0 <sup>+</sup>	1.40	0.106±0.03	340.6	570±170	34±10	0.20±0.03	2.39±0.3	-2.43	2.62
<sup>142</sup> Ba 2 <sup>+</sup> → 0 <sup>+</sup>	0.95	0.070±0.04	359.7	660±400	30±16	0.16±0.04	2.57±0.4		
<sup>144</sup> Ba 2 <sup>+</sup> → 0 <sup>+</sup>	1.08	0.70±0.03	199.4	1100±60	49±3	0.20±0.02	3.33±0.2	-2.17	2.20
<sup>146</sup> Ba 2 <sup>+</sup> → 0 <sup>+</sup>	1.09	0.86±0.06	181.0	1390±100	61±4	0.22±0.02	3.73±0.2		
<sup>146</sup> Ce 2 <sup>+</sup> → 0 <sup>+</sup>	0.93	0.26±0.05	258.6	880±180	39±8	0.17±0.02	2.97±0.2	-2.56	3.03
<sup>148</sup> Ce 2 <sup>+</sup> → 0 <sup>+</sup>	1.00	1.06±0.08	158.7	200±160	87±7	0.25±0.02	4.48±0.2	-3.30	4.56
<sup>150</sup> Ce 2 <sup>+</sup> → 0 <sup>+</sup>	1.03	3.60±1.0	97.1	3300±950	141±40	0.32±0.04	5.76±0.4		
<sup>154</sup> Nd 2 <sup>+</sup> → 0 <sup>+</sup>	0.97	7.7±2	72.8	2180±650	102±26	0.25±0.03	4.67±0.4		

<sup>a</sup>Q<sub>0</sub> calculated is from Ref. 7.

As mentioned above, six positions with respect to distance were used in the experiment: 0.008, 0.1250, 0.2500, 0.5000, 1.000, and 2.000 cm. Figure 2 shows an example of the intensities obtained for the 2<sup>+</sup> → 0 transition in <sup>102</sup>Zr. From these distances, the acceptance angle of the fission detectors and the velocities of the fission fragments the average velocity of the fragments that produced a specific isotope after neutron emission was determined by first taking the Z of that isotope and using the experimental data of Reisdorf, et al.<sup>4</sup> that gives the average preneutron mass (A\*) for the production of each charge. The mass of the isotope produced (A<sub>F</sub>) is then subtracted from this mass to obtain the average number of neutrons emitted ( $\bar{\nu} = A^* - A_F$ ). The number of neutrons emitted is then used along with the preneutron mass as indexes in the experimental data that gives the relationship of the total kinetic energy (E<sub>K</sub>) of the fission fragments to  $\bar{\nu}$  and A\* of Nifenecker, et al.<sup>2</sup> to determine E<sub>K</sub>. This value of E<sub>K</sub> and A\* are then used in Eq. (1) to define the average value of the velocity.

$$V_1 = \sqrt{\left(\frac{2}{A^*} - \frac{1}{126}\right) E_K} \quad (1)$$

The lengths (l) listed earlier for the distances from the source to detector (F1) are

converted by Eq. (2) before calculating the lifetimes,

$$\bar{l} = -l \left( \frac{\ell_n |\cos \theta|}{1 - \cos \theta} \right). \quad (2)$$

The angle θ is the acceptance angle of the fission fragment detectors. This correction was needed to define the length of the average flight path of the fragments. Using these distances and velocities of individual isotopes each position of the source is converted to a time between fission and the instant when a particular fragment of measured mass is stopped. This time is then used along with the gamma line yield at each position to determine the lifetime of each gamma transition.

The lifetimes of the gamma lines were then used to determine the reduced electric-quadrupole transition widths (B(E<sub>2</sub>)<sub>ex</sub>), intrinsic electric quadrupole moments (Q<sub>0</sub>) and β<sub>2</sub>. These parameters, which appear in Table 1, were obtained following the procedure of Stelson and Grodzins.<sup>5</sup> The isotopic assignments in Table 1 are taken from previous work of this group.<sup>6</sup> These isotopic assignments have since been partially confirmed by Khan, et al.<sup>7</sup> Figure 3 shows an example of the gamma ray spectra for different distances, in this case centered

around mass 148. The  $^{148}\text{Ce}$  line position is marked in the upper left in Fig. 3. This line shows no significant Doppler-shifted component at short times but at longer times the Doppler-shifted component becomes equivalent to the unshifted one. A small amount of  $^{146}\text{Ba}$  can also be seen in this figure. Figure 4 shows the results determining the total yield of these lines over the appropriate masses at each position. The figure shows one of the two examples of a two-component decay curve observed in this experiment. The two cases of multiple decay curves are  $^{146}\text{Ba}$  and  $^{110}\text{Ru}$ .

No attempt has been made to correct the data for the hyperfine interaction (HFI) which couples the nuclear and the electronic spins of the fission fragments. This effect is expected to be strong for highly ionized fission fragments. This correction is such as to decrease the lifetimes as reported in this experiment. The magnitude of the correction could be as large as 20% if the destruction of the fission fragment alignment by HFI occurred in a time comparable to the half life of the gamma transition. It

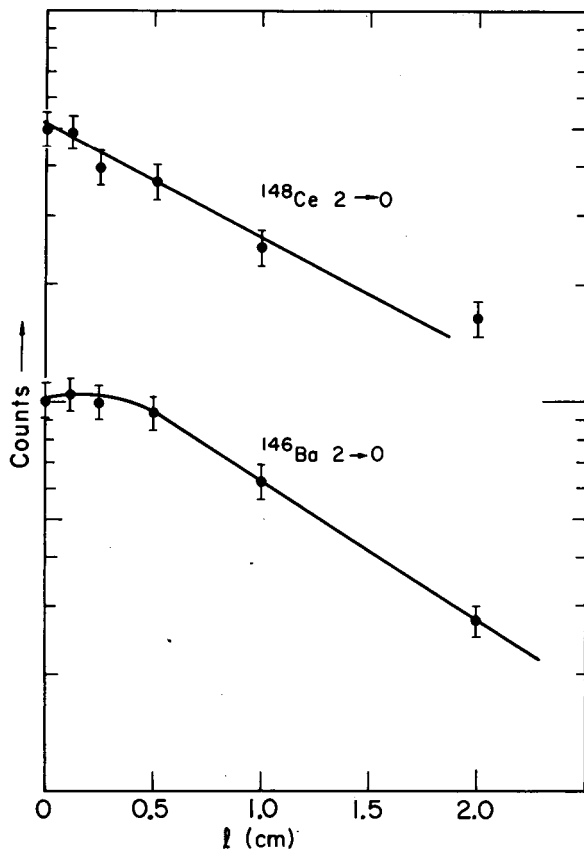


Fig. 4. Decay curves for  $^{148}\text{Ce}$  and  $^{146}\text{Ba}$ . (XBL737-3427)

is expected, however, that the characteristic time for the spin deorientation, should be much shorter than the half lives reported here and, therefore, that such effects are probably negligible.

The results of this experiment do not agree well with the previous results of our group<sup>6</sup> using a two-point decay curve. Figure 5 shows the values of  $\beta_2$  and  $B(E2)/B(E2)_{sp}$  obtained from both experiments. It is seen that the half-lives measured in this experiment are approximately 50% longer than those reported earlier. The results of this experiment are also compared with the calculations of Ragnarsson, et al.<sup>8</sup> In Fig. 6 it can be seen that the agreement between calculated values for prolate shapes and the experimental ones is remarkably good. This of course does not prove that the system is prolate because we cannot determine the sign of  $Q_0$ .

It should be noted that the previously reported large deformation of zirconium ( $\beta_2 \sim 0.6$ ) 102 is disproved in this experiment.

We wish to thank J. B. Hunter for help at various stages of the experiment and J. Blachot for checking of numerical calculations.

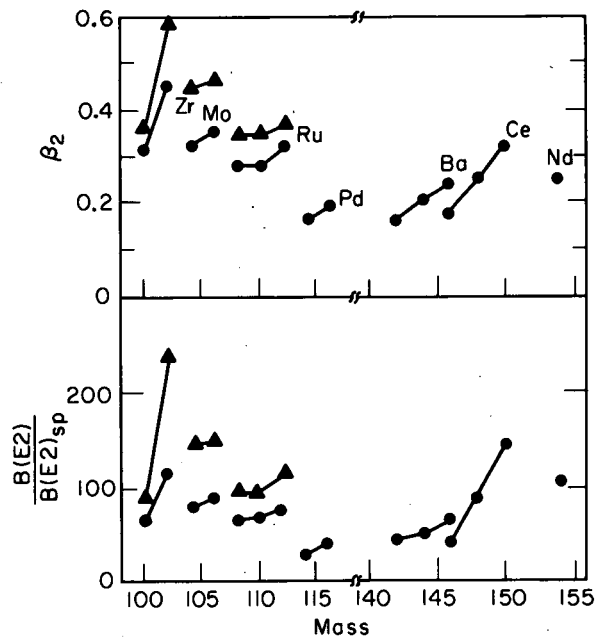


Fig. 5. Comparison of the  $\beta_2$   $B(E2)/B(E2)_{sp}$  values of the experiment of Cheifetz, et al. and this work. The  $\Delta$  are Cheifetz, et al. and the  $\circ$  are this work. (XBL737-3429)

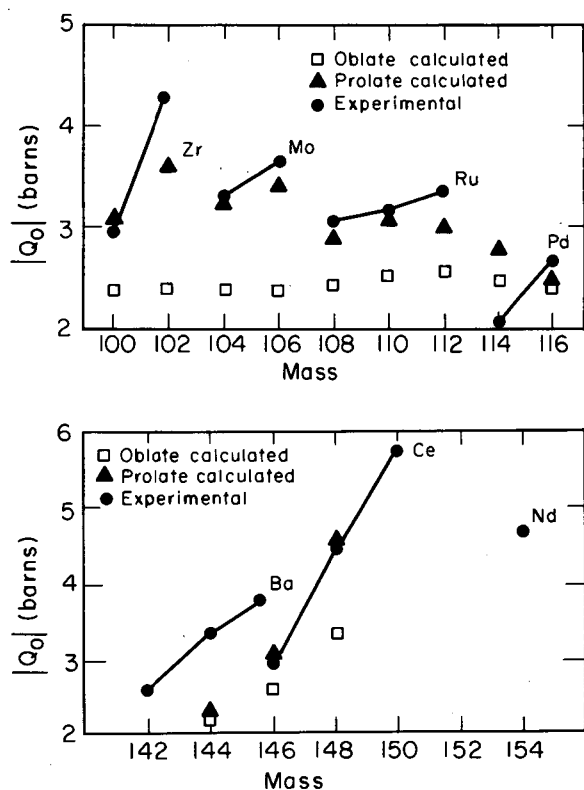


Fig. 6. A comparison of experimental and the calculated results of Ragnarsson, Ref. 7. (XBL737-3430)

### Footnote and References

\* Condensed from a report to be published in the *Translations of the Third Symposium on the Physics and Chemistry of Fission*, Rochester, New York, August 13-17, 1973. IAEA-SM174/62.

1. R. L. Watson, J. B. Wilhelmy, R. C. Jared, C. Ruge, H. R. Bowman, S. G. Thompson, J. O. Rasmussen, *Nucl. Phys.* **A141**, 449 (1970).
2. H. Nifenecker, C. Signarbieux, R. Babinet, J. Poitou, Conference paper no. SM 174/207. The numerical values were obtained by private communication.
3. J. T. Routti, S. G. Prussin, *Nucl. Instr. Methods* **72**, 125 (1969).
4. W. Reisdorf, J. P. Unik, H. C. Griffin, Glendenin, *Nucl. Phys.* **A177**, 337 (1971).
5. P. H. Stelson, L. Grodzins, *Nucl. Data* **A1**, 211 (1965).
6. E. Cheifetz, R. C. Jared, S. G. Thompson, J. B. Wilhelmy, International Conference on the Properties of Nuclei Far from the Region of Beta-Stability, CERN, 7-30, **V2**, 883 (1970).
7. T. A. Khan, D. Hofman, F. Horsch, to be published, *Nucl. Phys.* (1973).
8. Ragnarsson, International Conference on the Properties of Nuclei Far from the Region of Beta-Stability, CERN, 7-30, **V2**, 847 (1970).

### CORE POLARIZATION IN $^{134}\text{Te}^*$

R. A. Naumann,<sup>†</sup> J. B. Wilhelmy,<sup>‡</sup> R. C. Jared, H. Nifenecker,<sup>§</sup> and S. G. Thompson

The double magic nuclei and their adjacent isotopes have yielded much to the development of nuclear shell models. We report here on the enhancement of reduced transition probabilities with respect to their estimates based on the extreme single particle model. Our emphasis is on the newly discovered doubly magic nuclear region near the tin-132 ( $^{132}_{50}\text{Sn}_{82}$ ) core. Already data have been reported for the single particle and single hole nuclei  $^{133}_{51}\text{Sb}_{82}$  and  $^{134}_{50}\text{Sn}_{84}$  where the  $d^{1}_{5/2}$  and  $g^{1}_{7/2}$  proton states and  $g^{-1}_{7/2}$  neutron state are tentatively located.<sup>1</sup> The one-particle one-hole nucleus  $^{132}_{51}\text{Sb}_{81}$  has been investigated following beta decay of the  $40 \pm 1$  sec doubly magic tin-132.<sup>2</sup> The observed positive parity levels have been discussed in terms of the proton-neutron configurations

$$(\pi 1g_{7/2} \text{ or } 2d_{5/2})^1 \times (\nu 3s_{1/2} \text{ or } 2d_{3/2})^{-1}.$$

The low lying states of tellurium-134,  $^{134}_{52}\text{Te}_{82}$ , were first reported by John, Guy, and Wesolowski at Livermore.<sup>3</sup> The first three excited states were located at 1279, 1576 and 1691 keV and were corroborated as being the  $2^+$ ,  $4^+$  and  $6^+$  levels respectively through measurements of prompt fission gamma rays.<sup>4</sup> The Livermore group obtained a 162 nsec half life for the isomeric  $6^+ \rightarrow 4^+$  transition.<sup>3</sup> The wave function for the  $6^+$  state is expected to contain principally the components  $(1g_{7/2})^2$  and  $(1g_{7/2})^1(2d_{5/2})^1$  while the  $4^+$  and  $2^+$  state may contain in addition the  $(2d_{5/2})^2$  component. Heyde and co-workers<sup>5</sup> have calculated eigenfunctions and eigenvalues for a number of even

82-neutron isotones using these basis states and a Gaussian residual interaction containing both triplet and singlet terms. They report that the  $(g_{7/2})^2$  configuration has amplitudes of over 98% in the wavefunctions of both the  $6^+$  and  $4^+$  levels of tellurium-134. Heyde and co-workers also showed that the electric quadrupole lifetime for the  $6^+$  state could be well accounted for using such wavefunctions. Recently the group at Stockholm<sup>6</sup> have repeated this calculation with similar results.

Jared, Nifenecker and Thompson,<sup>7</sup> using a modification of the recoil plunger technique, have measured lifetimes in the 0.05 to 7 nsec range for several transitions de-exciting from prompt fission products formed in the spontaneous fission of  $^{252}\text{Cf}$ . Of particular interest for analysis is the 297 keV  $4^+ \rightarrow 2^+$  transition in  $^{134}\text{Te}$ . This level is populated by a prompt branch and by a branch decaying through the 162 nsec  $6^+$  level. By correcting for the contribution from the delayed  $6^+$  yield as given by John, Guy and Wesolowski<sup>3</sup> and more recently by Clark, Glendenin, and Talbert<sup>8</sup> we have fitted the experimental data of Jared, Nifenecker and Thompson<sup>7</sup> to obtain a half life of  $1.44 \pm$

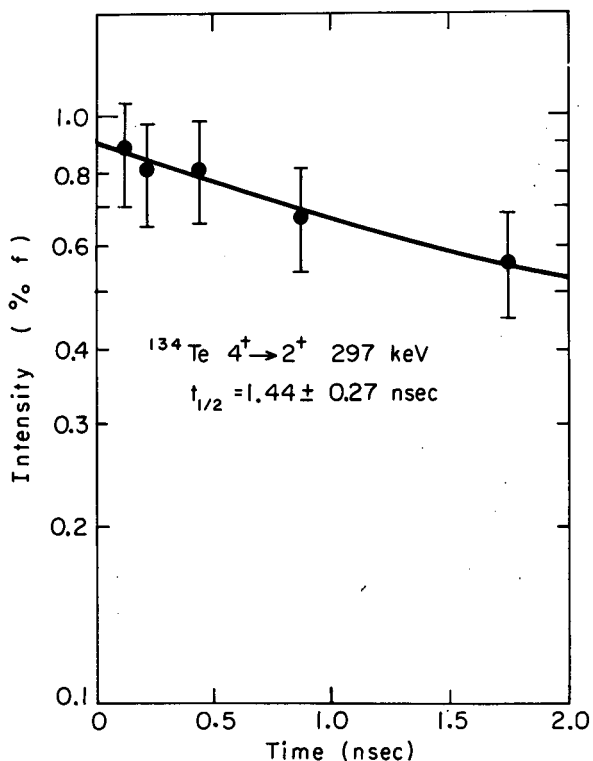


Fig. 1. Experimental points and fitted results for the 297 keV  $4^+ \rightarrow 2^+$  gamma ray observed in the prompt de-excitation of the  $^{252}\text{Cf}$  fission product  $^{134}\text{Te}$ . (XBL-742-2462)

0.27 nsec for the 297 keV transition. The experimental points and fit to the data are shown in Fig. 1.

The theoretical reduced E2 transition probability between the J and J terms of the  $j^2$  proton configuration is given by:

$$B(E2)_{\text{th}} = \frac{|\langle J' || E(2)_a + E(2)_b || J \rangle|^2}{(2J+1)}$$

The numerator may be expressed in terms of the reduced matrix element for the single particle state  $j$ :<sup>9</sup>

$$\langle J' || E(2)_a + E(2)_b || J \rangle = ((2J+1)(2J'+1))^{1/2} (-2) \begin{Bmatrix} J & J' & 2 \\ j & j & j \end{Bmatrix} \langle j || E2 || j \rangle,$$

where<sup>10</sup>

$$\langle j || E(2) || j \rangle = e_{\text{eff}} \left( \frac{(5)(2j+1)^{1/2}}{4\pi} \right) \langle j \ 1/2 \ 2 \ 0 | j \ 1/2 \rangle \langle j | r^2 | j \rangle,$$

and  $e_{\text{eff}}$  is the effective charge of the proton.

We have chosen the diagonal radial matrix elements from the relationships:

$$\langle j | r^2 | j \rangle = \frac{(N+3/2)\hbar}{m\omega}$$

Where  $\hbar\omega = 41 \text{ MeV}/A^{1/3}$ ,  $m$  = nucleon mass, and  $N$  = principal oscillator quantum number. For the case of tellurium-134 this leads to a value  $\langle g_{7/2} | r^2 | g_{7/2} \rangle = 28.7 \text{ fm}^2$ . The effective proton charge may now be evaluated from the ratio of the experimental and theoretical  $B(E2)$  values:  $e_{\text{eff}}/e = (B(E2)_{\text{exp}}/B(E2)_{\text{th}})^{1/2}$ . The results are shown in Table 1 for  $^{134}\text{Te}$ . The close agreement between the effective proton charge evaluated for the  $6^+$  and  $4^+$  states in tellurium-134 confirms the suggestion of Heyde and co-workers that these terms arise principally from the  $(1g_{7/2})^2$  proton configuration.

In Table 1 we also compare the effective proton charges evaluated from the measured lifetimes of other nuclei containing two protons, or two proton holes, beyond a doubly magic core following the same prescriptions used for tellurium-134. There is a consistency for the effective proton charge over the entire mass region, including the neutron rich region of tin-132. This consistency points to a near constant quadrupole core polarization throughout the periodic table independent of mass.

Table 1. Core polarization in nuclei: 2 protons, or 2 proton holes, removed from doubly closed shells.

Nucleus	Level	Half life (nsec)	$\Delta E$ (keV)	$\alpha_T^{(g)}$	$\langle j r^2 j\rangle$ (fm <sup>2</sup> )	$B(E2)_{Ex}$ (e <sup>2</sup> fm <sup>4</sup> )	$B(E2)_{Th}$ (e <sup>2</sup> fm <sup>4</sup> )	$e_{eff}/e$
<sup>210</sup> <sub>84</sub> Po <sub>126</sub>	(a) 6 <sup>+</sup>	38. ± 5	46.7	295	39.1	227. ± 37.	94.	1.56 ± 0.13
	4 <sup>+</sup>	1.8 ± 0.2	246.	0.24		283. ± 32.	136.	1.44 ± 0.08
<sup>134</sup> <sub>52</sub> Te <sub>82</sub>	(b) 6 <sup>+</sup>	162. ± 7	115.	1.06	28.5	85. ± 6.	28.	1.74 ± 0.06
	4 <sup>+</sup>	1.44 ± 0.27	297.	0.04		164. ± 31.	61.	1.64 ± 0.15
<sup>92</sup> <sub>42</sub> Mo <sub>50</sub>	(c) 8 <sup>+</sup>	191. ± 7	148.	0.30	25.1	32.3 ± 1.4	15.5	1.45 ± 0.03
	(c) 6 <sup>+</sup>	1.54 ± 0.05*(g)	330.	0.016		79. ± 2.5	38.6	1.43 ± 0.02
	(d) 2 <sup>+</sup>	(3.0 <sup>+1.5</sup> <sub>-1.0</sub> ) × 10 <sup>-4</sup>	1509.	--		244. <sup>+117.</sup> <sub>- 83.</sub>	49.	2.24 <sup>+0.48</sup> <sub>-0.42</sub>
<sup>54</sup> <sub>26</sub> Fe <sub>28</sub>	(e) 6 <sup>+</sup>	1.18 ± 0.03	411.		17.2	40.8 ± 1.0	10.2	2.00 ± 0.03
	(f) 2 <sup>+</sup>	(0.90 ± 0.10) × 10 <sup>-3</sup>	1408.			104. ± 10.	22.4	2.15 ± 0.10
<sup>50</sup> <sub>22</sub> Ti <sub>28</sub>	(e) 6 <sup>+</sup>	0.44 ± 0.02	524.		16.8	32.9 ± 1.6	9.7	1.84 ± 0.04
	(f) 2 <sup>+</sup>	(0.90 ± 0.23) × 10 <sup>-3</sup>	1554.			69.6 ± 17.4	21.4	1.80 ± 0.22

(a) Ref. 11. (b) Ref. 3. (c) Ref. 12. (d) Ref. 13. (e) Ref. 14. (f) Ref. 15. (g) 85% branch to 4<sup>+</sup> state. (h) Theoretical values taken from Ref. 16. For error propagation we have assumed a 10% uncertainty in  $\alpha_T$ .

#### Footnotes and References

\* Condensed from a report to be published in Physical Review Letters.

† Los Alamos Scientific Laboratory, Los Alamos, NM.

‡ Present address: Departments of Chemistry and Physics, Princeton University, Princeton, NJ.

§ Present address: CEA, Centre d' Études Nucleaires de Saclay, France.

1. G. B. Holm, S. Borg, B. Rydberg, CERN Report 70-30 (1970).

2. A. Kerek, G. B. Holm, P. Carlé and J. McDonald, Nucl. Physics A195, 159 (1972).

3. W. John, F. W. Guy and J. J. Wesolowski, Phys. Rev. C 2, 1451 (1970).

4. J. B. Wilhelmy, S. G. Thompson, R. C. Jared, and E. Cheifetz, Phys. Rev. Letters 25, 1122 (1970).

5. K. Heyde, M. Waroquier, G. VandenBerghe, Phys. Letters 35B, 211 (1971).

6. A. Kerek, G. B. Holm, S. Borg and L. E. deGeer, Nucl. Phys. A195, 177 (1972).

7. R. C. Jared, H. Nifenecker and S. G. Thompson, Third Symposium on the Physics and Chemistry of Fission, Rochester, N. Y., IAEA-SM-174/62, International Atomic Energy Agency, Vienna (1973). Preprint: Lawrence Berkeley Laboratory, Report LBL-1963.

8. R. G. Clark, L. E. Glendenin, and W. L. Talbert, Third Symposium on the Physics and Chemistry of Fission, Rochester, N. Y., IAEA-SM-174/86, International Atomic Energy Agency, Vienna (1973).



9. Bohr and Mottelson, Nuclear Structure Vol. I, (W. A. Benjamin Inc., (1969), p. 84.
10. Ibid. p. 363.
11. E. G. Funk, Jr., H. J. Prask, F. Schima, J. McNulty, and J. W. Mihelich, Phys. Rev. **129**, 757 (1963).
12. S. Cochavi, J. M. McDonald, and D. B. Fossan, Phys. Rev. C **3**, 1352 (1971).
13. D. H. Youngblood, R. L. Kozub, and J. C. Hill, Nucl. Phys. A **166**, 198 (1971).
14. S. Cochavi, D. B. Fossan, S. H. Henson, D. E. Alburger, and E. K. Warburton, Phys. Rev. C **2**, 2241 (1970).
15. P. H. Stelson, and L. Grodzins, Nuclear Data A **1**, 21 (1965).
16. R. S. Hager and E. C. Seltzer, Nuclear Data **4**, 1, (1968).

### SIMULTANEOUS EMISSION OF TWO LIGHT CHARGED PARTICLES IN SPONTANEOUS FISSION OF $^{252}\text{Cf}^*$

S. K. Kataria, E. Nardi, and S. G. Thompson

The process of nuclear fission accompanied by a third light-charged particle (LCP) has been the subject of many investigations.<sup>1</sup> Recently, Kapoor, et al.<sup>2</sup> found evidence for the simultaneous emission of two LCP in coincidence with fission fragments in the thermal neutron-induced fission of  $^{235}\text{U}$ . In the present work we have observed the occurrence of the simultaneous emission of two LCP in the spontaneous fission of  $^{252}\text{Cf}$ , we have identified the coincident LCP and obtained their energy distributions, and we have measured the angular correlation between the two particles.

Two semiconductor particle telescopes were placed on the opposite sides of a strong  $^{252}\text{Cf}$  source as shown in Fig. 1(a). The source

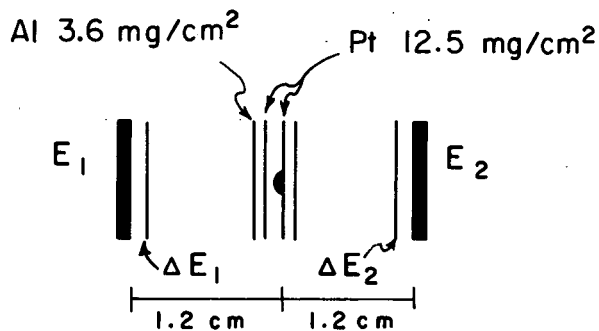


Fig. 1(a). The schematic diagram of the detector-source configuration used in Part 1 experiment. The first set of measurements were made using  $50\mu\text{eV}$   $\Delta E$  and  $48\mu\text{eV}$   $\Delta E_2$  counter telescopes. The second measurement used  $37\mu\text{eV}$   $\Delta E_1$  and  $24\mu\text{eV}$   $\Delta E_2$  counter telescopes.

(XBL735-3036)

strength was  $0.6 \times 10^7$  fissions per minute. Two measurements were made using different thicknesses for the  $\Delta E$  counters in the particle telescopes. The first measurement was carried out with a  $50\mu\text{eV}$   $\Delta E_1$  and a  $48\mu\text{eV}$   $\Delta E_2$  counter. The second measurement was carried out using a  $37\mu\text{eV}$   $\Delta E_1$  and a  $24\mu\text{eV}$   $\Delta E_2$  counter to study the low energy part of the alpha particle distributions in quaternary fission.

A four parameter data acquisition system was used to record the information from the coincidence events. The four parameter system was triggered by the occurrence of a fast coincidence between the two  $\Delta E$  counters. Therefore, all the two-fold events ( $\Delta E_1 - \Delta E_2$ ), three-fold events ( $\Delta E_1 - \text{TEL}_2$  and vice versa), and four-fold events ( $\text{TEL}_1 - \text{TEL}_2$ ) were recorded. The data analysis was done off-line. The particle identification was performed by using a power law approximation to the range-energy curves.<sup>3</sup>

The angular correlation experiment was carried out with a  $^{252}\text{Cf}$  source, stronger by an order of magnitude than the one used in the first experiment. With the new source, the true to chance rate decreased to a ratio of 2 to 1 within the two-telescope set up. Therefore, in order to have a reasonable true to chance ratio both telescopes were replaced by semiconductor detectors and the electronic configuration was also modified. Two time-pickoff units were used to obtain the timing signals which were fed to a time to amplitude converter (TAC). The two linear energy signals from the two counters and the linear time signal from the TAC were recorded event by event on the multiparameter data recording system. The time distribution obtained showed a time resolution of 3 nsec. The window on the time signal

was set at 6 nsec as compared to 40 nsec in the first part. The true to chance ratio varied from 20 to 1 for the 45° measurement to 8 to 1 for the 90° measurement.

Figure 1(b) shows the various configurations of the two detectors which were used to obtain the angular correlation between the two LCP. These measurements were divided into three sets. In the first set, the distance between the detectors and the source was 2.0 cm for the 90° and 180° measurements and 2.2 cm

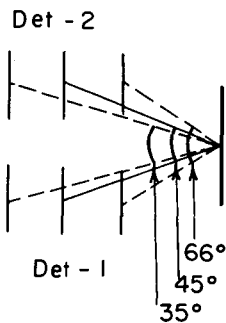
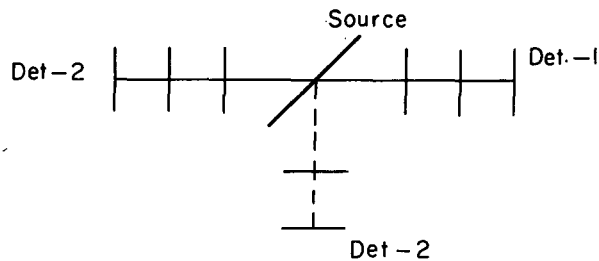


Fig. 1(b). The schematic diagram of the eight measurements of the Part 2 experiment. Three different distances were used for 180° and two distances were used for 90° measurements. Three measurements were made for 66°, 45° and 35° angles between the two detectors.

(XBL735-3031)

Table I. The total number of events for various types of coincidences between the two light-charged particles (LCP) emitted in the spontaneous fission of  $^{252}\text{Cf}$  observed in the experiment using  $50\mu\Delta E$  telescope systems. (p = protons, t = tritons, and  $\alpha$  = alpha particles)

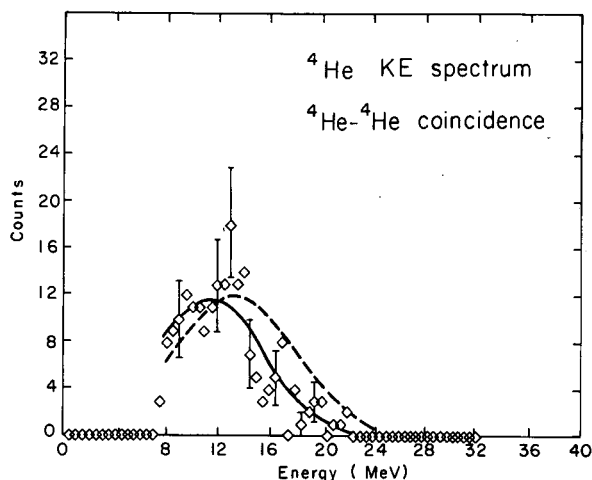
Telescope 1	Telescope 2	No. of events
p	- p	10
p	- t	0
p	- $\alpha$	16
t	- p	5
t	- t	1
t	- $\alpha$	66
$\alpha$	- p	12
$\alpha$	- t	82
$\alpha$	- $\alpha$	551

for the 66° measurement. In the second set these distances were 3.2 cm for the 90° and 180° measurement and 3.5 cm for the 45° measurement. The third set includes measurements for angles 180° and 35°; the corresponding distances were 4.5 cm and 4.75 cm. For the 90° and 180° measurements the effective thickness of the absorber foils were identical for both detectors (1.4 times thickness), whereas for 66°, 45°, and 35° the effective thickness of the absorber foils varied (1.2 - 1.15 times thickness).

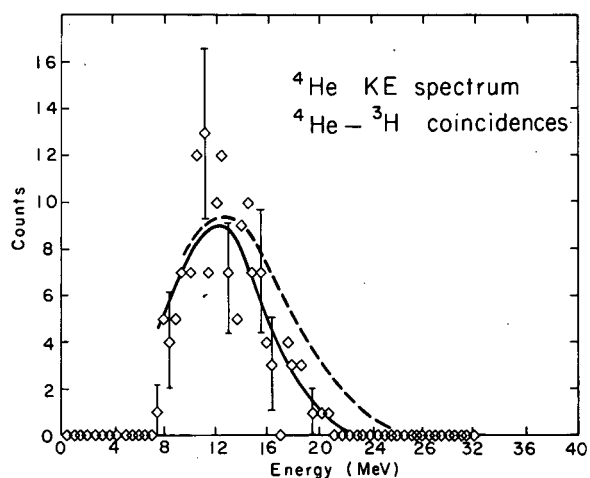
The coincident events were predominantly of the type  $^4\text{He}-^4\text{He}$  but  $^4\text{He}-^3\text{H}$  and  $^4\text{He}-^1\text{H}$  events were also observed. No coincident events involving particles heavier than  $Z = 2$  were observed. A significant part of the events involving  $^1\text{H}$  are due to the fast neutron-induced (n, p) reaction in the detectors in coincidence with long range alpha particles. However, the contribution of (n, p) reaction to the ( $^1\text{H}, ^4\text{He}$ ) events where the energy of  $^1\text{H}$  is larger than 5 MeV is insignificant.<sup>4</sup> Table I

Table II. The relative abundances of protons tritons and alpha particles normalized to unity, observed in each telescope for quaternary and ternary fission events with  $50\mu\Delta E$  telescopes in the experiment Set 1.

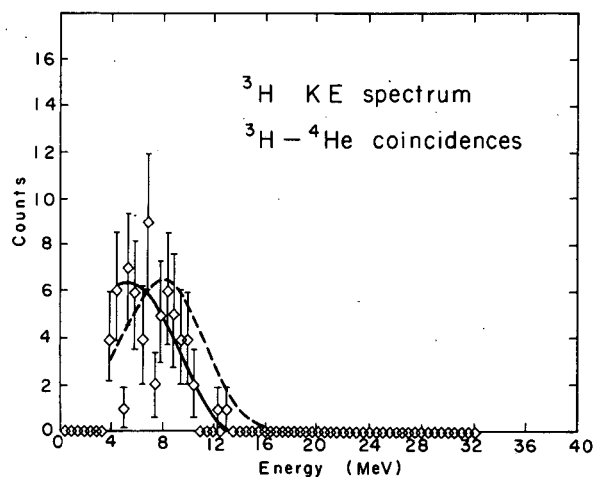
Relative Prob.	Quaternary		Ternary	
	Tel-1	Tel-2	Tel-1	Tel-2
Protons	$.035 \pm .01$	$.03 \pm .01$	$.03 \pm .01$	$.015 \pm .01$
Tritons	$.097 \pm .01$	$0.11 \pm .01$	$.09 \pm .01$	$.09 \pm .01$
Alphas	$0.87 \pm .01$	$0.85 \pm 0.01$	$.88 \pm .01$	$.895 \pm .01$
$\text{He}^6$			$.01 \pm .005$	$.01 \pm .005$



(a)  ${}^4\text{He}$  K.E. spectrum in  ${}^4\text{He} - {}^4\text{He}$  events with a  $24\mu$   $\Delta E$  telescope. (XBL735-3029)



(b)  ${}^4\text{He}$  K.E. spectrum in  ${}^4\text{He} - {}^3\text{H}$  events with a  $50\mu$   $\Delta E$  telescope. (XBL735-3028)



(c)  ${}^3\text{H}$  K.E. spectrum in  ${}^4\text{He} - {}^3\text{H}$  events with  $50\mu$   $\Delta E$  telescope. (XBL735-3026)

shows the observed number of various types of coincidence events using thick  $50\mu$   $\Delta E$  counter telescopes. Table II contains the relative yields of protons, tritons,  ${}^4\text{He}$  and  ${}^6\text{He}$  normalized to unity for each telescope in ternary and quaternary fission events. It can be seen that within the statistical error these relative yields in normal ternary fission events are equal to the corresponding relative yields in the fission events with two light-charged particles (quaternary fission).

Figures 2(a) through (c) show the energy distribution of alphas, tritons, and protons observed in the quaternary fission. The smooth curve passing through the experimental points is a calculated curve. It is obtained by fitting to the experimental spectrum a Gaussian distribution with  $\hat{E}$ ,  $\hat{\sigma}$  as the most probable energy and variance parameter; after making corrections for the energy loss in the absorber foils. These energy loss corrections were performed using a Monte Carlo technique to take into account the finite source-detector geometry. The fitted values of  $\hat{E}$  and  $\hat{\sigma}$  for various spectra are shown in Table III. The dashed curve shown in these figures is the corresponding energy distribution observed in normal ternary fission using the same telescopes. Figure 2(a) shows the same energy spectrum obtained in the second measurement with the  $24\mu$   $\Delta E$  counter telescope. The energy distribution of alpha particles in coincidence with tritons is shown in Fig. 2(b). From these figures it is concluded that the energy distributions of the alpha particles in quaternary fission is lower as compared to normal ternary fission by about 2 MeV as given in Table III. It can also be concluded that the alpha energy distribution in quaternary fission does not depend on the charge of the coincident light particle. The mean energy of the alpha particles does not depend on the energy of the coincident alpha particle as shown in Fig. 3. Figure 2(c) shows the energy distribution of tritons in coincidence with alpha particles. The energy spectrum in quaternary fission is seen to be lower as compared to the corresponding distribution in the normal ternary fission. The difference in most probable energy  $\hat{E}$  for tritons in quaternary and ternary fission is about 2.0 MeV.

The experimental results of the eight measurements are given in Table IV. The lower energy cutoff used in the off-line analysis of the data was 5.0 MeV in the two counters to reduce

Fig. 2. The kinetic energy distribution of LCP in quaternary fission. The dashed curve is the kinetic energy distribution of LCP in normal ternary fission. The continuous curve is the fitted curve as explained in the text.

Table III. Experimental and fitted parameters for energy distributions shown in Fig. 2(a) to (e).  $\hat{E}$  and  $\hat{\sigma}$  are the most probable energy and the variance parameters of the Gaussian distribution. Fitted  $\bar{E}$  and  $\bar{\sigma}$  represent the mean energy and the variance of the energy distribution with ( $E_{\min} = 8$  MeV for  $\alpha$ -particles and  $E_{\min} = 4.0$  MeV for tritons) computed after making corrections for the energy loss in the absorber cover foils to the Gaussian distribution. Experimental  $\bar{E}$  and  $\bar{\sigma}$  are the mean energies and the variance calculated from the experimentally observed energy distributions.

Identification	Fitted Parameters				Experimental	
	$\hat{E}$	$\hat{\sigma}$	$\bar{E}$	$\bar{\sigma}$	$\bar{E}$	$\bar{\sigma}$
Set-1. Alpha's in quaternary ( $\alpha$ - $\alpha$ ) events	$13.5 \pm 0.5$	4.0	12.9	2.8	$12.9 \pm 0.5$	2.9
Set-1. Alpha's in quaternary ( $\alpha$ -t) events	$14.00 \pm 0.8$	4.0	13.06	3.2	$12.75 \pm 0.5$	2.9
Set-1. Alpha's in ternary events	$16.1 \pm 0.2$	4.4	14.5	3.6	$14.2 \pm 0.2$	3.7
Set-2. Alpha's in quaternary ( $\alpha$ - $\alpha$ ) events	$14.0 \pm 0.6$	4.2	12.9	3.4	$12.7 \pm 0.6$	3.6
Set-2. Alpha's in ternary fission	$16.2 \pm 0.2$	4.4	14.2	4.2	$14.1 \pm 0.2$	4.2
Set-1. Tritons in quaternary (t- $\alpha$ ) events	$6.6 \pm 0.8$	2.6	7.2	1.9	$7.3 \pm 0.5$	2.1
Set-1. Tritons in ternary events	$8.8 \pm 0.5$	2.8	8.7	3.0	$8.8 \pm 0.5$	2.8

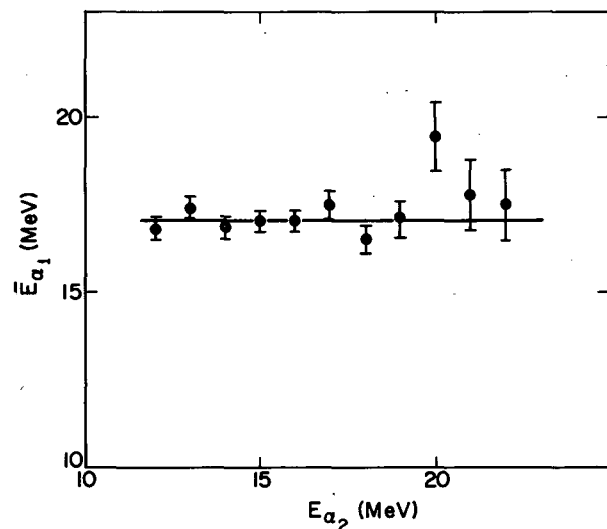


Fig. 3. The mean kinetic energy distribution of alpha particle detected in Telescope 1 plotted as a function of the kinetic energy of the coincident alpha particle detected in Telescope 2. (XBL7210-4219)

the contribution of the fast neutron induced reactions in the detector material which are in coincidence with the normal ternary fission events. Figure 4 shows the plot of the probability of quaternary fission versus  $\Theta$ .

The mean energies of particles detected in one counter does not depend on the energy of the particle detected in the other counter. This conclusion holds for all the measurements. Moreover, it is observed that the most probable energy  $\hat{E}$  of the particles in quaternary fission does not depend on the angle between the two counters as shown in Table V for four measurements. The total probability obtained by integrating  $P_4(\theta)$  is  $(1.5 \pm 0.5 \cdot 10^{-6})$  per binary fission.

The energy distributions of tritons and of alpha particles in quaternary fission are very much similar to the corresponding energy distributions in the normal ternary fission except for the fact that mean energies for these particles in quaternary fission are lower than in ternary fission. The angular correlation experiment shows that the yield at  $90^\circ$  is smaller than at  $30^\circ$  or  $180^\circ$ , although the yield at  $30^\circ$  is higher than the yield at  $180^\circ$ . It seems that the emission mechanism of light particles

Table IV. Summary of angular correlation experimental data.  $\bar{E}_1$  and  $\bar{E}_2$  are the mean energies of the distribution observed in detectors (F1) and (F2) with  $E_{\min} = 5$  MeV. Quantity P is a measure of the angular correlation as defined in the text.

Set-Det	Angle	Time (hr)	Events	P	Quaternary		Ternary	
					$\bar{E}_1$	$\bar{E}_2$	$\bar{E}_1$	$\bar{E}_2$
A.	60°	495	581	2.8 ± 0.3	10.1 ± 0.2	9.85 ± 0.2	12.61 ± 0.2	12.72 ± 0.2
	90	220	309	1.65 ± 0.2	10.7 ± 0.5	10.0 ± 0.5	12.20 ± 0.2	11.91 ± 0.2
	180	187	335	2.2 ± 0.2	9.2 ± 0.6	10.2 ± 0.4	11.77 ± 0.4	11.71 ± 0.2
B.	45°	520	410	10.2 ± 0.6	10.1 ± 0.2	9.8 ± 0.2	11.30 ± 0.2	12.20 ± 0.2
	90	520	113	1.5 ± 0.2	11.2 ± 0.5	9.9 ± 0.5	13.5 ± 0.3	12.7 ± 0.3
	180	384	109	2.3 ± 0.2	10.2 ± 0.5	10.2 ± 0.5	12.2 ± 0.3	12.7 ± 0.3
C.	35°	362	79	8.5 ± 1.0	9.5 ± 0.7	9.4 ± 0.7	11.91 ± 0.2	12.3 ± 0.2
	180	691	52	2.1 ± 0.5	9.3 ± 0.8	9.4 ± 0.8	12.37 ± 0.2	11.8 ± 0.2

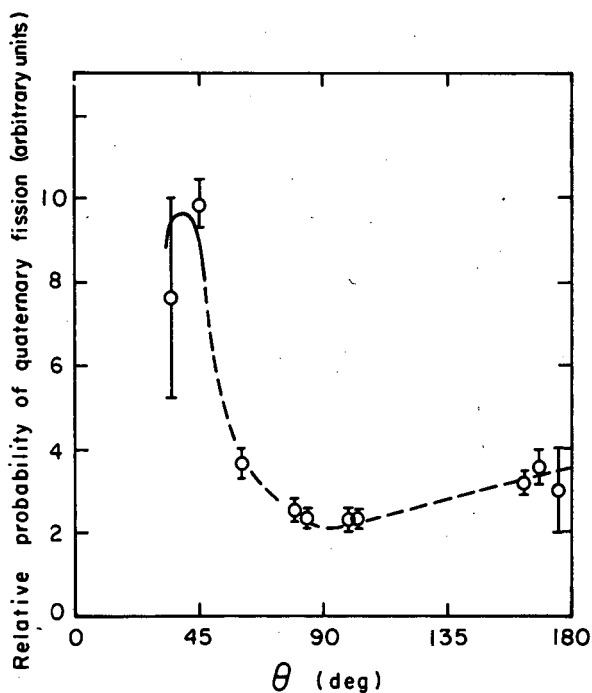


Fig. 4(a). Plot of the angular correlation between the two light-charged particles corrected for the energy loss in the absorber foils and the finite geometry of the detector-source geometry. (XBL735-3033)

in quaternary fission is similar to the emission mechanism of light particles in ternary fission. If one assumes that the light particles in ternary fission are produced at scission from one of the two fragments when the interaction between the two fragments has vanished, then the quaternary fission events represent the cases where each fragment has contributed one LCP. Under the assumption that each fragment can emit only one LCP with probability  $P_1$ , which does not depend on the other fragment, the total probability of quaternary fission is  $P_4 = P_1 P_2$ . The probability of ternary fission will be equal to  $P_1 + P_2$ . Taking the experimental value of  $P_1 + P_2 = 1/300$  and assuming  $P_1 = P_2$ ,  $P_4$  is equal to  $2.6 \times 10^{-6}$  per fission, which is in good agreement with the experimental value of  $P_4$ . This hypothesis is also consistent with the constancy of relative abundances of tritons and  $^4\text{He}$  in two types of fission events.

Under the assumption that each LCP in the quaternary fission has a sharply peaked angular distribution with respect to the motion of the fission fragment as in normal ternary fission and assuming that the two LCP are emitted statistically independent of each other, there is an angular correlation between the two LCP as shown in Fig. 4(b). The calculated curve is symmetrical around 90°. The magnitude of  $W(180^\circ)/W(90^\circ)$  quantity is of the order observed in the experiment. However, the experimental correlation is not symmetrical around 90° as calculated under the hypothesis.

Table V. Fitted parameters  $\hat{E}$  and  $\hat{\sigma}$  are the most probable energy and the variance parameters of the Gaussian distributions for alpha particles fitted to the experimental spectra observed in angular correlation experiment. The energy loss corrections used were based on assumed values of triton/alpha probability and the assumed parameters for triton energy distribution as observed in part 1 experiment. The fits were made only to four measurements.

Set	Detector	Quaternary		Ternary		
		$\hat{E}$	$\sigma$	$\hat{E}$	$\sigma$	
A 66°	i	13.15 ± 0.8	4.20	15.3 ± 0.5	4.72	
	ii	12.70 ± 0.8	3.65	16.30 ± 0.5	4.90	
	90°	i	14.08 ± 0.8	4.0	15.6 ± 0.5	4.6
		ii	15.0 ± 0.8	4.8	16.05 ± 0.5	4.21
180°	i	14.22 ± 0.8	3.63	15.0 ± 0.5	4.70	
	ii	13.5 ± 0.8	4.3	15.5 ± 0.5	4.45	
B 45°	i	11.81 ± 0.8	4.20	14.4 ± 0.	4.24	
	ii	12.88 ± 0.8	3.65	15.2 ± 0.5	4.20	

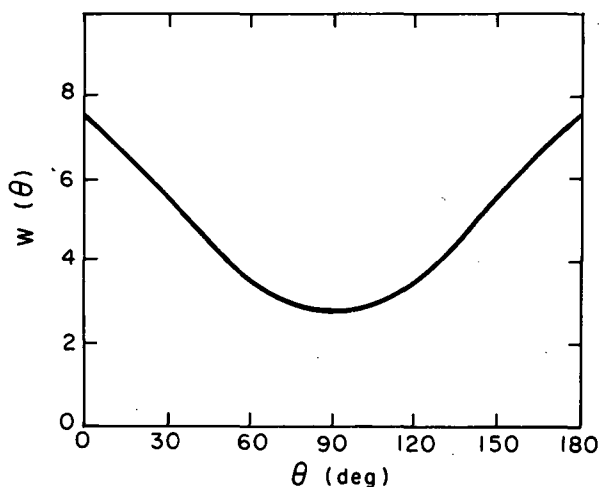


Fig. 4(b). The angular correlation expected for quaternary fission based on the angular distribution of light-charged particles in ternary fission. (XBL735-3034)

#### Footnote and References

\* This is a condensation of a paper presented at the Third Symposium on the Physics and Chemistry of Fission at Rochester, NY, August 13-17, 1973. (See LBL-1905).

1. I. Halpern, *Ann. Rev. Nucl. Sci.* **21**, 245 (1971).
2. S. S. Kapoor, R. K. Chaudhary, S.K. Kataria, S. R. S. Murthy, and V. S. Ramamurthy, presented at the Nuclear Physics and Solid State Physics Symposium, Chandigarh, India, December 28-31, 1972. (Proceedings to be published).
3. F. S. Goulding, D. A. Landis, J. Cerny, R. H. Pehl, *IEEE Trans. Nucl. Sci.* **NS-13**, 514 (1966).
4. S. W. Casper, J. Cerny, and R. C. Gatti, *Phys. Rev.* **154**, 1193 (1967).

CHARGE DISTRIBUTION OF THE FRAGMENTS EMITTED  
IN THE REACTION BETWEEN  $^{63,65}\text{Cu}$  AND 606-MeV  $^{84}\text{Kr}$

S. G. Thompson, L. G. Moretto, R. C. Jared, R. P. Babinet,  
R. C. Gatti, and J. L. Levinson

Very broad charge distributions have been observed for the particles emitted in the reaction between  $^{107,109}\text{Ag}$  and various heavy ions like  $^{14}\text{N}$  and  $^{40}\text{Ar}$ . These particles, characterized by low kinetic energies, appear to be the result of complete relaxation of the internal degrees of freedom. It is somewhat harder to decide whether the charge distributions can be interpreted as arising from statistical emission or whether such distributions are associated with various equilibrium processes.

In order to investigate the latter problem the charge distribution of the particles emitted in the reaction between  $^{63,65}\text{Cu}$  and  $^{84}\text{Kr}$  has been measured. The  $^{84}\text{Kr}$  beam has been provided by the Berkeley SuperHILAC. The experimental setup is the same used for the study of Ar-induced reactions and is described in another report. The telescope detector, obtained by combining a  $\Delta E$  gas proportional counter with an E solid state detector was placed at  $15^\circ$  with respect to the beam direction. The  $\Delta E$  and E pulses were amplified, digitized and recorded on magnetic tape. An off-line analysis of the data yielded an  $E_{\text{total}}$ ,  $\Delta E$  mass in which the ridges corresponding to individual charges could be identified. Atomic numbers as high as 36 could be identified, although in this high Z region the particles with adjacent Z were only partially separated. The kinetic energy distributions appeared to be low in energy and very broad. The breadth of these distributions seems to be due mainly to a kinematic effect which makes a fixed center of mass energy vary with angle very dramatically in the lab system. The kinetic energy distributions appeared to be free from experimental cut-offs and could be integrated, yielding the charge distribution shown in Fig. 1. The cross sections increase nearly exponentially with increasing atomic number up to  $Z = 22$ . The yields remain approximately constant from  $Z = 22$  to the neighborhood of the projectile

atomic number, where the yield again rises steeply. The increase in yield close to the Z of the projectile is also associated with a high energy component in the kinetic energy distribution which is absent for the other atomic numbers. Because of the different velocities of the various particles and because of the possibility of kinematic double solutions, it is not possible to relate the observed charge distributions with the charge distribution at a fixed angle in the center of mass. More work is in progress in order to evaluate the charge distribution as a function of center of mass angle.

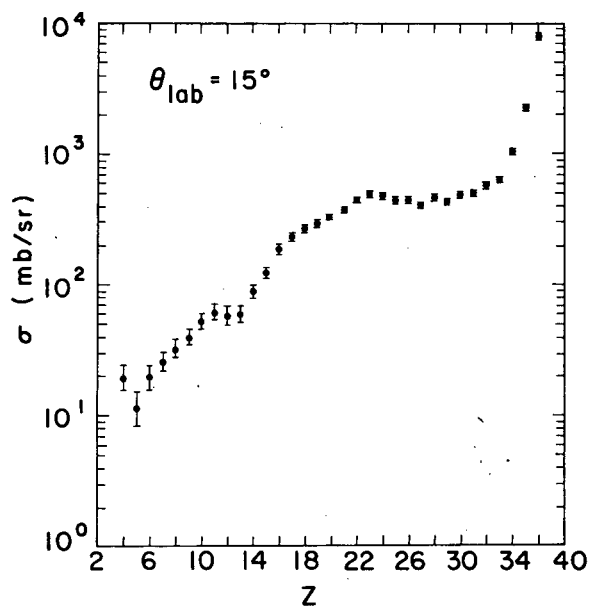


Fig. 1. Charge distribution for the particles emitted in the reaction between  $^{63,65}\text{Cu}$  with 606 MeV  $^{84}\text{Kr}$ . (XBL 742-2463)

STUDY OF THE CHARGED PARTICLES PRODUCED IN THE  
REACTION BETWEEN  $^{107, 109}\text{Ag}$  AND 288 MeV  $^{40}\text{Ar}$

S. G. Thompson, L. G. Moretto, R. C. Jared, R. C. Gatti, R. P. Babinet  
H. Gutbrod, D. Heunemann, J. C. Hunter, R. C. Schmitt, and J. L. Levinson

The reactions induced by large heavy ions are expected to enhance the role played by collective degrees of freedom and to exhibit substantial macroscopic features. The reaction between a  $^{107, 109}\text{Ag}$  target and a 288-MeV  $^{40}\text{Ar}$  seems to support such a view. A great variety of charged particles appear to be emitted in such a reaction. The details of the charge, kinetic energy and angular distributions may provide a suitable experimental ground for the testing of macroscopic phenomenological models.

The experiment has been performed by bombarding a thin Ag target with the 288-MeV Ar beam provided by the SuperHILAC. A schematic diagram of the equipment is shown in Fig. 1. Two  $\Delta E$ -E telescopes were used to identify the atomic number of the particles. One of the telescopes was composed of a solid state  $\Delta E$  detector ( $\sim 9 \mu\text{m}$  thick) and by a solid

state E detector ( $\sim 300 \mu\text{m}$  thick). The other telescope was composed of a  $\Delta E$  gas proportional counter and by an E solid state detector. The latter telescope appeared to be more versatile because of the possibility of changing the thickness of the  $\Delta E$  detector simply by changing the gas pressure.

Both telescopes were mounted on movable arms so that the angle at which the particles were collected could be changed. The linear pulses coming from both telescopes were properly amplified, digitized by means of a multiplexer and ADC system and fed to a PDP-9 computer together with the necessary identification pulses. The experimental data could be displayed on-line in the form of a  $\Delta E$ -E map by means of a storage oscilloscope. Furthermore, the data were recorded on magnetic tape which was used to produce, off-line, an E- $\Delta E$  map. Depending upon the angle and the telescopes, the atomic number of the identified particles ranged from 3-5 to above 18 (Fig. 2). The kinetic energy distributions, corrected for target thickness and dead layers, appear as broad gaussian-like peaks with a very low most probable energy. After transformation to the

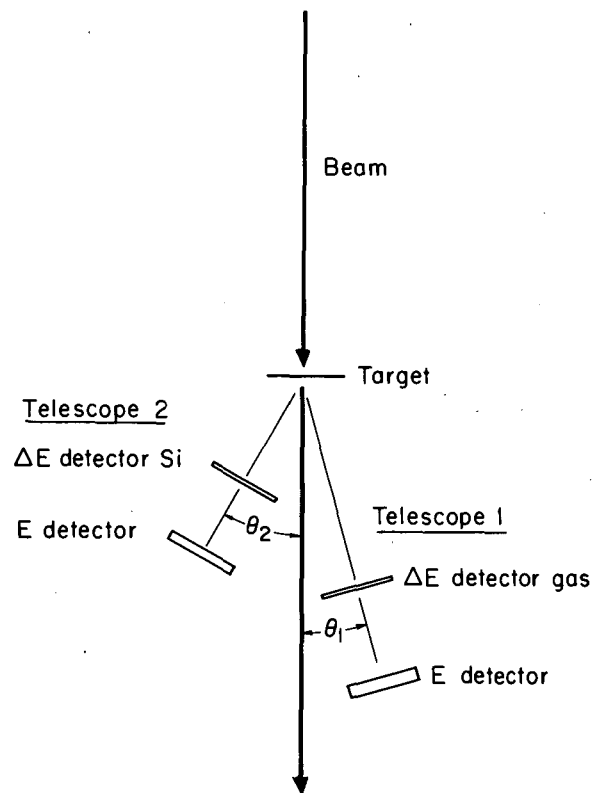


Fig. 1. Schematic diagram of the experimental apparatus. (XBL 7312-7023)

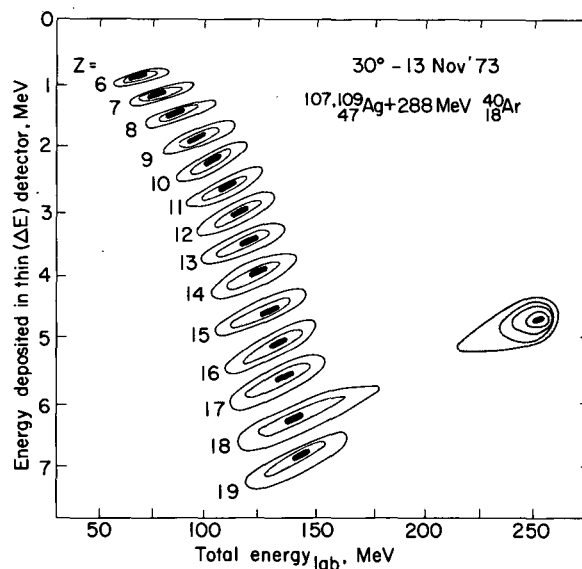


Fig. 2.  $\Delta E$ - $E_{\text{total}}$  map of the events detected by a gas  $\Delta E$  telescope. The high energy peak corresponding to  $Z = 18$  corresponds to the Ar elastic scattering. (XBL 7312-7026)



center of mass system, the kinetic energy distributions seem to be essentially independent of angle. The independence of the kinetic energy distributions upon angle supports the assumption of a two body decay. An example of the kinetic energy distributions in the lab system and in the center of mass system can be seen in Fig. 3. The most probable kinetic energies in the center of mass appear to be very low, in the neighborhood of the energies expected for two spheres or spheroids at their equilibrium deformation repelled by their Coulomb interaction (Fig. 4). This indicates that

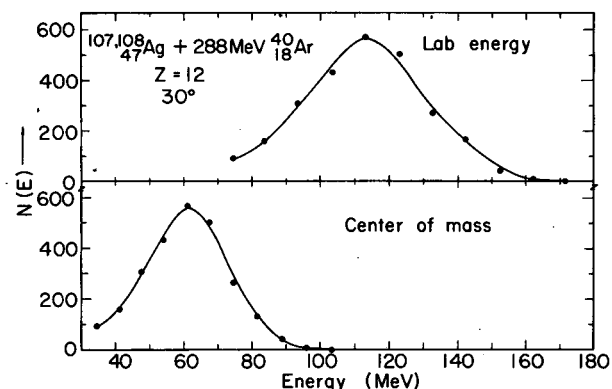


Fig. 3. Example of kinetic energy distribution in the laboratory and center of mass systems. (XBL7312-7025)

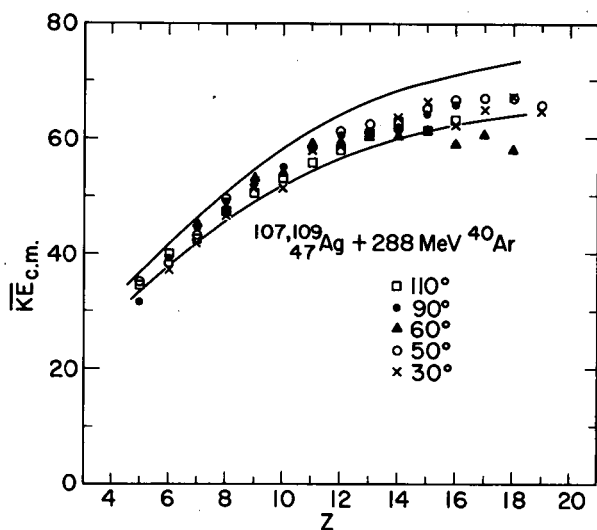


Fig. 4. Most probable kinetic energies in the center of mass system. The upper and lower lines correspond to the energies arising from the Coulomb repulsion of two spheres and two spheroids at equilibrium deformation respectively. Notice how the experimental energies appear to be almost independent of angle. (XBL7312-7027)

a large amount of the initial kinetic energy has disappeared and has been presumably distributed among the internal degrees of freedom of the system. Since the kinetic energy distributions are observed in their entirety and no instrumental cut-off is present, one can simply integrate the kinetic energy distribution associated with each of the Z's and obtain a meaningful cross section. The cross sections as a function of Z for various angles are shown in Fig. 5. The cross sections increase with atomic number and show a rather pronounced even-odd effect. All the cross sections initially decrease with angle but eventually become flat as one moves into the backward hemisphere. This can be seen best in the center of mass angular distributions shown in Fig. 6. These angular distributions are not symmetric about 90° as one might expect from a compound nucleus reaction. However there is a substantial cross section in the backward hemisphere.

The interpretation of these data at the moment is still very tentative because of various ambiguities. On one hand the kinetic energy distributions indicate, both with their most probable values and their widths, that a nearly complete thermalization of the kinetic energy has taken place. This is consistent with a compound nucleus emission for which a complete thermalization in the spectra of the emitted particles is a necessary condition. Still, one may envisage non-compound nucleus processes for which a complete relaxation takes place only

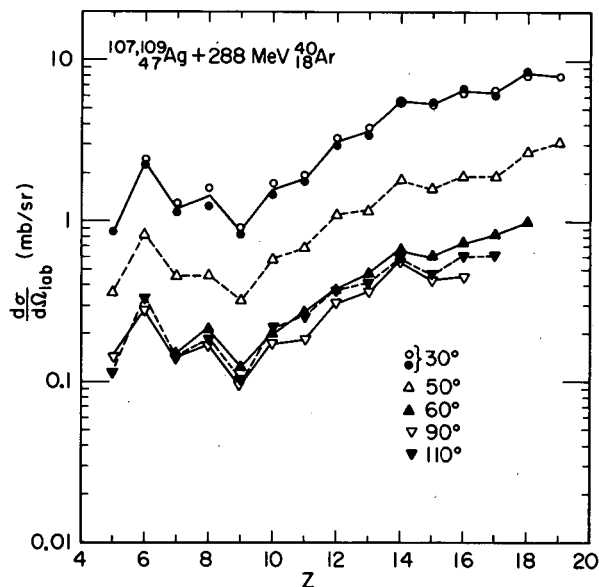
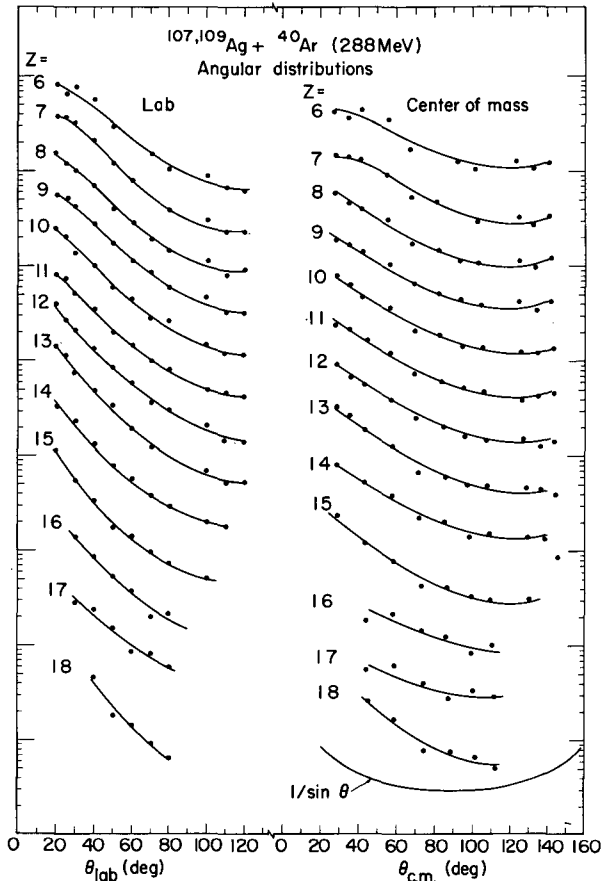


Fig. 5. Cross section for the production of particles as a function of atomic number for various angles. (XBL7312-7024)



insofar as the internal degrees of freedom are concerned, while the collective degrees of freedom (like the mass and charge asymmetry degrees of freedom) are not equilibrated. The angular distributions add support to this theory. The lack of symmetry about  $90^\circ$  indicates that the dynamical features associated with the incoming channel have not completely disappeared. A possible reason for the excess forward peaking may be the fact that the decay time is shorter or at least comparable with the nuclear rotation period.

So it seems possible to obtain a qualitative picture of the reaction in terms of collective and macroscopical features, but a quantitative phenomenological model has yet to be developed.

Fig. 6. Center of mass angular distributions for two different Z's. (XBL7312-7038)

### HIGHLY INELASTIC EMISSION OF HEAVY CHARGED PARTICLES IN THE REACTION BETWEEN $^{107,109}\text{Ag}$ AND $^{14}\text{N}$

L. G. Moretto, R. C. Jared, S. G. Thompson, S. K. Kataria,  
D. Heunemann, R. P. Babinet, R. C. Schmitt, and J. L. Levinson

The reaction between a  $^{107,109}\text{Ag}$  target and a  $^{14}\text{N}$  beam at various bombarding energies has been studied. In this reaction a large variety of particles is emitted; particles with atomic numbers ranging from 0 to  $\sim 18$  have been identified. The mechanism of emission of these particles is not very clear. On one hand the kinetic energy distributions seem to indicate that a near complete relaxation of the system has taken place and that a compound nucleus emission may be occurring. On the other hand the angular distributions seem to indicate that the process occurs on a time scale comparable with or shorter than one nuclear rotation period, thus suggesting a more direct process of emission. The purpose of

this experiment is to gather a set of experimental data, as complete as possible, in order to clarify the emission mechanism.

The schematic of the experiment is shown in the previous article. The thin ( $\sim 300 \mu\text{g}/\text{cm}^2$ ) self supporting Ag target was bombarded with a  $^{14}\text{N}$  beam obtained from the 88-inch cyclotron. The bombardments were made at three different energies: 100 MeV, 160 MeV, 250 MeV. The particles produced in the reactions were identified by means of two  $\Delta E$ -E telescopes. One of the telescopes was composed of two solid state detectors (a  $\Delta E$  counter  $\sim 9 \mu\text{m}$  thick and an E counter  $\sim 300 \mu\text{m}$  thick); the

other telescope was composed of a  $\Delta E$  gas proportional counter and an E solid state counter. The latter telescope appeared to be much more versatile than the solid state telescope because of the possibility of varying the thickness of the  $\Delta E$  counter simply by changing the gas pressure.

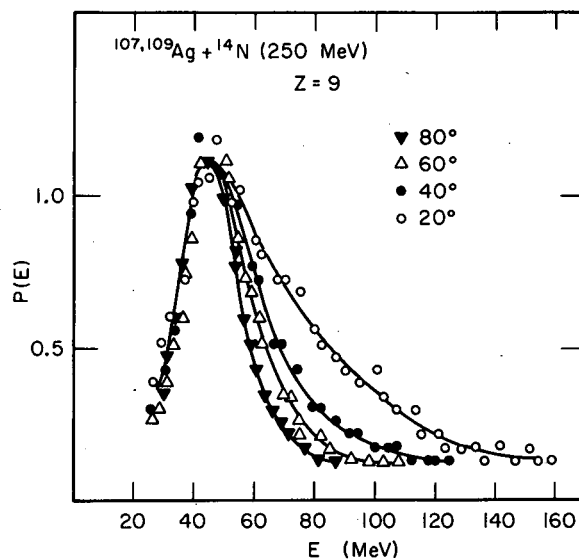
The measurements were performed at various angles, the smallest of them usually being the critical angle. In particular, at 160 MeV bombarding energy, the measurements were performed at angles as large as  $150^\circ$  in the laboratory system.

The linear pulses from the various detectors, after suitable amplification were digitized by means of a multiplexer-ADC system, fed to a PDP-5 computer and recorded on magnetic tape. The monitoring of the experiment was performed by means of a Landis-Goulding particle identifier. The magnetic tapes were used to generate, off-line, a  $\Delta E$ ,  $E_{\text{total}}$  map and a particle identification,  $E_{\text{total}}$  map which were used to obtain cross sections and kinetic energy distributions for the various atomic numbers.

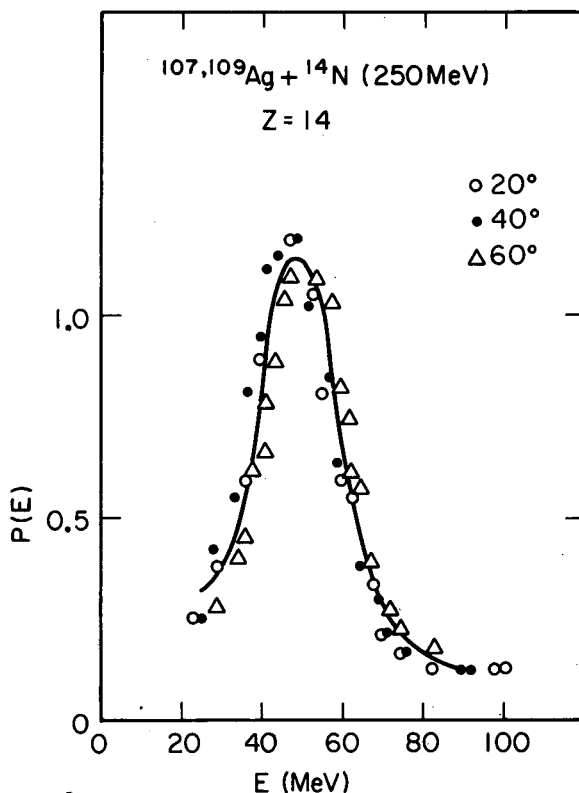
The observed kinetic energy distributions depend both upon the atomic number and the angle. At large angles, all the kinetic energy distributions show a rather broad peak at energies comparable with the Coulomb energy that we call a "relaxed peak" because of the very high degree of inelasticity involved. At smaller angles a similar picture is observed with the exception of the particles with atomic numbers in the neighborhood of that of the target. For these particles a very broad energy distribution is observed ranging from energies close to the projectile energy down to the neighborhood of the Coulomb barrier. The relaxed peaks, in which we are most interested, transform quite nicely into the center of mass if one assumes that a binary splitting occurs (Fig. 1). The center of mass most probable kinetic energies appear to depend rather weakly upon angle with the exclusion of those associated with atomic numbers close to the target. The center of mass most probable energies correlate rather nicely with the Coulomb energies associated with two touching spheres or two touching spheroids at equilibrium deformation (Fig. 2).

Since the relaxed peaks can be easily integrated, a meaningful cross section for each Z can be obtained (Fig. 3). These cross sections vary dramatically both with Z and with angle and show a remarkable even-odd effect.

The center of mass angular distributions appear to vary with Z. For atomic numbers close to that of the projectile, a strong forward distribution is observed while for atomic



a



b

Fig. 1. Examples of the kinetic energy distributions of the center of mass.  
(XBL 7310-4401, 7310-4402)

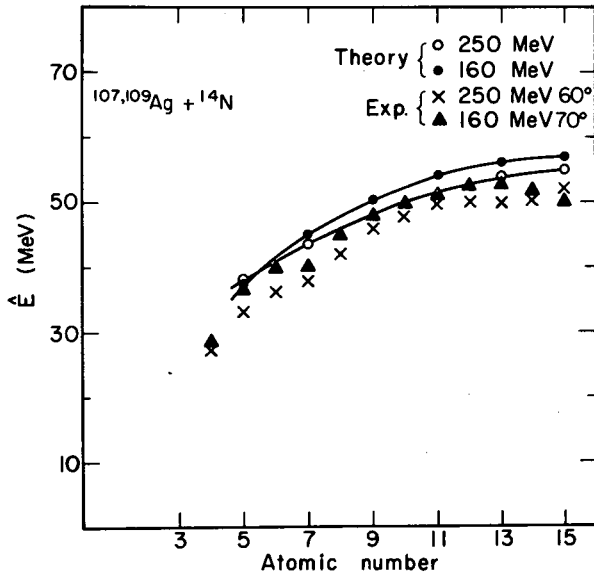


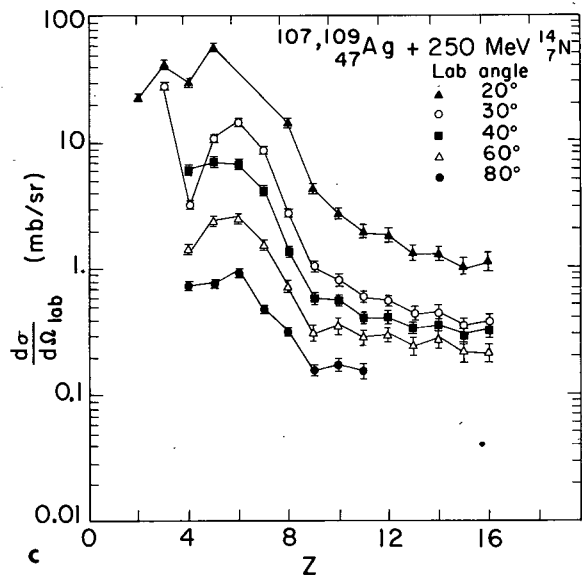
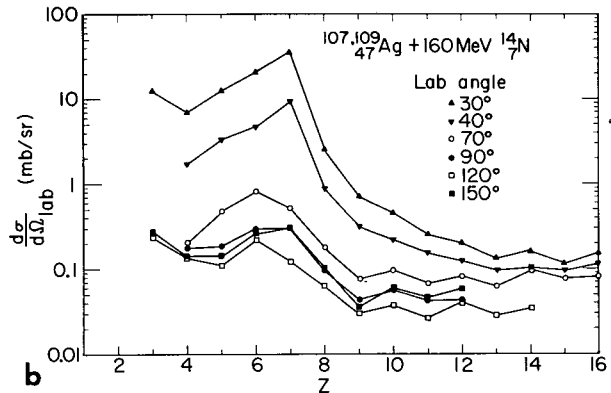
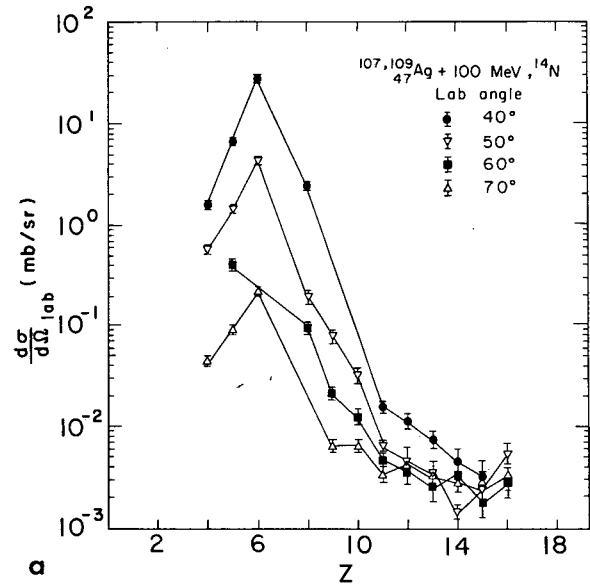
Fig. 2. Most probable kinetic energies in the center of mass. (XBL 7310-4398)

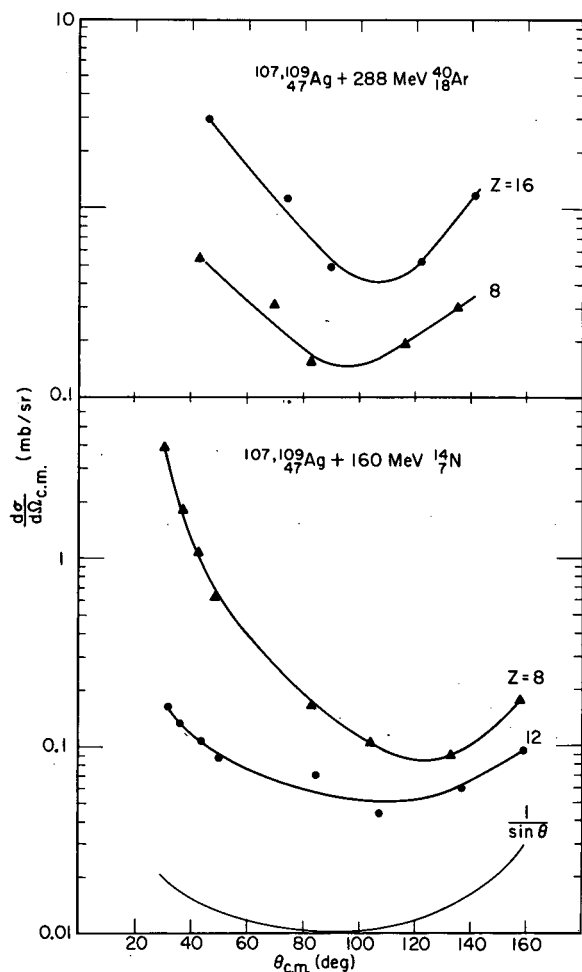
numbers away from the projectile the angular distributions become more and more symmetric about  $90^\circ$  (Fig. 4). In all the cases a rise in the backward direction is present.

The interpretation of these data remains uncertain. The kinetic energy distributions are consistent with complete relaxation and thus with a compound nucleus emission. A recent theory proposed by one of us and based upon the assumption of statistical emission can predict the kinetic energy distributions in satisfactory detail. The only indication of non-statistical emission can be seen for instance in Fig. 1a for  $Z = 9$  where at small angles a high energy tail is observed. In rather dramatic contrast with the kinetic energy distributions, the angular distributions, in general, do not show the symmetry about  $90^\circ$  typical of the compound nucleus emission. The forward peaking is always stronger than the backward peaking. Furthermore, the forward peaking is more substantial for atomic numbers close to that of the projectile. One could be tempted to assume that the backward peaking is due uniquely to the compound nucleus emission. In this way one could fit a  $1/\sin\Theta$  distribution to the backward angle data and extract the cross section for the compound nucleus reaction as well as for the direct component. This approach is perhaps too naive. A quantity more significant than  $d\sigma/d\Omega$  from the physical point of view is  $d\sigma/d\Theta = 2\pi \sin\Theta$

Fig. 3. Cross sections as a function of atomic number and angle for bombarding energies of (a) 100 MeV, (b) 160 MeV, and (c) 250 MeV.

(XBL 742-2452, 7312-7028, 742-2453)





$d\sigma/d\Omega$ . In fact the factor  $2\pi\sin\Theta$  is purely a geometrical factor which arises because of the orientation of the total angular momentum on a plane perpendicular to the beam direction. It follows that, if  $d\sigma/d\Theta$  does not decrease fast enough with angle, the cross section  $d\sigma/d\Omega$  may be rising in the backward direction.

In conclusion, the overall picture of this reaction seems to be quite consistent with a near complete relaxation of the intrinsic degrees of freedom. On the other hand the lack of symmetry of the angular distributions about  $90^\circ$  indicates that a residual coupling exists between the ingoing and outgoing channels. A possible explanation of this overall picture is related to the slow evolution of the completely relaxed system at the "ridge point" (which can be approximated by two spheroids in contact): If the potential energy is not too steep along the mass asymmetry coordinate and/or the nuclear matter flow is viscous, then the system may take a long time to evolve in the mass asymmetry direction while it may decay quite rapidly into two new fragments.

#### References

1. L. G. Moretto, Physics Letters **40B**, 185 (1972).

Fig. 4. Examples of angular distribution in the center of mass. (XBL 7312-7038)

### ANGULAR DISTRIBUTIONS OF FRAGMENTS PRODUCED IN THE BOMBARDMENT OF $^{107, 109}\text{Ag}$ AND $^{159}\text{Tb}$ WITH $^{14}\text{N}$

L. G. Moretto, R. C. Gatti, and S. G. Thompson

Telescope experiments have shown that the reaction of  $^{107, 109}\text{Ag}$  with  $^{14}\text{N}$  projectiles of various energies produces low kinetic energy fragments with various atomic numbers that, from the kinetic energy distributions alone, may be considered compound nucleus products. The same experiments have shown that the angular distributions in the center of mass present a backward-forward peaking, the forward peaking being more pronounced for the fragments with atomic number close to that of the projectile. In order to obtain a global view of the angular distributions for larger Z fragments, an experiment has been undertaken to measure full angular distributions

over the angular range  $170^\circ - 10^\circ$ . The detector is a strip of mica pressed against a cylindrical surface at whose center is the thin Ag target (see Fig. 1). The beam to which the target is exposed is collected by a Faraday cup and integrated by an electrometer. The particle tracks can be developed by chemical etching of the mica strip with hydrofluoric acid and can be observed by means of an optical microscope.

The Z detection threshold of mica depends upon energy. For energies of about 1.5 MeV/nucleon the threshold is about  $Z=15$ . In this way only the heavier fragments produced in the

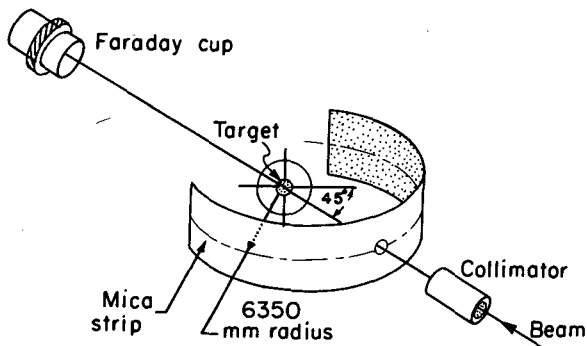


Fig. 1. Schematic drawing of the experimental apparatus. (XBL 742-2455)

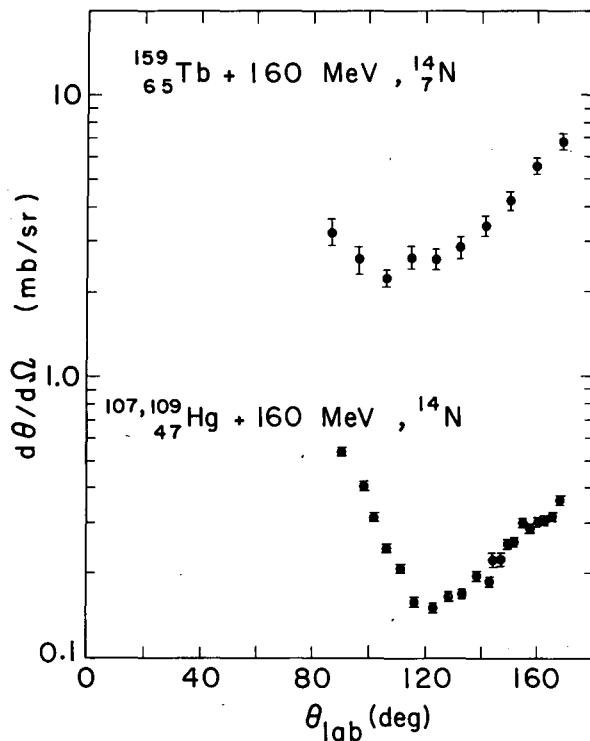


Fig. 2. Angular distributions in the laboratory system for the targets  $^{107,109}\text{Ag}$  and  $^{159}\text{Tb}$ . (XBL 742-2456)

reaction can be observed. Two targets,  $^{107,109}\text{Ag}$  and  $^{159}\text{Tb}$  have been exposed to the 160-MeV  $^{14}\text{N}$  beam.

The experimental data obtained for the two targets are shown in Fig. 2. A very dramatic

backward peaking is visible in both experiments. The data on the forward direction are compromised by the presence of a large number of shallow tracks which can be partially ascribed to the recoils of various transfer reactions and which interfere with the observation of the deeper tracks corresponding to the fragments of interest.

The data transformed into the center of mass, assuming an average mass  $A = A_{\text{tot}}/2$  and an average kinetic energy corresponding to a binary fission process, are shown in Fig. 3. A more meaningful way to plot the angular distribution is to plot  $d\sigma/d\Theta = 2\pi\sin\Theta d\sigma/d\Omega$ . The removal of the geometrical factor  $(2\pi\sin\Theta)^{-1}$  arising from the angular momentum alignment in a plane perpendicular to the beam should leave a constant distribution in the case of a compound nucleus reaction. The result of such a transformation can be seen in Fig. 4.

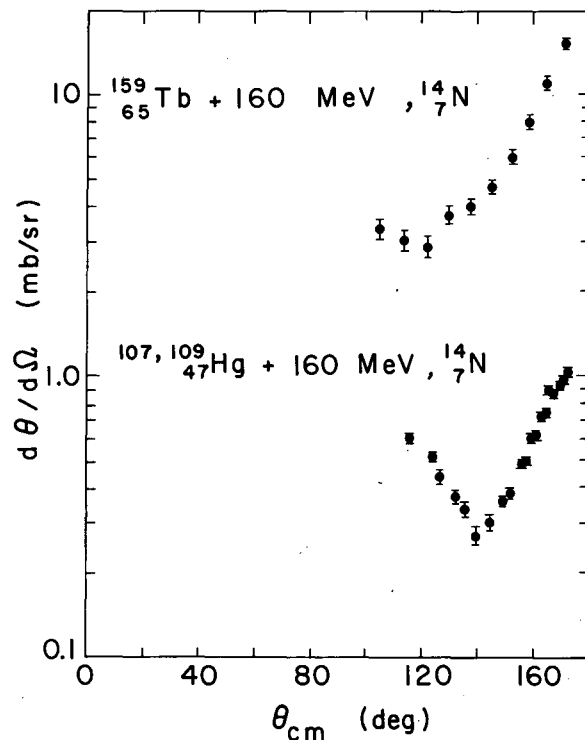


Fig. 3. Angular distribution in the center of mass system for the targets  $^{107,109}\text{Ag}$  and  $^{159}\text{Tb}$ . (XBL 742-2457)

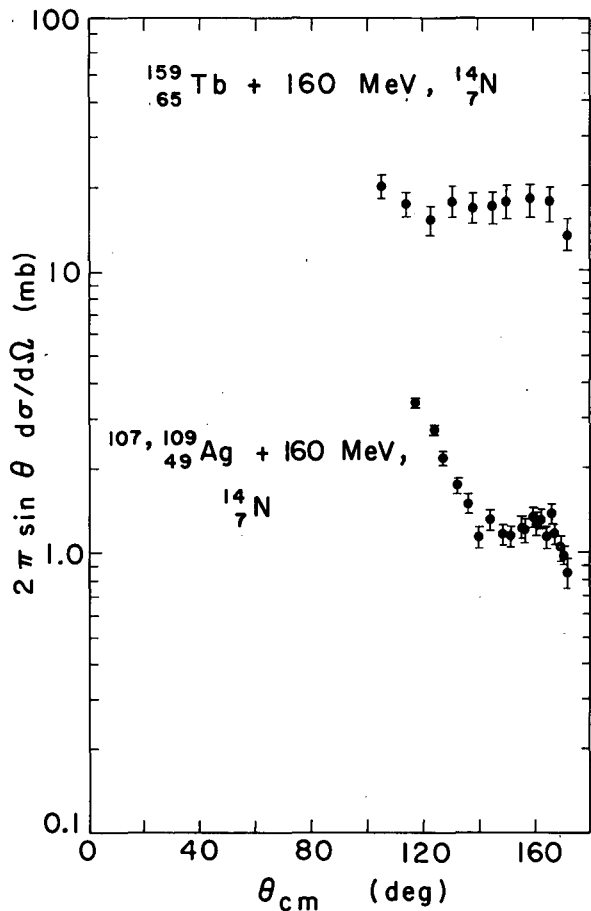


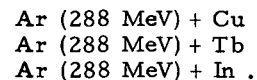
Fig. 4. Angular distributions as in Fig. 3 corrected for the rotational geometry factor  $2\pi \sin\theta$ . (XBL 742-2458)

### X-RAY ANALYSIS OF HEAVY ION REACTION PRODUCTS

R. C. Jared, R. P. Babinet, and S. G. Thompson

The x-rays produced by heavy ion reaction products are a valuable tool to use in the determination of the reaction mechanism. From the x-rays emitted some hours after the initial bombardment, it is possible to obtain information about the yields of the various products formed in the reaction. Using catcher foils at various angles, the angular distribution of the products can be determined. In addition, by using a stack of thin catcher foils, one can obtain some information about the kinetic energy distribution of these products. The study of heavy ion reaction products based on off-line x-ray spectra leads to ambiguous conclusions because of uncertainties about the mass-chain that produces the x-rays, as has been pointed out by Jared, Nifenecker, Moretto, and Thompson.<sup>1</sup> In this report we have only investigated the kinetic energies of

the reaction products. The range of ions of a given Z is determined by observing the relative yields of x-rays in several successive thin catcher foils mounted behind the target. In this framework the following reactions have been studied:



The results are shown in Figs. 1, 2, and 3 for the above reactions. In general, an x-ray spectrum of elements close to the target chemical element is observed in the target itself and in the first foils. These products seem to be obtained from a transfer reaction of some nucleons from the projectile to the target, and

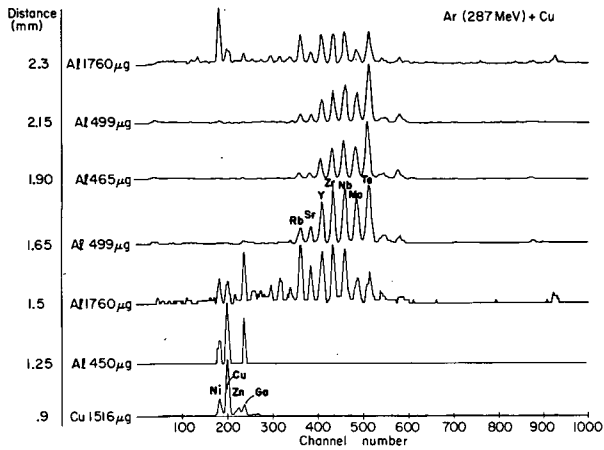


Fig. 1. The x-ray spectrum produced in various catcher foils for the reaction Cu + Ar (288 MeV). (XBL 7310-4361)

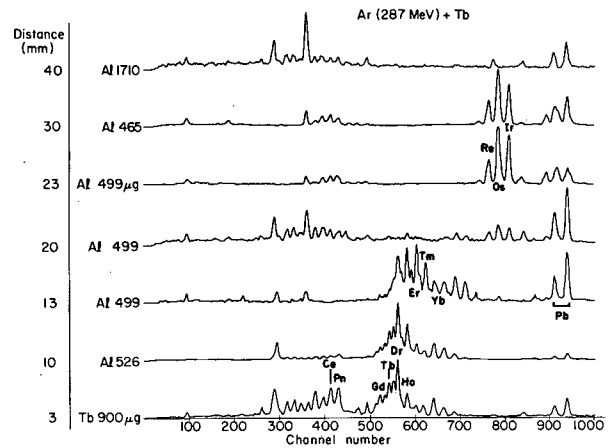


Fig. 3. The x-ray spectrum produced in various catcher foils for the reaction Tb + Ar (288 MeV). (XBL 7310-4363)

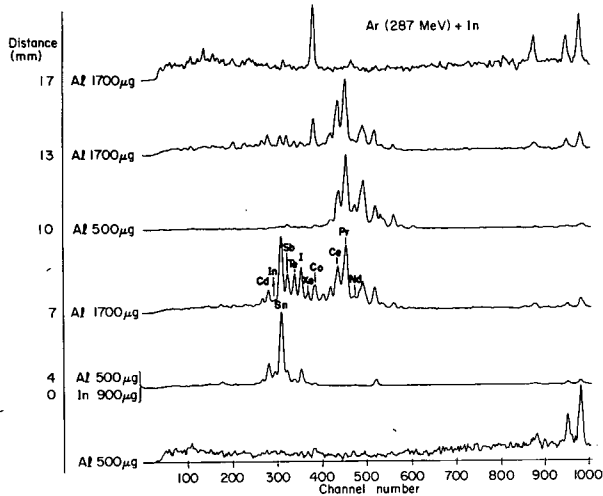


Fig. 2. The x-ray spectrum produced in various catcher foils for the reaction In + Ar (288 MeV). (XBL 7310-4362)

vice versa, giving a product with small kinetic energy. The large ranges observed for products whose  $Z$  is well above the target are in agreement with the range expected for the compound system with full momentum transfer. (In the case of the reactions considered, the ranges of the compound nucleus are given in Table I). Although the  $Z$  of these products are well below the  $Z$  of the compound system, it is expected, based on their ranges, that indeed they belong to the mass chain of the compound system.

These products are expected to be neutron deficient and consequently the mechanism of x-ray production is mainly electron capture. It is therefore expected that no strong selectivity effect should arise in this process, thus allowing quantitative results to be obtained from a precise analysis of the x-ray spectrum charge by charge. This, however, should not be true for the compound nucleus fission fragments which may not decay by

Table I. Range of recoiling compound nuclei.

Projectile	Target	Compound nucleus(CN)	Energy of the (CN)	~ Range in Al of the(CN)
${}^{40}_{18}\text{Ar}$	${}^{63}_{29}\text{Cu}$	${}^{103}_{47}\text{Ag}$	112 MeV	$\sim 3.8 \text{ mg/cm}^2$
${}^{40}_{18}\text{Ar}$	${}^{115}_{49}\text{In}$	${}^{155}_{67}\text{Ho}$	74 MeV $\sim 0.5 \text{ MeV/nucleon}$	$\sim 3.0 \text{ mg/cm}^2$
${}^{40}_{18}\text{Ar}$	${}^{159}_{65}\text{Tb}$	${}^{199}_{83}\text{Bi}$	58 MeV $\sim 0.3 \text{ MeV/nucleon}$	$\sim 2.2 \text{ mg/cm}^2$



electron capture and which could account for the observed yield well below the target Z. A more detailed analysis requires x-ray,  $\gamma$ -ray coincidence measurements in order to be able to determine the isotopes in the mass chains.

A more detailed treatment of this data has recently been presented by H. Nifenecker at the Seventh European Conference on Physics and Chemistry of Complex Nuclear Reactions. In summary we find that the use of off-line x-ray to determine the reaction mechanism in heavy ion reactions is a valuable tool that

gives a quick picture of the overall process. In order to make the results quantitative, however,  $\gamma$ -ray, x-ray coincidence measurements must be made to remove ambiguities concerning the mass chains produced in heavy ion reactions.

#### Reference

1. R. C. Jared, H. Nifenecker, L. G. Moretto, and S. G. Thompson, Nuclear Chemistry Annual Report, Lawrence Berkeley Laboratory, Report LBL-1666 (1972) p. 43.

### RADIOCHEMICAL YIELD DETERMINATION OF VARIOUS REACTION PRODUCTS IN THE REACTION OF $^{238}\text{U}$ WITH $^{40}\text{Ar}$ AND $^{84}\text{Kr}$ IONS

I. Binder, J. V. Kratz,\* J. O. Liljenzin,<sup>†</sup> A. E. Norris,<sup>‡</sup> and G. T. Seaborg

The chemical processing of heavy-ion bombarded uranium targets is the subject of another contribution to this report.<sup>1</sup> The chemical fractions that might include superheavy element atoms as represented by the homologous elements Tc through Te and Re through Po (i.e., the distillate, the superheavy element (SHE) fraction, and the lead fraction) are counted for alpha-particle and spontaneous fission activities using silicon surface barrier detectors with a thickness corresponding to the range of a 15-MeV alpha particle. The alpha particles are counted with a pulse-height analysis system. Spontaneous fission events are recorded simultaneously in the alpha detectors by setting a threshold at 15-MeV alpha-particle energy and counting events with higher energy release in a separate scaler.

For the low intensity krypton bombardments that have been performed to date, there is no evidence for unknown energy alpha groups, and no spontaneous fission event has been recorded during five months. (Similarly there is no evidence for superheavy elements from the argon bombardments.) This leads to an upper limit of the formation cross section for the superheavy elements 107 through 116 in the reaction  $^{84}\text{Kr}$  on  $^{238}\text{U}$  of less than  $10^{-31}\text{ cm}^2$  for an assumed half-life of ten days. The limits quoted by the Dubna group for the production of superheavy elements in similar reactions, namely  $^{76}\text{Ge}$  on  $^{238}\text{U}$  and  $^{74,76}\text{Ge}$  on  $^{232}\text{Th}$ , range from  $10^{-33}\text{ cm}^2$  to  $5 \times 10^{-35}\text{ cm}^2$ ,<sup>2</sup> which reflects the present availability of much higher intensity heavy-ion beams in that laboratory.

In addition to the search for superheavy

elements, it is of great interest to study the types and yield distributions of other reaction products formed in the same targets. Analysis of the gamma-ray activities in the various chemical fractions result in information about the formation of reaction products over a broad range of Z and A. This information is independent of the reaction mechanism involved.

The chemical fractions were counted periodically for a total of two to three weeks. After computer evaluation of the gamma-ray spectra, the identification of isotopes and their yield determinations were performed by comparison of the observed decay characteristics with a gamma-ray reference table, as described elsewhere.<sup>3</sup>

For the reaction of  $^{40}\text{Ar}$  with  $^{238}\text{U}$  (incident beam energy varying from 288 MeV down to reaction threshold, i.e., 200 MeV for reaction channels leading to binary fission<sup>4</sup>), 136 isotopes, distributed among 53 elements, were identified. Reaction product cross sections are plotted vs mass number in Fig. 1. These data were evaluated in terms of mass and charge distribution in a three-dimensional iterative procedure. On the whole, the resulting cross sections seem to imply at least three types of reaction channels as follows:

- 1) Nucleon transfer reactions with maximum cross sections centered on the projectile and target masses ("rabbit ears"). To obtain the integral cross section for transfer reactions, the yield data in the light rabbit ear were integrated using a log-normal distribution with the asymmetric tail on the lower mass side to

describe the mass yields. To describe charge distribution, isotopic yield dispersion curves were assumed to be Gaussian with a width of 2.8 mass units (FWHM). This value was taken from the results obtained by Volkov's group<sup>5</sup> for the yield dispersion of light transfer products in the reaction of  $^{40}\text{Ar}$  with  $^{232}\text{Th}$ .

2) There is a broad distribution of products originating from the binary fission of a composite system with a life-time long enough to permit complete charge and mass transfer (symmetric fission). To obtain the mass yield distribution curve, the following assumption were made about the charge distribution of fragments, and the results were checked against available experimental data:

- a. For each fragment mass  $A_f$  the yield of isobars is described by a Gaussian distribution.
- b. The dependence of the most probable nuclear charge  $Z_p$  on  $A_f$  was calculated for the different hypotheses: Unchanged charge density of the fragments (UCD), equal charge displacement (ECD), charge distribution according to minimum potential energy at the scission point (MPE), an empirical linear relation between  $Z_p$  and  $A_f$ .
- c. It was assumed that neutrons are evaporated from the fragments in a number proportional to the fragment mass  $\nu_f = (\nu/A_0)A_f$ . Furthermore, the final mass yield distribution curve was also assumed to be of a Gaussian shape. Free parameters in the iterative procedure are the width of the charge dispersion curves and its variation with mass, the width of the Gaussian mass yield distribution curve and the location of its maximum, and the total number of evaporated neutrons  $\nu$ .

With all the yield data between mass numbers 69 and 205 included in the least squares iterative calculation, the computation resulted in an unreasonably broad charge dispersion width, and the fissioning nucleus was calculated to be around  $A_0 = 250$ ,  $Z_0 = 100$ . As discussed below, it was then assumed that the fission product distribution from the composite system is superimposed upon another fission yield distribution and that the neutron-rich isotopes with mass numbers  $80 \leq A \leq 150$  should not be included in the mass yield calculation of the composite system fission. Then the fissioning nucleus was calculated to be close to  $^{278}\text{X}$  with  $\nu \approx 10$ , as expected. Although the calculations are not yet completed, the ECD assumption on the  $Z_p(A_f)$  dependence,

or a linear function  $Z_p = a + bA_f$ , seem to describe the data better than the other assumptions on the charge distribution. The Gaussian mass yield curve indicated in Fig. 1 is the result of the best linear fit. The width of the mass distribution is about 75 mass units (FWHM), and the width of the isotopic distributions at symmetric mass division is about 7.5 mass units (FWHM), which is in reasonable agreement with the results obtained by Oganesyan.<sup>6</sup>

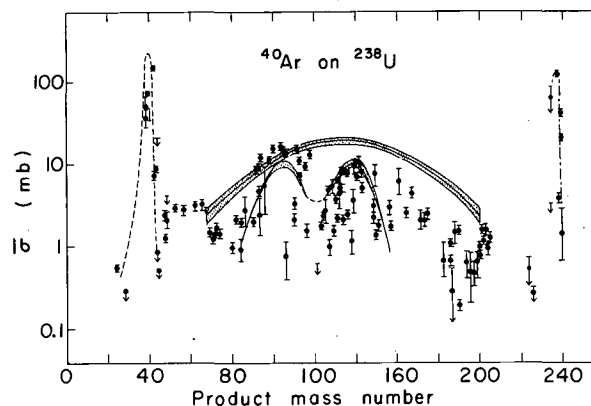


Fig. 1. Plot of the experimentally obtained cross sections for individual isotopes vs mass number in the reaction  $^{238}\text{U} + ^{40}\text{Ar}$ . Incident beam energy (Lab)  $\leq 288$  MeV. The broad band represents the calculated mass yield distribution and its error for the composite system fission after neutron evaporation. The double-hump distribution fits the excess yields of neutron-rich fission products.

(XBL 742-2466)

3) The failure to fit the yields of neutron-rich isotopes in the mass region 80 through 150 in the fission product mass distribution from the composite system fission suggested that there might be another fission yield distribution superimposed on the type 2) distribution. This assumption is supported by the isotopic yield distribution of iodine isotopes (Fig. 2) showing an excess yield of neutron-rich isotopes. Even though the yields of  $^{133}\text{I}$ ,  $^{134}\text{I}$ , and  $^{135}\text{I}$  in Fig. 2 are partially cumulative or cumulative yields, they cannot be explained in terms of the type 2) yield distribution. To integrate the neutron-rich distribution, yields derived from the type 2) distribution were subtracted from the data and the residues treated in a similar iterative procedure as described above. It was found that a double-hump yield distribution (see Fig. 1) similar to that observed for alpha-induced fission of  $^{238}\text{U}$  at moderate excitation energies

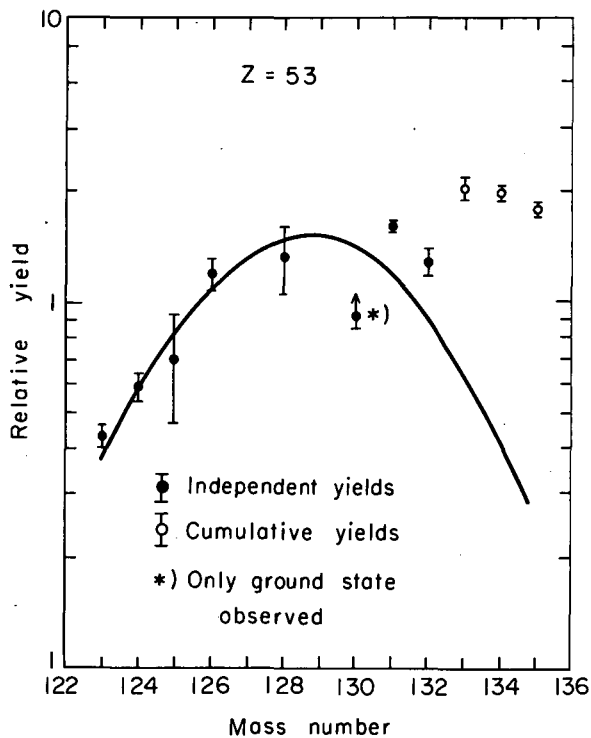


Fig. 2. Isotopic yield distribution for iodine isotopes ( $Z = 53$ ) in the reaction  $^{238}\text{U} + ^{40}\text{Ar}$ . (XBL 742-2464)

gives a slightly better fit to the data than a broad, singly-peaked Gaussian distribution. This might suggest that this fission type results from projectile-target interactions in which several nucleons and modest amounts of excitation energy are transferred.

Preliminary results of cross-section calculations for the different reaction channels observed in  $^{40}\text{Ar}$  on  $^{238}\text{U}$  are given in Table I.

Table I. Preliminary results on cross sections in the reaction of  $^{238}\text{U}$  with  $^{40}\text{Ar}$  ions. Incident beam energy (Lab)  $\leq 288$  MeV.

Transfer reactions	600 mbarn
Total fission cross section	$\sim 600$ mbarn
Fission of composite system	$\sim 450$ mbarn
Neutron-rich fission product distribution	$\sim 150$ mbarn
<b>Total reaction cross section</b>	<b><math>\sim 1200</math> mbarn</b>

The total fission cross section amounts to about 50% of the total reaction cross section.

The reaction of  $^{84}\text{Kr}$  with  $^{238}\text{U}$  (incident beam energy  $\leq 605$  MeV) has been investigated only in a few low-intensity bombardments so far. Cross sections of individual isotopes are plotted vs product mass number in Fig. 3. Due to large statistical variations in the gamma-ray spectra, errors are generally large. Nevertheless, a few conclusions might be drawn from Fig. 3. The general picture is rather similar to the one obtained for

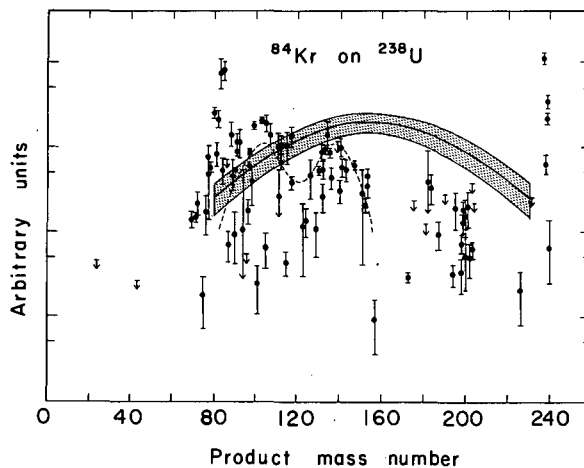


Fig. 3. Plot of the experimentally obtained cross sections for individual isotopes vs mass number in the reaction  $^{238}\text{U} + ^{84}\text{Kr}$ . Incident beam energy (Lab)  $\leq 605$  MeV. The broad band represents the estimated mass yield distribution and its error for the composite system fission after neutron evaporation. The dashed curve is intended to indicate qualitatively, that there is an excess of neutron-rich fission products similar to the one observed in  $^{238}\text{U} + ^{40}\text{Ar}$ . (XBL 742-2465)

$^{238}\text{U} + ^{40}\text{Ar}$ . From the yield distribution of the more neutron-deficient isotopes, it is concluded that there is again a broad symmetrical distribution of fission fragments from the fission of a composite system. This distribution is centered around mass number 155 and has a width of about 80-90 mass units (FWHM) which should be expected for the binary fission of the composite system. An estimate of the integrated cross section for this reaction channel is 300 millibarns. This is in contrast to the results obtained by the Orsay group<sup>7</sup> which reported an upper limit of 10 millibarns for the complete fusion of 500-MeV Kr ions with  $^{238}\text{U}$ . It may be that in the Orsay experiment the incident beam energy was not high enough for the formation of a composite system.

The isotopic yield distribution of iodine isotopes in  $^{238}\text{U} + ^{84}\text{Kr}$  is similar to the one observed for  $^{238}\text{U} + ^{40}\text{Ar}$  (Fig. 2). The excess of neutron-rich isotopes around mass numbers 100 and 135 suggests again that there is another yield distribution superimposed on the composite system fission product distribution. More intense bombardments are needed to allow a meaningful integration of both fission yield distributions.

#### Footnotes and References

\* On leave from Institut für Kernchemie, Universität Mainz, with a fellowship from Gesellschaft für Schwerionenforschung GSI, Darmstadt, Germany.

† Department of Nuclear Chemistry, Chalmers University of Technology, Göteborg, Sweden.

‡ Los Alamos Scientific Laboratory, Los Alamos, NM.

1. J. V. Kratz, J. O. Liljenzin, G. T. Seaborg, "Chemical Processing of Super-HILAC Targets" in Section III of this report.
2. Yu. Ts. Oganessian, Report JINR P7-7410, Dubna (1973).
3. I. Binder, M. Di Casa, J. V. Kratz, J. O. Liljenzin, A. E. Norris, "Computer-Aided Analysis of  $\gamma$ -Ray Spectra" in Section IV of this report.
4. T. Sikkeland, *Arkiv für Fysik* 36, 539 (1967).
5. A. G. Arthuk, V. V. Avdeichikov, G. F. Gridnev, V. L. Mikheev, V. V. Volkov, J. Wilczyński, Report JINR E7-5917, Dubna (1971) and A. G. Arthuk, G. F. Gridnev, V. L. Mikheev, V. V. Volkov, J. Wilczyński, Report JINR E7-6970, Dubna (1973).
6. Yu. Ts. Oganessian, Proceedings of the Second Symposium on Physics and Chemistry of Fission, I.A.E.A. Vienna, p. 489 (1969).
7. M. Lefort, Y. Le Beyec, J. Peter, Paper presented at the XIth Winter Meeting on Nuclear Physics, Villars, France (1973).
8. J. Péter, F. Hanappe, C. Ngô, B. Tamain, Paper presented at the I.U.P.A.P. Meeting, Munich (1973).

DEVIATIONS FROM ISOSPIN-IMPOSED SYMMETRY IN THE REACTION  
 ${}^4\text{He}(\vec{d}, t){}^3\text{He}^*$ 

 W. Dahme,<sup>†</sup> H. E. Conzett, F. J. Arvieux,<sup>‡</sup>  
 J. Birchall, and R. M. Larimer

The nuclear reaction  ${}^4\text{He}(\vec{d}, t){}^3\text{He}$  has received considerable attention since Gross, et al.<sup>1</sup> reported clear deviations from the forward-backward symmetry of the cross section that was predicted by Barshay and Temmer<sup>2</sup> to result from isospin conservation. The measured asymmetries were accounted for, in part, by the different Coulomb effects on the proton and neutron pick-up amplitudes in a DWBA calculation.<sup>3</sup> Since the calculated asymmetries were consistently smaller than those observed, it was suggested that some isospin impurity could be responsible for this remaining discrepancy. The entrance and exit channel potential parameters used in the calculation were obtained from optical model fits to elastic  $d + {}^4\text{He}$  and  ${}^3\text{H} + {}^3\text{He}$  cross-sections. Since polarization data were not available, the spin-orbit term of the potentials could not be well determined.

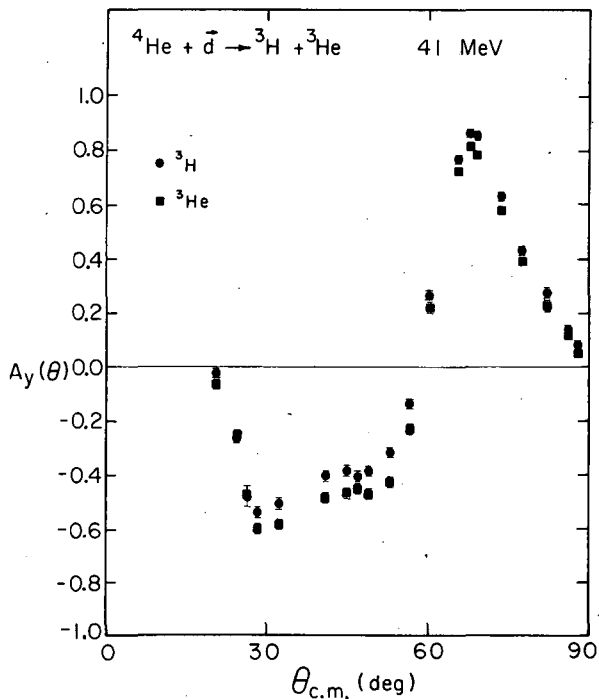


Fig. 1. Vector analyzing powers,  $A_y({}^3\text{H})$  and  $A_y({}^3\text{He})$ , in the  ${}^4\text{He}(\vec{d}, t){}^3\text{He}$  and  ${}^4\text{He}(\vec{d}, {}^3\text{He}){}^3\text{H}$  reactions, respectively, at 41 MeV.  
 (XBL 734-2722)

In order to provide data for a more complete and, perhaps, more sensitive testing of the DWBA calculations, we have measured the vector analyzing powers  $A_y(\theta)$  of the reactions  ${}^4\text{He}(\vec{d}, t){}^3\text{He}$  and  ${}^4\text{He}(\vec{d}, {}^3\text{He}){}^3\text{H}$  at  $E_d = 32.1$  and 41.0 MeV. Figures 1 and 2 show our results at 41 MeV. The analyzing powers reach substantial values, and the ratio  $R_A = A_y({}^3\text{H})/A_y({}^3\text{He})$  differs from 1.0 by as much as 20%. Similar results were obtained at 32.1 MeV, and these deviations of  $R_A$  from 1.0 provide further evidence for the breakdown of the symmetry imposed by isospin conservation.

It should be noted that the weaker assumption of charge-symmetry of the nuclear forces leads to equality of the cross sections (equivalent to symmetry about  $90^\circ$  because of the equal masses of the final state products) and the analyzing powers of these two (mirror) reactions. Thus, a more detailed and rigorous examination of the extent to which the Coulomb effects can explain the entire deviations of  $R_A = \sigma({}^3\text{H})/\sigma({}^3\text{He})$  and of  $R_A$  from 1.0 is clearly important.

An optical model analysis is underway of the recent 15 to 45 MeV elastic  $\vec{d} + {}^4\text{He}$  vector analyzing power data of Leemann, et al.<sup>4</sup> This will fix more definitely the entrance channel potential parameters, in particular the spin-orbit term. Our preliminary analysis points to a value of the spin-orbit term,  $V_{so}$ , considerably smaller than the 8 MeV used in the calculation of Gross, et al.

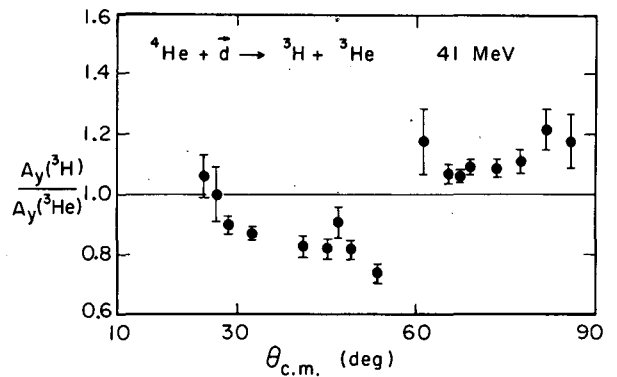


Fig. 2. The ratio  $R_A = A_y({}^3\text{H})/A_y({}^3\text{He})$  at 41 MeV.  
 (XBL 734-2723)

Since these are  $l = 0$  transfer reactions, there is no contribution to the analyzing powers from the DWBA form factor. Thus, the values reported here must result from the spin-orbit distortion of the exit and/or entrance channel wavefunctions. Since the entrance channel  $V_{SO}$  will be fixed by the  $\bar{d} + {}^4\text{He}$  elastic data, the reaction analyzing power data should determine the exit channel  $V_{SO}$ . In this way, a more detailed examination can be made of the effect of form factor variations on the deviations of  $R_O$  and  $R_A$  from unity.

#### Footnotes and References

\* Published in Proceedings of the International Conference on Nuclear Physics, edited by J. de Boer and H. J. Mang (North-Holland Publishing Company, Amsterdam, 1973), Vol. 1, p. 444.

† Present address: Sektion Physik, Universität München, D-8064 Garching, Germany.

‡ Present address: Institut des Sciences Nucléaires, Cedex 257, 38044 Grenoble, France.

1. E. E. Gross, E. Newman, W. J. Roberts, R. W. Rutkowski, and A. Zucker, *Phys. Rev. Letters* **24**, 473 (1970).
2. S. Barshay and G. M. Temmer, *Phys. Rev. Letters* **12**, 728 (1964).
3. E. E. Gross, E. Newman, M. B. Greenfield, R. W. Rutkowski, W. J. Roberts, and A. Zucker, *Phys. Rev. C* **5**, 602 (1972).
4. Ch. Leemann, H. E. Conzett, W. Dahme, J. Macdonald, and J. P. Meulders, *Bull. Am. Phys. Soc.* **17**, 562 (1972), and to be published.

### DEPOLARIZATION IN $\vec{p} - {}^9\text{Be}$ SCATTERING AND THE SPIN-SPIN INTERACTION

J. Birchall, F. J. Arvieux,<sup>†</sup> H. E. Conzett, W. Dahme,<sup>‡</sup>  
W. Haeberli,<sup>§</sup> and R. M. Larimer

Since Feshbach<sup>1</sup> proposed the existence of a nucleon-nucleus spin-spin interaction, several attempts have been made to determine  $V_{SS}$  in a spherical term such as  $-V_{SS}(r)\vec{\sigma} \cdot \vec{I}$  in the optical potential. Fisher et al.<sup>2</sup> recently summarized the results of investigations of the scattering of polarized neutrons on polarized targets. They concluded that  $V_{SS}$  could not be determined unambiguously from the data because of the failure of the theory to reproduce the energy dependence of the experimental results between 0.3 and 8.0 MeV. Another way to investigate  $V_{SS}$  is through the measurement of the depolarization parameter  $D$ ,<sup>3</sup> which for direct elastic scattering has the value 1.0 in the absence of the spin-spin term. Measurements of  $D$  have been made for several nuclei by Katori et al.<sup>4</sup> with 1.36 MeV neutrons, by Batty and Tschalär<sup>5</sup> with 50 MeV protons, and by Beurtey et al.<sup>6</sup> with protons near 20 MeV. The large deviations of  $D$  from 1.0 that were found by Katori et al. were attributed to compound elastic scattering. Only the proton measurements of Beurtey et al. were of sufficient accuracy to show values of  $D$  differing significantly from 1.0, but these results were for a single scattering angle. It has been pointed out recently by Sherif and Hussein<sup>7</sup> that measurements of angular distributions

of  $D$  are needed to determine both the form and strength of the spin-spin interaction. In particular, their DWBA calculations consider, in addition to the spherical spin-spin term, a tensor term of the form  $-\frac{1}{2} V_{ST}(r)[3(\vec{\sigma} \cdot \vec{r})(\vec{I} \cdot \vec{r}) - \vec{\sigma} \cdot \vec{I}]$ , and their results predict considerable sensitivity of the  $D$  parameter to the sign and strength of  $V_{ST}$ .

We have measured  $D$  as a function of angle for the elastic scattering of 25-MeV polarized protons from  ${}^9\text{Be}$ .  $D$  is related to the polarizations  $p_0$  and  $p_1$  of the incident and scattered beams and the analyzing power  $A_1$  of the target by

$$p_1 = (D p_0 + A_1)/(1 + A_1 p_0).$$

A high efficiency, high resolution proton polarimeter was used in these measurements. The polarization analyzer was a silicon target in the form of a semiconductor detector, as described by Frois et al.<sup>8</sup> Protons scattered from the silicon analyzer were detected in left and right side detectors placed at  $27^\circ$  with respect to the polarimeter axis. Beam incident on the polarimeter was monitored by means of a "zero-degree" detector placed directly behind the analyzer detector. High scattering efficiency was ensured by the use

of a thick analyzer (1 mm), and good energy resolution was obtained by adding the analyzer and left or right detector energy signals. The analyzing power  $A_1$  of the target was measured by means of the ratio of counts in the "zero-degree" detector for spin up and spin down incident beam.

Measurements of  $D$  have been made, so far, at laboratory angles of  $45^\circ$ ,  $57^\circ$ ,  $70^\circ$ , and  $85^\circ$ , which fall in an angular region where the calculations of Sherif and Hussein predict up to 10% deviations of  $D$  from 1.0. In addition,  $D$  has been measured for  $^{12}\text{C}$ , since its value in the scattering from this spin-zero nucleus should be unity. Our result for  $^{12}\text{C}$  is  $D(\theta_L = 61^\circ) = 0.988 \pm 0.015$ , which provides a very satisfactory check on the experimental procedures. Figure 1 shows our results for  $^9\text{Be}$  along with the predictions of Sherif and Hussein. These experimental deviations of  $D(\theta)$  from 1.0 provide perhaps the first clear qualitative evidence for the existence of a nucleon-nucleus spin-spin interaction. It is clear from the calculated curves that a quantitative determination of the tensor part of the interaction,  $V_{ST}$ , cannot be made from this depolarization experiment on  $^9\text{Be}$ . However,

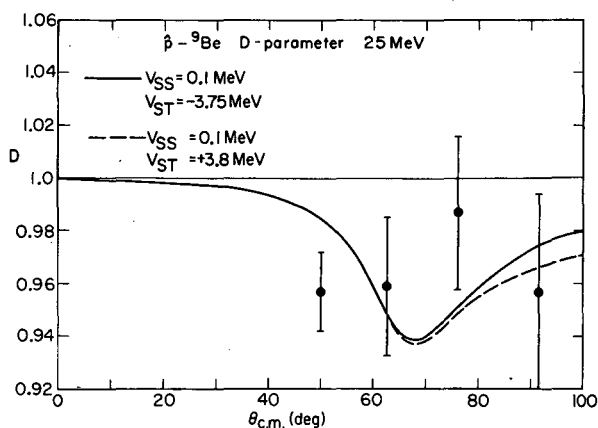


Fig. 1. The depolarization parameter,  $D(\theta)$ , in  $p\text{-}^9\text{Be}$  scattering at 25 MeV. The curves are calculated values from Sherif and Hussein (private communication).

(XBL 7310-4281)

$^{10}\text{B}$  is predicted to be suitable for that purpose.<sup>7</sup>

#### Footnotes and References

\*Published in Proceedings of the International Conference on Nuclear Physics, edited by J. de Boer and H. J. Mang (North-Holland Publishing Company, Amsterdam, 1973), Vol. 1, p. 371.

†Present address: Institut des Sciences Nucléaires, Cedex 257, 38044 Grenoble, France.

‡Present address: Sektion Physik, Universität München, D-8064 Garching, Germany.

§Department of Physics, University of Wisconsin, Madison, Wisconsin.

1. H. Feshbach, Nuclear Spectroscopy, Part B, edited by F. Ajzenberg-Selove
2. T. R. Fisher, H. A. Grench, D. C. Healey, J. S. McCarthy, D. Parks, and R. Whitney, Nucl. Phys. A **179**, 241 (1972).
3. L. Wolfenstein, Ann. Rev. Nucl. Sci. **6**, 43 (1956).
4. K. Katori, T. Nagata, A. Uchida, and S. Kobayashi, J. Phys. Soc. Japan **28**, 1116 (1970).
5. C. J. Batty and C. Tschalär, Nucl. Phys. A **143**, 151 (1970).
6. R. Beurtey, P. Catillon, and P. Schnabel, J. de Phys. **31**, Supp. C2, 96 (1970); Polarization Phenomena in Nuclear Reactions, edited by H. H. Barschall and W. Haerberli (Univ. of Wisconsin Press, Madison, 1971), p. 657.
7. H. S. Sherif and A. H. Hussein, Phys. Letters **41B**, 465 (1972); Phys. Rev. C **8**, 518 (1973).
8. B. Frois, J. Birchall, R. Lamontagne, R. Roy, and R. J. Slobodrian, Nucl. Instr. and Meth. **96**, 431 (1971).

THE DEPOLARIZATION PARAMETER IN  $\vec{p} - {}^{10}\text{B}$  ELASTIC SCATTERING AND THE SPIN-SPIN INTERACTION

J. Birchall, H. E. Conzett, F. N. Rad, S. Chintalapudi,\*  
and R. M. Larimer

Sherif and Hussein<sup>1</sup> have pointed out recently that the depolarization parameter (see preceding paper) is a sensitive probe of the spin-spin interaction in nucleon-nucleus elastic scattering. Other parameters, such as the cross-section and asymmetry, polarization and spin rotation parameters, are relatively insensitive.

Two types of spin-spin force are considered. A spherical term:

$$U_{ss}(r) = V_{ss} F_0(r) \underline{\sigma} \cdot \underline{I},$$

and a tensor term:

$$U_{st}(r) = -1/2 V_{st} F_t(r) [3(\underline{\sigma} \cdot \hat{r})(\underline{I} \cdot \hat{r}) - \underline{\sigma} \cdot \underline{I}],$$

where  $\underline{\sigma}$  and  $\underline{I}$  are the spins of the incident proton and the target nucleus, respectively, and  $\hat{r}$  is a unit vector in the direction of a line connecting the centers of the projectile and target. The depth  $V_{ss}$  and the form factor  $F_0(r)$  of the spherical term can be estimated from the nucleon-nucleon spin-spin interaction and the single nucleon wave function in the target nucleus.<sup>2</sup> The form and strength of the tensor interaction have not yet been estimated. An angular distribution of the D-parameter is required.  ${}^{10}\text{B}$ , which has a spin 3 ground state, is expected to have large deviations of the D-parameter from 1.0.

We have used a 26-MeV polarized proton beam at the 88-inch cyclotron to bombard a 62.9 mg/cm<sup>2</sup>  ${}^{10}\text{B}$  target. The polarization of the beam was continuously monitored by scattering from a  ${}^4\text{He}$  gas target downstream from the  ${}^{10}\text{B}$ , and by measuring the left-right asymmetry for scattering at  $\pm 117.5^\circ$  from the  ${}^4\text{He}$  using two detector telescopes. The polarization of the elastically scattered protons was measured by a polarimeter with high figure of merit and good energy resolution.<sup>3</sup> The polarimeter used a 1-mm thick silicon solid state detector as polarization analyzer and two side detectors at  $\pm 27^\circ$  to the polarimeter axis. Protons which passed unscattered through the analyzer detector were stopped in a "zero degree" detector. The zero degree collimation had the same angular width as the analyzer, with respect to the target center, but much reduced angular height. The analyzing power of the target was deduced from the spin up -- spin down count ratio in the zero-degree detector.

Geometrical errors in the determination of D were minimized by careful monitoring and adjustment of beam alignment during the runs, by deducing D from spin-up/spin-down ratios in each side detector and by obtaining results with the silicon polarimeter placed on each side of the beam. As a check on these procedures the D-parameter of  ${}^{12}\text{C}$  was measured at a number of angles (D for elastic scattering from a spin zero nucleus should be identically 1.0). Values of D consistent with 1.0 were found in each case.

Results of the  $\vec{p} - {}^{10}\text{B}$  D-parameter measurements are shown in Fig. 1. The curves are not fits to our data. They are calculations due to Sherif and Hussein,<sup>4</sup> the values of  $V_{st}$  being chosen to reproduce a data point from Saclay<sup>5</sup> at 65° c.m. and 19.8 MeV. As expected, the deviations of D from unity for  ${}^{10}\text{B}$  are quite large and the points obtained so far seem to indicate a tensor well depth of the order of -2 MeV. Further measurements are planned in order to add to the angular distribution of D.

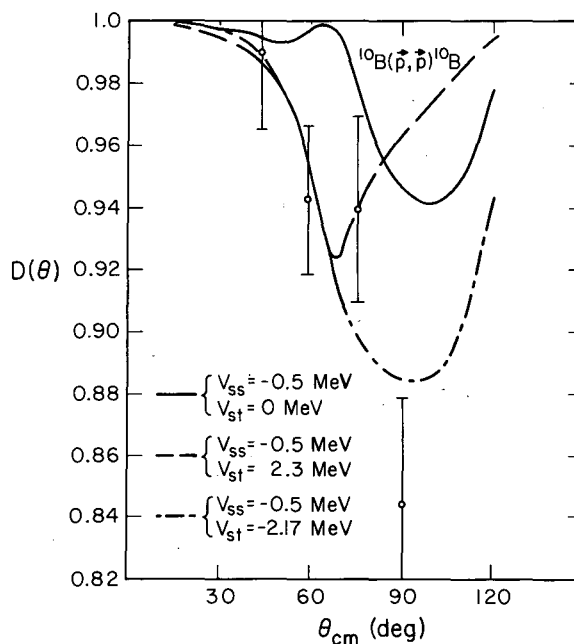


Fig. 1. The depolarization parameter,  $D(\theta)$ , in  $\vec{p} - {}^{10}\text{B}$  scattering at 25.3 MeV. The curves are calculated results at 19.8 MeV from Ref. 4. (XBL 7310-4281)



### Footnote and References

\* On leave from Bhabha Atomic Research Centre, India.

1. H. S. Sherif and A. H. Hussein, Phys. Letters 41B, 465 (1972).
2. G. R. Satchler, Particles and Nuclei 1, 397 (1971).
3. B. Frois, J. Birchall, R. Lamontagne, R. Roy and R. J. Slobodrian, Nucl. Instr. and Methods 96, 431 (1971). J. Birchall,

W. Dahme, J. Arvieux, R. M. Larimer and H. E. Conzett, Nuclear Chemistry Annual Report 1972, Lawrence Berkeley Laboratory Report LBL-1666 (1972), p. 365.

4. H. S. Sherif and A. H. Hussein, Phys. Rev. C 8, 518 (1973).
5. R. Beurtey, P. Catillon and P. Schnabel, J. de Phys. 31, Supp. C2, 96 (1970). P. Catillon in Polarization Phenomena in Nuclear Reactions, edited by H. H. Barschall and W. Haerberli (Univ. of Wisconsin Press, 1971) p. 657.

### IS THE $^{12}\text{C}(\vec{d}, d_0)$ REACTION A GOOD POLARIZATION STANDARD?<sup>†</sup>

J. Arvieux,<sup>†</sup> J. Birchall, H. E. Conzett, W. Dahme,<sup>‡</sup>  
W. Haerberli,<sup>§</sup> and R. M. Larimer

There has been a great development of polarized-ion sources associated with different kinds of accelerators, ranging from very low energy electrostatic generators up to the 12-GeV Argonne ZGS synchrotron. The widening of the energy range at which polarized beams are available emphasizes the need for good polarization standards that can be used to calibrate the polarized beams. Usually one relies on double-scattering experiments which give, for spin 1/2 particles, an absolute value of the polarization. For deuterons such an experiment would usually give an ambiguous answer, because the effects of the tensor polarizations,  $T_{2q}$ , cannot be separated from that of the vector polarization,  $iT_{11}$ . Hopefully, there are a few reactions in which the  $T_{2q}$  are small compared to  $iT_{11}$  so that an absolute value of the vector polarization can be derived. One such reaction is the  $^4\text{He}(\vec{d}, d)^4\text{He}$  elastic scattering at an incident beam energy  $E_d = 11.5$  MeV and laboratory scattering angle  $\theta_L = 88^\circ$ , at which a double-scattering experiment has been done at Los Alamos.<sup>1</sup> The result from this experiment is in good agreement with a later result that was achieved with a polarized beam from the Los Alamos Lamb-shift polarized-ion source, whose polarization was determined by the quench ratio method.<sup>2</sup> An independent measurement of  $iT_{11}$  at  $E_d = 11.5$  MeV,  $\theta_L = 87.8^\circ$  was made at Zurich.<sup>3</sup> The absolute calibration of the tensor polarization of the deuteron beam was made via the  $^{16}\text{O}(\vec{d}, \alpha)^{14}\text{N}^*(2.31)$  reaction,<sup>4</sup> and the theoretical ratio between vector and tensor polarization in the beam was then used to provide the absolute vector polarization value. The agreement between the values from the two laboratories is very good,

and this point can now be used as a deuteron vector polarization calibration standard. The value we have adopted is  $iT_{11}(E_d = 11.5 \text{ MeV}, \theta_L = 88^\circ) = -0.360 \pm 0.009$  which is the weighted mean value between the Zurich result,  $iT_{11} = -0.362 \pm 0.009$ , and the Los Alamos result,  $iT_{11} = -0.356 \pm 0.012$ . This value has been used at Berkeley<sup>5</sup> to normalize an angular distribution of  $iT_{11}$  in  $^4\text{He}(\vec{d}, d)^4\text{He}$  scattering at 15 MeV and the agreement with 15-MeV data from Los Alamos<sup>6</sup> is excellent.

The 15 MeV  $^4\text{He}(\vec{d}, d)^4\text{He}$  data have been also used in Grenoble to calibrate a  $^{12}\text{C}$  polarimeter from 20 to 30 MeV,<sup>7</sup> which has then been used to study the  $^4\text{He}(\vec{d}, d)^4\text{He}$  scattering between 20 and 30 MeV.<sup>8</sup> A comparison of preliminary data from Berkeley and Grenoble has shown very good agreement for the 20 and 30 MeV data but there was a 10% discrepancy at  $E_d = 25$  MeV. The possibility exists that the 25 MeV  $^{12}\text{C}$  calibration experiment could be the source of the discrepancy. If one looks at the  $^{12}\text{C}(\vec{d}, d_0)$  analyzing power angular distributions, one sees that the first (negative) maximum value of  $iT_{11}$  is  $iT_{11}(E_d = 20.4 \text{ MeV}, \theta_L = 40^\circ) = -0.287$  and  $iT_{11}(E_d = 25.2 \text{ MeV}, \theta_L = 45^\circ) = -0.711$ . This rapid variation with energy has been attributed<sup>9</sup> to compound nucleus effects in  $^{14}\text{N}$  at excitation energies around 30 MeV where a broad resonance has been observed in photonuclear scattering.<sup>10</sup> Rapid variations of  $iT_{11}$  are then likely to occur around  $E_d = 25$  MeV, and these could then explain the discrepancy between the Berkeley and Grenoble  $^4\text{He}(\vec{d}, d)^4\text{He}$  data.

To check this possibility we have measured  $iT_{11}$  in  $^{12}\text{C}(\vec{d}, d_0)$  elastic scattering at

$E_d = 20, 25$  and  $30$  MeV near the first maximum of  $iT_{11}$ . Near  $25$  MeV the incident energy was varied by steps of a few hundred keV. The experiment was done at the Berkeley 88-inch cyclotron. The purely vector polarized deuteron beam (intensity up to  $100$  nA, polarization of the order of  $82\%$  of the maximum possible  $iT_{11} = \sqrt{3}/3$ ) was sent in a first scattering chamber onto a gas target cell filled with one atmosphere of  $^4\text{He}$ . The beam energy, measured with an analyzing magnet was  $30.00 \pm 0.05$  MeV. Two telescopes set symmetrically left and right at  $\theta_L = 90^\circ$  detected and identified the scattered deuterons. The measured asymmetry, combined with the previously established value<sup>5</sup> of the analyzing power,  $iT_{11}(E_d = 30 \text{ MeV}, \theta_L = 90^\circ) = -0.321 \pm 0.010$ , served to monitor the beam polarization, which was very stable and changed by less than  $3\%$  during the course of the experiment. The unscattered beam was then sent into a second scattering chamber after having passed through aluminum energy degraders and a set of defining slits. There the beam was incident on a  $15 \text{ mg/cm}^2$   $^{12}\text{C}$  target, and the asymmetry was measured by two telescopes set symmetrically left and right at angles  $\theta_L$ .

In order to eliminate instrumental asymmetries, alternate runs were taken with the sign of the beam polarization reversed. The results of our vector analyzing power measurements near  $25$  MeV are given in Fig. 1. Our  $29.5$  MeV result agrees well with the value measured at Grenoble. Near  $25$  MeV there is a strong variation of  $iT_{11}$  with energy changes of a few hundred keV. These values must be compared with the Grenoble value  $iT_{11}(E_d = 25.2 \text{ MeV}, \theta_L = 47^\circ) = -0.711 \pm 0.050$ . Although the agreement is satisfactory, the higher precision of the present data clearly shows that  $^{12}\text{C}(d, d_0)$  elastic scattering is not a good reaction for a polarimeter around  $25$  MeV. A similar effect is observed at  $20$  MeV where there is a significant difference between our value and the Grenoble value, which can also be attributed to the difference in beam energies for the two experiments.

In conclusion,  $^{12}\text{C}(\vec{d}, d_0)^{12}\text{C}$  elastic scattering, if suitable as a polarization standard at  $30$  MeV, should not be used at present below this energy because of rapid variations of the analyzing power with angle and energy. A much more detailed survey of the analyzing powers in  $^{12}\text{C}(d, d_0)$  scattering below  $30$  MeV is required before it can be used with confidence as a standard polarization analyzer in that energy region. The  $^4\text{He}(\vec{d}, d)^4\text{He}$  elastic scattering exhibits a smooth dependence with angle and energy over a wide range from  $15$  to  $45$  MeV, and thus is more suitable as a polarization standard, although  $iT_{11}$  is smaller than for the  $^{12}\text{C}(\vec{d}, d_0)$  reaction.

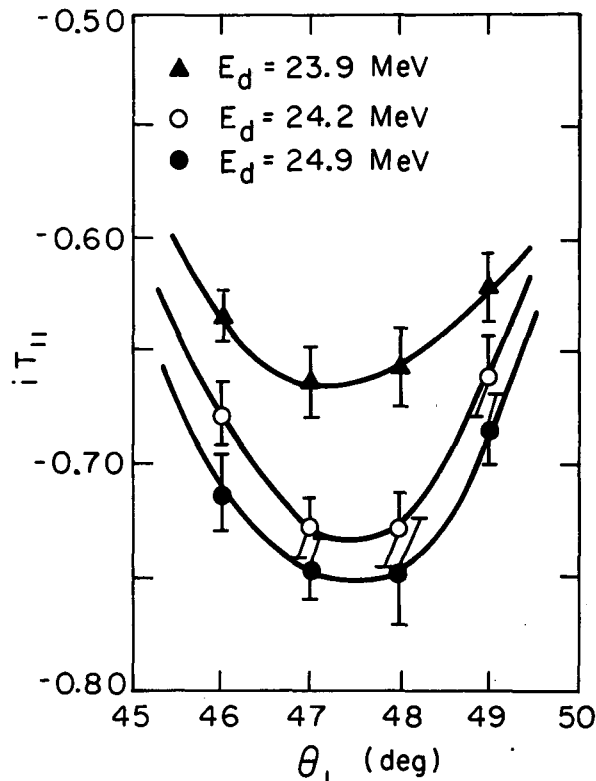


Fig. 1. Vector analyzing power,  $iT_{11}$ , in  $^{12}\text{C}(\vec{d}, d_0)$  as a function of  $\theta_L$ , the angle in the laboratory system for incident energies  $E_d$  near  $25$  MeV. The solid curves serve only to guide the eye. (XBL 741-2113)

#### Footnote and References

\* Condensed from LBL-2353, submitted to Nuclear Instruments and Methods.

† Present address: Institut des Sciences Nucléaires, Cedex 257, 38044.

‡ Present address: Sektion Physik, Univ. München, D-8046 Garching, Germany.

1. V. S. Starkovitch, Thesis, LASL Report LA-4191, July 1969, unpublished; G. G. Ohlsen, V. S. Starkovitch, W. G. Simon, and E. M. Bernstein, Phys. Letters **28B**, 404 (1969).

2. V. S. Starkovitch and G. G. Ohlsen, Polarization Phenomena in Nuclear Reactions, ed. by H. H. Barschall and W. Haerberli (Univ. of Wisconsin Press, Madison, 1971), p. 581; LASL Report LA-4465 MS, July 1970, unpublished.

3. V. König, W. Gruebler, A. Ruh, R. E. White, P. A. Schmelzbach, R. Risler, and P. Marmier, Nucl. Phys. A166 (1971) 393; W. Gruebler, V. König, P. A. Schmelzbach, and P. Marmier, Nucl. Phys. A134 (1969) 686.
4. B. A. Jacobsohn and R. M. Ryndin, Nucl. Phys. 24 (1961) 505.
5. Ch. Leemann, H. E. Conzett, W. Dahme, J. Macdonald, and J. P. Meulders, Bull. Am. Phys. Soc. 17 (1972) 562, and to be published.
6. R. A. Hardekopf, D. D. Armstrong, L. L. Catlin, P. W. Keaton, Jr., and G. P. Lawrence, LASL Report LA-5051, October 1972, unpublished.
7. G. Perrin, Nguyen Van Sen, A. Fiore, and J. Arvieux, Nucl. Instr. Methods 101 (1972) 603.
8. A. Fiore, J. Arvieux, Nguyen Van Sen, G. Perrin, R. Darves-Blanc, J. C. Gondrand, and F. Merchez, Proceedings of the International Conference on Few Particle Problems in the Nuclear Interaction, ed. by I. Slaus, S. A. Moszkowski, R. P. Haddock, and W. T. H. Van Oers (North-Holland Publishing Co., Amsterdam, 1972), p. 620.
9. G. Perrin, Nguyen Van Sen, J. Arvieux, A. Fiore, J. L. Durand, R. Darves-Blanc, J. C. Gondrand, F. Merchez, and C. Perrin, Nucl. Phys. A193 (1972) 215.
10. J. M. Loiseaux, J. M. Maison, and M. Langevin, J. Physique 28 (1967) 11.

#### THE $j$ -DEPENDENCE OF THE VECTOR ANALYZING POWER FOR $(d, {}^3\text{He})$ AND $(d, t)$ REACTIONS\*

B. Mayer,<sup>†</sup> H. E. Conzett, W. Dahme,<sup>‡</sup> D. G. Kovar,<sup>§</sup>  
R. M. Larimer, and Ch. Leemann

A number of experiments have shown that the vector analyzing power for  $(d, p)$  and  $(p, d)$  reactions with polarized incident particles depends strongly on the  $j$ -value of the transferred neutron for a given orbital angular momentum transfer.<sup>1,2</sup> Recently, this property, along with distorted-wave-Born-approximation (DWBA) fits to measured analyzing powers, has been exploited to provide spin assignments to a substantial number of states populated by these reactions in nuclei ranging from  $A = 40$ -187.<sup>3</sup> Also,  $J^\pi$  assignments of several states in  ${}^{209}\text{Pb}$  have been confirmed with this method.<sup>4</sup> It has been shown that the  ${}^{208}\text{Pb}(d, t){}^{207}\text{Pb}$  neutron pickup reaction with polarized deuterons near 12 MeV, also, shows a strong  $j$ -dependence of the vector analyzing power.<sup>4,5</sup> Since the same states can be reached via the  $(p, d)$  reaction, either reaction can be selected, in principle, to provide  $J^\pi$  assignments for the product nuclear states.

The  $(d, {}^3\text{He})$  proton transfer reaction, of course, provides another large number of states whose  $J^\pi$  values could be assigned or confirmed if the expected similar  $j$ -dependence of the vector analyzing power were established; and, the present lack of polarized neutron beams make the analogous  $(n, d)$  experiment unfeasible. We report here the results of an investigation that shows, indeed, a strong  $j$ -dependence of the vector analyzing power in the  ${}^{208}\text{Pb}(d, {}^3\text{He})$

${}^{207}\text{Tl}$  and  ${}^{12}\text{C}(d, {}^3\text{He}){}^{11}\text{B}$  reactions induced with vector polarized deuterons.

Data on the  ${}^{208}\text{Pb}(d, t){}^{207}\text{Pb}$  and  ${}^{12}\text{C}(d, t){}^{11}\text{C}$  reactions were taken concurrently so as to extend to higher energies the study of the  $j$ -dependence in those reactions.

The  ${}^{208}\text{Pb}(d, {}^3\text{He})$  and  ${}^{208}\text{Pb}(d, t)$  Reactions

The experiment was performed with a 30 MeV vector polarized deuteron beam from the Berkeley 88-inch cyclotron. The beam polarization was monitored continuously with a polarimeter placed downstream of the main scattering chamber. The analyser used was  ${}^4\text{He}$ , whose analyzing power in  $d-{}^4\text{He}$  elastic scattering was measured previously.<sup>6</sup> The vector polarization of the beam was typically  $p_y = 0.52$ .

The  $(d, {}^3\text{He})$  and  $(d, t)$  reactions populate essentially the  $3s_{1/2}$ ,  $2d_{3/2}$ ,  $1h_{11/2}$  and  $2d_{5/2}$  proton hole states and the  $3p_{1/2}$ ,  $2f_{5/2}$ ,  $3p_{3/2}$ ,  $1i_{13/2}$ , and  $2f_{7/2}$  neutron hole states in  ${}^{207}\text{Tl}$  and  ${}^{207}\text{Pb}$ , respectively. The angular distributions of the vector analyzing power,  $A_y(\theta)$ , exhibit a strong  $j$ -dependence for the  $2d$  states populated by the  $(d, {}^3\text{He})$  reaction (Fig. 1) and for the  $3p$  and  $2f$  states from the  $(d, t)$  reaction (Fig. 2). The sign of  $A_y(\theta)$  for  $j = l + \frac{1}{2}$  is opposite to that for  $j = l - \frac{1}{2}$  over most of the angular range studied, so the ease and unambiguity of  $j$ -assignment from such measurements

is clearly demonstrated. Moreover, the DWBA calculation gives a good qualitative account of this effect. In the DWBA calculations shown in Figs. 1 and 2, the deuteron optical potential was generated by fitting cross sections of deuteron elastic scattering from  $^{208}\text{Pb}$  at 27.5 MeV;<sup>7</sup> the  $^3\text{He}$  and triton optical potential parameters were those derived by Becchetti and Greenlees<sup>8</sup> from a global optical-model analysis.

The  $^{12}\text{C}(d, ^3\text{He})$  and  $^{12}\text{C}(d, ^3\text{He})$  and  $^{12}\text{C}(d, t)$  Reactions. The experiment was done at an incident deuteron energy of 45 MeV. The results are shown in Fig. 3. The  $^{12}\text{C}(d, ^3\text{He})$ ,  $^{11}\text{B}$  and  $^{12}\text{C}(d, t)^{11}\text{C}$  reactions give rise to very similar cross sections and vector analyzing powers. The small differences are within those that can be expected due to differences in Q-values and Coulomb effects. Therefore, in Fig. 3 the  $^{12}\text{C}(d, t)^{11}\text{C}$  experimental results are shown only for the first two levels. The analyzing powers for the  $l = 1$  transitions ( $p_{3/2}$  ground state,  $p_{1/2}$  2.14 MeV state) have quite different magnitudes but the angular distributions are in phase. Actually, even in (p, d)

reactions the j-dependence of the analyzing power is not always characterized by phase opposition over the whole angular range.<sup>2</sup>

The DWBA calculation with the optical-model parameters of Ref. 9 gives qualitative agreement with the analyzing power data for the  $p_{1/2}$  transition are reproduced but with a shift of about  $10^\circ$  between the calculated and experimental distributions. The DWBA does not at all reproduce the data for the transition to the  $p_{3/2}$  5.03 MeV state, even though the experimental angular distribution is qualitatively similar to that for the  $p_{3/2}$  ground state. Such difficulties were not unexpected since they are often encountered in DWBA calculations for reactions involving light nuclei.

In summary, a strong j-dependence of the vector analyzing power in (d,  $^3\text{He}$ ) reactions has been experimentally established for  $l = 2$  transitions in  $^{208}\text{Pb}$  and for  $l = 1$  transitions in  $^{12}\text{C}$ . Thus, this reaction can be used to determine spins of the many nuclear states that can be reached via proton transfer, in the same

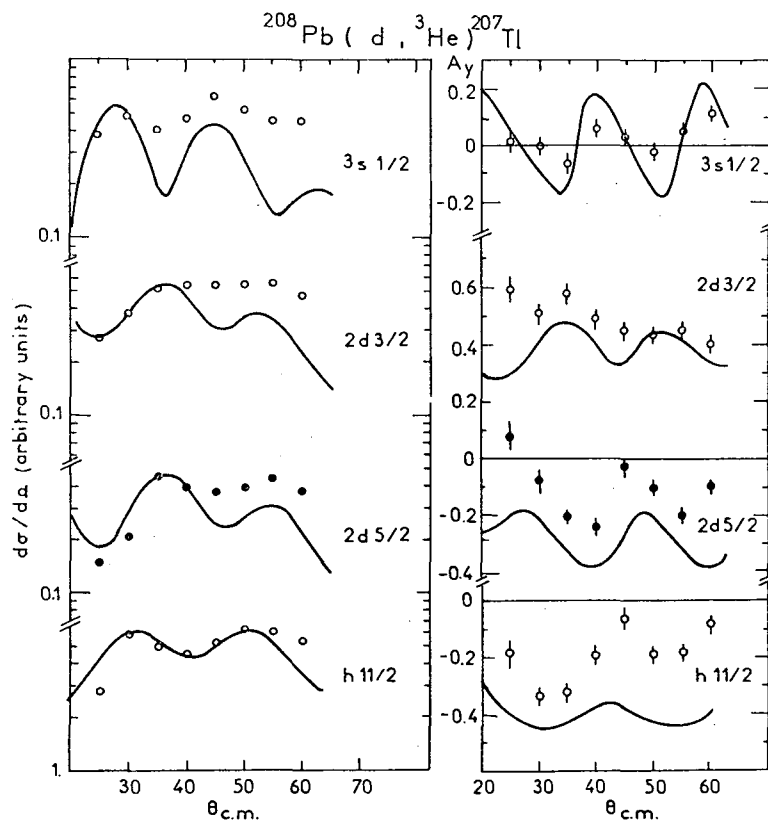


Fig. 1. Angular distributions of cross sections and vector analyzing power for the  $^{208}\text{Pb}(d, ^3\text{He})$   $^{207}\text{Tl}$  reaction at 30 MeV and DWBA predictions.

(XBL 743-527)

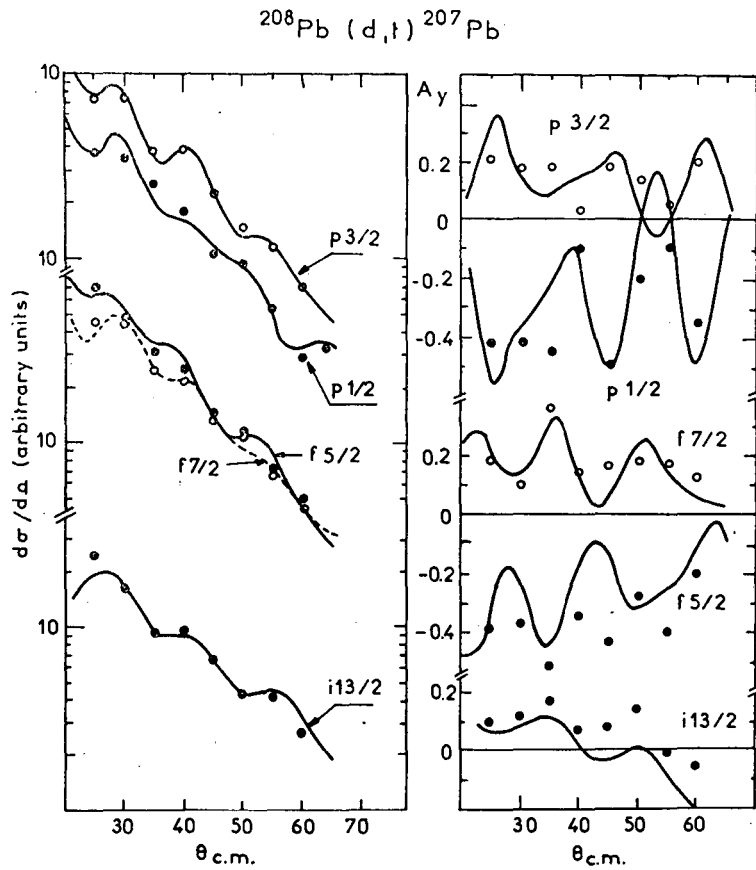


Fig. 2. Angular distributions of cross sections and vector analyzing power for the  $^{208}\text{Pb}(d,t)^{207}\text{Pb}$  reaction at 30 MeV and DWBA predictions.

(XBL 743-528)

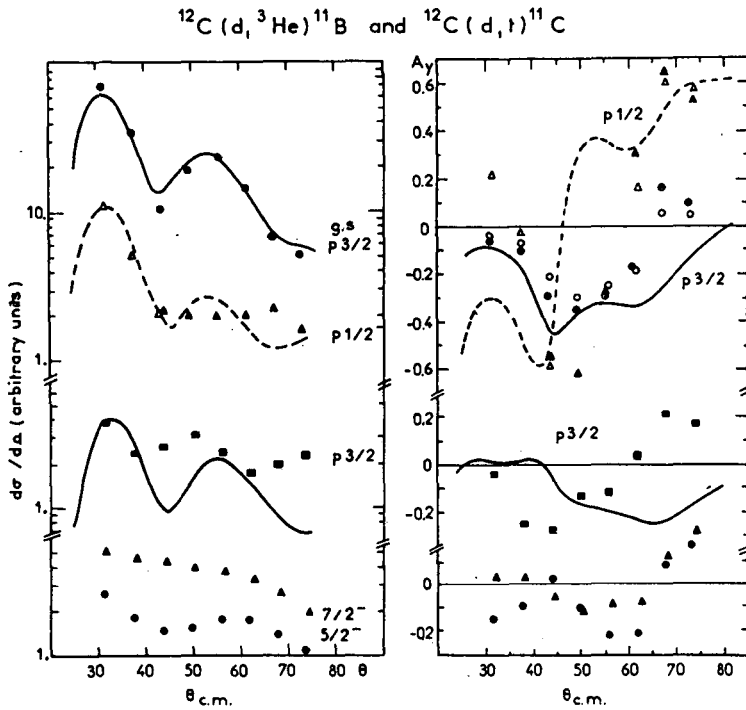


Fig. 3. Angular distributions of cross sections and vector analyzing for the  $^{12}\text{C}(d,^3\text{He})^{11}\text{B}$  (full dots) and  $^{12}\text{C}(d,t)^{11}\text{C}$  (empty dots) reactions at 45 MeV and DWBA predictions for  $^{12}\text{C}(d,^3\text{He})^{11}\text{B}$ .

(XBL 743-529)

manner as has been so successful in the neutron transfer experiments.

#### Footnotes and References

\* Condensed from LBL-2340, submitted to Phys. Rev. Letters.

† Present address: DPh-N/ME CEN Saclay, BP. 2 91120 Gif-Sur-Yvette, France.

‡ DAAD exchange student from the University of Munich, West Germany.

§ Present address: Argonne National Laboratory, Argonne, Illinois.

1. T. J. Yule and W. Haeberli, Phys. Rev. Letters 19, 756 (1967), Nucl. Phys. A117, 1 (1968); A. M. Baxter, J. A. R. Griffith, and S. Roman, Phys. Rev. Letters 20, 1114 (1968); A. A. Debenham, J. A. R. Griffith, M. Irshad, and S. Roman, Nucl. Phys. A151, 81 (1970); A. A. Debenham, J. A. R. Griffith, M. Irshad, O. Karban, and S. Roman, Nucl. Phys. A167, 289 (1971); D. C. Kocher and W. Haeberli, Nucl. Phys. A172, 652 (1971).
2. J. L. Escudié, J. C. Faivre, J. Gosset, H. Kamitsubo, R. M. Lombard, and B. Mayer, Phys. Rev. Letters 23, 1251 (1969); B. Mayer, J. Gosset, T. L. Escudié, and H. Kamitsubo, Nucl. Phys. A177, 205 (1971).
3. D. C. Kocher and W. Haeberli, Nucl. Phys. A196, 225 (1972); R. F. Casten, P. W. Keaton, Jr., and G. P. Lawrence, Phys. Rev. C7, 1016 (1973); R. D. Rathmell, P. J. Bjorkholm, and W. Haeberli, Nucl. Phys. A206, 459 (1973); J. A. Aymar, H. R. Hiddleston, S. E. Darden, and A. A. Rollefson, Nucl. Phys. A207, 596 (1973).
4. S. E. Vigdor, R. D. Rathmell, H. S. Liers, and W. Haeberli, Nucl. Phys. A210, 70 (1973).
5. H. S. Liers, R. D. Rathmell, S. E. Vigdor, and W. Haeberli, Phys. Rev. Letters 26, 261 (1971).
6. Ch. Leemann, H. E. Conzett, W. Dahme, J. MacDonald, and J. P. Meulders, Bull. Amer. Phys. Soc. 17, 562 (1972), and to be published.
7. J. Testoni, private communication.
8. F. D. Becchetti, Jr., and G. W. Greenlees, Polarization Phenomena in Nuclear Reactions, edited by H. H. Barschall and W. Haeberli (Univ. of Wisconsin Press, Madison, 1971) p. 682.
9. F. Hinterberger, G. Maierle, U. Schmidt-Rohr, P. Turek and G. J. Wagner, Nucl. Phys. A106, 161 (1968).

#### THE SCATTERING OF POLARIZED PROTONS FROM Si IN THE GIANT RESONANCE REGION OF $^{29}\text{P}^*$

C. R. Lamontagne,<sup>†</sup> B. Frois,<sup>†</sup> R. J. Slobodrian,<sup>†</sup>  
H. E. Conzett, Ch. Leeman, and R. de Swiniarski<sup>‡</sup>

Recent studies of inelastic proton scattering from a broad range of nuclei provide evidence for excitation of a giant quadrupole or monopole resonance just below the well known giant dipole resonance.<sup>1</sup> The proton widths of these broad states seem to imply that a resonance effect should be present in proton elastic scattering through this region of excitation. It should be observable provided that the shape elastic scattering, as described by the optical model (OM), is not dominant. While the scattering of protons (unpolarized and polarized) from helium is amenable to a detailed phase shift analysis,<sup>2</sup> the scattering from carbon and other nuclei has been analyzed by the optical model with varying degrees of sophistication.<sup>3-5</sup> It is well known that OM

parameters and wave functions are extensively used in the distorted wave Born approximation (DWBA) calculations of nuclear reactions.<sup>6</sup> The OM parameters for the proton-nucleus interactions are obtained from elastic scattering cross sections at and above 10-MeV laboratory energy. Experimental data and OM parameters are available at rather widely spaced energy intervals and smooth interpolations of them are usually assumed appropriate in applications. This results in monotonically varying parameters. However the validity of the latter and of the corresponding wave functions may be affected by resonances and, in particular, by the giant resonances present in nuclei. The region of the giant dipole resonance for  $^{29}\text{P}$  is located near

20 MeV in the  $^{28}\text{Si} + p$  channel, while the evidence for the quadrupole or monopole resonances in other nuclei would centre them about 2 MeV lower in energy.<sup>1</sup> No information on cross sections or polarizations has been available between 17 and 29 MeV<sup>7,8</sup> as is the case for most nuclei.

The polarized proton beam facility of the Berkeley 88-inch cyclotron was used to measure relative cross sections and asymmetries in the scattering from Si at 2-MeV intervals between 17 and 29 MeV inclusive. Four pairs of cooled silicon detectors were

used at symmetrical angles with respect to the beam, and geometrical asymmetries were compensated by performing measurements with two opposite spin orientations of the proton beam. The analyzing power  $A(\theta)$  was calculated from the left and right detector yields with both spin orientations of the beam, and the relative cross sections were obtained from averaging yields. Figure 1 shows the cross sections and analysing powers obtained; the solid lines correspond to best fits calculated with the optical model code Magali.<sup>9</sup>

It was conjectured by Satchler<sup>10</sup> sometime ago that the nature of the spin-orbit interaction

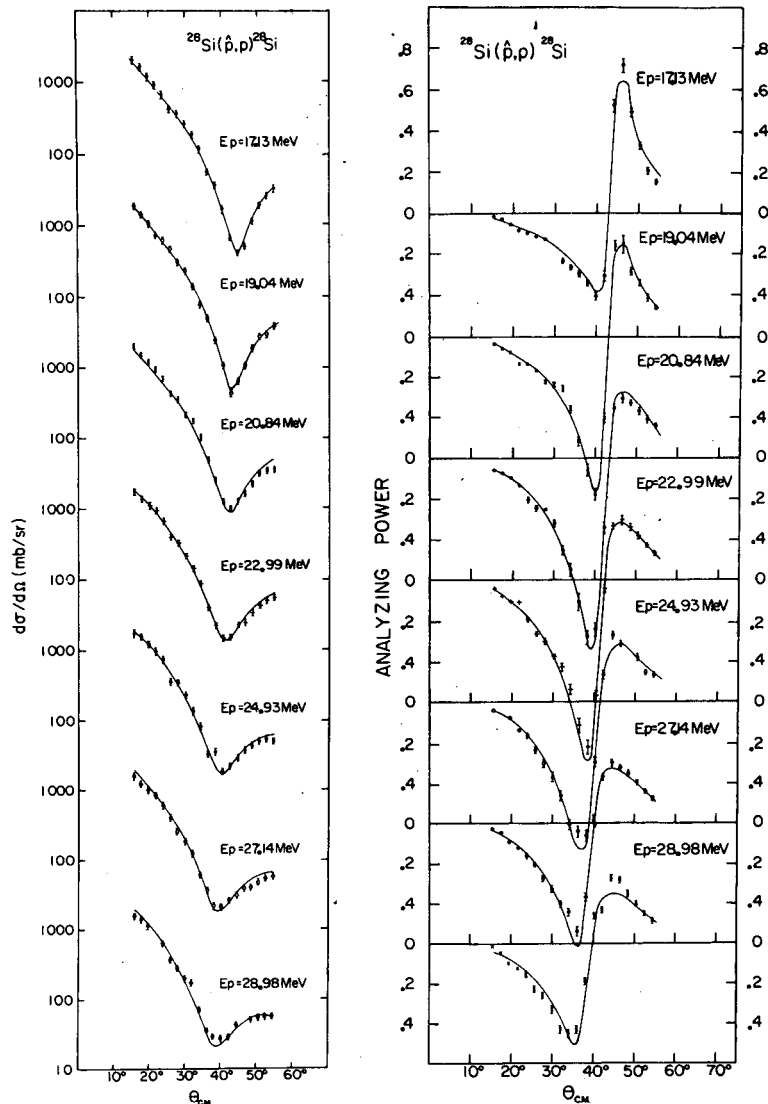


Fig. 1. Analyzing powers and cross sections obtained in the present experiment. Solid lines are optical model best fits.  
(XBL 743-524)

could be determined unambiguously from high quality polarization data, particularly at forward angles. Figure 2 shows indeed that the parameters obtained from the forward angle data fit successfully the full angular distributions at 17<sup>8</sup>, 25<sup>11</sup>, and 29<sup>8</sup> MeV. Figure 3 is a plot of the OM as functions of energy. The salient features are, firstly, a transition from a volume absorption  $W$  to a surface absorption  $W_d$  (with a fairly monotonic sum  $W + W_d$ )<sup>12</sup> and, secondly, a clear non-monotonic variation of the spin-orbit potential with a maximum near 21 MeV, corresponding well to the expected location of the giant dipole resonance.

The standard optical model calculation does not include contributions to the scattering from resonances other than those from single-particle potential scattering. Thus, it is possible that the anomalous behavior of the potential parameters found in this analysis is due to a giant resonance contribution to the

scattering which is not specifically included in the calculation.

An examination of the behavior with energy of the partial wave scattering amplitudes was made with the following results: The  $p_{1/2}$  and  $p_{3/2}$  amplitudes show stronger absorption between 17 and 25 MeV with best fit parameters than for those obtained with  $V_{SO}$  interpolated linearly, as would be expected for absorption through a giant dipole resonance. However, other amplitudes also show increased absorption, which is due to the fact that the OM potential has no specific  $l$ -dependence and thus, the effect of changes in the potential parameters cannot be limited to particular partial waves. A more detailed phase shift analysis should make it possible to identify a resonance effect in a particular partial wave. The extension to other nuclei of the experimental investigation of elastic proton scattering in the giant resonance regions is also planned.

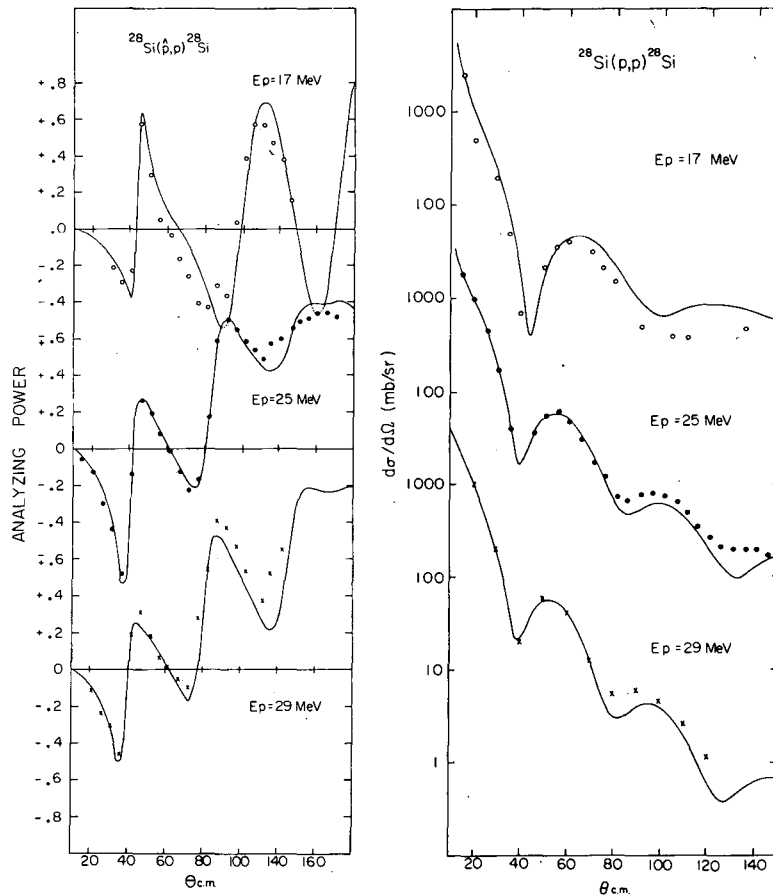


Fig. 2. Cross sections and analyzing powers at 17 MeV from ref. 7, at 25 MeV from ref. 11 and at 29 MeV from ref. 8. Solid lines are obtained from optical model fits with parameters identical to those of Fig. 1.

(XBL 743-525)



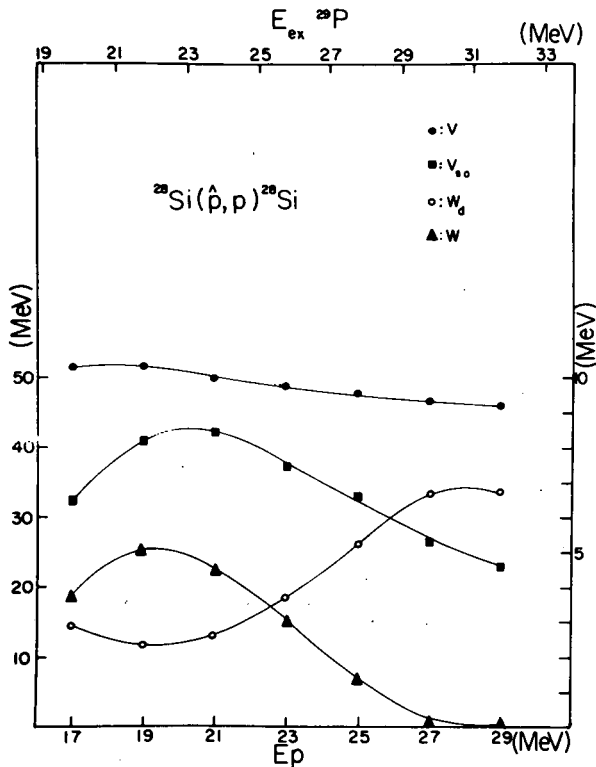


Fig. 3. Plot of optical model parameters for the best fits shown on figure 1. The sum  $W + W_d$  is approximately constant. The spin orbit potential  $V_{SO}$  shows a maximum near 20 MeV. The scale on the right is for  $W$ ,  $W_d$ , and  $V_{SO}$ . (XBL 743-526)

#### Footnotes and References

\*Condensed from Phys. Letters 45B, 465 (1973).

†Département de Physique, Université Laval, Québec 10e, Canada.

‡Institut des Sciences Nucléaires, Centre de Tri, 3844 Grenoble, France

1. M. B. Lewis and F. E. Bertrand, Nucl. Phys. A 196, 337 (1972); M. B. Lewis, Phys. Rev. Letters 29, 1257 (1972); G. R. Satchler, Nucl. Phys. A 195, 1 (1972); Particles and Nuclei (to be published).
2. G. R. Plattner, A. D. Bacher and H. E. Conzett, Phys. Rev. C 5, 1158 (1972).
3. P. E. Hodgson, Ann. Rev. of Nucl. Science 17, 1 (1967) and refs. therein.
4. F. D. Bechetti Jr. and J. W. Greenlees, Phys. Rev. 180, 1190 (1969).
5. F. Perey, in Polarisation Phenomena in Nuclear Reactions (H. H. Barschall and W. Haerberli, Eds.) and refs. therein, (University of Wisconsin Press, Madison 1971).
6. N. Austern, Direct Interaction Theories (John Wiley and Sons, 1970) and refs. therein.
7. D. J. Baugh, C. W. Greenlees, J. S. Lilley and S. Roman, Nucl. Phys. 65, 33 (1965) contains data at 17 MeV.
8. R. M. Craig, J. C. Dore, G. W. Greenlees, J. Lowe and D. L. Watson, Nucl. Phys. 83, 493 (1963) contains data at 29 MeV.
9. J. Raynal, 1969 D. Ph T/69, 42 (CEN Saclay).
10. G. R. Satchler, Nucl. Phys. A 92, 273 (1967).
11. R. de Swiniarski, H. E. Conzett, C. R. Lamontagne, B. Frois and R. J. Slobodrian, Can. J. Phys. 51, 1293 (1973).
12. The quality of the fits depends on the sum  $W + W_d$ , and weakly on the values of  $W$  and  $W_d$ .

THE SCATTERING OF POLARIZED PROTONS FROM  $^{24}\text{Mg}$ ,  $^{27}\text{Al}$ , AND  $^{32}\text{S}$  IN THE GIANT RESONANCE REGIONS OF  $^{25}\text{Al}$ ,  $^{28}\text{Si}$ , AND  $^{33}\text{Cl}$

J. Birchall, H. E. Conzett, C. R. Lamontagne,\*  
R. M. Larimer, R. Roy,\* and R. J. Slobodrian\*

The inelastic scattering of both unpolarized and polarized protons from several nuclei has recently provided evidence for the excitation of a giant quadrupole or monopole resonance just below the well known giant dipole resonance in the target nucleus.<sup>1</sup> Another way to investigate these giant resonances is via elastic proton scattering, since their proton widths imply that a resonance effect should be seen, provided that the shape elastic scattering is not completely dominant. Recent evidence for such an effect in  $^{29}\text{P}$  has been seen in  $\vec{p}$ - $^{28}\text{Si}$  elastic scattering between 17 and 29 MeV.<sup>2</sup>

We have extended to neighboring nuclei the measurements of cross sections and analyzing powers in elastic proton scattering in the giant resonance regions. Data were taken at 2-MeV intervals between 15 and 25 MeV for  $^{24}\text{Mg}$  and  $^{32}\text{S}$  and between 13 and 25 MeV for  $^{27}\text{Al}$ . These energy ranges include the region of giant dipole excitation of  $^{25}\text{Al}$ ,  $^{33}\text{Cl}$ , and  $^{28}\text{S}$ , respectively. Examples of our analyzing power data for  $^{27}\text{Al}$  and  $^{32}\text{S}$  are shown in Figs. 1 and 2. A rapid variation with energy of the forward maxima between laboratory scattering angles of  $30^\circ$  and  $50^\circ$  is clearly evident. This is shown in more detail in Fig. 3, where we have plotted the maximum analyzing power near  $40^\circ$ - $45^\circ$  as a function of energy. The broad peaking of these excitation functions

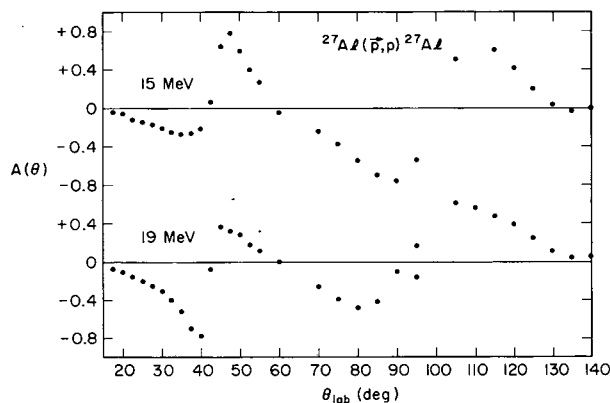


Fig. 1. Analyzing power,  $A(\theta_L)$ , in  $\vec{p}$ - $^{28}\text{Al}$  elastic scattering at 15 and 19 MeV.  
(XBL 743-2524)

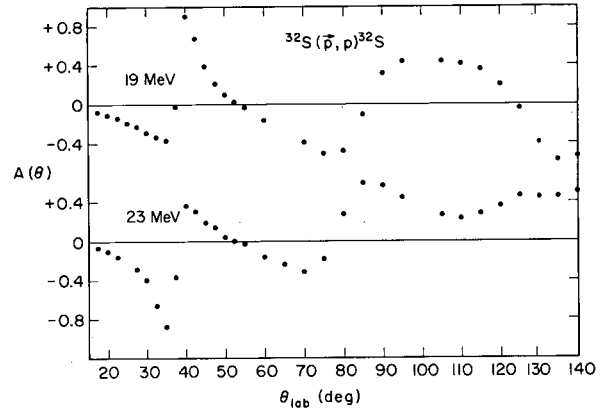


Fig. 2.  $A(\theta_L)$  in  $\vec{p}$ - $^{32}\text{S}$  elastic scattering at 19 and 23 MeV.  
(XBL 743-2525)

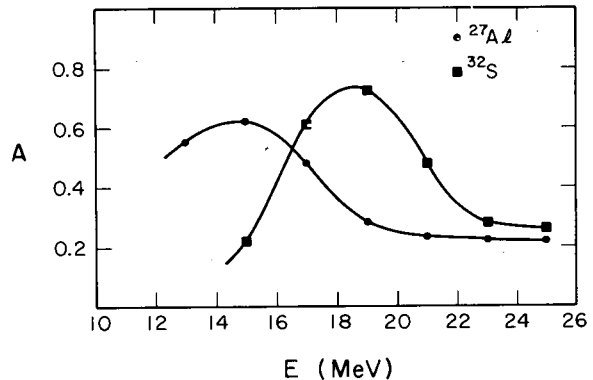


Fig. 3. Excitation functions of  $A(\approx 45^\circ)$  and  $A(\approx 40^\circ)$  in  $\vec{p}$ - $^{27}\text{Al}$  and  $\vec{p}$ - $^{32}\text{S}$  scattering, respectively.  
(XBL 743-2526)

is quite similar to that found in the  $\vec{p}$ - $^{28}\text{Si}$  scattering.<sup>2</sup> An optical model analysis of that data showed an anomalous energy dependence of the spin-orbit potential strength through the giant resonance region, so the behavior of our data suggests that a similar effect is present in the neighboring nuclei studied here.

Footnotes and References

\*August 1973 guest experimenters from Universite Laval, Quebec 10e, Canada.

1. M. B. Lewis and F. E. Bertrand, Nucl. Phys. A 196, 337 (1972); M. B. Lewis, Phys.

Rev. Letters 29, 1257 (1972); G. R. Satchler, Nucl. Phys. A 195, 1 (1972); Particles and Nuclei (to be published).

2. C. R. Lamontagne, B. Frois, R. J. Slobodrian, H. E. Conzett, Ch. Leemann, and R. de Swinarski, Phys. Letters 45B, 465 (1973).

A STUDY OF THE  $(\alpha, \alpha'n)$  REACTION ON VARIOUS TARGETS AT 90 MeV

D. R. Brown, I. Halpern, D. L. Hendrie, and H. Homeyer

In recent experiments done at the University of Washington cyclotron, the large broad peak seen at forward angles in the inelastic spectra of high energy alpha particles scattered from heavy targets<sup>1, 2</sup> was shown to have a large contribution from the  $(\alpha, {}^5\text{He}_{g.s.}) \rightarrow (\alpha, \alpha'n)$  reaction.<sup>3, 4</sup> In these experiments the alpha particles and neutrons from the breakup of  ${}^5\text{He}$  were detected in coincidence, and using the kinematics of the breakup process, the differential cross section for the reaction was deduced at a number of angles. From these data, the total cross section integrated over angle for the  ${}^{208}\text{Pb}(\alpha, {}^5\text{He}_{g.s.})\gamma^{207}\text{Pb}$  reaction was estimated to be about 69 mb at 42 MeV.<sup>3, 4</sup>

Having found so large a cross section for this reaction at 42 MeV, it was decided to repeat the study at the higher energies available at the 88-inch cyclotron. The higher energy studies also have an advantage over those at lower energy in that distortions of the  $\alpha$ -n correlation due to  ${}^5\text{He}$  breakup in the Coulomb field of the residual nucleus are less important.

In June 1973 we had a run using the 90 MeV  ${}^4\text{He}$  ion beam from the 88-inch cyclotron. In these measurements the energies and directions of neutrons and coincident  $\alpha$  particles were both measured. The experimental effort was divided into three parts:

1. The size of the  $(\alpha, {}^5\text{He}_{g.s.})$  reaction on  ${}^{12}\text{C}$ ,  ${}^{103}\text{Rh}$ ,  ${}^{208}\text{Pb}$ , and  ${}^{\text{nat}}\text{U}$  targets was measured in order to learn about the A dependence of the pickup process. Preliminary results indicate that although the reaction occurs in all targets studied, it is more copious in heavier targets.

2. Using a  ${}^{208}\text{Pb}$  target and a long flight path to give good time of flight and therefore good neutron energy resolution, data were taken specifically to determine which sharp final states in the residual  ${}^{207}\text{Pb}$  nucleus are populated by the  $(\alpha, {}^5\text{He}_{g.s.})$  reaction. Early results indicate that the  $3p$  states are favored.

3. Again using the  ${}^{208}\text{Pb}$  target, the in-plane angular correlation between the  $\alpha$  particle and the neutron was mapped out in a series of runs in which the  $\alpha$  counter was fixed and the neutron counter angle was varied. From these data we isolate production of final states of the unbound  $\alpha$ -neutron system other than the  ${}^5\text{He}_{g.s.}$ . Preliminary results here give evidence for the occurrence of quasi-elastic scattering. The analysis of all of these data is currently underway.

References

1. Gary M. Chenevert, Ph.D. Thesis, University of Washington, 1969, unpublished.

2. G. Chenevert, N. S. Chart, I. Halpern, G. Glasshauser, and D. L. Hendrie, Phys. Rev. Letters 27, 434 (1971).

3. D. R. Brown, I. Halpern, R. Haffner, K-L. Liu, and P. Russo, Bull. Am. Phys. Soc. 17, 927 (1972).

4. Nuclear Physics Laboratory Annual Report, University of Washington, (1973), p. 66.

## HIGHLY INELASTIC DEUTERON SCATTERING AT 45 MeV

H. Wieman, M. Zisman, I. Halpern, and D. Hendrie

The mechanisms for inelastic scattering in which large amounts of energy are transferred are still not fully understood. Measurements of  $(p, p')$ ,<sup>1</sup>  $(\alpha, \alpha')$ ,<sup>2</sup> and  $({}^3\text{He}, {}^3\text{He}')$ <sup>2</sup> for 40-100 MeV projectiles have shown that there is a large direct inelastic cross section that accounts for 10% or more of the total reaction cross section. In the case of the  $(\alpha, \alpha')$  reaction a portion of the observed  $\alpha'$  spectrum has been explained in terms of the  $(\alpha, {}^3\text{He})$  reaction<sup>3</sup> and considerable effort has been directed toward interpreting other portions of the  $\alpha'$  spectrum in terms of collective multipole resonances.

In pursuing the subject of highly inelastic scattering we have used 45 MeV deuterons from the 88-inch cyclotron to compare with the 90 MeV  $(\alpha, \alpha')$  results. The  $(d, d')$  spectra were measured at a number of angles for targets having  $A$  values from 27 to 208. If the main mechanism for the inelastic scattering is a quasi-elastic collision with a nuclear nucleon or other subunit, then one would expect that the deuteron, being weakly bound, could not in a single interaction lose a large amount of energy without breaking up. As a result, the  $(d, d')$  cross-section would be expected to be smaller than that for  $(\alpha, \alpha')$  and  $(p, p')$ , especially at backward angles. However, contrary to this simple picture, the cross sections we measured for  $(d, d')$  are roughly the same as those for comparable  $(\alpha, \alpha')$  and  $(p, p')$  measurements. An example of an observed spectrum [ $\text{Au}(d, d')$  at  $25^\circ$ ] is compared in Fig. 1 with Chenevert's  $25^\circ$  data for  $\text{Au}(\alpha, \alpha')$  and Bertrand's  $\text{Au}(p, p')$   $30^\circ$  data. The data analysis is in a preliminary stage so careful comparisons of angular distributions and total cross sections have not yet been made, but it is clear that the inelastic scattering spectra of the different projectiles are strikingly similar. For a realistic comparison, it should be mentioned that at  $25^\circ$  the  $(p, p')$  cross section is probably about a factor of two greater than it is for the  $30^\circ$  data shown. Deuteron breakup, although much more probable than  $(d, d')$ , apparently does not compete significantly with the inelastic channel.

There is some weak evidence for structure in the deuteron spectrum, including a peaking between 9-15 MeV of excitation, which is similar to the structure that has sometimes been interpreted in  $(p, p')$  and  $(\alpha, \alpha')$  in terms of giant multipole resonances. At the present time, however, we have not concentrated on this feature of the data.

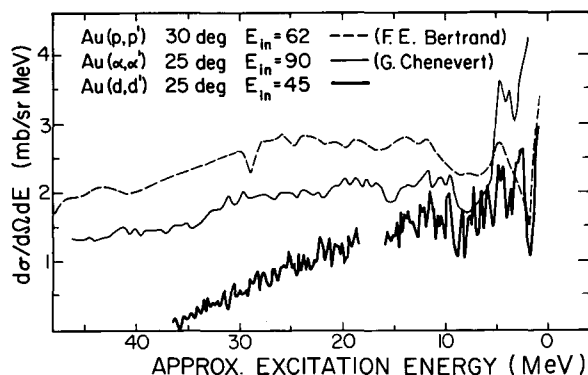


Fig. 1.  $\text{Au}(d, d')$  at  $25^\circ$  at an incident energy of 45 MeV.  $\text{Au}(p, p')$  at  $30^\circ$  at an incident energy of 62 MeV (F. E. Bertrand and R. W. Peelle).<sup>1</sup>  $\text{Au}(\alpha, \alpha')$  at  $25^\circ$  at an incident energy of 90 MeV (G. Chenevert).<sup>2</sup> (XBL 743-448)

## References

1. F. E. Bertrand and R. S. Peelle, Oak Ridge National Laboratory Report ORNL-4460, (1969) (unpublished).
2. Gary M. Chenevert, Ph.D. Thesis, University of Washington, 1969 (unpublished).
3. D. R. Brown, J. R. Calarco, I. Halpern, R. Heffner, K-L Liu, and P. A. Russo, Nuclear Physics Laboratory Annual Report, University of Washington (1972), p. 78 (unpublished).

THE  $^{12}\text{C}(^{14}\text{N}, ^{13}\text{N})^{13}\text{C}$  REACTION AT 100 MeV

R. M. DeVries, M. S. Zisman, J. G. Cramer, K-L. Liu,  
F. D. Becchetti, B. G. Harvey, H. Homeyer, D. G. Kovar,  
J. Mahoney, and W. von Oertzen

Recently it has been shown that the inclusion of "recoil" in numerical DWBA calculations of heavy ion transfer cross sections strongly affects the predicted differential cross sections in both shape and magnitude, particularly at higher energies, and explains many observations that were not previously understood.<sup>1,2</sup> In particular, the inclusion of recoil increases the number of  $l$ -transfers which can contribute to the cross section. This can be seen by considering the selection rules. The angular momentum selection rules for a reaction  $A(a, b)B$  are:

$$|l_1 - l_2| \leq l \leq l_1 + l_2$$

and

$$|j_1 - j_2| \leq l \leq j_1 + j_2$$

where

$a = b + x]_{l_1}^{j_1}$  and  $B = A + x]_{l_2}^{j_2}$ , i. e.,  $b$  and  $A$  are the cores between which  $x$  is transferred.

If recoil effects are not included, there is an additional "rule" which is an artifact of the "no-recoil" approximation. It is:  $(-1)^l = \Delta\pi$  where  $\Delta\pi$  is the change in parity from the initial to the final system. The  $l$ -values which satisfy this pseudo rule are called "normal"  $l$ 's and those which do not are called "non-normal"  $l$ 's. The contributions of these non-normal  $l$ -transfers to the cross section have

been found to be quite important in many heavy ion reactions.

One example of this was the successful analysis of single nucleon transfer reactions induced by  $^{14}\text{N}$  on  $^{12}\text{C}$  and  $^{11}\text{B}$  at high energies.<sup>1</sup> The relative lack of structure in some of the angular distributions for these reactions was explained by the complementary contribution of a "normal"  $l = 0$  transfer and a "non-normal"  $l = 1$  transfer, both of which were highly structured but out of phase with each other. In particular, the  $^{12}\text{C}(^{14}\text{N}, ^{13}\text{N})^{13}\text{C}_{g.s.}$  reaction at 78 MeV was well fit with the incoherent sum of these rapidly oscillating components, producing a smooth angular distribution in reasonable agreement with the data.

This explanation of a relatively structureless angular distribution is quite plausible, but it would be preferable to fit an angular distribution of the reaction  $^{12}\text{C}(^{14}\text{N}, ^{13}\text{N})^{13}\text{C}$  (3.09 MeV,  $2s_{1/2}$ ) which, according to the first of the above selection rules, will have only an  $l = 1$  contribution to the cross section. If this contribution has the same rapidly oscillating angular dependence found in the  $l = 1$  contribution to the  $^{13}\text{C}$  ground state cross section, then the experimental  $2s_{1/2}$  angular distribution would be expected to have pronounced oscillations.

To test this prediction, we have measured the  $^{14}\text{N} + ^{12}\text{C}$  elastic scattering and single

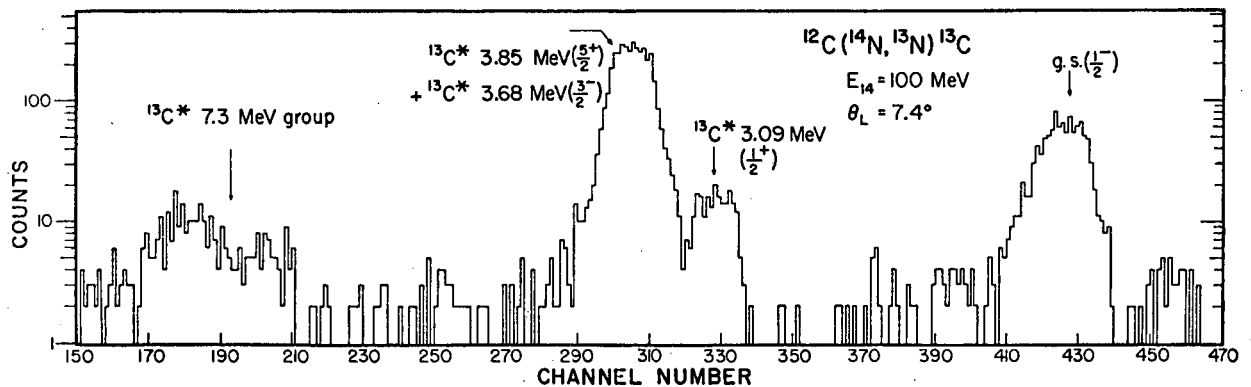


Fig. 1. Position spectrum for the  $^{12}\text{C}(^{14}\text{N}, ^{13}\text{N})^{13}\text{C}$  reaction. (XBL 743-449)

nucleon transfer differential cross sections at a bombarding energy of 100 MeV using an  $^{14}\text{N}$  beam from the Berkeley 88-inch cyclotron. The reaction products were analyzed with a magnetic spectrometer system.<sup>3</sup> A momentum spectrum for the transfer reaction is shown in Fig. 1, with the ground, 3.09 MeV, and 3.85-MeV states indicated. Since  $^{13}\text{N}$  is bound by only 1.94 MeV, no excited states of  $^{13}\text{N}$  are expected in the spectrum.

Figure 2 shows the angular distributions of the  $^{13}\text{C}$  states. Also shown for comparison is the measured elastic scattering angular distribution and its optical model fit. It can be seen clearly from Fig. 2 that the  $^{13}\text{C}$  ground state ( $1p_{1/2}$ ) does not oscillate while the angular distribution for the 3.09-MeV ( $2s_{1/2}$ ) state has pronounced oscillations, in qualitative agreement with the prediction given above. However, a serious discrepancy appears when the oscillations of the 3.09-MeV ( $2s_{1/2}$ ) angular distribution are compared with those of the elastic scattering angular distribution in Fig. 2. We see that the two distributions oscillate out of phase. The diffraction model for heavy ion transfer reaction<sup>4</sup> indicates that this phasing is characteristic of an even  $l$  transfer and, as has been previously mentioned, the transfer reaction is expected to populate the  $2s_{1/2}$  state with  $l=1$  only. It is possible that the diffraction model is too crude to give reliable predictions of such phasing. To investigate this question we must employ a more accurate theoretical treatment.

Exact finite range DWBA calculations including recoil were made using the program LOLA.<sup>2</sup> These are shown in Fig. 3. The ground state ( $1p_{1/2}$ ) angular distribution is reasonably well fit with the DWBA prediction which is an incoherent sum of  $l=0$  and  $l=1$  components and gives a product spectroscopic factor of 0.51. This number is in good agreement with the value determined in the 78 MeV-analysis<sup>2</sup> (0.53) and with the theoretical value of Cohen and Kurath<sup>5</sup> (0.42). The 3.85-MeV ( $1d_{5/2}$ ) angular distribution is also well-reproduced by the DWBA calculation, although in the case the measured spectroscopic factor (0.37) is less than the expected value of unity.

[Based on a comparison with high-resolution  $^{12}\text{C}(^7\text{Li}, ^6\text{Li})$  data,<sup>6</sup> the contribution to the 3.85-MeV peak from the unresolved  $1p_{3/2}$  level at 3.68 MeV is expected to be small.] However, the  $l=1$  prediction for the  $2s_{1/2}$  angular distribution is clearly out of phase with the data, as anticipated by the consideration of the diffraction model above, and the normalization shown in Fig 3 yields a spectroscopic factor (0.25) considerably smaller than expected. Curiously, the data bear an amazing resemblance in phase and shape to the  $l=0$  contribution to the ground state angular distribution.

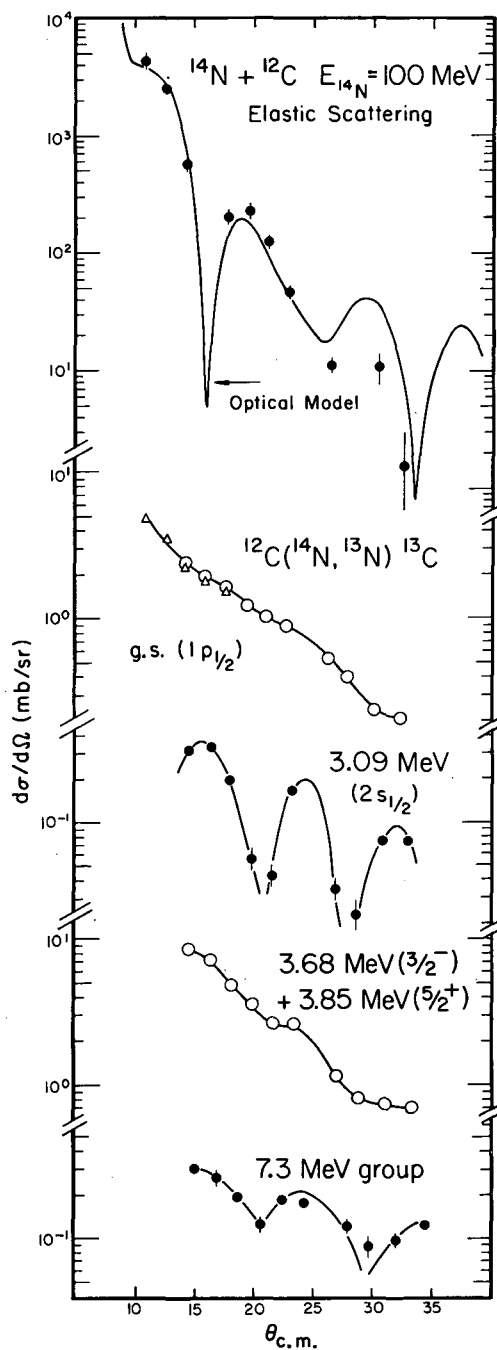


Fig. 2. Experimentally observed angular distributions. The elastic scattering optical model fit was obtained with the parameter set:  $V_0 = 145$  MeV,  $r_0 = 0.925$  F,  $a_0 = 0.816$  F,  $W_{\text{vol}} = 35.3$  MeV,  $r_1 = 1.30$  F,  $a_1 = 0.178$  F, where  $R = r_0 (12^{1/3} + 14^{1/3})$ . The triangular points in the  $^{13}\text{C}$  ground state angular distribution were obtained from measurements of the mirror reaction  $^{12}\text{C}(^{14}\text{N}, ^{13}\text{C})^{13}\text{N}_{\text{g.s.}}$ . The solid curves through the transfer reaction angular distributions are only to guide the eye. (XBL 743-450)

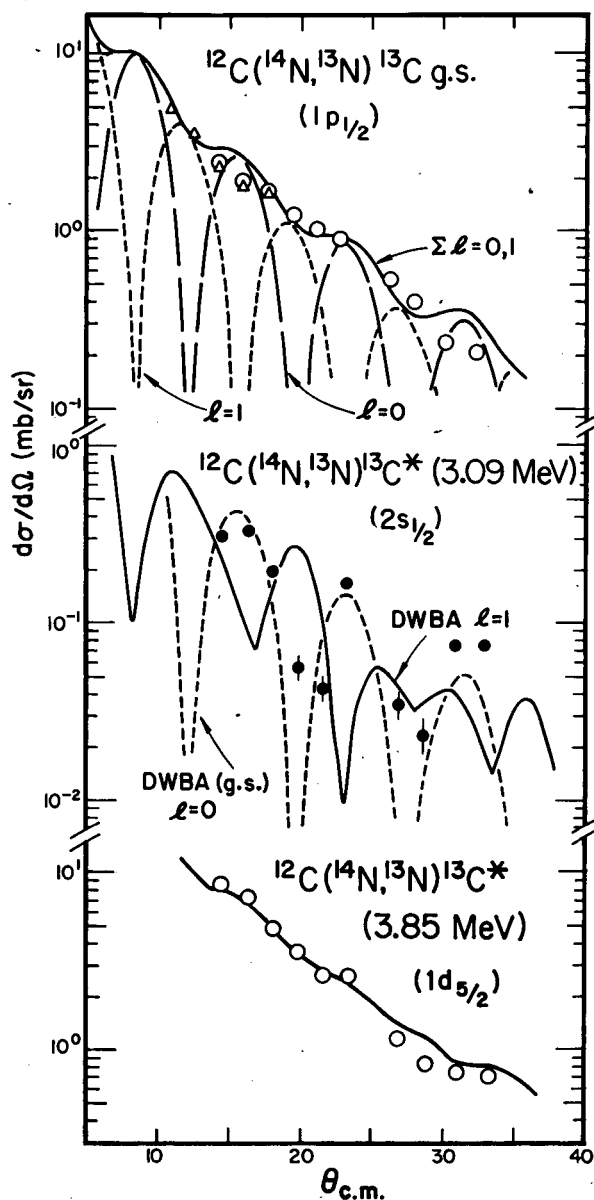


Fig. 3. DWBA calculations (using the optical parameters of Fig. 2) for the  $^{13}\text{C}$  ground, 3.09 MeV, and 3.85 MeV states. As discussed in the text, the 3.09 MeV excited state should be an  $l = 1$  transfer but seems to more closely resemble an  $l = 0$  transfer. (XBL 743-451)

We have investigated the dependence of these predictions on the optical model parameters used. Other parameter sets which fit the  $^{14}\text{N} + ^{12}\text{C}$  elastic scattering in this energy region<sup>7</sup> were tried in the DWBA calculations. Also investigated were the effects of small

changes in the bound state parameters (those used in the fits shown are  $r_0 = 1.25 F$  and  $a = 0.65 F$ ). None of these changes produced any discernable change in the phase of the angular distributions.

Since the finite range DWBA program LOLA has given good agreement with other oscillating angular distributions in this mass and energy region<sup>2</sup> (no  $2s_{1/2}$  states were studied, however) and has also correctly predicted the angular distribution of a  $2s_{1/2}$  state in the  $^{30}\text{Si}(^{16}\text{O}, ^{15}\text{N})^{31}\text{P}$  reaction at 42 MeV,<sup>8</sup> we must conclude that the fault does not lie with the code, and that the reaction process responsible for the population of the  $2s_{1/2}$  state is somehow not being correctly described.

In summary, we find that the ground and 3.85 MeV state angular distributions are well-reproduced by finite-range DWBA calculations but the 3.09 MeV state has a highly oscillatory angular distribution which is completely out of phase with the theoretical prediction. The explanation for the anomaly is presently unknown and further measurements should be undertaken to clarify the reaction mechanisms in this mass region.

#### References

1. R. M. DeVries and K. I. Kubo, *Phys. Rev. Letters* **30**, 325 (1973).
2. R. M. DeVries, *Phys. Rev. C* **8**, 951 (1973).
3. B. G. Harvey, et al., *Nucl. Instr. Methods* **104**, 21 (1972); M. S. Zisman, Lawrence Berkeley Laboratory Report No. LBL-1247, 1972, (unpublished).
4. K. R. Greider, in *Nuclear Reactions Induced by Heavy Ions*, (North-Holland, Amsterdam, 1970), p. 217; *A. Dar Phys. Letters* **7**, 339 (1963).
5. S. Cohen and D. Kurath, *Nucl. Phys.* **A101**, 1 (1967).
6. P. Schumacher, N. Ueta, H. H. Duhm, K. I. Kubo, and W. J. Klages, *Nucl. Phys.* **A212**, 573 (1973).
7. I. Kohno, S. Nakajima, T. Tonuma, and M. Odena, *J. Phys. Soc. Japan* **30**, 940 (1971); W. von Oertzen, M. Liu, C. Caverzino, J. C. Jacmart, R. Pongheon, M. Riou, J. C. Roynette, and C. Stephan, *Nucl. Phys.* **A143**, 34 (1970).
8. R. M. DeVries, *Phys. Rev. C* **8**, 1542 (1973).

THE ( $^{16}\text{O}$ ,  $^{14}\text{C}$ ) REACTION ON SPHERICAL AND DEFORMED NUCLEIW. von Oertzen,\* B. G. Harvey, D. L. Hendrie,  
H. Homeyer,<sup>†</sup> D. G. Kovar,<sup>‡</sup> and J. Mahoney

Measurements of two proton transfer<sup>1</sup> on spherical nuclei with closed neutron shell  $N = 82$  showed large cross sections, which appear enhanced due to the proton pairing interaction. The active proton shell model orbits in these nuclei are the same as the neutron orbits in the tin isotopes --  $3g_{1/2}$ ,  $2d_{5/2}$ ,  $2d_{3/2}$ ,  $h_{11/2}$ ,  $g_{9/2}$ ,  $h_{11/2}$ . The proton pairing interaction scatters the single particle strength over all these shells. The two proton transfer on these nuclei thus will be determined by a coherent action of many configurations.

We have measured the ( $^{16}\text{O}$ ,  $^{14}\text{C}$ ) reaction using the 104-MeV  $^{16}\text{O}$  beam from the 88-inch cyclotron at LBL on targets of  $^{142}\text{Nd}$ ,  $^{144}\text{Sm}$ ,  $^{148}\text{Sm}$ , and  $^{152}\text{Sm}$ . This study will allow a comparison of the two-proton transfer strength into the same proton configurations for different neutron numbers ( $^{144}\text{Sm}$ - $^{152}\text{Sm}$ ) and a comparison of the transfer strength on spherical ( $^{142}\text{Nd}$ ,  $^{144}\text{Sm}$ ,  $^{148}\text{Sm}$ ) and deformed nuclei ( $^{152}\text{Sm}$ ). The high incident energy turns out to be important to achieve comparable dynamical conditions for the three Sm isotopes. As shown in Fig. 1, the Q-value dependence of the ( $^{16}\text{O}$ ,  $^{14}\text{C}$ ) cross section is rather restrictive at lower energies due to the dominance of the Coulomb field.<sup>2</sup>

The  $^{14}\text{C}$  spectra were obtained with the magnetic spectrometer and a focal plane detector described previously.<sup>3</sup> The targets were made on  $^{12}\text{C}$  backings of  $20 \mu\text{g}/\text{cm}^2$  thickness, and had thicknesses between  $100$ - $200 \mu\text{g}/\text{cm}^2$ . The overall energy resolution was mainly determined by the target thickness and varied from 150 and 200 keV. Angular distributions were measured for the  $^{144}\text{Sm}(^{16}\text{O}, ^{14}\text{C})^{146}\text{Gd}$  reaction and the angle of maximum cross section was found to be at  $\sim 35^\circ$  ( $\sim 30^\circ$  Lab). Figure 2 shows a sample  $^{12}\text{C}$  spectrum on  $^{144}\text{Sm}$  at  $30^\circ$  lab scattering.

The ground state transition does dominate the spectra, although not as strongly as in (t,p) reactions on the tin isotopes<sup>4</sup> with the same neutron shell model orbits. The more complicated structure of the  $^{16}\text{O}$  compared to the triton, and the large cross sections of the heavy ion transfer reaction for larger angular momentum transfer, gives stronger transitions to excited states with spins of  $2^+$ ,  $4^+$ ,  $3^-$ , etc. At excitation energies above 5 MeV no selective population of states is seen and the high density of levels produces a continuum in the spectrum.

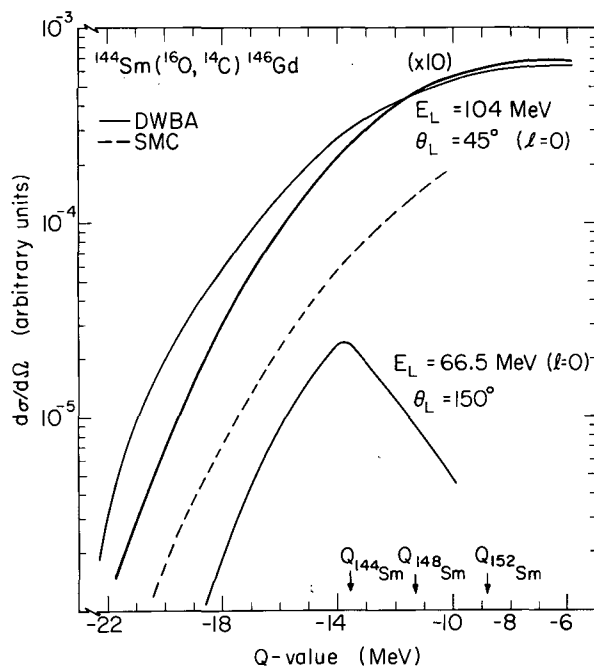


Fig. 1. Calculated Q-dependence of the ( $^{16}\text{O}$ ,  $^{14}\text{C}$ ) reaction as described in the text. (XBL 738-3967)

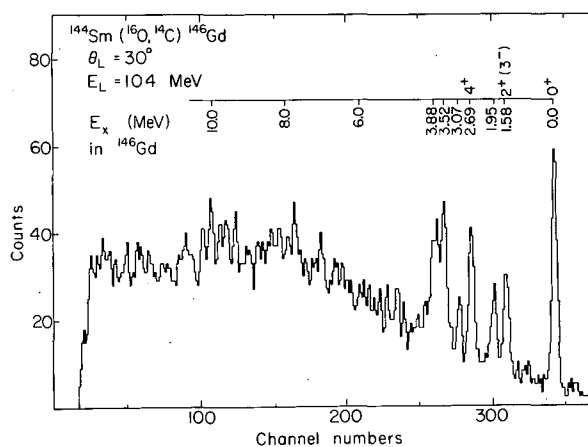


Fig. 2. A spectrum of the  $^{144}\text{Sm}(^{16}\text{O}, ^{14}\text{C})^{146}\text{Gd}$  reaction at  $\theta_L = 30^\circ$  using 104-MeV oxygen ions. (XBL 735-3001)



Table I. Transfer probabilities for ( $^{16}\text{O}$ ,  $^{14}\text{C}$ ) reactions (ground state transitions) at  $E_L = 104$  MeV and  $\theta_L = 30^\circ$ .

Target	$Q_0$ (MeV)	$d_0$ (fm)	$^{14}\text{C}/^{16}\text{O}$	CF	$P_{\text{tr}} (\times 10^{-5})$
$^{152}\text{Sm}$	-8.85	2.047	$1.2 \cdot 10^{-5}$	1.04	1.24
$^{148}\text{Sm}$	-11.3	2.086	$3.5 \cdot 10^{-5}$	1.55	5.4
$^{144}\text{Sm}$	-13.6	2.12	$4.6 \cdot 10^{-5}$	2.8	12.8
$^{142}\text{Nd}$	-11.78	2.05	$5.0 \cdot 10^{-5}$	1.85	9.2

$Q_0$  = Ground state Q-value.

$d_0$  = Average minimum distance  $\bar{R}_{\text{min}} = d_0 (A_1^{1/3} + A_2^{1/3})$ .

CF = Q-value dependence correction factor.

$P_{\text{tr}}$  = Reduced transfer probability.

For a comparison of the two-proton transfer strength Table I gives the experimental ratios  $^{14}\text{C}/^{16}\text{O}$  (or experimental transfer probability) for the different targets. From these values the absolute cross sections can be obtained by multiplying with the cross section for elastic scattering (in the incident channel) that is still Rutherford scattering at that angle. Due to the different ground state Q-values (also given in the table) the transfer probability has to be corrected for the Q-value dependence. The Q-value dependence of the cross section was obtained from DWBA calculations using as bound state a di-proton wavefunction with the appropriate quantum numbers corresponding to major oscillator shell of 3s and a fixed binding energy. A no recoil calculation was performed, and is displayed in Fig. 2 as the two solid lines for  $40^\circ$  and  $45^\circ$  c.m., which correspond to the calculated angle of maximum cross section. The factors CF given in the table are the ratios of calculated cross sections at the Q-value of maximum cross section. The reduced transfer probability  $P_{\text{tr}}$  given in the table then should reflect the variation of the two-proton transfer strength due to structure factors alone.

Whereas the transfer probability is the same for  $^{142}\text{Nd}$ , and  $^{144}\text{Sm}$  targets as expected from a pairing rotational model<sup>5</sup> we observe a distinctive decrease as function of increasing neutron number for the samarium isotopes. This decrease is probably due to the interaction of the protons with the neutrons outside the closed  $N = 82$  shell (which leads to a larger

binding energy of the two protons as reflected by the less negative Q-values) and which could lead to spreading of the  $l = 0$  transfer strength. However there are no obvious states in the spectra which contain the missing strength.

#### Footnotes and References

\* On leave from Max Planck Institut für Kernphysik, Heidelberg, Germany.

† On leave from Hahn-Meitner Institut, Berlin, Germany.

‡ Present address: Argonne National Laboratory, Argonne, Illinois.

1. W. von Oertzen, H. G. Bohlen, and B. Gebauer, Nucl. Phys. **A207**, 91 (1973).
2. Y. Cassagnou, M. Laméhin-Rachti, C. Levi, W. Mittig, and L. Papineau, Proceedings of the Symposium on Heavy Ion Transfer Reactions 1972, Argonne National Laboratory.
3. B. G. Harvey et al., Nucl. Inst. and Methods **104**, 21 (1972).
4. E. R. Flynn, J. G. Beery, and A. G. Blair, Nucl. Phys. **A154**, 225 (1970).
5. See for example, R. A. Broglia, O. Hansen and C. Riedel, Advances in Nucl. Phys. Vol. 6 (1973).

A STUDY OF THE  $^{208}\text{Pb}(^{16}\text{O}, ^{15}\text{O})^{209}\text{Pb}$  REACTION AND THE  
NEUTRON POTENTIAL,  $A > 200$

F. Becchetti,\* D. Kovar, B. G. Harvey, H. Homeyer,  
J. Mahoney, C. Maguire, D. K. Scott, and W. von Oertzen

The neutron levels in  $^{209}\text{Pb}$  have been studied via the  $^{208}\text{Pb}(^{16}\text{O}, ^{15}\text{O})$  reaction at a bombarding energy of 140 MeV. The experiments were performed at the 88-inch cyclotron using the magnetic spectrometer - focal plane system.

Of particular interest is the  $1j_{15/2}$  level in  $^{209}\text{Pb}$ . Spectroscopic factors for this state, measured previously using light ion reactions, vary from 0.2 to 1.0. In most light ion reaction the  $1j_{15/2}$  state is very weak due to momentum mismatch. In contrast, the ( $^{16}\text{O}, ^{15}\text{O}$ )

reaction preferentially excites this state. This can be seen in Fig. 1 where we display an  $^{15}\text{O}$  spectrum obtained at  $\theta_L = 40^\circ$ , which is near the grazing angle. We note the absence of any other strong excitation above  $E_x \approx 3$  MeV, although there appear to be groups between  $E_x = 3$  and 4.2 MeV. These latter groups are most likely  $j_{15/2}$  fragments.

We are analyzing the data with finite-range DWBA including recoil,<sup>1</sup> and have obtained preliminary results which indicate  $C^2S = 0.9$  for all states other than  $1j_{15/2}$  and  $C^2S = 0.5$  for the  $j_{15/2}$  level at 1.5 MeV.

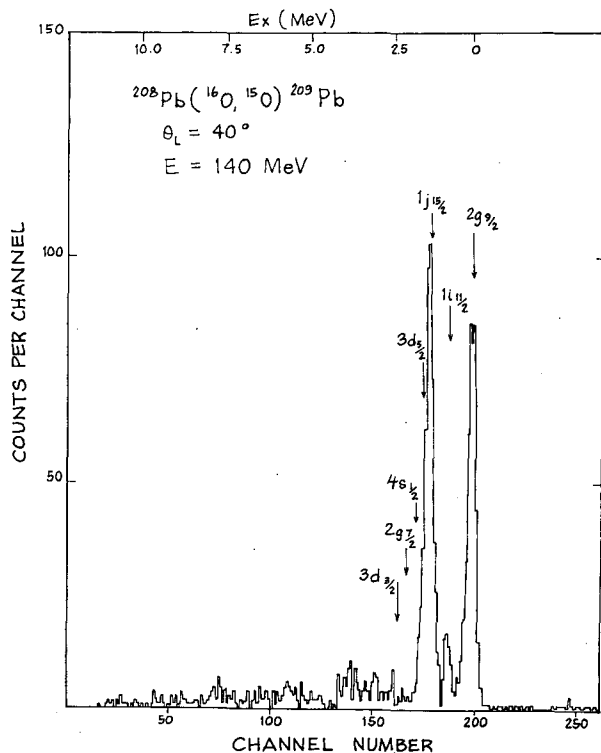


Fig. 1. (XBL 741-147)

We have compared the  $^{208}\text{Pb}(^{16}\text{O}, ^{15}\text{O})$  results with those obtained from the one proton transfers,  $^{208}\text{Pb}(^{16}\text{O}, ^{15}\text{N})$ . If we assume that  $^{15}\text{O}$  and  $^{15}\text{N}$  are mirror nuclei, then the ratio of ( $^{16}\text{O}, ^{15}\text{O}$ ) to ( $^{16}\text{O}, ^{15}\text{N}$ ) cross sections gives a measure of the radial distribution of valence neutrons in  $^{209}\text{Pb}$  relative to valence protons in  $^{209}\text{Bi}$ . Our results indicate that the neutron and proton distributions are similar in Pb, i. e.,  $\langle r^2 \rangle_n^{1/2} - \langle r^2 \rangle_p^{1/2} \leq 0.1$  fm. Among neutron potentials<sup>2</sup> used in the literature, the Zaidi potential<sup>2</sup> (Woods-Saxon,  $V = 51$  MeV,  $r = 1.19$  fm,  $a = 0.75$  fm,  $\lambda_{so} = 20.5$ ) gives results most consistent with our data.

#### Footnote and References

\* Present address: University of Michigan, Ann Arbor, MI 48105.

1. Program LOLA; R. DeVries (unpublished).
2. S. A. A. Saidi and S. Darmodj. Phys. Rev. Letters 19, 1446 (1967).

A STUDY OF THE TWO PROTON TRANSFER REACTIONS  
 $^{208}\text{Pb}(^{12}\text{C}, ^{10}\text{Be})^{210}\text{Po}$  AND  $^{208}\text{Pb}(^{16}\text{O}, ^{14}\text{C})^{210}\text{Po}$

F. D. Becchetti,\* D. G. Kovar,† B. G. Harvey, D. L. Hendrie,  
 H. Homeyer,‡ J. Mahoney, W. von Oertzen,‡ and N. K. Glendenning

Many shell model calculations have been performed predicting levels in nuclei consisting of a few particles or holes outside of a  $^{208}\text{Pb}$  core. Most of these nuclei can be studied with a variety of light ion reactions. To date, however, the levels in  $^{210}\text{Po}$  formed by transferring two protons directly to the  $^{208}\text{Pb}$  core have not been studied. We report the observation of levels in  $^{210}\text{Po}$  via the heavy ion two-proton transfer reactions:  $(^{12}\text{C}, ^{10}\text{Be})$  and  $(^{16}\text{O}, ^{14}\text{C})$ . The results are used to test predictions of available shell model wave-functions.

The experiments were performed using  $^{12}\text{C}$  ( $E_L = 78$  MeV) and  $^{16}\text{O}$  ( $E_L = 104, 140$  MeV) beams from the LBL 88-inch cyclotron. The beam was energy-dispersed across the target by a pair of analyzing magnets. Reaction products were detected in the focal plane of a dispersion-matched magnetic spectrometer with a position-sensitive proportional counter (6 horizontal wires,  $6 \times 45$  cm effective area) backed by a plastic scintillator.<sup>1</sup> In the present arrangement a time-zero detector<sup>2</sup> consisting of a thin ( $\sim 80$   $\mu\text{g}/\text{cm}^2$ ) NE111 plastic scintillator was placed at the entrance of the spectrometer. The signal from this detector and another from the final scintillator were used for the TOF measurement (replacing the cyclotron rf signal employed previously). Typical resolutions (FWHM) in the present experiment were  $\Delta E/\Delta X \sim 10\%$ , TOF  $\sim 1\%$  (2.5 nsec) and energy resolution  $\delta E/E \sim 0.15\%$  or approximately 100-150 keV for  $(^{12}\text{C}, ^{14}\text{C})$ , depending on the target thickness.

Both "thin" ( $\sim 100$   $\mu\text{g}/\text{cm}^2$ ) and "thick" ( $\sim 300$   $\mu\text{g}/\text{cm}^2$ ) targets consisting of  $^{208}\text{Pb}$  evaporated onto thin carbon foils (10-30  $\mu\text{g}/\text{cm}^2$ ) were used. Some of the targets also had a layer of carbon evaporated over the  $^{208}\text{Pb}$  so as to reduce evaporation and sputtering of the  $^{208}\text{Pb}$  from beam bombardment. In order to reduce the latter effects were limited the beam currents to  $\lesssim 300$  na (fully stripped ions). Cross sections were obtained from the particle yields relative to a monitor counter and the  $^{16}\text{O}(8^+)$  yield, which in turn, was normalized to Rutherford cross sections at forward angles. The energy of any particle could be determined from its position measurement to an accuracy  $\sim \pm 0.05\%$  ( $\pm 30$  to  $\pm 70$  keV).

Particle spectra obtained for the reactions  $^{208}\text{Pb}(^{12}\text{C}, ^{10}\text{Be})^{210}\text{Po}$ ,  $E(^{12}\text{C}) = 78$  MeV and

$^{208}\text{Pb}(^{16}\text{O}, ^{14}\text{C})^{210}\text{Po}$ ,  $E(^{16}\text{O}) = 104$  MeV are shown in Fig. 1. The  $^{12}\text{C}$  and  $^{16}\text{O}$  bombarding energies correspond to the same projectile

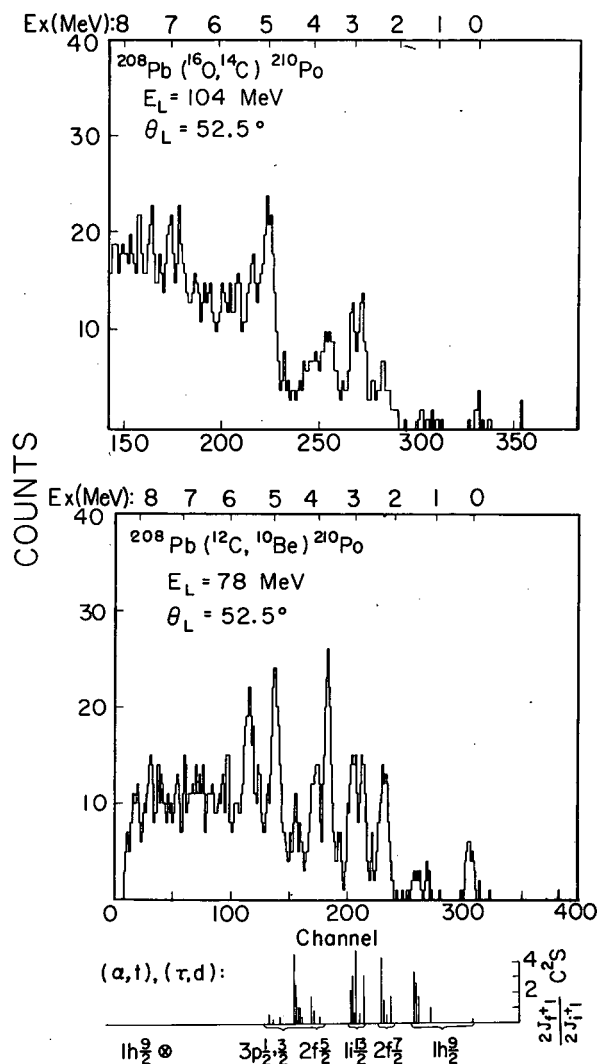


Fig. 1. Top: A comparison of  $(^{16}\text{O}, ^{14}\text{C})$  and  $(^{12}\text{C}, ^{10}\text{Be})$  spectra (thin target) near the grazing angle. The energy scales have been adjusted to be approximately the same. Bottom: Excitation energies and spectroscopic factors for  $^{210}\text{Po}$  levels  $[1h_{9/2} \oplus n l j]_J$  observed in  $^{209}\text{Bi}(\alpha, t)$  and  $^{209}\text{Bi}(^3\text{He}, d)$ .  
 (XBL-731-2013A)

velocities and nearly the same energy above the Coulomb barrier ( $\sim 20$  MeV greater). In Fig. 1 the angle ( $52.5^\circ$  lab) is near the peak in the measured angular distributions, which are similar for the two reactions or different levels. The shapes of the spectra reflect the strong Q-value dependence of heavy-ion reactions. This dependence results in a "Q-window" whose centroid,  $Q_{opt}$ , depends on the charge transfer and bombarding energy.

The data appear to indicate that the observed  $Q_{opt}$  values are slightly more positive than those given by the semi-classical approximation and considerably more negative than those given by DWBA. The exact shapes of the spectra, however, are complicated functions of both the Q-dependence of the reaction and the structure of the final states. Recoil effects are also important.

#### Angular Distributions

Angular distributions are shown in Figs. 2-3. A few forward angle points for some of the levels observed in ( $^{16}\text{O}, ^{14}\text{C}$ ) were obscured

by contaminants. The error bars shown reflect only the statistical errors (std. dev.) in the estimated total yield and background correction. The fluctuations in the data at  $E_x > 6$  MeV may not be significant owing to the level density and background at high excitation. The shapes of the angular distributions for  $E_x < 6$  MeV are essentially the same to within the errors indicated even though known states of very different spins ( $J^\pi = 0^+$  to  $8^+$ ) are shown.

In Table I we list the levels in  $^{210}\text{Po}$  believed to be  $[\pi l j \times \pi_9 / 2]$  and compare calculated spectroscopic factors relative to those of single particle states in  $^{209}\text{Bi}$  observed in  $^{208}\text{Pb}(^{12}\text{C}, ^{11}\text{B})$  and  $^{208}\text{Pb}(^{16}\text{O}, ^{15}\text{N})$  at the same bombarding energies. The results are consistent with light ion results<sup>3</sup> and we therefore conclude that the heavy-ion reactions proceed via a direct single-step transfer without appreciable core-excitation. As in the reaction  $^{208}\text{Pb} \rightarrow ^{209}\text{Bi}$  we observe a j-selectivity which depends on the structure of the projectile. The ( $^{16}\text{O}, ^{15}\text{N}$ ) reaction ( $n l j = 1 p_{1/2}$ ) favors final states involving transitions with the single particle orbits  $j = l + 1/2$  compared

Table I. Comparison of Spectroscopic Factors for  $^{210}\text{Po}$  and  $^{209}\text{Bi}$ .

Reaction	$E_x^a$ (MeV)	$d\sigma/d\Omega$ (mb/sr)	Assumed s.p. <sup>b</sup>	Ratio $C^2S(^{210}\text{Po})/C^2S(^{209}\text{Bi})$
$^{209}\text{Bi}(^{12}\text{C}, ^{11}\text{B})^{210}\text{Po}$ $E_L = 78$ MeV $\theta_L = 65$	1.18	$0.16 \pm 0.04$	$1h_{9/2}$	$0.73 \pm 0.08$
	1.52	$1.10 \pm 0.11$		
	2.37	$1.92 \pm 0.14$	$2f_{7/2}$	$0.70 \pm 0.06$
	2.94	$0.44 \pm 0.07$	$1i_{13/2}$	$0.89 \pm 0.10$
	3.20	$0.65 \pm 0.08$		
4-5.8	$2.12 \pm 0.21$	$2f_{5/2} - 3p$	$1.03 \pm 0.11$	
$^{209}\text{Bi}(^{16}\text{O}, ^{15}\text{N})^{210}\text{Po}$ $E_L = 104$ MeV $\theta_L = 67.5$	1.55	$0.25 \pm 0.02$	$1h_{9/2}$	$0.92 \pm 0.09$
	2.40	$2.64 \pm 0.08$	$2f_{7/2}$	$0.95 \pm 0.04$
	3.11	$0.79 \pm 0.04$	$1i_{13/2}$	$0.90 \pm 0.04$
	4-5.8	$3.33 \pm 0.13$	$2f_{5/2} - 3p$	$1.14 \pm 0.04$

<sup>a</sup>Excitation energy of centroid ( $\pm 50$  keV).

<sup>b</sup>States in  $^{210}\text{Po}$  assumed to be multiplets formed by coupling single particle configuration listed to  $^{209}\text{Bi}(1h_{9/2})$  g. s.

<sup>c</sup>Ratio of summed spectroscopic factors for levels in  $^{210}\text{Po}$  and  $^{209}\text{Bi}$  as deduced from cross section ratios using  $^{209}\text{Bi}$  data from Ref. 4.

to ( $^{12}\text{C}, ^{11}\text{B}$ ) ( $n\ell j = 1p_{3/2}$ ). Furthermore, single particle wave functions with large radial extension (large  $n$ ) are favored.

Since kinematic effects play a dominant role in heavy-ion reactions, it is necessary to account for these before attempting to deduce spectroscopic information. Fortunately DWBA theory appears to reproduce kinematic effects reasonably well, although some details remain questionable. We have used two methods to calculate form factors. Both methods are applicable for the simultaneous transfer of two nucleons (in contrast to a sequential transfer). One method computes the form factor as a matrix element of the sum of the shell model interactions that bind the transferred nucleons to the projectile core.<sup>5</sup> We refer to this as the "sum of interactions" (SI). The other method approximates the sum of the interactions by a single potential acting on the center-of-mass of the transferred nucleons.<sup>6</sup> We refer to this as the "center-of-mass interaction" (CMI). Both the CMI and SI methods yield a local form factor which depends only on the separation,  $R$ , between projectile and target core, and the angular momentum transfer. Both methods give the same qualitative results although quantitative differences exist. These differences are greatest when the transfer proceeds by states having small relative  $1s$  motion (e.g.,  $0^+ \rightarrow (1h_{9/2})^2 0^+$ ).

We have calculated angular distributions for ( $^{12}\text{C}, ^{10}\text{Be}$ ) and ( $^{16}\text{O}, ^{14}\text{C}$ ) using the DWBA program DWUCK<sup>7</sup> with form factors calculated with both CMI and SI methods, the former with a radial cut off at 8.5 fm. Some of the calculations are shown in Figs. 2-3 (SI form factor). The calculated shapes of the angular distributions are nearly independent of  $L$  or the nuclear configurations. The maxima in the DWBA angular distributions shift back in angle with increasingly negative  $Q$ -value whereas the experimental results do not. Results similar to those shown in Figs. 2 and 3 have also been observed for single nucleon transfers on  $^{208}\text{Pb}$ , and other mass regions. The discrepancies between theory and experiment appear to be associated with the optical model description of the distorted waves in DWBA, since the quality of the fits are correlated<sup>8</sup> with projectile orbit mismatch ( $Q - Q_{\text{opt}}$ ). We have estimated recoil effects by comparing "no-recoil" and "recoil" DWBA<sup>9</sup> calculation for a di-nucleon cluster transfer. The shapes of the angular distributions are not drastically altered by the inclusion of recoil, i.e., the discrepancies vs.  $Q$  value persist.

It is a distinguishing feature of heavy ion reactions that the nucleons transferred to and from the projectile can be in single particle states other than  $1s_{1/2}$ . This feature can

result in a  $j$ -selectivity such as that observed<sup>4</sup> in the ( $^{12}\text{C}, ^{11}\text{B}$ ) and ( $^{16}\text{O}, ^{15}\text{N}$ ) reactions. Similarly one might expect a  $j$ -selectivity for two-nucleon transfers from  $^{16}\text{O}$  and  $^{12}\text{C}$ . In the two-nucleon transfers considered here, however, such effects must enter via the structure factors rather than constraints on  $L$  since  $J_a = J_b = 0$ . We have considered projectile wave functions consisting of a  $0^+$  core plus two protons in the  $1p_{3/2}$  and  $1p_{1/2}$  shell, i.e.,  $\alpha 1p_{3/2}^2 + \beta 1p_{1/2}^2$  where  $\alpha^2 + \beta^2 = 1$ . The form factor for transitions to final states of the form  $(n\ell j)^2 0^+$  have then been calculated (SI method) vs. the  $(p_{1/2})$  mixing amplitude,  $\beta^2$ . One observes the following preferred  $0^+ \rightarrow 0^+$  transfers:  $(j_1^2)_{0^+}$  projectile configuration  $\rightarrow (j_2^2)_{0^+}$  target configuration  $(j_1^2)_{0^+}$  projectile to configuration  $\rightarrow (j_2^2)_{0^+}$  target configuration. Thus transitions involving pure  $jj$ -coupled wave functions (projectile and target) should exhibit a pronounced projectile dependence analogous to that observed for single nucleon transfers<sup>4</sup> (although the origin of the two effects are somewhat different).

Most of the  $j$ -selectivity is destroyed by small amounts of configuration mixing in the projectile wave functions. Thus, e.g., a 20 admixture of  $(p_{3/2})^2$  in  $^{16}\text{O}$  increases the ( $^{16}\text{O}, ^{14}\text{C}$ ) cross sections to  $j_2^2$  final states ( $3p_{1/2}^2, 2f_{5/2}^2, 1h_{9/2}^2$ ) by factors of 4 to 200. Even with "realistic" projectile wave functions,<sup>10</sup> however, measurable differences ( $\sim 2$ ) still exist between the calculated ( $^{12}\text{C}, ^{10}\text{Be}$ ) and ( $^{16}\text{O}, ^{14}\text{C}$ ) transition strengths.

The low-lying states of  $^{210}\text{Po}$  populated in two-proton transfers on  $^{208}\text{Pb}$  are expected to consist of levels formed by two protons in the shell model orbits  $n\ell j = 1h_{9/2}, 2f_{7/2}, 1i_{13/2}, 2f_{5/2}, 3p_{3/2}$  and  $3p_{1/2}$ . All states thus formed have positive parity except those involving the  $1i_{13/2}$  "intruder" level from the next higher oscillator shell.

We have calculated the relative peak cross sections to these levels (SI method, Cohen-Kurath wave functions (set a) were used for the projectiles.<sup>10</sup> Out of 52 states considered only 14 states are calculated to have strength  $\geq 10\%$  of the strongest transition ( $0^+ \rightarrow f_{7/2} p_{3/2} 2^+$ ). The strongest transitions are those involving the  $2f_{7/2}$  and  $3p_{3/2}$  single particle orbits (low  $\ell$ , large  $n$ ).

We have investigated two shell model calculations for  $^{210}\text{Po}$ : that of Kuo-Herling (KH) which uses matrix elements deduced from nucleon-nucleon scattering,<sup>11</sup> and that of Ma-True (MT), which uses matrix elements calculated from a phenomenological force<sup>12</sup> (central + multipolar). Both calculations reproduce many of the properties for nuclei  $A \sim 208$ :

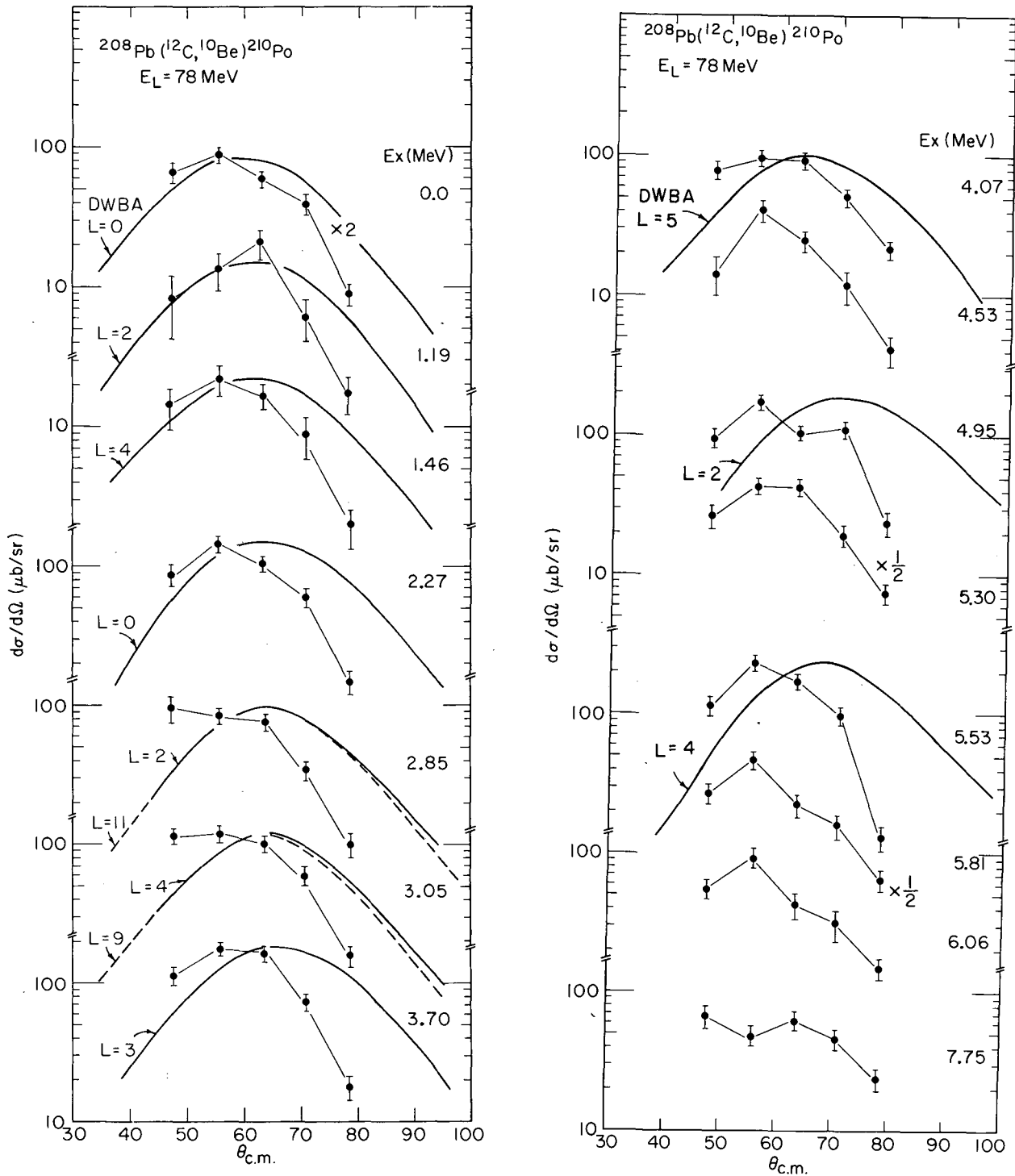


Fig. 2. Angular distributions for groups observed in  $^{208}\text{Pb}(^{12}\text{C}, ^{10}\text{Be})^{210}\text{Po}$ . The smooth curves are no-recoil DWBA calculations. The data points have been connected to guide the eye.  
(XBL 736-3081A)

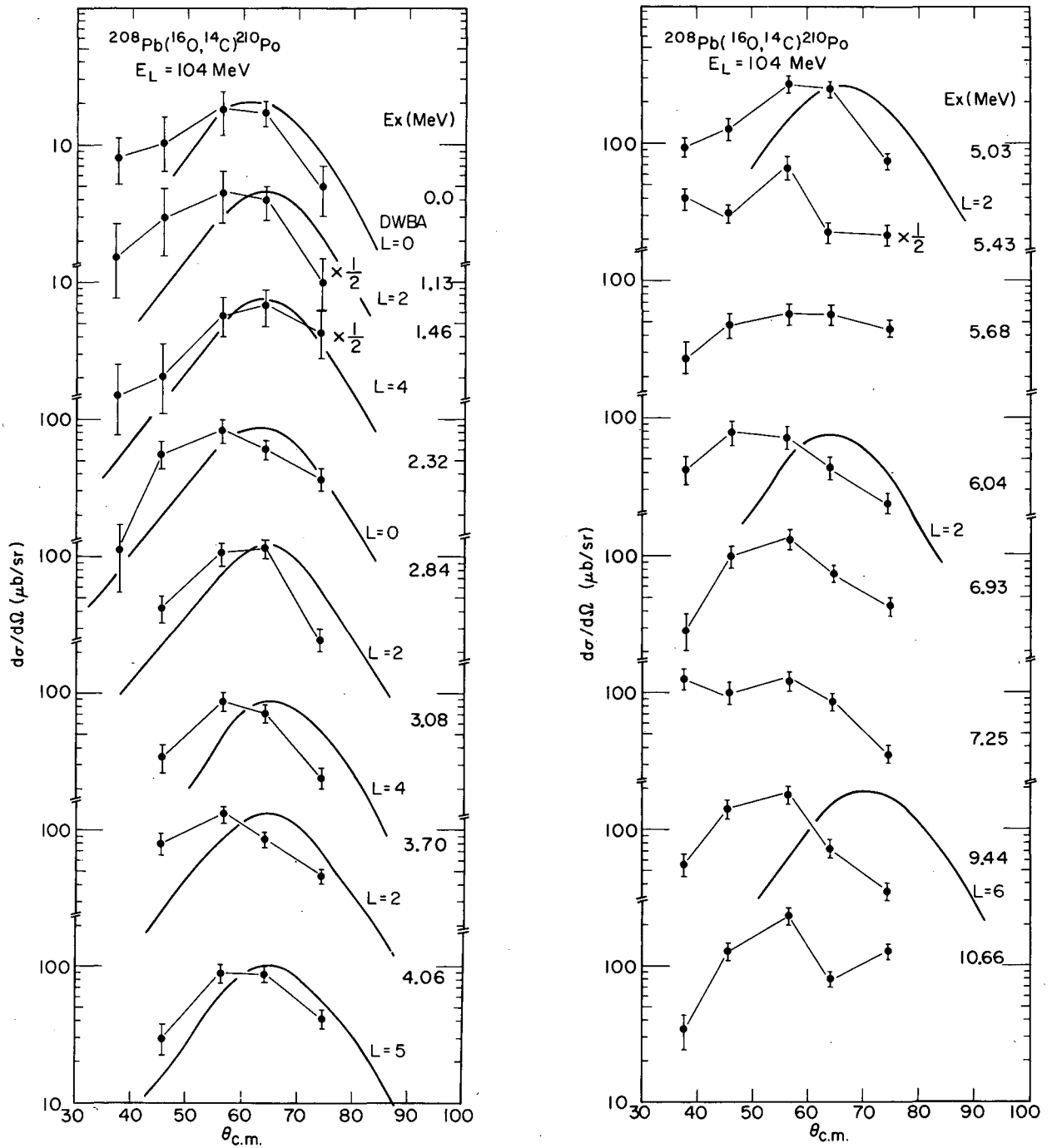


Fig. 3. Angular distributions for groups observed in  $^{208}\text{Pb}(^{16}\text{O}, ^{14}\text{C})$ . The smooth curves are no-recoil DWBA calculations. The data points have been connected to guide the eye.  
(XBL 736-3082B)

Levels in  $^{210}\text{Po}$

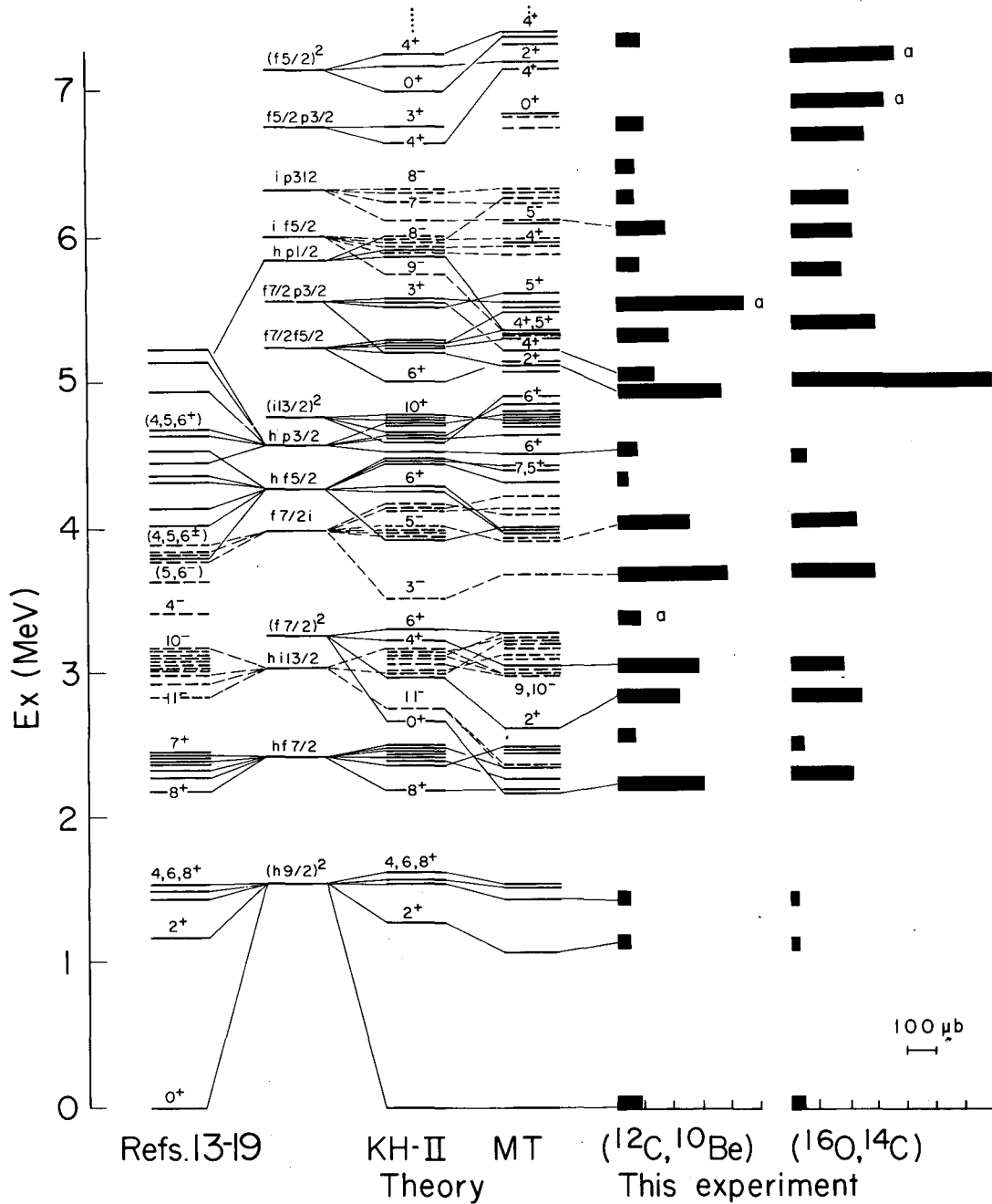


Fig. 4. A comparison of previously known and predicted levels in  $^{210}\text{Po}$  with groups observed in this experiment. The bar graphs represent integrated cross sections. Groups labeled "a" could be due to projectile excitation. Suggested level assignments are indicated by connecting lines: — positive parity; - - - negative parity.

(XBL 731-2172A)



energy levels, spectroscopic factors, transition rates, etc. In Fig. 4 we compare schematically predictions for levels in  $^{210}\text{Po}$  with previously reported levels and groups seen in the present experiment. The qualitative features of the spectra are reproduced, i.e., the number of levels and the distribution of transition strength, although the g.s. strength appears to be overestimated. Relatively few configurations dominate:  $(f_{7/2}p_{3/2})$ ,  $(f_{7/2}^2)$ ,  $(f_{7/2}i_{13/2})$ ,  $(f_{7/2}p_{1/2})$ ,  $(f_{7/2}^2f_{7/2})$ , with the strengths spread via configuration mixing. There appear to be more than one candidate for each observed

level  $E_x > 2$  MeV, however, and unfortunately, the calculated angular distributions are nearly independent of J. The likely candidates for the levels observed in  $(^{16}\text{O}, ^{14}\text{C})$  and  $(^{12}\text{C}, ^{10}\text{Be})$  are indicated in Fig. 4.

We may summarize the results presented above as follows:

(1) The two-proton transfer reactions  $^{208}\text{Pb}(^{12}\text{C}, ^{10}\text{Be})^{210}\text{Po}$  and  $^{208}\text{Pb}(^{16}\text{O}, ^{14}\text{C})^{210}\text{Po}$  selectively populate many previously unobserved levels in  $^{210}\text{Po}$ .

(2) The measured angular distributions show no reliable L or J signature, which precludes model-independent assignments.

(3) The theoretical calculations, however, exhibit features which are sensitive to the structure and spin of the projectile and target states and indicate that the levels observed are predominantly the  $(2f_{7/2})^2$   $0^+$ ,  $2^+$ ,  $4^+$ ,  $6^+$ ,  $(2f_{7/2}i_{13/2})$   $3^-$ ,  $5^-$ , and  $(2f_{7/2}^2p_{3/2})$   $2^+$ ,  $4^+$  states predicted by shell model calculations.

(4) The cross sections to the  $0^+$  (g.s.) and  $2^+$  (1.18 MeV) levels in  $^{210}\text{Po}$  are found to be enhanced by factors  $\sim 8$  and  $\sim 3$ , respectively, compared to those expected for pure  $(h_{9/2})^2$  configurations. Calculations using "realistic" projectile and target shell model wave functions, however, overestimate the  $0^+$  (g.s.) and  $2^+$  cross sections by factors of 2 to 15.

(5) The gross features of the observed spectra,  $E_x \lesssim 7$  MeV, are reproduced by the calculations, and in particular the differences in the  $(^{16}\text{O}, ^{14}\text{C})$  and  $(^{12}\text{C}, ^{10}\text{Be})$  spectra.

#### Footnotes and References

\*Present address: Cyclotron Laboratory, Physics Department, University of Michigan, Ann Arbor, Michigan 48105.

†Present address: Argonne National Laboratory, Argonne, Illinois.

‡Permanent address: Hahn-Meitner Institute, Berlin, Germany.

1. B.G. Harvey, J. Mahoney, F.G. Pühlhofer, F.S. Goulding, D.A. Landis, J.C. Faivre, D.G. Kovar, M.S. Zisman, J.R. Meriwether, S.W. Cospser, and D.L. Hendrie, Nucl. Instr. Methods 104, 21 (1972).
2. B.G. Harvey, H. Homeyer, J. Mahoney, and G. Gabor, 1972 LBL Progress Report, LBL-1666, p. 366 (unpublished).
3. R. Tickle and J. Bardwick, Phys. Letters 36B, 32 (1971); W.A. Lanford, W.P. W.P. Alford, and H.W. Fulbright, preprint.
4. D.G. Kovar, F.D. Becchetti, B.G. Harvey, F.G. Pühlhofer, J. Mahoney, D.W. Miller, and M.S. Zisman, Phys. Rev. Letters 29, 1023 (1972); D.G. Kovar et al., Phys. Rev. Letters 30, 1075 (1973).
5. N.K. Glendenning, Phys. Rev. 137, B102 (1965).
6. R. Broglia, T. Kammuri, R. Liotta, A. Winther, and B. Nilsson, J. Phys. 32, Suppl. 11-12, C6-151 (1971); R. Broglia, R. Liotta, A. Winther, B. Nilsson, and T. Kammuri, preprint.
7. P.D. Kunz, University of Colorado reports COO-535-606 and COO-535-613 (unpublished).
8. F.D. Becchetti, P.R. Chirstensen, V.I. Manko, and R.J. Mickles, Phys. Letters 43B, 279 (1973).
9. T. Sawaguri and W. Tobocman, J. Math. Phys. 8, 2223 (1967).
10. S. Cohen and D. Kurath, Nucl. Phys. A101, 1 (1967); S. Cohen and D. Kurath, Nucl. Phys. A141, 145 (1970).
11. G.H. Herling and T.T.S. Kuo, Nucl. Phys. A181, 113 (1972); T.T.S. Kuo and G.H. Herling, NRL Memorandum Report 2258 (1971).
12. C.W. Ma and W.W. True, submitted to Phys. Rev. C; W.W. True, private communication.

## ANALYSIS OF HEAVY ION INDUCED SINGLE NUCLEON TRANSFER REACTIONS

D. G. Kovar,\* F. D. Becchetti,<sup>†</sup> B. G. Harvey, D. L. Hendrie,  
H. Homeyer,<sup>‡</sup> J. Mahoney, and W. von Oertzen<sup>§</sup>

The single nucleon transfer reactions ( $^{16}\text{O}, ^{15}\text{N}$ ) and ( $^{16}\text{O}, ^{17}\text{O}$ ) on  $^{208}\text{Pb}$  were studied at  $^{16}\text{O}$  bombarding energies of 104, 140, and 216 MeV to investigate the energy dependence of the cross section. Of interest were the cross section changes in going to higher bombarding energies than have been used before and the ability of DWBA calculations to reproduce quantitatively the experimental results.

The reactions were studied at the 88-inch cyclotron using the magnetic spectrometer-proportional counter system described previously.<sup>1</sup> This system provided unambiguous particle identification and energy resolutions of the order of  $\Delta E/E = 0.15\%$ . Figures 1 and 2 show the spectra obtained for the one-proton stripping and one-neutron pickup reactions, respectively. Angular distributions obtained at all three bombarding energies showed typical bell shaped angular distributions peaked near the expected semi-classical grazing angle.

Strong population of the single-particle (hole) states in  $^{209}\text{Bi}$  ( $^{207}\text{Pb}$ ) was observed at all three bombarding energies. Figures 3 and 4 show the cross section dependence of these states on the bombarding energy. The pronounced  $j$ -dependence of the cross section, favoring the  $j = l + 1/2$  states at the lower energy,<sup>2</sup> disappears as one goes to higher energies and is not present at 216 MeV in the ( $^{16}\text{O}, ^{15}\text{N}$ ) reaction while in the ( $^{16}\text{O}, ^{17}\text{O}$ ) reaction the qualitative trend, although less clear, appears to be the opposite.

DWBA analysis of the angular distributions for the ( $^{16}\text{O}, ^{15}\text{N}$ ) reactions at 104 and 140 MeV has been reported previously.<sup>3</sup> It appears that (1) recoil effects are important and must be included for the extraction of reliable spectroscopic factors, and (2) there is a systematic  $Q$ -dependence in the angle of the cross section maximum that could not be reproduced in the DWBA calculations. Analysis has now been performed with exact finite range DWBA<sup>4</sup> which includes recoil effects explicitly. The results show (see Table I) that the large discrepancies in the relative spectroscopic factors obtained with no-recoil DWBA have been removed. The heavy ion results agree to about 40% with the results from light ion studies, except for the  $h_{9/2}$  state, whose spectroscopic factor is about a factor of 2 too large. However, the calculations do not reproduce the energy dependence of the cross sections which are

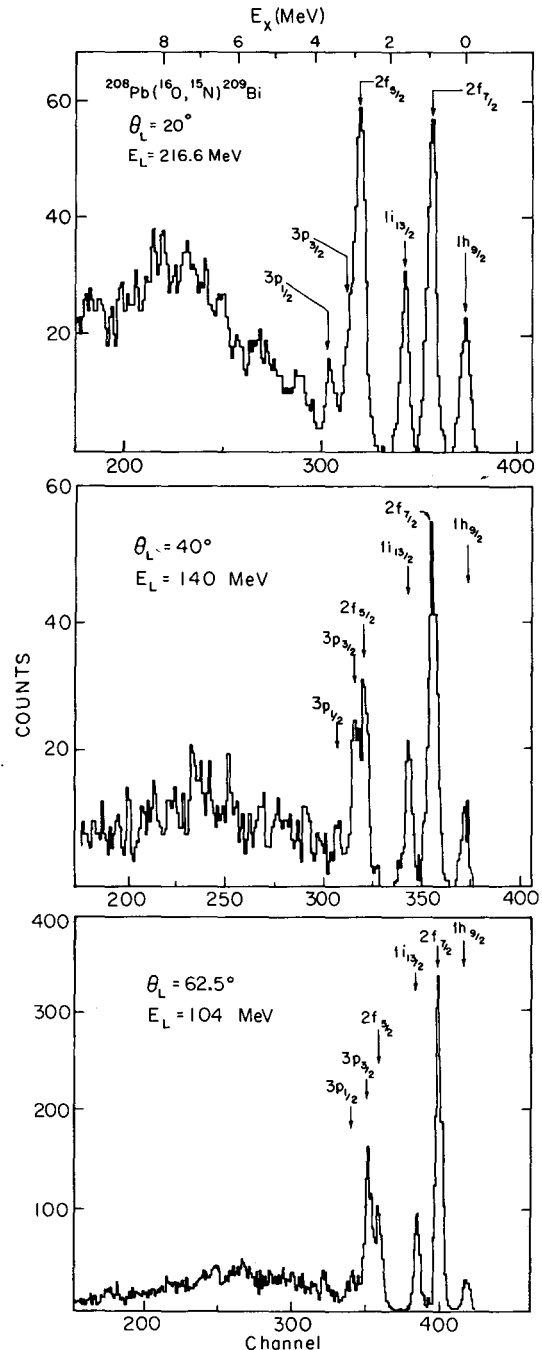


Fig. 1. Typical spectra obtained in the reaction  $^{208}\text{Pb}(^{16}\text{O}, ^{15}\text{N})^{209}\text{Bi}$  at bombarding energies 104 MeV, 140 MeV, and 216 MeV.

(XBL 743-582)

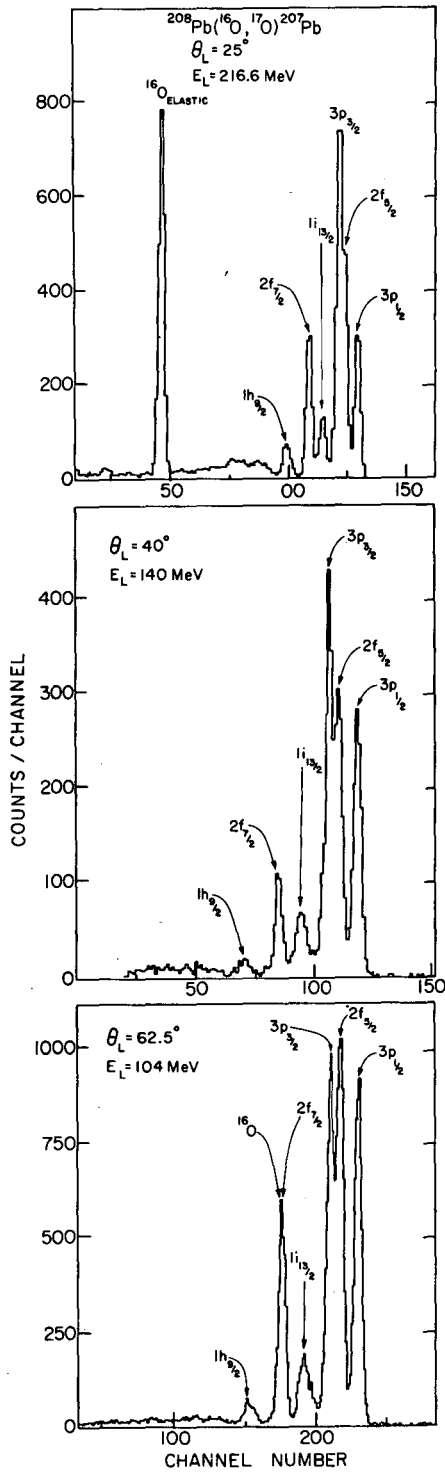


Fig. 2. Typical spectra obtained in the reaction  $^{208}\text{Pb}(^{16}\text{O}, ^{17}\text{O})^{207}\text{Pb}$  at bombarding energies 104 MeV, 140 MeV, and 216 MeV. (XBL 743-583)

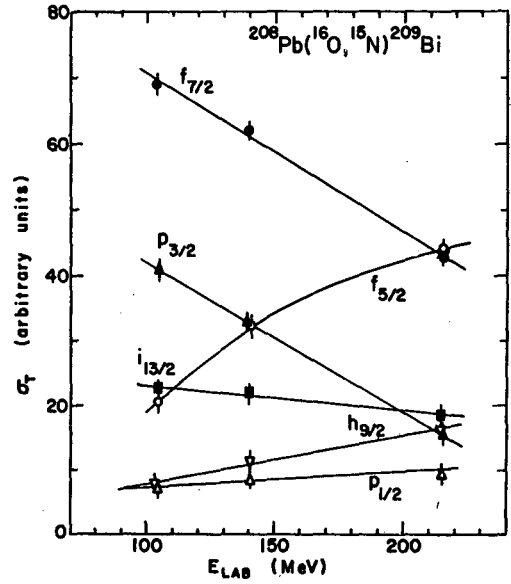


Fig. 3. Energy dependence of the cross section for the single-particle states populated in the  $^{208}\text{Pb}(^{16}\text{O}, ^{15}\text{N})^{209}\text{Bi}$  reaction. (XBL 743-584)

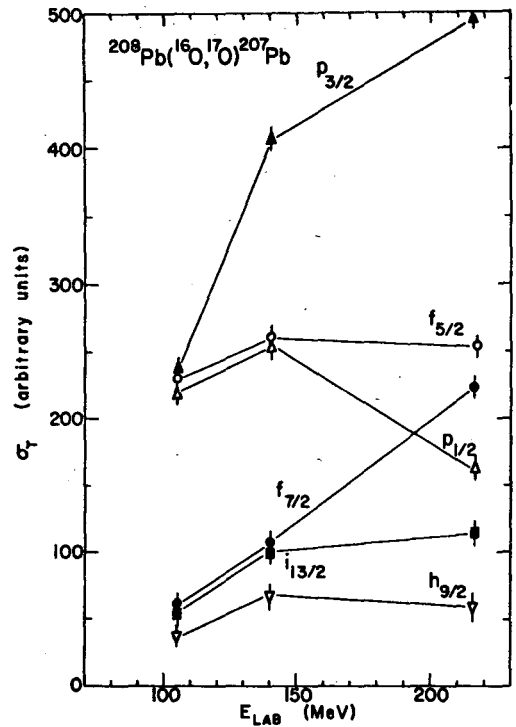


Fig. 4. Energy dependence of the cross section for the single-hole states populated in the  $^{208}\text{Pb}(^{16}\text{O}, ^{17}\text{O})^{207}\text{Pb}$  reaction. (XBL 743-585)

Table I. Spectroscopic Factors,  $^{208}\text{Pb}(^{16}\text{O}^{15}\text{N})^{209}\text{Bi}$ 

$E_x$ (MeV)	$nl_j$	No-Recoil DWBA			Exact Finite Range DWBA			( $^3\text{He}, d$ )
		104 MeV	140 MeV	216 MeV	104 MeV	140 MeV	216 MeV	
0.0	$1h_{9/2}$	6.33	8.00	7.08	2.60	2.08	0.62	1.00
0.90	$2f_{7/2}$	1.67	1.00	0.44	1.06	1.00	0.37	1.12
1.61	$1i_{13/2}$	1.38	0.83	0.37	0.96	0.87	--	0.94
2.84	$2f_{5/2}$	6.67	6.67	7.50	1.48	1.04	0.37	1.14
3.12	$3p_{3/2}$	1.92	1.00	0.42	1.48	0.96	0.35	1.08
3.64	$3p_{1/2}$	5.8-6.7	6.2-10.0	5.8-7.5	0.6-1.0	0.6-1.3	0.25-0.35	0.7-0.9

enhanced at higher energies, nor the constant angle of the cross section maximum that is found experimentally. Therefore, while significant improvements are made by analysis with exact finite range DWBA, there are still problems which need to be resolved. Work is in progress to investigate these problems and to analyze the ( $^{16}\text{O}, ^{17}\text{O}$ ) results.

#### References

\* Presently at Argonne National Laboratory, Argonne, Illinois.

† Presently at University of Michigan, Ann Arbor, Michigan.

‡ On leave from Hahn-Meitner Institut, Berlin, Germany.

§ On leave from Max Planck Institut für Kernphysik, Heidelberg, Germany.

1. B.G. Harvey, J. Mahoney, F.G. Pühlhofer, F.S. Goulding, D.A. Landis, J.-C. Faivre, D.G. Kovar, M.S. Zisman, J.R. Meriwether, S.W. Cosper, and D.L. Hendrie, Nucl. Inst. Meth. **104**, 21 (1972).

2. D.G. Kovar, F.D. Becchetti, B.G. Harvey, F.G. Pühlhofer, J. Mahoney, D.W. Miller, and M.S. Zisman, Phys. Rev. Lett. **29**, 1023 (1972).

3. D.G. Kovar, B.G. Harvey, F.D. Becchetti, J. Mahoney, D.L. Hendrie, H. Homeyer, W. von Oertzen, and N.A. Nagarajan, Phys. Rev. Lett. **30**, 571 (1973).

4. DWBA code LOLA; R. DeVries, private communication.

#### INDIRECT PROCESSES IN HEAVY-ION TRANSFER REACTIONS

D. K. Scott, N. K. Glendenning, B. G. Harvey, D. L. Hendrie,  
L. Kraus, C. Maguire, J. Mahoney, Y. Terrien, and K. Yagi

Heavy Ion induced transfer reactions are now used extensively for studies of nuclear structure, but many details of the reaction mechanism remain to be clarified. In particular, most theoretical analyses ignore the effect of indirect processes, although it is often assumed intuitively that these should play an even more important role than they are now known to do in light ion reactions. Recently quantitative calculations on the effect

of indirect processes on two neutron transfer reactions induced by heavy ions on Sn isotopes have been reported.<sup>1</sup> Here we compare these calculations with experimental data.

We have studied the two neutron pick-up reaction  $^{122}\text{Sn}(^{16}\text{O}, ^{18}\text{O})^{120}\text{Sn}$  at 104 MeV incident energy. The  $^{18}\text{O}$  ions were identified in the magnetic spectrometer by measuring  $(dE/dx)$  and time-of-flight.<sup>2</sup> The inverse

stripping reaction  $^{120}\text{Sn}(^{18}\text{O}, ^{16}\text{O})^{122}\text{Sn}$  at 100 MeV incident energy has been reported previously.<sup>3</sup> The spectrum for the pick-up reaction in Fig. 1 illustrates the strong enhancement of the  $\text{O}^+$  superfluid ground state over the collective  $2^+$  excitation, an effect well-known from the analogous (p, t) reaction on Sn isotopes. Most  $2n$  transfer data with heavy ions have not revealed this enhancement strongly.)<sup>4</sup> The background observed in the spectrum arose from inelastic scattering of the  $^{16}\text{O}$  beam in the  $7^+$  charge state, which almost coincides with  $^{18}\text{O}$  in the time-of-flight identification.

The measured differential cross sections for the  $\text{O}^+$  and  $2^+$  states in both the stripping and the pick-up reactions are shown in Fig. 2. The ground state cross sections have been normalized for the two reactions, and they agree closely in shape, although the time reversed reactions were not in fact performed at precisely the same center of mass energies. The cross sections are also normalized to the theoretical curves in the figure; the experimental peak for the ground state cross section was  $330 \mu\text{b}/\text{sr}$ .

Qualitatively the distributions for the  $\text{O}^+$  and  $2^+$  states in the pick-up reaction

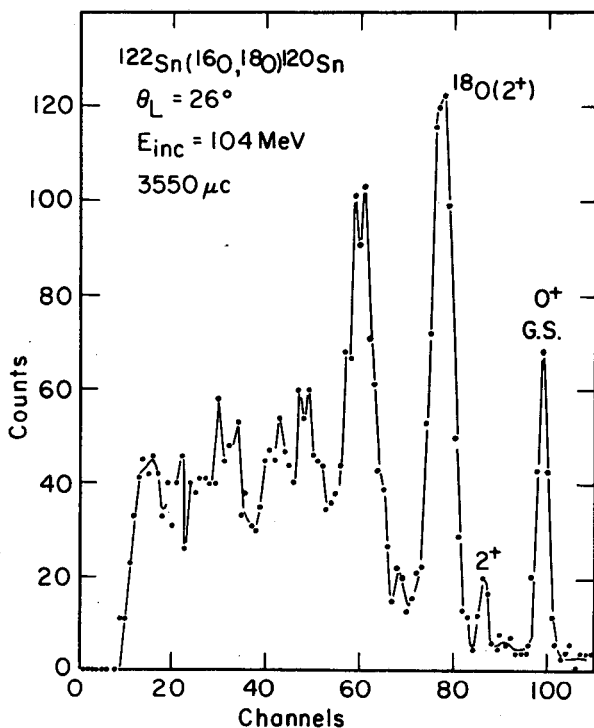


Fig. 1. Energy spectrum for the  $^{122}\text{Sn}(^{16}\text{O}, ^{18}\text{O})^{120}\text{Sn}$  reaction. (XBL 741-2191)

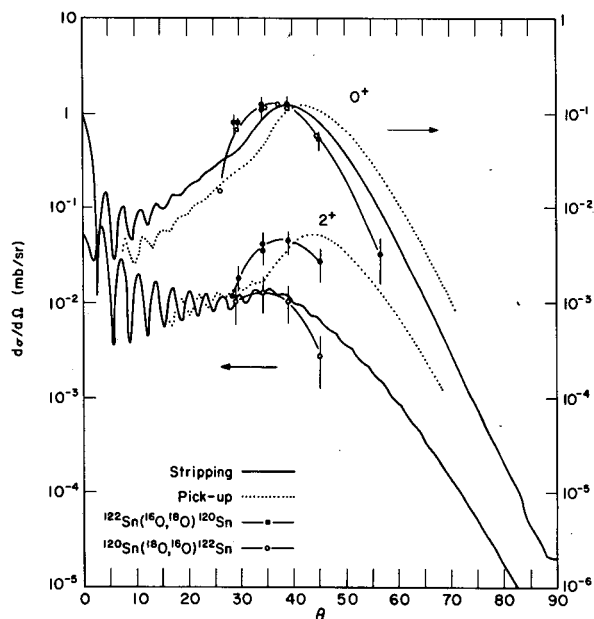


Fig 2. Differential cross sections for the reactions  $^{122}\text{Sn}(^{16}\text{O}, ^{18}\text{O})^{120}\text{Sn}$  at 104 MeV and  $^{120}\text{Sn}(^{18}\text{O}, ^{16}\text{O})^{122}\text{Sn}$  at 100 MeV incident energy. Also shown are theoretical calculations for the same transfers on the lighter Sn isotope pair  $^{112}\text{Sn}, ^{114}\text{Sn}$ . (XBL 743-2527)

$^{122}\text{Sn}(^{16}\text{O}, ^{18}\text{O})^{120}\text{Sn}$  show the usual classical maximum at  $\theta = 37^\circ$ , corresponding to a grazing collision in the combined coulomb and nuclear potential, whereas the  $2^+$  distribution in stripping has a tendency to flatten at forward angles. The results of a theoretical calculation for these reactions, made prior to the experiment and hence not at the same incident energies, is shown in Fig. 3. Here we see that the inclusion of indirect processes leads to a flattening of the  $2^+$  state in stripping and in addition, to a dip in the region of the classical maximum, due to the destructive interference between the direct and indirect contributions to the transition. In pick-up to the  $2^+$  state, this interference is constructive and the shape of the distribution is largely unperturbed. Also shown in the figure is the result of a calculation ignoring indirect contributions, in which all the distributions have the classical form.

As the data for Fig. 2 show, the minimum in the  $2^+$  stripping distribution is not observed. The magnitude of this dip is of course sensitively dependent on the value of deformation  $\beta_2$  assumed for the collective  $2^+$  states. The calculation used  $\beta_2 = 0.13$  for  $^{120}\text{Sn}$  and  $0.124$  for  $^{122}\text{Sn}$ , values derived from light ion inelastic scattering. However a measurement

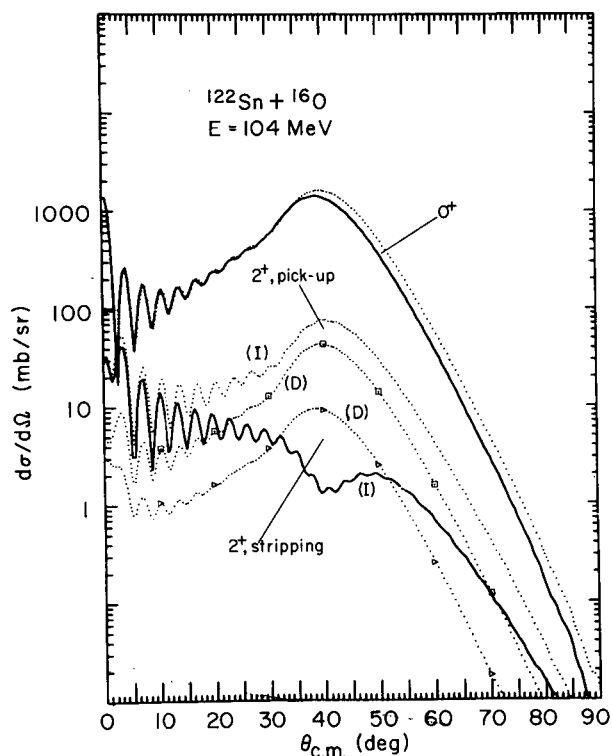


Fig. 3. Theoretical differential cross sections for the reactions  $^{122}\text{Sn}(^{16}\text{O}, ^{18}\text{O})^{120}\text{Sn}$  and  $^{120}\text{Sn}(^{18}\text{O}, ^{16}\text{O})^{122}\text{Sn}$  at 100 MeV incident energy. The effect of including indirect processes (I) or including only direct processes (D) is shown for the transitions to the  $2^+$  states. (XBL741-2195)

of elastic and inelastic scattering  $^{122}\text{Sn}(^{16}\text{O}, ^{16}\text{O})^{122}\text{Sn}$  (this report) indicates that this value is consistent with the heavy ion data. The optical potentials used in the transfer calculation ( $V = 40$  MeV,  $W = 15$  MeV,  $r_R = r_i = 1.31$  fm,  $a_R = a_i = 0.45$  fm) gave good agreement with the

elastic scattering and they have also been used successfully to describe the one-nucleon transfer reaction ( $^{16}\text{O}, ^{15}\text{N}$ ) on  $^{122}\text{Sn}$  (this report).

In Fig. 2, the data are compared with calculations for the lighter Sn isotopes  $^{112}\text{Sn}$ ,  $^{114}\text{Sn}$ . Here changes in the nuclear structure yield a stronger contribution from the direct process,<sup>5</sup> and qualitatively these calculations are in better agreement with our data (apart from an overall shift in the location of the maxima, due partly to differences between the energies used in calculation and experiment).

Detailed calculations relevant to the experimental data are in progress. However, the preliminary results reported here suggest that indirect processes in heavy-ion reactions can probably be calculated with the same confidence as for light ion reactions, and that the effect on differential cross sections could prove to be a sensitive means of studying nuclear structure and deformations.

#### References

1. N.K. Glendenning, and R.J. Ascutto, Phys. Letters **45B**, 85 (1973).
2. B.G. Harvey et. al., Nucl. Instr. Methods **104**, 21 (1972).
3. N. Anyas-Weiss et. al., Proceedings of International Conference on Nuclear Physics (Munich 1973) Vol. I, p. 485.
4. R.H. Siemssen, Proceedings of the Symposium on Two Nucleon Transfer and Pairing Excitations (Argonne 1972), p. 273.
5. N.K. Glendenning and R.J. Ascutto, Lawrence Berkeley Laboratory Report LBL-1987.

ELASTIC AND INELASTIC SCATTERING OF  $^{16}\text{O}$  ON  $^{122}\text{Sn}$  AT 104 MeV

Y. Terrien, N. K. Glendenning, B. G. Harvey, D. L. Hendrie,  
L. Kraus, C. Maguire, J. Mahoney, D. K. Scott, and K. Yagi

The elastic and inelastic scattering of  $^{16}\text{O}$  ions from  $^{122}\text{Sn}$  has been studied at an incident energy of 104 MeV. This experiment has been done in order to extract suitable optical model

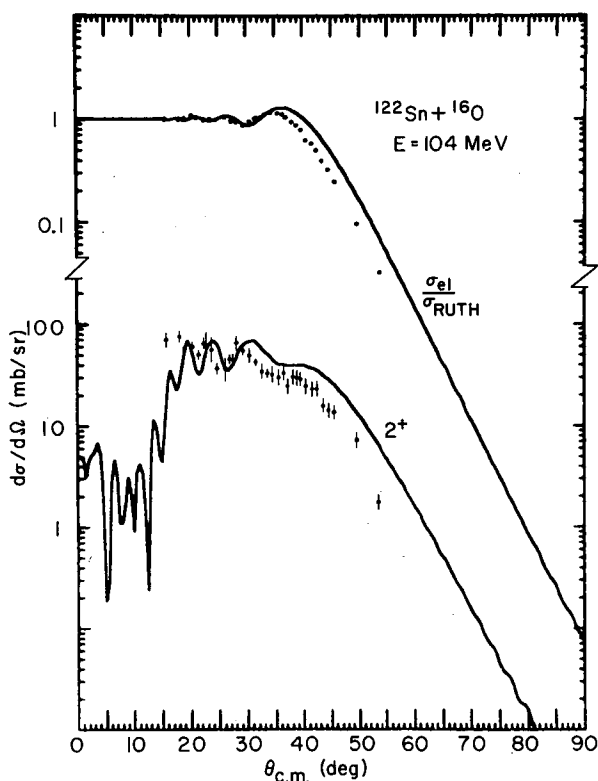


Fig. 1. Elastic and inelastic scattering of  $^{16}\text{O}$  on  $^{122}\text{Sn}$ : experimental and theoretical (coupled channels DWBA) angular distributions. (XBL741-2194)

(OM) parameters and the deformation parameter  $\beta_2$  of the lowest collective  $2^+$  state in  $^{122}\text{Sn}$ . Indeed, these quantities must be known as well as possible in order to estimate properly the importance of inelastic scattering as an intermediate step in the reaction  $^{122}\text{Sn}(^{16}\text{O}, ^{18}\text{O})^{120}\text{Sn}$ . Some preliminary calculations of elastic and inelastic scattering had been done<sup>1</sup> using the coupled channels Born approximation (CCBA), with a typical set of OM parameters<sup>2</sup>  $V = 40$  MeV,  $W = 15$  MeV,  $r_R = r_i = 1.31$  fm.,  $a_R = a_i = 0.45$  fm., and with  $\beta_2$  values taken from (pp') experiments and Coulomb excitation measurements for the nuclear and Coulomb parts of the form factor, respectively. As can be seen in Fig. 1, these  $\beta_2$  values seem to be suitable for heavy ion inelastic scattering also; both the amplitude and the shape of the  $2^+$  state cross section angular distribution are well reproduced by the calculation, except for the presence of an angular shift of about  $3^\circ$  which could be due to the fact that the calculations were done for an incident energy of 100 MeV instead of 104 MeV, the actual energy of the ingoing  $^{16}\text{O}$  particles in the experiment. Calculations on the experimental data are in progress.

## References

1. R. J. Ascutto and N. K. Glendenning, private communication.
2. F. Becchetti et al., Phys. Rev. C 6, 2215 (1972).

ANGULAR DISTRIBUTIONS FROM THE  $^{122}\text{Sn}(^{16}\text{O}, ^{15}\text{N})^{123}\text{Sb}$  REACTION

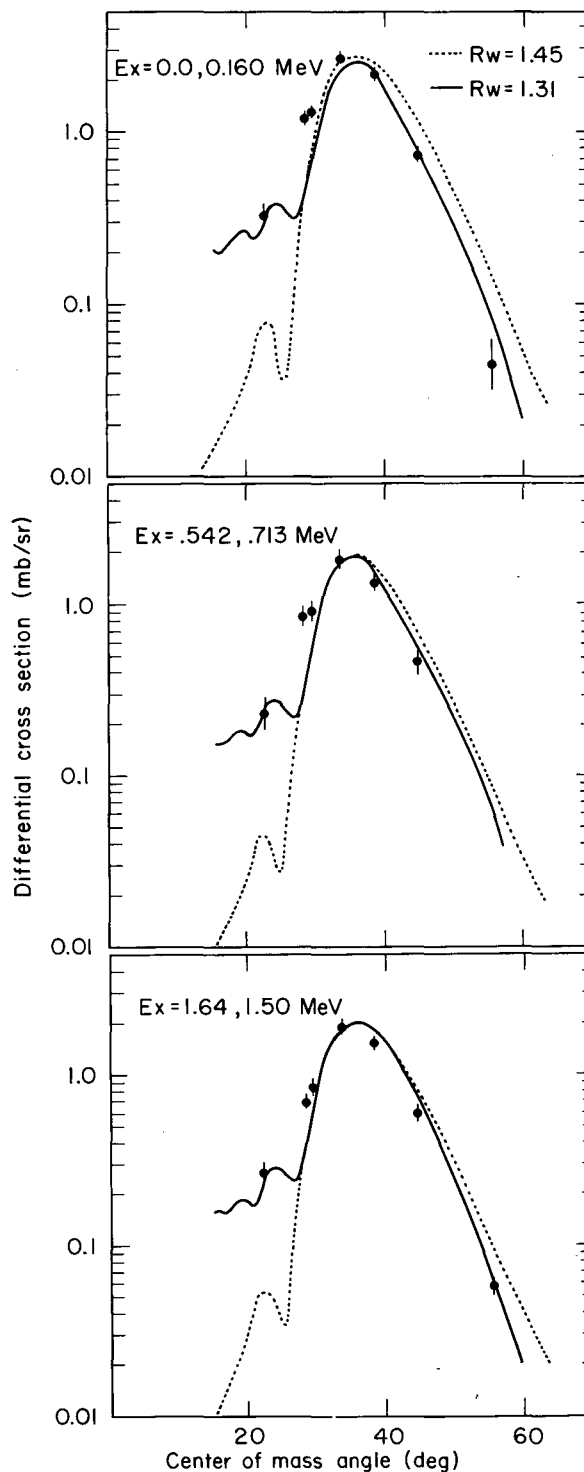
C. Maguire, B. G. Harvey, D. L. Hendrie, L. Kraus,  
J. Mahoney, D. K. Scott, Y. Terrien, and K. Yagi

One of the more ambiguous facets of heavy ion reaction analyses is the choice of optical model parameters to be used to describe the incoming and outgoing channels. For a given incident energy, projectile and target, the behavior of the form factor associated with the reaction curtails the extent to which the optical potential can be determined. In elastic and inelastic scattering, the outermost regions of the potential dominate the reaction while for two-nucleon transfer the steeply falling form factor makes the reaction more sensitive to the interior of the nucleus. One-nucleon transfer tests the potential somewhere between these two regions. In another study in this report, the  $^{122}\text{Sn}(^{16}\text{O}, ^{18}\text{O})^{120}\text{Sn}$  experiment has been analyzed on the basis of a coupled channels mechanism.<sup>1</sup> The theoretical fits are particularly dependent on the choice of the optical potential geometry and on the deformation parameters. To determine the latter, a separate series of elastic and inelastic angular distributions were measured. The scattering data, also given in this report, are very well fit by the optical potential used in the coupled channels calculation for the two-neutron transfer. A further test of the optical potential is afforded by the  $^{122}\text{Sn}(^{16}\text{O}, ^{15}\text{N})^{123}\text{Sb}$  reaction.

Table 1.

Energy	$j\pi$	$C^2S$
0.0	7/2+	6.7
0.16	5/2+	4.8
.54	3/2+	1.2
.72	1/2+	0.7
1.50	3/2, 5/2+	
1.64	11/2-	
Others up to 2.75 MeV		

Fig. 1. Angular distributions from the  $^{122}\text{Sn}(^{16}\text{O}, ^{15}\text{N})^{123}\text{Sb}$  reaction. The curves represent fits predicted by two optical potentials differing only in the value of the absorptive radius  $R_w$ . (XBL743-2522)





As it happens, the magnetic field of the spectrometer which is suitable for the ( $^{16}\text{O}$ ,  $^{18}\text{O}$ ) reactions also allows the detection of the  $^{15}\text{N}$  groups from the ground and excited states of  $^{123}\text{Sb}$ . These groups are well separated from the  $^{16}\text{O}$   $7^+$  background due to the differing energy losses. In fact good angular distributions were obtained for several groups, since the length of exposure at a given angle was determined by the much weaker yield of the  $^{18}\text{O}$  group.

With fifty protons, the tin isotopes have a closed proton shell. The single particle strength distribution has been studied in the ( $^3\text{He}$ , d) reaction as given in Table 1.<sup>2</sup> The resolution obtained in the ( $^{16}\text{O}$ ,  $^{18}\text{O}$ ) experiment,  $\sim 200$  keV, was insufficient to resolve the first two pairs of states. Since heavy ion induced angular distribution shakes are not sensitive to the angular momentum transferred, this lack of resolution was not critical for the present purposes. The primary interest here is the comparison of the theoretically predicted shape with the data. Shown in Fig. 1 are three angular distributions representing six states in  $^{123}\text{Sb}$ . Also shown are fits predicted using

Hankel function form factors and two sets of optical potentials differing only in the value of the absorptive radius. The shapes have been normalized directly to the data. The surprising result is that in contrast to the ( $^{16}\text{O}$ ,  $^{18}\text{O}$ ) experiment, the ( $^{16}\text{O}$ ,  $^{15}\text{N}$ ) data support a smaller value for the absorptive radius. The forward angle slope appears better reproduced with the smaller radius value than with the larger radius. The backward angles are fit equally well with both sets. These angular distributions will be studied further, to determine whether recoil effects, known to be important in single-nucleon heavy-ion transfer reactions,<sup>3</sup> will affect these conclusions.

#### References

1. R. Ascutto, N. Glendenning, Lawrence Berkeley Laboratory Report LBL-1990, 1973.
2. M. Conjeaud, et al., Nucl. Phys. A117, 449 (1968).
3. D.G. Kovar, et. al., Phys. Rev. Letters 30, 21, 1973.

### THE REACTION $^{208}\text{Pb}(^{20}\text{Ne}, \alpha)^{224}\text{Th}$

B. G. Harvey, D. L. Hendrie, D. K. Scott, J. Mahoney,  
C. F. Maguire, Y. Terrien, L. Kraus, and K. Yagi

Massive direct transfer reactions such as ( $^{20}\text{Ne}$ ,  $\alpha$ ) might be useful for the measurement of ground state masses, lifetimes and energy levels of very heavy nuclei far beyond those presently known. As a preliminary attempt, we have studied the reaction  $^{208}\text{Pb}(^{20}\text{Ne}, \alpha)^{224}\text{Th}$  to see whether  $\alpha$ -particles could be detected that corresponded to the formation of  $^{224}\text{Th}$  in its ground or first few excited states. The result was negative to an extent sufficiently spectacular to be worth reporting.

One kinematic difficulty with this reaction is that the high angular momentum of the  $^{20}\text{Ne}$  in a grazing collision cannot easily be carried away by a light particle such as an  $\alpha$ -particle to leave the  $^{224}\text{Th}$  in its  $J^\pi = 0^+$  ground state. It therefore seemed advisable to use a  $^{20}\text{Ne}$  beam with an energy very close to the Coulomb barrier so that low partial waves (in the ideal case the s-wave) would approach the target nucleus just within the range of the nuclear forces that induce the transfer reaction. To make sure that the beam energy was just right, we chose 99 MeV, slightly above the Coulomb barrier, and used a target of  $^{208}\text{Pb}$  that was 7 MeV thick for the  $^{20}\text{Ne}$  ions. At some depth

within the target, the  $^{20}\text{Ne}$  ion energy should therefore have just the value to allow low partial waves to approach within the range of nuclear forces without being captured to form a compound nucleus.

Alpha-particles were detected both with an E- $\Delta$ E silicon counter telescope in the scattering chamber, and with the spectrometer and focal plane detector system at a laboratory angle of  $110^\circ$ . No events above background were observed in the neighborhood of the  $^{224}\text{Th}$  ground state in either the telescope or the spectrometer.

In the spectrometer measurement, which was made only at  $110^\circ$  (lab), not even a single  $\alpha$ -particle event was observed in the first  $\sim 5$  MeV of excitation of  $^{224}\text{Th}$ . A single event would have corresponded to a differential cross section of only 70 nb/msr. The result was therefore negative to a gratifyingly clean extent. When the spectrometer field was reduced so that lower energy (evaporation?) particles fell on the focal plane, we observed  $\alpha$ -particles, tritons and deuterons, confirming that the detection system was indeed working properly.

SPECTROSCOPY OF NUCLEI FAR FROM STABILITY  
USING HEAVY ION TRANSFER REACTIONS

D. K. Scott, B. G. Harvey, D. L. Hendrie, L. Kraus,  
C. Maguire, J. Mahoney, Y. Terrien, and K. Yagi

The study of nuclei far from stability presents a challenge both to experimental and theoretical nuclear physics. The known limit of stability on the neutron excessive side extends far beyond the region where detailed spectroscopy has been carried out. Transfer reactions with heavy ions offer the possibility of studying such nuclei in detail. For example, while the (t, p) reaction has been used to probe nuclei two neutrons from stability, the first reaction available for 3n transfer is ( $^{11}\text{B}$ ,  $^8\text{B}$ ). Such reactions have proved difficult with conventional counter telescope techniques<sup>1, 2</sup> since the cross section is small compared to the background of  $^7\text{Li} + \alpha$  which simulates  $^8\text{B}$  events. In the one case where the reaction has been used to study  $^{28}\text{Mg}$ , there is a large discrepancy with other techniques for even the ground state mass.<sup>3</sup>

In this report we present preliminary data using the Berkeley magnetic spectrometer for the study of nuclei far from stability. Our primary interest lay in the  $^{26}\text{Mg}(^{11}\text{B}, ^8\text{B})^{29}\text{Mg}$  reaction, but it is interesting that the spectrometer accepts simultaneously the  $^{26}\text{Mg}(^{11}\text{B}, ^{13}\text{N})^{24}\text{Ne}$  and  $^{26}\text{Mg}(^{11}\text{B}, ^{11}\text{C})^{26}\text{Na}$  reactions. These two proton pick-up and charge exchange reactions lead also to exotic nuclei currently being investigated<sup>4, 5</sup> via the ( $^6\text{Li}$ ,  $^8\text{B}$ ) and ( $^7\text{Li}$ ,  $^7\text{Be}$ ) reactions. The detection of  $^8\text{B}$  has the advantage that the inherently more abundant two neutron transfer product  $^9\text{B}$  is particle unstable. The advantages of using the spectrometer are illustrated elsewhere in the report.

These initial experiments were done at 86 MeV incident energy with a thick  $500\ \mu\text{g}/\text{cm}^2$  target. The  $^8\text{B}$  was identified by measuring the time-of-flight ( $\alpha M/Q$ ), together with two independent determinations of  $(dE/dX)$  in the focal plane proportional counters on the spectrometer. The time zero detector was  $200\ \mu\text{g}/\text{cm}^2$  NE111 which, together with the target, gave rise to poor energy resolution for the heavier transfer products,  $^{13}\text{N}$  and  $^{11}\text{C}$ .

A spectrum for the ( $^{11}\text{B}$ ,  $^{13}\text{N}$ ), ( $^{11}\text{B}$ ,  $^{11}\text{C}$ ) and ( $^{11}\text{B}$ ,  $^8\text{B}$ ) reactions is shown in Fig. 1. The cross section for 2p pick-up was typically  $250\ \mu\text{b}/\text{sr}$ , and for exchange,  $100\ \mu\text{b}/\text{sr}$ . These cross sections are  $\sim 10$  times greater than the ( $^6\text{Li}$ ,  $^8\text{B}$ ) and ( $^7\text{Li}$ ,  $^7\text{Be}$ ) reactions, a fact which, for the 2p pick-up, can be partly understood on a cluster picture. The spectrum for  $^8\text{B}$ , which is plotted on an event-by-event basis, shows evidence for states, but at present it is not

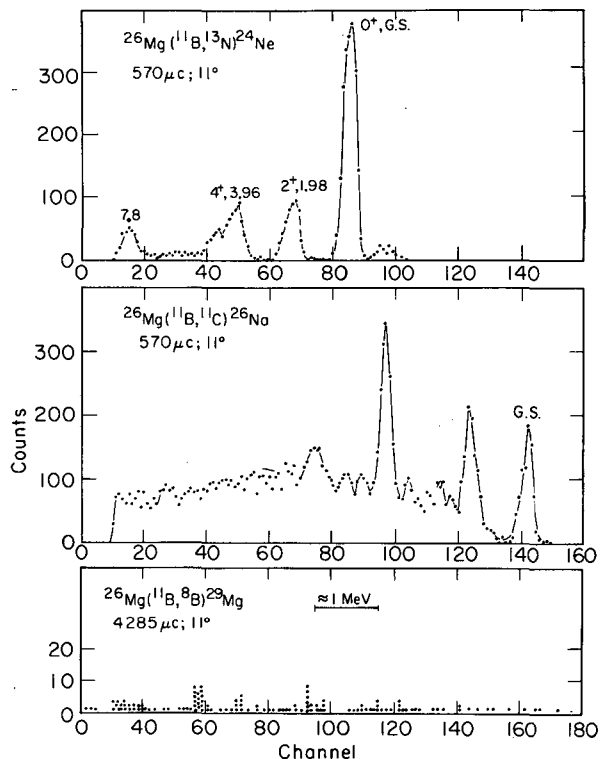


Fig. 1. Energy spectra for the reactions (a)  $^{26}\text{Mg}(^{11}\text{B}, ^{13}\text{N})^{24}\text{Ne}$ , (b)  $^{26}\text{Mg}(^{11}\text{B}, ^{11}\text{C})^{26}\text{Na}$ , and (c)  $^{26}\text{Mg}(^{11}\text{B}, ^8\text{B})^{29}\text{Mg}$  at 86 MeV incident energy and  $11^\circ$  in the laboratory.

(XBL741-2190)

possible to assign a ground state transition until a similar transfer leading to a known final nucleus with similar neutron structure is made in order to understand the selectivity of the heavy ion transfer. Work on the  $^{28}\text{Si}(^{11}\text{B}, ^8\text{B})^{31}\text{Si}$  reaction is in progress together with further study of  $^{29}\text{Mg}$  with better statistics and at other angles. The cross sections for the 3n transfer are  $\approx 100\ \text{nb}/\text{sr}$ .

#### References

1. D. K. Scott, et al., Proceedings of the 4th Atomic Mass Conference, (Plenum Press 1972) edited by J. H. Sandars and A. H. Wapstra, p. 54.
2. J. Cerny, private communication, 1974.

3. D. R. Goosman and D. Alburger, Phys. Rev. C 8, 1331 (1973).

4. J. Cerny, et. al., to be published.

5. G. C. Ball, et. al., Phys. Rev. Letters 28, 1069 (1972).

### FEASIBILITY OF ALPHA-TRANSFER STUDIES VIA THE $(\alpha, {}^8\text{Be})$ REACTION AT HIGH ENERGIES\*

G. J. Wozniak, N. A. Jelley, and J. Cerny

Although it has been apparent for some time that the  $(\alpha, {}^8\text{Be}_{g.s.})$  reaction is potentially one of the least controversial  $\alpha$ -pickup reactions, the original experiments by Brown et. al.<sup>1</sup> employing  $\alpha$ - $\alpha$  coincidence techniques showed that at 35.5 to 41.9 MeV bombarding energies, nondirect processes appeared predominant. We wish to show that direct processes appear to dominate at higher bombarding energies. The large  $\alpha$ -structure amplitude of  ${}^8\text{Be}$  should make  $(\alpha, {}^8\text{Be}_{g.s.})$  a most useful spectroscopic reaction with which to investigate theoretical  $\alpha$ -structure amplitudes in nuclei, such as those for the p-shell given by Kurath<sup>2</sup> and Rotter.<sup>3</sup>

To study the  $(\alpha, {}^8\text{Be})$  reaction, one must detect the particle unstable  ${}^8\text{Be}$  nucleus. Usually this is done either by coincidence techniques<sup>1</sup> or by the detection of both breakup  $\alpha$  particles in a single counter telescope.<sup>4</sup> Since the cross section is small ( $\sim 1$ -60  $\mu\text{b}/\text{sr}$ ) at 65 MeV, we have developed a new  ${}^8\text{Be}$  detection technique<sup>5</sup> with an appreciable probability of detecting the two breakup  $\alpha$  particles by using a divided collimator in front of a position-sensitive counter telescope with an angular acceptance larger than that of the  ${}^8\text{Be}$  breakup cone.

In these experiments we studied the  $(\alpha, {}^8\text{Be})$  reaction on several p-shell targets. A 65 MeV  $\alpha$  beam from the 88 inch cyclotron was used to irradiate targets of  ${}^{11}\text{B}$  (enriched to 98%),  ${}^{12}\text{C}$ , and  $\text{SiO}_2$  (as an oxygen target)<sup>6</sup> of thicknesses 210, 60, and 255  $\mu\text{g}/\text{cm}^2$ , respectively. A 125  $\mu\text{E}$   $\Delta\text{E}$  detector (1 cm in diameter) and a 300  $\mu\text{E}$  (PSD)<sup>7</sup> fed three high-rate amplifier systems and a pileup rejector which rejected events arising from different beam bursts. The amplifiers fed both a divider circuit, to obtain the position signal, and a particle identifier. Energy spectra gated by position and PI were collected on a Nuclear Data 4096 channel analyzer.

Figure 1 presents representative spectra of the  ${}^{11}\text{B}(\alpha, {}^7\text{Li}){}^8\text{Be}$  and  ${}^{11}\text{B}(\alpha, {}^8\text{Be}){}^7\text{Li}$  reactions as well as the  $(\alpha, {}^8\text{Be})$  reaction on  ${}^{16}\text{O}$  (each acquired in about two hours). One can clearly see from comparing Fig. 1(a) to 1(b) that there is total discrimination in the  $(\alpha, {}^8\text{Be})$

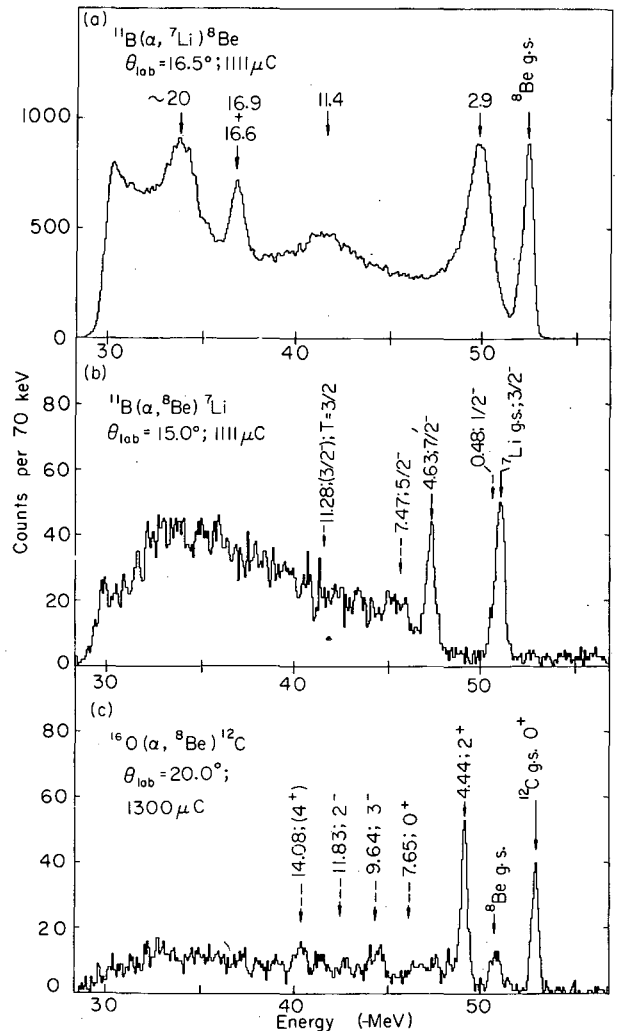


Fig. 1. Energy spectra taken at 65 MeV bombarding energy. Parts (a) and (b) show  ${}^7\text{Li}$  and  ${}^8\text{Be}$  energy spectra, obtained concurrently by setting appropriate PI and position gates, from the  ${}^{11}\text{B}(\alpha, {}^7\text{Li}){}^8\text{Be}$  and  ${}^{11}\text{B}(\alpha, {}^8\text{Be}){}^7\text{Li}$  reactions, respectively, after 1111  $\mu\text{C}$ . Part (c) shows an  ${}^8\text{Be}$  energy spectrum from the  ${}^{16}\text{O}(\alpha, {}^8\text{Be}){}^{12}\text{C}$  reaction for 1300  $\mu\text{C}$ . At this angle the ground state is relatively strongly populated. (XBL735-2818)

data against  ${}^7\text{Li}$  events. Our experimental  ${}^8\text{Be}$  energy resolution of  $\sim 450$  keV was principally determined by the width of the position gate ( $\approx 1.0^\circ$ ). The background observed above the  ${}^7\text{Li}$  and  ${}^{12}\text{C}$  ground state peaks is indicative of the contribution of  $\alpha$ - $\alpha$  pileup events to the  ${}^8\text{Be}$  spectra. Since the detection efficiency for  ${}^8\text{Be}_{2.9}^*$  was estimated to be 1/50 of that for the  ${}^8\text{Be}_{\text{g.s.}}$ , no contribution was observed<sup>8</sup> from the ( $\alpha$ ,  ${}^8\text{Be}_{2.9}^*$ ) reaction.

In the  ${}^{16}\text{O}(\alpha, {}^8\text{Be}){}^{12}\text{C}$  reaction only the  $0^+$  ground and  $2^+$  first excited states of  ${}^{12}\text{C}$  are observed to be strongly populated, as shown in Fig. 1(c). Transitions to the ( $4^+$ ), 14.08 MeV<sup>9</sup> and  $3^-$ , 9.64 MeV states are weakly seen though the ( $4^+$ ) level at back angles was observed strongly. There was no evidence of any significant excitation of the  $2^-$  unnatural parity state at 11.83 MeV nor the  $0^+$  level at 7.65 MeV. These observations are in qualitative agreement with expectations based on the predictions<sup>2,3</sup> of  $\alpha$ -structure amplitudes for  ${}^{16}\text{O}$  and differ from the earlier work on the  ${}^{16}\text{O}(\alpha, {}^8\text{Be}){}^{12}\text{C}$  reaction at  $E_\alpha = 41.9$  MeV. In that experiment<sup>1</sup> there was some evidence for excitation of the  $0^+$  state at 7.65 MeV and the average yield to the  $3^-$  state was roughly equal to that to the ground state at the angles studied. At 65 MeV, the ratio of the integrated cross sections  $\sigma(3^-)/\sigma(\text{g.s.})$  is less than 0.3.

The  ${}^{11}\text{B}(\alpha, {}^8\text{Be})$  reaction selectively populates the  $3/2^-$ , ground state and  $7/2^-$ , 4.63 MeV second excited state of  ${}^7\text{Li}$  and shows only a weak transition to the  $5/2^-$ , 7.47 MeV level, predicted to be S hindered in an LS coupling basis in direct transfer.<sup>10</sup> There was no indication of transitions to the  $T = 3/2$  state at 11.28 MeV which would be isospin forbidden. Also, we can place a limit of 15% of the ground state strength on the population of the  $\gamma_2^-$ , 0.48 MeV state. This weak strength to the  $1/2^-$  and  $5/2^-$  levels are consistent with the calculated  $\alpha$ -structure amplitudes<sup>2,3</sup> for  ${}^{11}\text{B}$ . Similar agreement with theory is obtained for the reaction on  ${}^{12}\text{C}$  (for which no spectrum is shown) in which only the  $0^+$  ground and  $2^+$  first excited states in  ${}^8\text{Be}$  are clearly populated. Transitions to the  $4^+$  level at 11.4 MeV in  ${}^8\text{Be}$  might be expected,<sup>2,3</sup> but its broad width<sup>9</sup> would make it difficult to observe. No population of the  $2^+$  (mixed isospin) states at  $\sim 16$  MeV was seen, consistent with the small calculated<sup>2</sup>  $\alpha$ -structure amplitude in  ${}^{12}\text{C}$ .

Angular distributions for ( $\alpha, {}^8\text{Be}$ ) reactions on  ${}^{12}\text{C}$  and  ${}^{16}\text{O}$  are shown in Fig. 2. Somewhat similar oscillatory behavior is seen for the two  $L = 0$  transfers to the  ${}^8\text{Be}$  and  ${}^{12}\text{C}$  ground states and a notably stronger strength at back angles occurs for the  $L = 2$  transfers. Forward angle measurements at 70 MeV on these targets produced quite similar differential cross sections

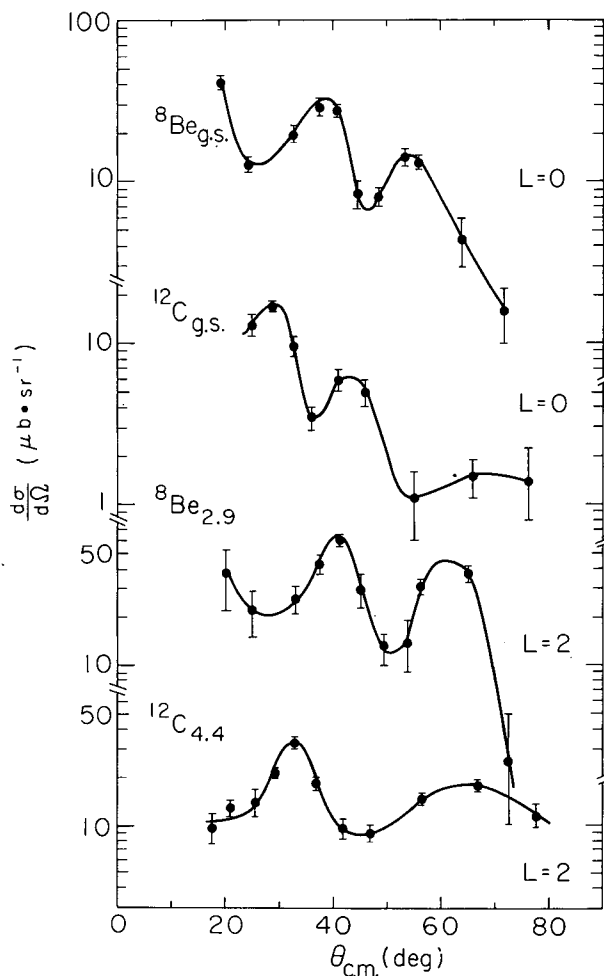


Fig. 2. Absolute differential cross sections for the strong transitions from the ( $\alpha, {}^8\text{Be}$ ) reaction on  ${}^{12}\text{C}$  and  ${}^{16}\text{O}$  targets. The absolute cross sections could be uniformly in error by as much as 20%. The curves drawn are meant to guide the eye. (XBL735-2987)

also indicating a dominant direct reaction mechanism. The  ${}^{11}\text{B}(\alpha, {}^8\text{Be}){}^7\text{Li}$  data (not shown) possessed relatively structureless angular distributions for the transitions to the ground and 4.63 MeV levels of  ${}^7\text{Li}$ , which is probably due to mixed  $L$  transfers.

To extract spectroscopic factors which can be quantitatively compared to theoretical predictions, one must account for kinematic effects which might affect the relative excitation of states. As a crude preliminary approximation one can neglect these effects and look at the ratio of yields at the first maximum. (A fairly extensive attempt was made to fit these data via the zero-range distorted wave Born approximation (DWBA) assuming an  $\alpha$ -cluster transfer. Unfortunately, only poor fits were obtained,

although at 65 MeV the angular momenta in the entrance and exit channels are well matched. This failure may be due to the fact that the  $^8\text{Be}$  optical potential is unknown; in addition neglect of finite range effects may contribute.) At the first maximum, the experimental ratios of the differential cross sections of the first excited to ground states of both  $^{12}\text{C}$  and  $^8\text{Be}$  are closely equal to 2, while the corresponding ratios of spectroscopic factors<sup>2,3</sup> are 5.5 and 1.3, respectively.

While it may require detailed excitation function studies to conclusively determine the direct nature of the ( $\alpha$ ,  $^8\text{Be}$ ) reaction at 65 MeV, the strong population of only those states which are predicted to have significant  $\alpha$ -structure amplitudes implies a dominant direct reaction mechanism. Hopefully a description of this  $\alpha$ -transfer process by an exact DWBA approach will enable quantitative tests to be made of spectroscopic predictions. Furthermore, using this relatively simple  $^8\text{Be}$  identifier, extensive comparisons with other  $\alpha$ -pickup reactions like ( $d$ ,  $^6\text{Li}$ ) and ( $^3\text{He}$ ,  $^7\text{Be}$ ) will be made possible.

#### Footnote and References

\* Condensed from Phys. Rev. Letters 31, 607 (1973).

1. R. E. Brown, J. S. Blair, D. Bodansky, N. Cue, and C. D. Kavaloski, Phys. Rev. 138, B1394 (1965).

2. D. Kurath, Phys. Rev. C 7, 1390 (1973).

3. I. Rotter, Fortschr. Phys. 16, 195 (1968).

4. G. J. Wozniak, H. L. Harney, K. H. Wilcox, and J. Cerny, Phys. Rev. Letters 28, 1278 (1972).

5. G. J. Wozniak, N. A. Jelley, and J. Cerny, see Instrumentation section.

6. A Si target was irradiated at  $\theta_{\text{lab}} = 20.0^\circ$  to understand the small background in the  $\text{SiO}_2$  data arising from  $^{24}\text{Mg}$  states populated by ( $\alpha$ ,  $^8\text{Be}$ ) on  $^{28}\text{Si}$ .

7. Our PSD was obtained from Edax International, Inc.

8. Events from the ( $\alpha$ ,  $^8\text{Be}_{2,9}^*$ ) reaction on light targets, if two-body, would have  $\sim 500$  keV higher energy than those from ( $\alpha$ ,  $^8\text{Be}_{\text{gs}}$ ) transitions to the same final states, due to a kinematic effect.

9. All excitation energies, spin and parity assignments quoted are from F. Ajzenberg-Selove and T. Lauritsen, Nucl. Phys. A114, 1 (1968) and A78, 1 (1966), except for the  $J^\pi$  assignments for levels of  $^7\text{Li}$  which are from R. J. Spiger and T. A. Tombrello, Phys. Rev. 163, 964 (1967).

10. A. N. Boyarkina, Academia Nauk, SSSR (english trans.) Physical Series 28, 255 (1964).

### MASSES FOR $^{43}\text{Ar}$ AND THE NEW ISOTOPES $^{45}\text{Ar}$ AND $^{46}\text{Ar}^*$

N. A. Jelley, K. H. Wilcox, R. B. Weisenmiller,  
G. J. Wozniak, and J. Cerny

In the region of light nuclei ( $A < 50$ ), masses of highly neutron-rich nuclides have been predicted by Garvey et. al.<sup>1</sup> by extrapolating away from the valley of stability on the basis of an independent particle model description of nuclear ground states. A simple alternative approach<sup>2</sup> based on a j-j coupling shell model description<sup>3</sup> for the ground states of even-even and even-odd nuclei, though not as general as that of Garvey et. al.,<sup>1</sup> has recently<sup>2,4</sup> been applied to describe successfully the masses of the known  $T_z = 5/2$  nuclei in the s-d shell. The very neutron-rich argon isotopes  $^{43}\text{Ar}$ ,  $^{45}\text{Ar}$ , and  $^{46}\text{Ar}$  extend far from stability ( $T_z = 7/2$  to 5), and their masses are of considerable interest not only as a means of investigating the effect of increasing neutron-excess

on nuclear binding energies, but also because in this region the predictions of Garvey et. al.<sup>1</sup> and those of the shell model differ significantly.

We have determined the previously unknown masses of  $^{43}\text{Ar}$ <sup>5</sup> and the two new isotopes  $^{45}\text{Ar}$  and  $^{46}\text{Ar}$ , as well as several excited states of  $^{43}\text{Ar}$  and  $^{45}\text{Ar}$ , by the  $^{48}\text{Ca}(\alpha, ^9\text{Be})$ ,  $^{48}\text{Ca}(\alpha, ^7\text{Be})$  and  $^{48}\text{Ca}(^6\text{Li}, ^8\text{B})$  reactions. Beams of 77.7 MeV  $\alpha$ -particles ( $\sim 1 \mu\text{A}$ ) and 80.1 MeV  $^6\text{Li}^{2+}$  ( $\sim 100 \text{ nA}$ ) from the 88-inch cyclotron were used to bombard a 96.25% isotopically enriched self-supporting  $^{48}\text{Ca}$  target ( $410 \mu\text{g}/\text{cm}^2$ ). In both experiments outgoing particles were detected by two counter telescopes located on opposite sides of the beam.

The method of data handling has been described previously<sup>4</sup> and involves in part a comparison of two particle identification signals to reduce background.

Figure 1(a) shows a  ${}^7\text{Be}$  energy spectrum from  ${}^{48}\text{Ca}$  obtained at  $\theta_{\text{lab}} = 32^\circ$ . Transitions arising from  ${}^{12}\text{C}$  and  ${}^{16}\text{O}$  contaminants in the target can be seen, as well as peaks (FWHM  $\sim 250$  keV) corresponding to the ground state of  ${}^{45}\text{Ar}$  and to a level at 3.25 MeV excitation. An energy calibration was obtained for the  ${}^7\text{Be}$  spectra by recording the  ${}^{28}\text{Si}(\alpha, {}^7\text{Be}){}^{25}\text{Mg}$  and  ${}^{40}\text{Ca}(\alpha, {}^7\text{Be}){}^{37}\text{Ar}$  reactions at intervals throughout the experiment. Adequate separation between the  ${}^7\text{Be}(\text{g.s.})$  and  ${}^7\text{Be}^*(0.429 \text{ MeV})$  transitions was obtained for  $(\alpha, {}^7\text{Be})$  on  ${}^{28}\text{Si}$ ,  ${}^{40}\text{Ca}$  and  ${}^{48}\text{Ca}$ , though not on  ${}^{12}\text{C}$  and  ${}^{16}\text{O}$ . Spectra at several angles between  $\theta_{\text{lab}} = 28^\circ$

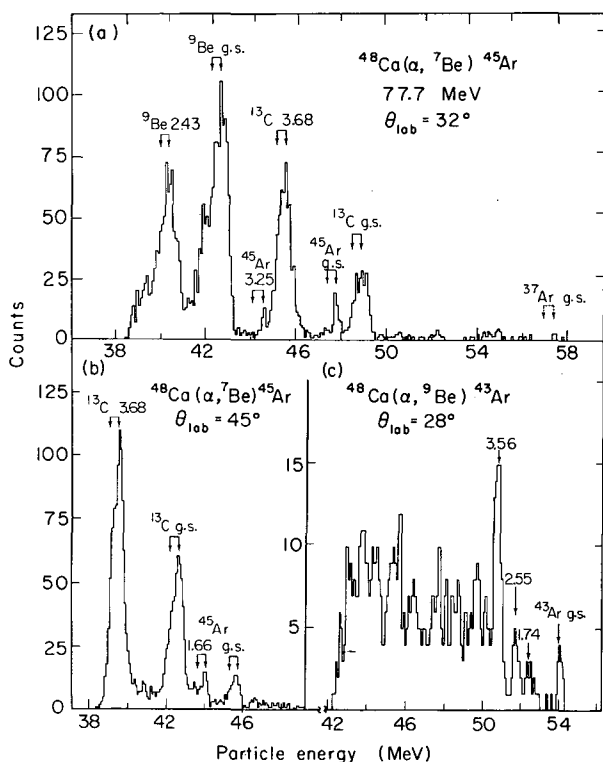


Fig. 1. (a) An energy spectrum from the reaction  ${}^{48}\text{Ca}(\alpha, {}^7\text{Be}){}^{45}\text{Ar}$  at  $\theta_{\text{lab}} = 32^\circ$  (7250  $\mu\text{Coul}$ ). The double arrows represent  ${}^7\text{Be}(\text{g.s.})$  and  ${}^7\text{Be}^*(0.429 \text{ MeV})$  transitions.

(b) As (a) but taken at  $\theta_{\text{lab}} = 45^\circ$  (30,000  $\mu\text{Coul}$ ).

(c) A composite spectrum of data taken with one counter telescope at  $\theta_{\text{lab}} = \pm 28^\circ$  from the reaction  ${}^{48}\text{Ca}(\alpha, {}^9\text{Be}){}^{43}\text{Ar}$  (17,000  $\mu\text{Coul}$ ). Contributions to this spectrum from the  $(\alpha, {}^9\text{Be})$  reaction on  ${}^{12}\text{C}$  and  ${}^{16}\text{O}$  fall below  $\sim 46$  MeV.

(XBL7311-4418).

and  $45^\circ$  [see Fig. 1(b)] were collected, kinematically confirming observation of the reaction  ${}^{48}\text{Ca}(\alpha, {}^7\text{Be}){}^{45}\text{Ar}$ , as well as enabling the region up to 5 MeV excitation to be seen. Over this angular range the cross-section to the ground state of  ${}^{45}\text{Ar}$  varied between 1.4 and 0.5  $\mu\text{b/sr}$ , and transitions to levels at  $1.66 \pm 0.05$ ,  $2.42 \pm 0.05$ , and  $3.25 \pm 0.07$  MeV excitation were identified. All states were seen at more than one angle.

For the  ${}^9\text{Be}$  spectra the  ${}^7\text{Be}$  energy calibration was used as a primary reference since it was well determined in the region of interest. Analysis of  ${}^9\text{Be}$  energy spectra from  ${}^{12}\text{C}$  and  $\text{SiO}_2$  targets showed that the ground state of the residual nucleus was always populated. A  ${}^9\text{Be}$  energy spectrum from  ${}^{48}\text{Ca}$  at  $\theta_{\text{lab}} = 28^\circ$  is shown in Fig. 1(c). Peaks are indicated corresponding to the ground state ( $d\sigma/d\Omega \sim 100$  nb/sr) and excited states at  $1.74 \pm 0.05$ ,  $2.55 \pm 0.05$ , and  $3.56 \pm 0.07$  MeV excitation in  ${}^{43}\text{Ar}$ . These and a state at  $4.74 \pm 0.10$  MeV were all seen at more than one angle.

For the  ${}^{48}\text{Ca}({}^6\text{Li}, {}^8\text{B}){}^{46}\text{Ar}$  data, an energy calibration was obtained by periodically collecting spectra from a carbon target, and from the position of the  ${}^{16}\text{O}({}^6\text{Li}, {}^8\text{B}){}^{14}\text{C}$  ground state peak arising from slight oxidation of the  ${}^{48}\text{Ca}$  target. A  ${}^8\text{B}$  energy spectrum from  ${}^{48}\text{Ca}$  at  $\theta_{\text{lab}} = 15^\circ$  is shown in Fig. 2(a). Identification of the peaks followed from comparison with spectra taken at  $\theta_{\text{lab}} = 15^\circ$  on  ${}^{40}\text{Ca}$ ,  ${}^{12}\text{C}$  and  $\text{SiO}_2$  (as an oxygen target). Spectra from  ${}^{12}\text{C}$  and  $\text{SiO}_2$  are shown in Figs. 2(b) and 2(c), respectively. (As was the case for the lighter targets, the level most strongly populated in the  ${}^{40}\text{Ca}({}^6\text{Li}, {}^8\text{B}){}^{38}\text{Ar}$  reaction was the ground state.) Observed kinematic shifts between  $\theta_{\text{lab}} = 10^\circ$  and  $17^\circ$  provided additional confirmation of peak assignments. The cross-section to the ground state of  ${}^{46}\text{Ar}$  was found to be  $\sim 1$   $\mu\text{b/sr}$  at forward angles. No transitions to excited states of  ${}^{46}\text{Ar}$  were observed; shell model calculations<sup>6</sup> predict the first excited state to be at  $\sim 2$  MeV excitation.

Analysis of the data gave the mass excesses of the argon isotopes as  ${}^{43}\text{Ar} = 31.98 \pm 0.07$  MeV,  ${}^{45}\text{Ar} = -29.727 \pm 0.06$  MeV, and  ${}^{46}\text{Ar} = 29.732 \pm 0.07$  MeV, which are compared in Fig. 3 to the predictions of Garvey et al.<sup>1</sup> and to those based on a shell model description of nuclear ground states. A preliminary value<sup>7</sup> ( $-32.27 \pm 0.04$  MeV) for the mass excess of  ${}^{44}\text{Ar}$  via the  ${}^{48}\text{Ca}({}^3\text{He}, {}^7\text{Be}){}^{44}\text{Ar}$  reaction is also compared.

In this shell model description, which is based on the approach given in the original work,<sup>3</sup> the mass excess of a nucleus with  $m$   $j$ -protons beyond a closed shell and  $n$   $j'$ -neutrons,  $M(\pi j^m \nu j'^n)$ , is related simply to that of the nucleus with no  $j'$ -neutrons,  $M(\pi j^m)$ , by the equation:

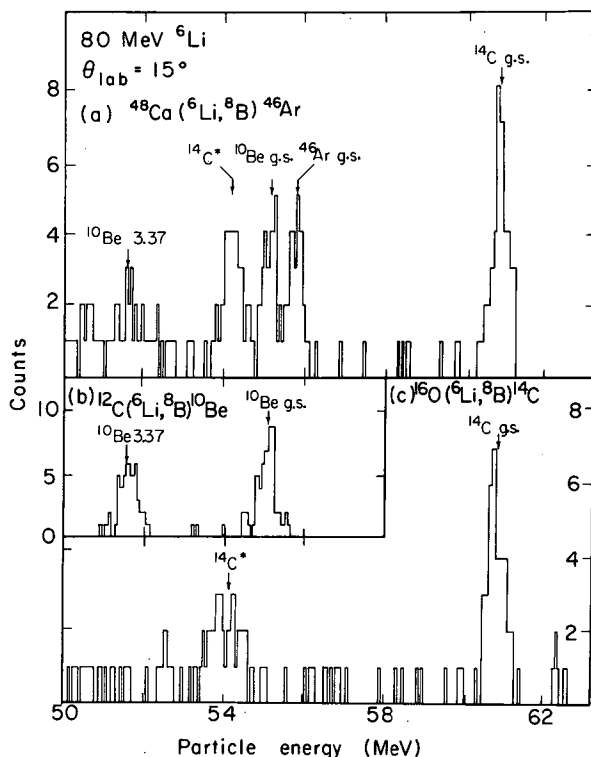


Fig. 2. Energy spectra from the ( ${}^6\text{Li}, {}^8\text{B}$ ) reaction taken at  $\theta_{\text{lab}} = 15^\circ$  on (a)  ${}^{48}\text{Ca}$  (6300  $\mu\text{coul}$ ), (b)  ${}^{12}\text{C}$ , and (c)  ${}^{16}\text{O}$ ; all are displayed with the same  ${}^8\text{B}$  energy scale.

(XBL7311-4417)

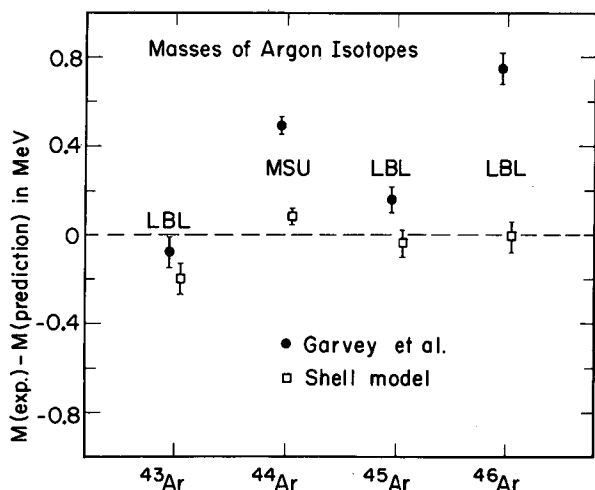


Fig. 3. Comparison of the difference between the measured mass excesses and predictions for the argon isotopes,  ${}^{43-46}\text{Ar}$ .

(XBL7311-4564)

$$M(\pi_j^m, \nu_j^n) = M(\pi_j^m) + \alpha_{j^m} + V(j'^n) + V(j^m, j'^n),$$

where  $\alpha_{j^m}$  denotes the sum of the kinetic energy and the interaction with the closed shells of each  $j'$ -neutron,  $V(j'^n)$  their mutual interaction energy, and  $V(j^m, j'^n)$  their interaction with the  $m$   $j$ -protons. The value of  $V(j^m, j'^n)$  simplifies considerably if no odd-odd nuclei are considered, depending then only on a single average interaction potential,  $V(jj')$ .<sup>1,8</sup> With this restriction we have determined the 14 parameters  $M(\pi_j^m)$ ,  $\alpha_{j^m}$ ,  $V(j'^n)$  and  $V(jj')$  for the 37 nuclei with  $\pi d_{3/2}$  or  $\nu f_{7/2}$  configurations by a least squares fit to the 24 known masses.<sup>9</sup> The root mean square deviation between the fitted and experimental values is 85 keV. The predicted values for the mass excesses of the high- $T_z$  argon isotopes are  ${}^{43}\text{Ar} = -31.78$ ,  ${}^{44}\text{Ar} = -32.35$ ,  ${}^{45}\text{Ar} = -29.69$ , and  ${}^{46}\text{Ar} = -29.72$  MeV.

As can be seen in Fig. 3, these predicted values agree well with the observed mass excesses of the argon isotopes. However, significant discrepancies between experiment and the predictions of Garvey et al.<sup>1</sup> are observed for  ${}^{44}\text{Ar}$  (490 keV) and  ${}^{46}\text{Ar}$  (750 keV). It will be particularly interesting to compare these measurements, both of masses and of excitation energies, with the results of large basis shell model calculations.<sup>6</sup> It would appear though, that the above shell model approach<sup>2</sup> to masses may be useful as an alternate predictive scheme for experimentalists studying highly neutron-rich light nuclei.

#### Footnote and References

\* Condensed from article submitted to Phys. Rev. Letters.

1. G. T. Garvey, W. J. Gerace, R. L. Jaffe, I. Talmi, and I. Kelson, Rev. Mod. Phys. **41**, S1 (1969).

2. N. A. Jelley, K. H. Wilcox, and J. Cerny, to be published.

3. S. Goldstein and I. Talmi, Phys. Rev. **105**, 995 (1957).

4. K. H. Wilcox, N. A. Jelley, G. J. Wozniak, R. B. Weisenmiller, H. L. Harney, and J. Cerny, Phys. Rev. Letters **30**, 866 (1973).

5. J. Hudis, E. Hagebø, and P. Patzelt, Nucl. Phys. **A151**, 634 (1970), and references therein.

6. D. H. Gloeckner, R. D. Lawson, and F. J. D. Serduke, submitted to Phys. Rev. Letters.

7. W. F. Steele, G. M. Crawley, and S. Maripuu, MSU Cyclotron Laboratory Report No. 98 (1973).

8. A. de-Shalit and I. Talmi, Nuclear Shell Theory (Academic Press Inc., New York, 1963).

9. A. H. Wapstra and N. B. Gove, Nucl. Data Tables 9, 265 (1971).

### ANALYZING POWERS IN $^{208}\text{Pb}(\vec{p}, t)^{206}\text{Pb}$ TRANSITIONS

J. A. Macdonald,<sup>†</sup> N. A. Jelley, and Joseph Cerny

In the past three years several studies have been made of the analyzing powers associated with the two-nucleon transfer ( $\vec{p}, t$ ) and ( $\vec{p}, ^3\text{He}$ ) reactions at medium energies on light targets<sup>1-3</sup> though, until now, few results<sup>4</sup> have been reported on any nucleus heavier than  $^{28}\text{Si}$ . DWBA analysis of analyzing powers as well as the differential cross sections of those reactions, however, has met with mixed results. It is of interest then to examine the ( $\vec{p}, t$ ) reaction on a heavy target for which the DWBA has been successful in describing the differential cross sections, and to see whether similar agreement is obtained for the analyzing powers. We have, therefore, used a polarized beam to investigate the  $^{208}\text{Pb}(\vec{p}, t)^{206}\text{Pb}$  reaction, for which good DWBA fits to the differential cross sections have been obtained in studies using unpolarized beams.<sup>5-8</sup>

Our experiments were carried out at the 88-inch cyclotron using a 40-MeV proton beam from the polarized-ion axial injection source. Beam polarization of  $|p_y| = 0.794 \pm 0.013$  was obtained and beam intensities of  $\sim 10$  to 50 nA on target were used. The beam polarization was monitored by a  $^4\text{He}$ -polarimeter, whose analyzing power is well known,<sup>9</sup> located downstream from the target chamber before the Faraday cup. The target was an evaporated 2-mg/cm<sup>2</sup> self supporting  $^{208}\text{Pb}$  metal foil enriched to  $>99\%$ . Two pairs of  $\Delta E$ -E counter telescopes were used, each pair being situated symmetrically on either side of the beam axis and feeding Goulding-Landis particle identifier systems. Angular distributions were obtained ranging from  $15^\circ$  to  $60^\circ$  in the center of mass, at intervals of  $2.5^\circ$ .

In our experiment the location of the polarimeter did not permit an absolute determination of the total integrated beam current, and absolute values of the differential cross section were obtained by a single normalization of the relative distributions to the literature.<sup>6-8</sup> Good agreement with previous measurements was obtained.

A representative spectrum is shown in Fig. 1 in which the analyzed transitions are

labelled. Figures 2 and 3 present the differential cross section ( $d\sigma/d\Omega$ ) and analyzing powers ( $A_y$ ), respectively. The following characteristics of the latter are noteworthy. First, the  $0^+$  ground state ( $L=0$ ) transition shows the most dramatic analyzing power behavior, extending to 0.85 at  $25^\circ$  c.m.

Furthermore, this analyzing power has an approximate derivative relationship to the differential cross section, i. e.,  $|A_y(\theta)| \propto d/d\theta(d\sigma/d\Omega)$ , which can simply follow from a spin-dependent distortion in the optical potential, as has been pointed out for elastic scattering and single nucleon stripping.<sup>10</sup> For transitions with  $L > 0$  the analyzing power is substantially smaller than for  $L=0$  and the phases for the  $0^+$ ,  $2^+$ ,  $4^+$ , and  $6^+$  transitions alternate as  $(-1)^{L/2}$ .

For processes such as these strong ( $p, t$ ) transitions to low-lying positive parity states in  $^{206}\text{Pb}$ , for which the dominant shell-model configurations belong to a single oscillator shell, Glendenning<sup>5</sup> has shown that the shape (but not the magnitude) of the differential

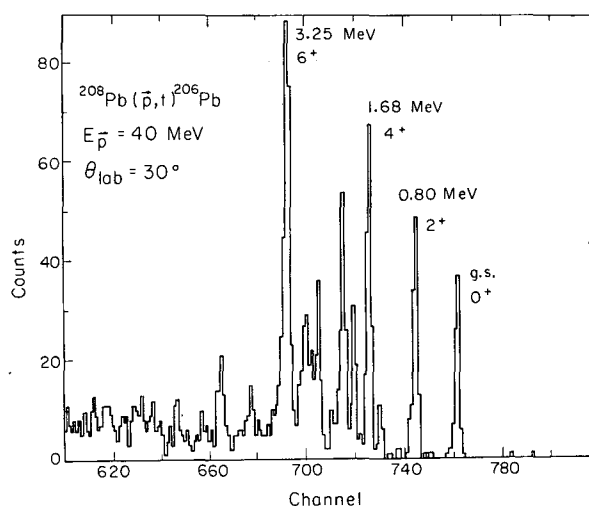


Fig. 1. Representative triton energy spectrum for  $^{208}\text{Pb}(\vec{p}, t)^{206}\text{Pb}$ . (XBL-734-2725)



cross section angular distribution can be calculated without a detailed knowledge of the nuclear wave function. Since the simple DWBA suggests<sup>10</sup> that the analyzing power will

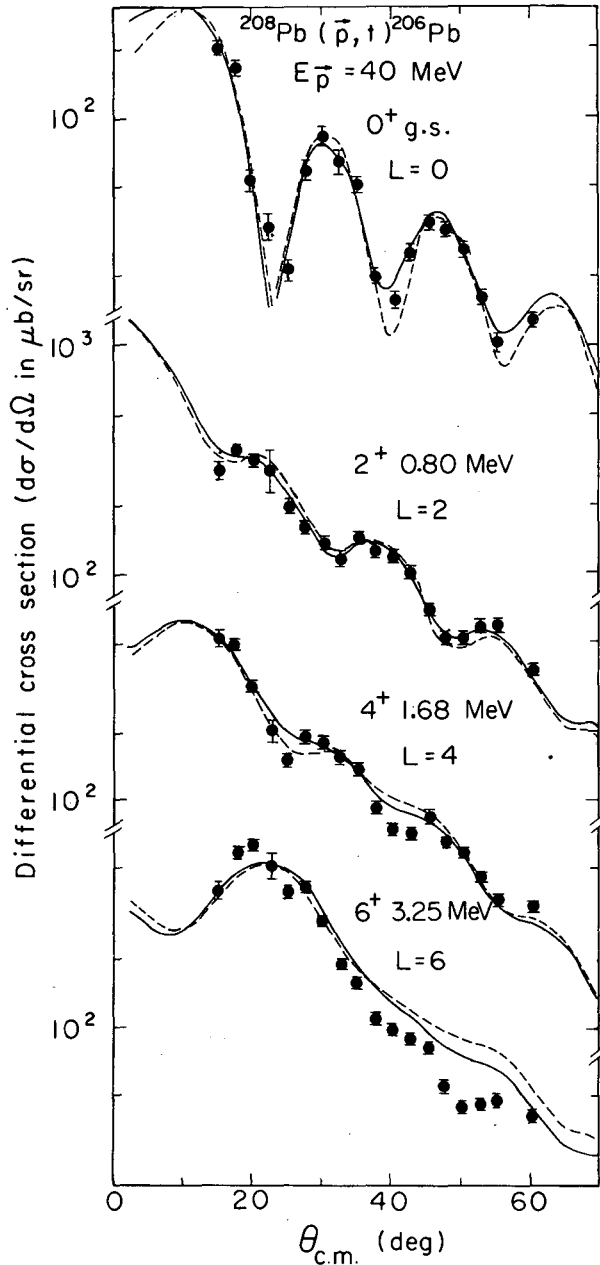


Fig. 2. Differential cross sections for transitions to states labelled in Fig. 1. The curves are separately normalized DWBA calculations: The dashed line is the result using optical parameters from Ref. 13; the solid curve was obtained by replacing the proton potential by one derived from Ref. 14. (XBL-734-3200)

$^{208}\text{Pb}(\bar{p}, t)^{206}\text{Pb}$   $E_{\bar{p}} = 40$  MeV

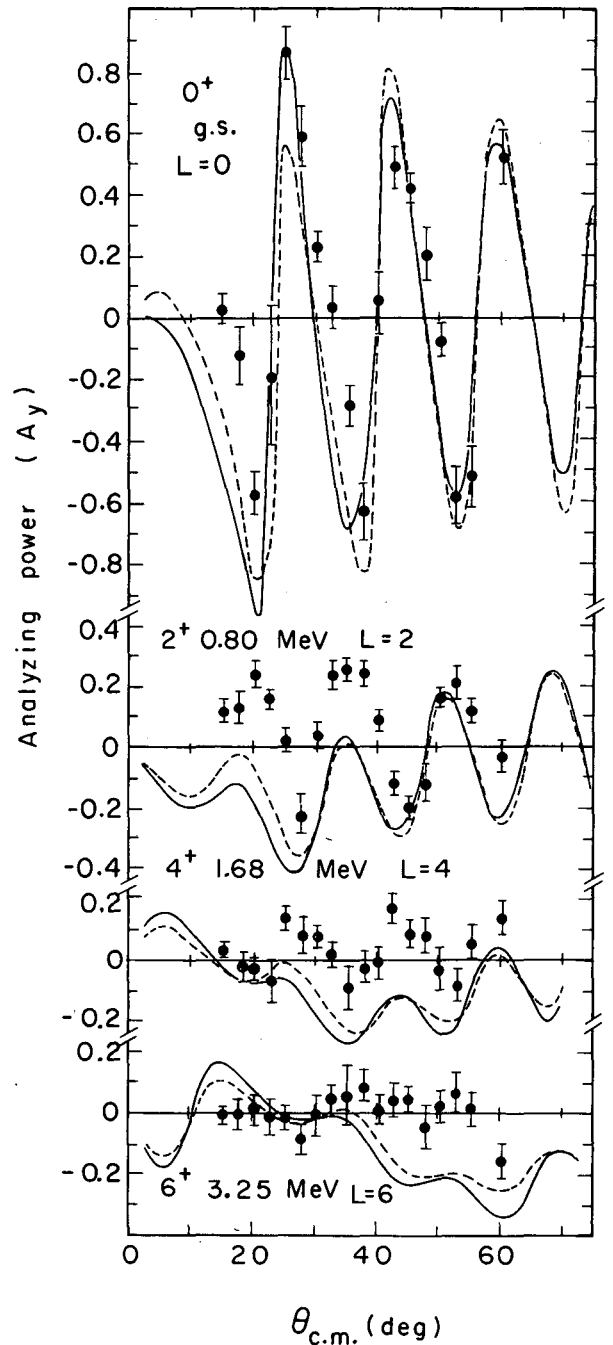


Fig. 3. Analyzing powers for the corresponding distributions of Fig. 2. The curves are DWBA fits as described in the caption to Fig. 2. (XBL-736-3199)

depend on the shape rather than on the magnitude of the cross section, one expects for these transitions that  $A_y$  is also affected by the nuclear structure in only a minimal way.

DWBA calculations have been undertaken using the program DWUUK<sup>11</sup> with structure factors from Ref. 6. Using a fixed set of optical parameters the expected insensitivity of the analyzing power calculations to the wave function was confirmed for the transition to the ground state with structure amplitudes derived from several different wave functions.<sup>6, 12</sup> Having established this, the optical parameters themselves were studied. The dashed curves for the ground state transition in Figs. 2 and 3 show that parameters used in previous  $^{208}\text{Pb}(p, t)$  DWBA studies<sup>13</sup> produce an acceptable fit to the differential cross section, though a poorer fit to the experimental analyzing power. However, if the proton optical potential derived from the global prescription of Becchetti and Greenlees<sup>14</sup> is used, as shown by the solid curve, it produces a good cross section fit and also better accounts for the analyzing power, particularly in predicting the large asymmetry at  $25^\circ$  and the lesser maxima at more backward angles.

In Figs. 2 and 3 calculations are also shown for the transitions to the  $2^+$ ,  $4^+$  and  $6^+$  states. One can see that the fits to these differential cross sections are good for both proton optical potentials. Agreement for the analyzing powers is poor in detail, although the predictions do oscillate in phase with the data.

The limited success of these DWBA calculations may be due in part to finite range effects which were neglected, and which are expected to be important if processes involving the nuclear interior are significant,<sup>15</sup> such as may be more the case for transitions to excited states. Suitable elastic scattering data with which to establish a proper triton optical potential would also remove some uncertainty in assessing the validity of the zero-range approximation. Nevertheless, this simple approach has been successful in accounting for the ground state transition as well as the phases and perhaps the overall magnitudes of the analyzing powers in the transitions to the excited states.

#### Footnotes and References

\* Condensed Physics Letters 48B, 237 (1973).

† Present address Chalk River Laboratories, AECL, Chalk River, Ontario.

1. J.C. Hardy, A.D. Bacher, G.R. Plattner, J.A. Macdonald, and R.G. Sextro, Phys. Rev. Letters 25, 298 (1970).
2. J.M. Nelson, N.S. Chant, and P. S. Fisher, Phys. Letters 31B, 445 (1970).
3. J.M. Nelson, N.S. Chant, and P. S. Fisher, Nucl. Phys. A156, 406 (1970).
4. Some results on  $^{176}\text{Yb}(\vec{p}, t)^{174}\text{Yb}$  with  $E_p = 16$  MeV have been reported recently: G. Igo, J.C.S. Chai, R.F. Casten, T. Udagawa, and T. Tamura, Nucl. Phys. A207, 289 (1973).
5. N.K. Glendenning, Phys. Rev. 156, 1344 (1967).
6. G.M. Reynolds, J.R. Maxwell, and N.M. Hintz, Phys. Rev. 153, 1283 (1967).
7. S.M. Smith, C. Moazed, A.M. Bernstein, and P.G. Roos, Phys. Rev. 169, 951 (1968).
8. S.M. Smith, P.S. Roos, A.M. Bernstein, and C. Moazed, Nucl. Phys. A158, 497 (1970).
9. A.D. Bacher, G.R. Plattner, H.E. Conzett, D.J. Clark, H. Grunder, and W.F. Tivol, Phys. Rev. C5, 1147 (1972).
10. L.S. Rodberg, Nucl. Phys. 15, 72 (1959); L.C. Biedenharn and G.R. Satchler, Helv. Phys. Acta, Suppl. 6, 372 (1961).
11. Written by P.D. Kunz, Oct. 1967 version, modified by J.C. Hardy to include the harmonic oscillator two-nucleon form-factor.
12. R.A. Broglia and C. Riedel, Nucl. Phys. A92, 145 (1967).
13. In Refs. 7 and 8 the proton potential was obtained from 40-MeV elastic scattering on  $^{208}\text{Pb}$ ; M.P. Fricke, E.E. Gross, B. M. Morton, and A. Zucker, Phys. Rev. 156, 1207 (1967). The triton potential is from Glendenning, Ref. 5.
14. F.D. Becchetti, Jr. and G. W. Greenlees, Phys. Rev. 182, 1190 (1969).
15. N. Austern, R.M. Drisko, E.C. Halbert, and G.R. Satchler, Phys. Rev. B3, 133 (1969).

ANALYZING POWERS FOR ( $\vec{p}$ ,  $^3\text{He}$ ) REACTIONS IN THE  $1p$ -SHELL\*

J. A. Macdonald,<sup>†</sup> Joseph Cerny, J. C. Hardy,<sup>†</sup>  
H. L. Harney,<sup>‡</sup> A. D. Bacher,<sup>§</sup> and G. R. Plattner<sup>||</sup>

In previous reports<sup>1,2</sup> we have described some of the ( $\vec{p}$ , t) results arising out of our study of two-nucleon transfer reactions in light nuclei induced by polarized protons. We present here some of the complementary ( $\vec{p}$ ,  $^3\text{He}$ ) results obtained in these experiments, which constitute an important further test for the reaction theory as well as for the nuclear structure of the states involved.

The relatively simple zero-range DWBA has enjoyed considerable success in describing the angular distributions of (p, t) and (p,  $^3\text{He}$ ) cross sections at forward angles ( $\theta_{\text{lab}} \leq 60^\circ$ ), e.g., Ref. 3. For this reason one might expect this model to adequately describe the experimental analyzing powers as well, since both quantities are simply related to the transition amplitude. However, previous reports<sup>4</sup> of inconsistencies between experiment and theory in the ratio of cross sections to certain mirror states is already evidence of some inadequacy in describing these two-nucleon transfer reactions with the simple DWBA, so that general comparisons of theoretical with experimental analyzing powers are of interest.

The experiments were performed at the 88-inch cyclotron, using the axial injection polarized ion source. Beam polarizations of  $|p_y| \approx 75 - 80\%$  can be typically achieved for protons with a beam current between 10 and 50 nA. For  $^{16}\text{O}$  and  $^{15}\text{N}$  targets, a beam energy of 43.8-MeV was used; for  $^{13}\text{C}$  the energy was 49.6-MeV. After passing through the gas target, the beam was recollimated before entering a polarimeter located downstream from the main scattering chamber. For the 49.6 MeV beam, the beam was degraded by an aluminum absorber to 40 MeV before entering the polarimeter because the polarimeter was not calibrated at the higher energy.<sup>5</sup>

Outgoing light reaction products were detected in four nearly identical semiconductor counter telescopes arranged in two pairs located symmetrically about the beam axis. The double collimators were arranged so that the angular acceptance was about  $1^\circ$  and the solid angle about  $1 \times 10^{-4}$  sr. For each telescope, the  $\Delta E$  and E signals were fed through charge-sensitive preamplifiers to remotely located linear amplifiers. After satisfying mutual fast coincidence requirements ( $2\tau \sim 100$  nsec), these signals were fed to a Goulding-Landis particle identifier.

Total energy signals from identified tritons and  $^3\text{He}$ 's were routed to a 4096-channel analyzer operated in  $16 \times 256$  channel mode, and then stored on magnetic tape for subsequent computer analysis.

For a transition involving a spin-dependent interaction potential, such as in the case for distorted waves generated by optical potentials including a spin-orbit term, the differential cross section can be written<sup>6</sup>

$$\frac{d\sigma}{d\Omega} \propto \sum_{M\mu_i\mu_f}^J \left| \sum_{\text{LST}} \sum_{\text{N}} G_{\text{NLSJT}}^{\text{LSJT}} B_{M\mu_i\mu_f} \right|^2$$

In order to evaluate the structure amplitude  $G$ , it is necessary to obtain the wave function for the center-of-mass motion of the transferred nucleons as they appear in the target nucleus and project out that component for which their relative motion is the same as that found for the corresponding nucleons in the  $^3\text{He}$  particle. Amplitudes  $G_{\text{NLSJT}}(jj')$  have been tabulated by Glendenning<sup>6</sup> for the transfer of nucleons from pure ( $jj'$ ) configurations. However, using an effective-interaction shell model calculation, Cohen and Kurath<sup>7</sup> have evaluated two particle fractional parentage factors  $\beta_{jj'\text{SJT}}$  between various nuclear states in the  $1p$  shell. Our spectroscopic amplitudes have been evaluated as follows:

$$G_{\text{NLSJT}} = \sum_{jj'} \beta_{jj'\text{SJT}} G_{\text{NLSJT}}(jj').$$

Zero-range DWBA calculations predicting differential cross-sections and analyzing powers for the reactions on  $^{16}\text{O}$ ,  $^{15}\text{N}$ , and  $^{13}\text{C}$  targets were performed using the program DWUCK. This code included a spin-orbit distortion in the optical potentials. The optical model parameters for the protons and mass-3 are from Refs. 3 and 8.

The  $^{16}\text{O}(\vec{p}, ^3\text{He})^{14}\text{N}$  results are shown in Fig. 1. Of particular interest are the  $1^+$  states in  $^{14}\text{N}$  at 0 and 3.95 MeV. Both transitions can go by  $L=0$  or 2 but the cfp's of Cohen and Kurath<sup>7</sup> indicate predominant  $L=2$  to the ground state and  $L=0$  to the 3.95-MeV state; the data for  $d\sigma/d\Omega$  clearly support this prediction, although the agreement is only qualitative for the 3.95-MeV transition. However, there is no agreement whatsoever for the  $A_y$  in either case, which is particularly surprising for the

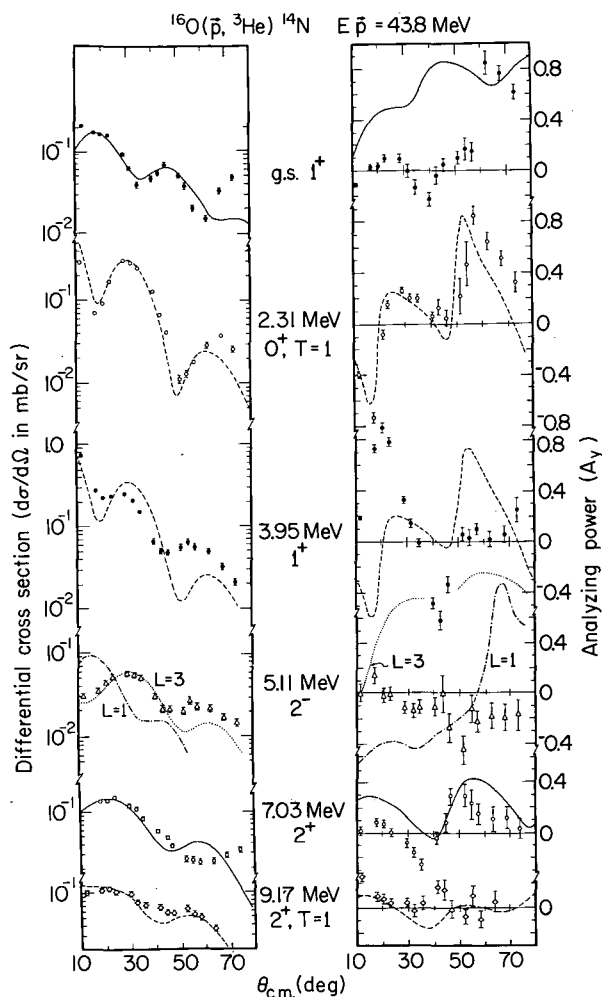


Fig. 1. Differential cross sections (left) and analyzing powers for observed  $^{16}\text{O}(\vec{p}, ^3\text{He})^{14}\text{N}$  transitions. The curves are obtained from DWBA calculations described in the text, and are separately and arbitrarily normalized to the data for  $d\sigma/d\Omega$  only. (XBL-7310-4284)

ground state, whose  $d\sigma/d\Omega$  is well fit.

The  $2^+$  states at 7.03 and 9.17 MeV are  $T=0$  and  $T=1$ , respectively, the latter being the analog of the 6.59 MeV  $2^+$  state in  $^{14}\text{O}$ . Figure 1 shows rather good DWBA agreement with the experimental  $d\sigma/d\Omega$  for both of these, primarily at forward angles for the  $T=0$  state. The calculated  $A_y$  for the  $T=0$  state is also in reasonable qualitative agreement with the data. However, the  $A_y$  measurements for the  $T=1$  state, and for its analog in  $^{14}\text{O}$ , disagree significantly with the calculations and are out of phase with the other observed  $L=2$  transitions.

The  $^{15}\text{N}(\vec{p}, ^3\text{He})^{13}\text{C}$  results are shown in Fig. 2. The transitions to the ground and first excited states both go by mixed  $L=0, 2$  and the wave functions indicate similar mixtures of  $L$  in both. The  $d\sigma/d\Omega$  data indeed are in good agreement with the theory. For the  $A_y$  data, the theory again suggests that these two transitions should be nearly identical, and the data show reasonable similarity, particularly at forward angles, but only fair agreement with the calculation in the same region.

The  $^{13}\text{C}(\vec{p}, ^3\text{He})$  transfers leading to states in  $^{11}\text{B}$  are shown in Fig. 3. As for the  $^{15}\text{N}$  target,  $(\vec{p}, ^3\text{He})$  on  $^{13}\text{C}$  is allowed to proceed in general through a complex admixture of transferred  $(J/L/S)$ . Though the theory reproduces  $d\sigma/d\Omega$  rather well for all these transitions, no agreement is obtained for  $A_y$  with the exception of the 12.94-MeV ( $1/2^-$ ,  $T=3/2$ ) transition, where fair qualitative agreement is obtained. The calculation for the 6.74-MeV ( $7/2^-$ ) transition, too, is qualitatively correct, but the magnitude is wrong by nearly a factor of 2.

To summarize, (also see Refs. 1 and 2) for transitions involving a single  $L$ -transfer the DWBA calculations predict that the analyzing power should generally (but not always) be

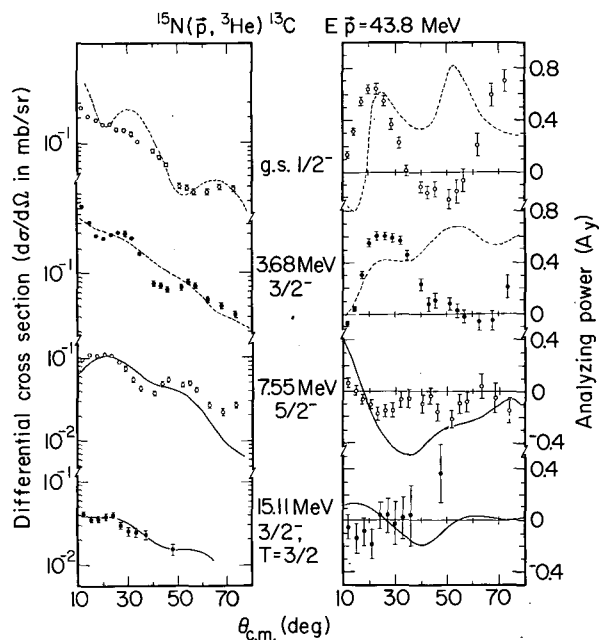


Fig. 2. Differential cross sections (left) and analyzing powers for  $^{15}\text{N}(\vec{p}, ^3\text{He})$  transitions to states in  $^{13}\text{C}$ . The curves show DWBA calculations described in the text, which are separately and arbitrarily normalized to the  $d\sigma/d\Omega$  data only. (XBL-7310-4286)

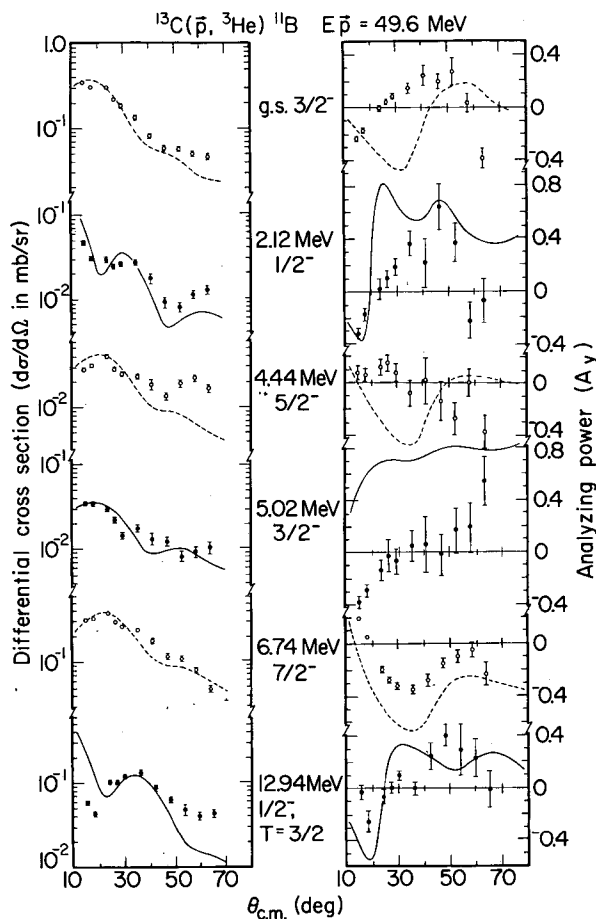


Fig. 3. Differential cross section (left) and analyzing powers for transitions observed in  $^{13}\text{C}(\vec{p}, ^3\text{He})^{11}\text{B}$ . The curves show DWBA calculations discussed in the text, and are separately and arbitrarily normalized to the data for  $d\sigma/d\Omega$  only. (XBL-7310-4288)

characteristic of this L-value. In fact, the data indicate that only in some of the particularly simple transitions such as  $(\vec{p}, t)$  reactions to ground and analog final states (not shown here) does the model give an acceptable account of the experimental results. In a large number of other apparently uncomplicated transitions this simple approach completely fails to predict the analyzing powers. Moreover, in these  $(\vec{p}, ^3\text{He})$  reactions, which are generally complex, the theory appears to be inadequate in treating most of the cases considered.

A major factor contributing to this difficulty is the choice of suitable optical potentials. For these targets and energies, the choice is not always obvious, especially for the mass-3 channel. Given the lack of complete optical model information for the applicable elastic scattering

processes, this source of uncertainty cannot be overcome.

A substantial effort has been made by a number of workers<sup>9</sup> to modify the DWBA formalism to eliminate the need for the zero-range approximation. With respect to analyzing powers, Nelson et al.<sup>10</sup> have had some success in improving fits to the few cases they considered by including a finite range routine, but it is not obvious that the large changes needed to achieve good agreement with some of the data presented here could be obtained in this way. Also, by assuming a simple direct process in these calculations, the effects of multiple-step processes have been neglected. The extent to which such factors affect the analyzing power in these cases is not known and should also be examined.

#### Footnotes and References

\* Condensed from LBL-2317, submitted to Phys. Rev. C.

† Present address: Chalk River Nuclear Laboratories, AECL, Chalk River, Ontario K0J 1J0, Canada.

‡ Present address: Max-Planck-Institut für Kernphysik, Heidelberg, West Germany.

§ Present address: Physics Department, Indiana University, Bloomington, Indiana 47401.

|| Present address: University of Basel, Basel, Switzerland.

1. J.C. Hardy, A.D. Bacher, G.R. Plattner, J.A. Macdonald, and R.G. Sextro, Phys. Rev. Letters 25, 298 (1970).

2. J.A. Macdonald, H.L. Harney, Joseph Cerny, and A.D. Bacher, Nuclear Chemistry Annual Report 1972, Lawrence Berkeley Laboratory Report LBL-1666 (1972), p. 67.

3. D.G. Fleming, J.C. Hardy, and J. Cerny, Nucl. Phys. A162, 225 (1971).

4. D.G. Fleming, J. Cerny, and N.K. Glendenning, Phys. Rev. 165, 1153 (1968).

5. A.D. Bacher, G.R. Plattner, H.E. Conzett, D.J. Clark, H. Grunder, and W.F. Tivol, Phys. Rev. C5, 1147 (1972).

6. I.S. Towner and J.C. Hardy, Advan. Phys. 18, 401 (1969); N.K. Glendenning, Ann. Rev. Nucl. Sci. 13, 191 (1963); Phys. Rev. 137, B102 (1965); Lawrence Berkeley Laboratory Reports UCRL-18268 and UCRL-18269 (unpublished).

7. S. Cohen and D. Kurath, Nucl. Phys. A141, 145 (1970).

8. C.M. Perey and F.G. Perey, Nucl. Data Tables 10, 539 (1972).

9. e.g., N. Austern, R.M. Drisko, E.C. Halbert, and G.R. Satchler, Phys. Rev. 133,

B3 (1964); E. Rost and P.D. Kunz, Nucl. Phys. A162, 376 (1971); L.A. Charlton, Phys. Rev. C8, 146 (1973).

10. J.M. Nelson, N.S. Chant, and P.S. Fisher, Nucl. Phys. A156, 406 (1970).

### THE BETA-DELAYED PROTON DECAY OF $^{25}\text{Si}$

R. G. Sextro, R. A. Gough, and J. Cerny

As part of an effort to obtain more complete information on  $\beta^+$ -delayed proton emission from the  $T_z = -3/2$ ,  $A = 4n + 1$  series of nuclides, protons following the decay of  $^{25}\text{Si}$  have been observed. The energies and intensities of such proton decays can be used to determine excitation energies in the beta-decay daughter and the preceding beta-decay transition strengths feeding these levels.

The  $^{24}\text{Mg}(^3\text{He}, 2n)^{25}\text{Si}$  experiments were done with beams of 29.5 and 40 MeV from the 88-inch cyclotron. In order to obtain high-resolution low-background particle spectra, a helium-jet transport system was used, the details of which are given elsewhere.<sup>1</sup>

The  $^{25}\text{Si}$  delayed proton spectrum shown in Fig. 1 was obtained using a  $10\text{-}\mu\text{m } \Delta E$ - $250\text{-}\mu\text{m } E$

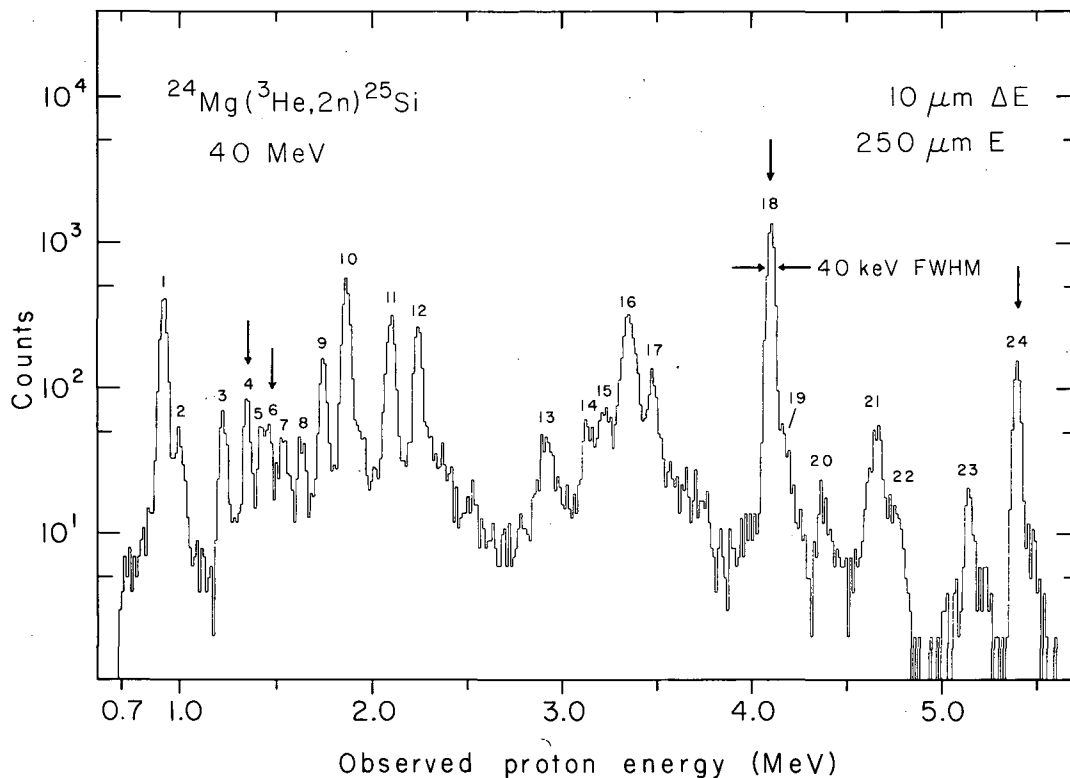


Fig. 1. Identified protons following decay of  $^{25}\text{Si}$ . Energies corresponding to the peak numbers are given in Table I. The vertical arrows denote decays of the  $T = 3/2$  analogue level. (XBL 7311-6804)

$\mu\text{m E}$  detector telescope at a beam energy of 40 MeV. Additional data (not shown here) were acquired using both thinner and thicker  $\Delta E$  detectors in order to span a large proton range—from 600 keV to  $\sim 8.5$  MeV.

No known  $\beta^+$ -delayed protons could originate from any likely target contaminants. However, at 40 MeV the beta-delayed proton precursor  $^{21}\text{Mg}$  (Ref. 1) could be produced via the  $^{24}\text{Mg}({}^3\text{He}, \alpha 2n)$  reaction; no proton peaks associated with its decay were seen. The

half-lives exhibited by all statistically significant peaks in the spectra were found to be consistent with that of  $^{25}\text{Si}$ . Combining several independent measurements, our resulting  $^{25}\text{Si}$  half-life is  $222.6 \pm 5.9$  msec, which agrees with the previous values of  $225 \pm 6$  msec (Ref. 2) and  $218 \pm 4$  msec (Ref. 3). The weighted average of these determinations gives  $220.7 \pm 2.9$  msec which has been used for all subsequent calculations and results quoted here.

The energy of the lowest  $T = 3/2$  state has

Table I. Proton energies following decay of  $^{25}\text{Si}$  and energy levels in  $^{25}\text{Al}$ . Underlined numbers preceding each entry correspond to peak numbers in Fig. 1. (All energies in MeV  $\pm$  keV)

Proton energies (c.m.) corresponding to decays to the following levels in $^{24}\text{Mg}$					Deduced <sup>a</sup> energies in $^{25}\text{Al}$
	g. s.	1.369	4.123	4.233	
<u>7</u>	$1.586 \pm 15$	-- <sup>b</sup>			$3.857 \pm 15$
<u>10</u>	$1.927 \pm 1^c$	--			$4.197 \pm 1$
<u>12</u>	$2.311 \pm 1^c$	<u>1</u> $0.943 \pm 2^c$			$4.582 \pm 1$
	x <sup>b</sup>	<u>5</u> $1.464 \pm 20$			$5.104 \pm 20$
<u>13</u>	$3.017 \pm 15$	x <sup>b</sup>			$5.288 \pm 15$
<u>14</u>	$3.239 \pm 20$	x			$5.510 \pm 20$
<u>15</u>	$3.332 \pm 20$	x			$5.603 \pm 20$
	x	<u>11</u> $2.162 \pm 10$			$5.802 \pm 10$
<u>21</u>	$4.846 \pm 15$	<u>16</u> $3.473 \pm 15$	x	--	$7.115 \pm 11$
<u>22</u>	$4.968 \pm 20$	<u>17</u> $3.606 \pm 15$	x	x	$7.243 \pm 12$
	x	x	<u>2</u> $1.034 \pm 25$	x	$7.428 \pm 25$
<u>23</u>	$5.367 \pm 15$	x	<u>3</u> $1.264 \pm 15$	x	$7.648 \pm 11$
<u>24</u>	$5.631 \pm 3^c$	<u>18</u> $4.263 \pm 3^c$	<u>6</u> $1.506 \pm 20$	<u>4</u> $1.391 \pm 15$	$7.902 \pm 3$
	x	<u>19</u> $4.347 \pm 40$	x	x	$7.987 \pm 40$
	x	<u>20</u> $4.556 \pm 20$	<u>9</u> $1.801 \pm 10$	<u>8</u> $1.684 \pm 15$	$8.193 \pm 8$

<sup>a</sup>The excitation energies are calculated using a proton separation energy of  $2.271 \pm 0.001$  MeV.

<sup>b</sup>Energetically allowed proton decays below the experimental energy range ( $\leq 600$  keV) are denoted by --, while those within the detectable range, but unobserved are marked by x.

<sup>c</sup>These proton energies were used as energy calibrants.

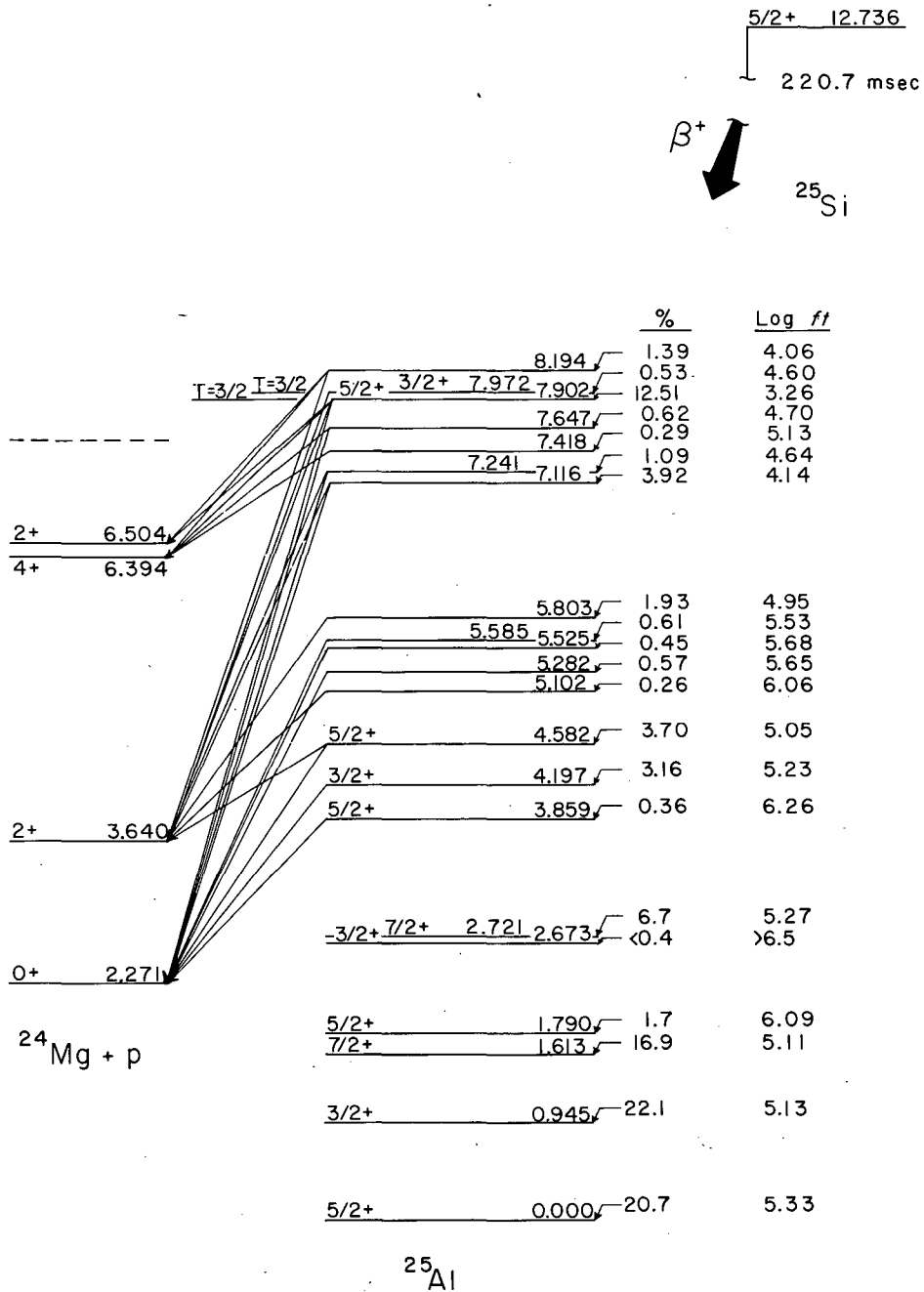


Fig. 2. Proposed decay scheme for  $^{25}\text{Si}$ . The excitation energies are averages of previous values and those listed in Table I.

(XBL 7311-6824)



been determined by several techniques: radiative capture,<sup>4</sup> resonance scattering<sup>5</sup> and particle transfer reactions.<sup>6</sup> The energies of the prominent proton decays to the  $^{24}\text{Mg}$  ground- and first-excited states (peaks 24 and 18, respectively, in Fig. 1) serve as energy calibrants. Likewise, the low-energy peaks from known<sup>7</sup> states at 4.197 and 4.582 are also energy calibration points.

The center-of-mass energies for the 24 proton peaks and assignments to levels in  $^{25}\text{Al}$  are listed in Table I. The ground state spin and parity of  $^{25}\text{Si}$  is assumed to be  $5/2^+$ , analogous to that for the  $^{25}\text{Na}$  ground state, and the lowest  $T = 3/2$  states in  $^{25}\text{Al}$  and  $^{25}\text{Mg}$  (Ref. 8). Therefore, allowed beta-decay from  $^{25}\text{Si}$  will populate those levels with  $J^\pi = (3/2, 5/2 \text{ or } 7/2)^+$  in  $^{25}\text{Al}$ . Energy levels up to 5 MeV in excitation have been extensively investigated<sup>7,9</sup>; it is unlikely that any new levels fed by allowed beta decay exist in this energy region. Above 5 MeV, recent studies<sup>9</sup> have accurately located many new levels. No new levels have been postulated on the basis of the present delayed proton results. In fact, agreement between those excitation energies inferred from the present results and the previous values is excellent.

The present work confirms many of the earlier delayed proton observations.<sup>3</sup> The higher resolution data discussed here resolve some of the broad proton groups in the earlier data into two or more distinct peaks, and identify additional peaks in the decay spectrum. The  $T = 3/2$  state decays to the ground- and first-excited states in  $^{24}\text{Mg}$  were identified previously, however the lower intensity decays to the second and third excited states were first observed in the present data.

The assignments listed in Table I indicate that no states between 5.9 and 7.0 MeV give rise to observable proton decay peaks. The earlier Brookhaven work<sup>3</sup> shows three levels in this range of excitation—at 6.15, 6.70, and 6.92 MeV. No decays corresponding to the first of these were seen, while for the latter two, the proton peaks were assigned to other states. Finally, the earlier assignment of a peak to the 8.97 MeV state (originally thought to be the second  $T = 3/2$  state) is now known to be incorrect on the basis of its recently measured  $J^\pi = 1/2^+$ .<sup>10</sup> The present assignment of this peak to a state at 7.65 MeV is shown in Table I.

Absolute  $\beta^+$ -decay branching ratios and  $ft$  values can be obtained from the relative proton intensities, and the calculated strength for the superallowed beta-decay to the  $T = 3/2$  state. Assuming isospin purity for this level, the  $\log ft$  is 3.26 (Ref. 11). The resulting branching ratios and  $\log ft$  values for all beta-decays to  $^{25}\text{Al}$  are shown as part of the decay scheme displayed in Fig. 2. The branching ratios for beta decay to states below 3 MeV are calculated from comparison to the mirror  $^{25}\text{Na}$  negatron decay.<sup>12</sup> A comparison of the mirror beta-decay transition strengths gives  $(ft)^+/(ft)^- = 1.17 \pm 0.04$ , consistent with the earlier determination.<sup>12</sup>

### References

1. R. G. Sextro, R. A. Gough, and J. Cerny, *Phys. Rev. C* **8**, 258 (1973).
2. R. McPherson and J. C. Hardy, *Can. J. Phys.* **43**, 1 (1965).
3. P. L. Reeder, A. M. Poskanzer, R. A. Esterlund, and R. McPherson, *Phys. Rev.* **147**, 781 (1966).
4. G. C. Morrison, D. H. Youngblood, R. C. Barse, and R. E. Segel, *Phys. Rev.* **174**, 1366 (1968).
5. B. Teitelman and G. M. Temmer, *Phys. Rev.* **177**, 1656 (1969).
6. W. Benenson, E. Kashy, and I. D. Proctor, *Phys. Rev. C* **7**, 1143 (1973).
7. H. Röpke, H. J. Brundiers, and G. Hammel, *Nucl. Phys.* **A153**, 211 (1970).
8. J. C. Hardy and D. J. Skyrme, in *Isobaric Spin in Nuclear Physics*, edited by J. D. Fox and D. Robson (Academic, New York, 1966) p. 701.
9. C. P. Browne, J. D. Goss, and A. A. Rollefson, *Phys. Rev. C* **8**, 1805 (1973).
10. J. A. Becker, R. E. McDonald, L. F. Chase, Jr., and D. Kohler, *Phys. Rev.* **188**, 1783 (1969).
11. J. C. Hardy and B. Margolis, *Phys. Lett.* **15**, 276 (1965).
12. D. E. Alburger and D. H. Wilkinson, *Phys. Rev. C* **3**, 1957 (1971).

## HIGH-RESOLUTION MEASUREMENTS OF BETA-DELAYED PROTONS FROM $^{37}\text{Ca}$ AND $^{41}\text{Ti}$

R. G. Sexto, R. A. Gough, and J. Cerny

Although beta-delayed proton decay in light nuclei has been well-established for the  $A = 4n+1$ ,  $T_z = -3/2$  nuclei,  $^{37}\text{Ca}$  and  $^{41}\text{Ti}$  are among those nuclides which have not been previously studied<sup>1</sup> with high-resolution techniques. Through the use of a helium-jet transport (described in Ref. 2) and particle identification, we have been able to observe all significant particle decays from  $^{37}\text{Ca}$  and  $^{41}\text{Ti}$  spanning a proton energy range from  $\sim 0.6$  to 8.5 MeV.

These nuclides were produced using  $^3\text{He}$  beams from the 88-inch cyclotron for bombardment of  $^{36}\text{Ar}$  and  $^{40}\text{Ca}$  targets; the  $^{37}\text{Ca}$  experiments were done at 40 MeV, while the  $^3\text{He} + ^{40}\text{Ca}$  experiments used 29.5, 36.5 and 60-MeV beams in order to establish relative peak intensities as a function of bombarding energy. At some of these bombarding energies, competing reaction products can potentially complicate the proton spectra. All but  $^{40}\text{Sc}$  can be eliminated on the basis of half-life, known beta-delayed proton peak energies, or beta-decay systematics. In order to ascertain the contribution of delayed-protons from  $^{40}\text{Sc}$  in the proton spectra obtained from  $^3\text{He}$  bombardment of  $^{40}\text{Ca}$ , data were also acquired from the  $^{40}\text{Ca}(p, n)^{40}\text{Sc}$  reaction at 20 MeV.

The reactions on the  $^{40}\text{Ca}$  target were done using 1.0 to 1.5-mg/cm<sup>2</sup> thick targets, while in order to investigate the  $^{36}\text{Ar}(^3\text{He}, 2n)^{37}\text{Ca}$  reaction, a gas target system was developed for use with the helium jet. The very thin ( $\sim 200 \mu\text{g}/\text{cm}^2$ ) exit window in this target required the use of a Hg-filled Toepler pump to maintain a pressure differential of  $\lesssim 15$  Torr, while operating at a target box pressure of 1100 Torr (absolute).

We have previously reported<sup>3</sup> a new determination of the excitation energy of the lowest  $T = 3/2$  state in  $^{41}\text{Sc}$ , which disagrees substantially with the previous value. This reassignment has recently been confirmed using  $^{40}\text{Ca}(p, p)$  resonance results.<sup>4</sup> After averaging with our delayed-proton data, the proton decay energy has been used as an energy calibrant. Similarly, proton decays from the well-known  $T = 3/2$  states in  $^{25}\text{Si}$  and  $^{37}\text{Ca}$  have been used as calibration points,<sup>3</sup> along with low energy protons from decay of accurately known levels in  $^{25}\text{Al}$  (see the contribution on beta-delayed proton decay of  $^{25}\text{Si}$  elsewhere in this Annual Report).

Delayed protons following  $^3\text{He}$  and proton bombardments of  $^{40}\text{Ca}$  targets are shown in Fig. 1; parts (a) and (b) were obtained using the  $^3\text{He}$  beam energies indicated, while the spectrum shown in part (c) was taken using 20-MeV protons. A more complete spectrum from the 60-MeV  $^3\text{He}$  bombardment of  $^{40}\text{Ca}$  is shown in Fig. 2. Finally, a delayed-proton spectrum from  $^{37}\text{Ca}$  is shown in Fig. 3 for the energy region between 2 and  $\sim 4$  MeV.

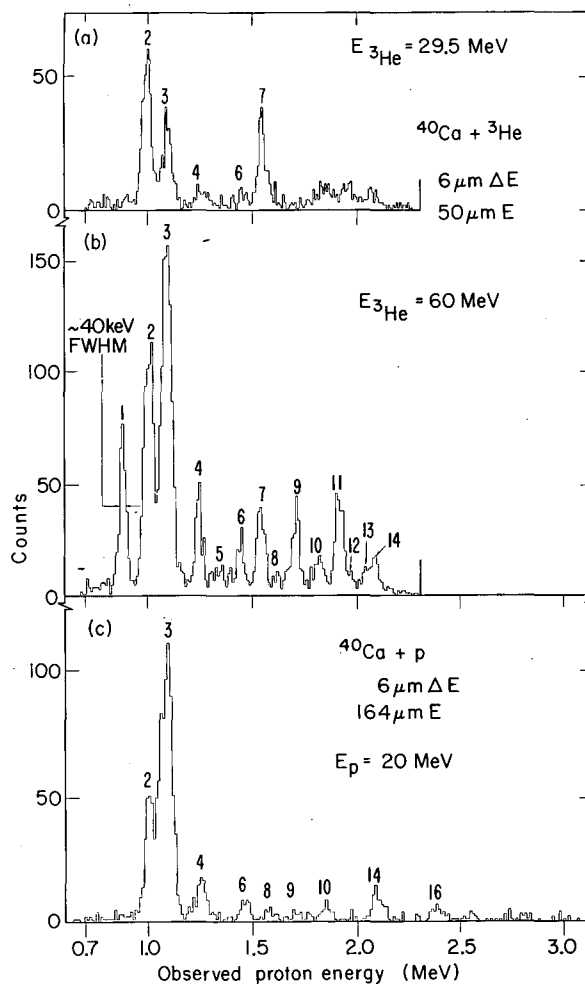


Fig. 1. Identified protons following  $^3\text{He}$  or proton bombardment of  $^{40}\text{Ca}$ . The peak numbers refer to peaks in Tables I and II.  
(XBL 738-4004)

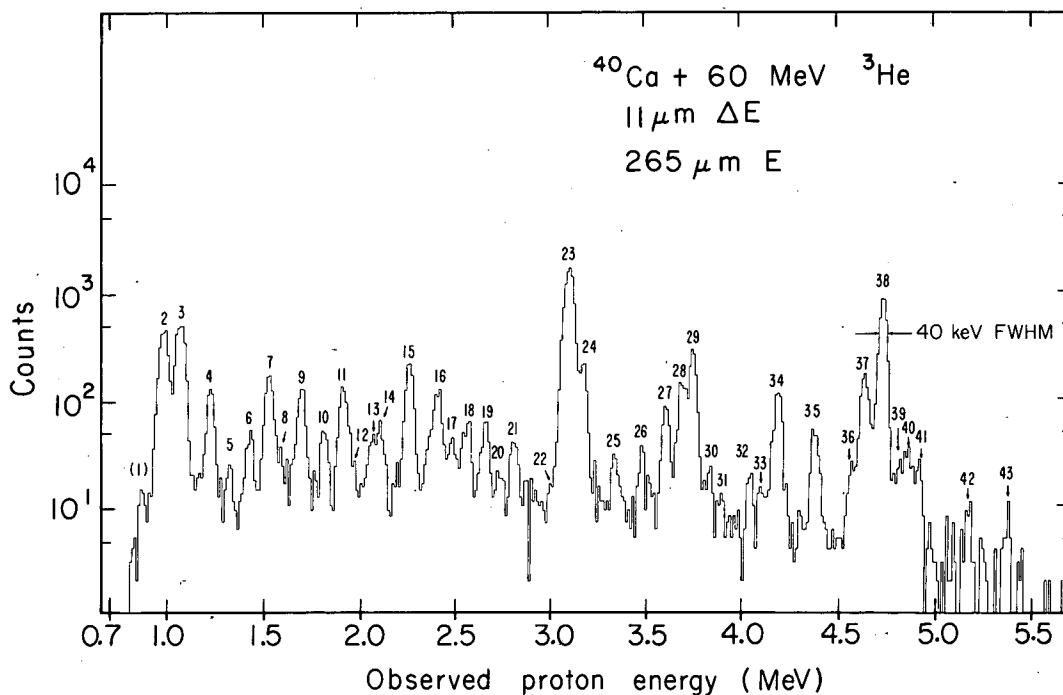


Fig. 2. Delayed protons following  ${}^3\text{He}$  bombardment at 60 MeV. The intensity of peak 1 is reduced due to an electronic cut-off. (XBL 738-4007)

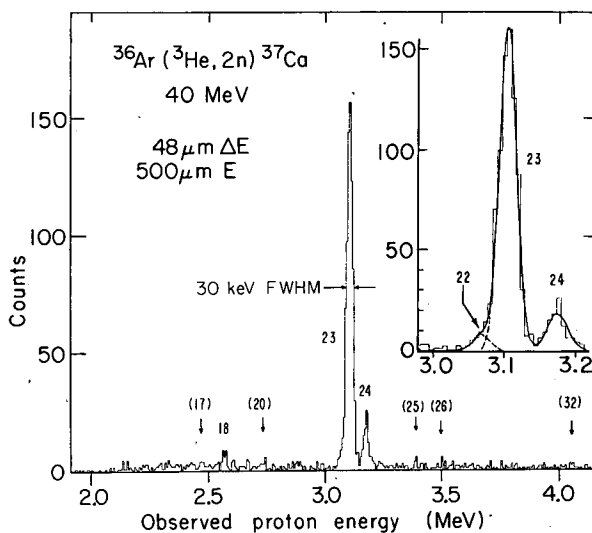


Fig. 3. Delayed protons from  ${}^{37}\text{Ca}$ . The three main groups are shown in the inset along with the Gaussian fits to each peak. (XBL 738-4005)

Half-life data were acquired for each of these three nuclides. Our half-life measurements for  ${}^{40}\text{Sc}$  and  ${}^{37}\text{Ca}$  agree with the previously reported values; since the present results do not statistically alter the established half-lives, we have adopted  $182.4 \pm 0.7$  msec for  ${}^{40}\text{Sc}$  and  $175 \pm 3$  msec for  ${}^{37}\text{Ca}$ . The present results for  ${}^{41}\text{Ti}$  are not, however, consistent with the former value of  $88 \pm 1$  msec.<sup>1</sup> The earlier data, obtained with a 32-MeV  ${}^3\text{He}$  beam, could have been affected by contamination from  ${}^{37}\text{Ca}$  produced in the  ${}^{40}\text{Ca}({}^3\text{He}, \alpha 2n)$  reaction. We have used the present result of  $80 \pm 2$  msec for the  ${}^{41}\text{Ti}$  half-life; this value is based on peaks associated solely with the decay of  ${}^{41}\text{Ti}$ .

The center-of-mass proton energies and the excitation energy inferred for each decay peak are given in Tables I and II for  ${}^{37}\text{Ca}$  and  ${}^{41}\text{Ti}$  respectively. For the case of  ${}^{37}\text{Ca}$ , all protons are assumed to arise from decays to the  ${}^{36}\text{Ar}$  ground state; the deduced energy levels listed in Table I all agree with previously determined excitation energies. Similarly for  ${}^{41}\text{Ti}$ , states up to  $\sim 6$  MeV in excitation should predominantly decay to the  ${}^{40}\text{Ca}$  ground state, based on penetrabilities for the various

Table I. Eneter-of-mass proton energies and energies of levels in  $^{37}\text{K}$ . (All energies in MeV  $\pm$  krV).

Peak number	Proton energy	Deduced energy <sup>a</sup> in $^{37}\text{K}$
1	0.894 $\pm$ 15	2.751 $\pm$ 15
9	1.757 $\pm$ 10	3.614 $\pm$ 10
11	1.979 $\pm$ 10	3.836 $\pm$ 10
17	2.568 $\pm$ 20	4.425 $\pm$ 20
18	2.652 $\pm$ 20	4.509 $\pm$ 20
20	2.822 $\pm$ 20	4.679 $\pm$ 20
22	3.149 $\pm$ 15	5.006 $\pm$ 15
23	3.190 $\pm$ 3 <sup>b</sup>	5.047 $\pm$ 3
24	3.262 $\pm$ 10	5.119 $\pm$ 10
25	3.432 $\pm$ 30	5.289 $\pm$ 30
26	3.585 $\pm$ 20	5.442 $\pm$ 20
32	4.159 $\pm$ 20	6.016 $\pm$ 20

<sup>a</sup>The excitation energies were computed using a proton separation energy of  $1.857 \pm 0.001$  MeV.

<sup>b</sup>Used as part of the energy calibration.

possible decay modes. Above this energy, decays to  $^{40}\text{Ca}$  excited states have been observed,<sup>5</sup> and some of our assignments follow these inelastic scattering results, as can be noted from Table II. Again the agreement with previous excitation energies is excellent, with the one new assignment to a level at  $\sim 3.56$  MeV based on comparison to the  $^{41}\text{Ca}$  mirror.<sup>6</sup>

From the assumption of isospin purity for the  $T=3/2$  state in  $^{37}\text{K}$ , the  $\log ft$  for beta decay to this state can be calculated to be 3.30. The relative proton intensities then lead to absolute branching ratios and  $\log ft$  values for other states fed by allowed beta decay. These branching ratios and  $ft$  values are shown as part of the  $^{37}\text{Ca}$  decay scheme in Fig. 4. The ground state decay branch is from the mirror, while the branch to the 1.368-MeV state is calculated from the remaining unassigned beta-decay strength.

Since the ground state of  $^{41}\text{Sc}$  is  $7/2^-$ , beta decay from  $^{41}\text{Ti}$  ( $3/2^+$ ) is first-forbidden unique. All excited states in  $^{41}\text{Sc}$  are unbound, hence absolute beta decay branching ratios can be determined directly from the relative proton intensities. The resulting

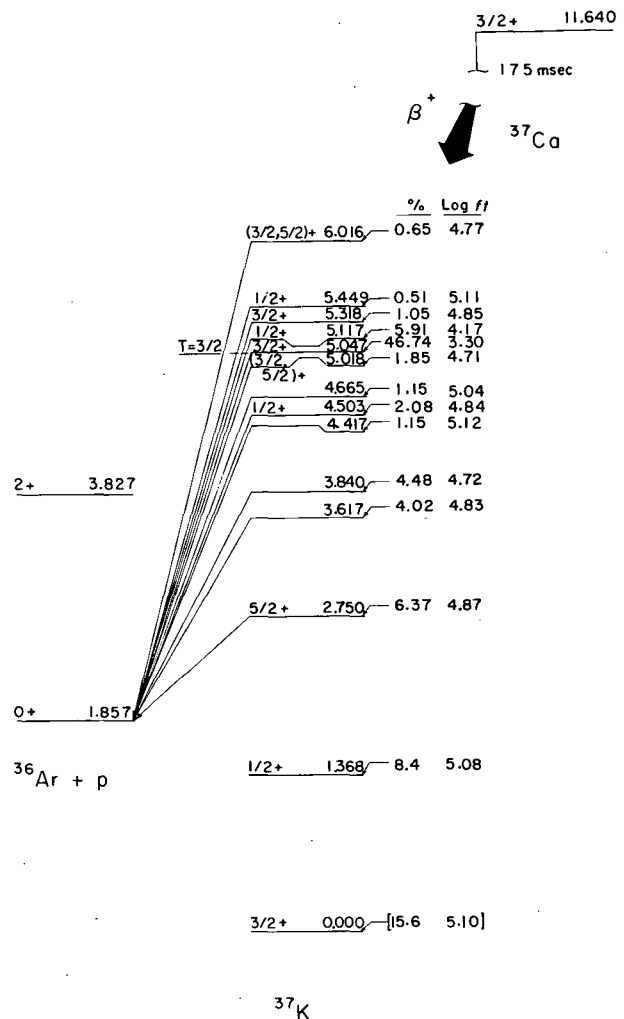


Fig. 4. Proposed decay scheme for  $^{37}\text{Ca}$ . The excitation energies are from Table I, averaged with the previous values.

(XBL 7310-4297)

branching ratios and  $\log ft$  values are given in Fig. 5 as part of the  $^{41}\text{Ti}$  decay scheme. Comparing the observed beta-decay strength for the superallowed decay with the calculated value gives the degree of isospin mixing for this  $T=3/2$  state in  $^{41}\text{Sc}$ . In the extreme case where the Gamow-Teller matrix element is zero (where deviations between the observed and predicted values can only be due to isospin impurities), the isospin purity is  $(92.6 \pm 3.8)\%$ .

Such mixing might predominantly occur with the nearby state at 5.838 MeV, which, noting Fig. 5, exhibits significant beta-decay strength. Similar impurities have been observed in the  $T=3/2$  states in  $^{17}\text{F}$  and  $^{33}\text{Cl}$  (Ref. 7).

Table II. Center-of-mass proton energies and excitation energies in  $^{41}\text{Sc}$ . (All energies in MeV  $\pm$  keV).

Peak number	Final state in $^{40}\text{Ca}$	Proton energy	Deduced energy level in $^{41}\text{Ti}$ <sup>a</sup>
2	g. s.	1.025 $\pm$ 15	2.111 $\pm$ 15
7	g. s.	1.585 $\pm$ 15	2.671 $\pm$ 15
15	g. s.	2.328 $\pm$ 10	3.414 $\pm$ 10
16	g. s.	2.470 $\pm$ 20	3.556 $\pm$ 20
19	g. s.	2.729 $\pm$ 20	3.815 $\pm$ 20
21	g. s.	2.885 $\pm$ 15	3.971 $\pm$ 15
23	g. s.	3.155 $\pm$ 15	4.241 $\pm$ 15
24	g. s.	3.227 $\pm$ 20	4.313 $\pm$ 20
25	g. s.	3.423 $\pm$ 30	4.509 $\pm$ 30
26	g. s.	3.575 $\pm$ 20	4.661 $\pm$ 20
27	g. s.	3.696 $\pm$ 15	4.782 $\pm$ 15
28	g. s.	3.783 $\pm$ 15	4.869 $\pm$ 15
29	g. s.	3.843 $\pm$ 10	4.929 $\pm$ 10
30	g. s.	3.933 $\pm$ 25	5.019 $\pm$ 25
31	g. s.	4.002 $\pm$ 25	5.088 $\pm$ 25
34	g. s.	4.292 $\pm$ 15	5.378 $\pm$ 15
35	g. s.	4.489 $\pm$ 15	5.575 $\pm$ 15
36	g. s.	4.679 $\pm$ 20	5.765 $\pm$ 20
37	g. s.	4.755 $\pm$ 10	5.841 $\pm$ 10
38	g. s.	4.853 $\pm$ 4 <sup>b</sup>	5.939 $\pm$ 4
39	g. s.	4.954 $\pm$ 25	6.040 $\pm$ 25
40	g. s.	4.999 $\pm$ 20	6.085 $\pm$ 20
4	3.737	1.279 $\pm$ 15	6.102 $\pm$ 15
41	g. s.	5.049 $\pm$ 20	6.135 $\pm$ 20
42	g. s.	5.307 $\pm$ 30	6.393 $\pm$ 30
12	3.353	2.033 $\pm$ 25	6.472 $\pm$ 25
13	3.737	2.115 $\pm$ 30	6.938 $\pm$ 30

<sup>a</sup>The proton separation energy used for these calculations is  $1.086 \pm 0.001$  MeV.

<sup>b</sup>Used as part of the energy calibration.

<sup>c</sup>Assigned to the same state.

## Footnote and References

Condensed from LBL-1955, to be submitted to Nuclear Physics.

1. A. M. Poskanzer, R. McPherson, R. A. Esterland, and P. L. Reeder, *Phys. Rev.* **152**, 995 (1966).

2. R. G. Sextro, R. A. Gough, and J. Cerny, *Phys. Rev. C* **8**, 258 (1973).

3. R. A. Gough, R. G. Sextro, and J. Cerny, *Phys. Letters* **43B**, 33 (1973).

4. T. A. Trainor, T. B. Clegg, and W. J. Thompson, *Bull. Am. Phys. Soc.* **18**, 602 (1973).

5. A. Marinov, Ch. Drory, E. Navon, J. Burde, and G. Engler, *Nucl. Phys.* **A145**, 534 (1970).

6. S. M. Smith, A. M. Bernstein, and M. E. Rickey, *Nucl. Phys.* **A113**, 303 (1968); K. K. Seth, A. Saha, and L. Greenwood, *Phys. Rev. Lett.* **31**, 552 (1973).

7. J. C. Hardy, J. E. Esterl, R. G. Sextro, and J. Cerny, *Phys. Rev. C* **3**, 700 (1971).

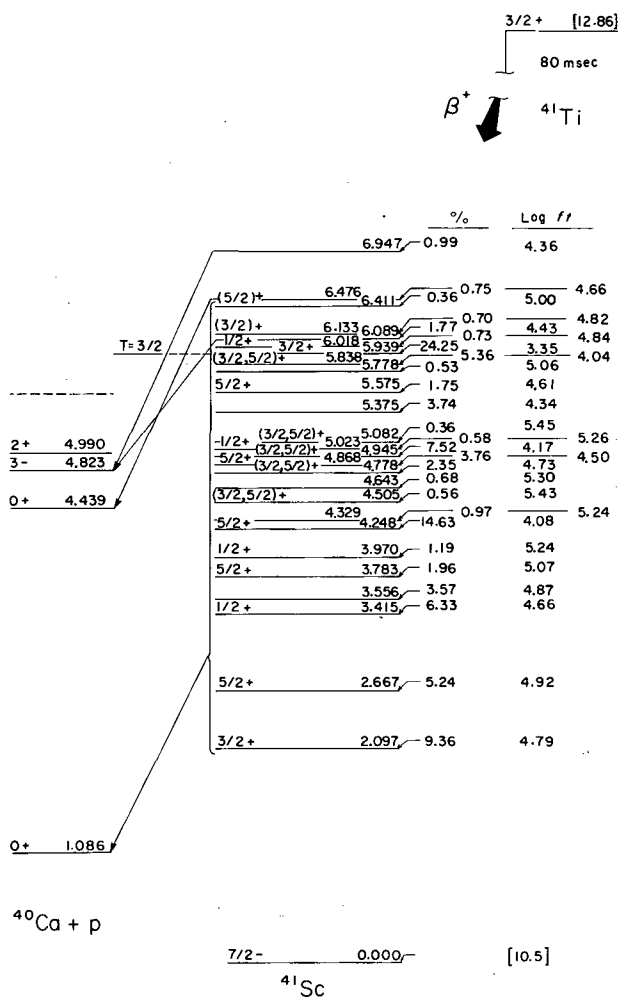


Fig. 5. Proposed  $^{41}\text{Ti}$  decay scheme. The excitation energies are from Table II, averaged with the previous results (XBL 7310-4298)

### THE DISCOVERY OF TWO ISOTOPES, $^{14}\text{Be}$ AND $^{17}\text{B}$ , AT THE LIMITS OF PARTICLE STABILITY

J. D. Bowman,<sup>†</sup> A. M. Poskanzer, R. G. Korteling,<sup>‡</sup> and G. W. Butler<sup>§</sup>

$\Delta E$ -E and time-of-flight techniques were used to observe the products of the interaction of 4.8-GeV protons with a uranium target. Two new isotopes,  $^{14}\text{Be}$  and  $^{17}\text{B}$ , were observed to be particle stable and the existence of  $^{18}\text{C}$  was confirmed. Two other isotopes,  $^{12}\text{Li}$  and  $^{16}\text{B}$  were shown to be particle unstable. The new isotope  $^{17}\text{B}$  recently had been predicted to be particle stable, but the observation of  $^{14}\text{Be}$  was doubly surprising because it was thought to be unstable on the basis of both theoretical predictions and previous experimental results.

A few years ago it was believed that all the particle-stable isotopes of the elements up

through boron had been discovered. It was predicted<sup>1</sup> that  $^{14}\text{Be}$  was unbound by 2.4 MeV and  $^{17}\text{B}$  by 4.0 MeV. In addition there was an experiment showing the particle instability of  $^{14}\text{Be}$ .<sup>2</sup> This result was from a heavy ion transfer experiment in which the yield was more than a factor of 10 lower than that expected from systematics. A year ago, Thibault and Klapisch<sup>3</sup> recalculated the masses and predicted  $^{17}\text{B}$  bound by 0.6 MeV and  $^{14}\text{Be}$  unbound by 1.5 MeV. The present experiment was stimulated by this recalculation that predicted  $^{17}\text{B}$  to be the lightest undiscovered isotope.

The method of production was the interaction

of high energy protons with a uranium target, an approach which had been quite fruitful in the past. A uranium target  $28 \text{ mg/cm}^2$  thick was placed in the 4.8-GeV external proton beam of the Bevatron. Fragments were identified in a  $\Delta E$ -E telescope in which the two detectors were separated by 25 cm. The time-of-flight of the fragments between the two detectors was recorded together with the  $\Delta E$  and E values. The time-of-flight and the E signals were used to identify the mass number of the fragments, and the  $\Delta E$ -E information was used to distinguish the elements. The telescope of silicon detectors was at  $90^\circ$  to the beam and consisted of a  $25 \text{ }\mu\text{m}$   $\Delta E$  detector and a  $67\text{-}\mu\text{m}$  E detector, both collimated to  $4 \times 6 \text{ mm}$ . The E detector was at a distance of 42 cm from the target with a veto detector immediately behind it to reject particles which did not stop in the E detector. All the detectors were cooled to  $-23^\circ\text{C}$ . Most of the electronics including the preamplifiers had been used in a previous experiment and have already been described.<sup>4</sup> The timing resolution (FWHM) in the present experiment for  $^{11}\text{B}$  fragments which deposited 20 MeV in the E counter was 290 ps, giving a mass resolution at mass 11 of 4.4%.

A problem encountered in the previous experiment<sup>4</sup> was the background from accidental coincidences which obscured the interesting regions of possible new isotopes. Thus, for the present experiment pulse width discrimination was introduced to eliminate spurious events caused by two pulses occurring within a time shorter than could be distinguished by a pile-up rejector. The time between the leading edge and cross-over of each signal was measured with a resolution (FWHM) of 130 ps for the  $\Delta E$  detector and 70 ps for the E detector. Signals proportional to the pulse widths were also recorded for each event. They were corrected for walk with pulse height in the off-line data analysis and then windows at  $1/4$  the peak height were set on these signals, which reduced the background a factor of 80. Also introduced in the present experiment were a new method for analyzing time-of-flight data and a new algorithm for particle identification.

In a data taking period of three weeks at an average beam intensity of  $6 \times 10^{11}$  protons per pulse (10 pulses per minute), 12 million events of the elements Li through N were recorded. Stability over this long data collection period was achieved by having two separate pulsers feed tagged simulated events to the preamplifiers which allowed two point stabilization of the data. Events were selected which had E signals between 10 and 60 MeV, time-of-flight signals between 10.6 and 27 ns, and met the above requirements of the pulse width discriminators. The wide energy window was achieved by correcting the E signals for the

dead layer on the E counter, and by correcting the time-of-flight signals for walk with both E and  $\Delta E$ . The E and time-of-flight signals were then used to calculate the mass number (A) of each fragment. The  $\Delta E$ -E signals were used to calculate a particle identification signal and then the calculated mass number was used to remove the mass dependence in order to calculate the atomic number (Z). Thus, a two parameter display of yield versus Z and A was obtained in which each isotope appeared as a mountain peak as shown in Fig. 1. It was observed that there was a small amount of tailing of the yield to low Z. This was evaluated at masses 10 and 13 where  $^{10}\text{Li}$  and  $^{13}\text{Be}$  were known not to exist. Thus, by knowing the form of this tailing and normalizing it at the point one half Z higher, this small effect could be subtracted out when taking mass yield cuts at constant Z. These final graphs<sup>5</sup> are shown in Fig. 2 for the elements Li, Be, and B.

Figure 2 clearly shows all the known particle stable isotopes of Li, Be, and B, and in addition, two new isotopes,  $^{14}\text{Be}$  and  $^{17}\text{B}$ . In Fig. 1 these isotopes appeared as peaks. There are 150  $^{14}\text{Be}$  events and 50  $^{17}\text{B}$  events. Nuclei known to be particle-unstable ( $^8\text{Be}$ ,  $^9\text{B}$ ,  $^{10}\text{Li}$ , and  $^{13}\text{Be}$ ) are missing in Fig. 2, and in addition it is clear from the figure that  $^{12}\text{Li}$  and  $^{16}\text{B}$  are particle-unstable. The case of  $^{13}\text{Li}$  is less clear. Although there are 1400  $^{11}\text{Li}$  events and no  $^{13}\text{Li}$  events, one cannot conclude that  $^{13}\text{Li}$  is particle-unstable because of the expected low yield. Approximate production cross sections were determined for

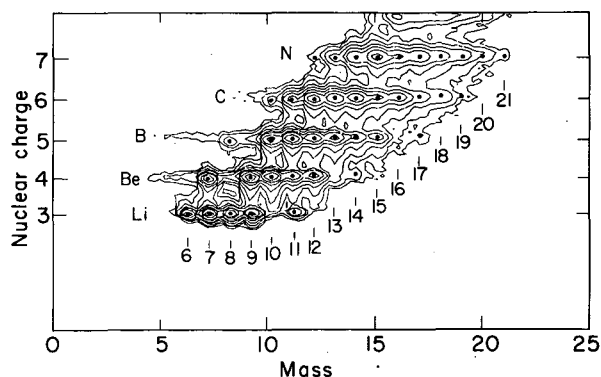


Fig. 1. Contour plot of nuclear charge (Z) vs mass number (A). The solid points indicate the positions of the peaks. For the weak peaks, the position of the points are based on extrapolations from the clearly resolved peaks. The lowest contour is at the three-count level, and there are two logarithmically-spaced contour levels per decade (XBL 738-3925)

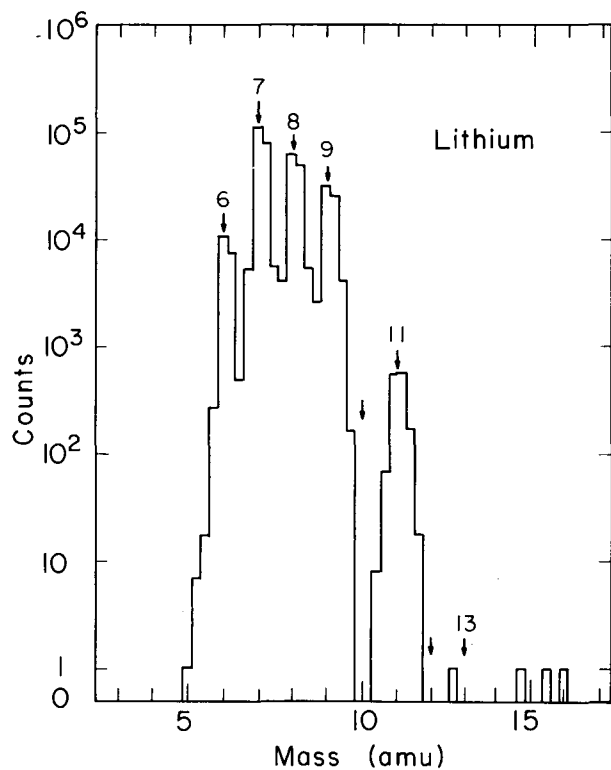
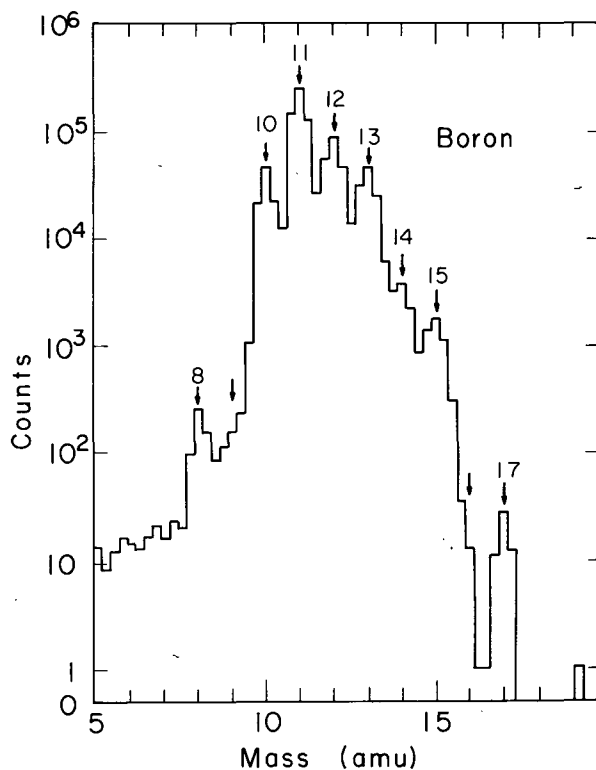
**a****c**

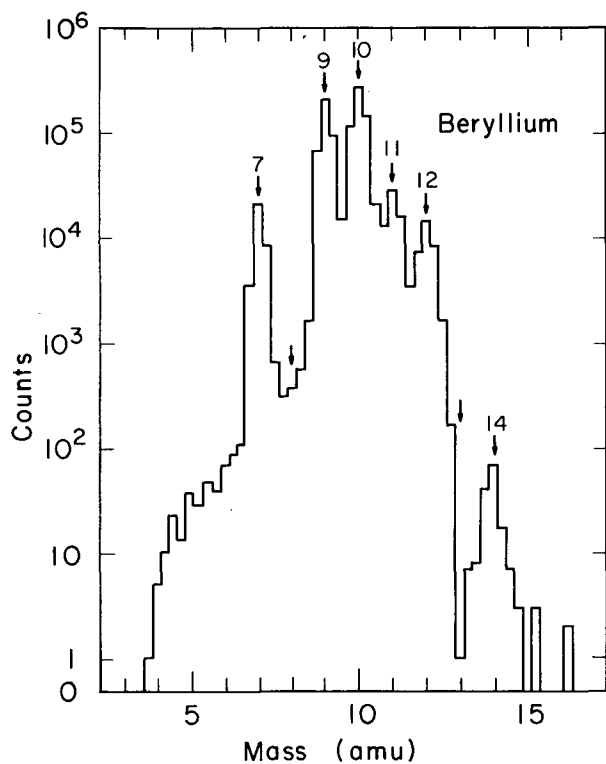
Fig. 2. Mass number distributions selected on the atomic numbers of Li, Be, and B. Arrows for the new and missing isotopes point to the expected positions of the peaks based on the positions of the main isotopes.

(XBL 738-3918)

(XBL 738-3917)

(XBL 738-3916)

$^{14}\text{Be}$ ,  $^{17}\text{B}$ ,  $^{18}\text{C}$ , and  $^{19}\text{C}$ , and upper limits estimated for  $^{13}\text{Li}$ ,  $^{19}\text{B}$ ,  $^{20}\text{C}$ , and  $^{22}\text{N}$ .

**b**

After the appearance of the clear peak for  $^{14}\text{Be}$  in Fig. 2, it was realized that the very recent measurement<sup>6</sup> of the mass of  $^{14}\text{B}$  drastically affects the prediction for  $^{14}\text{Be}$ . Thibault and Klapisch had assumed  $^{14}\text{B}$  to be just bound, but Ball, Costa, Davies, Forster, Hardy, and McDonald<sup>6</sup> found it to be bound by 1.0 MeV. Using this mass and the Garvey-Kelson transverse relation<sup>1</sup> one now happily predicts that  $^{14}\text{Be}$  is bound by 0.4 MeV. The discrepancy with the heavy ion transfer experiment<sup>2</sup> must have been due to the long linear extrapolation used for the systematics in that study.

#### Footnotes and References

\*Condensed from Phys. Rev. Letters 9, 614 (1973) and Phys. Rev. C 9, (March 1974).



† Present address: Los Alamos Scientific Laboratory, Los Alamos, N.M.

‡ Permanent address: Simon Fraser University, Burnaby, B.C., Canada.

§ Permanent address: Los Alamos Scientific Laboratory, Los Alamos, N.M.

1. G. T. Garvey and I. Kelson, Phys. Rev. Letters 16, 197 (1966).

2. A. G. Artukh, V. V. Avdeichikov, J. Ero, G. F. Gridnev, V. L. Mikheev, V. V. Volkov, and J. Wilczynski, Phys. Letters 33B, 407 (1970).

3. C. Thibault and R. Klapisch, Phys. Rev. C6, 1509 (1972).

4. G. W. Butler, A. M. Poskanzer, and D. A. Landis, Nucl. Instr. Methods 89, 189 (1970).

5. The small tailing to low masses which can be seen in the figure for Be and B results from a dead time in the veto detector circuitry.

6. G. C. Ball, G. J. Costa, W. G. Davies, J. S. Forster, J. C. Hardy, and A. B. McDonald, Phys. Rev. Letters 31, 395 (1973).

### FRAGMENTS FROM URANIUM IRRADIATED BY 2.1-GeV/NUCLEON DEUTERONS AND ALPHA PARTICLES

A. M. Poskanzer, J. D. Bowman,\* and A. M. Zebelman

We are planning to study fragment production from uranium by the relativistic heavy ions of the Bevalac. By comparing the results with those for incident protons,<sup>1</sup> we expect to learn if the heavy ions deposit more energy in the target nucleus or induce collective effects not seen with incident protons. We have begun initial studies using the deuteron and alpha particle beams presently available. So far we have used a telescope consisting of a 50- $\mu\text{m}$   $\Delta E$  counter and a 380- $\mu\text{m}$  E counter.

Energy spectra for He, Li, and Be isotopes at 90° to the beam were obtained. The data for incident alpha particles are shown in Fig. 1. Because of a lack of accurate beam monitors at present, the data have been normalized so that the  $^4\text{He}$  spectrum has the same peak cross section as for incident protons.<sup>1</sup> The ratios of the energy spectra for incident deuterons and alpha particles compared to incident protons are shown in Fig. 2. It is evident that the shapes of the energy spectra with incident deuterons are almost the same as for incident protons, while the spectra for incident alpha particles exhibit interesting differences. From the ratios one can see that there is a broadening of the energy spectra with incident alphas, with both a shift to lower energies and a flattening of the high energy tails. The flatter tails imply higher temperatures and therefore higher deposition energies with the incident alphas.

Brief measurements were also made at

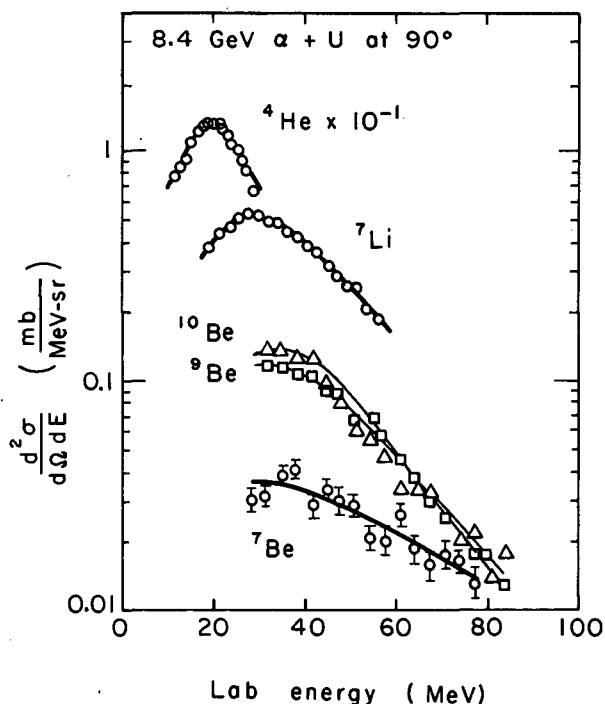


Fig. 1. Laboratory energy spectra at 90° to the beam from the irradiation of uranium with 8.4 GeV alpha particles.

(XBL-741-2028)

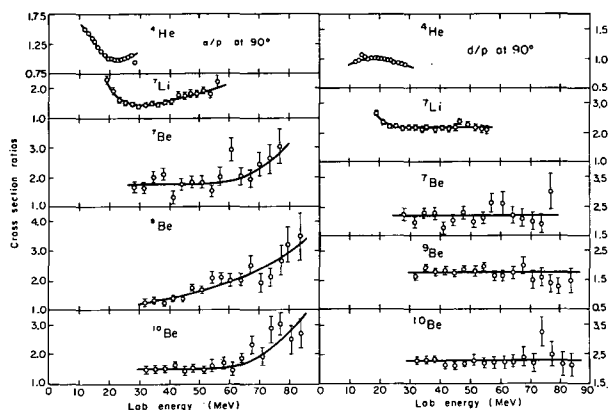


Fig. 2. Ratios of the energy spectra at 90° to those for incident protons. On the right are the ratios for incident deuterons/protons and on the left, incident alphas/protons.

(XBL-741-2029)

Table I. Most probable fragment energies (MeV)

Frag- Projec- ment tile	Lab Angle			Shift 25° - 155°	
	25°	90°	155°		
<sup>4</sup> He	P	21.0	20.55	19.4	1.6
	α	20.1	19.5	18.8	1.3
<sup>7</sup> Li	P	32.9	30.7	26.5	6.4
	α	34	29.8	26	8

25° and 155° to the beam. Table I gives the most probable fragment energies at all three angles. It is seen that the forward-backward energy shifts are not significantly greater with incident alphas than with incident protons. This implies that the forward momentum transfer is not appreciably greater with incident alphas. Table II gives the forward-backward intensity ratios, obtained by integrating the energy spectra with extrapolations to both higher and lower

Table II.  $d\sigma/d\Omega(25^\circ)/d\sigma/d\Omega(155^\circ)$ .

Projectile	Fragment	
	<sup>4</sup> He	<sup>7</sup> Li
P	1.3	1.6
α	2.5	4.4

energies. It is seen that with incident alphas the angular distributions are considerably more forward peaked. This, combined with the lack of shift of the energies, implies a most direct process in the case of the incident alphas.

These conclusions are all tentative. It is planned to extend the data to both lower and higher fragment energies, and to study heavier emitted fragments.

#### Footnotes and References

\* Present address: Los Alamos Scientific Laboratory, Los Alamos, New Mexico.

1. A. M. Poskanzer, G. W. Butler, and E. K. Hyde, Phys. Rev. C3, 882 (1971).

### ON-LINE MASS-SPECTROMETRIC MASS MEASUREMENTS OF NEUTRON RICH ISOTOPES OF Li, Na, and K\*

R. Klapisch, C. Thibault, C. Rigaud, A. M. Poskanzer  
L. Lessard, W. Reisdorf

Fragmentation of heavy nuclei by high energy protons can be used to produce neutron rich isotopes of the light elements. In the case of the alkali elements, Li, Na, K, detailed information is obtained when a special mass spectrometer is used on-line in an extracted beam of the CERN proton synchrotron. Energetic recoils that result from the interaction of intense ( $1.5 \cdot 10^{12}$ ) proton bursts with a 2 g/cm<sup>2</sup> U target are captured in heated graphite foils from which alkali elements diffuse very quickly to be ionized on a hot rhenium

surface. The ions are accelerated (10 kV, DC) and mass analyzed by a single stage magnetic prism. After the exit slit, they are refocused by electrostatic quadrupole lenses, through a thick shielding wall, onto an electron multiplier thus capable of counting single ions despite the intense background environment of the accelerator.

The mass of a short-lived Na isotope can be measured by comparing the acceleration potential necessary to get exactly the same

deflection in a fixed magnetic field as for a sodium isotope of known mass. This was shown to give accuracies better than  $10^{-5}$  for  $^{27-30}\text{Na}$  despite the low resolving power (500 FWHM) of the instrument.

In a more recent experiment this technique has been further improved. Better ground conditions allowed the study of decay properties and mass measurements of still rarer isotopes. The accuracy has been improved by a better resolving power (1000 FWHM) and by the continuous monitoring of systematic errors through a comparison of the unknown mass to two known ones instead of one.

As a result the mass excess of  $^{11}\text{Li}$  is determined to be  $40.94 \pm 0.08$  MeV making it bound by only  $170 \pm 80$  keV. Preliminary values are  $10.6 \pm 0.8$  MeV for  $^{31}\text{Na}$  and  $16.4 \pm 1.1$  MeV for  $^{32}\text{Na}$ . It is expected that the final analysis will show some improvement in the uncertainties. The masses of  $^{27-30}\text{Na}$  were remeasured and will now be known with an accuracy of 100 to 200 keV. The masses of  $^{48-49}\text{K}$  have also been measured.

## HIGH ENERGY ELASTIC SCATTERING BY RECOIL DETECTION

A. M. Poskanzer, A. M. Zebelman, and V. Viola

A test of the feasibility of studying proton-nucleus elastic scattering at GeV energies by detecting only the recoil nucleus was made. In the usual experiment the scattered proton is accurately measured and a highly analyzed incident beam is used. However, if one measures the laboratory kinetic energy,  $E$ , of the recoil nucleus, one may obtain directly the square of the momentum transfer,  $|t|$ , by  $|t| = 2 A m_0 E$ . Thus, instead of measuring the 5-GeV proton scattered at a few degrees to the beam, the idea is to try to measure the recoil nucleus having a typical energy of the order of 10 MeV and a lab angle of about  $86^\circ$ . Kinematic calculations show that at this angle one is insensitive to the energy resolution of the beam. At the same time, in inelastic scattering to an excited state, the kinetic energy of the recoil is decreased by about the excitation energy of this excited state.

In general, the separation of a ground state from a first excited state requires an energy resolution of the order of 1 MeV. This should be easier to obtain for the low energy recoil than for the scattered proton, except

A comparison of the results with different mass predictions shows that the Garvey-Kelson mass relations give the best overall fit but that there are significant and interesting differences. It is shown, for instance, that the odd-even effect in binding energies is less pronounced than predicted.

### Footnote and References

\* With the exception of the support of one of the authors (A. M. P.) by LBL, this work was mainly supported by the Laboratoire Rene Bernas du Centre de Spectrometrie de Masse, 91406 Orsay, France.

1. R. Klapisch, C. Thibault, A. M. Poskanzer, R. Prieels, C. Rigaud, and E. Roeckl, *Phys. Rev. Letters* **29**, 1254 (1972), and references therein.
2. R. Klapisch, R. Prieels, C. Thibault, A. M. Poskanzer, C. Rigaud, and E. Roeckl, *Phys. Rev. Letters* **31**, 118 (1973).

that the kinematic shift of the recoil particle is quite large (3-10 MeV/deg), thus demanding that high angular resolution be attained. However, not only does one need a detector with high angular resolution, but of equal importance are problems of finite target size, multiple scattering in the target and in the detector, and the emittance of the proton beam itself. The detection system was a telescope of silicon semiconductor detectors consisting of a transmission  $\Delta E$  detector and a position-sensitive E detector. In this manner we were able to identify the recoil nucleus, measure its kinetic energy, and achieve good angular resolution. An experiment using recoil detection was recently done for 400-GeV proton-proton elastic scattering,<sup>1</sup> but without particle identification or the use of a position sensitive detector.

Two test experiments were carried out: proton-proton elastic scattering and proton- $^7\text{Li}$  elastic scattering. These experiments were done with the Bevatron 4.8-GeV proton beam focused to a profile 12 mm wide by 25 mm high. The proton-proton experiment was

done with a  $0.9 \text{ mg/cm}^2$  thick Mylar target, 1 mm wide and about 40 mm in height. The target for the proton- $^7\text{Li}$  experiment was made by evaporating  $0.4 \text{ mg/cm}^2$  of natural Li onto the Mylar. The  $\Delta E$  detectors were  $65 \mu\text{m}$  and  $22 \mu\text{m}$  thick for the proton-proton and proton- $^7\text{Li}$  experiments, respectively. The same position-sensitive detector,  $400 \mu\text{m}$  thick, was used for both experiments. A  $0.5 \text{ mm}$  thick rectangular Cu collimator  $4 \text{ mm}$  wide and  $6 \text{ mm}$  high was placed between the  $\Delta E$  and E detectors. The telescope was  $400 \text{ mm}$  from the target in the proton-proton experiment and thus subtended an angle of  $0.5^\circ$ ; in the proton- $^7\text{Li}$  experiment the telescope was  $200 \text{ mm}$  from the target and subtended  $1.0^\circ$ . The data were stored and processed by a computer system which displayed the particle identifier spectrum, the position spectrum, and energy spectra sorted on particle identity and position.

The peaks in the energy spectra were about twice the background. The centroids of the peaks for the proton-proton and the proton- $^7\text{Li}$  experiments are plotted versus the laboratory angle in Figs. 1 and 2, respectively. The smooth curves shown are those calculated for elastic scattering; the agreement confirms that the energies of the peaks shift with angle as expected for elastic scattering. The average FWHM of the peaks in the proton-proton case was  $1.2 \text{ MeV}$  but in the proton- $^7\text{Li}$  case was  $4 \text{ MeV}$ . This poor value for  $^7\text{Li}$  means that

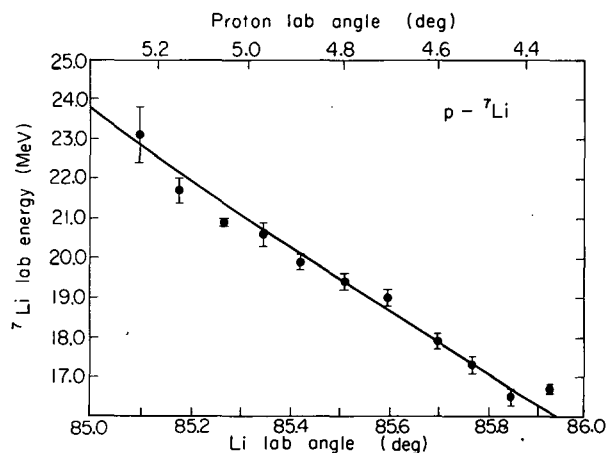


Fig. 1. Graph of the energies for the centroids of the peaks observed in the recoil proton energy spectrum versus the recoil proton lab angle. The smooth curve shows the dependence of lab energy on lab angle calculated from two body kinematics. The curve was normalized to the data by shifting it a few tenths of a degree, well within the uncertainties of alignment. (XBL-741-2103b)

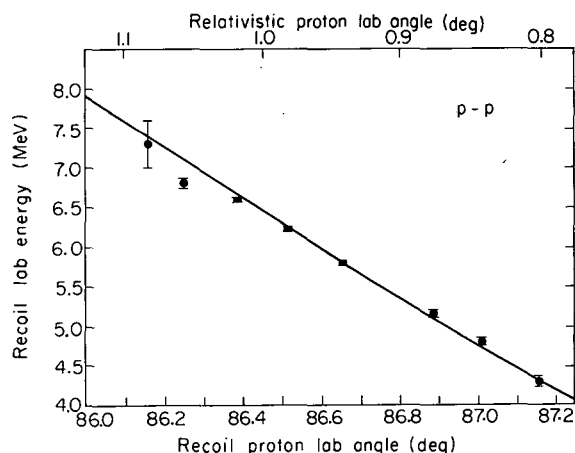


Fig. 2. Same as Fig. 1 for proton- $^7\text{Li}$  scattering. (XBL-741-2103a)

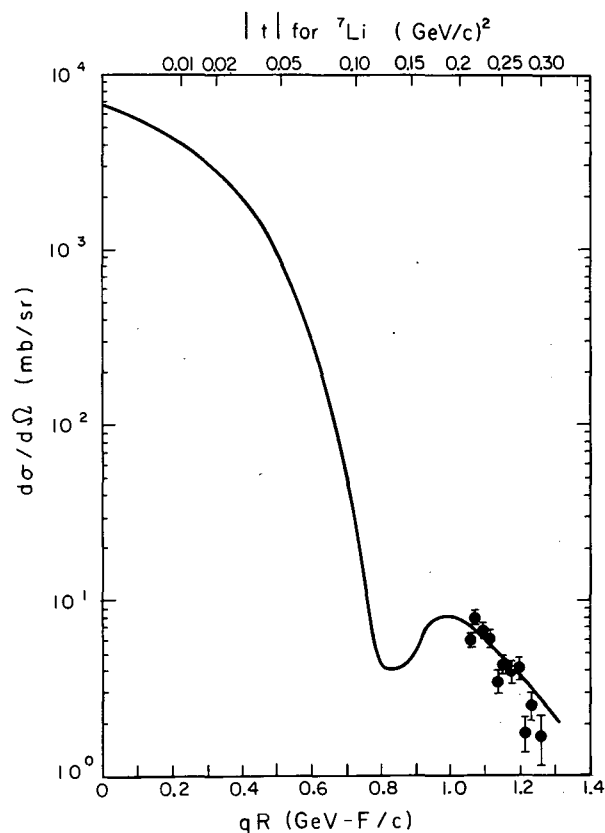


Fig. 3. Comparison of the data in Ref. 1 on proton- $^{12}\text{C}$  elastic scattering at  $1 \text{ GeV}$  and the  $^7\text{Li}$  data collected in the present work. The  $^7\text{Li}$  data have been approximately normalized to the smooth curve. The abscissa at the top gives the range of  $|t|$  covered by the data. (XBL-741-2102)

we did not separate the first excited state at 0.4 MeV from the ground state. For the proton case, we believe that multiple scattering in the target was the main contributor to the resolution. For the  ${}^7\text{Li}$  case, we calculated a contribution of 1.5 MeV each from multiple scattering in the target, the width of the target, and the convergence of the beam. However, this still does not fully account for the 4 MeV resolution observed.

In Fig. 3, the areas of the peaks are plotted on a qR graph showing the 1-GeV proton- ${}^{12}\text{C}$  elastic data,<sup>2</sup> in order to illustrate the region of the differential cross section curve covered in this one measurement. In summary, we have detected the recoils from high energy proton-proton and proton-nucleus

scattering, but problems remain with the energy resolution, counting rate, and range of momentum transfers easily studied.

### References

1. V. Bartenev, R. A. Carrigan, Jr., I-Hung Chiang, R. L. Cool, K. Goulianos, D. Gross, A. Kuznetsov, E. Malanud, A. C. Melissinos, B. Morozov, V. Nikitin, S. L. Olsen, Y. Pilipenko, V. Popov, R. Yamada, and L. Zolin, *Phys. Rev. Letters* **31**, 1367 (1973).
2. H. Palevsky, J. L. Friedes, R. J. Sutter, G. W. Bennett, G. J. Igo, W. D. Simpson, G. C. Phillips, D. M. Corley, N. S. Wall, R. L. Stearns, and B. Gottschalk, *Phys. Rev. Letters* **18**, 1200 (1967).

## FREE-PARTICLE COLLISIONS IN PROTON AND PION-INDUCED NUCLEAR REACTIONS

N. P. Jacob, Jr. and S. S. Markowitz

At high energies ( $\geq 0.1$  GeV), simple "knockout" reactions of the form  $(a, aN)$ , where  $a$  is the incident projectile and  $N$  is a nucleon, are feasible tools for investigating free-particle type collisions in nuclear matter.<sup>1</sup> Since the predominant mechanism for such reactions involves a "quasi-free" initial collision between projectile and a target nucleon, and the unhindered escape of both collision partners, it is anticipated that changes in cross sections for these reactions would reflect similar changes in free-particle cross sections.

The most recent studies<sup>2-3</sup> for  $(p, 2p)$  reactions exhibit such an effect. The excitation functions for the  ${}^{25}\text{Mg}(p, 2p){}^{24}\text{Na}^2$  and the  ${}^{142}\text{Ce}(p, 2p){}^{141}\text{La}^3$  reactions rise by factors of  $1.19 \pm 0.05$  and  $1.47 \pm 0.13$  respectively, between 0.4 GeV and 1.0 GeV, and slowly decreases above 1.0 GeV. This can be correlated to a marked factor of 2 rise in total free pp scattering<sup>4, 5</sup> between the same energies. These results, while demonstrating evidence for free-particle collisions in  $(p, 2p)$  reactions, are inconsistent with the idea that the free-particle ratio of  $2.0 \pm 0.1$  would be more greatly reduced in reactions on heavy nuclei than light nuclei, due to greater attenuation factors for particle scattering. It was thus the goal of the initial phase of this research to obtain precise  $(p, 2p)$  excitation functions on some medium mass nuclei, separated appreciably in mass so as to examine the effect of increasing nuclear size and thus attenuation on free-particle effects. The target

nuclei chosen,  ${}^{48}\text{Ti}$  and  ${}^{74}\text{Ge}$ , not only met these qualifications, but were considered still light enough to expect that free-particle collisions would be preserved and not washed out by nuclear matter.

All cross sections in this work were determined by standard foil irradiations in the

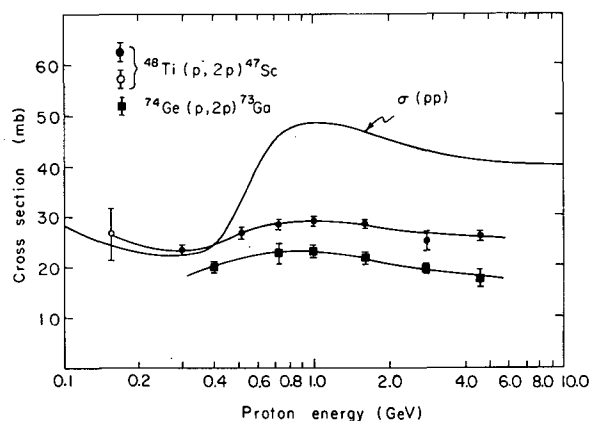


Fig. 1. Excitation functions for the  ${}^{48}\text{Ti}(p, 2p){}^{47}\text{Sc}$ ,  ${}^{74}\text{Ge}(p, 2p){}^{73}\text{Ga}$  and free pp reactions. The solid circles and squares are from this work. The point at 155 MeV is taken from Ref. 7. Free particle pp cross sections are taken from Ref. 4 below 0.5 GeV and from Ref. 5 above 0.5 GeV. (XBL-7312-7000)

internal proton beams of the LBL 184-inch synchrocyclotron or the Bevatron, and subsequent analysis by gamma counting. The excitation functions for the  $^{48}\text{Ti}(p, 2p)^{47}\text{Sc}$  and the  $^{74}\text{Ge}(p, 2p)^{73}\text{Ga}$  reactions are shown in Fig. 1. As seen, pp scattering is not washed out in these medium mass nuclei. For each (p, 2p) excitation function a slight but significant rise occurs between 0.3 GeV and 1.0 GeV. This rise is much less than the rise in the free-particle excitation function due to effects of the struck proton momentum and attenuation of the incoming and outgoing particles by the nuclear matter.

The results of this and previously published work are summarized in Table I.

Table I. Ratio of cross sections at 1.0 GeV to that at 0.4 GeV.

Reaction	$\sigma_{1.0}/\sigma_{0.4}$
free pp	$1.98 \pm 0.08$
$^{25}\text{Mg}(p, 2p)^{24}\text{Na}$	$1.19 \pm 0.05^a$
$^{48}\text{Ti}(p, 2p)^{47}\text{Sc}$	$1.17 \pm 0.04$
$^{74}\text{Ge}(p, 2p)^{73}\text{Ga}$	$1.16 \pm 0.05$
$^{142}\text{Ce}(p, 2p)^{141}\text{La}$	$1.47 \pm 0.13^b$

<sup>a</sup>Ref. 2.

<sup>b</sup>Ref. 3.

Apparently, attenuation factors do not obliterate free-particle effects even with increasing

mass number of the target. Furthermore, it appears from the data that the reduction in the free pp scattering ratio is about constant regardless of nuclear size.

The second phase of this research has begun the study of ( $\pi, \pi n$ ) reactions on light nuclei. The pioneering work of Reeder and Markowitz<sup>6</sup> demonstrates evidence for (3, 3) pion-nucleon resonance scattering in the  $^{12}\text{C}(\pi^-, \pi^-n)^{11}\text{C}$  reaction. While results are still preliminary, work on the  $^{19}\text{F}(\pi^-, \pi^-n)^{18}\text{F}$  also shows similar structure in its excitation function at 200 MeV, but to a lesser extent. Future experiments will use  $^{14}\text{N}$  and  $^{16}\text{O}$  as target systems.

#### References

1. J. R. Grover and A. A. Caretto, Jr., *Ann. Rev. Nucl. Sci.* 14, 51 (1964).
2. P. L. Reeder, *Phys. Rev.* 1795 (1969).
3. S. Meloni and J. B. Cumming, *Phys. Rev.* 136, B1359 (1964).
4. V. S. Barashenkov and V. M. Maltsev, *Fortschr. Physik* 9, 549 (1961).
5. D. V. Bugg, D. C. Salter, G. H. Stafford, R. F. George, K. F. Riley, and R. J. Tapper, *Phys. Rev.* 146, 980 (1966).
6. P. L. Reeder and S. S. Markowitz, *Phys. Rev.* 133, B639 (1964).
7. J. P. Cohen, G. Albuoy, and N. Poffe, *J. Phys. (Paris)* 26, 427 (1965).

## THE NUCLEAR DROPLET MODEL FOR ARBITRARY SHAPES

W. D. Myers and W. J. Swiatecki

### Introduction

The Droplet Model was introduced in Ref. 1 as a refinement of the Liquid Drop Model of average nuclear properties. It is a model which takes into account effects associated with the deviations of neutron and proton densities from constant bulk values, and the deviations of the effective boundaries of the neutron and proton distributions from a common surface. The theory developed in Ref. 1 was specialized from the outset to spherical shapes. The purpose of the work presented here was to derive the equations of the Droplet Model in their full generality, for arbitrary shapes.

In Refs. 1-4 the background and motivation for the Droplet Model have already been discussed. We will not repeat that material here except to stress once again that the Droplet Model deals only with smooth, average nuclear properties and shell effects are outside the scope of the model.

The degrees of freedom of the model must first be defined, together with the constraints arising from the conservation of neutrons and protons. Then the potential energy of the Droplet Model may be written as a function of the degrees of freedom (in terms of Taylor expansions about the Liquid Drop Model configuration as starting point). If this energy is minimized with respect to all degrees of freedom except the geometrical shape of the system then a Droplet Model mass formula results that is a function of the neutron and proton numbers and the shape.

### Degrees of Freedom

In general two functions of position  $\rho_N(\mathbf{r})$  and  $\rho_Z(\mathbf{r})$ , whose spatial integrals are  $N$  and  $Z$ , can specify the time-averaged distribution of  $N$  neutrons and  $Z$  protons in a nucleus. In the idealized case of distributions with sharp surfaces, i. e. such that  $\rho_N$  and  $\rho_Z$  are almost constant within two surfaces  $\Sigma_N$  and  $\Sigma_Z$  and zero outside, the shapes of the surfaces  $\Sigma_N$  and  $\Sigma_Z$  and the functions  $\rho_N$  and  $\rho_Z$  together constitute the degrees of freedom describing the configuration of the system. Under certain assumptions this remains true for leptodermous systems in which the density distributions are no longer sharp, but the degree of diffuseness is small, so that the densities fall from their bulk values to zero in a thin region around the surfaces  $\Sigma_N, \Sigma_Z$  (thin compared to the dimensions of the system). Such thin-skinned density

distributions may be thought of as derived from the sharp generating density distributions by a normal shift of neutrons (or protons) from layers just inside the surface  $\Sigma_N$  (or  $\Sigma_Z$ ) to layers just outside, according to some diffuseness prescription.

The Droplet Model of saturating, leptodermous, two-component systems (such as nuclei) results from making expansions of properties of interest (such as the energy) in powers of three small quantities (functions of position). These are as follows: the small deviations of the two generating densities  $\rho_N$  and  $\rho_Z$  from the corresponding standard nuclear matter values, and the small (variable) separation between the effective sharp surfaces  $\Sigma_N$  and  $\Sigma_Z$ .

By following the procedures outlined in Ref. 5, the original degrees of freedom  $\Sigma_N, \Sigma_Z, \rho_N, \rho_Z$  may be transformed to the set

- $\Sigma$ , the mean shape of the system,
- $\bar{\epsilon}$ , a scale factor,
- $\tilde{\epsilon}$ , the density nonuniformity function,
- $\bar{\delta}$ , the average relative neutron excess in the bulk,
- $\tilde{\delta}$ , the neutron excess nonuniformity function,
- $\tilde{\tau}$ , the neutron skin nonuniformity function.

These are related, of course, by the constraints of particle number conservation.

### The Energy

In the Droplet Model, as in the Liquid Drop Model, there are three components in the energy: a volume energy  $E_V$ , a surface energy  $E_S$  and a Coulomb energy  $E_C$ . The volume energy is assumed to be an integral over the volume inside  $\Sigma$  of an energy density which is a function of the generating densities  $\rho_N$  and  $\rho_Z$  (or equivalently of  $\epsilon$  and  $\delta$ ). The surface energy is assumed to be an integral over the surface  $\Sigma$  of a surface energy density  $\gamma$  which is a function of the conditions prevailing in the immediate neighborhood of the relevant point on the surface. The possibility of splitting up the main part of the nuclear energy into a volume and a surface term has its roots in the approximately leptodermous nature of most nuclei, as a result of which the major modifications of the energy caused by

the presence of the surface can be localized to a relatively thin surface region. The limitations imposed by shell effects have been illustrated in Ref. 3. Methods to supplement a leptodermous treatment of nuclei by incorporation of shell effects are reviewed in Refs. 6-8, and are a subject of continued study.

For the present we assume the validity of the leptodermous approach and write the total energy, including Coulomb energy as

$$\begin{aligned}
 E(N, Z; \Sigma, \bar{\epsilon}, \tilde{\epsilon}, \bar{\delta}, \tilde{\delta}, \tilde{\tau}) \\
 = \left[ -a_1 + J\bar{\delta}^2 + \frac{1}{2}K\bar{\epsilon}^2 - L\bar{\epsilon}\bar{\delta}^2 + \frac{1}{2}M\bar{\delta}^4 \right] A \\
 + \rho_0 \int_V (J\tilde{\delta}^2 + \frac{1}{2}K\tilde{\epsilon}^2) + A^{2/3} a_2 B_s (1 + 2\bar{\epsilon}) \\
 + \frac{1}{3} \rho_0 r_0 \int_S (F\bar{\epsilon} + H\tau^2 + 2P\tau\bar{\delta} - G\bar{\delta}^2) + A^{1/3} a_3 B_k \\
 + c_1 \frac{Z^2}{A^{1/3}} B_c (1 - \bar{\epsilon}) \\
 - \frac{1}{2} e \rho_0 \int_V (3\tilde{\epsilon} + \tilde{\delta}) v - \frac{1}{4} e \rho_0 r_0 \int_S \tau \tilde{v} \\
 - c_3 \frac{Z^2}{A} - (c_4/2^{1/3}) Z.
 \end{aligned}$$

where the notation is explained in detail in Ref. 5.

After minimization with respect to  $\bar{\delta}$ ,  $\tilde{\delta}$ ,  $\bar{\epsilon}$ ,  $\tilde{\epsilon}$  and  $\tau$  the Droplet Model energy formula may be written in the form:

$$\begin{aligned}
 E(N, Z; \text{shape}) = \left[ -a_1 + J\bar{\delta}^2 - \frac{1}{2}K\bar{\epsilon}^2 + \frac{1}{2}M\bar{\delta}^4 \right] A \\
 + \left[ a_2 + \frac{9}{4}(J^2/Q)\bar{\delta}^2 \right] A^{2/3} B_s + a_3 A^{1/3} B_k \\
 + c_1 Z^2 A^{-1/3} B_c - c_2 Z^2 A^{1/3} B_r - c_5 Z^2 B_w - c_3 Z^2 A^{-1} \\
 - (c_4/2^{1/3}) Z,
 \end{aligned}$$

where

$$\begin{aligned}
 \bar{\delta} &= \left[ 1 + \frac{3}{16} (c_1/Q) Z A^{-2/3} B_v \right] / \left[ 1 + \frac{9}{4} (J/Q) A^{-1/3} B_s \right] \\
 \bar{\epsilon} &= \left[ -2a_2 A^{-1/3} B_s + L\bar{\delta}^2 + c_1 Z^2 A^{-4/3} B_c \right] / K.
 \end{aligned}$$

The quantities  $B_i$  being the shape dependences. These are discussed in detail in Refs. 5 and 9.

A preliminary, but illustrative, set of values for the parameters entering the theory is,

$$a_1 = 15.986 \text{ MeV,}$$

$$a_2 = 20.76 \text{ MeV,}$$

$$a_3 = 0 \text{ MeV,}$$

$$J = 36.5 \text{ MeV,}$$

$$Q = 17 \text{ MeV,}$$

$$K = 240 \text{ MeV,}$$

$$L = 100 \text{ MeV,}$$

$$M = 0 \text{ MeV,}$$

$$r_0 = 1.175 \text{ fm}$$

$$b = 0.99 \text{ fm}$$

Similar fits have been discussed previously in Refs. 10 and 11.

### Density Distributions

If, in addition to the energy, one is interested in displaying the equilibrium density distributions of the  $N$  neutrons and  $Z$  protons associated with the assumed shape  $\Sigma$ , one proceeds as follows. The shape  $\Sigma$  is first constructed with a volume determined by the mass number  $A$  and the equilibrium value of the scale parameter  $\bar{\epsilon}$ . The internal distributions of neutrons and protons can then be constructed with the aid of  $\epsilon$  and  $\delta$ . The separate surfaces  $\Sigma_N$  and  $\Sigma_Z$  are found with the aid of the function  $\tau$  and the final step is diffusing the surfaces. This could be achieved by folding in a short-range function into the generating densities, or simply by constructing an appropriate fall-off profile whose effective sharp surface coincides with  $\Sigma_N$  or  $\Sigma_Z$ , as the case may be. The surface width  $b$  of this profile should be about 0.99 fm, to agree with experiment.

### Footnote and References

\*Condensed from LBL-1957 (submitted to Ann. Phys.). See Ref. 5.

1. W. D. Myers and W. J. Swiatecki, Ann. Phys. **55**, 395 (1969).

2. W. D. Myers, Proceedings of the Third International Conference on Atomic Masses, Winnipeg, 1967.

3. C. F. Tsang, Ph.D. Thesis, Lawrence Radiation Laboratory Report UCRL-18899 (1969).

4. W. D. Myers, in "Dynamic Structure of Nuclear States," Proceedings of the 1971 Mont Tremblant International Summer School, University of Toronto Press (1972).

5. W. D. Myers and W. J. Swiatecki, Lawrence Berkeley Laboratory Report LBL-1957 (1973).



6. S.G. Nilsson, et al., Nucl. Phys. A131, 1 (1969).
7. J.R. Nix, Ann. Rev. Nucl. Sci. 22, 65 (1972).
8. M. Brack, et al., Rev. Mod. Phys. 44, 320 (1972).
9. R.W. Hasse, Ann. Phys. 68, 377 (1974).
10. S. Ludwig, et al., Nucl. Phys. A203, 627 (1973).
11. J.W. Truran, A.G.W. Cameron, and E. Hilf, Proceedings of the International Conference on the Properties of Nuclei Far from the Region of Beta-Stability, Leysin, Switzerland, August 1970.

## THE DYNAMICS OF CHARGED VISCOUS LIQUID DROPS

C. T. Alonso

In reactions involving very heavy nuclei, such macroscopic properties as viscosity and elasticity can influence the mechanism of the reaction, and there is some justification for examining the rheological behavior of nuclear matter. Furthermore, most collision-fusion reactions occur at high enough excitations that the dynamics lie more or less in the classical hydrodynamic regime. In this approximation, quantum mechanical effects can be applied to the classical bulk motion in a quasi-classical manner. For example, closed-shell effects can be represented by a variable elasticity that has relative maxima at the magic numbers.

The rheology of nuclear matter during compound nucleus formation is probably that of a viscous liquid and not that of an elastic solid. This can be inferred from a crude estimate of the relaxation time  $\lambda$  for nuclear stresses, assuming the nucleus to be a rheological Maxwell body.<sup>1</sup> This time is given by  $\lambda = \eta/\mu$ , where  $\eta$  is the nuclear viscosity and  $\mu$  is a nuclear modulus of rigidity. Estimating that  $\eta = 0.10 \text{ MeV dsec/fm}^3$  (where  $\text{dsec} = 10^{-22} \text{ sec}$ ), and  $\mu = 0.5 \text{ MeV/fm}^3$ , we find that  $\lambda = 0.20 \text{ dsec}$ . The physical interpretation of  $\lambda$  is that for reactions that take place during times  $\delta t \gg \lambda$ , the nucleus behaves like a viscous liquid. Even interpenetration reactions that take place at the speed of light would require about 0.10 dsec duration for heavy nuclei, so we conclude that if this estimate of  $\lambda$  is correct, colliding nuclei in heavy ion accelerator experiments should be described not as elastic solids but as viscous liquids.

Making the reasonable assumption that the nuclear fluid is incompressible (or more particularly that nuclear flow has a low Mach number; we estimate it to be around Mach 0.1 in accelerator collisions, so shock waves are not a problem) the four equations that apply are the equation of continuity

$$\bar{\nabla} \cdot \bar{U} = 0, \quad (1)$$

the Navier-Stokes equation

$$(\partial/\partial t + \bar{U} \cdot \bar{\nabla}) \bar{U} = \frac{-\nabla P}{\rho} + \frac{\bar{F}}{m} + \frac{\eta}{\rho} \nabla^2 \bar{U}, \quad (2)$$

and the quasi-static Maxwell equations

$$\bar{\nabla} \cdot \bar{E} = \rho_c / \epsilon_0 \quad (3)$$

$$\bar{\nabla} \times \bar{E} = 0. \quad (4)$$

Here  $\bar{U}$  represents the velocity field relative to a fixed Eulerian mesh,  $P$  is the fluid pressure,  $\rho$  is the mass density,  $\eta$  the viscosity,  $\bar{E}$  the electric field, and  $\rho_c$  the charge density. The general term  $\bar{F}/m$  contains all the external forces to be applied to the drop.

By integrating the above bulk equations over the free surface we obtain the boundary conditions at the free surface. Physically these reflect the property that liquids can support no shear stress and that the normal stress at the surface defines the opposing fluid pressure at the surface. It can be shown that the resultant stress on a free surface must vanish even though the surface is accelerating, for the surface has no inertia associated with it.<sup>2</sup> The appropriate boundary condition becomes

$$\bar{n} \cdot \bar{T}^{\text{out}} - \bar{T}^{\text{in}} = 0 \quad (5)$$

where  $\bar{n}$  is the normal to the surface and  $\bar{T}$  is a general tensor whose divergence equals the right side of the Navier-Stokes equation. For a general charged viscous liquid drop the tensor  $\bar{T}$  is composed of four separate tensors:

$$\bar{T}_{ab} = P_{ab} + S_{ab} + V_{ab} + M_{ab} \quad (6)$$

where

$$P_{ab} = -\delta_{ab} P \text{ (normal fluid pressure)} \quad (7)$$

$$S_{ab} = \delta_{ab} \gamma \left( \frac{1}{R_1} + \frac{1}{R_2} \right) \text{ (surface tension) (8)}$$

$$V_{ab} = \frac{\partial U_a}{\partial x_b} + \frac{\partial U_b}{\partial x_a} \text{ (viscous stress) (9)}$$

$$M_{ab} = \epsilon (E_a E_b - \frac{1}{2} \delta_{ab} E^2) \text{ (Maxwell stress) (10)}$$

If the dielectric constant of nuclear matter is unity, that is, if nuclear matter is not polarizable, then the electric field is continuous over the surface and the Maxwell stress does not enter into the boundary condition (5). However it is interesting to point out that if there is a tangential Maxwell stress of the surface it can lead to deformation into a prolate or an oblate spheroid, with convective flow in the interior of the drop.

A salient characteristic of this problem is that the interesting dynamics enter through the surface boundary conditions. The bulk dynamics are preset by the surface pressure and the surface velocity through Eqs. (1) and (2). Another interesting point is that in this problem, flow that is once irrotational at any time must remain irrotational for all time, regardless of the value of the viscosity. Thus calculations that are initialized in an irrotational manner are forced to develop irrotationally, and rotational motion can only be studied if a problem is initialized with a rotational flow field. In particular, head-on accelerator collisions, which by definition involve an irrotational flow field due to the constant initial velocity profile of the incoming drops, must develop in an irrotational manner.

In general these equations are not analytically solvable and one must resort to computer solutions by means of finite differences. We are in the process of developing such a code, which is designated by the name SQUISH. The bare hydrodynamics in SQUISH are based on the SMAC (Simplified Marker And Cell) technique developed at Los Alamos by F. Harlow and A. Amsden.<sup>3</sup> The tensors (7), (8), and (9) and the electrostatic bulk force have been programmed into SQUISH; other forces such as elastic stresses and angular momentum are in the development stage.

The SQUISH code is limited by computation time to cases of axial symmetry; it can only treat head-on collisions. Its three main advantages over existing dynamical treatments are that it contains

- (1) a free surface calculation that requires no parameterization,
- (2) a free-flow calculation that can be rotational or irrotational, and
- (3) provisions for including bulk properties like viscosity and elasticity. Thus the final

version of SQUISH is expected to yield the following information about the classical dynamics of collisions, fusions, and fissions:

- (1) free surface shape and energy
- (2) free-flow velocity field (rotational or irrotational)
- (3) kinetic energy profile
- (4) Coulomb energy profile
- (5) free-flow moment of inertia
- (6) quadrupole moment
- (7) viscosity dependence of above
- (8) energy dependence of above
- (9) spin angular momentum dependence of above
- (10) elasticity dependence of above
- (11) Coriolis forces.

This is an ambitious program and the present incomplete version includes calculations (1) through (8). The other calculations are in various stages of development.

The first full test that we applied to the code was to simulate the viscosity dependence of surface oscillations. When the surface tension force predominates, these are called Rayleigh oscillations and the free surface is given, in the limit of small viscosity and small amplitude, ( $\eta/\omega\rho R_0^2 \ll 1$ ) by<sup>4,5</sup>

$$R = R_0 (1 + A_n e^{-\beta t} \cos \omega t P_n(\theta)) \quad (11)$$

where

$$\beta = (n-1)(2n+1) \frac{\eta}{\rho R_0^2} \quad (12)$$

with characteristic frequency

$$\omega^2 = n(n-1)(n+2) \frac{\gamma}{\rho R_0^3} \quad (13)$$

For uranium nuclei the period of the undamped oscillation is approximately 16 dsec.

When SQUISH is initialized at  $t=0$  with an  $A_2=0.25$  shape, and the program is allowed to cycle in small time steps, the shape evolution that it predicts (by applying Eqs. (1) and (2) to movable markers in the finite difference cells) is shown in Fig. 1. The correspondence between Eqs.(11)-(13) and the free surface predicted by SQUISH is very close ( $\pm 0.05$  fm) for both of the viscosities shown. Thus we feel that the surface tension has been reliably programmed. Note in Fig. 1 that a kinematic viscosity of  $0.5 \text{ fm}^2/\text{dsec}$  results in a virtually undamped oscillation, while a viscosity of  $2.0$  damps the oscillation to a sphere in about a quarter period, so the critical nuclear viscosity lies inside this range.

Wong has pointed out that the experimental observation of undamped  $\beta$ -vibrations in nuclei indicates viscosities below  $0.5 \text{ fm}^2/\text{dsec}$ .<sup>6</sup>

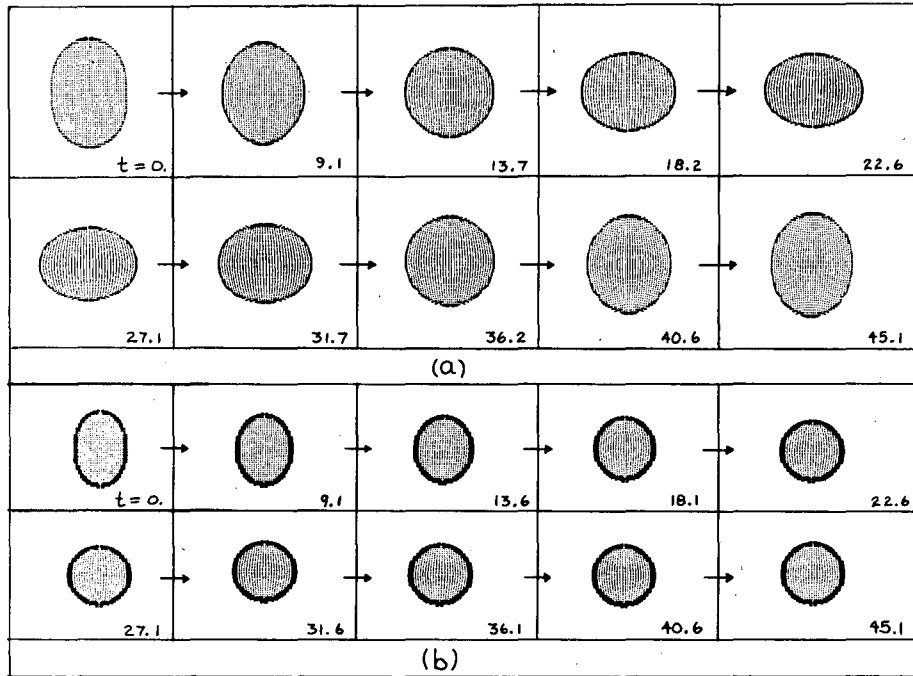


Fig. 1. Viscous Rayleigh Oscillations: These frames describe the time time evolution of a viscous uncharged uranium-like nucleus with two different values of viscosity. The time units at the bottom of each frame are in 0.35 dsec. The theoretical period for the undamped oscillation is 45 time units. In both case (a) and case (b) the drop is initialized at rest with  $R_0 = 7.57$  fm and  $A_2 = 0.25$ . The drops in (a) and (b) are identical except for viscosity; the difference in size is due only to different scaling in the computer plotting. The surface tension coefficient in both cases is  $\gamma = 1.154$  MeV/fm<sup>2</sup>. In case (a) the kinematic viscosity is  $\nu = 0.5$  fm<sup>2</sup>/dsec, and the oscillation proceeds almost undamped through a complete period. In case (b) the kinematic viscosity is  $\nu = 2.0$  fm<sup>2</sup>/dsec, and the oscillation damps to a sphere in about a quarter period. Thus the critical nuclear viscosity should be around 1.0 fm<sup>2</sup>/dsec. (XBB 741-144)

However it can be argued that the corresponding nonobservation of high-energy  $\beta$ -vibrations indicates high viscosities at high energies (i. e., temperatures), so there may be a strong temperature dependence to the nuclear viscosity. This temperature dependence may not be the same as that shown by other Fermi liquids at low temperatures (for example the viscosity of liquid He<sup>3</sup> goes as  $T^{-2}$ ) because of superfluid properties at low temperatures.

Wong has shown that the addition of a body charge to the droplet does not change the nature of the oscillation [Eq. (11)], but it changes the characteristic frequency to<sup>6</sup>

$$\omega^2 = \frac{\gamma}{\rho R_0^3} n(n-1)(n+2) - \frac{2}{3\epsilon_0} \frac{n(n-1)}{2n+1} \frac{\rho_c^2}{\rho} \quad (14)$$

For uranium the effect of the charge is to increase the period from 16 dsec to about 25 dsec. In Fig. 2 are shown two Coulomb oscillations at two different values of the fissility parameter  $x = 1/2(E_{\text{Coulomb}}/E_{\text{surface}})$ . The sequence 2-a has an initial shape well within the saddle point and it oscillates with noticeable damping. The sequence 2-b has a fissility of 0.9, and its initial shape is outside the saddle-point, so it begins to fission instead of oscillating.

Further studies of the code have included head-on Coulomb trajectories of two equal droplets, for which the theoretical rigid-body time from the turning-point is given by

$$T = \frac{a^{3/2}}{A} \left\{ [x(x-1)]^{1/2} + \frac{1}{2} \ln \left[ \frac{x^{1/2} + (x-1)^{1/2}}{x^{1/2} - (x-1)^{1/2}} \right] \right\} \quad (15)$$

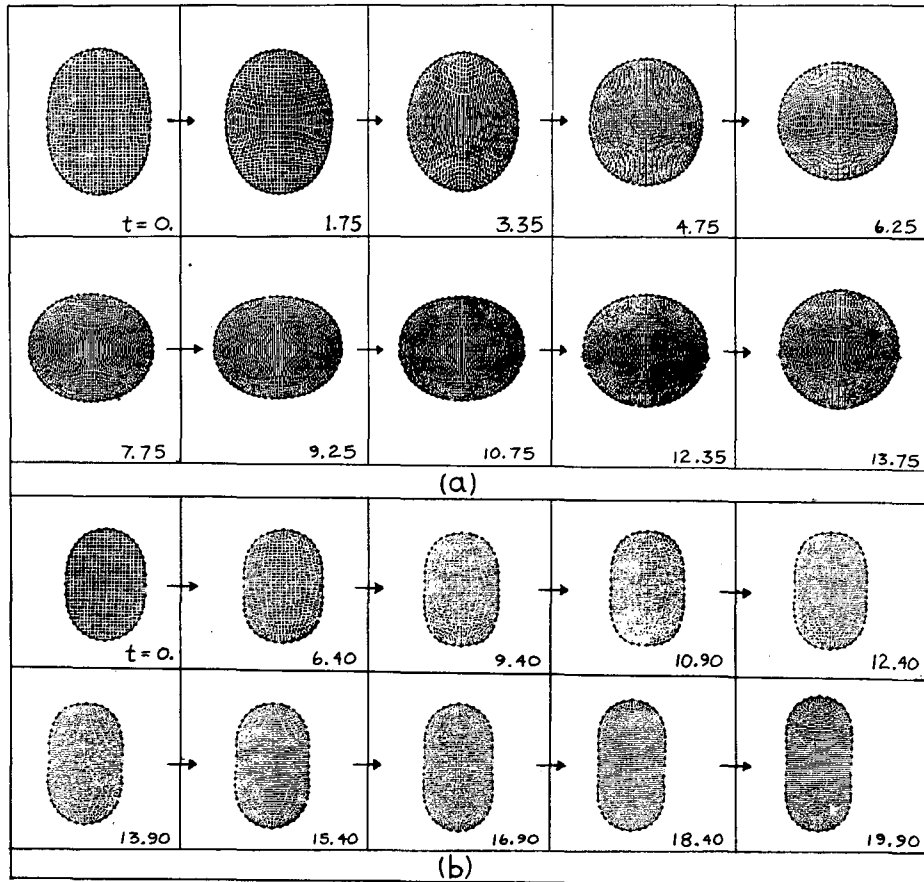


Fig. 2. Viscous Coulomb Oscillations: These frames follow the evolution in time of a viscous nucleus with two different values of the fissility parameter  $x = 1/2(E_{\text{Coul}}/E_{\text{surface}})$ . The time in dsec ( $=10^{-22}$ sec) is given in the lower right corner of each frame. In case (a) the fissility is  $x = 0.3$ , so the droplet is well within the saddle shape and the nucleus oscillates stably, damping slowly to a sphere because of its fairly high viscosity. The theoretical period of the charged oscillation is  $T = 16$  dsec. In case (b) the fissility is  $x = 0.9$  and the droplet is outside the saddle shape, so it begins to fission. (XBB 741-145)

and the velocity of the center of mass by

$$V_{\text{cm}} = \frac{A}{2a^{\frac{1}{2}}} \left( \frac{x-1}{x} \right)^{\frac{1}{2}} \quad (16)$$

where  $ax$  is the center separation,  $a$  is the minimum separation, and  $A = (Q^2/\pi\epsilon_0 M)^{\frac{1}{2}}$ . Values of  $V_{\text{cm}}(t)$  from SQUISH for two droplets started close together at rest reproduce these theoretical values to 2%, with better accuracy at the higher viscosities. Some evidence for dynamic deformation is noted in these runs but it is rather small.

Work is now progressing on fusions and fissions, which have their own characteristic problems. The fission is complicated by velocity initialization problems as well as by the fact

that it should really contain some quantum aspects due to its adiabatic, low-temperature development. If a droplet is started out near the saddle point it takes a long time for any real motion to develop, but if it is not started near the saddle point the correct initial velocity field is unknown.

Fusion problems are much easier to initialize due to the uniform incoming velocities, but the necking process requires special handling. At the moment when the two nuclei touch, there is a cusp in their united surface which imposes high surface tensions and this must be handled by a special program which rounds off the cusp microscopically. The fusion problem is being actively worked on at

this time. We hope to begin a set of complete fusion and fission simulations, including computer-generated movies, in the near future.

### References

1. Landau and Lifshitz, Theory of Elasticity, 2nd ed., (Pergamon Press, 1970) p. 162.
2. J. R. Melcher, Field-Coupled Surface Waves (MIT Press, 1963) p. 14.
3. F. Harlow and A. Amsden, J. Comp. Physics 6, 322 (1970).
4. Lord Rayleigh, Proc. Roy. Soc. (London) 29, 71-97 (1879).
5. H. Lamb, Hydrodynamics, 6th ed., (Dover Press, 1932) p. 640.
6. H. H. Tang and C. Y. Wong, "Vibrations of a Viscous Liquid Sphere," submitted to J. of Fluid Mech.

## MACROSCOPIC NUCLEAR PROPERTIES

J. Randrup

The macroscopic properties of nuclei play an important role in the analysis and interpretation of many recent and current experiments performed at this and other laboratories. In the theoretical attempts to understand the macroscopic aspects of nuclear material, the Thomas-Fermi model in the Seyler-Blanchard modification has proved a rich and varied source of useful first estimates. For example, it was used by Myers and Swiatecki<sup>1</sup> to obtain the preliminary values for the various constants entering in their droplet model. In the following the model is shortly described and some applications of particular interest in connection with heavy-ion reactions are presented.

### Model

Consider some many-particle system in its ground state. The basic Thomas-Fermi assumption is that locally the system behaves as the equivalent uniform system, in other words, that the particles are uniformly distributed within the locally available momentum space. Furthermore, the local sum-over-states is approximated by a continuous momentum-space integration. Considering only systems with identical neutron and proton densities this means that the matter density  $\rho$  and the kinetic-energy density  $\tau$  are connected with the local Fermi momentum  $P_F(\vec{r})$  in the following way.

$$\rho(\vec{r}) = \frac{t}{h^3} \int^{P_F} d^3 \vec{p} = \frac{4\pi}{3} t \frac{P_F^3}{h^3} \quad (1)$$

$$\tau(\vec{r}) = \frac{t}{h^3} \int^{P_F} \frac{p^2}{2m} d^3 \vec{p} = \frac{3}{5} \frac{P_F^5}{2m} \rho \quad (2)$$

Here  $t$  denotes the degeneracy; in the present

case  $t = \text{spin} \times \text{isospin} = 4$ . It is understood that the densities vanish in the classically forbidden regions (where  $P_F^2$  is negative).

In order to describe nuclear material Seyler and Blanchard<sup>2</sup> introduced the following phenomenological two-body interaction

$$V_{12} = -C g\left(\frac{r_{12}}{a}\right) \left(1 - p_{12}^2/b^2\right), \quad g(r) = \frac{e^{-r}}{r} \quad (3)$$

This interaction is basically of the Yukawa type, but is modified with a momentum-dependent factor in order to reproduce the saturating character of the nuclear forces. The Yukawa range  $a$  is a natural unit of length in the problem, and the saturation momentum  $b$  is a natural unit of momentum. The interaction strength  $C$  is positive in order to produce an attractive interaction.

The presence of a two-body interaction in the many-particle system gives rise to an effective single-particle potential  $V_{\text{eff}}$  (in this case momentum-dependent) acting on the individual particles. With the definitions

$$R(\vec{r}_1) = -C \int g\left(\frac{r_{12}}{a}\right) \rho(\vec{r}_2) d^3 \vec{r}_2 \quad (4)$$

$$T(\vec{r}_1) = \frac{C}{b^2/2m} \int g\left(\frac{r_{12}}{a}\right) \tau(\vec{r}_2) d^3 \vec{r}_2, \quad (5)$$

the effective single-particle potential may be written

$$V_{\text{eff}} = R(1 - p^2/b^2) + T \quad (6)$$

It is convenient to introduce the static potential  $U=R+T$  and the effective mass  $B$ ,  $1/2B = 1/2m - R/b^2$ . Notice that both of these functions are momentum-independent. The effective single-particle Hamiltonian may then be written

$$H_{\text{eff}}(\vec{r}) = p^2/2B(\vec{r}) + U(\vec{r}) \quad (7)$$

Furthermore, the total-energy density  $e(\vec{r})$  becomes

$$e(\vec{r}) = \tau(\vec{r}) + \frac{1}{2} \int_{\text{P}_F} V_{\text{eff}}(\vec{r}) d^3 \vec{p} = \frac{1}{2}((1+m/B)\tau + U\rho) \quad (8)$$

In this way it is thus possible, given any system described by densities  $\rho$  and  $\tau$ , to calculate the interaction and total energies in the presence of the Seyler-Blanchard two-body interaction. An iteration scheme is provided by the connection

$$E_F = P_F^2(\vec{r})/2B(\vec{r}) + U(\vec{r}) \quad (9)$$

which, by virtue of (1) and (2), makes it possible to solve for new densities  $\rho'$  and  $\tau'$  in the field generated by the old densities  $\rho$  and  $\tau$ . This iteration scheme gives a stable and relatively fast convergence towards the self-consistent equilibrium solution.

If the system considered is spherical or semi-infinite the problem reduces to a one-dimensional one. In the applications presented here, we have only to consider semi-infinite systems. In that case there is invariance with respect to translation in directions parallel to the surface plane (transversal directions). Hence the folding in (4) and (5) simplifies:

$$\int \frac{e^{-r_{12}/a}}{r_{12}/a} f(x_2) d^3 \vec{r}_2 = 2\pi a^2 \int e^{-x_{12}/a} f(x_2) dx_2 \quad (10)$$

The physical parameters entering the model, namely  $C$  (strength),  $a$  (range) and  $b$  (saturation momentum), are determined so as to reproduce the prescribed values of the volume energy coefficient  $a_v$ , the surface-energy coefficient  $a_s$  and the nuclear radius constant  $r_0$  (see Ref. 1 for details). Following this reference we choose  $C=328.61$  MeV,  $a=0.62567$  fm and  $b=392.48$  MeV/c. The average nucleon mass  $m$  is  $938.903$  MeV/c<sup>2</sup>.

#### Analytic Approximation

The equilibrium distribution resulting from an unrestricted variation of the densities represents the self-consistent solution for the many-particle system in presence of the two-body interaction. In the semi-infinite case,

the distribution is constant inside the system and decreases through the surface region (which has a width of the order of the range  $a$ ). From the point when the local Fermi momentum is zero the density vanishes. The behavior in the neighborhood of this end point  $x_0$  is as a three-halves power,  $\rho(x) \approx (x_0 - x)^{3/2}$ .

For the application of the model it is useful to have a simple analytic approximation to the true equilibrium distribution. For that purpose we have studied the family of distributions

$$\rho(a;x) = \rho_0 \left(1 - e^{-x/a_{\text{TF}}}\right)^{3/2} \quad (11)$$

For this family the surface-energy coefficient  $a_s$  (and other properties) may be considered a function of the surface-width parameter  $a_{\text{TF}}$ , and a minimization of  $a_s$  with respect to variations of  $a_{\text{TF}}$  leads to an approximation to the self-consistent distribution, as obtained by an unrestricted variation. In Table I certain characteristic surface properties of the approximative solution are compared to those of the true solution. It is evident, that the approximation is very good in most respects. In the following we shall refer to this approximation as the TF distribution.

Table I. Comparison of some characteristic surface properties of the density distributions obtained by a restricted variation (using the TF distribution  $\rho_{\text{TF}}(x) \approx (1 - e^{-x/a_{\text{TF}}})^{3/2}$ ,  $a_{\text{TF}} = 1.322 a_{\text{Yuk}}$  and an unrestricted variation (self-consistent Thomas-Fermi minimization, Ref. 1).

Comparison	Restricted Variation	Full Variation
Surface location $C$	1.6926	1.8842
Surface width $b$	1.4205	1.3936
10%-90% width $t_{10-90}$	3.236	3.180
Surface flare $\gamma$	-1.748	-1.728
Surface energy $a_s$	18.583	18.560

#### Proximity Forces

It can be shown<sup>3</sup> that the force between two gently curved leptodermous systems may be written

$$F(s) = 4\pi \bar{R} \gamma(s) \quad (12)$$

Here  $s$  measures the surface separation (for example, the smallest distance between the equivalent sharp surfaces,  $\Delta x_s$ ). The factor  $\bar{R}$  is the reduced radius of the two surfaces

and thus depends only on the geometry. The factor  $\gamma(s)$  is the interaction-energy coefficient for the corresponding two flat (semi-infinite) systems, at the same separation  $s$ . Thus, this function  $\gamma$ , the proximity-force function, is universal in the sense that it depends only on the types of surfaces involved and not on the actual geometry of these systems.

The model described above may be applied to yield a first estimate of the proximity-force function  $\gamma$ . To do this we consider two semi-infinite nuclear systems with density profiles equal to their asymptotic equilibrium shape. All degrees of freedom apart from the separation  $s$  are considered frozen. The two frozen systems are then pushed towards each other without any adjustment of the surface profiles, and the corresponding surface-energy coefficient is calculated at each separation.

The resulting function is displayed in Fig. 1. As the two systems start feeling each other there is an exponential gain in energy, but as the two densities are forced to overlap appreciably a large repulsion will develop. The resulting minimum has a depth approximately equal to the asymptotic surface-energy coefficient  $\gamma_0$ . However, due to the skewness of the surface profiles, the two distributions never add up to a completely uniform distribution and consequently the depth is somewhat smaller. Similarly, the minimum does not occur at precisely zero separation between the two mean surfaces. The difference in the minimum value and  $\gamma_0$  may be estimated rather accurately by the quadratic compressibility formula.<sup>1</sup>

One may obtain the interaction energy between the two curved systems by integrating the force (12). This leads to the formula

$$\epsilon(s) = \int_s^\infty F ds' = 4\pi \bar{R} \int_s^\infty \gamma(s') ds' = 4\pi \bar{R} E(s) \quad (13)$$

The associated universal proximity-energy function  $E(s)$  is displayed in Fig. 2. Note that it predicts an interpenetration equilibrium depth of 1.2 fm ( $\approx r_0$ ) which is the depth at which  $\gamma$  changes sign.

#### Unfreezing the Surface Diffuseness

In the preceding section we have discussed how a first estimate of the proximity force may be obtained by considering completely frozen systems. Clearly, this assumption must be relaxed in a more realistic treatment of the problem. As a first step towards a finer description of approaching nuclear systems we have tried to unfreeze the surface-diffuseness degree of freedom. When two nuclear surfaces are brought closer and closer together, the mutual attraction at large separation will cause

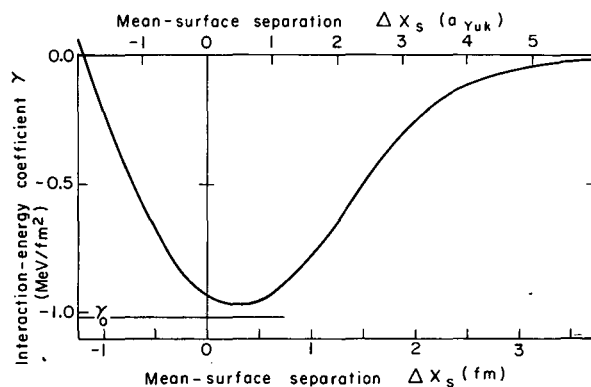


Fig. 1. Interaction-energy coefficient  $\gamma$  for two semi-infinite symmetric systems, frozen to their asymptotic profiles.  $\gamma$  is plotted as function of the mean-surface separation  $\Delta x_s$ . The calculation is performed within the Seyler-Blanchard modification of the Thomas-Fermi model with the standard choice of parameters, as described in the text. The function  $\gamma$  is referred to as the proximity-force function.

(XBL 743-2507)

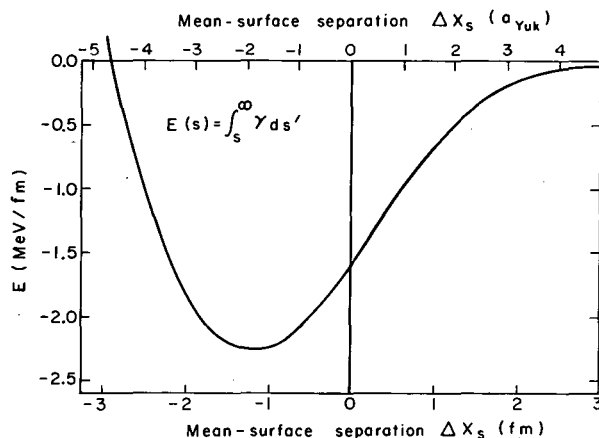


Fig. 2. The proximity-energy function  $E(s) = \int_s^\infty \gamma ds'$  associated with the proximity-force function  $\gamma$  described in Fig. 1. (XBL 743-2508)

a gradual increase in the equilibrium surface diffuseness and this change may severely influence the development of a heavy-ion r process.

For the purpose of studying this effect we have considered two semi-infinite nuclear systems of the type described above. This time,

however, we have allowed the surface-diffuseness to vary freely for each value of the mean-surface separation  $\Delta x_s$ . Thus, for each  $\Delta x_s$ , we have calculated the interaction-energy coefficient  $\gamma$  as function of the diffuseness parameter  $a_{TF}$ . The results of this calculation are displayed in Fig. 3.

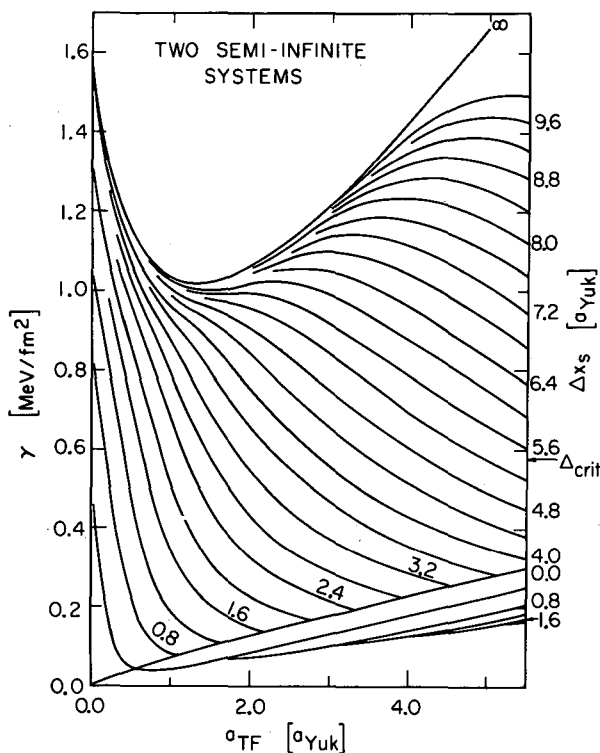


Fig. 3. Interaction-energy coefficient  $\gamma$  as function of surface-diffuseness  $a_{TF}$ , for several fixed mean-surface separations  $\Delta x_s$ . The critical separation  $\Delta_{crit}$ , for which the curve has a point of inflexion, is indicated. Same model as in Fig. 1. The turnover for small values of  $\Delta x_s$  is due to the skewness of the Thomas-Fermi distribution. (XBL 743-2476)

The qualitative features are as follows. For large separations, of course, there will be a minimum near the asymptotic value of  $a_{TF}$ ,  $a_{TF} = 1.322 a_{Yuk}$ . But if the diffuseness increases sufficiently the systems will eventually prefer to collapse into one system. As the separation  $\Delta x_s$  decreases, this barrier against collapse also decreases and its maximum moves towards smaller values of  $a_{TF}$ . At the same time the minimum occurs for larger and larger diffuseness. Ultimately, at a certain critical separation  $\Delta_{crit}$ , the two extrema coincide and there is no stable solution apart from the one corresponding to a uniform system.

As can be seen from the figure, this investigation indicates a critical distance of approximately  $\Delta_{crit} \approx 5.5 a_{Yuk} = 3.44$  fm. This value of the critical distance corresponds closely to the point where the two Thomas-Fermi density distributions touch each other. The point of inflexion occurs for a diffuseness-parameter value of  $a_{TF} \approx 1.9 a_{Yuk}$ . This value is almost 50% larger than the original equilibrium value for well separated surfaces. Hence the nuclear surfaces change appreciably before the collapse occurs.

Thus, our studies indicate the existence of a critical separation at which the nuclear surfaces lose stability against collapse. A detailed dynamical study of how this process occurs and how the subsequent neck-healing develops is of course of greatest interest in connection with heavy-ion reactions and we are currently investigating various aspects of this phenomenon.

#### References

1. W. D. Myers and W. J. Swiatecki, *Ann. Phys.* **55**, no. 3 (1969), 395.
2. R. G. Seyler and C. H. Blanchard, *Phys. Rev.* **124**, no. 1 (1961) 227; *Phys. Rev.* **131**, no. 1 (1963) 355.
3. J. Randrup, W. J. Swiatecki, and C. F. Tsang, to be published.



## QUANTIZATION OF THE SEYLER-BLANCHARD MODEL

J. Randrup

The Thomas-Fermi model described in the preceding article yields a reasonable description of many nuclear properties. It neglects, however, some important effects originating from the quantal nature of the nuclear system. For example, the model fails to produce an exponential density tail in the classically forbidden region outside the system and the density ripples due to the phase relations imposed by the presence of the nuclear surface. Such quantum effects may influence the macroscopic surface properties and give significant contributions to, for example, the surface-energy and curvature-energy coefficients as well as increase the overall diffuseness of the surface region (this diffuseness comes out too small in the Thomas-Fermi calculation). Hence it is desirable to quantize the model in order to study the macroscopic quantal properties of nuclear material. In the following it will be shown how this is possible and furthermore how the established quantum model may be cast into a useable form by means of Langer's WKB-type approximation.<sup>2</sup> In order to study specifically the quantum effects we have stayed as close as possible to the non-quantal model described above, hence developing what might be called a quantization at the Seyler-Blanchard model.

The standard Thomas-Fermi model, as it has been described in the preceding contribution, does not explicitly treat exchange effects. However, the phenomenological Seyler-Blanchard interaction with its momentum dependence will to some extent compensate for that. This important effect is more properly treated in the refined Thomas-Fermi-Dirac model and must of course also be taken into account in a full-scale quantum approach. But here we are concerned with the specific effects of quantizing the Thomas-Fermi model and hence it is appropriate to describe the system in the Hartree approximation. Thus, the system is thought of as a many-particle system, each of the particles being in a certain state  $\psi_i$  and the total system being described by the corresponding uncorrelated-product wave function  $\psi = \prod \psi_i$ .

For the matter density  $\rho$  and the kinetic energy density  $\tau$  we then have

$$\rho = \sum \psi_i^* \psi_i = \frac{t}{h^3} \int^{P_F} \psi^* \psi d^3p \quad (1)$$

$$\tau = \sum \psi_i^* \frac{p^2}{2m} \psi_i = \frac{t}{h^3} \int^{P_F} \psi^* \frac{p^2}{2m} \psi d^3p \quad (2)$$

The two-body interaction  $V_{12}$  via which the particles interact may now be a differential operator. With this interaction specified the self-consistent state of the system may be obtained by a standard variational procedure.<sup>1</sup> This leads to the effective single-particle potential operator  $V_i^{\text{eff}} = \sum \langle V_{ij} \rangle_j$ . Thus, we are provided with an iteration scheme completely analogous to the preceding non-quantal one, and in fact the Thomas-Fermi model comes out as a special case corresponding to solving the effective Schrödinger equation in a simple WKB-type approximation where tails are neglected.

### The Two-Body Interaction

In the non-quantal model the (Seyler-Blanchard) two-body interaction is of the form

$$V_{12} = -C g(r_{12}) (1 - p_{12}^2/b^2) \quad (3)$$

In the quantization process, the momenta change to differential operators and there is no unique way to quantize a product like  $g(r)p^2$ . However, after some studies, we have been led to consider the following quantization rule the natural one,

$$V_{12} \rightarrow -C (g(r_{12}) - \{\vec{p}_{12}, g(r_{12}), \vec{p}_{12}\}) \quad (4)$$

Here the brackets symbolize the appropriately symmetrized product,  $\{a, b, a\} = \frac{1}{4}(a^2b + 2aba + ba^2)$ . This particular choice is the only one leading to form invariance in the sense that the effective single-particle potential operator may be written

$$V_i^{\text{eff}} = -C \sum \langle g_{ij} \rangle_j - \frac{1}{b^2} \{\vec{p}_i, \sum \langle g_{ij} \rangle_j, \vec{p}_i\} - \frac{1}{b^2} \sum \langle \{p_j, g_{ij}, p_j\} \rangle_j \quad (5)$$

Note that this form is quite analogous to the non-quantal case.

### Effective Single-Particle Equation

With the choice of quantization rule described above, the effective single-particle potential operator may be written

$$V_{\text{eff}} = R - \frac{1}{b^2} \vec{p} R \vec{p} + T \quad (6)$$

where  $R$  and  $T$  are defined as in the preceding article, Eqs. (4) and (5). Defining, as before, the effective static potential  $U = R + T$  and the (position-dependent) effective mass  $B$  by  $1/2B = 1/2m - R/b^2$ , the corresponding

effective single-particle Hamiltonian becomes

$$H_{\text{eff}} = \vec{p} \frac{1}{2B} \vec{p} + U \quad (7)$$

Again, notice the great formal similarity with the non-quantal case.

At present we concentrate on a semi-infinite system. Hence there is translational invariance in the transversal directions (directions parallel to the surface) and we may assume the single-particle wave functions to have the following form,

$$\psi(\vec{r}, \vec{p}) = \sqrt{2} s(x, p_x, p_{\perp}) e^{iyp_y/\hbar} e^{izp_z/\hbar} \quad (8)$$

Here,  $s$  may be considered real and the normalization is such that  $s = \sin$  in the bulk region of the system.

Since we now have  $\vec{p}^2 = -\hbar^2 \partial_x^2 + p_{\perp}^2$  the resulting equation for  $s$  becomes

$$\left( \frac{d}{dx} \frac{-\hbar^2}{2B(x)} \frac{d}{dx} + \frac{p_{\perp}^2}{2B(x)} + U(x) - E(p_x, p_{\perp}) \right) s(x, p_x, p_{\perp}) = 0 \quad (9)$$

The connection between the momentum quantum numbers  $p_x$  and  $p_{\perp}$  and the energy  $E$  is  $(p_x^2 + p_{\perp}^2)/2B_0 + U_0 = E$  where the subscript 0 refers to the asymptotic bulk region of the system.

### Method of Solution

The burden of work on obtaining the stationary solution of the problem lies in solving the effective single-particle Schrödinger Eq. (9). In our investigations we have benefited from the existence of a very good approximate solution, introduced by Langer<sup>2</sup> and in the following referred to as the Langer approximation.

Consider an equation of the form  $u'' + Q^2 u = 0$  and assume that there is one turning point  $x_t$ , determined by  $Q(x_t) = 0$ , where  $Q = |Q^2|^{1/2}$ . Then the Langer approximation to the solution may be expressed as  $u_L \approx |\xi|^{1/4} \text{Ai}(\xi) Q^{-1/2}$ . Here  $\text{Ai}$  is the real Airy function and  $\xi = \text{sgn}(\xi) \cdot \left(\frac{3}{2} |\xi|\right)^{2/3}$  where  $\xi$  is the associated action variable,  $\xi = \int_x^x Q dx'$ . The relative error

introduced by this approximation is equal to  $S''/S$  where  $S = Q^{-1/2} |\xi|^{1/6}$ . Studies of simple cases indicate that this approximation is very good and in most cases almost indistinguishable from the true solution.

The actual Eq. (9) is not immediately of the required form since the variable mass introduces a linear differential term. This term may be eliminated, however, by transforming to a constant-mass system  $y(x)$ , where  $y$  satisfies  $y' \sim B$ . Since the constant of proportionality only affects the resulting normalization we assume it to be unity in the bulk,  $y' = B/B_0$ . Then we have

$$Q^2 = \frac{2B}{\hbar^2} (E - U) \left(\frac{B_0}{B}\right) = q^2 \cdot \left(\frac{B_0}{B}\right) \quad (10)$$

where  $q$  is the local wave number for the system. The appropriately normalized Langer solution to Eq. (9) is then

$$s = \sqrt{\pi} \left(\frac{q_0}{q} \cdot \frac{B}{B_0}\right)^{1/2} |\xi|^{1/4} \text{Ai}(\xi) \quad (11)$$

Transforming now back to the original  $x$  variable we find

$$\xi \equiv \int_{y_t}^y Q dy' = \int_{x_t}^x q dx' \quad (12)$$

Hence  $\xi$  is identical to the usual WKB variable associated with the system. Consequently, Eq. (11) holds also in terms of the original  $x$  variable. Thus, we have generalized the Langer approximation to systems with a non-constant mass.

For the Airy function entering in the solution a fast and very accurate code has been established, and a computer program has been set up for the treatment of the entire problem. Numerical investigations based on the presented model are in progress and quantitative results are expected in the near future.

### References

1. L. I. Schiff, Quantum Mechanics, (McGraw-Hill, New York, 1955), p. 285.
2. R. E. Langer, Phys. Rev. **51**, 669 (1937).

## PROXIMITY FORCES

J. Randrup, W. J. Swiatecki,\* and C. F. Tsang

For certain physical systems such as homogeneous solids, fluids or the heavier atomic nuclei, for which there exists a surface region that is thin compared to the size of the object under consideration (leptodermous systems), the potential energy of the system may be decomposed into a volume term and a surface term. The surface term is proportional to the area of the effective sharp surface bounding the object. For a simply-connected system the above decomposition is accurate if the principal radii of curvature of the surface are everywhere much larger than the thickness of the surface region. Moreover, when this condition is satisfied, correction terms to the surface energy (such as the curvature correction) may be derived by expansions in powers of the ratio of the thickness of the surface to the size of the system, thus making the expression for the potential energy even more accurate. Such a series expansion has been useful in discussing the average binding energies (masses) of atomic nuclei, and one might have thought that, apart from effects associated with the discreteness of nucleons (shell effects) there was no more to the problem of average nuclear energies than the calculation of the above series expansions to a sufficiently high order. This is not the case. Thus, when the surface of the system becomes contorted into features whose characteristic dimensions are of the order of the thickness of the surface region itself, the above series expansions become useless. This failing is by no means of merely academic interest; it may be serious for a system with a thin neck, on the verge of dividing into two fragments (as in nuclear fission), or in the case of two sub-systems about to come into contact (as in nuclear reactions induced by heavy projectiles). In the latter case in particular, when the system is not simply connected, a calculation of the surface energies of the two pieces, no matter how accurately it is corrected for the curvatures of the two surfaces, can never give rise to the (strong) attraction that in practice appears when the effective sharp surfaces approach each other to within a distance comparable with the surface thickness.

Various attempts to remedy these failings have been made in the past. They range from microscopic computer calculations on individual pairs of nuclei (by Greiner and collaborators and Brueckner and collaborators), through the introduction of a schematic (Yukawa) pseudo-interaction by Krappe and Nix, to recent estimates of certain aspects of the

nucleus-nucleus attraction by Wilczyński and others.

We have found it possible to derive simple expressions for the additional potential energy (or forces) associated with certain of the more important types of violently contorted surfaces which should enable one to complement in a useful way the usual series expansions of average nuclear potential energy. We shall call these additional forces "proximity forces" because they arise from the proximity of elements of the contorted surface, the contortion being such that different pieces of the surface actually face each other across a small gap or crevice.

Consider then a system where surface elements face each other across a gap of variable width  $D$ . Over regions of the gap or crevice where the angle between the facing surface elements is small, and the surface, apart from being folded over, is otherwise only gently curved, the interaction energy of the two surfaces may be written as an integral of an interaction energy per unit area of the gap. This interaction energy per unit area, say  $e(D)$ , is approximately equal to the interaction energy of two parallel surface elements of unit area at the appropriate separation  $D$ . Hence the proximity energy  $E_p$  may be written as

$$E_p = \int_{\text{gap}} e(D) d\sigma + \text{corrections.} \quad (1)$$

The integral is over the area of the gap and the "corrections" arise from the limited validity of the assumption that the contorted surface can be represented as a gap with almost parallel faces.

The qualitative appearance of the function  $e(D)$  follows from its definition as the interaction energy of two plane, parallel unit elements of surface at a distance  $D$ . For  $D$  greater than the thickness of the surfaces (2 or 3 fermis in the case of nuclei)  $e(D)$  tends rapidly to zero. For small values of  $D$ ,  $e(D)$  becomes negative, and for  $D=0$  it is approximately equal to minus twice the surface energy per unit area of the material of which the system is composed. This is because at  $D=0$  the two juxtaposed density distributions have added up to an approximately constant bulk value, so that the net effect of bringing the surfaces together from infinity has been to destroy two unit areas of surface. Thus

$$e(o) \approx - 2\gamma, \quad (2)$$

where  $\gamma$  is the surface energy coefficient (about 1 MeV/fm<sup>2</sup> for nuclear matter, about 75 ergs/cm<sup>2</sup> for water).

If one continues on to negative values of  $D$ , adding up the two density distributions without allowing them to get out of each other's way, the function  $e(D)$  will begin to increase, will go through zero and will eventually grow without limit, reflecting the energy cost of doubling the density in the overlap region. It follows that  $e(D)$  exhibits a minimum, and this minimum occurs in fact near  $D=0$  (where  $-e(D) = 2\gamma$ ). This is because it is at this separation that the total density is approximately equal to the standard bulk density, and the bulk energy of a stable system is stationary (a minimum) with respect to deviations of the density from the standard value.

With this understanding of the appearance of the function  $e(D)$ , we shall illustrate the consequences of Eq. (1) by considering two spherical systems whose effective sharp surfaces (with radii  $R_1$  and  $R_2$ ) are separated by a least distance  $s$ . Take the  $z$ -axis along the line of closest approach and the  $x, y$  axes in a plane at right angles. The proximity energy is then, approximately,

$$E_p = \iint dx dy e(D). \quad (3)$$

We are assuming that the radii  $R_1, R_2$  are much larger than the thickness of the surfaces, and that all degrees of freedom of the density distributions (including the shapes of the surfaces) are frozen. The two systems are thus taken to be gently curved and undeformable. To evaluate  $E_p$  under these assumptions consider the Taylor expansion of the gap width  $D$

$$D = s + \frac{1}{2} D_{xx} x^2 + \frac{1}{2} D_{yy} y^2 + \dots,$$

where  $D_{xx}, D_{yy}$  are the second derivatives of  $D$  with respect to  $x$  or  $y$ , evaluated at  $x=y=0$ . In the case of spheres one easily verifies that  $D_{xx} = D_{yy} = 1/\hat{R}$ , where  $\hat{R}$  is the "reduced radius" of the system, given by  $\hat{R} = R_1 R_2 / (R_1 + R_2)$ . Changing variables from  $x, y$  to  $\xi, \eta$  defined by  $\xi = \sqrt{D_{xx}/2} x, \eta = \sqrt{D_{yy}/2} y$ , we have  $D = s + \rho^2$ , where  $\rho^2 = \xi^2 + \eta^2$ . Hence the proximity potential may be written as

$$\begin{aligned} E_p(s) &= \frac{2}{\sqrt{D_{xx} D_{yy}}} \iint d\xi d\eta e(D) \\ &= \frac{2}{\sqrt{D_{xx} D_{yy}}} \int_0^\infty 2\pi \rho d\rho e(D) \\ &= \frac{2\pi}{\sqrt{D_{xx} D_{yy}}} \int_{D=s}^\infty dD e(D). \end{aligned} \quad (4)$$

In the last two lines the integration is extended to infinity, although the precise upper limit doesn't matter because the integrand  $e(D)$  is essentially zero there.

The force between the two spheres is given by

$$\begin{aligned} F(s) &= - \frac{dE_p}{ds} = \frac{2\pi}{\sqrt{D_{xx} D_{yy}}} e(s) \\ &= 2\pi \hat{R} e(s). \end{aligned} \quad (5)$$

This equation expresses the following Proximity Force Theorem: the force between two gently curved undeformable bodies (as a function of the least separation  $s$ ) is proportional to the interaction potential between two flat unit elements of the surfaces, the proportionality factor being a measure of the curvatures of the two surfaces.

For two spheres the factor is  $2\pi$  times the reduced radius  $\hat{R}$ . (In the more general case of two arbitrary gently curved surfaces, each characterized in the vicinity of the line of closest approach by two principal radii of curvature,  $A_1$  and  $B_1$  for surface 1, and  $A_2$  and  $B_2$  for surface 2, it may be shown that the factor  $D_{xx} D_{yy}$  is given by

$$\begin{aligned} D_{xx} D_{yy} &= \frac{1}{A_1 B_1} + \frac{1}{A_2 B_2} + \left( \frac{1}{A_1 A_2} + \frac{1}{B_1 B_2} \right) \sin^2 \alpha \\ &+ \left( \frac{1}{A_1 B_2} + \frac{1}{A_2 B_1} \right) \cos^2 \alpha. \end{aligned}$$

Here  $\alpha$  is the azimuthal angle around the  $z$ -axis between the principal planes of curvature of the two surfaces in the vicinity of the line of closest approach. For spheres  $A_1 = B_1 = R_1, A_2 = B_2 = R_2$ , and one verifies that  $1/\sqrt{D_{xx} D_{yy}}$  reduces to  $\hat{R}$ .

For positive values of  $s$  the force  $F$  given by Eq. (5) is negative (an attraction). This attraction is strongest where  $-e(s)$  is a maximum, which we saw occurs at  $s \approx 0$ . Hence the maximum attraction between two undeformable, gently curved objects occurs near the point where their effective sharp surface are in contact, and is given by

$$F_{\max} \approx 2\pi \hat{R} e(0) = -4\pi \hat{R} \gamma. \quad (6)$$

(or  $-\frac{4\pi\gamma}{\sqrt{D_{xx}D_{yy}}}$  in the general case).

This equation expresses the remarkable result that the maximum attraction between undeformable, gently curved bodies may be written without any knowledge of the nature of the cohesive interactions between the particles constituting the bodies, provided only the surface energy coefficient  $\gamma$  is known.

Under the conditions stated (undeformable, gently curved bodies) Eq. (6) would apply equally well to the contact force between ordinary solids (where the attraction is due to molecular forces), or to nuclei, where the attraction is due to nucleon-nucleon forces. The magnitude of the force predicted by Eq. (6) may be illustrated as follows. With a nominal value of  $\gamma$  equal to 100 ergs/cm<sup>2</sup> (the surface energy of solids is of this order of magnitude, for example 300 ergs/cm<sup>2</sup> for mica) we find that two equal spheres with radii of 5 cm should attract each other with a force given by

$$F_{\max} = 3100 \text{ dynes} = 3.2 \text{ g weight.}$$

Cohesive forces between smooth curved surfaces of mica, rubber and gelatin have in fact been found experimentally to have this order of magnitude.<sup>1,2</sup>

In the case of nuclei the surface energy coefficient  $\gamma$  is about 1 MeV/fm<sup>2</sup> and for two equal spheres with radii 5 fm (corresponding approximately to medium nuclei with mass number 76) we find

$$F_{\max} \approx 31 \text{ MeV/fm.}$$

In order to calculate the force between two nuclei in its dependence on the separation  $s$  one has to use Eq. (5), whose right hand side is a product of a geometrical factor  $2\pi\hat{R}$  depending on the two nuclei in question, and a

universal function of distance  $e(s)$ , independent of the nuclei. The semi-quantitative appearance of  $e(s)$  has been sketched out above, but in order to calculate  $e(s)$  in detail one needs to have a theory describing the structure of the nuclear surface region, so that one may take two flat nuclear surfaces and calculate their interaction energy as a function of the separation. Such a calculation of  $e(s)$  has been performed by J. Randrup, using W. D. Myers' theory of the nuclear surface based on the nuclear Thomas-Fermi method. Using this result one may also evaluate the integral over  $e(D)$  that appears in Eq. (4) and which enables one to write the potential (rather than the force) acting between two nuclei as a product of a geometrical factor and a universal function of  $s$ . It turns out that this universal function may be represented in a rather rough approximation as a linear function times an exponential for  $s > 0$  and a parabola for  $s < 0$ , so that the final formula for the predicted nucleus-nucleus proximity potential may be written as follows

$$E_p(s) = -4\pi \hat{R} \gamma s_0 \begin{cases} \frac{5}{3} \left(1 + \frac{s}{s_0}\right) e^{-\frac{8}{5} \left(\frac{s}{s_0}\right)} & \text{for } s > 0 \\ \frac{5}{3} - \left(\frac{s}{s_0}\right) - \frac{1}{2} \left(\frac{s}{s_0}\right)^2 & \text{for } s < 0. \end{cases} \quad (7)$$

In calculating  $\hat{R}$  a reasonable value for the nuclear radius constant would be 1.18 fm. A formula for  $\gamma$  based on the Myers-Swiatecki Lysekil mass formula would read

$$\gamma = 0.9517 \left[ 1 - 1.7826 \left( \frac{N-Z}{A} \right)^2 \right] \text{ MeV/fm}^2,$$

where  $N, Z, A$  are the total numbers of neutrons, protons and nucleons in both nuclei. The parameter  $s_0$  allows one some freedom to scale the predicted potential  $E_p$ , while preserving the condition

$\left. \frac{dE_p}{ds} \right|_{s=0} = 4\pi \hat{R} \gamma$ . Randrup's numerically calculated curve for  $E_p$  is represented roughly by a choice  $s_0 \approx 1$  fm.

Caution should be exercised in using formula of Eq. (7). Its proper domain of applicability is to the mapping of the average nuclear potential energy surface (for not too small systems) in a very small subspace of the total configuration space defined by the requirement of undeformability (all degrees of freedom of the two individual nuclei are frozen). In trying to compare the potential  $E_p$  directly with results of nucleus-nucleus scattering experiments one should remember

that nuclei are not undeformable. Perhaps the gross features of Eq. (7) would nevertheless show up in scattering experiments at sufficiently high energies (especially in grazing collisions) where there might not be enough time during the collision for the nuclear density distributions to deform appreciably. It might also be argued that in the analysis of elastic nucleus-nucleus collisions a formula based on the assumption of undeformability is actually the relevant one, since any excitation of the degrees of freedom of the individual nuclei would tend to take the system out of the channel for elastic scattering.

A second reservation on the indiscriminate use of Eq. (7) stems from the assumption that  $R_1$  and  $R_2$  should be much larger than the thickness of the nuclear surface. Even for heavy nuclei this condition is not satisfied accurately, and when one of the nuclei is as light as oxygen or neon, very serious corrections to Eq. (7) are to be expected.

We are at present studying such higher order corrections to the proximity forces. We are also investigating (together with J. Blocki) formulae analogous to Eq. (7), but arising from the application of Eq. (1) to an axially symmetric crease (rather than a gap), such as might occur in the post-contact stages of the fusion of two nuclei.

#### Footnote and References

\*Theoretical Physics Group, LBL.

1. J. N. Israelischoili and D. Tabor, "The Measurement of Van der Waals Dispersion Forces in the Range 1.5 to 130 mm," Proc. Roy. Soc. London A 331, 19 (1972).
2. K. L. Johnson, K. Kendall, and A. D. Roberts, Proc. Roy. Soc. London A 324, 301 (1971).

### COMPOUND NUCLEUS FORMATION IN HEAVY ION COLLISIONS\*

C. F. Tsang

Heavy ion reactions have been the way in which new elements with  $Z = 102$  to  $Z = 105$  were synthesized.<sup>1</sup> In these reactions projectiles up to  $^{22}\text{Ne}$  were used and extremely powerful techniques were developed to detect very small cross-sections. To make heavier elements,  $Z = 106$  and  $107$  as well as the predicted superheavy elements, projectiles as heavy as  $^{86}\text{Kr}$  may become necessary. In these cases, various problems connected with the use of heavy ions such as angular momentum and viscosity effects become more critical and cross-sections are much reduced. Thus it may become crucial to obtain a better understanding of the compound nucleus formation so as to find the optimal conditions under which heavy ion collisions may lead to the production of new elements.

Several experimental observations have strong bearings on the theoretical study of compound nucleus formation. The first is the observation at Berkeley several years ago that to make the same final product  $^{244}\text{Fm}$ , the cross-section is several orders of magnitude lower when a  $^{40}\text{Ar}$  projectile is used than the case when  $^{16}\text{O}$  is used. The second is the recent exhaustive Dubna attempt in the production of superheavy nuclei by bombarding a Th target with a  $^{74,76}\text{Ge}$  beam, in which

only an upper limit for the very low cross-section is estimated for the synthesis. In contrast to this, a third experiment done at Berkeley to make Yb isotopes by bombarding a  $^{80}\text{Se}$  target with a  $^{84}\text{Kr}$  projectile yields quite measurable cross-sections. All these experiments have to be understood within our theory.

Our picture of a heavy ion reaction is as follows. Before the projectile and target nuclei come into contact, the process is well understood in terms of Rutherford scattering. Now, after the compound nucleus is formed from the two nuclei, its de-excitation to the ground-state product has been studied to a large extent in terms of evaporations, instability against centrifugal forces and fission. It is in between these two stages that very little is known, and it is here that we concern ourselves in the present study. Two questions need to be settled. The first is, when the two nuclei touch, will they stick together by means of nuclear interactions, or will they be repelled by Coulomb and centrifugal forces? The second question is, if the two nuclei are able to stick together (in the two-tangent spheres configuration), will they flow together into a compound nucleus, or will they elongate and fission?

To answer the first question, we study the competition between the forces involved. Earlier studies show that it is a good approximation to assume that the interacting nuclei do not deform during the short time scale of the collision. Coulomb, and centrifugal forces are well-known. For the nuclear attractive force we wrote a simple formula based on a Thomas-Fermi calculation of two semi-infinite slabs of nuclear matter. We call this the proximity force, being the force acting between two nuclei when they are in close proximity to each other. This force is discussed in more detail elsewhere in this Annual Report.

Figure 1 displays the condition when the force balance is such that the system will stick together. This is expressed in terms of the fissility parameter  $x$  of the composite system as a function of the fractional size of one of the two colliding nuclei:

$$U = \frac{A_1}{A_1 + A_2}$$

for a series of angular momentum values, expressed in terms of a parameter  $y$  defined as  $y = (\text{Rotational energy of the system}) / (2 \times \text{surface energy of sphere with same total mass})$ , where values of rigid moment of inertia are assumed. Thus for zero angular momentum and equal sizes of the projectile and target, the system will stick if  $x \leq 6/5$ .

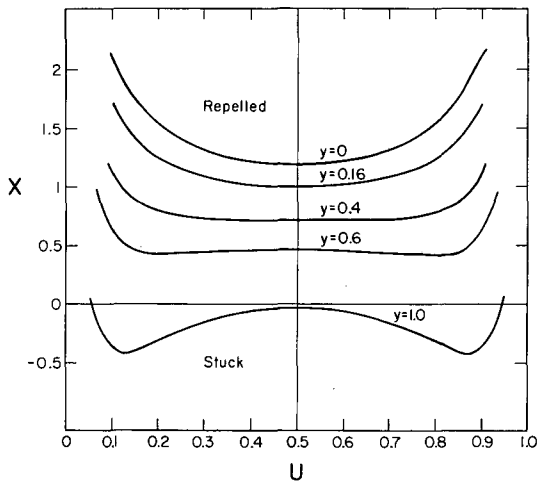


Fig. 1. Critical fissility parameter for the sticking of two spheres as a function of  $U = A_1 / (A_1 + A_2)$  for a series of angular momentum values expressed in terms of the ratio ( $y$ ) of the rotational energy to twice the surface energy of an equivalent sphere. For each curve sticking is possible for smaller values of  $x$ , i. e., below the curve.

(XBL-742-2431)

The limit will be higher for asymmetric systems ( $U \neq 0.5$ ), and the limit will decrease as the angular momentum goes up due to the disruptive centrifugal effect. This has some relevance to the Dubna experiment of  $(Xe + U)$  which has an  $x$  value of 1.225 and  $U$  value of 0.364. It can be seen from the graph that most of its partial waves are under the condition that they will not stick (hence only direct reaction products will be observed), and only in cases where angular momenta are close to zero the system will stick. In fact it is observed that the cross-section of direct reaction products in this reaction is greater than that of the fission-like product by a ratio of 4:1.

To answer the second question, we construct a measure of compactness of the system in its tangent-sphere configuration as well as in its fission saddle point shape. Then we can determine whether the tangent-sphere configuration is inside or outside the fission saddle point. If it is outside, then the fission forces

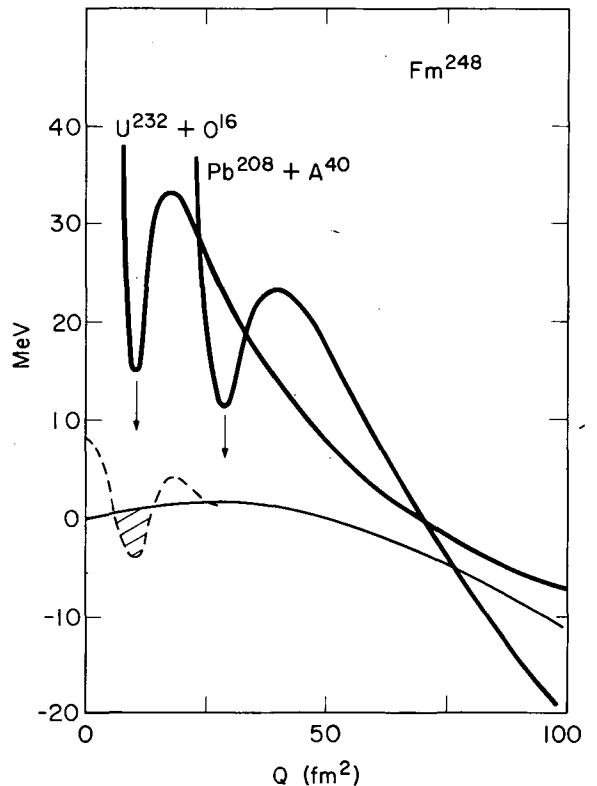


Fig. 2. Potential energy as a function of the quadrupole moment of the mass distribution. The lower curve is the energy along the fission path of  $^{248}\text{Fm}$ . The two upper curves are for two-sphere systems,  $(^{16}\text{O} + ^{232}\text{U})$  and  $(^{40}\text{Ar} + ^{208}\text{Pb})$  respectively.

(XBL-742-2426)

are present and tend to push to system to fission. If it is inside, the system would have a relatively high probability of fusing into a compound nucleus. We made many attempts to construct such a measure, which, we demand, should be simple, have reasonable behaviors near the sphere and also for two spheres at infinity, as well as being able to distinguish the asymmetry of the system. We finally ended up using the quadrupole moment of the mass distribution of the system around its center of mass.

Figure 2 displays the potential energy as a function of the quadrupole moment of the mass distribution. The lower curve is the energy along the fission path of  $^{248}\text{Fm}$ . Along this curve the system takes the usual fission shapes, including neck formation, elongation, etc. Each of the two curves above it represents the energy of two spheres coming together. The rapid rise in energy on the left end of the curve is due to the doubling of density when the two spheres overlap each other. The small minimum in this curve is the position that the two spheres will be in when they come together, and they de-excite by deforming away from

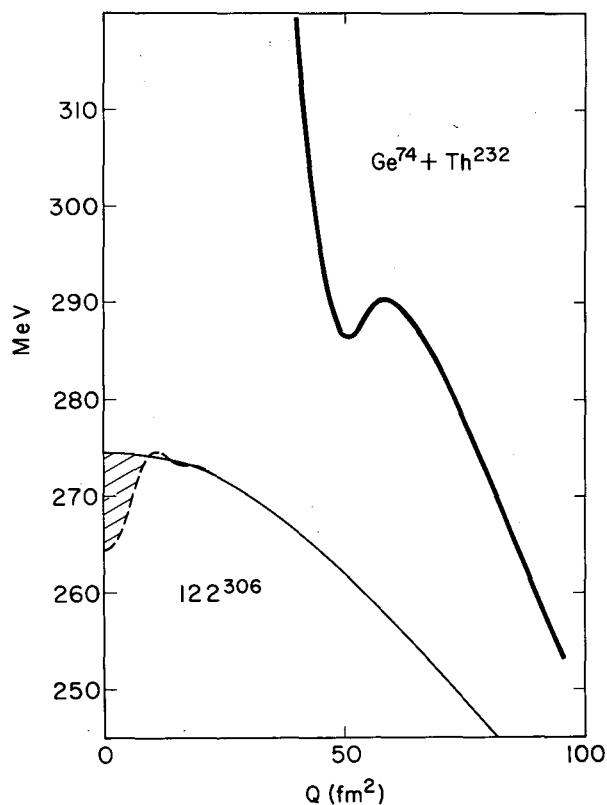


Fig. 3. Same as Fig. 2, but for ( $^{74}\text{Ge} + ^{232}\text{Th}$ ) system. (XBL-742-2428)

two spheres. One can see the obvious difference between the two curves, one representing the reaction ( $^{16}\text{O} + ^{232}\text{U}$ ) and the other ( $^{40}\text{Ar} + ^{208}\text{Pb}$ ). It is seen ( $^{40}\text{Ar} + ^{208}\text{Pb}$ ) is outside the  $^{248}\text{Fm}$  saddle point shape and experiences fission forces whereas ( $^{16}\text{O} + ^{232}\text{U}$ ) is well inside. This explains semi-quantitatively the difference in production cross sections between the two reactions. Figure 3 shows a similar plot for the reaction ( $^{74}\text{Ge} + ^{232}\text{Th}$ ), where it is seen that the two-sphere system is outside the fission saddle point, making it very difficult for the compound nucleus to form. The situation is somewhat better for the case of ( $^{48}\text{Ca} + ^{248}\text{Cm}$ ) where the two-sphere system is still outside, but not too far from the fission saddle point; there may be a finite probability of populating the compound nucleus well. This might be helped by an extra push provided by an increase in the bombarding energy. Figure 4 shows the case where the different combinations ( $^{40}\text{Ar} + ^{118}\text{Sn}$  or  $^{84}\text{Kr} + ^{74}\text{Ge}$ ) of projectile and target with the same compound nucleus ( $^{158}\text{Er}$ ) make little difference in compound nucleus formation except for angular momentum effects. In this case almost any reaction is inside the large saddle point shape.

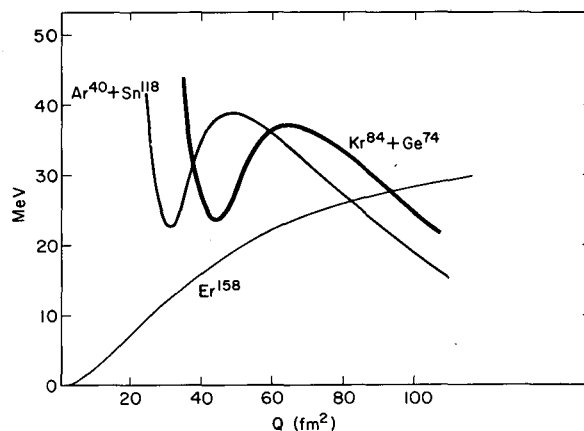


Fig. 4. Same as Fig. 2, but for ( $^{40}\text{Ar} + ^{118}\text{Sn}$ ) and ( $^{84}\text{Kr} + ^{74}\text{Ge}$ ) with  $^{158}\text{Er}$  the compound system. (XBL-742-2429)

#### Footnote and References

\* This work was done in collaboration with W. J. Swiatecki of the LBL Theoretical Physics Group.

1. See for example, A. Ghiorso, LBL-213 (1971).



## FRICTIONAL EFFECTS IN HEAVY ION COLLISIONS\*

C. F. Tsang

In the study of collisions between two large nuclei, the role of frictional forces between them turns out to be an important one in understanding various phenomena. Two examples may be mentioned: The first is the problem of multi-nucleon transfer between two heavy ions in which a reduction of cross-section is observed as a function of maximum angular momentum produced in the reactions. One suggested explanation is that there exists a critical orbital angular momentum between the two nuclei above which multi-nucleon transfer probability is greatly reduced. It is easy to see that the presence of frictional forces between the nuclei will cause part of the orbital angular momentum to be converted into the respective spins of the two nuclei, so that a constant value of critical orbital angular momentum is no longer a valid concept. Such a critical value depends on the amounts of spins produced, which in turn, depends on the magnitude of the frictional forces as well as the dynamic process. The second example is the problem of two nuclei colliding to form a compound nucleus. In some cases, such as in attempts to make a superheavy nucleus, this depends on the energy that is available to push the two nuclei together. If frictional forces are large, this energy will quickly be converted into heat (or single-particle excitations) and will then not be available to push them together. Thus an estimation of the magnitude of frictional forces may be very important in studying the possibility of making a compound nucleus.

The approach we have taken is to write a Rayleigh dissipation function for the frictional forces between two colliding nuclei.

$$R = \frac{1}{2}k \int \rho_1 \rho_2 \vec{v}_{12}^2 d\tau$$

where the integration is over the overlap of the two nuclei;  $\rho_1$  and  $\rho_2$  are the densities due to the two respective nuclei at the volume element  $d\tau$ ;  $\vec{v}_{12}$  is the relative velocity at this point and  $k$  is an adjustable frictional coefficient. What this dissipation function implies is a frictional force given by

$$\vec{F} = -k \int \rho_1 \rho_2 \vec{v}_{12} d\tau.$$

With the Rayleigh dissipation function, the Lagrange equations of motion may be written and solved. Only four degrees of freedom are assumed: the distance between the two nuclei, the orbital angular motion represented by the angle of a line joining the centers of the two

nuclei relative to a fixed laboratory frame, and the two spins. The forces present, in addition to the dissipative frictional force are Coulomb, centrifugal, and proximity forces. The latter is the short range nuclear force that is described in more detail elsewhere in these reports.

We are able to reduce the four equations of motion into one integro-differential equation. This equation was solved numerically. In the case of grazing reactions, in which a very small overlap of the two nuclei may be assumed, certain approximations can be made and the equation may be solved analytically. With the frictional coefficient as the only adjustable parameter, all properties of the collision process at any time may be calculated for a given heavy ion collision with the bombarding energy and the impact parameter given. These include the heat dissipated, the orbital angular momentum and spins at any point of motion, the angle of deflection, and the kinetic energy of the final products.

We present in Fig. 1 a specific result, chosen because it points to a way of determining the magnitude of the frictional coefficient. It was recently pointed out by Wilczynski<sup>1</sup> in studying the transfer products in ( $^{40}\text{Ar} + ^{232}\text{Th}$ )

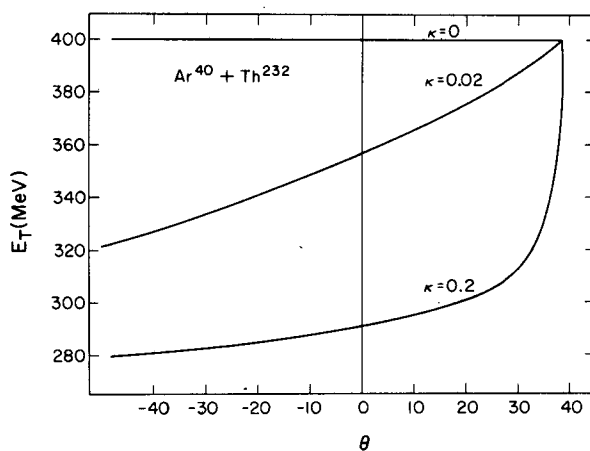


Fig. 1. Kinetic energy of the final products,  $E_T$ , as a function of the deflection angle  $\theta$  for the grazing reaction ( $^{40}\text{Ar} + ^{232}\text{Th}$ ) for various values of the frictional coefficient  $\kappa$ . The Myers and Swiatecki Lysekil mass formula parameters are used in this calculation.

(XBL-742-2425)

reactions that frictional forces are responsible for the reduction of the kinetic energy of the product as its angle of deflection is decreased from its grazing value. Figure 1 is such a plot with these quantities obtained from our calculation for three values of our fictional coefficient in a dimensionless unit,  $k$ . For the intermediate value  $k = 0.02$ , it is seen that as the angle deviates from grazing towards negative values, the kinetic energy is decreased. Physically, as the projectile and target nuclei overlap, the nuclear interaction causes the angle of deflection to deviate from the grazing value, and at the same time the frictional force causes the kinetic energy to be reduced. Thus, for  $k = 0$ , there is no frictional force, and the curve in Fig. 1 displays no decrease in energy. On the other hand, for a larger value of  $k = 0.2$ , the decrease in kinetic energy is much faster,

reaching a limiting value corresponding to the case where the spins of the two nuclei and the rotation of the whole system have the same angular velocity and there is no rubbing between the nuclei. By a comparison of such a calculation with experimental measurements, one would expect to be able to determine the frictional force between two heavy ions in a grazing collision to within possibly a factor of 2 or so.

#### Footnote and Reference

\* This work was done in collaboration with W.J. Swiatecki of the Theoretical Physics Group.

1. J. Wilcznski, Niels Bohr Institute preprint (1973).

## TOTAL REACTION CROSS SECTIONS FOR HEAVY IONS

J. R. Alonso and J. O. Rasmussen

The cross section calculation program discussed in the previous annual report<sup>1</sup> has been modified using the formulae developed below to allow for a reduction in running time by a factor of about 100 with essentially no loss of accuracy.

Basically, the total reaction cross section can be written as

$$\sigma = \frac{\pi}{k^2} \sum_{\ell=0}^{\infty} (2\ell+1) \rho_{\ell} \quad (1)$$

where  $\rho_{\ell}$  is the reaction probability for each partial wave. One way of evaluating  $\rho_{\ell}$ , due originally to T. D. Thomas,<sup>2</sup> consists of taking the potential  $V_{\ell}$  for each  $\ell$  value and calculating the absorption of the incident wave function by this potential by finding the transmission of the  $\ell$ 'th wave over or through the barrier. A calculational simplification is made by assuming that the barrier is an inverted parabola of characteristic width

$$\hbar\omega_{\ell} = \sqrt{\frac{\hbar^2}{\mu} \frac{d^2 V_{\ell}}{dr^2}} \quad (2)$$

( $\mu$  = reduced mass)

so that the transmission through the barrier is given by the Hill-Wheeler formula<sup>3</sup>

$$\rho_{\ell} = 1 / \{ 1 + \exp[2\pi(B_{\ell} - E)/\hbar\omega_{\ell}] \} \quad (3)$$

C. Y. Wong<sup>4</sup> first suggested that by making the assumption that the barrier location and

width are independent of  $\ell$ , the reaction cross section, given by the combination of Eqs. (1) and (3), can be easily integrated over  $\ell$  values to give the following closed form expression:

$$\sigma_{\text{fusion, spherical}} = \frac{R^2 \hbar\omega_0}{2E} \times \ln \left\{ 1 + \exp \left[ \frac{2\pi}{\hbar\omega_0} (E - B_0) \right] \right\} \quad (4)$$

This expression, which is valid for spherical nuclei, represents a considerable saving in calculations, since the sum over partial waves has been eliminated. The accuracy of this formula can be evaluated from Table I, which shows a comparison of cross section calculated by Eq. (4) and by the full sum over partial waves (up to  $\ell = 120$ ). Although the cross sections range over 10 orders of magnitude the two calculations never vary by more than 30%.

In order to generalize this approach to include the effects of nuclear deformation on the cross sections, we have used Wong's original assumptions, and have parametrized the nuclear deformation in terms of the barrier height at different nuclear orientation angles. For each nuclear orientation the Hill-Wheeler transmission formula has been replaced by two exponential functions smoothly joined at the point where the incident energy equals the barrier height at that orientation. In the resulting expressions the total cross section is

Table I. Comparison of fusion cross-sections for  $^{12}\text{C} + ^{235}\text{U}$  calculated by summing over partial waves, and using C. Y. Wong's formula with the  $l$  dependence integrated out.

$E_{\text{lab}}$ (MeV)	Cross-Sections (mb)	
	Sum over $l$ waves	Closed form expression
46.9	4.01E-7	2.90 E-7
48.9	2.98E-6	2.24 E-6
50.9	2.22E-5	1.72 E-5
52.9	1.65E-4	1.33 E-4
54.9	1.24E-3	1.03 E-3
56.9	9.25E-3	7.97 E-3
58.9	6.89E-2	6.18 E-2
60.9	0.511	0.478
62.9	3.69	3.63
64.9	23.1	24.2
66.9	88.2	98.6
68.9	183.	216.
70.9	272.	339.
72.9	347.	457.
74.9	410.	569.
76.9	463.	675.
78.9	507.	776.
80.9	548.	872.
82.9	593.	963.
84.9	641.	1050.
94.9	912.	1430.
103.9	1160.	1710.
123.9	1600.	2180.

then given as an integral over  $l$  values and over all orientation angles of the nucleus. Three separate regions are considered, depending on whether the incident energy  $E$  is above, or below the barrier for any orientation, or within the range of barrier heights between  $B_0$  and  $B_{90}$ . In all cases the  $l$  integral is easily solved, leaving only the integral over the nuclear orientation angles. In the expression below, the parameter  $\mu$  is  $\cos \theta$ , where  $\theta$  is the angle of the impact point with respect to the nuclear symmetry axis. For  $E$  between  $B_0$  and  $B_{90}$ ,  $\mu_0$  is the angle at which the barrier equals the incident energy. For all larger angles (smaller  $\mu$  values) the barrier is above  $E$ , and vice versa. Introducing the following definitions,

$$\delta B = \frac{2\pi}{\hbar\omega} (B_{90} - B_0) \quad (5)$$

and

$$\delta E = \frac{2\pi}{\hbar\omega} (E - B_{90}),$$

we can then write the resulting formulae as follows,

$$\text{I. } E < B_0: \quad \sigma_{\text{fusion}} = \frac{\hbar\omega}{E} \frac{R^2}{4} e^{\delta E} \int_0^1 d\mu e^{\mu^2 \delta B} \quad (6)$$

$$\text{II. } B_0 < E < B_{90}: \quad \sigma_{\text{fusion}} = \frac{\hbar\omega}{E} \frac{R^2}{4} \left\{ e^{\delta E} \int_{\mu_0}^1 d\mu e^{\mu^2 \delta B} + e^{-\delta E} \int_0^{\mu_0} d\mu e^{-\mu^2 \delta B} \right\} + \frac{\pi R^2}{E} \left\{ (E - B_{90})(1 - \mu_0) + 1/3 (B_{90} - B_0)(1 - \mu_0^3) \right\} \quad (7)$$

$$\text{III. } E > B_{90}: \quad \sigma_{\text{fusion}} = \frac{\hbar\omega}{E} \frac{R^2}{4} e^{-\delta E} \int_0^1 d\mu e^{-\mu^2 \delta B} + \frac{\pi R^2}{E} \left\{ (E - B_{90}) + 1/3 (B_{90} - B_0) \right\} \quad (8)$$

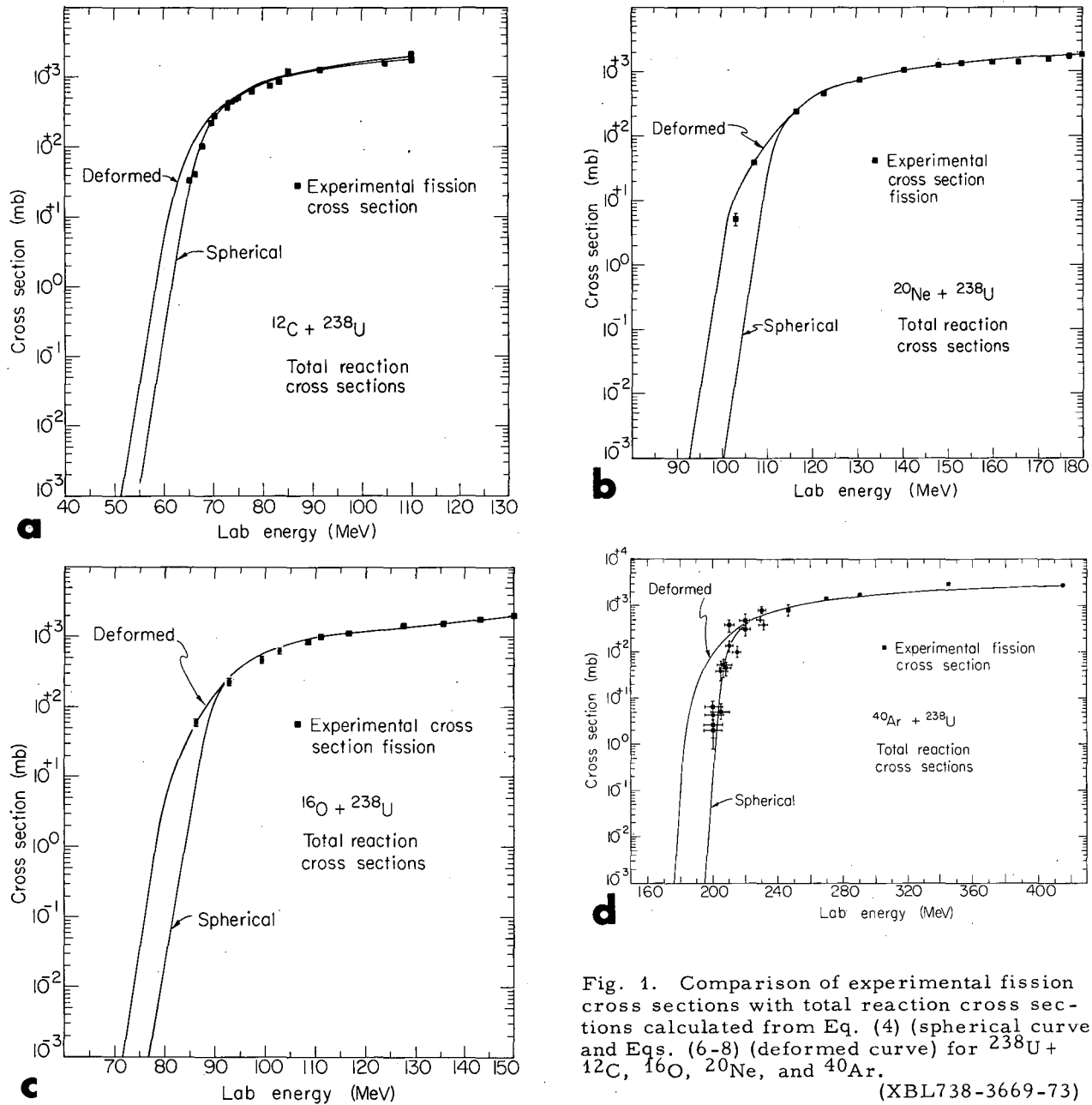


Fig. 1. Comparison of experimental fission cross sections with total reaction cross sections calculated from Eq. (4) (spherical curve) and Eqs. (6-8) (deformed curve) for  $^{238}\text{U} + ^{12}\text{C}$ ,  $^{16}\text{O}$ ,  $^{20}\text{Ne}$ , and  $^{40}\text{Ar}$ .  
(XBL738-3669-73)

In the limit of zero deformation, Eq. (8) reduces to Wong's equation, for  $E \gg B$ , but Eq. (6) is in error by a factor of 2 for  $E \ll B$ , because of the difference between our joined exponential functions and the Hill-Wheeler transmission formula at energies far below the barrier. The error is not serious, though, as the cross section varies by orders of magnitude for small energy changes in this region.

Calculations have been made using these formulae for comparison with experimental

fission cross sections for  $^{238}\text{U} + ^{12}\text{C}$ ,  $^{16}\text{O}$ ,  $^{20}\text{Ne}$ , and  $^{40}\text{Ar}$ . The first three were measured by Viola and Sikkeland,<sup>5</sup> the last by Sikkeland.<sup>6</sup> For the uranium target the difference between the total reaction cross section and the fission cross section is insignificant. Figure 1 shows these comparisons. Note that the C + U curves are identical to those shown in the last Annual Report.<sup>1</sup> There is a substantial predicted difference in barriers between the spherical and deformed calculations and in all cases except argon a set of parameters can be found which

consistently fits the available data to the deformed predictions. The deviation in the case of Ar+U is quite substantial. The increase in the barrier is in all probability due to phenomena outside the scope of our model which must be important for the interaction of two very heavy nuclei. These may be dynamical deformation effects causing a flattening of the poles, or Coulomb effects brought about by the fact that the shape of the touching nuclei at the moment of contact is outside the saddle point shape for the compound system so that more kinetic energy may be required to drive the nuclei together to cause fusion.<sup>7</sup>

It is clear that new models must be devised to explain interactions between very heavy nuclei, however we feel confident that our model is accurate and quite useful for total reaction cross sections for projectiles of  $Z \leq 10$ .

### References

1. J. Alonso, Nuclear Chemistry Annual Report 1972, LBL-1666, p. 124.
2. T. D. Thomas, Phys. Rev. 116, 703 (1959).
3. D. L. Hill and J. A. Wheeler, Phys. Rev. 89, 1102 (1953).
4. C. Y. Wong, to be published.
5. V. Viola and T. Sikkeland, Phys. Rev. 128, 767 (1962).
6. T. Sikkeland, Ark. Fyz, 36, 539 (1966).
7. W. Swiatecki and C. F. Tsang, private communication.

## ON SUBCOULOMB TRANSFER REACTIONS

M. A. Nagarajan

A detailed study of the systematics of nucleon transfer between heavy ions at low energies has been made by Buttle and Goldfarb.<sup>1</sup> They found that the recoil effects were important, especially for heavy targets, and suggested an approximate method for the inclusion of the recoil corrections. Their approximation relied on the assumption that the largest contribution to the transfer arises from a configuration where the nucleon to be transferred lies along the line joining the centers of mass of the heavy ions at their distance of closest approach.

An approximate treatment of recoil corrections had been suggested by the author<sup>2</sup> and had been applied to the analysis of spectroscopic factors in the reactions of proton transfer with <sup>12</sup>C and <sup>16</sup>O ions on <sup>208</sup>Pb target.<sup>3</sup> The analysis displayed the importance of the recoil effects in correctly predicting the  $j$  dependence<sup>4</sup> and the energy dependence of the transfer cross-section. Recently, the first order recoil correction has been calculated exactly<sup>5</sup> and it has been found that at projectile energies just greater than the Coulomb energy, the first order calculations agree very well with exact calculations.

We have tried to calculate the first order

recoil effects exactly in the case of subcoulomb transfer reactions. Following Buttle and Goldfarb,<sup>1</sup> we assume that the relative motion between the heavy ions can be approximated by a pure Coulomb function and use the identity that the gradient of the Coulomb function is given by

$$\vec{\nabla} \chi_c^{(-)}(\vec{K}, \vec{r}) = [-i\vec{K} + iK \frac{\vec{r}}{r} + K \vec{\nabla}_K \left(\frac{1}{r}\right)] \chi_c^{(-)}(\vec{K}, \vec{r}) \quad (1)$$

where  $\vec{\nabla}$  refers to a derivative with respect to the vector  $\vec{r}$ , while  $\vec{\nabla}_K$  refers to a derivative with respect to the vector  $\vec{K}$ . The above identity, Eq. (1), makes it simple to evaluate the first order recoil corrections, if one uses it in conjunction with the properties of Coulomb integrals enumerated by Buttle and Goldfarb.<sup>1</sup> One can show that the gradient of the Coulomb function has two components, one along the momentum vector  $\vec{K}$  and the other along the radial vector  $\vec{r}$ . The component along  $\vec{K}$  causes a change in the angular momentum selection rule, introducing the angular momentum due to recoil. It takes into account the fact that the two ions are in relative motion at the instant of transfer. The component along  $\vec{r}$  merely renormalizes the magnitude of the cross-section without affecting its angular dependence.

Buttle and Goldfarb had studied the properties of the Coulomb integrals and had predicted the transfer amplitude to have a symmetry direction along the direction of the momentum of the residual nucleus. If the residual nucleus were left in an excited state, a consequence of the above symmetry will be to predict the distribution of the de-excitation gamma ray to be symmetric around the direction of the recoil momentum of the residual nucleus. From Eq. (1), one can show that the effect of the recoil correction would be to breakdown the symmetry. It would be of interest to study the particle-gamma correlation in heavy ion induced transfer reactions.

Calculation incorporating the first order recoil corrections as exemplified by Eq. (1)

are now in progress.

### References

1. P. J. A. Buttle and L. J. B. Goldfarb, Nucl. Phys. A176, 299 (1971).
2. M. A. Nagarajan, Nucl. Phys. A196, 34 (1972).
3. D. G. Kovar et al., Phys. Rev. Letters 30, 1075 (1973).
4. D. G. Kovar et al., Phys. Rev. Letters 29, 1023 (1972).
5. A. J. Baltz, private communication.

## ON THE SYSTEMATICS OF THE INTERFERENCE BETWEEN DIRECT AND INDIRECT MODES IN TWO-NUCLEON PICKUP AND STRIPPING REACTIONS BETWEEN HEAVY IONS.\*

Norman K. Glendenning and R. J. Ascutto<sup>†</sup>

We reported earlier on the  $^{120}\text{Sn}(^{18}\text{O}, ^{16}\text{O})$  reaction which exhibited a strong destructive interference between the direct and indirect modes of exciting the  $2^+$  state in  $^{122}\text{Sn}$ .<sup>1</sup> Here we point out that the interference is of opposite sign in the stripping and pickup reactions to vibrational states. This is illustrated in Figs. 1 and 2 for both heavy and light tin isotopes. Since both direct and indirect modes have cross sections which are peaked near the grazing angle,<sup>1</sup> the interference can actually produce a dip at the grazing angle if the indirect amplitudes are sufficiently close in magnitude to the direct. This is calculated to be the case for the  $2^+$  state of the heavy tin isotopes (Fig. 1) where the dip is readily apparent for the stripping reaction. This is in contrast to the pickup reaction where the interference is constructive and the resultant cross section therefore has the "normal" shape. The indirect modes are calculated to be unimportant for the ground state transition. They are not as strong in the light isotopes even for the  $2^+$  and consequently no interference dip occurs there (Fig. 2).

At this point we note that the details of our results depend upon the structure of the nuclei. These calculations employed a two-quasiparticle description of the vibrational state.<sup>2</sup> An R. P. A. calculation could have produced quantitatively different results. However, both descriptions would have led to

an opposite sign of the interference for stripping and pickup though they would not necessarily agree on the absolute sign. The parentage amplitudes connecting the four states shown in Fig. 3 are given by Refs. 3 and 4.

$$\beta_{ab0}(\text{O}_A \leftrightarrow \text{O}_{A+2}) \approx \left(\frac{2j_a+1}{2}\right)^{\frac{1}{2}} V_a U_b \delta_{ab} \quad (1)$$

$$\beta_{abJ}(\text{O}_{A+2} \leftrightarrow \text{J}_A) = \left(\frac{2J+1}{1+\delta_{ab}}\right)^{\frac{1}{2}} [V_a V_b \psi_{ab} - U_a U_b \phi_{ab}] \quad (2)$$

$$\beta_{abJ}(\text{O}_A \leftrightarrow \text{J}_{A+2}) = -\frac{1}{1+\delta_{ab}} \left(\frac{1}{2}\right)^{\frac{1}{2}} [U_a U_b \psi_{ab} - V_a V_b \phi_{ab}] \quad (3)$$

$$\beta_{ab0}(\text{J}_A \leftrightarrow \text{J}_{A+2}) \approx \beta_{ab0}(\text{O}_A \leftrightarrow \text{O}_{A+2}) \quad (4)$$

where  $\beta$  is defined in general as

$$\beta_{abJ} = [2J_p + 1)(1 + \delta_{ab})]^{\frac{1}{2}} \langle \Phi_{J_p}(A+2) || [d_a^+ d_b^+] || \Phi_{J_p}(A) \rangle \quad (5)$$

where  $d_a^+$  creates a particle in the state  $n_a l_a j_a$ . In the production of the  $2^+$  state in both stripping and pickup reactions, transitions 1 and 4 are indirect, while 2 is the direct amplitude for pickup and 3 is the direct amplitude for stripping. The opposite sign of these amplitudes, 2 and 3, is what determines their

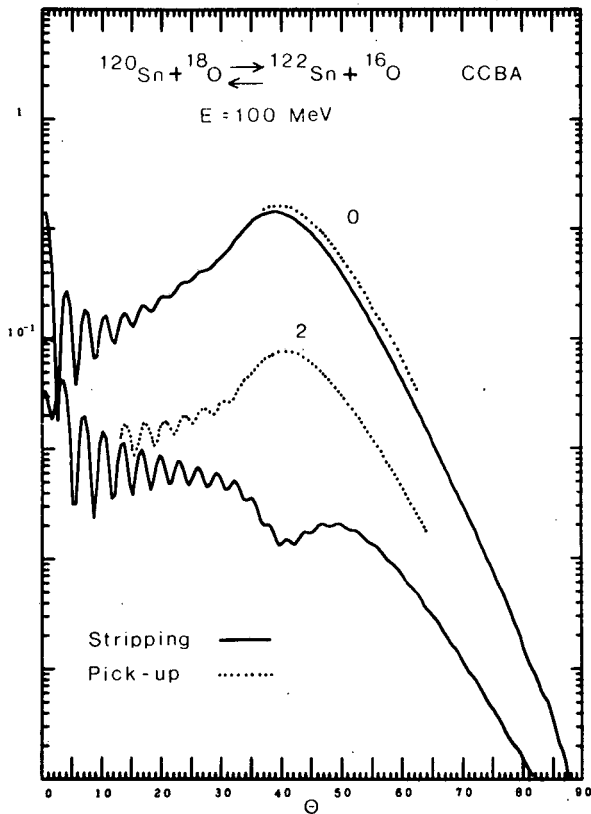


Fig. 1. The stripping and pickup cross sections for the ground state and  $2^+$  state, computed with direct and indirect transitions (CCBA). The indirect transitions almost cancel each other for the ground state. However, for the  $2^+$ , they interfere destructively with the direct transitions for the stripping reaction, producing the dip at the grazing angle. For the pickup reactions, they interfere constructively and preserve the characteristic peak at the grazing angle. The two ground state cross sections would be time-reversed reactions except for the finite  $Q$ -value and the use of the 100-MeV incident energy for each. (XBL-738-1086)

opposite interference characteristics with the direct modes.

The situation is different for production of the ground state. Both 2 and 3 are the lowest order indirect modes and since they are of opposite sign they tend to cancel each other accounting for the weak indirect contribution to the ground state transitions.

We have so far remarked on the opposite signs of the two parentage amplitudes. For two quasiparticle states (TDA) the  $\phi$  are zero

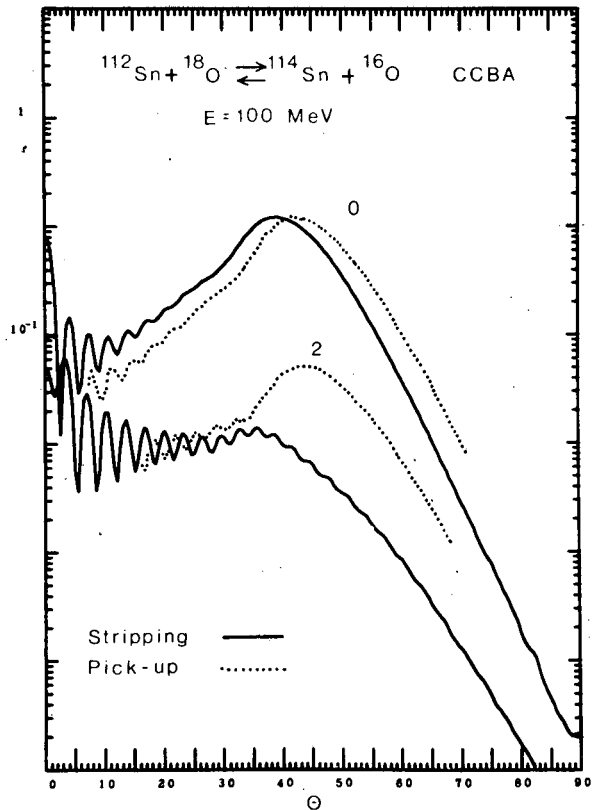


Fig. 2. This figure contains material analogous to Fig. 1 for the light end of the tin isotopes. Here the indirect transitions are weaker compared to the direct than was the case for the heavy isotopes of Fig. 1. Consequently the difference in the  $2^+$  states is smaller. Cross sections are in mb/sr. The top scale refers to the  $0^+$  and the bottom to the  $2^+$  state. (XBL-738-1087)

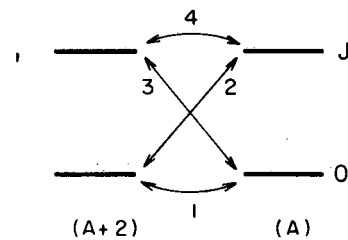


Fig. 3. The parentage amplitudes, Eqs. (1)-(4) correspond to the four connections shown here. The transitions 2 and 3 have opposite sign. Since they are each a segment of the two second-order transitions to the ground in both pickup and stripping, they tend to cancel each other, yielding a small second order contribution to the ground state. For the  $2^+$  state however, 2 is direct for a pickup reaction and 3 is direct for stripping, while 1 and 4 are segments of the second-order routes. The opposite sign of 2 and 3 implies opposite interference of direct and indirect transitions in stripping compared to pickup. (XBL-739-1244)

and the  $\psi_{ab}$  are to be identified with the quasi-particle amplitudes  $\eta_{ab}$  of our earlier paper.<sup>4</sup> In this case the absolute sign of the interference is that illustrated by our figures, and is destructive for stripping. However, the form of the parentage amplitudes admits a more complex behaviour. For example, through a series of isotopes the relative importance of  $\psi$  and  $\phi$  could change. At the same time the U and V factors are changing. It could then happen that the absolute sign of the  $\beta$ 's would be opposite for light and heavy members of an isotopic series, and that in the neighborhood of the change, the two amplitudes would not necessarily have opposite signs. A systematic study of pickup and stripping reactions throughout a series of isotopes (or isotones for proton transfer) is therefore likely to yield structural details that have not been accessible in other experiments.

#### Appendix

The parameters and nature of the calculation reported here were described in Ref. 1 except that here we generated single-particle states in a Woods-Saxon potential, all having a binding of one-half of the two neutron separation energy. These are used as the basic

states from which the nuclear states are built. Earlier we had used an average potential. The difference in the final results is slight.

#### References

\*To appear in Phys. Letters.

†Wright Nuclear Structure Laboratory, Yale University.

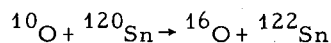
1. R. J. Ascutto and N. K. Glendenning, Phys. Letters 45B, 85 (1973) and Symposium on Heavy-Ion Transfer Reactions, Argonne, Ill. (1973) 513. Figure 9 in the Symposium also shows the effect of changing the sign of the interference.
2. R. Arvieu and M. Veneroni, Compt. Rend. 250, 992 (1960); R. Arvieu, Annales de Physique (Paris) 8, Series 13 (1963).
3. S. Yoshida, Nucl. Phys. 33, 685 (1962).
4. R. J. Ascutto and N. K. Glendenning, Phys. Rev. C2, 415 (1970).

## THE EFFECT OF INDIRECT TRANSITIONS ON TWO NUCLEON TRANSFER BETWEEN HEAVY IONS

Norman K. Glendenning and R. J. Ascutto\*

In this paper we report our calculation of the effect of indirect transitions on two-nucleon transfer cross sections between heavy ions. These processes involve an inelastic transition in the target or final nucleus as an intermediate step compared to the direct particle transfer from initial to final state. This work is a natural outgrowth of our earlier investigations on such effects on light nuclide induced reactions, where our calculations indicated strong higher order contributions.<sup>1</sup> This prediction was most dramatically confirmed in the case of (p, t) reactions on deformed nuclei.<sup>2</sup> It would be surprising if they did not play an important role in heavy ion reactions and the present note suggests they do, and proposes a very interesting Q-dependence of the ratio of indirect to direct amplitudes and of the shape of the angular distribution.

We have performed our calculation for the following reaction at 100 MeV.



First we describe briefly the nature of the structure of the nuclei which is relevant to this reaction. The ground state of  $^{18}\text{O}$  is treated as an inert core of  $^{16}\text{O}$  plus two neutrons which may occupy the  $s_{1/2}$ ,  $d_{3/2}$  and  $d_{5/2}$  orbitals in a Woods-Saxon potential which binds them at approximately the energies observed in  $^{17}\text{O}$ . The interaction matrix elements between pairs of neutrons in each of these configurations is assumed to be of the pairing force type of such a strength that the binding energy of the last two neutrons is correct. Two states of each tin nucleus are included, the ground and the collective  $2^+$  state. The former is described as a BCS vacuum state, and the latter as a collective two-quasi-particle state. The neutron orbitals of Sn are generated from a Woods-Saxon potential corresponding to the average parameters of Myers.<sup>3</sup> The form factor for the transfer of two nucleons based on these nuclear descriptions is shown in Fig. 1. The projected wave function, or form factor, is more complicated to obtain than in (t, p) reactions, because of the



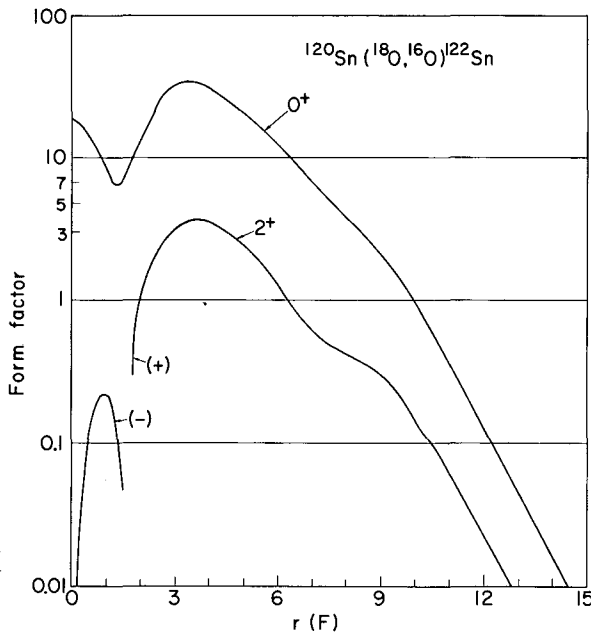


Fig. 1. The form factors for two neutron transfer from  $^{18}\text{O}$  to  $^{120}\text{Sn}$  for the ground and  $2^+$  states. The maximum occurs at approximately a separation distance between O and Sn corresponding to  $\odot$  lying along a radius of Sn. (XBL-733-2385)

necessity to retain the finite range of the interactions. It is defined by the following identity for transfer from the pure configuration  $(j^2)\text{O}$  in the projectile to the configuration  $(j_1 j_2)J$  in the residual nucleus:

$$\iint dr_1 dr_2 \psi_{(j_1 j_2)J}^{M^*}(r_1', r_2') \times \{V(r_1) + V(r_2)\} \psi_{(j^2)\text{O}}(r_1, r_2) \equiv U_J(R) Y_J^{M^*}(\hat{R}) \quad (1)$$

Here  $V$  is the Woods-Saxon potential which binds the neutrons in  $^{18}\text{O}$ ,  $R$  is the vector joining the core of the projectile ( $^{16}\text{O}$ ) to the target nucleus ( $^{120}\text{Sn}$ ),  $r_1$  and  $r_2$  are the coordinates of the two neutrons with respect to the projectile core, while  $r_1'$  and  $r_2'$  are their coordinates with respect to the target nucleus.

$$r_1' = r_1 + R. \quad (2)$$

For mixed configurations, such as we use, the form factor is obtained by weighting such form factors by the product of parentage amplitudes for the light and heavy nuclei involved. We note from Fig. 1 that the  $J=0$  form factor is

considerably bigger than the  $J=2$ . For this reason, we include only the monopole transition connecting the  $2^+$  states, although in principle they can be connected by  $J=2$  and 4 as well. The reduction of the left side of Eq. (1) to a form  $U_J(R)$  is complicated and we do not discuss it here.

The inelastic transitions are computed on the basis of the macroscopic vibrational model. The nuclear deformation parameter  $\beta_2$  for the tin isotopes are taken from an analysis of proton scattering.<sup>4</sup> We use the same optical model parameters as Becchetti et al.<sup>5</sup> in their analysis of  $^{16}\text{O} + ^{208}\text{Pb}$  scattering. These authors find the deformation parameter obtained in proton experiments consistent with their determination in the heavy ion experiment. For this reason we can have considerable confidence in our estimate of the strength of the inelastic processes. We determine the strength of the Coulomb quadrupole term in the interaction by using the experimentally determined<sup>6</sup> value of  $B(E2)$ . The nuclear and charge deformation are shown in Table I. The nuclear field is deformed according to

$$V[r-R(\theta)] = V(r-R) - \beta_2 R_T \frac{\partial V}{\partial R} Y_2(\theta) \quad (3)$$

where

$$R(\theta) = R_p + R_T [1 + \beta_2 Y_{20}(\theta)] \quad (4)$$

Table I. Nuclear and charge quadrupole deformation constants which are to be associated with radii of  $r_0 = 1.12$  and  $r_c = 1.2$ , respectively.

	$\beta_N$	$\beta_C$
$^{120}\text{Sn}$	0.13	0.112
$^{122}\text{Sn}$	0.124	0.118

corresponding to a spherical projectile of "radius"  $R_p$  and a vibrational target of radius  $R_T$ . Of course it is  $R_p + R_T$  which is to be identified with the optical model radius which is typically parameterized as  $r_0(A_p^{1/3} + A_T^{1/3})$ . It is the product  $\beta_2 R_T$  which is determined for us by the proton scattering experiment which the sum  $R_p + R_T$  is determined by the analysis of heavy ion elastic scattering. We have relied upon an extrapolation of the optical potential from Pb to Sn. We checked this by using an alternative potential determined by Morrison<sup>7</sup> for  $^{16}\text{O} + ^{48}\text{Ca}$ . These two rather different parameterizations are shown in

Table II. They yield elastic, inelastic and transfer cross sections which are virtually the same for fine and this gives us confidence that the results presented below do not contain any uncertainty attributable to optical model parameters or deformation.

Table II. Two sets of optical model parameters which yield virtually the same elastic and reaction cross sections for O+Sn at E = 100 MeV. The optical model radius is  $r_o(A_p^{1/3} + A_T^{1/3})$  and the charge radius is  $r_c A_T^{1/3}$ .

	V	W	$r_o$	$\alpha$	$r_c$
Becchetti <sup>5</sup>	-40	-15	1.31	0.45	1.2
Morrison <sup>7</sup>	-100	-40	1.22	0.5	1.2

In our calculations we include the inelastic coupling between the ground and collective  $2^+$  state in both tin nuclei, to all orders, and the first order particle transfer from the ground state of the target to both states of the final nucleus and the monopole transition from the  $2^+$  state of the target to the  $2^+$  state of the final nucleus. We do not consider those transitions in which either oxygen nucleus is excited. The method by which we include the indirect transition is the so-called source term method.<sup>8</sup>

The result of a coupled channel calculation for 100 MeV oxygen ions which includes the effects of inelastic excitation of the tin nuclei is shown in Fig. 2. The ground state is barely altered so we show no comparison, but the  $2^+$  state is strongly affected by the additional modes of excitation. In particular, the direct transition, shown by a dashed line, interferes destructively with the indirect modes of excitation and produces an angular distribution in which the expected peak at the grazing angle is absent. Instead a poor angular resolution experiment would observe a monotonically decreasing distribution, fairly flat at first, and then falling rapidly after the grazing angle, or peak in the ground state cross section. This is in marked contrast with the DWBA prediction.

Of course there is a continuous evolution from the dashed curve to the solid as a function of deformation constants  $\beta$ , or collectivity of the intermediate states. As remarked earlier, we determined the appropriate values from other experiments, and such values, listed in Table I, were used in the calculation shown in Fig. 2.

The Q value of this reaction is 2.8 MeV. It is interesting to know how the balance between direct and indirect amplitudes depends on Q, since as is well known, the magnitude of the cross sections depend strongly on the

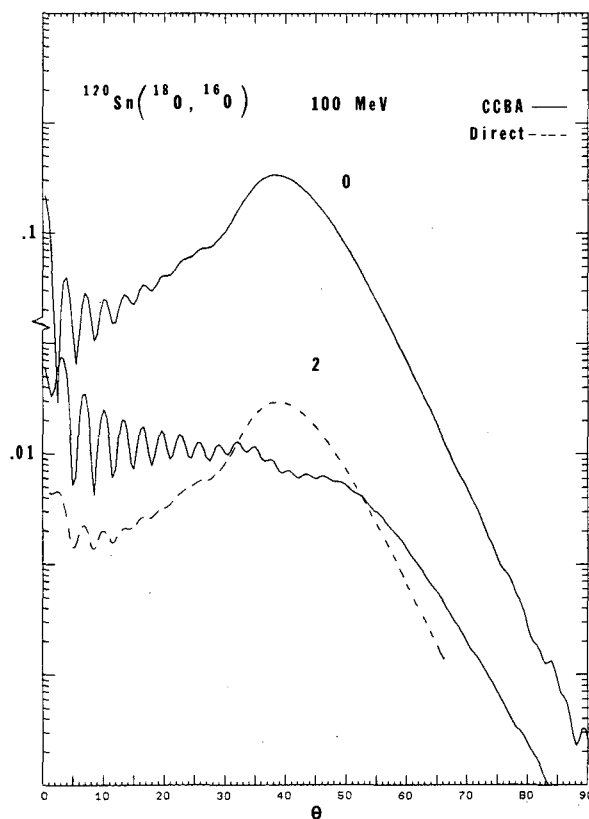


Fig. 2. Differential cross section in mb/sr for exciting the ground and  $2^+$  states in  $^{122}\text{Sn}$ , computed in the coupled channel calculation in which the direct and indirect routes are included. Compare with the direct route alone for the  $2^+$  state. For the ground, the direct route is almost the whole contribution so no comparison is shown. (Note that the scale is split for the two levels.) (XBL-733-249)

Q. In Fig. 3 we show what would result if the Q had the less favorable value of -6 MeV. Comparing with Fig. 2 we see that the ground state cross section and the direct cross section to the  $2^+$  cross section has fallen only by about a factor of 30. This indicates that the indirect amplitudes are not attenuated as strongly as the direct in unfavorable Q situations.<sup>9</sup> Also we note that the shape of the  $2^+$  cross section has changed considerably in comparison with Fig. 2 owing to a change in angular distribution of the indirect amplitudes.

From this comparison we learn that, other things being similar, an unfavorable Q value emphasizes the contribution of multiple step transitions to particle transfer.

In the present calculation the excited  $2^+$

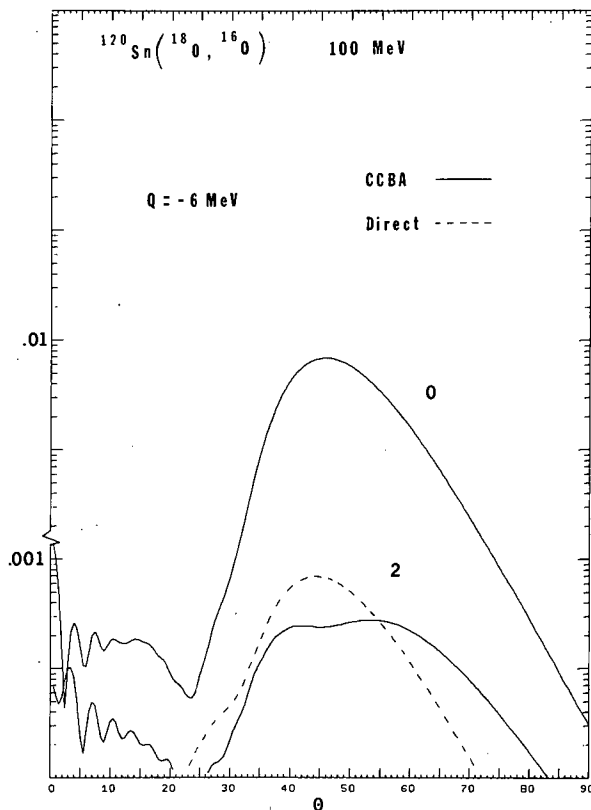


Fig. 3. Fictitious situation with  $Q$  of reaction changed from correct value of 2.8 MeV to -6 MeV. Compare with Fig. 2, noting that the direct contribution to the  $2^+$  state has been drastically attenuated by the unfavorable  $Q$ , while the overall cross section which includes the indirect routes is much less affected.

(XBL-733-252)

state is strongly effected by the indirect transitions while the ground state is not. This can be understood in terms of the stronger  $J = 0$  form factor shown in Fig. 1 which favors the  $O(A) \rightarrow 2(A) \rightarrow 2(A+2)$  transition over the direct  $O(A) \rightarrow 2(A+2)$ . However, in other nuclei, the  $J = 2$  form factor may be larger than the  $J = 0$  which could then cause the indirect transition  $O(A) \rightarrow 2(A+2) \rightarrow O(A+2)$  transition to be more important than the direct ground state transition. This would lead to a reversal of the situation in tin.

On the basis of these calculations we suggest that, under appropriate circumstances, higher order processes will be very strong in

heavy ion particle transfer reactions. The simple angular distribution which consists of a strong peak at a grazing is characteristic of single-step transition. The contribution of indirect transitions changes this, leading to a fairly flat distribution to the grazing angle, and then falling off. We found that the ratio of indirect to direct transitions increases as the  $Q$  value departs from the optimum value, suggesting that such effects will be seen in experiments on a series of isotopes for which the  $Q$  value changes over a few MeV.

#### Footnotes and References

\*Wright Nuclear Structure Laboratory, Yale University, New Haven.

1. R. J. Ascutto and N. K. Glendenning, Phys. Rev. C 2 (1970) 1260; N. K. Glendenning and R. S. Macintosh, Nucl. Phys. A168 (1971) 575.
2. R. J. Ascutto, N. K. Glendenning and B. Sorensen, Phys. Rev. Lett. 34B (1971) 17; Nucl. Phys. A183 (1972) 60; T. Tamura et al., Phys. Rev. Lett. 25 (1970) 1507 and errata 26 (1971) 156.
3. W. D. Myers, Nucl. Phys. A145 (1970) 387; table 1.
4. O. Beer et al., Nucl. Phys. A147 (1970) 326 table 2 and 9.
5. F. D. Becchetti et al., Phys. Rev. C 6 (1972) 2215.
6. P. H. Stelson and L. Grodzins, Nuclear Data A1 (1965) 21.
7. G. C. Morrison, J. de Phys. 32 (1971) No. 11-12.
8. R. J. Ascutto and N. K. Glendenning, Phys. Rev. 181 (1969) 1396; Phys. Rev. C 2 (1970) 415, and Nucl. Phys. A188 (1972) 185.
9. From consideration of classical Coulomb trajectories one expects a  $Q$ -dependence of the form  $\exp(-\alpha|Q-Q_{\text{opt}}|^2)$ .<sup>10</sup> If the reaction goes in two steps with associated values  $Q_1$  and  $Q_2$  so that  $Q = Q_1 + Q_2$ , then the same consideration leads to a  $Q$ -dependence which is like  $\exp(-\alpha|Q_1 - Q_{\text{opt}}|^2 - \alpha|Q_2 - Q_{\text{opt}}|^2)$ . The latter is much more favorable than the former especially if  $Q_1 \sim Q_2$ .
10. D. M. Brink, Phys. Letters 40B (1972) 37.

THE SENSITIVITY OF THE FORWARD CROSS SECTION  
IN TRANSFER REACTIONS BETWEEN HEAVY IONS  
TO THE EDGE OF THE NUCLEAR FIELD\*

Norman K. Glendenning and R. J. Ascutto<sup>†</sup>

In this note we focus attention on the cross section in heavy ion reactions at angles smaller than the grazing angle,  $\theta_g$ . Under classical subcoulomb conditions, such scattering events would correspond to large impact parameters or distant collisions where the field is weak and causes little deflection. Of course, distant orbits cannot very effectively contribute nucleon transfer reactions, especially when more than one nucleon is transferred, because of the exponential decay of the bound state wave functions. However, in the classical scattering of particles in a field, such as that which acts between heavy ions, there exist also small impact parameter orbits which lead to forward scattering, for energies above the barrier, as was pointed out long ago by Ford and Wheeler.<sup>1</sup> Nuclei on such orbits can very easily transfer particles. They are, however, subject to absorption, because of their close encounter.

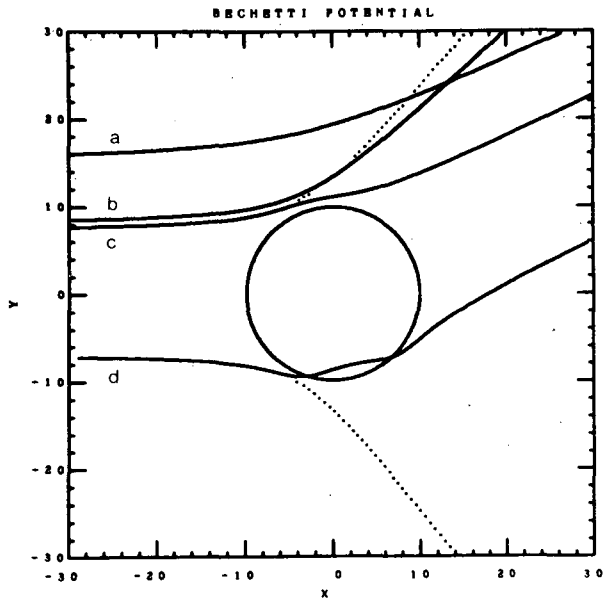


Fig. 1. Four classical orbits in the real part of the potential of Table I are plotted, three of which, having impact parameters a, c and -d, ( $d < c$ ) scatter to the same angle  $\theta$ . The orbit b feels a stronger repulsion than a and therefore scatters to a larger angle. The circle marks the half value of the Woods-Saxon nuclear potential. The orbits are for  $^{18}\text{O}$  scattered by  $^{120}\text{Sn}$  at 100 MeV lab energy. Dotted lines show pure Coulomb orbits.

(XBL 7310-1381)

However, this is precisely our interest in them. We claim that forward angle scattering in transfer reactions can be used as a very sensitive probe of the edge of the nuclear potential acting between heavy ions.

The situation is illustrated schematically in Fig. 1. The distant orbit, a, is only slightly deflected by some small angle,  $\theta$ , say. A closer orbit, b, since it feels a stronger repulsive field, is scattered to a larger angle.

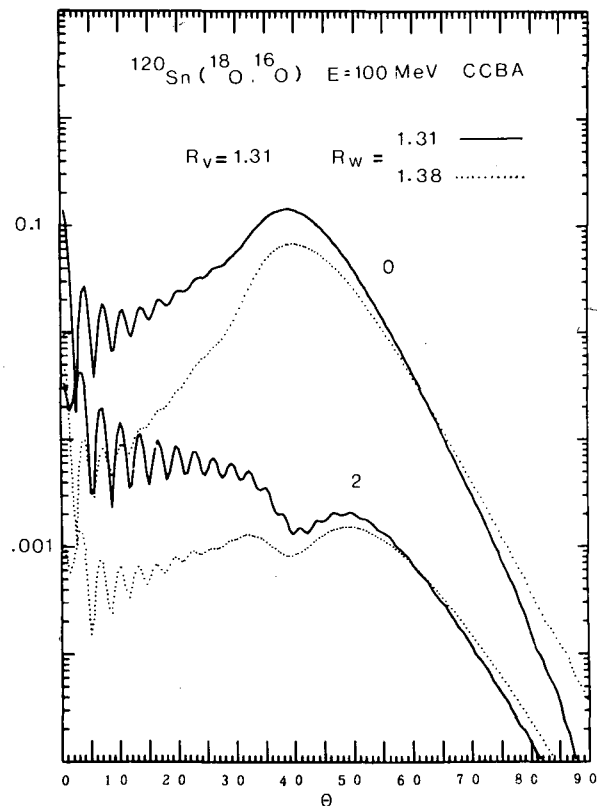


Fig. 2. Differential cross sections for the  $0^+$  and  $2^+$  state are compared for two values of the radius of the imaginary potential one of which (dotted curve is 5% larger than the other). The shape of the  $2^+$  cross section has been strongly altered from the classical shape exhibited by the  $0^+$  by strong two-step processes which interfere destructively with the direct for stripping reactions as discussed in Ref. 2. Cross sections are in mb./sr. and the two scales refer respectively to the  $0^+$  and  $2^+$  states.

(XBL 739-1249)

However, the two closer orbits c and d ( $d < c$ ) feel a net attraction and scatter to the same angle  $\theta$  as a. The orbits such as c and d are the ones of interest here.

In Fig. 2 we show calculated cross sections for the reaction  $^{120}\text{Sn}(^{18}\text{O}, ^{16}\text{O})^{122}\text{Sn}$  leading to the ground and collective  $2^+$  state in  $^{122}\text{Sn}$ , for  $E = 100$  MeV, an energy significantly above the coulomb barrier ( $\sim 50$  MeV). The solid lines correspond to the optical model parameters listed in Table I. The ground state cross section shows the characteristic peak at the grazing angle while the  $2^+$  cross section exhibits a dip there due to destructive interference between direct and indirect modes of producing this state. This we have discussed separately.<sup>2</sup> The comparison we wish to make is with the dashed curve, which corresponds to a 5% increase in the radius of the imaginary potential. We see that this very modest change in the potential results in a difference in the ratio of forward to grazing angle cross section of more than a factor of 10, which is a very large amplification factor. (If the forward angle cross section for the ground state is hard to measure experimentally, because of low cross section, we suggest a wide angle encounter to integrate out the ripples and speed up data taking.)

Table I. Optical Potential Parameters: the radius of the nuclear part is  $r_o(A_P^{1/3} + A_T^{1/3})$  and the charge radius  $r_c A_T^{1/3}$

V	W	$r_o$	a	$r_c$
-40	-15	1.31	.45	1.2

Of course the question immediately comes to mind as to whether the effect of changing the radius of the imaginary potential relative to the real might not be more easily detected in the elastic cross section. This is not the case as shown in Fig. 3 where we see a high precision experiment would be required to distinguish the two cross sections. Even then the multiple ambiguities in the optical model fit to elastic cross sections might not yield a unique determination. Nor would inelastic cross sections, or one nucleon transfer reactions be as appropriate for the measurement of this effect. For in such reactions, distant orbits, a, would make a larger contribution to the forward angle cross section, thus masking the effect produced on the close orbits c and d by the edge of the nuclear potential.

Since the de Broglie wave length of the

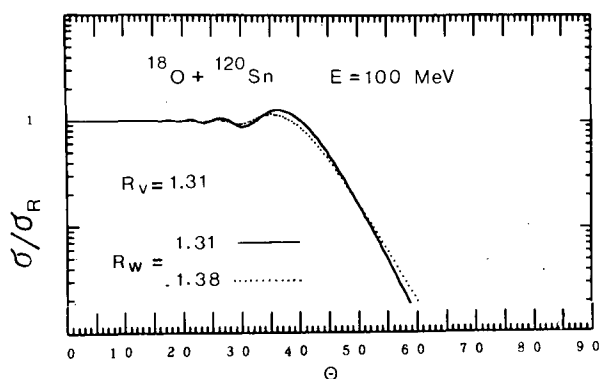


Fig. 3. The elastic cross sections in the entrance channel corresponding to the reaction of Fig. 2 for the two cases there, showing the weak sensitivity of the elastic cross section to  $R_v - R_w$  compared to the two-nucleon transfer cross section. The optical model parameters are listed in Table I for the solid line.

(XBL 739-1248)

relative motion between heavy ions in typical collisions is very short compared to the nuclear dimensions, there is a close correspondence between impact parameter and angular momentum. This makes it especially interesting to examine the S matrix elements as a function of L. We anticipate being able to relate rather directly, changes in such a plot to changes in the interaction region, such as potential radii or slope of the tail of bound state wave functions of transferred particles. Such a plot for the transfer reaction leading to the ground state of  $^{122}\text{Sn}$  is shown in Fig. 4, and corresponds to the cross section shown by a solid line in Fig. 2. The absolute value of the S matrix element is plotted versus integer values of L. These points are joined exhibiting a very smooth behavior of S. The sudden fall on the low side of the peak corresponds to the sudden onset of absorption.<sup>3</sup> The slower fall off on the high L side is governed by the tail of the transfer form factor. The points plotted on the figure indicate S matrix values in the case where the imaginary radius has been increased by 5% (dotted line of Fig. 2). Here as anticipated we see the lower L region is affected but not the higher region.

It is also noteworthy that the peak in the S matrix is very little affected by the change in imaginary radius, whereas our calculations (not shown) indicate a considerable shift if the real radius is also increased. We conclude that the trajectories are principally determined by the real potential, while the imaginary potential produces little deflection.

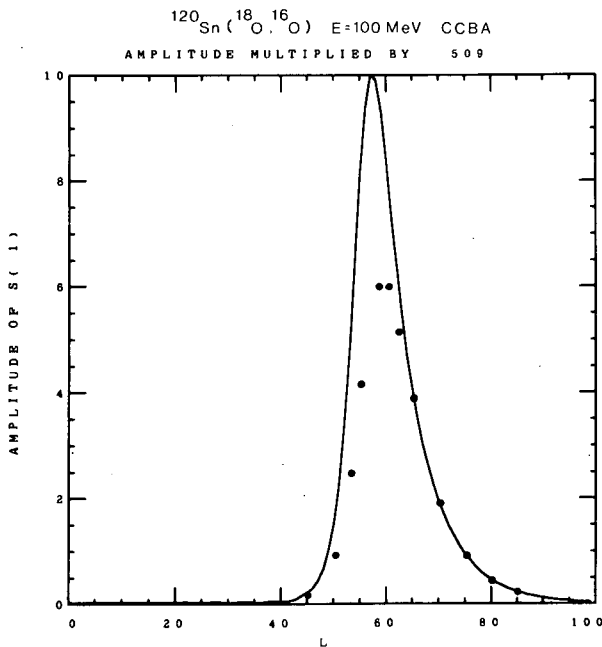


Fig. 4. The absolute value of the S matrix elements for the  $0^+$  state are plotted as a function of  $L$  and the points (for integer  $L$ ) joined. The solid lines of this and Fig. 2 correspond as do the dots. (XBL 7310-1382)

The forward angle ripples in the differential cross section are, we believe, the result of interference between pairs of close impact orbits from opposite sides of the nucleus, such as  $c$  and  $d$  in Fig. 1. This phenomenon is likely to be very general for heavy ion transfer reactions, especially where more than one nucleon is transferred, for it depends only on a sufficiently high localization in  $L$ . The frequency of the ripples is determined by the angular momentum  $L_0$  corresponding to the peak in the S matrix (angle between peaks is  $\Delta\theta = \pi/L_0$ ). Indeed, if the S matrix were a delta function  $\delta(L - L_0)$ , then the angular distribution

would be given by  $|Y_{L_0}(\theta)|^2$ . The ripples will be damped according to the width  $\Delta L$  of  $S$ . So, for example, we see that the ripples are more damped in the dotted curve of Fig. 2 corresponding to widths at half maximum of  $\Delta L = 14$  and 11, respectively, for the dotted and solid S matrix shown in Fig. 4.

To summarize, the ratio of the cross sections of two-nucleon transfer reactions, measured at forward angle and at the grazing angle, is a very sensitive probe of the relationship between the radius of the real and imaginary nuclear potentials. Such measurements should prove very useful in determining the details of the potential at the edge, which is of decisive importance in predicting cross sections of heavy ion reactions. The location of the edge of the imaginary potential relative to the real is also important in connection with the question of nuclear molecules. However, this kind of measurement should be made for the  $0^+$  state since it is very little affected by second-order processes. In contrast, second-order processes can strongly alter the forward cross-section, and are responsible for the forward peak in the  $2^+$  state.<sup>2</sup>

#### Footnotes and References

\* Physics Letters, **48B**, 6 (1974).

† Wright Nuclear Structure Laboratory, Yale University, New Haven, CT.

1. K. W. Ford and J. A. Wheeler, *Ann. of Physics* (N. Y.) **7** (1959) 259.
2. R. J. Ascutto and N. K. Glendenning, *Symposium on Heavy-Ion Transfer Reactions*, Argonne (1973) 513; *Phys. Letters* **45B** (1973) 85.
3. We use absorption only to mean loss to other channels than the elastic, inelastic and transfer channels explicitly treated in the calculation: We do not imply fusion!

## ABRASION AND ABLATION OF HEAVY IONS\*

J. D. Bowman,<sup>†</sup> W. J. Swiatecki, and C. F. Tsang

We have begun exploring some simple interpretations of the Bevatron Heavy Ion experiment. The particular data we are concerned with are those of Heckman, Lindstrom, Greiner, and Bieser.<sup>1</sup> In their experiments, a beam of  $^{16}\text{O}$  with 2.1 GeV/nucleon is passed through a target, and the cross-section is measured for the conversion of  $^{16}\text{O}$  into various secondary beams corresponding to a loss of 1, 2, 3 protons and also for removing  $^{16}\text{O}$  entirely from the beam.

The range of targets used was H, C, S, Cu, and Pb. In addition to  $^{16}\text{O}$  beams,  $^{12}\text{C}$  and  $^4\text{He}$  beams were also studied. In other experiments the isotopic composition of the emerging secondary beams and other fine details were analyzed, but we have limited our studies to understanding these cross-sections.

An obvious question arises: Can these data be understood in terms of a shearing off of a piece of the  $^{16}\text{O}$  as it zooms through the target material? For example, what cross-sections does one predict if one assumes nuclei to be sharp spheres with an equivalent sharp radius of  $r_0 A^{1/3}$  ( $r_0 \approx 1.2 F$ ), and that the  $^{16}\text{O}$  is such a sharp sphere (radius  $R_1$ ) which gets a piece gouged out of it every time it encounters a Pb target nucleus (radius  $R_2$ )? The calculation is of course, rather trivial. It involves two steps. First we want to calculate the relative volume  $\Delta Z/Z$  of the oxygen swept out by the Pb, the geometrical problem of the volume of intersection of a cylinder of radius  $R_2$  with a sphere of radius  $R_1$ . We call this process abrasion, with  $Z_{abr}$  giving the number of protons swept out. The answer will be a function of the impact parameter  $b$ , the distance between the line of motion of the  $^{16}\text{O}$  and the center of the Pb target nucleus.

Secondly, the remaining nucleus after the abrasion has a concave cylindrical surface where there used to be a convex spherical surface. Its surface energy is quite a few MeV higher than that of its ground state spherical shape. This extra energy will frequently be dissipated by the emission (evaporation) of neutrons, protons, or  $\alpha$  particles, in times of  $10^{-17}$  or  $10^{-18}$  sec. From the geometry of the gouged out remaining nucleus we can calculate its excess surface energy, say  $\Delta E_s$ . (The surface energy of nuclei is known as about 1 MeV/ $F^2$ .) It takes about 10 MeV to evaporate a nucleon, so the average number of protons

evaporated will be about

$$\Delta Z_{abl} \sim \frac{\Delta E_s}{20 \text{ MeV}}$$

So the final number of protons lost is

$$\Delta Z(b) = \Delta Z_{abr}(b) + \Delta Z_{abl}(b)$$

where the first part follows from the geometry of the volume sheared off and the second from the geometry of the area sheared off. A typical abrasion-ablation curve is shown in Fig. 1 as a function of the overlap depth  $l$  in fermi.

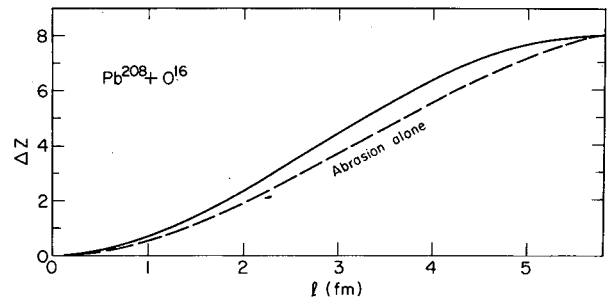


Fig. 1. Abrasion-ablation curve for 2.1-MeV/N  $^{16}\text{O}$  on  $^{208}\text{Pb}$ , showing the number of protons stripped off the  $^{16}\text{O}$  nucleus as a function of overlap depth  $l$ . The broken line is the result when only abrasion is considered. The full line is the result with the inclusion of ablation.

(XBL-737-3325)

We can now calculate the range of impact parameters  $b_{\text{lower}} < b < b_{\text{upper}}$  for removing say, one proton from the  $^{16}\text{O}$  and then calculate the cross section for producing nitrogen from oxygen by

$$\sigma(0 \rightarrow N) = \pi \left( b_{\Delta Z=1.5}^2 - b_{\Delta Z=0.5}^2 \right)$$

Nothing is adjustable in such a calculation and one wonders what will come out, 10 mb, 100 mb, or 1000 mb to compare with the 323 mb for the case of Pb as a target. How will the answer depend on target mass?

Table I summarizes the experimental results together with our estimates at this stage of the game (using  $r_0 = 1.2$ ). The following points are observed:

1. Calculated cross sections are in the right ballpark, but are

Table I.

	<u>H</u>	<u>C</u>	<u>S</u>	<u>Cu</u>	<u>Pb</u>
$^{16}\text{O} \rightarrow \text{N}$	$\sigma_1 = 64 \pm 11\%$ (121)*	$104 \pm 6\%$ (208)	$121 \pm 8\%$ (263)	$164 \pm 7\%$ (299)	$323 \pm 7\%$ (419)
$^{16}\text{O} \rightarrow \text{C}$	$\sigma_2 = 58 \pm 14\%$ (67)	$130 \pm 5\%$ (130)	$139 \pm 8\%$ (181)	$190 \pm 6\%$ (219)	$258 \pm 7\%$ (286)
$^{16}\text{O} \rightarrow \text{B}$	$\sigma_3 = 34 \pm 17\%$ (45)	$61 \pm 8\%$ (97)	$73 \pm 10\%$ (142)	$86 \pm 9\%$ (175)	$123 \pm 11\%$ (239)
$^{16}\text{O} \rightarrow \text{not O}$	$\sigma_{\text{Tot}} = 315 \pm 7\%$ (343)	$935 \pm 2\%$ (743)	$1310 \pm 4\%$ (1100)	$1820 \pm 2\%$ (1500)	$3100 \pm 2\%$ (2700)

\* Numbers in parentheses give the calculated cross-sections according to a "clean-cut" version of abrasion-ablation theory, (assuming sharp surfaces for the nuclei).

2. Too high by a factor of about 2 for  $\text{O} \rightarrow \text{N}$ ,  $\text{O} \rightarrow \text{B}$ , not so much for  $\text{O} \rightarrow \text{C}$  (an odd-even effect that might be associated with the odd-even variations of nucleon binding energies, which would influence the evaporation), and
3. Total cross sections are too low.

While the cross-section predictions are generally in the right ballpark, the second and third observations imply, on closer examinations (not described here), a very serious deficiency in the model examined so far.

This kind of discrepancy is what one would arrive at by examining the physics of the collision more closely. When a nucleon or even a collection of extremely energetic nucleons zips through  $^{16}\text{O}$  one does not really expect a piece of the  $^{16}\text{O}$  to be ripped off instantaneously. What one expects is for the fast nucleon(s) to zip through, leaving behind recoiling target nucleons and ( $\pi$ ) mesons. The recoil velocities are smallish (50-100 MeV we are told) so on a fast time scale nothing much happens at first. The region of overlap (the swiped region) far from having been swept clean, is a region where energy and even rest mass (of the pions) has been deposited. Moreover the directions of the recoiling nucleons and pions are not well collimated forward; the partners of elastic n-n collisions actually go mostly at angles close to  $90^\circ$  to the beam. So what one has is a hot region (a bruise) with 50-100 MeV nucleons and

pions radiating out. Those directed away from the  $^{16}\text{O}$  will indeed escape, but others, perhaps half, will irradiate the  $^{16}\text{O}$ , heat it up and make it lose more nucleons than one had thought.

So our present tendency is to go away from a clean-cut abrasion to a dirty, gangrenous bruise that develops into a boil (and raises the patient's temperature). The end result is the loss of a leg from a bruised foot!

To develop a theory of such a process there seem to be two necessary elements:

1. A phenomenological theory of the deposition of mass, energy and momentum in the swiped region (the bruise). Perhaps the concept of a volume friction will be useful.
2. The dispersal of the bruise: partly by direct sublimation and partly by transfer of energy to the oxygen and subsequent evaporation.

Figure 2 is an attempt to imagine what the result might be of carrying out a calculation in which two fast nuclei (comparable in size) collide and the energy (and momentum) dissipation is described by a friction term which is a function of the overlap of the two density distributions  $\rho_1(\vec{r})$  and  $\rho_2(\vec{r})$ . For example, one might try to describe the rate of energy dissipation (i. e., energy taken out of the collective kinetic energies and converted into internal excitations



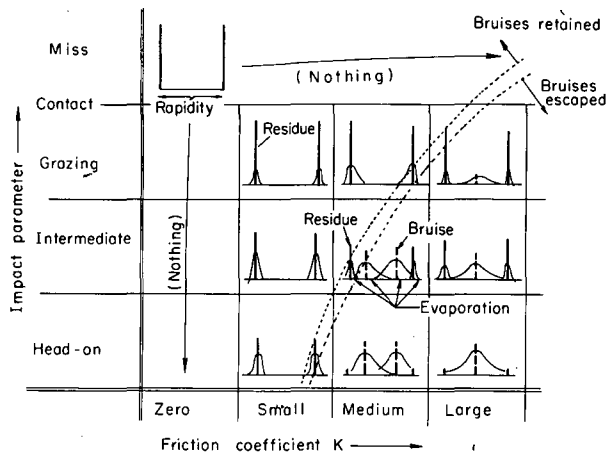


Fig. 2. Rapidity diagrams for various impact parameters and frictional strength. See text for details. (XBL-737-3448)

and meson production) by a term of the form

$$\frac{dE}{dt} = -K \int \rho_1(\vec{r}) \rho_2(\vec{r}) f(\vec{v}_{12}^2) d^3\vec{r}$$

Here  $f$  is some increasing function of the square of the relative velocity  $\vec{v}_{12}$  between the mass elements of the two fragments at the point  $\vec{r}$  and  $K$  is a friction or dissipation coefficient.

Figure 2 shows a set of 10 velocity (or rapidity) diagrams representing various possible results of such a collision as a function of the impact parameter and the magnitude of the friction coefficient  $K$ . If the impact parameter is greater than the contact value, or if  $K=0$ , there is essentially no interaction and the rapidity diagram shows two delta functions corresponding to the unperturbed projectile and target.

At the other extreme, if two comparable nuclei collide head on and the friction is large enough to soak up all the kinetic energy (i.e., the nuclei are brought to rest in the center of mass frame), one would find a single fireball centered in the middle of the rapidity plot, though there might be a large spread extending even to the edges of the rapidity diagram.

If  $K$  is imagined decreased (but we still confine ourselves to a head-on collision) then

the two nuclei will begin to pass through each other, but with reduced velocities. The single central hump in the rapidity diagram will then split into two humps, which move to the edges of the diagram as the friction goes to zero.

On the other hand if the friction is kept large but the impact parameter is increased, one expects the overlapping portions of the nuclei (the bruises) to be brought to rest but the nonoverlapping portions to keep going with approximately their initial velocities. One would then see three humps in the rapidity diagram, two at the edges and one in the center. The area of the central hump representing the stopped overlapping region would go to zero as the impact parameter tends to the contact value.

If, with an intermediate impact parameter, the friction is decreased, then the overlapped portions of the nuclei will not be brought to rest but will pass through each other with diminished velocities. One then expects four humps as shown in the central one of the  $3 \times 3$  set of pictures in Fig. 2. As the friction coefficient  $K$  is decreased, the two middle humps move out towards the edges. At some critical value of  $K$  there will in fact come a stage where the momentum deposited in the bruises by the frictional force is not large enough to tear them away, and below that critical value only the side humps would be present. The critical friction at which this happens would be a function of the impact parameter, and the dotted line across Fig. 2 is meant to be an indication of the existence of such a critical locus.

The widths of all the humps are not intended to be to scale. Evaporation from the excited residues or bruises would be one factor contributing to the widths, but other dynamical or pre-equilibrium processes might be equally or more important.

#### Footnotes and References

\* Summary of contribution to the Berkeley Summer Study on High Energy Heavy Ion Reactions, 1973, LBL-2908.

† Present address: Los Alamos Scientific Laboratory, Los Alamos, NM.

1. H.H. Heckman, P.J. Lindstrom, D.E. Greiner, F.S. Bieser, Lawrence Berkeley Laboratory preprint. (The data in the preprint is preliminary).

## RELATIVISTIC HEAVY-ION ELASTIC SCATTERING

W. L. Wang and R. G. Lipes\*

We investigate relativistic heavy-ion scattering in terms of a coherent droplet model, where the colliding nuclei are treated as droplets of nuclear matter with no internal structure. The interaction between nuclei is assumed to be proportional to the amount of interpenetrating matter. We take the matter distribution from electron scattering experiments, and relate the interaction parameter by the optical theorem to the total cross section.

The model we use is the coherent-droplet model first proposed by Chou and Yang<sup>1</sup> in their discussion of elementary particle scattering. We have the S-matrix at impact parameter  $b$  as

$$S(\vec{b}) = \exp \left[ ix \int d^2b' \rho_A(\vec{b}') \rho_B(\vec{b} - \vec{b}') \right] \quad (1)$$

where  $x$  is a constant and  $\rho(\vec{b})$  are the two-dimensional densities (or the blackness of the objects).<sup>5</sup> The complete elastic scattering amplitude is

$$F(\vec{q}) = \frac{ik}{2\pi} \int d^2b \exp[i\vec{q} \cdot \vec{b}] \{1 - S(\vec{b})\} \quad (2)$$

where  $\vec{q}$  is the momentum transfer,  $k$  is the incident momentum, and  $q^2 = 2k^2(1 - \cos \theta)$ . We may convert Eqs. (1) and (2) into a partial wave scattering amplitude by introducing the following correspondence:  $(kb \leftrightarrow l + 1/2)$ , and write the partial wave amplitude  $S(b) \rightarrow S_l(k)$  as

$$S_l(k) = \exp \left[ ix \left( \frac{k^2}{2\pi} \right) \int d(\cos \theta) P_l(\cos \theta) G_A(q) G_B(q) \right] \quad (3)$$

where  $G(q)$ 's are the nuclear form factors, the complete scattering amplitude  $F(q)$  is then

$$F(q) = \frac{1}{2ik} \sum_l (2l+1) \{S_l(k) - 1\} P_l(\cos \theta) \quad (4)$$

The total cross section is given by the optical theorem as

$$\sigma_{\text{tot}}(k) = \frac{4\pi}{k} \text{Im}[F(q=0)] \quad (5)$$

In the asymptotic energy region, the total cross section may be taken to be simply the geometric value:

$$\sigma_{\text{tot}} = 2\pi(R_A + R_B)^2 \quad (6)$$

where  $R_A$  and  $R_B$  are the radii of the colliding nuclei.

Before we discuss our results, we would like to recall the diffraction pattern of black-sphere scattering, where the ratio of the differential cross sections is given simply by

$$\left( \frac{d\sigma}{dt} \right) / \left( \frac{d\sigma}{dt} \right)_{t=0} = 4 \left| \frac{J_1(qR)}{qR} \right|^2, \quad (7)$$

where  $J_1(qR)$  is the first order Bessel function. The effective radius is  $R=R_1+R_2$ . Equation (7) displays the well known Fraunhofer diffraction. We shall see that in the case of nucleus-nucleus and particle-nucleus collisions, this diffraction pattern is very rapidly attained, especially when the nucleus has a relatively sharp surface region.

Since the diffraction pattern may be determined approximately by Eq. (7), it is also interesting to mention an approximate scaling for the forward differential cross section. Let us denote the forward scattering cross sections of nuclei 1 and 2, and nuclei 3 and 4 by  $(d\sigma_{12}/dt)_{t=0}$  and  $(d\sigma_{34}/dt)_{t=0}$  respectively. For the black-sphere scattering, the optical theorem and Eq. (6) give

$$\frac{(d\sigma_{12}/dt)_{t=0}}{(d\sigma_{34}/dt)_{t=0}} = \frac{(R_1 + R_2)^4}{(R_3 + R_4)^4} \quad (8)$$

Equations (7) and (8) provide us with a useful relation for a first-order estimate of any heavy-ion elastic scattering at high energies.

We have performed calculations at incident kinetic energies of 2.1 GeV/nucleon for  $^4\text{He}$ ,  $^{12}\text{C}$ , and  $^{16}\text{O}$ , and obtain the differential cross sections, which are shown in Fig. 1. The solid lines indicate the purely diffractive scattering; the dashed lines show the results with a complex value of  $\beta$ . The imaginary part is 0.5 of the real part. Our purpose is to show that, even for such large  $\beta$ , the diffraction pattern still remains.

The most interesting feature of our study is the regularity of the diffraction minima, expressed in terms of the values of  $qR$ . To illustrate this property further, we plot the relative cross section  $(d\sigma/dt)/(d\sigma/dt)_{t=0}$  versus  $qR$  in Fig. 2. It is quite interesting that the cross section of  $^{16}\text{O}$ - $^{16}\text{O}$  is nearly equal to that of  $^{12}\text{C}$ - $^{12}\text{C}$  scattering at all momentum transfers.

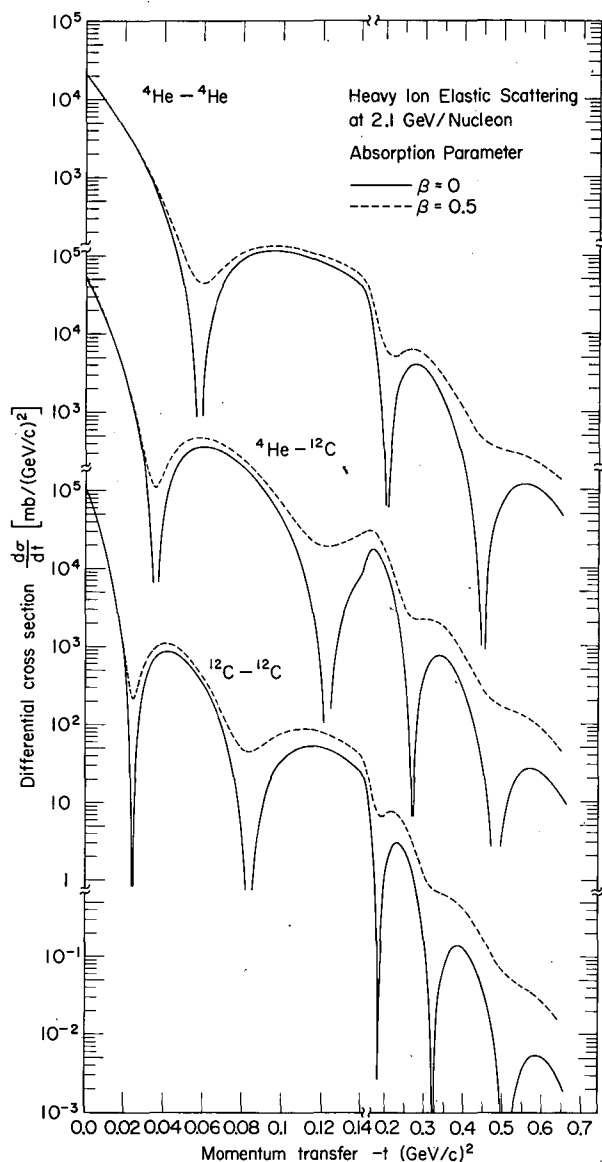


Fig. 1. Differential cross sections for  ${}^4\text{He}$ - ${}^4\text{He}$ ,  ${}^4\text{He}$ - ${}^{12}\text{C}$  and  ${}^{12}\text{C}$ - ${}^{12}\text{C}$  elastic scattering. The solid line is obtained using a purely imaginary  $x$ , i. e.,  $x=ix_0$ ; the dashed line corresponds to  $x=(\beta+i)x_0$ , with a large real part  $\beta=0.5$ . The diffraction patterns shown here are independent of the incident energy.

(XBL-738-3726)

To test this model, we suggest the following experiments:

1. scattering of nuclei with very diffused surface, e. g., deuteron or helium, to study the large momentum transfer, and
2. scattering of nuclei heavier than  ${}^{12}\text{C}$

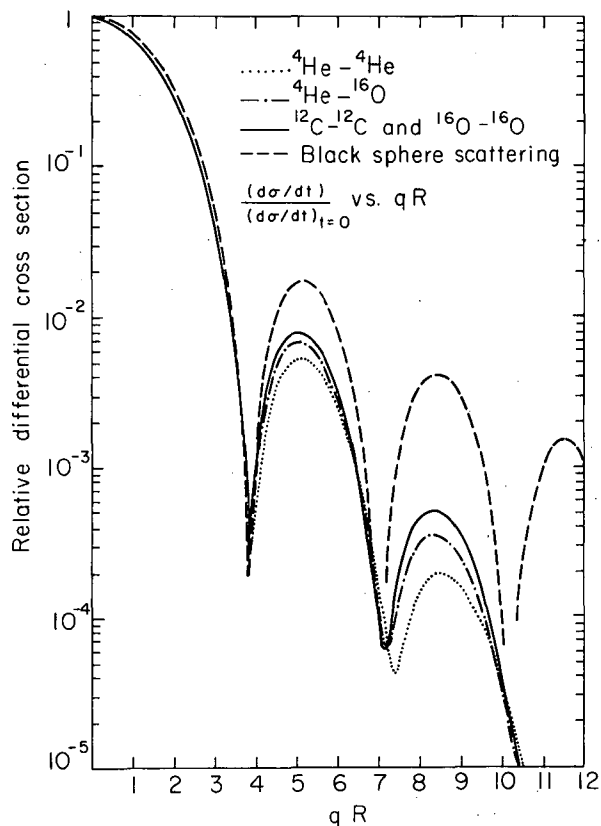


Fig. 2. Differential cross sections in "scaling coordinates". We plot relative cross section,  $(d\sigma/dt)_{t=0}$  to the forward cross section  $(d\sigma/dt)_{t=0}$ , versus  $qR$ , where  $q$  is the momentum transfer and  $R$  is the effective radius  $R=R_1+R_2$ . The differential cross sections seem to scale. The  ${}^{12}\text{C}$ - ${}^{12}\text{C}$ ,  ${}^{12}\text{C}$ - ${}^{16}\text{O}$ , and  ${}^{16}\text{O}$ - ${}^{16}\text{O}$  are essentially indistinguishable on this plot. The  ${}^4\text{He}$  scattering deviates from the asymptotic form, probably due to its diffused surface. The long dashed line is the prediction of a sharp cut-off model (black sphere scattering).

(XBL-739-4016)

to study the asymptotic behavior of the diffraction pattern.

It would also be interesting to use beams of various energies to determine the energy where the interaction becomes asymptotic.

#### Footnotes and References

\* Present address: California Institute of Technology, Pasadena, California 91109.

1. T. T. Chou and C. N. Yang, Phys. Rev. Letters **20**, 1213 (1968); Phys. Rev. **170**, 1591 (1968); Phys. Rev. **175**, 1832 (1968).

DIFFERENTIAL  $K_L \rightarrow K_S$  REGENERATION IN COHERENT  
PRODUCTION MODEL AND OPTICAL MODEL

W. L. Wang and Fumiyo Uchiyama\*

We investigate the high-energy  $K_L \rightarrow K_S$  regeneration process in nuclei in terms of a coherent production model,<sup>1,2</sup> and an optical model which explicitly treats  $K_L$  as a mixture of  $K_0$  and  $\bar{K}_0$  particles.<sup>3,4</sup> We show that it is not necessary to introduce a large neutron skin to interpret the data of Foeth et. al.,<sup>4</sup> if the finite range of strong interaction is taken into account properly in the density distribution. The coherent production model and the optical model, with very different physical interpretations, give very similar results. We also show that these models represent two ways of summing the multiple scattering series in the particular case of  $K_L \rightarrow K_S$  regeneration. In conclusion, we discuss the unique and important feature of using nuclear regeneration scattering to study scattering theories, as compared to other high-energy particle-nucleus scattering.

In the coherent production model, the differential cross section for the coherent regeneration process may be written as

$$\left(\frac{d\sigma}{dt}\right)_{K_L A \rightarrow K_S A} = \left(\frac{d\sigma_0}{dt}\right)_{t=0} |F(t)|^2, \quad (1)$$

where  $t = -(\text{momentum transfer})^2$  and  $d\sigma_0/dt|_{t=0}$  is the forward regeneration cross section of a nucleon. The amplitude  $F(t)$  is related to the multiple scattering of the incident and outgoing particles with the nucleus, and also to the fact that the regenerating nucleon is bound. We may write  $F(t)$  as

$$F(t) = \int_0^\infty e^{i\vec{q} \cdot \vec{b}} T(\vec{b}) e^{-\frac{1}{2}(1-i\alpha_{KN}) \sigma_{KN} T(\vec{b})} d^2b, \quad (2)$$

where  $\vec{q}$  is the momentum transfer,  $q^2 = -t$ , and  $\vec{b}$  the impact parameter. In Eq. (2), the neutron and proton distributions are taken to be the same. The total  $K_L$ - and  $K_S$ -nucleon average cross sections are the same (neglecting weak interactions) and denoted as  $\sigma_{KN}$ . The nuclear effects enter in the form of the two-dimensional density  $T(\vec{b})$ ,

$$T(\vec{b}) = A \int_{-\infty}^{\infty} \rho(\vec{r}) dz, \quad (3)$$

where  $\rho(\vec{r})$  is the nuclear density distribution (normalized to unity). For Cu and Pb, we assume a spherical symmetric Woods-Saxon density distribution, with half-radius about

0.6 fm larger and the diffuseness about 0.1 fm larger than those determined from electron scattering.

In the optical model, the regeneration amplitude for  $K_S$  is

$$F_R^{\text{Opt}} = \frac{i}{2} [F - \bar{F}] \quad (4)$$

where we denote  $K_0$ - and  $\bar{K}_0$ -nucleus scattering amplitudes as  $F$  and  $\bar{F}$ , respectively. These amplitudes may be related to  $K_0$ - and  $\bar{K}_0$ -nucleon interactions. We have

$$F(q^2) = \frac{ik}{2\pi} \int e^{i\vec{q} \cdot \vec{b}} [1 - e^{iP(\vec{b})}] d^2b \quad (5)$$

where  $P(\vec{b})$  is a phase shift function. In the case of  $K_0$ -nucleus scattering, we may write

$$P(\vec{b}) = \frac{i}{2} \left[ \frac{Z}{A} (1 - i\alpha_{K_0 p}) \sigma_{K_0 p} T_p(\vec{b}) + \left(1 - \frac{Z}{A}\right) (1 - i\alpha_{K_0 n}) \sigma_{K_0 n} T_n(\vec{b}) \right] \quad (6)$$

where  $\sigma_{K_0 N}$  are the total  $K_0$ -N cross sections,  $\alpha_{K_0 N}$  are the ratios of the real to imaginary parts of the forward  $K_0$ -N scattering amplitudes. The two-dimensional densities  $T_N(\vec{b})$  are related to Eq. (3) to the proton and neutron densities, which are assumed to have a Woods-Saxon form. For  $\bar{K}_0$ -nucleus scattering, we also use Eq. (5), with the K-nucleon parameters in  $P(\vec{b})$  appropriately changed for  $\bar{K}_0$ .

The results of our calculation are shown in Figs. 1 and 2. We have shown that both models reproduce the experimental data very well, the diffraction pattern being sensitive to nuclear gross size and the normalization to the elementary regeneration parameters. Furthermore, we find no necessity for introducing a neutron radius larger than the proton radius.

We have also shown that the two models are formally equivalent.<sup>5</sup> However, the coherent production formalism may provide us a simpler framework to study separately the nucleon regeneration amplitudes and the nuclear effects. The optical model, on the other hand, provides directly a relation to the  $K_0$  and  $\bar{K}_0$  elastic scattering amplitudes, which allows us to interrelate these amplitudes and study their detailed behavior. The interrelation of various elastic and regeneration scattering amplitudes is especially useful since we may also calculate

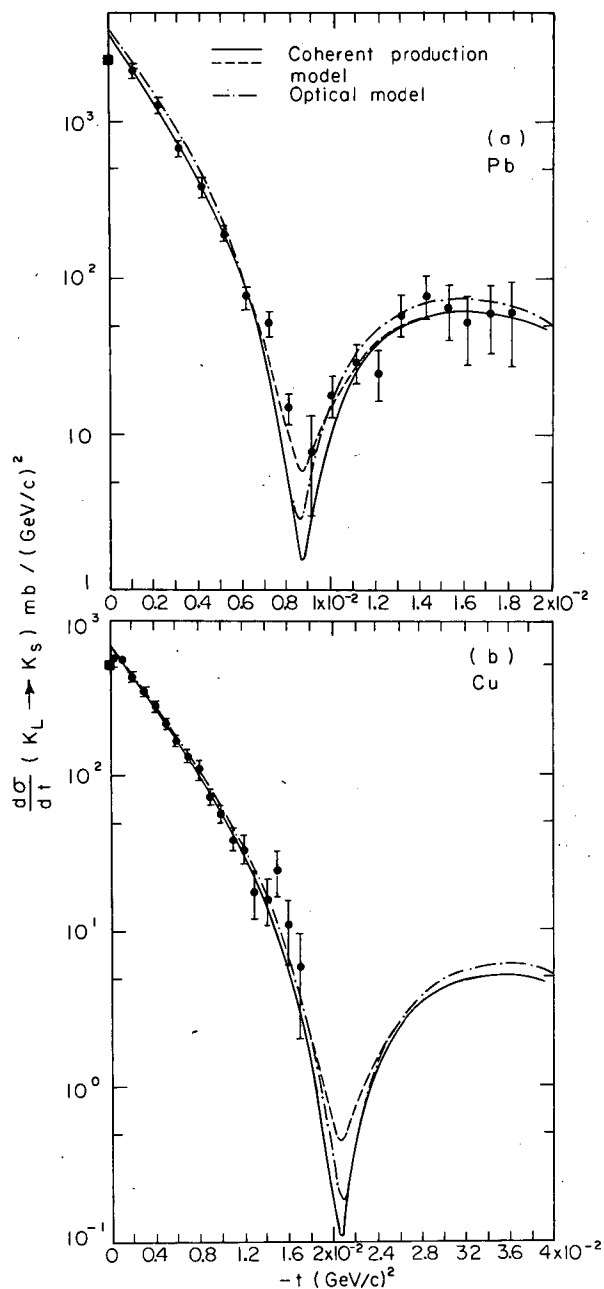


Fig. 1. Differential  $K_L \rightarrow K_S$  regeneration cross section for (a) Pb and (b) Cu. The  $K_L$  incident momentum is 4 GeV/c. The solid lines are the results of the coherent production model, using the parameter  $\alpha = -0.112$  as determined from Ref. 2; the dashed lines are the results of the same calculation using  $\alpha = -0.224$ . These two values of  $\alpha$  give identical results except near the diffraction minimum. The dash-dot lines are the results of the optical model calculations, using the same density distribution for neutrons and protons. The parameters of these calculations are given in Ref. 5. The data are from Foeth et al.<sup>4</sup>

(XBL-7310-4277)

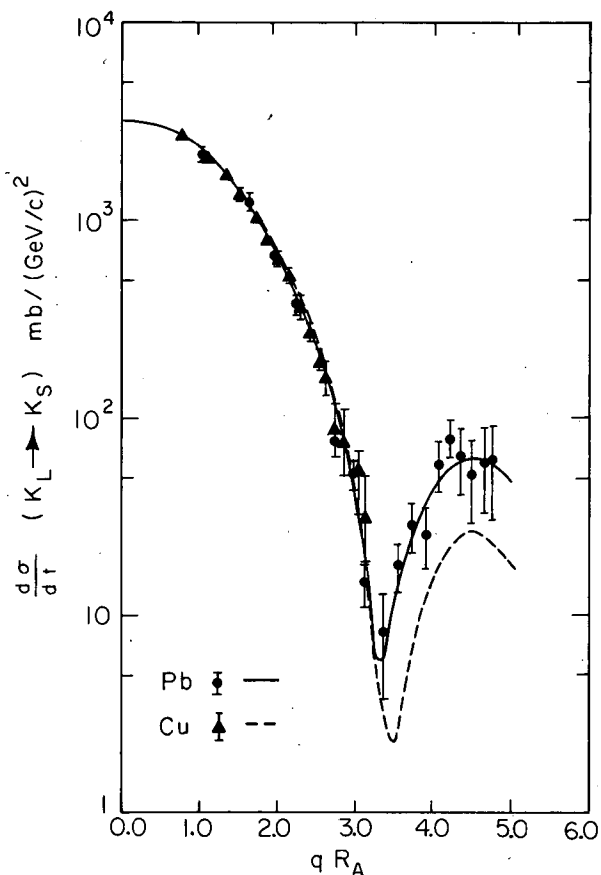


Fig. 2. The differential regeneration cross section plotted in the scaling coordinates. The copper and lead data are seen to have a simple scaling property.  $R$  is the half radius,  $R = 1.2 \times A^{1/3}$  fm of the target. The copper data is multiplied by 4.8, in agreement with the estimate of the black sphere diffraction model. The differential cross sections are more forward peaked than the elastic  $K_0$  and  $\bar{K}_0$  differential cross section, which show the usual diffraction pattern due to strong absorption. The data are from Foeth et al.<sup>4</sup>

(XBL-7310-4271)

the regeneration amplitude directly from the coherent production model.

Quite importantly, we find that the nuclear regeneration process provides a framework of unique interest in the study of various nuclear multiple-scattering formalisms. In most other types of high-energy projectiles, the (uninteresting) diffractive phenomenon prevails so that the main differential cross sections are not sensitive to the model used. We have now a non-diffractive process (the regeneration) which should serve as a much better test of the scattering theory. It may also be argued that large

momentum transfer processes with other projectiles should serve the same purpose. However, at large momentum transfers, other more complicated contributions generally occur and these are difficult to take into account.

In this work, we have shown that the basic character of the differential cross section is related to an overall nuclear matter distribution. This may not remain true in detail when more refined data are available, particularly beyond the first minimum. It would also be useful to extend the experiments to lower energies and lighter nuclei, where various nuclear multiple-scattering theories are most likely to give different results.

## ANGULAR DISTRIBUTION AND POLARIZATION OF $^{16}\text{O}(\gamma, n_0)^{15}\text{O}^*$

W. L. Wang and C. M. Shakin

We report a calculation of the angular distribution and polarization of the photoneutrons from  $^{16}\text{O}$  in the giant dipole region.

We have previously studied the nuclear compound states responsible for generating the intermediate structure in the photonuclear cross section of  $^{16}\text{O}$ .<sup>1</sup> We have shown, in a doorway-state formalism, that the intermediate resonances in the giant dipole region could be due to coupling of three-particle, three-hole (secondary doorway) states to the one-particle, one-hole giant dipole (doorway) states. Such configuration mixing redistributes the strength of the dipole transition and thus modifies the energy variation of the photodisintegration amplitudes. For detailed theoretical formalism and comparison to the experimental data, see Ref. 1. In the present calculation, we find that a consistent interpretation of the angular distribution and polarization may be obtained either by (I) assuming a phenomenological giant quadrupole (E2) resonance, or (II) by modifying the phase difference between the E1 amplitudes. In Case II, we do not require any E2 resonance to fit the data, or alternatively, the magnitudes of the E2 amplitudes used can be taken to be in reasonable agreement with those extracted from the polarized-proton capture experiment. The result of Case (I) has been discussed in a preliminary report.<sup>2</sup>

In the giant dipole region, the most important photodisintegration amplitudes are the E1 amplitudes. For  $^{16}\text{O}$ , these amplitudes have

## Footnotes and References

\* Particle Data Group, LBL.

1. K.S. Kolbig and B. Margolis, Nucl. Phys. B6, 85 (1968).
2. Fumiyo Uchiyama, Phys. Rev. D (Feb. 1974).
3. A. Bohm et. al., Phys. Letters 27B, 594 (1968).
4. H. Foeth et. al., Phys. Letters 31B, 544 (1970).
5. W.L. Wang and F. Uchiyama, Lawrence Berkeley Laboratory Report LBL-2313 (to be published).

been calculated in Ref. 1; they contain rather complicated energy dependence, which may be represented by the following T-matrix

$$T = \langle \psi_0^{(-)} | H_Y | 0 \rangle + \sum_d \frac{\langle \psi_0^{(-)} | H_{pd} | \phi_d \rangle \langle \phi_d | H_Y | 0 \rangle}{E - E_d - \Delta_d - \Delta_x + \frac{1}{2}(\Gamma_d + \Gamma_x)} \quad (1)$$

where  $|0\rangle$  is the  $^{16}\text{O}$  ground state, and  $H_Y$  the photonuclear interaction. The doorways,  $|\phi_d\rangle$ , are the usual 1p-1h (Tamm-Dancoff) dipole states at  $E_d = 22.3$  MeV and 24.3 MeV. The mixing of 3p-3h secondary-doorway states (with the dipole states) causes the shift and width,  $\Delta_d$  and  $\Gamma_d$ , to have rapid energy dependence which gives rise to intermediate resonances in the T-matrix. The shift  $\Delta_x$  and  $\Gamma_x$  are parameters as discussed in Ref. 1. The channel wave functions  $|\psi_0^{(-)}\rangle$  included  $s_{1/2}$  and  $d_{3/2}$  continuum neutrons coupled to a  $p_{1/2}$  hole state in the case of the ground-state cross section,  $^{16}\text{O}(\gamma, n_0)^{15}\text{O}$ .

In Case II of our study, the phases of the E1 amplitudes are modified, as to be discussed. For E2 amplitudes we may parameterize the E2 T-matrix as,

$$T_{\ell_j}(E2) = D_{\ell_j} + \sqrt{\frac{5}{4\pi k_\gamma}} \frac{\sqrt{\Gamma_{\ell_j}} \sqrt{\Gamma_Y(E2)}}{E - E_q + i\Gamma_q/2} \quad (2)$$

where  $D_{\ell_j}$  is the direct amplitude. The E2 resonance is assumed to be at energy  $E_q$  and

have a total width  $\Gamma_q$ .  $\Gamma_\gamma(E2)$  is the total ground-state photoabsorption width. For simplicity we take  $E_q$  and  $\Gamma_q$  to be constants. This assumption of an E2 resonance occurs only in our Case I study, where we take  $E_q = 23$  MeV and  $\Gamma_q = 4$  MeV. The  $\gamma$ -width  $\Gamma_\gamma$  is chosen to exhaust the E2 sum rule and  $\Gamma_j$  is determined from a fit to the angular distribution data.

The result of our calculation is shown in Figs. 1 and 2. We have shown that the E1 photodisintegration amplitudes obtained in the doorway-state formalism are adequate to interpret the experimental data, provided that we modify our E1 phase differences, which may simply be due to the inaccuracy in the potential scattering phase shifts. The conjecture of an E2 resonance in the dipole region, however,

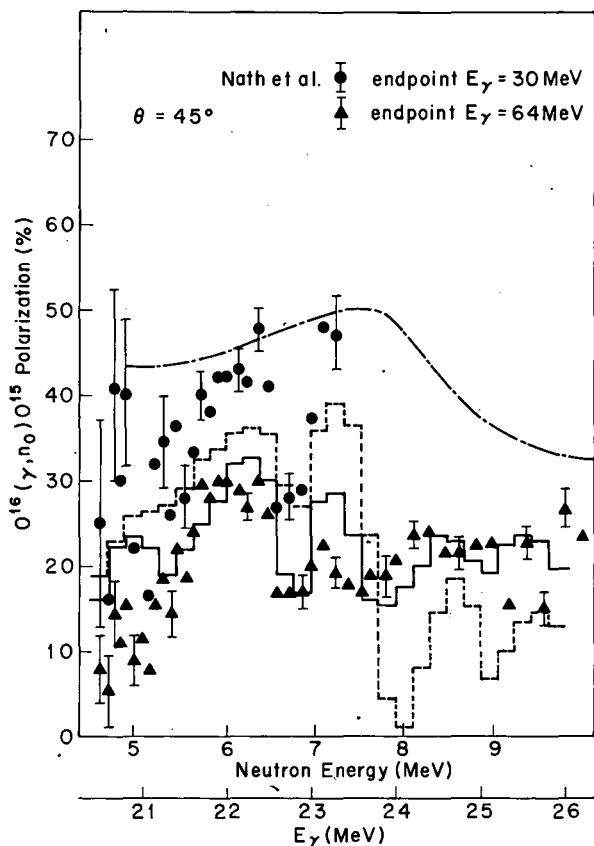


Fig. 1. Polarization at  $\theta = 45^\circ$ . Case I. The dashed line is the result of the E1 approximation; the solid line shows the effect of including the E2 resonance. The dash-dot line is the result of a coupled-channel calculation of Buck and Hill.<sup>3</sup> The data are from Nath et al.<sup>4</sup> The calculation is carried out at 0.2 MeV intervals. (XBL-7310-1344)

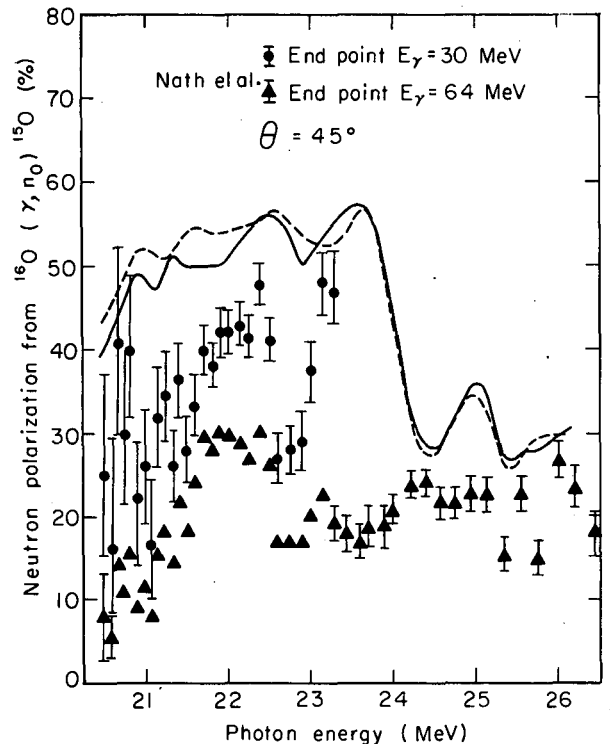


Fig. 2. The polarization at  $45^\circ$ . Case II. The dashed line is obtained by modifying the E1 phase difference  $\Delta_{ds}$  (see Ref. 2), assuming no E2 amplitudes. The solid line shows the effect of E2 amplitudes in the same calculation with modified  $\Delta_{ds}$ .

(XBL-7310-4218)

remains as possibility; a more definite answer would require more experimental and theoretical investigations.

#### References

1. W. L. Wang and C. M. Shakin, Phys. Rev. C 5, 1898 (1972).
2. W. L. Wang and C. M. Shakin, Phys. Rev. Letters 30, 301 (1973); W. L. Wang, Proc. Int'l. Conf. on Photonuclear Reactions and Applications (March 26-30, 1973), Pacific Grove, California, edited by B. L. Berman.
3. B. Buck and A. D. Hill, Nucl. Phys. A95, 271 (1967).
4. R. Nath, F. W. K. Firk, and H. L. Schultz, Nucl. Phys. A194, 49 (1972); R. Nath et al., Nucl. Instr. Methods 98, 385 (1972).

## COUPLED CHANNEL ALPHA DECAY THEORY FOR ODD-MASS NUCLEI

A. J. Soinski, D. G. Raich,  
J. O. Rasmussen, and E. A. Rauscher

In the alpha decay of spheroidal nuclei, the noncentral electromagnetic field permits the exchange of energy between internal nuclear excitation and the external alpha particle. The only noncentral couplings of importance are those involving the collectively enhanced rotational E2 transitions of deformed nuclei. Starting with boundary conditions set at the spheroidal nuclear surface, the formal problem involves the outward propagation of the alpha particle wave function through the anisotropic barrier out to some distance where coupling effects are negligible.

The nuclei  $^{253}\text{Es}$  and  $^{255}\text{Fm}$ , both spin  $7/2$ , are ideal cases for applying an exact numerical treatment because alpha transitions to the favored bands of the daughters have been well studied,<sup>1</sup> and angular distribution data from low temperature nuclear alignment experiments are also available.<sup>2</sup> Including the  $l = 0, 2$ , and 4 partial waves, nine coupled differential equations must be solved for decays to the five lowest states of the daughter rotational band.

The results of the numerical integration will check two commonly used assumptions. The first is that near the nuclear surface the favored alpha waves have zero projection of orbital angular momentum along the cylindrical

symmetry 3-axis of the daughter nucleus. Subject to this  $m_l = 0$  constraint, we wish to determine if the coupled channel treatment can reproduce both the experimental relative intensities to the spin  $7/2, 9/2, 11/2, 13/2$ , and  $15/2$  states of the daughter and the angular distribution data. The second assumption to be tested is that the relative intensities of a given  $l$ -wave are given by the square of a Clebsch-Gordan coefficient times the calculated spherical barrier penetrability for the alpha group (Bohr, Fröman, Mottelson formula).<sup>3</sup>

The general form of the coupled second-order differential equations has been given by Perlman and Rasmussen.<sup>4</sup> The nine coupled equations have eighteen linearly independent solutions. A set of solutions was found by integrating inward from large radius (150 f) with eighteen different starting conditions. From the resulting 18 solutions we construct the solutions of physical interest by linear combination, such that the solutions asymptotically go over to purely outgoing Coulomb waves with phase shifts  $\phi_{lI_f}$ . The solutions are constrained to be purely real at the inner radius (10 f), and the restriction to only  $m_l = 0$  components in the nuclear frame at 10 f leaves only two adjustable parameters  $a_2$  and  $a_4$ , the amplitude of d-wave and g-wave relative to s-wave at the inner radius.

Table I. Percentage intensities for favored rotational band alpha decay.

$I_f$	$^{253}\text{Es}$ intensities			$^{255}\text{Fm}$ intensities	
	Theory ( $\gamma=0$ )	Theory ( $\gamma=0.018$ )	Experiment	Theory ( $\gamma=0$ )	Experiment
7/2	90.82	90.07	90.0	93.99	93.3
9/2	5.56	6.43	6.6	4.31	5.2
11/2	1.056	0.93	0.85	0.827	0.62
13/2	0.0865	0.1060	0.079	0.0886	0.090
15/2	0.0087	0.0070	0.010	0.0074	0.0080
$a_2$	0.85736	1.03368		0.78109	
$a_4$	-0.10103	-0.27276		-0.20541	



The latest alpha intensity data of Ahmad and collaborators<sup>1</sup> for  $^{253}\text{Es}$  and  $^{255}\text{Fm}$  were corrected for small contributions of  $l = 6$  waves. Values of  $a_2$  and  $a_4$  were then found such that the error in the five measured intensities was minimized by logarithmic least squares.

Table I compares theory and experiment. There are three other sets of  $a_2$  and  $a_4$  values with different signs giving good fits, but we exclude them on the basis of the microscopic theory of Poggenburg et al.<sup>5</sup> The  $\gamma = 0$  results contain the strict constraint to  $m_l = 0$  alpha waves, and the  $\gamma = 0.018$  results relaxing that constraint will be discussed later. Though the fit of  $\gamma = 0$  results is fairly good, examination of Table I reveals a systematic discrepancy. The intensity ratio of the second to the first excited state is significantly larger than theory in both nuclei studied. Such a deviation from BFM theory had been noted for favored bands of many alpha emitters, but it is only now clear that the coupled channel treatment does not affect that discrepancy. We conclude that the leading order intensity relations (which assume only  $m_l = 0$  alpha waves) are violated for favored alpha decay and that significant non-zero components, at least for d-waves, are present on a spherical surface near the nucleus. Furthermore this discrepancy is not removed by simple Coriolis band-mixing. In lieu of a better model we have recalculated intensities with the inclusion of a "rotational attenuation factor"  $\exp\{-\gamma[I_f(I_f+1) - I_i(I_i+1)]\}$  which reduces alpha amplitudes on the inner surface by an exponential argument which is proportional to the excited state energy. Such a functional form might be a manifestation of a sloping inner barrier, as given by optical model nuclear potentials. However, from Table I we see that the inclusion of the rotational attenuation factor, while correcting the 11/2 to 9/2 intensity ratio, makes the 13/2 to 15/2 intensity ratio worse.

Table II shows an  $l = 4$  branching comparison of our coupled-channel results with the BFM formula.<sup>3</sup> Comparison is made with Asaro et al.,<sup>6</sup> where the alpha barrier penetrability was calculated for a pure Coulomb barrier cutting off at a definite nuclear radius. The other BFM comparison is from Poggenburg et al.,<sup>5</sup> where an optical-model nuclear potential was used. It is seen that the  $\gamma = 0$  coupled channel results for  $l = 4$  branching are very close to the earlier results with the BFM formula, thus confirming the theoretical validity of approximating alpha branching by the product of the barrier penetrability times the square of the appropriate Clebsch-Gordan coefficient. However, there is a regime of higher  $l = 4$  hindrance where channel coupling in the  $\gamma = 0$  calculations causes deviations from the BFM branching approximation. This can be seen in Fig. 1 where  $l = 4$  branching ratios are plotted as a function of  $a_4$  with  $a_2 = 0.89$  and  $\gamma = 0$ . The values at  $a_4 = -0.101$  are given in Table II. In the vicinity of  $a_4 = 0.2$  the hindrance factors are highest, and the deviations in branching ratio are substantial.

In Table II we see that the rotational attenuation factor greatly alters the g-wave in the ground decay group. The s- and d-wave interference in the ground group makes a large contribution to the  $P_4(\cos\theta)$  term in the alpha angular distribution function. In Table III we compare the data and the predictions of various calculations for the angular distribution coefficients from low temperature alignment experiments on  $^{253}\text{Es}$ .<sup>2</sup> The inclusion of a small ( $\gamma = 0.006$ ) rotational attenuation factor gives the best agreement between theory and experiment, although the relative intensities of 11/2 and 9/2 groups are not as good as with the larger ( $\gamma = 0.018$ ) factor.

In summary there seems to be a small but

Table II. Theoretical branching of the  $l = 4$  alpha groups for  $^{253}\text{Es}$ .

$I_f$	BFM-sharp	BFM-sloping	Coupled channel	
	(Asaro et al.) <sup>6</sup>	(Poggenburg et al.) <sup>5</sup>	( $\gamma=0$ )	( $\gamma=0.018$ )
7/2	(1)	(1)	(1)	(1)
9/2	2.57	2.486	2.499	1.934
11/2	2.10	1.994	2.010	1.139
13/2	0.65	0.632	0.626	0.254
15/2	0.065	0.063	0.063	0.0169

Table III.  $^{253}\text{Es}$  nuclei aligned in neodymium ethylsulfate. Alpha decay counting rate at 0.01 K relative to that at 4 K for two angles ( $0^\circ$  and  $90^\circ$ ) with respect to the crystalline c-axis.

	$W(0^\circ)$	$W(90^\circ)$			
Experimental	1.872(7)	0.521(4)			
Theoretical:					
1. Bohr, Fröman, Mottelson as applied by Asaro et al. <sup>6</sup>	1.882	0.540			
2. Mang Shell Model as applied by Poggenburg et al. <sup>5</sup>	1.837	0.566			
3. Numerical integration, this work					
	$a_2$	$a_4$	$\gamma$		
	0.8574	-0.1010	0.0	1.794	0.575
	0.9190	-0.1413	0.006	1.882	0.531
	1.0337	-0.2728	0.018	2.024	0.458

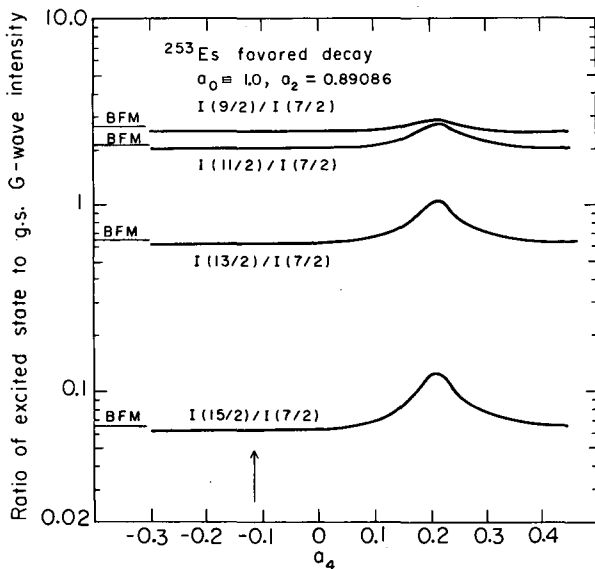


Fig. 1. Logarithm of the ratio of the  $l = 4$  intensity in excited states of the  $K = 7/2 + [633]$  band of  $^{249}\text{Bk}$  to that of the ground state for  $a_2 = 0.86$ . Bohr, Fröman, and Mottelson ratios (Table II) hold for most values of  $a_4$ .  
(XBL-743-2690)

systematic violation of the leading order intensity relations for favored  $l = 2$  alpha groups. The special effects of channel coupling do not spoil the accuracy of the simple Clebsch-Gordan branching expressions for  $l = 4$  until one

encounters higher  $l = 4$  hindrance factors than are found in either  $^{253}\text{Es}$  or  $^{255}\text{Fm}$ .

#### References

1. I. Ahmad, F. T. Porter, M. S. Freedman, R. F. Barnes, R. K. Sjoblom, F. Wagner, J. Milsted, and P. R. Fields, *Phys. Rev. C* **2**, 390 (1971); and I. Ahmad, private communication, (1973).
2. A. J. Soinski, R. B. Frankel, Q. O. Navarro, and D. A. Shirley, *Phys. Rev. C* **2**, 2379 (1970).
3. A. Bohr, P. O. Fröman, and B. R. Mottelson, *Kgl. Danske. Videnskab. Selskab, Mat.-Fys. Med.* **29**, No. 10 (1955).
4. I. Perlman and J. O. Rasmussen, in *Handbuch der Physik*, edited by S. Flügge (Springer-Verlag, Berlin, 1957), Vol. 42, p. 169.
5. J. K. Poggenburg, H. J. Mang, and J. O. Rasmussen, *Phys. Rev.* **181**, 1697 (1969), and J. K. Poggenburg, Ph.D. Thesis, Lawrence Berkeley Laboratory Report UCRL-16187 (1965) (unpublished).
6. F. Asaro, S. G. Thompson, F. S. Stephens, and I. Perlman, in *Proceedings of the International Conference on Nuclear Structure at Kingston, Ontario, 1960*, edited by D. A. Bromley and E. Vogt (University of Toronto Press, Toronto, 1960), p. 553. Our numbers are from a recalculation given in Ref. 2.

**EXTENSION OF ALPHA DECAY RATE THEORY TO SPHERICAL  
ODD-ODD NUCLEI ( $^{210}\text{At}$ )**

A. Shihab-Eldin, L. J. Jardine, and J. O. Rasmussen

Theoretical calculations of alpha decay rates of nuclei in the  $^{208}\text{Pb}$  region, using shell-model wave functions of the nucleons outside the closed shells, have been successfully carried out.<sup>1,2,3</sup> A finite Gaussian internal wave function for the alpha particle was used by Mang<sup>1</sup> and Harada.<sup>2</sup> Later, Rasmussen<sup>3</sup> showed that a simple delta-function approximation gave greatly simplified formulas, and essential agreement with the sophisticated theories.

### I. Outline of Theory

We have carried out the more involved angular momentum recouplings and fractional parentage expansion to extend the formulation of Ref. 3 to the alpha decay of the odd-odd  $^{210}\text{At}$  nucleus. As was outlined in Ref. 3, the alpha decay constant,  $\lambda_L$ , is given as follows:

$$\lambda_L = \frac{2\gamma_L^2}{\hbar} \left( \frac{\rho}{G_L^2 + F_L^2} \right)_{r=R_0} \quad (1)$$

where  $\left( \frac{\rho}{G_L^2 + F_L^2} \right)_{r=R_0}$  is the penetration factor

and  $\gamma_L^2$  is the reduced  $\alpha$  width given by

$$\gamma_L = C \sum_{J_N J_P} b_{J_N J_P}^T F_P(j_1 j_2 J_P) F_N(j_3 j_4 J_N) G(J_P J_N L) \quad (2)$$

where

$$C = \left( \frac{\hbar^2 R_0}{2M} \right)^{\frac{1}{2}} \left( \frac{4\pi S^3}{3} \right)^{\frac{3}{2}} R_1 R_2 R_3 R_4 \quad (3)$$

and

$$F_P(j_1 j_2 J_P) = (2j_1 + 1)^{\frac{1}{2}} (-1)^{j_1} (J_P j_1 0 - 1/2 | j_2 - 1/2) \quad (4)$$

$$F_N(j_3 j_4 J_N) = (2j_3 + 1)^{\frac{1}{2}} (-1)^{j_3} (J_N j_3 0 - 1/2 | j_4 - 1/2) \quad (5)$$

$$G(J_P J_N L) = (2J_P + 1)^{\frac{1}{2}} (L J_P 0 0 | J_N 0) \quad (6)$$

The factor  $b_{J_N J_P}^T$  is a product of fractional parentage coefficients (FPC) and recoupling coefficients derived from recoupling of the parent state in terms of the daughter state and the four nucleons forming the alpha particle as will be shown later by Eq. (14).

To calculate this factor, we assume a pure shell model configuration for the initial ground state (5+) of  $^{210}_{85}\text{At}$  which arises from a coupling between the proton and neutron configurations which are internally coupled to  $9/2^-$  and  $1/2^-$ , respectively; and we write this initial state as

$$|\psi_i\rangle = |(\pi(h_{9/2})^3_{9/2} (\nu(f_{5/2})^6_{0} \nu(p_{1/2}))_{1/2})_{J_i=5}\rangle \quad (7)$$

We now use the fractional parentage expansion<sup>4</sup> to rewrite the proton configurations of Eq. (8) as:

$$|\pi(h_{9/2})^3_{9/2}\rangle = \sum_{J_P} \alpha_{J_P} |(\pi(h_{9/2})^2_{J_P} \pi(h_{9/2})_{9/2})\rangle \quad (8)$$

where in the notation of Ref. 4,  $\alpha_{J_P}$  is given by

$$\alpha_{J_P} = [((h_{9/2})^2_{J_P} (h_{9/2})_{9/2} | (h_{9/2})^3_{9/2})] \quad (9)$$

Similarly for the neutrons we may write

$$\begin{aligned} & |(\nu(f_{5/2})^6_{0} \nu(p_{1/2}))_{1/2}\rangle \\ &= \sum_{J_N} \alpha_{J_N} |((\nu(f_{5/2})^4_{J_N} \nu(f_{5/2})^2_{J_N}) \nu(p_{1/2}))_{1/2}\rangle \quad (10) \end{aligned}$$

where

$$\alpha_{J_N} = [((f_{5/2})^4_{J_N} (f_{5/2})^2_{J_N} | (f_{5/2})^6_0)] \quad (11)$$

For configurations of the final  $^{206}_{83}\text{Bi}$  daughter populated by the alpha decay, we will consider

$$(\pi(h_{9/2}) \nu(f_{5/2})^{-1})_{J=2,3,4,5,6,7} \text{ (unfavored decay)}$$

and

$$(\pi(h_{9/2}) \nu(f_{5/2})^{-2} \nu(p_{1/2}))_{J=4,5} \text{ (favored decay)}$$

For the favored decay (transitions removing a  $(f_{5/2})^2$  neutron pair, no further internal recoupling of the neutron configuration of Eq. (10) is needed. However, for the unfavored decay (removal of a  $(f_{5/2} p_{1/2})$  neutron pair), we can recouple the neutron configuration of Eq. (10) by using Racah coefficients for the recoupling of the three angular momenta.<sup>4</sup> Further, we need only to consider components of Eq. (10) with  $J_N = 0$  and we may write

$$\begin{aligned}
& |(\nu(f_{5/2})_0^6 \nu(p_{1/2}))^{1/2}\rangle \\
&= \sum_{J_N} (-)^{1/2+5/2+J_N+0} \sqrt{\hat{J}_N \cdot \hat{0}} \times \begin{Bmatrix} 5/2 & 1/2 & J_N \\ 1/2 & 5/2 & 0 \end{Bmatrix} \\
&\quad (12) \\
&\times |((\nu(f_{5/2})\nu(p_{1/2}))_{J_N} \nu(f_{5/2})^{-1})^{1/2}\rangle
\end{aligned}$$

The selection rule ( $L_\alpha + J_N + J_P$  must be even) of Eq. (6), coupled with the additional restrictions that  $L_\alpha$  (no parity change) and  $J_P$  (protons in same orbit) are both even, requires that only even values of  $J_N$  are allowed. Furthermore, for the favored alpha decay only  $J_N=0$  is allowed while for the unfavored decay only  $J_N=2$  can contribute; thus, the summation over  $J_N$  in Eq. (10) reduces to a single term.

Using these properties, we can rewrite Eq. (7) (aside from a constant factor), explicitly showing the FPC for the unfavored decay, as

$$\begin{aligned}
|\psi_i\rangle &= \sum_{J_P} C_1 \alpha_{J_P} [[(\pi(h_{9/2})_{J_P}^2 \pi(h_{9/2}))^{9/2} \\
&\quad \otimes ((\nu(f_{5/2})\nu(p_{1/2}))_{J_N=2} \nu(f_{5/2}))^{1/2}]_{J_i=5}] \\
&\quad (13)
\end{aligned}$$

where  $C_1$  is the recoupling coefficient from Eq. (12) for  $J_N=2$ . One can consider this initial state as composed of four angular momenta ( $J_P, 9/2, J_N(=2)$ , and  $5/2$ ) with a certain order of coupling. Use of a 9-j symbol allows this state to be expressed as a linear combination of states composed of the same four angular momenta but with a different coupling order<sup>4</sup> appropriate to the formation of an alpha particle in the following way:

$$\begin{aligned}
|\psi_i\rangle &= C_1 \sum_{L_\alpha} \alpha_{J_P} \sqrt{9/2 \ 1/2 \ \hat{L}_\alpha \ \hat{J}_f} \begin{Bmatrix} J_P & J_N & L_\alpha \\ 9/2 & 5/2 & J_f \\ 9/2 & 1/2 & J_i \end{Bmatrix} \\
&\quad (14) \\
&\times [[(\pi(h_{9/2})_{J_P}^2 (\nu(f_{5/2})\nu(p_{1/2}))_{J_N=2} L_\alpha (\pi(h_{9/2}) \\
&\quad \nu(f_{5/2}))_{J_f}]_{J_i=5}].
\end{aligned}$$

For the favored decay we can rewrite Eq.(7) as

$$\begin{aligned}
|\psi_i\rangle &= \sum_{J_P} \alpha_{J_P} [[(\pi(h_{9/2})_{J_P}^2 \pi(h_{9/2}))^{9/2} \\
&\quad \otimes ((\nu(f_{5/2})_{J_N=0}^2 \nu(p_{1/2}))^{1/2})_{J_i=5}] \cdot \alpha_{J_N=0} \\
&\quad (15)
\end{aligned}$$

where the four angular momenta we want to recouple are  $J_P, 9/2, J_N(=0)$  and  $1/2$ . When these

are recoupled as in Eq. (14), the 9-j symbol reduces to a 6-j symbol<sup>4</sup> and the following result is obtained:

$$\begin{aligned}
|\psi_i\rangle &= \sum_{J_f J_P L_\alpha} \alpha_{J_P} \sqrt{9/2 \ \hat{J}_f} \begin{Bmatrix} J_f & J_i & L_\alpha \\ 9/2 & 9/2 & 1/2 \end{Bmatrix} \\
&\quad (16) \\
&\times [[(\pi(h_{9/2})_{J_P}^2 \nu(f_{5/2})_{J_N=0}^2) L_\alpha (\pi(h_{9/2}) \\
&\quad \nu(p_{1/2}))_{J_f}]_{J_i=5}] \cdot \alpha_{J_N=0}
\end{aligned}$$

For each final state of the daughter nucleus,  $|J_d\rangle$ , only terms of Eqs. (14) and (16) with  $J_f=J_d$  will contribute. Similarly, for each possible alpha decay constant of a given  $L$ , only the term with  $L_\alpha=L$  will contribute to the summation.

## II. Results

In Table I we present the theoretical alpha decay rates from the  $5+$  ground state of  ${}^{210}_{85}\text{At}$  to all members of  ${}^{206}_{83}\text{Bi}$  multiplets ( $(\pi(h_{9/2})\nu(f_{5/2})^{-1})_{J=2,3,4,5,6,7}$  and  $(\pi(h_{9/2})\nu(f_{5/2})^{-2}\nu(p_{1/2}))_{J=4,5}$ . We also show the experimental relative intensities of the alpha groups measured by Ref.6. There is overall agreement between the experimental and theoretical alpha decay rates, and the agreement between relative intensities of alpha groups to levels within the same multiplets is even better. In particular, the absence of any feeding to the  $2_1^+$  and  $3_1^+$  members of the  $(\pi(h_{9/2})\nu(f_{5/2})^{-1})$  multiplet and the  $4_2^+$  member of the  $(\pi(h_{9/2})\nu(f_{5/2})^{-2}\nu(p_{1/2}))$  multiplet relative to the other spin members of the multiplets is predicted rather well.

However, the calculation fails to predict the proper feeding strength to the  $4_1^+$  and  $5_1^+$  states relative to the  $6_1^+$  ground state. Part of this discrepancy might be accounted for if constructive mixing in the lowest  $4_1^+$  and  $5_1^+$  states occurs from the higher-lying  $4_2^+$  and  $5_2^+$  states which belong to different configurations. The calculation also fails to predict the proper relative feeding strengths to states belonging to different configurations or multiplets; for example, the feeding to the  $5_1^+$  and  $5_2^+$  states. Many factors can contribute to this latter failure. Among them is the sensitivity of the nucleon radial wave functions to the choice of connection radii. Also, the delta function model does not take into account the finiteness of the  $\alpha$ -particle wave packet, nor does it provide for interchannel coupling.<sup>3</sup>

It is interesting, also, to note that the calculation reveals that the  $L=2$  alpha waves ( $\lambda_2$ ) are invariably the dominant mode of decay for each transition, even in the case of

Table I. A comparison of the experimental<sup>1</sup> and theoretical relative alpha intensities in the decay of  $^{210}_{85}\text{At}$ .

	$^{206}\text{Bi}$ configurations <sup>a</sup>		Relative $\alpha$ intensity	
	$J^\pi$	E(keV)	Experimental <sup>b</sup>	Calculated <sup>c</sup>
$(\pi(h_{9/2})\nu(f_{5/2}^{-1}p_{1/2}^{-2}))_{J^\pi}$	$6_1^+$	0	100	100
	$4_1^+$	60	$26 \pm 2$	14
	$3_1^+$	70	n. o. <sup>e</sup>	0.3
	$5_1^+$	83	$95 \pm 6$	$11^d$
	$7_1^+$	140	$14 \pm 2$	15
	$2_1^+$	409	n. o. <sup>e</sup>	0.005
$(\pi(h_{9/2})\nu(p_{1/2}^{-1}f_{5/2}^{-2}))_{J^\pi}$	$5_2^+$	167	$83 \pm 6$	$83^d$
	$4_2^+$	200	n. o. <sup>e</sup>	0.3

<sup>a</sup>Spin and energy assignments were taken from Refs. 7 and 8.

<sup>b</sup>Experimental relative intensities were taken from Ref. 6.

<sup>c</sup>The value of the parameter  $R_0$  used was 8 fm.

<sup>d</sup>Discussed in text. Relative antisymmetry factors treated as in Ref. 9.

<sup>e</sup>Alpha groups not observed by Ref. 6 can be given an upper limit of  $\leq 5$ .

Table II. Relative intensity strength  $\lambda_L$ , for various orbital angular momentum groups in  $\alpha$ -transitions in arbitrary units for each transition.

Orbital angular momentum	Transition	$5^+ \rightarrow 6_1^+$	$5^+ \rightarrow 5_1^+$	$5^+ \rightarrow 7_1^+$	$5^+ \rightarrow 5_2^+$	$5^+ \rightarrow 4_2^+$
0		forbidden	8.55(-31)	forbidden	1.15(-25)	forbidden
2		1.64(-28)	1.75(-29)	2.29(-28)	4.56(-27)	1.22(-28)
4		1.85(-32)	5.85(-31)	8.43(-31)	1.04(-27)	1.04(-28)
6		4.91(-33)	4.56(-32)	8.16(-32)	8.96(-29)	2.50(-29)
8		4.86(-34)	8.48(-34)	3.36(-33)	forbidden	forbidden

the  $J_1=5^+ \rightarrow 5_1^+$  which has an allowed  $L=0$  mode. An exception to this is the  $J_1=5^+ \rightarrow 5_2^+$  (favored decay) where the  $L=0$  mode is the dominant one. In Table II we compare the relative contributions (in arbitrary units for each transition) from the various  $\lambda_L$  modes for some selected transitions to the two  $^{206}\text{Bi}$  multiplets. The theoretical mixing ratios of Table II might be subjected to experimental test by various alpha angular correlation experiments.

Further refinement of the calculation is possible with the use of more realistic wave functions that include configuration mixing, rather than the simple "pure" shell model states employed in the present calculation.

#### References

1. H. J. Mang, Z. Phys. 148, 582 (1957).
2. K. Harada, Prog. Theor. Phys. 26, 667 (1961).
3. J. O. Rasmussen, Nucl. Phys. 44, 93 (1963).
4. A. de-Shalit and I. Talmi, Nuclear Shell Theory (Academic Press, New York, 1963), p. 509.
5. J. Blomqvist and S. Wahlborn, Ark. Fys. 16, No. 46 (1960).
6. N. A. Golovkov, Sh. Guetkh, B. S. Dzhelapov, Yu. V. Norseev, V. A. Khalkin, and V. G. Chumin, Izv. Fiz. 33, 1622 (1969) (translated page 1489).
7. M. Fujioka, M. Kanbe, and K. Hisatake, Phys. Rev. Letters 31, 114 (1973).
8. L. J. Jardine and A. Shihab-Eldin, Bull. Am. Phys. Soc. 18, 1379 (1973); and unpublished results.
9. I. S. Towner and J. C. Hardy, Adv. in Phys. 18, No. 74, 401 (1969).

### BACKBENDING AND ROTATION ALIGNMENT

F. S. Stephens, P. Kleinheinz,  
R. K. Sheline, and R. S. Simon

It is now clear that a rather sudden structural change occurs in the ground-state rotational band of a considerable number of rare-earth even nuclei at high angular momenta.<sup>1,2</sup> These irregularities are such that two or three rotational transitions in the region of  $I \approx 12-20$  become lower in energy with increasing  $I$ , whereas transitions above and below this  $I$ -region have the normal (rotational) monotonic increase in energy with  $I$ . If the moment-of-inertia,  $\mathcal{J}$ , is plotted against the square of the rotational frequency,  $\omega^2$ , such a behavior produces a "backbending" curve (larger  $\mathcal{J}$  but smaller values for  $\omega^2$ ). There has recently been considerable interest in determining the nature of the structural change responsible for this behavior. We have examined the  $Z$  and  $N$  dependence of backbending in the rare-earth region as given by a model based on the rotation alignment of two  $i_{13/2}$  neutrons.<sup>3</sup> This model ascribes backbending to a crossing of the ground-state and such a 2-quasiparticle band. The important parameters in this model are the rotational moment of inertia, the position of the fermi surface, and the deformation (both quadrupole and hexadecapole). To fix these (and other) parameters most reliably, we propose a comparison with the observed rotation alignment of a single  $i_{13/2}$  neutron

in the adjacent odd- $A$  nuclei.

It is clear that most of the parameters entering into the 2-quasiparticle calculation for even-even nuclei also enter in much the same way into the 1-quasiparticle calculation of the lowest  $i_{13/2}$  band in an odd-mass nucleus. Such bands are observed throughout the rare-earth region and backbending in the even nuclei should be related to the characteristics of these bands in the adjacent odd-mass nuclei if the rotation-alignment model is correct. We will attempt to make this comparison, first in a qualitative way, and then more quantitatively.

If we look at the lowest  $i_{13/2}$  band in an odd-neutron rare-earth nucleus one characteristic feature of the energies is the presence of a term whose sign alternates as  $I$  increases. This alternation of energies is the beginning of the rotation-alignment process, and can be traced back to the Coriolis-induced amplitude of the  $\Omega = 1/2$  orbital in the wave function, and further, to its decoupling term. Thus, this oscillation is related to the extent of alignment, though it is not a direct measure of it. Therefore, it seems to be of interest to compare the size of this term with the degree of backbending

in the adjacent even nuclei. In Fig. 1 we have plotted all the information on rotational levels of even nuclei in the rare-earth region from  $N \approx 90$  through  $Z \approx 76$ . A figure similar in this respect has been given by Sorensen.<sup>2</sup> In Fig. 2 we have plotted the rotational levels of the lowest  $i_{13/2}$  band in the odd-mass nuclei. The effects of the alternating energy term are apparent. The rotation-alignment model would imply some correlation between the size of the alternating energy term and backbending. Comparison of Figs. 1 and 2 suggests that this may well be the case, but a more quantitative comparison would be helpful.

One of the effects that Coriolis mixing has on the levels of the lowest mixed band is a compression of the band, that is, an increase in the apparent moment of inertia. This compression is a result of the fact that, while all the levels of the band are lowered, the higher spin levels are lowered more. This lowering of the levels in the lowest band is exactly what causes the 2-quasiparticle band in even-even

nuclei to drop below the ground-state band according to the rotation-alignment model. It seems clear that the lowering in the 1-quasiparticle system of levels will be closely related to that in the 2-quasiparticle system, and the band compression is an indirect measure of the former of these. Thus a correlation between backbending and the 1-quasiparticle band compression is strongly suggested.

It is not difficult to arrive at a quantitative expression for the compression of the lowest  $i_{13/2}$  band in the odd-neutron nuclei. If the band is decoupled (rotation aligned), then the  $I = 17/2$  to  $13/2$  separation should be just the average  $I = 2$  to  $0$  separation in the two adjacent even nuclei. Thus, the ratio,  $6 E(17/2 \rightarrow 13/2) / 32 \bar{E}(2 \rightarrow 0)$ , should be  $6/32 = 0.188$  if the band is decoupled. This ratio should be 1.00 if the band is not mixed at all. This "compression factor" for the odd nuclei has been included in Figs. 1 and 2, and we have drawn a rough contour line for a compression

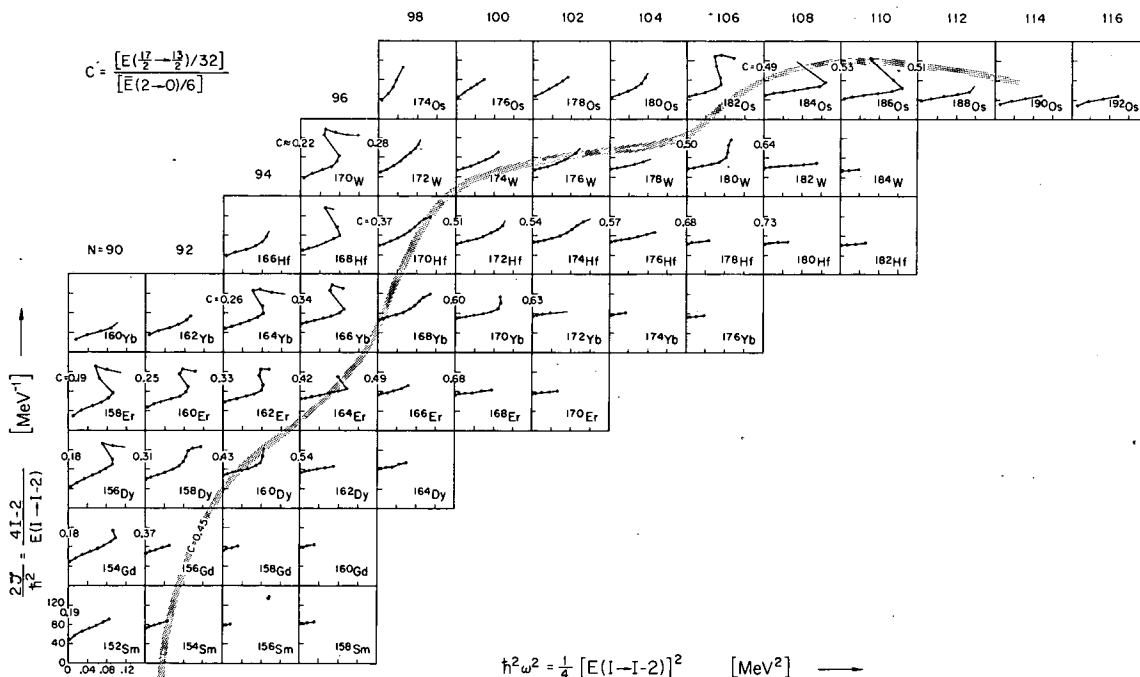


Fig. 1. Ground-band level energies in doubly-even rare-earth nuclei. The plots give the moment-of-inertia  $\frac{2I}{\hbar^2}$  versus the square of the rotational frequency  $\hbar^2\omega^2$ , both quantities derived from the transition energy. In a few cases where more than one possible choice exists, the lowest-energy transition is always used. Tentatively assigned band members are indicated by an omitted dot. The compression factors  $C$  and the contour line for  $C = 0.45$  are derived from the  $17/2^+ \rightarrow 13/2^+$  level spacings observed in the odd- $N$  nuclei (Fig. 2), and from the mean value  $\bar{E}(2 \rightarrow 0)$  of the  $2^+$  energies in the adjacent even nuclei. The data are taken from a recent compilation by Saethre et al. (Nucl. Phys. A207, 486 (1973). (XBL 7312-6974)

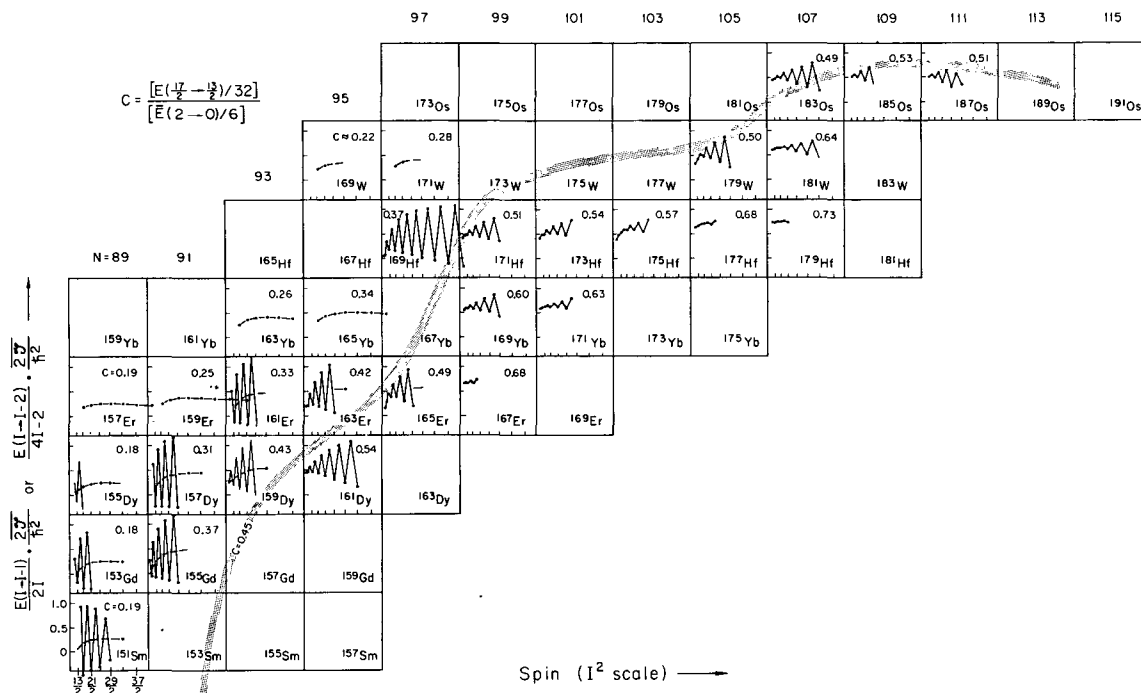


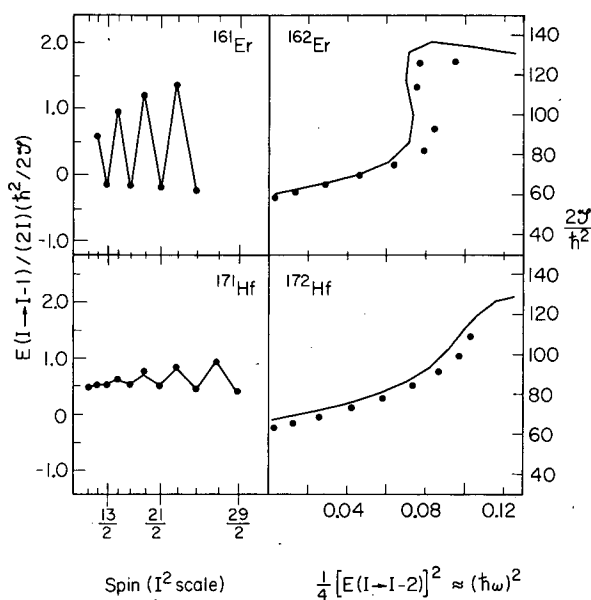
Fig. 2. The  $i_{13/2}$  yrast level energies in odd- $N$  rare-earth nuclei. The plots give the apparent  $\hbar^2/2\mathcal{I}$  as derived from the transition energy (in units of the mean value of  $\hbar^2/2\mathcal{I}$  in the neighboring even-even isotopes) versus the square of the spin of the upper level. In this plot an unperturbed rotational band gives a horizontal line (with the ordinate close to one), a band following the equation  $E = AI(I+1) + BI^2(I+1)^2$  gives a straight line with the slope  $B$ . The compression factor  $C$  derived from the  $17/2^+ \rightarrow 13/2^+$  transition energy is indicated for each nucleus. In several nuclei with  $N \leq 99$  only one E2 cascade was observed, which establishes the energy-favored band members with  $I = j, j+2, \dots$ ; these points are connected by a broken line to indicate the absence of the alternate band members. (For illustrative purposes this is also done for several complete bands). Dots are omitted for tentatively assigned band members. The source of the original data is given in Ref. 4. (XBL 7312-6973)

factor of 0.45. It is apparent that these numbers correlate rather closely with the size of the alternating energy term. Furthermore, the contour line approximately divides the backbending even nuclei from those that do not seem to backbend, though more data are badly needed in the lower right portions of Figs. 1 and 2. We find the correlation between compression factor and backbending, as indicated in Fig. 1, quite encouraging, and will now test these ideas by direct calculation.

For the direct calculations we picked two pairs of nuclei:  $^{161}\text{Er}$  and  $^{162}\text{Er}$  (which backbends), and  $^{171}\text{Hf}$  and  $^{172}\text{Hf}$  (which does not backbend). The Coriolis effects were treated

exactly the same in the one-particle (odd-mass) and two-particle (even-even) calculations. Two parameters were varied in the one-particle case to fit the observed  $i_{13/2}$  band in the odd-mass nucleus, and then these values for the parameters were used in the even-even cases. A more detailed account of this calculation has been given elsewhere.<sup>4</sup> The results are shown in Fig. 3 and the agreement with the data for the even-even cases is excellent. Such calculations need to be improved and extended, but seem to lend strong support to the proposal that backbending in this region is due to an intersection of the ground band with a rotation-aligned 2-quasiparticle band based on  $i_{13/2}$  neutrons.





- References
1. A. Johnson and Z. Szymanski, Physics Reports 7C, 181 (1973).
  2. R.A. Sorensen, Rev. Mod. Phys. 45, 353 (1973).
  3. F.S. Stephens and R.S. Simon, Nucl. Phys. A183, 257 (1972).
  4. F.S. Stephens, P. Kleinheinz, R. K. Sheline, and R. S. Simon, Lawrence Berkeley Laboratory Report LBL-1911, submitted to Nuclear Physics.

Fig. 3. A comparison of experimental (dots) and calculated (lines) properties of levels in the pairs of nuclei  $161, 162\text{Er}$  and  $171, 172\text{Hf}$ . The plots are of the same type as those in Figs. 1 and 2. The left side of the figure shows the fits obtained for the lowest  $i_{13/2}$  band in the odd-mass nucleus of each pair, and the right side shows the results for the even-even nucleus calculated using the same parameters. (XBL-736-3105)

### CONFIGURATION MIXING OF TWO-QUASI-PARTICLE STATES IN EVEN-EVEN DEFORMED NUCLEI\*

H. Massmann,<sup>†</sup> J. O. Rasmussen,<sup>‡</sup> T. E. Ward,<sup>§</sup>  
P. E. Haustein,<sup>||</sup> and F. M. Bernthal<sup>¶</sup>

In the past several years interesting measurements have been made concerning band-mixing in even-even nuclei. The even-even nuclei around  $^{178}\text{Hf}$  are interesting because of their prolific isomerism. Khoo et al.<sup>1</sup> carried out measurements of excited bands in  $^{176}\text{Hf}$ . Their analysis shows that the  $K^\pi = 6^+$  bands at 1333.1 and 1761.5 keV are highly mixed between two-quasi-proton and two-quasi-neutron configurations with a mixing ratio of 38:62. Also the two  $K^\pi = 1^+$  bands in  $^{176}\text{Hf}$  at 1672.3 and 1862.8 keV are mixed in a ratio of 30:70. Studies by Helmer and Reich<sup>2</sup> and by Ward et al.<sup>3</sup> indicate that the 1147-keV state (mainly two-quasi-neutron) and the 1480 keV state (mainly two-quasi-proton) in  $^{178}\text{Hf}$  are highly mixed (mixing ratio 34:66). Another case of highly mixed configuration occurs in  $^{174}\text{Yb}$ , where the two  $K^\pi = 5^-$  states at 1886 and 2383 keV have a mixing ratio of 35:65 (deduced from their  $ft$  values).

One can obtain at least a qualitative explanation by considering that the two states interact with one another through the residual proton-neutron interaction. If the off-diagonal matrix element is denoted by

$$m \equiv \langle \psi_{n_1 n_2} | V_{\text{res}}^{n-p} | \psi_{p_1 p_2} \rangle \quad (1)$$

the mixing ratio between the two states is denoted by  $\chi = \beta^2/\alpha^2$  and the energy difference of the like-spin members of the two bands of the configurations considered is denoted by  $\Delta\lambda$ , then one finds that these quantities are related by:

$$m = \frac{\Delta\lambda\sqrt{\chi}}{1+\chi} \quad (2)$$

But  $m$  is related to  $p$ - $n$  force with BCS superfluid wave functions (for the case of parallel angular momentum projections  $\Omega_{n_1} + \Omega_{n_2}$  and  $\Omega_{p_1} + \Omega_{p_2}$ ) as follows:

$$m = \left( u_{n_1} v_{n_2} u_{p_1} v_{p_2} + v_{n_1} u_{n_2} v_{p_1} u_{p_2} \right) \cdot \left( \langle n_1 \bar{p}_2 | V_{np} | \bar{n}_2 p_1 \rangle - \left( u_{n_1} v_{n_2} v_{p_1} u_{p_2} + v_{n_1} u_{n_2} u_{p_1} v_{p_2} \right) \langle n_1 \bar{p}_1 | V_{np} | \bar{n}_2 p_2 \rangle \right) \quad (3)$$

Table I. Fit of energy splittings of Gallagher-Moszkowski pairs.

Nucleus	Configuration		$K^\pi$		$\Delta E_{th}$	$\Delta E_{th}$	$\Delta E_{exp}$
	Proton	Neutron	$\Sigma_n + \Sigma_p = 0$	$\Sigma_n + \Sigma_p = 1$	$r_o = 1.5 fm$	$r_o = 1.0 fm$	
					(keV)	(keV)	(keV)
$^{164}Ho$	$7/2^- (523)\uparrow$	$1/2^+ (400)\uparrow$	$3^-$	$4^-$	118	124	102
		$3/2^+ (402)\downarrow$	$5^-$	$2^-$	-123	-131	-85
		$3/2^- (521)\uparrow$	$2^+$	$5^+$	165	159	171
$^{166}Ho$	$7/2^- (523)\uparrow$	$1/2^- (521)\downarrow$	$4^+$	$3^+$	-147	-156	-171
$^{168}Tm$	$1/2^+ (411)\downarrow$	$5/2^- (512)\uparrow$	$3^-$	$2^-$	-242	-231	-234
		$7/2^+ (633)\uparrow$	$4^+$	$3^+$	-138	-145	-157
$^{170}Tm$	$1/2^+ (411)\downarrow$	$5/2^- (512)\uparrow$	$3^-$	$2^-$	-239	-236	-232
$^{174}Lu$	$7/2^+ (404)\downarrow$	$3/2^- (521)\uparrow$	$5^-$	$2^-$	-59	-58	-90
		$1/2^- (521)\downarrow$	$3^-$	$4^-$	93	69	80
$^{176}Lu$	$7/2^+ (404)\downarrow$	$1/2^- (510)\uparrow$	$4^-$	$3^-$	-130	-138	-118
$^{182}Ta$	$7/2^+ (404)\downarrow$	$1/2^- (510)\uparrow$	$4^-$	$3^-$	-127	-135	-174 <sup>a)</sup>
		$3/2^- (512)\downarrow$	$2^-$	$5^-$	166	168	154 <sup>b)</sup>

More recent experimental values (R. G. Helmer, R. C. Greenwood and C. W. Reich, Nucl. Phys. A168, 449 (1971)) are: a)-100; b) 140.

Here  $u$  and  $v$  represent the usual BCS amplitudes and were obtained by solving the BCS equations (blocking was not taken into account). The matrix elements in Eq. (3) represent the off-diagonal matrix elements of the effective neutron-proton potential between Nilsson wave functions.

The effective neutron-proton potential was taken to be of finite-range Gaussian central form

$$V_{np} = \exp(-r^2/r_o^2) (V_{TE} P_{TE} + V_{TO} P_{TO} + V_{SE} P_{SE} + V_{SO} P_{SO}) \quad (4)$$

where  $P_{TE}$ ,  $P_{TO}$ ,  $P_{SE}$ ,  $P_{SO}$  are the projection operators for the spin triplet (T), or singlet (S) and even (E) or odd (O) relative orbital angular momentum.

We used two different forces in our calculations, force I with  $r_o = 1.5$  fm, force II with  $r_o = 1.0$  fm. The potential strengths were derived (up to a common additive constant; this because a pure Wigner force does not contribute to the splitting) by doing a least square fit of energy splittings of Gallagher-Moszkowski pairs. We did not include in the

Table II. Potential strength of forces used in this work.

Force Component	Force I ( $r_o = 1.5$ fm) (MeV)	Force II ( $r_o = 1.0$ fm) (MeV)
$V_{TE}$	-117	-262
$V_{SO}$	-72	+35
$V_{TO}$	-62	-169
$V_{SE}$	-25	-51

fit the cases involving  $K=0$  or  $K=1$  bands, which are the most susceptible to higher order corrections (this because of the higher level densities of low  $K$  bands). The result of the fitting procedure is shown in Table I. Table II shows the optimum force strength so obtained. The Wigner strength was adjusted to get the best agreement with the experimental band mixing matrix elements. The matrix elements

$$\langle np | V_{np} | n'p' \rangle$$

were calculated from a sophisticated program

of Dr. Gordon Struble. Table III shows the agreement between the experimental and calculated band mixing matrix elements. The agreement is quite satisfactory, though somewhat better for the shorter range force II.

Table III. Comparison of theoretical and experimental mixing matrix elements (keV)

Case	$ m_{th} $ (Force I)	$ m_{th} $ (Force II)	$ m_{exp} $
$m_8^-(^{178}\text{Hf})$	133	158	158
$m_6^+(^{176}\text{Hf})$	203	199	208
$m_5^-(^{174}\text{Hf})$	270	249	235
$m_1^+(^{176}\text{Hf})$	12	25	88
$m_8^-(^{180}\text{Hf})$	122	144	
$m_6^+(^{174}\text{Hf})$	194	190	$< 0.3\Delta\lambda$
$m_6^+(^{174}\text{Yb})$	129	126	

### Footnotes and References

\* Condensed from LBL-1693. (Phys. Rev. C, May, 1974).

† On leave from Facultad de Ciencias, U. de Chile.

‡ J.S. Guggenheim Fellow., 1973.

§ Cyclotron Laboratory, Indiana University, Bloomington, Indiana.

|| Department of Chemistry and Heavy Ion Accelerator Lab., Yale University

¶ Department of Chemistry and Physics and Cyclotron Lab., Michigan State University, Lansing, Michigan.

1. T. L. Khoo, J. C. Waddington, R. A. O'Neil, Z. Preibirz, D. G. Burke, and M. W. Johns, Phys. Rev. Letters 28, 1717 (1972).

2. R. G. Helmer and C. W. Reich, Nucl. Phys. A114, 649 (1968).

3. T. E. Ward, Y. Y. Chu, and J. B. Cumming (private communication).

## TWO CORIOLIS MIXED ROTATIONAL BAND EXPANSION FOR DEFORMED ODD-MASS NUCLEI

H. Massmann,\* J. O. Rasmussen,<sup>†</sup> and W. Ribbe<sup>‡</sup>

Multi-band Coriolis-mixed rotational band calculations like the ones done by C. Alonso,<sup>1</sup> and Baznat et. al.,<sup>2</sup> have done much to explain the rotational band energies of odd-mass deformed nuclei. This way one solves the complete problem at once, one obtains physical meaningful parameters, and one obtains also the mixing ratio between all the bands considered. The problem with this approach is that it is somewhat cumbersome to use; there are too many parameters which may not be known (band head energies, attenuation factors for the Coriolis matrix elements) and unless data on higher bands and spectroscopic factors are known, the sets of parameters obtained are far from unique.

On the other extreme, one has the traditional rotational (one) band power series expansion which can be derived from the multi-band expansion by means of the perturbation theory and the condition

$$\frac{\hbar^2}{2\mathcal{I}} \langle j_+ \rangle \ll |E_{I,K} - E_{I,K+1}| \quad (1)$$

$\mathcal{I}$  is the moment-of-inertia,  $\langle j_+ \rangle$  the effective Coriolis matrix element. The traditional (one) band expansion is

$$E_I = E_0 + A(I(I+1) - K^2) + B(I(I+1) - K^2) + \dots + (-1)^{I+K} \frac{(I+K)!}{(I-K)!} \left\{ A_{2K} + B_{2K} (I(I+1) - K^2) + \dots \right\} \quad (2)$$

This expression works well in many cases, the energies are given by a simple analytic expression, and it is easily used (that is, the fits converge immediately and parameters are unique). However, in many cases, when the inequality (1) does not hold, then the expansion (2) becomes meaningless. In those cases the magnitude of the fitted parameters depend on

Table I

..... Nuclei .....								
	$^{181}_{74}\text{W}107$		$^{161}_{67}\text{Ho}94$		$^{249}_{97}\text{Bk}152$		$^{171}_{71}\text{Lu}100$	
Bands considered	$9/2^+(624)$	$7/2^+(633)$	$1/2^+(411)$	$3/2^+(411)$	$7/2^+(633)$	$5/2^+(642)$	$9/2^-(514)$	$7/2^-(523)$
Band heads (keV)	0	953.6	212.2	298.7	0	389.18	469.5	662.0
$A = \frac{\hbar^2}{2\mathcal{I}}$ (keV) This work:	9.654	--	12.40	14.33	4.605	5.33	11.20	14.11
Bunker & Reich:	10.3	--	(12.5)	--	--	--	11.3	14.0
B (eV)	-1.931	--	-8.53	-11.4	2.75	3.69	-1.06	-1.69
$A_{2K}$ (keV)	$0.830 \times 10^{-10}$	$-0.163 \times 10^{-7}$	-9.049	0.1406	$-0.574 \times 10^{-8}$	$0.670 \times 10^{-3}$	$-0.410 \times 10^{-10}$	$0.845 \times 10^{-8}$
Number of levels fitted	12	1	12	7	6	5	7	2
$\alpha$ (keV)	15.05		13.37		4.968		12.66	
$\beta$	$4.53 \times 10^{-4}$		$7.47 \times 10^{-4}$		$-6.48 \times 10^{-4}$		0.108	
$\alpha_{2K}$ (keV)	$-1.603 \times 10^{-6}$		-8.979		$0.6686 \times 10^{-3}$		$0.830 \times 10^{-6}$	
$ j_+ $	4.98		0.5790		2.491		1.635	
$ \langle K   j_+   K+1 \rangle _{th}$	5.6		0.56		6.1		4.4	
$\Sigma (E_{th} - E_{exp})^2$	25.637		436.5		2.96		0.352	
Other Bands	$11/2^+(615)$		$5/2^+(413)$		$9/2^+(642)$		$5/2^-(532)$	
Assignment	1160.	4.86	~925.	0.62	~930.	5.65	~1700.	5.1
Band head (keV)	$5/2^+(642)$		$5/2^+(402)$		$3/2^+(652)$		$11/2^-(505)$	
	1606.	6.18	~1700	2.33	~970	6.50	> 3000	3.3
			$1/2^+(420)$					
			> 2000	2.82				

how many parameters were used on the expansion and on the number of levels included in the fit.

When condition (1) is violated, then the mixing between the two bands is large. The question arises, can one do any progress with a calculation which mixes just those two bands and represents the mixing with the other bands through the perturbation expansions? Very simple two-band expansions with fixed moment-of-inertia were already used by Kerman<sup>3</sup> in 1956 with application to  $^{183}\text{W}$ . The expression we used is given by:

$$\begin{vmatrix} M_{11} - E_1 & M_{12} \\ M_{21} & M_{22} - E_1 \end{vmatrix} = 0 \quad (3)$$

where

$$M_{11} = E_{K>}^0 + \alpha \frac{I(I+1) - K_{>}^2}{1 + \beta(I(I+1) - K_{>}^2)}$$

$$M_{22} = E_{K<}^0 + \alpha \frac{I(I+1) - K_{<}^2}{1 + \beta(I(I+1) - K_{<}^2)}$$

$$+ \alpha 2K_{<} \frac{(-1)^{I+K_{<}} \frac{(I+K_{<})!}{(I-K_{<}^2)!}}{[1 + \beta(I(I+1) - K_{<}^2)]^{2K_{<}}}$$

$$M_{12} = M_{21} = \alpha \frac{\langle j_{+} \rangle \sqrt{I(I+1) - K_{>}K_{<}}}{1 + \beta(I(I+1) - K_{>}K_{<})}$$

The two solutions of this quadratic equation give the energy levels of the upper and lower band. (Of course,  $K_{>} = K_{<} + 1$ .) Parameter  $\alpha$  is the rotational constant ( $\hbar^2/2\mathcal{I}$ ) (the same  $\alpha$  is used in the two bands to reduce the number of parameters, but this condition should probably be relaxed to better simulate the interaction with the neglected bands).  $\beta$  is the softness parameter and so,  $\alpha/[1 + \beta(I(I+1) - K_{>}K_{<})]$  allows for a variable moment-of-inertia.  $\langle j_{+} \rangle$  is related to Coriolis matrix element connecting the two bands.

Table I shows the results of some of the cases studied by doing a least-squares fit on the energy levels.

For  $^{181}\text{W}$ , a multi-band analysis was done by Lindblad et al.<sup>4</sup> The admixture of  $9/2^{+}(624)$  and  $7/2^{+}(633)$  into the rotational ground band

(mainly  $9/2^{+}(624)$ ) is shown in Fig. 1. One observes that with  $|\langle j_{+} \rangle| = 4.98$  one gets a good agreement between the two-band fit and multi-band fit. The  $9/2^{+}(624)$  admixture in the multi-band fit is lower because there is also some admixture of other levels (although small) in the ground band, and when comparing with the two-band fit, one should really add it to the  $9/2^{+}(624)$  component. One also sees that the energy differences are fitted very well (see Fig. 2). That the fit is sensitive to  $|\langle j_{+} \rangle|$  can be seen by fixing it at some other value. If  $|\langle j_{+} \rangle|$  is fixed at 1.77, one gets a much poorer fit and the amount of admixture of  $7/2^{+}(633)$  in the ground band becomes very different from what the multi-band fitting procedure gives.

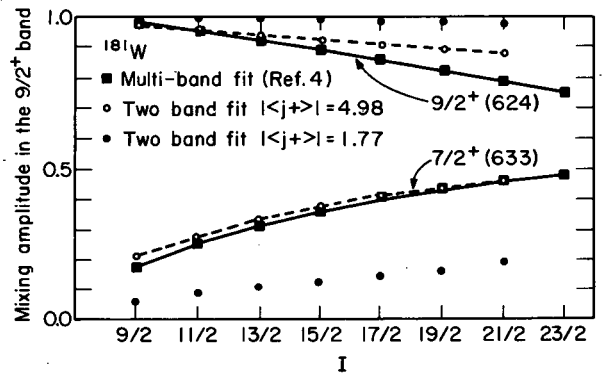


Fig. 1. Mixing amplitudes of the  $9/2^{+}(624)$  and  $7/2^{+}(633)$  configuration in the  $9/2^{+}$  band of  $^{181}\text{W}$ . (XBL-744-2827)

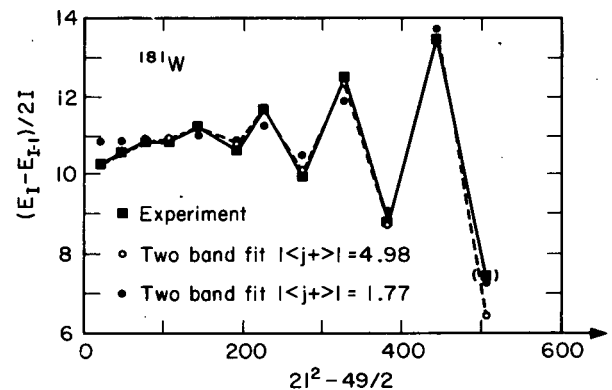


Fig. 2. Comparison of the experimental and fitted energy levels for  $^{181}\text{W}$ . (XBL-743-2509)

Table II. Comparison of experimental and fitted energy levels for  $^{249}\text{Bk}$ .

Spin	$7/2^+(633)$		$5/2^+(642)$	
	$E_{\text{exp}}$	$E_{\text{fit}}$	$E_{\text{exp}}$	$E_{\text{fit}}$
5/2	—	—	389.18	390.05
7/2	0.	-0.144	428.96	428.22
9/2	41.79	41.72	475.01	474.78
11/2	93.75	93.74	541.94	541.83
13/2	155.84	155.59	598.07	598.29
15/2	229.26	230.31		718.18
17/2	311.90	311.32		748.86
19/2		416.76		988.05

In Fig. 3 the experimental and calculated energy differences versus spin are plotted for  $^{249}\text{Bk}$ . (The nine experimental points plotted are fitted by only four parameters). The agreement is very good. The experimental energies were recently measured by Hoff.<sup>5</sup> In Table II the experimental and calculated energy levels are given.

$^{161}\text{Ho}$  is a typical case where the mixing of the two bands is large, and inequality (1) does not hold. The fits with the traditional expansion depend very much on how many levels are fitted and how many parameters are used

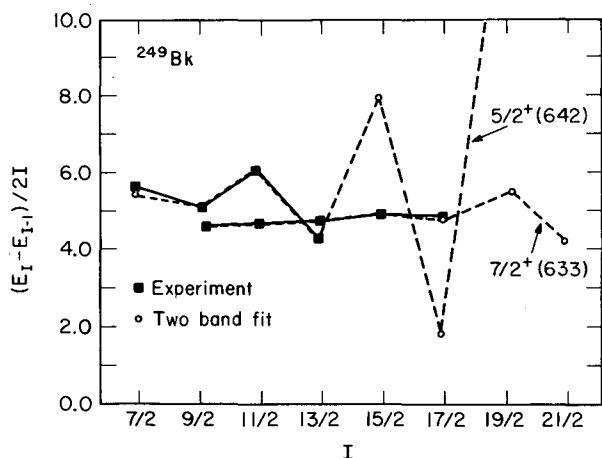


Fig. 3. Comparison of the experimental and fitted energy levels for the  $5/2^+(642)$  and  $7/2^+(633)$  rotational bands. All the experimental points on the figure are fitted for both bands simultaneously with only four parameters. (XBL-743-2510)

on the fit. In Fig. 4 one can observe how well a four and five parameter fit (without including  $E_0$ ) does. In all cases shown, the fit was done only up to  $I=13/2$  (that is seven energy levels). One sees that the traditional expansion fails completely in predicting the higher spin levels. The fit with the two band mixing expansion does better than both of them (note that only four parameters are used and at the same time seven levels of the upper band are also fitted).

To conclude, we would like to say that the two band mixing expansions seems to work well

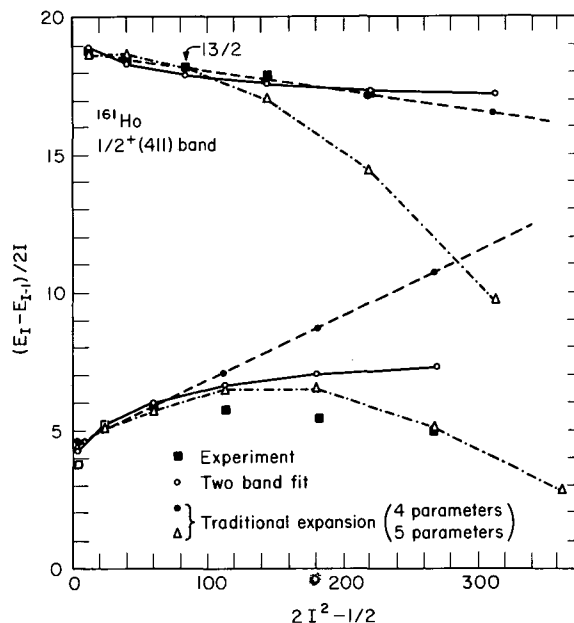


Fig. 4. Comparison of the traditional and two-band energy fitting for  $^{161}\text{Ho}$ . (XBL-743-2511)

when the mixing is mainly between two bands. Thus, some physical insight can be gained without going to the sophisticated multi-band fitting formalism. One should keep in mind that the parameters one gets out of this theory are still renormalized parameters, due to the neglected interaction with the other bands. Also often, at least three or more bands contribute significantly to the mixing, and then only a multi-band calculation would be meaningful.

#### Footnotes and References

\* On leave from Facultad de Ciencias, U. de Chile.

† J. S. Guggenheim Fellow.

† Present address: Hahn-Meitner Institut, West Berlin, Germany.

1. C. T. Alonso and J. O. Rasmussen, LBL Nuclear Chemistry Annual Report (1972).
2. M. I. Baznat, N. I. Pyatov, and M. I. Chernej, *Physica Scripta* **6**, 227 (1972).
3. A. K. Kerman, *Dan. Mat. Fys. Medd.* **30**, no. 15 (1956).
4. Th. Lindblad, H. Ryde, and P. Kleinheinz, *Nucl. Phys.* **A210**, 253 (1973).
5. R. Hoff, private communication.

## NUMBER-DISPLACEMENT DEGREES OF FREEDOM IN NUCLEAR ROTATIONAL THEORY†

John O. Rasmussen and Chin W. Ma\*

In theoretical calculations of the nuclear rotational spectrum, several specific collective degrees of freedom have been considered as influencing deviations from the  $I(I+1)$  energy spacings. There are the proton and neutron pairing correlations involved in the Coriolis antipairing (CAP) effect. There are the  $\beta$ - and  $\gamma$ -vibrational degrees of freedom involved in shape-change effects. There is also a fourth-order cranking effect that may be expressed in terms of an additional collective degree of freedom as

$$E = \sum_i \frac{1}{2} C_i (X_i - X_{i0})^2 + I(I+1)/2J(X_i), \quad (1)$$

where  $X_i$  ( $i = 1, 2, 3, \dots$ ) describes the various degrees of freedom,  $C_i$  is the spring constant associated with the  $i$ th degree of freedom, and  $J(X_i)$  is the moment of inertia. The rotational solution may be obtained by minimizing the total energy of Eq. (1) with respect to each of the  $X_i$  at a given angular momentum  $I$ .

In this note we shall identify a new degree of freedom which will affect both the moment of inertia and the potential energy of Eq. (1). What interests us here is the fact that the even-parity orbital systems and odd-parity orbital systems make separable contributions to the moment of inertia, since the operator  $j_x$  has even parity. Thus, it is possible that the nuclear system could change its moment of inertia by shifting nucleons between the two orbital systems of opposite parity. In other

words, the nuclear system might assume unequal chemical potentials ( $\lambda_+$  and  $\lambda_-$ ) for the different-parity orbital systems in order to minimize the total energy for a given angular momentum.

The potential energy term corresponding to the separation of  $\lambda_+$  and  $\lambda_-$  is easily derived in the limit of the continuous model, where the discrete distributions of Nilsson orbital energies are replaced by a density function  $\rho$ . Let  $\rho_+$  and  $\rho_-$  be the number of Nilsson orbitals per energy interval for positive parity and negative parity, respectively. The number of nucleons transferred for a given change of chemical potential  $\lambda$  is, by definition of  $\rho$ ,

$$dn = 2\rho d\lambda, \quad (2)$$

noting that Nilsson orbitals are doubly degenerate. Thus, conservation of particle number gives the condition

$$\rho_+ d\lambda_+ = -\rho_- d\lambda_- . \quad (3)$$

The new degree of freedom will be characterized by  $\sigma$ , the difference of the chemical potentials:

$$\sigma \equiv \lambda_+ - \lambda_- . \quad (4)$$

The fundamental definition of the chemical potential is

$$\lambda_{\pm} = dE/dn_{\pm} .$$

Integrating in the continuous model, using Eqs. (2) - (4), we obtain the desired spring constant  $C_\sigma$  associated with the number-displacement degree of freedom

$$C_\sigma = 2\rho_+ \rho_- / (\rho_+ + \rho_-). \quad (5)$$

The effect of the new degree of freedom can be estimated by calculating its contribution to the correction term  $BI^2(I+1)^2$  in an expansion of the rotational energy.<sup>2</sup> The general form of the coefficient B is given by<sup>1</sup>

$$B = -\sum \frac{1}{8C_i J^4} \left( \frac{\partial J}{\partial X_i} \right)^2 \quad (6)$$

Equation (6) shows that each degree of freedom makes an additive contribution which is inversely proportional to the spring constant  $C_i$  and directly proportional to the square of the corresponding partial derivative of the moment of inertia.

TABLE I. Derivatives of cranking moment of inertia with respect to chemical potentials (all in units of  $\text{MeV}^{-2}$ ).

Nucleus	$\epsilon$	$\epsilon_4$	$\frac{\partial 2J}{\partial \lambda_{+p}}$	$\frac{\partial 2J}{\partial \lambda_{-p}}$	$\frac{\partial 2J}{\partial \sigma_p}$	$\frac{\partial 2J}{\partial \lambda_{+n}}$	$\frac{\partial 2J}{\partial \lambda_{-n}}$	$\frac{\partial 2J}{\partial \sigma_n}$
<sup>152</sup> Sm	0.202	-0.036	7.42	22.80	-11.5	44.32	19.40	24.0
<sup>162</sup> Dy	0.256	-0.006	5.46	17.97	-9.17	37.16	17.38	19.8
<sup>178</sup> Hf	0.250	0.052	0.30	8.83	-5.40	25.65	5.66	15.7

We have calculated the various derivatives of moments of inertia with respect to chemical potentials  $\lambda_+$  and  $\lambda_-$  for protons and neutrons for several nuclei in the rare-earth region, and they are presented in Table I. It can be shown from Eqs. (3) and (4) that

$$\frac{\partial J}{\partial \sigma} = \left[ \rho_- \frac{\partial J}{\partial \lambda_+} - \rho_+ \frac{\partial J}{\partial \lambda_-} \right] \rho^{-1}. \quad (7)$$

These contributions to B from Eqs. (6) and (7) are summarized in Table II along with comparison values of the total CAP contribution according to Marshalek<sup>3</sup> and the experimental B value.

Including these new degrees of freedom ( $\sigma$  effect) actually makes worse the disagreement with experiment in Refs. 1 and 3, where the CAP contribution  $B_\Delta$  alone often exceeds the experimental. However, the disagreement of cranking-model calculations with experiment is a much broader question which we do not address here.

It is evident that the  $\sigma$ -effect contributions due to the number-displacement degree of freedom are very significant and cannot be neglected. Of course, more realistic calculations should be made of the spring constant  $C_\sigma$  without using the continuous model, but we do not expect a qualitative change from the estimates here. The  $\sigma$  degrees of freedom may alter the role of subshell irregularities in the Coriolis antipairing effect.

TABLE II. Number-displacement effect calculations and comparison of CAP values.

Nucleus	$\rho_p$ ( $\text{MeV}^{-1}$ )	$\rho_n$ ( $\text{MeV}^{-1}$ )	$C_{\sigma p}$ ( $\text{MeV}^{-1}$ )	$C_{\sigma n}$ ( $\text{MeV}^{-1}$ )	$B_{\sigma p}$ ( $\text{MeV}^{-1}$ )	$B_{\sigma n}$ (eV)	$B_{\text{expt}}$ (eV)	$B_\Delta^a$ (eV)
<sup>152</sup> Sm	2.32	3.40	1.09	1.48	10.2	33.1	193	33.7
<sup>162</sup> Dy	2.20	3.03	1.03	1.32	1.33	4.86	10.8	13.1
<sup>178</sup> Hf	2.68	2.88	1.26	1.25	0.67	5.79	13.1	19.4

<sup>a</sup>From Ref. 3.

#### Footnotes and References

<sup>†</sup>Condensed version of article in Phys. Rev. Letters 31, 317 (1973).

\* Physics Department, Indiana University, Bloomington, Indiana.

1. C. W. Ma and J. O. Rasmussen, Phys. Rev.

C 2, 798 (1970).

2. A. Bohr and B. R. Mottelson, Kgl. Dan. Vidensk. Selsk, Mat.-Fys. Medd. 27, No. 16 (1953).

3. E. R. Marshalek, Phys. Rev. 158, 993 (1967).



**EXPONENTIAL DEPENDENCE OF THE NUCLEAR MOMENT-OF-INERTIA  
ON PAIRING CORRELATION AND THE PAIRING STRETCH MODEL  
FOR NUCLEAR ROTATION<sup>†</sup>**

Chin W. Ma\* and John O. Rasmussen

The Exponential Dependence

One of the central problems in the study of deformed nuclei is how to calculate the moment-of-inertia  $J$ .<sup>1</sup> The moment-of-inertia can be calculated using the well known second order cranking formula of Inglis<sup>2</sup> and Belyaev<sup>3</sup>

$$J = 2\hbar^2 \sum_{\Omega_\alpha > 0} \frac{|\langle \alpha' | j_x | \alpha \rangle|^2}{E_{\alpha'} + E_\alpha} (U_{\alpha'} V_\alpha - V_{\alpha'} U_\alpha)^2 \quad (1)$$

where  $|\alpha\rangle$  is the single particle wave function with  $\alpha$  representing the appropriate quantum numbers;  $\Omega_\alpha$  is the magnetic quantum number along the symmetry axis;  $U_\alpha$  and  $V_\alpha$  are the probability amplitudes of the orbital  $\alpha$  in the presence of pairing; and  $E_\alpha$  is the quasi-particle energy. Following our previous treatment,<sup>4</sup> we parametrize  $U_\alpha$  and  $V_\alpha$  by introducing a pairing correlation parameter  $\nu$ . The quantity  $\nu/G$  is the effective number of Nilsson orbitals participating in the pairing correlation. If  $\nu=0$ , we have a sharp Fermi surface with no pairing correlation. If  $\nu=\Delta$ , where  $\Delta$  is the pairing gap parameter, we have the BCS ground state.

In what follows we shall vary the pairing correlation parameter  $\nu$  for a given fixed pairing strength  $G$  to study the behavior of  $J$  as expressed by Eq. (1).

We have carried out cranking model moment-of-inertia calculations for a range of  $\nu$  values for rare-earth nuclei, and the results are plotted in Fig. 1 for protons. A striking result of our calculations is the degree to which the calculated moments-of-inertia conform to

an exponential dependence on the pairing correlation parameters  $\nu_p$  and  $\nu_n$ , as is evident in the excellent straight line behavior in the  $\ln J$  vs.  $\nu$  plots of Fig. 1. This exponential dependence is valid for a wide range of  $\nu$  values above the lower limit  $\nu_L$  which is about 20% - 30% of the energy gap  $\Delta$  of the BCS ground state. For  $\nu$  values smaller than  $\nu_L$  there are usually some deviations.

We have also directly calculated the moment-of-inertia at zero pairing ( $\nu=0$ ) which we denoted as  $J_0$ . Note that in general  $J_0$  does not equal the extrapolated value  $J^{(0)}$ . The difference between  $J_0$  and  $J^{(0)}$  is an indication of the degree of deviation from the exponential dependence at small  $\nu$ . The resulting  $J_0$  for several rare-earth nuclei together with the corresponding rigid-body values are listed in Table I for comparison. It is seen from Table I that there are often substantial deviations of  $J_0$  from  $J_{rig}$ .

Two-Dimensional Pairing Stretch Model

It seemed of interest to proceed further to make a two-dimensional pairing modification of the Diamond, Stephens, Swiatecki stretch model.<sup>5</sup> Whereas their equation reads

$$E = \frac{\hbar^2}{6B\beta^2} I(I+1) + \frac{1}{2} C(\beta - \beta_0)^2, \quad (2)$$

we write an analogous equation in the two pairing coordinates  $\nu_p$  and  $\nu_n$  as

$$E = \frac{\hbar^2}{2J(\nu_p, \nu_n)} I(I+1) + V_{PBCS}(\nu_p) + V_{PBCS}(\nu_n). \quad (3)$$

Table I. Cranking moments-of-inertia with no pairing (all units in MeV<sup>-1</sup>)

Z	A	$\left(\frac{2J_0}{\hbar^2}\right)_p$	$\left(\frac{2J_0}{\hbar^2}\right)_n$	$\left(\frac{2J_0}{\hbar^2}\right)_{total}$	$\left(\frac{2J}{\hbar^2}\right)_{rigid}$
66	162	60.22	102.68	162.90	143.96
68	168	40.98	76.39	117.37	153.66
70	172	40.65	82.38	123.03	159.66
72	178	38.05	76.30	114.35	168.12
74	182	22.03	55.73	77.76	173.49

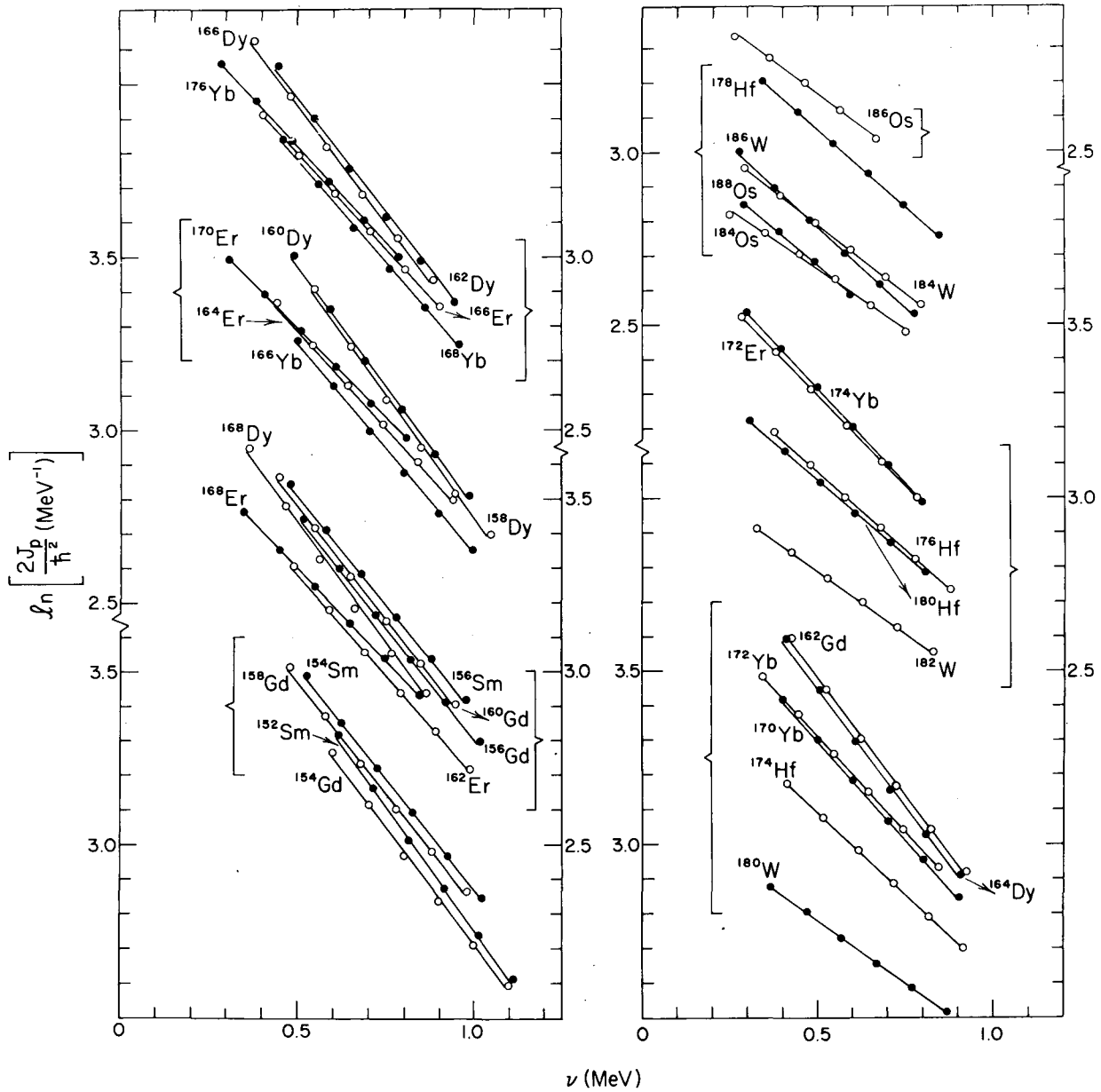


Fig. 1. This plot illustrates for proton systems of deformed nuclei the near-exponential dependence of theoretical cranking moments-of-inertia on pairing. The logarithm of the calculated moment-of-inertia is plotted vs. the pairing correlation parameter  $\nu$  (particle number and pairing strength  $G$  held constant). The points are theoretical calculations with no reference to experiment. (XBL 736-830)

The kinetic energy term will now be expressed in the exponential form found by cranking. Although cranking calculations will reproduce the general trend of experimental moments-of-inertia, cranking moments and higher order correction terms do not agree quantitatively with experiment.<sup>6</sup> Thus, in applying the exponential relation, we shall introduce two adjustable correction factors  $a$  and  $b$  to allow adjustment of the calculated constants  $J_{0p}$ ,  $J_{0n}$ ,  $\gamma_p$  and  $\gamma_n$  as given in Table I. The moment-of-inertia in Eq. (3) now reads

$$J(v_p, v_n) = aJ_{0p} \exp(-b\gamma_p v_p) + aJ_{0n} \exp(-b\gamma_n v_n) \quad (4)$$

The two correction-factors  $a$  and  $b$  are fixed by essentially forcing our calculations to fit the  $2^+ \rightarrow 0^+$  and  $4^+ \rightarrow 2^+$  transition energies.

The number-projected BCS energy that plays the role of potential energy is calculated in the continuous model (cf. Eq. (4.20) of Ref. 3). The Berkeley minimum search routine MINSER was used to find the minimum of the energy function (Eq. 3) for successive even values of spin. These calculations were carried out for five well-deformed nuclei  $^{162}_{66}\text{Dy}$ ,  $^{168}_{68}\text{Er}$ ,  $^{172}_{70}\text{Yb}$ ,  $^{178}_{72}\text{Hf}$ , and  $^{182}_{74}\text{W}$ . Table II summarizes the results for rotational transition energies, comparing both with experiment and with the three-parameter, "extended-VMI model"  $\chi^2$  fits of Saethre et. al.<sup>7</sup> In general, our two-parameter model calculations agree as well with experiment as the three-parameter extended VMI (variable moment-of-inertia) model  $\chi^2$  fits of Saethre et. al.<sup>7</sup> However, we get a more rapid increase of apparent moment-of-inertia at high spin than extended VMI, though we do not get "back-bending."

Table II. Ground band transition energies  $E_I - E_{I-2}$  (keV)

Nucleus	I	This calculation	Extended VMI 3-parameter $\chi^2$	Experimental
$^{162}_{66}\text{Dy}$	2	80.70	80.660	80.660
	4	185.16	185.005	185.005
	6	282.72	282.863	282.864
	8	370.96	372.9	372.6
	10	448.78	455.3	453.7
	12	516.09	530.8	526.2
	14	573.44	600.3	
16	621.67	664.8		

Table II (continued)

$^{168}_{68}\text{Er}$	2	79.80	79.7994	79.7998
	4	184.50	184.283	184.281
	6	285.27	284.634	284.646
	8	380.40	379.545	379.536
	10	468.67	468.5	
	12	549.37	551.7	
	14	622.20		
	16	687.10		
	18	744.15		
$^{172}_{70}\text{Yb}$	2	78.73	78.72	78.74
	4	181.57	181.53	181.52
	6	279.57	279.73	279.74
	8	370.72	372.0	371.5
	10	453.74	457.8	(458.3)
	12	528.00	537.4	(538.1)
	14	593.38	611.3	
	16	650.01	680.2	
	18	698.12		
$^{178}_{72}\text{Hf}$	2	93.20	93.119	93.181
	4	213.63	213.503	213.444
	6	325.62	325.533	325.562
	8	426.12	426.377	426.371
	10	513.60	515.2	
	12	587.69	592.7	
	14	648.69		
	16	697.04		
	18	732.70		
$^{182}_{74}\text{W}$	2	100.09	100.102	100.102
	4	229.34	229.319	229.317
	6	349.29	350.69	351.02
	8	456.65	464.1	464.0
	10	549.80	571.5	567.6
	12	628.41	676.4	

We note that in no case has there been a pairing collapse. The reason that pairing collapse does not occur here up to spins above the Mottelson-Valatin limit may be mainly due

to our inclusion of a particle-number projection term in the pairing energy. Such projection always stabilizes pairing.

We hope that the physical insights of this model will be of value as a guide to future calculations on the challenging problem of nuclear rotational moment-of-inertia.

#### Footnotes and References

† Condensed version of article Phys. Rev. C9, 1083 (1974).

\* Physics Department, Indiana University, Bloomington, Indiana 47401.

1. We shall use ordinary J for the moment-of-inertia, rather than the script letter in common usage. There should not be any confusion with angular momentum, for which the symbol I is used.

2. D.R. Inglis, Phys. Rev. 96, 1059 (1954).

3. S. T. Belyaev, Kgl. Danske Videnskab. Selskab. Mat.-Fys. Medd. 31, No. 11 (1959).

4. C. W. Ma and J. O. Rasmussen, Phys. Rev. C 2, 798 (1970).

5. R. M. Diamond, F. S. Stephens, and W. J. Swiatecki, Phys. Letters 11, 315 (1964).

6. S. G. Nilsson and O. Prior, Kgl. Danske Videnskab. Selskab, Mat.-Fys. Medd. 32, No. 16 (1961). E. R. Marshalek, Phys. Rev. 139B, 770 (1965); 158, 993 (1967).

7. O. Saethre, S. A. Hjorth, A. Johnson, S. Jägare, H. Ryde, and Z. Szymanski, Nucl. Phys. A207, 486 (1973).

## CRANKING MODEL CALCULATION OF $^{162}\text{Er}$ HIGH-SPIN ROTATIONAL STATES INCLUDING $i_{13/2}$ RECOUPLING

C. W. Ma\* and J. O. Rasmussen

As seen in the two preceding reports,<sup>1,2</sup> our nuclear rotational energy calculations with Coriolis antipairing and particle-number conservation do not exhibit backbending at spins as low as experimentally observed in 92-96 neutron nuclei. Our calculations use rotational kinetic energy expressions from cranking calculations including fourth order. In seeking further improvements, we have gone back to our matrix diagonalization approach<sup>3</sup> of five years ago in treating the cranking velocity  $\omega$  to all orders for the high-j orbitals ( $i_{13/2}$  neutron and  $h_{11/2}$  proton systems). This approach is analogous to the diagonalization of the Coriolis interaction, as carried out by Stephens and Simon.<sup>4</sup> They have identified backbending with the crossing of the ground band with a band of predominantly two quasi-particle character. Their calculation was done for fixed pairing correlation, and we here wish to include Coriolis anti-pairing effects. Results here reported are constrained to a fixed deformation.

#### Basic Assumptions of Calculation

Consider the cranking model equations

$$(H - \omega J_x) \psi_\omega = W_\omega \psi_\omega \quad (1)$$

$$\langle \psi_\omega | J_x | \psi_\omega \rangle = \sqrt{I(I+1)} \quad (2)$$

The energy of a rotational state is

$$E_{\text{tot}}(\omega) = \langle \psi_\omega | H | \psi_\omega \rangle - \langle \psi_\omega | H | \psi_0 \rangle \quad (3)$$

By eliminating  $\omega$  between Eqs. (2) and (3) one can obtain a relation between  $E_{\text{tot}}$  and I which can then be compared with the experimental data.

Since the operator  $J_x$  has positive parity, Eq. (1) can be solved separately for the proton even parity orbitals ( $P^+$ ), the proton odd parity orbitals ( $P^-$ ), the neutron even parity orbitals ( $N^+$ ) and the neutron odd parity orbitals ( $N^-$ ).

We consider first the fourth-order cranking solutions for the low-j orbitals (odd-parity neutrons and even-parity protons)

$$E_{\text{tot}}^{4\text{th}}(\omega) = \frac{1}{2} \omega^2 (J_0 + 3C_4 \omega^2) \quad (4)$$

$$\langle J_x \rangle^{4\text{th}}(\omega) = \omega (J_0 + 2C_4 \omega^2) \quad (5)$$

For the contribution of odd-parity protons to energy and to angular momentum, the cranking equations are solved by diagonalizing all two quasi-particle excitations in  $5h_{11/2}$ . The dimension of the matrix is  $37 \times 37$ . We further notice that the  $5h_{11/2}$  Nilsson wave function is very pure, and the mixing of the other j-orbitals is in general less than 10%; thus we simply assume that the wave functions of the  $5h_{11/2}$  are all pure and can be described by a good-j basis  $|jm\rangle$ . The energies of the  $5h_{11/2}$  states, however, will still be chosen as the exact Nilsson energies.

For the even-parity neutrons we diagonalize only the  $6i_{13/2}$  and neglect the other  $N^+$  orbitals. The dimension of all two quasi-particle excitations in  $6i_{13/2}$  is  $50 \times 50$ . Our total energy can be expressed as

$$E_{\text{tot}}(\omega) = \frac{1}{2} \omega^2 (J_o^{P+} + J_o^{N-}) + \frac{3}{2} \omega^4 (C_4^{P+} + C_4^{N-}) \\ + E(\omega)_{5h_{11/2} \text{ diagonalization}} \quad (6) \\ + E(\omega)_{6i_{13/2} \text{ diagonalization}}.$$

The  $\langle J_x \rangle$  is

$$\langle J_x \rangle = \omega (J_o^{P+} + J_o^{N-}) + 2\omega^3 (C_4^{P+} + C_4^{N-}) \quad (7) \\ + \langle J_x \rangle_{5h_{11/2} \text{ diagonalization}} \\ + \langle J_x \rangle_{6i_{13/2} \text{ diagonalization}}.$$

#### Single Particle Basis and Pairing

The single particle basis and pairing parameters follow exactly those of Nilsson et al.<sup>5</sup> They are

$$\begin{aligned} \kappa_p &= 0.0637, & \mu_p &= 0.60 \\ \kappa_n &= 0.0637, & \mu_n &= 0.42 \\ g_0 &= 19.2 \text{ MeV}, & g_1 &= 7.4 \text{ MeV} \\ \epsilon_2 &= 0.242, & \epsilon_4 &= -0.007. \end{aligned} \quad (8)$$

There is no adjustable parameter in the present calculation.

#### Coriolis-Antipairing (CAP) Effect

For a given  $\omega$ , we try to minimize

$$\delta \langle H - \omega J_x \rangle = 0 \quad (9)$$

by varying the pairing parameter  $\nu$  under the constraint

$$\langle \psi_o | N | \psi_o \rangle = n \quad (10)$$

i.e., only the average number of particles of the ground state is conserved. We find it very important to include the fixed-particle-number correction in studying the CAP effect. In the present calculation this is approximately taken into account by adding a term

$$-G \sum_{k \neq l > 0} U_k V_k^3 U_l^3 V_l / \sum_{k > 0} U_k^2 V_k^2 \quad (11)$$

to the BCS ground state energy.

#### Discussion

**Level-crossing.** Figure 1 shows the level-crossing between the lowest state ( $n=1$ ) and the second lowest state ( $n=2$ ) for the  $6i_{13/2}$  neutron system. The level-crossing in  $6i_{13/2}$

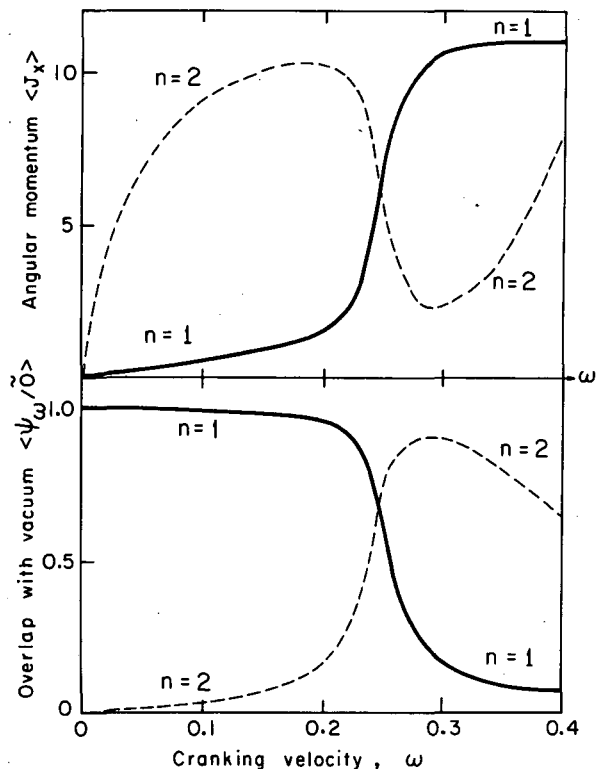


Fig. 1. Angular momentum contribution  $\langle J_x \rangle$  (above) and overlap with BCS vacuum (lower) for the  $i_{13/2}$  neutron system in  $^{162}\text{Er}$ . The abscissa is the cranking velocity  $\omega$ .

(XBL-743-2512)

occurs at  $\omega \approx 0.24$  MeV.

**CAP effect.** Figure 2 shows the CAP effect for both proton and neutron in the  $\nu_c$  vs  $\omega$  plot and also in the  $\nu_c$  vs I plot.

The proton pairing decreases only by 10% up to spin 18, the neutron pairing decreases by 30%. There is no pairing collapse in either case.

**Backbending.** Figure 3 compares the energy  $E(I)$  with the experimental data. The calculated results are obtained with the CAP effect. Table I lists results with and without CAP.

We are able to obtain backbending, although it occurs at  $12^+ \rightarrow 10^+$  instead of at the experimental place of  $16^+ \rightarrow 14^+$ . The level-crossing is responsible for the backbending. The curve before the level-crossing and the curve after the level-crossing do not have the same slope, so they don't join smoothly. We also have preliminary results reducing the pairing

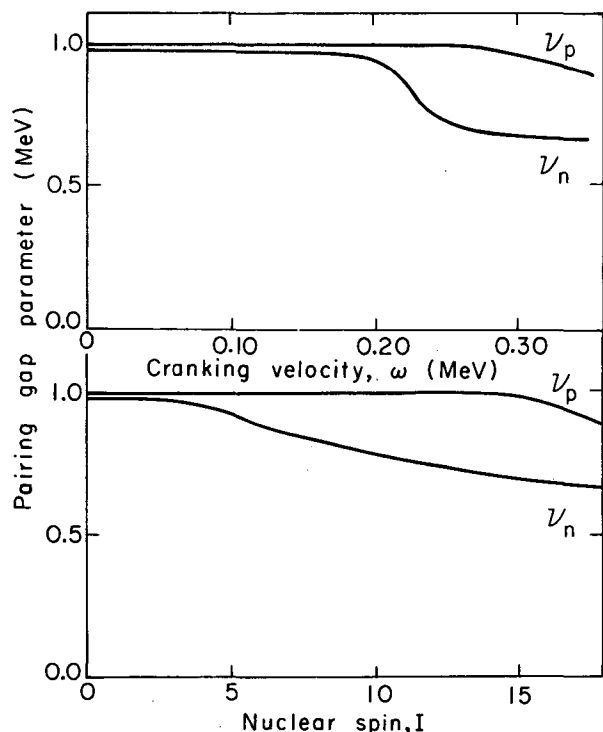


Fig. 2. This figure illustrates the Coriolis antipairing with plots of proton and neutron gap parameters as a function of cranking velocity  $\omega$  (above) and total nuclear spin I (below). (XBL-743-2513)

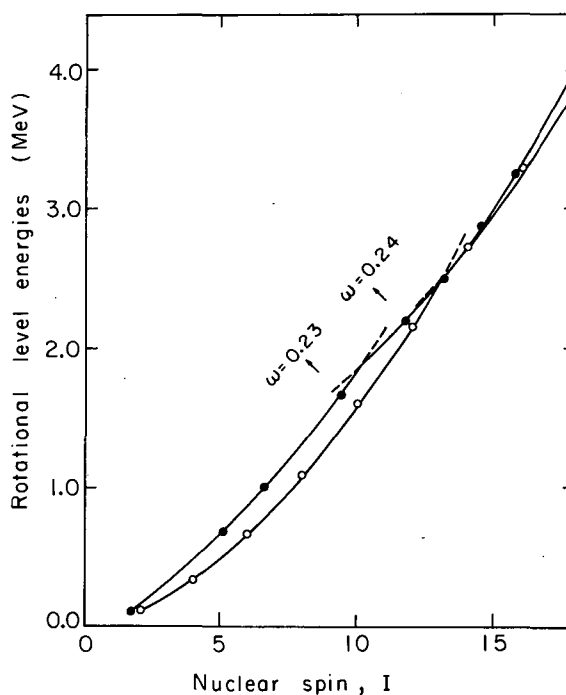


Fig. 3. Theoretical (solid dots) and experimental (open circles) rotational level energies in  $^{162}\text{Er}$ . The backbending points are indicated by crossing curves with dashed extensions. (XBL-743-2514)

strength constant  $g_0$  from the Nilsson et al.<sup>5</sup> value of 19.2 to 18.8 MeV (see Eq. (8)), as is proper consistent with the particle number conservation correction. The theoretical back-bending moves to the  $14 \rightarrow 12$  transition both with and without CAP, and overall agreement with experiment is improved.

In our present calculation the level-crossing in  $6i_{13/2}$  occurs at  $\omega \approx 0.24$ . The proton  $5h_{11/2}$  also shows a level-crossing although at much higher  $\omega$ , namely  $\omega \approx 0.39$ . Hence, we can predict that there will be a second backbending at high spin, corresponding to the level-crossing in  $5h_{11/2}$ .

We did not allow ourselves any free parameters to renormalize the cranking inertial parameters as in Refs. 1 and 2. With such adjustment the theoretical breakpoint for backbending would move up in spin.

Our results are consistent with the general results of the elaborate Hartree-Fock-Bogoliubov calculations of Banerjee, Dalafi, Ring, and Mang.<sup>6</sup> They find some general decrease

Table I. Experimental and theoretical rotational energies in  $^{162}\text{Er}$ .

Experimental			Theoretical			
$E_I(\text{keV})$	$\Delta E_{I, I-2}(\text{keV})$	$E_I(\text{keV})$	No CAP		With CAP	
			$E_I(\text{keV})$	$\Delta E_{I, I-2}(\text{keV})$	$E_I(\text{keV})$	$\Delta E_{I, I-2}(\text{keV})$
0	0	0			0	
2	102	102	141	141	140	140
4	329	227	457	316	456	316
6	666	337	886	429	860	404
8	1096	430	1368	482	1324	464
10	1602	506	1846	478 <sup>a</sup>	1830	506
12	2164	562	2348	502	2242	412 <sup>a</sup>
14	2744	580	2878	530	2732	490
16	3290	546 <sup>a</sup>	3466	588	3320	588
18	3844	554	4160	694	3998	678

<sup>a</sup>Denotes first backbending transition.

in pairing but attribute the backbending in  $^{162}\text{Er}$  to the sudden decoupling in the  $i_{13/2}$  orbitals.

We hope to further refine our calculation, allowing for additional degrees of freedom and extending the calculations to other nuclei.

#### Footnotes and References

\*Physics Department, Indiana University, Bloomington, Indiana.

1. C. W. Ma and J. O. Rasmussen, Phys. Rev. C 9, 1083 (1974), cf. also digest version in this annual report.

2. S. Y. Chu, J. O. Rasmussen, and C. W. Ma, preceding report, cf. also Bull. Am.

Phys. Soc. (Ser. II) 18, 1584 (1973).

3. C. W. Ma, Ph.D. Thesis, Physics Department, University of California, Berkeley, June 1969 (unpublished).

4. F. S. Stephens and R. S. Simon, Nucl. Phys. A183, 257 (1972).

5. S. G. Nilsson et al., Nucl. Phys. A131, 1 (1969).

6. B. Banerjee, H. R. Dalafi, P. Ring, and H. J. Mang, in Proceedings of the International Conference on Nuclear Physics, Munich, 1973, edited by J. de Boer and H. J. Mang (North-Holland Publishing Co., Amstertsam, 1973), Vol. I, p. 198.

## THREE-DIMENSIONAL PAIRING STRETCH MODEL CALCULATIONS

S. Y. Chu, J. O. Rasmussen and C. W. Ma\*

At present, for many even-even deformed nuclei, the ground rotational bands are known up to very high spin members. The energies exhibit considerable deviations from the simple  $I(I+1)$  rule. A large number of studies have been directed at understanding these deviations. Usually the following effects are considered as the most important sources of these deviations:

- (1) the Coriolis antipairing effect of proton and neutron (Mottelson-Valatin effect<sup>1</sup>)
- (2) the quadrupole stretching (Bohr-Mottelson model<sup>2</sup>)
- (3) the fourth-order cranking effect (as in Harris expressions<sup>3</sup>)
- (4) the special decoupling of nucleons in high angular momentum orbitals (such as,  $i_{13/2}$  neutrons, as pointed out by Stephens and Simon<sup>4</sup>).

We are reporting results of a large variational calculation in the framework of the new (1969) Nilsson model.<sup>5</sup> This 1969 model includes hexadecapole as well as quadrupole deformation and diagonalizes more than 10 oscillator shells without truncation. We also include the pairing interaction by the BCS method, but we include in the BCS energy the important particle-number projection. The moments of inertia and derivatives with respect to deformation and pairing parameters are calculated with the Inglis-Belyaev cranking expression.<sup>6,7</sup> At each spin the program searches for the total energy minimum in the space of three coordinates. The three coordinates are pairing correlation for protons and for neutrons and quadrupole deformation. In order to study the fourth-order cranking effect, we have calculated both with and without the theoretical fourth order cranking coefficient. At this stage, the physics corresponding to the special decoupling of nucleons in high  $j$ -orbitals is not included.

The total Hamiltonian reads like this:

$$H = E_{\text{BCS}}^{(p)} + E_{\text{BCS}}^{(n)} + E_{\text{rot}}$$

The BCS energy expression is as follows:

$$E_{\text{BCS}} = \sum_i e_i 2v_i^2 - G \left( \sum_i u_i v_i \right)^2 - G \left( \frac{\sum_i u_i^3 v_i^3}{\sum_i u_i^2 v_i^2} \right)$$

There is one such equation for protons and one for neutrons. With this potential alone the

calculation gives too small a value for equilibrium quadrupole deformation. Therefore, we have added a correction of the form of the leading order term in the liquid drop Coulomb energy:

$$H_{\text{corr}} = -\alpha \epsilon^2$$

Here  $\epsilon$  is Nilsson's quadrupole deformation parameter, coefficient  $\alpha$  is empirically adjusted to force the equilibrium deformation to equal the experimental value. The required  $\alpha$  values are considerably larger than the Coulomb term would give, but we attribute this difference to an incorrect surface energy from the Nilsson model.

In the rotational kinetic energy  $E_{\text{rot}}$ , the moments of inertia are based on cranking model calculations. Numerical calculations of Ref. 8 show that these moments of inertia have exponential dependence on pairing parameters  $\nu$ . The calculations here reported improve upon the rotational energy calculations of Ref. 8 in that the full PBCS energy sum is made, instead of using the continuous model, and we also include quadrupole deformation as a third variational parameter. Therefore, in our calculation, we have taken the moment of inertia as a sum of four terms, the contributions of proton and neutron systems of even and odd parity with constants from cranking calculations as in Ref. 8, except that we split up the contributions of opposite parities. We introduce two renormalization factors, as in Ref. 8. One of them is to adjust the magnitude of the total moment of inertia, the other to adjust the pairing dependence. These two factors are adjusted to fit the experimental transition energies from spin 6 to 4 and from 4 to 2. After these two constants are fixed, we proceed to calculate the other members of ground rotational bands. We also include fourth-order cranking by solving angular velocity  $\omega$  with the Harris equations.

$$\langle J \rangle = \sqrt{I(I+1)\hbar} = J\omega + 2C_4\omega^3$$

$$E_{\text{rot}} = \frac{1}{2} J\omega^2 + \frac{3}{2} C_4\omega^4$$

We have made calculations for  $^{152}\text{Sm}$ ,  $^{154}\text{Sm}$ ,  $^{158}\text{Dy}$ ,  $^{160}\text{Dy}$ ,  $^{162}\text{Dy}$ ,  $^{164}\text{Dy}$ ,  $^{162}\text{Er}$ ,  $^{164}\text{Er}$ ,  $^{166}\text{Yb}$ , and  $^{170}\text{Yb}$ . Since there is insufficient space here we will present only a sampling of the results.



In Figs. 1 and 2 it is seen that our theoretical energies have no backbending. In this regard these calculations agree with the earlier continuous model calculations of Ma and Rasmussen.<sup>8</sup> Pairing collapse and accompanying backbending do not occur until higher spins than is the case for experiment, the particle-number conserving term in the BCS energy pushing the collapse to higher spin than the Mottelson and Valatin estimate.<sup>1</sup> We thus feel that the experimental backbending for  $^{162}\text{Er}$ ,

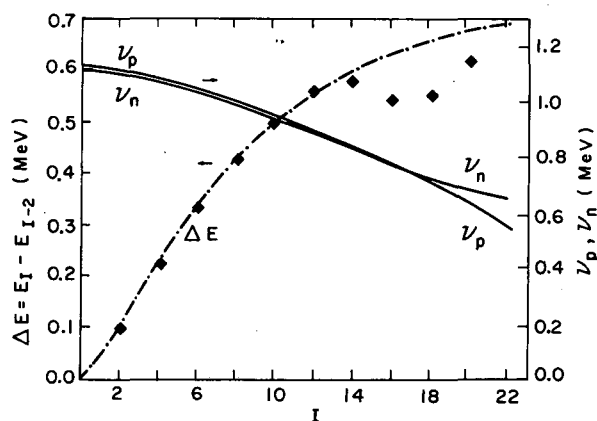


Fig. 1. The broken line shows the calculated transition energies of spin  $I$  to  $I-2$  of  $^{162}\text{Er}$ . The scale is on the left. The diamonds mark the experimental values. The pairing parameters  $\nu_p$  and  $\nu_n$  are plotted with solid lines, and the scale is on the right axis.

(XBL743-2515)

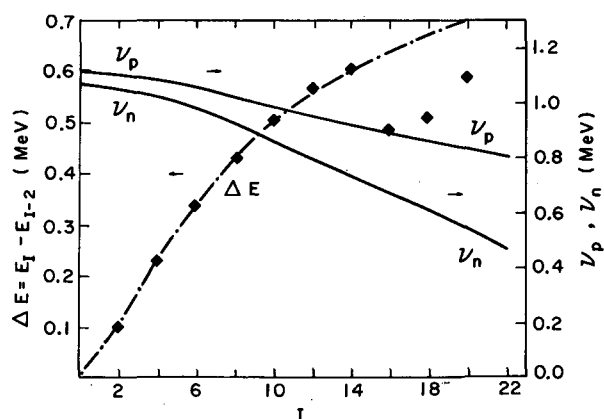


Fig. 2. The broken line shows the calculated transition energies of spin  $I$  to  $I-2$  of  $^{166}\text{Yb}$ . The scale is on the left. The diamonds mark the experimental values. The pairing parameters  $\nu_p$  and  $\nu_n$  are plotted with solid lines, and the scale is on the right axis.

(XBL743-2516)

$^{166}\text{Yb}$ , and neighboring nuclei is primarily due to special recoupling effects of the  $i_{13/2}$  neutrons, as Stephens and Simon have stressed and as early calculations of Chin Ma indicated.<sup>9</sup>

In Fig. 3 the fit of  $^{168}\text{Yb}$  is quite good until spin 22, where the neutron pairing drops abruptly, and our moment of inertia formulas are not good approximations. The pairing collapse here contrasts with Fig. 2, and the difference probably arises as a consequence of the neutron subshell for  $^{168}\text{Yb}$ , where neutron pairing is more fragile. We have also calculated the rotational  $g$ -factors and  $B(E2)$  values for all states.

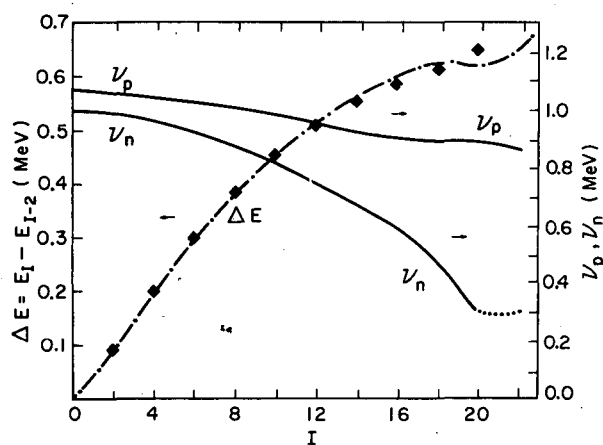


Fig. 3. The broken line shows the calculated transition energies of spin  $I$  to  $I-2$  of  $^{168}\text{Yb}$ . The scale is on the left. The diamonds mark the experimental values. The pairing parameters  $\nu_p$  and  $\nu_n$  are plotted with solid lines, and the scale is on the right axis.

(XBL743-2517)

### References

\* Physics Department, Indiana University, Bloomington, Indiana.

1. B.R. Mottelson and J.G. Valatin, Phys. Rev. Letters 5, 511 (1960).
2. A. Bohr and B.R. Mottelson, Kgl. Dan. Vid. Selsk. Mat. Fys. Medd. 27, No. 16 (1953).
3. S.M. Harris, Phys. Rev. 138, 509 (1965).
4. F.S. Stephens and R.S. Simon, Nucl. Phys. A183, 257 (1972).
5. S.G. Nilsson et. al., Nucl. Phys. A131, 1 (1969).

6. D.R. Inglis, Phys. Rev. 96, 1059 (1954).  
 7. S. T. Belyaev, Kgl. Dan. Vid. Selsk. Mat. Fys. Medd. 31, No. 11 (1959).  
 8. See preceding report from C. W. Ma and

J. O. Rasmussen, Phys. Rev. C 9, 1083 (1974).

9. Cf. Fig. 17 of C. W. Ma, Ph.D. Thesis, Physics Department, University of California, Berkeley, June 1969 (unpublished).

### MICROSCOPIC CALCULATION OF THE HIGHER-ORDER EFFECTS IN NUCLEAR QUASI-ROTATIONAL SPECTRUM

C. W. Ma\* and C. F. Tsang

The variable-moment-of-inertia model,<sup>1</sup> which has been very successful in describing the low-spin as well as the high-spin nuclear rotational energies  $E$ , can be expressed as follows:

$$E = \frac{1}{2} C (J - J_0)^2 + \frac{I(I+1)}{2J}, \quad (1)$$

$$\frac{\partial E}{\partial J} = 0,$$

where  $J_0$  is the moment-of-inertia of the nucleus and  $C$  is called the force constant; both of them can be determined experimentally by fitting to the energy levels.

We have attempted to calculate microscopically the parameter  $J_0$  and  $C$ . First the nucleons are considered to move in a deformed potential with pairing interaction acting between them. The pairing strength and the detailed shape of the deformed potential are taken to

be similar to those in the work of Nilsson et al.,<sup>2</sup> except that we have now readjusted several neutron levels around neutron number  $N=104$  and 108 in order to reproduce better the experimental levels. Next, based on the cranking model of Inglis,<sup>3</sup> the moment-of-inertia  $J_0$  can be evaluated by the Belyaev formula.<sup>4</sup>

The force constant  $C$  can also be expressed microscopically as

$$C^{-1} = \sum_i \frac{1}{C_i} \left( \frac{\partial J_0 / \hbar^2}{\partial X_i} \right)^2 = \sum_i K_{Xi} \quad (2)$$

where  $X_i$  ( $i=1-5$ ) are variables associated respectively with the  $P_2$  deformation, the  $P_4$  deformation, the proton pairing, the neutron pairing, and the fourth-order cranking; and  $C_i$  are the corresponding force constants. In

Table I. Sample results for the force constant  $C_{VMI}^{-1}$  and the separate contributions from various higher order effects. The experimental values of  $C_{VMI}^{-1}$  are taken from Ref. 1. All units are in  $\text{MeV}^{-3}$ .

Nucleus	$K_{22}$	$K_{44}$	$K_{v_p}$	$K_{v_n}$	$4C$	$C_{VMI}^{-1}$ (calc.)	$C_{VMI}^{-1}$ (exp.)
<sup>152</sup> Sm	13	15	30.35	43.39	80.43	182.2	595
<sup>158</sup> Gd	3	5	42.53	79.72	92.29	222.5	245
<sup>162</sup> Dy	4	3	45.58	92.22	105.1	249.8	195
<sup>166</sup> Er	2	1	42.27	122.30	106.8	274.4	240
<sup>170</sup> Yb	3	0	32.66	88.03	75.84	199.5	160
<sup>178</sup> Hf	1	0	17.55	75.96	82.23	176.7	135
<sup>182</sup> W	0	0	11.77	227.45	46.35	285.6	98
<sup>186</sup> Os	1	1	21.05	58.22	63.54	144.8	162

Table II. Sample results for the moment-of-inertia, B coefficient and the force constant calculated with  $G_0/A = 18.0$  MeV, the results of Marshalek<sup>7</sup> are also listed for comparison.

Nucleus	..... This calculation.....			..... Marshalek <sup>a</sup> .....	
	$\frac{2J_0}{\hbar^2}$ (MeV <sup>-1</sup> )	-B (eV)	$C_{VMI}^{-1}$ (MeV <sup>-3</sup> )	$\frac{2J_0}{\hbar^2}$ (MeV <sup>-1</sup> )	-B (eV)
<sup>152</sup> Sm	55.57	77.0	367	46.77	221
<sup>154</sup> Sm	78.02	50.0	927	72.31	37.5
<sup>156</sup> Gd	70.69	54.4	680	66.53	43.0
<sup>158</sup> Gd	69.66	33.2	391	74.96	26.7
<sup>160</sup> Dy	66.06	42.5	405	68.45	37.4
<sup>162</sup> Dy	70.74	37.6	471	74.02	33.4
<sup>166</sup> Er	73.17	45.8	656	73.96	33.7
<sup>168</sup> Er	71.40	25.4	330	74.96	25.0
<sup>172</sup> Yb	73.90	27.9	416	75.93	30.0
<sup>174</sup> Yb	76.61	25.9	446	77.82	27.8
<sup>176</sup> Hf	73.30	40.2	580	67.43	42.6
<sup>178</sup> Hf	66.44	26.0	253	64.10	44.0
<sup>184</sup> W	54.67	31.0	139	53.48	68.5
<sup>186</sup> W	46.41	56.4	131	48.40	99.1

<sup>a</sup> See Ref. 7

the present calculations, the fixed-particle-number corrections have been included in evaluating the pairing force constant. We have also applied the Strutinsky<sup>6,2</sup> method to take into account the shell-correction effect in evaluating the  $P_2$  and  $P_4$  shape force constant.

Some of the results of calculation were presented in the Nuclear Chemistry Annual Report of 1972. Since then we have investigated details of individual contributions to the force constant from various effects. It is shown in Table I that the neutron and proton Coriolis-antipairing and the fourth-order cranking corrections give the main contributions, while centrifugal stretching effects are relatively small. We have also investigated the effect of varying the pairing strength on our results. In Table II we display the results for slightly reduced pairing strength  $G_0/A = 18.0$  MeV (compared with the usual value of 19.2 MeV). With this value the calculated moment of inertia are much improved. Our calculations are compared with those of Marshalek<sup>7</sup> who used the B coefficient, defined as

$$B = -\sum_i \frac{1}{8C_i J_0^4} \left( \frac{\partial J}{\partial X_i} \right)_{x_{i0}}^2$$

The two calculations yield similar results at the middle of the rare-earth region, though discrepancies occur at both ends of the region. Various other investigations, including shifting of single particle levels, were also made. These investigations are to be published.

#### References

- \*Physics Department, Indiana University, Bloomington, Indiana.
1. M. A. J. Mariscotti, G. Scharff-Goldhaber, and B. Buck, Phys. Rev. 178, 1864 (1969).
  2. S. G. Nilsson, C. F. Tsang, A. Sobiczewski, Z. Szymanski, S. Wycech, C. Gustafson, I. L. Lamm, P. Moller, and B. Nilsson, Nucl. Phys. A131, 1 (1969).
  3. D. R. Inglis, Phys. Rev. 96, 1059 (1954).

4. S.T. Belyaev, Kgl. Danske Videnskab. Selskab, Mat. Fys. Medd. 31, No. 11 (1959).

5. C.W. Ma and J.O. Rasmussen, Phys. Rev. C 2, 798 (1970).

6. V.M. Strutinsky, Nucl. Phys. A95, 420 (1967).

7. E.R. Marshalek, Phys. Rev. 139, B770 (1965); 158, 993 (1967); Phys. Rev. Letters 20, 214 (1968).

### STATISTICAL PROPERTIES OF A PAIRED SYSTEM WITH FIXED QUASI-PARTICLE NUMBER

L. G. Moretto and T. Clements

Ordinarily a nuclear reaction begins by means of the excitation of one or a few degrees of freedom, either intrinsic or collective. Frequently the system relaxes from the initial simple configuration into more and more complicated configurations leading eventually to the compound nucleus formation. The evolution of the system from the initial configuration to the compound nucleus is governed by the law of increasing entropy at constant energy. The methods used to describe such entropization are generally based upon the master equation and require the knowledge of the level densities of the system for fixed number of particle-hole excitations or "quasi-particles". So far the models used for the description of systems with fixed quasi-particle numbers are various versions of the independent particle model of which the shell model is the most common version. In the present paper the effect of residual interactions not included in the shell model is accounted for by means of the pairing Hamiltonian. This Hamiltonian is diagonal in the quasi-particle space and has the form:

$$H = \sum (\epsilon_k - \lambda - E_k) + 2 \sum n_k E_k + \frac{\Delta^2}{G}$$

where  $\epsilon_k$  are the single particle energies,  $\lambda$  is the particle chemical potential,  $G$  is the pairing strength,  $E_k = \sqrt{(\epsilon_k - \lambda)^2 + \Delta^2}$  are the quasi-particle energies,  $n_k$  are the quasi-particle occupation numbers, and  $\Delta$  is the gap parameter given by the equation:

$$\frac{2}{G} = \sum \frac{1 - 2n_k}{E_k}$$

In order to fix the quasi particle number we introduce the auxiliary Hamiltonian:

$$H' = H + \xi Q = \sum (\epsilon_k - \lambda - E_k) + \frac{\Delta^2}{G} + 2 \sum n_k (E_k - \xi)$$

where  $Q$  is the quasi-particle number and  $\xi$  is the quasi particle chemical potential.

The auxiliary Hamiltonian can be used to obtain the Grand Partition Function,  $e^{\Omega}$ :

$$\Omega = -\beta \sum (\epsilon_k - \lambda - E_k) - \beta \frac{\Delta^2}{G} + 2 \sum \ln [1 + \exp(-\beta(E_k - \xi))]$$

where  $\beta = 1/T$  is the reciprocal of the temperature. The gap equation takes the form:

$$\sum \frac{1}{E_k} \tanh \frac{1}{2} \beta (E_k - \xi) = \frac{2}{G}$$

The other thermodynamical quantities can be obtained by differentiation of  $\Omega$ :

$$Q = \frac{1}{\beta} \frac{\partial \Omega}{\partial \xi} = 2 \sum \frac{1}{1 + \exp \beta(E_k - \xi)}$$

$$E = \frac{\partial \Omega}{\partial \beta} = \sum \epsilon_k \left[ 1 - \frac{\epsilon_k - \lambda}{E_k} \tanh \frac{1}{2} \beta (E_k - \xi) \right] - \frac{\Delta^2}{G}$$

$$N = \frac{\partial \Omega}{\partial \lambda} = \sum \left[ 1 - \frac{\epsilon_k - \lambda}{E_k} \tanh \frac{1}{2} \beta (E_k - \xi) \right]$$

In order to study the properties of such a system, we apply the above formalism to the uniform model, characterized by the density of doubly degenerate single particle states  $g$  and by the ground state gap parameter  $\Delta_0$ .

First we consider the zero temperature case ( $\beta \rightarrow \infty$ ). The gap equation can be integrated analytically and gives:

$$\xi = \frac{1}{2} \sqrt{\frac{\Delta}{\Delta_0}} (\Delta + \Delta_0).$$

The quasi-particle equation gives

$$Q = 4g \sqrt{\xi^2 - \Delta^2}.$$

The combination of the above two equations gives the dependence of  $\Delta$  upon  $Q$ :

$$Q = 2g \sqrt{\frac{\Delta}{\Delta_0}} (\Delta_0 - \Delta).$$

As can be seen in Fig. 1, this function is double-valued from  $Q = 0$  to  $Q = Q_{\max} = \frac{4}{3\sqrt{3}} g\Delta_0$ . In fact the function is triple-valued,  $\Delta = 0$  always being a solution of the gap equation. In order to decide which of the three values of  $\Delta$  is the physically acceptable solution, we can check the stability of the solutions by considering the  $E, Q$  graph. The energy equation can also be integrated analytically and gives:

$$E = \frac{1}{2} g(\Delta_0^2 - \Delta^2) \left(1 - \frac{\Delta}{\Delta_0}\right) \quad \text{for } \Delta > 0$$

$$E = \frac{1}{2} g(\Delta_0^2 + \frac{Q^2}{8g}) \quad \text{for } \Delta = 0.$$

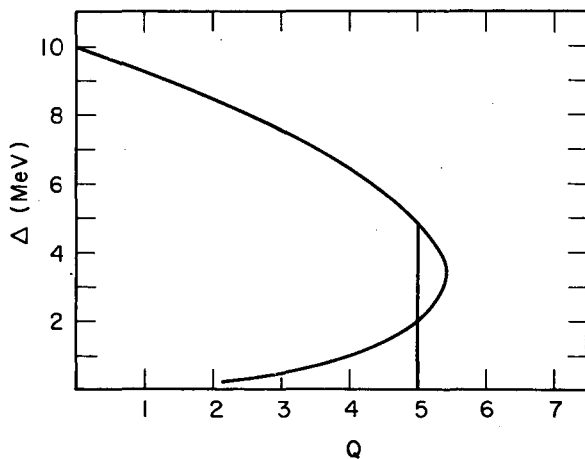


Fig. 1. Dependence of  $\Delta$  upon  $Q$  at zero temperature. The thin line indicates the region where the paired solution becomes unstable. (XBL-743-2518)

A plot of  $E$  vs  $Q$  shown in Fig. 2 presents a loop which the physical solution must bypass. Consequently the gap parameter drops abruptly from a finite value to zero.

Similar features can be observed for  $T > 0$ , with the difference that the free energy  $F = -\Omega T + \xi Q$  must be considered instead of the energy. In this case, the abrupt disappearance of the gap parameter at the bypass of the free energy loop takes the form of a first order phase transition.

In Fig. 3 the phase diagram in the  $T, Q$

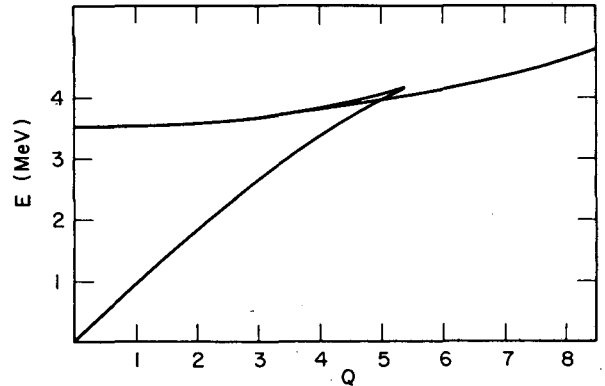


Fig. 2. Dependence of the energy upon  $Q$  at zero temperature. The loop represents a region of unstable solutions. (XBL-744-2826)

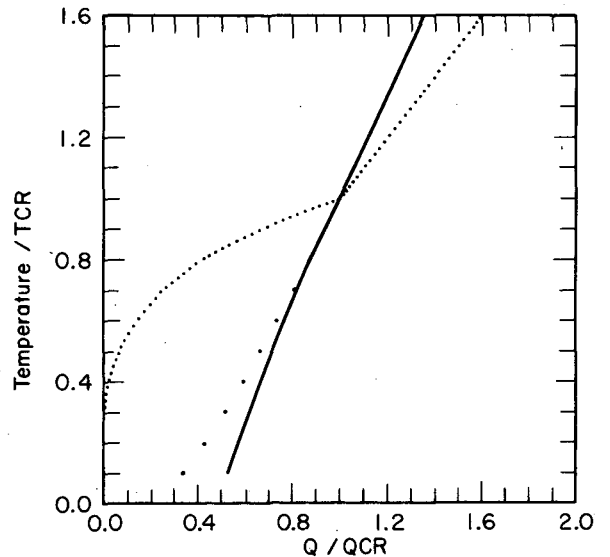


Fig. 3. Phase diagram in the  $T, Q$  plane. In the region to the left of the solid line the system is paired; in the region to the right the system is unpaired. The dotted line crossing the phase boundary at the critical temperature corresponds to the most probable quasi-particle number. (XBL-743-2519)

plane, can be seen. The solid line corresponds to the boundary between paired and unpaired phase. Below the critical temperature of the unrestricted system, the transition is first order, above is second order. The dotted line, crossing the phase boundary at the critical temperature, represents the most probable quasi-particle number as a function of temperature. This is the path followed by the unrestricted system and corresponds to  $\xi = 0$ . Figure 4 presents the lines of constant  $\Delta$  in the T, Q plane. It can be observed that at constant Q, the gap parameter increases with increasing temperature. In fact even for the Q values where  $\Delta = 0$  at T = 0 a sufficiently large

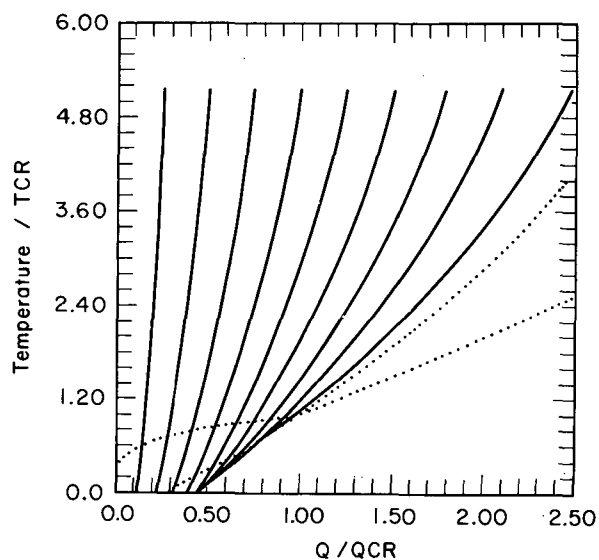


Fig. 4. Lines of constant  $\Delta$  in the T, Q plane. (XBL-743-2520)

temperature increase will bring the pairing correlation back. This is another example of the so called "thermally assisted pairing correlation" which is due to the diminished anti-blocking effect of the quasi-particles due to an increase in temperature.

Finally, Fig. 5 shows the lines of constant entropy in the E, Q plane. This graph is perhaps the most useful since it can easily be read at constant energy and gives an immediate information concerning the relaxation of the system towards the equilibrium number of quasi-particles.

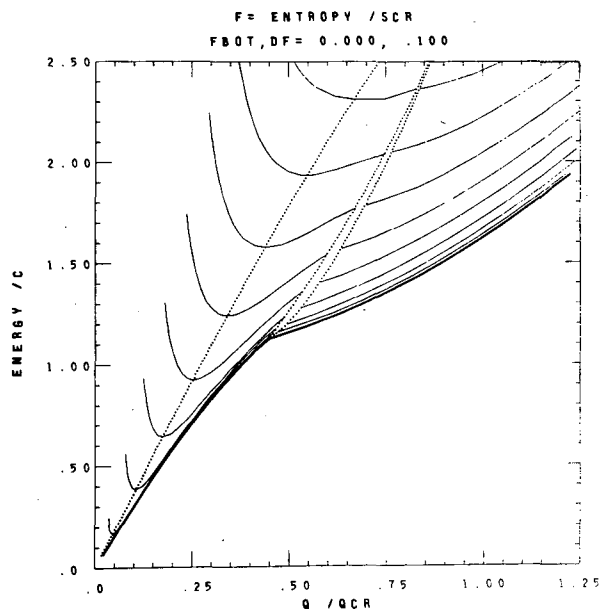


Fig. 5. Lines of constant entropy in the E, Q plane. (XBL-743-455)

### FINITE TEMPERATURE CALCULATION OF ANGULAR VELOCITIES AND MOMENTS OF INERTIA IN ROTATING NUCLEI

L. G. Moretto

In this work a very simple pairing model is used to calculate the zero and finite temperature behavior of the angular velocity and of the moment of inertia as a function of angular momentum. The model is characterized by three parameters: the density  $g$  of the equidistant, doubly degenerate, single particle levels; the average  $z$  projection  $m$  of the single particle angular momentum; the gap parameter  $\Delta_0$  corresponding to zero temperature and zero angular momentum.

The properties of the system are contained in the grand potential  $\Omega$

$$\Omega = -\beta g \int_{-S}^{+S} d\epsilon \left[ \epsilon - E + \frac{1}{\beta} \left\{ \ln [1 + \exp -\beta(E - \gamma m)] + \ln [1 + \exp -\beta(E + \gamma m)] \right\} \right] - \frac{\beta \Delta^2}{G} \quad (1)$$

where  $\beta = \frac{1}{T}$  is the reciprocal of the temperature,  $\epsilon$  is the energy of the single particle levels measured with respect to the constant chemical potential,  $E = [\epsilon^2 + \Delta^2]^{1/2}$ ,  $\gamma$  is the angular velocity and  $G$  is the pairing strength. The pairing cut-off  $S$  is taken to be much larger than the gap parameter throughout the calculation:  $S \gg \Delta_0$ .

By suitable differentiation of the grand potential, all the other thermodynamical equations are obtained. The case in which  $T = 0$  can be worked out analytically and is considered first. The angular momentum equation yields:

$$I = 2mg [(\gamma m)^2 - \Delta^2]^{1/2}. \quad (2)$$

The gap equation can also be integrated explicitly, producing the following relationship between  $\Delta$  and  $\gamma$ :

$$\frac{1}{2} \frac{\Delta_0^2 - \Delta^2}{\Delta_0} = [(\gamma m)^2 - \Delta^2]^{1/2}. \quad (3)$$

By means of Eqs. (2) and (3) one obtains the following important relations:

$$\frac{\Delta}{\Delta_0} = \left(1 - \frac{I}{I_{cr}}\right)^{1/2} \quad \text{for } I \leq I_{cr} \quad \Delta = 0 \quad \text{for } I \geq I_{cr} \quad (4)$$

$$\gamma = \frac{I_{cr}}{\mathfrak{I}_R} \left(2 - \frac{I}{I_{cr}}\right) \quad \text{for } I \leq I_{cr} \quad \gamma = \frac{I}{\mathfrak{I}_R} \quad \text{for } I \geq I_{cr} \quad (5)$$

$$\mathfrak{I} = \frac{I}{\gamma} = \mathfrak{I}_R \frac{I/I_{cr}}{2 - \frac{I}{I_{cr}}} \quad \text{for } I \leq I_{cr} \quad = \mathfrak{I}_R \quad \text{for } I \geq I_{cr} \quad (6)$$

where  $I_{cr} = \underline{g} \underline{m} \Delta_0$ ,  $\mathfrak{I}_R = 2 \underline{m}^2 \underline{g}$ .

The Eq. (4) gives the dependence of the gap parameter  $\Delta$  upon angular momentum. The gap parameter decreases as the angular momentum increases and vanishes at the critical angular momentum  $I_{cr}$ . The effect of superfluidity on the moment of inertia is quite visible in Eq. (6). The moment of inertia vanishes at zero angular momentum, and it increases monotonically as the angular momentum increases from zero to its critical value. Above the critical angular momentum the superfluidity disappears and the moment of inertia attains its rigid value. More peculiarly, the angular velocity  $\gamma$ , given by Eq. (5), decreases with increasing angular momentum in the interval  $0 \leq I \leq I_{cr}$ . For values of the

angular momentum larger than  $I_{cr}$  the angular velocity increases proportionally to the angular momentum. This behavior generates a very pronounced back-bend in the plot of the moment of inertia versus the square of the angular velocity.

By integrating the energy equations and subtracting the ground state energy one obtains the yrast function, namely the region of the highest angular momentum states at a given energy, or conversely, the region of the lowest energy states at a given angular momentum:

$$E_y = \begin{cases} \frac{I_{cr}^2}{\mathfrak{I}_R} \frac{I}{I_{cr}} \left(2 - \frac{I}{I_{cr}}\right) & \text{for } I \leq I_{cr} \\ \frac{I_{cr}^2}{\mathfrak{I}_R} + \frac{I^2}{2\mathfrak{I}_R} & \text{for } I \geq I_{cr} \end{cases} \quad (7)$$

Above the critical angular momentum, the yrast line is a parabola typical of an object rotating with a rigid moment of inertia. Below the critical angular momentum the yrast line is also a parabola but it has a negative instead of a positive second derivative.

The case in which  $T > 0$  will now be considered. It is well known that at zero angular momentum the gap parameter decreases with increasing temperature and vanishes at the critical temperature  $T_{cr}$  given by:

$$T_{cr} = 2 \Delta_0 / 3.5. \quad (8)$$

It follows that the system is characterized by three critical quantities  $I_{cr}$ ,  $T_{cr}$ ,  $\mathfrak{I}_R$  which can be related to the physical parameters of the system as follows:

$$I_{cr} = \underline{g} \underline{m} \Delta_0; \quad T_{cr} = 2 \Delta_0 / 3.5; \quad \mathfrak{I}_R = 2 \underline{g} \underline{m}^2. \quad (9)$$

Since these three critical quantities contain all the physical information on the model, it is possible to scale every specific physical situation by means of the following three reduced variables: the reduced angular momentum  $I/I_{cr}$ , the reduced temperature  $T/T_{cr}$  and the reduced moment of inertia  $\mathfrak{I}/\mathfrak{I}_R$ .

In Fig. 1 the yrast line is shown together with higher energy-angular momentum isotherms and with the line of the critical energies. One can see that the yrast line has negative second derivative everywhere below the critical angular momentum; the lower isotherms have positive second derivatives at

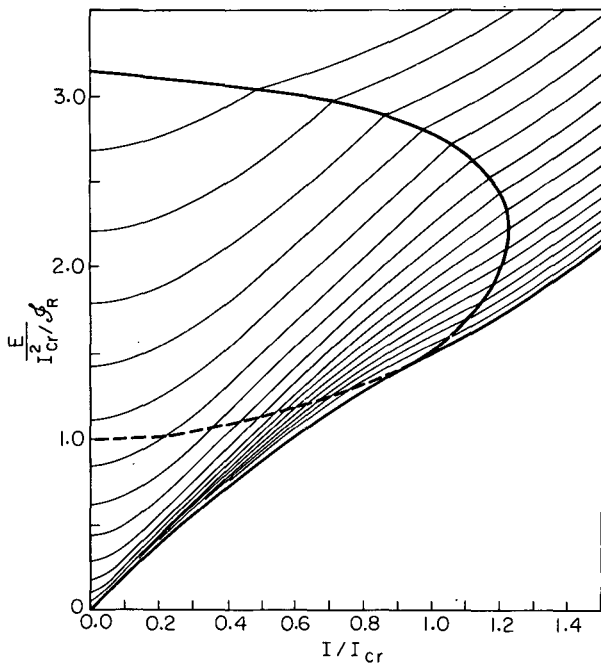


Fig. 1. Yrast line and higher isotherms. The energy scale is expressed in units of condensation energy. The isotherm next to the yrast line is at  $T/T_{cr} = 0.158$  and the following isotherms are in steps of  $0.0526 T_{cr}$ . The dashed line represents the yrast line of the unpaired system. The upper line crossing the various isotherms represents the boundaries between the paired and unpaired region. (XBL 733-2511)

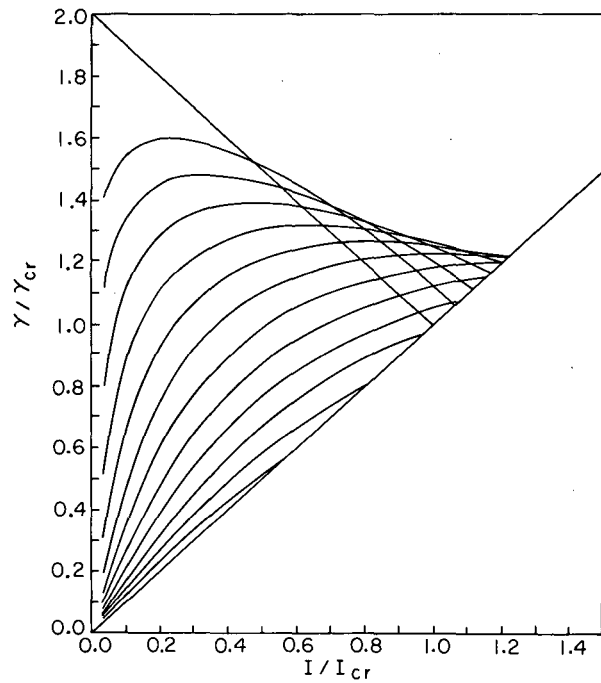


Fig. 2. Reduced angular velocity as a function of the reduced angular momentum for various temperatures. The rising diagonal line represents the angular velocity of an unpaired system. The upper line corresponds to  $T/T_{cr} = 0$ . The next isotherm is at  $T/T_{cr} = 0.158$  and the following isotherms are in steps of  $0.04 T_{cr}$ . (XBL 733-2481)

low angular momentum and negative second derivatives at high angular momentum; the higher isotherms have positive second derivatives everywhere. This behavior is better appreciated in Fig. 2 where the angular velocity is plotted as a function of angular momentum for various temperatures. At  $T = 0$ , as predicted by Eq. (5), the angular velocity decreases as the angular momentum increases. At higher temperatures the angular velocity goes from zero to a maximum and then decreases. At the highest temperatures the angular velocity increases monotonically with angular momentum. At and above the critical angular momenta, the angular velocity becomes independent of temperature and increases proportionally to the angular momentum.

The dependence of the moment of inertia on the square of the angular velocity is shown in Fig. 3. The back-bending is extremely pronounced at  $T = 0$ , it is attenuated as the temperature increases until, at a temperature

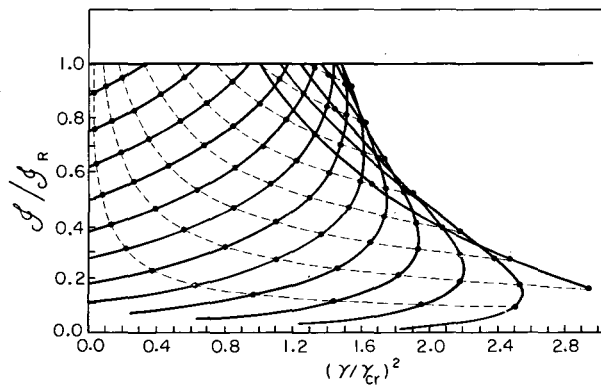


Fig. 3. Moment of inertia versus the square of the angular velocity for various temperatures (solid lines). The  $T/T_{cr} = 0$  isotherm is incomplete on the right. The next isotherm is at  $T/T_{cr} = 0.158$  and the following isotherms are in steps of  $0.04 T_{cr}$ . The dashed lines are lines of constant angular momentum in steps of  $1/7 I_{cr}$ . (XBL 733-2480)



$\frac{T}{T_{cr}} \approx 0.53$ , it disappears. Above this temperature and below the critical temperature the moment of inertia increases regularly with the square of the angular velocity. The back bending is associated with the presence of negative

second derivatives in the energy angular momentum isotherms and with the presence of negative first derivatives in the angular velocity angular momentum isotherms.

## PAIRING AND SPIN DISTRIBUTION EFFECTS ON THE YRAST LINE

L. G. Moretto

The superfluid properties of nuclei are best established at zero temperature. Therefore the interaction between pairing and angular momentum should be best observed along the yrast line, namely along the locus of the lowest energy levels at the various angular momenta.

Some anomalies in the rotational bands of deformed nuclei have been attributed to the disappearance of pairing with increasing angular momentum. Such effects should be more pronounced and more easily understood in spherical nuclei. In these nuclei the effective moment of inertia is more sensitive to pairing. In fact the moment of inertia of any object tends towards its rigid value with increasing deformation independently from the flow of matter.

The detailed shape of the yrast line depends also upon the local fluctuations of spacings and spins occurring at the Fermi surface. In order to single out the features which are associated with the angular momentum and pairing interaction, the shell effects can be eliminated by using a uniform model where the level spacing is constant. In this case the yrast line, for a spherical nucleus, is completely determined by the pairing strength  $G$ , by the density  $g$  of the doubly degenerate single particle levels and by the distribution of the single particle spin projections  $p(m)$ . It will be shown that the spin projection distribution is most important in determining both the slope and the curvature of the yrast line. In the present study two extreme spin projection distributions are used. The first is a  $\delta$  function:  $p(m) = \delta(m-m)$ . The second is a rectangular distribution:  $p(m) = \text{constant}$  for  $0 \leq m \leq m_x$  and  $p(m) = 0$  for  $m > m_x$ ,  $m_x$  being the largest possible spin projection.

The first spin projection  $p(m) = \delta(m-m)$  has been used before with the analytical results shown in a previous contribution. In this case the dependence of the angular velocity  $\gamma$ , of the moment of inertia  $\mathcal{J}$  and of the yrast energy  $E_y$ , upon the angular momentum  $I$  is

shown by means of thin lines in Figs. 1-3. In Fig. 1 it is seen that below the critical angular momentum,  $\gamma$  is a decreasing function of  $I$ . This is immediately reflected upon the shape of the yrast line since  $\gamma = dE/dI$ . Thus it can be seen from Fig. 3 that the yrast line

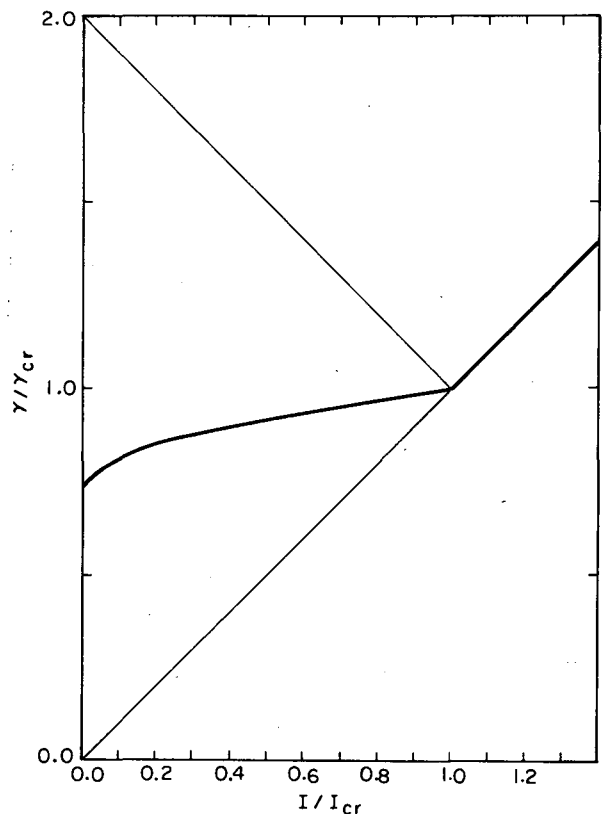


Fig. 1. Dependence of the angular velocity upon the angular momentum for a  $\delta$  function spin projection distribution (upper thin line) and for a rectangular spin projection distribution (thick line). The two calculations are normalized to the same critical angular momentum  $I_{cr}$ . (XBL 735-2831)

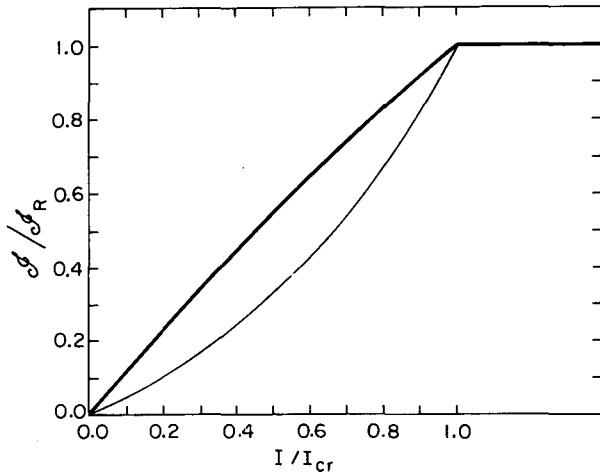


Fig. 2. Moment of inertia as a function of angular momentum. The thin and thick lines refer to the two different models as in Fig. 1. (XBL 735-2834)

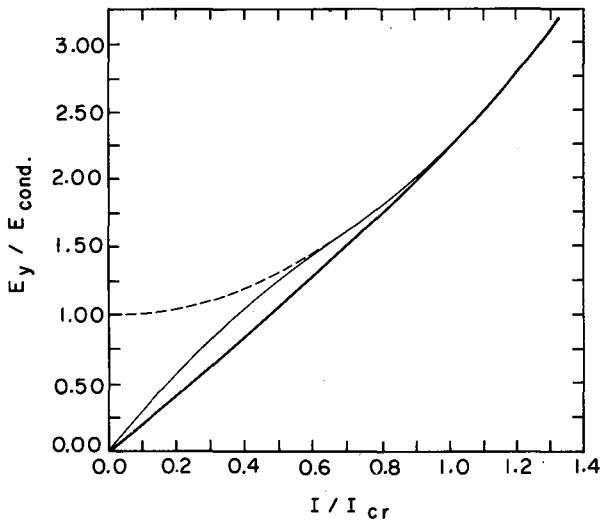


Fig. 3. Yrast line for the two models as indicated in Fig. 1. The two calculations are normalized to reproduce the same rigid moment of inertia and the same condensation energy. The dashed line merging first into the thin and later into the thick solid line is a parabola corresponding to the yrast line for the unpaired system. (XBL 735-2858)

below the critical angular momentum is characterized by a negative second derivative. This can be understood qualitatively as follows. Every broken pair generates two quasi-particles which, because of the constant spin

projections, contribute always the same amount of angular momentum. Thus the angular momentum is proportional to the number of quasi-particles. On the other hand the energy cost of two quasi-particles decreases with the number of quasi-particles already present, because of the blocking effects. Therefore the energy will increase less and less as the angular momentum increases.

The second spin projection distribution  $p(m) = \text{constant}$  for  $m \leq m_x$   $p(m) = 0$  for  $m > m_x$  does not lead to an equivalently elegant analytical formalism. However it is very interesting because it closely simulates the case of a spherical nucleus where the Fermi surface is sampling all the  $2J+1$  spin projections of a given  $J$  shell.

The angular momentum equation can be integrated analytically and yields:

$$I = \frac{2}{3} \frac{g}{\gamma^2 m_x} [\gamma^2 m_x^2 - \Delta^2]^{3/2}. \quad (1)$$

Similarly the gap equation becomes:

$$\begin{aligned} \frac{1}{2} \frac{\gamma m_x}{\Delta^2 \Delta_0} \left\{ (\Delta^2 + \Delta_0^2) \left( 1 - \frac{\Delta^2}{\gamma^2 m_x^2} \right)^{1/2} - (\Delta_0^2 - \Delta^2) \right\} \\ = \sinh \left( 1 - \frac{\Delta^2}{\gamma^2 m_x^2} \right)^{1/2}. \end{aligned} \quad (2)$$

These two equations define the two functions  $\Delta = \Delta(I)$  and  $\gamma = \gamma(I)$ . Unfortunately these two functions cannot be expressed analytically. However, it is feasible to calculate the value of  $\gamma$  at  $I=0$  ( $\Delta = \Delta_0$ ) and at  $I = I_{cr}$  ( $\Delta = 0$ ):

$$\gamma_{I=0} = \frac{\Delta_0}{m_x}; \quad \gamma_{cr} = \frac{e}{2} \frac{\Delta_0}{m_x}, \quad (3)$$

where  $e$  is the base of the natural logarithms. We can see immediately that, contrary to the previous case, the angular velocity  $\gamma$  increases in going from  $I=0$  to  $I = I_{cr}$ . Such an increase is monotonic as shown in Fig. 1 by the thick solid curve. The critical angular momentum is given by the relation:

$$I_{cr} = \frac{e}{3} g m_x \Delta_0. \quad (4)$$

The moment of inertia as a function of angular momentum is shown in Fig. 2 by the thick solid curve. Its rigid value, assumed when  $I = I_{cr}$  is:

$$\mathfrak{I}_R = \frac{2}{3} g m_x^2. \quad (5)$$

By comparing the two models at constant gap parameter  $\Delta_0$  and at constant rigid moment of inertia it appears that the rectangular distribution predicts a larger critical angular momentum than the  $\delta$  distribution:

$$\frac{I_{cr}^{(2)}}{I_{cr}^{(1)}} = \frac{e}{\sqrt{3}}. \quad (6)$$

From Fig. 3, and remembering that  $\gamma = dE/dI$ , it is concluded that the yrast line should be characterized by a positive second derivative in the paired region. This is in contrast with the previous model which predicts a negative second derivative for the yrast line.

The yrast energy at the critical angular momentum can be calculated directly:

$$E_{y_{I=I_{cr}}} = \frac{1}{2} g \Delta_0^2 + \frac{I_{cr}^2}{2\mathfrak{I}_R} = \frac{1}{2} g \Delta_0^2 \left(1 + \frac{e^2}{6}\right) \approx 2.23 E_{cond}, \quad (7)$$

where  $E_{cond} = 1/2 g \Delta_0^2$  is the condensation energy due to the pairing correlation. It is interesting to note that the previous model predicts  $E_{y_{I=I_{cr}}} = 1.5 E_{cond}$ .

The complete yrast line is shown in Fig. 3 by the thick solid curve, and it does indeed

show a slightly positive second derivative in the paired region.

The reason for such a behavior can be qualitatively understood as follows. The first two quasi-particles which are produced occupy the highest portion of the spin projection distribution, generating a certain amount of angular momentum. The next quasi-particles must occupy a lower portion of the spin projection distribution, thus generating less angular momentum per quasi-particle. In other words as the angular momentum increases it takes more quasi-particles to generate a fixed amount of angular momentum. This is in contrast with the previous model where the same number of quasi-particles always produces the same amount of angular momentum. Because of this effect, the flaring out of the previous yrast line is more than compensated by the extra energy needed to produce the extra number of quasi-particles.

It is interesting to realize that a decreasing angular velocity as a function of angular momentum with the consequent negative second derivative of the yrast line is responsible for a back bending in the plot of the moment of inertia versus the square of the angular velocity. It has been shown here that such a back bending depends critically upon the spin projection distribution. A systematic study of these features of the yrast lines should provide a strong test for our understanding of the pairing interaction in nuclei.

## INFLUENCE OF PAIRING AND OF THE SPIN PROJECTION DISTRIBUTION ON THE "CLASSICAL" ISOTHERMAL ROTATIONS OF A NUCLEUS

L. G. Moretto

It has been shown that the main effect of angular momentum on the nuclear level density can be accounted for on one hand by the rotational phase space of the nucleus as a whole, on the other by the unavailability of the rotational energy to excite the intrinsic degrees of freedom. This rotation and the associated rotational phase space need not be associated with well defined rotational quantum states. In fact such a rotation is present even in the case of a spherical nucleus where no quantum mechanical rotation is possible. These rotational features are essentially "classical" in nature insofar as the rotational strength is shared by all the states. Along the same line, individual

levels may not show any distinct rotational characteristics, while the envelope of many levels shows an energy angular momentum dependence typical of a rotor. This is expected to be the case for the yrast line of a spherical nucleus: the individual yrast levels may not show a rotational behavior individually, since they are not part of a rotational band. However their envelope is expected to show distinct rotational features. A similar consideration should hold also for nuclei at temperatures larger than zero. The existence of rotational features in the energy-angular momentum isotherms allows one to extract other rotational quantities like the angular velocity and the moment of

inertia.

A model with uniform single particle spacing and uniform spin projection distribution is characterized by a constant moment of inertia whose value corresponds to the "rigid" value. A shell model with nonuniform spacing and spin projection distribution still yields a "rigid" moment of inertia. However such a moment of inertia is not constant insofar as changes in temperature and in angular momentum can lead to the occupation of levels with widely different spin projections. In general the presence of residual interactions still leads to a rigid moment of inertia. Only special residual interactions such as those of the pairing kind produce moments of inertia which deviate dramatically from their rigid value. Such interactions are responsible for a superfluid condensation which leads to a highly correlated motion of the nucleons.

The effects of the pairing correlation on the rotational properties of nuclei are best observed when the interference of the shell structure is eliminated. This can be achieved by the use of the uniform model. In this special version of the uniform model the level scheme consists of a set of equidistant, doubly degenerate levels with a density  $g$  and with a constant spin projection  $m$ . The information concerning the strength of the pairing interaction is contained in the ground state gap parameter  $\Delta$ . An important advantage of this model is the fact that the chemical potential is a constant because of the symmetries inherent to the single-particle scheme. For this reason the particle equation can be disregarded and the chemical potential can be set equal to zero.

For a nucleus, where the particle number is small, large fluctuations are to be expected which do remove the sharp phase transition. In order to appreciate the extent to which the system can fluctuate in its superfluid behavior, let us consider the Hamiltonian:

$$H = 2 \sum_k v_k^2 (\epsilon_k - \lambda) + G \left[ \sum_k u_k v_k (1 - 2n_k) \right]^2 + 2 \sum_k n_k (\epsilon_k - \lambda) (u_k^2 - v_k^2), \quad (1)$$

where  $n_k$  are the quasiparticle occupation numbers and, for simplicity, we disregard the quasiparticle spin projection.

The BCS treatment consists in finding out the value of  $\Delta$  which minimizes the Hamiltonian

at fixed occupation numbers  $n_k$ . In fact it is easy to verify that the condition  $\frac{\partial H}{\partial \Delta} = 0$  corresponds to the gap equation. In order to estimate the extent of the fluctuations one must calculate the second derivative at the equilibrium value of the gap parameter,  $\Delta_{eq}$ :

$$\frac{\partial^2 H}{\partial \Delta^2} \Big|_{\Delta=\Delta_{eq}} = \Delta_{eq}^2 \sum_k \frac{1-2n_k}{E_k^3} \left( 1 - \frac{G \Delta_{eq}}{2} \sum_k \frac{1-2n_k}{E_k^3} \right). \quad (2)$$

In the absence of quasiparticles and for the uniform model one obtains:

$$\frac{\partial^2 H}{\partial \Delta^2} \Big|_{\Delta=\Delta_{eq}} = 2g(1-gG) \approx 2g. \quad (3)$$

This implies that, for very small temperatures, the fluctuations in  $\Delta$  have a width:

$$\sigma \approx \sqrt{\frac{T}{g}} \propto \sqrt{\frac{T}{N}}. \quad (4)$$

In other words the width of the fluctuations is inversely proportional to the square root of the number of particles. Such a proportionality is, of course, retained even for the more general expression of the second derivative. Consequently one does expect that a sharp phase transition may occur in a macroscopic superconductor. On the other hand, on the same basis, such a transition should be washed out when the number of particles is small, like in a nucleus. Because of the finite width of the probability distribution in  $\Delta$ , and of the presence of higher moments, the use of average quantities is more significant than the use of the corresponding most probable quantities. The probability distribution in  $\Delta$  is given by:

$$P(\Delta, \gamma) \propto \exp(-(\Omega - \mu M)). \quad (5)$$

Thus the average angular velocity  $\bar{\gamma}$  and the average gap parameter  $\bar{\Delta}$  are given by:

$$\bar{\gamma} = \frac{\int \gamma P(\Delta, \gamma) d\Delta d\gamma}{\int P(\Delta, \gamma) d\Delta d\gamma}, \quad \bar{\Delta} = \frac{\int \Delta P(\Delta, \gamma) d\Delta d\gamma}{\int P(\Delta, \gamma) d\Delta d\gamma}. \quad (6)$$

The plot of the average angular velocity versus angular momentum for various temperatures is

is shown in Fig. 1. Close to the critical region the most probable angular velocity reaches abruptly its rigid value generating a cusp, while the average angular velocity approaches asymptotically its rigid value. This shows how in a real nucleus one should not expect a phase transition in going from the paired to the unpaired configuration. In Fig. 2 the average moment of inertia is shown as a function of angular momentum. The rigid moment of inertia is attained asymptotically at all temperatures. Notice that, even for  $T=T_{cr}$ , the moment of inertia is still smaller than its rigid value because of the persistence of the pairing correlation. Similarly in Fig. 3 the average moment of inertia is plotted versus the square of the average angular velocity. Again one notices a smooth fold over which, for the lowest temperatures, constitutes the upper part of an S

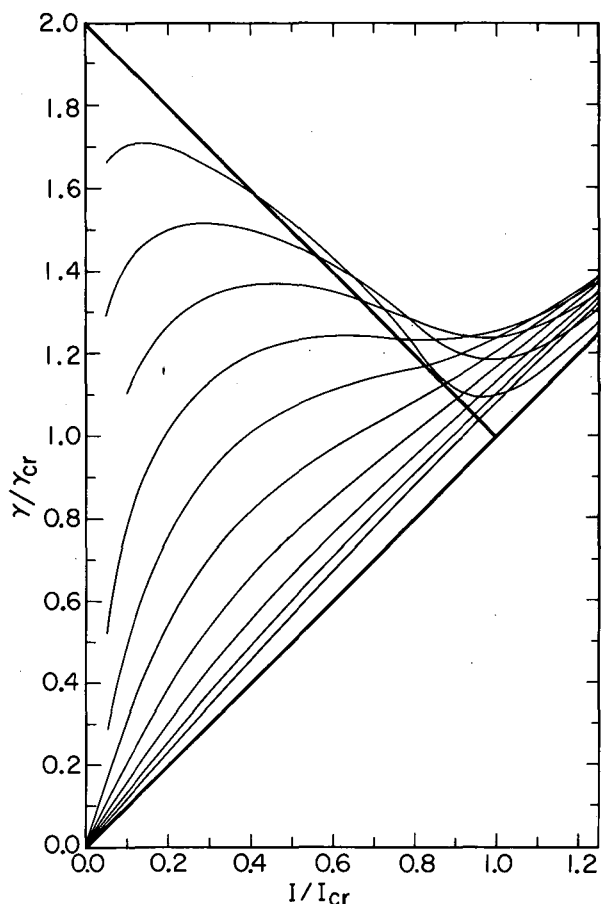


Fig. 1. Average angular velocities as a function of angular momentum for various temperatures (thin lines). The lowest temperature is  $T = 0.1 T_{cr}$ ; the upper temperature is  $T = T_{cr}$ . The thick lines correspond to the zero temperature limit of the angular velocity with and without pairing. (XBL 7311-4585)

shaped curve. In this calculation pairing extends above the critical temperature: consequently the isotherm corresponding to  $T=T_{cr}$  shows a moment of inertia smaller than its rigid value.

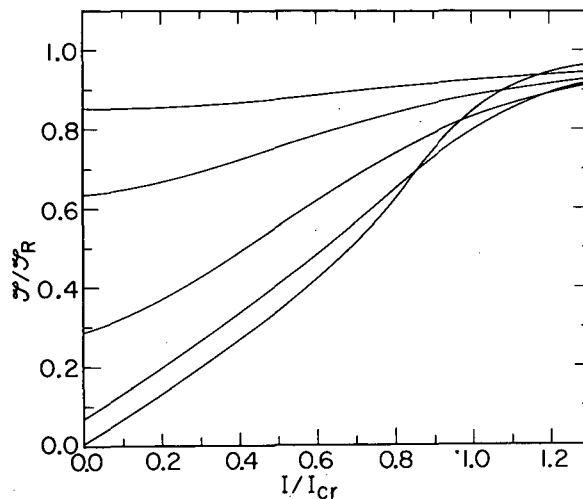


Fig. 2. Average moment of inertia as a function of angular momentum. The lowest curve corresponds to  $T = 0.2 T_{cr}$ ; the upper curve corresponds to  $T = T_{cr}$ . (XBL 7311-4589)

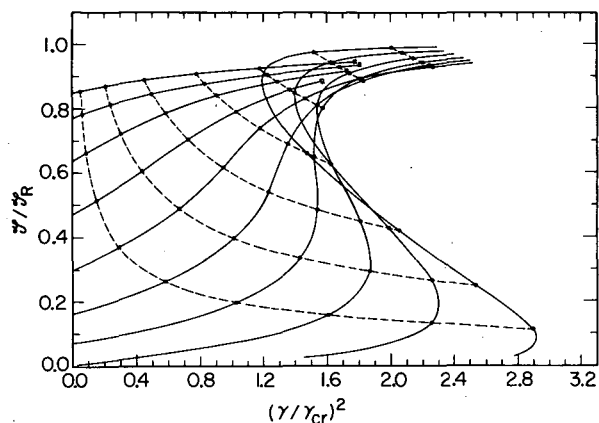


Fig. 3. Average moment of inertia versus the square of the average angular velocity (solid lines). The lowest temperature is  $T = 0.1 T_{cr}$ ; the upper temperature is  $T = T_{cr}$ . The dashed curves correspond to constant angular momentum value (from  $I = 0.2 I_{cr}$  to  $I = 1.4 I_{cr}$ ). (XBL 7311-4587)

A semianalytical study of the properties of simple models has been carried out in the previous sections. It is now interesting to investigate in detail the properties of more realistic models. The shell model, applied to a spherical nucleus, in conjunction with the pairing Hamiltonian lends itself to a sufficiently simple numerical calculation. In order to simplify the display of the various quantities the calculations are limited to individual nuclear components, neutrons or protons. For a fixed temperature, angular momentum and particle number, the gap equation, the momentum equation, and the particle equation can be solved to give the gap parameter  $\Delta$ , the angular velocity  $\gamma$  and the chemical potential  $\lambda$ . The angular velocity  $\gamma$  is displayed in Fig. 4 as a function of angular momentum for various temperatures for the neutron component of  $^{220}\text{Rn}$ . The lowest isotherms show very strong fluctuations due to shell effects for angular momenta above the critical value. For angular momenta lower than the critical value, the dependence of  $\gamma$  on angular momentum shows a flatter behavior, which, at the lowest isotherm does indeed resemble the dependence predicted by the uniform model with a rectangular spin projection distribution (see preceding report). So the shell model indicates that at the lowest temperatures the angular velocity tends to become almost constant with angular momentum. Furthermore there is no evidence that the angular velocity decreases with angular momentum. This implies that no backbending is to be expected. The same figure indicates that as the temperature increases, both pairing and shell

effects disappear. When the temperature is sufficiently high the linear dependence of  $\gamma$  on  $I$ , typical of a rigid rotor, is observed.

In Fig. 5 the moment of inertia is displayed versus the angular momentum for various temperatures. The lowest isotherms show the dramatic decrease of moment of inertia due to

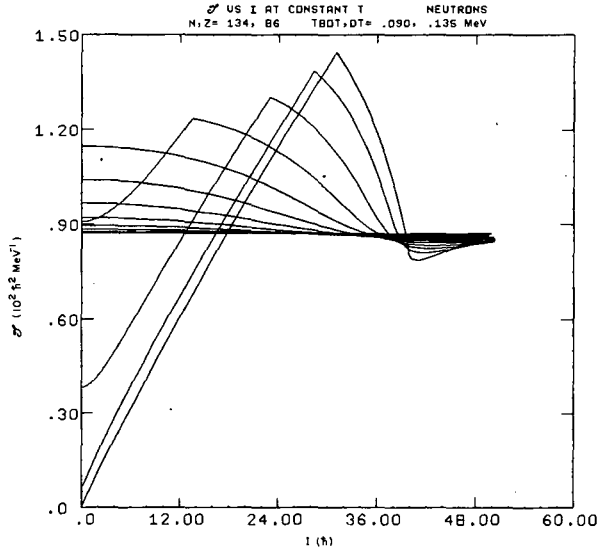


Fig. 5. Shell model calculation of the moment of inertia vs angular momentum for the neutron component of  $^{220}\text{Rn}$ . (XBL 7311-4578)

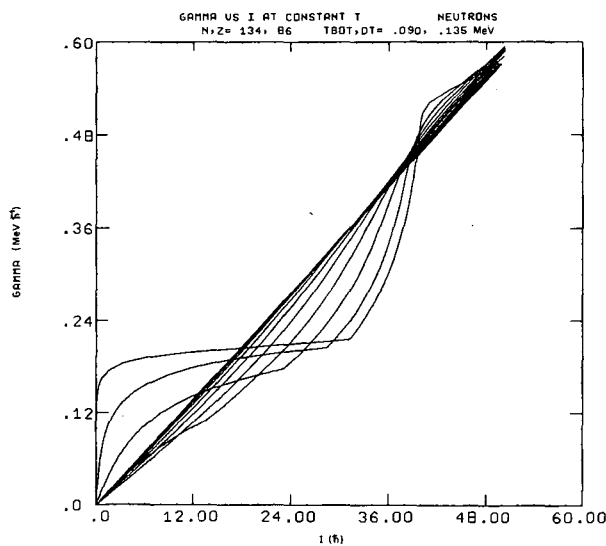


Fig. 4. Shell model calculation of the angular velocity vs angular momentum for the neutron component of  $^{220}\text{Rn}$ . (XBL 7311-4577)

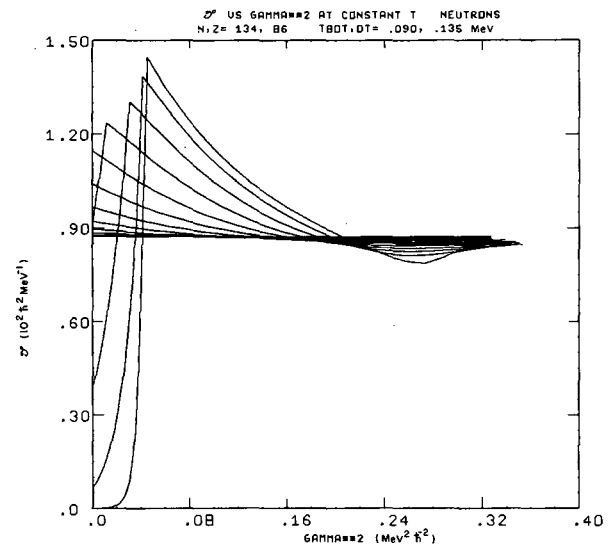


Fig. 6. Shell model calculation of the moment of inertia vs the square of the angular velocity for the neutron component of  $^{220}\text{Rn}$ . (XBL 7311-4579)

pairing. The antipairing effect of the angular momentum is visible in the rapidly rising moment of inertia as the angular momentum increases. The cusps appearing in the lowest isotherms are associated with the disappearance of pairing. In the vicinity of these cusps the moment of inertia assumes values much above the average. This is due to the presence of a high spin level ( $g_0/2$ ) close to the Fermi surface. Its role decreases as the angular momentum increases because the quasiparticles occupy higher levels with lower spin. The higher isotherms show a rapid flattening of the fluctuations with the consequent achievement of

a constant moment of inertia at all angular momenta. In Fig. 6 the moment of inertia is plotted versus the square of the angular velocity for various temperatures. The main feature of this diagram is the absence of the backbending. The angular velocity for the lowest isotherm remains almost constant, without backbending, while the moment of inertia rapidly increases. The constancy of angular velocity with angular momentum at low temperatures suggests that the dynamical behavior of the system is closer to that of an oscillator than to that of a rotor.

### SUPERFLUID PROPERTIES OF EXCITED NUCLEI ARISING FROM A $\delta$ -FORCE RESIDUAL INTERACTION

L. G. Moretto and S. K. Kataria\*

The short range residual interaction in nuclei is usually accounted for by means of the pairing Hamiltonian.

$$H = \sum_{\pm k} \epsilon_k a_k^\dagger a_k - \sum_{k, k'} G_{kk'} a_{k'}^\dagger a_{k'}^\dagger a_k^- a_k \quad (1)$$

where  $\epsilon_k$  are the single particle energies,  $a_k^\dagger$  and  $a_k^-$  are the residual interaction matrix elements. Matrix elements,  $G_{kk'}$ , when calculated for a  $\delta$ -force residual interaction, can vary by as much as one order of magnitude depending upon the single particle states  $k, k'$ . In this work the statistical functions describing excited nuclei have been calculated on the basis of the Nilsson shell model and of a  $\delta$ -force matrix elements.<sup>1</sup> A comparison is made with calculations performed on the basis of a constant pairing strength  $G$ .<sup>2</sup>

The logarithm  $\Omega$  of the grand partition function can be derived from the Hamiltonian:<sup>3</sup>

$$\Omega = -\beta \sum_k (\epsilon_k - \lambda - E_k) + 2 \sum_k \ln [1 + \exp(-\beta E_k)] - \beta \sum_{kk'} G_{kk'} \chi_k \chi_{k'} \quad (2)$$

where  $\beta$  is the inverse of the temperature,  $\lambda$  is the chemical potential,  $E_k = [(\epsilon_k - \lambda)^2 + \Delta_k^2]^{1/2}$  and  $\Delta_k$  is related to  $\chi_k$ 's by the relation:

$$\Delta_k = \sum_{k'} G_{kk'} \chi_{k'}$$

All the other thermodynamical equations can be obtained by a suitable differentiation of  $\Omega$ . For instance, the gap equation takes the form:

$$\frac{\partial \Omega}{\partial \Delta_k} = 0 \quad \text{or} \quad \Delta_k = \frac{1}{2} \sum_{k'} G_{kk'} \Delta_{k'} \frac{\tanh \frac{1}{2} \beta E_{k'}}{E_{k'}} \quad (3)$$

The level density is

$$\rho(E, N) = \frac{\exp S}{(2\pi)^{3/2} D^{1/2}} \quad (4)$$

where  $D = \det[\partial^2 \Omega / \partial a_i \partial a_j]$ ,  $a_i$  being the Lagrange multipliers used to fix the constants of motion of the system.

In the present calculations the single particle eigenvalues  $\epsilon_k$  have been obtained using the Nilsson model. The matrix elements  $G_{kk'}$  have been computed on the basis of a  $\delta$ -force residual interaction. The strength of the  $\delta$ -interaction has been chosen so that the gap parameters  $\Delta_k$  at the Fermi surface reproduce the overall experimental even-odd mass differences. The particle equation and the set of gap equations (Eq. (3)) have been solved simultaneously by means of an iteration procedure.

Figure 1 shows the temperature dependence of the gap parameters  $\Delta_k$  associated with each level  $k$  for the proton component of the nucleus  $^{220}_{86}\text{Rn}$ . It is seen that in ground state the gap parameters for different levels are different. Furthermore, it is interesting to notice that all the gap parameters  $\Delta_k$  vanish at a common critical temperature. In the constant G approximation all the gap parameters are identically equal. At the critical temperature the system undergoes a second-order phase transition which appears in the specific heat as a discontinuity. Figure 2(a) shows the temperature dependence of the denominator of the level density expression

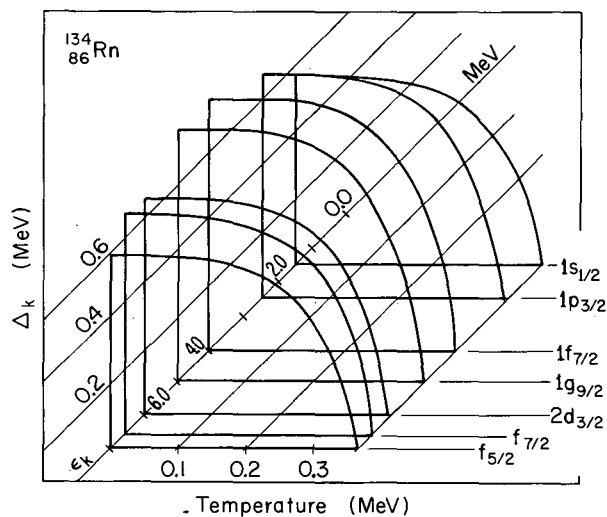


Fig. 1. The temperature dependence of the gap parameters  $\Delta_k$  for the proton component of  $^{220}_{86}\text{Rn}$  is shown for few selected levels.  $\epsilon_k$  denotes the single particle energy eigenvalue. All the gap parameters  $\Delta_k$  become zero at the same temperature. (XBL 736-3202)

(Eq. (4)) for the  $\delta$ -force matrix elements. Figures 2(b) and 2(c) show the variation of the nuclear entropy and nuclear level density with temperature.

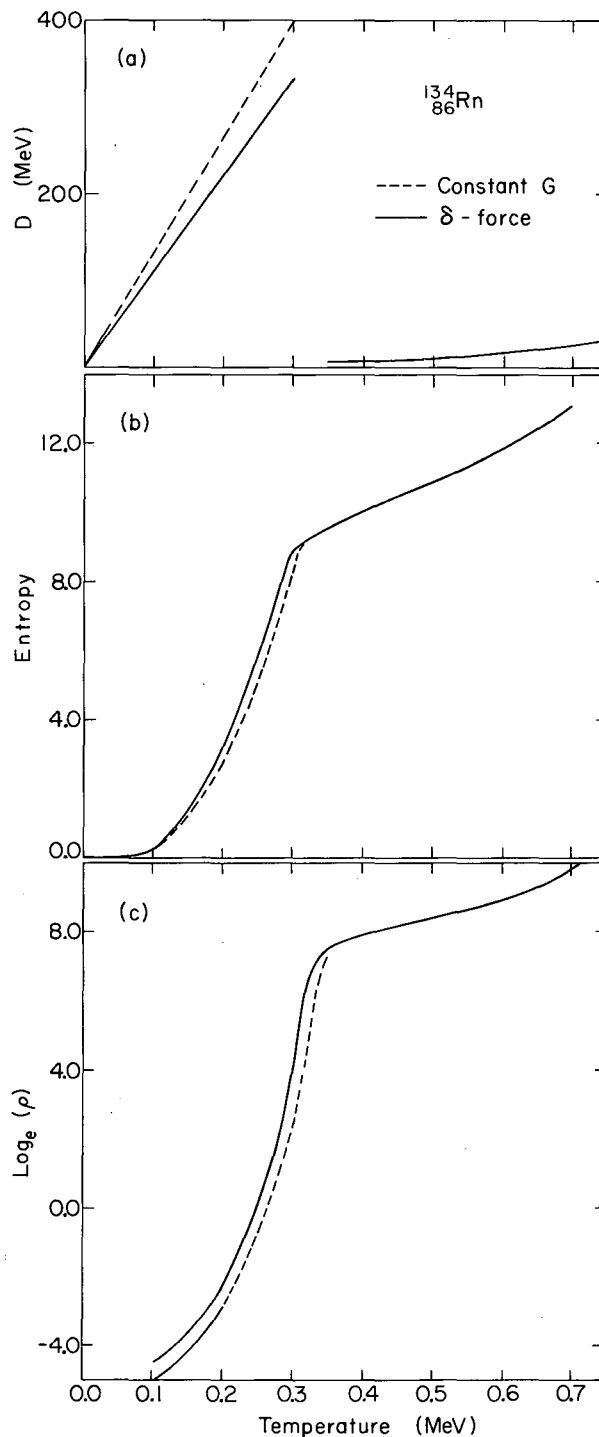


Fig. 2. The temperature dependence of the thermodynamical quantities for the proton component of the nucleus  $^{220}_{86}\text{Rn}$ . (a) The denominator in the level density expression. (b) The nuclear entropy. (c) The nuclear level density. The continuous lines refer to the calculation with  $\delta$ -force pairing matrix elements and the dashed lines are associated with the use of constant G-matrix elements. The magnitude of the pairing strength G was adjusted so as to match the  $\Delta$  with the gap parameter  $\Delta_F$  obtained with  $\delta$ -force. (XBL 736-3228)



The validity of the constant-G approximation has been studied by calculating the various statistical thermodynamic functions. The pairing strength  $G$  was chosen so as to match the gap parameter  $\Delta$  to the gap parameter  $\Delta_k$  associated with the level closest to the Fermi surface, calculated on the basis of the  $\delta$ -interaction. The temperature dependence of the matched  $\Delta$  and  $\Delta_k$  for a single nucleon component is shown in Fig. 3. One notices that the critical temperature of the system with  $\delta$ -force matrix elements is different from the

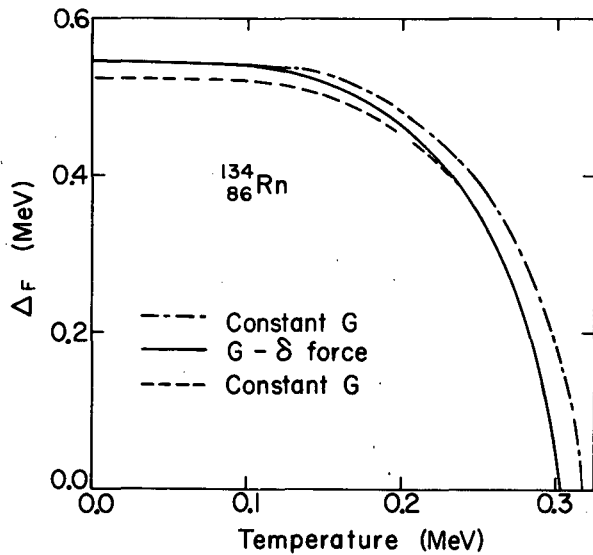


Fig. 3. The temperature dependence of the gap parameters  $\Delta$  for the proton component of  $^{220}\text{Rn}$  for the level closest to the Fermi surface for the three cases. The continuous curve is obtained by using the  $\delta$ -force pairing matrix elements. The dashed curves are obtained within the constant  $G$  approximation. The dashed curve (--) is obtained by matching the condensation energy with constant  $G$  and the condensation energy with  $\delta$ -force matrix elements. The dashed curve (- - -) is obtained by matching the gap parameter  $\Delta$  in the constant  $G$  approximation to the gap parameter  $\Delta_F$  for the level nearest to the Fermi surface calculated with the  $\delta$ -force. (XBL 736-3206)

critical temperature obtained from the constant  $G$  calculations. A lower critical temperature for the proton component of the system with  $\delta$ -force  $G$ -matrix elements as compared to the case with constant  $G$  matrix elements is observed for most of the cases analyzed. Another possible way of comparing the two formalisms is that of matching the condensation energies:

$$CE = \sum_{k=1}^{\infty} \left\{ \epsilon_k \left( 1 - \frac{\epsilon_k^{-\lambda}}{E_k} \right) - \frac{1}{2} \frac{\Delta_k^2}{E_k} \right\} - \sum_{k=1}^{N/2} \epsilon_k.$$

When this is done, the gap parameter  $\Delta$  does not agree with the  $\Delta_k$  at the Fermi surface. However, the critical temperatures for these two systems do match for the few cases analyzed. Figure 2(a) shows the denominators of the level density expression (Eq. (7)) for the two formalisms where the constant- $G$  gap parameter  $\Delta$  is matched to the  $\Delta_k$  closest to the Fermi surface. Figures 2(b), 2(c) show the behavior of the entropy and of the logarithm of nuclear level density on the temperature for the two formalisms.

The calculations have been performed for the neutron components too. A similar behavior is observed for those cases. It is concluded that the effect of the approximation of constant matrix element  $G$  on the nuclear entropy or nuclear level density is not a serious one, provided one has the correct prescription to estimate an effective pairing strength  $G$ .

#### Footnote and References

\* On leave from Bhabha Atomic Research Centre, Bombay, India.

1. J. D. Immele and G. L. Struble, Nucl. Phys. **A187**, 459 (1972).
2. L. G. Moretto, Nucl. Phys. **A182**, 641 (1972).
3. M. Sano and S. Yamasaki, Prog. Theor. Phys. **29**, 397 (1963).

**STUDIES ON STATISTICALLY EXCITED SHELL MODEL NUCLEI:  
THE DEPENDENCE OF THE SHELL STRUCTURE AND OF THE PAIRING  
CORRELATION UPON ANGULAR MOMENTUM**

L. G. Moretto

The complete formalism describing the statistical properties of a nucleus in terms of pairing, angular momentum and excitation energy is presented below. All of the quantities refer to a single nuclear component.

The logarithm of the grand partition function is:

$$\Omega = -\beta \sum (\epsilon_k - \lambda - E_k) + \sum \ln [1 + \exp(-\beta(E_k - \gamma m_k))] + \sum \ln [1 + \exp(-\beta(E_k + \gamma m_k))] - \beta \frac{\Delta^2}{G}. \quad (1)$$

In this expression  $\epsilon_k$  and  $m_k$  are the single particle energies and spin projections respectively;  $\beta$ ,  $\alpha = \beta\lambda$  and  $\mu = \beta\gamma$  are the Lagrange multipliers which fix the energy, the particle number and the angular momentum projection respectively;  $G$  is the pairing strength;  $\Delta$  is the gap parameter; the quasiparticle excitation  $E_k$  is given by:  $E_k = [(\epsilon_k - \lambda)^2 + \Delta^2]^{1/2}$ . The quantity  $\beta$  is also the reciprocal of the temperature and  $\lambda$  is identified with the chemical potential. The gap parameter  $\Delta$  is obtained as a function of  $\beta$ ,  $\lambda$ ,  $\gamma$  by solving the gap equation:

$$\sum \frac{1}{2E_k} \left[ \tanh \frac{1}{2} \beta(E_k - \gamma m_k) + \tanh \frac{1}{2} \beta(E_k + \gamma m_k) \right] = \frac{2}{G}. \quad (2)$$

The constants of motion are the particle number  $N$ , the total energy  $E$ , the angular momentum projection  $M$ . These quantities are given by the following expressions:

$$N = \sum \left[ 1 - \frac{\epsilon_k - \lambda}{2E_k} \left\{ \tanh \frac{1}{2} \beta(E_k - \gamma m_k) + \tanh \frac{1}{2} \beta(E_k + \gamma m_k) \right\} \right], \quad (3)$$

$$E = \sum \epsilon_k \left[ 1 - \frac{\epsilon_k - \lambda}{2E_k} \left\{ \tanh \frac{1}{2} \beta(E_k - \gamma m_k) + \tanh \frac{1}{2} \beta(E_k + \gamma m_k) \right\} \right] - \frac{\Delta^2}{G}, \quad (4)$$

$$M = \sum m_k \left[ \frac{1}{1 + \exp\beta(E_k - \gamma m_k)} - \frac{1}{1 + \exp\beta(E_k + \gamma m_k)} \right]. \quad (5)$$

The above equations, together with the gap equation define  $\Delta$ ,  $\lambda$ ,  $\beta$ , and  $\gamma$  as a function of  $N$ ,  $E$ ,  $M$ ,  $G$ ,  $\epsilon_k$ , and  $m_k$ . The entropy is given by:

$$S = \sum \ln [1 + \exp(-\beta(E_k - \gamma m_k))] + \sum \ln [1 + \exp(-\beta(E_k + \gamma m_k))] + \beta \sum \frac{1}{1 + \exp\beta(E_k - \gamma m_k)} + \beta \sum \frac{1}{1 + \exp\beta(E_k + \gamma m_k)}. \quad (6)$$

The level density is given by:

$$\rho(E, N_i, M) = \frac{\exp S}{(2\pi)^{n/2} D^{1/2}}. \quad (7)$$

The index  $i$  indicates that more than one component may be present (in the present case one has neutrons and protons) and  $n$  is equal to the number of Lagrange multipliers introduced in the formalism. The quantity  $D$  is given by:

$$D = \det \left| \frac{\partial^2 \Omega}{\partial a_i \partial a_j} \right|, \quad (8)$$

where the  $a_i$ 's indicate the Lagrange multipliers.

In this formalism only the  $z$  component  $M$  of the total angular momentum is accounted for, while no explicit mention is made about the total angular momentum  $I$ . However, for a spherically symmetric system, the formalism is indeed complete. Because of such a symmetry, the laboratory fixed  $z$  axis can be made to coincide with the body fixed  $z'$  axis and both can be aligned within the quantum mechanical uncertainty with the angular momentum direction. In this case the whole physical effects of the angular momentum are taken up by the  $z$  projection and it is possible to identify and substitute  $M$  and  $I$ . This is correct in the classical limit; in the quantum mechanical

limit the substitution should be  $M \rightarrow \sqrt{I(I+1)} \sim I + \frac{1}{2}$ .

However, in the evaluation of the level densities one has to account for the statistical factor associated with angular momentum. In order to determine such an effect we use the procedure suggested by Bethe:

$$\rho(E, I) = \rho(E, M) - \rho(E, M+1), \quad (9)$$

or, with good approximation

$$\rho(E, I) = - \frac{d}{dM} \rho(E, M) \Big|_{M=I+1/2}. \quad (10)$$

In order to evaluate such a derivative one can write approximately:

$$\rho(E, M) \approx f(E, I) e^{-M^2/2\sigma^2}, \quad (11)$$

where

$$\sigma^2 = \frac{I}{\beta\gamma}. \quad (12)$$

In such an expression  $f(E, I)$  and  $\sigma^2$  depend on  $I$  through the quantities which describe the intrinsic nuclear properties. The derivative can now be taken:

$$\rho(E, I) = \frac{2I+1}{2\sigma^2} f(E, I) e^{-(I+\frac{1}{2})^2/2\sigma^2} \quad (13)$$

$$= \frac{2I+1}{2\sigma^2} \rho(E, M = I+1/2). \quad (14)$$

Such an approximation permits a straightforward evaluation of the total level density. In Fig. 1 the denominator of the level density for the nucleus  $^{194}\text{Pt}$  is shown. In many of the isotherms two discontinuities are visible corresponding to the neutron and proton pairing phase transition. In Figs 2-4 the natural logarithms of the level densities for  $^{194}\text{Pt}$ ,  $^{198}\text{Hg}$ , and  $^{220}\text{Rn}$  are presented as a function of energy and angular momentum. The effects of closeness to the  $^{208}\text{Pb}$  shell on the pairing properties can be easily observed especially by means of the superfluid boundaries for the neutron and proton components. Especially visible is the limited extension of the proton paired phase in  $^{198}\text{Hg}$  (Fig. 3). The upsweep of the constant level density lines close to zero angular momentum is due to the  $2I+1$  dependence of the level densities.

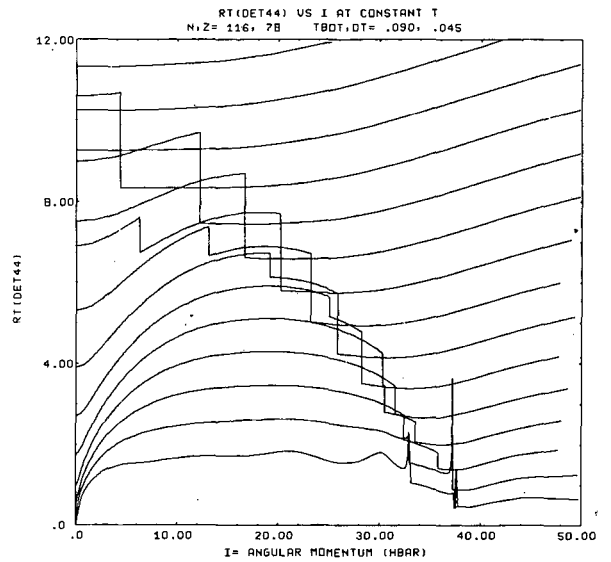


Fig. 1. Square root of the denominator determinant (in MeV) for the nucleus  $^{194}\text{Pt}$  as a whole, as a function of temperature and angular momentum. The two discontinuities associated with the proton and neutron phase transitions are observed in many isotherms.

(XBL 733-274)

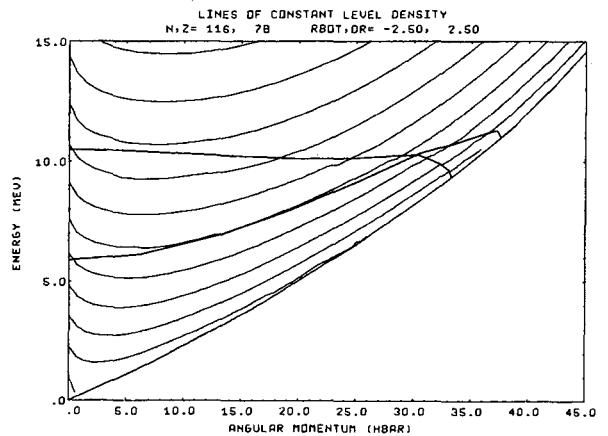


Fig. 2. Lines of constant natural logarithm of the level density in the energy angular momentum plane for  $^{194}\text{Pt}$ . The yrast line and the boundaries of the neutron and proton superfluid phases are also shown.

(XBL 734-2613)

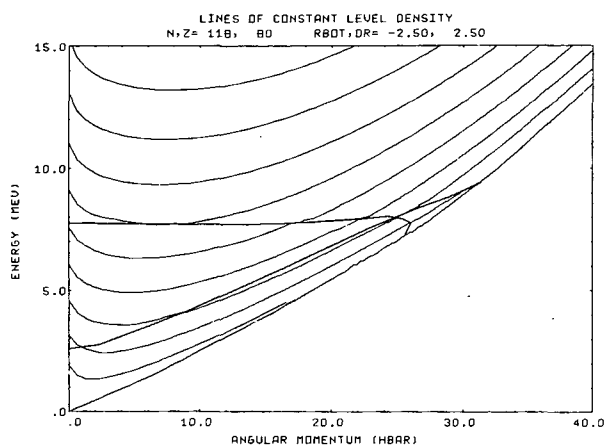


Fig. 3. Same as Fig. 2 for  $^{198}\text{Hg}$ .  
(XBL 734-2618)

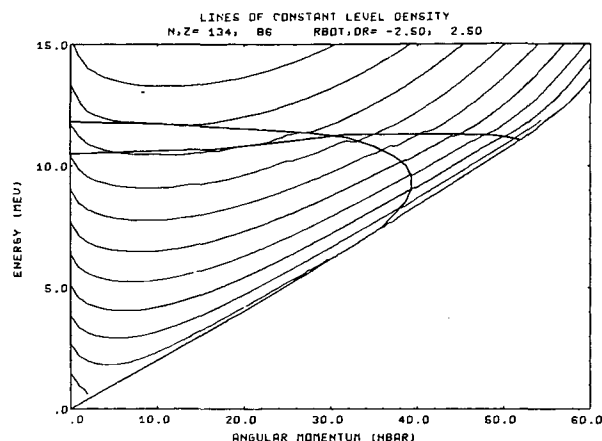


Fig. 4. Same as Fig. 2 for  $^{220}\text{Ru}$ .  
(XBL 734-2612)

### LARGE SUPERFLUIDITY ENHANCEMENT IN THE PENETRATION OF THE FISSION BARRIER

L. G. Moretto and R. P. Babinet

The standard pairing formalism generates a Hamiltonian, diagonal in quasi-particle space, whose expectation value can be expressed as follows:

$$\langle H \rangle = \langle H(n_k, \Delta) \rangle = 2 \sum v_k^2 (\epsilon_k - \lambda) + 2 \sum n_k (\epsilon_k - \lambda) (u_k^2 - v_k^2) - G \left[ \sum u_k v_k (1 - 2n_k) \right]^2 \quad (1)$$

where the  $n_k$  are the quasi-particles occupation numbers,  $\Delta$  is the gap parameter which expresses the diffuseness of the Fermi surface due to the residual interaction,  $\epsilon_k = \epsilon_k(\alpha)$  are the single particle levels,  $\lambda$  is the chemical

potential;  $v_k^2 = 1 - u_k^2 = \frac{1}{2} \left( 1 - \frac{\epsilon_k - \lambda}{E_k} \right)$  and

$E_k = [(\epsilon_k - \lambda)^2 + \Delta^2]^{1/2}$ . The gap parameter is usually determined by the condition:

$$\frac{\partial \langle H \rangle}{\partial \Delta} = 0, \quad (2)$$

which is called the gap equation. Such a condition, which requires  $\langle H \rangle$  to be stationary with respect to  $\Delta$ , is relevant to physical situations where the static, or equilibrium properties of a system are to be determined.

This is not the case when the quantum-mechanical penetration of a fission barrier is considered. The penetration of a multidimensional barrier implies a dynamical motion whose semiclassical trajectory must be determined not by considering the potential energy only, but by applying a dynamical principle such as the least action principle.

It follows that the application of the gap equation (2) to the problem of barrier penetrability is not appropriate and a new gap equation, defining the gap parameter in the frame work of the more general dynamical problem, should be obtained.

The action integral for the problem of barrier penetration is:

$$S = \int_a^b \sqrt{2B(V-E)} d\alpha, \quad (3)$$

where  $\alpha$  is the deformation coordinate,  $a$  and  $b$  are classical turning points,  $B$  is the inertia associated with the coordinate  $\alpha$ ,  $V$  is the potential energy and  $E$  is the total energy. Such an expression depends upon the gap parameter  $\Delta$  through both the inertia  $B$  and the potential energy  $V$ .

The potential energy  $V$  can be identified with the expectation value of the pairing Hamiltonian expressed as a function both of the deformation  $\alpha$  and of the gap parameter  $\Delta$ . In order to approximate the dependence of  $\langle H \rangle$  with respect to  $\Delta$  when  $\Delta = \Delta_0$ ,  $\Delta_0$  being the stationary value of  $\Delta$ . If the single particle Hamiltonian is approximated by the uniform model, one obtains:

$$\left. \frac{\partial^2 \langle H \rangle}{\partial \Delta^2} \right|_{\Delta = \Delta_0} = 2g \left( 1 - \frac{gG}{2} \right) \approx 2g, \quad (4)$$

where  $g$  is the total density of the doubly degenerate single particle levels inclusive of neutrons and protons.

The potential energy  $V(\alpha)$  can be expressed in quadratic approximation as:

$$V(\alpha) = V_0(\alpha) + g(\Delta - \Delta_0)^2, \quad (5)$$

where  $V_0(\alpha)$  is the "shape" of the barrier which corresponds to a value of  $\Delta$  equal to its stationary value  $\Delta_0$ . Similarly the inertia, which can be obtained by the cranking model, is given, for the uniform model, by the expression:

$$B = \hbar^2 \left\langle \left( \frac{\partial \epsilon_k}{\partial \alpha} \right) \right\rangle^2 \frac{g}{3\Delta^2} \sim \frac{K}{\Delta^2}. \quad (6)$$

In order to correct the limiting form of this equation at large  $\Delta$ , the following expression can be postulated:

$$B = \frac{K}{\Delta^2} + \beta, \quad (7)$$

where  $\beta$  is the irrotational limit of the inertia.

By substituting (7) and (5) in (3) one obtains:

$$S = \int_a^b d\alpha \sqrt{2 \left( \frac{K}{\Delta^2} + \beta \right) \left\{ V_0(\alpha) - E + g(\Delta - \Delta_0)^2 \right\}}. \quad (8)$$

The least action principle requires that the integral  $S$  be an extremum, namely  $\delta S = 0$ . In other words a function  $\Delta(\alpha)$  must be found which minimizes the integral (8). Since Eq. (10) does not contain the derivative of  $\Delta$  with respect to  $\alpha$ , the variational condition reduces to the algebraic equation:

$$\frac{d}{d\Delta} \left[ \left( \frac{K}{\Delta^2} + \beta \right) \left\{ V_0(\alpha) - E + g(\Delta - \Delta_0)^2 \right\} \right] = 0. \quad (9)$$

This equation is the gap equation relevant to

the dynamical problem. By setting  $\beta = 0$ , a very simple expression is obtained:

$$\frac{\Delta}{\Delta_0} = 1 + \frac{V_0(\alpha) - E}{g\Delta_0^2}. \quad (10)$$

Before penetrating the barrier, at the classical turning point given by the equation  $V_0(\alpha) - E = 0$ , the gap parameter is  $\Delta = \Delta_0$ ; in other words the solution for  $\Delta$  is the same as that given by Eq. (2). As the system dives into the barrier, the least action principle tends to decrease the inertia by increasing  $\Delta$ . The gap parameter is prevented from increasing indefinitely by the restoring force originated by the potential energy. The effect is very large indeed. By using the following round numbers:  $g = 7 \text{ MeV}^{-1}$ ,  $\Delta_0 = 1 \text{ MeV}$ , and  $V_0(\alpha) - E = 7 \text{ MeV}$ , one obtains  $\Delta = 2\Delta_0$ . The effect of such a pairing increase can be incorporated into an effective potential  $V^*$ :

$$V^*(\alpha) - E = \frac{V_0(\alpha) - E}{1 + \frac{V_0(\alpha) - E}{g\Delta_0^2}}. \quad (11)$$

Again, by using the above mentioned parameters, it appears that the deeper the system dives into the barrier, the more the effective barrier is reduced; in particular, by using the numerical values of the parameters mentioned above, the height of the effective barrier is reduced by a factor of two with respect to the true barrier. It is clear that such a dramatic reduction of the barrier must have a substantial effect on the spontaneous fission half-lives.

In Fig. 1, a plot of  $\frac{\Delta}{\Delta_0}$  is shown as a

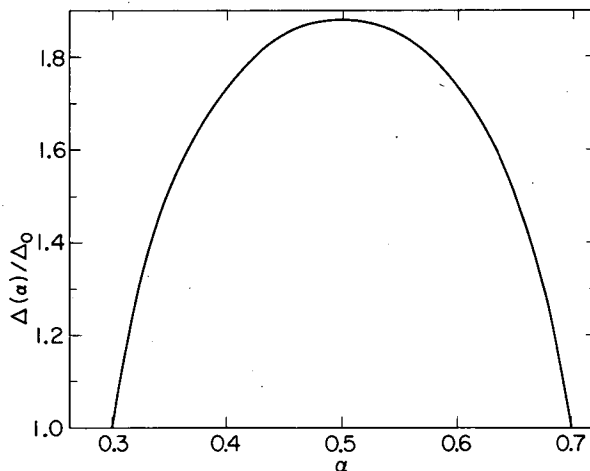


Fig. 1. Enhancement of the gap parameter in the penetration of the fission barrier.

(XBL 7312-6965)

function of  $\alpha$ . This calculation, applied to the uniform model, has been performed by substituting Eq. (9) and Eq. (4) into Eq. (3), and using the following parameters:

$$B = 1666 \frac{\Delta_0^2}{\Delta^2} + 225 \hbar^2 \text{ MeV}^{-1}, \quad \Delta_0 = 0.775 \text{ MeV},$$

$V = 6 - \frac{1}{2} 269 (\alpha - \alpha_0)^2 \text{ MeV}$  and  $E = 0$ . These quantities are expected to be realistic for an actinide nucleus. In Fig. 2, the effective potential energy is shown as a function of deformation. The overall features are still the same as those estimated by Eq. (12) and Eq. (13).

A limitation of the above treatment is related to the fact that  $\Delta$  should be considered as a true dynamical variable instead of a

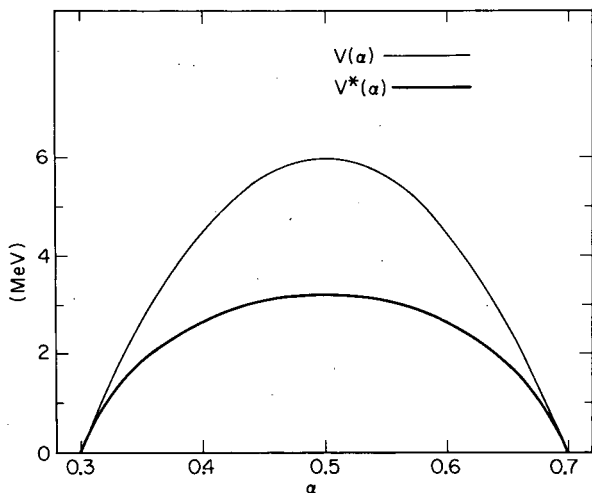


Fig. 2. Effective fission barrier  $V^*(\alpha)$  (thick line) as compared with the true fission barrier  $V(\alpha)$  (thin line). (XBL 7312-6964)

simple parameter. In other words, one should account for the kinetic energy associated with  $\Delta$  as well as for the potential energy. Consequently, the inertia becomes a tensor, and the action becomes:

$$S = \int \sqrt{2 \left[ B_{\alpha\alpha} + 2B_{\alpha\Delta} \frac{d\Delta}{d\alpha} + B_{\Delta\Delta} \left( \frac{d\Delta}{d\alpha} \right)^2 \right]} \sqrt{V_0(\alpha) - E + g(\Delta - \Delta_0)^2} d\alpha. \quad (12)$$

For the uniform model:

$$B_{\alpha\Delta} \approx 0 \quad B_{\Delta\Delta} = \hbar^2 \frac{g}{6\Delta^2}.$$

In this case the variational equation  $\delta S = 0$  becomes a rather complicated differential equation. Fortunately, it turns out that

$B_{\Delta\Delta} \left( \frac{d\Delta}{d\alpha} \right)^2 \ll B_{\alpha\alpha}$ , as can be checked by using Eq. (10) to calculate  $\frac{d\Delta}{d\alpha}$ .

The problem of the barrier penetrability needs to be further pursued by means of more realistic models. Some indication of the effect discussed above may exist in low energy induced fission. Fission fragment angular distributions, measured very close to the barrier of the compound nuclei  $^{210}\text{Po}$  and  $^{211}\text{Po}$  have led to the tentative conclusion of anomalously large values of the gap parameter at the saddle point. Such conclusions, however, seem to be incompatible with higher energy fission excitation function. This effect could find a possible justification along the following lines. The penetration into higher levels in induced fission is expected to depend upon the rate of increase of the level density. This rate is substantial at energies close to the top of the barrier thus leading to a larger value of the gap parameter. At higher excitation energies the rate of increase of the level density diminishes thus reducing the penetration and accounting for a normal excitation function.

**THEORETICAL PREDICTIONS OF FISSION HALF-LIVES OF ELEMENTS  
WITH Z BETWEEN 92 AND 106\***

J. Randrup,<sup>†</sup> C. F. Tsang, P. Möller,<sup>‡</sup>  
S. G. Nilsson,<sup>‡</sup> and S. E. Larsson<sup>§</sup>

In the last few years rather refined calculations of the fission barriers have been carried out taking into account both reflection asymmetric (e. g.,  $P_3$  and  $P_5$ ) degrees of freedom<sup>1-4</sup> at the second barrier peak and axially asymmetric degrees of freedom<sup>5, 6</sup> at the first barrier peak. It therefore seems appropriate to now use the wealth of experimental information<sup>7</sup> on the fission half-lives to obtain some semiempirical information on the fission inertial masses. It is our hope to develop an alternative method by this approach for calculating the fission half-lives of heavy and super-heavy elements that are not yet observed.

The theoretical fission barriers used are taken from Ref. 4 when available, or else calculated as described there and in Ref. 8 (Ref. 8 describing calculations of barriers for odd-even nuclei). They have subsequently been modified to take into account the effects of the  $\gamma$ -degree of freedom as given in Ref. 5 as well as a readjusted surface energy term in the liquid-drop energy part of the potential energy. The theoretical barriers thus calculated are in very good agreement with experiment except for the second barrier of  $^{232}\text{Th}$  and the first barrier of light Th and U isotopes.

For the calculation of fission half-lives, the choice of the actual fission-path coordinate proves to be rather important. The  $\epsilon$ -coordinate has a singular behavior for large distortions and thus the corresponding metric does not seem very well suited for an intuitive grasp of the fission problem. Instead, we choose the "equivalent center-of-mass separation",  $r$ . The transformation from  $\epsilon$  to  $r$  is simply given by

$$r = 3/4 R_0 \left( \frac{1 + 1/3\epsilon}{1 - 2/3\epsilon} \right)^{2/3},$$

$$R_0 = r_0 A^{1/3}. \quad (4)$$

This formula is strictly valid only for purely ellipsoidal shapes and equal-mass fragments, but we shall assume it to hold for more general distortions.

Hydrodynamical calculations<sup>9, 10</sup> of the fission inertia (in terms of the  $r$  coordinate and under the assumption of "y-family" shapes yields an inertial function which decreases from the spherical values of  $(32/15)\mu$

to the asymptotic value  $\mu$  for two separated fragments (cf. Fig.1),  $\mu$  being the reduced mass of the final two-fragment system. Since these calculations are based on the assumption of irrotational flow of the nuclear matter, they underestimate severely the true inertial mass. More realistic calculations yield a fluctuating inertial mass reflecting the specific single-particle structure of the particular nucleus under consideration. For the present first approach, however, we have confined ourselves to consider only a smooth inertial function. It also appears probable that the fissioning nucleus in its motion through deformation space circumvents the higher peaks of the inertia tensor.

Various considerations lead us to consider a trial inertial function of the following type

$$B_r = B_r^{\text{rigid}} + k(B_r^{\text{irrot}} - B_r^{\text{rigid}}), \quad (5)$$

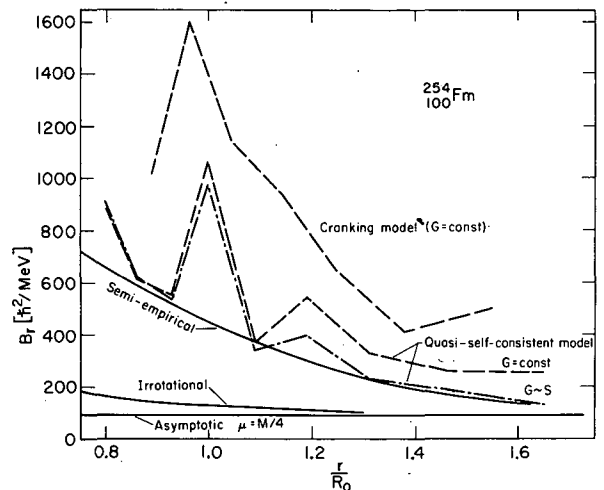


Fig. 1. Comparison of various inertial-mass functions  $B_r$  (here shown for  $^{254}\text{Fm}$ ). The lower curve represents the irrotational-flow calculation, while the kinded upper curves correspond to various microscopic models: Upper dashed: Cranking model,  $G = \text{constant}$ , Lower dashed: Quasi-self consistent model,  $G = \text{constant}$ , Dot-dashed: Quasi-self consistent model,  $G \sim S$ . The smooth curve in between is the determined best one-parameter semi empirical inertial-mass function (corresponds to  $k = 6.5$  in Eq. (5)). (XBL 737-3449)

where  $B_r^{\text{rigid}} = \mu$  is the mass corresponding to a rigid separation of the two fragments, and  $B_r^{\text{irrot}}$  is the mass corresponding to irrotational flow during the fission process. Thus  $k$  is an adjustable parameter describing the contribution to the inertial mass from the internal nuclear motion,  $k$  being unity for purely irrotational flow. As mentioned above, we expect from the microscopic calculations  $k$  to be considerably larger than that. This inertial function is of the same type as was used by Nix et al.<sup>9</sup> For simplicity we shall here assume equal-mass fragments and furthermore approximate the difference multiplying  $k$  by an exponential. The explicit form of  $B_r$  thus becomes

$$B_r = \frac{M}{4} \left[ 1 + k \frac{17}{15} e^{-(r - 3/4 R_o)/d} \right]. \quad (6)$$

Here  $M$  is the mass of the fissioning nucleus and accounts for the general scaling property of the inertial mass. The fall-off parameter  $d$  is taken to be that of the irrotational inertia,  $d = R_o/2.452$ .

The above trial inertial function, with only one adjustable parameter  $k$ , is used in connection with the established fission-barriers to fit optimally the spontaneous fission half-lives for all the actinide nuclei (see Fig. 2). From a minimization of the mean logarithmic deviation of the calculated half-lives from the experimental values the parameter  $k$  is found to equal 6.5. For this value of  $k$  the experimental half-lives are reproduced to within a factor of 25 on the average. Considering the span in half-lives, stretching over 30 decades, we find this parametric fit satisfactory for the present simple approach. We also believe a basis is established for a rather reliable half-life estimate in the close-lying mass regions. In particular, the longest-lived even-even isotope of element 106 is predicted to occur for  $N = 152$  with a half-life around 100  $\mu\text{sec}$ . The prediction for odd- $N$  isotopes of element 106 is discussed in the next section.

The fast fall-off with  $N$  of the Fm isotope half-lives (Fig. 2) also deserves some comments. Thus between  $^{256}\text{Fm}$  and  $^{258}\text{Fm}$  there is a shortening in half-lives by a factor of almost  $10^8$ . Theoretically the same fall-off factor occurs instead between  $^{258}\text{Fm}$  and  $^{260}\text{Fm}$ . Thus for  $^{258}\text{Fm}$  the second minimum as well as the second peak remain above the ground-state energy marked by a dashed line

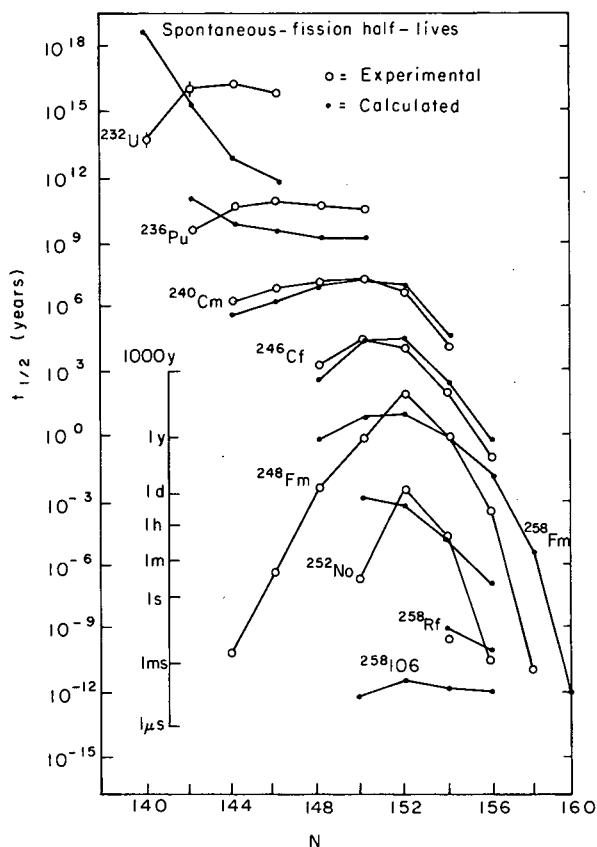


Fig. 2. Spontaneous-fission half-lives. Full circles: experimental values.<sup>7</sup> Open circles: calculated values with the determined semi-empirical inertia shown in Fig. 1. The mean logarithmic deviation is 1.4. Also half-lives predicted for the element 106 are shown.

(XBL 733-2429)

(assumed equal to the ground-state potential-energy minimum plus a 0.5 MeV zero-point beta-vibrational energy). For  $^{260}\text{Fm}$ , on the other hand, only the first peak rises above the dashed line, leading to a radical diminishing of the WKB integral and reflected in the rapid fall-off in half-life. Empirically this transition appears to occur between  $^{256}\text{Fm}$  and  $^{258}\text{Fm}$ .

A special problem is constituted by the shape-isomeric nuclei. This special group of nuclei was not included in the sample



employed when fitting the inertial-mass function. As is seen from Fig. 3, the obtained semiempirical inertial function yields isomeric half-lives being too long by six orders of magnitude on the average. However, the  $\epsilon_4$  degree of freedom is expected to have a relatively large influence on the isomeric fission. In Fig. 3 we have displayed the isomeric half-lives when the  $\epsilon_4$  dependence of the  $r$  coordinate is taken into account. It is seen that indeed this brings the calculated values into much better agreement with experiment. It should be added that a consistent inclusion of this effect does not appreciably change the good overall fit to the ground-state half-lives.

The large deviations for the U isotopes probably reflect the complicated structure of the second barrier region as found in the modified-oscillator model.<sup>4</sup> The possible experimental consequences of this structure were first pointed out in Ref. 13. In addition to this, the parametrization employed here may be somewhat insufficient for the rather extended barriers for these nuclei.

The odd-A nuclei are found to have considerably prolonged half-lives relative to their even-even neighbors. In Fig. 4 we have plotted the logarithm of the relative hindrance factor associated with odd-proton and neutron number, respectively. In several of the cases the ground-state intrinsic orbital is known and the assignment is then shown in the figure. The hindrance factor is typically of the order of  $10^5$  but varies in magnitude between  $10$  and  $10^{10}$ . Particularly large hindrance factors appear to be associated with the  $[734 \frac{9}{2}]$

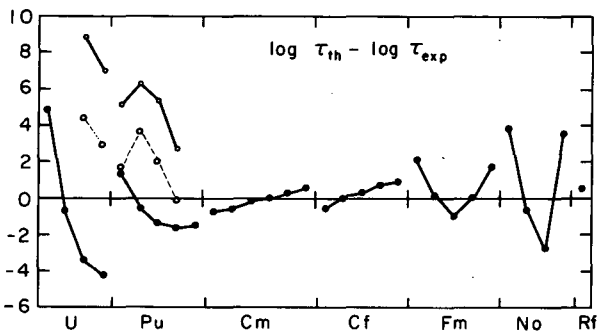


Fig. 3. Deviations of calculated half-lives from experimental values. In addition to the normal half-lives (full circles) also the results for some isomeric states are shown (open circles). The broken lines connect results obtained by including the effect of  $\epsilon_4$  on the  $r$ -coordinate, while all other points are calculated without this refinement.

(XBL 737-3271)

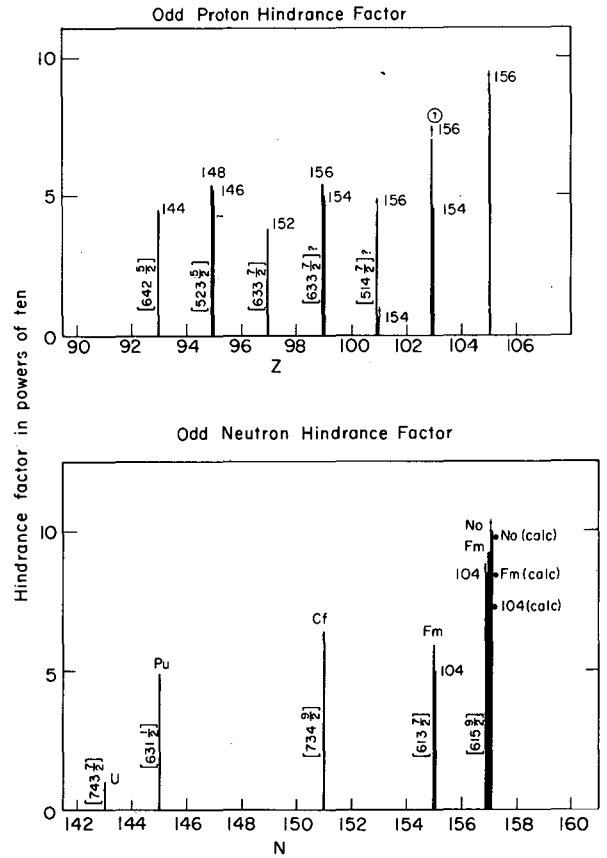


Fig. 4. Spontaneous fission half-life hindrance factors for odd-Z and odd-N nuclei, as obtained by comparing their empirical half-lives with values obtained by interpolation among adjacent even-even nuclei half-lives. The calculated hindrance factors for  $N = 157$  are displayed as dots for comparison.

(XBL 734-2629)

and the  $N = 157$  orbital, which latter we surmise to be  $[615 \frac{9}{2}]$ . The assignment is unclear since for the calculated ground-state deformation of  $\epsilon = 0.23$  there are several orbitals available close to each other above  $N = 152$ . For the distortion of  $\epsilon = 0.23$   $9/2+$  actually appears first as the 161st orbital. The reason that we associate  $[615 \frac{9}{2}]$  with the  $N = 157$  ground state with some confidence is that  $^{257}\text{Fm}$  is known to decay by an unhindered alpha transition to this orbital in  $^{253}\text{Cf}$ . In this latter nucleus the orbital assignment is fairly certain. The particular stability at  $N = 157$  exhibited for all of the heavy elements, Cf, Fm, No and element 104, was pointed out to us by G. T. Seaborg.<sup>14</sup> The relevance of this finding for the production of prospective still heavier elements is

obvious and we have been investigating the question of whether  $N = 157$  can be expected to yield increased stability also for larger  $Z$ -values.

By studying the specialization energy associated with an odd particle we have estimated the extra hindrance factor increasing the half-lives of nuclei having  $9/2+$  as the odd-particle orbital under the two simplifying assumptions: First, degrees of freedom in addition to  $\epsilon$  and  $\epsilon_4$ , namely  $\epsilon_3$  and  $\epsilon_5$  (reflection asymmetry) and  $\gamma$  (axial asymmetry) can be neglected for the calculation of the effect of the increase in the potential-energy surface. Second, the odd-particle influence on the inertial mass involved in the barrier penetration may be neglected. Under these assumptions we obtain hindrance factors for the different  $N = 157$  cases as shown in Fig. 4 to the right of the experimental bars drawn in the figure for three  $N = 157$  nuclei. The agreement appears surprisingly good. Thus for Fm, No and  $Z = 104$ , the theoretical calculations including only the potential-energy effect appear to reproduce the empirical findings very well. For the element,  $Z = 106$ ,  $N = 157$ , however, the calculations predict a much smaller hindrance factor ( $\sim 10^3$ ). In view of the somewhat unsatisfactory simplifying assumptions made we do not expect more than qualitative agreement for the odd-A effect.

#### Footnotes and References

\*Published in Nucl. Phys. A217, 22 (1973).

†On leave from the University of Aarhus, Denmark.

‡On leave from Lund Institute of Technology, Lund, Sweden.

§Lund Institute of Technology, Lund, Sweden.

1. P. Möller and S. G. Nilsson, Phys. Letters 31B 283 (1970).
2. H. C. Pauli, T. Ledergerber and M. Brack, Phys. Letters 34B, 264 (1971).
3. H. C. Pauli and T. Ledergerber, Nucl. Phys. A175 545 (1971).
4. P. Möller, Nucl. Phys. A192 529 (1972).
5. S. E. Larsson, S. G. Nilsson and I. Ragnarsson, Phys. Letters 38B 269 (1972).
6. U. Götz, H. C. Pauli and K. Junker, Phys. Letters 39B 436 (1972).
7. Compilations by K. Hulet, E. Hyde, R. Vandenbosch and V. Viola and S. V. Jackson, private communications (1972).
8. S. G. Nilsson, G. Ohlén, C. Gustafsson and P. Möller, Phys. Letters 30B, 437 (1969).
9. J. R. Nix, Nucl. Phys. A130 241 (1969).
10. E. O. Fiset and J. R. Nix, Nucl. Phys. A193, 647 (1972).
11. J. Krumlinde, private communication, to be published.
12. A. Sobiczewski, private communication, to be published.
13. P. Moller and J. R. Nix, Physics and Chemistry of Fission (IAEA, Rochester, 1973).
14. G. T. Seaborg, private communication, 1972.

## THE SUPERHEAVY ELEMENTS: A BRIEF REVIEW

C. F. Tsang

An invited article<sup>1</sup> for The Physics Teacher has been written that gives a brief summary of the status of superheavy element research. First, the basic ideas behind the prediction of the possible existence of superheavy nuclei are explained. Starting with a simple knowledge of the liquid drop model of the nucleus and of the occurrence of magic numbers in the nuclear shell model, an attempt is made

to explain to the general reader how developments in the understanding of the connections between these two models in 1965 led to the realization of the possible existence of a group of elements beyond the present periodic table. These relatively stable elements are referred to as "an island of stability." Many studies of the occurrence of magic numbers point toward the proton number 114 and the neutron

number 184 as being the position around which these nuclei lie. Detailed studies with a method incorporating both the liquid drop and the shell models enabled the first comprehensive estimate of the stability of these nuclei to be made in 1968. Since then, improved estimates have been made by several groups. Qualitatively, all the calculations confirm the idea that if these nuclei could be made, they would live long enough to be studied. In fact, it is predicted that some of these nuclei may have half-lives comparable to the age of the solar system.

The first experimental attempts to make superheavy elements were made in 1967 with a heavy ion linear accelerator. The results were negative mainly because, using the heavy ion projectiles available at the time, the reaction fell far short of the island of stability. From 1968 to 1972, attention has been turned to the search for these elements in nature. This search was based on the assumption that if these elements were made during the formation of the solar system they might live long enough to be detected in minute quantities in appropriate ores. Comprehensive efforts by Berkeley, Dubna, Mainz, and other groups have not, so far, yielded positive results. Search in cosmic rays has also been made without success. One may attribute these results to the possibility that conditions existing during the formation of our solar

system or in cosmic ray sources were not favorable to the formation of superheavy nuclei. Furthermore, theoretical values of half-lives are subject to large uncertainties and they may turn out to be much less than the age of the solar system or the age of cosmic rays, but nevertheless may be observed if they are made in accelerators.

Thus most of the current attention is focused on formation by means of heavy ion reactions. Recently developed heavy ion accelerators can yield beams of heavy ions never before obtained. Experiments have been performed in Orsay and Dubna, and further experiments are planned in Berkeley, getting closer and closer to the center of the island of stability. Many aspects of heavy ion reactions have not been fully understood, such as viscosity, inertia, and angular momentum effects, and these may have important bearings on whether one is able to make a superheavy nucleus by means of the collision of a heavy ion with the target nucleus. Both theoretical and experimental studies are currently underway to study these effects.

#### Reference

1. Two of the other more detailed reviews are: J. R. Nix, *Physics Today* (April 1972) p. 30. S. G. Thompson and C. F. Tsang, *Science* **178**, 1047 (1972).

### NUCLEAR MASSES, DEFORMATIONS, AND SINGLE-PARTICLE ORBITALS FOR MEDIUM-HEAVY AND HEAVY NUCLEI

C. F. Tsang, I. Ragnarsson,<sup>†</sup> S. G. Nilsson<sup>†</sup>  
P. Möller,<sup>†</sup> and J. R. Randrup

A summary is made of the calculated nuclear masses, single-particle orbitals, deformations and fission barriers for nuclei ranging from  $A \approx 100$  to  $A \approx 300$  along the line of beta-stability, thus including the predicted superheavy region. The calculation is based on the modified oscillator single particle potential well, using recently adjusted parameters. The Strutinsky Prescription is applied to extract shell effects which are combined with the Myers-Swiatecki liquid drop mass formula to yield deformation energy surfaces. For comparison, the energy surfaces are also calculated using Myers and Swiatecki droplet mass formula for the case of actinide nuclei. Some of the material have been published in various journals,<sup>1</sup> but this paper is an attempt to give, in one place, a complete

summary of the efforts of the Lund-Berkeley group during the last few years. The compilation includes:

1. A table and a figure showing modified-oscillator potential parameters  $\kappa$  and  $\mu$  as a function of  $A$ .
2. Single-particle level diagrams for regions with mass numbers around 110, 140, 165, 187, 208, 225, 242, 255 and 298.
3. Contours of shell correction energies as a function of neutron and proton numbers.
4. Ground state masses for nuclei from  $A = 100$  to 300.
5. Ground state deformation values for all nuclei under study in terms of both  $(\epsilon, \epsilon_4, \epsilon_6)$

and  $(\beta_2, \beta_4, \beta_6)$  values.

6. For the actinide nuclei, masses, deformations and barrier properties are given both using the liquid drop mass formula and using the droplet formula. Nuclear deformations for very neutron-rich isotopes of actinide elements are also displayed. These calculations take into account the effects of reflection and axial asymmetries.

7. A comparison of experimental single-particle levels and calculated levels is also made for the actinide region.

#### Footnotes and References

\*To be submitted to Nuclear Data.

†Department of Mathematical Physics, Lund University, Lund, Sweden.

1. See, for example, S. G. Nilsson, C. F. Tsang, A. Sobiczewski, Z. Szymanski, S. Wycech, C. Gustafson, I. L. Lamm, P. Möller, and B. Nilsson, Nucl. Phys. A131 1 (1969); P. Moller, Nucl. Phys. A192, 529 (1972).

## II. Chemical and Atomic Physics

*Heavy Ion Induced Atomic Reactions*

*Atomic and Molecular Spectroscopy*

*Photoelectron Spectroscopy and Hyperfine Interactions*

## RADIATIVE CAPTURE AND BREMSSTRAHLUNG OF BOUND ELECTRONS INDUCED BY HEAVY IONS\*

P. Kienle,<sup>†</sup> M. Kleber,<sup>†</sup> B. Povh,<sup>††</sup> R. M. Diamond,  
F. S. Stephens, E. H. Grosse,<sup>‡</sup> M. R. Maier,<sup>‡</sup> and D. Proetel<sup>†</sup>

The characteristics of x-ray emission, induced by atomic collisions of fast ( $v/c > 0.1$ ), highly stripped Ar( $17^+$ ), Ne( $10^+$ ), and N( $7^+$ ) ions, was investigated using gas targets. Three types of beam-associated processes have been observed: (i) non-radiative electron transfer into outer projectile orbits, followed by emission of characteristic x-rays, (ii) radiative electron capture<sup>1</sup> of weakly bound electrons into empty inner orbits of the projectile, (iii) bremsstrahlung of strongly bound electrons in the Coulomb field of the fast projectile.

Figure 1 shows sample x-ray spectra from the He and Ne gas targets. Besides the K x-rays in the Ar run, which have energies expected for transitions in Ar( $16^+$ ), one sees broad lines. They are beam associated, because their peak energies change only with the energy and the species of the projectile, but not appreciably with the target atom. In agreement with Ref. 1 we assign these broad x-ray lines to radiative capture of bound electrons from He or Ne into (mainly) K orbits of the

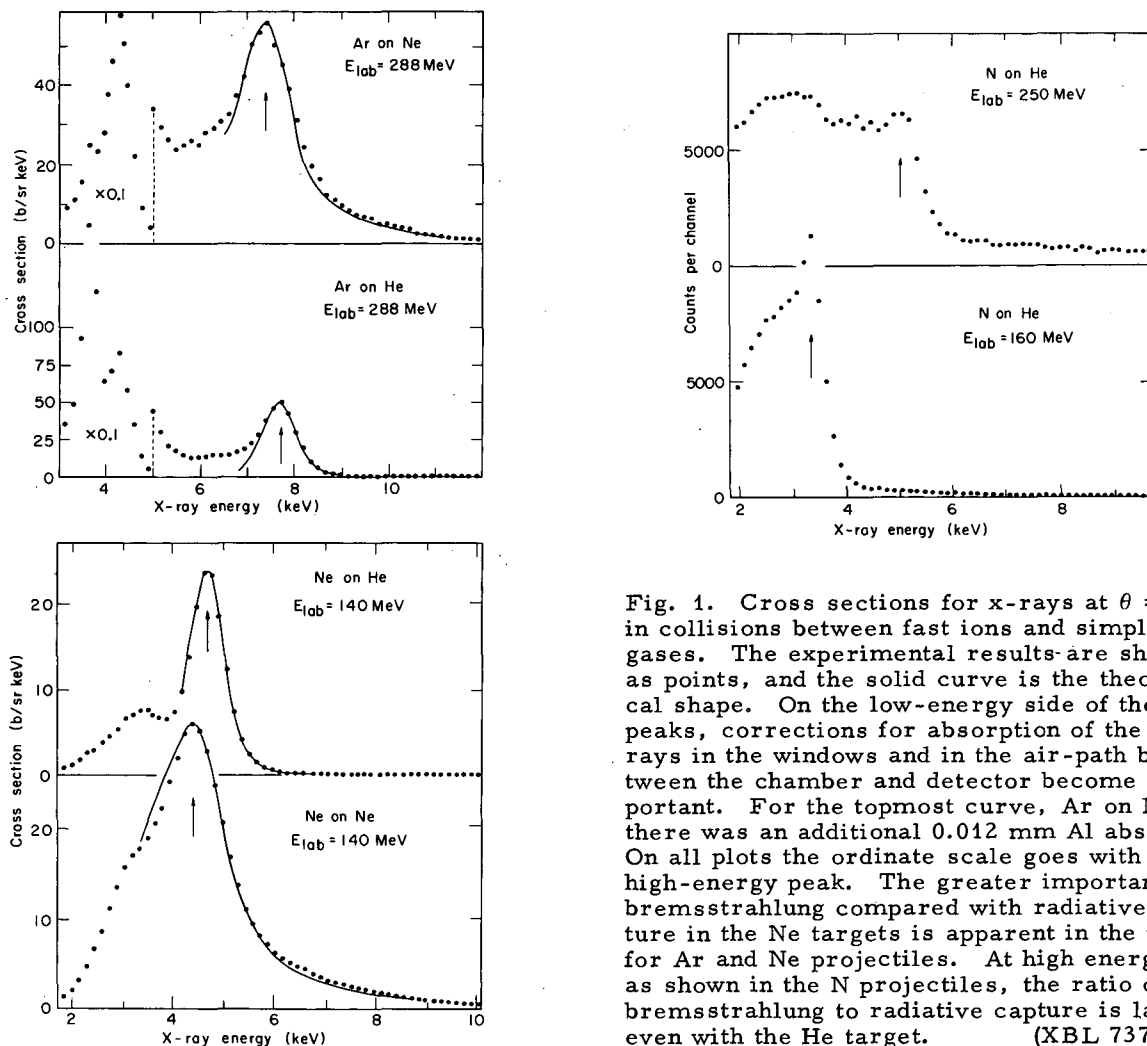


Fig. 1. Cross sections for x-rays at  $\theta = 90^\circ$  in collisions between fast ions and simple gases. The experimental results are shown as points, and the solid curve is the theoretical shape. On the low-energy side of the peaks, corrections for absorption of the x-rays in the windows and in the air-path between the chamber and detector become important. For the topmost curve, Ar on Ne, there was an additional 0.012 mm Al absorber. On all plots the ordinate scale goes with the high-energy peak. The greater importance of bremsstrahlung compared with radiative capture in the Ne targets is apparent in the plots for Ar and Ne projectiles. At high energies, as shown in the N projectiles, the ratio of bremsstrahlung to radiative capture is large even with the He target. (XBL 737-937)

highly stripped projectiles. If one considers the electrons quasifree, with an intrinsic momentum  $\vec{p}_i$  in a potential  $U_i$ , moving with a momentum  $\vec{k}$  towards the projectile considered at rest, one can intuitively derive the radiation frequency  $\omega$  when the electron is captured in an orbit with a binding energy  $E_f$ :

$$\frac{(\vec{p}_i + \vec{k})^2}{2m_e} + U_i = \hbar\omega + E_f$$

or

$$\hbar\omega = (E_i - E_f) + \frac{k^2}{2m_e} + \frac{\vec{k} \cdot \vec{p}_i}{m_e}. \quad (1)$$

This energy for the capture maximum is in fair agreement with the experimental results. The cross section for such radiative capture can be calculated by the "impact parameter" method.<sup>2</sup> In the energy region where the cross section is peaked, it can be factorized into two parts; one contains the properties of the projectile, and the other, those of the target. The latter enters in the form of its Compton profile,<sup>3</sup> and thus reflects the momentum distribution of the electrons in the target.

In addition, in the spectra of all targets with  $Z > 6$  we observed high-energy tails, such as those shown in Fig. 1. These radiation tails must have a different origin, because their intensity relative to the capture spectrum increases with larger beam velocities. With 17.8 MeV/n  $^{14}\text{N}$ , they become quite marked. We assign this radiation component to bremsstrahlung from strongly bound electrons. The cross section for bremsstrahlung radiated by an electron during a collision with a heavy particle of charge  $Z$  and velocity  $v$  is classically given by<sup>4</sup> (we use atomic units):

$$\frac{d^2\sigma_B}{d\Omega d\omega} \approx \frac{2}{c\pi\omega} \left( \frac{Z \sin\theta}{cv} \right)^2 \ln \left( \frac{\rho_{\max}}{\rho_{\min}} \right). \quad (2)$$

For a given frequency  $\omega$  one has  $\rho_{\max} \approx v/\omega$ , because for impact parameters larger than  $\rho_{\max}$  the collision time  $\tau \approx \rho/v$  is too long to produce significant radiation at that frequency. For bound electrons the quantum limit on the impact parameter is the limit down to which the electron can be localized. The upper

limit to the bremsstrahlung spectrum  $\omega_{\max} \approx v/\rho_{\min} \approx v/a$  increases with decreasing orbital radius  $a$ . Thus, strongly bound 1s electrons lead to high-frequency bremsstrahlung.

In summary, we have established the main features which determine the spectral distribution of the capture radiation of weakly bound electrons by fast ( $v/c \approx 0.12$ ) heavy ions. The radiation frequency is connected by a simple dispersion relation [Eq. (1)] to the momentum component  $p_z$  of the captured electron. The cross section for a given frequency is proportional to the probability to find an electron with the corresponding momentum component  $p_z$ . In addition, a new radiation process was found, a type of bremsstrahlung of strongly bound electrons. Bremsstrahlung becomes important in the x-ray spectrum at the highest beam velocities, because its cross section drops more slowly with increasing beam energy than that for radiative capture. At lower beam velocities the capture radiation becomes more important, whereas at still lower velocities (which we did not study) one would expect that the radiative-capture process should turn into transitions between quasimolecular states formed during a slow collision.

#### Footnotes and References

\* Condensed from Phys. Rev. Letters 31, 1099 (1973); LBL-1961.

† Permanent address: Technische Universität München, Munich, W. Germany.

†† Permanent address: Universität Heidelberg, Heidelberg, W. Germany.

‡ Permanent address: Max Planck Institut für Kernphysik, Heidelberg, W. Germany.

1. H. W. Schnopper, H. D. Betz, J. P. Delville, K. Kalata, A. R. Sohval, K. W. Jones, and H. E. Wegner, Phys. Rev. Letters 29, 898 (1972).

2. G. F. Drukarev, Bull. Acad. Sci. USSR, Phys. Ser. 24, 981 (1960); D. R. Bates and R. McCarroll, Adv. Phys. 11, 39 (1962).

3. M. Cooper, Adv. Phys. 20, 453 (1971).

4. For discussion and references see J. D. Jackson, Classical Electrodynamics (Wiley, New York, 1962), p. 509.

CHEMICAL EXPERIMENTS USING ACCELERATED HEAVY  
IONS AT THE BEVATRON

M. E. Jayko and A. Chatterjee

Preliminary investigations have been conducted in this Laboratory with Bevatron-produced high-energy ions. This was done in anticipation of the new Bevalac facility which will make possible many studies in radiation chemistry and radiation biochemistry which have not before been feasible. To initiate a program we have started with a study of heavy ions from the Bevatron. The results are expected to contribute significantly to the understanding of radiobiological data.

The Fricke-ferrous sulfate dosimeter is presently being used as a chemical monitor of the Bevatron heavy-ion beam.

Ferrous sulfate solutions (ranging in concentration from  $10^{-2}$  to  $10^{-4}$  molar) were irradiated with 230-MeV/n carbon ions. In water the range of such energetic carbon ions is about 10.9 cm. The LET increases along the path with a large increase at the Bragg peak just before it comes to a stop. For a 230-MeV/n carbon ion penetrating through water, the ratio between the Bragg peak ionization and the entrance ionization is greater than six. Since heavy ions exhibit different LETs at various segments of the track, a multicompartmented cell was used so that LET effects along the track could be studied in a single experiment. A schematic diagram of the cell and the experimental arrangement is shown in Fig. 1.

The target cells, made of quartz, had seven compartments (2 cm in diameter with windows 0.071-in. thick set 1.8 cm apart), each compartment containing a volume of 6 mliters. Irradiation time varied with beam intensity with the total dose being  $1 - 2 \times 10^3$  rads. Ferric yields were measured according to the method of J. Weiss et al.<sup>4</sup> and the relative yields are shown in Fig. 2.

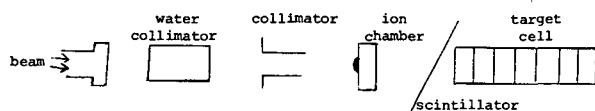


Fig. 1. A schematic representation of the experimental arrangement. (XBL742-330)

The ferrous concentration is given as a relative yield; absolute yields (G values) will only be possible after more precise information concerning the dose is available. Experiments to obtain this information are now in progress. The  $G(\text{Fe}^{3+})$  depends upon the LET of the radiation and is greatest when the LET is low; nevertheless, there is an increase in yield at the Bragg peak. There are other factors such as the availability of oxygen and the back reactions of the products capable of oxidizing ferrous ion which affect the yield and cannot yet be applied to the problem in a quantitative manner. One study which could have great significance is the relationship between track structure and chemical products. The relative yield of  $\text{Fe}^{3+}$  is an interesting example showing a decrease with depth initially, then rising near the Bragg ionization peak, falling sharply immediately thereafter.

We wish to thank Dr. Warren M. Garrison and C. A. Tobias for helpful discussions.

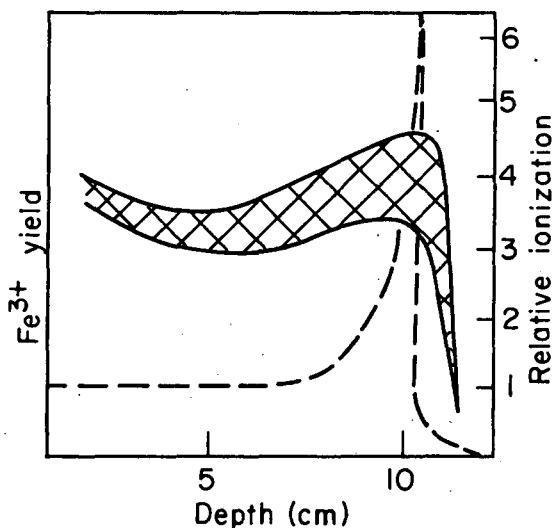


Fig. 2. The relative yield of  $\text{Fe}^{3+}$  at various depths of the multicompartmented cell.  $\text{Fe}^{3+}$  yield at all concentrations fell within the hatched area. The dashed curve is the Bragg ionization curve. (XBL742-331)



LIFETIME OF THE  $2^3S_1$  STATE OF HELIUM-LIKE ARGON  
( $Z = 18$ ) AND HELIUM-LIKE TITANIUM ( $Z = 22$ )

H. Gould, R. Marrus,\* and R. W. Schmieder†

The  $2^3S_1$  state of helium-like ions decays to the  $1^1S_0$  ground state primarily by relativistically induced magnetic-dipole radiation. The existence of this single-photon process was first noted by Breit and Teller<sup>1</sup> in connection with the metastable state of hydrogen, and the theory for radiative decay of helium-like ions in the  $2^3S_1$  state has now been considered by many authors.<sup>2</sup> The most detailed calculations of the lifetime of this state have been made by G. W. F. Drake<sup>3</sup> who finds that  $\tau(2^3S_1) = 212.4 \times 10^{-9}$  sec for helium-like argon and  $\tau(2^3S_1) = 27.4 \times 10^{-9}$  sec for helium-like titanium.

The single-photon decay of the  $2^3S_1$  state was first noted<sup>4</sup> in the x-ray spectra of helium-like ions excited in the solar corona and has subsequently been observed in the laboratory in the spectra of  $Ar^{16+}$  (Ref. 5) and  $He I$ .<sup>6</sup> A beam-foil measurement of this lifetime in  $Ar^{16+}$  using the 412-MeV argon beam from the old Berkeley heavy-ion linear accelerator (HILAC) yielded as a result  $\tau(2^3S_1) = 172 \pm 30 \times 10^{-9}$  sec in rough agreement with the theory. In this report, the results of a new series of measurements on this decay are reported.

The systems studied were helium-like  $Ar^{16+}$  and  $Ti^{20+}$  obtained from the new Berkeley heavy-ion accelerator (superHILAC).

A schematic of the apparatus used is illustrated in Fig. 1. It is similar in basic idea to that employed in our previous work described in Ref. 5, but much of the hardware has been rebuilt and some of the dimensions changed. The argon emerging from the superHILAC is magnetically deflected into our apparatus and passes through a thin carbon foil (23 or 53  $\mu\text{g}/\text{cm}^2$ ) mounted on a movable track with a total travel of 1.6 meters. The fraction of two-electron ions excited to the  $2^3S_1$  state by the foil is sufficient for experimentation over the energy range  $2.4 \text{ MeV}/\text{amu} \leq 7.2 \text{ MeV}/\text{amu}$  employed in this experiment. The beam subsequently passes in front of a pair of collimating slits mounted in front of the detectors which permits them to detect x-rays emitted only by those argon ions which radiate in front of the open slits. The beam is then collected in a Faraday cup and the integrated current recorded. A 0.6-cm-diameter collimating slit mounted between the track and the cup ensured that any and all ions passing through the foil and between the detectors must also strike the Faraday cup. In this way, the integrated current measured at the cup provides a reliable normalization of the number of metastable ions passing in front of the detectors. That this is indeed the case was established by varying the aperture of the collimator and noting that the measured lifetime was independent of this parameter.

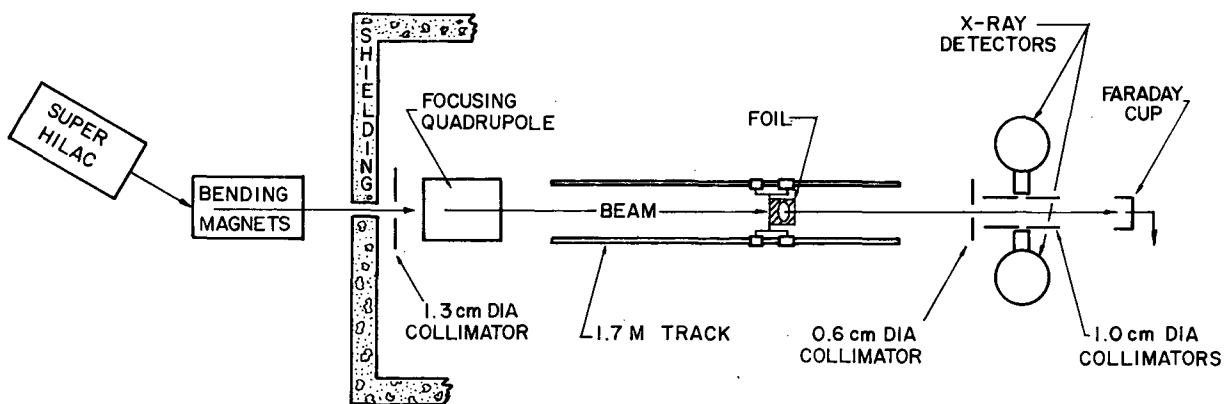


Fig. 1. Schematic of the apparatus. (XBL 732-197)

The spectra associated with decays-in-flight of the two beams is shown in Fig. 2. For the argon, a single peak is observed at an energy of 3.1 keV with a signal/noise ratio of about 100/1. A similar single peak at an energy of 4.7 keV is observed with the titanium beam. That this peak is associated with the decay of the  $2^3S_1$  state had already been established in our previous work.<sup>5</sup> The lifetime is determined by integrating the total number of counts under the peak for a fixed integrated beam current, and plotting this number versus foil-detector separation. Twenty-seven decay curves were taken with argon beams ranging in energy from 96.4 to 288.4 MeV, and eight

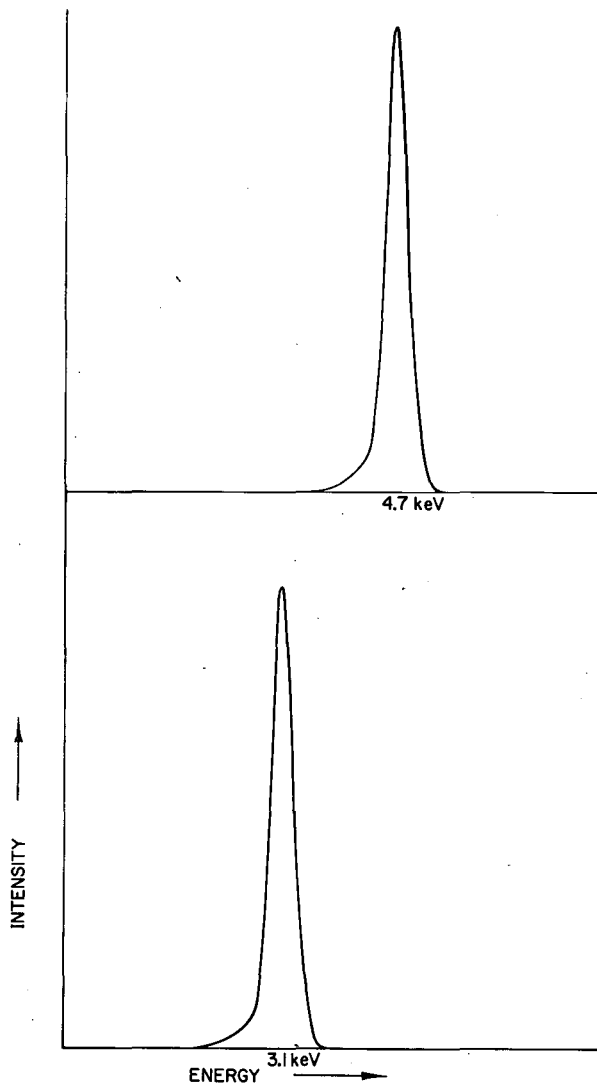


Fig. 2. Energy spectrum of the observed x-rays. (XBL 736-832)

decay curves were taken with titanium, at energies of 115.7 and 346 MeV. The results of these decay curves are given in Table I.

The absence of other spectral lines is ensured by placing the track so that the foil is never closer than 0.8 meter to the detectors. This is sufficiently far so that all other excited atomic levels of argon ions or titanium ions present in the beam will have become thoroughly depopulated by decay to the ground state. In this connection, it should be noted that the  $2^3P_0$  level decays to the  $2^3S_1$  level with a theoretical lifetime of about  $5.5 \times 10^{-9}$  sec for  $Ar^{16+}$  and about  $4.5 \times 10^{-9}$  sec for  $Ti^{20+}$ . In order that the measured lifetime of  $2^3S_1$  not be influenced by cascading from this state, it is important that sampling of the decay curve be started only after several mean lives have elapsed. Under this condition, it is possible to place an upper limit on the measured decay rates due to this cascading mechanism. For the geometry and beam energies used here the effect on our lifetime will

Table I. Lifetimes of the  $2^3S_1$  state of helium-like argon measured at different beam energies

96.4 MeV	138.4 MeV	183.2 MeV	288.4 MeV
163±17	188±18	183.5±21	178.5±38
174±34	173±9	213±17	186.5±34
154±32	164±8	171±15	192±26
158.5±23	177±11	212±28	183±32
169±13		200±17	167±14
163.5±11			136±12
174±24			135±25
170±13			
172±12			
173±26			
179±13			

Lifetimes of the  $2^3S_1$  state of helium-like titanium measured at different beam energies

115.7 MeV	
25.2±0.5	26.7±1.0
25.9±0.9	25.9±1.0
24.7±1.0	27.2±0.8
24.9±0.7	27.4±0.8

always be less than 0.5%, independent of the relative populations of the two states at the foil.

Pressure quenching as a possible source of error has been investigated. The lifetime measurements were performed at an ambient pressure of about  $3 \times 10^{-6}$  Torr. By increasing the pressure to  $10^{-5}$  Torr, we find that the effect on the lifetime due to pressure quenching is less than 0.5%.

A further possible source of systematic error arises from detector pile-up. It is noted during the runs with the argon beam that the normalized count rate in the detector decreases if the argon beam current is increased. This effect arises from occasional multi-MeV particles (probably neutrons) which enter the detectors. Detector recovery from these events is very slow, giving rise to a dead time. These nuclear events are produced when the argon beam strikes metal surfaces that are present, principally the lead collimating slits, and the number of these events noticeably decreases when the energy of the argon beam is decreased to 2.41 MeV/amu—slightly below the Coulomb barrier for the lead-argon system. A study was made at 2.41 MeV/amu to determine if there was a dependence of the measured lifetime on the average beam current. A small but statically significant effect was observed. Over the observed range of beam currents, it was found that the measured lifetime increased with increased beam current at a rate of about  $5(3) \times 10^{-9}$  sec per nA. The data reported in this experiment were taken mainly at 0.5 nA. A correction for this effect of  $2.5 \times 10^{-9}$  sec was made to all of our measured argon lifetimes, and the error in this correction is incorporated into our stated error. The detectors were modified for runs with the titanium beam and no measurable pile-up effect was observed. The modified detectors were also used in an argon run and no significant change in the lifetime was found.

Table I contains a summary of the lifetime data. The final results are: for  $\text{Ar}^{16+}$ ,  $\tau(2^3S_1) = 172(12) \times 10^{-9}$  sec;  $\text{Ti}^{20+}$ ,  $\tau(2^3S_1) = 25.8(1.3) \times 10^{-9}$  sec. The lifetime values represent a weighted average of all the individual results, where the weighting factor is the statistical one, and is independent of our method for handling background subtraction. The stated error contains a two-standard deviation contribution from statistics, a contribution from uncertainty in the pile-up correction for the argon, and a contribution from uncertainty in the velocity. The final result is corrected for degrading of the beam energy by the foil and relativistic time dilation.

The measured value of the argon lifetime is

in good agreement with our previous measurement<sup>7</sup> but in apparent disagreement with the theory, whereas the titanium result reflects a possible disagreement. Therefore, a thorough search for systematic effects was made which might explain the disagreement. During one or more of the runs, the following parameters were varied: foil thickness and material, foil holder diameter, collimator diameters, collimator material, collimator-detector separation, separation between collimators, direction of foil travel, distance of the detectors from beam center line, Faraday cup target, and residual gas pressure. No systematic effect was found. We can not, of course, rule out the possibility that the discrepancy is somehow an artifact of the basic experimental method. Although we have not been able to find a plausible model to suggest that this is the case, we are nevertheless currently attempting to remeasure these lifetimes by an independent method. In this connection, it should be noted that both the argon and titanium lifetimes were measured with the identical apparatus. We are also planning measurements of this lifetime in higher-Z elements.

Many people have contributed to the success of this work. It is a pleasure to acknowledge the encouragement and support of Albert Ghiorso. The nuclear chemistry electronics group directed by Fred Goulding provided and serviced the solid state detector systems. Douglas McDonald was primarily responsible for the engineering and Warren Harnden, Mike Nitschke, William Davis, and Richard Eppley assisted in various phases of the work.

#### Footnotes and References

\*Partly supported by a fellowship from the John S. Guggenheim Foundation.

†Present Address: Sandia Laboratories, Livermore, California.

1. G. Breit and E. Teller, *Astrophys. J.* **91**, 215 (1940).
2. G. Feinberg and J. Sucher, *Phys. Rev. Letters* **26**, 681 (1971); G. W. F. Drake, *Phys. Rev. A* **5**, 1979 (1972); H. R. Griem, *Astrophys. J.* **156**, 1103 (1969); I. L. Beigman and V. I. Safronova, *Sov. Phys. —JETP* **33**, 1102 (1971).
3. G. W. F. Drake, *Phys. Rev. A* **3**, 908 (1971).
4. A. H. Gabriel and C. Jordan, *Nature* **221**, 947 (1969); *Monthly Notices Roy. Astron. Soc.* **145**, 241 (1969).

5. R. Marrus and R. W. Schmieder, Phys. Letters 32A, 431 (1970).

6. J. R. Woodworth and H. W. Moos, Phys.

Rev. Letters 30, 775 (1973).

7. R. Marrus and R. W. Schmieder, Phys. Rev. A 5, 1160 (1972).

### K-VACANCY PRODUCTION IN 150-MeV Kr + Kr COLLISIONS

R. Anholt, W. E. Meyerhof,\* F. S. Stephens, Jr.,  
R. M. Diamond, J. de Boer, D. Proetel, and P. O. Tjöm

In connection with an investigation of K vacancy production in a symmetric heavy-ion collision,<sup>1</sup> we have studied the production of K x rays in Kr + Kr collisions. Basing himself on earlier work with Fano, Lichten<sup>2</sup> has proposed that in a symmetric collision in which a  $2p\pi_u$  vacancy is available early in the collision [see inset in Fig. 1 for molecular-orbital

(MO) notation], the dominant process of K vacancy formation is electron promotion: as the collision partners come together an electron from the  $2p\sigma_u$  MO can make a transition to the  $2p\pi_u$  MO (by rotational coupling) thereby creating a vacancy in the  $2p\sigma_u$  MO, which on separation of the atoms becomes a  $1s$  vacancy. The important role of the original  $2p\pi_u$  vacancy has been confirmed experimentally.<sup>3</sup> Even for  $Z > 10$ , if there is no  $2p$  vacancy in the projectile or the target, the  $2p\sigma_u \rightarrow \pi_u$  electron promotion process can still play a dominant role, particularly in solids, because of the possibility of two-collision processes:<sup>4</sup> the projectile can obtain a  $2p$  vacancy in a first collision and can carry this vacancy into the second collision, where a  $2p\sigma_u$  electron can be promoted into the vacancy,<sup>u</sup> as described above. Nevertheless, as  $Z$  is increased, one can expect the two-collision mechanism to diminish to a point where it is overtaken by other, one-collision processes.<sup>1</sup> This expectation is based on the facts that (1) the lifetime of a  $2p$  vacancy decreases<sup>5</sup> roughly as  $1/Z$  and (2) the cross section for "hitting" the L shell of the second atom decreases approximately as  $1/Z^2$ . The yield of a two-collision process relative to a one-collision process therefore decreases roughly as  $1/Z^3$ .

We wanted to compare the K vacancy production cross sections for Kr + Kr ( $Z = 36$ ) collisions in a gaseous target with Br + Br ( $Z = 35$ ) measurements<sup>6</sup> made with a solid KBr target in order to determine whether in the latter case the two-collision process is still dominant. If the two-collision process is in fact still dominant in a solid target for  $Z = 35$ , the Kr + Kr cross section measured in the gas should fall below the Br + Br cross section, assuming proper scaling in bombarding energy.<sup>1</sup>

First, to assure ourselves that in the Kr gas target a one-collision process is operative, we measured the yield of Kr K x-rays as a function of gas pressure in a gas cell.<sup>7</sup> A 290-MeV Kr beam from the SuperHILAC entered the cell through a 0.5-mil Al window.

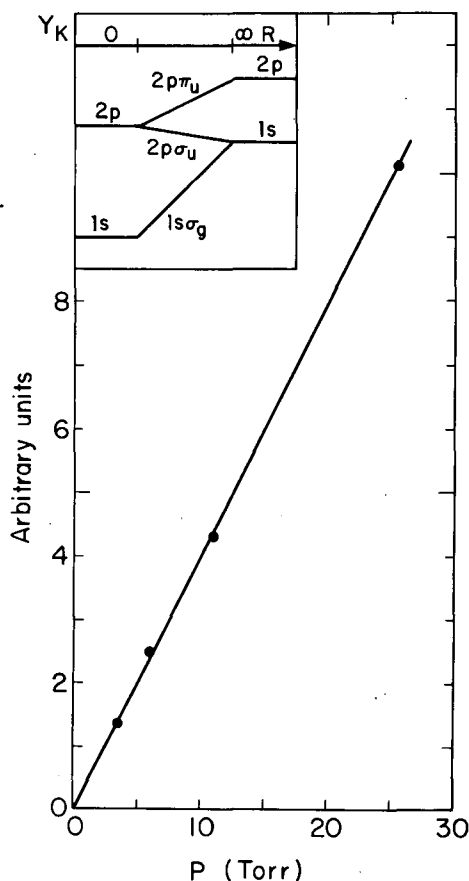


Fig. 1. Kr + Kr K x-ray yield versus gas pressure. Inset shows selected schematic MO levels for a symmetric collision.

(XBL 742-2328)

X-rays were detected with an LBL-made intrinsic Ge x-ray detector through 1-mil Be windows in the cell and detector. Figure 1 shows that between 3 and 30 Torr the yield is linear with pressure; if a two-collision process were operative, the yield should vary as the square of the pressure.

At a given bombarding energy, at pressures higher than 50 Torr, the yields begin to decrease. This is due to the variation of the cross section with energy, for at higher pressures the projectile loses considerable energy going through the gas cell. From the calculated energy loss and the measured cross sections we obtain the results shown in Fig. 2 for

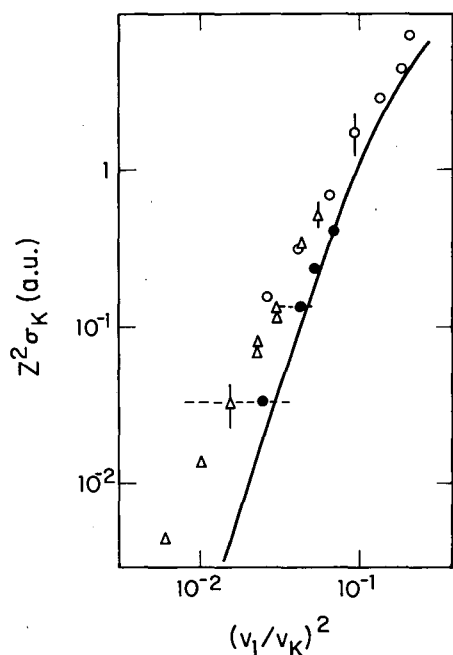


Fig. 2. Scaled K vacancy production cross sections versus reduced bombarding energy (1 a. u. =  $2.8 \times 10^{-17}$  cm<sup>2</sup>). All K x-ray production cross sections have been corrected with the neutral-atom fluorescence yield (Ref. 5). The abscissa is equal to  $(E_1/M_1)/(U_K/m)$ , where  $E_1, M_1$  = kinetic energy and mass of projectile,  $U_K$  = K binding energy,  $m$  = mass of electron. On the Kr + Kr points, the dashed horizontal bars indicate the energy spread of the beam across the effective length of the gas target. Triangles are Br + Br results,<sup>6</sup> open circles are Cl + Ar results.<sup>8</sup> (XBL 742-2329)

the points below the maximum energy. The energy scaling law is discussed in Ref. 1. For the present it is important only to note that the Kr + Kr cross sections fall below the line of Br + Br cross sections. (This result is not quite consistent with Cl + Ar measurements by Winters et al.,<sup>8</sup> also shown in Fig. 2. For this purpose, the Cl + Ar results are considered as symmetric, by doubling the Cl K x ray production cross sections and correcting by the Cl fluorescence yield).<sup>5</sup> It would appear, therefore, that in Br + Br collisions in a solid the two-collision mechanism is dominant; any one-collision process should be of the order of magnitude of the Kr + Kr results. Very likely, the one-collision process in Kr + Kr collisions, as well as in Br + Br, is one of direct excitation from the  $2p\sigma$  MO to the continuum, or to vacant, bound states below the continuum.<sup>1</sup> The solid line in Fig. 2 represents the expected  $2p\sigma \rightarrow$  continuum excitation cross section, based on calculations of Thorson and co-workers.<sup>9</sup> The Kr + Kr results lie quite close to this curve.

#### Footnotes and References

\* On leave from Department of Physics, Stanford University, California.

1. W. E. Meyerhof, to be published.
2. W. Lichten, Phys. Rev. **164**, 131 (1967).
3. B. Fastrup, G. Hermann, and Q. C. Kessel, Phys. Rev. Letters **27**, 771 (1971).
4. F. W. Saris and D. J. Bierman, Phys. Letters **35A**, 199 (1971).
5. W. Bambynek et al., Rev. Mod. Phys. **44**, 716 (1972).
6. H. Kubo, F. C. Jundt, and K. H. Purser, Phys. Rev. Letters **31**, 674 (1973); W. E. Meyerhof et al., to be published.
7. P. Kienle et al., Phys. Rev. Letters **31**, 1099 (1973).
8. L. Winters et al., Phys. Rev. Letters **31**, 1344 (1973).
9. V. Sethuraman, W. R. Thorson, and C. F. Lebeda, Phys. Rev. A **8**, 1316 (1973).

THE MOLECULAR ORBITAL X-RAY YIELD IN  
SYMMETRIC COLLISIONS

R. Anholt and J. O. Rasmussen

Several groups have recently reported evidence for a quasimolecular x-ray, observed in collisions between heavy ions and various targets.<sup>1-3</sup> Spectra taken with high-resolution solid state detectors generally show a broad continuum beginning at the separated atom (SA) x-ray peaks and merging into the background at the united atom (UA) x-ray energy. Such a spectrum is shown in Fig. 1, this one being for Br on a solid KBr target.<sup>3</sup> The region due to molecular orbital (MO) x-rays is roughly inside the dotted lines in this figure. Above this line are the  $K\alpha$  and  $K\beta$  peaks of Br and an intense continuum stretching down to 20 keV. This continuum is thought to be due

partly to radiative capture and partly to electron bremsstrahlung.

The main molecular levels responsible for the production of these MO x-rays are shown in the upper right hand corner of Fig. 1. If there is a vacancy in the  $1s\sigma_g$  orbital, it may be filled radiatively at any internuclear distance,  $R$ , by electrons from higher molecular orbitals. A  $1s\sigma_g$  vacancy may be created in a one-collision process or a two-collision process. With the former the vacancy is created by Coulomb excitation or by some other mechanism and is filled in the same collision. In a

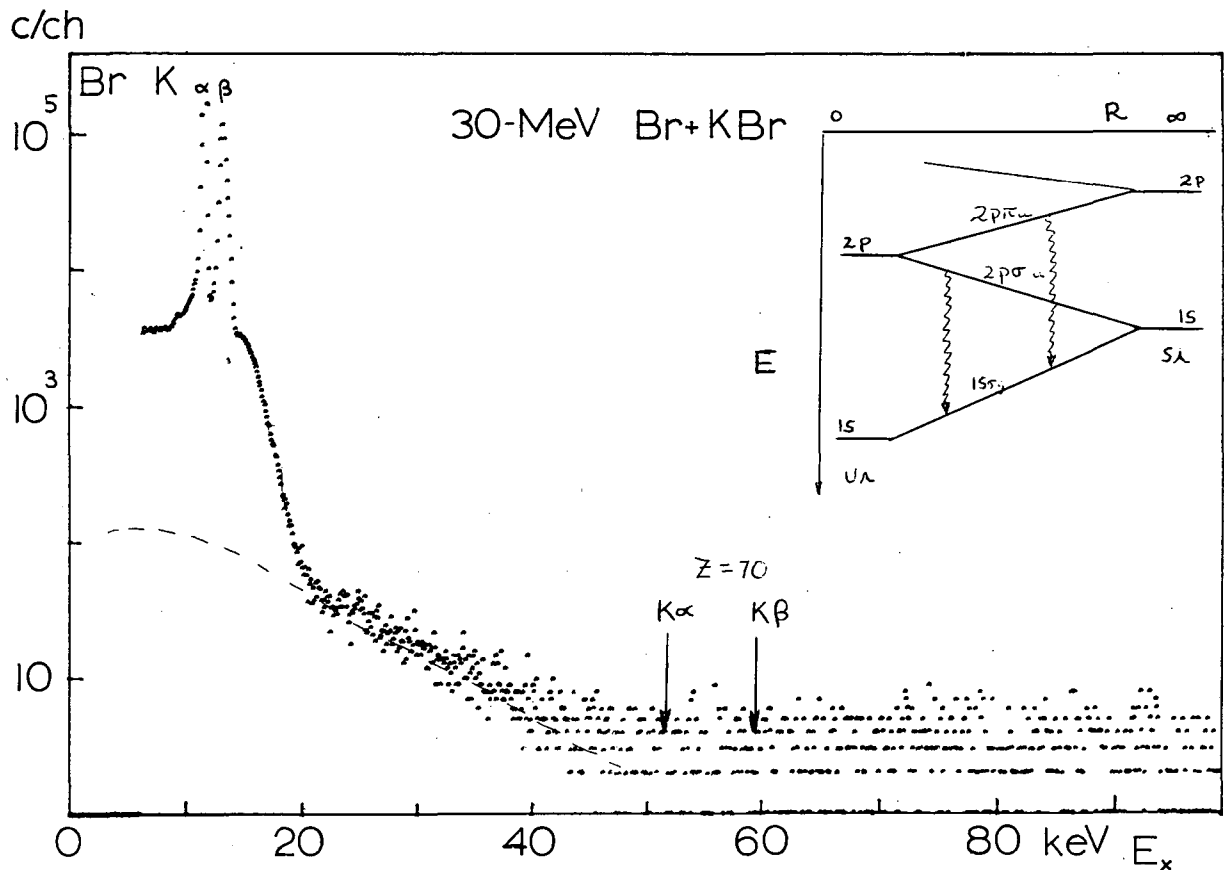


Fig. 1. X-ray spectrum for 30-MeV Br on solid KBr from the work of Meyerhof et al. Room background has not been subtracted. A 0.063-in. Al absorber has been used.

(XBL 7312-7235)

two-collision process, for which our calculations apply, the vacancy is carried into the collision, having been formed in some prior encounter. For this process, one finds that the differential MO yield normalized to the total number of projectile K vacancies can be written as:

$$\frac{1}{Y_K} \frac{dY}{dE} = 4\pi n_2 f(w) R^2 \frac{dR}{dE} \frac{\lambda(R)}{\lambda} \left(1 - \frac{d_0}{R}\right)^{1/2} \omega_K,$$

where  $n_2$  is the target atom density,  $E$  is the photon energy,  $\lambda(R)/\lambda$  is the ratio of the radiative MO transition probability at  $R$  to the radiative SA transition probability,  $\omega_K$  is the SA fluorescent yield,  $d_0$  is the distance of closest approach at zero impact parameter, and  $f(w)$  is the Demkov transfer probability<sup>4</sup> which depends on the separation of the  $1s$  levels of the collision partners and on the velocity of the incoming ion and gives the probability that a projectile K vacancy will correlate to the  $1s\sigma_g$  orbital. For symmetric collisions, a K vacancy has approximately a 50% probability of going into the  $2p\sigma_u$  and a 50% probability of going into the  $1s\sigma_g$ . Thus  $f(w)$  is  $1/2$ . In a symmetric collision the number of projectile K vacancies,  $Y_K$  in this expression, can be taken as  $1/2$  of the total number of vacancies as measured by the  $K\alpha$  and  $K\beta$  x-ray peaks.

It is important to note two things about this expression. The first is that the yield per projectile K vacancy is independent of the projectile velocity except for the small factor of  $d_0/R$ . The portion of the atoms that radiate MO-x rays depends only on the relative size the MO region ( $4\pi R^2 dR$ ) compared to the total volume that one atom occupies,  $1/n_2$ . The second thing to note is that since the distance  $R$  corresponding to a molecular x-ray of some fraction of the UA K x-ray energy scales as  $1/Z$ , this MO volume and hence the differential MO yield will go as  $1/Z^3$ .

To obtain  $\lambda(R)$  and  $dR/dE$  in this expression we have used hydrogen molecular ion wavefunctions to calculate dipole transition probabilities between the  $2p\sigma_u$ ,  $2p\pi_u$ ,  $3p\sigma_u$ ,  $3p\pi_u$ ,  $4p\sigma_u$ , and  $4f\sigma_u$  and the  $1s\sigma_g$  orbital. These were scaled up to the appropriate  $Z$ ; the dipole transition probabilities go as  $Z^4$ , energies go as  $Z^2$ , while the internuclear distance goes as the inverse of  $Z$ . The reason we chose to use hydrogenic quantities instead of attempting a many-body calculation is that at least for  $H_2^+$ , the use of hydrogenic wavefunctions is far more accurate than L. C. A. O. and various small basis set expansions. Furthermore, if one compares nonrelativistic one-electron energies and transition rates for hydrogenic atoms with experiment and with many-body calculation for atoms, the error in taking the hydrogenic values is not too large for

$35 < Z < 100$ , and can be accounted for in a straightforward way. For instance, for the transition  $2p \rightarrow 1s$ , the ratio of the the hydrogenic transition energy to the average experimental value goes from 0.95 for  $Z = 35$  to 1.17 for  $Z = 100$ . The ratio of the transition rates for the same transition goes from 0.70 to 0.78 over the same range of  $Z$ .

Figure 2 gives the normalized MO yield for Br on a solid  $Br_2$  target. Here, we compare our hydrogenic calculations with experiment and with Meyerhof's calculation.<sup>6</sup> The two lie very close to experiment, as is shown, though our calculations do not reach the correct UA endpoint. This deficiency lies in the use of unscreened nonrelativistic energies, so to correct for this one can use experimental K-L and K-M energy differences for atoms and hydrogenic values of these energies to derive a scaling factor or calibration curve that corrects the  $H_2^+$  energies for many-electron and relativistic effects. The resulting energies will then be constrained to go to the correct

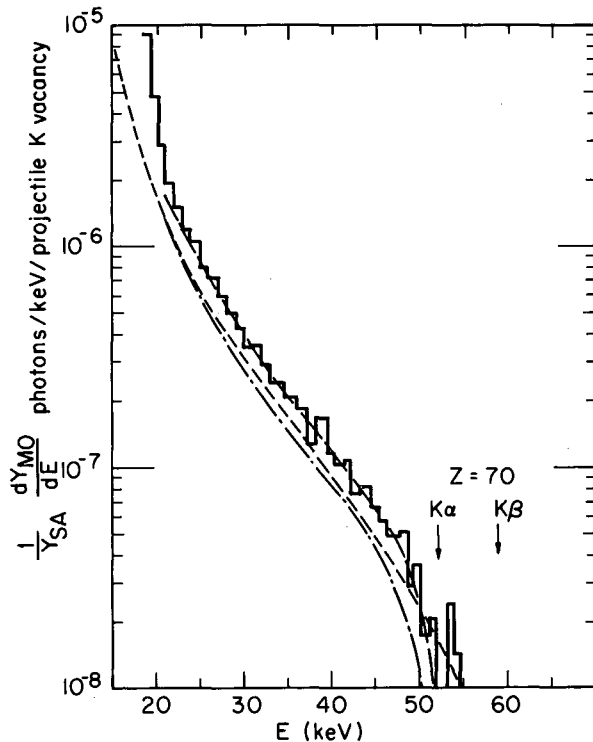


Fig. 2. Normalized differential MO yield for Br on  $Br_2$ . Meyerhof's theory<sup>6</sup> (short dashed line) is based on atomic transition probabilities and  $dR/dE$  is for the  $2p\pi_{3/2} \rightarrow 1s\sigma_{1/2}$  transition. The long dashed line is for calculations with nonrelativistic one-electron wavefunctions. The dash-dot line is with scaled energies and transition probabilities (see text).

(XBL 7312-7009)

UA and SA limits at  $R = 0$  and  $\infty$ . Using relativistic, many-electron, calculated transition probabilities for atoms,<sup>5</sup> the  $H_2^+$  transition probabilities may be corrected also. The use of this energy and transition-rate dependence gave the fit (shown in Fig. 2) which not only approached the correct endpoint, but accurately reproduced the experimental intensity as well.

We have applied this model to other systems where results have been made available. In the case of I on NaI, the two-collision process does not explain the yield observed in that experiment.<sup>6</sup> Apparently the one-collision process dominates there, the two-collision process having decreased as  $1/Z^3$ .

#### References

1. J. R. MacDonald, M. Brown, and T. Chiao, Phys. Rev. Letters 30, 471 (1973).
2. F. W. Saris, W. F. Van der Weg, H. Tawara, and R. Laubert, Phys. Rev. Letters 28, 717 (1972).
3. W. E. Meyerhof, T. K. Saylor, S. M. Lazarus, W. A. Little, B. B. Triplett, and L. F. Chase, Jr., Phys. Rev. Letters 30, 1279 (1973).
4. W. E. Meyerhof, Phys. Rev. Letters 31, 1341 (1973).
5. J. H. Scofield, Phys. Rev. 179, 9 (1969).
6. W. E. Meyerhof, to be published.

### THEORETICAL X-RAY TRANSITION PROBABILITIES FOR HIGH-Z SUPERHEAVY ELEMENTS

R. Anholt and J. O. Rasmussen

As a result of recent interest in x-ray transitions<sup>1</sup> and positron emission<sup>2</sup> during collisions between very heavy ions where the combined atomic number of the target and projectile exceeds 100, we undertook a program to calculate radiative transition probabilities for superheavy atoms.

Dirac-Hartree-Fock<sup>3</sup> (DHF) wavefunctions for neutral atoms with  $Z = 92, 112, 130, 150, 160,$  and  $170$  were obtained from J. B. Mann at the Los Alamos Scientific Laboratory, and fully relativistic expressions for transition rates of various parities and multiplicities<sup>4</sup> were used to calculate transition rates to the K,  $L_1, L_2,$  and  $L_3$  shells for these atomic numbers.

Some results for K transitions are shown in Fig. 1 and are compared with similar work with Relativistic-Hartree-Fock-Slater (RHFS) wavefunctions<sup>5</sup> (calculations up to  $Z = 126$ ) and with one-electron (point nucleus) Dirac wavefunctions. The behavior of the K- $L_3$  and K- $L_2$  transition rates as  $Z$  approaches 137 calculated with one electron Dirac wave functions and as  $Z$  approaches 170 is similar. The reason for this behavior is that as one

approaches a stronger central field, the  $1s$  wavefunction is pulled in closer and closer toward the nuclear center, while the L- and M-shell wavefunctions are not pulled in as fast. This means that the overlap between the K- and outer-shell wavefunction will begin to decrease, reducing the integral over the appropriate Bessel-function-weighted overlap.

The behavior of the K- $M_2$  transition rate in this figure is even more surprising. The reason for it, however, is similar. Here the product of the major component of the wavefunctions  $\psi_{1s} \times \psi_{3p_{1/2}}$  has one node. For  $Z < 130$  the product  $\psi_{1s} \times \psi_{3p_{1/2}}$  multiplied by the appropriate spherical Bessel function has a radial region of positive integrand which makes a greater contribution than the negative region. For still higher atomic numbers, however, the contribution of the  $1s$  wavefunction becomes smaller near the origin, and the magnitude of the positive contribution is less than that of the negative contribution at  $Z = 150$ . The dipole matrix element essentially changes sign; thus, at some point between  $Z = 130$  and  $150$ , the K- $M_2$  transition rate approaches zero, and past 150, rises again.



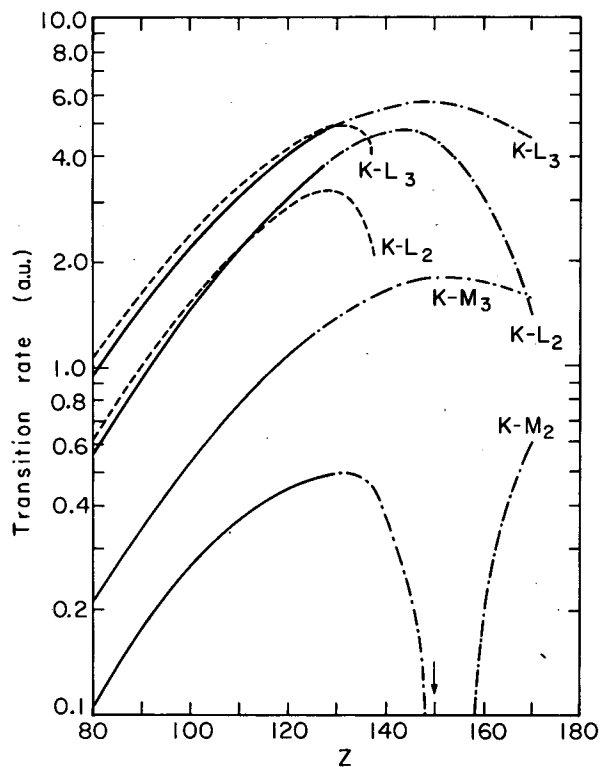


Fig. 1. K-L<sub>2</sub>, K-L<sub>3</sub>, K-M<sub>2</sub>, and K-M<sub>3</sub> transition rates vs Z in units of a. u. (1 a. u. =  $4.132 \times 10^{16}$  sec<sup>-1</sup>). Calculations made by Lu, Malik, and Carlson (solid lines) and by ourselves using hydrogenic Dirac wavefunctions (dashed line) and Dirac-Hartree-Fock wavefunctions (dash-dot-dash line). (XBL 738-3716)

#### References

1. P. H. Mokler, H. J. Stein, and P. Armbruster, *Phys. Rev. Letters* **29**, 827 (1972).
2. B. Müller, J. Rafelski, and W. Greiner, *Z. Phys.* **257**, 183 (1972).
3. J. B. Mann and J. T. Waber, *J. Chem. Phys.* **53**, 2397 (1970); *Atomic Data* **5**, 201 (1973).
4. H. R. Rosner and C. P. Bhalla, *Z. Phys.* **231**, 347 (1970).
5. C. C. Lu, F. B. Malik, and T. A. Carlson, *Nucl. Phys.* **A175**, 289 (1972).

SPECTRA AND ENERGY LEVELS OF  $V \text{ V}^*$ C. H. H. Van Deurzen,<sup>†</sup> J. G. Conway, and  
S. P. Davis<sup>‡</sup>

To excite and separate the spectra of vanadium a vacuum sliding-spark light source was used connected in a series LCR electrical circuit ( $L$  = inductance,  $C$  = capacitance,  $R$  = resistance). The vacuum sliding spark light source is able to excite and separate higher ionized atomic states as the circuit parameters  $L$ ,  $C$ ,  $R$ , and the voltage  $V_0$  across the capacitor are varied. Lines belonging to a given state of ionization were identified by observing their common intensity behavior with current. In the sliding-spark spectrum lines of oxygen, silicon, and carbon spectra are also present due to the excitation of the spacer material, especially at peak currents greater than 400A. Several different spectrographs were employed to observe the spectra from 500 to 950 Å. They are listed in Table I, along with their figures of merit. Kodak spectroscopic plates were used: short-wavelength radiation (SWR) plates in the vacuum region, and I-0, I-F, I-N, and I-Z plates in the air region.

To obtain good excitation of  $V \text{ V}^*$  a peak current of 1000 A was selected. The electrical circuit parameters were  $L = 13 \mu\text{H}$ ,  $C = 24 \mu\text{F}$ ,  $R_{\text{added}} < 1 \Omega$ , and  $V_0 = 1160 \text{ V}$ . The current-pulse full width at half maximum was 56  $\mu\text{sec}$  and the spark was triggered 15 times per sec. The  $V \text{ V}^*$  spectrum was photographed from 450 to 2800 Å with the 3-m normal-incidence vacuum spectrograph (2.78 Å/mm dispersion), and from 2600 to 8500 Å with the 5.2-Å/mm spectrograph in air. The triplet at 483 Å was photographed in the first four orders, and the lines at 962 and 978 Å were photographed in the first and second order. The lines at 285 and 286 Å appeared in the second and third order.

Calibration spectra below 2680 Å were obtained from a water-cooled copper hollow cathode with Ge and Si in the cathode,<sup>1-3</sup> and above 2680 Å from a ThI electrodeless lamp.<sup>4-6</sup> Plate measurements were made on a 25-cm Grant comparator; 25-40 calibration lines were used on every 25-cm plate. When fitted with a sixth-order polynomial, the wavelengths of the calibration lines deviated from their interferometric value by not more than  $\pm 1.5 \mu \times$  (plate factor).

The vanadium lines obtained in multiorders showed an rms deviation of 0.002 Å (except the lines of 285 and 286 Å, which agreed to  $\pm 0.01$  Å) when the wavelengths were reduced to the first order; the values listed are the average values. The error limits in the vanadium wavelengths are estimated to be 0.004 Å in vacuum and 0.008 Å in air.

Intensities were estimated visually from the plates on a scale 1-350.

Table II lists 59 classified lines of  $V \text{ V}^*$ , 46 of which are newly classified. The lines marked h appeared hazy, apparently caused by blending with impurity lines or with lines from lower ionization stages of vanadium. The line at 4293.74 Å blends with a V III line at 4293.47 Å.

The level analysis was begun on the basis of the levels reported by Gibbs and White.<sup>7</sup> The wavelengths reported by them for the 483-Å triplet and 490-Å doublet are about 0.1 Å too large and 0.3 Å too small, respectively, and the lines at 285 and 286 Å (3d-4f) were wrongly classified—the 4f levels are inverted in

Table I. Spectrograph characteristics.

Mounting	Focal length (m)	Grooves/mm	$m\lambda$ (at blaze) (order $\times$ Å)	$m \frac{d\lambda}{dx}$ (order $\times$ Å/mm)
Ebert, air	3.4	79	225900	17.5
Ebert, air	3.4	600	5000	5.2
Czerny-Turner, air	0.75	600	7000	20
Eagle, vacuum	3.0	1200	1380	2.78

Table II. Classified lines of V V.

Level combination Odd                  Even	Wave number ( $\text{cm}^{-1}$ )	Wavelength ( $\text{\AA}$ )	Intensity
$4f^2F_{5/2} - 3d^2D_{3/2}$	349675	285.98	1
$4f^2F_{7/2} - 3d^2D_{5/2}$	348628	286.84	2
$4p^2P_{3/2} - 3d^2D_{3/2}$	207660.2	481.556	3
$4p^2P_{3/2} - 3d^2D_{5/2}$	207035.9	483.008	30
$4p^2P_{1/2} - 3d^2D_{3/2}$	206393.7	484.511	20
$5p^2P_{3/2} - 4s^2S_{1/2}$	203874.6	490.498	4
$5p^2P_{1/2} - 4s^2S_{1/2}$	203356.6	491.747	2
$4p^2P_{1/2} - 6s^2S_{1/2}$	197461.0	506.429	1
$4p^2P_{3/2} - 6s^2S_{1/2}$	196196	509.694	2
$4p^2P_{1/2} - 5s^2S_{1/2}$	121822.9	820.864	20
$6p^2P_{3/2} - 4d^2D_{3/2}$	121773.0	821.200	1
$6p^2P_{3/2} - 4d^2D_{5/2}$	121628	822.18	6h
$6p^2P_{1/2} - 4d^2D_{3/2}$	121516.7	822.932	3
$4f^2F_{7/2} - 7g^2G$	121080.7	825.895	2
$4f^2F_{5/2} - 7g^2G_{7/2}$	120656.7	828.798	1
$4p^2P_{3/2} - 5s^2S_{1/2}$	120556.6	829.486	30
$3p^53d^2\ ^2F_{7/2} - 4d^2D_{5/2}$	103946.2	962.036	15
$3p^53d^2\ ^2F_{5/2} - 4d^2D_{3/2}$	102232.0	978.168	10
$3p^53d^2\ ^2F_{5/2} - 4d^2D_{5/2}$	102087.6	979.551	1
$4f^2F_{7/2} - 6g^2G$	100771.5	992.344	10
$4f^2F_{5/2} - 6g^2G_{7/2}$	100348.0	996.532	5
$5p^2P_{1/2} - 7s^2S_{1/2}$	91575	1092.00	1h

Table II. (continued)

Level combination Odd                  Even	Wave number ( $\text{cm}^{-1}$ )	Wavelength ( $\text{\AA}$ )	Intensity
$5p^2P_{3/2} - 7s^2S_{1/2}$	91056.3	1098.222	2
$4p^2P_{1/2} - 4d^2D_{3/2}$	87508.7	1142.744	15
$4p^2P_{3/2} - 4d^2D_{5/2}$	86387.0	1157.581	25
$4p^2P_{3/2} - 4d^2D_{3/2}$	86242.5	1159.522	6
$4f^2F_{7/2} - 5g^2G$	67108.8	1490.118	20
$4f^2F_{5/2} - 5g^2G_{7/2}$	66684.2	1499.605	10
$4p^2P_{3/2} - 4s^2S_{1/2}$	59516.6	1680.204	100
$4p^2P_{1/2} - 4s^2S_{1/2}$	58250.4	1716.725	50
$5p^2P_{3/2} - 4d^2D_{3/2}$	58115.5	1720.710	4
$5p^2P_{3/2} - 4d^2D_{5/2}$	57971.2	1724.995	15
$5p^2P_{1/2} - 4d^2D_{3/2}$	57597.6	1736.183	10
$4f^2F_{5/2} - 4d^2D_{3/2}$	55772.9	1792.984	25
$4f^2F_{5/2} - 4d^2D_{5/2}$	55628.5	1797.639	6h
$4f^2F_{7/2} - 4d^2D_{5/2}$	55205.4	1811.418	30
$5p^2P_{1/2} - 6s^2S_{1/2}$	52355.0	1910.038	4
$5p^2P_{3/2} - 6s^2S_{1/2}$	51836.9	1929.126	9
$4f^2F_{7/2} - 5d^2D_{5/2}$	38791.2	2577.130	20
$4f^2F_{5/2} - 5d^2D_{5/2}$	38368.6	2605.523	4h
$4f^2F_{5/2} - 5d^2D_{3/2}$	38301.3	2610.098	10
$5p^2P_{1/2} - 5d^2D_{3/2}$	36476.7	2740.666	10
$5p^2P_{3/2} - 5d^2D_{5/2}$	36025.4	2774.998	15

Table II. (continued)

$5p^2P_{3/2} - 5d^2D_{3/2}$	35958.8	2780.144	3
$6h^2H - 5g^2G$	33886.8	2950.13	8w
$6p^2P_{3/2} - 5d^2D_{3/2}$	27698.54	3609.269	2
$6p^2P_{1/2} - 7s^2S_{1/2}$	27654.33	3615.039	2h
$6p^2P_{3/2} - 5d^2D_{5/2}$	27631.96	3617.966	15h
$6p^2P_{1/2} - 5d^2D_{3/2}$	27442.94	3642.887	8
$6p^2P_{3/2} - 7s^2S_{1/2}$	27399.03	3648.724	4
$5p^2P_{3/2} - 5s^2S_{1/2}$	23800.99	4200.322	20
$5p^2P_{1/2} - 5s^2S_{1/2}$	23283.2	4293.74	20b
$7h^2H - 6g^2G$	20463.86	4885.299	7w
$6h^2H - 7i^2I$	20276.12	4930.533	15w
$6p^2P_{1/2} - 6d^2D_{3/2}$	18883.64	5294.115	4
$6p^2P_{3/2} - 6d^2D_{5/2}$	18665.21	5356.070	8
$6p^2P_{3/2} - 6d^2D_{3/2}$	18628.07	5366.750	1
$3p^53d^2\ ^2F_{7/2} - 5g^2G_{9/2}$ ?	18368.12	5442.704	3
$6p^2P_{3/2} - 6s^2S_{1/2}$	11820.50	8457.555	1

h = hazy; b = blend; w = wide.

V V. Four lines between the  $3p^6$  and  $3p^53d^2$  configurations were observed. The triplet at 962 Å has been classified as the  $3p^64d\ ^2D - 3p^53d^2\ ^2F^0$  combination and places the latter term about  $80\text{ cm}^{-1}$  below the value reported by Gabriel, Fawcett and Jordan.<sup>8</sup> The line at 5442 Å has been tentatively assigned to the  $3p^65g\ ^2G_{9/2} - 3p^53d^2\ ^2F_{7/2}^0$  transition which constitutes a double electron jump. The 18 newly found levels and the corrected values for the previously reported levels are presented in Table III. The combination cycles close to within a few units in the first decimal place of

the wave number. The uncertainty in the levels relative to the ground state is estimated to be about  $3\text{ cm}^{-1}$ , resulting from the uncertainty in the 4p-3d triplet. Figure 1 shows the energy level diagram for quadruple ionized vanadium.

From the present investigation the ionization energy of the  $V^{4+}$  ion may be corrected from the previously reported value of  $526\,100\text{ cm}^{-1}$  to

$$E_{\text{ion}} = 526\,524 \pm 5\text{ cm}^{-1}. \quad \text{V V}$$

Table III. Energy levels of V V.

Symbol	Energy (cm <sup>-1</sup> )	Interval (cm <sup>-1</sup> )	Term value (cm <sup>-1</sup> )	n <sup>*</sup>	Δ n <sup>*</sup>
4s <sup>2</sup> S <sub>1/2</sub>	148143.3		378380.7	2.692652	
5s <sup>2</sup> S <sub>1/2</sub>	328216.9		198307.1	3.719424	
6s <sup>2</sup> S <sub>1/2</sub>	403854.8		122669.2	4.729084	
7s <sup>2</sup> S <sub>1/2</sub>	443074.2		83449.8	5.733663	
8s <sup>2</sup> S <sub>1/2</sub>	(466065) <sup>a</sup>		(60459)		
4p <sup>2</sup> P <sub>1/2</sub> <sup>0</sup>	206393.7	1266.2	320130.3	2.927395	0.005807
4p <sup>2</sup> P <sub>3/2</sub> <sup>0</sup>	207659.9		318864.1	2.933302	
5p <sup>2</sup> P <sub>1/2</sub> <sup>0</sup>	351499.9	518.0	175024.1	3.959095	0.005871
5p <sup>2</sup> P <sub>3/2</sub> <sup>0</sup>	352017.9		174506.1	3.964966	
6p <sup>2</sup> P <sub>1/2</sub> <sup>0</sup>	415419.6	255.6	111104.4	4.969117	0.005725
6p <sup>2</sup> P <sub>3/2</sub> <sup>0</sup>	415675.2		110848.8	4.974842	
3d <sup>2</sup> D <sub>3/2</sub>	0.0	623.6	526524.0	2.282631	0.001353
3d <sup>2</sup> D <sub>5/2</sub>	623.6		525900.4	2.283984	
4d <sup>2</sup> D <sub>3/2</sub>	293902.4	144.4	232621.6	3.434154	0.001066
4d <sup>2</sup> D <sub>5/2</sub>	294046.8		232477.2	2.435220	
5d <sup>2</sup> D <sub>3/2</sub>	387976.7	66.6	138547.3	4.449854	0.001070
5d <sup>2</sup> D <sub>5/2</sub>	388043.3		138480.7	4.450924	
6d <sup>2</sup> D <sub>3/2</sub>	434303.2	37.2	92220.8	5.454191	0.001100
6d <sup>2</sup> D <sub>5/2</sub>	434340.4	(22.7)	92183.6	5.455291	
7d <sup>2</sup> D <sub>3/2</sub>	(460702)		(65822)		
7d <sup>2</sup> D <sub>5/2</sub>	(460725)		(65799)		
4f <sup>2</sup> F <sub>5/2</sub> <sup>0</sup>	349675.3	-423.2	176848.7	3.938618	-0.004704
4f <sup>2</sup> F <sub>7/2</sub> <sup>0</sup>	349252.1		177271.9	3.933914	
5g <sup>2</sup> G <sub>7/2</sub>	416359.5	1.4	110164.5	4.990269	
5g <sup>2</sup> G <sub>9/2</sub>	416360.9		110163.1	4.990301	
6g <sup>2</sup> G	450023.5		76500.5	5.988426	
7g <sup>2</sup> G	470332.5		56191.5	6.987302	
8g <sup>2</sup> G	(483514)		(43010)		
6h <sup>2</sup> H <sup>0</sup>	450247.2		76276.8	5.997201	
7h <sup>2</sup> H <sup>0</sup>	470487.3		56036.7	6.996946	
3p <sup>5</sup> 3d <sup>2</sup> 2F <sub>5/2</sub> <sup>0</sup>	396134.4	1858.6	130389.6	4.586943	0.033045
3p <sup>5</sup> 3d <sup>2</sup> 2F <sub>7/2</sub> <sup>0</sup>	397993.0		128531.0	4.619988	

<sup>a</sup>Predicted levels.

## Footnotes and References

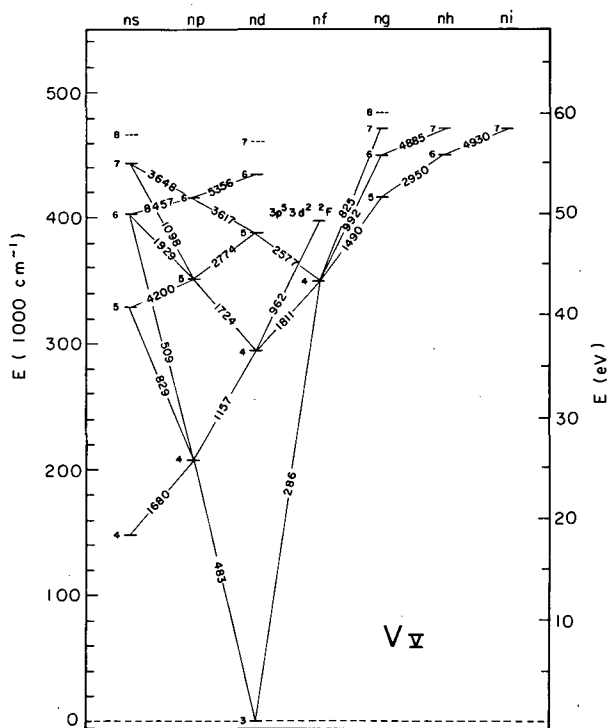


Fig. 1. Energy-level diagram for  $V V$ . The figures give the approximate wavelength of the leading line in each multiplet. Dotted lines are the next predicted terms.

(XBL 734-2601)

\*For a more complete discussion the reader is referred to LBL-1657, by C. H. H. Van Deurzen, May 1973.

†Present address: Department of Physics, University of British Columbia, Vancouver 8, Canada.

‡Physics Department, University of California, Berkeley.

1. V. Kaufman, L. J. Radziemsky, Jr., and K. L. Andrews, *J. Opt. Soc. Am.* **56**, 911(1966).

2. L. J. Radziemsky, Jr., K. L. Andrews, V. Kaufman, and U. Litzen, *J. Opt. Soc. Am.* **57**, 336 (1967).

3. V. Kaufman and J. F. Ward, *J. Opt. Soc. Am.* **56**, 1591 (1966).

4. F. P. J. Vabro, *J. Opt. Soc. Am.* **58**, 484 (1968).

5. D. Goorvitch, F. P. J. Vabro, and A. L. Clúe, *J. Opt. Soc. Am.* **59**, 971 (1969).

6. A. Giacchetti, R. W. Stanley, and R. Zalubas, *J. Opt. Soc. Am.* **60**, 474 (1970).

7. R. C. Gibbs and H. E. White, *Phys. Rev.* **33**, 162 (1929).

8. A. H. Gabriel, B. C. Fawcett, and C. Jordon, *Proc. Phys. Soc.* **87**, 825 (1966).

### THE PREDICTION OF CORE-LEVEL BINDING-ENERGY SHIFTS FROM CNDO MOLECULAR ORBITALS\*

D. W. Davis and D. A. Shirley

A theory was developed for calculating core-level binding-energy shifts with potential models that employ "intermediate-level" molecular-orbital wavefunctions. The relaxation-energy term in atomic core-level binding energies was considered first. The ground-state potential model (GPM) and relaxation-potential model (RPM) were then developed for calculating core-level binding energy shifts in molecules from CNDO<sup>1</sup> wavefunctions. It was shown that neglect of certain two- and three-center integrals in these models limits their accuracy when unlike molecules are compared. The models were modified by calculating  $\langle r^{-1} \rangle$  integrals, to be sensitive to

bond directions of p orbitals. The pp' modification, in which a subset of the neglected integrals is retained to recover invariance to coordinate transformations, was thereby necessitated. The GPM approach yields shifts in very good agreement with experiment when comparisons are restricted to similar molecules. The RPM version gives better agreement, especially over wider classes of molecules. It also provides relaxation energies  $V_R$  that can be combined with *ab initio* orbital energies to give binding energies. One application of these potential models is discussed below.

Detailed comparisons with experiment<sup>2-5</sup> have shown that GPM predictions based on CNDO/2 wavefunctions give core-level shifts in excellent agreement with experiment, provided that only similar molecules are compared. "Similar" in this context would preclude comparison of large and small molecules, of molecules with different numbers of bonds to the central atom, of cyclic or unsaturated molecules with saturated, straight-chain molecules, and perhaps of fluorine-substituted with unsubstituted hydrocarbons. In fact only the first three restrictions are quantitatively very important. Thus standard deviations of from 0.1 to 0.4 eV in comparisons between theoretical GPM C(1s) shifts and experiment were obtained for fluorinated alkanes,<sup>4</sup> benzenes,<sup>3</sup> ethanes,<sup>5</sup> and ethylenes.<sup>5</sup> The advantages of comparing only molecules with the same number of bonds to the central atom have been noted for O(1s) shifts.<sup>5</sup>

The atomic-charge (or  $\dot{A}$ CHARGE) analysis,<sup>3</sup> which has been reported in several very similar variants,<sup>3,6,7</sup> is closely related to the GPM model in its point-charge version. The difference is that ACHARGE yields an experimental set of atomic charges  $\{q_i\}$  from the measured binding-energy shifts  $\{\delta_i\}$  through solution of the equation

$$\vec{\delta} = \underline{\underline{A}} \vec{q},$$

where the matrix elements  $A_{ij}$  depend only on molecular geometry and atomic integrals. ACHARGE atomic charges generally show very good to excellent agreement with CNDO charges. We have illustrated this conclusion by plotting in Fig. 1 the two sets of charges for H, C, and F as derived from fluorinated hydrocarbons.<sup>3,5</sup> These values of  $q(\text{ACHARGE})$  were all obtained from binding energies measured in gases. We believe that they are to be preferred over results from solids,<sup>6,7</sup> for which lack of a suitable reference level precludes a rigorous determination of shifts. The good agreement in Fig. 1 suggests that chemists may have in binding-energy shifts an operational means for determining that elusive quantity, the atomic charge.

The RPM method is likely to be of particular value in calculating shifts for cases in which variations in the relaxation energy,  $V_R$  can affect the observed shifts. Thus the N(1s) shifts in several small molecules are predicted much better by RPM than by GPM calculations, with standard deviations of 1.3 and 2.35 eV, respectively.<sup>4</sup>

The C(1s) shift in carbon monoxide is very badly predicted by the GPM method because CO is compared with larger molecules. The

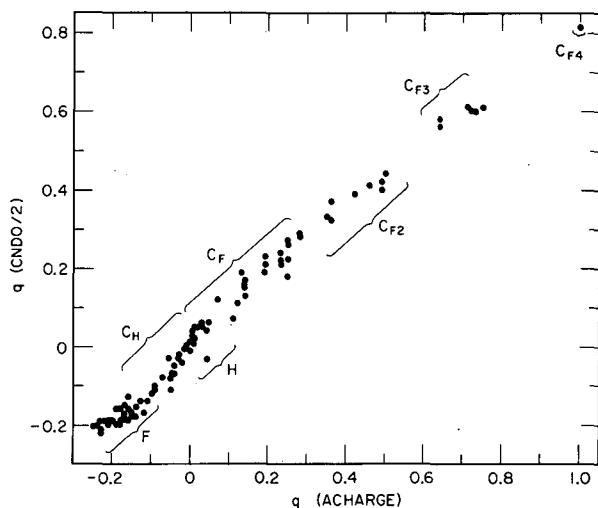


Fig. 1. Atomic charges on C, F, and H in units of  $|e|$  from CNDO/2 calculations, versus charges derived from ACHARGE analysis of binding energy shifts, for 27 fluorinated hydrocarbons. The range of charges found on the following types of atom are indicated: F, H, and carbon bonded to H ( $C_H$ ); to fluorine ( $C_F$ ) and to two, three, or four fluorines ( $C_{F2}$ ,  $C_{F3}$ ,  $C_{F4}$ ). (XBL 738-3695)

predicted value for  $E_B(\text{C } 1s; \text{CO})$  is relatively too low in GPM because CO has a much smaller value of  $V_R$  than the other molecules. The RPM approach brings CO into reasonable agreement.<sup>4</sup>

There are also cases in which poor agreement between GPM predictions and experiment is obtained even though chemically similar compounds are being compared. Ammonia and the methylamines provide an example. The GPM theory predicts  $E_B(\text{N } 1s)$  to increase by 1 eV from  $\text{NH}_3$  to  $(\text{CH}_3)_3\text{N}$ , whereas it in fact decreases by 0.8 eV, in excellent agreement with RPM predictions.<sup>5</sup> Similar behavior has been observed and explained in nitroxides.<sup>8</sup>

A solid state problem of some interest is the relative C(1s) binding energies in graphite and diamond. The most accurate experimental values of  $E_B(\text{C } 1s)$  for these two cases are<sup>9,10</sup>

$$E_B^F(\text{C } 1s, \text{ diamond}) = 284.44(7) \text{ eV},$$

$$E_B^F(\text{C } 1s, \text{ graphite}) = 284.68(20) \text{ eV}.$$

Since the graphite work function is known to be 4.6 V,<sup>11</sup> we also have its binding energy relative to the vacuum level,



$$E_B^V(\text{C } 1s, \text{ graphite}) = 289.3 \text{ eV.}$$

CNDO calculations for these (infinite) lattices are of course not possible, but we have calculated C(1s) relaxation energies using the RPM method for a number of two-dimensional hexagonal arrays of carbon atoms, to simulate the graphite lattice. The outer carbons were taken as being bonded to avoid "dangling bonds" and open orbitals, so this calculation was in fact done on the most central carbon atoms in the planar aromatic molecules benzene, anthracene, etc., as shown in Table I. There is a clear tendency for  $V_R[\text{C}(1s)]$  to increase with increasing molecular size. We plotted  $V_R$  against  $(n_C = \text{number of carbons})^{-1/2}$  and extrapolated to  $n_C^{-1/2} = 0$  to obtain the limiting value

$$V_R(\text{graphite}) \approx V_R(\text{C}_6\text{H}_6) + (1.6 \pm 0.2) \text{ eV.}$$

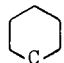
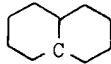
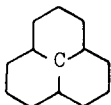
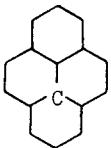
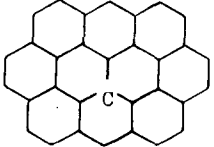
The  $n_C^{-1/2}$  plot was chosen in the expectation

that the excess positive charge in the relaxed final state would go to a radius  $R \propto n_C^{1/2}$  on the outside of the molecule, when it would exert a potential  $V \sim e^2/R \sim e^2/n_C^{1/2}$  on the hole state. A  $1/n_C$  extrapolation would yield essentially the same result. Since the measured C(1s) binding energy in benzene is 290.4 eV,<sup>3</sup> an additional relaxation energy of 1.6 eV would give  $E_B(\text{graphite, theory}) = 288.8 \text{ eV}$ . An alternative estimate of 289.3 eV was obtained by extrapolating the RPM estimates of  $E_B$ , and comparing with the benzene value. Thus we estimate a "best value" of

$$E_B(\text{graphite, theory}) = 289.0 \pm 0.3 \text{ eV,}$$

in good agreement with the experimental value of 289.3 eV. Thus it is possible to make an estimate of a core-level binding energy in a solid from RPM theory. A similar estimate was made for diamond, based on only methane and neopentane. The result was

Table I. Potential at carbon atoms in molecules simulating graphite environment (in eV).

Molecule <sup>a</sup>	$n_C$	$V(Z)$	$V(Z+1)$	$V_R$
	6	88.31	123.68	17.69
	10	87.79	123.93	18.07
	13	88.03	125.36	18.66
	16	87.77	125.03	18.63
	32	87.91	126.18	19.14

<sup>a</sup>Potential is calculated at carbon indicated by "C."

$$E_B(\text{diamond, theory}) = 288.2 \pm 0.5 \text{ eV.}$$

This could be compared with experiment if the work function of diamond were known.

The two models for calculating core-level binding-energy shifts from CNDO wavefunctions may be summarized as follows:

1. In both cases the core-level shifts are approximated by shifts in the potential at the nucleus:  $\Delta E_B \approx \Delta V_n$ . Thus the spatial extent of the core state is neglected, as are shifts in exchange terms involving it.

2. In the point-charge modification of GPM or RPM, the potential due to other atoms is approximated by a term of the form  $\Sigma q/R$ . This version is most directly comparable with the ACHARGE model.

3. In the  $pp'$  modification of GPM or RPM,  $r^{-1}$  integrals are calculated. For invariance to coordinate transformations this necessitates retention of certain additional ( $pp'$ ) terms in the potential.

4. In the RPM approach, the effect of a core hole state on the potential is simulated by repeating the CNDO calculation with the nuclear charge on the central atom increased by one unit. Binding energy shifts are then given by  $-(1/2)\Delta[V_n(Z) + V_n(Z+1)]$ , and the relaxation energy by  $(1/2)[V_n(Z+1) - V_n(Z)]$ .

All these modifications are remarkably successful in predicting core-level binding-energy shifts. The  $pp'$  modification of RPM is the soundest theoretically and it also agrees best with experiment.

#### Footnotes and References

\*From LBL-1970 and J. Electr. Spectroscopy, to be published.

1. J. A. Pople and D. L. Beveridge, Approximate Molecular Orbital Theories (McGraw-Hill, New York, 1970).
2. D. W. Davis, D. A. Shirley, and T. D. Thomas, J. Chem. Phys. 56, 671(1972).
3. D. W. Davis, D. A. Shirley, and T. D. Thomas, J. Am. Chem. Soc. 94, 6565 (1972).
4. D. W. Davis and D. A. Shirley, Chem. Phys. Letters 15, 185 (1972).
5. D. W. Davis, M. S. Banna, and D. A. Shirley, Lawrence Berkeley Laboratory Report LBL-1909; J. Chem. Phys., to be published.
6. G. D. Stucky, D. A. Matthews, J. Hedman, M. Klasson, and C. Nordling, J. Am. Chem. Soc. 94, 8009 (1972).
7. D. T. Clark, D. B. Adams, and D. Kilcast, Chem. Phys. Letters 13, 439 (1972).
8. D. W. Davis, R. L. Martin, M. S. Banna, and D. A. Shirley, J. Chem. Phys., to be published.
9. R. G. Cavell, S. P. Kowalczyk, L. Ley, R. A. Pollak, B. Mills, D. A. Shirley, and W. Perry, Phys. Rev. B 7, 5313 (1973).
10. F. R. McFeely, private communication, August 1973.
11. H. F. Ivey, Phys. Rev. 76, 567 (1949).

### ELECTRON PARAMAGNETIC RESONANCE OF $^{239}\text{Pu}^{3+}$ AND $^{243}\text{Am}^{4+}$ IN $\text{CeO}_2$ AND OF $^{241}\text{Pu}^{3+}$ IN $\text{ThO}_2$ †

W. Kolbe, N. Edelstein, C. B. Finch, and M. M. Abraham

The most pronounced difference in electronic properties between the lanthanide and actinide series is the further breakdown of Russell-Saunders coupling in the latter because of the increasingly larger effects of spin-orbit coupling. For example, the  $^6\text{H}$  term contributes 96% to the ground ( $J = 5/2$ ) state of the  $f^5$  configuration for  $\text{Sm}^{3+}(4f^5)$ , while contributing only 66% to the  $\text{Pu}^{3+}(5f^5)$  ground state.<sup>1</sup> The resulting admixture of other terms into the ground state changes the

behavior of the actinide ion (relative to the rare-earth ion) when it is placed in a crystal-line environment. Edelstein et al.<sup>1</sup> calculated the respective fourth- and sixth-order crystal-field operator equivalent factors for  $\text{Sm}^{3+}$  and  $\text{Pu}^{3+}$ , using intermediate coupled wavefunctions. They found a sign reversal for the fourth-order parameter in the case of the actinide ion. Since the fourth-order term predominates, this calculation showed that the  $\text{Pu}^{3+}$  crystal-field splittings under  $O_h$  symmetry

would be inverted with respect to  $\text{Sm}^{3+}$  in the same symmetry. For an eightfold-coordinated cubic site, the ground state for the  $\text{Sm}^{3+}$  ion should be the fourfold degenerate  $\Gamma_8$ , while for the  $\text{Pu}^{3+}$  ion the  $\Gamma_7$  doublet should lie lowest.

The  $\text{Sm}^{3+}$  ion has never been observed in cubic symmetry, but  $^{239}\text{Pu}^{3+}$  has been observed in an eightfold-coordinated cubic site in five different crystals of the fluorite type:  $\text{ThO}_2$ ,  $\text{CaF}_2$ ,  $\text{SrF}_2$ ,  $\text{BaF}_2$ , and  $\text{SrCl}_2$ .<sup>1,2</sup> Additionally,  $^{241}\text{Am}^{4+}$  and  $^{243}\text{Am}^{4+}$  (which are isoelectronic to trivalent plutonium) have also been observed in the  $\text{ThO}_2$  host.<sup>2</sup> Although in each case the observed ground state was a  $\Gamma_7$  doublet as expected, it was found that the measured isotropic  $g$  values were different for each host. This was due to the differing magnitudes of the crystal field which produced various admixtures of excited crystal-field

states into the ground state.<sup>1</sup> Indeed, the experimental  $g$  values for  $\text{Pu}^{3+}$  were found to vary monotonically with the relative strengths of the cubic crystalline electric fields in these hosts. This crystal-field-produced admixture of excited states also explained qualitatively the large variation in the observed hyperfine parameters.<sup>3</sup>

The fluorite-type host  $\text{CeO}_2$  has a lattice constant smaller than the five aforementioned crystals, and therefore the magnitude of its crystal field should be the largest of all the six hosts. The cubic field splitting of the  $4f^7$  ion  $\text{Gd}^{3+}$  in  $\text{CeO}_2$ , however, was observed to be smaller than in  $\text{ThO}_2$  in spite of the larger crystal field strength anticipated.<sup>4</sup> This anomalous situation is believed to be due to the almost pure S ground state for the half-filled  $4f$  shell, where the mechanisms for lifting the

Table I. Spin-Hamiltonian parameters for  $5f^5$  configuration ions.

Matrix	$ g $	$ A $ ( $10^{-4} \text{ cm}^{-1}$ )		$B_4^a$ ( $\text{cm}^{-1}$ )	Ref.
		$^{239}\text{Pu}^{3+}$	$^{241}\text{Pu}^{3+}$		
$\text{CeO}_2$	$1.333 \pm 0.001$	$22.4 \pm 0.2$		-5400	b
$\text{ThO}_2$	$1.3124 \pm 0.0005$	$65.4 \pm 0.2$		-5130	c
$\text{CaF}_2$	$1.297 \pm 0.002$	$66.95 \pm 0.03$	$46.1 \pm 0.6$	-4945	b
			$48.07 \pm 0.10$		d
$\text{SrF}_2$	$1.250 \pm 0.002$	$84.6 \pm 1.0$		-4440	e
$\text{BaF}_2$	$1.187 \pm 0.004$	$102 \pm 3$		-3820	e
$\text{SrCl}_2$	$1.1208 \pm 0.0005$	$127.9 \pm 0.4$		-3190	c

---

Matrix	$ g $	$ A $ ( $10^{-4} \text{ cm}^{-1}$ )		Ref.
		$^{241}\text{Am}^{4+}$	$^{243}\text{Am}^{4+}$	
$\text{CeO}_2$	$1.3120 \pm 0.0005$		$22.1 \pm 0.2$	b
$\text{ThO}_2$	$1.2862 \pm 0.0005$	$45.7 \pm 0.1$	$45.3 \pm 0.1$	c

<sup>a</sup> Values of  $B_4^a$  were calculated assuming that  $B_6^a/B_4^a = -0.2$ .

<sup>b</sup> This work.

<sup>c</sup> Reference 2.

<sup>d</sup> W. Kolbe and N. Edelstein, unpublished, reported in Ref. 8.

<sup>e</sup> Reference 1.

degeneracy are not understood.<sup>5</sup> Recently, the analogous  $5f^7$  ion  $\text{Cm}^{3+}$  has been shown to exhibit a larger splitting in  $\text{CeO}_2$  than in  $\text{ThO}_2$ .<sup>6</sup> The agreement in this case with the predictions of the crystal field model is again a result of the larger intermediate-coupling effects present for the actinide ion; the  $8S$  ground state of  $\text{Gd}^{3+}$  is approximately 97% pure, while that of  $\text{Cm}^{3+}$  is only 79%.<sup>7</sup> Thus in the case of  $\text{Gd}^{3+}$ , where the effects of intermediate coupling are small, other mechanisms<sup>5</sup> become important and appear to dominate.

We report here the EPR observation of both  $^{239}\text{Pu}^{3+}$  ( $I=1/2$ ) and  $^{243}\text{Am}^{4+}$  ( $I=5/2$ ) in the fluorite-type host,  $\text{CeO}_2$ . The results are in agreement with the above arguments about relative crystal field strengths. We have also observed the EPR spectrum of  $^{241}\text{Pu}^{3+}$  ( $I=5/2$ ) in  $\text{ThO}_2$ , and present an additional value for the ratio of the magnetic moments  $\frac{241\mu}{239\mu}$  of trivalent plutonium for comparison with the results summarized by Edelstein.<sup>8</sup> The data are given in Table I.

As mentioned above, the range of  $g$  values observed in the various hosts results from the mixing of excited  $J$  states into the ground state by the crystalline electric field. In the earlier work of Edelstein et al.<sup>1</sup> intermediate coupled wavefunctions were used, taking into account only the admixture of the two lowest  $J$ -manifolds,  $J=5/2$  and  $7/2$ , by the crystal field. In order to better approximate the effects of higher  $J$ -manifolds, we have carried out an additional calculation in which we have simultaneously diagonalized the electrostatic, spin-orbit, and crystal field Hamiltonians, using a truncated basis set consisting of 40 of the 73 terms of the  $f^3$  configuration. Lam and Chan<sup>9</sup> have recently pointed out the importance of including the effects of higher  $J$ -manifolds.

Since only one experimental number,  $g$ , is known for each host, it is necessary to assume some value for the ratio of the crystal field parameters  $B_6/B_4$ .<sup>10</sup> For convenience, the ratio was chosen to be  $-0.2$ ,<sup>1</sup> and the resultant values of  $B_4$  are listed in Table I. These values differ somewhat from those reported in the previous work,<sup>1,2</sup> but the general trend is still apparent. As can be seen from the table, the magnitude of the parameter  $B_4$  is found to vary monotonically throughout the series of fluorite host lattices. The results of Lam and Chan,<sup>9</sup> for the range of crystal field parameters considered by them, are in agreement with the values presented here. A calculation following the methods of Edelstein and Mehlhorn<sup>3</sup> but using the wavefunctions described above to interpret the hyperfine parameters is in progress but not completed at this time.

In conclusion, these actinide results show

that the crystal-field interaction in  $\text{CeO}_2$  is indeed the strongest of the six fluorite hosts studied. Only in the case of the  $S$ -state ion  $\text{Gd}^{3+}$ , whose ground state is predominantly orbitally nondegenerate (resulting in much weaker crystal field interactions), does this pattern appear to be violated.

#### Acknowledgments

We gratefully acknowledge the cooperation of O. L. Keller and the staff members of the ORNL Transuranium Research Laboratory whose radiation containment facilities were essential for the work reported here.

#### Footnote and References

† In press, J. Chem. Phys.

1. N. Edelstein, H. F. Mollet, W. C. Easley, and R. J. Mehlhorn, J. Chem. Phys. **51**, 3281 (1969). The calculation of the intermediate-coupled wavefunctions reported in this reference was based on the optically derived spin-orbit and electrostatic parameters of  $\text{Sm}^{3+}$  [W. T. Carnall, P. R. Fields and K. Rajnak, *ibid.* **49**, 4424 (1968)] and  $\text{Pu}^{3+}$  [J. G. Conway and K. Rajnak, *ibid.* **44**, 348 (1966)].
2. M. M. Abraham, L. A. Boatner, C. B. Finch, and R. W. Reynolds, Phys. Rev. B **3**, 2864 (1971).
3. N. Edelstein and R. Mehlhorn, Phys. Rev. B **2**, 1225 (1970); M. M. Abraham, L. A. Boatner, C. B. Finch, and R. W. Reynolds, Phys. Rev. B **3**, 2864 (1971).
4. M. M. Abraham, L. A. Boatner, C. B. Finch, E. J. Lee, and R. A. Weeks, J. Phys. Chem. Solids **28**, 81 (1967); M. M. Abraham, E. J. Lee, and R. A. Weeks, *ibid.* **26**, 1249 (1966).
5. B. G. Wybourne, Phys. Rev. **148**, 317 (1966).
6. W. Kolbe, N. Edelstein, C. B. Finch, and M. M. Abraham, J. Chem. Phys. **58**, 821 (1973); *ibid.* **56**, 5432 (1972).
7. W. T. Carnall and B. G. Wybourne, J. Chem. Phys. **40**, 3428 (1964); B. G. Wybourne, Spectroscopic Properties of Rare Earths (Interscience, New York, 1965), p. 204.
8. N. Edelstein, Phys. Letters **33A**, 233 (1970).
9. D. J. Lam and S. K. Chan, Phys. Rev. B **6**, 307 (1972).

10. B. G. Wybourne, Spectroscopic Properties of Rare Earths (Interscience, New York, 1965). The tensor operator coefficients  $B_4$  and  $B_6$  are given by  $B_4 = 8B_4/\beta$  and

$B_6 = 16B_6/\gamma$ , where  $B_4$  and  $B_6$  are the spin-Hamiltonian parameters, and  $\beta$  and  $\gamma$  are Steven's operator-equivalents are used by K. R. Lea, M. J. M. Leask, and W. P. Wolf, *J. Phys. Chem. Solids* 23, 1381 (1962).

### CALCULATION OF THE CRYSTAL FIELD SPLITTINGS OF $\text{Sm}^{3+}$ LEVELS IN $\text{LaCl}_3$ WITH INCLUSION OF J MIXING\*

K. Rajnak,\* R. Mehlhorn,<sup>†</sup> and N. Edelstein

Energy levels of  $\text{Sm}^{3+}$  in  $\text{LaCl}_3$  have been measured by Magno and Dieke.<sup>1</sup> A crystal field calculation by Axe and Dieke<sup>2</sup> (including J mixing) for the  $^6\text{H}$  and  $^6\text{F}$  multiplets reproduced 39 observed levels with an rms deviation of  $\pm 3.2 \text{ cm}^{-1}$ . Further assignments of higher levels and some additional data were included in the book of Dieke.<sup>3</sup> Some assignments of the centers of gravity (often estimated from one observed crystal field component) were made from a least-squares fitting procedure by Carnall, Fields, and Rajnak<sup>4</sup> who included the configuration interaction parameters  $\alpha$ ,  $\beta$ , and  $\gamma$ .<sup>5</sup> The fit was quite unsatisfactory, however. The rms deviation was  $119 \text{ cm}^{-1}$  (vs  $\sim 50$  for most other rare earth ions). Two levels whose identification was quite certain had deviations of  $\sim 200 \text{ cm}^{-1}$ . Furthermore  $\alpha$  was determined to be  $16 \text{ cm}^{-1}$  whereas it was  $22 \text{ cm}^{-1}$  for  $\text{Sm}^{3+}$  in solution. It was impossible to determine a value for  $\gamma$ . Any attempt to include  $\gamma$ , even if it were not allowed to vary, immediately led to a  $\sim 10 \text{ cm}^{-1}$  and large errors in all the parameters. This difficulty arose because  $\gamma$  is essentially dependent on seniority number. Consequently assignment of rather high levels is required before  $\gamma$  can be determined.

In the present work we took the free ion parameters of Carnall et al. and the crystal field parameters<sup>6</sup> of Axe and Dieke and diagonalized the matrices for the electrostatic, spin-orbit, and crystal field interactions simultaneously. Truncation of the basis vectors was necessary, however, since the  $f^5$  configuration contains 73 LS states. We chose to include only 42 states: all the sextets and quartets except the 4S and 4I2, and the following doublets: 2P1, 2P3, 2P4, 2D1, 2D2, 2D4, 2D5, 2F1, 2F2, 2F4, 2F5, 2F6, 2F7, 2H6, 2I4, 2K1, 2K4, and 2K5.<sup>7</sup> Limiting the J values to  $J \leq 15/2$  leads to three matrices to be diagonalized:  $\mu = 1/2$ , rank = 184;  $\mu = 3/2$ , rank = 178;  $\mu = 5/2$ , rank = 172, where  $\mu = J_z \pmod{6}$ .

Comparison of the results of diagonalization of these matrices with the crystal field parameters set equal to zero and the free ion calculation of Carnall et al. gave a value for the truncation error of each J level. For the levels below  $20\,100 \text{ cm}^{-1}$  these errors were  $\sim 20 \text{ cm}^{-1}$ , but were much larger for some higher states. The exclusion of 2L1 and 2L3 from the basis vectors resulted in a large error for the  $J = 15/2$  levels, particularly the one at  $\sim 20\,300 \text{ cm}^{-1}$ . Comparison of the calculated centers of gravity from a complete diagonalization including the crystal field matrix elements with those from the truncated eigenvectors with the crystal field parameters equal to zero gave a crystal field shift for each J level. When a correction was made for the truncation error, crystal field shifts were  $\leq \pm 25 \text{ cm}^{-1}$  except for the  $J = 9/2$  at  $20\,500 \text{ cm}^{-1}$ . Since this was one of the levels with a very large truncation error, the larger shift ( $-44 \text{ cm}^{-1}$ ) may not be meaningful. The  $J = 15/2$  and  $J = 11/2$  at  $20\,300$  and  $21\,000 \text{ cm}^{-1}$  are so badly J mixed that it is impossible to determine a center of gravity for the levels independently. Consequently no crystal field shift could be computed.

Having ascertained that J mixing does not cause appreciable shifts of the center of gravity of the levels, we then used the results of the crystal field calculation (including splitting factors) to make some additional assignments and corrected a couple of the centers of gravity chosen by Carnall et al. A new free ion fit to these centers of gravity was carried out, fixing  $\gamma = 800 \text{ cm}^{-1}$  (near the value for  $\text{Sm}^{3+}$  in solution). The rms deviation was reduced to  $54 \text{ cm}^{-1}$ . A "complete" diagonalization with these new free ion parameters (see Table I) gave considerable improvement for some of the levels and allowed some additional assignments to be made. These new assignments were insufficient to determine  $\gamma$  by fitting, however.

Table I. Parameters for  $\text{Sm}^{3+}$  in  $\text{LaCl}_3$  ( $\text{cm}^{-1}$ ).

---

$E^1$	=	$5465.27 \pm 17.21$
$E^2$	=	$25.40 \pm 0.30$
$E^3$	=	$547.62 \pm 1.65$
$\zeta$	=	$1153.8 \pm 8.9$
$\alpha$	=	$24.29 \pm 1.98$
$\beta$	=	$795.72 \pm 98.4$
$\gamma$	=	800
$B_0^2$	=	161.70
$B_0^4$	=	182.00
$B_0^6$	=	710.24
$B_6^6$	=	448.14

---

The results are remarkably good considering the truncation of the basis states and the fact that no fitting of the crystal field parameters was carried out. J mixing does occur and makes the interpretation of some levels difficult, but it is considerably less than had been expected. The crystal field parameters determined by Axe and Dieke for the  $^6\text{H}$  and  $^6\text{F}$  multiplets seem to represent the higher multiplets reasonably well. Detailed consideration of the crystal field splittings of the higher states is made difficult by the truncation errors, however. Such an approximate calculation did prove valuable in understanding the over-all structure of the energy levels and allowed computation of an improved set of free ion parameters. Further progress on the analysis of  $\text{Sm}^{3+}$  in  $\text{LaCl}_3$  must await the ability to carry out least-squares fits on large matrices and computations with a larger basis set than that chosen here. One must be very cautious about fitting free ion parameters with a truncated basis set, however. The  $g$  values as well as energies should be fit. If such a complete fit is carried out, it should

also include the additional three-body operators of configuration interaction.<sup>8,9</sup>

We would like to thank John Conway and H. M. Crosswhite for helpful discussion. One of us (K.R.) would like to thank the Lawrence Berkeley Laboratory for its hospitality.

#### Footnotes and References

\* Present address: 524 Wealthy, Kalamazoo, Mich. 49007.

† Physiology and Anatomy Department, University of California, Berkeley, Calif. 94720.

1. M. S. Magno and G. H. Dieke, *J. Chem. Phys.* **37**, 2354 (1962).

2. J. D. Axe and G. H. Dieke, *J. Chem. Phys.* **37**, 2364 (1962).

3. G. H. Dieke, *Spectra and Energy Levels of Rare Earth Ions in Crystals* (Wiley, New York, 1968).

4. W. T. Carnall, P. R. Fields, and K. Rajnak, *J. Chem. Phys.* **49**, 4424 (1968).

5. See B. G. Wybourne, *Spectroscopic Properties of Rare Earths* (Wiley, New York, 1965), for all definitions.

6. The values used here correspond to the definitions of Wybourne, not those originally used by Axe and Dieke.

7. Notation is that of C. W. Nielson and G. F. Koster, *Spectroscopic Coefficients for the  $p^n$ ,  $d^n$ , and  $f^n$  Configurations* (Tech. Press, Cambridge, Mass. 1963).

8. K. Rajnak and B. G. Wybourne, *Phys. Rev.* **132**, 280 (1963).

9. B. R. Judd, *Phys. Rev.* **141**, 4 (1966).

GEOMETRIES OF THE METHOXY RADICAL  
( ${}^2E$  AND  $A {}^2A_1$  STATES) AND THE METHOXIDE ION\*

D. R. Yarkony, H. F. Schaefer III, and S. Rothenberg<sup>†</sup>

Ab initio self-consistent-field electronic structure calculations have been performed on the methoxy radical ( $\text{CH}_3\text{O}$ ) in its ground and first excited electronic states and on the methoxide ion ( $\text{CH}_3\text{O}^-$ ). The geometries of the three species have been predicted by varying the total energy with respect to the CH and CO bond distances and the OCH bond angle. The three geometries are qualitatively quite different, particularly the CO bond distances. A small Jahn-Teller distortion is predicted for the  ${}^2E$   $\text{CH}_3\text{O}$  ground state. The excited  ${}^2A_1$  state of  $\text{CH}_3\text{O}$  is predicted to lie at 3.6 eV. The results are summarized in Table I.

Footnotes

\*Published in J. Amer. Chem. Soc. 96, 656 (1974).

<sup>†</sup>Present address: Information Systems

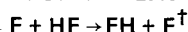
Design, 7817 Oakport St., Oakland, California 94621.

Table I. Geometry predictions for  $\text{CH}_3\text{O}$  and  $\text{CH}_3\text{O}^-$ . For comparison the experimental methanol geometry is indicated. (Bond distances are given in Å.)

Molecule	State	r (CH)	r (CO)	$\theta(\text{OCH})$
$\text{CH}_3\text{O}$	${}^2E$	1.08	1.44	109°
$\text{CH}_3\text{O}$	${}^2A_1$	1.08	1.65	102°
$\text{CH}_3\text{O}^-$	${}^1A_1$	1.12	1.39	114°
$\text{CH}_3\text{OH}$	${}^1A'$	(1.093) <sup>a</sup>	1.434	109.5°

<sup>a</sup>Not determined experimentally. Value in parentheses is that for  $\text{CH}_4$ .

BARRIER HEIGHT FOR THE EXCHANGE REACTION

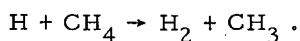


S. V. O'Neil, H. F. Schaefer III, and C. F. Bender\*

The two classic systems for the study of reactive quantum mechanical tunneling are<sup>1-3</sup>

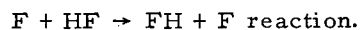


and



The merits of these two systems with respect to tunneling are at least three: a) both are relatively simple reactions, b) both have relatively high barrier heights ( $\sim 10$  kcal), and c) both involve the transfer of the lightest atom, hydrogen. Thus  $\text{H} + \text{H}_2$  and  $\text{H} + \text{CH}_4$  are amenable to detailed calculation, and at thermal energies tunneling should contribute a significant fraction of the reactive cross sections.

A related system which might be considered a candidate for reactive tunneling is the



Although the experimental activation energy is not known for the above reaction, in recent years it has been assumed<sup>1</sup> to be low, no more than 6 kcal. There are two reasons for this assumption. The first is Johnston's bond energy bond order (BEBO) method, which predicts the 6-kcal barrier. As ab initio theorists, we tend to be skeptical of empirical schemes such as BEBO. However, Truhlar<sup>4</sup> has recently shown that BEBO is remarkably accurate for the  $\text{H} + \text{H}_2$  and  $\text{F} + \text{H}_2$  reactions. Not only does BEBO accurately reproduce the activation energies, but it also predicts minimum energy paths within 0.03 Å of those obtained from the most elaborate available ab initio calculations.<sup>5,6</sup> Thus the BEBO method for these two systems is far more accurate than could have been anticipated, and one should consider seriously the 6-kcal prediction for  $\text{F} + \text{HF}$ .

The second indirect piece of evidence against the existence of a substantial barrier for  $F + HF$  is the report by Pimentel and co-workers<sup>7</sup> of the observation of the linear molecules  $ClHCl$ ,  $BrHBr$ , and  $IHI$  in noble gas matrices. By analogy with  $H_3$ ,  $FH_2$ , and the general London-Eyring-Polanyi-Sato<sup>8</sup> (LEPS) view of potential surfaces, the saddle point for the  $X + HX$  exchange reactions should also occur for the linear symmetric ( $D_{\infty h}$ )  $XHX$  configuration. Thus the work of Pimentel suggests that for  $Cl + HCl$ ,  $Br + HBr$ , and  $I + HI$ , there should be no barrier at all. This prediction is in turn not consistent with the kinetic studies of Klein, Persky, and Weston,<sup>9</sup> who found (by somewhat unconventional means) the barrier for  $Cl + HCl$  exchange to be  $\sim 10$  kcal. In addition, Milligan and Jacox<sup>10</sup> have challenged the conclusions of Pimentel, voicing their opinion that the matrix isolated species are in reality  $ClHCl^-$ ,  $BrHBr^-$ , and  $IHI^-$ . Very recently, however, Pimentel's conclusions have been supported by the BEBO calculations of Truhlar, Olson, and Parr.<sup>11</sup> In addition to predicting  $ClHCl$ ,  $BrHBr$ , and  $IHI$  to be bound by 1.56, 3.02, and 6.77 kcal, Truhlar et al. find vibrational frequencies in reasonable agreement with Pimentel's experimental values.

In the present communication we report ab initio calculations on linear symmetric  $FHF$ . Since the minimum energy path must pass through at least one geometry at which the two  $HF$  bond distances are equal, the lowest energy symmetric  $FHF$  provides a lower limit to the barrier height for  $F + HF \rightarrow FH + F$ .

Two basis sets of contracted Gaussian functions<sup>12</sup> have been used in the present work. The first, a double zeta (DZ) set, is designated  $F(9s5p/4s2p)$ ,  $H(4s/2s)$ . This is the same basis used in our previous calculations<sup>13,14</sup> of the  $F + H_2$  and  $H + F_2$  surfaces. The second basis, termed double zeta plus polarization (DZ + P), is described by the notation  $F(9s51d/4s2p1d)$ ,  $H(4s1p/2s1p)$ . This second basis set yielded a surface<sup>6</sup> approaching quantitative accuracy for  $F + H_2$ .

Electron correlation was explicitly taken into account using multiconfiguration first-order wavefunctions.<sup>15</sup> The form of this type of wavefunction is determined by symmetry considerations. Since  $F + HF$  refers to the same molecule as  $H + F_2$ , the reader is referred to our work<sup>14</sup> on  $H + F_2$  for the list of configurations actually included. For linear  $FHF$  the first-order wavefunction constructed from the DZ + P basis includes 670 configurations. The orbitals of the multiconfiguration wavefunctions were optimized by the iterative natural orbital method.<sup>16</sup>

Our results are summarized in Table I. The first point to be made is that electron correlation lowers the predicted barrier by about 30 kcal. This is consistent with the earlier a priori calculations<sup>6,13</sup> on  $F + H_2$ . Unlike the  $F + H_2$  calculations, however, we see here that the larger basis set yields a slightly higher barrier than the DZ set. All four calculations yield qualitatively similar results for the barrier location.

Table I. Predicted barrier heights for  $F + HF \rightarrow FH + F$ . See text for a brief description of the different wave functions.

Property		Wavefunction		
		r(H-F) (Å)	Barrier (kcal)	Total energy (hartrees)
DZ	SCF	1.087	53.8	-199.3307
DZ	CI	1.126	21.8	-199.4327
DZ+P	SCF	1.083	53.7	-199.3578
DZ+P	CI	1.099	23.9	-199.4676

The result of the present quantum mechanical calculations is almost completely unexpected, in light of previous thinking about the  $F + HF$  potential surface.<sup>17</sup> We think the calculations reported are sufficiently reliable that the true barrier height is unlikely to be less than 18 kcal/mol. In that case  $F + HF$  may replace  $H + H_2$  and  $H + CH_4$  as the model system for the study of reactive tunneling.

#### Footnotes and References

<sup>†</sup>Published in Proc. Natl. Acad. Sci. USA **71**, 104 (1974); LBL-1665.

\*Permanent address: Lawrence Livermore Laboratory, University of California, Livermore, California 94550.

1. H. S. Johnston, Gas Phase Reaction Rate Theory (Ronald Press, New York, 1966).

2. Reactive tunneling in the  $H + H_2$  has been considered by several authors. For a particularly interesting recent treatment, see J. D. Doll, T. F. George, and W. H. Miller, J. Chem. Phys. **58**, 1343 (1973).

3. For the definitive discussion of reactive tunneling in  $H + CH_4$ , see H. S. Johnston, Adv. Chem. Phys. **3**, 131 (1961).

4. D. G. Truhlar, J. Am. Chem. Soc. **94**, 7584 (1972).



5. I. Shavitt, R. M. Stevens, F. L. Minn, and M. Karplus, *J. Chem. Phys.* **48**, 2700 (1968). For an even more accurate linear  $H_2$  surface, see B. Liu, *J. Chem. Phys.* **58**, 1925 (1973).
6. C. F. Bender, S. V. O'Neil, P. K. Pearson, and H. F. Schaefer, *Science* **176**, 1412 (1972).
7. P. N. Noble and G. C. Pimentel, *J. Chem. Phys.* **49**, 3165 (1968); V. Bondybey, G. C. Pimentel, and P. N. Noble, *J. Chem. Phys.* **55**, 540 (1971); P. N. Noble, *J. Chem. Phys.* **56**, 2088 (1972).
8. P. J. Kuntz, E. M. Nemeth, J. C. Polanyi, S. D. Rosner, and C. E. Young, *J. Chem. Phys.* **44**, 1168 (1966).
9. F. S. Klein, A. Persky, and R. E. Weston, *J. Chem. Phys.* **41**, 1799 (1966).
10. D. E. Milligan and M. E. Jacox, *J. Chem. Phys.* **53**, 2034 (1970); **55**, 2550 (1971).
11. D. G. Truhlar, P. C. Olson, and C. A. Parr, *J. Chem. Phys.* **57**, 4479 (1972).
12. T. H. Dunning, *J. Chem. Phys.* **53**, 2823 (1970).
13. C. F. Bender, P. K. Pearson, S. V. O'Neil, and H. F. Schaefer, *J. Chem. Phys.* **56**, 4626 (1972).
14. S. V. O'Neil, P. K. Pearson, H. F. Schaefer, and C. F. Bender, *J. Chem. Phys.* **58**, 1126 (1973).
15. H. F. Schaefer, *The Electronic Structure of Atoms and Molecules: A Survey of Rigorous Quantum Mechanical Results* (Addison Wesley, Reading, Mass. 1972).
16. C. F. Bender and E. R. Davidson, *J. Phys. Chem.* **70**, 2675 (1966).
17. In discussing our result with colleagues, the only indirect support we have been able to locate comes from the semiempirical LEPS potential surface used by N. Blais for his classical trajectory study of the  $H + F_2$  reaction (Los Alamos Scientific Laboratories Report LA-4687). Blais found good agreement with experiment for the distribution of product vibrational energy. After concluding our study, we asked Dr. Donald L. Thompson of Los Alamos to obtain the  $F + HF \rightarrow FH + F$  barrier from Blais's surface. The barrier height found was  $\sim 25$  kcal, in good agreement with the values reported here.

#### THEORETICAL SUPPORT FOR THE ASSIGNMENT OF X-OGEN TO THE $HCO^+$ MOLECULAR ION\*

U. Wahlgren,<sup>†</sup> B. Liu,<sup>†</sup> P. K. Pearson, and  
H. F. Schaefer III

The first unidentified interstellar microwave line was reported in 1970 by Buhl and Snyder,<sup>1</sup> who, appropriately enough, named this line the X-ozen line. They were originally<sup>1</sup> able to detect X-ozen at  $89.190 \pm 0.002$  GHz in five galactic sources: W3 (OH), Orion, L134, Sgr A ( $NH_3A$ ), and W51. The first two candidates suggested for X-ozen were HNC and  $HCO^+$ , the former the suggestion of Herzberg (noted by Buhl and Snyder<sup>1</sup>) and the latter that of Klemperer.<sup>2</sup> Since then Snyder and Buhl<sup>3</sup> have concluded that a second unidentified line (at 90.665 GHz) is more likely to be due to HNC, and very recent *ab initio* calculations<sup>4</sup> have unquestionably ruled out HNC as a candidate for X-ozen.

Klemperer's proposed assignment was made by noting that the HC bond distance in

HCN is  $1.06 \text{ \AA}$  and the CO bond distance in  $CO^+$  is  $1.115 \text{ \AA}$ . Assuming these same bond distances are valid for  $HCO^+$ , Klemperer predicted the  $J = 0 \rightarrow 1$  pure rotational line to occur at 89.246 GHz, in very close agreement with X-ozen,  $89.190 \pm 0.002$  GHz. However, this is not the only plausible choice of bond distances for  $HCO^+$ . For example, one might assume  $r_e(CO)$  to be the same as in the iso-electronic CO molecule ( $1.128 \text{ \AA}$ ), and take  $r_e(HC)$  from the  $CH^+$  ion ( $1.131 \text{ \AA}$ ). This second assumed geometry suggests that the  $J = 0 \rightarrow 1$  transition of  $HCO^+$  could occur in the vicinity of 85.7 GHz, far from the X-ozen line. Generally, for any linear triatomic molecule, there will be a locus of pairs of bond distances which fit an observed rotational line. If we assume that X-ozen is  $HCO^+$  and the difference ( $B_e - B_0$ ) is the same for  $HCO^+$

as for the isoelectronic HCN molecule, then the  $B_e$  value of  $\text{HCO}^+$  is 44.785 GHz. Some points on the appropriate locus of acceptable linear geometries are seen in Table I. Our chemical intuition (see also Sutton<sup>5</sup>) suggests that geometries outside this range are not very plausible. Shorter CO bond distances seem unlikely *per se*, while longer value of  $r_e(\text{CO})$  necessitate unreasonably small HC bond distances.

Table I. Locus of geometries (for  $\text{HCO}^+$ ) which yield a rotational constant  $B_e = 44.785$  GHz. (Bond distances are in Å.)

$r_e(\text{HC})$	$r_e(\text{CO})$
1.1244	1.100
1.1144	1.102
1.1043	1.104
1.0942	1.106
1.0840	1.108
1.0737	1.110
1.0634	1.112
1.0530	1.114
1.0425	1.116
1.0319	1.118
1.0213	1.120

This year Buhl and Snyder<sup>6</sup> have reported four new galactic sources of the X-ogen emission line. Thus there is little question that X-ogen is an important interstellar species. In addition, Klemperer's hypothesis (that X-ogen is  $\text{HCO}^+$ ) has been taken quite seriously, in particular the implication that polyatomic molecular ions may play an important role in the chemistry of the interstellar medium.<sup>7-11</sup> For example, the existence of a substantial interstellar abundance of  $\text{H}_2\text{CN}^+$  could be used<sup>11</sup> to explain both the unexpected DCN/HCN ratio<sup>12</sup> of  $6 \times 10^{-3}$  and the formation of the HNC molecule.

Thus it is clear that either the confirmation or denial of  $\text{HCO}^+$  as X-ogen would be extremely important. To date it has not proved possible to obtain a laboratory microwave spectrum of  $\text{HCO}^+$ . In addition, a search<sup>6</sup> for the  $\text{H}^{13}\text{CO}^+$  rotational line analogous to X-ogen (assuming it is  $\text{H}^{12}\text{CO}^+$ ) proved fruitless. With these avenues temporarily exhausted, it is our opinion that *ab initio* theoretical studies provide the fastest route to a

partial clarification of this question. Accordingly, in the present paper we present the results of such a study.

Our first set of calculations was completely analogous to that reported earlier for HNC<sup>4</sup>. A large contracted Gaussian basis set (the reader is referred elsewhere<sup>13</sup> for a fairly thorough discussion of the methods mentioned here), designated H (6s 1p/3s 1p), C (11s 6p 1d/6s 3p 1d), O (11s 6p 1d/6s 3p 1d), was employed. Following the self-consistent-field (SCF) calculations, extensive configuration interaction (CI) was carried out using the MOLECULE-CI program of Roos and Siegbahn.<sup>14</sup> All singly- and doubly-excited configurations (a total of 6343) were included with respect to the SCF configuration  $3\sigma^2 4\sigma^2 1\pi^4 5\sigma^2$ . Thus this type of wavefunction explicitly includes the effects of electron correlation.

A second series of calculations was carried out using a very large basis set of Slater functions: H (3s 2p 1d), C (5s 4p 2d 1f), O (5s 4p 2d 1f). Experience suggests<sup>15</sup> that such a basis should yield SCF total energies within 0.001 hartree = 0.027 eV of the Hartree-Fock limit. The ALCHEMY program<sup>16</sup> was used for these SCF calculations. No CI was attempted with this larger basis set.

The Slater basis SCF calculations yielded a C-O bond distance 0.004 Å shorter than that obtained from the Gaussian basis SCF calculation. Assuming that the Slater basis SCF bond distances are sufficiently close to the Hartree-Fock limit, and that basis set and correlation corrections are independent, then the C-O bond distance predicted by the Gaussian basis CI might be 0.004 Å longer than the exact value. However, we should be least mention that the usual effect of electron correlation is an opposite one, namely to lengthen bond distances predicted at the Hartree-Fock level of theory. Thus it is by no means inconceivable that our Gaussian-basis CI bond distances are significantly more accurate than 0.004 Å.

The calculation labeled "Gaussian Basis CI" in Table II, by far our most accurate, predicts the  $\text{HCO}^+$  rotational line to occur 0.17 GHz higher than that of X-ogen. Assuming the calculated C-O bond distance to be 0.004 Å too large, the transition would occur at 89.9 GHz, which is 0.7 GHz too high. This provides an upper limit to the error in the calculation. However, considering the results obtained earlier for HCN<sup>4</sup> and the discussion of the previous paragraph, it seems reasonable to conclude that the error in the calculation is significantly smaller than 0.7 GHz, and to identify the X-ogen line as being due to the  $J = 0$  to  $J = 1$  transition for  $\text{HCO}^+$ . In fact, it seems fair to say that the present

Table II. Predicted properties of the  $\text{HCO}^+$  molecular ion. See text for a brief description of the different calculations. Bond distances are given in Å. The theoretical  $\Delta E$  values were obtained assuming  $(B_e - B_0) = 0.19$  GHz, the experimental value<sup>a</sup> for HCN.

	Total Energy (hartrees)	$r_e$ (HC)	$r_e$ (CO)	$B_e$ (GHz)	$\Delta E$ (J = 0 $\rightarrow$ J = 1)
Gaussian Basis SCF	-113.0073	1.089	1.0779	46.82	93.26
Slater Basis SCF	-113.0218	1.087	1.0740	47.11	93.84
Gaussian Basis CI	-113.3064	1.095	1.1045	44.87	89.36
Klemperer estimates <sup>b</sup>	--	1.060	1.1150	44.63	88.88
X-ogen <sup>c</sup>	--	--	--	--	89.189 $\pm$ 0.002

<sup>a</sup>Herzberg, G., Electronic Spectra of Polyatomic Molecules (Van Nostrand Reinhold, New York, 1967).

<sup>b</sup>Reference 2.

<sup>c</sup>Reference 6.

ab initio results reduce the creditability gap associated with Klemperer's admittedly un-tuitive prediction. A calculation of this precision cannot establish with complete certainty that X-ogen is  $\text{HCO}^+$ . A laboratory microwave measurement, the interstellar detection of an isotopic  $\text{HCO}^+$  molecule or a much larger calculation, including explicit calculation of  $B_0 - B_e$ , would be required for this purpose. Finally, we point out that our assumption<sup>†</sup> that  $2(B_e - B_0)$  for  $\text{HCO}^+$  is the same as that for the isoelectronic HCN molecule is subject to an uncertainty, perhaps as large as 0.2 GHz.

#### Footnotes and References

\*Published in Nature Phys. Sci. 246, 4 (1973).

†Present address: IBM Research Laboratory, Monterey and Cottle Roads, San Jose, California 95114.

1. D. Buhl and L. E. Snyder, Nature 228, 267 (1970).

2. W. Klemperer, Nature, 227, 1230 (1970).

3. L. E. Snyder and D. Buhl, Bull. Am. Astr. Soc. 4, 227 (1972).

4. P. K. Pearson, G. L. Blackman, H. F. Schaefer, B. Roos, and U. Wahlgren, Astrophys. J. Lett. 184, L19 (1973).

5. L. E. Sutton, Tables of Interatomic Distances and Configuration in Molecules and Ions (Chemical Society, London, 1958).

6. D. Buhl and L. E. Snyder, Astrophys. J. 180, 791 (1973).

7. M. T. Leu, M. A. Biondi, and R. Johnsen, Phys. Rev. A 8, 420 (1973).

8. W. D. Watson, Astrophys. J. Lett. 183, L17 (1973).

9. A. Dalgarno, M. Oppenheimer, and R. S. Berry, Astrophys. J. Lett. 183, L21 (1973).

10. A. Dalgarno, E. Herbst, S. Novick, and W. Klemperer, Astrophys. J. Lett. 183, L131 (1973).

11. W. D. Watson, Astrophys. J. 183, (1973).

12. K. B. Jefferts, A. A. Penzias, and R. W. Wilson, Astrophys. J. Lett. 179, L57 (1973).

13. H. F. Schaefer, The Electronic Structure of Atoms and Molecules: A Survey of Rigorous Quantum Mechanical Results (Addison Wesley, Reading, Mass., 1972).

14. B. Roos, Chem. Phys. Lett. 15, 153 (1972).

15. A. D. McLean and M. Yoshimine, Intern. J. Quantum Chem. 1S, 313 (1967).

16. A. D. McLean, in Proceedings of the Conference on Potential Energy Surfaces in Chemistry, edited by W. A. Lester, 87 (IBM Research, San Jose, Calif., 1971); P. S. Bagus, in Selected Topics in Molecular Physics, edited by E. Clementi, 187 (Berlag Chemie, Weinheim/Bergstr., Germany, 1972).

HNC MOLECULE IN INTERSTELLAR SPACE?  
SOME PERTINENT THEORETICAL CALCULATIONS\*

P. K. Pearson, G. L. Blackman, H. F. Schaefer III,  
and U. Wahlgren<sup>†</sup>

Introduction

The assignment of an emission line from the galactic sources W51 and DR21 to the HNC molecule by Snyder and Buhl<sup>1</sup> has aroused a fair amount of interest. Metz<sup>2</sup> included this development in a summary of the year's "interesting, important, and exciting activities" in physics. Since HNC has heretofore been observed only in frozen-inert-gas matrices,<sup>3</sup> study of its rotational spectrum has been impossible, and little information has been available on which to make this assignment. In fact, the assignment was made on the basis of the bond lengths which Milligan and Jacox<sup>3</sup> assumed for their studies.

In view of the difficulty of making measurements on this evanescent molecule, this emission line seems to provide a good opportunity for the illustrative use of electronic structure theory. We have, accordingly, performed ab initio calculations to determine the bond lengths, the dipole moment, and the quadrupole coupling constant for the HNC molecule.

Theoretical Approach

In the first set of calculations carried out, we adopted a (9s 5p 1d/4s 2p 1d) basis set of contracted Gaussian functions centered on the C and N atoms. For hydrogen a (4s 1p/2s 1p) basis was chosen. This sort of basis set is termed "double zeta plus polarization," and is generally reliable for predicting one-electron properties and molecular geometries within the self-consistent-field (SCF) approximation. For a fairly thorough discussion of basis sets, see the book by Schaefer.<sup>4</sup>

The equilibrium geometries of HNC and HCN within the self-consistent-field framework were determined by repeated calculation of the electronic energies with various sets of bond lengths. The calculated total energy for the predicted geometry was -92.88972 hartrees.

Calculations were performed on a Univac 1108 using the MOLE Quantum Chemistry System described by Rothenberg et al.<sup>5</sup> Each point in the geometry search required 35 to 40 minutes of computer time.

The second series of calculations began

near the linear equilibrium geometry predicted from the calculations described above. A larger basis set was used (11s 6p 1d/6s 3p 1d) on C and N and (6s 1p/3s 1p) on H. Electron correlation was taken into account using the configuration interaction (CI) method and programs developed by Roos<sup>6</sup> in Stockholm. All singly- and doubly-excited configurations with respect to the SCF configuration  $4\sigma^2 2\sigma^2 3\sigma^2 4\sigma^2 1\pi^4 5\sigma^2$  were included, a total of 6343 configurations. Assuming the linear HNC predicted above, the H-N and N-C bond distances were optimized to yield the lowest possible total energy, -93.16916 hartrees. About 25 minutes of IBM 360/195 machine time was required for a single geometry.

Results

The predicted geometries of HNC are given in Table I, together with the calculated dipole moment and nuclear quadrupole coupling constant. For reference, these quantities are also presented for HCN.

The first point to be made is that the most reliable theoretical HCN geometry, that obtained from the 6343 configuration wave functions, is in very close agreement with experiment.<sup>6</sup> This agreement, particularly for the C-N distance, is probably in part fortuitous, as we are inclined to believe that such a calculation should yield bond distances reliable only to  $\pm 0.003 \text{ \AA}$ . This latter reliability should accordingly be attached to our HNC geometry predictions.

The table shows that the calculated and experimental  $B_e$  values are nearly identical. Since only the  $B_0$  value is available for the species identified by Snyder and Buhl,<sup>1</sup> it is important to point out the relationship between  $B_0$  and  $B_e$ . From Herzberg,<sup>7</sup>

$$B_0 = B_e - \frac{1}{2} \alpha_1 - \alpha_2 - \frac{1}{2} \alpha_3$$

for HCN and HNC. Using the vibration-rotation interaction constants  $\alpha$  recommended for HCN by Herzberg,<sup>7</sup>  $B_e$  is found to be 0.19 GHz greater than  $B_0$ .

The emission signal of Snyder and Buhl<sup>1</sup> was reported at 90.665 GHz. Using the  $B_e$  value obtained for HNC by our CI calculations,

Table I. Predicted properties of HCN and HNC

	HCN			HNC	
	SCF	CI	Experiment	SCF	CI
R(C-N), Å	1.137	1.153	1.153 <sup>a</sup>	1.159	1.169
R(H-C), Å	1.063	1.068	1.066 <sup>a</sup>		--
R(H-N), Å	--	--	--	0.986	0.995
B <sub>e</sub> (GHz)	45.66	44.53	44.51 <sup>b</sup>	46.29	45.43
eq Q( <sup>14</sup> N), MHz	-3.65	--	-4.71 <sup>c</sup>	0.93	--
μ, debye	3.22	--	2.98 <sup>d</sup>	2.91	--

<sup>a</sup>Reference 6.  
<sup>b</sup>Reference 7.  
<sup>c</sup>Reference 8.  
<sup>d</sup>Reference 9.

a value of 90.86 GHz is obtained. Assuming that ( $B_e - B_0$ ) is the same for HNC as for HCN, the HNC emission is predicted to occur at 90.48 GHz. In either case the theoretical HNC line differs by about 0.2 GHz or 0.2% from that of Snyder and Buhl. Thus HNC becomes an excellent candidate for the emitting species. In this regard it is worth noting that our calculations predict HNC to lie 0.63 eV above HCN, with a substantial barrier to isomerization. In the future we hope to explore the dynamics of this simple chemical reaction in considerable detail.

Another test of this assignment would be provided by the hyperfine structure of the observed line, produced by the interaction of the

<sup>14</sup>N nuclear quadrupole moment with the electric field gradient (see Fig. 1). Our SCF calculations predict a quadrupole coupling constant  $eqQ = 0.93$  MHz [using the value of  $Q(^{14}\text{N}) = 0.016$  barn from McLean and Yoshimine<sup>10</sup> and O'Konski and Ha<sup>11</sup>]. An error of 50% must be allowed, however, in light of the expected accuracy of this sort of calculation in predicting field gradients, and the fact that the magnitude of the calculated field gradient is rather small. Nonetheless, it would be of some interest to see whether the observed line exhibits hyperfine structure consistent with a coupling constant of this sign and approximate magnitude. The figure illustrates the hyperfine structure that would be produced by a quadrupole coupling constant of 0.93 MHz.

#### Footnotes and References

\*Published in *Astrophys. J. Letters* **184**, L49 (1973).

†Present address: IBM Research Laboratory, Monterey and Cottle Roads, San Jose, California 95114.

1. L. E. Snyder and D. Buhl, *Bull. Am. Astr. Soc.* **3**, 388 (1971).

2. W. D. Metz, *Science* **179**, 670 (1973).

3. D. E. Milligan and M. E. Jacox, *J. Chem. Phys.* **39**, 712 (1963); **47**, 278 (1967).

4. H. F. Schaefer, *The Electronic Structure of Atoms and Molecules, A Survey of Rigorous Quantum Mechanical Results* (Addison Wesley, Reading, Mass., 1972).

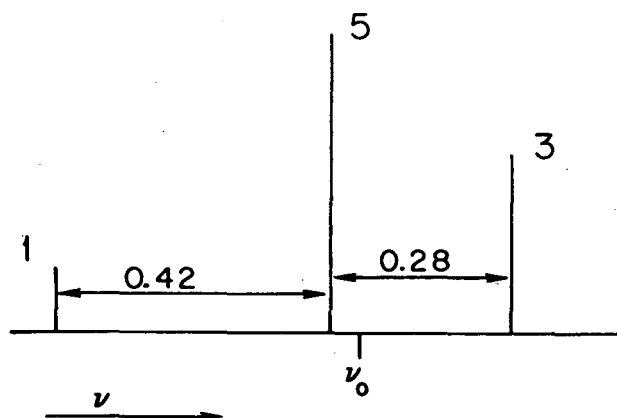


Fig. 1. Hyperfine structure of the  $J = 0 \leftarrow 1$  line of HNC, as predicted for  $eqQ(^{14}\text{N}) = 0.93$  MHz. (XBL 734-2756)

5. S. Rothenberg, P. Kollman, M. Schwartz, E. Hayes, and L. C. Allen, Intern. J. Quantum Chem. 3S, 715 (1970).
6. V. W. Laurie, and D. R. Herschbach, J. Chem. Phys. 37, 1687 (1962).
7. G. Herzberg, Electronic Spectra of Polyatomic Molecules (Van Nostrand Reinhold Company, New York, 1966).
8. F. LeLucia and W. Gordy, Phys. Rev. 187, 58 (1969).
9. R. D. Nelson, D. R. Lide, and A. A. Maryott, Selected Values of Electric Dipole Moments for Molecules in the Gas Phase, Natl. Std. Ref. Data Ser-NBS 10 (U. S. Govt. Printing Office, Washington, D. C., 1967).
10. A. D. McLean and M. Yoshimine, Bull. Am. Phys. Soc. 13, 373 (1968).
11. C. T. O'Konski and T.-K. Ha, J. Chem. Phys. 49, 5354 (1968).

### PROBABLE NONEXISTENCE OF XENON MONOFLUORIDE AS A CHEMICALLY BOUND SPECIES IN THE GAS PHASE\*

D. H. Liskow, H. F. Schaefer III, P. S. Bagus<sup>†</sup> and B. Liu<sup>†</sup>

The long-range interaction between Xe and F may be expressed as the sum of two terms:<sup>1</sup> a) the induction energy due to the permanent quadrupole moment of the F atom and the polarizability of the Xe atoms and b) the dispersion attraction due to the polarizabilities of the two atoms. Assuming no chemical attraction between Xe and F, the long-range terms will yield an attractive potential well similar to that found<sup>2</sup> for Xe - Ne, where the bond distance  $r_e(\text{Xe} - \text{Ne})$  is 3.8 Å, and the dissociation energy  $D_e$  is 0.15 kcal/mol.

However, following the discovery of XeF<sub>2</sub>, XeF<sub>4</sub>, and XeF<sub>6</sub> during the past decade, many workers have assumed<sup>3</sup> that XeF is a chemically bound species, with a dissociation energy of ~ 20 kcal/mol. This assumption is based in large part on the electron spin resonance (ESR) experiments of Falconer and Morton.<sup>4</sup> They reported the ESR spectrum of XeF in crystals of XeF<sub>4</sub> subjected to  $\gamma$  radiation at 77° K. Furthermore, kinetic studies have suggested the existence of XeF as an intermediate in water oxidation<sup>5</sup> and in NO and NO<sub>2</sub> oxidation<sup>6</sup> by XeF<sub>2</sub>. Finally, it is thought<sup>7, 8</sup> that the decomposition of both XeF<sup>+</sup>OsF<sub>6</sub><sup>-</sup> and FXeOSO<sub>2</sub>F involves the XeF radical.

In the present communication we report the results of *ab initio* electronic structure calculations on the lowest  $2\Sigma^+$  and  $2\Pi$  states of XeF. This study is the logical extension of our earlier work<sup>9, 10</sup> on the krypton fluorides. The chosen basis set of Slater-type functions centered on Xe and F is shown in Table I. The properties of the F atom basis are well understood.<sup>9-11</sup> For the  $1S$  ground state of the Xe

atom, the present basis yields a self-consistent-field (SCF) energy of -7232.1204 hartrees, which may be compared to the numerical Hartree-Fock results of Mann,<sup>12</sup> -7232.14 hartrees, and Fischer,<sup>13</sup> -7232.153 hartrees. In either case, it is seen that the present basis set for xenon yields an SCF total energy within 1 eV of the nonrelativistic Hartree-Fock limit.

The present calculations were carried out using the ALCHEMY program.<sup>14</sup> Xe plus F( $2P_u$ ) can give rise to electronic states of  $2\Sigma^+$  and  $2\Pi$  symmetry, and single-configuration SCF calculations were carried out for both states. The internuclear separations chosen ranged from 3.0 bohrs (1 bohr = 0.5292 Å) to 10.0 bohrs. In addition, a wide variety of configuration interaction (CI) calculations were carried out for the  $2\Sigma^+$  ground state. Of these CI calculations, only results from the first-order wavefunctions are given. Detailed descriptions of the first-order wavefunction have been given elsewhere.<sup>9-11</sup> Our wavefunction included all configurations in which not more than one of the 11 valence electrons occupied an orbital beyond the valence shell. The valence shell consisted of all molecular orbitals which correlated in the separated atom limit with the 2p orbital of F and the 5p orbital of Xe. For  $2\Sigma^+$  XeF, using the basis set described earlier, there were 354 configurations in this first-order wavefunction. The most extensive wavefunction investigated contained 2142 configurations, including in addition all double excitations from the occupied valence  $\sigma$  orbitals. However, the qualitative result was the same as that found with the first-order wavefunction.

Table I. Basis set of Slater functions,  $r^{n-1} e^{-\zeta r}$ , for calculations of xenon fluorides

Atom	Type	Orbital $\zeta$	Exponent
Xe	1s	55.110	
	1s	36.545	
	2s	26.283	
	2s	22.451	
	3s	14.881	
	3s	12.067	
	4s	7.620	
	4s	5.566	
	5s	3.518	
	5s	2.173	
	2p	30.678	
	2p	21.424	
	3p	13.721	
	3p	10.709	
	4	7.422	
	4p	5.036	
	5p	3.516	
	5p	2.016	
	3d	20.469	
	3d	11.964	
4d	7.727		
4d	5.233		
4d	3.379		
5d	2.0		
5d	1.2		
4f	3.5		
4f	2.5		
F	1s	11.011	
	1s	7.917	
	2s	3.096	
	2s	1.946	
	2p	6.165	
	2p	3.176	
	2p	1.612	
	3d	4.0	
	3d	2.0	
	4f		

Figure 1 summarizes our results for diatomic XeF. There it is seen that both the  $2\Sigma^+$  state yields a significantly less repulsive curve. However, even in the latter case, the  $2\Sigma^+$  ground state is repulsive by ~20 kcal/mol at the experimental XeF<sub>2</sub> bond distance, 2.117 Å = 4.0 bohrs, the potential curve is repulsive by 10 kcal/mol. Thus it is clear that the present theoretical study predicts XeF to be a bound species only in the van der Waals sense of our first paragraph. That is, we predict no chemical bond between Xe and F.

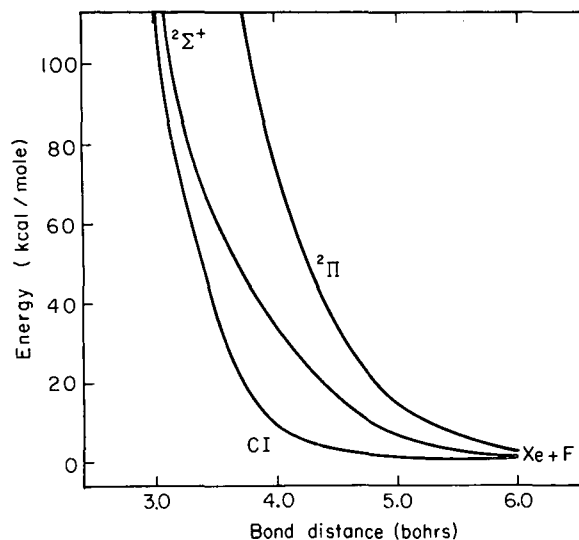


Fig. 1. Potential energy curves for xenon monofluoride. The curves labeled  $2\Sigma^+$  and  $2\Pi$  are the results of single-configuration SCF calculations. The curve labeled CI refers to the 354 configuration first-order wavefunctions. The potential curves have been shifted to yield the same dissociation limit,  $X(1S) + F(2P_u)$ . (XBL 731-2079)

Since the experiments of Falconer and Morton<sup>4</sup> were carried out in the solid state, it is conceivable that there is no conflict between their work and ours. For example, the dissociative XeF radical might somehow be trapped in the XeF<sub>4</sub> crystal long enough to produce an ESR spectrum.

It should be noted that preliminary elastic scattering molecular beam experiments by Lee<sup>15</sup> support our contention that XeF is not a chemically bound species. Finally, Klemperer<sup>16</sup> plans to determine the dipole moment of XeF using recently developed methods for studying van der Waals-bound molecules. A small dipole moment ( $\leq 0.1$  debye) would be consistent with the present theoretical results.

#### Footnotes and References

\* Published in J. Amer. Chem. Soc. **95**, 4056 (1973).

† Permanent address: IBM Research Laboratory, Monterey and Cottle Roads, San Jose, California 95114.

1. J. O. Hirschfelder, C. F. Curtiss, and R. B. Bird, Molecular Theory of Gases and Liquids (Wiley, New York, 1954).

2. J. M. Parson, T. P. Schafer, F. P. Tully, P. E. Siska, Y. C. Wong, and Y. T. Lee, *J. Chem. Phys.* **53**, 2123 (1970).
3. N. Bartlett and F. O. Sladky, *The Chemistry of Krypton, Xenon, and Radon*, in *Comprehensive Inorganic Chemistry* (Pergamon Press, London, 1973).
4. W. E. Falconer and J. R. Morton, *Proc. Chem. Soc. (London)* 1963, **95**; J. R. Morton and W. E. Falconer, *J. Chem. Phys.* **39**, 427 (1963).
5. V. A. Legasov, V. N. Prusakov, B. B. Chaivanov, *Russ. J. of Phys. Chem.* **42**, 610 (1968).
6. H. S. Johnston and R. Woolfolk, *J. Chem. Phys.* **41**, 269 (1964).
7. F. O. Sladky, P. A. Bulliner, and N. Bartlett, *J. Chem. Soc. (London)* **1969**, 2179.
8. M. Wechsberg, P. A. Bulliner, F. O. Sladky, R. Mews, and N. Bartlett, *Inorg. Chem.* **11**, 3063 (1972).
9. B. Liu and H. F. Schaefer, *J. Chem. Phys.* **55**, 2369 (1971).
10. P. S. Bagus, B. Liu, and H. F. Schaefer, *J. Am. Chem. Soc.* **94**, 6635 (1972).
11. H. F. Schaefer, *The Electronic Structure of Atoms and Molecules: A Survey of Rigorous Quantum Mechanical Results* (Addison-Wesley, Reading, Mass., 1972).
12. J. B. Mann, Los Alamos Scientific Laboratory Report LA-3690, July 1967.
13. C. F. Fischer, *Some Hartree-Fock Results for the Atoms Helium to Radon*, Department of Mathematics, University of British Columbia, January 1968.
14. A system of programs developed by B. Liu, M. Yoshimine, P. S. Bagus, and A. D. McLean. For a description see: a) A. D. McLean, p. 87 in *Proceedings of the Conference on Potential Energy Surfaces in Chemistry* (RA18, IBM Research Laboratory, San Jose, Calif., 1971); b) P. S. Bagus, p. 187 in *Selected Topics in Molecular Physics* (Verlag Chemie, Weinheim/Bergstr., Germany, 1972).
15. Y. T. Lee, personal communication.
16. W. Klemperer, personal communication.

## POTENTIAL ENERGY SURFACES FOR SIMPLE CHEMICAL REACTIONS

### H. F. Schaefer III

During the past year, an area of particular emphasis within the Berkeley Electronic Structure Theory Group has been the prediction of potential surfaces for reactive systems. Only within the past two years has it become possible to make reliable *a priori* calculations of surfaces for systems with more than three or four electrons.

#### Simplest Halogen Atom Plus Alkali Dimer Potential Surface: $F + Li_2 \rightarrow LiF + Li$

Rigorous electronic-structure calculations have been carried out to investigate some features of the potential energy surface for the chemical reaction  $F + Li_2 \rightarrow LiF + Li$ . The basis set of contracted Gaussian functions was of "double zeta plus polarization" quality, with an additional set of p functions on F added to describe  $F^-$ . Single-configuration and two-configuration self-consistent-field calculations are reported here. A minimum energy path was obtained for the collinear reaction, but the

most important feature determined was the nature of the potential minimum due to the  $FLi_2$  complex. For linear  $F-Li-Li$ , this complex is bound by 4 kcal/mol relative to separated  $LiF + Li$ . The attraction is much stronger, 34 kcal, for  $C_{2v}$  geometry, and this species is predicted to have a bond angle of  $99^\circ$  and  $Li-F$  bond distance of 1.79 Å. Several excited electronic states of  $FLi_2$  are discussed briefly. A contour map of the linear potential surface is shown in Fig. 1.

#### Avoided Intersection of Potential Energy Surfaces: The $(H^+ + H_2, H + H_2^+)$ System

Nonempirical electronic structure calculations have been carried out on the two lowest  $^1A_1$  states of  $H_3^+$ . When one proton is infinitely separated from the other two, these  $^1A_1$  potential surfaces cross each other. The nature of this avoided intersection is examined by means of potential curves, contour diagrams, and perspective plots (see Figs. 2 and 3).



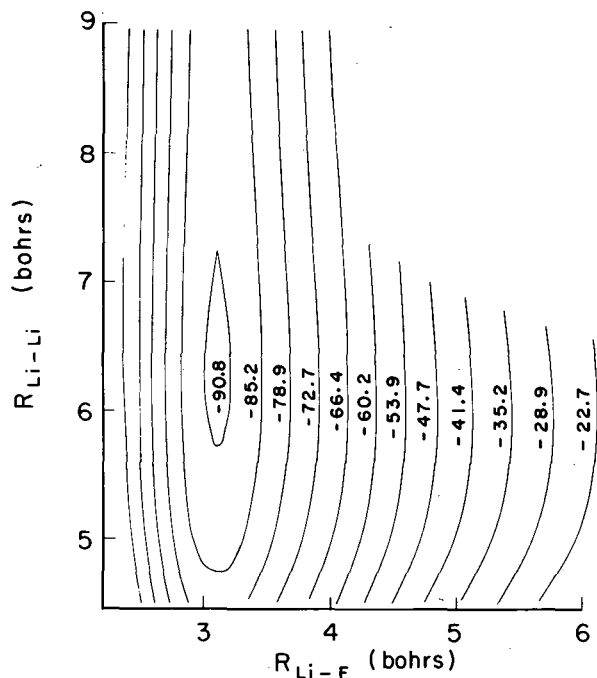


Fig. 1. Collinear contour map for the F-Li-Li potential energy surface in the self-consistent-field approximation. (XBL 7211-4393)

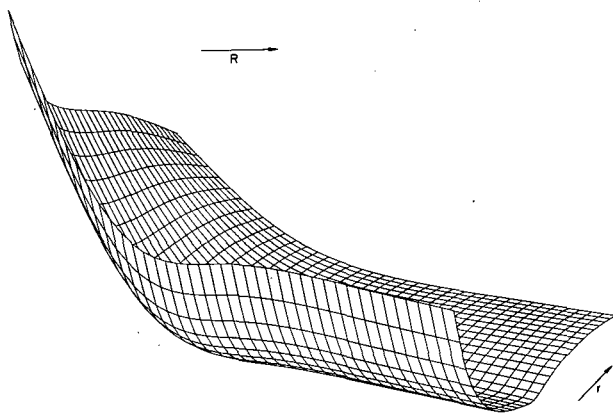


Fig. 2. Perspective plot of the lowest  $^1A_1$  potential energy surface of  $H_3^+$ . (XBL 733-2469)

Surface hopping is discussed within a Landau-Zener-Stuckelberg (LZS) framework, and the LZS assumptions concerning the surfaces are shown to be reasonable near the avoided intersection. *Ab initio* LZS parameters are compared with those obtained from the semiempirical diatomics-in-molecules surfaces of Preston and Tully. The agreement is good, better than might have been anticipated.

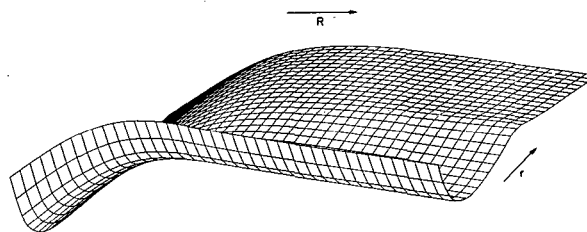


Fig. 3. Perspective plot of the first excited  $^1A_1$  potential surface of  $H_3^+$ . (XBL 733-2468)

Potential Energy Surfaces Related to the Ion-Molecule Reaction  $C^+ + H_2$  (Ref. 3)

The  $C^+ + H_2$  ion-molecule reaction has been studied by several experimental groups and appears destined to become the focal point of much experimental and theoretical activity. *Ab initio* self-consistent-field and configuration interaction calculations have accordingly been carried out for this system. A double zeta basis set of contracted Gaussian functions was employed and as many as 570 configurations included. For isosceles triangle configurations ( $C_{2v}$  point group) the  $^2A_1$ ,  $^2B_1$ , and  $^2B_2$  potential surfaces were considered, while for linear geometries ( $C_{\infty v}$ ) the  $^2\Sigma^+$  and  $^2\Pi$  surfaces were studied. Properties reported include minimum energy paths and energy profiles (see, for example, Fig. 4) for the various processes considered. The intuitive correlation diagram of Mahan and Sloane is made semiquantitative in reliability. Pathways of  $CH_2^+$  complex formation will depend crucially on the  $C_s$  potential surface.

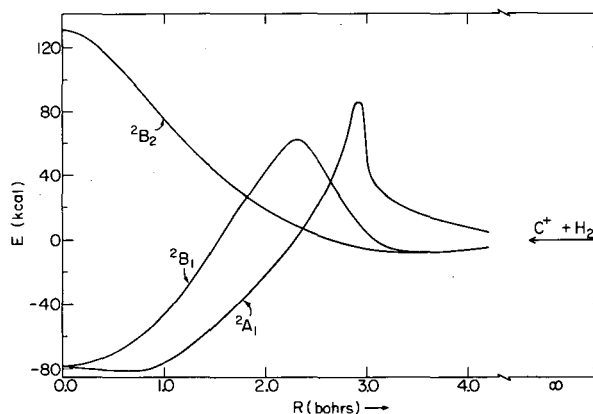
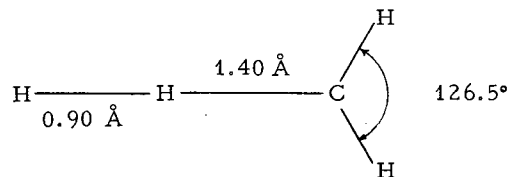


Fig. 4. Energy profiles along the  $C_{2v}$  minimum energy paths for  $C^+ + H_2 \rightarrow CH_2^+$ . (XBL 7310-4163)

Reaction Pathways for the Triplet Methylene  
Abstraction  $\text{CH}_2(^3\text{B}_1) + \text{H}_2 \rightarrow \text{CH}_3 + \text{H}$  (Ref. 4)

A theoretical study of the reaction of triplet methylene with molecular hydrogen has been carried out. A contracted Gaussian basis set of double zeta quality was employed. Following the determination of each self-consistent-field wavefunction, configuration interaction was performed including all singly- and doubly-excited configurations (a total of 649). The potential surface was studied in three dimensions and a total of 780 points computed. From these data, several approximations to the minimum energy path have been computed and compared. The reaction exothermicity is computed to be 5.37 kcal/mol, in good agreement with experiment, 4.5 kcal/mol. The predicted barrier height is 15.5 kcal/mol, a result consistent with the lack of any observed reaction between  $\text{CH}_2(^3\text{B}_1)$  and  $\text{H}_2$  at 300°K. The predicted barrier is 4.2 kcal/mol less than that obtained by Carr using the bond-energy bond-order (BEBO) method. The saddle-point geometry is predicted to be



References

1. P. K. Pearson, W. J. Hunt, C. F. Bender, and H. F. Schaefer, *J. Chem. Phys.* **58**, 5358 (1973). Also LBL-1605.
2. C. W. Bauschlicher, S. V. O'Neil, R. K. Preston, H. F. Schaefer, and C. F. Bender, *J. Chem. Phys.* **59**, 1286 (1973). Also LBL-1664.
3. D. H. Liskow, C. F. Bender, and H. F. Schaefer, *J. Chem. Phys.* **60**, (1974). Also LBL-2302.
4. C. P. Baskin, C. F. Bender, C. W. Bauschlicher, and H. F. Schaefer, *J. Am. Chem. Soc.* **96**, (1974). Also LBL-2324.

## ELECTRONIC STRUCTURE OF SIMPLE INORGANIC MOLECULES

H. F. Schaefer III

The purpose of this article is to summarize theoretical work carried out at Berkeley during the past year<sup>1-7</sup> on the electronic structure of inorganic molecules. Our theoretical studies are a priori in that they involve the rigorous application<sup>8</sup> of the variational principle to Schrödinger's equation within the Born-Oppenheimer approximation.

### Iron Trifluoride<sup>1</sup>

We first discuss the neutral molecule  $\text{FeF}_3$ . An essentially "double zeta" basis set of contracted Gaussian functions was used. Calculations were carried out for three different F-Fe-F angles, 120°, 109.471°, and 90°. The high-spin  $^6\text{A}_1$  state is predicted to be the ground state and have a planar or nearly planar equilibrium geometry. For planar geometry, the low-spin  $^2\text{A}_1$  state is predicted to lie 7.66 eV above the high-spin state. A Walsh-like analysis (see Fig. 1) is used to discuss the possible geometries of other transition metal trifluorides. The electronic structure is further discussed on the basis of Mulliken populations, and a variety of molecular properties are reported.

### Status of Ab Initio Molecular Structure Predictions

In a review article presented at the Dartmouth conference on the Critical Evaluation of Chemical and Physical Structural Information, I surveyed the reliability of molecular geometries predicted from quantum mechanical electronic structure calculations. Given a modest amount of information about the basis set and from of the wavefunction (self-consistent-field or some type of configuration interaction), one can reasonably estimate the expected geometrical uncertainties. These guidelines are discussed with respect to several examples for which accurate experimental data are available including the  $\text{C}_3$  hydrocarbons, the  $\text{CH}_3\text{NC}$  and  $\text{CH}_3\text{CN}$  molecules, and the diatomics  $\text{CH}$  and  $\text{CH}^+$ . Finally some recent purely predictive studies of the Berkeley electronic structure group were described. The molecules discussed include  $\text{LiO}_2$ ,  $\text{FeF}_3$ ,  $\text{HF}_2$ ,  $\text{XeF}$ , and  $\text{HNC}$ .

### Geometry of the $\text{LiO}_2$ Radical<sup>3</sup>

Quantum mechanical calculations have been

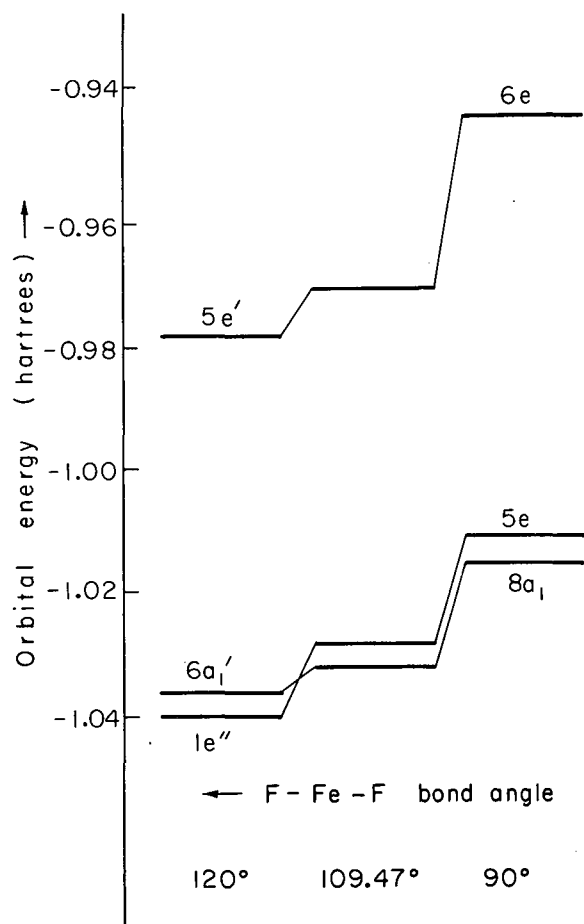


Fig. 1. Diagram of  $\text{FeF}_3$  orbital energies for those orbitals corresponding to the d-orbitals of  $\text{Fe}^{3+}$  in a crystal field picture.

(XBL 7211-4373)

carried out for the two lowest electronic doublet states of the lithium dioxide molecule. The results are pertinent to possible crossed molecular beam experiments and to matrix isolation spectroscopy. A qualitative discussion of the electronic structure changes accompanying the  $\text{Li} + \text{O}_2$  and  $\text{LiO} + \text{O}$  reactions is given. For the quantitative calculations, a contracted Gaussian basis set was used, designated  $\text{Li} (9s\ 4p/4s\ 2p)$ ,  $0 (9s\ 5p/4s\ 3p)$ . For isosceles triangle configurations, the  ${}^2A_2$  state is the electronic ground state, with equilibrium geometry  $r(\text{LiO}) = 1.82\ \text{\AA}$  and  $\theta(\text{O-Li-O}) = 44.5^\circ$ . The  ${}^2B_2$  state is predicted to lie 14 kcal/mol higher with  $r(\text{LiO}) = 1.76\ \text{\AA}$ , and  $\theta(\text{O-Li-O}) = 46.5^\circ$ . For  $C_{\infty v}$  geometry the  ${}^2\Pi$  state bond distances were predicted,  $R(\text{Li-O}) = 1.62\ \text{\AA}$  and  $R(\text{O-O}) = 1.35\ \text{\AA}$ . There appears to be little or no barrier between the  $C_{2v}$  and  $C_{\infty v}$  forms.

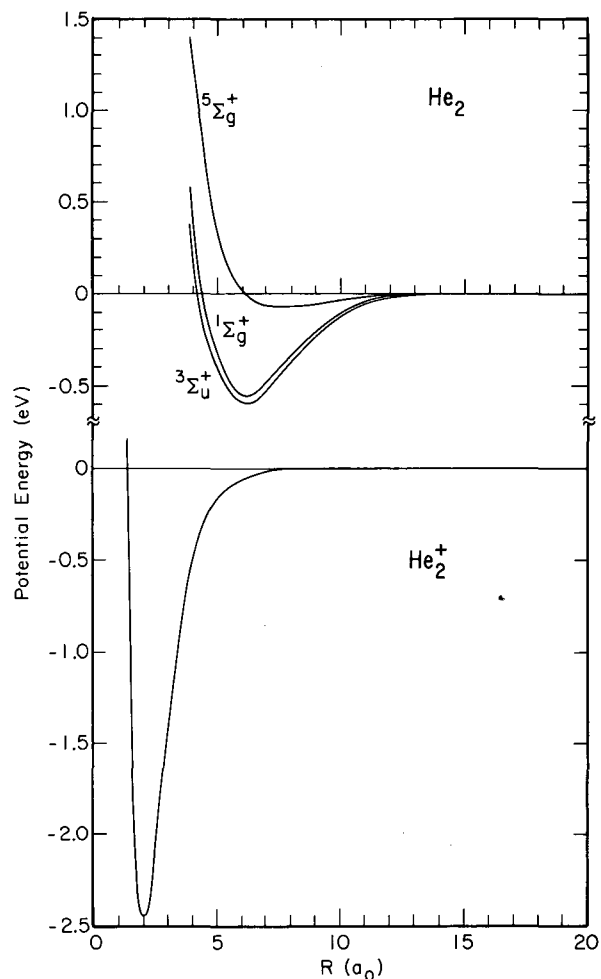


Fig. 2. Potential energy curves for the ground state of  $\text{He}_2^+$  and the states of  $\text{He}_2$  arising from two  $1s2s^3S$  He atomic states. (XBL 735-6092)

#### Penning and Associative Ionization of Triplet Metastable Helium Atoms<sup>4</sup>

Potential energy curves for the  $1\Sigma_g^+$ ,  $3\Sigma_u^+$ , and  $5\Sigma_g^+$  states which arise from two triplet metastable helium atoms ( $1s2s^3S$ ) have been calculated by a large configuration interaction expansion and are seen in Fig. 2. From the potential curves for the  $1\Sigma_g^+$  and  $3\Sigma_u^+$  auto-ionizing states, cross sections for Penning and associative ionization have been calculated; the total ionization cross section for thermal energy (0.026-eV) collisions, for example, is computed to be  $94\ \text{\AA}^2$ . In this low-energy region the orbiting model is seen to be adequate for determining the total ionization cross section, but not the more specific cross sections.

Interaction Potential Between Two  
Rigid HF Molecules<sup>5</sup>

As a prelude to the study of energy transfer in the HF-HF system, the potential energy surface for the interaction of two rigid HF molecules has been calculated within the ab initio self-consistent-field framework. A  $H(4s\ 1p/2s\ 1p)$ ,  $F(9s\ 5s\ 1d/4s\ 2p\ 1d)$  basis set of contracted Gaussian function was employed. The number of unique points on the surface is greatly reduced by symmetry, and only 294 points were required to give a fairly complete description of the four-dimensional surface. The coordinate system chosen is given in Fig. 3. Parts of the surface are illustrated by a series of contour maps, one of which is seen in Fig. 4. Some preliminary attempts to fit the surface to an analytic form are described. The equilibrium geometry of  $(HF)_2$  is predicted.

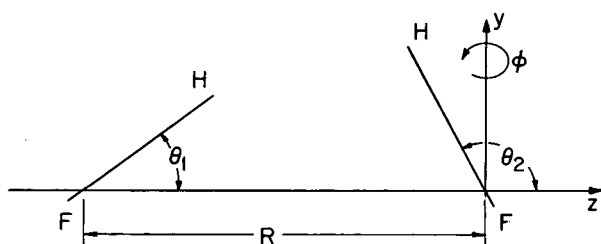


Fig. 3. Coordinate system chosen for HF-HF.  $R$  is the distance between the two HF centers of mass. The angle  $\phi$  is defined with respect to the indicated  $y$  axis;  $\phi$  is the angle of rotation of the right-hand HF molecule about this  $y$  axis. (XBL 738-3761)

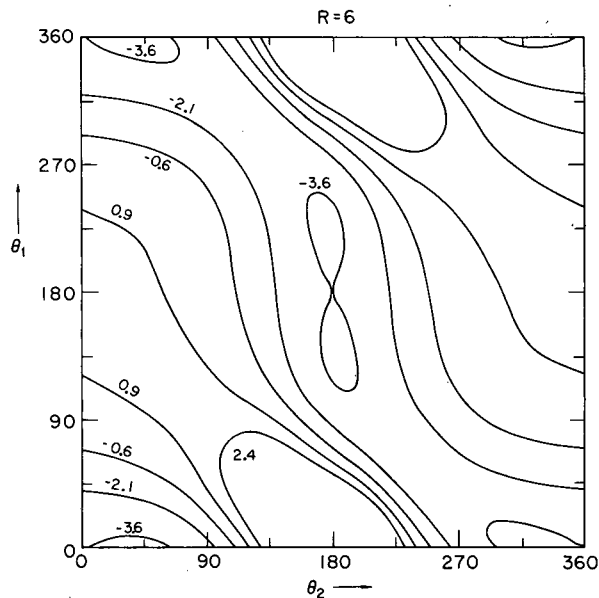


Fig. 4. Contour map of that part of the HF-HF potential surface with  $R = 6$  bohrs and  $\phi = 0^\circ$  (planar).  $\theta_1$  and  $\theta_2$  are defined in Fig. 3, and contours are marked in kcal/mol relative to two infinitely separated HF molecules. Each HF molecule has fixed internuclear separation 1.723 bohrs. XBL 737-3456

Distortion of Atomic Orbitals Within Molecules<sup>6</sup>

The importance of the flexibility of atomic orbitals in a molecular environment has been investigated for several phosphorous-containing diatomic molecules. The results, summarized in Table I, indicate the degree to which atomic Hartree-Fock orbitals are suitable for molecular electronic structure studies.

Table I. Summary of results for PH, PC, PN, PO, and PF. Except for hydrogen in PH, a  $(5s\ 4p/2s\ 1p)$  basis was used for each lighter atom. Energies are given in kcal/mol relative to the fully contracted result.

Phosphorous basis set	PH	PC	PN	PO	PF
Bond distance ( $\text{\AA}$ )	1.533	1.558	1.491	1.473	1.590
$(7s\ 5p/3s\ 2p)$	0.00	0.00	0.00	0.00	0.00
$(7s\ 5p/4s\ 3p)$	-6.79	-26.85	-38.37	-35.86	-19.91
$(7s\ 5p/5s\ 4p)$	-7.57	-28.06	-39.79	-37.09	-20.58
$(7s\ 5p/6s\ 5p)$	-7.61	-28.66	-40.42	-37.60	-21.20

Table II. Summary of *ab initio* predictions for the triplet states of HCN.  
(Bond distances are given in Å.)

Symmetry	$T_e$ (eV)	$r_e$ (HC)	$R_e$ (CN)	$\theta_e$ (HCN)	Most important configurations	Coef- ficients
$1^3A'$	4.42	1.081	1.294	128.6	$5a'^2$ $6a'$ $1a''^2$ $7a'$	0.9548
$1^3A''$	5.46	1.099	1.365	117.0	$5a'^2$ $6a'^2$ $1a''$ $7a'$	0.9673
$2^3A'$	5.91	1.063	1.320	160.0	$5a'^2$ $6a'^2$ $1a''$ $2a''$	0.8400
					$5a'^2$ $6a'$ $1a''^2$ $7a'$	0.5200
$2^3A''$	6.85	1.061	1.314	157.4	$5a'^2$ $6a'$ $1a''^2$ $2a''$	0.8285
					$5a'^2$ $6a'^2$ $1a''$ $7a'$	0.4951
$3^3A'$	6.98	1.081	1.250	132.6	$5a'$ $6a'^2$ $1a''^2$ $7a'$	0.8794
					$5a'^2$ $6a'^2$ $1a''$ $2a''$	0.3689
$3^3A''$	7.41	1.045	1.237	180	$5a'$ $6a'^2$ $1a''^2$ $2a''$	0.9537

#### Geometries of the Excited Electronic States of HCN<sup>7</sup>

Nonempirical electronic structure calculations have been carried out for the ground state and 12 low-lying ( $< 10$ -eV) excited states of HCN. A contracted Gaussian basis set of essentially double zeta quality was employed. A new theoretical approach, which should be widely applicable, was applied to the excited electronic states. First one selects a physically meaningful set of orbitals, which, hopefully, will be about equally suitable for all the electronic states of interest. After selecting a single configuration to describe each electronic state, configuration interaction is performed including all configurations differing by one orbital from any of the selected reference configurations. The method appears to be one of the simplest capable of treating several states of the same symmetry. The predicted geometries have been compared with the experimental results of Herzberg and Innes, as well as the appropriate Walsh diagram. The *ab initio* calculations and the Walsh diagram concur that Herzberg and Innes's assignment of the  $\tilde{B}^1A''$  state, with bond angle  $114.5^\circ$ , is incorrect. Although the theoretical predictions are in several cases at variance with the Walsh diagram, these differences can in most cases be justified in terms of a breakdown of the single-configuration picture of electronic structure. One modification of Walsh's diagram is suggested, a change in the shape of the  $5a'$  orbital binding energy. Without this modification, the Walsh prediction is in serious disagreement with Herzberg and Innes's  $141^\circ$  bond angle for the  $\tilde{C}^1A'$  state. The present theoretical study predicts a bond

angle of  $141.2^\circ$  for the third  $^1A'$  electronic state of HCN. The triplet state results are summarized in Table II.

#### References

1. R. W. Hand, W. J. Hunt, and H. F. Schaefer, *J. Amer. Chem. Soc.* **95**, 4517 (1973). Also LBL-1632.
2. H. F. Schaefer, *Advances in Chemistry* \_\_, (1974).
3. S. V. O'Neil, H. F. Schaefer, and C. F. Bender, *J. Chem. Phys.* **59**, 3608 (1973). Also LBL-1913.
4. B. J. Garrison, W. H. Miller, and H. F. Schaefer, *J. Chem. Phys.* **59**, 3193 (1973). Also LBL-1825.
5. D. R. Yarkony, S. V. O'Neil, H. F. Schaefer, C. P. Baskin, and C. F. Bender, *J. Chem. Phys.* **60**, (1974). Also LBL-1969.
6. C. W. Bauschlicher and H. F. Schaefer, *Chem. Phys. Letters* **23**, (1974).
7. G. M. Schwenzer, S. V. O'Neil, H. F. Schaefer, C. F. Baskin, and C. F. Bender, *J. Chem. Phys.* **60**, (1974). Also LBL-1983.
8. H. F. Schaefer, *The Electronic Structure of Atoms and Molecules: A Survey of Rigorous Quantum Mechanical Results* (Addison-Wesley, Reading, Mass., 1972).

## ESCA\*

D. A. Shirley

A comprehensive review article on electron spectroscopy was written for the review series *Advances in Chemical Physics*. The article was too lengthy and detailed to describe in a short report, but an outline appears below.

A

- I. Introduction
- II. Chemical Shifts in Core Electron Binding Energies
  - II. A. General Comments
  - II. B. Theoretical Descriptions Based on the Calculation of Binding Energies
    - II. B. 1. Methods Involving Both Initial and Final States
      - II. B. 1.a. General Background
      - II. B. 1.b. Results for Atoms and Ions
      - II. B. 1.c. Results for Molecules
    - II. B. 2. Methods Involving the Initial State Only
      - II. B. 2.a. Connection Between Hole-State and Frozen-Orbital Calculations
      - II. B. 2.b. Comparison of Orbital Energy Differences with Experiment
  - II. C. Quantum-Mechanical Methods Not Involving Binding-Energy Calculations
    - II. C. 1. Potential Models
    - II. C. 2. The ACHARGE Approach
    - II. C. 3. Atomic Charge Correlations
    - II. C. 4. Thermochemical Estimates

- II. D. Correlations of Binding-Energy Shifts with Other Properties
  - II. D. 1. Correlations with Other Binding Energy Shifts
  - II. D. 2. Correlations with Diamagnetic Shielding Constants
  - II. D. 3. Correlations with "Pauling Charges" and Electronegativity
  - II. D. 4. Correlations with "Group Shifts"

B

- III. Valence-Shell Structure
  - III. A. Introduction
  - III. B. Valence Bands in Metals
  - III. C. Valence Orbitals: Cross Sections
  - III. D. Valence Orbitals in Inorganic Anions
- IV. Multiplet Splitting
  - IV. A. Introduction
  - IV. B. Multiplet Splitting in Atoms
  - IV. C. Multiplet Splitting in Molecules
  - IV. D. Multiplet Splitting in Salts
  - IV. E. Multiplet Splitting in Metals

The main purpose of this article was to summarize the theoretical situation regarding chemical shifts in core-electron binding energies as of early 1972, based on the literature published up to that time. To this end the various theoretical methods then available for calculating core-level shifts were classified according to a general scheme, from the most rigorous approaches including relaxation energies through "potential model" theories, to schemes based on such empirical concepts as electronegativity. When the theoretical methods were thus arrayed their similarities could be discerned, and several enlightening relationships emerged.

One example will be given. Thomas<sup>1</sup> found an excellent correlation between core-level shifts and ligand electronegativities. When one attempts to put this relation on a quantitative base by relating core-level shifts to "Pauling charges" as determined from Pauling's electronegativity-ionicity equation

$$I = 1 - \exp[-0.25(X_A - X_B)^2], \quad (1)$$

however, the correlation disappears. The reason for this is that the ionicity appears to be linearly related to the electronegativity. We propose the relation

$$I = 0.129 (X_A - X_B). \quad (2)$$

With Eq. (2) we can reconcile the electronegativity with the potential model, obtaining for the C(1s) binding-energy shifts in halogenated methanes the equation

$$\begin{aligned} \Delta E_B &= k \Delta q_C + \Delta V \\ &= (22)(0.129) \sum_{i=1}^4 (X_x(i) - X_H) - e^2(0.129) \\ &\times \left[ \sum_{i=1}^4 \left( \frac{X_x(i) - X_C}{R_{CX}} \right) - \frac{4(X_H - X_C)}{R_{CH}} \right]. \quad (3) \end{aligned}$$

Shifts based on this equation are plotted, together with experimental shifts, in Fig. 1. This approach combines the advantages of preserving the excellent agreement found by Thomas and of giving both a quantitative relationship between  $\Delta E_B$  and a reasonable set of

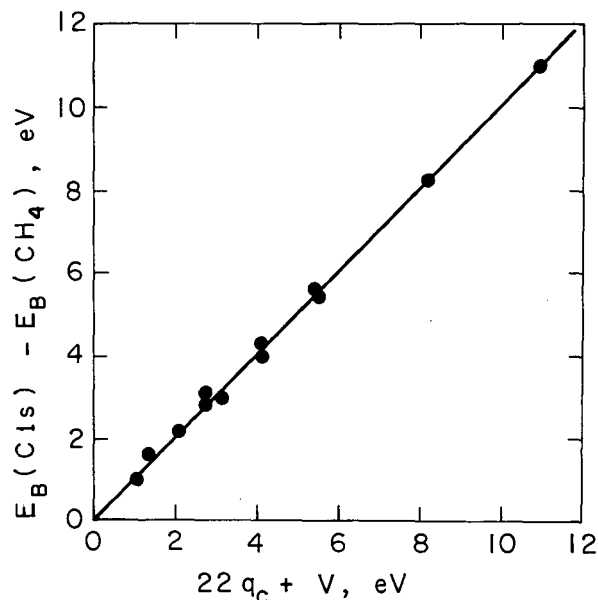


Fig. 1. Binding energy shifts in halomethanes versus predictions of a potential model based on Eqs. (2) and (3). (XBL 721-2243)

charges on the carbon atom. We conclude, therefore, that Eq. (2) gives a better measure of ionicity than does Eq. (1).

#### Footnote and References

\* Condensed from LBL-610 and D. A. Shirley, *Advan. Chem. Phys.* 23, 85 (1973).

1. T. D. Thomas, *J. Am. Chem. Soc.* 92, 4184 (1970).

### X-RAY PHOTOEMISSION STUDY OF Gd, Tb, AND Dy 4f AND VALENCE BANDS

F. R. McFeely, S. P. Kowalczyk, L. Ley,  
and D. A. Shirley

High-resolution 4f-shell and valence-band spectra of metallic Gd, Tb, and Dy have been observed under ultrahigh vacuum conditions ( $8 \times 10^{-11}$  Torr). Detailed structure in the 4f-shell final states identifies the transitions as ( $4f^7 \rightarrow 4f^6$ ) in Gd, ( $4f^8 \rightarrow 4f^7$ ) in Tb, and ( $4f^9 \rightarrow 4f^8$ ) in Dy, thereby further confirming the tripositive character of the ion cores in

rare earth metals. However, large differences were observed in the valence-band spectra of these three metals, in contrast to the very similar initial-state densities obtained from APW calculations.<sup>1</sup> In the Gd valence-band spectrum a peak appears near the Fermi energy  $E_F$ , while both Tb and Dy show free-electron-like plateaus.

Valence-band and 4f spectra are shown in Fig. 1. The use of monochromatized Al  $K\alpha_{1,2}$  x-rays permitted direct observation of the Fermi edge and resolution of valence-band and 4f structural features not observed in previous

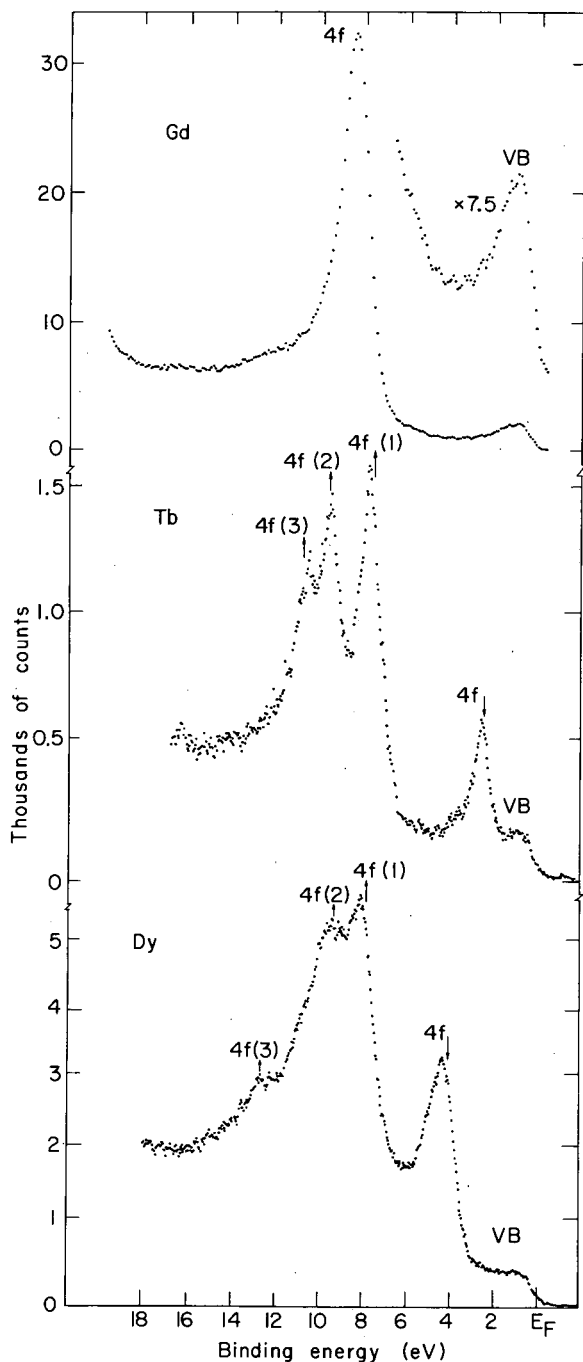


Fig. 1. X-ray photoemission spectra of the 4f and valence band region of Gd, Tb, and Dy. (XBL 736-3185)

XPS studies of rare-earth metals<sup>2</sup> and trifluorides.<sup>3</sup> The results of Hagström and co-workers<sup>2</sup> on these metals were completely confirmed. The overall shapes and energy spacings of the 4f peaks agreed well with the trifluoride results of Wertheim, et al.,<sup>3</sup> which were used diagnostically in conjunction with optical data.<sup>4</sup>

Table I lists the binding energies of major features in the spectra and final-state assignments for the 4f peaks. The relative positions of the component 4f peaks in each spectrum agree well with optical levels, which have been assigned up to  $40,000\text{ cm}^{-1}$  (5 eV). The peaks are spaced slightly more widely in the XPS spectra, as expected, because the ionic charge in the  $Z^{4+}(4f^n)$  final state is one greater than for the comparison optical ion ( $Z=1$ )<sup>3+</sup>(4f<sup>n</sup>). Herbst, Lowy, and Watson<sup>5</sup> have thoroughly discussed the absolute binding energies of 4f electrons in rare-earth metals. Our 4f binding energies agree well with their calculated values. The 4f binding energies agree well for Tb but there is a discrepancy of about 0.8 eV for Gd and Dy with earlier experimental work.<sup>2</sup> This is probably due to the fact that we could not determine the Fermi level directly. We have also independently estimated a relaxation energy<sup>6</sup> of 7-10 eV for 4f photoemission from rare-earth metals, in good agreement with their quantity ( $\Delta - \epsilon_{4f}$ ). It should be emphasized that the 4f structure that appears practically in the valence bands in the spectra in Fig. 1 isn't really there in the initial-state density, where the 4f shell would be a single peak ~10 eV further below  $E_F$ . The 4f hole states are "intruders" that invade the valence-band region on photoemission via a larger relaxation energy.

The 4f structure is most conveniently interpreted in terms of exchange splitting, as discussed by Wertheim, et al.<sup>3</sup> Thus in Gd the initial state is  $4f^7(^8S)$ , with all seven 4f spins parallel. The final state can only be  $^7F$ , which is the lowest term in  $\text{Eu}^{3+}(4f^6)$ , and indeed only one narrow peak is observed, at  $E_B=8.62$  eV. The width of this peak (1.25 eV FWHM) must arise in part from splitting of the  $^7F$  term into the seven levels  $^7F_J$ , with  $0 \leq J \leq 7$  (in the optical spectrum of  $\text{Eu}^{3+}$  these levels are distributed over about 0.6 eV).

The valence-band spectrum of Gd shows a well-resolved peak of ~1.5 eV FWHM after a (rather uncertain) correction for inelastic scattering. This peak has its maximum within 0.5 eV of  $E_F$  and is in good agreement both with APW theory<sup>1</sup> and with Eastman's UPS results.<sup>7</sup> This high density of states at  $E_F$  in Gd is important in explaining both the large saturation magnetization and the electronic heat capacity.<sup>1</sup>



Table I. Binding energies (eV) and FWHM of characteristic features of 4f-VB spectra of Gd, Tb, and Dy.<sup>a</sup>

	VB maximum	4f ↓	4f (1) ↑	4f (2) ↑	4f (3) ↑	Intensity Ratio $\Sigma 4f_{\uparrow} / 4f_{\downarrow}$	
Gd	$E_B^F$	1.08(10) <sup>b</sup>	---	8.62(10); $7_F^c$	---	---	$\infty$
	FWHM	1.50(5)	---	1.25(10)	---	---	
Tb	$E_B^F$	---	2.63(10); $8_S$	7.80(10) $6_P, 6_I, 6_D$	9.53(10)	10.51(10)	
	FWHM	---	0.80(5)	1.20(5)	1.36(5)	1.32(5)	$7.4 \pm 0.4$
Dy	$E_B^F$	---	4.47(10); $7_F$	8.23(10); $5_D, 5_L$	9.53(10)	12.82(10)	
	FWHM	---	1.8(1)	1.8(1)	2.5(1)	2.2(1)	$2.7 \pm 0.4$

<sup>a</sup>Relative energies difference between features are accurate to within 0.05 eV.

<sup>b</sup>Value in parenthesis is the absolute error in the last place.

<sup>c</sup>Assignments from optical data (Ref. 4).

The Tb 4f sextet structure (or majority-spin structure, in the terminology of Wertheim, et al.<sup>3</sup>) shows the distinct peaks and a shoulder. Probably the peak at 7.8 eV is the analog of the  $6_P$ ,  $6_I$ , and  $6_D$  terms between 32,000 and 41,000  $\text{cm}^{-1}$  in the optical spectrum of Gd<sup>3+</sup> (Ref. 4). The other peak and shoulder must arise from higher, as yet unassigned levels.

The valence-band XPS spectrum of Tb does not show a definite maximum near  $E_F$ , but instead is completely flat for at least 1 eV. The valence-band XPS spectrum of Dy is flat for 3 eV below  $E_F$ , in striking contrast to the APW valence-band density of states. It is even clearer in Dy than in Tb that there is no peak in the spectrum near  $E_F$ , because the interfering 4f minority-spin peak is farther below  $E_F$ .

The Dy 4f spectrum shows a strong resemblance to the optical spectrum of Tb<sup>3+</sup>(4f<sup>8</sup>). There is a well-resolved minority-spin peak (the  $7_F$  term) at  $E_F - 4.5$  eV, and a majority-spin (quintet) structure of at least three peaks, the first lies 3.7 eV from the  $7_F$ -term peak, in good agreement with the  $\sim 26\,000$   $\text{cm}^{-1}$  (3.2 eV)

gap in the Tb<sup>3+</sup> optical levels between the mean energy of the  $7_F$  term and a group of levels near 28 000  $\text{cm}^{-1}$  of  $5_D$  and  $5_L$  character. Additional optical levels in the 33 000-36 000  $\text{cm}^{-1}$  region in Tb<sup>3+</sup> are probably responsible for at least part of the other major component of the quintet peak. A third, smaller component presumably corresponds to as-yet-unassigned optical levels.

In summary, the rare earth metals Gd, Tb, and Dy are clearly shown to have tripositive 4f<sup>7</sup>, 4f<sup>8</sup>, and 4f<sup>9</sup> ion-core configurations, in agreement with earlier XPS studies and other measurements. The valence-band spectra, however, vary markedly, in contrast to expectations based on band-structure calculations.

#### References

1. J. O. Dimmock and A. J. Freeman, Phys. Rev. Letters **13**, 750 (1964) (Gd:APW); S. C. Keeton and T. L. Loucks, Phys. Rev. **168**, 672 (1968) (Gd, Dy: RAPW); C. Jackson, Phys. Rev. **178**, 949 (1969) (Tb: RAPW).

2. P. O. Hedén, H. Löfgren, and S. B. M. Hagström, *Phys. Rev. Letters* **26**, 432 (1971); S. B. M. Hagström, in *Electron Spectroscopy*, edited by D. A. Shirley (North-Holland, 1972), p. 515; P. O. Hedén, H. Löfgren, and S. B. M. Hagström, *Phys. Stat. Sol. (b)* **49**, 724 (1972).

3. G. K. Wertheim, A. Rosencwaig, R. L. Cohen, and H. J. Guggenheim, *Phys. Rev. Letters* **27**, 505 (1971).

4. G. H. Dieke, *Spectra and Energy Levels of Rare Earth Ions in Crystals*, edited by

H. M. Crosswhite and Hannah Crosswhite (Interscience, 1968), p. 142.

5. J. E. Herbst, D. N. Lowy, and R. E. Watson, *Phys. Rev. B* **6**, 1913 (1972).

6. L. Ley, S. P. Kowalczyk, F. R. McFeely, R. A. Pollak, and D. A. Shirley, *Phys. Rev. B*, to be published.

7. D. E. Eastman, *Sol. St. Comm.* **7**, 1697 (1969).

### X-RAY PHOTOEMISSION FROM SODIUM AND LITHIUM\*

S. P. Kowalczyk, L. Ley, F. R. McFeely, R. A. Pollak,<sup>†</sup>  
and D. A. Shirley

We have observed x-ray photoelectron spectra from clean surfaces of sodium and lithium. Figure 1 shows the Na 1s and Li 1s lines with their characteristic plasmon loss structures. The Na 1s, Na 2s, Na 2p, and Li 1s lines each show a surface plasmon loss peak, plus 5, 4, 3, and 2 bulk plasmon peaks, respectively. Plasmon energies  $\hbar\omega_p$  are set out in Table I. The Na  $\hbar\omega_p$  (bulk) values agree quite well with electron-loss results.<sup>1-6</sup> They also definitely favor the free-electron plasma model prediction of  $(4\pi ne^2/m)^{1/2}$  over the core-polarization corrected values<sup>1, 7</sup> in sodium. For lithium our  $\hbar\omega_p$  (bulk) values are intermediate between those of Kunz<sup>1</sup> and of Fellenzer,<sup>5</sup> lower than theory. The ratio  $\omega_p$ (bulk)/ $\omega_p$ (surface) is quite close to the theoretical  $\sqrt{2}$ , although the surface plasmon peaks are poorly resolved.

Core-level binding energies relative to the Fermi level,  $E_B^F$ , and to the vacuum level  $E_B^V = E_B^F + (\text{work function})$ , are set out in Table II. The  $E_B^V$  results are systematically lower than  $E_B$  values for free atoms, as estimated either from optical<sup>8</sup> plus x-ray<sup>9</sup> data or from theoretical free-atom values.<sup>10</sup> The latter two are in excellent agreement (Table II). These results appear to provide particularly clear examples of extra-atomic relaxation. The last column in Table II gives estimates of extra-atomic relaxation shifts from a simple "equivalent-cores" model<sup>11</sup> that assumes complete screening in the atomic cell, using Mann's<sup>12</sup> Slater integrals. In this model the Li 1s shift, for example, would be given by

$$\Delta E_{ea} = E_B(\text{atom}) - E_B^V \approx \frac{1}{2} \mathcal{F}(1s\ 2s)_{\text{beryllium}}$$

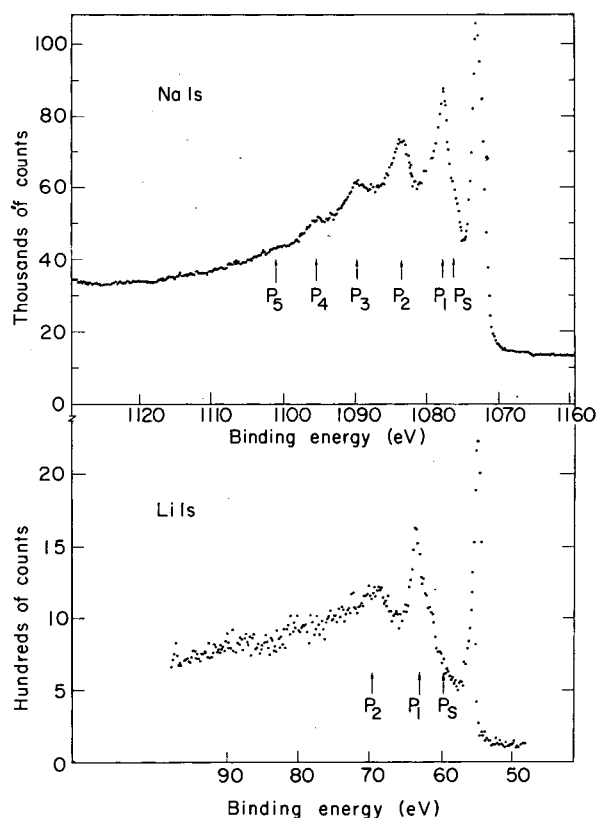


Fig. 1. Sodium and lithium 1s lines, with characteristic plasmon structure. The Li  $P_1$  peak is slightly enhanced in this spectrum from Na 2s contamination. (XBL 734-2752)

Table I. Plasmon energies (eV).

Line	$E(P_1)^a$	$E(P_2)$	$E(P_3)$	$E(P_4)$	$E(P_5)$	$\overline{E(P)}^b$	$E(P_S)$	$\overline{E(P)}/E(P_S)$	$E(P)_{th}$	$E(P)_{th}^{*c}$	$E(P)_e^d$	$E(P_S)_e^d$
Na 1s	5.8(1)	5.8(1)	5.9(1)	5.9(2)	5.9(2)	5.83(4)	4.0(1)	1.45	5.95 <sup>1, e</sup>	5.58 <sup>1</sup>	5.71(10) <sup>1</sup>	3.85(10) <sup>1</sup>
Na 2s	5.9(1)	5.8(1)	5.8(2)	5.8(1)	---	5.80(2)	4.1(1)	1.41			5.85(5) <sup>2</sup>	3.82(10) <sup>2</sup>
Na 2p	5.8(1)	5.9(1)	5.7(2)	---	---	5.77(6)	4.0(2)	1.44			5.87 <sup>3</sup>	4.01(17) <sup>3</sup>
Na VB	6.0(2)	5.0(3)	---	---	---	5.5(2)	4.0(3)	1.38			5.4(2) <sup>4</sup>	
Auger <sup>1</sup> D (KL <sub>23</sub> L <sub>23</sub> )	5.7(2)	5.7(2)	5.7(3)	---	---	5.7(1)	---	---				
Auger <sup>1</sup> P (KL <sub>1</sub> L <sub>23</sub> )	5.5(3)	5.9(3)	---	---	---	5.7(2)	---	---				
Li 1s	7.5(3)	7.3(3)	---	---	---	7.4(2)	5.0(3)	1.48	8.02 <sup>1</sup>	7.96 <sup>1</sup>	7.12(10) <sup>1</sup>	4.20(10) <sup>1</sup>
											8 <sup>5</sup>	4.6 <sup>5</sup>
												5.2 <sup>6</sup>

<sup>a</sup>Energy of peak N-Energy of peak N-1.

<sup>b</sup>Average of all the bulk plasmon energies.

<sup>c</sup>Free electron theory corrected for core polarization.

<sup>d</sup>Other measurements.

<sup>e</sup>Superscripts denote references in text.

Table II. Binding, Auger, and relaxation energies (eV).

Line	$E_{B,K}^F$ <sup>a</sup>	$E_{B,K}^V$ <sup>b</sup>	$E^A$ (th) <sup>c</sup>	$E^A$ (opt) <sup>e</sup>	$\Delta E^A$ (th)	$\Delta E^A$ (opt)	$\Delta E^A$ (calc)
Na 1s	1071.7(1)	1074.0	1079 <sup>c</sup>	1079.1	5.0	5.1	5.3 <sup>f</sup>
Na 2s	63.4(1)	65.7	71.9 <sup>c</sup>	71.1	6.2	5.4	5.0 <sup>f</sup>
Na 2p	30.4(1)	32.7	36.6 <sup>c</sup>	38.1	3.9	5.4	5.1 <sup>f</sup>
Auger <sup>1</sup> D (KL <sub>23</sub> L <sub>23</sub> )	994.2(1)	991.9	975.8 <sup>d</sup>	977.2	16.1	14.7	16.8 <sup>g</sup>
Auger <sup>1</sup> P (KL <sub>1</sub> L <sub>23</sub> )	954.7(1)	952.4	937.1 <sup>d</sup>		15.3		16.8 <sup>g</sup>
Li 1s	54.8(1)	57.2	---	64.9	---	7.7	6.4 <sup>f</sup>

<sup>a</sup> Binding energy or kinetic energy relative to  $E_F$ (Au).

<sup>b</sup> Work-function corrections of 2.3 eV (Na) or 2.4 eV (Li) were made.

<sup>c</sup> From Ref. 10.

<sup>d</sup> Estimated from binding energies, without relaxation.

<sup>e</sup> From data in Refs. 8 and 9.

<sup>f</sup> Estimated as in Ref. 11.

<sup>g</sup> Estimated as in Ref. 13.

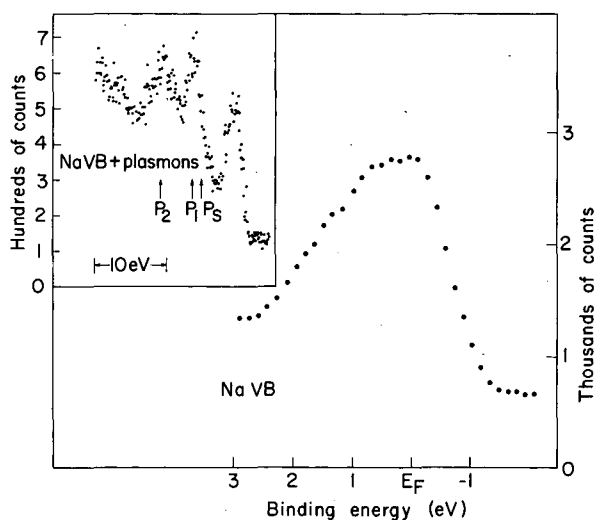


Fig. 2. Sodium KLL Auger spectrum, with plasmons.

(XBL 734-2750)

where  $\mathcal{F} = (F^0 - \frac{1}{2}G^0)$  is the two-electron interaction between the K hole and the screening electron. The very good agreement of the last column in Table II with the preceding two strongly supports this model.

Auger energy shifts from extra-atomic relaxation are even larger, because two holes are screened in the final state. Again a simple "equivalent cores" screening model<sup>13</sup> predicts extra-atomic relaxation energies in (Table II, Column 8) very good agreement with experiment. The sodium KLL Auger spectrum is shown in Fig. 2. The predicted energy in this case is, for the sodium <sup>1</sup>D line,

$$\Delta E_{ea} = \mathcal{F} (2p\ 3s)_{Al} + \mathcal{F} (2p\ 3p)_{Al} - \mathcal{F} (1s\ 3s)_{Mg}$$

Free-atom Auger energies were estimated, using optical and x-ray data, both from one-electron binding energies<sup>13</sup> (Columns 4 and 6) and from NaII and NaIII states<sup>8</sup> (Columns 5 and 7). These large Auger extra-atomic relaxation energies should be very useful in surface-physics studies.

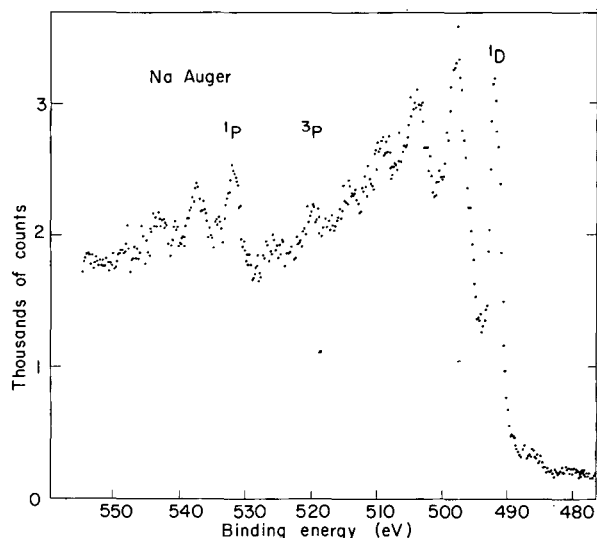


Fig. 3. Sodium valence band. The data has been treated by adding four channels and then performing a sliding linear fit to three adjacent points. Insert shows a wider unsmoothed scan, with plasmons. (XBL 734-2808)

The valence-band spectrum of sodium (Fig. 3) agrees roughly in shape and width with the x-ray emission spectrum.<sup>14,15</sup> An approximate  $E^{1/2}$  dependence of intensity on energy is observed, as expected, because sodium is the most free-electron-like of the alkali metals.<sup>16</sup> The reduced valence-band width was  $3.1 \pm 0.1$  eV if measured from the high-energy edge, or  $2.5 \pm 0.1$  eV if measured from  $E_F(\text{Au})$ . The latter value agrees well with the x-ray emission data of Crisp and Williams.<sup>15</sup> Of course x-ray photoemission and x-ray emission and absorption are very different processes, and the spectra need not be identical.

Our spectrum does not show the excitonic structure observed in x-ray emission<sup>15,17-19</sup> and attributed to the Nozieres-De Dominicis singularity.<sup>20</sup>

#### Footnotes and References

\* Condensed from LBL-1682. Published in *Phys. Rev. B* **8**, 3583 (1973).

† Present address: IBM Thomas J. Watson Research Center, Yorktown Heights, NY 10598.

1. C. Kunz, *Phys. Letters* **15**, 312 (1965).
2. J. B. Swan, *Phys. Rev.* **135**, A1467 (1964).
3. J. L. Robins and P. E. Best, *Proc. Roy. Soc.* **79**, 110 (1962).
4. R. E. Palmer and S. E. Schnutterly, *Phys. Rev. B* **4**, 2329 (1971).
5. H. Fellenzer, *Z. Physik* **165**, 419 (1961).
6. I. Lindau, H. Löfgren, and L. Walldin, *Phys. Letters* **36A**, 293 (1971).
7. D. Pines, *Elementary Excitations in Solids* (W. A. Benjamin, 1963).
8. C. E. Moore, "Atomic Energy Levels", NBS Circular 467 (1949).
9. J. A. Bearden, *Rev. Mod. Phys.* **39**, 78 (1967).
10. K. Siegbahn, *et al.*, *Nova Acta Regiae Soc. Sci. Upsaliensis Ser. IV*, Vol. 20 (1967). Appendix II.
11. L. Ley, S. P. Kowalczyk, F. R. McFeely, R. A. Pollak, and D. A. Shirley, *Phys. Rev. B*, **8**, 2392 (1973).
12. J. B. Mann, "Atomic Structure Calculations I. Hartree-Fock Energy Results for the Elements Hydrogen to Lawrencium," LA-3690, TID 4500.
13. S. P. Kowalczyk, R. A. Pollak, F. R. McFeely, L. Ley, and D. A. Shirley, *Phys. Rev. B*, **8**, 2387 (1973).
14. D. H. Tomboulian, *Handbuch der Physik XXX*, edited by S. Flügge (Springer-Verlag, Berlin, 1957), p. 246; and references therein.
15. R. S. Crisp and S. E. Williams, *Phil. Mag.* **6**, 625 (1961).
16. F. S. Ham, *Phys. Rev.* **128**, 2524 (1962).
17. C. Kunz, R. Haensel, G. Keitel, P. Schreiber, and B. Sonntag, NBS Special Publications 323 (1971), p. 275.
18. G. D. Mahan, *Phys. Rev.* **163**, 612 (1967).
19. G. D. Mahan, NBS Special Publication 323 (1971), p. 253.
20. P. Nozieres and C. T. De Dominicis, *Phys. Rev.* **178**, 1097 (1969).

X-RAY PHOTOEMISSION STUDIES OF DIAMOND, GRAPHITE,  
AND GLASSY CARBON VALENCE BANDS\*

F. R. McFeely, S. P. Kowalczyk, L. Ley, R. G. Cavell,  
R. A. Pollak, and D. A. Shirley

The element carbon is in many respects unique among the Group IV elements in its solid-state properties. In its diamond modification it structurally resembles the small-band-gap tetrahedral semiconductors silicon, germanium, and grey tin, while it is, in contrast to these materials, a very good insulator. At ordinary temperature and pressure, however, the thermodynamically stable form of carbon is not diamond, but graphite, a semi-metallic form without an analog in the group IV series. It is of interest to compare the valence bands of the two forms of carbon because the different coordination--trigonal in graphite and tetrahedral in diamond--suggests substantial differences in their chemical bonding. While the simple tight-binding description of these two forms in terms of  $sp^2$  and  $sp^3$  bonding must be greatly modified to provide a realistic band structure, vestiges of s and p character in the bands should still be manifest through cross-section modulation in the photoemission spectrum.

Using a simple but qualitatively correct model, it is possible to relate the intensities observed from the valence bands to the cross-sections of the atomic states from which they arise. This is particularly interesting for carbon since the  $2s/2p$  cross section ratio is  $\sim 13$ . This gives us a probe sensitive to the s-like parts of the valence bands, which are inaccessible in a K x-ray emission experiment.

The spectra of the forms of carbon are shown in Fig. 1. The diamond spectrum was compared to x-ray emission results and theoretical densities of states. The results are summarized in Fig. 2. As previously indicated, the intensities of the XPS spectrum are "reversed" from those of the K x-ray emission spectrum, amplifying the s-like parts of the bands. When this cross section is considered, the agreement between theory and experiment is quite satisfying.

In oversimplified terms, one can consider the difference in electronic structure between diamond and graphite to be due to the " $\pi$  bands" in graphite, which take one p orbital per atom and do not mix with the " $\sigma$ -bands", this can be seen from the XPS and K x-ray emission spectra shown in Fig. 3. As would be expected, the s-like regions in the XPS spectrum are even more dominant than in diamond, since they are

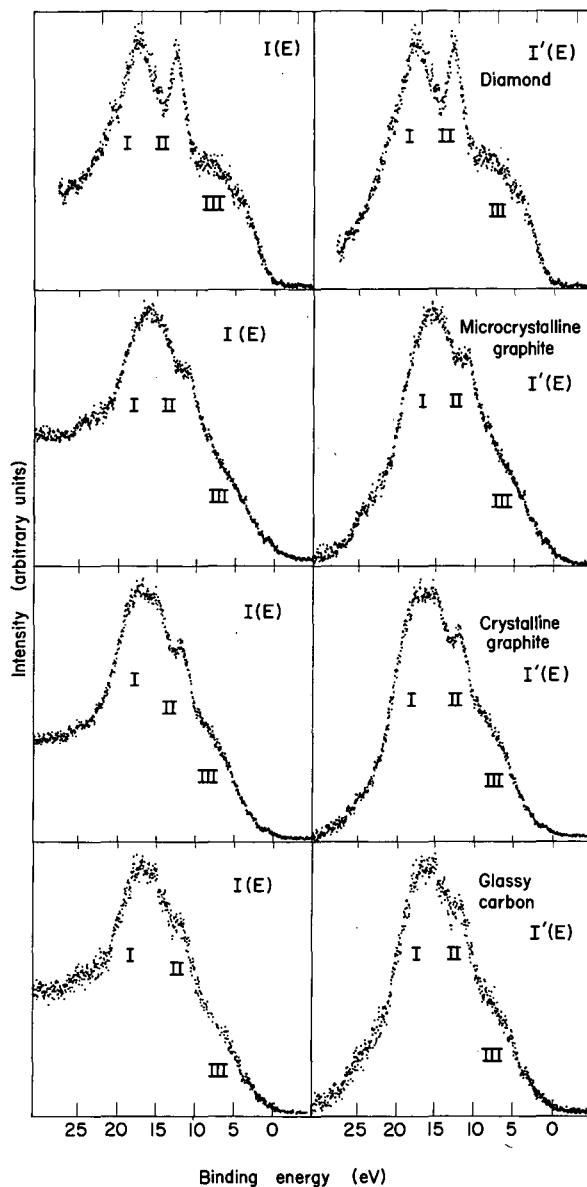


Fig. 1. Valence-band XPS spectra, before [I(E)] and after [I'(E)] correction for inelastic losses, of diamond, single-crystal graphite, polycrystalline graphite, and glassy carbon. (XBL 7310-4310)

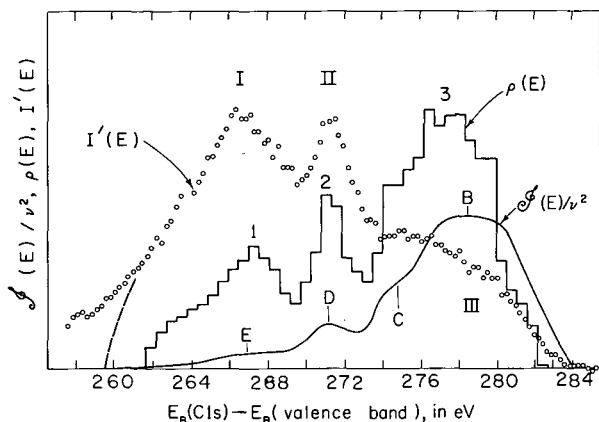


Fig. 2. Comparison for diamond of the XPS spectrum  $I'(E)$  (this work), the K x-ray emission spectrum  $I(E)/\nu^2$  (Ref. 12) and the calculated density of states (Ref. 11). Characteristic features are denoted by roman numerals for  $I'(E)$ , arabic numerals for  $I(E)$ , and letters for  $\rho(E)/\nu^2$ . Abscissa pertains to  $I'(E)$  and  $\rho(E)/\nu^2$ , as described in text:  $\rho(E)$  was drawn by aligning peak 2 with peak II in  $I'(E)$ . Ordinates are linear and start from zero. Dashed line indicates extrapolation of  $I'(E)$  to zero at the bottom of the valence bands to eliminate an artificial tail.

(XBL 739-4099)

admixed with one less p function. The x-ray emission experiment shows a nearly complete lack of p-state density in the lower regions of the valence bands.

In examining the spectrum of glassy carbon, the following observations can be made: 1) The spectrum resembles that of graphite more than diamond in the region of Peak III, showing a gradual decrease in intensity rather than a sharp cutoff, 2) The total width of the intense part of  $I'(E)$  is nearer that of graphite than that of diamond. Defining this width  $W$  as the energy separation between the points in  $I'(E)$  of half the maximum height on the low-energy side and of quarter height on the high-energy side, we find  $W = 15.5$  eV (graphite), 18 eV diamond, and 16 eV (glassy carbon), 3) Peak I is intermediate in relative intensity between diamond and graphite, and 4) The valley between Peaks I and II is filled in.

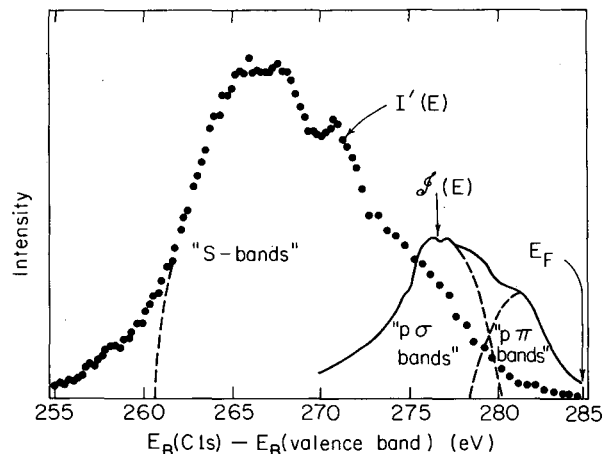


Fig. 3. Relation between photoemission valence-band spectra and x-ray emission energies, discussed in text. Because these are excited (hole) states the relationship between spectral energies is rigorous. Intensities can vary quite differently across the valence band, however, because the two spectroscopies involve different transitions. Thus in Fig. 2 the s-like bands are emphasized in XPS and the p-like bands in K x-ray emission relative to  $\rho(E)$ .

(XBL 739-4098)

It is actually not surprising that the XPS spectrum of the amorphous material should resemble the crystalline cases so closely. As Weaire and Thorpe have pointed out and numerous XPS experiments have demonstrated, the gross features of the density of states depend on atomic properties and the short-range order in the crystal, while the long-range order is responsible for the fine structure. The filling-in of the valley between Peaks I and II is an example of the kind of fine-structure change observed earlier in amorphous materials. The other features noted above are consistent with glassy carbon possessing both trigonally and tetrahedrally coordinated carbons, with more of the former than the latter.

A number of models for the structure of glassy carbon have been proposed on the basis of x-ray diffraction data. Our results do not rule out any of these, although they specifically support those that include both trigonal and tetrahedral bonding.

## X-RAY PHOTOEMISSION FROM ZINC: EVIDENCE FOR EXTRA-ATOMIC RELAXATION VIA SEMILOCALIZED EXCITONS

L. Ley, S. P. Kowalczyk, F. R. McFeely, R. A. Pollak,\*  
and D. A. Shirley

In this paper we report an x-ray-photoelectron-spectroscopy (XPS) study on metallic zinc. A high-purity single crystal of zinc was irradiated with monochromatized  $\text{AlK}\alpha_{1,2}$  x rays in a Hewlett-Packard 5950A ESCA Spectrometer that had been modified to operate at pressures  $\leq 10^{-9}$  Torr after baking. Energies for core levels and satellites are due to extrinsic and possibly also intrinsic discrete energy losses.

In the valence band region (Fig. 1) we find a 3d band peak centered at  $10.18 \pm 0.10$  eV below  $E_F$ . The 4s, 4p band is low and flat, and the Fermi edge is clearly visible, with a (signal)/(background) ratio of  $> 50$ . Unfortunately none of the published theoretical band-structure calculations on zinc<sup>1-4</sup> were accompanied by density-of-states plots, so it is not clear whether the calculated 4s, 4p bands would be in more than qualitative agreement with Fig. 1.

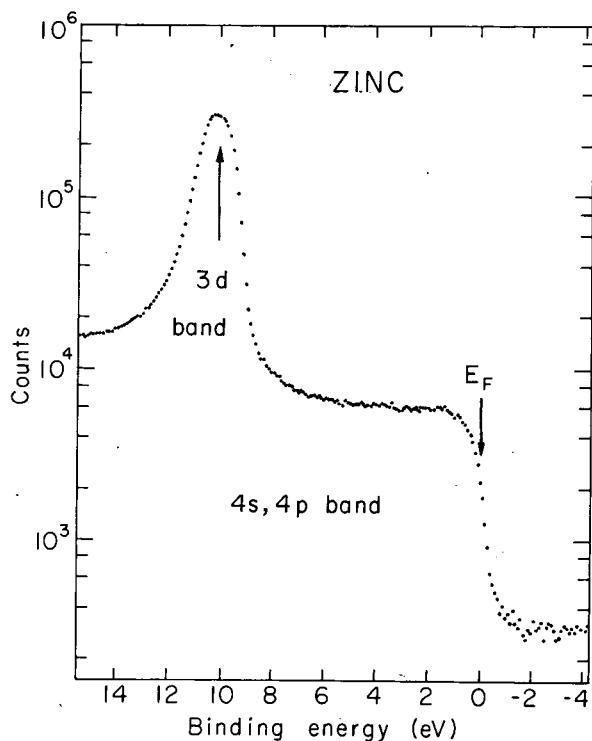


Fig. 1. XPS valence-band spectrum of zinc, on a semilogarithmic scale.

(XBL 732-2353)

The previous experimental studies of zinc<sup>5-9</sup> give results in only fair agreement among themselves.

The analysis of these data raises the question of the extent to which valence-band photoemission spectra of metals are distorted by differential relaxation, relative to the one-electron orbital energies obtained in bandstructure calculations.

The atomic relaxation energy  $E_R$  which is observed as the difference between the orbital energy  $\epsilon$  as obtained from a HF calculation and the experimental binding energy  $E_B$ ,

$$E_B = -\epsilon - E_R,$$

is well understood in terms of the rearrangement of the passive orbitals upon ionization,<sup>10</sup> as long as we neglect correlation energies.

A comparison of binding energies of quasi-core levels obtained in free atoms and conductors (compare Table II) establishes a positive energy difference

$$\Delta E_B = E_B(\text{atom}) - E_B(\text{conductor})$$

of the order of 3 eV.

We have extended this comparison to a wide range of elements and orbitals. The results can be summarized as indicating that  $\Delta E_B$  is always positive for atomic core levels, falling in a rather wide range of values up to  $\sim 15$  eV. This shift cannot be assigned with certainty to any single effect, but we believe that extra-atomic relaxation is the dominant factor. This interpretation is supported by the rather good detailed agreement with experiment shown by an "extra-atomic relaxation" model derived in the following section. There is, however, another effect that may also be important; namely, a change in the magnitude of the core level's orbital energy  $\epsilon$  in the solid relative to that in the gas. This change could apparently have either sign, depending on the details of the local bonding structure. It is difficult to estimate the magnitude of  $\Delta\epsilon = \epsilon(\text{solid}) - \epsilon(\text{atoms})$ , but we would expect it to be rather small for core levels, probably in the 1-2 eV range or less in most cases. It is difficult to see how  $\Delta\epsilon$  would be substantially larger than



this. If  $\Delta\epsilon$  were very large for the 3d orbital in zinc, for example, very strong chemical bonds would have to be present. In fact the cohesive energy of zinc is less than 1 eV.

We therefore believe that extra-atomic relaxation, rather than the  $\Delta\epsilon$  effects, is dominant in the observed binding-energy shifts from atoms to metals. Indeed this should come as no surprise: It is simply a very direct experimental manifestation of "screening" of an excess charge—the hole—on an "impurity" by the itinerant electrons. Friedel suggested twenty years ago<sup>11, 12</sup> that screening of an impurity charge should be accomplished by the formation of an occupied semilocalized (exciton) state about the impurity via the dropping down of a conduction-band state below  $E_F$  at the impurity site. We assume that the outgoing photoelectron will interact repulsively with this nascent valence band state as the latter forms adiabatically during photoemission. This would be in complete analogy with atomic relaxation of the valence orbitals during photoemission from core states.<sup>10</sup> Here, too, it would result in a lowering of the binding energy. In order to calculate this additional interaction, we have to know the wavefunction of  $|E\rangle$  the newly formed excitonic state.

The Friedel sum rule states, that an impurity of charge  $z$  relative to the lattice atoms will have its charge screened by net positive phase shifts in the conduction electron partial L waves. This does not indicate directly how to calculate  $\Delta E_B$  because the wave function of the exciton state is now known. It is, however, expected that this state will be composed mainly of L waves corresponding to the symmetry of the lowest unbound states in the conduction band, e. g., the p wave in zinc, the d wave in iron, or the s (and p) wave in sodium. Furthermore, the wave function  $|E\rangle$  of the exciton state, while oscillatory, will of course resemble an atomic wave function at the impurity ion core. We are now in the position to calculate  $\Delta E_B$  along lines quite analogous to those given in Ref. 10 for the calculation of the atomic relaxation.

Figure 2 is a plot of the experimental values of  $\Delta E_B$  (averaged over core levels) against values calculated on the above model. It shows that the two quantities are correlated. It also shows that  $\Delta E_B(\text{theo.}) > \Delta E_B(\text{expt})$  on the average, which is expected because this model is based on the highly-localized atomic states; it must therefore overestimate  $\Delta E_B$  somewhat.

The correlation in Fig. 2 is encouraging, but more dramatic evidence for the validity of this model can be obtained by studying trends. In Fig. 3 experimental and theoretical shifts are plotted against atomic number for the 3d series and for the rare-gases implanted into

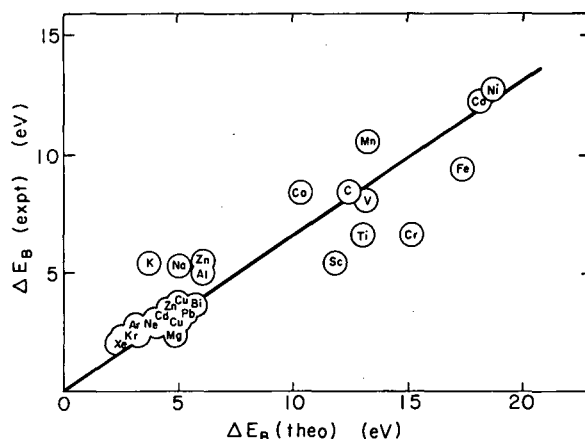


Fig. 2. Experimental excess binding energies in solids versus theoretical extra-atomic relaxation energies based on model described in text. Line through points has a slope of 0.66. (XBL 732-2352)

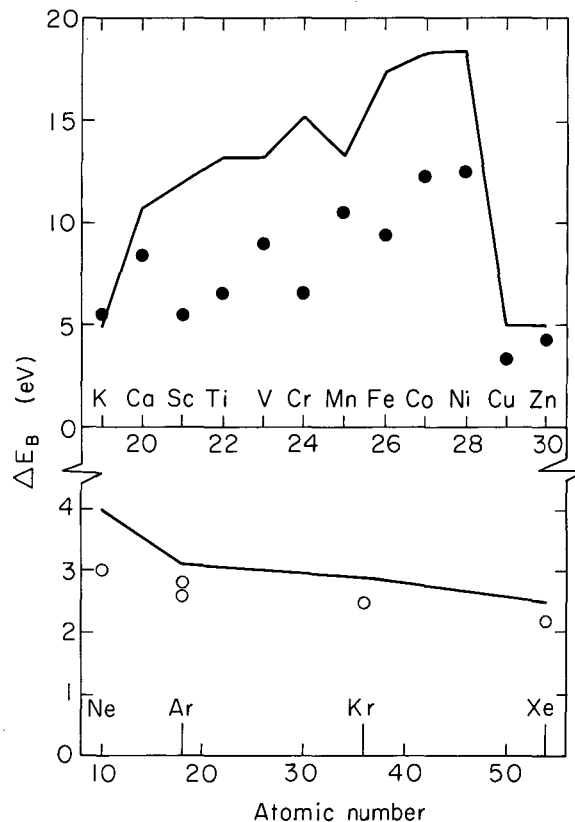


Fig. 3. Experimental excess binding energies (points) and theoretical estimates based on atomic-orbital approximation to exciton states, using model described in text (lines connecting calculated points). Top panel: Results for 3d series metals. Note break at filled d shell, from Cu to Zn. Bottom panel: Rare gases embedded in metals. (XBL 732-2351)

conductors. The trends agree well in both series. Of special note is the sharp break in  $\Delta E_B$  between Ni and Cu. This occurs because in Ni (atomic configuration  $d^8s^2$ ) there are d states immediately above  $E_F$ . The screening of a hole-state charge on the "impurity" is thus achieved mainly by the d wave. The exciton state is thus d-like, and it interacts relatively strongly with the hole state. By contrast, in Cu (atomic configuration  $3d^{10}4s$ ) the d band is filled and screening must occur mostly via the s and p waves. The atomic approximation to the exciton state thus involves integrals such as  $F^0(2s, 4s)$ , which are smaller. It would be difficult to reproduce this dramatic break in  $\Delta E_B$  at the top of the 3d series without explicitly considering atomic properties.

Two major conclusions can be drawn from this work: First, relaxation effects are important in zinc, even for the 3d band. The question, "do the 3d bands lie below the bottom of the 4s, 4p bands?" is too simply stated. When its phraseology is refined, it has two answers. If one adds, "... in the photoemission spectrum?" the answer is "No, see Fig. 1." If one adds instead, "... in the initial state?" the answer is "Almost certainly

yes." It seems evident that atomic relaxation of the Zn(3d) orbitals amounts to about 4 eV and extra-atomic relaxation to about 3.4 eV. The binding energy  $E_B(3d)$  is thus less than the orbital energy (Koopman's theorem) estimates by 7.4 eV. Extra-atomic relaxation accompanying photoemission from the 4s, 4p bands is probably about the same size or a little smaller [i.e.,  $F^0(4s, 4p) \approx F^0(3d, 4p)$ ] while atomic relaxation is smaller or even negative. Hence we would expect the 3d peak in the XPS spectrum to move ~5 eV closer to  $E_F$  relative to the 4s, 4p bands than their relative positions in a self-consistent Hartree-Fock calculation.

The second major conclusion from this work is that semilocalized exciton states accompanying photoemission have been identified through their effects on core-level binding energies in conductors. An approximate theoretical model was developed and used to estimate the extra-atomic relaxation energy accompanying the formation of these states. The model overestimates the effect somewhat, as expected, but it reproduces experimental trends very well. It appears to provide a first step toward a quantitative understanding of extra-atomic relaxation in metals.

Table I. Experimental energies (in eV).

Feature	$E_B^F$	FWHM	Rel. intensity <sup>a</sup>
2s peak	1196.16(25)	5.5(5)	0.19
2p <sub>1/2</sub> peak	1045.09(15)	1.94(5)	0.58
2p <sub>3/2</sub> peak	1021.96(15)	2.00(5)	1
2p satellites	~ 9 and 14 eV below each 2p peak	2 broad peaks, 8-10 eV total width	0.30(5) relative to each 2p
2p <sub>1/2</sub> - 2p <sub>3/2</sub> splitting	23.15(5)	---	---
3s peak	139.88(15)	2.62(10)	0.035
3p <sub>1/2</sub> peak	91.31(15)	2.6(2)	0.039
3p <sub>3/2</sub> peak	88.70(15)	2.6(2)	0.067
3p splitting	2.60(2)	---	---
3d peak	10.18(10)	1.45(2)	0.042
4s, p bands	0 to $\geq 10$	$\geq 10$	0.006

<sup>a</sup>These ratios are accurate to about  $\pm 10$

Table II. Comparisons of  $E_B^{\text{nd}}$  and  $E_B^{\text{nd}}$  in gases and metals (in eV).

Level	$E_B^{\text{F}^{\text{a}}}$	$\phi^{\text{b}}$	$E_B^{\text{V}^{\text{c}}}$	$E_B^{\text{(atomic)}}$	$\Delta E_B$
Cu(3d)	3.0(1)	4.5	7.5	10.44	2.9
Zn(3d)	10.18(15)	3.7	13.88	17.31	3.4
Cd(4d <sub>3/2</sub> )	11.46(9)	3.9	15.36	18.28	2.9
Cd(4d <sub>5/2</sub> )	10.47(9)	3.9	14.37	17.58	3.2
Pb(4f <sub>7/2</sub> )	136.4(2)	4.05	140.5	144.0(5)	3.5
Bi(4f <sub>7/2</sub> )	157.0(2)	4.3	161.3	164.9(5)	3.6

<sup>a</sup>Binding energy with respect to the Fermi-level

<sup>b</sup>Work function.

<sup>c</sup>Binding energy with respect to the vacuum level:  $E_B^{\text{V}} = E_B^{\text{F}} + \phi$ .

#### Footnotes and References

\*Present address: IBM, Thomas J. Watson Research Center, Yorktown Heights, NY 10598.

1. W. A. Harrison, *Phys. Rev.* **126**, 497 (1962).
2. L. F. Mattheiss, *Phys. Rev.* **134**, A970 (1964).
3. R. W. Stark and L. M. Falicov, *Phys. Rev. Letters* **19**, 795 (1967).
4. F. Borghese and P. Denti, *Nuovo Cimento* **3B**, 34 (1971).
5. A. E. Sandstrom, in *Handbuch der Physik*, edited by S. Flugge (Springer-Verlag, Berlin, 1957), Vol. XXX.

6. C. Nordling, *Arkiv Fysik* **15**, 397 (1959).
7. P. O. Nilsson and I. Lindau, *J. Phys. F* **1**, 854 (1971).
8. S. Hanzely and R. J. Liefeld, in "Electronic Density of States" (NBS Special Publication 323, December 1971), p. 319.
9. R. T. Poole, R. C. G. Leckey, J. G. Jenkin, and J. Liesegang, private communication.
10. D. A. Shirley, *Chem. Phys. Letters* **16**, 220 (1972).
11. J. Friedel, *Phil. Mag.* **43**, 1531 (1952).
12. J. Friedel, *Advan. Phys.* **3**, 446 (1954).

## X-RAY PHOTOEMISSION STUDIES OF THE ALKALI HALIDES\*

S. P. Kowalczyk, F. R. McFeely, L. Ley, R. A. Pollak,<sup>†</sup>  
and D. A. Shirley

The spectra obtained for the valence-band regions of several alkali halides are shown in Figs. 1-3. In light of the well-known ionic nature of these crystals it is not surprising that the uppermost valence-band peaks strongly resemble core-level peaks. In Fig. 4 the theoretical band structures calculated by Cohen et al.<sup>1-4</sup> by the EPM method of Ge, GaAs, ZnSe, and NaCl are shown along with the valence band XPS spectra.<sup>5</sup> The bands are in all cases grouped as would be expected from atomic-structure considerations, in a group of three bands nearest the Fermi level and a single band at lower energy. The lowest level has in all cases  $\Gamma_1$  symmetry and may be characterized quite unequivocally as an s-like level. The other three bands have  $\Gamma_{25}^1$  symmetry in the tetrahedral case and  $\Gamma_{15}$  in the octahedral NaCl lattice. It is therefore quite tempting to classify these three bands as p-like. It is clear however that in the case of Ge, where the s-like band (band 1) and the lowest p-like band (band 2), are degenerate at the X point, this artificial categorization of the bands by labels reflecting their supposed atomic parentage is misleading.

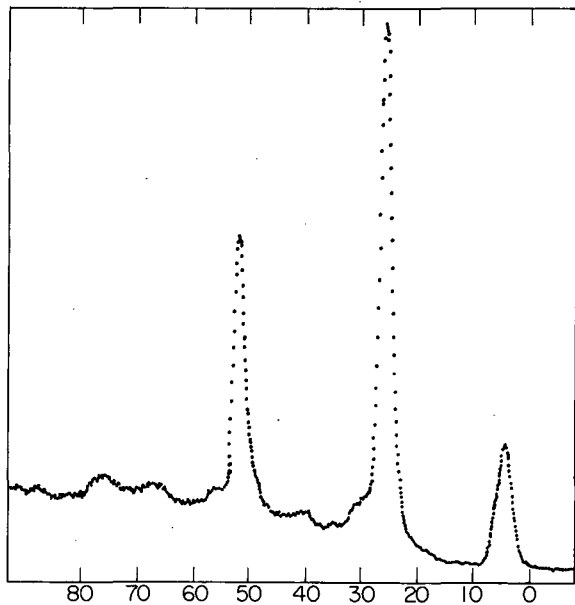


Fig. 1. X-ray photoemission spectrum of the valence band region of LiF.  
(XBL 738-3763)

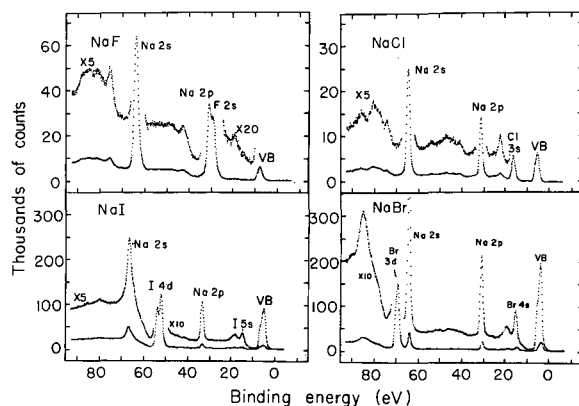


Fig. 2. X-ray photoemission spectra of the valence band region of the sodium halides.  
(XBL 736-3234)

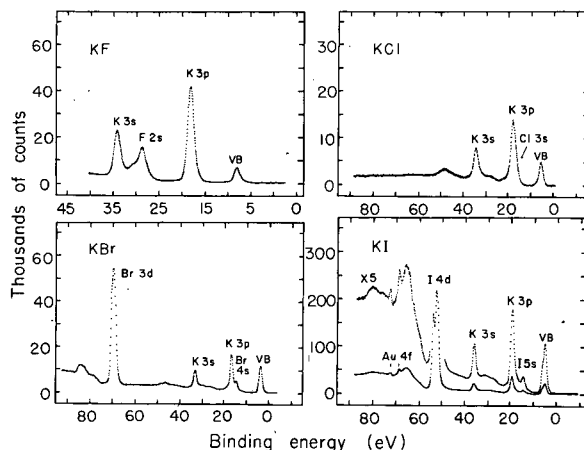


Fig. 3. X-ray photoemission spectra of the valence band region of the potassium halides.  
(XBL 736-3233)

The similarity of bands 1 and 2 in the Group IV elements is demonstrated by both experimental and theoretical results. Cavell et al.<sup>6</sup> studied the variation of the XPS cross sections across the valence bands for diamond, Si, and Ge. These results showed that the XPS cross section of the peaks corresponding to band 2 in each case followed quite closely that of band 1,

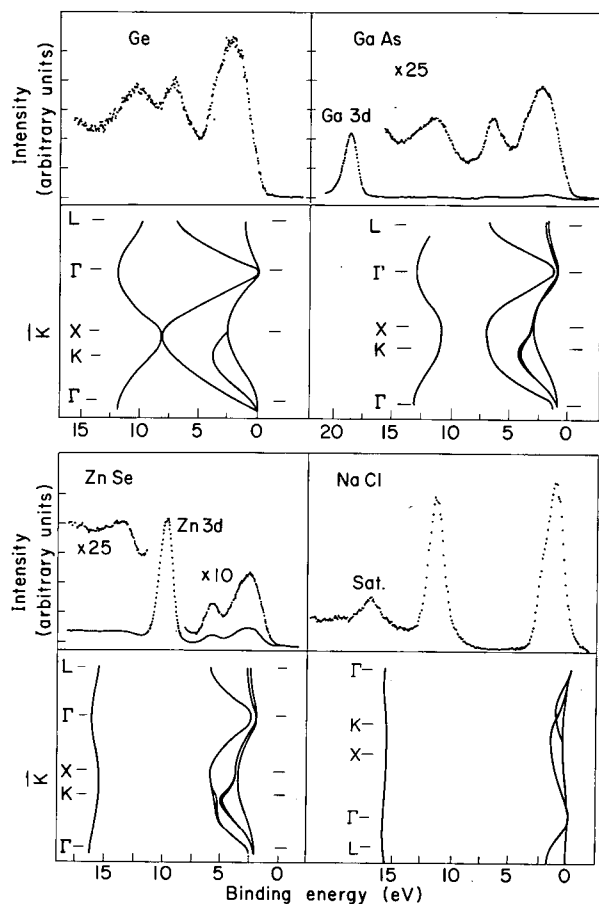


Fig. 4. X-ray photoemission spectra and band structures of Ge, GaAs, ZnSe, and NaCl. The upper row shows the uncorrected experimental spectra. The lower row shows the corresponding band structure of EPM calculations of Refs. 3-6. (XBL 7310-4347)

the s-like band, and was very different from that of bands 3 and 4, the p-like bands. Charge-density calculations were also performed on each of the four bands of Ge by Walter and Cohen.<sup>7</sup> They showed that the charge distributions of bands 1 and 2 are practically identical, and are very s-like. Bands 3 and 4 were found to be very similar to each other also, and both very p-like.

In progressing along this series to GaAs, definite changes are apparent in both the photoemission spectrum and in the calculated band structure. The primary difference in the photoemission spectrum is that the band 1 peak has split off somewhat from the peaks due to bands 2-4 and has moved to higher binding energy. This is reflected as well in the band structure. On the basis of these changes, one

would expect that band 1 is becoming more s-like and band 2 more p-like. The calculated charge densities bear out this expectation. Band 1 in GaAs is almost completely localized on the As site and is virtually undistorted from spherical symmetry. Band 2 is less profoundly changed from the case of Ge but is definitely more p-like. These changes in the bands can be readily understood in terms of a simple argument based on the increased electronic charge on the anion.

In ZnSe the analogous changes are observed, with band 1 becoming almost completely core-like and band 2 showing a high degree of p character. It is evident that the effect of increasing the antisymmetric part of the potential is to progressively unmix the s-p bands 1 and 2 into purer atomic-like states.

If a localized state description were valid for the alkali halides the XPS spectrum would be that of essentially atomic orbitals in a cubic crystal field. Since p-orbitals are not split by a cubic field, the only structure in the alkali halide "valence bands" would be due to spin-orbit splitting. If a band structure picture were valid, dispersion in the band structure could give rise to extra structure in the valence-band peaks.

Figures 5 and 6 shows expanded spectra of

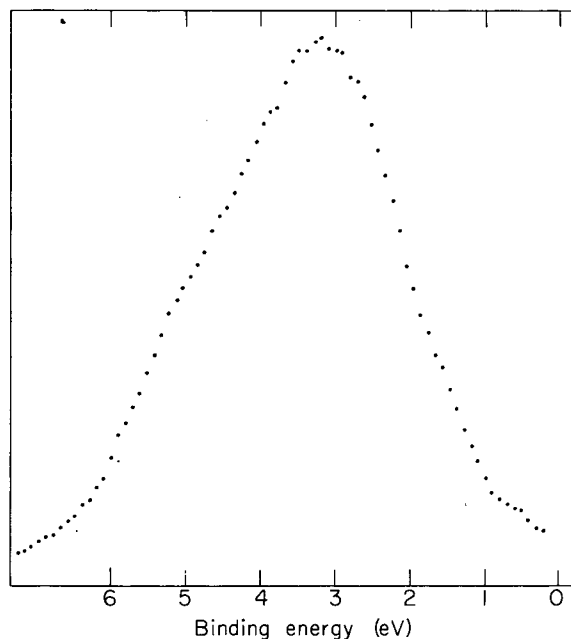


Fig. 5. The outermost p band of LiF. (XBL 738-3762)

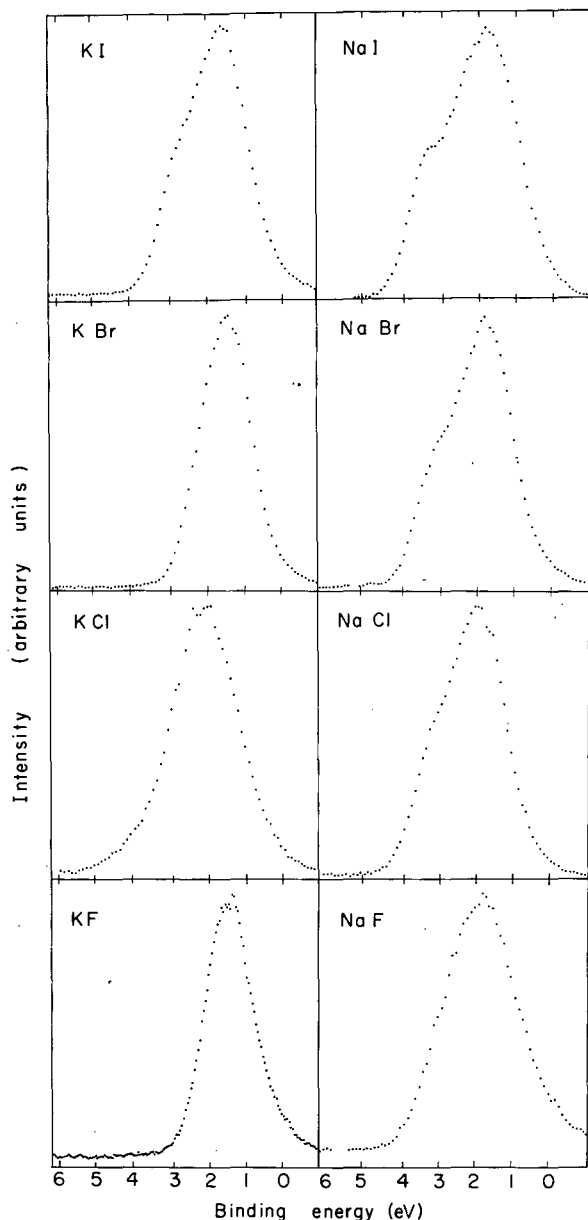


Fig. 6. The outermost p band of the sodium and potassium halides. (XBL 737-3287)

the outermost p bands of each of the nine salts studied in this work. In three of the salts (KF, KCl, NaF) there is only one fairly symmetrical peak nominally corresponding to bands 2-4. This indicates that the p-bands retain a good deal of their atomic character in the solid.

In contrast to the above cases, the "valence bands" of LiF, NaCl, NaBr, NaI, KBr, and KI

show definite structure on the high binding energy side.

We reject a spin-orbit interpretation of this structure for several reasons. In Table I we compare the atomic spin-orbit splittings<sup>8</sup> of the appropriate halogen levels with the splittings of the two features in the alkali-halide valence bands. In every case the separation of the features in the solid is larger than that predicted by spin-orbit splitting. In several cases--NaCl, NaBr, NaI, and especially LiF--the features are split much more than could be accounted for by spin-orbit splitting alone. Also, the large effect in the spectra of the change from Na<sup>+</sup> to K<sup>+</sup> in the chlorides argues against the structure being due to localized chlorine states.

A further strong argument in favor of a band picture is provided by the systematic evolution in the valence-band photoemission spectra and theoretical band-structure calculation of bands 1 and 2 in progressing from Group IV to III-V to II-VI to I-VII crystals.

Table II lists binding energies of the outer core levels in these salts, relative to the top of the valence bands.

In many photoemission spectra of solid samples, peaks appear at energies of roughly 5-50 eV below the primary photoemission peak. These can be of two distinct types: 1) intrinsic satellite lines due to additional final states which may be reached in the photoemission process, and 2) extrinsic structure due to energy losses suffered by the photoelectron as it escapes the crystal. Table III lists the energy of the loss structure observed in this work and the value of losses observed in externally produced electron beams passing through the alkali halides.<sup>9</sup> For example in NaCl, the losses associated with the Na core peaks agree well with Best's data and are thus extrinsic loss peaks. However from Fig. 7, it can be seen that the loss structure of the Cl 2p is different.

An interpretation of this peak as a final state satellite is supported by the observation of a 6-eV satellite from the Cl 3s in the spectrum of LiCl by Wertheim and Rosencwaig,<sup>10</sup> as well as in the soft x-ray spectrum of Fischer and Braun.<sup>11</sup>

Table I. Comparison of atomic spin-orbit splitting of outer-most halogen level with splitting of observed features in valence bands of the alkali halides of this study.

	Atomic spin-orbit splitting <sup>a</sup>	LiX <sup>b</sup>	NaX <sup>b</sup>	KX <sup>b</sup>
F	0.05	1.68	---	---
Cl	0.11		1.13	---
Br	0.46		1.28	---
I	0.94		1.48	1.08

<sup>a</sup>Ref. 8.  
<sup>b</sup>This work.

Table II. Binding energies (eV) of the outer core levels of the sodium and potassium halides.<sup>a</sup>

		<u>LiF</u>							
		VB(1)	3.54						
		VB(2)	5.22						
		F 2s	24.90						
		Li 1s	50.77						
		<hr/>							
		<u>NaF</u>		<u>NaCl</u>		<u>NaBr</u>		<u>NaI</u>	
VB	2.06	VB(1)	1.47	VB(1)	1.67	VB(1)	1.67	VB(1)	1.67
F 2s	23.20	VB(2)	2.60	VB(2)	2.95	VB(2)	3.15	VB(2)	3.15
Na 2p	24.77	Cl 3s	12.58	Br 4s	12.83	I 5s	11.21	I 5s	11.21
Na 2s	57.46	Na 2p	27.03	Na 2p	28.21	Na 2p	29.29	Na 2p	29.29
		Na 2s	59.77	Na 2s	61.00	I 4d <sub>5/2</sub>	47.68	I 4d <sub>5/2</sub>	47.68
				Br 3d	66.21	I 4d <sub>3/2</sub>	49.35	I 4d <sub>3/2</sub>	49.35
						Na 2s	61.96	Na 2s	61.96
		<hr/>							
		<u>KF</u>		<u>KCl</u>		<u>KBr</u>		<u>KI</u>	
VB	1.38	VB	1.87	VB	1.27	VB(1)	1.48	VB(1)	1.48
K 3p	13.01	K 3p	14.07	K 3p	14.17	VB(2)	2.56	VB(2)	2.56
F 2s	22.24	K 3s	30.11	Br 4s	16.24	I 5s	10.82	I 5s	10.82
K 3s	27.75			K 3s	30.21	K 3p	15.55	K 3p	15.55
				Br 3d	65.68	K 3s	31.59	K 3s	31.59
						I 4d <sub>5/2</sub>	47.48	I 4d <sub>5/2</sub>	47.48
						I 4d <sub>3/2</sub>	49.10	I 4d <sub>3/2</sub>	49.10

<sup>a</sup>Energies are relative to the top of the valence band and are given to  $\pm 0.1$  eV.

Table III. Loss structure observed in this work and characteristic energy losses (CEL) reported by Best.<sup>a</sup>

		<u>LiF</u>							
		Li 1s	4.13, 15.0, 23.91, ~36.0						
		F 2s	2.95, 5.81, 8.46						
		CEL	14.5, 17.0, 24.9, 43.2						
<u>NaF</u>		<u>NaCl</u>		<u>NaBr</u>		<u>NaI</u>			
F 2p	11.5	Na 2p	9.4, 12.4, 15.4, 21.6	Br 3d	14.7, 19.8	Na 2s	12.4		
CEL	11.6	Na 2s	9.5, 12.7, 15.5, 20.8	Br 4s	15.1	I 4p	14.7, ~30		
		Cl 2p	18.6	Na 1s	8.64, 13.7	I 4s	~12		
		Cl 2s	10.0, 15.3,	CEL	7.6, 13.9, 20.8	I 3p <sub>1/2</sub>	~12.6		
		Na 1s	9.4, 12.6, 15.3, 21.4			Na 2s	12.6		
		CEL	8.7, 12.7, 15.5, 22.2			I 5p	12.8		
						CEL	12.3, 17.8		
							25.9, 33.1		
<u>KF</u>		<u>KCl</u>		<u>KBr</u>		<u>KI</u>			
K 2s	11.4, 28.5	K 3s	10.6, 13.4, 14.8, 22.7	K 3s	10.1, 12.8, 14.9	K 2s	10.4		
K 2p	11.3, 28.9	K 3p	~11	Br 3d	9.7, 14.1, ~27	CEL	8.0, 11.2		
F 1s	7.4, 11.7, ~28	K 2p	8.1, 11.39, 25.9	CEL	9.2, 12.5, 18.2,				
CEL	10.1, 12.4, 17.1,	Cl 2p	17.1, 26.5		22.0, 25.4, 28.0				
	22.5, 26.9, 31.0	CEL	10.2, 13.8, 19.6, 23.0, 26.4						

<sup>a</sup>Ref. 9.



## Footnotes and References

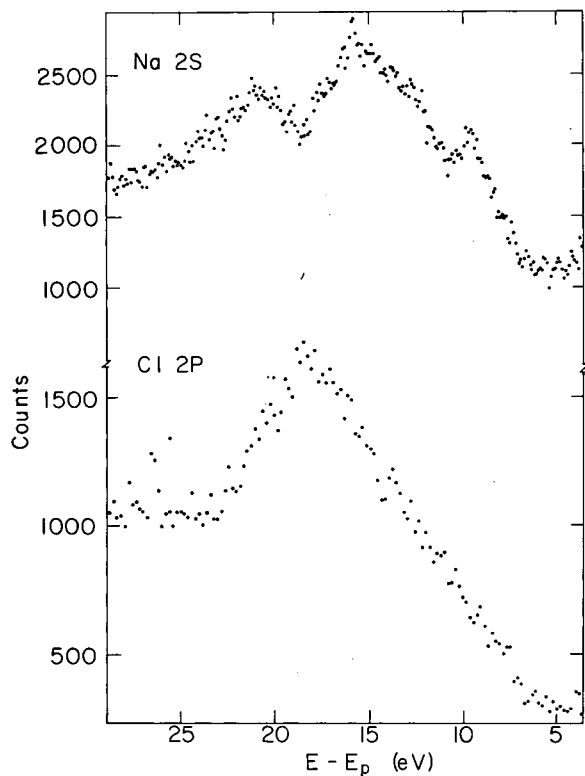


Fig. 7. The loss structure of the Cl 2p and Na 2s levels of NaCl. (XBL 736-3235)

## Acknowledgments

We would like to thank Dr. Norman Edelstein for the crystals used in these experiments.

\* Condensed from LBL-1945. To be published in Phys. Rev. B (Apr. 1, 1974).

† Present address: IBM T. J. Watson Research Center, Yorktown Heights, NY 10598.

1. M. L. Cohen and T. K. Bergstresser, Phys. Rev. **141**, 789 (1966).
2. R. L. Zucca, J. P. Walter, Y. R. Shen, and M. L. Cohen, Solid State Comm. **8**, 627 (1970).
3. J. P. Walter and M. L. Cohen, Phys. Rev. B **1**, 2661 (1970).
4. C. Y. Fong and Marvin L. Cohen, Phys. Rev. **185**, 1168 (1969).
5. R. A. Pollak, L. Ley, S. P. Kowalczyk, D. A. Shirley, J. D. Joannopoulos, D. J. Chadi, and Marvin L. Cohen, Phys. Rev. Letters **29**, 1103 (1972).
6. R. G. Cavell, S. P. Kowalczyk, L. Ley, R. A. Pollak, B. Mills, D. A. Shirley, and W. Perry, Phys. Rev. B **7**, 5313 (1973).
7. John P. Walter and Marvin L. Cohen, Phys. Rev. B **4**, 1877 (1971).
8. C. E. Moore, "Atomic Energy Levels" (U.S. Dept. of Commerce, NBS Circular, No. 467), Vol. 1 (1949); Vol. 2 (1952); Vol. 3 (1958).
9. P. E. Best, Proc. Phys. Soc. **79**, 133 (1962).
10. G. K. Wertheim and A. Rosencwaig, Phys. Rev. Letters **26**, 1179 (1971).
11. D. W. Fischer and W. L. Braun, Anal. Chem. **37**, 902 (1965).

## ELECTRONIC DENSITY OF STATES AND BONDING IN CHALCOPYRITE-TYPE SEMICONDUCTORS

Carmen Varea de Alvarez,\* Marvin L. Cohen,\*  
L. Ley, S. P. Kowalczyk, F. R. McFeely,  
D. A. Shirley, and R. W. Grant†

We have calculated the valence-band density of states  $N(E)$  and measured the x-ray photoemission (XPS) spectrum  $I(E)$  for the chalcopyrite-type semiconductor  $ZnGeP_2$ .  $I(E)$  was also measured for  $CdSnAs_2$ . In  $ZnGeP_2$

the shapes of  $N(E)$  and  $I(E)$  agreed very well, allowing us to correlate structure in  $I(E)$  explicitly with Zn-P and Ge-P bonds through contour plots of electron charge densities integrated over selected energy intervals,  $\rho_{\Delta E}(\vec{r})$ .

This approach appears promising for a detailed understanding of bonding in chalcopyrite-type compounds and other ternary or more complex materials.

The  $A^{II}B^{IV}C^V$  compounds are ternary analogues of the  $B^{III}C^V$  zincblende semiconductors (e.g.,  $ZnGeP_2$  is the analogue of GaP) in which alternate cation sites are occupied by atoms of the Group II and Group IV elements surrounded in tetrahedral coordination by Group V anions. The ternary compounds therefore possess an essential complication that is absent in their binary analogues--two kinds of bonds. The present work represents the first attempt to relate features in  $N(E)$  or  $I(E)$  to different bonds in a relatively complex material, thereby extending a correlation that is obvious for the diamond and zincblende lattices.<sup>1</sup> The photoelectron spectra were measured in a Hewlett-Packard 5950 ESCA Spectrometer (which uses monochromatized  $AlK_{\alpha}$  x-rays) modified to operate at pressures well below  $10^{-9}$  Torr. Samples of the single crystals were fractured inside the spectrometer immediately before the measurements. Valence-band spectra  $I(E)$  referred to the top of the valence band are shown in Fig. 1. The intense peaks corresponding to emission of core-like Zn 3d and Cd 4d electrons have been truncated to exhibit the valence s and p contributions more clearly. The unperturbed shape of the d peaks is indicated by solid curves in Fig. 1.

In a typical zincblende semiconductor,  $I(E)$  exhibits the following prominent structure:<sup>1</sup> A broad peak (peak I) near the top of the valence band, separated from a second narrower peak (peak II) by a small valley, followed by a gap which separates this structure from the lowest energy peak III. States in peak I correspond to electrons near the bonding sites, peak II contains electrons which are mostly s-like around the cation and some charge piled up in the bonding region, and peak III contains electrons which are s-like around the anion. This is also the general structure of  $I(E)$  in the chalcopyrite-type semiconductors (compare Fig. 1).

Starting at the top of the valence band,  $I(E)$  rises in both compounds to an intense, broad peak at a binding energy of 2-4 eV (peak I). This peak exhibits a wealth of fine structure. After a well defined minimum at 6.2 eV in  $ZnGeP_2$  and 5.7 eV in  $CdSnAs_2$ , the intensity rises again. In  $CdSnAs_2$  a blunt hump is observed around 7.0 eV (peak II) with a satellite at 8.3 eV. Beyond 8.5 eV  $I(E)$  follows closely the sharp onset of the leading edge of the 4d peak. Valence-band contributions to  $I(E)$  cannot be distinguished at higher binding energies.

In  $ZnGeP_2$  a second region of high valence-electron density can be identified around 7.0 eV

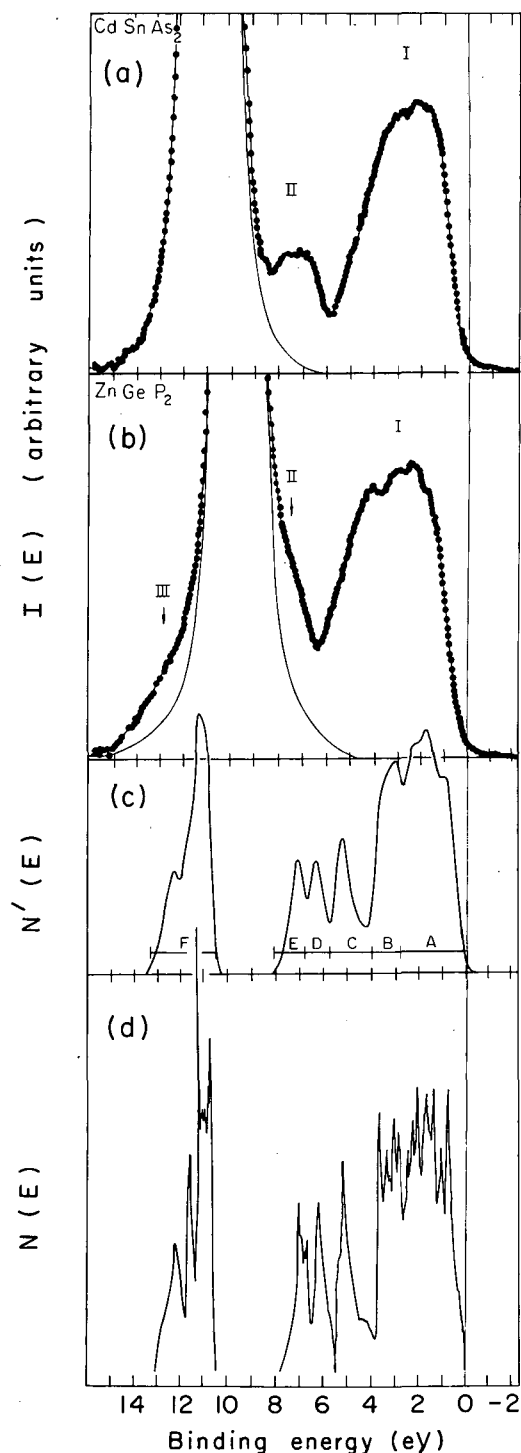


Fig. 1. (a) XPS spectrum for  $CdSnAs_2$ , (b) XPS spectrum for  $ZnGeP_2$ , (c) Broadened theoretical density of states for  $ZnGeP_2$ , (d) Calculated valence band density of states for  $ZnGeP_2$ . (XBL 7310-4205)

on the leading edge of the Zn 3d peak. There is a shoulder on the low energy (high binding energy) side of the Zn 3d peak which we interpret as due to a third valence band peak centered at  $\sim 12.5$  eV with a total width of about 4 eV at its base.

Figure 1 also contains  $N(E)$  for  $\text{ZnGeP}_2$  deduced from a band structure calculation employing the empirical pseudopotential method (EPM).<sup>2</sup> Critical points in the band structure show up as sharp structure in  $N(E)$ . To facilitate comparison with experiment a Gaussian broadened curve  $N'(E)$  is also shown. Figure 2 shows  $\rho_{\Delta E}(\vec{r})$ . The energy intervals  $\Delta E$  were chosen through analysis of  $N'(E)$ ;  $\rho_{\Delta E}(\vec{r})$  was then calculated for each interval by restricting the band indices and k-states to give electron states in the desired energy range  $\Delta E$ .

Referring to Fig. 1 we see that the highest energy (lowest binding energy) valence-band structure, which corresponds to peak I in the zincblende case, is split into two regions, A and B. Using the  $\rho_A(\vec{r})$  and  $\rho_B(\vec{r})$  of Fig. 2, we see that these regions contain electrons in the Zn-P and Ge-P bonds, respectively. Peak I is therefore split by the energy difference in the two bonds. The Ge-P bond appears to be a stronger covalent bond (i. e., it lies lower in energy) than the Zn-P bond, as would be expected on chemical grounds.

The peak-II region splits into three peaks C, D, and E. For  $\text{ZnGeP}_2$  in the C region charge concentrates on Zn with some charge in the Ge-P bond while region D and show charge accumulating on Ge. This order is expected because the Ge potential is deeper than that of Zn. In the XPS spectra, peak II is partially hidden by the d-peaks. In  $\text{CdSnAs}_2$ , by measuring the relative areas under the experimental spectrum and comparing this with the theoretical curve of  $\text{ZnGeP}_2$ , we conclude that the structure in the region between 6.5 eV and 7.5 eV probably corresponds to the D and C unresolved doublet. The satellite at 8.3 eV is interpreted as arising from region E. In the theoretical  $N'(E)$  the region of peak III is labeled F. There are 8 electrons in this region and  $\rho_F(\vec{r})$  shows that the electrons are mostly s-like around the anion, i. e., the P site. This is the same configuration found in zincblende-type semiconductors. It is expected, as the phosphorous 3s subshell is tightly enough bound to be nearly corelike.

The above analysis illustrates the advantages of dealing with both  $\rho_{\Delta E}(\vec{r})$  and  $N(E)$ . We have concentrated on  $\text{ZnGeP}_2$  in this work, but the results should be general for the chalcopyrite-type compounds. The possibility of identifying certain features in  $I(E)$  with well-defined

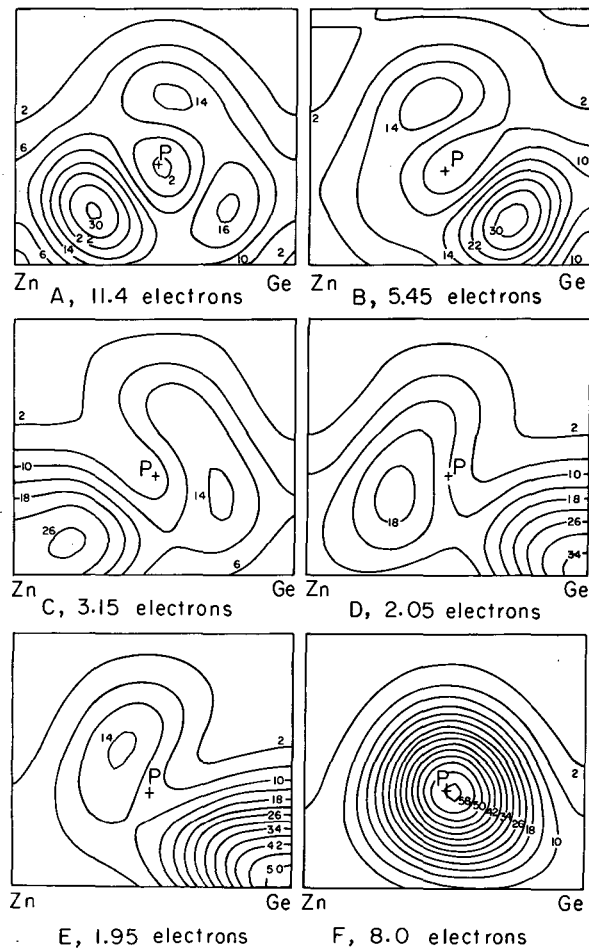


Fig. 2. Calculated electronic charge density contour plots for  $\text{ZnGeP}_2$  corresponding to density of states peaks A, B, C, D, E, and F. The plots are normalized to the number of electrons contained in each peak. This value is given for each plot. (XBL 7310-4206)

charge distributions and specific bonds should be especially useful in the analysis of complex or amorphous materials, which as yet defy a realistic theoretical treatment.

#### Acknowledgement

We thank H. Nadler of the Science Center, Rockwell International for growing the  $\text{ZnGeP}_2$  crystal.

#### Footnotes and References

\* Supported in part by National Science Foundation Grant GP 35688.

† Present address: Science Center, Rockwell International, Thousand Oaks, CA 91360.

1. L. Ley, S. Kowalczyk, R. Pollak, and D. A. Shirley, *Phys. Rev. Letters* **29**, 1088 (1972); and R. A. Pollak, L. Ley, S. Kowalczyk, D. A. Shirley, J. D.

Joannopoulos, D. J. Chadi, and M. L. Cohen, *Phys. Rev. Letters* **29**, 1103 (1972).

2. C. Varea de Alvarez and M. L. Cohen, *Phys. Rev. Letters* **30**, 979 (1973).

### TOTAL VALENCE BAND DENSITIES OF STATES OF III-V AND II-VI COMPOUNDS FROM XPS

L. Ley, R. A. Pollak,\* F. R. McFeely,  
S. P. Kowalczyk, and D. A. Shirley

The technical importance and the wealth of band structure calculations on binary semiconductors with an average of 4 valence electrons led us to a comprehensive survey of the total valence-band density of states (DOS) of 14 of these compounds.

We measured the x-ray photoelectron spectra (XPS) of cubic GaP, GaAs, GaSb, InP, InAs, InSb, ZnS, ZnSe, ZnTe, CdTe, and HgTe, and of hexagonal ZnO, CdS, and CdSe. Spectra in the 0-50 eV binding energy range were obtained from freshly-cleaved single crystals, using monochromatized  $AlK_{\alpha}$  (1486.6 eV) radiation.

The binding energies of the outermost d-levels were determined relative both to the top of the valence band ( $E_B^V$ ) and to the Fermi level of a thin layer of gold that was vapor deposited after each run ( $E_B^F$ ). The quoted energies,  $E_B^V$ , are accurate to  $\pm 0.15$  eV in most cases, and those relative to the Fermi level to  $\pm 0.09$  eV.

These data also yielded measures of sample charging during the x-ray bombardment and the position of the Fermi level  $E_F$ . The general trend is for charging to increase with band gap. The materials with small fundamental band gaps charge to values near or less than the band gap, and those with large gaps charge to values near or greater than the band gap.

$E_F$  does not show any preferential position with respect to the band gap as has been suggested from earlier data,<sup>1,2</sup> obtained under less favorable conditions. Evidence for an apparent increase in core d-level spin-orbit splitting over free atom values was interpreted as possibly due to the effects of the tetrahedral crystal field experienced by the atom in the zincblende structure. A tetrahedral field would not only lift part of the degeneracies of the  $d_{5/2}$  and  $d_{3/2}$  levels, but would also increase the average separation of the resulting

groups. A straightforward calculation shows that measurable effects of the latter kind would render the splitting into sublevels unobservable.

The s, p valence-band spectra show three main peaks with considerable structure on the "least-bound" peak. A generalized VB spectrum is shown in Fig. 1. The energies of features labeled in Fig. 1 are set out in Table I for the 14 semiconductors studied. These energies are generally in quite good agreement with those obtained for some of the compounds from UV-photoemission.<sup>3</sup>

The great expenditures in calculating the band structure throughout an irreducible part of the Brillouin zone has limited available theoretical densities of states of relatively few compounds. Therefore, in order to compare our experimental data with as wide a

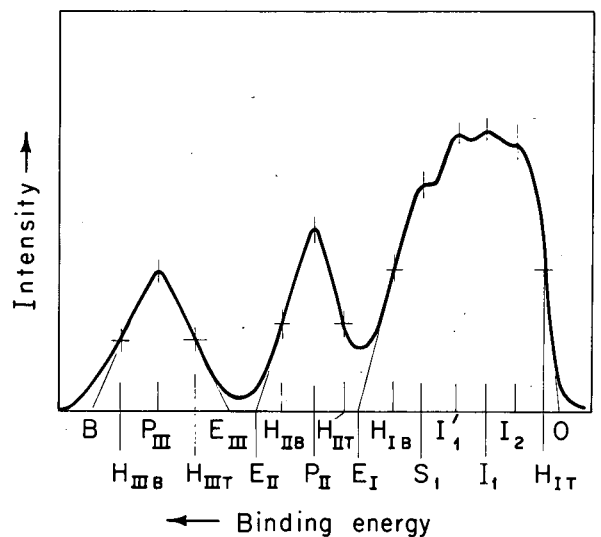


Fig. 1. Generalized photoelectron spectrum for the binary semiconductors. For an explanation of the labeled features see text. (XBL 735-2813)

Table I. Binding energies of characteristic valence-band features from top of valence bands (in eV).<sup>a</sup>

Material	H <sub>IT</sub>	I <sub>2</sub>	I <sub>1</sub>	I' <sub>1</sub>	S <sub>1</sub>	H <sub>IB</sub>	E <sub>I</sub>	H <sub>IIT</sub>	P <sub>II</sub>	H <sub>IIB</sub>	E <sub>II</sub>	E <sub>III</sub>	H <sub>IIT</sub>	P <sub>III</sub>	H <sub>IIB</sub>	B
GaP	0.7	1.7	2.4	--	3.5	4.0	--	5.4	6.5	7.0	7.4	8.2	9.1	10.3	12.2	13.4
GaAs	1.0	1.8	2.4	2.9	3.8	--	--	--	6.6	7.5	8.1	9.0	10.0	11.4	13.3	14.4
GaSb	0.8	1.7	2.1	--	3.4	3.7	4.4	5.5	6.4	7.1	7.4	8.6	9.2	10.0	11.1	11.9
InP	0.7	--	1.8	--	2.7	3.6	--	--	5.4	6.2	6.9	7.8	8.6	9.7	10.8	11.6
InAs	0.6	1.7	2.1	--	3.0	3.5	--	--	5.8	6.3	6.9	8.5	9.4	10.5	11.6	12.6
InSb	1.0	2.0	2.5	--	3.2	3.5	4.2	--	5.9	6.5	7.2	8.4	8.9	10.0	11.1	12.0
ZnO	2.1	--	2.9	--	≈3.8	--	--	--	5.9	6.6	7.0	≈18	19.8	20.7	23.1	24.8
ZnS	0.8	2.0	2.6	--	3.2	4.0	--	--	4.9	5.9	6.4	11.4	11.8	12.4	13.3	13.8
ZnSe	0.8	1.6	1.9	--	2.6	3.5	--	--	5.2	5.8	6.0	11.6	12.1	12.7	14.6	15.8
ZnTe	0.7	(1.2)	1.7	(2.2)	2.8	3.4	--	--	5.1	5.8	6.3	11.3	11.5	11.9	12.7	13.4
CdS	0.8	(1.3)	1.6	--	(2.1)	3.1	--	--	4.1	4.8	5.5	--	--	--	--	--
CdSe	0.8	1.5	1.9	--	--	--	--	--	4.3	5.1	5.5	--	--	--	--	--
CdTe	0.6	1.5	1.8	--	(2.5)	2.9	(3.6)	--	4.5	5.2	5.6	--	--	--	--	--
HgTe	0.7	1.5	2.1	--	--	3.3	--	--	5.3	6.0	6.5	--	--	--	--	--

<sup>a</sup>See Fig. 1 and text for definition of points. Accuracy is ±0.1 eV.

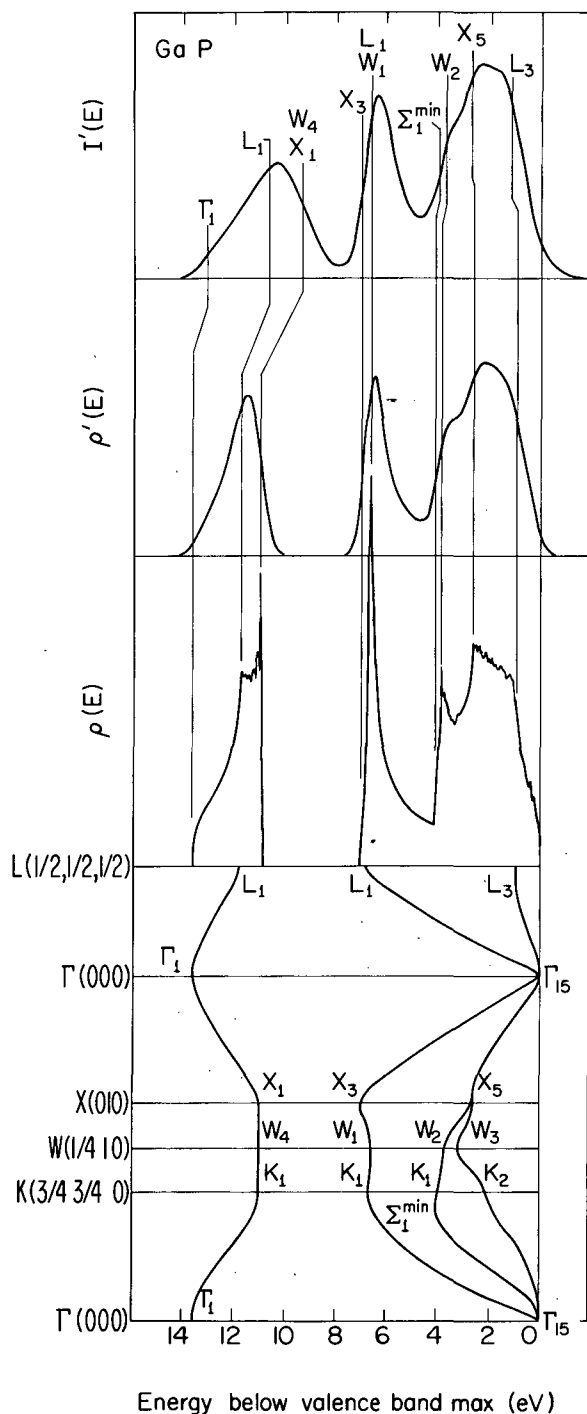


Fig. 2. Band structure, density of states  $\rho(E)$ , broadened density of states  $\rho'(E)$ , and corrected valence-band spectrum  $I'(E)$  for GaP. Band structure and  $\rho(E)$  are taken from Ref. 4. (XBL 733-2509)

range of calculations as possible, it was necessary to derive from the spectrum corrected for inelastic losses,  $I'(E)$ , the energies of selected symmetry points. The theoretical densities of states  $\rho(E)$  for five cubic binary compounds as calculated by the empirical pseudopotential method (EPM)<sup>4</sup> have been broadened with a Gaussian of 0.7 eV FWHM at the top and 0.8 eV FWHM at the bottom of the valence band, to account for finite instrumental resolution plus lifetime broadening which increases with increasing binding energy. Figure 2 shows as an example the close resemblance of this broadened density of states  $\rho'(E)$  with the experimental spectrum  $I'(E)$  for GaP. The positions of characteristic features in the theoretical density of states  $\rho(E)$  which are associated with the energies  $E_i$  of critical points can be related to corresponding features in the broadened density of states  $\rho'(E)$ . Applying the same criteria which determine  $E_i$  in  $\rho'(E)$  to  $I'(E)$  yields in turn experimental values for  $E_i$ . The similarity in the band structure of all the cubic binary semiconductors allows an extension of this procedure to spectra for which no theoretical densities of states are yet available.

The energies of the symmetry points  $L_3$ ,  $X_5$ ,  $W_2$ ,  $\Sigma_1^{\min}$ ,  $W_1$ ,  $X_3$  ( $L_1$ ),  $X_1$ ,  $L_1$  and  $\Gamma_1$  obtained for the eleven cubic compounds, are the first comprehensive set of absolute energy levels in the valence bands of binary semiconductors.

A comparison with theoretical band structure results from EPM, OPW, OPW (adj), SCOPW, APW, KKR, and ROPW ( $X_{\alpha\beta}$ )<sup>5</sup> methods, where available, show, that ROPW ( $X_{\alpha\beta}$ )<sup>5</sup> energies agree very well with experiment, on the whole. In particular, they predict the important "ionicity gap"  $X_1 - X_3$  quite well.

#### Footnotes and References

\*Present Address: IBM Watson Research Center, Yorktown Heights, NY 10598.

1. W. Gudat, E. E. Koch, P. Y. Yu, M. Cardona, and C. M. Penchina, Phys. Stat. Sol. (b) **52**, 505 (1972).
2. C. J. Veseley, R. L. Hengehold, and D. W. Langer, Phys. Rev. **5B**, 2296 (1972).
3. D. E. Eastman, W. D. Grobman, and J. Freeouf, to be published.
4. J. Chelikowsky, D. J. Chadi, and M. L. Cohen, to be published.
5. J. P. van Dyke and F. Hermann, private communication.

## CORE-LEVEL BINDING ENERGY SHIFTS IN SMALL MOLECULES\*

D. W. Davis,<sup>†</sup> M. S. Banna, and D. A. Shirley

Chemical shifts in binding energies of core-level electrons are of interest because they can provide information about the relative distribution of valence electrons within molecules. In this work we report x-ray photoemission measurements of a number of shifts in small molecules in the gaseous state. The binding energy,  $E_B$ , is given by the equation

$$E_B + K = h\nu$$

where  $K$  represents the experimentally determined kinetic energy, and  $h\nu$  is the energy of the exciting radiation, in this case  $MgK\alpha_{1,2}$  (1253.6 eV). Measurements were made in the Berkeley iron-free spectrometer<sup>1</sup> using sample pressures of  $(2 - 5) \times 10^{-2}$  Torr. Further details are given elsewhere.<sup>2</sup> Core level shifts were obtained relative to selected reference gases, usually bled in simultaneously with the gas under study. The peak positions were obtained by fitting the spectra with Lorentzian peak shapes. Some experimental shifts are listed in Table I.

To interpret our results, we use two models. In the "relaxation potential model" or RPM,<sup>3</sup> shifts are predicted by the equation

$$\Delta E_B = -\Delta V_a - \Delta V_R.$$

Here  $V_a$  is the initial-state electrostatic potential energy at nucleus  $a$ , where the ionized core electron was localized. It is given by

$$V_a = \sum_i \psi_i^*(i) (e^2/R_{ia}) \psi_i(i) d\tau_i - \sum_{j \neq a} Z_j'/R_{aj},$$

where  $\psi_i$  is the molecular orbital for electron  $i$ . In our calculations, the contribution of the core electrons at the host atom to  $V_a$  is neglected; therefore  $i$  is summed over valence electrons only.  $Z_j'$  equals the charge on nucleus  $j$ ,  $Z_j$ , minus the number of core electrons centered at nucleus  $j$ .  $V_R$  represents the final-state contribution to binding energies, and is given by the equation

$$V_R = \frac{1}{2} (V_a^+ - V_a),$$

where  $V_a^+$  is the potential energy at the nucleus in the final-state molecular ion with a core vacancy at nucleus  $a$ .<sup>4</sup> The valence orbitals  $\psi_i^+$  were approximated by simply increasing  $Z_a$  to  $Z_a + 1$  and recomputing the wavefunctions.<sup>3a</sup> CNDO/2 wavefunctions were used to get the  $\psi_i^+$ 's. In the GPM approach,<sup>3</sup>  $\Delta V_R$  is neglected, i. e.,  $\Delta E_B = -\Delta V_a$ .

The RPM is superior to the GPM for the prediction of core-level shifts for a single element in diverse molecular environments. This is so because it can account for the increase in  $V_R$  with the number of atomic centers in a molecule and when ligands are added to the host atom. The effect of  $V_R$  upon core-level chemical shifts is illustrated by the trend

Table I. Experimental chemical shifts.

Compound	Reference	Core level <sup>a</sup>	$E_B(\text{compound}) - E_B(\text{Ref})$ (eV)
$C_6H_6$	$CH_4$	C 1s	-11.54(2)
$CHF_3$	$CH_4$	C 1s	-2.72(3)
$CH_2F_2$	$CH_4$	C 1s	-5.52(4)
$CH_2F_2$	$CH_4$	F 1s	-1.83(10)
$CH_3CH_3$	$CH_4$	C 1s	-11.20(4)
$CH_3CH_2F$	$CH_4$	C 1s	-8.57(5), -10.77(5)
$CH_3CH_2F$	$CH_4$	F 1s	-3.20(6)
$CH_3CHF_2$	$CH_4$	C 1s	-5.91(4), -10.34(4)
$CH_3CHF_2$	$CH_4$	F 1s	-2.22(6)

in the N(1s) shifts in methyl amines (Fig. 1). The GPM theory fails to predict this trend while the RPM gives results falling within 0.2 eV of the predicted values.

The GPM model can be applied successfully to interpret shifts among similar molecules. An example of this are the fluorinated ethanes (Fig. 2) and the fluorinated ethylenes (Fig. 3).

One can obtain empirical atomic charges from core-level shifts using the ground state potential model.<sup>2</sup> If the off-diagonal matrix elements of  $R_{ia}^{-1}$  between atomic orbitals are neglected and if the remaining matrix elements are treated as if they contained only s orbitals,  $V_a$  becomes simply:

$$V_a = -[q_a e^2 \langle 1/R_a \rangle + \sum_{j \neq a} e^2 q_j / R_{aj}] + Z'_a e^2 \langle 1/R_a \rangle.$$

Here  $\langle 1/R_a \rangle$  is the expectation value of  $1/r$  for the valence electrons in atom a, and  $q_j = Z_j - p_j$ , where  $Z'_j$  is the atomic number minus the number of core electrons and  $p_j$  is the valence-shell population. Thus the expression for chemical shifts becomes:

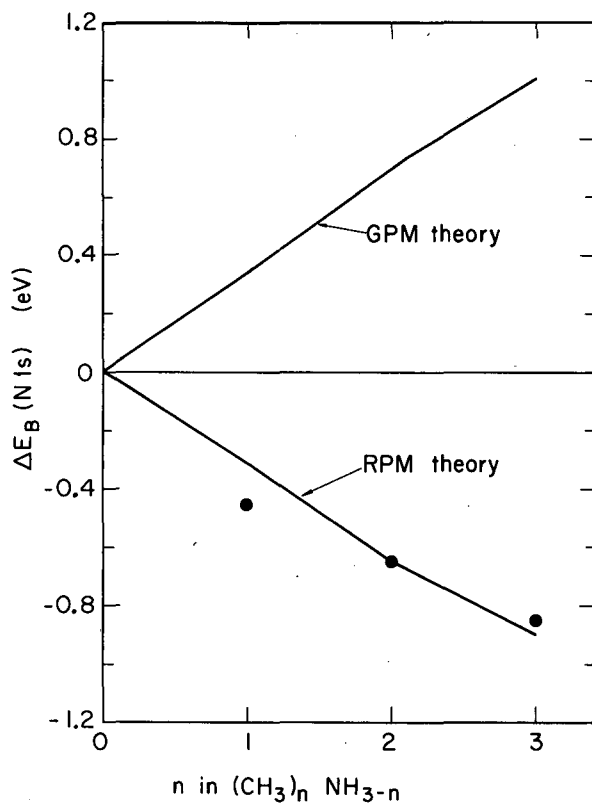


Fig. 1. The N(1s) binding-energy shifts in methylamines, relative to NH<sub>3</sub>, versus the number of methyl groups. Points are experimental results, from Ref. 8, while lines connect theoretical points calculated from ground-state potential model (GPM) and from relaxation potential model (RPM). Clearly relaxation dominates the binding energy shifts for the methylamines. (XBL 736-3160)

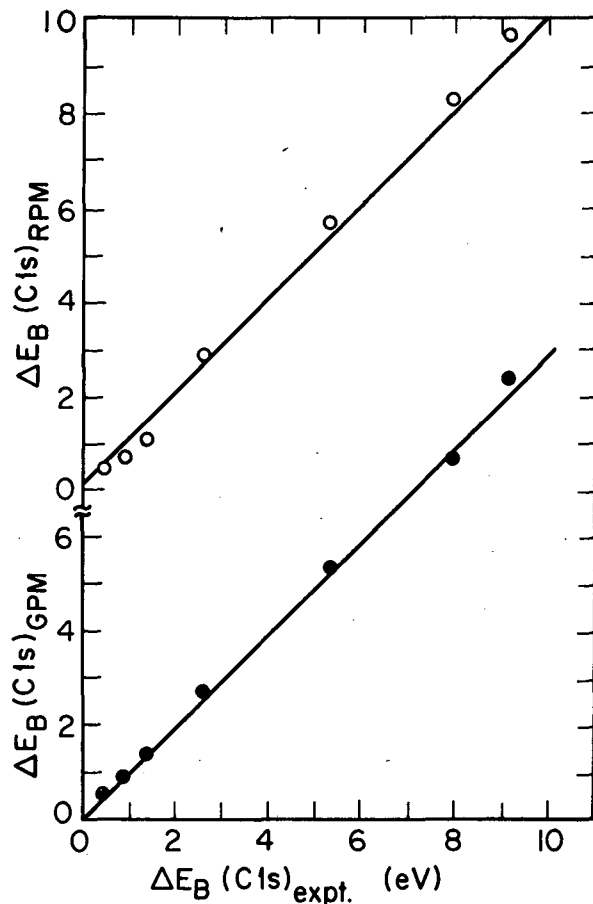


Fig. 2. Plot of theoretical (GPM and RPM) C(1s) shifts in fluoroethanes versus experimental values, with ethane as a reference. Open circles are RPM, filled circles GPM predictions. Both lines have unit slope. Standard deviations of theoretical values are 0.14 eV (GPM), 0.31 eV (RPM). These results show that  $\Delta V_R$  is exaggerated in RPM calculations. Compounds in order of increasing  $\Delta E_B$  are: (C<sub>2</sub>H<sub>6</sub>), C<sup>\*</sup>H<sub>3</sub>CH<sub>2</sub>F, C<sup>\*</sup>H<sub>3</sub>CHF<sub>2</sub>, C<sup>\*</sup>H<sub>3</sub>CF<sub>3</sub>, C<sup>\*</sup>H<sub>2</sub>FCH<sub>3</sub>, C<sup>\*</sup>HF<sub>2</sub>CH<sub>3</sub>, C<sup>\*</sup>F<sub>3</sub>CH<sub>3</sub>, C<sub>2</sub>F<sub>6</sub>. (XBL 736-3156)



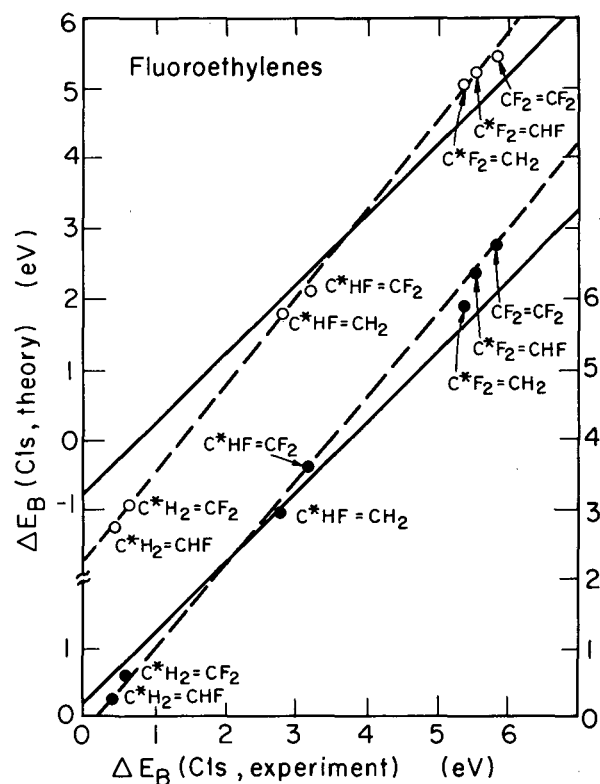


Fig. 3. Plot of RPM (open circles) and GPM (filled circles) theoretical C 1s shifts for fluorinated ethylenes, relative to  $C_2H_4$ , against experimental values. Solid lines are fits for unit slope (standard deviations are 0.38 (GPM) and 0.53 (RPM)), while dashed lines were fitted with slopes variable (standard deviations 0.12 (GPM) and 0.07 (RPM)). Host atoms are noted by asterisks. (XBL 736-3225)

$$\Delta E_B^a = E_B^a(\text{sample}) - E_B^a(\text{reference}) = q_a e^2 \langle 1/R_a \rangle + \sum_{j \neq a} e^2 q_j / R_{aj} - Z'_a e^2 \langle 1/R_a \rangle + V_a(\text{reference}).$$

The above is a linear equation. One also has the electroneutrality condition  $\sum_j q_j = 0$ . Thus the  $q_j$ 's can be calculated if enough shifts are measured. This model is called ACHARGE.<sup>2a</sup> Using  $e^2 \langle 1/R_a \rangle_C = 22.0 \text{ eV}/|e|$  for carbon 1s shifts and  $e^2 \langle 1/R_a \rangle_F = 32.5 \text{ eV}/|e|$  for fluorine 1s shifts<sup>2a</sup> we have computed charge distributions in fluoromethanes, fluoroethanes and fluoroethylenes, a sample of which is shown in Table II. Both these charges and those obtained from CNDO/2 give a negative charge

Table II. Derived atomic charges.

Compound	Atom <sup>a</sup>	$q^b$ (ACHARGE)	$q^b$ (CNDO/2)
$CH_3 - CH_3$	C	0. (assumed)	0.
	H	0. (assumed)	0.
$H_3C^1 - C^2H_2F$	$C^1$	-0.02	-0.04
	$C^2$	0.23	0.21
	F	-0.23	-0.21
	$\bar{H}$	0.002	0.01
$H_3C^1 - C^2F_2H$	$C^1$	-0.05	-0.08
	$C^2$	0.49	0.42
	F	-0.23	-0.21
	$\bar{H}$	0.006	0.04
$H_2C^1 = C^2FH$	$C^1$	-0.05	-0.11
	$C^2$	0.25	0.22
	$\bar{H}$	0.004	0.03
	F	-0.21	-0.19
$H_2C^1 = C^2F_2$	$C^1$	-0.14	-0.18
	$C^2$	0.50	0.44
	H	0.03	0.06
	F	-0.21	-0.19

<sup>a</sup>  $\bar{H}$  denotes an average of all hydrogen charges.

<sup>b</sup> Charges are given in units of  $|e|$ .

for the carbon  $\beta$  to a fluorine atom, contrary to the intuitive notion that electronegative substituents tend to withdraw electrons from all other atoms in the molecule.

#### Footnotes and References

\* Condensed from LBL-1909.

<sup>†</sup> Present Address: University of Pittsburgh, Department of Chemistry, Pittsburgh, PA 15260.

1. C. S. Fadley, S. B. M. Hagström, M. P. Klein, and D. A. Shirley, *J. Chem. Phys.* **48**, 3779 (1968).
2. a) D. W. Davis, D. A. Shirley, and T. Darrah Thomas, *J. Am. Chem. Soc.* **94**, 6565 (1972); b) G. D. Stucky, D. A. Matthews, J. Hedman, M. Klasson, and C. Nordling, *J. Am. Chem. Soc.* **94**, 8009 (1972).
3. a) D. W. Davis and D. A. Shirley, *Chem. Phys. Letters* **15**, 185 (1972); b) D. W. Davis and D. A. Shirley, to be published.
4. L. Hedin and A. Johansson, *J. Phys. B, Ser. 2*, **2**, 1336 (1956).

ANOMALOUS MULTIPLET-SPLITTING INTENSITY RATIOS  
IN K-LEVEL XPS SPECTRA OF NO AND O<sub>2</sub>

P. S. Bagus,\* M. Schrenk,\* D. W. Davis, and D. A. Shirley

When photoelectrons are ejected from atomic core levels of paramagnetic molecules<sup>1</sup> or salts,<sup>2</sup> multiplet splitting may be observed in the characteristic photoelectron peaks. This splitting arises from final state multiplet structure established by coupling of the open core shell with the valence shells. The simplest case is one in which a valence level of character  $2S+1L$  (or  $2S+1\Lambda$  for molecules) couples to a core  $s$  electron. Two peaks are observed: a lower binding-energy, higher-multiplicity peak corresponding to the final state  $2S+2L$ , and a second peak associated with the final state  $2SL$ . The intensity ratio of these two peaks is nominally the multiplicity ratio  $(S + 1)/S$ .

Positive deviations from the  $(S + 1)/S$  intensity ratio have been observed in a number of cases, and this may be a rather general phenomenon. Simple theory suggests that correlation effects, which affect both the multiplet splitting energy and the intensity ratio, are largest when the photoelectron is ejected from a core state having the same principal quantum number as the unpaired valence orbital, and are much less important otherwise. Thus deviations from multiplet ratios in second-row elements are not expected a priori.

Inspection of the published spectra<sup>1</sup> for O<sub>2</sub> and NO confirms that the multiplet ratios  $4\Sigma/2\Sigma = 2$  and  $3\Pi/1\Pi = 3$  are approximately satisfied, but especially in the O<sub>2</sub> case there is apparent evidence for a positive deviation. In particular the peak heights in the partially-resolved spectra stand in a ratio of 2:1, implying that this ratio would increase on resolution of the peaks. This result is surprising, because it seems very unlikely that the correlation effect mentioned above could be large enough to account for sizable deviations in these 1s spectra. It is also disquieting. Multiplet structure in photoemission spectra has potential as a diagnostic tool for studying spin-density distributions. To apply it in this way one should first assess and understand deviations from the multiplet intensity ratios. To this end, we present below both experimental and theoretical results which show that the intensity ratios of the 1s photoelectron multiplet peaks do indeed depart significantly from the final-state multiplicity ratios in NO and O<sub>2</sub>. The measured and calculated (in parentheses) ratios are, for NO(N 1s),  $R(3\Pi/1\Pi) = 3.43(8):1$  (3.09:1) and for O<sub>2</sub>(O 1s) $R(4\Sigma/2\Sigma) = 2.47(3):1$  (2.28:1). These values are in every case

larger than the multiplicity ratios.

Gaseous O<sub>2</sub> and NO were subjected to irradiation by MgK $\alpha_{1,2}$  X-rays in the Berkeley Iron-Free Spectrometer. Photoelectrons were analyzed at an energy resolution of 0.06%. The experiments were carried out at room temperature with sample pressures in the  $(1 - 5) \times 10^{-2}$  Torr range. The spectrometer current was stepped in 0.1 milliamperes ( $\sim 0.1$  eV) intervals. Counting was continued in each case until  $\sim 5 \times 10^3$  counts were obtained in the peak channels.

The spectra were analyzed to yield intensity ratios by least-squares fitting with Lorentzian peaks. A further refinement was made in the peak shape beyond simply using Lorentzians. The incident MgK $\alpha_{1,2}$  characteristic X-ray is of course a doublet, consisting of a lower-energy, lower-intensity component from the  $(2p_{1/2} \rightarrow 1s)$  transition in addition to the stronger  $(2p_{3/2} \rightarrow 1s)$  component. The relative intensities of these components should be about 1:2 and their energy separation about 0.3 eV, as judged by x-ray data on neighboring elements. Thus, in addition to using a single Lorentzian line (version L1), we also fitted the spectra with a line shape that was a composite of two Lorentzians, of relative intensity 1:2. Two versions of this approach were used. In the first, denoted as L2, these two components ( $\alpha_1$  and  $\alpha_2$ ) were separated by 0.40 eV. In the other case, L2', they were separated by 0.32 eV, a figure obtained from relativistic Hartree-Fock-Slater results.<sup>3</sup> In Table I the intensity ratios and weighted variances from all six data sets are listed. It is very encouraging that the derived intensity ratios are quite insensitive to whether fitting procedure L1, L2, or L2' was used. It is especially pleasing that the two-Lorentzian fits give significantly improved variances. We emphasize that use of two rather than one Lorentzian in this way does not constitute the addition of a new parameter, but rather a change in the line shape to recognize the known structure of the exciting radiation.

The theoretical determination of relative intensities and intensity ratios that we present follows from the use of the sudden approximation (SA) as described by Åberg.<sup>4</sup> The SA is applied using Hartree-Fock (HF) wavefunctions computed for the initial ground states and final 1s-hole states of NO and O<sub>2</sub>.<sup>5,6</sup> In the SA, the probability that the ionization of spin

Table I. Experimental final-state intensity ratios, R, of the N 1s ( $^3\Pi/{}^1\Pi$ ) peaks in NO and the O 1s ( ${}^4\Sigma/{}^2\Sigma$ ) peaks in O<sub>2</sub> following X-ray photomission. Results of three fitting procedures (L1, L2, and L2', explained in text) are given.

Spectrum	Fit L1		Fit L2		Fit L2'	
	R	Variance	R	Variance	R	Variance
NO(N 1s) Run 1	3.64(23)	3.2	3.52(16)	1.6	3.57(17)	1.9
NO(N 1s) Run 2	3.48(14)	2.8	3.34(9)	1.5	3.38(10)	1.6
O <sub>2</sub> (O 1s) Run 1	2.52(8)	3.1	2.47(8)	2.2	2.48(7)	1.7
O <sub>2</sub> (O 1s) Run 2	2.53(9)	6.1	2.51(6)	2.4	2.49(6)	2.7
O <sub>2</sub> (O 1s) Run 3	2.55(10)	10.0	2.53(5)	2.8	2.52(6)	4.5
O <sub>2</sub> (O 1s) Run 4	2.41(10)	4.2	2.41(7)	2.1	2.39(7)	2.3

Final adopted values: R(NO, N 1s) = 3.43(8); R(O<sub>2</sub>, O 1s) = 2.47(3).

orbital  $\psi_i$  will leave the N - 1 electron system in state n is simply

$$P_n^{(-i)} = |C_n^{(-i)}|^2 = |\langle \Phi_n | \psi_0^{(-i)} \rangle|^2. \quad (1)$$

The probability that the target will be left in some other final state is  $1 - P_n^{(-i)}$ . The N - 1 electron overlap matrix element of Eq. (1) is evaluated by forming determinants of the overlap integrals between the non-orthogonal sets of orbitals  $\psi_k$  determined for  $\psi_0$  and  $\phi_l^{\pi}$  determined for  $\Phi_n$ .<sup>7</sup> Now in NO, for example, the molecular orbital (MO configuration of the ground state is:

$$\psi_0(X^2\Pi) = 1\sigma^2 2\sigma^2 3\sigma^2 4\sigma^2 5\sigma^2 1\pi^4 2\pi^1 ({}^2\Pi);$$

where  $1\sigma$  is an O 1s orbital and  $2\sigma$  a N 1s orbital. The final "normal" hole state configurations upon ionization of the O 1s or N 1s electron are:

$$\Phi(N\ 1s\text{-hole}) = 1\sigma^1 ({}^2\Sigma^+) 2\sigma^2 3\sigma^2 4\sigma^2 5\sigma^2 1\pi^4 2\pi^1 ({}^2\Pi)$$

$$\Phi(O\ 1s\text{-hole}) = 1\sigma^2 2\sigma^1 ({}^2\Sigma^+) 3\sigma^2 4\sigma^2 5\sigma^2 1\pi^4 2\pi^1 ({}^2\Pi);$$

where the open core shell and the  $2\pi$  shell may couple to either  ${}^3\Pi$  or  ${}^4\Pi$ . In terms of determinants of  $\langle \psi_k | \phi_l \rangle$ , the intensities of the 1s-hole singlet or triplet final-state peaks are proportional to

$$P(O\ 1s\text{-hole}, {}^{2S'+1}\pi) = [(2S' + 1)/4]$$

$$\times [D_{11}^{\sigma} D_{22}^{\sigma} D^{\pi} (D_{22}^{\pi})^3]^2$$

$$P(N\ 1s\text{-hole}, {}^{2S'+1}\pi) = [(2S' + 1)/4]$$

$$\times [D_{22}^{\sigma} D_{22}^{\sigma} D^{\pi} (D_{22}^{\pi})^3]^2;$$

where  $S' = 0$  or  $1$ . Here  $D^{\sigma}$  is the  $5 \times 5$  determinant with elements  $(D^{\sigma})_{ij}$  given by

$$(D^{\sigma})_{ij} = \langle \psi_{i\sigma}(\text{ground state}) | \phi_{j\sigma}(\text{hole state}) \rangle,$$

and  $D^{\pi}$  is the analogous  $2 \times 2$  determinant for the  $\pi$  orbitals.

We have found that the integrals  $\langle \psi_{1\pi} | \phi_{1\pi} \rangle$  are consistently smaller for the low-spin coupling ( ${}^1\Pi$  or  ${}^2\Sigma^-$ ) than for the high-spin coupling of the hole states. This is true also for  $\langle \psi_{2\pi} | \phi_{2\pi} \rangle$  except for the N 1s-hole states of NO, where the integral for  ${}^1\Pi$  coupling is 0.0005 larger than for  ${}^3\Pi$  coupling. The differences between the values of the integrals for the different couplings are small:

$$\frac{\langle \psi_{1\pi}(\text{NO ground state}) | \phi_{1\pi}(\text{NO, N-1s hole } {}^3\Pi) \rangle}{\langle \psi_{1\pi}(\text{NO ground state}) | \phi_{1\pi}(\text{NO, N-1s hole } {}^1\Pi) \rangle} = \frac{0.9747}{0.9670} = 1.008$$

and

$$\frac{\langle \psi_{1\pi}(\text{O}_2\ \text{ground state}) | \phi_{1\pi}(\text{O}_2^+, {}^4\Sigma^-) \rangle}{\langle \psi_{1\pi}(\text{O}_2\ \text{ground state}) | \phi_{1\pi}(\text{O}_2^+, {}^2\Sigma^-) \rangle} = \frac{0.9093}{0.8792} = 1.033.$$

Table II. Calculated relative intensities, P, for the normal single 1s-hole states of NO and O<sub>2</sub> and intensities for multiple excitation, P<sub>M</sub>. Calculated and observed values, in parenthesis, of the intensity ratios, R, for the multiplet peaks (<sup>3</sup>Π/<sup>1</sup>Π for NO and <sup>4</sup>Σ<sup>-</sup>/<sup>2</sup>Σ<sup>-</sup> for O<sub>2</sub>).

Quantity	Calculated value (observed value)	% Deviation from multiplicity ratio
<u>NO</u>		
P(N 1s-hole, <sup>3</sup> Π)	0.568	--
P(N 1s-hole, <sup>1</sup> Π)	0.184	--
R(N 1s-hole <sup>3</sup> Π/ <sup>1</sup> Π)	3.09:1(3.43:1)	3%(14.3%)
P <sub>M</sub> (N 1s-hole)	0.248	--
P(O 1s-hole, <sup>3</sup> Π)	0.544	--
P(O 1s-hole, <sup>1</sup> Π)	0.177	--
R(O 1s-hole <sup>3</sup> Π/ <sup>1</sup> Π)	3.08:1	2.7%
P <sub>M</sub> (O 1s-hole)	0.280	--
<u>O<sub>2</sub></u>		
P(1s-hole, <sup>4</sup> Σ <sup>-</sup> )	0.406	--
P(1s-hole, <sup>2</sup> Σ <sup>-</sup> )	0.178	--
R( <sup>4</sup> Σ <sup>-</sup> / <sup>2</sup> Σ <sup>-</sup> )	2.28:1(2.47:1)	14%(23.5%)
P <sub>M</sub>	0.417	--

However, the ratios above are effectively taken up to the eighth power to determine their contributions to the intensity ratios of the respective peaks. (This is an oversimplified statement: expansion of the determinants yields complicated expressions). Small differences in the values of orbital overlap integrals can thus lead to large effects in the intensity ratios. Substitution of the calculated overlap integrals into the appropriate determinants yielded intensity ratios in excess of the multiplet values, as shown in Table II, wherein the results are summarized. We conclude that the overlap effect is responsible for at least part of the observed deviation.

#### Footnote and References

\* IBM Research Laboratory, San Jose, CA.

1. J. Hedman, P. F. Hedén, C. Nordling, and K. Siegbahn, *Phys. Letters* **29A**, 178 (1969).
2. C. S. Fadley, D. A. Shirley, A. J. Freeman, P. S. Bagus, and J. V. Mallow, *Phys. Rev. Letters* **23**, 1397 (1969).
3. C. C. Lu, T. A. Carlson, F. B. Malik, T. C. Tucker, and C. W. Nestor, Jr., *Atomic Data* **3**, 1 (1971).
4. T. Åberg, *Ann. Acad. Sci. Fenn. AVI*, 308, 1 (1969), and references contained therein; *Phys. Rev.* **156**, 142 (1967).
5. P. S. Bagus and H. F. Schaefer, *J. Chem. Phys.* **55**, 1474 (1971); NO wavefunctions.
6. P. S. Bagus and H. F. Schaefer, *J. Chem. Phys.* **56**, 224 (1972); O<sub>2</sub> wavefunctions.
7. P. O. Löwdin, *Phys. Rev.* **97**, 1474 (1955).

## MULTIPLY SPLITTING IN 1s HOLE STATES OF MOLECULES\*

D. W. Davis, R. L. Martin, M. S. Banna, and D. A. Shirley

The core level x-ray photoemission spectra of paramagnetic molecules show multiplet structure. This can qualitatively be understood by noting that in a system containing one or more unpaired spins, the ionization of a core electron leads to at least two final states; one in which the remaining core electron is coupled parallel to the valence spins,

and one in which the spins are anti-parallel. The energies of the two final states will not be identical. Thus one expects to see two peaks in the core-level spectrum, separated by the energy difference between the two final states. This phenomenon is termed multiplet splitting of core-level binding energies.<sup>1,2</sup> The present work reports the observation of multiplet

Table I. 1s electron binding energies and multiplet splittings (eV)

Molecule <sup>a</sup>	Binding energy <sup>b</sup>	Linewidth (FWHM)	Multiplet splitting <sup>c</sup>
$\underline{N}_2\overline{F}_4$	412.5(5) <sup>d</sup>	1.02(4)	
$N_2\underline{F}_4$	694.1(5) <sup>e</sup> 694.6(5) <sup>e</sup>	1.40(8) <sup>f</sup>	
$\underline{N}\overline{F}_2$	414.4(5) <sup>g</sup> 412.5(5) <sup>g</sup>	0.82(4)	1.934(41)
$N\underline{F}_2$	695.3(5) <sup>g</sup> 694.5(5) <sup>g</sup>	1.40(8)	0.720(8)
$\underline{N}\overline{O}_2$	413.3(5) <sup>d</sup> 412.6(5) <sup>d</sup>	0.94(3)	0.702(35)
$N\underline{O}_2$	542.0(5) <sup>h</sup> 541.3(5) <sup>h</sup>	0.97(4)	0.666(41)
$(\underline{C}\overline{F}_3)_2\underline{N}\overline{O}$	408.9(5) <sup>o</sup> 408.4(5) <sup>o</sup>	1.1(1)	0.5(1)
$(\underline{C}\overline{F}_3)_2\underline{N}\underline{O}$	540.6(5) <sup>o</sup> 539.8(5) <sup>o</sup>	1.3(1)	0.8(1)
$(\underline{C}\overline{F}_3)_2\underline{N}\overline{O}$	695.3(5) <sup>o</sup> 694.7(5) <sup>o</sup>	1.59(8) <sup>i</sup>	0.6(1)
$(\underline{C}\overline{F}_3)_2\underline{N}\underline{O}$	299.7(5) <sup>o</sup> 299.3(5) <sup>o</sup>	1.00(8) <sup>j</sup>	0.4(1)
$\underline{O}_2$	544.2(5) <sup>k</sup> 543.1(5) <sup>k</sup>	0.80(31)	1.122(25)
$\underline{N}\underline{O}$	411.5(5) <sup>l</sup> 410.1(5) <sup>l</sup>	0.81(3)	1.421(24)
$N\underline{O}$	543.6(5) <sup>l</sup> 543.1(5) <sup>l</sup>	0.80(4)	0.548(49)
$\underline{D}\underline{T}\underline{B}\underline{N}\underline{O}^m$	407.2(5) <sup>d</sup> 406.6(5) <sup>d</sup>	1.03(12)	0.590(70)
$\underline{D}\underline{T}\underline{B}\underline{N}\underline{O}^m$	537.0(5) <sup>n</sup> 536.4(5) <sup>n</sup>	0.76(5)	0.525(45)

Table I. (continued)

<sup>a</sup>The ionized atom is underlined. The cases  $\underline{O}_2$ , NO, and DTBNO have been reported previously. In this work they were redone incorporating the  $K_{\alpha_{1,2}}$  doublet in the fitting procedure.

<sup>b</sup>Standard deviation in the last digit is given parenthetically.

<sup>c</sup>Fits were obtained by constraining the linewidths to be equal.

<sup>d</sup>Referenced to  $N_2$ .

<sup>e</sup>Referenced to F 1s of  $CH_3F$ . Splitting in F 1s line believed to be due to inequivalent fluorines in  $N_2F_4$  (see text) and not the presence of any  $NF_2$ .

<sup>f</sup>FWHM constrained to be the same as that in  $NF_2$  in obtaining fit.

<sup>g</sup>Absolute binding energies for  $NF_2$  were obtained from the observed shifts from  $N_2F_4$  when both were referenced to neon, coupled with the  $N_2F_4$  absolute binding energies referenced as in d and e.

<sup>h</sup>Referenced to  $O_2$ .

<sup>i</sup>FWHM constrained to be that of F 1s in  $CF_3H$  in obtaining a fit.

<sup>j</sup>FWHM constrained to be that of C 1s in  $CF_3H$  in obtaining a fit.

<sup>k</sup>Ref. 8.

<sup>l</sup>Ref. 2.

<sup>m</sup>Abbreviation is for ditertiary butyl nitroxide.

<sup>n</sup>Referenced to  $H_2O$ .

<sup>o</sup>Referenced to neon.

splitting in several molecules and examines an expression for the magnitude of the splitting based on multiplet hole theory and semi-empirical INDO wavefunctions.

The C, N, O, and F(1s) binding energies of the compounds studied are reported in Table I. All but  $N_2F_4$  are paramagnetic.  $NO_2$  and  $NF_2$  were produced by heating  $N_2O_4$  and  $N_2F_4$ , respectively, in a special cell constructed for this purpose. The spectra of some of the more interesting cases are shown in Figs. 1 and 2.

The most fruitful approach for estimating the magnitude of the multiplet splitting involves multiplet hole theory<sup>3</sup> (MHT). MHT determines the difference in the total energies of the two final states directly. In particular, a useful theorem for discussing the splitting in s-type core orbitals is provided by Van Vleck's Theorem, which states that the difference in

energy between the two final states of spin  $(S_k+1/2)$  and  $(S_k-1/2)$  formed by coupling an s-electron to the configuration  $a^k$  in an atomic system is given by (1).

$$\Delta_s = (2S_k+1)k_{as} \quad (1)$$

Here  $S_k$  is the spin quantum number of the  $a^k$  configuration and  $K_{as}$  is the exchange integral between the orbital containing the unpaired spin(s) and the s-orbital being coupled to it. In attempting to generalize Eq. (1) to molecular systems, we would require that the splitting be given by the spin multiplicity of the parent configuration multiplied by the appropriate exchange integral between a molecular orbital and the core orbital. The approach we have used for obtaining the molecular orbitals and hence the exchange integral is based on the semi-empirical INDO method.<sup>4</sup> This method utilizes the unrestricted Hartree-Fock formalism and introduces a slight

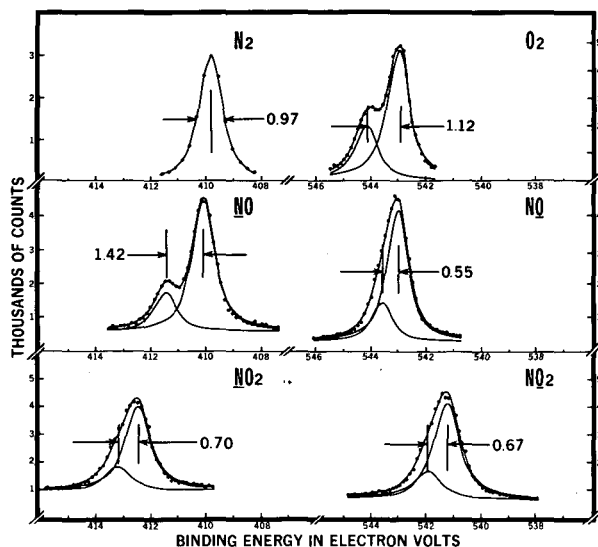


Fig. 1. Nitrogen and oxygen 1s peaks in diamagnetic  $N_2$ ; paramagnetic  $O_2$ ; paramagnetic  $NO$ ; and the paramagnetic species  $NO_2$  (150-170°C). (XBL 736-752)

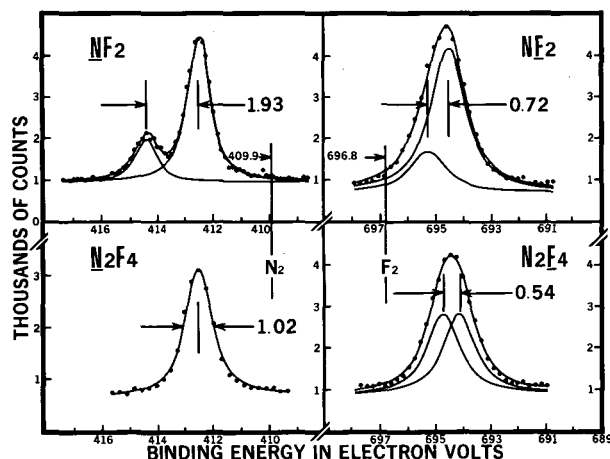


Fig. 2. Nitrogen and fluorine 1s peaks in  $NF_2$  (180-200°C) and room temperature  $N_2F_4$ . Vertical bars indicate binding energies in  $F_2$  and  $N_2$ . (XBL 736-753)

modification of Eq. (1). Within this approximation the expression for the splitting is

$$\Delta_{1s} = (2S_k + 1) \sum_{\mu} \rho_{\mu} k_{1s, \mu} \quad (2)$$

where  $\mu$  runs over the atomic orbitals on the

center being ionized, and  $\rho_{\mu}$  is the unpaired spin density in orbital  $\mu$ .

Strictly speaking, the spin densities and exchange integrals necessary for the evaluation of Eq. (2) are described by the wavefunction for the ion, i. e., the wavefunction for the system with a 'hole' in the core s-orbital. It is possible, however, to use the ground-state wavefunctions as approximations to the final-state wavefunctions (in the spirit of Koopmans' Theorem). In this version of the frozen-orbital approach, the valence-orbital spin densities would be obtained from an INDO calculation on the parent molecule, while the MHT "hole state" approach would obtain the spin densities directly from hole state wavefunctions. Since INDO does not include the 1s orbitals in the basis set, a direct hole-state calculation is not possible. The molecular orbitals of the hole state, however, can be rather well approximated by the "equivalent cores" technique.<sup>5,6</sup> This is based on the fact that a 1s electron shields essentially one unit of nuclear charge from the valence orbitals. Thus the valence orbitals of atomic nitrogen with a hole in the 1s shell closely resemble those of atomic oxygen. In the specific application to this problem, the multiplet splitting in  $O_2$ , for example, would be obtained in the hole-state approach from spin densities and exchange integrals appropriate to  $FO^+$ . Since photoemission is a fast process, the molecular geometry used for a calculation on the hole state is the same as that for the parent molecule. The experimental and calculated splittings, along with the geometries used for the calculations, are summarized in Table II. Figure 3 compares splittings calculated by the frozen-orbital approach with experiment. The equivalent-core hole state results are compared with experiment in Fig. 4.

It is clear from the figures that the MHT hole state results are superior to the frozen orbital estimates. The MHT hole state predictions 'track' experimental values, being  $\sim 0.3 \pm 0.1$  eV low, while the other model is much more erratic. The case of  $O_2$  is most striking, and can be used to illustrate the differences in the two methods. The frozen orbital approach predicts a splitting of 2.91 eV while the hole-state method gives 1.05 eV, in excellent agreement with the experimental value of 1.12 eV. The major cause of the discrepancy between the two approaches lies in the phenomenon of spin migration accompanying photoemission. The INDO method places 1.0 unpaired electrons on each oxygen in the  $O_2$  molecule. Upon ionization of one of the  $O(1s)$  electrons, the molecular orbitals of  $O_2$  rearrange to place more total electron density on the ionized center. The total spin density

Table II. Comparison with calculated splittings (eV).

Molecule		Experiment	Hole-State MHT	Frozen orbital MHT
NF <sub>2</sub> <sup>a</sup>	Δ <sub>N</sub> 1s	1.93	1.85	1.40
	Δ <sub>F</sub> 1s	0.72	-- <sup>d</sup>	0.11
NO <sub>2</sub> <sup>b</sup>	Δ <sub>N</sub> 1s	0.70	0.62	0.86
	Δ <sub>O</sub> 1s	0.67	0.27	0.54
O <sub>2</sub> <sup>b</sup>	Δ <sub>O</sub> 1s	1.12	1.05	2.91
	Δ <sub>O</sub> 1s	1.42	0.96	1.04
NO <sup>b</sup>	Δ <sub>N</sub> 1s	1.42	0.96	1.04
	Δ <sub>O</sub> 1s	0.55	0.35	0.63
DTBNO <sup>c</sup>	Δ <sub>N</sub> 1s	0.59	0.20	0.46
	Δ <sub>O</sub> 1s	0.53	0.16	1.34

<sup>a</sup>INDO calculation used geometry from M. D. Harmony and R. J. Myers, *J. Chem. Phys.*, **35**, 1129 (1961)

<sup>b</sup>Geometry from L. E. Sutton, ed. *Tables of Interatomic Distances and Configuration in Molecules and Ions* (London, The Chemical Society, Burlington House, 1958).

<sup>c</sup>Ditertiary butyl nitroxide; R(N-O) = 1.28 Å; R(N-C) = 1.47 Å, R(C-C) = 1.52 Å, R(CH) = 1.1 Å, ∠ONC = 115°, ∠NCC = 109.45°, ∠CCH = 109.45; the tertiary carbons, the nitrogen atom and the oxygen were assumed planar.

<sup>d</sup>It is not possible to perform an "equivalent cores" hole state calculation in this case since it would involve the neon atom which is not accounted for in the INDO parameterization.

on the ionized center, however, decreases from 1.0 to 0.3 electrons. This is the main source of the reduced value of the predicted splitting using the MHT hole state method.

A second contribution arises from the equivalent-cores approach. The dominant term in Eq. (2) for the frozen-orbital method comes from the spin density in the O(2p) orbitals and hence from the 1s-2p atomic exchange integral for oxygen. In contrast, the hole-state approach uses the exchange integral for fluorine, which is ~ 0.7 eV larger than that for oxygen. The decrease in the predicted splitting from the frozen-orbital to the equivalent-cores approximation thus arises from a decrease in the spin density on the ionized center in the final state, which more than compensates for the increased exchange integral.

The absolute values of the binding energies deserve comment. Figure 1 shows a steady increase in the N(1s) binding energy from N<sub>2</sub> to NO to NO<sub>2</sub>. Chemical intuition would predict such an ordering as negative charge is

successively drawn away from the nitrogen through oxidation. The N(1s) binding energy in NF<sub>2</sub> is greater than that for NO<sub>2</sub>, in agreement with the relative electronegativities of fluorine and oxygen. The O(1s) binding energy decreases from O<sub>2</sub> to NO to NO<sub>2</sub>. The intuitive approach used above would predict the O(1s) binding energies as O<sub>2</sub> > NO ≈ NO<sub>2</sub>. We believe the rather substantial (~ 2 eV) shift between NO and NO<sub>2</sub> is, in large part, due to electron density migration toward the hole in the final state. Although this "extra atomic relaxation" also affects the N(1s) shifts, the increased oxidation of the nitrogen in NO<sub>2</sub> (vs NO) apparently overrides the relaxation effect, and the N(1s) binding energy is greater for NO<sub>2</sub>.

The N(1s) and O(1s) peaks in (CF<sub>3</sub>)<sub>2</sub>NO and ((CH<sub>3</sub>)<sub>3</sub>C)<sub>2</sub>NO are of special interest. They are both shifted toward lower binding energies relative to NO. This may be interpreted in terms of inductive electron donation by the alkyl groups during photoemission. The fact that the N(1s) and O(1s) binding energies are



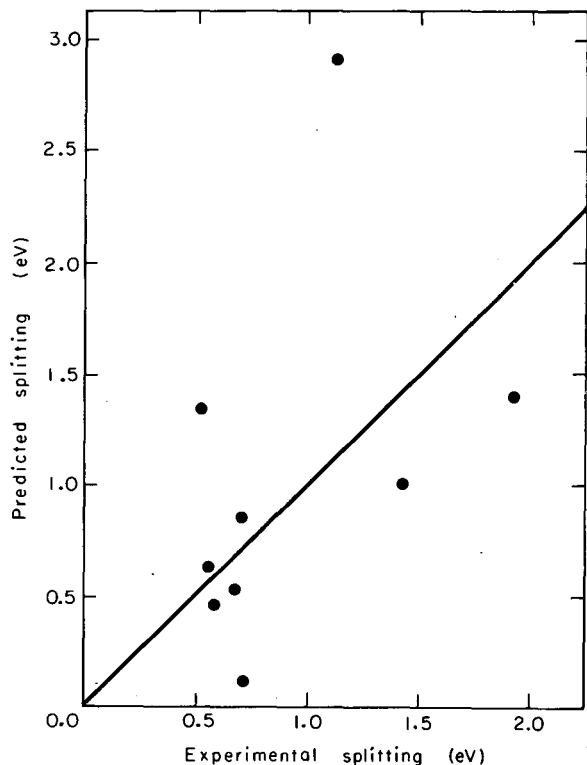


Fig. 3. MHT "frozen orbital" predictions vs. experimental splittings. The diagonal line has a slope of unity. (XBL 7310-4242)

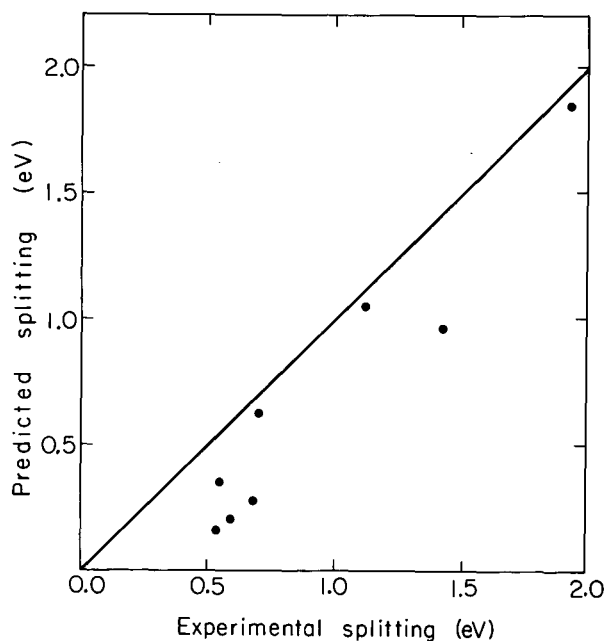


Fig. 4. Splittings predicted by the MHT "hole state" approach vs. the experimental splittings. The diagonal line has unit slope. (XBL 735-3004)

lower for the di-tertiary butylnitroxide than bis-trifluoromethyl nitroxide is qualitatively in line with the organic chemists' concept of strong inductive electron donation by a tertiary-butyl group. Tertiary carbons can stabilize positive charge more readily than secondary carbons, and they in turn more readily than primary carbons.<sup>7</sup> This is the basis of the general rule concerning the order of reactivity of alkyl halides in  $S_N1$  reactions. Since the intermediate in these reactions is a carbonium ion, those species which tend to stabilize the carbonium ion transition state react more rapidly. Because tertiary carbons can stabilize the transition state more effectively than secondary, etc., the order of reactivity found is  $3^\circ > 2^\circ > 1^\circ$ . This process can only be properly understood in terms of charge transfer between the initial (ground) state and the final (or transition) state; a discussion that includes the initial state alone is simply not adequate. The same is true in explaining core-level binding-energy shifts. This point is made especially cogently by the results of INDO calculations on NO, DTBNO, and  $(CF_3)_2NO$ , presented in Table III. On the basis of ground state properties alone one would not expect a large shift in the  $N(1s)$  binding energies from NO to DTBNO: the observed shift arises almost entirely from electron transfer from the t-butyl groups to the nitrogen atom in the final hole state (extra atomic relaxation). This transfer enhances the loss of the  $N(1s)$  electron since it stabilizes the positive ion in the final state. The relationship between core-level binding energy shifts and other chemical properties (such as basicity) suggests that further study is warranted.

#### Footnote and References

\*Condensed from LBL-1915, to be published in *J. Chem. Phys.*, Oct. 1973.

1. J. Hedman, P. F. Heden, C. Nordling, and K. Siegbahn, *Phys. Lett.*, **29A**, 178 (1969).
2. D. W. Davis and D. A. Shirley, *J. Chem. Phys.* **56**, 669 (1972).
3. A. J. Freeman, P. S. Bagus, and J. V. Mallow, private communication.
4. J. A. Dople, D. L. Beveridge, and P. A. Dobosh, *J. Chem. Phys.* **44**, 3289 (1966).
5. W. L. Jolly and D. N. Hendrickson, *J. Am. Chem. Soc.* **92**, 1863 (1970).
6. D. W. Davis and D. A. Shirley, *Chem. Phys. Letters* **15**, 185 (1972).
7. It now appears that alkyl groups stabilize

both positive and negative saturated ions in the gas phase relative to hydrogen. The concept of an alkyl group stabilizing a positive charge through inductive electron donation may thus be lost. Brauman and Blair have postulated that the stabilization arises from the polarizability of the alkyl group and its proximity to the charged center. Whatever

the mechanism, the effect still remains. See, for example, Brauman and Blair, *J. Am. Chem. Soc.* **92**, 5986 (1970).

8. D. A. Shirley, in *Advances in Chemical Physics*, edited by I. Prigogine and S. A. Rice, Vol. 23, p. 85 (1973).

### CHARACTERISTIC ENERGY LOSS STRUCTURE OF SOLIDS\* FROM X-RAY PHOTOEMISSION SPECTRA

R. A. Pollak,<sup>†</sup> L. Ley, F. R. McFeely,  
S. P. Kowalczyk, and D. A. Shirley

X-ray photoemission from solids can be conceptualized as a three-step process: 1) excitation of an electron from the ground state to a free-electron-like state of high kinetic energy within the solid, 2) passage of this photoelectron to the surface of the solid, and 3) escape of the electron from the solid. Conservation of energy requires that the measured kinetic energy of the photoelectron be equal to the x-ray photon energy minus the total energy expended in steps 1-3. In practice XPS spectra are usually corrected by subtracting structure associated with steps 2 and 3, and structure associated with step 1 is then related to the eigenvalue spectrum of the system. This paper deals instead with the spectral structure that results from energy-loss phenomena during steps 2 and 3 of the photoemission process. Our objective is to relate the low-energy loss structure observed in XPS studies of nine clean metals to characteristic energy losses obtained by other methods.

Among the most prominent features in the XPS loss spectra are those due to plasmons. A plasmon is a collective rarefaction-compression wave in the valence electron gas. Before discussing individual results we should comment on the distinction between extrinsic and intrinsic plasmons. An electron passing through a solid can create extrinsic plasmons by coupling between its longitudinal electric field and electron density fluctuations. Many plasmon resonance energies have been determined by measuring the energy losses of electrons reflected from solid surfaces or transmitted through thin films.<sup>1</sup> Almost all structure observed in the spectra reported below can in fact be attributed to this type of plasmon energy loss. In addition to extrinsic plasmons, many-body calculations<sup>2</sup> predict intrinsic plasmon structure resulting from plasmons coupled to core electrons. This type of plasmon excitation is intrinsic to the photoemission

of a core electron that is coupled with the surrounding plasma rather than to a free electron passing through a plasma. The total spectral density in this model consists of a sharp quasi-particle peak with a broader plasmon satellite structure at a higher "binding" energy.

#### Systematics

The systematic variation of the plasmon structure for Ag to Te is illustrated in Fig. 1.

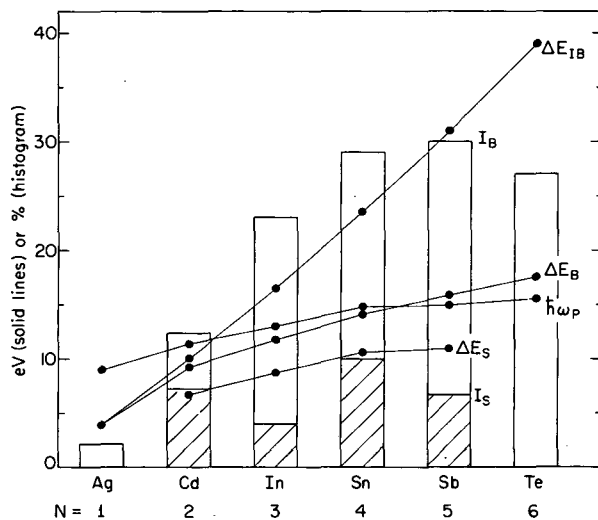


Fig. 1. Systematic of plasmon losses in Ag, Cd, In, Sn, Sb, and Te.  $\Delta E_{IB}$  is the onset-interband-transition energy ( $4d \rightarrow E_F$ ),  $\Delta E_B$  is the measured bulk plasmon energy,  $\Delta E_S$  is the measured surface plasmon energy,  $\hbar\omega_p$  is the calculated free electron bulk plasmon energy, and  $I_B$  and  $I_S$  are the intensity of the bulk and surface plasmon intensity respectively relative to the zero-loss peak. (XBL 7211-4394)

The interband transition ( $4d \rightarrow E_F$ ) energy  $\Delta E_{IB}$  is a strong function of atomic number, varying from 3.9 eV in Ag to 39 eV in Te. The free electron plasmon energy,

$$\hbar\omega_p = \hbar \left( \frac{4\pi n e^2}{m} \right)^{1/2}, \quad (1)$$

varies smoothly from 9 eV in Ag where  $N$ , the number of valence electrons, is 1 to 15.6 eV in Te ( $N = 6$ ). Here  $n$  is the number density of the electron plasma and  $m$  is the free electron mass. The measured bulk plasmon energy  $\Delta E_B$  rises smoothly from 3.9 eV in Ag to 17.6 eV in Te. The difference ( $\hbar\omega_p - \Delta E_B$ ) decreases from Ag to Sn, changes sign between Sn and Sb then increases slightly in magnitude in Te. The surface plasmon energy  $\Delta E_S$  obeys the expected free-electron relation

$$\Delta E_B = \sqrt{2} \Delta E_S,$$

to within an error of  $\pm 0.05$  in the coefficient. The intensities (areas) relative to the parent, zero-loss peak for the bulk plasmon ( $I_B$ ), and surface plasmon ( $I_S$ ) are shown as histograms in Fig. 1. The intensity  $I_B$  of the bulk plasmon loss increases smoothly from a minimum of 2% in Ag to a value of about 28% in Sn, Sb, and Te. The surface plasmon intensity showed more varied behavior. This is not unexpected because  $I_S$  is much more sensitive to surface conditions than  $I_B$ .

For Ag and Cd, in which interband transitions play an important role, the characteristic loss structure cannot be completely explained by combinations of one surface and one bulk loss alone. We thought it might be possible, however, to relate the observed losses at energies above 10 eV to those at 7.8 eV (Ag) and 9.3 eV (Cd) by assuming that the number of valence electrons participating in these higher-energy plasma oscillations is increased over the number that participate in the low-energy oscillations by 10, the number of electrons in the filled 4d shell. To test this hypothesis we parameterized Eq. (1) to

$$\hbar\omega_p = C\sqrt{n}, \quad (2)$$

which retains the  $\sqrt{n}$  dependence of the bulk plasma oscillations. Adjusting  $C$  to reproduce the 7.8 eV (Ag) and 9.3 eV (Cd) losses for  $n = 1$  and  $n = 2$  respectively, we obtained for  $n = 11$  and  $n = 12$ , values for the loss energies that are in fair agreement with the observed

(but otherwise unexplained) losses around 20 eV in the two metals.

The above interpretation is supported by other data. In Ag, the real part of the dielectric constant,  $\epsilon_1$ , crosses through zero near 7.8 eV and exhibits a local minimum at 25 eV.<sup>3</sup> In addition, the imaginary part,  $\epsilon_2$ , is small ( $\sim 0.7$ ) at 25 eV.<sup>3</sup> Both observations support our description of the 25 eV loss in Ag as plasmonlike. The necessary adjustment of  $C$  in Eq. (2) implies an effective electron mass,  $m_{eff}$ , for these collective excitations. The agreement between  $\hbar\omega_p$  as calculated from Eq. (2) and the experimental values could be further improved, by taking the difference in effective mass for s- and d-electrons into account.

Reducing the bulk plasmon energies calculated above by a factor of  $1/\sqrt{2}$ , we obtain energies that are consistent with an interpretation of the losses at 18.8 eV and 13.9 eV as surface plasmons. This interpretation is supported for Ag by a recent investigation by Pratesi and Rovida,<sup>4</sup> who find that the loss peak at 18 eV is surface sensitive, a condition commonly observed for surface plasmons.

#### Footnote and References

\*Condensed from LBL-1971. To be published in *J. Electr. Spectrosc.*

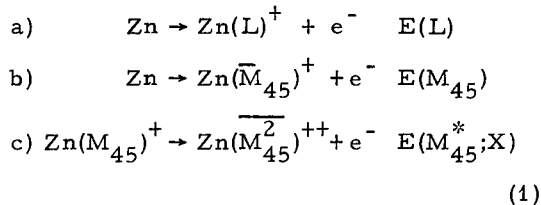
†Present address: IBM T. J. Watson Research Center, Yorktown Heights, NY 10598.

1. H. Raether, *Springer Tracts in Mod. Phys.*, **38**, 84 (1965).
2. B. I. Lundqvist, *Phys. Kondens. Materie*, **6**, 193 (1967); **6**, 206 (1967); **7**, 117 (1968); **9**, 236 (1969); Lars Hedin, Bengt Lundqvist, and Stig Lundqvist, in *Proc. 3rd Int. Mat. Res. Symp., Electronic Density of States*, Nat. Bur. Stand. (U.S.), Spec. Pub. 323 (1971).
3. M. Schlicher, *Z. Physik*, **250**, 87 (1972).
4. F. Pratesi and G. Rovida, *J. Electr. Spectrosc.*, **1** 296 (1972/73).

THE  $L_2, 3M_{45}M_{45}$  AUGER SPECTRA OF METALLIC COPPER AND  
ZINC: THEORY AND EXPERIMENT\*

S. P. Kowalczyk, R. A. Pollak,<sup>†</sup> F. R. McFeely,  
L. Ley, and D. A. Shirley

The  $LM_{45}M_{45}$  Auger process can be written as the algebraic sum of three simple steps. In Zn, for example, these may be written



where the energy of each process is written on the right, and X denotes the term designation of the two-hole final state. Here steps (a) and (b) are simply the ionizations of an L or  $M_{45}$  electron, the energies of these steps are just the appropriate binding energies, referred to the Fermi energy. Our experimental binding-energy values are given in Table I. Step (c) is more complicated. It is also an  $M_{45}$  binding energy, but in this case with a hole already in the 3d shell (the  $M_{45}$  shell) in the initial state.

Table I. Core level binding energies (eV)<sup>a</sup>

Metal	$E(L_2)$	$E(L_3)$	$E(M_{45})$
Cu	952.6(2)	932.8(2)	3.0(1)
Zn	1044.9(2)	1021.9(2)	9.9(1)

<sup>a</sup>Error in tenths place appears parenthetically.

The energy of step (c) in Eq. (1) can be related to that of step (b), the one-electron binding energy  $E(M_{45})$ . Two additional terms are necessary, however. The first, denoted  $\mathcal{F}(M_{45}M_{45}; X)$ , accounts for multiplet  $\mathcal{F}$  coupling in the final state X. The "multiplet" term is easily worked out for the  $d^8$  configuration using multiplet coupling theory<sup>1</sup> and Mann's Slater integrals.<sup>2</sup> The calculated values of  $\mathcal{F}(X)$  are given in Table II. The dynamic relaxation energy,  $E_R$ , accompanying photoemission is also taken into account implicitly, by using the empirical 3d binding energies. By dynamic relaxation energy we mean the amount by which the 3d binding energy is lowered from the orbital-energy

Table II. Multiplet energies  $\mathcal{F}(M_{45}M_{45}; X)$  for  $3d^8$ , in eV<sup>a</sup>

Element	X = <sup>1</sup> S				
Cu	31.4	26.3	26.9	25.9	23.9
Zn	35.2	29.4	30.2	28.9	26.7

<sup>a</sup>Using  $F^0, F^2, F^4$  values from Ref. 2.

(Koopmans' theorem<sup>3</sup>) estimate through relaxation of the passive orbitals during electron emission. From the optimized Hartree-Fock-Slater results of Rosén and Lindgren,<sup>4</sup>  $E_R$  has a value of 5.3 eV for a Cu 3d electron in atomic copper.

The second term that must be combined with  $E(M_{45})$  in order to give an accurate estimate of  $E(M_{45}^*; X)$  in Eq. (1) is a correction term accounting for an additional relaxation energy, which we shall denote as  $R(M_{45}M_{45})$ . This is a static relaxation energy. It is the amount by which the binding energy of the second 3d electron (step (c) of Eq. (1)) is reduced because its Hartree-Fock potential is made more repulsive when the passive electrons relax toward the hole left by the first 3d electron, in step (b) of Eq. (1).

Having considered these two contributions to step (c), we can now write  $E(M_{45}^*; X)$  as

$$E(M_{45}^*; X) = E(M_{45}) + \mathcal{F}(M_{45}M_{45}; X) - R(M_{45}M_{45}) \quad (2)$$

To calculate  $R(M_{45}M_{45})$  we shall first formally divide it into two parts,

$$R(M_{45}M_{45}) = R(M_{45}M_{45})_a + R(M_{45}M_{45})_e, \quad (3)$$

where the atomic static relaxation term  $R(M_{45}M_{45})_a$ , is the static relaxation energy, discussed previously<sup>5, 6</sup> that a free copper or zinc atom would have, and  $R(M_{45}M_{45})_e$  is an additional extra-atomic relaxation energy that arises from electronic relaxation toward the 3d hole from the surrounding lattice. It is relatively straightforward to estimate  $R(M_{45}M_{45})_a$  because, following the work of Hedin and Johansson,<sup>7</sup> this term should be

twice the dynamic relaxation contribution  $E_R(M_{45})$ .<sup>5,6,8</sup> Using Rosén and Lindgren's value of 5.3 eV quoted above for Cu, we therefore have

$$R(M_{45}M_{45};Cu)_a \approx 10.6 \text{ eV.}$$

We could just use the above estimate for Zn as well, with little additional error, but it is also possible to improve on this estimate somewhat. The atomic relaxation energy can be divided into inner-shell, intrashell, and outer-shell contributions. Following Hedin and Johansson,<sup>7</sup> we infer that the first two should be essentially the same for Cu( $3d^{10}4s$ ) and Zn( $3d^{10}4s^2$ ). The additional outer-shell relaxation energy arising from the additional 4s electron in Zn may be estimated from Mann's integrals,<sup>2</sup> using the equivalent-cores method,<sup>5,6</sup> as 1.7 eV. Thus  $R(M_{45}M_{45};Zn)_a \approx 12.3$  eV. The extra-atomic term should be quite sensitive to the environment, and probably the most important consequence of our analysis is to call attention to the magnitude of this environment-sensitive term in the Auger energy. In the cases at hand we are dealing with metals, and it seems safe to assume that the extra unit of charge induced on one atom in the periodic lattice by the appearance of a hole in the filled 3d shell will be completely screened by the conduction electrons.

We can estimate the screening length of an electron gas for a point charge from the Fermi-Thomas model as<sup>9</sup>

$$l \sim (E_F/6\pi n e^2)^{1/2}. \quad (4)$$

This estimate gives  $l \sim 0.5$  Å for both Cu and Zn. Such a short screening length implies that the localized 3d hole must be almost totally screened by the induced screening charge on the hole-state atom itself. If we assume this to be the case an upper limit for  $R(M_{45}, M_{45})_e$  would be given by the electrostatic energy of interaction between a 3d electron and a 4s or 4p electron. Using Mann's tables,<sup>2</sup> we find 9.6 eV and 11.0 eV for the 3d, 4s interactions in atomic Cu and Zn, respectively, and 9.6 eV for the 3d, 4s interaction in atomic gallium, the first element with a 4p electron in its ground state. Since the nominal configurations of Cu and Zn are  $d^{10}s$  and  $d^{10}s^2$ , we shall use the 3d, 4s energy for estimating  $R_e$  in Cu and the (gallium) 3d, 4p energy for  $R_e$  in Zn.

Combining the two relaxation energies, we have

$$R(M_{45}M_{45}) \lesssim 20.2 \text{ eV} \quad (6)$$

for both Cu and Zn. Combining this with

Table III.  $L_{2,3}M_{45}M_{45}$  Auger energies in Cu and Zn(eV)

Final state, X	Copper		Zinc			
	Expt.	Eq. (7)	Expt.	Eq. (7)		
$L_2M_{45}M_{45}$	$1S$	(932.8)	935.4	1010.4(4)	1010.0	
		(934.2)				
	$3P$		940.5		1015.8	
		$1G$	937.8(2)	939.9	1014.9(2)	1015.0
			$1D$		940.9	
$3F$	940.6	942.9	1017.9(3)	1018.5		
$L_3M_{45}M_{45}$	$1S$	(913.6)	915.6	986.6(3)	986.9	
		(915.8)				
	$3P$		920.7		992.7	
		$1G$	918.0(2)	920.1	991.8(2)	991.9
			$1D$		921.1	
$3F$	920.6	923.1	995.2(3)	995.4		

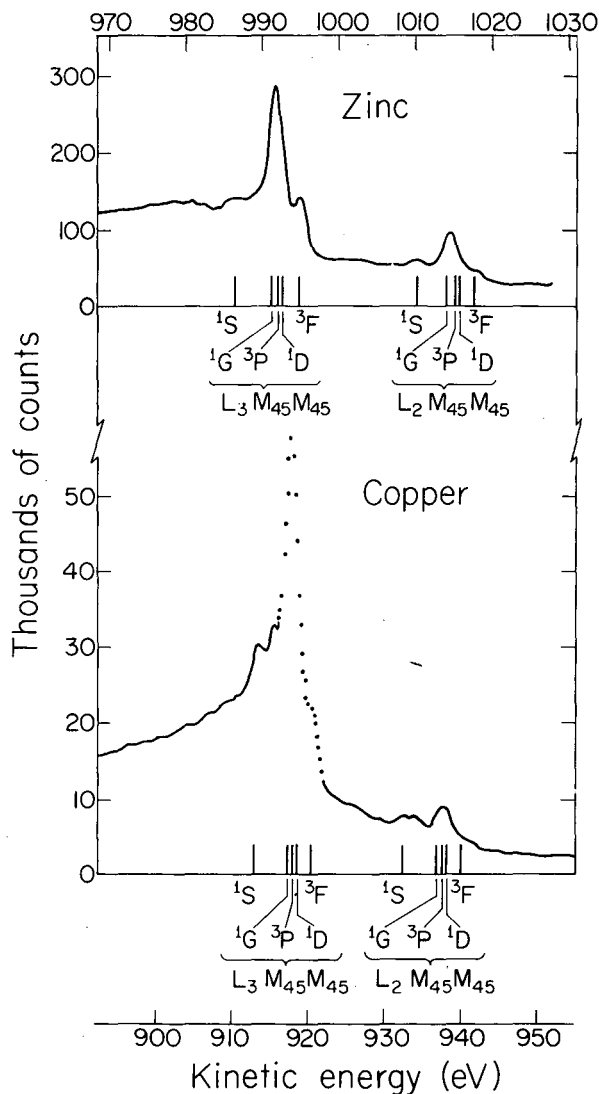


Fig. 1. Experimental  $L_{2,3}M_{45}M_{45}$  Auger spectra from copper and zinc. Kinetic energy scales are given relative to the Fermi energy. Multiplet structures from theory described in text are shown as lines under spectra. They have been moved down in energy relative to values in Table III by 0.5 eV (Zn) and 3 eV (Cu) to facilitate comparison of multiplet structure with experiment. (XBL 7212-4880).

Eqs. (1) and (2), and using the energies in Tables I and II, we have calculated the theoretical Auger energies

$$E(L_{2,3}M_{45}M_{45};X) = E(L_{2,3}) - 2E(M_{45}) - \mathcal{F}(M_{45}M_{45};X) + R(M_{45}M_{45}). \quad (7)$$

The results are set out in Table III.

Experimental Auger spectra over the regions of interest are shown in Fig. 1, and experimental values of the Auger energies are also listed in Table III for comparison with the theoretical values. Agreement between experiment and our theoretical values is excellent. It appears that Eq. (7) provides, for the first time, a framework within which it is possible to predict quantitative values of Auger energies in metals in some detail.

In Zn the main line within each group is interpreted as arising from the three levels  $3P$ ,  $1G$ , and  $1D$ , which are predicted to be nearly degenerate. Since the relative intensities of these three components are unknown, we can only say that the experimental energy of the main  $L_3M_{45}M_{45}$  line,  $991.8 \pm 0.2$  eV, agrees exactly with the predicted energy of the  $1G$  component (991.9 eV) and is up to 1.3 eV lower than that of the highest-energy component,  $1D$  (993.2 eV). The two extreme levels of  $d^8$ ,  $1S$  and  $3F$ , are also in nearly exact agreement with experiment for the Zn ( $L_3M_{45}M_{45}$ ) group and nearly as good for the Zn ( $L_2M_{45}M_{45}$ ) group, with a maximum discrepancy of only 0.6 eV.

Copper has more theoretical uncertainties *a priori*. The width of the  $d$  band and its proximity to  $E_F$  weaken the quantitative validity of using localized atomic functions. Thus copper is a test case for studying the extent to which an atomistic approach will give reasonable results in spite of theoretical ambiguities. In this context the agreement between theory and experiment in Table III is very good.

#### Footnotes and References

\* Condensed from LBL 1641. Published in Phys. Rev. B8, 2387 (1973).

† Present address: IBM T. J. Watson Research Center, Yorktown Heights, NY 10598

1. J. C. Slater, Quantum Theory of Atomic Structure (McGraw-Hill, 1960), Vol. II, pp. 286, 294.

2. J. B. Mann, "Atomic Structure Calculations. I. Hartree-Fock Energy Results for the Elements Hydrogen to Lawrencium," Los Alamos Scientific Laboratory Report LASL-3690 (1967).

3. T. Koopmans, *Physica* 1, 104 (1933).

4. A. Rosén and I. Lindgren, *Phys. Rev.* 176, 114 (1968).

5. D. A. Shirley, Chem. Phys. Letters 17, 312 (1972).  
 6. D. A. Shirley, Chem. Phys. Letters 16, 220 (1972).  
 7. L. Hedin and G. Johansson, J. Phys. B2, 1336 (1969).

8. D. A. Shirley, "Theory of KLL Auger Energies Including Static Relaxation," to be published in Physical Review A (March 1974).  
 9. C. Kittel, Quantum Theory of Solids (John Wiley and Sons, 1963), Chap. 6.

### THE RELATIVE EFFECT OF EXTRA-ATOMIC RELAXATION ON AUGER AND ESCA SHIFTS IN TRANSITION METALS AND SALTS\*

S. P. Kowalczyk, L. Ley, F. R. McFeely,  
 R. A. Pollak,<sup>†</sup> and D. A. Shirley

#### Auger Energies and One-Electron Binding Energies

The Auger transition ( $ijkl$ ) can be broken up into three steps:



The energies of steps (1a) and (1b) are simple one-electron binding energies  $E(j)$  and  $E(k)$ , which can be used directly. The binding energy in step (1c) must be modified, however, to account for the effects on  $E(l)$  of electronic relaxation in step (1b) and of two-hole coupling in the final state. As discussed earlier,<sup>1-3</sup> these two effects yield an energy  $E(l)^*$  for step (1c) of the form

$$E(l)^* = E(l) + \mathcal{F}(kl;X) - R(kl), \quad (2)$$

in which  $\mathcal{F}(kl;X)$  is the interaction energy between the  $k$ - and  $l$ -holes in the final state  $X$  and  $R(kl)$  is the relaxation energy. The Auger energy is then given as

$$E(j, k, l;X) = E(j) - E(k) - E(l) - \mathcal{F}(kl;X) + R(kl). \quad (3)$$

The  $\mathcal{F}(kl;X)$  term is readily calculable<sup>2,3</sup> using standard multiplet coupling theory and tabulated Slater integrals.<sup>4</sup> We can write  $R$  as the sum of an atomic relaxation energy  $R_a$ , arising mainly from the collapse of other electronic orbitals of the host atom toward the  $k$  hole in step (1b), plus an extra-atomic relaxation<sup>3</sup> term  $R_e$ .

There are two important contributions to  $R_a$ : outer-shell relaxation and intra-shell relaxation.<sup>1,2</sup> For the cases discussed below (the Na KLL and Zn LMM transitions) the intrashell effect is dominant. The intrashell relaxation energy can be estimated as twice the dynamic intrashell relaxation energy  $E_R$  (intrashell).<sup>3</sup> Calculations of  $E_R$  are available from optimized Hartree-Fock-Slater calculations on hole states.<sup>5</sup>

Extra-atomic relaxation  $R_e$  occurs through a flow of electronic charge toward the host atom during step 1b. We have discussed  $R_e$  in terms of a simple screening model<sup>3,6</sup> which gives the Auger energy of metal as

$$E(jkl;X) = E(j) - E(k) - E(l) - \mathcal{F}(kl;X) + 2E_R(l) + \mathcal{F}(l,c)_k. \quad (4)$$

In an application to the  $L_3M_{45}M_{45}$  Auger spectra of Cu and Zn, Eq. (4) gave very good results.<sup>3</sup>

#### The Use of Optical Data on Free Atoms

As an alternative to using Eq. (4) to predict Auger energies in metals, we can derive Auger energies for free atoms,  $E^A(jkl)$ , from optical data,<sup>7</sup> usually in combination with x-ray energies<sup>8</sup> and/or calculated atomic binding energies.<sup>5,9</sup> Estimating  $E^A(jkl)$  from free-atom one-electron binding energies  $E^A(i)$ , by going through a three-step process similar to Eq. (1a,b,c) for free atoms, it is easy to derive the relation

$$E^A(jkl;X) = E^A(j) - E^A(k) - E^A(l) - \mathcal{F}(kl;X) + 2E_R(l), \quad (5)$$

which differs in form from Eq. (4) only in

Table I. Energies in the atomic copper  
( $L_3M_{45}M_{45}; {}^1D$ ) Auger transition (in eV).

Quantity in Eq. (5)	Identity this quantity	Numerical value	Reference
$E^A(j)$	$E(L_3)$	940.1	a, b
$E^A(k)$	$E(M_{45})$	10.44	b
$E^A(l)$	$E(M_{45})$	10.44	b
$\mathcal{F}(k, l; X)$	$\mathcal{F}(M_{45}M_{45}; {}^1D)$	25.9	b
$E_R(l)$	$E_R(3d)$	5.3	c

<sup>a</sup>The  $\alpha_{12} L_{III} M_{IV} V$  x-ray energy was taken from Ref. 8. The optical 3d energy was taken from Ref. 7.

<sup>b</sup>Ref. 7.

<sup>c</sup>This is termed the "reorganization energy" in Ref. 5.

Table II. Summary of results for the ( $L_3M_{45}M_{45}; {}^1D$ ) energy in copper

Method	Est. quantity	$R_e$ (expt) (eV)	$R_e$ (theo) (eV)
$E_B$ (solids)	$E^F({}^1D) - \mathcal{F}(M_{45}, c)$	911.5	$\mathcal{F}(M_{45}, c) = 6.5$ 11.0
$E_B$ (atoms)	$E^A({}^1D)$	903.9	$R_e(TA) = 9.6$ 15.5
$E_B$ (atoms, 2-hole states)	$E^A({}^1D)$	902.4	$R_e(TA) = 11.1$ 15.5

having no extra-atomic relaxation term. To apply this result to the ( $L_3M_{45}M_{45}; {}^1D$ ) Auger transition in atomic copper, for example, we can use the data collected in Table I to find

$$E^A(L_3M_{45}M_{45}; {}^1D)_{Cu} = 903.9 \text{ eV,}$$

for atomic copper. The Auger energy in a solid, referred to the Fermi can be compared directly to that in an atom by correcting for the work function  $\phi$ . The two Auger energies also differ by the total Auger extra-atomic relaxation, which we shall denote by  $R_e(TA)$ . Thus

$$E^F(jkl) = E^A(jkl) + e\phi + R_e(TA). \quad (6)$$

We find  $R_e(TA) = 9.6$  eV for the copper ( $L_3M_{45}M_{45}; {}^1D$ ). We may relate, Eqs. (5) and (6) and also derive a method for estimating  $R_e(TA)$  theoretically, by going once again through a three-step sequence as in Eq. (1), but this time relating the energy of each step in the metal to that in the free atom. This gives

$$E^F(jkl) = E^A(jkl) + e\phi + \mathcal{F}(lc)_k + \frac{1}{2} [\mathcal{F}(lc) + \mathcal{F}(kc) - \mathcal{F}(jc)]. \quad (7)$$

Thus the total Auger extra-atomic relaxation is given by

$$R_e(TA) = \mathcal{F}(lc)_k + \frac{1}{2} [\mathcal{F}(lc) + \mathcal{F}(kc) - \mathcal{F}(jc)]. \quad (8)$$

from Eqs. (6) and (7). Thus from Eq. (8), we have for copper

$$R_e(TA, CuL_3M_{45}M_{45}; {}^1D) = 15.5 \text{ eV.}$$

Another approach that also employs optical data is based on the use of the one- and two-hole states in free atoms that correspond to the initial and final states in the Auger transition. This gives  $R_e(TA) = 11.1$  eV, which is in better agreement with the theoretical estimate of 15.5 eV. Results for copper are collected in Table II.



Extra-Atomic Relaxation and Auger Energies  
in Zinc and Sodium Salts

To assess the extent to which variations in extra-atomic relaxation energy can affect Auger energies, we have selected the (KLL;  $^1D$ ) transition in sodium and the (L<sub>3</sub>M<sub>45</sub>M<sub>45</sub>;  $^3P$ ,  $^1G$ ,  $^1D$ ) peak in zinc as examples that are sufficiently well-characterized for this study.

To analyze the sodium data we can use all three methods discussed above, and they all show quite good agreement. We shall use two-hole optical states data to calculate the atomic Auger energies  $E^A(\text{KLL}; ^1D)$  and to provide an empirical value of the combination of terms  $- \mathcal{F}(kl; X) + 2E_R(l)$  in Eq. (5). This quantity will be used to derive extra-atomic relaxation energies in the solids. The mean energy of the  $1s^2 2s^2 2p^4 (^1D) 3s$  state in Na I lies 101.92 eV above the ground state of Na I.<sup>7</sup> We can estimate the Auger energy as

$$E^A(\text{KLL}; ^1D) = E^A(K) - E^A(1s^2 2s^2 2p^4 (^1D) 3s) = 977.2 \text{ eV},$$

in good agreement with the value reported for Na vapor.<sup>10</sup> We can combine the above result (977.2 eV) with Eq. (5),  $E(K) = 1079.1 \text{ eV}$ , and  $E(L_{23}) = 38.02 \text{ eV}$  to obtain a reliable empirical estimate of

$$- \mathcal{F}(2p, 2p; ^1D) + 2E_R(2p) = -25.96 \text{ eV}.$$

The extra-atomic relaxation energies in the solids in Table III were obtained from the

relation

$$R_e = E^F(\text{KLL}; ^1D) - E^F(1s) + 2E^F(2p) + 25.86 \text{ eV}, \quad (9)$$

which follows from Eq. (4).

It is not always feasible to calculate  $R_e$  in solids from Auger and binding-energy data in the way described above. Unfortunately, neither binding energy shifts nor Auger shifts alone are very meaningful, because there is no reliable reference energy if these energies are compared from one solid to another. A meaningful energy shift does exist, however; it is the shift in the difference energy between the binding energy of one of the final state holes and the apparent binding energy in the XPS spectrum of the Auger line,  $E_B(jkl) = h\nu - E(jkl)$ , where  $h\nu$  is the photon energy. Substituting this relation into Eq. (9), with  $\mathcal{F}(l, c) = R_e$ , we have

$$E(l) - E_B(jkl) = E(j) - E(k) - h\nu - \mathcal{F} + 2E_R + R_e.$$

Now  $E(j) - E(k)$  is the energy of an x-ray connecting two core states. It shifts very little with changes of environment. The combination of terms  $-\mathcal{F} + 2E_R$  is an atomic property which should also be constant from one material to another, and of course  $h\nu$  doesn't vary. Thus to a very good approximation,

$$\Delta[E(l) - E_B(jkl)] = \Delta R_e. \quad (10)$$

Table III. Energy parameters for the Na(KLL;  $^1D$ ) Auger transition (in eV)

Sample	$E(1s)^a$	$E(2p)^a$	$E(\text{KLL}; ^1D)^a$	$R_e^d$	$\Delta[E(2p) - E_B(\text{KLL})]^e$
metal	1071.7	30.4	994.2	9.2	(8.7)
NaI	1070.3	28.3	991.9	4.1	4.3
oxide <sup>b</sup>	1075.2	32.8	986.8	3.1	3.7
NaF	(1066.8) <sup>c</sup>	24.8	991.9	(-0.2)	(0)

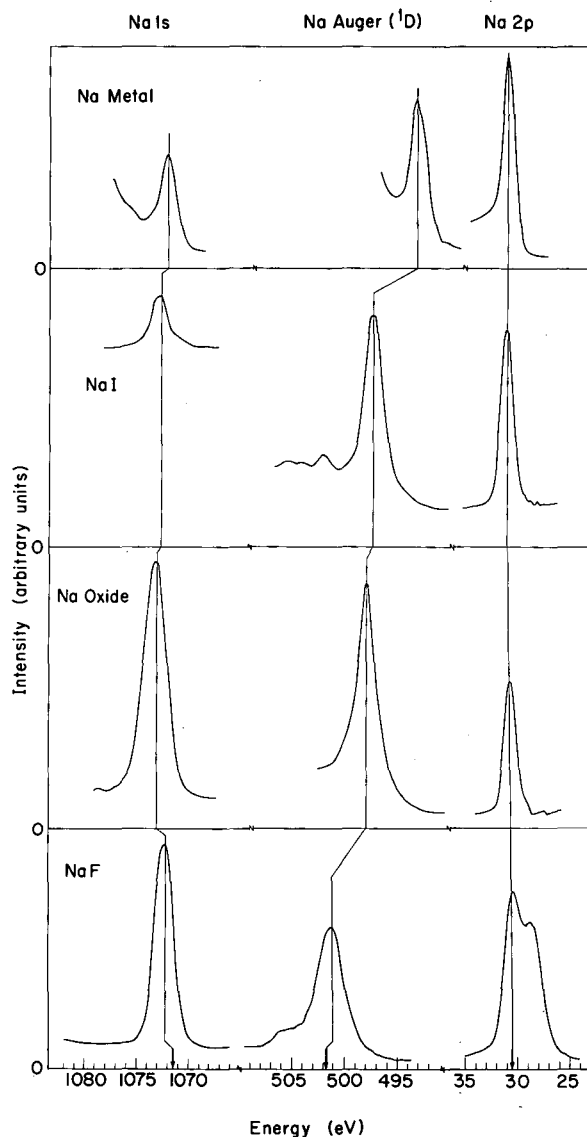
<sup>a</sup>Reference energies: top of valence bands (NaI and NaF); sodium Fermi level (metal and oxide).

<sup>b</sup>Thin oxide layer in metal.

<sup>c</sup>Estimated using  $E(1s) - E(2p) = 1042.0 \text{ eV}$ .

<sup>d</sup>From Eq. (9).

<sup>e</sup>See Eq. (10). NaF was used as the reference.



That this relationship holds well for Na is shown by comparing the last two columns of Table III. The relative shifts in  $E_B(\text{KLL}; {}^1\text{D})$  and  $E(2p)$  for Na, as well as the constancy of  $E(1s) - E(2p)$ , is illustrated in Fig. 1.

The  $L_3M_{45}M_{45}$  transition in zinc was studied in the metal,<sup>3</sup> in single crystals of ZnO, and  $\text{ZnF}_2$ . The equation

$$R_e(\text{Zn}) = E^F(L_3M_{45}M_{45}) - E^F(2p_{3/2}) + 2E^F(3d) + \mathcal{G}(3d, 3d; {}^1\text{D}) - 2E_R, \quad (11)$$

can be used to obtain  $R_e$  for the  ${}^1\text{D}$  peak in zinc. Again the extra-atomic relaxation term  $R_e$  is larger in the metal than in the oxide or fluoride, as expected (Table IV). The apparent binding energy shift  $E(3d) - E_B({}^1\text{D})$  increases by 5.2 eV from  $\text{ZnF}_2$  to Zn metal, in reasonable agreement with the 4.0 eV increase in  $R_e$ . Thus the Auger shifts in zinc and zinc compounds behave as expected, in agreement with the sodium results.

Returning now to the relation between Auger shifts  $\delta E(jkl; X)$  ESCA shifts  $\delta E(i)$ , we can derive from Eq. (3) the variation of these

Fig. 1. Sodium 1s, 2p, and  ${}^1\text{D}$  Auger lines as observed in an XPS spectrum, plus free-atom energies. The 2p peaks are made to coincide. For the measured energies see Table III. The 1s peaks nearly coincide, showing that the energy difference  $E(1s) - E(2p)$  is nearly constant, while large shifts arising from differences in extra-atomic relaxation are observed in the  ${}^1\text{D}$  Auger lines. The free atom values are denoted by the arrows and bold lines. The lower binding energy component of the doublet in the Na 2p region in the NaF spectra is the F 2s peak. (XBL 736-3179)

Table IV. Energy parameters for the  $\text{Zn}(L_3M_{45}M_{45}; {}^1\text{D})$  Auger transition (in eV)

Sample	$E^F(2p_{3/2})$	$E^F(3d)$	$E^F(L_3M_{45}M_{45}; {}^1\text{D})$	$R_e^a$	$\Delta[E(3d) - E_B({}^1\text{D})]$
metal	1021.96 <sup>b</sup>	10.18 <sup>b</sup>	991.8 <sup>b</sup>	6.8	5.2
ZnO	1022.2	10.44	987.4	2.7	1.0
$\text{ZnF}_2$	1021.5	10.9	985.9	2.8	(0)

<sup>a</sup>From Eq. (10).

<sup>b</sup>From Ref. 3.

shifts between two environments as

$$\delta E(jk\ell;X) = \delta E(j) - \delta E(k) - \delta E(\ell) + \delta R(k\ell). \quad (12)$$

Equation (12) displays explicitly the important role played by changes in relaxation energy  $\delta R(k\ell)$  relative to ESCA shifts. Applying this relation to the (KLL;  $^1D$ ) transition in sodium, and using the data in Table III, we have for the shifts from metal to oxide:  $\delta R = 6.1$  eV. Thus the shift in relaxation energy (-6.1 eV) is much more important than the net binding-energy shift (-1.3 eV) in determining the Auger shift of -7.4 eV in this case.

#### Acknowledgements

We gratefully acknowledge gifts of ZnO single crystal from Prof. G. A. Somorjai, ZnF<sub>2</sub> single crystal from Dr. R. Feigelson, and NaF and NaI from Dr. N. M. Edelstein.

#### Footnotes and References

\* Condensed from LBL-1916. Published in Phys. Rev. B 9, 831, (1974).

† Present Address: IBM, T. J. Watson Research Center, Yorktown Heights, N. Y. 10598.

1. D. A. Shirley, Chem. Phys. Letters 17, 312 (1972).
2. D. A. Shirley, Phys. Rev. A7, 1520 (1973).

3. S. P. Kowalczyk, R. A. Pollak, F. R. McFeely, L. Ley, and D. A. Shirley, Phys. Rev. B, 8, 2387 (1973).

4. J. B. Mann, "Atomic Structure Calculations I. Hartree-Fock Energy Results for the Elements Hydrogen to Lawrencium", LA-3690, (1967).

5. U. Gelius and K. Siegbahn, "ESCA Studies of the Molecular Core and Valence Levels in the Gas Phase", UUIP-794 (unpublished) (September, 1972).

6. L. Ley, S. P. Kowalczyk, F. R. McFeely, R. A. Pollak, and D. A. Shirley, Phys. Rev. B, 8, 2392 (1973).

7. C. E. Moore, "Atomic Energy Levels" (U. S. Dept. of Commerce, NBS Circular No. 467) Vol. 1 (1949); Vol. 2 (1952); Vol. 3 (1958).

8. J. A. Bearden, Rev. Mod. Phys. 39, 78 (1967).

9. K. Siegbahn, C. Nordling, A. Fahlman, R. Nordberg, K. Hamrin, J. Hedman, G. Johansson, T. Bergmark, S.-E. Karlsson, I. Lindgren, and B. J. Lindberg, ESCA - Atomic, Molecular and Solid State Structure by Means of Electron Spectroscopy, Nova Acta Regiae Soc. Sci. Upsaliensis Ser. IV, Vol. 20 (1967).

10. Kenneth D. Sevier, Low Energy Electron Spectroscopy (John Wiley and Sons, 1972). Reference is made to work by H. Hilling on sodium vapor Auger lines.

## THEORY OF KLL AUGER ENERGIES INCLUDING STATIC RELAXATION\*

D. A. Shirley

In an Auger process an atom loses energy by a transition from an initial state possessing in inner-shell vacancy to a final state in which the inner vacancy is filled but two new vacancies are present further out. An electron is ejected in this transition. The Auger electron's kinetic energy is termed the "Auger energy" of the transition.

This report gives the results of a theory that predicts E(KLL), the KLL Auger energies of the elements, in terms of one-electron binding energies and two-electron Coulomb and exchange integrals. The application of this theory to KL<sub>1</sub>L<sub>1</sub> energies alone was reported earlier.<sup>1</sup> In this report the theory is

applied to predict all nine KLL components. The key innovation in this work is the recognition of a previously overlooked "static" relaxation-energy term that has a considerable effect on E(KLL). Inclusion of this term allows the accurate prediction of KLL Auger energies, without resorting to multiparameter fits of experimental Auger energies. Theoretical values of E(KLL) are derived and found to be in excellent agreement with experiment.

Asaad and Burhop<sup>2</sup> made a major advance in the understanding of the KLL Auger spectrum by considering the effect of intermediate coupling in the two-hole final state. For the

nine observable KLL lines they found expressions of the form

$$\begin{aligned} E(KL_1L_1; {}^1S) &= E(K) - 2E(L_1) - F^0(20, 20), \\ E(KL_2L_3; {}^1D) &= E(K) - E(L_2) - E(L_3) \\ &\quad - F^0(21, 21) + \frac{2}{25} F^2(21, 21) \\ &\quad + \frac{3}{4} \zeta - \left\{ \left[ \frac{3}{25} F^2(21, 21) + \frac{1}{4} \zeta \right]^2 \right. \\ &\quad \left. + \frac{1}{2} \zeta^2 \right\}^{1/2}, \end{aligned} \quad (1)$$

and seven similar equations that are omitted here for brevity. The notation in Eqs. (1) is standard. The final-state-term symbol is included in the expression for the Auger energy. One-electron binding energies are given as  $E(K)$ , etc. Two-electron integrals have their usual notation. Coulomb and exchange integrals will be denoted as  $J$  and  $K$ , respectively, while the component Slater integrals are denoted as  $F^k$  and  $G^k$ . The spin-orbit coupling constant is denoted as  $\zeta$ . The spin-orbit coupling constant is denoted as  $\zeta$ . It can be obtained empirically from the empirical binding energies by using the relation  $\zeta = 2[E(L_2) - E(L_3)]/3$ .

The Asaad-Burhop equations were firmly anchored on multiplet theory,<sup>3</sup> and their predictions were qualitatively correct. Tables of Auger energies were compiled by fitting these equations to a few accurately-determined experimental energies, using the Slater integrals as parameters to be adjusted empirically.<sup>4-6</sup> Mann<sup>7</sup> has recently calculated accurate values of the Slater integrals of the elements, and these agree very poorly with the values determined empirically by fitting Auger energies to Eq. (1). We attribute this discrepancy to the omission in the Asaad-Burhop theory of a very important "static" relaxation term  $R$ , which accounts for the more repulsive environment experienced by an  $L$  electron after another  $L$  electron has been ionized. This indirect repulsive interaction increases the Auger energy. The  $R$  term can be calculated by a method described earlier for  $KL_1L_1$  energies.<sup>1</sup>

Using this approach, we can write as the general expression for the KLL' Auger energy associated with the final state  $X$ ,

$$\begin{aligned} E(KLL'; X) &= E(K) - E(L) \\ &\quad - E(L') - \mathcal{G}(KLL'; X) + R(X). \end{aligned} \quad (2)$$

Denoting the intrashell contribution to  $R$  by  $r$ , neglecting the negligible contribution of inner-shell relaxation, and using the equivalent-cores approximation, we have for the  $L$  shell

$$\begin{aligned} R(21) &= r + \sum_{\substack{\ell' \\ n' > 2}} \frac{N(n'\ell')}{(4\ell'+2)} f(\ell\ell') \Delta[F^0(2\ell, n'\ell')] \\ &\quad - \Delta \sum_k [g_k(\ell\ell) G^k(2\ell, n'\ell')]. \end{aligned} \quad (3)$$

Here  $F^0$  and  $G^k$  are Slater integrals that appear in the expansions of the Coulomb and exchange integrals, respectively.  $N(n'\ell')$  is the population of the  $n'\ell'$  subshell. The coefficients  $f(\ell\ell')$  and  $g(\ell\ell')$  are readily evaluated using standard multiplet theory. They have been given earlier.<sup>8</sup>

The full equations that were used to calculate the Auger energies are:

$$\begin{aligned} E(KL_1L_1) &= E(K) + R - 2E(L_1) - F^0(2s, 2s) \\ E(KL_1L_2 {}^1P_1) &= E(K) + R - E(L_1) - E(L_2) \\ &\quad - F^0(2s, 2p) + \frac{3}{4} \zeta - \left\{ \left[ \frac{1}{3} G^1(2s, 2p) - \frac{1}{4} \zeta \right]^2 \right. \\ &\quad \left. + \frac{1}{2} \zeta^2 \right\}^{1/2} \\ E(KL_1L_3 {}^3P_1) &= E(K) + R - E(L_1) - E(L_2) \\ &\quad - F^0(2s, 2p) + \frac{3}{4} \zeta + \left\{ \left[ \frac{1}{3} G^1(2s, 2p) - \frac{1}{4} \zeta \right]^2 \right. \\ &\quad \left. + \frac{1}{2} \zeta^2 \right\}^{1/2} \\ E(KL_1L_2 {}^3P_0) &= E(K) + R - E(L_1) \\ &\quad - E(L_2) - F^0(2s, 2p) + \frac{1}{3} G^1(2s, 2p) \\ E(KL_1L_3 {}^3P_2) &= E(K) + R - E(L_1) \\ &\quad - E(L_2) - F^0(2s, 2p) + \frac{1}{3} G^1(2s, 2p) + \frac{3}{2} \zeta \\ E(KL_2L_3 {}^1D_2) &= E(K) + R - 2E(L_2) - \\ &\quad - F^0(2p, 2p) + \frac{2}{25} F^2(2p, 2p) + \frac{9}{4} \zeta \\ &\quad - \left\{ \left[ \frac{3}{25} F^2(2p, 2p) + \frac{1}{4} \zeta \right]^2 + \frac{1}{2} \zeta^2 \right\}^{1/2} \\ E(KL_3L_3 {}^3P_2) &= E(K) + R - 2E(L_2) - F^0(2p, 2p) \\ &\quad + \frac{2}{25} F^2(2p, 2p) + \frac{9}{4} \zeta + \left\{ \left[ \frac{3}{25} F^2(2p, 2p) + \frac{1}{4} \zeta \right]^2 + \frac{1}{2} \zeta^2 \right\}^{1/2} \\ E(KL_3L_3 {}^3P_0) &= E(K) + R - 2E(L_2) \\ &\quad - F^0(2p, 2p) - \frac{1}{10} F^2(2p, 2p) \\ &\quad + \frac{3}{2} \zeta + \left\{ \left[ \frac{3}{10} F^2(2p, 2p) - \frac{1}{2} \zeta \right]^2 + 2\zeta^2 \right\}^{1/2} \\ E(KL_2L_2 {}^1S_0) &= E(K) + R - 2E(L_2) \\ &\quad - F^0(2p, 2p) - \frac{1}{10} F^2(2p, 2p) + \frac{3}{2} \zeta \\ &\quad - \left\{ \left[ \frac{3}{10} F^2(2p, 2p) - \frac{1}{2} \zeta \right]^2 + 2\zeta^2 \right\}^{1/2}. \end{aligned} \quad (4)$$

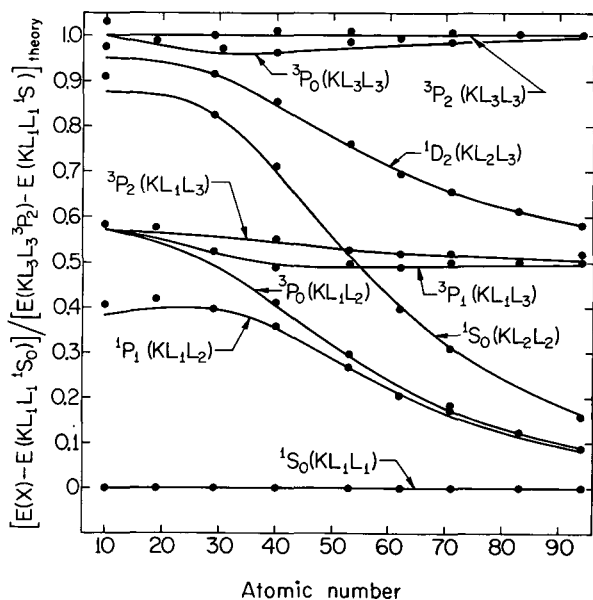
TABLE I. Predicted *KLL* Auger energies (eV).

El.	Z	R	$^1S_0$	$^1P_1$	$^3P_1$	$^3P_0$	$^3P_2$	$^1D_2$	$^3P_2$	$^3P_0$	$^1S_0$
			$KL_1L_1$	$KL_1L_2$	$KL_1L_3$	$KL_1L_2$	$KL_1L_3$	$KL_2L_3$	$KL_3L_3$	$KL_3L_3$	$KL_2L_2$
Ne	10	6	751	774	785	785	785	806	809	809	802
Na	11	8	922	948	961	961	961	986	989	989	981
Mg	12	10	1101	1131	1145	1145	1145	1174	1178	1178	1168
Al	13	12	1296	1332	1348	1348	1348	1383	1388	1387	1376
Si	14	14	1511	1550	1568	1568	1569	1607	1612	1611	1599
P	15	16	1739	1781	1800	1800	1801	1841	1848	1847	1833
S	16	18	1980	2032	2053	2052	2052	2103	2110	2109	2094
Cl	17	20	2247	2302	2325	2324	2326	2379	2386	2384	2368
Ar	18	22	2524	2584	2608	2607	2609	2666	2674	2672	2654
K	19	25	2814	2880	2906	2905	2908	2970	2979	2976	2957
Ca	20	28	3121	3194	3221	3220	3223	3292	3302	3299	3279
Sc	21	31	3451	3529	3557	3555	3560	3633	3645	3640	3619
Ti	22	33	3793	3880	3910	3907	3913	3995	4008	4003	3980
V	23	36	4163	4256	4286	4283	4290	4376	4390	4384	4360
Cr	24	39	4552	4647	4679	4676	4685	4772	4789	4781	4754
Mn	25	42	4953	5054	5088	5083	5094	5187	5205	5196	5167
Fe	26	45	5373	5480	5515	5509	5522	5620	5640	5631	5598
Co	27	48	5806	5922	5959	5953	5968	6073	6095	6085	6049
Ni	28	51	6265	6385	6423	6416	6433	6541	6566	6554	6516
Cu	29	54	6734	6863	6903	6894	6914	7030	7058	7045	7002
Zn	30	57	7216	7351	7393	7382	7405	7525	7556	7542	7495
Ga	31	58	7713	7744	7873	7884	7778	7802	7904	8009	7782
Ge	32	60	8218	8367	8414	8398	8430	8562	8602	8586	8524
As	33	61	8749	8903	8953	8934	8970	9105	9149	9132	9063
Se	34	62	9283	9447	9500	9478	9518	9662	9710	9693	9616
Br	35	63	9839	10012	10069	10043	10089	10241	10295	10276	10188
Kr	36	65	10411	10592	10653	10623	10675	10834	10894	10874	10775
Rb	37	67	10994	11184	11249	11214	11273	11437	11505	11484	11372
Sr	38	68	11593	11792	11863	11822	11889	12060	12136	12114	11987
Y	39	70	12211	12419	12497	12449	12524	12703	12787	12764	12622
Zr	40	72	12849	13065	13150	13095	13179	13364	13457	13433	13274
Nb	41	73	13501	13725	13819	13756	13850	14042	14145	14120	13942
Mo	42	75	14176	14409	14512	14439	14544	14744	14858	14832	14633
Tc	43	76	14862	15105	15217	15135	15251	15459	15583	15557	15337
Ru	44	78	15570	15820	15944	15851	15980	16194	16331	16304	16059
Rh	45	80	16294	16554	16689	16584	16726	16948	17099	17071	16801
Pd	46	81	17034	17303	17452	17333	17491	17720	17887	17858	17556
Ag	47	83	17793	18070	18233	18100	18273	18510	18692	18662	18331
Cd	48	85	18563	18849	19028	18880	19069	19313	19512	19481	19119
In	49	85	19347	19642	19839	19673	19881	20134	20351	20320	19920
Sn	50	86	20149	20454	20668	20485	20712	20973	21209	21177	20740
Sb	51	87	20968	21282	21517	21313	21562	21831	22090	22057	21576
Te	52	88	21806	22130	22386	22161	22432	22710	22991	22957	22433
I	53	88	22659	22992	23271	23024	23319	23604	23909	23874	23303
Xe	54	89	23516	23862	24166	23894	24216	24514	24846	24810	24186
Cs	55	90	24415	24766	25095	24798	25146	25447	25805	25769	25093
Ba	56	92	25320	25680	26038	25713	26090	26400	26788	26751	26018
La	57	93	26239	26613	27001	26646	27054	27377	27795	27758	26963
Ce	58	95	27190	27573	27993	27606	28047	28377	28829	28790	27930
Pr	59	96	28161	28553	29007	28587	29063	29402	29889	29850	28920
Nd	60	98	29153	29556	30047	29590	30104	30453	30978	30937	29933
Pm	61	99	30160	30574	31104	30609	31162	31521	32085	32044	30962
Sm	62	101	31188	31613	32183	31648	32243	32611	33217	33175	32010
Eu	63	103	32238	32762	33288	32707	33348	33725	34378	34335	33078
Gd	64	104	33305	33750	34412	33786	34474	34861	35561	35517	34167
Tb	65	105	34393	34850	35560	34886	35623	36020	36769	36725	35277
Dy	66	107	35503	35970	36733	36006	36797	37204	38007	37962	36407

## THEORY OF KLL AUGER ENERGIES INCLUDING STATIC...

TABLE I. (Continued)

El.	Z	R	$^1S_0$ $KL_1L_1$	$^1P_1$ $KL_1L_2$	$^3P_1$ $KL_1L_3$	$^3P_0$ $KL_1L_2$	$^3P_2$ $KL_1L_3$	$^1D_2$ $KL_2L_3$	$^3P_2$ $KL_3L_3$	$^3P_0$ $KL_3L_3$	$^1S_0$ $KL_2L_2$
Ho	67	109	36 633	37 110	37 929	37 147	37 995	38 411	39 271	39 226	37 557
Er	68	110	37 781	38 270	39 148	38 307	39 214	39 641	40 561	40 514	38 728
Tm	69	112	38 953	39 453	40 393	39 490	40 460	40 898	41 881	41 833	39 921
Yb	70	113	40 146	40 657	41 662	40 696	41 731	42 180	43 227	43 180	41 138
Lu	71	115	41 359	41 882	42 956	41 921	43 026	43 486	44 604	44 555	42 374
Hf	72	117	42 588	43 123	44 269	43 162	44 340	44 811	46 003	45 953	43 627
Ta	73	118	43 832	44 379	45 601	44 418	45 673	46 155	47 423	47 373	44 893
W	74	120	45 097	45 657	46 961	45 697	47 034	47 529	48 879	48 828	46 185
Re	75	121	46 387	46 961	48 349	47 001	48 423	48 930	50 366	50 314	47 501
Os	76	122	47 694	48 280	49 760	48 321	49 835	50 355	51 883	51 830	48 834
Ir	77	123	49 026	49 625	51 198	49 666	51 275	51 807	53 430	53 376	50 190
Pt	78	124	50 382	50 993	52 666	51 035	52 744	53 287	55 010	54 956	51 571
Au	79	126	51 761	52 385	54 163	52 427	54 242	54 799	56 628	56 573	52 976
Hg	80	127	53 160	53 795	55 683	53 838	55 763	56 329	58 269	58 213	54 397
Tl	81	129	54 567	55 221	57 224	55 264	57 305	57 890	59 946	59 889	55 842
Pb	82	130	56 007	56 673	58 800	56 717	58 882	59 479	61 659	61 601	57 306
Bi	83	132	57 468	58 153	60 405	58 197	60 488	61 103	63 409	63 351	58 804
Po	84	133	58 939	59 640	62 030	59 685	62 115	62 745	65 190	65 131	60 307
At	85	135	60 450	61 165	63 695	61 210	63 781	64 424	67 011	66 951	61 846
Ru	86	136	62 006	62 725	65 401	62 770	65 488	66 136	68 869	68 809	63 410
Fr	87	137	63 552	64 292	67 125	64 338	67 213	67 882	70 772	70 711	64 999
Ra	88	138	65 134	65 895	68 892	65 941	68 981	69 670	72 726	72 664	66 622
Ac	89	139	66 754	67 519	70 688	67 566	70 778	71 471	74 699	74 636	68 250
Th	90	140	68 379	69 167	72 516	69 214	72 607	73 322	76 731	76 667	69 920
Pa	91	141	70 056	70 856	74 393	70 904	74 485	75 212	78 809	78 745	71 622
U	92	142	71 748	72 567	76 302	72 615	76 395	77 141	80 938	80 873	73 353
Np	93	143	73 486	74 317	78 703	74 366	78 797	79 554	84 002	83 936	75 115
Pu	94	144	75 257	76 103	80 266	76 153	80 362	81 134	85 360	85 293	76 916
Am	95	145	77 116	77 956	82 349	78 006	82 446	83 211	87 669	87 601	78 763
Cm	96	146	78 928	79 620	84 422	79 670	84 519	85 137	90 003	89 935	80 279
Bk	97	147	80 660	81 562	86 447	81 613	86 546	87 373	92 323	92 254	82 431
Cf	98	148	83 352	84 224	89 496	84 276	89 596	90 393	95 731	95 661	85 064
Es	99	149	85 294	86 187	91 748	86 239	91 849	92 666	98 294	98 224	87 047
Fm	100	150	87 286	88 190	94 050	88 242	94 152	94 980	100 908	100 837	89 061



The new recommended Auger energies are presented in Table I. We have elected to present the full table rather than giving a detailed comparison between these predicted Auger energies and experimental values.<sup>9</sup> The agreement with experiment is generally excellent, however. Figure 1 shows a graphical comparison on a reduced plot in which the energy scale was not adjusted.

Fig. 1. Reduced KLL Auger-energy differences for the elements. Here  $E(X)$  is the experimental energy of component X. The nine components are labeled on the plot. In the ordinate ratio the denominator is always the total theoretical spacing, from Table I. The curves are theoretical, obtained by using theoretical energies from Table I in the numerator. Filled circles were obtained by using experimental values from Ref. 9 in the numerator. Thus there is no scaling to fit experiment to theory. (XBL 731-2081)

Footnotes and References

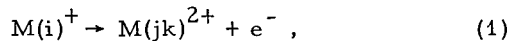
\*Based on LBL-1640, published in Phys. Rev. A 7 1520 (1973).

1. D. A. Shirley, Chem. Phys. Letters 17, 312 (1972).
2. W. N. Asaad and E. H. S. Burhop, Proc. Roy. Soc. (London) 72, 369 (1958).
3. J. C. Slater, Quantum Theory of Atomic Structure (McGraw-Hill, 1960), Vol. II, p. 294.
4. O. Hörnfeldt, F. Fahlman, and C. Nordling, Ark. Fys. 23, 115 (1962).
5. O. Hörnfeldt, Ark. Fys. 23, 235 (1962).
6. K. Siegbahn, C. Nordling, A. Fahlman, R. Nordberg, K. Hamrin, J. Hedman, G. Johansson, T. Bergmark, S.-E. Karlsson, I. Lindgren, and B. Lindberg, ESCA-Atomic, Molecular and Solid State Structure by Means of Electron Spectroscopy, Nova Acta Regiae Soc. Sci. Upsaliensis Ser. IV, Vol. 20 (1967).
7. J. B. Mann, "Atomic Structure Calculations I. Hartree-Fock Energy Results for the Elements Hydrogen to Lawrencium", Los Alamos Scientific Laboratory Report LASL-3690 (1967).
8. D. A. Shirley, Chem. Phys. Letters 16, 220 (1972).
9. Kenneth D. Sevier, Low Energy Electron Spectroscopy (John Wiley and Sons, 1972).

THEORY OF AUGER SATELLITE ENERGY SHIFTS\*

D. A. Shirley

A normal Auger transition takes an atomic system from a one-hole initial state to a two-hole final state, with the energy difference going into the kinetic energy of the ejected electron. Thus the Auger energy of the transition

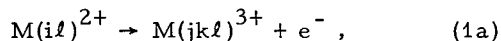


which carries element M from an initial state with a hole in the  $i$  orbital to a final state with holes in the  $j$  and  $k$  orbitals, is given by

$$E(ijk) = E(i) - E(jk). \quad (2)$$

Here  $E(i)$  and  $E(jk)$  are the total energies of the  $i$  and  $jk$  hole states.

Recently, Auger spectra in several heavy elements have shown Auger satellites.<sup>1,2</sup> These are Auger transitions that occur in the presence of additional, "spectator" vacancies which are present both before and after the transitions. An  $l$  satellite on the above  $(ijk)$  transition would involve the process



going from a two-hole initial state to a three-hole final state. This  $l$  satellite transition would be denoted  $(ijk(\ell))$ , and its energy would be given by

$$E(ijk(\ell)) = E(i\ell) - E(jk\ell). \quad (2a)$$

This report describes the development of a simple theoretical scheme for estimating the shift in energy of the satellite line relative to the main line in an Auger transition,

$$\Delta E(ijk(\ell)) \equiv E(ijk(\ell)) - E(ijk). \quad (3)$$

Let us consider Fig. 1, in which the hole states that have a spectator vacancy  $l$  are built up from the corresponding "regular" Auger hole states  $i$  and  $jk$  in a three-step Gedanken experiment. The first step takes the system to a hypothetical state in which an electron has been removed from orbital  $l$  without taking into account the presence of the  $i$  hole. The energy change of this process is just the binding energy of an  $l$  orbital in a free atom,  $E(l)$ .

In the second step the direct interaction between the  $i$  and  $l$  holes is added. The energy of the two-hole state is thus increased by this repulsive interaction an amount  $\mathcal{F}(i\ell)$ . From standard multiplet-coupling theory  $\mathcal{F}(i\ell)$  can be expressed in terms of two-electron Coulomb and exchange integrals. Thus, if the  $i$  and  $l$  orbitals were in an  $s$  and a  $p$  shell, for example, we could write  $\mathcal{F}(i\ell)$  in terms of Slater integrals as<sup>3</sup>

$$\mathcal{F}(i\ell) = F^0(i\ell) - \frac{1}{6} G^1(i\ell), \quad (4)$$

and similarly for other cases.

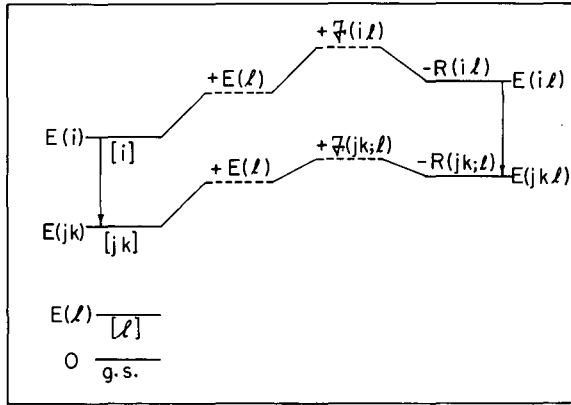


Fig. 1. Energy-level diagram illustrating the formation of the "spectator" hole states  $i\ell$  and  $jk\ell$  from the "regular" hole states  $i$  and  $jk$ , by a hypothetical three-step process. Corresponding Auger transitions are shown. (XBL 739-4105)

The third step in Fig. 1 involves the "indirect" interaction between orbitals  $i$  and  $\ell$ . These are brought about through the separate influence of the holes in orbitals  $i$  and  $\ell$  on the remaining "passive" occupied orbitals. The passive orbitals relax toward the attractive hole in orbital  $i$ . Electrons in these orbitals will then produce a different effective electrostatic potential at orbital  $\ell$ . The difference, which Hedin and Johansson<sup>4</sup> termed the "polarization potential"  $V_p$ , will increase the energy of the two-hole state by a relaxation energy

$$R(i\ell) = \langle \ell | V_p(i) | \ell \rangle = \langle \ell | \sum_m [V(\ell m)_i - V(\ell m)] | \ell \rangle. \quad (5)$$

Here  $V(\ell m)$  is the operator that describes the two-electron interaction between orbitals  $\ell$  and  $m$ , including both Coulomb and exchange contributions, in the neutral atom. The corresponding operator for an ion with a hole in the  $i$  orbital is denoted by  $V(\ell m)_i$ . The sum is taken over all occupied orbitals  $m$ .

After considering the analogous three steps for the  $jk\ell$  hole state and combining the energies for the three steps in each case, we have

$$\begin{aligned} E(i\ell) &= E(i) + E(\ell) + \mathcal{F}(i\ell) - R(i\ell) \\ E(jk\ell) &= E(jk) + E(\ell) + \mathcal{F}(jk;\ell) - R(jk;\ell). \end{aligned} \quad (6)$$

The signs of the  $\mathcal{F}$  and  $R$  terms indicate that

hole-hole interactions are repulsive, whereas relaxation of electrons toward a hole in an inner shell has an attractive effect on another such hole (or that this relaxation increases the binding energy of the corresponding electron<sup>5</sup>). From Eqs. (2), (2a), (3), and (6), the Auger shift can be expressed as

$$\Delta E(ijk(\ell)) = \mathcal{F}(i\ell) - \mathcal{F}(jk;\ell) - R(i\ell) + R(jk;\ell). \quad (7)$$

By assuming that the hole-state interactions are pair wise additive, we may rewrite this equation as

$$\begin{aligned} \Delta E(ijk(\ell)) &= \mathcal{F}(i\ell) - \mathcal{F}(j\ell) - \mathcal{F}(k\ell) - R(i\ell) \\ &\quad + R(j\ell) + R(k\ell). \end{aligned} \quad (8)$$

The  $\mathcal{F}$  terms can be calculated by simply using tabulated ground-state Coulomb and exchange integrals. This approach was discussed and used successfully for treating KLL Auger energies earlier.<sup>5</sup>

Before estimating the relaxation terms  $R$  we note that Hedin and Johansson subdivided two-electron relaxation effects involving holes into inner-shell, intra-shell, and outer-shell interactions. By explicit calculations on hole states the inner-shell effects were shown to be negligible. Intra-shell effects tend to be small in comparison with outer-shell terms, especially for core-level holes in large atoms, for which outer-shell terms dominate. In the version of the model used below, only outer-shell terms are considered and the "equivalent-cores" approximation is made. This approximation is well-known, in an empirical form, in x-ray spectroscopy, having been used as early as 1921 by Wenzel<sup>6</sup> in connection with x-ray satellites. In this form it involves estimating the energy of an x-ray transition in element  $Z$  in the presence of a core-electron hole by using the measured transition energy in element  $Z + 1$ . Thus the shielding of the outer orbitals by a core hole is taken as equivalent to that of a positive charge in the nucleus.

The quantum-mechanical version of the equivalent cores models is also a good approximation. Because the radii of electronic shells in a given atom increase dramatically with each unit increase in principal quantum number  $n$ , it suffices, for estimating the interaction with a hole in shell  $n$ , to approximate the radial wave functions of orbitals with  $n' > n$  by those of the corresponding orbitals in the next higher element. The additional interaction of these orbitals with holes in shells of  $n' < n$  is then given by<sup>7</sup>



Table I.  $L_3M_{45}M_{45}(M_{45})$  Auger satellite energy shifts (in Rydbergs).

Element	Z	$\mathcal{F}(2p\ 3d)$	$\mathcal{F}(3d\ 3d)$	R(2p 3d)	R(3d 3d)	$\Delta E(L_3M_{45}M_{45}(M_{45}))$	$\Delta E_{\text{expt}}$
Yb	70	11.45	8.94	4.96	4.73	-1.93(-26 eV)	
Re	75	12.46	9.75	5.41	5.18	-2.14(-29 eV)	
Hg	80	13.47	10.56	5.87	5.64	-2.24(-30.5 eV)	
Bi	85	14.47	11.37	5.93	5.70	-2.80(-38 eV)	-36(5) eV <sup>a</sup>
Th	90	15.48	12.19	5.22	4.99	-4.14(-56 eV)	
Am	95	16.49	13.00	5.60	5.30	-4.51(-61 eV)	-56 eV <sup>b</sup>
Fm	100	17.50	13.82	5.98	5.68	-4.76(-65 eV)	

<sup>a</sup>Ref. 1.  
<sup>b</sup>Ref. 2.

$$R(n''\lambda'', n'\lambda') = \sum_{\substack{n'\lambda', \\ n' > n, n''}} N(n'\lambda') [\mathcal{F}(n''\lambda'', n'\lambda')_{Z+1} - \mathcal{F}(2p, n'\lambda)_Z] - \mathcal{F}(n''\lambda'', n'\lambda')_Z] \quad (12)$$

$$R(3d\ 3d) = \sum_{n' > 3} N(n'\lambda) [\mathcal{F}(3d, n'\lambda)_{Z+1} - \mathcal{F}(3d, n'\lambda)_Z]$$

Here  $\lambda$  is the orbital angular momentum quantum number,  $N(n'\lambda')$  is the occupation number of the  $n'\lambda'$  subshell, and the sum is taken over all occupied states with  $n' > n$ .

Using this model shifts here predicted for  $L_3M_{45}M_{45}(M_{45})$  transitions in elements with atomic number  $70 \leq Z \leq 100$ . Comparisons with experiment have been made where possible.

For  $L_3M_{45}M_{45}(M_{45})$  transitions Eq. (9) takes the specific form

$$\Delta E(L_3M_{45}M_{45}(M_{45})) = \mathcal{F}(2p\ 3d) - 2\mathcal{F}(3d\ 3d) - R(2p\ 3d) + 2R(3d\ 3d). \quad (10)$$

Standard multiplet theory<sup>3</sup> gives

$$\begin{aligned} \mathcal{F}(2p\ 3d) &= F^0(2p\ 3d) - (1/15) G^1(2p\ 3d) \\ &\quad - (3/70) G^3(2p\ 3d) \\ \mathcal{F}(3d\ 3d) &= F^0(3d\ 3d) - (2/63) F^2(3d\ 3d) \\ &\quad - (2/63) F^4(3d\ 3d). \end{aligned} \quad (11)$$

Similar expressions can be written for the terms  $\mathcal{F}(2p, n'\lambda)$  and  $\mathcal{F}(3d, n'\lambda)$  that make up the relaxation terms

$$R(2p\ 3d) = \sum_{n' > 3} N(n'\lambda) [\mathcal{F}(2p, n'\lambda)_{Z+1}$$

Numerical values of  $\Delta E(L_3M_{45}M_{45}(M_{45}))$  were calculated from Eqs. (10) - (12) using Mann's<sup>8</sup> values of the Slater integrals. Results are given in Table I for intervals of  $\Delta Z = 5$ . The shifts increased regularly by a factor of 2.5 from  $Z = 70$  to  $Z = 100$ , although the estimated values of  $R$  varied erratically near  $Z = 90$ . The calculated values of  $\Delta E(L_3M_{45}M_{45}(M_{45}))$  show excellent agreement with experiment in the two elements for which measurements are available: -38 eV vs  $-36 \pm 5$  eV<sup>1</sup> in bismuth and -61 eV vs -56 eV<sup>2</sup> in americium. We conclude that this model gives realistic estimates of Auger satellite shifts.

#### Footnotes and References

\*Brief version of LBL-1953, Phys. Rev. A, to be published in early 1974.

1. S. K. Haynes, N. Velinsky, and L. J. Velinsky, Nucl. Phys. A90, 573 (1967).

2. Melvin S. Freedman and Fred T. Porter, Proceedings of the International Conference on Inner Shell Ionization Phenomena and Future Applications, April 17-22, 1972 (USAEC Technical Information Center, Oak Ridge, Tennessee), p. 680.

3. J. C. Slater, Quantum Theory of Atomic Structure (McGraw-Hill, New York, 1960), Vol. 2, p. 294.
4. L. Hedin and A. Johansson, *J. Phys.* **B2**, 1336 (1969).
5. D. A. Shirley, *Phys. Rev. A* **7**, 1520 (1973).
6. G. Wenzel, *Ann. d. Physik* **66**, 437 (1921); *Zeits. f. Physik* **31**, 445 (1921).
7. D. A. Shirley, *Chem. Phys. Letters* **16**, 220 (1972).
8. J. B. Mann, Los Alamos Scientific Laboratory Report LASL-3690 (1967).

### QUADRUPOLE COUPLING AT $^{193}\text{Ir}$ NUCLEI IN IRON\*

D. Salomon and D. A. Shirley

Hyperfine magnetic fields at nuclei of solute atoms occupying substitutional sites in ferromagnetic lattices are well-known. Quadrupole hyperfine structure may also be present in such solutes, even in a cubic host lattice such as iron. Quadrupole interactions could arise from solute-solute effects, lattice distortion at the impurity site, spin-orbit interactions in combination with nonzero  $\langle S_z \rangle$ , or perhaps from effects peculiar to domain walls. Recently two values have been reported for the quadrupole splitting of  $^{193}\text{Ir}$  in iron. Aiga and Itoh<sup>1</sup> saw clearly resolved satellites at  $\Delta\nu (= |e^2qQ/2h|) = 2.5$  MHz above and below the main line in the spin-echo NMR spectrum of  $\text{Ir}_{0.003}\text{Fe}_{0.997}$ . Wagner and Potzel<sup>2</sup> analyzed the  $^{193}\text{Ir}$  Mössbauer spectrum of an  $\text{Ir}_{0.03}\text{Fe}_{0.97}$  alloy to yield  $e^2qQ/2h = 1.6 \pm 0.3$  MHz. The disagreement between these two values leaves the situation regarding induced quadrupole structure at solutes in ferromagnets in a rather unsatisfactory state, because  $\text{Ir}(\text{Fe})$  is an important prototype for such systems. In an attempt to resolve this discrepancy we have studied a very dilute alloy by Mössbauer spectroscopy.

Mössbauer source experiments were performed, in order to study  $\text{Fe}(\text{Ir})$  systems sufficiently dilute that solute-solute interactions could be neglected. It has become increasingly clear in recent years that even a 1% solution in a ferromagnetic host cannot be regarded as dilute in the above sense. The compositions of our alloys were  $\leq 0.1$  atomic percent osmium.

The Mössbauer absorption spectrum from one sample is shown in Fig. 1. The resolution of the eight components is considerably better than that obtained by Wagner and Potzel, suggesting that the spectrum of their 3% alloy was seriously affected by inhomogeneous broadening. Our spectra were analyzed using the hyperfine spin Hamiltonian

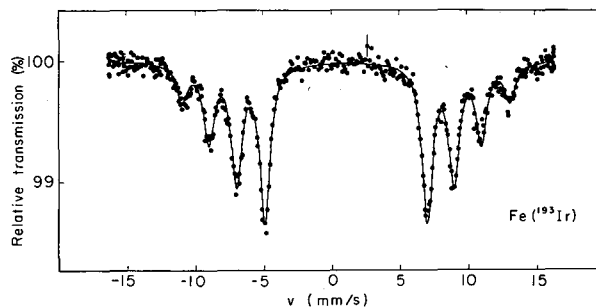


Fig. 1. Mössbauer absorption spectrum of a  $\text{Fe}(^{193}\text{Ir})$  source against a  $90 \text{ mg/cm}^2$  Ir absorber at  $4.2^\circ\text{K}$ , with a least-squares fit. The derived line width was  $\Gamma/2 = 0.460(8) \text{ mm}(\text{sec})$ . If the lines are numbered 1 through 8 from the left, the quadrupole interaction is manifest as a barely perceptible relative shift of lines 1, 4, 5, and 8 to the right. (XBL 734-2753)

$$\mathcal{H} = -g\mu_N H_{\text{hf}z} I_z + \frac{e^2qQ}{4I(2I-1)} [3I_z^2 - I(I+1)], \quad (1)$$

to yield the parameters given in Table I.

In making comparisons of our data with the earlier results, also set out in Table I, it is important to bear in mind the differences among the three experiments. The NMR measurements detected  $^{193}\text{Ir}$  nuclei in domain walls, while most of the Mössbauer signal involved nuclei within domains. In the Mössbauer spectra, but not the NMR spectrum, the sign of  $e^2qQ$  is detectable. Finally the concentration of Ir in the 3 atomic percent sample studied by Wagner and Potzel was so high as to compromise its value as a dilute  $\text{Fe}(\text{Ir})$  system.

Table I. Derived parameters for  $^{193}\text{Ir}(\text{Fe})$ 

Sample	$\nu_0$ (MHz)	$e^2qQ/2h$ (MHz)	$H_{\text{hf}}$ (kOe) <sup>a</sup>	Isomer Shift	Ref.
Os <sub>0.001</sub> Fe <sub>0.999</sub>	119.5(4)		-2.13(37)	1.017(7) mm/sec	This work
Os <sub>0.001</sub> Fe <sub>0.999</sub>	119.6(4)		-1.98(34)	1.027(8) mm/sec	This work
Average	119.6(3)		-2.05(25)	1.022(5) mm/sec	This work
Ir <sub>0.003</sub> Fe <sub>0.997</sub>	119.0		2.5 <sup>c</sup>	--	1
Ir <sub>0.03</sub> Fe <sub>0.97</sub>	121.4(1.7) <sup>b</sup>		-1.6(3)	--	2

<sup>a</sup>Derived using  $g(1/2)/g(3/2) = 8.874(13)$  and  $\mu(3/2) = 1.0591 \mu_N$ , as in Ref. 2.  
<sup>b</sup>Derived from parameters given in Ref. 2.  
<sup>c</sup>Only absolute value measured.

We note that the average ground-state hyperfine frequency  $\Delta\nu_\mu = g(3/2) \mu_N H_{\text{hf}}$  given by Aiga and Itoh agrees quite well with our value (119.0 MHz vs 119.6(3) MHz). Thus the hyperfine fields in domains and walls appear to be essentially the same.

Because of the large perturbative effect of neighboring solute atoms on NMR spectra in alloys of a few percent concentration, manifest as intense satellite lines,<sup>3</sup> together with the large field gradients that these neighbors probably create, one might expect the value of  $e^2qQ$  obtained from the Ir<sub>0.03</sub> Fe<sub>0.97</sub> alloy<sup>2</sup> to bear little relation to the NMR value.<sup>1</sup> In fact, as Table I shows, the earlier value agrees with ours in sign and is surprisingly close in magnitude. The reason for this behavior is of some interest because of its general applicability in comparing Mössbauer and NMR spectra. To understand this result let us consider first a case in which the quadrupole coupling arises entirely through spin-orbit interaction plus spin polarization. In a 3% (or even 1%) alloy, near-neighbor interactions would lead to various hyperfine magnetic fields statistically distributed among the solute atoms, and most likely the quadrupole interaction would be completely obscured in an NMR spectrum. The Mössbauer spectrum is sensitive to the sign of  $e^2qQ$ , however. By applying Eq. (1) to the excited and ground states, taking differences, allowing  $H_{\text{hf}}$  to vary slightly, and performing a weighted sum, it is easily shown that  $e^2qQ$  contributes coherently to the average, shifting the energy of each line by  $e^2qQ/4$ , with the sign of the shift for each component determined by whether the corresponding ground-state  $|\mu_I|$  value is  $3/2$  or  $1/2$ . Thus in Fig. 1, for example, the two lines at ca - 5 and -7 mm/sec are separated in energy by  $e^2qQ$  more than those at ca +7

and +9 mm/sec. Thus the presence of magnetic satellites arising from solute-solute interactions would have little effect on the value of  $e^2qQ$  derived from a Mössbauer spectrum.

If solute near neighbors induce substantial field gradients the situation is changed somewhat, but not as much as one might expect. The magnetic interaction is still dominant, and the quantization axis is essentially along  $\vec{H}_{\text{hf}}$ . Since the contributions to the field-gradient tensor arising from  $\langle S_z \rangle$  plus  $\vec{l} \cdot \vec{s}$  would, if taken alone, have a principal axis collinear with  $H_{\text{hf}}$ , this ( $\langle S_z \rangle$  plus  $\vec{l} \cdot \vec{s}$ ) interaction is not affected by the magnetic hyperfine interaction: it gives diagonal contributions to the energy matrix and contributes linearly to shifts in the spectral lines as indicated above. In contrast, contributions to the quadrupole interaction from near neighbors will be practically random relative to  $\vec{H}_{\text{hf}}$ . The diagonal components of this interaction will have both positive and negative signs, and they alone would contribute incoherently to line shifts, in the ensemble average. Since the two quadrupole interactions have different principal axes, the net effect of the neighbor-induced quadrupole interaction is a reduction of the observed quadrupole shifts, as is apparently observed in the Ir<sub>0.03</sub> Fe<sub>0.97</sub> alloy.

In summary, this work strongly supports the existence of quadrupole interactions in dilute Fe(Ir) systems and establishes the sign of  $e^2qQ$  as negative, in agreement with the more concentrated alloy results of Wagner and Potzel. Taken together, the three studies to date may be interpreted in terms of a quadrupole interaction at Ir nuclei in iron that arises through spin-orbit plus spin-polarization ( $\vec{l} \cdot \vec{s}$  plus  $\langle S_z \rangle$ ) effects, and that is present both in domains and in walls. The apparent

value of  $e^2qQ$  decreases slowly with concentration, as expected. The magnetic hyperfine field is the same within 0.3% between domains and walls, but appears to increase in the 3% alloy.

#### Footnotes and References

\*From LBL-1956, and Phys. Rev. B, to be published.

1. M. Aiga and J. Itoh, J. Phys. Soc. (Japan) 31, 1844 (1971).

2. F. Wagner and W. Potzel, in Hyperfine Interactions in Excited Nuclei, ed. by G. Goldring and R. Kalish (Gordon and Breach, New York, 1971), Vol. 2, p. 681.

3. J. I. Budnick, T. J. Burch, S. Skalski, and K. Raj, Phys. Rev. Letters 24, 511 (1970).

### SUPERTRANSFERRED HYPERFINE INTERACTION: PERTURBED ANGULAR CORRELATION OF $^{111}\text{mCd}$ IN $\text{KNiF}_3$ , $\text{KCoF}_3$ AND $\text{RbMnF}_3$

H. H. Rinneberg and D. A. Shirley

Perturbed angular correlation (PAC) of  $^{111}\text{mCd}$  as a dilute impurity in magnetically ordered transition metal salts has been found to be an effective tool in the study of supertransferred hyperfine interactions.<sup>1</sup> The PAC spectra of Cd in antiferromagnetic  $\text{KNiF}_3$  ( $T_N = 253.5^\circ\text{K}$ ),  $\text{KCoF}_3$  ( $T_N = 114^\circ\text{K}$ ) and  $\text{RbMnF}_3$  ( $T_N = 82.9^\circ\text{K}$ ) are shown in Fig. 1. Well resolved magnetic hyperfine structure is observed in each case. We include the spectra of  $\text{RbMnF}_3$  at  $77^\circ\text{K}$ . The decrease in sublattice magnetization is shown by the decrease in precession frequency. The observed hyperfine fields at the Cd nucleus ( $4^\circ\text{K}$ ) are:  $105.6(\pm 1.5)\text{kOe}$  ( $\text{KNiF}_3$ )  $74.4(\pm 1.0)\text{kOe}$  ( $\text{KCoF}_3$ ) and  $113.5(\pm 1.5)\text{kOe}$  ( $\text{RbMnF}_3$ ).

The perovskites  $\text{KNiF}_3$  and  $\text{RbMnF}_3$  are simple cubic antiferromagnets (Type G).  $\text{KCoF}_3$  has the same magnetic structure but with the magnetic transition a slight tetragonal distortion occurs. Within the experimental error no deviation of the observed spectrum from the simple cubic case (i. e., no quadrupole splitting) was found. We therefore neglect this distortion.

The  $\text{Cd}^{2+}$  enters substitutionally for a transition metal ion. It is octahedrally surrounded by six magnetic ions which are connected to the impurity by linear  $\text{Me}^{2+}\text{-F-Cd}^{2+}$  bonds. In the antiferromagnetic state the six lowest transition metal ions belong to the same sublattice.

The hyperfine fields at the Cd site are caused by supertransferred spin densities in Cd orbitals. Because of the cubic symmetry all dipole fields cancel. Similarly spin densities transferred into p and d orbitals of  $\text{Cd}^{2+}$  do not contribute except via core polarization. We neglect these contributions since

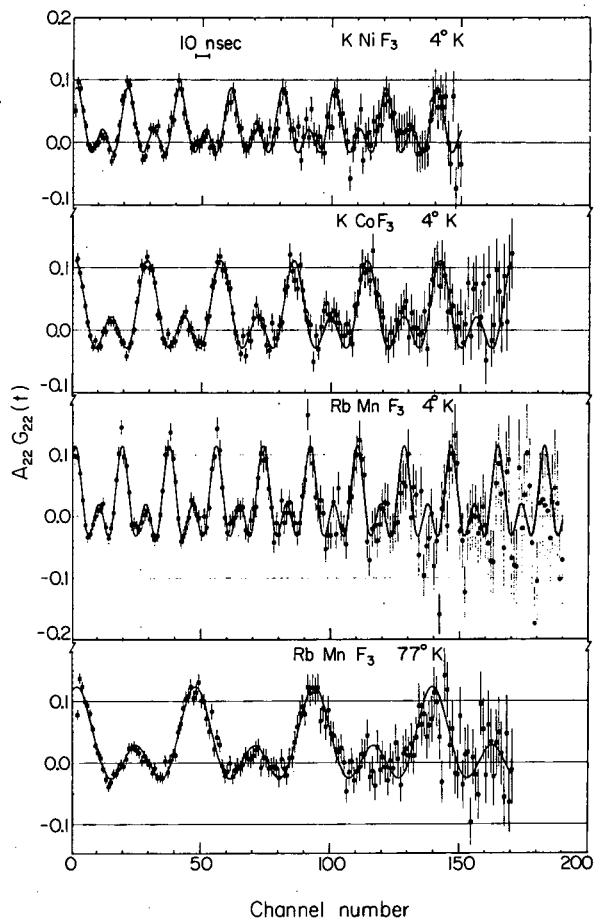


Fig. 1. Time differential PAC spectra of  $^{111}\text{mCd}$  in antiferromagnetic  $\text{KNiF}_3$ ,  $\text{KCoF}_3$ , and  $\text{RbMnF}_3$ . (XBL 734-2591)

they should be much smaller than those caused by spin densities directly transferred into S orbitals of  $\text{Cd}^{2+}$ . It is well known from NMR measurements,<sup>2,3</sup> there are fractional spin densities  $f_s, f_\sigma$  and  $f_\pi$  in fluorine 2s,  $2p_\sigma$  and  $2p_\pi$  orbitals, arising from overlap and covalency in the transition metal fluorine bond. These spin densities are in turn transferred into Cd ns orbitals by overlap. Since  $f_s$  is usually much smaller than the densities in p-orbitals only the overlap of  $2p_\sigma$  orbitals with Cd s orbitals is considered. The hyperfine fields at the Cd nucleus are therefore proportional to the spin density  $f_\sigma$  of the transition metal-fluorine bond. To a good approximation one obtains for the ratio of the measured hyperfine fields

$$\frac{H_{\text{hf}}(\text{Cd in KCoF}_3)}{H_{\text{hf}}(\text{Cd in KNiF}_3)} = \frac{\frac{1}{2} \left( \frac{\langle S \rangle}{S} \right)_{\text{Co}} \cdot \frac{f_\sigma^{\text{Co}}}{f_\sigma^{\text{Ni}}}}{\frac{1}{2} \left( \frac{\langle S \rangle}{S} \right)_{\text{Ni}} \cdot \frac{f_\sigma^{\text{Ni}}}{f_\sigma^{\text{Ni}}}}$$

Here the different zero spin deviations have been taken into account.<sup>4</sup> Since  $f_\sigma^{\text{Ni}}$  is known unambiguously from ( $f_\pi^{\text{Ni}} = 0, f_\sigma^{\text{Ni}} = 3.8\%$ ),<sup>3</sup> we obtain for  $\text{KCoF}_3$  and  $\text{RbMnF}_3$

$$f_\sigma = 2.6\%(\text{Co-F}) \text{ and } f_\sigma = 3.8\%(\text{Mn-F}).$$

The first value is in good agreement with the value ( $2.4 \pm 1.0\%$ ) obtained by Thornley et al.<sup>5</sup> from the fluorine superhyperfine structure of  $\text{CoF}_6^{3-}$ . Since NMR or ESR experiments yield only the difference  $f_\sigma - f_\pi$  a second measurement is generally needed to obtain the spin densities individually. From neutron diffraction data of antiferromagnetic  $\text{MnF}_2$  Nathans<sup>6</sup> obtained  $f_\sigma^{\text{Mn-F}} = 1.2\%$ . Because of

the small amount of spin density transferred into the fluorine  $2p_\sigma$  orbital, the covalency of the Mn-F bond was considered to be anomalously low.

Our value  $f_\sigma^{\text{Mn-F}} = 3.8\%$  resolves this anomaly. Generally spin densities determined by neutron diffraction seem to be too low. This is supported by recent ENDOR measurements<sup>7</sup> on  $\text{Mg}(\text{Ni})^{17}\text{O}$  and PAC data<sup>8</sup> of  $^{111}\text{mCd}$  in antiferromagnetic  $\text{NiO}$ ,  $\text{CoO}$ , and  $\text{MnO}$ .

#### Footnote and References

\* Condensed from LBL-1673.

1. H. H. Rinneberg and D. A. Shirley, Phys. Rev. Letters 30, 1147 (1973).
2. R. G. Shulman and V. Jaccarino, Phys. Rev. 108, 1219 (1957).
3. R. G. Shulman and S. Sugano, Phys. Rev. 130, 506 (1963).
4. J. Owen and D. R. Taylor, J. Appl. Phys. 39, 791 (1968).
5. J. H. M. Thornley, C. G. Windsor, and J. Owen, Proc. Roy. Soc. A 284, 252 (1965).
6. R. Nathans, S. J. Pickert, and P. J. Brown, J. Appl. Phys. 34, 1182 (1963).
7. P. Freund et al., to be published.
8. H. H. Rinneberg and D. A. Shirley, to be published.

### III. Physical, Inorganic, and Analytical Chemistry

*X-Ray Crystallography*

*Physical and Inorganic Chemistry*

*Radiation Chemistry*

*Applications of Activation Analysis*

*Environmental*

THE CRYSTAL AND MOLECULAR STRUCTURE OF  
TRIPHENYLMETHYLPHOSPHONIUM 1, 1, 1-TRICARBONYL-4,  
6-DICARBA-1-MANGANA-CLOSO-NONABORATE(1-)\*

F. J. Hollander, D. H. Templeton, and A. Zalkin

The  $(B_6C_2H_8)Mn(CO)_3^-$  ion was synthesized by Hawthorne and Pitts,<sup>1</sup> and a tentative structure was assigned to it on the basis of IR and NMR spectroscopic data.<sup>2</sup> This study of the triphenylmethylphosphonium (TPMP) salt, undertaken to verify the structure by x-ray crystallographic means, confirms that it is triphenylmethylphosphonium 1, 1, 1-tricarbonyl-4, 6-dicarbonyl-1-mangana-closo-nonaborate(1-).<sup>3</sup>

Clear, orange-red, needle-like crystals of the compound were supplied to us by M. Frederick Hawthorne as prepared by A. Denise Pitts. Optical extinction between crossed polarizers was very sharp. The space group is  $P\bar{1}$  with cell dimensions  $a = 11.216(5) \text{ \AA}$ ,  $b = 11.285(4) \text{ \AA}$ ,  $c = 11.464(5) \text{ \AA}$ ,  $\alpha = 105.79(1)^\circ$ ,  $\beta = 104.46(1)^\circ$ ,  $\gamma = 98.04(1)^\circ$ . The density measured by flotation in a mixture of n-hexane and carbon tetrachloride was  $1.25 \text{ g/cm}^3$  compared to  $1.29 \text{ g/cm}^3$  calculated for  $Z = 2$ . The measured density is low due to difficulties in getting the solution to wet the crystals. Intensity data were collected with a manual diffractometer using Zr-filtered MoK $\alpha$  radiation using a stationary-crystal stationary-counter technique.

A three-dimensional Patterson synthesis yielded the position of the Mn atom, and the remainder of the non-hydrogen atoms were found by successive refinements and Fourier synthesis. The expected structure of the anion was recognized, and the atoms expected to be carbon were labeled as such. A difference Fourier map showed peaks at all the positions where hydrogen atoms were expected. All non-hydrogen atoms were then allowed to refine with anisotropic thermal parameters, and the individual isotropic thermal parameters of the hydrogens were allowed to refine. The final cycle of full-matrix least squares brought the shifts of all parameters to less than 2% of their calculated standard deviations. The final  $R_1$  was 0.042 for 2862 reflections, and the weighted  $R_2$  was also 0.042.

The compound consists of discrete cations and anions. The triphenylmethylphosphonium cation exhibits a pseudo-threefold axis of symmetry along the P-C(3) bond, the phenyl groups being tilted so as to form a propeller (Fig. 1). The environment of the phosphorus is nearly regular tetrahedral. The hydrogens

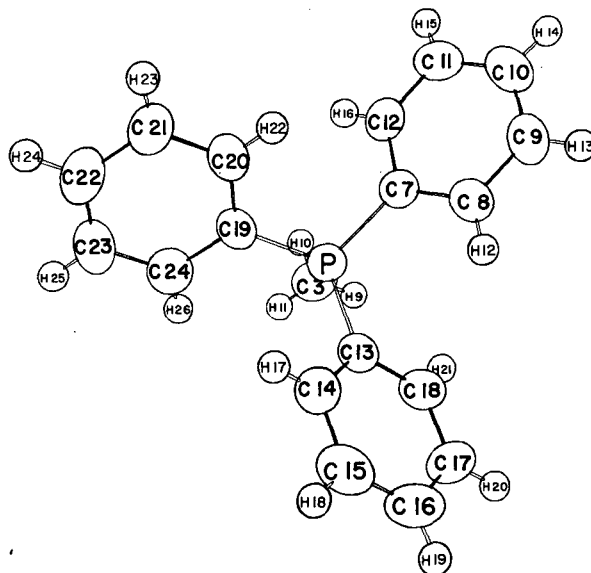


Fig. 1. Conformation and labeling of the cation. Perspective view roughly down the pseudo-threefold axis. Thermal ellipsoids have been scaled to enclose 50% probability. Hydrogen atoms have been given an artificial isotropic thermal parameter of  $2.0 \text{ \AA}^2$ . (XBL 724-666)

on the methyl group are staggered with respect to the carbons on the phosphorus as expected. The phenyl groups are very closely planar, with each atom less than one standard deviation from the mean plane. Two of the phenyls have the P-C bond bent slightly but significantly out of the plane, with P out of the plane by  $0.025 \text{ \AA}$ . All C-H distances are normal for X-ray crystallographic studies. The average C-C bond length in the phenyl groups is  $1.374(2) \text{ \AA}$ , uncorrected for thermal motion. The results from this study are consistent with the results of Fritchie<sup>4</sup> on another TPMP salt. The average values of chemically equivalent bonds are within the sum of their standard deviations of each other. The primary difference between the TPMP ions in the two studies is that in this study the ion assumes the expected propeller configuration, whereas in Fritchie's study packing forces distort it considerably.

The  $(B_6C_2H_8)Mn(CO)_3$  anion results in this work confirm the structure proposed for both the  $B_6C_2H_8^{2-}$  ligand and for the entire anion.<sup>1,2</sup> The anion possesses an almost exact non-crystallographic mirror plane running through the Mn, B(3) and B(6) (Fig. 2). Variations from mirror symmetry for the carborane cage atoms, including hydrogens, are all less than twice the standard deviations of their positions. The carbons of the carbonyl groups also conform well to the mirror symmetry, but the oxygen atoms deviate from this

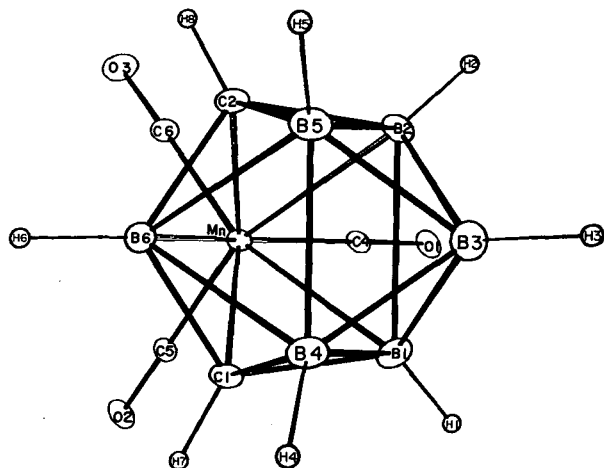


Fig. 2. Conformation and labeling of the anion. Perspective view parallel to the non-crystallographic mirror plane. (XBL 724-661)

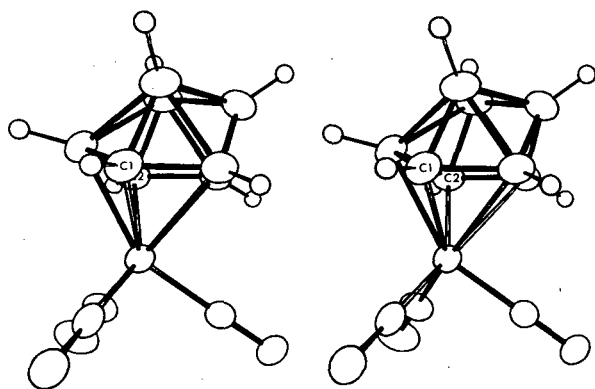


Fig. 3. Stereoscopic view of the anion. The view direction is approximately perpendicular to the non-crystallographic mirror plane. Temperature ellipsoids have been scaled to enclose 20% probability. Hydrogens have been given artificial thermal parameters of  $2.0 \text{ \AA}^2$ . (XBL 724-664)

symmetry by as much as five standard deviations. In addition, the carbonyl groups are very closely radial about the manganese. These observations confirm Hawthorne's spectroscopic conclusions,<sup>2</sup> and the slight deviations of the oxygens can undoubtedly be attributed to crystal packing forces.

The packing of the cations and the anions can be seen in Fig. 4. In a crude approximation it may be described as CsCl-type packing, but this approximation would be more accurate if the *b* axis were shorter and *a* and *c* were longer.

We thank Professor Hawthorne and Dr. Pitts for the crystals used in this research.

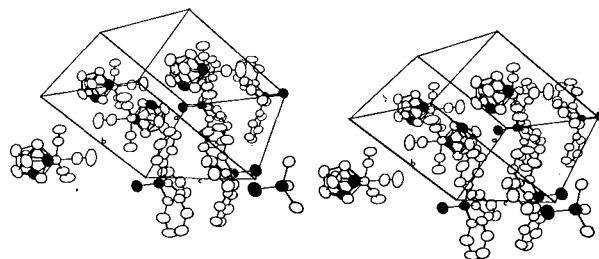


Fig. 4. Stereoscopic view of the contents of the unit cell. The methyl carbons and the carbons in the anion are solid black. The phosphorus atoms have been stippled. Labeled axes are positive from the origin. Hydrogen atoms and the cations in the *b* direction have been omitted for clarity, as have the phenyl groups of the foremost cation. (XBL 724-723)

#### Footnotes and References

\* Condensed from LBL-1661. Published in *Inorg. Chem.* **12**, 2262 (1973).

1. M. F. Hawthorne and A. D. Pitts, *J. Am. Chem. Soc.* **89**, 7115 (1967).
2. A. D. George and M. F. Hawthorne, *Inorg. Chem.* **8**, 1801 (1969).
3. Named according to Fig. 14, *Inorg. Chem.* **7**, 1945 (1968).
4. C. J. Fritchie, Jr., *Acta Crystallogr.* **20**, 107 (1966).



CRYSTAL STRUCTURE OF  $[\text{XeF}_5^+][\text{AsF}_6^-]^*$ 

N. Bartlett, F. J. Hollander,<sup>†</sup>  
D. H. Templeton, and A. Zalkin

Complexes of  $\text{XeF}_6$  with  $\text{F}^-$  acceptors were discovered in three separate laboratories.<sup>1-3</sup> The 1:1 complexes with  $\text{AsF}_5$  and  $\text{BF}_3$  were formulated on the basis of infrared evidence, by Bartlett et al.,<sup>2</sup> as  $\text{XeF}_5^+$  salts. Although the crystal structure determination of  $[\text{XeF}_5^+][\text{PtF}_6^-]$  (Ref. 4) and its relative  $[\text{XeF}_5^+][\text{RuF}_6^-]$  (Ref. 5) gave firm structural support for the vibrational justification<sup>6</sup> for  $[\text{XeF}_5^+][\text{AsF}_6^-]$ , it was clear from the powder data that this salt was not isostructural with its transition metal analogues  $\text{XeF}_5^+\text{MF}_6^-$  (M = Ru, Rh, Os, Ir, Pt), in which series an isostructural relationship was assured.<sup>5</sup> It is usual for crystal structures of  $\text{AsF}_6^-$  salts to differ from those adopted by Sb and transition metal analogues.<sup>7</sup> It appeared probable that the coordination of the  $\text{XeF}_5^+$  species in  $\text{XeF}_5^+\text{AsF}_6^-$  would differ from that observed in  $\text{XeF}_5^+\text{PtF}_6^-$ . Moreover, although the vibrational data provided strong circumstantial evidence for the salt formulation, firmer evidence was desirable. The formulation of the  $\text{XeF}_6 \cdot \text{AsF}_5$  complex became a matter of greater interest when Bartlett and Sladky demonstrated<sup>8</sup> that  $\text{XeF}_4$  was a poorer fluoride donor than  $\text{XeF}_2$  and would not form a complex with  $\text{AsF}_5$  under ordinary temperatures and pressures. The 1:1  $\text{XeF}_6 \cdot \text{AsF}_5$  complex was prepared and single crystals were grown as described by Bartlett and Wechsberg.<sup>6</sup> The selected crystal of  $\text{F}_{11}\text{AsXe}$  was a plate of approximate dimensions  $0.28 \times 0.16 \times 0.04$  mm. The crystal has monoclinic symmetry and the systematic absences indicate uniquely the space group  $\text{P}2_1/\text{c}$  with  $a = 5.886(3)$ ,  $b = 16.564(10)$ ,  $c = 8.051(4)$  Å,  $\beta = 91.564(35)^\circ$ ,  $V = 784.6$  Å<sup>3</sup>,  $Z = 4$ ,  $d_c = 3.51$  g/cm<sup>3</sup>. Diffraction data were collected at room temperature on a four-circle automatic diffractometer using a  $\theta$ - $2\theta$  scan technique with Mo K $\alpha$  radiation, monochromatized with a graphite monochromator. A total of 1382 independent data were recorded of which 925 had  $I > \sigma(I)$ .

The three-dimensional Patterson function revealed the positions of the two heavy atoms in the asymmetric unit, and a subsequent electron density map revealed 11 additional major peaks which were designated as fluorine. With all atoms anisotropic the final refinement yielded a conventional R factor of 0.12 for 925 reflections; including zero weighted reflections,  $R = 0.14$ . The weighted R factor ( $R_2$ ) = 0.13. The standard deviation of an observation of unit weight was 1.57.

The atomic arrangement is compatible with the salt formulation  $\text{XeF}_5^+\text{AsF}_6^-$ . The atomic arrangement revealed by the structure shows  $\text{XeF}_5$  and  $\text{AsF}_6$  groups which make close contacts to define the  $(\text{XeF}_5\text{AsF}_6)_2$  rings shown in Fig. 1. These rings have a form which is almost identical to that of the rings in the  $(\text{XeF}_5)_2\text{PdF}_6$  structure.<sup>9</sup> In this unit each  $\text{XeF}_5$  group makes bridging contacts to two  $\text{AsF}_6$  groups, via one F-ligand on one  $\text{AsF}_6$  group and two F-ligands of the other. Three F-ligands (in cis relationship to one another) of each  $\text{AsF}_6$  group each have bridging interaction with xenon.

The  $\text{XeF}_5$  group has essentially the same shape and size as the  $\text{XeF}_5$  group in  $\text{XeF}_5\text{PtF}_6$  (Ref. 4),  $\text{XeF}_5\text{RuF}_6$  (Ref. 5),  $(\text{XeF}_5)_2\text{PdF}_6$  (Ref. 9) and in crystalline  $\text{XeF}_6$  (Ref. 10) and as in those cases is consistent with designation as  $\text{XeF}_5^+$  (see Ref. 9). The  $\text{AsF}_6^-$ , is nevertheless close enough in size and shape to be so designated. The average As-F distance is

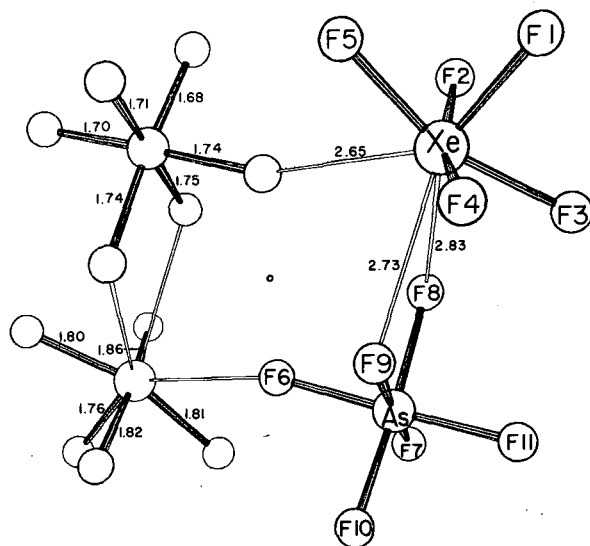


Fig. 1. Configuration and bond distances for  $\text{XeF}_5^+\text{AsF}_6^-$ . Perspective view roughly perpendicular to the  $bc$  plane showing the cation-anion clusters about the center of symmetry at  $1/2, 0, 1/2$ . Estimated standard deviation for all bond lengths shown is 0.02 Å.

(XBL 734-665)

1.72 Å with an average deviation of 0.03 Å. The As-F distance, corrected for libration, is 1.74 with an average deviation of 0.02.

This structure confirms that xenon hexafluoride donates fluoride ion to generate the  $\text{AsF}_6^-$  ion. The discovery that  $\text{XeF}_2$  and  $\text{XeF}_6$  each form complexes with  $\text{AsF}_5$ , but that  $\text{XeF}_4$  does not, was made by Bartlett and Sladky,<sup>8</sup> and they exploited this finding to effect a chemical purification of  $\text{XeF}_4$ . Evidently  $\text{XeF}_4$ , as Bartlett and Sladky had supposed, must be an inferior  $\text{F}^-$  donor compared with either  $\text{XeF}_2$  or  $\text{XeF}_6$ . Only  $\text{SbF}_5$  (which is the best  $\text{F}^-$  acceptor) forms  $\text{XeF}_3^+$ <sup>11,12</sup> with  $\text{XeF}_4$ .

The structure of  $\text{XeF}_5^+\text{AsF}_6^-$  (Figs. 1 and 2) is not like those of  $\text{XeF}_5^+\text{RuF}_6^-$  (Ref. 5) and  $\text{XeF}_5^+\text{PtF}_6^-$  (Ref. 4) in that each  $\text{XeF}_5^+$  is coordinated to 4 F ligands of four separate anions. Nevertheless, as has been discussed previously,<sup>9</sup> the  $\text{XeF}_5^+$  size and shape is not significantly different from that seen in the other  $\text{XeF}_5^+$  salts (including  $\text{XeF}_6$  itself). Moreover, the  $\text{XeF}_5^+$  coordination in  $(\text{XeF}_5)_2^+\text{PdF}_6^{2-}$  (Ref. 9) is almost exactly the same as that seen here.

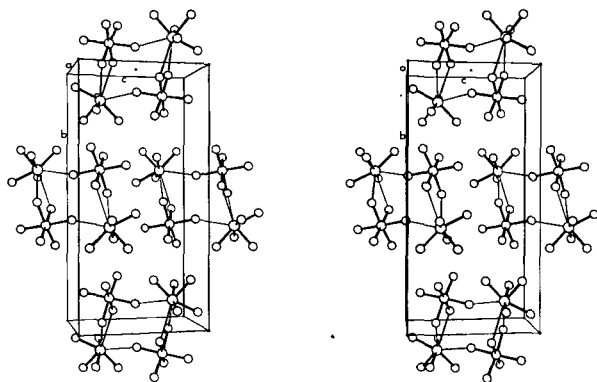


Fig. 2. Stereoscopic view of the  $\text{XeF}_5^+\text{AsF}_6^-$  structure. (XBL 724-724)

### Footnotes and References

\* Condensed from LBL-1170; to be published in *Inorganic Chemistry*, 1974.

† Present address: University of Iowa, Iowa City, Iowa.

1. G. L. Gard and G. H. Cady, *Inorg. Chem.* **3**, 1745 (1964).
2. N. Bartlett, S. Beaton, and N. K. Jha, Abstracts, 148th National Meeting of the American Chemical Society, Chicago, Ill., Sept. 1964, No. K3.
3. H. Selig, *Science* **144**, 537 (1964)
4. (a) N. Bartlett, F. Einstein, D. F. Stewart, and J. Trotter, *Chem. Commun.* (1960) 550 and (b) *J. Chem. Soc. A* (1967) (1190).
5. N. Bartlett, M. Gennis, D. D. Gibler, B. K. Morrell, and A. Zalkin, *Inorg. Chem.* **12**, 1717 (1973).
6. N. Bartlett and M. Wechsberg, *Z. anorg. u. allgem. Chemie* **385**, 5 (1971).
7. D. Babel, *Structure and Bonding* **3**, 1 (1967).
8. N. Bartlett and F. O. Sladky, *J. Amer. Chem. Soc.* **90**, 5316 (1968).
9. K. Leary, D. H. Templeton, A. Zalkin, and N. Bartlett, *Inorg. Chem.* **12**, 1726 (1973).
10. R. D. Burbank and G. R. Jones, *Science* **168**, 248 (1970).
11. R. J. Gillespie, B. Landa, and G. J. Schrobilgen, *Chem. Commun.* (1971) 1543.
12. D. E. McKee, C. J. Adams, A. Zalkin, and N. Bartlett, *Chem. Commun.* (1973) 26 and D. E. McKee, A. Zalkin, and N. Bartlett, *Inorg. Chem.* **12**, 1713 (1973).

CRYSTAL STRUCTURE OF  $[\text{XeF}_5^+]_2 [\text{PdF}_6^{2-}]^*$ 

K. Leary, D. H. Templeton, A. Zalkin, and N. Bartlett

In the course of experiments<sup>1</sup> aimed at a more convenient synthesis of palladium tetrafluoride<sup>2</sup> we obtained the  $\text{XeF}_6$  adducts of  $\text{PdF}_4$ ,  $2\text{XeF}_6 \cdot \text{PdF}_4$  and  $4\text{XeF}_6 \cdot \text{PdF}_4$ . These stoichiometries are similar to those reported previously by Pullen and Cady<sup>3</sup> for the  $\text{XeF}_6$  adducts of the germanium and tin tetrafluorides. Although Raman data<sup>1</sup> indicated that the  $\text{PdF}_4$  adducts were  $[\text{XeF}_5^+]_2 [\text{PdF}_6^{2-}]$  and  $[\text{Xe}_2\text{F}_{11}^+]_2 [\text{PdF}_6^{2-}]$ , respectively, full structural investigations were desirable. Such ionic formulations are consistent with  $\text{XeF}_6$  being a good base.<sup>4</sup> Comparison of the geometry of the cation in a doubly charged anion environment with that of the cation in singly charged anion salts<sup>4-6</sup> was also of interest. Suitable single crystals of the 2:1 adduct for high-quality x-ray structural investigation proved to be readily preparable. The structure has been determined and is reported in this paper.

$2\text{XeF}_6 \cdot \text{PdF}_4$  was prepared as described in a forthcoming paper.<sup>1</sup> Suitable crystalline samples were obtained by heating the compound in a Monel bomb to 400° under fluorine pressure (1000 psi). The bomb was cooled slowly to room temperature (~20°/h). Yellow, needle-shaped crystals were found adhering to the walls of the bomb. The crystal chosen for data collection was a small yellow needle. The crystals are orthorhombic, with  $a = 9.346(6)$ ,  $b = 12.786(7)$ ,  $c = 9.397(6)$  Å,  $V = 1122.9$  Å<sup>3</sup>,  $Z = 4$ , and  $d_c = 3.91$  g/cm<sup>3</sup>. The unit cell volume satisfies Zachariasen's criterion<sup>7</sup> for close-packed fluoride lattices, the effective volume per fluorine atom being 17.6 Å<sup>3</sup>. The space group is  $\text{Pca}2_1$ .

Diffraction data were collected at room temperature on a Picker automatic four-circle diffractometer using Mo K $\alpha$  radiation. A three-dimensional Patterson synthesis revealed the positions of two of the three heavy atoms. Full-matrix least-squares and a subsequent Fourier synthesis yielded the positions of the third heavy atom and several of the fluorine atoms. The refinement proceeded routinely down to  $R = 0.075$ , but the structure settled into a false minimum. After much experimentation involving location of atoms across symmetry elements (and pseudosymmetry elements), to generate a chemically acceptable arrangement, the  $R$  value dropped to 0.060. Subsequent refinement yielded an  $R$  value of 0.020. At this point the data were reordered to satisfy the noncentric symmetry and to take advantage of anomalous

dispersion. Two polarities must be considered. Least-squares refinement yielded  $R = 0.0260$  (including zero-weight data),  $R = 0.0241$  (excluding zero-weight data), and  $R_w = 0.0274$  for the polarity with mostly negative  $z$  coordinates. For the polarity with mostly positive  $z$  coordinates,  $R = 0.0256$  (including zero-weight data),  $R = 0.0237$  (excluding zero-weight data), and  $R_w = 0.0267$ . The magnitudes of the  $z$  parameters of the two forms did not differ by more than one standard deviation. We describe here the arbitrarily chosen structure with the mostly positive  $z$  atomic parameters. A final difference Fourier showed that the largest residual electron density was  $-1.7$  e/Å<sup>3</sup>.

This analysis was hampered by several special problems: the structure deviates very little from the symmetry of another space group,  $\text{Pca}$ ; the heavy atoms contribute little or nothing to the phasing of many of the reflections; the absolute polarity is not easy to establish. These problems are discussed in more detail in the full paper.

The asymmetric structural unit contains two crystallographically distinct  $\text{XeF}_5$  groups and a  $\text{PdF}_6$  group. The structural unit is illustrated in Figs. 1 and 2.

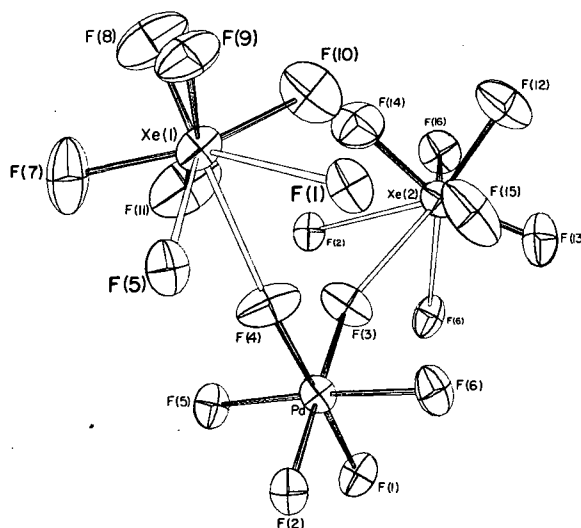


Fig. 1. The formula unit in  $[\text{XeF}_5^+]_2 [\text{PdF}_6^{2-}]$ .  
(XBL 724-6188)

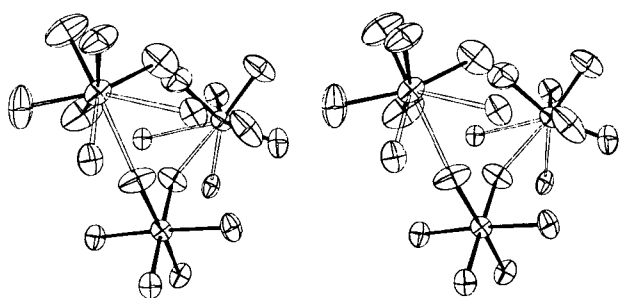


Fig. 2. Stereogram of the formula unit in  $[\text{XeF}_5^+]_2[\text{PdF}_6^{2-}]$ . (XBL 742-355)

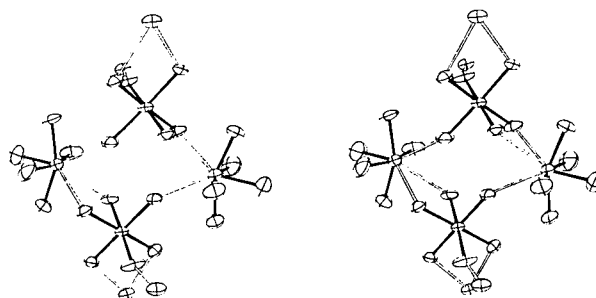


Fig. 4. Stereogram of the  $[\text{XeF}_5^+][\text{AsF}_6^-]$ -like rings in  $[\text{XeF}_5^+]_2[\text{PdF}_6^{2-}]$ . (XBL 742-356)

Each Xe atom of each  $\text{XeF}_5$  group makes one short contact with one  $\text{PdF}_6$  group [i.e.,  $\text{Xe}(2)-\text{F}(3)$ ,  $\text{Xe}(1)-\text{F}(4)$ ] and two somewhat longer contacts to a second  $\text{PdF}_6$  group. These Xe...F contacts link  $\text{XeF}_5$  groups into "rings" containing two species of each kind as shown in Figs. 3-5. These "rings" are linked by the further involvement of the  $\text{PdF}_6$  groups in adjoining "rings." There is a striking resemblance of the four-membered "ring" in this structure to that previously observed in  $[\text{XeF}_5^+][\text{AsF}_6^-]$ .<sup>6</sup>

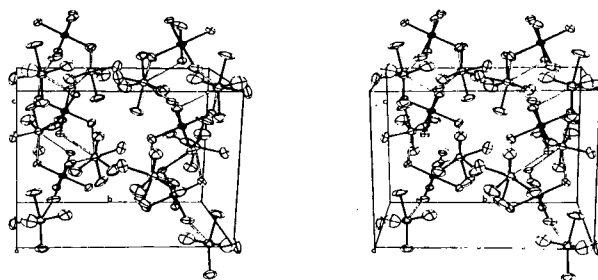


Fig. 5. Stereogram of the  $[\text{XeF}_5^+]_2[\text{PdF}_6^{2-}]$  unit cell, showing the packing of linked  $[\text{XeF}_5^+][\text{AsF}_6^-]$ -like rings. (XBL 742-357)

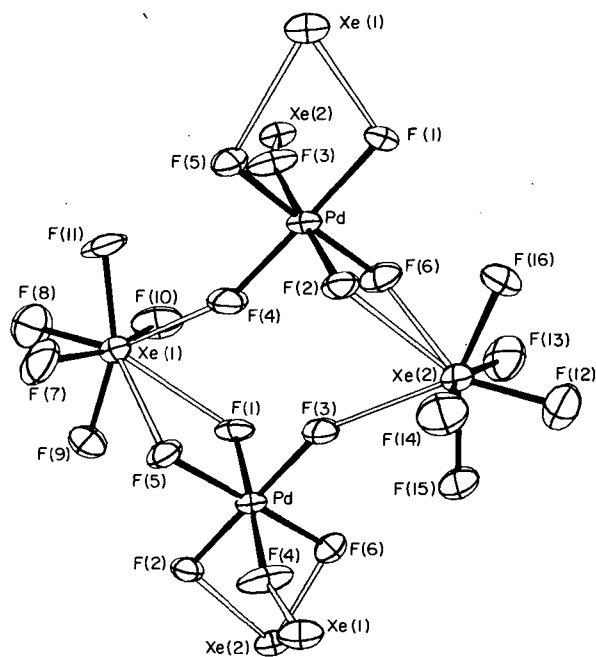


Fig. 3. The  $[\text{XeF}_5^+][\text{AsF}_6^-]$ -like rings in  $[\text{XeF}_5^+]_2[\text{PdF}_6^{2-}]$ . (XBL 725-6264)

The structure of  $[\text{XeF}_5]_2[\text{PdF}_6]$  is of most interest at this time for the geometry of the cation has previously been established by x-ray single-crystal analysis in the salts  $[\text{XeF}_5^+][\text{MF}_6^-]$  ( $M = \text{Pt},^5 \text{Ru},^5 \text{As}^6$ ) and crystalline  $\text{XeF}_6$  itself has been formulated<sup>8</sup> as  $[\text{XeF}_5^+]\text{F}^-$ . There are barely any significant differences between  $\text{XeF}_5^+$  species in different lattices, including  $\text{XeF}_5^+$  in crystalline  $\text{XeF}_6$ . The common geometry of the  $\text{XeF}_5$  moiety in all of the quoted structures and its close similarity<sup>5,9</sup> to the geometry of the neutral molecule  $\text{IF}_5$  provide compelling evidence for the cation  $\text{XeF}_5^+$ .

The coordination behavior of the  $\text{XeF}_5^+$  species not only supports the discrete nature of the species but also provides evidence of steric activity of the Xe(VI) nonbonding valence-electron pair. Figures 1-5 show that each  $\text{XeF}_5$  species in  $[\text{XeF}_5]_2[\text{PdF}_6]$  is coordinated to three F ligands of two  $\text{PdF}_6$  groups such that the three F ligands lie approximately on a conical surface, the axis of which is coincident with the symmetry axis of the  $\text{XeF}_5$ .

But if we describe  $\text{XeF}_5^+$  as a pseudooctahedral species in which the nonbonding valence-electron pair occupies the Xe coordination site trans to the axial bond, the position of the F ligands "on the conical surface" is seen to be appropriate; since then the Xe valence "pair" is avoided, and the positive charge of the cation (which we can anticipate will be centered essentially at the xenon atom) is least shielded.

#### Footnote and References

\*Condensed from LBL-1171, published in *Inorg. Chem.* **12**, 1726 (1973).

1. K. Leary and N. Bartlett, to be submitted for publication.
2. N. Bartlett and P. R. Rao, *Proc. Chem. Soc., London*, 393 (1964).
3. K. E. Pullen and G. H. Cady, *Inorg. Chem.* **5**, 2077 (1966); **6**, 1300 (1967).
4. F. O. Sladky and N. Bartlett, *J. Amer. Chem. Soc.* **90**, 5316 (1968).
5. (a) N. Bartlett, F. Einstein, D. F. Stewart, and J. Trotter, *J. Chem. Soc. A*, 1190 (1967); (b) N. Bartlett, M. Gennis, D. D. Gibler, B. K. Morrell, and A. Zalkin, *Inorg. Chem.* **12**, 1717 (1973).
6. N. Bartlett, B. DeBoer, F. Hollander, F. O. Sladky, D. Templeton, and A. Zalkin, to be submitted for publication.
7. W. H. Zachariasen, *J. Amer. Chem. Soc.* **70**, 2147 (1948).
8. R. D. Burbank and G. R. Jones, *Science* **168**, 248 (1970).
9. G. R. Jones, R. D. Burbank, and N. Bartlett, *Inorg. Chem.* **9**, 2264 (1970).

### STRUCTURE OF NdSBr AND ISOSTRUCTURAL RARE EARTH SULFO BROMIDES\*

N. Savigny,<sup>†</sup> A. Zalkin,  
C. Adolphe,<sup>†</sup> and D. H. Templeton

The compound NdSBr was first prepared in the laboratory of inorganic chemistry of Faculté de Pharmacie de Paris<sup>1</sup> as part of a group of five isostructural monoclinic sulfobromides: PrSBr( $\beta$ ), NdSBr, SmSBr, GdSBr, and TbSBr.<sup>2</sup> Diffraction patterns of a crystal (which was later recognized to be twinned) were interpreted on the basis of an incorrect unit cell, and the structure determination encountered difficulties.

At Berkeley the twinning was discovered, and dimensions for the monoclinic unit cells (space group  $P2_1/b$ ) were calculated:

	a (Å)	b (Å)	c (Å)	$\gamma$ (deg)
PrSBr( $\beta$ )	6.98	6.93	7.09	99.30
NdSBr	6.94	6.91	7.05	99.28
SmSBr	6.86	6.86	7.01	99.32
GdSBr	6.80	6.81	6.96	99.23
TbSBr	6.75	6.77	6.89	99.33

Intensity data were collected on a Picker FACS-1 diffractometer using Mo K $\alpha$  radiation. The geometry of the twinning caused superposition of reflections from both individuals if  $k = 3n$ . We measured 344 independent reflections with  $k \neq 3n$  to avoid the effects of this superposition. These data were quite sufficient to determine the 9 coordinates and 18 thermal parameters which describe the structural model. The coordinates are:

	x	y	z
Nd	0.3177 (1)	0.2106 (1)	0.4647 (1)
S	0.5543 (7)	0.0083 (7)	0.2396 (6)
Br	0.0847 (3)	0.2872 (3)	0.1160 (3)

Neodymium is coordinated to seven atoms. It is surrounded on one side by four sulphur atoms, on the other side by three bromine atoms. The average Nd - S distance is 2.80 Å.

The structure of NdSBr is closely related to that of the monoclinic form of  $\text{EuI}_2$ .<sup>3</sup> We find in it the same polyhedron with seven apices around the rare earth atom and the same kind of layers. There is also a great analogy to the structure of the orthorhombic CeSI type<sup>4</sup> which exists for several sulfobromides of lighter rare earth elements. It contains similar layers, but the manner of stacking is different.

#### Footnotes and References

\* Condensed from Acta Crystallogr. B29, 1532 (1973).

† Department of Physics, Faculté de Pharmacie, Paris.

1. C. Dagron, J. Etienne, and P. Laruelle, Second International Conference on Solid Compounds of Transition Elements, Euschede (Pays-Bas), June 1967.
2. C. Dagron and F. Thevet, C.R. Acad. Sci. Fr. 271, Series C, 677 (1970).
3. H. Bärnighausen and N. Schultz, Acta Crystallogr. B25, 1104 (1969).
4. J. Etienne, Bull. Soc. Fr. Mineral. Cristallogr. 92, 134 (1969).

### CRYSTAL STRUCTURES OF THE FLUOSILICATE HEXAHYDRATES OF COBALT, NICKEL AND ZINC\*

S. Ray,<sup>†</sup> A. Zalkin, and D. H. Templeton

Fluosilicate hexahydrates of several bivalent metals have been considered to be isomorphous with a large number of salts with the general formula  $\text{MG}_6\text{LR}_6$ , where M is a bivalent metal; G may be water or ammonia; L is a quadrivalent element like Si, Sn, Ti, or Zr; and R may be Cl, or CN. These crystals have a rhombohedrally-distorted CsCl-type packing and similar cell dimensions, except for possible doubling of axes.<sup>1-3</sup> Pauling<sup>4</sup> determined a structure in space group  $R\bar{3}$  for  $\text{NiSnCl}_6 \cdot 6\text{H}_2\text{O}$ , and this result has been widely regarded as typical for the entire series. The oxygen and chlorine atoms are arranged in nearly regular octahedra with identical orientations and dimensions, and this structure must be regarded as approximate at best. In a neutron-diffraction study of  $\text{FeSiF}_6 \cdot 6\text{H}_2\text{O}$ , Hamilton<sup>5</sup> deduced the space group to be  $R\bar{3}m$ . Disorder was postulated to explain this enhancement of symmetry because it gave better agreement with the data than did the alternative of twinning of crystals of  $R\bar{3}$  symmetry. The structure is a superposition of two components, each of symmetry  $R\bar{3}$ , related to each other by a mirror. The component structure resembles that determined by Pauling except for significant differences in the dimensions and orientations of the two kinds of octahedra.

A phase transition occurs near 230° K in  $\text{MnSiF}_6 \cdot 6\text{H}_2\text{O}$  (Ref. 6) and near 250° K in  $\text{CoSiF}_6 \cdot 6\text{H}_2\text{O}$  (Refs. 7 and 8). While studying these transitions we became interested in the room-temperature structures of this series of salts and learned that they are remarkably diverse in spite of the close isomorphism in the

sense of similar axial ratios. We have examined crystals of fluosilicate hexahydrates of Mg, Mn, Co, Ni, Cu, and Zn with the result that all are different from the Fe salt and only the Co, Ni, and Zn salts have the typical cell dimensions and space group. The Cu salt also exhibits space group  $R\bar{3}$  but with a four-times larger cell. The Mn compound has a primitive hexagonal cell rather than a rhombohedral one, a fact also reported by Kodera, Torii, and Osaki.<sup>9</sup> In our work at 23° C we observed crystals of the Mg salt to be of lower symmetry than trigonal, but twinned. Syoyami and Osaki<sup>10</sup> discovered a transition at about 25° in this salt, with space group  $R\bar{3}m$  above the transition. They determined the structure of the low-temperature form to be monoclinic, space group  $P2_1/c$ . The present paper describes the structures of the Co, Ni, and Zn salts; they differ significantly from the structure reported by Pauling<sup>4</sup> for  $\text{NiSnCl}_6 \cdot 6\text{H}_2\text{O}$ .

The salts  $\text{CoSiF}_6 \cdot 6\text{H}_2\text{O}$ ,  $\text{NiSiF}_6 \cdot 6\text{H}_2\text{O}$ , and  $\text{ZnSiF}_6 \cdot 6\text{H}_2\text{O}$  were prepared by dissolving, respectively, cobalt carbonate, nickel carbonate, and metallic zinc in fluosilicic acid and slowly evaporating the filtered solutions. Crystals were selected from crops recrystallized from aqueous solution by slow evaporation.

The Co crystal selected for study was a hexagonal (almost triangular) prism. Intensity data were collected with Zr-filtered Mo radiation and a card-controlled automatic diffractometer using the  $\theta$ - $2\theta$  scan technique. The measurements included 2666 reflections of which 721 were independent; 60 of these had

observed intensity less than the estimated standard deviation.

The Ni crystal was of rhombohedral shape. A computer-controlled four-circle diffractometer was used for the diffraction experiments with Cu K $\alpha$  radiation using the  $\theta$ - $2\theta$  scan technique. A total of 1873 reflections were measured, of which 298 were independent. Only 4 of these had intensity less than the standard deviation.

The Zn crystal was a regular hexagonal prism. Intensities were measured with Mo K $\alpha$  radiation of 726 independent reflections, of which 92 were less than the standard deviation.

The crystal data are as follows:

CoSiF $_6$ ·6H $_2$ O: reddish pink hexagonal prisms.

Hexagonal cell:  $a = 9.366(2)$ ,  $c = 9.730(4)$  Å,  $Z = 3$ .

Rhombohedral cell:  $a = 6.306(3)$  Å,  
 $\alpha = 95^\circ 55(4)'$ ,  $Z = 1$ .

Space group:  $R\bar{3}$ ;  $D_m = 2.07$ ,  $D_x = 2.08$   
g/cm $^3$ .

NiSiF $_6$ ·6H $_2$ O: apple green rhombohedra.

Hexagonal cell:  $a = 9.313(3)$ ,  $c = 9.623(2)$  Å,  $Z = 3$ .

Rhombohedral cell:  $a = 6.261(2)$  Å,  
 $\alpha = 96^\circ 6(5)'$ ,  $Z = 1$ .

Space group:  $R\bar{3}$ ;  $D_m = 2.12$ ,  $D_x = 2.13$   
g/cm $^3$ .

ZnSiF $_6$ ·6H $_2$ O: colorless hexagonal prisms.

Hexagonal cell:  $a = 9.363(3)$ ,  $c = 9.690(5)$  Å,  $Z = 3$ .

Rhombohedral cell:  $a = 6.297(3)$  Å,  
 $\alpha = 96^\circ 3(6)'$ ,  $Z = 1$ .

Space group:  $R\bar{3}$ ;  $D_m = 2.12$ ,  $D_x = 2.13$   
g/cm $^3$ .

The structure was determined in much the same way in each case. Atoms were assigned coordinates similar to those of one of the lower symmetry ( $R\bar{3}$ ) components of FeSiF $_6$ ·6H $_2$ O.<sup>5</sup> For the Co salt a Fourier synthesis of  $\Delta F$  showed two prominent but unequal peaks, one on each side of the assumed position of F. The only satisfactory explanation of this was the assumption of a disordered model. Fractional atoms, referred to as F(1) and F(2), were assigned to these two positions with occupation

factors adding to unity. A  $\Delta F$  map at this stage showed clearly the positions of the two hydrogen atoms. Introduction of these atoms with isotropic temperature factors and occupation factors for F(1)/F(2) = 0.43/0.57 yielded  $R = 0.033$  [excluding data where  $I < \sigma(I)$ ],  $R = 0.038$  (all data), and  $R_2 = 0.038$ .

In the case of NiSiF $_6$ ·6H $_2$ O with occupancy factors F(1)/F(2) = 0.33/0.67,  $R = 0.022$  (with or without the four zero-weighted data) and  $R_2 = 0.040$ .

In the refinement of ZnSiF $_6$ ·6H $_2$ O, the occupancy ratio was F(1)/F(2) = 0.33/0.67, and with this ratio  $R = 0.018$ , excluding reflections with  $I < \sigma(I)$ ,  $R = 0.023$  (all reflections), and  $R_2 = 0.021$ .

Except for minor numerical details the three salts have the same crystal structure. An unusual feature of this structure, for which we have no satisfactory explanation, is the disorder of F between two sites, unrelated by any symmetry element and with unequal occupancy factors. The distances between alternate sites are 0.71, 0.60, and 0.66 Å, respectively, in the Co, Ni, and Zn salts. We assume that all the F atoms in a particular SiF $_6$ <sup>2-</sup> ion are in the same type of site, because otherwise there would be unsatisfactory F-F distances. According to this model, the disorder involves two orientations of the fluosilicate ion about 30° apart with respect to rotation about the 3-fold axis.

The water molecules are nearly regular octahedra, as are the F atoms. These octahedra are packed according to a rhombohedrally distorted CsCl-type structure. The densest packing is in columns of alternate cations and anions along the 3-fold axis (Fig. 1). Three hydrogen bonds connect each pair of adjacent octahedra in a column, while one hydrogen bond connects an octahedron to each of its six neighboring octahedra in other columns. This topology of hydrogen bonding is the same for either F site and is also the same as that which Hamilton<sup>5</sup> deduced for each component of his structure. It would not exist in the Pauling<sup>4</sup> structure because in that arrangement each O would have two equidistant F neighbors in the same column (Fig. 2). This latter arrangement permits closer packing of spherical atoms, but provides too many acceptors for hydrogen bonds. Any rotation of one kind of octahedron relative to the other makes one neighbor closer than the other, with a rotation of 60° giving the maximum difference. In the FeSiF $_6$ ·6H $_2$ O structure the oxygen atoms are twisted about 40° from the Pauling<sup>4</sup> structure, in each component of the disorder model. In the present structures it is the fluorine atoms which are twisted, F(1) about 50° and F(2) about 20°.

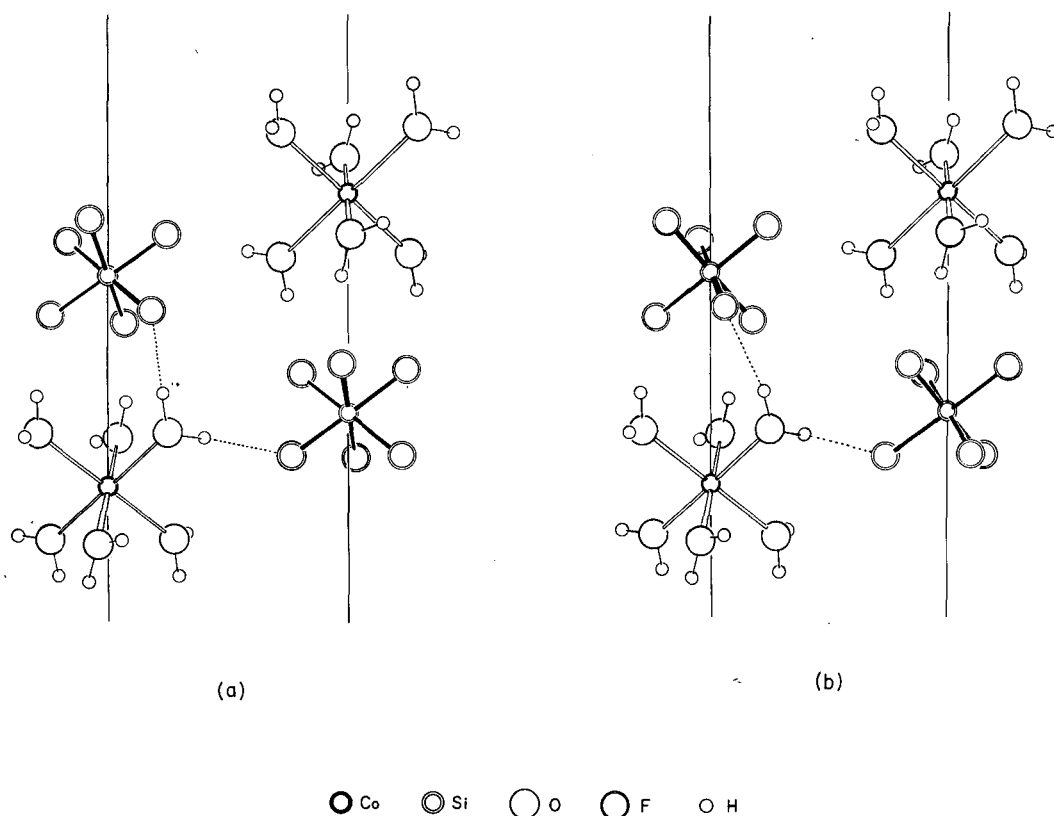


Fig. 1. Two neighboring columns in the structure of  $\text{CoSiF}_6 \cdot 6\text{H}_2\text{O}$ . Fluorine atoms are shown in (a) according to the F(1) positions and in (b) according to F(2). (XBL 696-619)

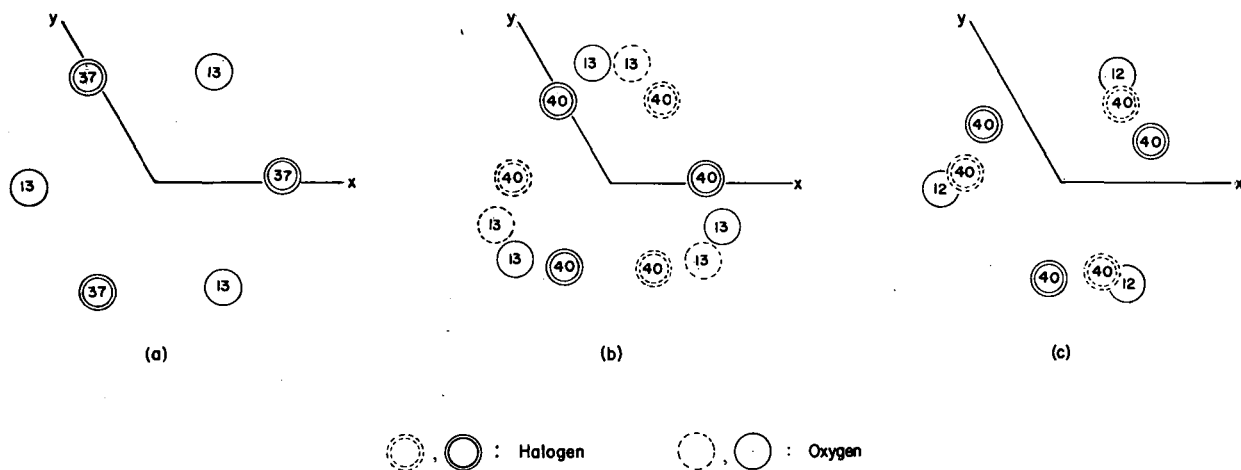


Fig. 2. Relative orientation of oxygen atoms on the top face of a water octahedron and halogen atoms on the bottom face of the adjacent octahedron in (a)  $\text{NiSnCl}_6 \cdot 6\text{H}_2\text{O}$  (Pauling<sup>2</sup>), (b)  $\text{FeSiF}_6 \cdot 6\text{H}_2\text{O}$  (Hamilton<sup>5</sup>, and (c)  $\text{CoSiF}_6 \cdot 6\text{H}_2\text{O}$  (this study). The numbers indicate values of the z coordinates ( $\times 100$ ), and broken circles indicate the alternate sites according to the disorder models. (XBL 704-878)



Footnotes and References

\* Condensed from LBL-1932; published in Acta Crystallogr. B29, 2741-2747 (1973).

† Present address: Dept. of Magnetism, Indian Association for the Cultivation of Science, Calcutta-32, India.

1. O. Hassel, Z. Phys. Chem. 126, 118-126 (1927).
2. O. Hassel, Z. Krist. 79, 531-532 (1931).
3. O. Hassel and J. Richter-Salvesen, Z. Phys. Chem. 128, 345-361 (1927).
4. L. Pauling, Z. Kristallogr. 72, 482-492 (1930).
5. W. C. Hamilton, Acta Crystallogr. 15, 353-360 (1962).
6. I. Tsujikawa and L. Couture, J. Phys. Radium 16, 430-431 (1955).
7. S. Ray, Indian J. Phys. 38, 176-177 (1964).
8. M. Majumdar and S. K. Datta, J. Chem. Phys. 42, 418-426 (1965).
9. E. Koderá, A. Torii, and K. Osaki, J. Phys. Soc. Japan 32, p.863 (1972).
10. S. Syoyama and K. Osaki, Acta Crystallogr. B28, 2626-2627 (1972).

**CRYSTAL STRUCTURE OF COPPER FLUOSILICATE HEXAHYDRATE\***

S. Ray,<sup>†</sup> A. Zalkin, and D. H. Templeton

In a previous communication<sup>1</sup> we mentioned the diverse structures which exist for the fluosilicate hexahydrates of divalent metals, which earlier had been believed to be like the structures determined by Pauling<sup>2</sup> for  $\text{NiSnCl}_6 \cdot 6\text{H}_2\text{O}$ . In the present paper we describe the structure of  $\text{CuSiF}_6 \cdot 6\text{H}_2\text{O}$ , which is significantly different from all the others.

Copper fluosilicate was prepared by dissolving metallic copper in fluosilicate acid. On slow evaporation at room temperature ( $\sim 23^\circ\text{C}$ ), deep blue crystals of the hexahydrate appeared, which were recrystallized from aqueous solution. The crystals obtained were susceptible to rapid efflorescence on exposure to the atmosphere (relative humidity  $\sim 50\%$ ), and had to be sealed in quartz capillaries for the diffraction experiment. Intensity data were collected with an automatic diffractometer and a  $\theta$ - $2\theta$  scan. A total of 1868 data was collected, of which 592 were independent; 235 of these had intensity less than the standard deviation, and were given zero weight in the least-squares refinement. The crystal data are as follows:

Hexagonal cell constants:

$$a = 18.180 \pm 0.002 \text{ \AA}, \quad c = 9.857 \pm 0.002 \text{ \AA}.$$

Rhombohedral cell constants calculated from the above:

$$a = 10.998 \pm 0.002 \text{ \AA}, \quad \alpha = 111^\circ 29' \pm 3'.$$

Four formula units per rhombohedral cell.

Space group:  $R\bar{3}$ .

$$D_m = 2.207 \text{ g/cm}^3, \quad D_x = 2.215 \text{ g/cm}^3.$$

It was assumed that, as in other hexahydrated fluosilicates, this structure consists of columns, extending in the  $c$  direction, built up of alternating  $\text{Cu}(\text{H}_2\text{O})_6$  and  $\text{SiF}_6$  octahedra. But in this case the neighboring columns are not identical, and the cell dimensions are doubled in the plane normal to the 3-fold axis. Accordingly the Cu and Si atoms were given special positions in the hexagonal cell. Four independent atoms each of O and F were assigned general positions. Cu(1), with site symmetry  $\bar{3}$ , was surrounded by six equivalent O(1); each of the Cu(2), with site symmetry  $\bar{1}$ , was surrounded by O(2), O(3), O(4), and their centrosymmetric equivalents related by inversion through the position of the particular Cu(2). Similar labeling was adopted for Si and F. A Patterson map indicated that while the oxygen octahedra surrounding Cu(1) and Cu(2) had the same orientation, there were two possible orientations for the corresponding  $\text{SiF}_6$  octahedra. After some initial setback in the matter of choice, all the O and F atoms were assigned satisfactory positions. With the hydrogen atoms held fixed in their calculated positions, varying only their common isotropic thermal parameter, refinement reduced  $R$  to 0.040 (0.077 including zero-weighted data),  $R_2$  to 0.043, and the goodness of fit to 1.12.

It is interesting to compare the present structure with that of  $\text{CoSiF}_6 \cdot 6\text{H}_2\text{O}$ , as described in our previous communication.<sup>1</sup> The basic features in both the cases are the columns of alternating octahedra. In the cobalt compound we have two disordered positions unequally occupied by the fluorine atoms. In the present case there is no disorder; instead, we have two very different types of column appearing alternately along the hexagonal  $a$ -axis. The columns of the first type, containing  $\text{Cu}(1)$  and  $\text{Si}(1)$  atoms, have the  $\bar{3}$  axes passing through them. The constituent  $\text{Cu}(\text{H}_2\text{O})_6$  and  $\text{SiF}_6$  octahedra are regular within the experimental limits, and oriented in the same way as the corresponding octahedra in  $\text{CoSiF}_6 \cdot 6\text{H}_2\text{O}$ , with the fluorine in the position with lower occupancy. The neighboring column, containing  $\text{Cu}(2)$  and  $\text{Si}(2)$ , both with site symmetry  $\bar{1}$ , is very different. While the  $\text{SiF}_6$  octahedron is still almost regular, there is a distinct tetragonal distortion in the  $\text{Cu}(\text{H}_2\text{O})_6$  octahedron. This is very significant, because previously  $\text{CuSiF}_6 \cdot 6\text{H}_2\text{O}$ , like the other hexahydrated fluosilicates, was supposed to be isomorphous with  $\text{NiSnCl}_6 \cdot 6\text{H}_2\text{O}$ , with one formula unit per rhombohedral unit cell, and consequently, the water octahedron surrounding the  $\text{Cu}^{2+}$  ion was considered trigonally distorted. With such assumption, Bleaney and Ingram<sup>3</sup> used mixed crystals of  $\text{CuSiF}_6 \cdot 6\text{H}_2\text{O}$  and  $\text{ZnSiF}_6 \cdot 6\text{H}_2\text{O}$  in their study of paramagnetic resonance, and Abragam and Pryce<sup>4</sup> gave theoretical interpretation of the results thus obtained, assuming that the  $\text{Cu}^{2+}$  ion was subjected to a ligand field of trigonal symmetry. The  $\text{Cu}:\text{Zn}$  ratio in the mixed crystal used in the experiment has not been mentioned in the paper of Bleaney and Ingram. Assuming that the  $\text{Cu}^{2+}$  ion concentration was very low, it is quite probable that the structure of the mixed crystal resembled that of  $\text{ZnSiF}_6 \cdot 6\text{H}_2\text{O}$ , and consequently the  $\text{Cu}^{2+}$  ions may indeed have been in a ligand field with trigonal symmetry. In that case there should be no objection to the said studies, except that the results obtained do not relate to the actual ligand field in  $\text{CuSiF}_6 \cdot 6\text{H}_2\text{O}$ . A careful study of paramagnetic resonance with the "undiluted" salt would then be worthwhile. It would also be interesting to prepare mixed crystals with different  $\text{Cu}:\text{Zn}$  ratio, and find out for what maximum concentration of  $\text{Cu}^{2+}$  the structure resembles that of  $\text{ZnSiF}_6 \cdot 6\text{H}_2\text{O}$ .

Figure 1 shows a portion of the structure in orthogonal projection on the  $xz$  plane. One of each kind of hydrogen atom is identified. The bonds  $\text{O}(1)\dots\text{F}(1)$  and  $\text{O}(1)\dots\text{F}(2)$  follow that same pattern as in  $\text{CoSiF}_6 \cdot 6\text{H}_2\text{O}$ . But while each of  $\text{F}(1)$ ,  $\text{F}(2)$ , and  $\text{F}(3)$  takes part

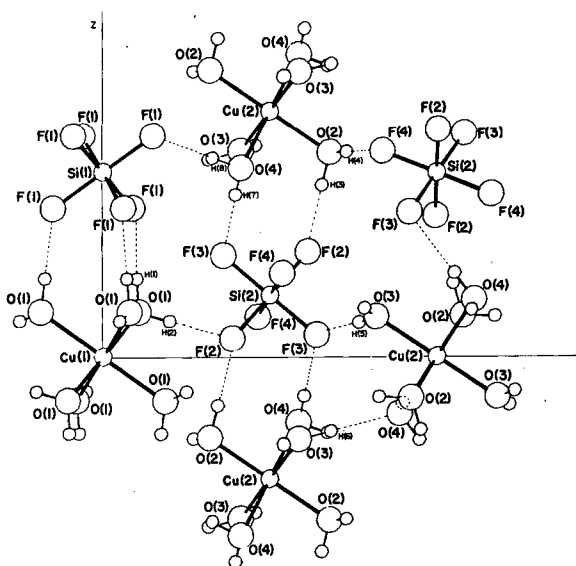


Fig. 1. Structure of  $\text{CuSiF}_6 \cdot 6\text{H}_2\text{O}$ , orthogonal projection on  $xz$ -plane.

(XBL 708-1692)

in two hydrogen bonds,  $\text{F}(4)$  seems to participate in only one; there appears an  $\text{O}(3)\dots\text{O}(4)$  bond instead. This makes the hydrogen bond configuration in this case rather different from that in  $\text{CoSiF}_6 \cdot 6\text{H}_2\text{O}$ , where each F atom participates in two hydrogen bonds.

#### Footnotes and References

\* Condensed from LBL-1935; published in *Acta Crystallogr.* **B29**, 2748-2751 (1973).

† Present address: Dept. of Magnetism, Indian Association for the Cultivation of Science, Calcutta-32, India.

1. S. Ray, A. Zalkin, and D. H. Templeton, LBL-1932 (1973).
2. L. Pauling, *Z. Kristallogr.* **72**, 482-492 (1930).
3. B. Bleaney and D. J. E. Ingram, *Proc. Phys. Soc.* **A63**, 408-409 (1950).
4. A. Abragam and M. H. L. Pryce, *Proc. Phys. Soc.* **A63**, 409-411 (1950).

## SODIUM CHROMATE TETRAHYDRATE\*

H. Ruben, I. Olovsson,<sup>†</sup>  
A. Zalkin, and D. H. Templeton

$\text{Na}_2\text{CrO}_4 \cdot 4\text{H}_2\text{O}$  is monoclinic,  $P2_1/c$ , with  $a = 6.184(4)$ ,  $b = 11.165(4)$ ,  $c = 12.20(1)_3 \text{ \AA}$ ,  $\beta = 104.95(10)^\circ$ ,  $Z = 4$ ,  $d_x = 1.91 \text{ g/cm}^3$ . The crystals were grown from aqueous solution at 25-29°.  $\text{Na}_2\text{SeO}_4 \cdot 4\text{H}_2\text{O}$  is isomorphous with  $a = 6.22(2)$ ,  $b = 11.18(4)$ ,  $c = 12.18(4) \text{ \AA}$ , and  $\beta = 105(1)^\circ$ .

Sodium chromate crystallizes as the decahydrate (below 19.5°), the hexahydrate (19.5-25.9°) and the tetrahydrate (25.9-63°)<sup>1</sup>, and a sesquihydrate is reported to be stable in the neighborhood of 70°.<sup>2</sup> We determined the structure of the tetrahydrate as a by-product of a study of several decahydrates.<sup>3</sup>

A yellow crystal was enclosed in a thin-wall quartz capillary to prevent gain or loss of water. Intensities of 1844 independent reflections were measured using Zr-filtered Mo K $\alpha$  radiation with the stationary-crystal stationary-counter technique. Systematic absences corresponded to  $P2_1/c$ . No correction was made for absorption,  $\mu = 15.7 \text{ cm}^{-1}$ , nor extinction. Zero weight was assigned to 537 reflections with  $I < \sigma(I)$ .

The sodium and chromium positions were deduced from a three-dimensional Patterson function, and oxygen atoms were found with a subsequent difference map. Hydrogen positions were derived from an analysis of the hydrogen bonding; only three of the eight hydrogen peaks were observable in the difference maps. The positional and anisotropic thermal parameters of all of the atoms with the exception of hydrogen were refined by least squares. The  $R_1$  index was 0.11 for all 1844 data, and 0.068 for the 1307 nonzero weighted data; the weighted index,  $R_2$  was 0.061. The goodness of fit was 1.02. In the final cycle no parameter shifted more than 0.02  $\sigma$ .

Each of the eight hydrogen atoms can be assigned unambiguously to a hydrogen bond. Only one of these bonds is from one water molecule to another; all of the others are between water and chromate oxygen atoms.

The two sodium ions are each coordinated to oxygen atoms from both water and chromate ions. Na(1) is at the center of a distorted octahedron of six oxygen atoms with Na-O distances ranging from 2.36 to 2.46  $\text{ \AA}$ . Na(2) is coordinated to five oxygen atoms at distances from 2.35 to 2.38  $\text{ \AA}$ .

The chromate ion is moderately distorted from regular tetrahedral shape. The O-Cr-O bond angles range from 108.5 to 111.5°. The average Cr-O bond length is 1.639  $\text{ \AA}$  when uncorrected for thermal motion, and is 1.649  $\text{ \AA}$  after correction for thermal motion assuming the "riding" model. The individual bond lengths vary from 1.605 to 1.675  $\text{ \AA}$  (uncorrected) and this variation appears to be statistically significant. We attribute it to hydrogen bonding and other crystal packing effects because the Cr-O distance is longer when oxygen has a larger number of sodium and hydrogen neighbors. McGinnety<sup>4</sup> has discussed similar effects in potassium chromate.

## Footnotes and References

\* Condensed from LBL-1931; published in *Acta Crystallogr.* **B29**, 2963-2964 (1973).

<sup>†</sup> Present address: Institute of Chemistry, University of Uppsala, Uppsala, Sweden.

1. *Gmelins Handbuch Der Anorganischen Chemie* (Verlag Chemie, GMBH, Weinheim, 1962), Vol. 52B, pp. 468-472.
2. H. J. Borchardt, *J. Phys. Chem.* **62**, 166-169 (1958).
3. H. W. Ruben, D. H. Templeton, R. D. Rosenstein, and I. Olovsson, *J. Amer. Chem. Soc.* **83**, 820-824 (1961).
4. J. A. McGinnety, *Acta Crystallogr.* **B28**, 2845-2852 (1972).

THE CRYSTAL STRUCTURE OF N, N' -BIS(2, 2, 6, 6-TETRAMETHYLPIPERIDYL-4)  
SUCCINIC ACID DIAMIDE DIHYDRATE,  $C_{22}H_{42}O_2N_4 \cdot 2H_2O^*$

H. Ruben, A. Zalkin, and D. H. Templeton.

$C_{22}H_{42}O_2N_4 \cdot 2H_2O$  crystallizes in the monoclinic space group  $P2_1/c$  with cell dimensions  $a = 13.069(6)$ ,  $b = 13.029(6)$ ,  $c = 15.658(6)$  Å,  $\beta = 99.96(5)^\circ$ ,  $Z = 4$ ,  $d_x = 1.09$  g/cm<sup>3</sup>. The title compound was synthesized by Joss and Calvin.<sup>1</sup> An automatic diffractometer using graphite-monochromated Cu K $\alpha$  x-rays,  $\theta$ - $2\theta$  scan technique, and a scintillation counter was used to measure all of the reflections within the quarter sphere of reflection out to a  $2\theta$  angle of  $124.5^\circ$ , yielding 4160 unique data, of which 3767 were greater than their estimated standard deviation.

The positions of all the nonhydrogen atoms, including two unexpected water molecules, were obtained from an E map phased by the application of "direct" methods. Hydrogen positions were calculated from the known chemical geometry. Full-matrix least-squares refinements were performed on all of the positional, anisotropic thermal (for the heavy atoms), and isotropic thermal (hydrogen atoms) parameters. As the number of parameters would produce a matrix that exceeds the capacity of our computer, we alternately refined half of the structure at a time. For the final refinements, all of the heavy-atom parameters were refined jointly with the hydrogen atoms fixed; this was followed with a refinement of

all the hydrogen atoms with the heavy atoms fixed. The final R factor, for all of the reflections was 0.049, and for the 3767 non-zero-weighted reflections was 0.044. The weighted R factor,  $R_w$ , was 0.065. The goodness of fit was 1.93.

The biradical of this compound, where the hydrogen atoms of the two piperidyl nitrogen atoms are replaced by oxygen radicals, has been prepared.<sup>1</sup> Stable biradicals of such compounds have been proposed as a flexible strain gauge, which when attached to a membrane or a macromolecule at two points would deform together with the support and transduce the strain into the interaction-dependent features of the ESR spectrum.<sup>2,3</sup> This structure determination was undertaken to provide accurate geometrical details in anticipation of such work.

Two crystallographically different, but chemically identical, molecules are centered about the centers of symmetry at  $(1/2, 1/2, 1/2; 1/2, 0, 0)$  and  $(0, 0, 0; 0, 1/2, 1/2)$  respectively. Each of the molecules is an extended chain (Fig. 1). The distances between the piperidyl nitrogen atoms, which are at opposite ends of the chains, are 14.45 and 14.24 Å respectively for

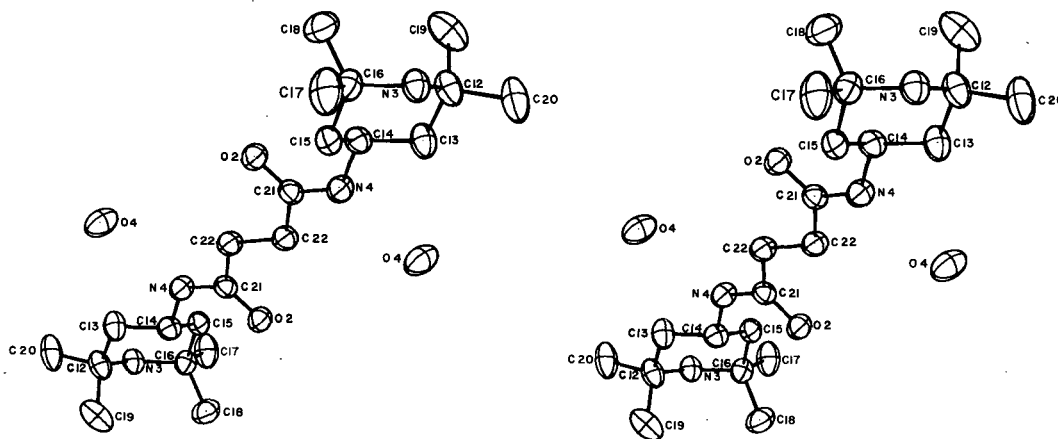


Fig. 1. Stereoscopic view of molecule II.  
(XBL 731-583)

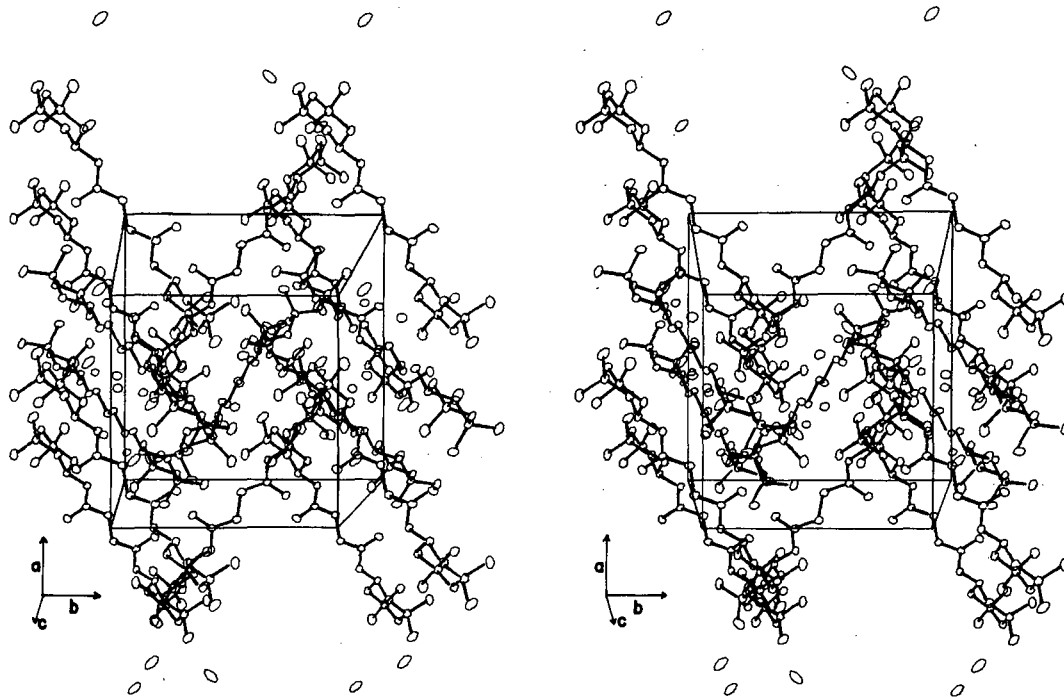


Fig. 2. Stereoscopic view of a unit cell showing the packing.

(XBL 713-580)

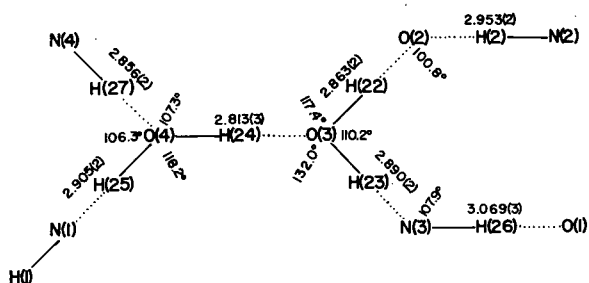


Fig. 3. Schematic diagram of the hydrogen bonding.  
(XBL 729-1871)

the two molecules. A stereoscopic view of the packing is shown in Fig. 2.

Chemically equivalent bond lengths in the two molecules differ by two or three times as much as would be expected according to the estimated standard deviations. Because a full matrix could not be used, the estimated standard deviations may be too low. Thermal motion, for which no correction was practicable, may also contribute to these differences. Thus the corresponding bond lengths in the two molecules may be regarded as identical.

The bond angles exhibit differences which correspond to slightly different conformations for the two molecules, and these differences, while minor, are definitely outside the experimental error.

An extensive hydrogen bond system, shown in Fig. 3, involves all of the hydrogen atoms associated with oxygen and nitrogen, with the exception of H(1). We attribute the conformational differences to this hydrogen bonding or other packing effects.

#### Footnote and References

\* Condensed from LBL-1936; to be published in *Acta Crystallogr.*

1. R. Joss and M. Calviñ, *J. Org. Chem.* **37**, 2015-2018 (1972).
2. M. Calvin, H. H. Wang, G. Entine, D. Gill, P. Ferruti, M. A. Harpold, and M. P. Klein, *Proc. Nat. Acad. Sci. U.S.A.* **63**, 1-8 (1969).
3. P. Ferruti, D. Gill, M. P. Klein, H. H. Wang, G. Entine, and M. Calvin, *J. Amer. Chem. Soc.* **92**, 3704-3713 (1970).

THE STRUCTURE OF THE  $10\pi$  ELECTRON CYCLOOCTATETRAENE DIANION IN  
 POTASSIUM DIGLYME 1, 3, 5, 7-TETRAMETHYLCYCLOOCTATETRAENE DIANION,  
 $[\text{K}(\text{CH}_3\text{OCH}_2\text{CH}_2)_2\text{O}]_2[\text{C}_8\text{H}_4(\text{CH}_3)_4]^{1-}$

S. Z. Goldberg, K. N. Raymond  
 C. A. Harmon, and D. H. Templeton

One of the first successes of quantum chemistry in its application to organic compounds was the explanation of the unusual stability of "aromatic" compounds. The Hückel  $4n+2$  rule for single carbocyclic rings is the most generally used result.<sup>2</sup> Probably the two most important predictions of this rule were the instability of uncomplexed cyclobutadiene and the conversion of the alternating double-bond tub geometry of the  $8\pi$  electron cyclooctatetraene molecule to a symmetrical planar  $10\pi$  electron dianion.<sup>3</sup> Many physical studies have been carried out on the dianion and much speculation has been made regarding its planar geometry. We have determined the structures<sup>4-9</sup> of several lanthanide and actinide complexes and others have examined transition metal complexes,<sup>10,11</sup> but as yet no definitive structural data have been available for cyclooctatetraene dianion itself. We report here the results of such a study. The anion, a tetramethyl substituted derivative of cyclooctatetraene, offers two advantages: the puckering of the ring can be determined by observing the deviation of the methyl groups from the carbocyclic ring, and the thermal libration of the ring in the solid state is expected to be diminished relative to the unsubstituted ring due to intermolecular interactions.

The compound was obtained as a by-product in the synthesis of the cerium complex,  $[\text{K}(\text{CH}_3\text{OCH}_2\text{CH}_2)_2\text{O}][\text{Ce}(\text{C}_8\text{H}_4(\text{CH}_3)_4)_2]$ .<sup>12</sup> When crystallized from the dimethyl ether of diethyleneglycol, diglyme, potassium bis(1, 3, 5, 7-tetramethylcyclooctatetraene)-dianion,  $[\text{K}(\text{CH}_3\text{OCH}_2\text{CH}_2)_2\text{O}]_2[\text{C}_8\text{H}_4(\text{CH}_3)_4]^{1-}$ , is obtained as bright yellow crystals which are extremely sensitive to oxygen and water. Several of these crystals were mounted in thin-walled quartz capillaries under an argon atmosphere. The composition and structure of the compound were established by the diffraction analysis.

As predicted by the Hückel theory this  $10\pi$  electron anion is aromatic with eightfold molecular symmetry and average C-C bond lengths of  $1.407(6)$  Å. The geometry of this free dianion thus compares very closely with the dianion in its metal complexes. Yellow air-sensitive crystals of potassium diglyme bis(1, 3, 5, 7-tetramethylcyclooctatetraene)dianion,

$[\text{K}(\text{CH}_3\text{OCH}_2\text{CH}_2)_2\text{O}]_2[\text{C}_8\text{H}_4(\text{CH}_3)_4]$ , crystalline in space group  $\overline{P}1(C_{1h})^{13}$  with  $a=9.757(3)$ ,  $b=10.026(4)$ ,  $c=8.793$  Å,  $\alpha=97.15(1)$ ,  $\beta=112.35(1)$ ,  $\gamma=109.95(1)^\circ$  with  $\rho_{\text{calc}}=1.16$  g/cm<sup>3</sup> for  $Z=1$ . All atoms, including hydrogen atoms, have been located and their positions and thermal parameters refined by full-matrix least-squares procedures to a conventional R factor of 5.5% for 855 reflections with  $F^2 > 3\sigma(F^2)$  collected with an automated x-ray diffractometer. The structure consists of an ion trimer which lies on an inversion center (Figs. 1 and 2). The two potassium ions are related by inversion and lie on either side of the cyclooctatetraene ring such that all the K-C bond lengths are equal and average  $3.003(8)$  Å. The opposite side of each potassium ion is coordinated by the three ether oxygens at an average

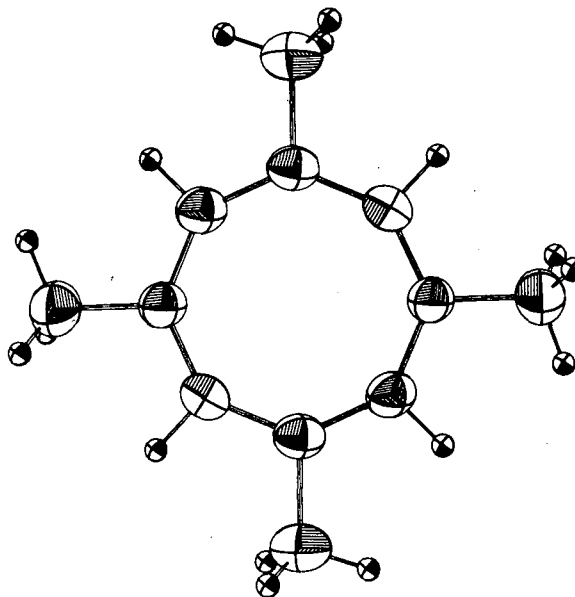


Fig. 1. A perspective drawing of the 1, 3, 5, 7-tetramethylcyclooctatetraene dianion. Thermal ellipsoids enclose 40% of the electron distribution. For clarity the isotropic thermal parameters for the hydrogens were set as  $1.0$  Å<sup>2</sup>. The ring carbon at the far left is  $C_1$  and the atoms are numbered in sequence for counter clockwise motion around the ring.  
 (XBL 742-339)

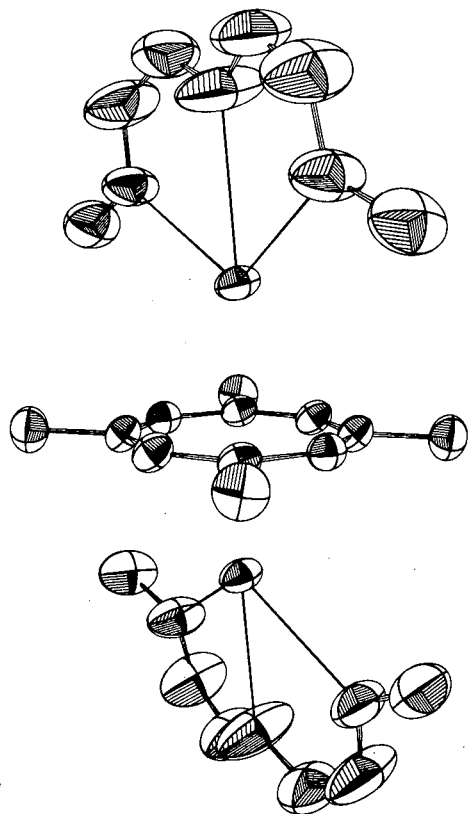


Fig. 2. A perspective drawing of  $[\text{K}((\text{CH}_3\text{OCH}_2\text{CH}_2)_2\text{O})_2[\text{C}_8\text{H}_4(\text{CH}_3)_4]]$ . Thermal ellipsoids enclose 30% of the electron density. Hydrogen atoms are not shown. The leftmost ring carbon is  $\text{C}_3$  and numbering proceeds in sequence for clockwise motion around the ring. In the lower diglyme molecule the leftmost atom is  $\text{O}_1$  and the remainder of the numbering is sequential.

(XBL 742-340)

distance of  $2.835(14)\text{ \AA}$ . All atoms in the carbocyclic ring lie in the plane to within experimental error and the ring is not significantly puckered; the two independent methyl groups are bent out of the plane of the ring by only  $0.5$  and  $2.6^\circ$ . A crystal packing diagram is shown in Fig. 3.

The crystallographic symmetry requires that the two potassium atoms be equidistant from the ring center. The observed distance is  $2.375(3)\text{ \AA}$ . The normal to the plane of the ring is nearly parallel to the K-K vector; the angle between them is  $0.9^\circ$ .

As can be seen in Fig. 3, the thermal motion increases within each  $[\text{K}((\text{CH}_3\text{OCH}_2\text{CH}_2)_2\text{O})_2]$

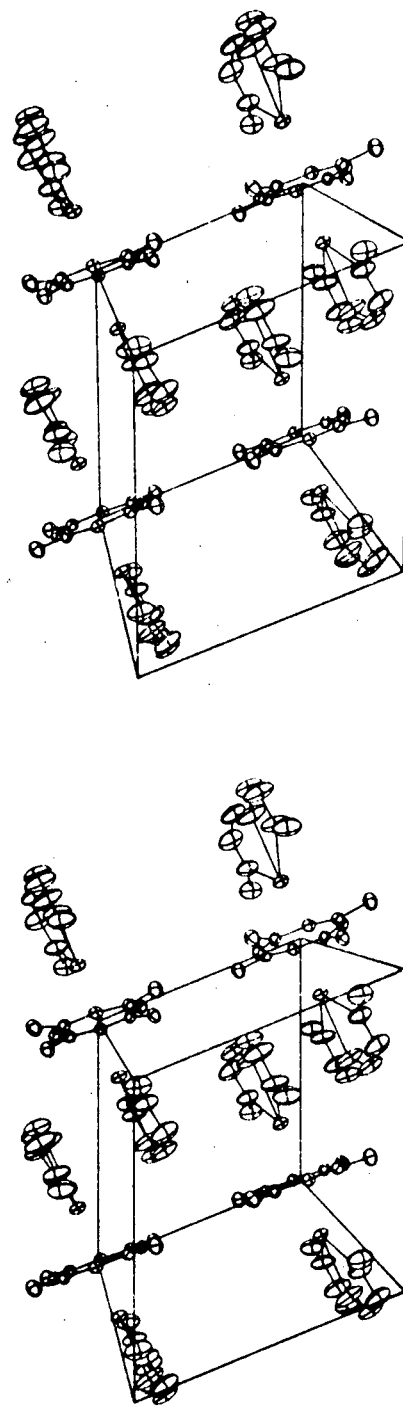


Fig. 3. A stereoscopic view of the unit cell for  $[\text{K}((\text{CH}_3\text{OCH}_2\text{CH}_2)_2\text{O})_2[\text{C}_8\text{H}_4(\text{CH}_3)_4]]$ . The a axis is horizontal, the c axis is vertical, and the b axis goes into the drawing. Thermal ellipsoids enclose 20% of the electron distribution. Only the molecules on the back face are shown. Hydrogens have been omitted.

(XBL 742-341)

[C<sub>8</sub>H<sub>4</sub>(CH<sub>3</sub>)<sub>4</sub>] trimeric unit on going outward from the center of the cyclooctatetraene ring. The ring itself is packed quite firmly in its position while the diglyme rings occupy relatively large holes in the structure.

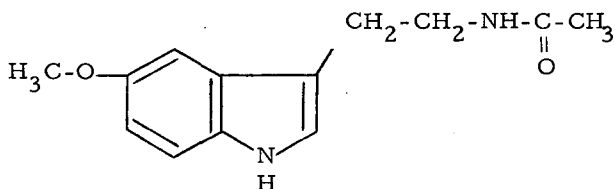
#### Footnote and References

1. Condensed from a report accepted for publication in J. Amer. Chem. Soc.
2. E. Hückel, Z. Physik **70**, 204 (1931); **76**, 628 (1932); International Conference on Physics, London, 1934, Vol. II (The Physical Society, London, 1935), p. 9; Z. Elektrochem. **43**, 752 (1937).
3. A. Streitwieser, Jr., Molecular Orbital Theory for Organic Chemists (Wiley, New York, 1961).
4. A. Zalkin, K. N. Raymond, J. Amer. Chem. Soc. **91**, 5667 (1969).
5. A. Avdeef, K. N. Raymond, K. O. Hodgson, and A. Zalkin, Inorg. Chem., **11**, 1083 (1972).
6. K. O. Hodgson, D. Dempf, and K. N. Raymond, Chem. Commun. 1592 (1971).
7. K. O. Hodgson and K. N. Raymond, Inorg. Chem. **12**, 458 (1973).
8. K. O. Hodgson and K. N. Raymond, Inorg. Chem. **11**, 171 (1972).
9. K. O. Hodgson and K. N. Raymond, Inorg. Chem. **11**, 3030 (1972).
10. H. Dierks and H. Dietrich, Acta Crystallogr. **B24**, 58 (1968).
11. H. Dietrich and M. Soltwish, Angew. Chem. **81**, 785 (1969).
12. C. A. Harmon (Ph.D. thesis), University of California, Berkeley, California (1973).
13. International Tables for X-ray Crystallography, Vol. I (Kynoch Press, Birmingham, England, 1969).

### THE CRYSTAL AND MOLECULAR STRUCTURE OF MELATONIN\*

W. G. Quarles, D. H. Templeton, and A. Zalkin

Melatonin, C<sub>13</sub>H<sub>16</sub>N<sub>2</sub>O<sub>2</sub>, is formed in the pineal gland of the human brain by N-acetylation of serotonin,<sup>1</sup> followed by methylation.<sup>2</sup> Its molecular structure is:



We studied its crystal structure as we did that of 5-methoxytryptamine<sup>3</sup> to gain evidence of the conformations which these and similar molecules might have in biological systems.

The crystals are monoclinic, space group P2<sub>1</sub>/c, with a = 7.707(2), b = 9.252(2), c = 17.077(4) Å, β = 96.78(3)° at 23°C. There are four molecules in a unit cell, giving a calculated density of 1.276 g/cm<sup>3</sup> versus a measured density of 1.272 g/cm<sup>3</sup>. There were

2275 θ-2θ scan data collected with an automatic diffractometer using Mo Kα x-rays and a scintillation counter; there is a total of 1140 independent reflections.

The phases of 151 strong reflections were determined by Sayre's Eq. (4), and the E map for the "best" solution showed the 17 nonhydrogen atoms which were refined by least squares with anisotropic thermal parameters. The 16 hydrogen atoms were recognized among the 19 highest peaks in a Fourier synthesis and were included in the calculation with isotropic thermal parameters. R<sub>1</sub> was 0.036 for the 900 reflections included in least squares and 0.054 for 1140 reflections; R<sub>2</sub> was 0.033. The standard deviation of an observation of unit weight was 1.01.

As seen in Figs. 1 and 2, the ethylamine side chain is in the fully extended (trans) conformation, and the entire molecule except for hydrogen atoms is approximately planar. Atoms C(12) and C(13) are respectively 0.31 and 0.62 Å from a mean plane through the indole ring system, but all other nonhydrogen



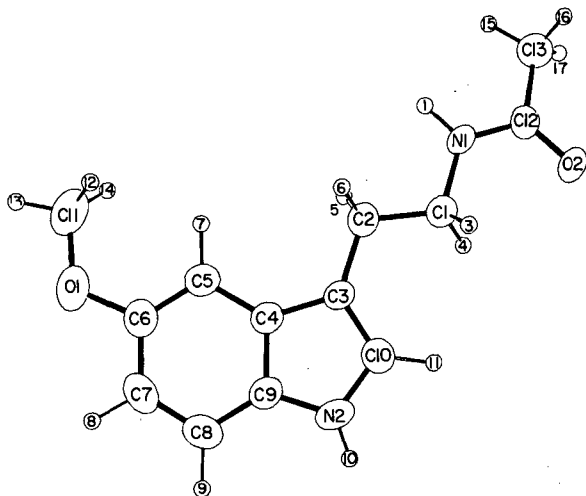


Fig. 1. Atomic numbering in melatonin.  
(XBL 735-646)

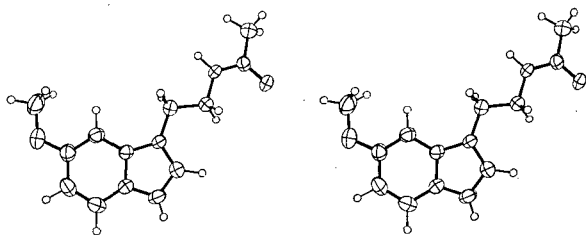


Fig. 2. Molecular conformation.  
(XBL 735-645)

atoms are closer than  $0.18 \text{ \AA}$  to this plane. Each of the nine atoms of the ring system deviates from this plane by  $0.019 \text{ \AA}$  or less. This small but statistically significant deviation from planarity of the ring system consists predominantly of a twist of the pyrrole ring, and the benzene ring is quite flat. Atoms C(3), C(10), and N(2) are  $0.038$ ,  $0.040$ , and  $-0.007 \text{ \AA}$  from the mean plane of the benzene ring. In 5-methoxytryptamine<sup>3</sup> we found the pyrrole ring to be flat, but the benzene ring to be nonplanar by similar small amounts. In crystals of bufotenin<sup>5</sup> two kinds of molecules are crystallographically independent and exhibit two other patterns of slight nonplanarity of the indole ring system. These facts suggest that the nonplanarity in each case is the result of packing forces, and that it has no significance concerning the structure of the isolated molecule.

A comparison of the bond distances in melatonin and in 5-methoxytryptamine, excluding the C(1)–C(2) bond, reveals that those in melatonin are systematically shorter by about  $0.007 \text{ \AA}$ . After a correction of this amount, the differences are quite consistent with the estimated standard deviation according to a probability plot.<sup>6</sup> Falkenberg<sup>7</sup> gave average values for many of these bond distances based on our results and five other accurate structure determinations (two of which included two independent molecules in the same crystal). Compared to these average bond lengths, our results tend to be low by  $0.002 \text{ \AA}$  for melatonin and high by  $0.005 \text{ \AA}$  for 5-methoxytryptamine. Probably at least part of these effects are the result of thermal motion, for which no correction has been made. Perhaps radiation damage to the 5-methoxytryptamine crystal also makes a contribution.

The various C–C bonds in the aromatic ring system differ in length by as much as  $0.05 \text{ \AA}$ , a variation far greater than the small discrepancies discussed above, and this variation is rather consistent in the various crystals. We regard it as a genuine effect of the electronic structure of these molecules.

The C(1)–C(2) bond length is  $1.534(4) \text{ \AA}$  in 5-methoxytryptamine,  $1.501(4) \text{ \AA}$  in melatonin, and various intermediate values in the other crystals listed by Falkenberg.<sup>7</sup> We cannot identify the cause of this discrepancy. The conformation difference between gauche and trans does not offer a simple explanation because serotonin picrate monohydrate<sup>8</sup> is gauche with C–C =  $1.513(4) \text{ \AA}$ , in agreement with several cases which are trans.

We attribute no special significance to the conformations of the side chains found in these crystals, but consider them to be the result of crystal packing. Falkenberg<sup>7</sup> reports 11 gauche and 9 trans examples among 20 indoleamines, and also a considerable variety of torsion angles where the ethylamine is attached to the ring. We assume that melatonin and similar compounds can exist in either conformation in various environments.

The molecules of melatonin are connected by weak hydrogen bonds between nitrogen and oxygen, N(1)–H(1)···O(2) and N(2)–H(10)···O(2); N–O =  $2.96$  and  $2.90 \text{ \AA}$ , respectively. These bonds connect the molecules in infinite sheets parallel to *b* and *c*. The molecules are arranged in the crystal as shown in Fig. 3.

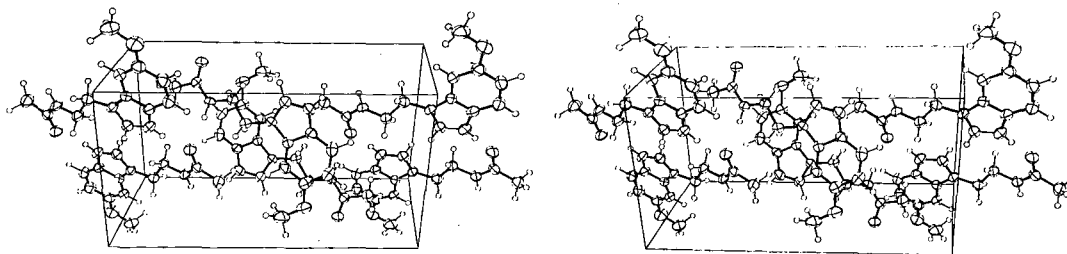


Fig. 3. Molecular packing: a toward back, b down, c to the left.

(XBL 735-644)

#### Footnote and References

\* Condensed from LBL-1933; published in *Acta Crystallogr.* **B30**, 99-103 (1974).

1. A. B. Lerner, J. D. Case, and Y. Takahashi, *J. Biol. Chem.* **235**, 1992-1997 (1960).
2. J. Axelrod and H. Weissbach, *Science* **131**, 1312 (1960).
3. W. G. Quarles, D. H. Templeton, and A. Zalkin, LBL-1934.
4. R. E. Long, *The Crystal and Molecular Structures of 7, 7, 8, 8-Tetracyanoquinodimethane and Cyclopropanecarboxamide, and a*

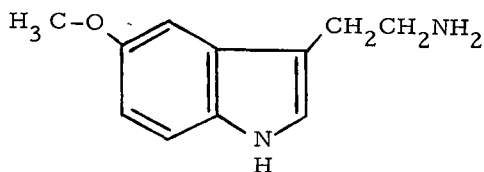
*Program for Phase Determination (thesis), University of California, Los Angeles, California (1965).*

5. G. Falkenberg, *Acta Crystallogr.* **B28**, 3219-3228 (1972).
6. W. C. Hamilton and S. C. Abrahams, *Acta Crystallogr.* **A28**, 215-218 (1972).
7. G. Falkenberg, *The Molecular Structure of Some Psychoactive Indolealkylamines and Related Substances (thesis), Karolinska Institutet, Stockholm (1972).*
8. U. Thewalt and C. E. Bugg, *Acta Crystallogr.* **B28**, 82-92 (1972).

### THE CRYSTAL AND MOLECULAR STRUCTURE OF 5-METHOXYTRYPTAMINE\*

W. G. Quarles, D. H. Templeton, and A. Zalkin

Serotonin and related molecules have attracted widespread attention because of their involvement in the function of the central nervous system.<sup>1</sup> We have studied the crystal structures of two of these substances, because molecular dimensions and conformations are relevant to studies of biological function. In this paper we describe the structure of 5-methoxytryptamine:



In the following paper we describe the structure of melatonin and compare the dimensions of these closely related molecules.

Crystals of 5-methoxytryptamine from the Regis Chemical Company, Chicago, were well-formed, thin, colorless, transparent plates. They were stable when stored at 5° C over Drierite, but turned brown when exposed to the atmosphere for a month. Exposure to x-rays hastened the color change and caused diffraction intensities to decrease, but the decrease was only 1 or 2% during the three-day period in which the intensity data were collected. The crystals are monoclinic, space group *Pc* with  $a = 6.110(2)$ ,  $b = 9.532(3)$ ,  $c = 8.831(3)$  Å,  $\beta = 98.72(4)^\circ$  at 23° C. There are two molecules in a unit cell, giving a calculated density of 1.245

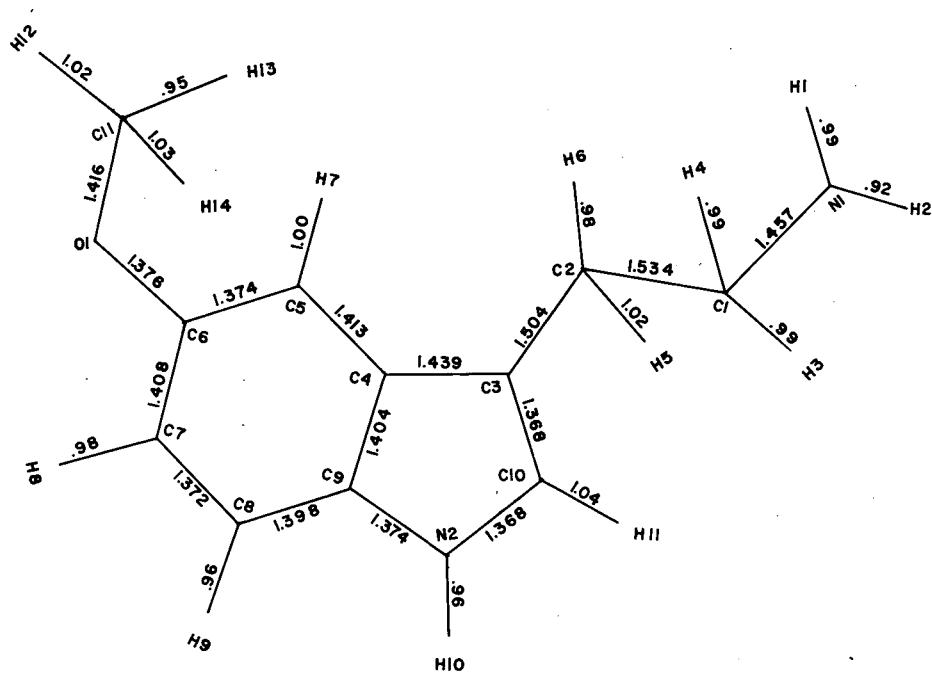


Fig. 1. Bond distances (Å)  
(XBL 704-827)

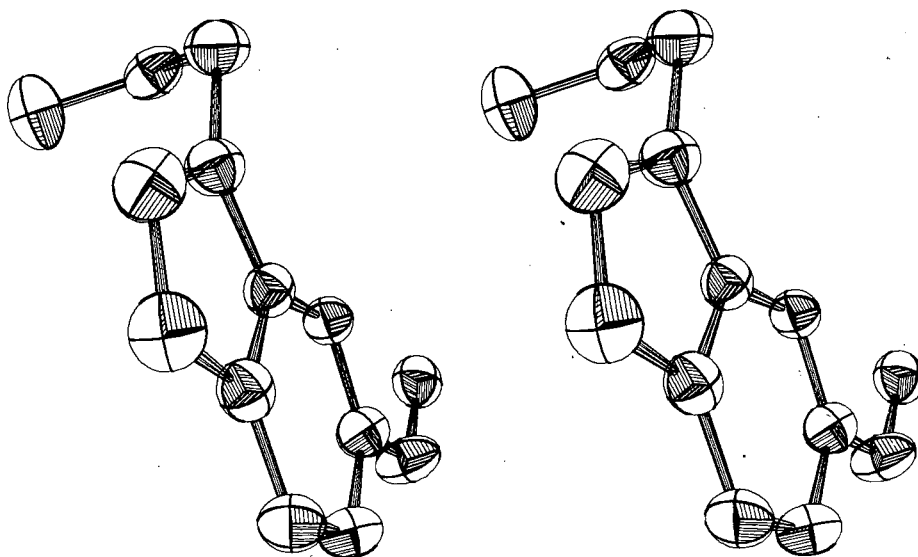


Fig. 2. Molecular conformation.  
(XBL 704-836)

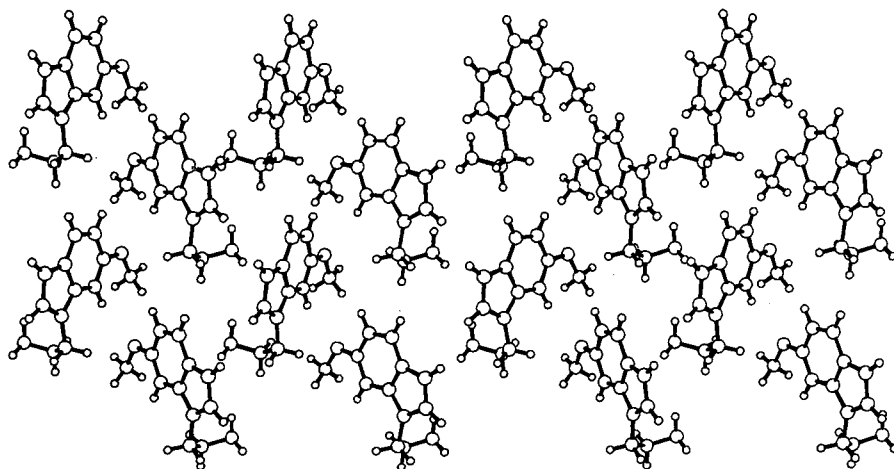


Fig. 3. Molecular packing: viewed down *a*, with *b* horizontal and *c* vertical.  
(XBL 734-460)

$\text{g}/\text{cm}^3$  versus a measured density (by flotation in ethylene chloride and ethyl acetate) of  $1.242 \text{ g}/\text{cm}^3$ . There were 1604  $\theta$ - $2\theta$  scan data collected with an automatic diffractometer using Cu K $\alpha$  x-rays and a scintillation counter.

The orientation of the molecule was suggested by the Patterson function, and the structure was determined by a method described by Quarles.<sup>2</sup> The positions of all the hydrogen atoms with isotropic thermal parameters were included in the least-squares refinements. All of the heavy atoms were refined anisotropically. The final R value was 0.025 for 746 non-zero weighted data, and 0.028 when the 61 zero weighted data were included. The weighted  $R_2$  was 0.026 and the standard deviation of a reflection of unit weight was 1.11.

The resulting bond distances are shown in Fig. 1. The molecular conformation is shown in Fig. 2. The ethylene side chain is bent into the gauche or synclinal conformation. The bond distances and angles are in good agreement with corresponding values for melatonin, with which they will be compared elsewhere, and with the results for several other similar molecules which have been reviewed by Falkenberg.<sup>3</sup> The nine atoms of the indole ring system are very nearly planar, but deviations from planarity are significant in comparison to the estimated standard deviations, about  $0.004 \text{ \AA}$ . The largest deviation from a mean plane is  $0.015 \text{ \AA}$ . Seven of the atoms, however, are within  $0.004 \text{ \AA}$  of a plane fitted to the pyrrole ring; the other two atoms, C(7) and C(8), are respectively  $0.040$  and  $0.036 \text{ \AA}$  to one side of this plane. Atoms O(1) and C(2), the first atoms of the side chains, are  $0.006$  and  $0.007 \text{ \AA}$ , respectively, from this same plane. Deviations from planarity of similar magnitude have been observed in melatonin

and in other indole derivatives for which the structures have been determined with high precision,<sup>4-6</sup> but no consistent pattern of the deviations is evident.

The molecules are connected by hydrogen bonds of the type N(2)-H(10)...N(1), with the N-N distance  $2.916(3) \text{ \AA}$  and the N-H-N angle  $170(3)^\circ$ . The molecules connected by these bonds form strings running in the [101] direction. Otherwise there are no close intermolecular interactions. The packing of the molecules is shown in Fig. 3.

#### Footnote and References

\* Condensed from LBL-1934; published in *Acta Crystallogr.* **B30**, 95-98 (1974).

1. S. Garattini and L. Valzelli, *Serotonin* (Elsevier, Amsterdam, 1965).
2. W. G. Quarles, X-ray Structure Investigation of Some Substituted Indoles, and the X-ray Crystal Structure of 1,1'-Bishomocubane (thesis), University of California, Berkeley.
3. G. Falkenberg, The Molecular Structure of Some Psychoactive Indolealkylamines and Related Substances (thesis), Karolinska Institutet, Stockholm (1972).
4. G. Falkenberg, (1972b). *Acta Crystallogr.* **B28**, 3219-3228 (1972).
5. G. Falkenberg and D. Carlström, *Acta Crystallogr.* **B27**, 411-418 (1971).
6. J. Bergman, S. Abrahamsson, and B. Dahlén, *Tetrahedron* **27**, 6143-6149 (1971).

STRUCTURE OF 5-HYDROXY-2, 3-NORBORNANE DICARBOXYLIC  
ACID  $\gamma$ -LACTONE,  $C_9H_{10}O_4$ \*

G. Chapuis, A. Zalkin, and D. H. Templeton

Crystals of this norbornane derivative,  $C_9H_{10}O_4$  are monoclinic, space group  $P2_1/n$ ;  $a = 22.421(8)$ ,  $b = 6.685(2)$ ,  $c = 10.914(4)$  Å,  $\beta = 94.34(5)^\circ$ ,  $Z = 8$ ,  $D_x = 1.483$  g/cm<sup>3</sup>.

Recently Koshland and co-workers<sup>1</sup> stressed the importance of orientation factors to chemical reaction velocities with special reference to the catalytic power of enzymes. To explore this hypothesis, they studied the relative velocities of some intramolecular lactonization, using norbornane derivatives which provides a rigid geometrical frame.<sup>2</sup> This crystallographic study was undertaken for one of these compounds to obtain an accurate description of its molecular geometry. The crystals were kindly supplied to us by Prof. D. E. Koshland and D. Hackney.

The intensities were measured with an automatic diffractometer using graphite monochromatized Mo K $\alpha$  radiation and a  $\theta$ - $2\theta$  scan technique. A total of 2143 unique reflections were obtained, of which 1667 with  $I > \sigma(I)$  were used for the least-squares refinements. The crystal structure was solved by direct methods using the MULTAN program<sup>3</sup> and refined by our full-matrix least squares. The final residual values obtained were  $R_1 = 0.042$  and  $R_2 = 0.042$ ; for all the data  $R_1 = 0.065$ . In the last stage of refinement the polar hydrogen model<sup>4</sup> has been used in connection with the

hydrogen scattering factor. The molecule is shown in the schematic diagram in Fig. 1. The crystal consists of hydrogen-bonded dimers where one molecule is related to the other by a noncrystallographic center of symmetry. Due to the strains in the norbornane molecules, the C-C bonds and angles depart significantly from the average values. The short C-C bonds C(2)-C(8), C(3)-C(9), C(11)-C(17), C(12)-C(18) are due to a delocalization of unsaturation from the carbonyl groups. The bond angles  $94,3(2)$ ,  $94.5(2)$ ,  $97.7(2)$ , and  $98.1(2)^\circ$  for C(1)-C(7)-C(4), C(10)-C(16)-C(13), C(3)-C(4)-C(5), and C(12)-C(13)-C(14) are characteristic for norbornane derivatives.

Figures 2 and 3 show the molecular conformation and packing. A statistical comparison of the interatomic distances of the two molecules by a probability plot<sup>5</sup> yielded a slope of 1.0, which indicates that the two molecules have identical dimensions within the accuracy of the determination.

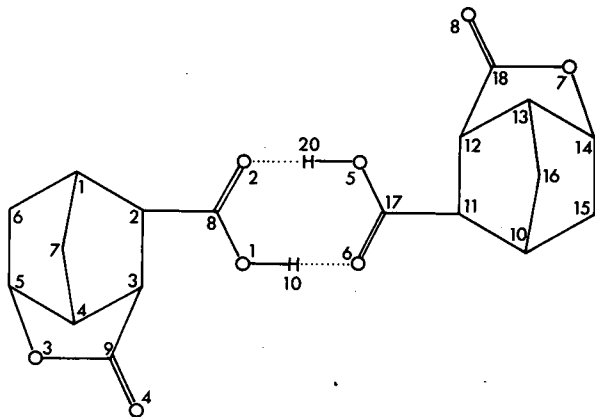


Fig. 1. Schematic diagram of the two asymmetric molecules of the norbornane derivative. (XBL-732-159)

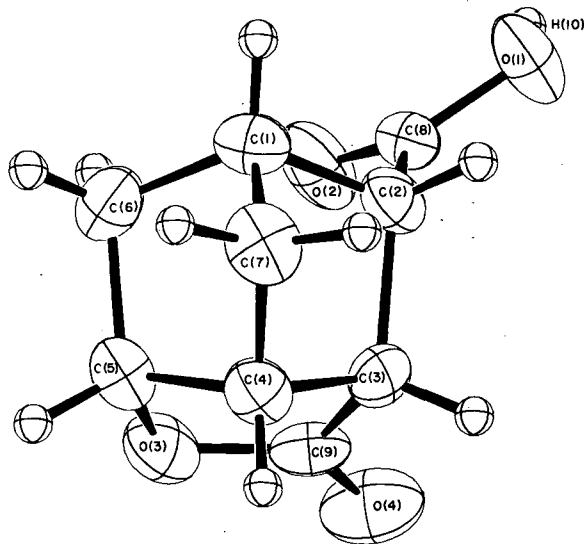


Fig. 2. Perspective view of one molecule with 50% probability thermal ellipsoids. For hydrogen atoms an arbitrary temperature parameter of  $1.0 \text{ \AA}^2$  was given. (XBL 732-158)

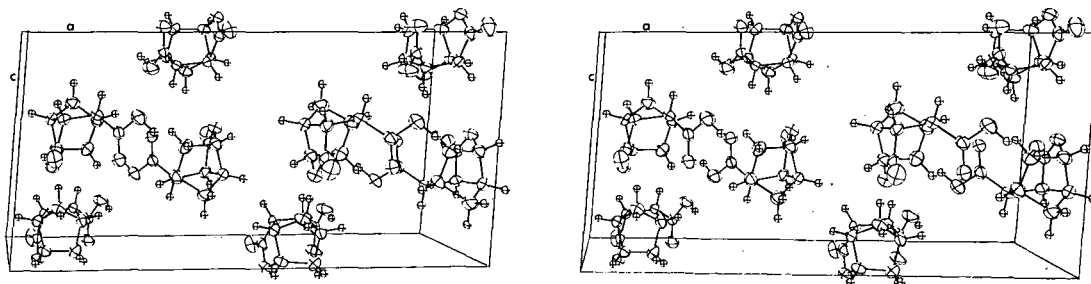


Fig. 3. Stereoscopic pair of a unit cell. The view direction is along the monoclinic b axis.  
(XBL-732-160)

#### Footnote and References

\* Condensed from LBL-1696; published in Acta Crystallogr. B29, 2642 (1973).

1. D. E. Koshland, K. W. Carraway, Jr., G. A. Dafforn, J. D. Gass, and D. R. Storm, Cold Spring Harbor Symposia on Quantitative Biology, Vol. XXXVI, 1971.

2. D. R. Storm and D. E. Koshland, J. Amer. Chem. Soc. 94, 5805-5814 (1972).

3. G. Germain, P. Main, and M. M. Woolfson, Acta Crystallogr. A27, 368-376 (1971).

4. D. H. Templeton, A. J. Olson, A. Zalkin, and L. K. Templeton, Acta Crystallogr. A28, Part S4, S252 (1972).

5. W. C. Hamilton and S. C. Abrahams Acta Crystallogr. A27, 368-376 (1971).

## CHEMICAL PROCESSING OF SUPERHILAC TARGETS

J. V. Kratz,\* J. O. Liljenzin,<sup>†</sup> and G. T. Seaborg

Uranium targets are being irradiated with heavy ions,  $Z \geq 18$ , for two reasons. One goal is to search for superheavy elements, which might be produced in such reactions. Secondly, to obtain information basic to an understanding of heavy nuclei collision reactions, the same

targets are used to measure yields of other reaction products.

The search for superheavy elements is based on a chemical separation of a super-heavy element fraction from the actinide ele-

## CHEMICAL PROCESSING OF HEAVY-ION BOMBARDED URANIUM TARGETS

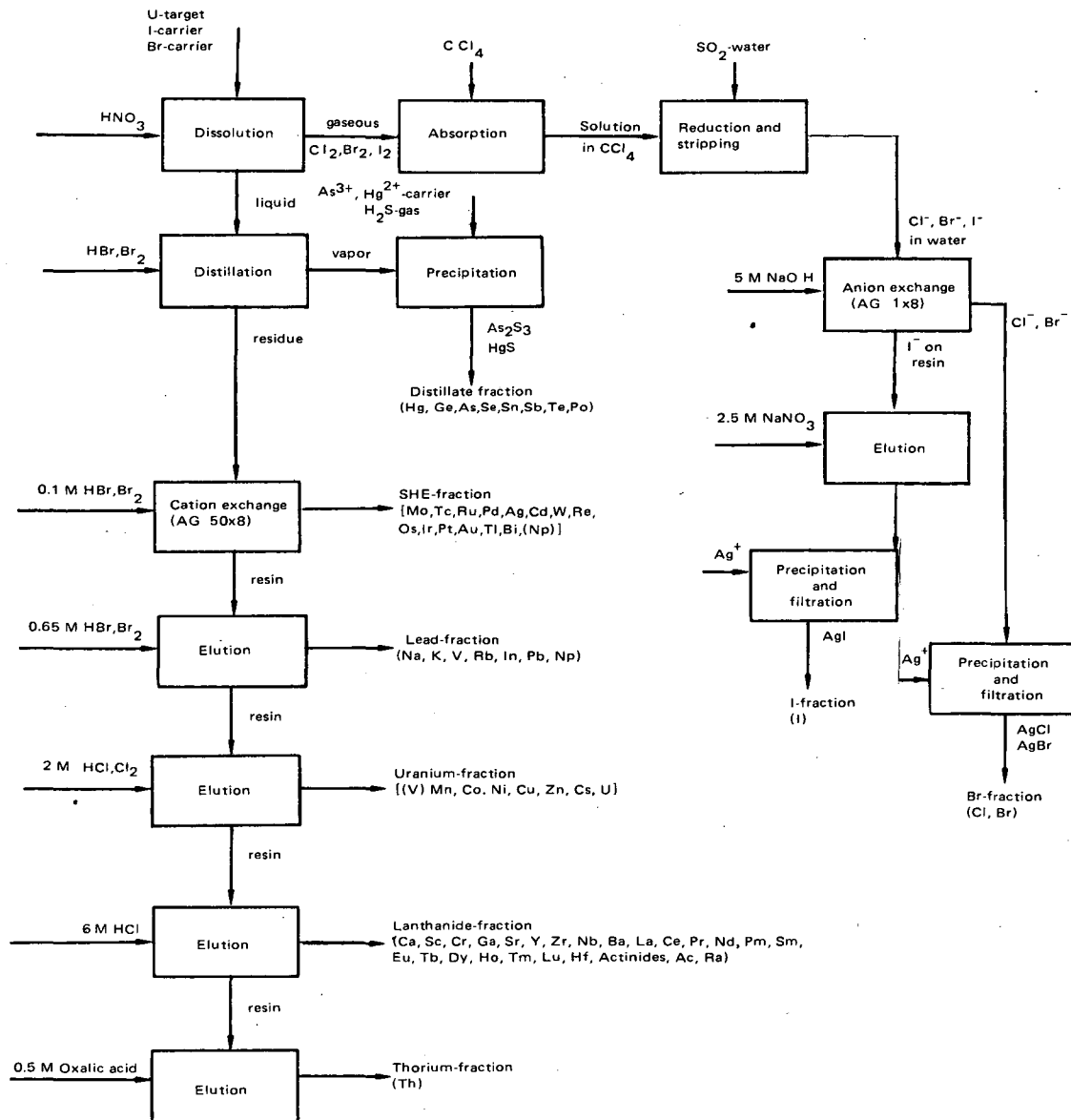


Fig. 1. Separation scheme for the processing of heavy-ion bombarded uranium targets. Elements identified in a certain fraction are indicated below the respective fraction names.

XBL 743-535

ments, including the bulk target material. Any superheavy elements that might be produced would be eluted from a cation exchange column as a group (elements 107 through 116) in the form of bromide complexes.<sup>1</sup> In addition to the cation exchange group separation for superheavy elements, further separation steps based on volatility and different degrees of complexing in HBr/Br<sub>2</sub> or HCl solutions are performed to separate the remaining reaction products into a limited number of chemical fractions, which are suitable for yield measurements by  $\gamma$ -ray spectroscopy. The experimental conditions were studied using radioactive tracers and by processing several uranium targets bombarded with <sup>40</sup>Ar ions. The final separation scheme, illustrated in Fig. 1, separates the uranium target into 8 chemical fractions. The procedure is described as follows.

Natural uranium metal foils, 12.7  $\mu$ m thick and 12.7 mm diameter (30 mg), were bombarded at 7.2 MeV/amu incident beam energy and then dissolved in the presence of 35  $\lambda$  each of 1 M HBr and HI added as carriers, in a closed glass apparatus. Bromine and iodine vapors were distilled into a CCl<sub>4</sub> trap. After back extraction into SO<sub>2</sub>-water, which was made 1 M in NaOH, the halides were loaded onto an AG 1-X8 column (3  $\times$  50 mm) in the OH<sup>-</sup> form. Bromide was eluted in 5 M NaOH followed by the elution of iodide in 2.5 M NaNO<sub>3</sub>.<sup>2</sup> The chemical yields of bromine and iodine (typically ~95% and ~70%, respectively) were determined using the Volhard titration method. The AgBr and AgI precipitates were then filtered onto a membrane filter (15 mm diameter) and mounted on standard Al-plates for  $\gamma$ -ray counting.

The nitric acid in the dissolver vessel was destroyed by fuming with concentrated HBr and evaporating to dryness three times. Volatile bromides were collected together with the aqueous distillate in an empty glass trap. After the addition of As<sup>3+</sup> and Hg<sup>2+</sup> carriers (0.1 mg each) to the distillate, a sulfide precipitate from this solution was filtered onto a membrane filter. The filter was mounted uncovered, dried, and counted for  $\alpha$ -particle, spontaneous fission, and  $\gamma$ -ray activities. Chemical yields for the volatilized elements have to be determined via known amounts of tracer activities added to the dissolver vessel prior to the volatilization.

The solid residue in the dissolver vessel was then dissolved in 0.1 M HBr/Br<sub>2</sub> and transferred to an AG 50W-X8 cation exchange column. This column was prepared by loading a standard heavy-walled glass column with 1 ml of resin as shown in Fig. 2. The upper part of the resin was used to absorb the large amount of target material; actually 1/7 of the

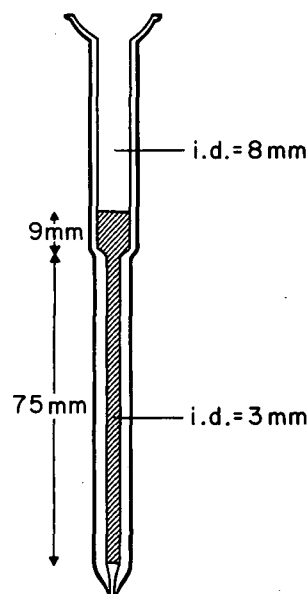


Fig. 2. AG 50W-X8 cation exchange column for the processing of 30 mg uranium targets.

XBL 742-2367

capacity of the column was used by the uranium. Columns with (stepwise) decreasing inner diameter are known to offer certain advantages in the chromatographic separation of small quantities from bulk materials.<sup>2</sup> The successive eluate fractions (Fig. 1) were collected in small glass beakers and evaporated nearly to dryness. These solutions, together with successive portions of 1 M HBr solution used for washing the beakers, were then transferred onto 15-mm circular microscope cover glass discs and evaporated to dryness. The glass discs were mounted on Al-cards and counted periodically for  $\alpha$ -particle, spontaneous fission and  $\gamma$ -ray activities.

In the I, Br and distillate fractions, chemical yields are typically between 50 and 100%; thus, chemical yield determinations are necessary. In the other five chemical fractions, quantitative elutions take place, and no chemical yield determinations need to be performed. Complications arise for a few elements, e.g., Mo, Np, V, which are distributed among two or more fractions. For isotopes of these elements, the initial activities from different fractions are summed to obtain the total reaction yields. Many elements are not listed in Fig. 1. Isotopes of these elements have not been detected in the separations performed to date, because of unfavorable half-lives, low  $\gamma$ -quantum yields, or too low formation cross sections. Through use of this separation



scheme (Fig. 1), yields of more than 100 isotopes of 53 elements have been determined in the reaction  $^{238}\text{U} + ^{40}\text{Ar}$ , and a smaller number in the reaction  $^{238}\text{U} + ^{84}\text{Kr}$ . These results are the subject of another contribution to this report.<sup>3</sup>

#### Footnotes and References

\* On leave from Institut für Kernchemie, Universität Mainz, with a fellowship from Gesellschaft für Schwerionenforschung GSI, Darmstadt, Germany.

† Department of Nuclear Chemistry, Chalmers University of Technology, Göteborg, Sweden.

1. J. V. Kratz, J. O. Liljenzin, G. T. Seaborg, Group Separations for Superheavy Elements, Nuclear Chemistry Annual Report 1972, LBL-1666, p. 308 (1972).

2. O. Samuelson, Ion Exchange Separations in Analytical Chemistry, Wiley, New York (1963).

3. I. Binder, J. V. Kratz, J. O. Liljenzin, A. E. Norris, G. T. Seaborg, in Section of this annual report.

### COVALENCY EFFECTS ON THE LIGAND FIELD SPLITTINGS OF OCTAHEDRAL $5f^1$ COMPOUNDS

N. Edelstein, D. Brown,\* and B. Whittaker\*

Over the past thirty years the problem of covalency in d transition metal complexes has been thoroughly studied both theoretically and experimentally.<sup>1</sup> For octahedral complexes the simple model of d electron orbitals interacting with ligand orbitals within a molecular orbital framework has proved useful since it enables parameters which describe the bonding in the complex to be determined from experimental data. This same model has been applied to f transition ions in octahedral symmetry but there have been very few experimental measurements.<sup>2-4</sup> We have now obtained the optical spectra of two octahedral Pa(IV) compounds. The results, combined with earlier measurements by Ryan<sup>5</sup> and others<sup>6,7</sup> on U(V) complexes and the analysis of spectral data available<sup>2</sup> for NpF<sub>6</sub>, have enabled us to provide a preliminary, qualitative analysis of the trends in bonding in these  $5f^1$  compounds.

$(\text{NEt}_4)_2\text{PaCl}_6$  and  $(\text{NEt}_4)_2\text{PaBr}_6$  (Et = C<sub>2</sub>H<sub>5</sub>) were prepared as reported previously.<sup>8</sup> Absorption spectra were recorded with a Cary Model 14 spectrophotometer using the technique recently described elsewhere.<sup>9</sup> Spectra were recorded for  $(\text{NEt}_4)_2\text{PaCl}_6$  at 85, 300 and 500 K and for the hexabromo-analogue at 77 and 300 K.

The spectra obtained for  $(\text{NEt}_4)_2\text{PaBr}_6$  are illustrated in Fig. 1, and the measured peak positions and assignments for this compound and for  $(\text{NEt}_4)_2\text{PaBr}_6$  are listed in Table I. The estimated accuracy of measurement is  $\pm 20\text{\AA}$ . The two groups of peaks at  $\sim 1.7\ \mu\text{m}$  were present in the spectrum of  $\text{NEt}_4\text{Cl}$  and in that of  $(\text{NEt}_4)_2\text{UCl}_6$  and are attributed to transitions within the tetraethylammonium cation.

Formally, the Hamiltonian to describe the system is:<sup>10,11</sup>

$$\begin{aligned} &= H_{\text{SO}} + H_{\text{CF}} \\ H_{\text{SO}} &= \zeta(r) (\vec{s} \cdot \vec{l}) \\ H_{\text{CF}} &= B_0^4 [C_0^{(4)} + \sqrt{5/14} (C_{-4}^{(4)} + C_4^{(4)})] + B_0^6 [C_0^{(6)} \\ &\quad - \sqrt{7/2} (C_{-4}^{(6)} + C_4^{(6)})] \end{aligned} \quad (1)$$

where  $\zeta(r)$  (from now written as  $\zeta$ ) the spin orbit coupling constant, and  $B_0^4$  and  $B_0^6$ , the crystal field parameters, are used as parameters to be evaluated from the experimental data. The operators  $\vec{s}$  and  $\vec{l}$ , the spin and orbital angular momentum respectively, and the  $C_q^{(k)}$ , the tensor operators used to describe the crystal field, depend only on the angular co-ordinates and the matrix elements of these operators may be readily evaluated.<sup>11</sup>

The energy level diagram derived from the above Hamiltonian (for the special case  $B_0^6 = 0$  and used for illustrative purposes only) is shown in Fig. 2. The right side of the figure represents the limit of strong spin orbit coupling and no crystal field while the left side represents the limit of strong crystal field and zero spin orbit coupling. The splittings of the f orbitals in a strong crystal field may be represented by the two parameters  $\theta$  and  $\Delta$  which are linearly related to the previously defined crystal field parameters by,

$$\begin{aligned} b_4 &= B_0^4/33, b_6 = (-5/429) B_0^6 \\ \theta &= 8b_4 - 56b_6 \\ \Delta &= 10b_4 + 84b_6 \end{aligned} \quad (2)$$

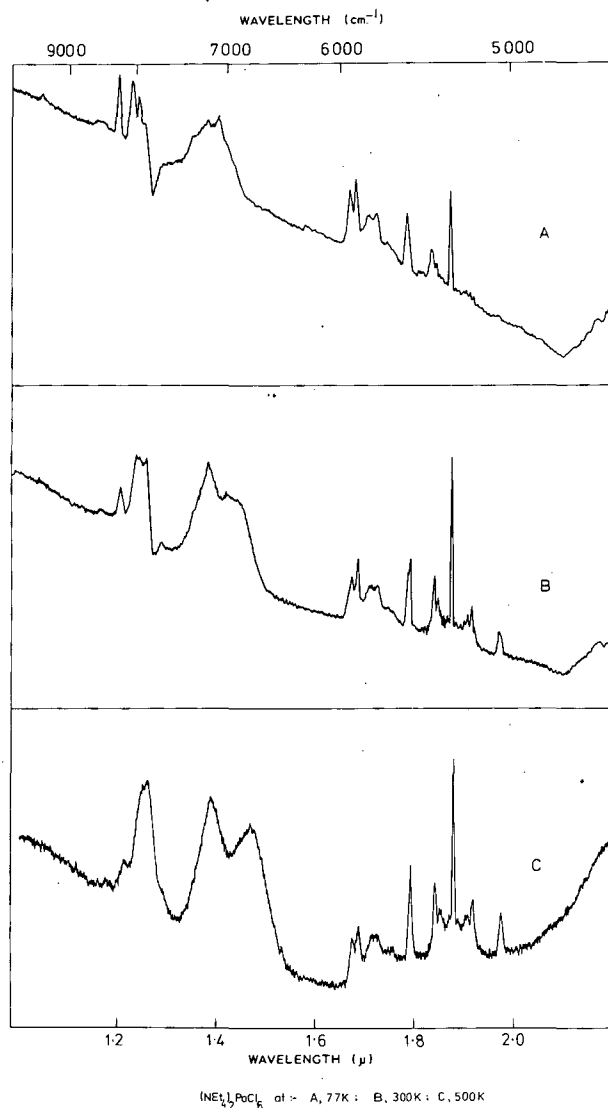


Fig. 1. Spectra of  $[(C_2H_5)_4N]_2PaCl_6$ . (A) 77°K, (B) 300°K, (C) 500°K.

XBL 743-515

As the ratio of the spin orbit coupling constant to the crystal field splitting changes the levels shift and in the intermediate region are labelled by their group theory representations as shown in Fig. 2. This diagram approximately represents the energy levels of the Pa compounds for the ratio

$$\frac{(7/2\xi/18b_4)}{1 + (7/2\xi/18b_4)} \approx 0.6 \quad (3)$$

We assign the optical absorption bands to transitions from the ground  $\Gamma_7$  level to the  $\Gamma_7'$ ,  $\Gamma_8'$ , and  $\Gamma_6$  states (Table I). Our spectra are remarkably similar to those of Ryan<sup>5</sup> for  $UX_6$  compounds (X = F, Cl, Br) and our

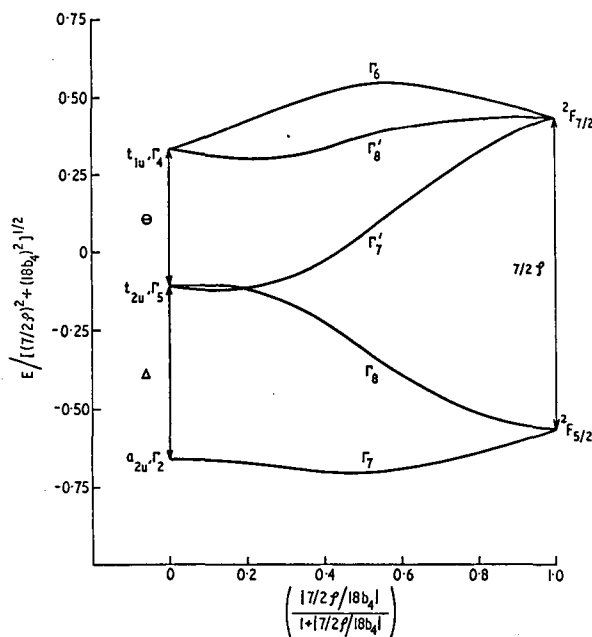


Fig. 2. Energy level splittings of the f orbitals in octahedral symmetry vs the ratio of the relative strengths of crystal field splittings and spin orbit splittings. (Drawn for  $B_0^6 = 0$ ).

XBL 743-513

assignments are based on the arguments he gave and which we will not repeat.

In addition to the above optical data, g value measurements are available for the ground state for  $PaCl_6^{2-}$ ,<sup>12</sup>  $UCl_6$ ,<sup>7</sup>  $UF_6$ ,<sup>6</sup> and  $NpF_6$ .<sup>13</sup> We have assumed for fitting purposes (to be described later) that the bromide complexes have the same g values as the chloride compounds. The g values for  $Cs_2PaCl_6$  and  $NpF_6$  were empirically determined to be negative, so we have assumed all the compounds have negative g values.

In a strong octahedral field the seven f orbital levels are split into two triplets,  $t_{2u}$  and  $t_{1u}$ , and one singlet  $a_{2u}$ . The ordering of the levels from geometric arguments is as shown in Fig. 2.

If we use these strong crystal field states as our basis states, the energy matrices are<sup>2,3,6</sup>

$$\begin{array}{l} \Gamma_7 \\ \Gamma_8 \\ \Gamma_6 \end{array} \begin{array}{l} 0 \\ (3)^{\frac{1}{2}}\xi \\ (3)^{\frac{1}{2}}\xi \quad \Delta - \frac{1}{2}\xi \\ \Delta + \frac{1}{4}\xi \quad \frac{3}{4}(5)^{\frac{1}{2}}\xi \\ \frac{3}{4}(5)^{\frac{1}{2}}\xi \quad \Delta + \theta - \frac{3}{4}\xi \\ \Delta + \theta + \frac{3}{2}\xi \end{array} \quad (4)$$

Table I. Experimental spectral results for  $\text{PaCl}_6^{2-}$  and  $\text{PaBr}_6^{2-}$  complexes.

$(\text{NEt}_4)_2\text{PaCl}_6$ at 500°K			$(\text{NEt}_4)_2\text{PaCl}_6$ at 300°C			$(\text{NEt}_4)_2\text{PaCl}_6$ at 77°K			$(\text{NEt}_4)_2\text{PaBr}_6$ at 300°K			
Band position (cm <sup>-1</sup> )	Int. <sup>a</sup>	Vibrational freq. (cm <sup>-1</sup> )	Band position (cm <sup>-1</sup> )	Int. <sup>a</sup>	Vibrational freq. (cm <sup>-1</sup> )	Band position (cm <sup>-1</sup> )	Int. <sup>a</sup>	Vibrational freq. (cm <sup>-1</sup> )	Band position (cm <sup>-1</sup> )	Int. <sup>a</sup>	Vibrational freq. (cm <sup>-1</sup> )	
$\Gamma_7 - \Gamma_6$	8264	m	+264	8271	s	+260	8306	s	+261	7664	s	+184
	-	-	-	8081	b	+70	8130	s	+85	7539	s	+59
	8000	s	0	(8011) <sup>b</sup>	-	0	8045	w, sh	0	(7480) <sup>b</sup>	-	0
	7936	s	-62	7943	s	-68	7980	m	-65	7422	s	-58
	7760	vw, sh	-240	7752	w	-259				7308	w	-172
									7232	w	-248	
$\Gamma_7 - \Gamma_{8'}$	7204	b		7273	b		7385	sh				
	6840	b		7008	b		7293	b		6943	vb	
							7102	b		(6751) <sup>b</sup>	b	
						6978	vw, sh		(6676) <sup>b</sup>	b		
$\Gamma_7 - \Gamma_{7'}$	5593	s	+255	5590	s	+260	5590	s	+257	5547	s	+182
	5444	s	+106	5444	s	+114	5441	s	+108			
	5405	s	+67	5405	sh	+75	5405	sh	+72	5431	b	+66
	5365	vw	+31	5372	vw	+42	5370	vw	+37			
	5338	s	0	5330	s	0	5333	s	0	5365	s	0
	5285	vw	-53	5271	vw	-39						
	5263	s	-75	5256	sh	-76				5307	b	-58
	5225	s	-113	5227	s	-103						
5079	s	-259	5080	s	-250				5181	s	-184	

<sup>a</sup>Key is as follows: s, sharp; b, broad; m, medium; w, weak; vw, very weak; sh, shoulder.

<sup>b</sup>Values in parentheses are estimated.

If, instead of this procedure, we had used molecular orbital wavefunctions,<sup>3,4,6</sup> we would have obtained a similar set of energy matrices which would have included in the most general case four orbital reduction factors plus the parameters  $\Delta$ ,  $\theta$ , and  $\zeta$ . The above  $g$  value equation would also contain an orbital reduction factor. In this paper we are concerned primarily with the qualitative changes of the parameters as the charge on the central ion is varied, or the halide ligand is changed. For this reason, and also because we have insufficient data to justify using more parameters, we have used only the three parameters  $\theta$ ,  $\Delta$ , and  $\zeta$  to fit the experimental data. The crystal field parameters  $\theta$  and  $\Delta$ , incorporate in their empirical values the sum of the electrostatic and covalent effects. Calculations based on the electrostatic point charge model fail to give the

correct magnitude, or in some cases the correct trends, to these two parameters for the compounds studied in this work. Similar effects have been found previously in studies of rare earth ions in fluorite type crystals.<sup>14</sup> We therefore assume covalent effects dominate the empirical values of  $\theta$  and  $\Delta$ . The values of  $\zeta$  found empirically will be an average of the spin orbit interactions in the  $t_{1u}$  and the  $t_{2u}$  orbitals corresponding to setting the orbital reduction factors equal to unity.

The results of the fitting procedure are shown in Table II. The agreement between the experimental and calculated levels is reasonably good. For  $\text{UCl}_6^-$  and  $\text{UBr}_6^-$  the fits are less satisfactory because the  $g$  values did not correlate well with the optical data. The calculated magnetic splittings are very sensitive

Table II. Results of the fitting of the spectral data for  $5f^1$  compounds.

Compound		Energy ( $\text{cm}^{-1}$ )			g	Parameters ( $\text{cm}^{-1}$ )		
		$\Gamma_7-\Gamma_6$	$\Gamma_7-\Gamma_{8'}$	$\Gamma_7-\Gamma_{7'}$		$\theta$	$\Delta$	$\zeta$
$(\text{NEt}_4)_2\text{PaCl}_6$	Calc.	8029	6988	5347	-1.115	1873	1634	1523
	Exp. <sup>a</sup>	8011	7022	5330	-1.141 <sup>b</sup>			
$(\text{NEt}_4)_2\text{PaBr}_6$	Calc.	7509	6767	5401	-1.100	1268	1707	1535
	Exp. <sup>a</sup>	7480	6828	5365	-1.150 <sup>c</sup>			
$(\text{Ph}_4\text{As})\text{UF}_6$	Calc. <sup>d</sup>	16135	13424	7427	-0.556	6882	4479	1885
	Exp. <sup>d</sup>	15900	13715	7413	-0.700 <sup>e</sup>			
$(\text{NEt}_4)\text{UCl}_6$	Calc.	11646	9903	6917	-0.927	3371	2936	1913
	Exp. <sup>d</sup>	11470	10190	6801	-1.1 <sup>f</sup>			
$(\text{NEt}_4)\text{UBr}_6$	Calc.	10689	9369	6955	-0.931	2375	2935	1925
	Exp. <sup>d</sup>	10555	9620	6823	-1.1 <sup>c</sup>			
$\text{NpF}_6$	Calc.	28380	24025	9348	-0.604	17498	5619	2433
	Exp. <sup>g</sup>	27000	24000	9350	-0.604 <sup>h</sup>			

<sup>a</sup>this work; <sup>b</sup>Ref. 12; <sup>c</sup>estimated value; <sup>d</sup>Ref. 5; <sup>e</sup>Ref. 6; <sup>f</sup>Ref. 7; <sup>g</sup>Ref. 2;

<sup>h</sup>Rev. 17.

to the value of the orbital reduction factor and this less satisfactory fit could be due to our assumption of unity for this parameter. These discrepancies are now being investigated. However, the most dramatic changes occur in the parameters  $\theta$  and  $\Delta$ .

Figure 3 shows the variations of  $\theta$  and  $\Delta$  in the  $5f^1$  compounds. There are three distinct trends. First, as the ligand is fixed, the splittings increase with higher oxidation state, i. e.,  $\theta + \Delta$  increases as we change from Pa(IV)  $\rightarrow$  U(V)  $\rightarrow$  Np(VI). Second, if we fix the oxidation state, the splittings decrease as we

change from the most electronegative to the least electronegative halide ion. And third,  $\theta$  changes much more rapidly than  $\Delta$  in the second case, for a fixed metal ion oxidation state.

The increase in the total splitting for a fixed halide ion with increasing oxidation state follows qualitatively the trends expected. A more positive metal ion will draw charge from the ligand and result in increased covalent bonding which will increase the ligand field splittings. However we also expect increased covalency as we change the ligand from

$\text{F}^- \rightarrow \text{Cl}^- \rightarrow \text{Br}^-$ , but the total ligand field splitting  $\Delta + \theta$  decreases.

This same trend has been found for 3d transition metal complexes. Owen and Thornley<sup>1</sup> have shown that the ligand field splitting for these ions can be represented approximately as  $(\alpha_\sigma^2 - \alpha_\pi^2)(E_d - E_p)$ , where  $\alpha_\sigma$  and  $\alpha_\pi$  are the coefficients of the  $\sigma$  and  $\pi$  combinations of ligand wavefunctions in the molecular orbital wavefunction.  $E_d$  and  $E_p$  are the binding energies of the outer d metal ion electrons and the outer p shell ligand electrons. They suggest the quantity  $(\alpha_\sigma^2 - \alpha_\pi^2) \times (E_d - E_p)$  could vary from  $\text{F}^- \rightarrow \text{Cl}^- \rightarrow \text{Br}^-$  in such a way so as to cause the observed trends. It can readily be shown (following Owen and Thornley) for  $f^1$  compounds in octahedral symmetry that,

$$\theta \approx (\alpha_\pi^2 + \alpha_\sigma^2 - \alpha_\pi'^2)(E_f - E_p) \quad (5)$$

$$\text{and } \Delta \approx (\alpha_\pi'^2)(E_f - E_p)$$

where  $\alpha_\pi$  and  $\alpha_\sigma$  are the ligand admixture coefficients for the  $t_{1u}$  state,  $\alpha_\pi'$  is the ligand admixture coefficient for the  $t_{2u}$  state, and  $E_f$  is the binding energy of the outermost f electrons.

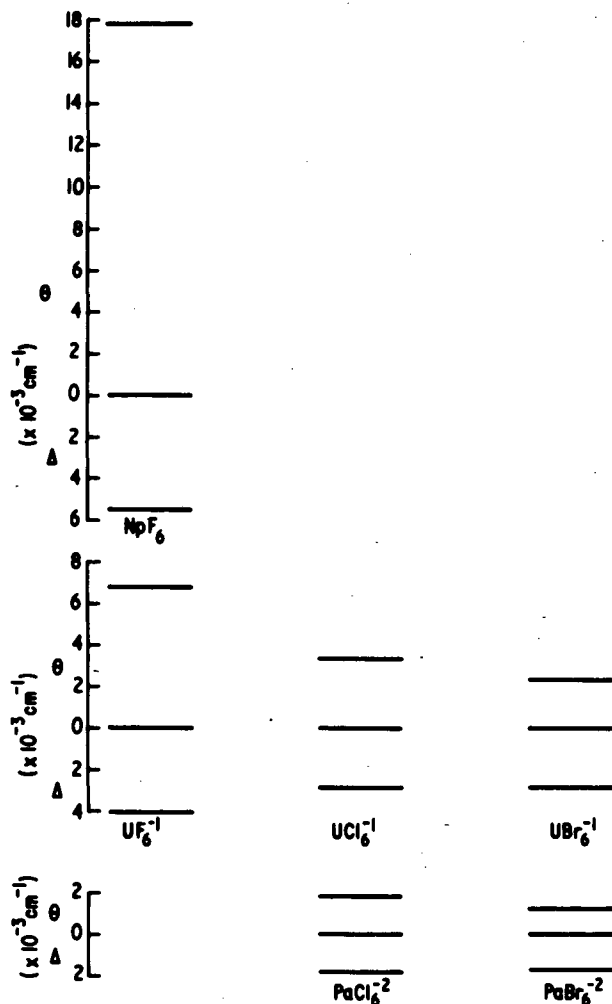


Fig. 3. Ligand field splittings  $\Delta$  and  $\theta$  for various octahedral  $5f^1$  compounds.

XBL 743-514

Equation 5 states the total ligand field splitting ( $\theta + \Delta$ ) depends on  $(\alpha_\pi^2 + \alpha_\sigma^2)(E_f - E_p)$ . We suggest that, similarly to the d series, this quantity could vary in such a way so as to explain the gross variations of  $(\Delta + \theta)$  as the halide ion is changed and the metal ion oxidation state is kept fixed.

Let us now consider the changes in  $\theta$  and  $\Delta$  as the metal ion is fixed but the halide ion changes. The fact that  $\theta$  changes much more rapidly than  $\Delta$  suggests from Eq. 5 that  $(\alpha_\pi^2 + \alpha_\sigma^2 - \alpha_\pi^2)$  changes much more rapidly than  $\alpha_\pi^2$ . Now  $\alpha_\pi$  and  $\alpha_\sigma$  both involve the same ligand orbital so we expect changes in  $\pi$  bonding to leave  $\theta$  relatively unaffected since these effects will tend to cancel. The quantity  $\Delta$  will depend directly on  $\pi$  bonding effects. Experimentally, however,  $\Delta$  does not vary drastically compared to  $\theta$ . It appears therefore, that there are large changes in  $\sigma$  bonding as the

halide ion is changed and the  $\pi$  bonding is relatively unaffected. Jørgenson et al.<sup>15</sup> have suggested that  $\sigma$  antibonding effects could adequately explain ligand field splittings in f electron compounds. Our results again point out the importance of  $\sigma$  antibonding.

Further work is now in progress to extend the number of compounds and the spectral range for which observations have been made, to perform accurate magnetic measurements on all the compounds, and to use the molecular orbital theory to fit the observations.

Part of this work was done while one of us (N.E.) was a visitor at the Physical Chemistry Laboratory, Oxford University. He would like to thank the Laboratory for its hospitality.

#### Footnotes and References

1. J. Own and J. H. M. Thornley, Rept. Prog. Phys. **29**, 675 (1966).
2. J. C. Eisenstein and M. H. L. Pryce, Proc. Roy. Soc. (London) **A255**, 181 (1960).
3. J. H. M. Thornley, Proc. Phys. Soc. (London) **88**, 325 (1966).
4. H. G. Hecht, W. B. Lewis, and M. P. Eastman, Chemical Dynamics, Vol. 21 in *Advances in Chemical Physics*, J. O. Hirschfelder and D. Henderson, Editors (Wiley - Interscience, New York, 1971), p. 351.
5. J. L. Ryan, J. Inorg. Nucl. Chem. **33**, 153 (1971).
6. P. Rigney, J. Dianoux, and P. Plurien, J. Phys. Chem. Solids **32**, 1175 (1971).
7. J. Selbin, J. D. Ortego, and G. Gritzner, Inorg. Chem. **7**, 976 (1968).
8. D. Brown and P. J. Jones, J. Chem. Soc. (A) **719** (1967).
9. D. Brown, J. F. Edwards and B. Whittaker, AERE-R7480 (1973).
10. B. G. Wybourne, *Spectroscopic Properties of Rare Earths* (John Wiley and Sons, Inc., New York, 1965).
11. There are a number of different conventions used for the crystal field parameters. We believe the formulation which is used in the theory of tensor operators is the most convenient. For the  $f^1$  system the "operator equivalent" convention has been used most frequently in the literature and the relationship is given by the equations
 
$$A_4^0 \langle r^4 \rangle = B_0^4 / 8; \quad A_6^0 \langle r^6 \rangle = B_0^6 / 16$$

12. J. D. Zxe, M. J. Stapleton and C. D. Jefferies, *Phys. Rev.* 121, 1630 ( 961).
13. C. A. Hutchinson, Jr. and B. Weinstock, *J. Chem. Phys.* 32, 56 (1960).
14. J. D. Axe and G. Burns, *Phys. Rev.* 152, 331 ( 961).
15. C. K. Jørgenson, R. Pappalardo and H. Schmidtke, *J. Chem. Phys.* 39, 422 (1963).

AN ELEMENTARY MOLECULAR ORBITAL CALCULATION ON  
 $U(C_8H_8)_2$  AND ITS APPLICATION TO THE ELECTRONIC  
STRUCTURES OF  $U(C_8H_8)_2$ ,  $Np(C_8H_8)_2$ , and  $Pu(C_8H_8)_2$

R. G. Hayes\* and N. Edelstein

Since the first preparation of the cyclooctatetraene compounds of actinide elements, <sup>1a</sup> their electronic structure has been the object of considerable interest. Thus far, cyclooctatetraene compounds of Th, <sup>1a</sup> U, <sup>1a</sup> Np, <sup>1b</sup> and Pu <sup>1b</sup> have been reported, as have compounds with some substituted cyclooctatetraenes. <sup>2</sup> These compounds have been given the trivial names of -cene, <sup>1a</sup> by supposed analogy with the iron series cyclopentadienes, so one speaks of uranocene, neptunocene, and so on.

In the original report on these compounds, a qualitative discussion of their electronic structure was given, in which they were supposed to be similar to the iron series bis(cyclopentadienyl) compounds, except that the orbitals of the rings and of the metal which were involved in bonding had one more node in going around the figure axis of the molecule. These were the  $e_2$  orbitals of the cyclooctatetraene rings and the  $f_{\pm 2}$  orbitals of the metal. Increased hydrolytic stability of  $U(C_8H_8)_2$ , over ionic cyclooctatetraenides, was offered as evidence for the proposed covalency of the compounds.

A number of physical measurements on cyclooctatetraene compounds have subsequently appeared, which provide information about the electronic structure of the compounds. Firstly, crystallographic work has shown the compounds to be sandwich compounds, and  $U(C_8H_8)_2$  has  $D_{8h}$  symmetry. <sup>3</sup> The magnetic susceptibilities of  $U(C_8H_8)_2$ ,  $Np(C_8H_8)_2$ , and  $Pu(C_8H_8)_2$  have been reported. <sup>1b</sup> Mössbauer absorption of  $Np(C_8H_8)_2$  has been reported. <sup>1</sup>

Finally, the <sup>1</sup>H nmr of uranocene and of 1, 3, 5, 7, 1', 3', 5', 7' -octamethyluranocene has been studied <sup>2, 4</sup> and the chemical shifts have been resolved into contact and pseudocontact contributions.

The integration of these data into a model of the electronic structure of the compounds has been only moderately successful. The Mössbauer isomer shift is most easily inter-

preted and suggest that the charge on Np in neptunocene is about +3.5. <sup>1b</sup> The susceptibility data from  $U(C_8H_8)_2$ ,  $Np(C_8H_8)_2$ , and  $Pu(C_8H_8)_2$  between 4.2 and 45° K have been fit to the Curie-Weiss law.  $Pu(C_8H_8)_2$  is diamagnetic.  $U(C_8H_8)_2$  and  $Pu(C_8H_8)_2$  have magnetic moments of 2.43 and 1.81 BM, respectively. These data have been interpreted by assuming that the interaction of the metal with the rings may be described using a weak axial crystal field, a crystal field weak enough to leave J a good quantum number. <sup>1b</sup> This accounts for the diamagnetism of  $Pu(C_8H_8)_2$ , since a crystal field which leaves  $J_z = \pm 4$  lowest in  $U(C_8H_8)_2$  and  $J_z = \pm 9/2$  lowest in  $Np(C_8H_8)_2$  leaves  $J_z = 0$  lowest in  $Pu(C_8H_8)_2$ . The magnetic moments associated with the proposed ground states of  $U(C_8H_8)_2$  and  $Np(C_8H_8)_2$  are of the right magnitude, but rather large (3.20 and 3.27 BM, respectively, assuming LS coupling).

The nmr data, interpreted with the aid of the crystal structure to calculate the pseudocontact shifts, suggest that the contact shifts arise from spin density in the cyclooctatetraenide  $\pi$  orbitals, because the ring proton and methyl proton shifts are similar in magnitude but opposite in sign. The shifts correspond, however, to negative spin density in the ligand  $\pi$  orbitals, so a simple interpretation in terms of bonding is not possible. One finds a number of mechanisms discussed in the literature which might lead to such a distribution in spin density. Some of these are considered in Ref. 3. A rather strong covalency involving the  $f_{\pm 2}$  orbitals, coupled with strong spin polarization by unpaired electrons in the non-bonding metal orbitals, could be responsible for the effect, but so might polarization of orbitals composed of ring  $\pi$  orbitals and metal 6d orbitals.

As a next step in the analysis of the electronic structure of such compounds, we have performed simple molecular orbital calculations in an attempt to estimate the energies and the compositions of the one electron orbitals

derived from metal *f* orbitals. We have used these results to calculate the magnetic moments of the various ions in order to see if the calculations yield plausible results. We have performed these calculations two ways. Firstly, we have estimated the ground states, including interelectronic repulsion and spin-orbit coupling in a minimal way. Secondly, we have done relatively exact calculations in which we have approximated the molecular interactions by a crystal field.

The results appear in Table I. Interelectronic repulsion parameters and spin-orbit constants used were:  $U^{+4}$ ,  $F_2 = 206.1 \text{ cm}^{-1}$ ,  $F_4 = 30.09 \text{ cm}^{-1}$ ,  $F_6 = 4.516 \text{ cm}^{-1}$ ,  $\zeta = 1638.0 \text{ cm}^{-1}$ ;  $Np^{+4}$ ,  $F_2 = 211.8 \text{ cm}^{-1}$ ,  $F_4 = 25.30 \text{ cm}^{-1}$ ,  $F_6 = 2.96 \text{ cm}^{-1}$ ,  $\zeta = 1985 \text{ cm}^{-1}$ ;  $Pu^{+4}$ ,  $F_2 = 242.9 \text{ cm}^{-1}$ ,  $F_4 = 34.535 \text{ cm}^{-1}$ ,  $F_6 = 3.911 \text{ cm}^{-1}$ ,  $\zeta = 2429.0$ .<sup>7</sup> The LS basis states used for the  $5f^2$  and  $5f^3$  configurations were complete. For the  $5f^4$  configuration we included only the quintets and triplets.

Table I. Properties Predicted for Actinocene Compounds Using Wolfsberg-Helmholz Level Scheme and an Accurate Inclusion of Spin-Orbit Coupling and Interelectronic Repulsion.<sup>a</sup>

$U(C_8H_8)_2$			$Np(C_8H_8)_2$			$Pu(C_8H_8)_2$		
$J_z$	$E, \text{ cm}^{-1}$	$g_{  }$	$J_z$	$E, \text{ cm}^{-1}$	$g_{  }$	$J_z$	$E, \text{ cm}^{-1}$	$g_{  }$
$\pm 3$	-1667.3	4.479	$\pm 5/2$	-1224.1	3.779	$\pm 0$	-3203.7	0
$\pm 2$	-464.0	3.394	$\pm 3/2$	-879.1	1.463	$\pm 1$	-2331.0	2.944
$\pm 4$	-223.2	7.040	$\pm 9/2$	-269.0	6.791	$\pm 3$	-1630.1	2.694
0	192.4	0	$\pm 7/2$	-208.6	6.219	$\pm 4$	-565.6	5.741
$\pm 1$	120.8	1.754	$\pm 1/2$	276.5	0.327 <sup>b</sup>	$\pm 2$	171.5	4.796

<sup>a</sup>Unless noted,  $g_{\perp} = 0$ . <sup>b</sup> $g_{\perp} = 3.930$ .

The ground states shown in Table I yield the following values for  $\pi_{\text{eff}}$ :  $U(C_8H_8)_2$ , 2.24 BM;  $Np(C_8H_8)_2$ , 1.89 BM;  $Pu(C_8H_8)_2$ , 0.00 BM.

Simple molecular orbital calculations suggest that the ground electronic states of  $U(C_8H_8)_2$ ,  $Np(C_8H_8)_2$ , and  $Pu(C_8H_8)_2$  are somewhat different from those predicted by a weak crystal field model,<sup>1b</sup> which predicts ground states having  $|J_z| = 4, 9/2, 0$ , respectively. The models agree that  $Pu(C_8H_8)_2$  should be diamagnetic, as is observed. The magnetic moments are predicted somewhat more accurately by the results of the molecular orbital calculations.

The charge on the metal in  $U(C_8H_8)_2$  is calculated to be +3.17, rather less than that deduced for  $Np(C_8H_8)_2$ . The electron donation to the metal is due almost entirely to the filled  $\pm 2_1$  states, as Streitwieser's original model predicted.<sup>1a</sup> Charges were calculated in the usual way, dividing up the overlap charge equally. The use of the same molecular orbitals for  $Np(C_8H_8)_2$  and  $Pu(C_8H_8)_2$  as calculated for  $U(C_8H_8)_2$  would give these metals the same charge.

The electronic structure predicted by the molecular orbital model is certainly consistent with a mechanism in which proton hyperfine

interaction is produced by spin polarization, but one could hardly say that the calculations demonstrate the importance of this mechanism. The mechanism would require polarization of the filled  $\pm 2_1$  orbitals, which are delocalized, by the two electrons in the  $\pm 1_3$  and  $\pm 3_1$  orbitals, which are localized on the metal. The observed proton coupling constants in these compounds are around 1 MHz,<sup>2</sup> which corresponds to a spin density of 0.0167 per carbon  $\pi$  orbital, or a total spin density of 0.1336 per molecular orbital. This is large, but not entirely unreasonable, since the orbital to be admixed by the exchange polarization,  $\pm 2_3$ , is only 1.2 eV away.

The molecular orbital calculations seem to have isolated the feature of the electronic structure of the actinocenes which is responsible for their ground states, the fact that the one-electron orbitals lie in two groups with  $\pm 1, \pm 3$  below  $\pm 2, 0$ . The resulting ground state provides a reasonable interpretation of the properties observed in these compounds. It is impossible to say, however, whether or not the calculations are scaled correctly and this question will probably not be resolved until the optical spectra are assigned. On the computational side, we could readily predict either a larger or a smaller scale factor by changing the details of the calculation in a

reasonable way. The overlaps are calculated for a +4 metal ion and uncharged C, so are probably too small. On the other hand, the assumed VSIP for uranium (8.0 eV) may well be too large.

Much of this work was carried out while R. G. H. was a visiting faculty member in the Department of Chemistry, University of California, Berkeley, to which he is grateful for support. We wish to thank Professor A. Streitwieser, Jr., for many helpful discussions.

#### Footnotes and References

\*University of Notre Dame.

1. (a) A. Streitwieser, Jr. and U. Muller-Westerhoff, *J. Amer. Chem. Soc.* **90**, 7364

(1968); (b) D. G. Karraker, J. A. Stone, E. R. Jones, Jr., and N. Edelstein, *ibid.*, **92**, 4841 (1970).

2. A. Streitwieser, Jr., D. Dempf, G. N. LaMar, D. G. Karraker, and N. Edelstein, *J. Amer. Chem. Soc.* **93**, 7343 (1971).

3. A. Zalkin and K. M. Raymond, *J. Amer. Chem. Soc.* **91**, 5667 (1969).

4. N. Edelstein, G. N. LaMar, F. Mares, and A. Streitwieser, Jr., *Chem. Phys. Lett.*, **8**, 399 (1971).

5. E. R. Menzel and J. B. Gruber, *J. Chem. Phys.* **54**, 3857 (1971).

6. J. Conway, *J. Chem. Phys.* **41**, 904 (1964).

### PREPARATION OF DI- $\pi$ -CYCLOOCTATETRAENE COMPLEXES OF URANIUM, THORIUM, AND PLUTONIUM BY DIRECT REACTION OF THE METALS WITH CYCLOOCTATETRAENE

D. F. Starks and A. Streitwieser, Jr.

We report the practical preparation of the di- $\pi$ -cyclooctatetraene complexes of uranium, thorium, and plutonium by direct reaction of the finely divided metals with cyclooctatetraene. These organometallic sandwich compounds have been prepared previously the reaction of cyclooctatetraene dianion with  $\text{UCl}_4$ ,<sup>1</sup>  $\text{ThCl}_4$ ,<sup>2</sup> and  $[(\text{C}_2\text{H}_5)_4\text{N}]_2\text{PuCl}_6$ ,<sup>3</sup> respectively, in accord with the common preparation of metallocene compounds by reaction of a ligand anion with a metal salt.

Previous preparations of metallocenes from the free metal include the treatment of magnesium<sup>4</sup> or iron<sup>5</sup> with cyclopentadiene at 300-600° to produce  $\text{Mg}(\text{C}_5\text{H}_5)_2$  and  $\text{Fe}(\text{C}_5\text{H}_5)_2$ , respectively, in reactions that may require the prior formation of cyclopentadienyl salts with liberation of hydrogen. A more direct transition metal analogy to our synthesis is the preparation of dibenzenechromium,  $\text{Cr}(\text{C}_6\text{H}_6)_2$ , in centigram amounts by the co-condensation of vapors of chromium and benzene onto a cold surface.<sup>6</sup>

The present experiments made use of pyrophoric uranium prepared from uranium hydride as described by Seaborg and Katz.<sup>7</sup> Several cycles of formation and decomposition of the hydride gave a finely divided reactive metal.

Reactions were generally run in sealed Pyrex tubes with care taken to exclude air and water. Uranium hydride was formed and de-

composed on a vacuum line, and dried and degassed cyclooctatetraene was condensed into an intermediate volumetrically calibrated tube and then onto the uranium. The Pyrex tube containing the uranium-cyclooctatetraene mixture was sealed off and heated in a tube furnace. Yields of  $\text{U}(\text{C}_8\text{H}_8)_2$  were determined by triturating the sample with tetrahydrofuran under an inert atmosphere and measuring the absorbance of the 615-nm peak. The presence of uranocene was established unambiguously by the characteristic cascade of bands in the 600-700-nm region.<sup>1</sup> The reaction could be run with either uranium or cyclooctatetraene as the limiting reagent. The highest yield observed, 57%, was obtained in an experiment with excess uranium at 150° for 2.5 hr. The product was also isolated by sublimation from the crude reaction mixture.

An interesting and significant feature of this preparation is the apparent catalytic effect of traces of mercury. Yields were low in the complete absence of mercury; the presence of a mercury manometer on the vacuum line is sufficient to provide the catalytic effect. One especially noteworthy feature of this effect is that previous studies of the mercury-uranium system<sup>8</sup> indicate that their mutual solubility is very small.

The analogous thorium compound di- $\pi$ -cyclooctatetraenethorium(IV) or thorocene<sup>2</sup> was formed in the same fashion via heating finely divided thorium metal, prepared from



thorium hydride, with cyclooctatetraene at 150°. Due to its relative insolubility the thorocene formed was characterized by placing the reaction product inside a quartz cuvette and subliming a thin film of thorocene on the walls of the cuvette. The thorocene isolated in this manner showed a uv spectrum identical with that of a sublimed film of thorocene prepared from ThCl<sub>4</sub> and K<sub>2</sub>C<sub>8</sub>H<sub>8</sub> ( $\lambda_{\text{max}}$  at 275 and 333 nm). Yields were not determined in the thorium reaction although they appear to be generally lower than in the uranium reaction.

A similar procedure was used with 1.5 mmol of plutonium, <sup>239</sup>Pu. A single small chunk was converted to finely divided metal by several cycles of hydride formation and decomposition and was treated with 0.30 mmol of dried and degassed cyclooctatetraene at 160° for 15 min in the absence of mercury. A red sublimate resulted which had the spectrum reported for Pu(C<sub>8</sub>H<sub>8</sub>)<sub>2</sub>.<sup>3</sup>

The present preparations provide a dramatic demonstration of the thermodynamic stability of the actinide cyclooctatetraene complexes. Treatment of pyrophoric uranium with cyclopentadiene under the same conditions used to form uranocene failed to produce any detectable amounts of the known compounds U(C<sub>5</sub>H<sub>5</sub>)<sub>3</sub><sup>9</sup> or U(C<sub>5</sub>H<sub>5</sub>)<sub>4</sub>.<sup>10</sup>

Further studies are under way concerning this direct reaction. Experiments are in progress employing other actinide metals and substituted cyclooctatetraenes.

We thank Dr. N. Edelstein and Dr. T. Parsons for the use of thorium and plutonium metals. This work was supported in part by National Science Foundation Grant No. GP-31803.

#### Footnotes and References

1. A. Streitwieser, Jr. and U. Muller-Westerhoff, *J. Amer. Chem. Soc.* **90**, 7364 (1968); A. Streitwieser, Jr., U. Muller-Westerhoff, G. Sonnichsen, F. Mares, D. G. Morrell, K. O. Hodgson, and C. A. Harmon, *J. Amer. Chem. Soc.* submitted for publication.
2. A. Streitwieser, Jr. and N. Yoshida, *J. Amer. Chem. Soc.* **91**, 7528 (1969).
3. D. G. Karkaker, J. A. Stone, E. R. Jones, Jr., and N. Edelstein, *J. Amer. Chem. Soc.* **92**, 4841 (1970).
4. W. A. Berber, *J. Inorg. Nucl. Chem.* **4**, 373 (1957).
5. S. A. Miller, J. A. Tebboth, and J. F. Tremaine, *J. Chem. Soc.* 632 (1952).
6. P. L. Timms, *Chem. Commun.* 1033 (1969); *J. Chem. Educ.* **49**, 782 (1972).
7. G. T. Seaborg and J. J. Katz, *The Actinide Elements* (McGraw-Hill, New York, 1954), p. 138 ff.
8. A. F. Messing and O. C. Dean, ORNL-2871, Oak Ridge National Laboratory, Oak Ridge, Tenn (1969); Y. Kobayashi and T. Ishimori, *J. Inorg. Nucl. Chem.* **31**, 981 (1969).
9. B. Kanellakopoulos, E. O. Fischer, E. Dornberger, and F. Baumgartner, *J. Organometal. Chem.* **24**, 507 (1970).
10. E. O. Fischer and Y. Hristidu, *Z. Naturforsch B17*, 275 (1962).

#### DI- $\pi$ -CYCLOOCTATETRAENEPROTACTINIUM

D. F. Starks, T. C. Parsons, A. Streitwieser, Jr.,  
and N. Edelstein

Protactinium (at. no. 91) lies between thorium and uranium in the periodic table. It shows a similarity to these elements in having a common +4 oxidation state but the lone 5f electron remaining in this oxidation state is readily lost to give a +5 oxidation state in many compounds. Only one organometallic compound of protactinium has been reported, tetrakis (cyclopentadienyl)protactinium(IV).<sup>1</sup> Consequently, there is a special interest in the preparation of di- $\pi$ -cyclooctatetraeneprotactinium; this compound is expected to be a D<sub>8h</sub>

sandwich complex by analogy with the uranium<sup>2,3</sup> and thorium<sup>4,5</sup> compounds.

#### Experimental

All work involving Pa was done in negative pressure containment glove boxes. Air and water sensitive materials were handled in a rebuilt argon-atmosphere glove box or in a vacuum line housed in a glove box. All solvents were carefully dried and degassed prior to use. Milligram amounts of Pa materials

were weighed on a Cahn Gram Electrobalance with a remote weighing assembly inside an argon glove box.

**Ligands.** A solution of  $K_2C_8H_8$  was prepared as described<sup>2,3</sup> previously by direct reaction of cyclooctatetraene with finely divided potassium in THF. Dry  $K_2C_8H_8$  (CAUTION: Violently pyrophoric, exploded on contact with oxygen) was obtained after vacuum transfer of solvent and was sealed in glass ampoules. The magnesium salt,  $MgC_8H_8$ , was obtained as a precipitate in the reaction between  $MgBr_2$  and  $K_2C_8H_8$  in THF.<sup>6</sup> A light green material was obtained after filtration and washing with fresh THF.

**Protactinium Starting Materials.** An aqueous HF solution of Pa salts was treated dropwise with concentrated ammonium hydroxide to precipitate milligram amounts of hydrated Pa oxide. After centrifugation and washing, the Pa oxide was allowed to air dry for 72 hr to form a ball which could be transferred readily. Protactinium pentachloride was prepared from the hydrated oxide through reaction with thionyl chloride at 400°.<sup>7</sup> Protactinium tetrachloride was obtained through the reduction of  $PaCl_5$  with aluminum powder.<sup>8</sup>

All Pa starting materials were routinely identified through x-ray powder pattern techniques prior to use. Thorium and uranium tetrafluorides were obtained from Research Organic/Inorganic and used without further purification.

**Di- $\pi$ -Cyclooctatetraeneprotactinium.** A dilute solution of 1.5 mg (4.0  $\mu$ mol) of protactinium tetrachloride in 15 ml of tetrahydrofuran was mixed under argon with 1.5 mg (8.2 mol) of dry  $K_2C_8H_8$ . The reaction mixture was transferred to the vacuum line, and the THF was stripped off. After evacuation to less than  $10^{-5}$  Torr, the bottom of the reaction flask was heated with a soft blue flame. A golden yellow sublimate was obtained which was characterized by the x-ray powder pattern as  $Pa(C_8H_8)_2$ .

In one experiment with  $PaCl_5$  in a more concentrated solution of THF, polymerization of the solvent rapidly occurred to a viscous mass apparently because of Pa radiation.

**Formation of  $U(C_8H_8)_2$  and  $Th(C_8H_8)_2$  from the Tetrafluorides.** A mixture of 14 mg (0.045 mmol) of uranium tetrafluoride and 13 mg (0.10 mmol) of dry  $MgC_8H_8$ , ground together in a mortar and pestle, was evacuated to  $10^{-6}$  Torr. Reaction and concomitant sublimation of uranocene was effected through gentle heating with a soft blue flame. The resultant 1.4% yield of uranocene sublimate was identified through its characteristic cascade of absorp-

tion bands in the 600-700 nm region. Thorium tetrafluoride was allowed to react with  $MgC_8H_8$  in the same manner and produced a sublimate of thorocene,  $Th(C_8H_8)_2$ , which was identified through its x-ray powder spectrum. One attempt to prepare the protactinium compound in an analogous fashion did not succeed, probably because the sample of protactinium tetrafluoride used was impure and could not be completely characterized.

**Powder Pattern Techniques.** X-ray powder patterns were obtained using a 57.3 mm Debye-Scherrer camera modified for easy loading of long capillaries. A Jarrell-Ash Microfocus x-ray source was employed using  $Cu K_\alpha$  radiation with Ni filter. A Norelco film reader was employed with a vernier scale readable to 0.05 mm. Films were uncorrected for shrinkage which was determined to be less than 0.05 mm.

Two different Pa  $(C_8H_8)_2$  samples were photographed and were found to be identical within experimental error. Each film contained eleven reflections and was measured twice. The reflections could be indexed by comparison with the calculated powder patterns for  $U(C_8H_8)_2$  and  $Th(C_8H_8)_2$ .<sup>9,10</sup> The resultant four sets of data were fitted by a least squares refinement to the lattice constant of a monoclinic unit cell.<sup>11</sup>

## Results and Discussion

The reaction of stoichiometric amounts of  $K_2C_8H_8$  and  $PaCl_4$  resulted in a golden yellow sublimate which the x-ray powder pattern showed to be  $Pa(C_8H_8)_2$ . The average values of the observed  $Pa(C_8H_8)_2$  reflections are compared with the calculated values for the thorium and uranium analogues in Table I. The absence of unidentified reflections indicates that this sublimate is pure  $Pa(C_8H_8)_2$ . Table II shows the lattice constants of  $Pa(C_8H_8)_2$  compared with those obtained from single crystal studies on the thorium and uranium analogues.

Powder pattern analysis of the unsublimable white residue from the reaction of  $PaCl_4$  with  $K_2C_8H_8$  demonstrated the presence of KCl. Consequently, the net reaction appears, as expected, to be



The high radioactivity of protactinium and the small amount of material available unfortunately hinders further study of the chemistry of the compound. However, one of the significant aspects of the complex is expected to be the electronic spectrum. With a single 5f electron this spectrum should be interpretable and should provide evidence concerning electronic structure. This research is currently in progress.

Table I. Partial powder pattern data for di- $\pi$ -cyclooctatetraeneactinides.

<u>h</u> <u>k</u> <u>l</u>	$U(C_8H_8)_2^a$		$Pa(C_8H_8)_2^b$		$Th(C_8H_8)_2^a$	
	<u>2<math>\theta</math></u>	<u>Int.</u>	<u>2<math>\theta</math></u>	<u>Int.</u>	<u>2<math>\theta</math></u>	<u>Int.</u>
0 1 1	13.20	10.0	13.27 (0.04) <sup>c</sup>	S <sup>d</sup>	13.06	10.0
-1 0 1	14.09	6.0	14.14 (0.04)	M	14.13	5.8
1 1 0	16.24	6.1	16.19 (0.02)	S	16.19	6.0
1 0 1	16.25	3.1			16.20	3.0
0 0 2	16.88	2.6	16.87 (0.04)	M	16.75	2.6
0 2 0	20.38	1.3	20.26 (0.07)	M-	20.14	1.3
-1 1 2	22.05	2.4	21.99 (0.07)	M-	21.97	2.4
-1 2 1	24.86	2.5	24.77 (0.03)	M-	24.69	2.5
1 1 2	24.88	1.1			24.70	1.1
0 1 3	27.44	1.4	27.47 (0.03)	W+	27.21	1.3
-2 1 1	27.57	1.5			27.62	1.4
2 1 1	29.91	1.6	29.95 (0.06)	W+	29.87	1.6
1 0 3	30.22	1.1			30.00	1.1
0 3 1	31.96	1.6	31.84 (0.06)	W+	31.58	1.6
2 2 0	32.82	1.4	32.84 (0.06)	W+	32.72	1.4
2 0 2	32.83	1.1			32.74	1.1

<sup>a</sup>Calculated (Ref. 9) from the reported structure (Ref. 10).

<sup>b</sup>Average values from four films.

<sup>c</sup>Maximum deviation from the average.

<sup>d</sup>Estimated intensities; S = strong, M = medium, W = weak.

Table II. Lattice constants for di- $\pi$ -cyclooctatetraeneactinides.

Lattice Parameters	$U(C_8H_8)_2^a$	$Pa(C_8H_8)_2$	$Th(C_8H_8)_2^a$
a, Å	7.084 (0.003) <sup>b</sup>	7.09 (0.02) <sup>b</sup>	7.0581 (0.0011) <sup>b</sup>
b, Å	8.710 (0.003)	8.75 (0.02)	8.8192 (0.0017)
c, Å	10.631 (0.005)	10.62 (0.02)	10.7042 (0.0018)
$\beta$ , deg	98.75 (0.03)	98.5 (0.2)	98.44 (0.03)

<sup>a</sup>Ref. 11.

<sup>b</sup>Estimated Standard Deviations.

During a preliminary preparation of  $Pa(C_8H_8)_2$  by reaction of  $PaCl_4$  with  $K_2C_8H_8$ , an excess of the latter compound was used.

The product sublimate contained Pa as demonstrated by its pronounced radioactivity and the presence of  $Pa(C_8H_8)_2$  bands in the x-ray

powder pattern. However, this pattern contained additional intense bands which were subsequently identified as belonging to  $K_2C_8H_8$ . Independent experiments showed that  $K_2C_8H_8$  has substantial volatility and does give a yellow sublimate. The gas phase structure of  $K_2C_8H_8$  is probably that of a planar cyclooctatetraene dianion ring with a potassium cation centered above and below the ring plane.

In the course of these studies we sought a solvent-free preparation of di- $\pi$ -cyclooctatetraeneactinides that could be adapted to protactinium. The direct reaction of the finely divided metal with cyclooctatetraene provides one such route<sup>12</sup> but pure protactinium metal is difficult and laborious to prepare.<sup>13</sup> The recent preparation of cyclooctatetraenemagnesium<sup>6</sup> as a non-volatile solid gave impetus to another preparation. A mixture of solid  $MgC_8H_8$  with either  $UF_4$  or  $ThF_4$  gave on heating under vacuum a sublimate in low yield of the corresponding di- $\pi$ -cyclooctatetraeneactinide. This method promised to be a useful route to such sandwich compounds despite the low yield, because the product is isolated directly as a pure sublimate. It should apply to  $PaF_4$  but the single experiment tried thus far did not succeed. The small sample of protactinium fluoride that we had available was black and may have contained acidic impurities.

The present preparation of  $Pa(C_8H_8)_2$  completes the isostructural series of di- $\pi$ -cyclooctatetraene complexes with the lower actinides, Th, U, Np,<sup>14</sup> and Pu.<sup>14</sup> Analogous compounds of the higher actinides americium and curium have not yet been reported but would be expected to be similar to the lanthanide complexes,  $[Ln(C_8H_8)_2]K$  ( $Ln = Y, La, Ce, Pr, Nd, Sm, Gd, Tb$ ),<sup>15</sup> because of the predominance of the +3 oxidation state in these elements.

Part of this work was performed under the auspices of the U. S. Atomic Energy Commission; part was supported by NSF grant No. GP-31803. We are pleased to acknowledge helpful discussions with Professors G. T. Seaborg, K. N. Raymond, N. Bartlett and Dr. A. Zalkin.

#### References

1. F. Baumgaertner, E. O. Fischer, B.

Kanellakopoulos and P. Lauberau, *Angew. Chem., Int. Ed. Engl.* **8**, 202 (1969).

2. A. Streitwieser, Jr. and U. Muller-Westerhoff, *J. Amer. Chem. Soc.* **90**, 7364 (1968).

3. A. Streitwieser, Jr., U. Muller-Westerhoff, G. Sonnichsen, F. Mares, D.G. Morrell, K. O. Hodgson and C.A. Harmon, *J. Amer. Chem. Soc.* **95**, 0000 (1973).

4. A. Streitwieser, Jr. and N. Yoshida, *J. Amer. Chem. Soc.* **91**, 7528 (1969).

5. J. Goffart, J. Fuger, B. Gilbert, B. Kanellakopoulos, and G. Duyckaerts, *Inorg. Nucl. Chem. Lett.* **8**, 403 (1972).

6. H. Lehmkuhl, S. Kintopf, and K. Mehler, *J. Organometal. Chem.* **46**, C1 (1972).

7. D. Brown and P. J. Jones, *J. Chem. Soc. (A)*, 874 (1966).

8. D. Brown and P. J. Jones, *J. Chem. Soc. (A)*, 719 (1967).

9. Deane K. Smith, LBL Report UCRL-7196 (1963).

10. A. Avdeef, K. N. Raymond, K. O. Hodgson, and A. Zalkin, *Inorg. Chem.* **11**, 1083 (1972).

11. Donald E. Williams, Ames Laboratory Report IS-1052 (1964).

12. D. F. Starks and A. Streitwieser, Jr., *J. Amer. Chem. Soc.* **95**, 3423 (1973).

13. R. L. Dod (Ph.D. Thesis), University of California, Lawrence Berkeley Laboratory Report LBL-659 (1972).

14. D. G. Karraker, J. A. Stone, E. R. Jones, Jr., and N. Edelstein, *J. Amer. Chem. Soc.* **92**, 4841 (1970).

15. K. O. Hodgson, F. Mares, D. F. Starks and A. Streitwieser, Jr., *J. Amer. Chem. Soc.* **95**, 0000 (1973).

### THE PREPARATION, CRYSTALLOGRAPHIC AND SPECTRAL PROPERTIES OF THE OCTAHEDRAL HEXAFLUOROPROTACTINATE (VI), $(NET_4)_2PaF_6$

D. Brown,\* B. Whittaker,\* and N. Edelstein

As part of a detailed study<sup>1</sup> of the trends in bonding of  $5f^1$  compounds we recently reported optical spectral data for the octahedral compounds  $(NET_4)_2PaCl_6$  and  $(NET_4)_2PaBr_6$ , to-

gether with an analysis of data available for certain 6-co-ordinate hexahalogenouranates (V) and neptunium hexafluoride. The trends in the ligand field parameters,  $\theta$  and  $\Delta$ , were ex-

plained qualitatively in terms of molecular orbital theory with large variations in  $\sigma$  bonding dominating the total ligand field splitting as the halide ion was varied with a fixed metal ion oxidation state. At that time the only protactinium (IV) fluoro-complexes known were<sup>2</sup>  $(\text{NH}_4)_4\text{PaF}_8$ , a series of the type  $\text{M}^{\text{I}}\text{Pa}_6\text{F}_{31}$  ( $\text{M}^{\text{I}} = \text{Na}, \text{K}$  and  $\text{Rb}$ ), all of which contain 8-co-ordinate Pa(IV) ions, and  $\text{LiPaF}_5$ , in which the Pa(IV) ion is 9-co-ordinate. Indeed, although a variety of actinide (IV) fluorocomplexes of the types  $\text{M}^{\text{I}}\text{M}^{\text{IV}}$  and  $\text{M}^{\text{II}}\text{M}^{\text{IV}}\text{F}_6$  ( $\text{M}^{\text{I}} =$  univalent cation,  $\text{M}^{\text{II}} =$  divalent cation, and  $\text{M}^{\text{IV}} =$  an actinide element) were known,<sup>2</sup> the available structural information indicated that the actinide (IV) ions were either 8- or 9-co-ordinate. Thus, no 6-co-ordinate actinide fluoro-complexes had been identified although structural and/or optical spectral data were not available for all the compounds (e. g.,  $\delta\text{-Na}_2\text{UF}_6$ ,  $\beta\text{-}$  and  $\delta\text{-(NH}_4)_2\text{UF}_6$ , and  $\text{Cs}_2\text{UF}_6$ ).

As a preliminary to the attempted preparation of octahedral Pa(IV) fluorocomplexes we had studied the reaction between  $\text{UF}_4$  and an excess of  $\text{NEt}_4$  in water, which yields only  $\text{NEt}_4\text{UF}_5$ , when Dr. J. L. Ryan (Batelle Northwest) informed us<sup>3</sup> that he had prepared octahedral complexes of the type  $(\text{NEt}_4)_2\text{M}^{\text{IV}}\text{F}_6$  ( $\text{M}^{\text{IV}} = \text{U}, \text{Np}$ , and  $\text{Pu}$ ) by reactions in propylene carbonate. Using a slightly modified procedure with the same solvent we have now prepared  $(\text{NEt}_4)_2\text{PaF}_6$  in two crystal modifications and report here the spectral and crystallographic properties of both modifications together with some of their chemical properties. The optical spectra indicate that both forms contain octahedrally co-ordinated Pa(IV) ions and are interpreted in terms of two ligand field parameters,  $\theta$  and  $\Delta$ , and the spin orbit coupling constant  $\zeta$ , and the resulting values are compared with those available for other octahedral  $5f^1$  compounds. X-ray diffraction and infrared results are also provided for  $(\text{NEt}_4)_2\text{UF}_6$  which has only been obtained in one crystal form, that being isostructural with  $\beta\text{-(NEt}_4)_2\text{PaF}_6$ .

#### Crystallographic and Chemical Properties

$\beta\text{-(NEt}_4)_2\text{PaF}_6$  crystallizes from reasonably concentrated solutions in oxygen-free propylene carbonate, e. g., 0.14 to 0.2 g  $^{231}\text{Pa}$  ml<sup>-1</sup>, on the addition of an equal volume of acetone. The second crop of crystals, obtained following the addition of an additional larger volume of acetone, is invariably  $\alpha\text{-(NEt}_4)_2\text{PaF}_6$ . The  $\beta$ -modification has also been obtained as the product of a single reaction in oxygen-free methyl cyanide. This product, however, was not pure and the use of this solvent was not pursued in view of the decomposition of  $(\text{NEt}_4)_2\text{UF}_6$  in methyl cyanide noted by Ryan et al.<sup>3</sup> On standing at room temperature (25°C) for a period of three weeks  $\beta\text{-(NEt}_4)_2\text{PaF}_6$  transforms com-

pletely to  $\alpha\text{-(NEt}_4)_2\text{PaF}_6$ , which is apparently the most stable phase of the hexafluoroprotactinate (IV) whereas only the  $\beta$ -phase has so far been obtained for the uranium (IV) analogue. It has not been possible to reverse the  $\beta \rightarrow \alpha(\text{NEt}_4)_2\text{PaF}_6$  transformation by cooling the  $\alpha$ -phase in liquid nitrogen, nor has the  $\beta \rightarrow \alpha$  change been observed under similar conditions using freshly prepared  $\beta\text{-(NEt}_4)_2\text{PaF}_6$ , or  $\beta\text{-(NEt}_4)_2\text{UF}_6$  (cf., the  $\beta \rightarrow \alpha\text{-(NEt}_4)_2\text{ThCl}_6$  transformation which occurs on cooling in liquid nitrogen). Attempts to obtain  $\alpha\text{-(NEt}_4)_2\text{UF}_6$  by heating the  $\beta$ -phase in a sealed x-ray capillary at  $\sim 90^\circ\text{C}$  resulted in decomposition of the material, whilst crystallization from large volumes of propylene carbonate-acetone mixtures (cf., preparation of  $\alpha\text{-(NEt}_4)_2\text{PaF}_6$ ) again yielded only the  $\beta$ -phase. Our observations indicate that  $\beta\text{-(NEt}_4)_2\text{PaF}_6$  is only obtained by crystallization from concentrated solution, behaviour which is similar to that recently found<sup>4</sup> for  $\alpha\text{-U(acac)}_4(\text{acac}, \text{acetylacetonone})$ . It is possible, although not established, that the ready transformation  $\beta \rightarrow \alpha\text{-(NEt}_4)_2\text{PaF}_6$  is associated with radiation damage since no similar change occurs with  $\beta\text{-(NEt}_4)_2\text{UF}_6$  and the sample of  $\text{PaF}_4$  available contained approximately 7 years growth of the intensely radioactive  $^{231}\text{Pa}$  decay chain.

$\alpha\text{-(NEt}_4)_2\text{PaF}_6$  possesses face-centered cubic symmetry, space group  $\text{O}_h^5\text{-Fm}3\text{m}$  with  $a_0 = 13.22 \pm 0.01 \text{ \AA}$ . A partial list of indexed  $\sin^2 \theta$  values is shown in Table I together with visually estimated intensities. It is interesting to note that orthorhombic  $(\text{NEt}_4)_2\text{UCl}_6$  is reported to undergo a reversible phase change at  $94^\circ\text{C}$  to become face-centered cubic and, indeed, the x-ray powder pattern of  $\beta\text{-(NEt}_4)_2\text{UF}_6$  can be indexed on the basis of a slightly smaller orthorhombic cell than that of  $(\text{NEt}_4)_2\text{UCl}_6$  ( $a_0 = 14.23$ ,  $b_0 = 14.73$ ,  $c_0 = 13.33 \text{ \AA}$ , space group  $\text{D}_{2h}^{13}\text{-Fmmm}$ ) with the same space group. Refinement of the orthorhombic unit cell dimensions showed those originally designated  $a_0$  and  $b_0$  to be equal within experimental error, and we therefore report the corresponding tetragonal unit cell, which has  $a_0 = 12.80 \pm 0.01$  and  $c_0 = 13.54 \pm 0.01 \text{ \AA}$ . However, without single crystal data it is obviously not possible to be absolutely certain of the symmetry. A partial list of indexed  $\sin^2 \theta$  values is shown in Table II together with visually estimated intensities. Relatively poor powder patterns were obtained for  $\beta\text{-(NEt}_4)_2\text{PaF}_6$  and an insufficient number of lines could be measured accurately enough to allow a reliable calculation of the unit cell.

Both  $(\text{NEt}_4)_2\text{PaF}_6$  and  $(\text{NEt}_4)_2\text{UF}_6$  are air-sensitive compounds, the former undergoing oxidation to unidentified protactinium (IV) species, and the latter rapidly deliquescing to form a green solution. The addition of aqueous ammonia to  $(\text{NEt}_4)_2\text{PaF}_6$  results in the forma-

Table I. Partial x-ray powder diffraction of  $\alpha$ -(NEt<sub>4</sub>)<sub>2</sub>PaF<sub>6</sub>.

Sin <sup>2</sup> $\theta$ obs	Sin <sup>2</sup> $\theta$ calc	h, k, l	I <sup>a</sup>	Sin <sup>2</sup> $\theta$ obs	Sin <sup>2</sup> $\theta$ calc	h, k, l	I <sup>a</sup>
0.0104	0.0102	1, 1, 1	S	0.1463	0.1462	5, 3, 3	W+
0.0136	0.0136	2, 0, 0	M	0.1502	0.1496	6, 2, 2	W+
0.0272	0.0272	2, 2, 0	S-	0.1738	0.173	5, 5, 1	M-
0.0376	0.0374	3, 1, 1	S		0.1734	7, 1, 1	
0.0413	0.0408	2, 2, 2	M-	0.1773	0.1768	6, 4, 0	M-
0.0538	0.0543	4, 0, 0	W+	0.1908	0.1904	6, 4, 2	M-
0.0640	0.0646	3, 3, 1	M	0.2008	0.2006	5, 5, 3	M-
0.0673	0.0681	4, 2, 0	M+		0.2006	7, 1, 3	
0.0820	0.0816	4, 2, 2	M	0.2278	0.2278	7, 3, 3	W-
-.0921	0.0918	5, 1, 1	M+	0.2313	0.2312	8, 2, 0	W
	0.0918	3, 3, 3			0.2312	6, 4, 4	
0.1086	0.1088	4, 4, 0	W+	0.2442	0.2448	8, 2, 2	W-
0.1189	0.1190	5, 3, 1	M+	0.2543	0.2550	5, 5, 5	VW-
0.1222	0.1224	4, 4, 2	M-		0.2550	7, 5, 1	
	0.1224	6, 0, 0		0.2822	7, 5, 3	VW-	
0.1361	0.1360	6, 2, 0	M-	0.2827	0.2822		9, 1, 1

<sup>a</sup>Visually estimated; S, strong; M, medium; W, weak; VW, very weak.

Table II. Partial x-ray powder diffraction pattern of  $\beta$ -(NEt<sub>4</sub>)<sub>2</sub>UF<sub>6</sub>.

Sin <sup>2</sup> $\theta$ obs	Sin <sup>2</sup> $\theta$ calc	h, k, l	I <sup>a</sup>	Sin <sup>2</sup> $\theta$ obs	Sin <sup>2</sup> $\theta$ calc	h, k, l	I <sup>a</sup>
0.0104	0.0104	1, 1, 1	S	0.1165	0.1164	0, 0, 6	M-
0.0128	0.0128	0, 0, 2	M-		0.1168	3, 3, 4	
0.0143	0.0143	2, 0, 0	M-	0.1232	0.1230	5, 3, 0	M-
0.0163	0.0165	1, 0, 2	W-		0.1231	5, 1, 3	
0.0206	0.0202	1, 1, 2	W-	0.1260	0.1262	5, 3, 1	M-
0.0220	0.0213	2, 1, 1	W-	0.1306	0.1302	6, 0, 0	M-
-.0274	0.0273	2, 0, 2	S-		0.1308	2, 0, 6	
0.0289	0.0288	2, 2, 0	M+	0.1444	0.1447	6, 2, 0	M-

Table II. continuation

0.0363	{ 0.0358	3, 0, 1	M+	0.1523	{ 0.1521	5, 3, 3	W
	0.0361	3, 1, 0			{ 0.01516	5, 4, 1	
	0.0362	1, 1, 3			0.1572	0.1567	
0.0391	0.0393	3, 1, 1	S-	0.1702	0.1712	4, 3, 5	W-
0.0418	0.0418	2, 2, 2	M-	0.1747	{ 0.1743	4, 0, 6	W+
0.0477	0.0472	2, 1, 3	W-		0.1748	5, 3, 4	
					0.1749	5, 1, 5	
0.517	0.0516	0, 0, 4	W				
0.0574	0.0579	4, 0, 0	W+	0.1838	{ 0.1842	5, 5, 1	W
	{ 0.0646	4, 1, 1			0.1842	7, 1, 1	
0.0650	{ 0.0650	3, 3, 0	M+	0.1883	0.1882	6, 4, 0	W
	0.0652	3, 1, 3		0.1950	{ 0.1947	3, 1, 7	W
0.0682	0.0683	3, 3, 1	W+		0.1950	7, 2, 1	
0.0707	0.0707	4, 0, 2	M	0.2010	0.2011	6, 4, 2	W-
0.0722	0.0722	4, 2, 0	M	0.2097	0.2099	7, 3, 0	W
0.0805	{ 0.0806	2, 2, 4	M-	0.2129	0.2131	7, 3, 1	W-
	0.0808	0, 0, 5		0.2217	0.2210	7, 2, 3	VW-
0.0853	0.0852	4, 2, 2	M	0.2319	0.2317	8, 0, 0	W-
0.0875	{ 0.0870	4, 0, 3	M	0.2388	{ 0.2385	7, 4, 1	W-
	0.0879	3, 1, 4			0.2391	7, 3, 3	
0.0935	0.0936	4, 1, 3	W-	0.2465	{ 0.2462	8, 2, 0	VW-
0.0943	0.0940	5, 1, 0	W-		0.2468	6, 0, 6	
	0.0941	3, 3, 3			0.2529	0.2527	
0.0971	0.0972	5, 1, 1	M+	0.2600	{ 0.2593	8, 2, 2	W-
0.1055	0.1050	5, 2, 0	W-		0.2605	6, 6, 0	
0.1095	{ 0.1096	4, 0, 4	W				
	0.1007	2, 2, 5					

<sup>a</sup>Visually estimated; S, strong; M, medium; W, weak; VW, very weak.

tion of the characteristic, black protactinium (IV) hydroxide which, in the presence of air, turns white within minutes. Both compounds are appreciably soluble in propylene carbonate and methyl cyanide but fail to dissolve in acetone, isopentane, carbon tetrachloride and

ether. Shortly after dissolution of  $(\text{NEt}_4)_2\text{PaF}_6$  in commercial methyl cyanide (water content 0.3%) containing oxygen, a gelatinous precipitate, presumably hydrous protactinium (V) oxide, is formed. The thermal instability of  $\beta\text{-(NEt}_4)_2\text{UF}_6$  has been mentioned above; dur-

ing attempts to obtain solid state spectral data above room temperature,  $\alpha$ -(NEt<sub>4</sub>)<sub>2</sub>PaF<sub>6</sub> was observed to decompose rapidly at ~ 420K.

### Infrared and Raman Spectra

Two infrared- and three Raman-active fundamental modes of vibration are predicted by group theory for regular octahedral molecules of the type MX<sub>6</sub> belonging to the point group C<sub>h</sub>. Thus, the three gerade model  $\nu_1$  (a<sub>1g</sub>),  $\nu_2$  (e<sub>g</sub>) and  $\nu_5$  (t<sub>2g</sub>) give rise to Raman active fundamentals whilst the two t<sub>1u</sub> modes,  $\nu_3$  and  $\nu_4$ , are permitted as fundamentals in the infrared. The t<sub>2u</sub> mode,  $\nu_6$ , is totally forbidden. Two infrared modes are in fact observed for both  $\alpha$ - and  $\beta$ -(NEt<sub>4</sub>)<sub>2</sub>PaF<sub>6</sub> and for  $\beta$ -(NEt<sub>4</sub>)<sub>2</sub>UF<sub>6</sub>. These occur at 404 (vs) and 148 (m) cm<sup>-1</sup> for both modifications of (NEt<sub>4</sub>)<sub>2</sub>PaF<sub>6</sub>, and at 406 (vs) and 155 (m) cm<sup>-1</sup> for  $\beta$ -(NEt<sub>4</sub>)<sub>2</sub>UF<sub>6</sub>. A weak shoulder at 378 cm<sup>-1</sup> in the spectrum of  $\beta$ -(NEt<sub>4</sub>)<sub>2</sub>UF<sub>6</sub> may indicate

slight distortion from perfect octahedral symmetry. Our value for  $\nu_3$  is in excellent agreement with that reported by Ryan et al.<sup>3</sup> for (NEt<sub>4</sub>)<sub>2</sub>UF<sub>6</sub>. As discussed below, vibronic bands associated with both  $\nu_3$  and  $\nu_4$  are observed in the electronic spectra of the hexafluoroprotactinates (IV).

Attempts to obtain Raman data for  $\beta$ -(NEt<sub>4</sub>)<sub>2</sub>UF<sub>6</sub> have unfortunately been unsuccessful. Both the solid compound and solutions in propylene carbonate exhibit strong, broadband fluorescence. This is apparently due to impurities in tetraethylammonium fluoride since this material exhibits the same fluorescence. Repeated recrystallization of NEt<sub>4</sub>F from ethanol-acetone mixtures and treatment of propylene carbonate solutions with either activated charcoal or alumina failed to remove the fluorescence. Although it can be partially "burned out" by prolonged exposure to the Raman beam, we were still unable to reliably

Table III. Spectral results for  $\alpha$ -(NEt<sub>4</sub>)<sub>2</sub>PaF<sub>6</sub>.

$\alpha$ -(NEt <sub>4</sub> ) <sub>2</sub> PaF <sub>6</sub> at 300K			$\alpha$ -(NEt <sub>4</sub> ) <sub>2</sub> PaF <sub>6</sub> at 85K			
Band position (cm <sup>-1</sup> )	Int.	Vibrational Freq. (cm <sup>-1</sup> )	Band position (cm <sup>-1</sup> )	Int.	Vibrational Freq. (cm <sup>-1</sup> )	
$\Gamma_7 - \Gamma_8$	{	12,048	w, sh	12,084	w	+638
		11,600	m	11,593	st	+147
				(11,446) <sup>b</sup>	-	0
				11,299	st	-147
		11,111	st, b	11,111	sh	-335
$\Gamma_7 - \Gamma_8$	{	9,881	m, b	10,504	w	
				10,060	m	
		9,276	m, b	9,862	m	
$\Gamma_7 - \Gamma_7$	{	6,094	st, s	6,105	st, s	+407
		5,838	st, s	5,843	st, s	+145
		5,690	st, s	5,698	st, s	0
		5,543	m	5,552	w	-146
		5,280	w			-410

<sup>a</sup>s, sharp; st, strong; sh, shoulder; m, medium; w, weak; b, broad.

<sup>b</sup>Values in parentheses are estimated.



identify bands which could be assigned to  $\nu_1$ ,  $\nu_2$  or  $\nu_5$ .

### Electronic Spectra

Solid state transmission spectra were obtained for  $\alpha$ -( $\text{NEt}_4$ )<sub>2</sub>PaF<sub>6</sub> (0.4 to 2.0  $\mu$ ) and the measured peak positions and assignments for this compound are shown in Table III. The estimated accuracy of measurement is  $\pm 10 \text{ \AA}$ .

Peaks at  $\sim 1.17$ , 1.37 and 1.68  $\mu$  were present in the spectra of  $\text{NEt}_4\text{F}$  and were attributed to transitions within the tetraethylammonium cation. The rest of the spectrum is similar to those we reported earlier<sup>1</sup> for the octahedral complexes ( $\text{NEt}_4$ )<sub>2</sub>PaCl<sub>6</sub> and ( $\text{NEt}_4$ )<sub>2</sub>PaBr, and the optical absorption bands are again assigned to transitions from the ground  $\Gamma_7$  level to the  $\Gamma_7'$ ,  $\Gamma_8'$  and  $\Gamma_6$  states (Table IV). Not unexpectedly, however, the observed bands have

Table IV. Comparison of calculated and experimental transition energies.

Compound		Energy ( $\text{cm}^{-1}$ )			g
		$\Gamma_7-\Gamma_6$	$\Gamma_7-\Gamma_8$	$\Gamma_7-\Gamma_7$	
( $\text{NEt}_4$ ) <sub>2</sub> PaF <sub>6</sub>	Calc. <sup>a</sup>	11537	9586	5717	-0.704
	Exp.	11446	9708	5698	(-0.75) <sup>b</sup>

<sup>a</sup>Parameters used to obtain these results are given in Table V.

<sup>b</sup>Value in parentheses is estimated.

shifted appreciably to lower wavelengths.  $\beta$ -( $\text{NEt}_4$ )<sub>2</sub>PaF<sub>6</sub> exhibits an identical spectrum.

The spectrum of  $\alpha$ -( $\text{NEt}_4$ )<sub>2</sub>PaF<sub>6</sub> is dominated by vibronic bands as were those recorded<sup>1</sup> for the hexachloro- and hexabromo-protactinate (IV), and the mean values obtained for the vibrational transition, 147 and 407  $\text{cm}^{-1}$ , compare favourably with those observed directly for  $\nu_4$  and  $\nu_3$ , respectively, in the infrared spectra of both  $\alpha$ - and  $\beta$ -( $\text{NEt}_4$ )<sub>2</sub>PaF<sub>6</sub>. A further similarity with the spectra of ( $\text{NEt}_4$ )<sub>2</sub>-PaCl<sub>6</sub> and ( $\text{NEt}_4$ )<sub>2</sub>PaBr<sub>6</sub> is the splitting observed for the  $\Gamma_8'$  level in octahedral symmetry. Data available on similar splittings observed for a range of uranium (V) complexes are summarized and discussed elsewhere.<sup>5</sup> The shifts to lower wavelength observed with decreasing temperature for the bands associated with the  $\Gamma_8'$  and  $\Gamma_6$  levels are associated with the smaller contribution from vibronic transitions

to the low energy side of the bands at lower temperatures.

The 300 K spectrum shows broad unresolved features for the higher energy transitions which makes their assignment difficult. Therefore, the assignment at 85 K shown in Table III was used to fit the ligand field splittings,  $\theta$  and  $\Delta$ , and the spin orbit coupling constant,  $\zeta$ . In order to have a check on these parameters the g value for PaF<sub>6</sub><sup>2-</sup> was estimated as -0.75 (cf., the values available for the UF<sub>6</sub><sup>-</sup> ion and NpF<sub>6</sub> are<sup>1</sup> -0.700 and -0.604, respectively). The experimental and calculated values are compared in Table IV. The values obtained for  $\theta$ ,  $\Delta$ , and  $\zeta$  are compared in Table V with those for other 5f<sup>1</sup> octahedral compounds. It can readily be seen that the PaF<sub>6</sub><sup>2-</sup> parameters fit the trends observed in the other 5f<sup>1</sup> compounds. The parameter  $\Delta$  changes less with increasing oxidation state or increasing elec-

Table V. Values of the ligand field parameters  $\theta$  and  $\Delta$  and the spin-orbit coupling constant  $\zeta$  for 5f octahedral compounds.

Compounds	Parameters ( $\text{cm}^{-1}$ )			Compound	Parameters ( $\text{cm}^{-1}$ )			Compound	Parameters ( $\text{cm}^{-1}$ )		
	$\theta$	$\Delta$	$\zeta$		$\theta$	$\Delta$	$\zeta$		$\theta$	$\Delta$	$\zeta$
$\alpha$ -( $\text{NEt}_4$ ) <sub>2</sub> PaF <sub>6</sub>	4502	3074	1508	(Ph <sub>4</sub> As)UF <sub>6</sub>	6882	4479	1885	NpF <sub>6</sub>	17498	5619	2433
( $\text{NEt}_4$ ) <sub>2</sub> PaCl <sub>6</sub>	1873	1634	1523	( $\text{NEt}_4$ )UCl <sub>6</sub>	3371	2936	1913				
( $\text{NEt}_4$ ) <sub>2</sub> PaBr <sub>6</sub>	1268	1707	1535	( $\text{NEt}_4$ )UBr <sub>6</sub>	2375	2935	1925				

tronegativity of the halide ion for a fixed oxidation state than does  $\theta$ . Qualitatively this trend has been correlated with changes in  $\sigma$  bonding dominating the total ligand field splittings.

Further magnetic and optical measurements in progress on the  $5f^4$  compounds will enable more quantitative conclusions to be drawn.

#### Footnotes and References

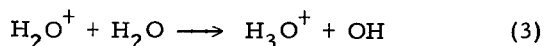
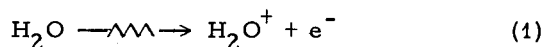
\* Chemistry Division, AWRE, Harwell, England.

1. N. Edelstein, D. Brown and B. Whittaker, *Inorg. Chem.*
2. R. A. Penneman, R. B. Ryan and A. Rosenzweig, *Structure and Bonding*, in press (1973).
3. J. L. Ryan, personal communication 1973; J. L. Ryan, J. M. Cleveland and G. H. Bryan, *Inorg. Chem.*, in press.
4. D. Brown and B. Whittaker, unpublished observations 1973.
5. D. Brown, B. Whittaker, and N. Edelstein, Report AERE-R-7481 (1973).

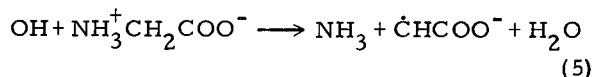
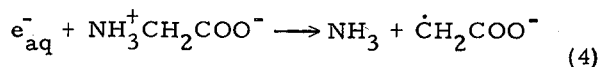
COMPARATIVE RADIATION CHEMISTRY OF GLYCINE  
AND ITS OLIGOPEPTIDE DERIVATIVES\*

W. M. Garrison

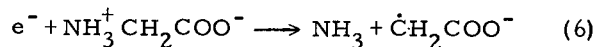
Major aspects of the radiation chemistry of the simpler  $\alpha$ -amino acids in aqueous systems may be represented in terms of the radiation-induced steps<sup>1</sup>



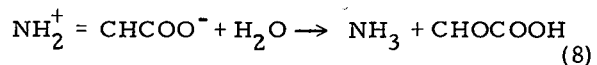
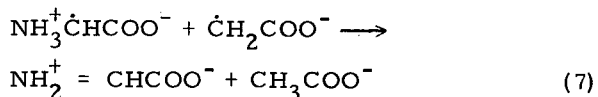
which reactions in dilute solutions of the amino acid are followed by<sup>2</sup>



where  $e_{\text{aq}}^-$  represents the hydrated electron. The evidence is that in concentrated solution the amino acid reacts directly with  $e^-$  prior to its hydration,<sup>3</sup> i. e.,

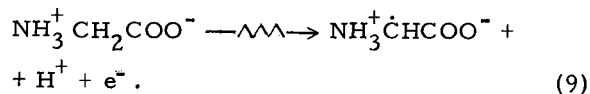


where  $k_6/k_4 \sim 10^3$ . The subsequent steps



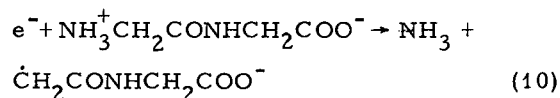
lead to formation of fatty acid and ketoacid as major organic products.

The radiation chemistry of the simpler  $\alpha$ -amino acids in the solid state involves ionic processes of a similar form.<sup>2</sup> In the case of the solid, the radiation-induced step is written

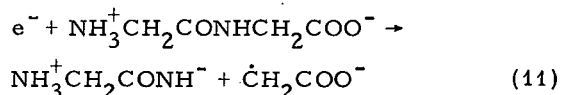


The electron formed in step 9 is captured via the analogue of step 6 and the subsequent reactions 7 and 8 occur on dissolution of the irradiated solid.

Reductive deamination via reaction akin to steps 4 and 6 also occur in the radiolysis of oligopeptides both in aqueous solution and in the solid state, i. e.,



However, in the peptide case there is also competing reaction of the type



Specific contributions of reactions of type 10 and 11 in the radiolysis of oligopeptide derivatives of glycine are being quantitatively evaluated.

Footnotes and References

\* Condensed version of paper presented at the Joint U. S.-Japan Conference on "Processes and Intermediates in the Radiation Chemistry of Condensed Phases," Catalina Island, California, February 5-9, 1973.

1. I. Dragnic, Radiation Chemistry of Water, (Academic Press, New York, 1971).

2. W. M. Garrison, Radiation Res. Rev. **3**, 305 (1972).

3. J. E. Aldrich, M. J. Bronskill, R. K. Wolff, and J. W. Hunt, J. Chem. Phys. **55**, 530 (1971).

## SCAVENGER EFFECTS IN THE RECOIL TRITIUM REACTIONS OF CYCLOHEXENE

D. C. Fee\* and S. S. Markowitz

Many recoil tritium experiments have used scavengers to remove thermalized tritium atoms and radical intermediates from the system before such species can yield products which might be confused with high-energy tritium reactions.<sup>1</sup> The yield of products formed solely by high energy (hot) reactions will remain unchanged over a wide range of scavenger concentrations. The yield of products formed by both thermal and hot processes will decrease rapidly with the addition of scavenger until a plateau is reached where the yield becomes relatively insensitive to scavenger concentration. In this region all thermal reactions, except with the scavenger, have presumably been suppressed and the yield is due entirely to hot reactions.<sup>2</sup>

The comparative efficiency of sulfur dioxide and oxygen as radical scavengers has recently been determined in the T + cyclohexene gas phase system.<sup>3</sup> In this system, one scavengeable thermal reaction product is cyclohexane- $\dot{t}$  which results largely from thermal addition of T to the double bond to form a cyclohexyl- $\dot{t}$  radical. This radical then abstracts a hydrogen atom from the bulk system to form cyclohexane- $\dot{t}$ . The cyclohexane- $\dot{t}$  yield exhibited identical scavenger plateaus with sulfur dioxide and oxygen scavenging. Ethylene- $\dot{t}$  and butadiene- $\dot{t}$  are primarily high energy products from the unimolecular decomposition of excited cyclohexene- $\dot{t}$  formed by direct substitution.<sup>4</sup> The ethylene- $\dot{t}$  yield exhibited identical scavenger plateaus with sulfur dioxide and oxygen scavenging. The butadiene- $\dot{t}$  yield was unaffected by sulfur dioxide scavenging but increased anomalously by nearly 50% with oxygen scavenging. We decided to investigate how the butadiene- $\dot{t}$  yields varied with differing scavengers.

### Results

The comparative efficiency of H<sub>2</sub>S, butadiene-d<sub>6</sub>, O<sub>2</sub> and SO<sub>2</sub> as radical scavengers

has been determined in the T + cyclohexene gas phase system. The T was produced by recoil in the <sup>3</sup>He(n,p)T reaction. Direct tritium substitution on cyclohexene yields cyclohexene- $\dot{t}$  which may undergo unimolecular decomposition to produce butadiene- $\dot{t}$ . In unscavenged samples butadiene- $\dot{t}$  is selectively depleted by reactions with H atoms produced by radiolysis. Neither SO<sub>2</sub> nor H<sub>2</sub>S is sufficiently reactive with H atoms to protect butadiene- $\dot{t}$  from such depletion. The "hot" butadiene- $\dot{t}$  yield can only be determined by means of O<sub>2</sub> or butadiene-d<sub>6</sub> scavenging. All products except butadiene- exhibit normal behavior with O<sub>2</sub>, SO<sub>2</sub> or H<sub>2</sub>S scavenging.

### Footnotes and References

\* Submitted in partial fulfillment of the Ph. D. Requirement, University of California, Berkeley, Department of Chemistry. Thesis reference LBL-1687, June 1973. Condensed from *J. Inorg. Nucl. Chem.* 35, 2153 (1973); details therein. Present Address: Aerospace Research Laboratories, Wright-Patterson Air Force Base, OH 45433.

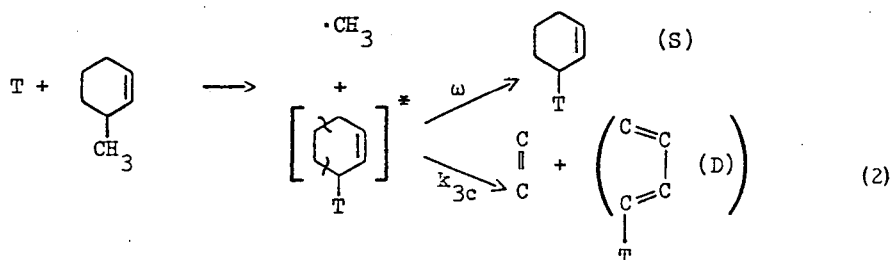
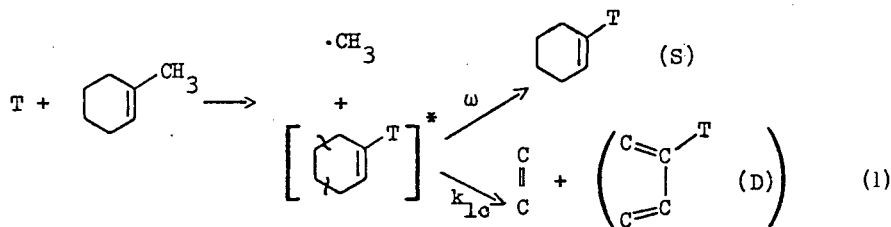
1. R. L. Wolfgang, *Progress in Reaction Kinetics* (edited by G. Porter) Vol. 3. Pergamon Press, Oxford (1965).
2. J. Hawke and R. L. Wolfgang, *Radiochim. Acta* 14, 116 (1970).
3. D. C. Fee, S. S. Markowitz and J. K. Garland, *Radiochim. Acta* 17, 135 (1972).
4. R. W. Weeks and J. K. Garland, *J. Phys. Chem.* 73, 2508 (1969); and *J. Am. Chem. Soc.* 93, 2380 (1971).

RECOIL TRITIUM REACTIONS WITH METHYLCYCLOHEXENE:  
A TEST OF THE ASSUMPTION OF ENERGY RANDOMIZATION  
PRIOR TO UNIMOLECULAR DECOMPOSITION\*

D. C. Fee<sup>†</sup> and S. S. Markowitz

For many years, the role of translational energy in promoting virtually all chemical reactions has been emphasized. One method of producing translationally excited ("hot") atoms for chemical studies is by nuclear reaction and resulting recoil. Recoil tritium atom reactions have now been observed with over one hundred

parent molecules.<sup>1-3</sup> We propose to use recoil tritium atom reactions with methylcyclohexene to test the RRKM<sup>4-5</sup> assumption of energy randomization prior to unimolecular decomposition. This is shown in Eqs. (1) and (2).



If  $k_{1c} = k_{3c}$ , excited cyclohexene-t molecules decompose with the same probability regardless of the site of energy input. That is, energy randomization occurs prior to unimolecular decomposition. If  $k_{1c} \neq k_{3c}$ , energy non-randomized unimolecular decomposition occurs.

In chemical activation studies such as this,  $k_a$ , the apparent rate constant of unimolecular decomposition, is determined from<sup>6</sup>

$$k_a = \omega \left( \frac{D}{S} \right) = Z \left( \frac{D}{S} \right) P \quad (3)$$

where  $\omega = ZP$  = collision frequency;  $Z$  is the collision number;<sup>7</sup>  $P$  is the sample pressure in Torr;  $D$  is the yield of decomposition product; and  $S$  is the yield of collisionally stabilized product (that is,  $S$  is the yield of activated molecules which were collisionally stabilized prior to unimolecular decomposition).

We assumed that possible differences in the average energy of excitation of cyclohexene-1-t versus that of cyclohexene-3-t could be estimated using the RRK formulation of the energy dependence of the unimolecular rate constant,<sup>5</sup> namely,

$$k_a = A \left[ \frac{E - E_0}{E} \right]^{s-1} \quad (4)$$

where  $k_a$  is alternately  $k_{1c}$  or  $k_{3c}$  as determined from the stabilization ( $S$ )/decomposition ( $D$ ) ratios from Eqs. (1) and (2) respectively;  $E_0$  and  $A$  for the unimolecular decomposition of cyclohexene are given in Eq. (5), the  $s$  parameter is taken as  $s = 24$  from the unimolecular decomposition of cyclohexene-t following recoil T-for-H substitution;<sup>8</sup> and  $E$  is the average energy deposited in the cyclohexene-t molecule following recoil T-for-methyl substitution on methylcyclohexene.

$$k_a = 10^{15.3} \exp(-66,900 \text{ cal/kT}) = A \exp(-E_0/kT) \quad (5)$$

The results for 7 mole% nitric oxide (NO) scavenged samples are in Table I. The effective collisional deactivation pressure in the sample defined as

$$P_{\text{eff}} = 1.0 P_{\text{C}_7\text{H}_{12}} + 0.17 P_{\text{He}} + 0.24 P_{\text{NO}} \quad (6)$$

Each sample contained 300 Torr of  $^3\text{He}$  (at 135°C) and a variable amount of nitric oxide and methylcyclohexene isomer ( $\text{C}_7\text{H}_{12}$ ). On a pressure for pressure basis,  $^3\text{He}$  is estimated to be only 17 (nitric oxide 24) as effective as methylcyclohexene in collisionally deactivating excited methylcyclohexene-t molecules.<sup>10</sup> The use of the effective pressure for the P in Eq. (3) is an attempt to correct for the effect of a weak collider in the system,  $^3\text{He}$  or NO. Otherwise, it is assumed that only a single collision between an activated methylcyclohexene-t molecule and an unlabeled methylcyclohexene

molecule is necessary for complete deactivation of the excited methylcyclohexene-t species. We point out that this "strong collision"<sup>4</sup> assumption may not be valid at the high energies of excitation encountered in recoil tritium experiments.

Considering the range of unimolecular rate constants<sup>7</sup> and the uncertainties of this method,  $k_{1c}$  and  $k_{3c}$  in Table I are nearly equivalent. The near equivalence of the unimolecular rate constants and the average energies of excitation for cyclohexene-1-t and cyclohexene-3-t (from T-for-methyl substitutions on 1-methylcyclohexene and 3-methylcyclohexene, respectively) shows that (a) the RRK-RRKM assumption of energy randomization prior to unimolecular decomposition is valid for the recoil-tritium-initiated unimolecular decomposition of cyclohexene, and (b) a T-for-methyl substitution reaction leaves an average energy of excitation of 6.0 to 6.5 eV in the resultant tritiated molecule. This is in good agreement with a previous estimate of 6 to 7 eV.<sup>11</sup>

Table I. The unimolecular decomposition of cyclohexene-t at 135°C<sup>a</sup>

Effective Pressure (Torr)	S/D (Eq. 6)	S/D (Eq. 7)	$k_{1c}$ ( $10^9 \text{ sec}^{-1}$ )	$k_{3c}$ ( $10^9 \text{ sec}^{-1}$ )	$E_{1c}$ (eV)	$E_{3c}$ (eV)
360	2.8	1.7	1.6 <sup>c</sup>	2.7	6.4	6.5
970	3.2	1.6	3.4	6.7	5.9	6.1

<sup>a</sup> Activated cyclohexene-t molecules formed by recoil T-for-methyl substitution with methylcyclohexene.

<sup>b</sup> Effective pressure =  $1.0 P_{\text{C}_7\text{H}_{12}} + 0.17 P_{\text{He}} + 0.24 P_{\text{NO}}$ .

<sup>c</sup> Determined with an estimated<sup>10</sup> collision diameter for cyclohexene of  $5.47 \times 10^{-8}$  cm and  $6.12 \times 10^{-8}$  cm for methylcyclohexene.

#### Footnotes and References

\* Condensed from LBL-1910; J. Phys. Chem. **78**, 354 (1974).

† Submitted in partial fulfillment of the Ph. D. requirements at the Department of Chemistry, University of California, Berkeley. Thesis of D. C. Fee, LBL-1687, June 1973.

1. F. S. Rowland, Molecular Beams and Reaction Kinetics, Ch. Schlier, editor (Academic Press, New York, 1970).

2. D. S. Urch, MTP International Review of Science, Inorg. Chem. Ser. **8**, 149 (1972).

3. F. S. Rowland, MTP International Review of Science, Phys. Chem. Ser. **9**, 109 (1972).

4. For Rice, Ramsperger, Kassel, and Marcus. See R. A. Marcus, J. Chem. Phys. **20**, 359 (1952). R. A. Marcus and O. K. Rice, J. Phys. and Colloid. Chem. **55**, 894 (1951).

5. O. K. Rice and H. C. Ramsperger, J. Am. Chem. Soc. **49**, 1617 (1927). O. K. Rice and

- H. C. Ramsperger, *J. Am. Chem. Soc.* **50**, 617 (1928). L. S. Kassel, *J. Phys. Chem.* **32**, 225 (1928). L. S. Kassel, *J. Phys. Chem.* **32**, 1065 (1928).
6. J. D. Rynbrandt and B. S. Rabinovitch, *J. Phys. Chem.* **75**, 2164 (1971).
7. P. J. Robinson and K. A. Holbrook, *Unimolecular Reactions* (Wiley-Interscience, New York, 1972) p. 164.
8. D. C. Fee and S. S. Markowitz, *J. Phys. Chem.* **78**, 347 (1974).
9. W. Tsang, *Int. J. Chem. Kinetics* **2**, 311 (1970). W. Tsang, *J. Phys. Chem.* **76**, 143 (1972).
10. Estimated from tabulated collisional deactivation efficiency data and collision diameters found in: S. C. Chan, B. S. Rabinovitch, J. T. Bryant, L. D. Spicer, T. Fujimoto, Y. N. Lin, and S. P. Pavlou, *J. Phys. Chem.* **74**, 3160 (1970).
11. Estimated from the stabilization (S)/decomposition (D) ratio of methylcyclobutane-t following T-for-H substitution on 1,3-dimethylcyclobutane. See C. T. Ting and F. S. Rowland, *J. Phys. Chem.* **74**, 445 (1970).

### RECOIL TRITIUM REACTIONS WITH CYCLOHEXENE AND ALKENES: DETERMINATION OF RATE PARAMETERS\*

D. C. Fee<sup>†</sup> and S. S. Markowitz

We are interested in the study of recoil tritium atoms.<sup>1,2</sup> Recoil tritium studies are often limited by the lack of knowledge of the energy of the tritium atom when it reacts. The tritium atom is produced via nuclear recoil with an energy (192 keV, 1 eV = 23 kcal/mole) which is virtually infinite on the chemical scale. The tritium ion (atom) undergoes a series of energy-losing collisions with its environment until it enters the energy region below 20 eV where reactions which produce stable tritium-labeled products are thought to occur. The tritiated product distribution that is experimentally measured is the summation of tritium atom reactions at all energies from 20 to 0.02 eV (thermal energies). Experimental determinations of the tritium atom energy distribution in the 20 to 0.02 eV range have not been made.<sup>1,2</sup> Attempts to calculate a theoretical tritium atom energy distribution that would explain the existing recoil tritium reaction data have not been too successful.<sup>1,2</sup>

In recoil tritium reactions, the only well known energy "bench mark" is that T-for-H substitution deposits an average excitation energy of 5 eV in the resultant tritiated molecule.<sup>3,4</sup> This relatively high energy of excitation, unless removed by collision, may cause the tritiated molecule to undergo unimolecular decomposition. In fact, analysis of the pressure dependence of the unimolecular decomposition of cyclobutane-t (following T-for-H substitution) with the RRKM theory (Rice, Ramsperger, Kassel and Marcus) of unimolecular reactions<sup>5,6</sup> led to the 5 eV figure.

Because of the lack of knowledge of the energy of the tritium atom when it reacts and

because the average energy of excitation is not too useful in analyzing competing unimolecular reaction channels, kinetic parameters often cannot be extracted from recoil tritium reaction studies. Even the simplest concepts of rate processes include an explicit energy dependence (see Refs. 5 and 6). In this paper, we attempt to show that kinetic parameters can be determined from selected, carefully designed recoil tritium experiments, namely, (1) studying the pressure dependence of the unimolecular decomposition of excited tritiated molecules following T-for-H substitution, and (2) studying the pressure dependence of the unimolecular decomposition of an excited tritiated alkyl radical following T atom addition to an alkene.

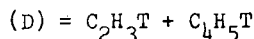
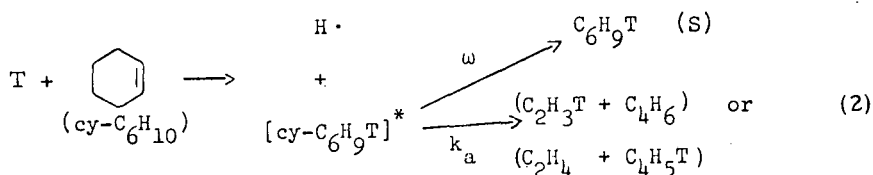
#### Determination of the s Parameter in the RRK Treatment of Cyclohexene Unimolecular Decomposition

The unimolecular decomposition of cyclohexene to give primarily ethylene and butadiene has been well established. The unimolecular rate constant is

$$k_a = 10^{15.3} \exp(-66,900 \text{ cal/kT}) = A \exp(-E_0/kT) \quad (\text{Ref. 7}) \quad (1)$$

The recoil tritium reaction scheme is shown in Eq. (2)

where  $\omega$  = ZP = collision frequency,  
P = cyclohexene pressure in Torr,  
Z = collision number,<sup>8</sup>  
S = collisional stabilization product, and  
D = unimolecular decomposition product.



The apparent rate constant of unimolecular decomposition,  $k_a$ , is given by<sup>9</sup>

$$k_a = \omega(D/S) = Z(D/S) P. \quad (3)$$

The S/D ratio should vary linearly with pressure for a unimolecular process. The collision frequency at the pressure where S/D = 1 is  $k_a$ .

The unimolecular formation of ethylene-t and butadiene-t as shown in Eq. (2) was confirmed by the linear pressure dependence of the stabilization (S)/decomposition (D) ratio shown in Fig. 1. Here, the pressure represents the total effective collisional deactivation pressure in the sample capsule. Each sample contained 98 Torr of  $^3\text{He}$  at 135°C and a variable pressure of cyclohexene. Relative colli-

sional deactivation efficiencies estimated from published sources<sup>10</sup> show that on a pressure-for-pressure basis  $^3\text{He}$  is only 20% as effective as cyclohexene ( $\text{C}_6\text{H}_{10}$ ) in deactivating excited cyclohexene molecules. Hence the "effective" collisional deactivation pressure of cyclohexene in the capsule is defined as

$$P_{\text{effective}} = P_{\text{C}_6\text{H}_{10}} + 0.2 P_{^3\text{He}}. \quad (4)$$

The use of the effective pressure for the P in Eq. (3) is an attempt to correct for the effect of a weak collider in the system,  $^3\text{He}$ . Otherwise, it is assumed that only a single collision between an activated cyclohexene-t molecule and an unlabeled cyclohexene molecule is necessary for complete deactivation of the excited cyclohexene-t species. We point out that this "strong collision"<sup>5</sup> assumption may not be valid at the high energies of excitation encountered in recoil tritium experiments.

The least squares fitted line of the S/D ratio versus pressure [actually log (S/D) versus log (pressure)] was extrapolated to S/D = 1.0. The pressure at which S/D was 1.0 was 0.50 Torr.

The apparent rate constant,  $k_a$ , for the unscavenged unimolecular decomposition of cyclohexene-t to ethylene-t or butadiene-t was calculated from Eq. (3) as  $5.1 \times 10^6 \text{ sec}^{-1}$ . The calculation of Z was made with an estimated<sup>10</sup> collision diameter for cyclohexene of  $5.47 \times 10^{-8} \text{ cm}$ . Using this value of  $k_a$  and an average excitation energy (following T-for-H substitution) of 5 eV for the E in Eq. (5), the s parameter in the RRK treatment<sup>6</sup> of the unimolecular decomposition of cyclohexene was determined as  $s = 24$ . The A and  $E_0$  used were from Eq. (1).

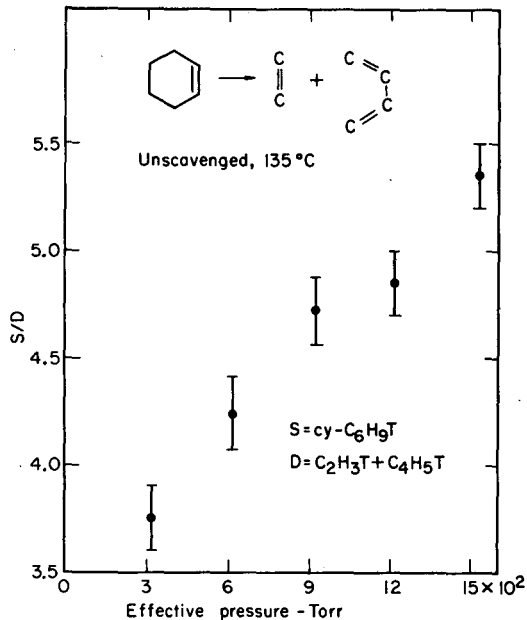


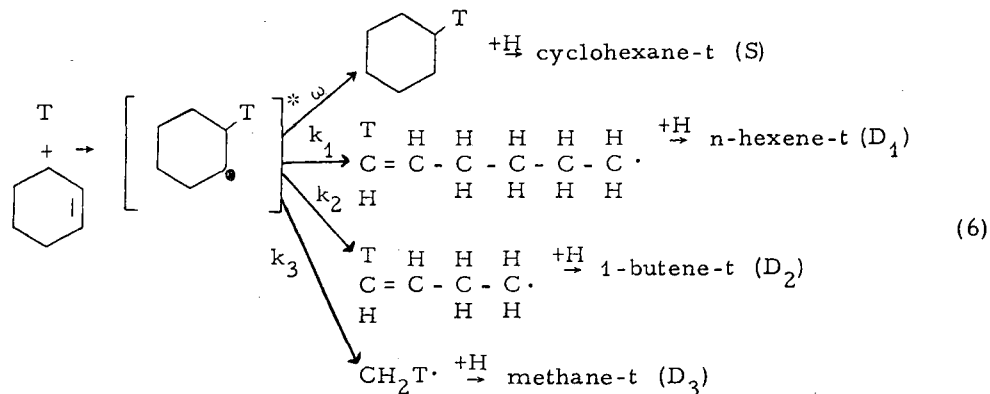
Fig. 1. The unimolecular decomposition of cyclohexene-t to give ethylene-t or butadiene-t; unscavenged data at 135 C. Activated cyclohexene-t molecules are formed by recoil T-for-H substitution. The abscissa is the effective pressure = cyclohexene pressure + 0.2 (helium-3 pressure). (XBL 735-2820)

$$k_a = A \left[ \frac{E - E_0}{E} \right]^{s-1} \quad (5)$$



Determination of the Apparent Rate Constants of the Unimolecular Decomposition/Isomerization of Cyclohexyl Radicals.

We propose the following reaction scheme for excited cyclohexyl-t radicals formed by the addition of a recoil tritium atom to cyclohexene.



gen atom to form a tritiated alkane or alkene; this is indicated by the + H over the arrow in Eq. (6), or (b) add to the double bond of cyclohexene. With H<sub>2</sub>S scavenging, all the radicals react rapidly with H<sub>2</sub>S to obstruct a hydrogen atom before they add to cyclohexene.<sup>11</sup> The data are shown in Fig. 2.

The rate constants  $k_1$  and  $k_2$  were determined from extrapolation of  $S/D$  versus effective pressure to  $S/D = 1$ . The calculation of  $Z$  was made with an estimated collision diameter of  $5.67 \times 10^{-8}$  cm for cyclohexyl-t radicals.<sup>10</sup> The values of the calculated rate constants at 135°C and the pressure at which  $S/D = 1$  were:

The site of the tritium label in the n-hexenyl-t radical and the 1-butenyl-t radical shown in Eq. (6) is purely arbitrary and is shown only for the sake of material balance along the reaction path. In unscavenged T + cyclohexene systems, tritiated radical products, once collisionally stabilized, may (a) abstract a hydro-

$k_1 = 8.4 \times 10^3 \text{ sec}^{-1}$  ( $7.9 \times 10^{-4}$  Torr),  
 $k_2 = 3.4 \times 10^4 \text{ sec}^{-1}$  ( $3.2 \times 10^{-3}$  Torr).  
 Using Eq. (4) to determine  $k_3$  at each effective pressure and comparing  $k_3$  with  $k_1$  and  $k_2$  values similarly derived allowed  $k_3$  to be estimated as  $5 \times 10^2 \text{ sec}^{-1}$ . The large uncertainty in the cyclohexane-t/methane-t ratio, as indicated by the large error bars in Fig. 2, prevented meaningful extrapolation over a large pressure range to the pressure of which  $S/D = 1$ .

We conclude that rate parameters can be determined in carefully designed recoil tritium experiments.

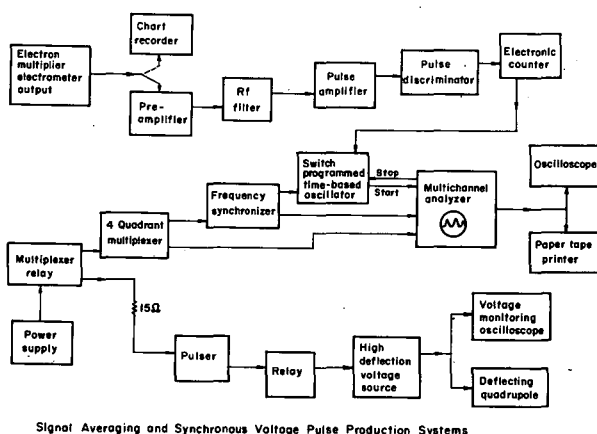


Fig. 2. The unimolecular decomposition of cyclohexyl-t radicals to n-hexene-t, 1-butene-t or methane-t; H<sub>2</sub>S scavenged data at 135 C. Activated cyclohexyl-t radicals are formed by recoil T atom addition to cyclohexene. The abscissa is the effective collisional deactivation pressure (in the sample capsule) defines as: effective pressure = cyclohexene pressure) + 0.5 (hydrogen sulfide pressure).  
 (XBL 736-3187)

### Footnotes and References

\* Condensed from LBL-1906, J. Phys. Chem. (in press).

† Submitted in partial fulfillment of the Ph. D. requirements, Department of Chemistry, University of California, Berkeley, Ph. D. Thesis of D. C. Fee, LBL-1687, June 1973.

1. F. S. Rowland, MTP Int. Rev. Sci., Phys. Chem. Series 9, 109 (1972).

2. D. S. Urch, MTP Int. Rev. Sci., Inorg, Chem. Ser. 8, 149 (1972).

3. E. K. C. Lee and F. S. Rowland, J. Am. Chem. Soc. 85, 897 (1963).

4. A. Hosaka and F. S. Rowland, J. Phys. Chem. 75, 3781 (1971).

5. R. A. Marcus and O. K. Rice, J. Phys. and Colloid. Chem. 55, 894 (1951). R. A. Marcus, J. Chem. Phys. 20, 359 (1952).

6. O. K. Rice and H. C. Ramsperger, J. Am. Chem. Soc. 49, 1617 (1927). O. K. Rice and H. C. Ramsperger, J. Am. Chem. Soc. 50, 617 (1928). L. S. Kassel, J. Phys. Chem. 32, 225 (1928). L. S. Kassel, J. Phys. Chem. 32, 1065 (1928).

7. W. Tsang, Int. J. Chem. Kinetics 2, 311 (1970). W. Tsang, J. Phys. Chem. 76, 143 (1972).

8. P. J. Robinson and K. A. Holbrook, Unimolecular Reactions (Wiley-Interscience, New York, 1972) p. 164.

9. J. D. Rynbrandt and B. S. Rabinovitch, J. Phys. Chem. 75, 2164 (1971).

10. S. C. Chan, B. S. Rabinovitch, J. T. Bryant, L. D. Spicer, T. Fujimoto, Y. N. Lin, and S. P. Pavlon, J. Phys. Chem. 74, 3160 (1970).

11. D. C. Fee and S. S. Markowitz, J. Inorg. Nucl. Chem. 35, 2153 (1973).

### RECOIL TRITIUM REACTIONS WITH ALKENES: FORMATION OF "POLYMER-T"\*

D. C. Fee<sup>†</sup> and S. Markowitz

Recoil tritium reactions have now been observed with over one hundred parent molecules.<sup>1-3</sup> The main reaction channels observed for recoil tritium atoms are:

- (1) Abstraction to form HT.
- (2) T-for-H substitution to form a tritiated parent molecule.
- (3) Addition to a double bond to form an excited alkyl-t radical.

The excited alkyl-t radical, unless collisionally stabilized, may undergo unimolecular decomposition/isomerization.<sup>4-5</sup>

Collisionally stabilized alkyl-t radicals are also capable of further reaction. The concentration of radiolysis produced radicals [formed by the recoiling ions following the <sup>3</sup>He(n, p)T reaction] is kept low to make radical-radical reactions negligible. Therefore, the only reactions of collisionally stabilized alkyl-t radicals in <sup>3</sup>He-hydrocarbon systems are:

- (1) Abstraction of a hydrogen atom to form an alkane-t species.
- (2) Addition to the double bond of the parent hydrocarbon initiating a tritiated radical chain.

The chain termination step is abstraction of a hydrogen atom. Tritiated dimers have been observed by radio-gas-chromatography.<sup>6-7</sup>

Tritiated products not eluted in the normal forward flow of the radio-gas-chromatographic analyses have been recovered and monitored as "polymer-t."<sup>8</sup> While the "polymer-t" data does not indicate the chemical composition of the tritiated products, it does allow crude separation by volatility. Low (molecular weight) "polymer-t" is back flushed from the chromatographic columns. Medium "polymer-t" is washed from a stainless steel capillary tube (operated at 25°C) connecting the sample crusher to the chromatographic column. High "polymer-t" is washed from the walls of the sample capsule in which the recoil tritium reaction took place.

Recently we reported scavenger effects on the "polymer-t" yield in T + cyclohexene reactions.<sup>9</sup> A glaring inconsistency developed in the "polymer-t" data when H<sub>2</sub>S was employed as scavenger. The rate constant at 25°C for the reaction of alkyl radicals with H<sub>2</sub>S (via H atom abstraction to form an alkane) is larger than with alkenes by several orders of magnitude.<sup>9</sup> Consequently, with H<sub>2</sub>S scavenging, all cyclohexyl-t radicals from T + cyclohexene reactions (at 25°C) should be monitored as cyclohexane-t. In H<sub>2</sub>S scavenged T + cyclohexene reactions, the expected increase in the cyclohexane-t should be accompanied by an

equal decrease in the 'polymer-t' yield. Experimentally the decrease in polymer-t yield was only 48% of the increase in the cyclohexane-t yield. We decided to critically re-examine the method of recovery and analysis of 'polymer-t'.

The new data is shown in Table I. With H<sub>2</sub>S scavenging, the tritiated radicals formed by T + cyclohexene reactions are assumed to react with H<sub>2</sub>S (to give products monitored by radio-gas-chromatography) rather than with cyclohexene (to give 'polymer-t'). With O<sub>2</sub> or SO<sub>2</sub> scavenging, the tritiated radicals are

assumed to react with O<sub>2</sub> or SO<sub>2</sub> rather than with cyclohexene.<sup>9</sup> The identity of the O<sub>2</sub> or SO<sub>2</sub> scavenged species is unknown. The O<sub>2</sub> and SO<sub>2</sub> scavenged tritiated species are monitored as 'polymer-t'. Therefore, a decrease in the sum of gas phase product yields from H<sub>2</sub>S to O<sub>2</sub> or SO<sub>2</sub> scavenging should be marked by an equal increase in 'polymer-t'. Two things should be noted: (1) No correction was necessary for <sup>35</sup>S activity (from the <sup>34</sup>S(n, γ)-<sup>35</sup>S reaction) that could be included in our measurements as <sup>35</sup>S was incorporated into the 'polymer-t'. Even with the highest SO<sub>2</sub> or H<sub>2</sub>S pressures, the total <sup>35</sup>S activity is less

Table I. T + alkene reaction data<sup>a</sup> at 25 C

Alkene	Scavenger	'Polymer-t' yield				Cyclohexane-t yield	Sum of gas phase product yields <sup>b</sup>
		Low	Medium	High	Sum		
Cyclohexene	H <sub>2</sub> S	2.0	2.1	33.6	37.7	109	201
	O <sub>2</sub>	3.8	11.1	79.4	94.3	0.5	48
	SO <sub>2</sub>	1.8	3.7	167	173	0.7	43
							Butane-t yield
1-Butene	H <sub>2</sub> S	8.2	3.3	10.6	22.1	135	304
	O <sub>2</sub>	21.7	5.0	18.0	44.7	2.8	148
	SO <sub>2</sub>	3.5	2.8	132	138	3.8	150

<sup>a</sup> Tritiated product yields relative to yield of tritiated parent compound as 100.

<sup>b</sup> Sum of all tritiated product yields monitored by radio-gas-chromatography except HT and the tritiated parent compound.

than 1% of the 'polymer-t' activity. And<sup>2</sup>, in contrast to previously reported data,<sup>8-12</sup> corrections for sample quenching were made for the data in Table I. The previously held assumption was that only trace (10<sup>-12</sup> mole) amounts of radioactive material was being recovered so that sample quenching was not important. This assumption was invalid. For example, the increase in total 'polymer-t' yield when corrections are made for quenching (versus assuming a constant efficiency of counting for all sample vials) ranged from 10 to 30% for the T + cyclohexene data. The high 'polymer-t' samples were quenched the most.

As shown by the T + cyclohexene reaction data in Table I, 85% of the 'polymer-t' expected

from the material balance arguments is recovered with SO<sub>2</sub> scavenging versus 35% with O<sub>2</sub> scavenging. Similarly for the T + 1-butene reaction data in Table I, 75% of the 'polymer-t' expected from material balance arguments is recovered with SO<sub>2</sub> scavenging versus 15% with O<sub>2</sub> scavenging. The increase in 'polymer-t' yield from O<sub>2</sub> to SO<sub>2</sub> scavenging is in the high 'polymer-t' grouping. This may indicate that the SO<sub>2</sub> scavenged species are more soluble in toluene than the O<sub>2</sub> scavenged species. The difference in efficiency of 'polymer-t' recovery with SO<sub>2</sub> scavenging for cyclohexene versus 1-butene (85% versus 75%) may indicate that the efficiency of the recovery process depends slightly upon the chemical nature of the 'polymer-t'.

We conclude that:

(1) The recovery and analysis of 'polymer-t' from T + alkene reactions by the method described may be only 75 to 85% complete. Although the recovery of 'polymer-t' may not be complete, the large amount of 'polymer-t' recovered supports the proposed mechanism of 'polymer-t' formation.

(2) The efficiency of recovery of 'polymer-t' is strongly dependent upon the scavenger used. With SO<sub>2</sub> scavenging, a higher percentage of the 'polymer-t' is recovered than with O<sub>2</sub> scavenging.

#### Footnotes and References

\* Condensed from LBL-1949; submitted to J. Inorg. Nucl. Chem.

† Submitted in partial fulfillment of the Ph. D. requirements, Department of Chemistry, University of California, Berkeley, Ph. D. Thesis of D. C. Fee, LBL-1687, June 1973. Present address: Aerospace Research Laboratories, Wright-Patterson Air Force Base, OH 45433.

1. F. S. Rowland, MTP Int. Rev. of Sci., Phys. Chem. Ser. 9, 149 (1972).
2. D. S. Urch, MTP Int. Rev. of Sci., Inorg. Chem. Ser. 8, 149 (1972).
3. F. S. Rowland, Molecular Beams and Reaction Kinetics, edited by Ch. Schlier, Academic Press, New York (1970), p. 108.
4. R. Kushner and F. S. Rowland, J. Phys. Chem. 76, 190 (1972).
5. D. C. Fee and S. S. Markowitz, J. Phys. Chem. 78, 347 (1974).
6. R. Kushner and F. S. Rowland, J. Phys. Chem. 75, 3771 (1971).
7. K. I. Mahan and J. K. Garland, J. Phys. Chem. 75, 1031 (1971).
8. J. K. Garland, Anal. Letters 1, 273 (1968).
9. D. C. Fee and S. S. Markowitz, J. Inorg. Nucl. Chem. 35, 2153 (1973).

## METASTABLE TRANSITIONS IN THE MASS SPECTRA OF DIMETHYLNITROSAMINE AND RELATED COMPOUNDS\*

A. S. Newton

The mass spectrum of dimethylnitrosamine (DMNA), also called N-nitrosodimethylamine, is interesting because it contains several metastable ions, one of which is unusual, and further because the fragmentation pattern involves extensive rearrangements. It is well known that DMNA and other nitrosamines are carcinogenic. Magee<sup>1</sup> has recently reviewed the evidence and points out that the nitrosamines themselves may be pre-carcinogens, i. e., they may not themselves induce the tumor, but a more active decomposition product may be the ultimate carcinogen. This ultimate carcinogen may be a carbonium ion derived from the nitrosamine.

DMNA is the simplest nitrosamine. It is readily synthesized from dimethylamine and nitrous acid. The mass spectrum was first investigated by Collin.<sup>2</sup> Collin correctly identified the M/z = 18 peak as NH<sub>4</sub><sup>+</sup> ion formed by a rearrangement mechanism. Collin observed but did not explain the peculiar shape of the low mass side of the mass 18 peak. Nor did he comment on similar but less pronounced behavior of M/z = 15 peak in the mass spectrum. Gowenlock, Jones and Major<sup>3</sup> studied

the appearance potentials of some ions in DMNA and related compounds in order to determine bond energies and thermodynamic properties of some of the ions and radicals involved in the fragmentation. Further studies on the mass spectra of nitroso compounds have been reported by Schroll, Cooks, Klemmensen and Lawesson.<sup>4</sup>

A study of the mass spectrum of DMNA in the mass region of 3 to 12 shows that significant metastable peaks occur at the apparent masses 3.81, 5.36, and 7.36. These peaks are each linear in intensity with pressure as shown in Fig. 1, hence they each arise from a unimolecular dissociation process. Metastable supressor cutoff curves identify these peaks as arising from the following transitions:

(M/z)*	Mass Transition	Ion Transition
3.81	59 <sup>+</sup> = 15 <sup>+</sup> + 44	CH <sub>3</sub> NNO <sup>+</sup> = CH <sub>3</sub> <sup>+</sup> + N <sub>2</sub> O
5.36	42 <sup>+</sup> = 15 <sup>+</sup> + 27	CH <sub>3</sub> NCH <sup>+</sup> = CH <sub>3</sub> <sup>+</sup> + HCN
7.36	44 <sup>+</sup> = 18 <sup>+</sup> + 26	CH <sub>3</sub> NCH <sub>3</sub> <sup>+</sup> = NH <sub>4</sub> <sup>+</sup> + C <sub>2</sub> H <sub>2</sub>

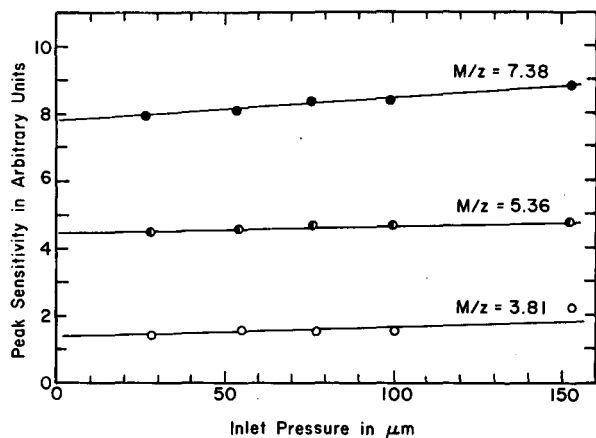


Fig. 1. Linearity with pressure of the intensity of metastable ions in the mass spectrum of N-nitrosodimethylamine. (XBL-742-358)

In each of these metastable transitions, the co-product of the fragment ion is a molecule of great stability. The transition to form  $\text{NH}_4^+$  from  $\text{CH}_3\text{NCH}_3^+$  involves the rearrangement of four H atoms and two C atoms. An intermediate three-membered ring is necessary for this to occur. A protonated ethylene imine is a suggested structure of the intermediate ion.

Kinetic energy release and half lives have been determined for the transitions leading to the 5.36 and 7.36 peaks. For the transition to the mass 5.36 ion, the kinetic energy release is  $0.020 \pm 0.005$  eV and the apparent half life is  $1.3 \pm 0.3$   $\mu\text{sec}$ . For the transition to the mass 7.36 ion, the kinetic energy release is  $0.040 \pm 0.01$  eV, and the half life is  $1.1 \pm 0.3$   $\mu\text{sec}$  or  $1.6 \pm 0.5$   $\mu\text{sec}$ , these two half lives being based on the change in peak intensity with time for

the mass 7.36 peak and the mass 18 peak respectively. These half lives are operational half lives applicable to the narrow range of time at which measurements can be made. Because the dissociation of these ions should be described by the quasi-equilibrium theory of mass spectra, a continuous distribution of half lives should be found. The observation of the same half life for the change in masses 7.36 and 18 suggests that nearly all the  $\text{NH}_4^+$  ions are formed by the metastable process, and that little of the 18 peak is formed in fast fragmentation processes.

The rise in baseline before the mass 18 and 15 peaks respectively are shown in Fig. 2.

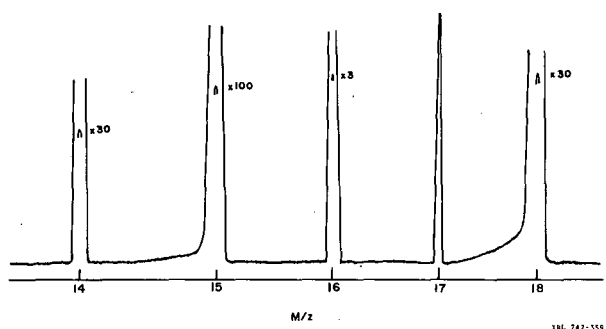


Fig. 2. Mass spectrum of N-nitrosodimethylamine in the mass region of 14 to 18. (XBL-742-359)

This behavior is rare among mass spectra, but it is shown by those compounds which fragment to dimethylamino ions. The fraction of the total peak height for these peaks which is represented by the slope before the peak is independent of the ion accelerating voltage.

Table I. Ratios of peak intensities in the mass spectra of compounds with the structure  $(\text{CH}_3)_2\text{N}-\text{X}$ .

Compound	Ratio x 100 of peak intensities <sup>a</sup>					
	5.36/42	5.36/15	15/42	7.36/44	7.36/18	18/44
$(\text{CH}_3)_2\text{NNO}$	0.055	0.069	80.2	1.37	0.41	333
$(\text{CH}_3)_2\text{NH}$	0.053	0.046	112.6	0.15	0.94	15.9
$(\text{CH}_3)_2\text{NCH}_3$	0.058	0.069	84.5	0.25	0.60	40.8
$(\text{CH}_3)_2\text{NNH}_2$	0.050 <sup>b</sup>	0.058	83.8	0.21 <sup>c</sup>	0.05 <sup>c</sup>	423

<sup>a</sup> Metastable ion peaks scanned at MV = 11300, other peaks at MV = 45240.

<sup>b</sup>  $(M/z)^* = 5.36$  interfered with by another metastable at  $(M/z)^* = 5.49$ , resulting from the transition  $59^+ = 18^+ + 41$ .

<sup>c</sup>  $(M/z)^* = 7.36$  interfered with by another metastable at  $(M/z)^* = 7.20$ , resulting from the transition  $45^+ = 18^+ + 27$ .

The rise results from the fragmentation of mass 44 to 18 or mass 42 to 15 respectively in the region of the ion source between the first slit and the focus slits. The voltage gradient in this region is low and ions spend relatively long times in their initial acceleration.

Intensity ratios of peaks in the mass spectrum of DMNA have been compared to the ratios of peaks in the mass spectra of compounds with the  $(\text{CH}_3)_2\text{NX}$  structure. The results in Table I show that for X equal NO, H,  $\text{CH}_3$ , or  $\text{NH}_2$ , the ratio of intensity of peaks at mass 5.36 to 15 or 5.36 to 42 are very close to constant. This suggests that the mass 42 ion dissociates by the same pathway regardless of the parent compound from which the ion is derived. This is not true for the mass 7.36, 18 and 44 peaks however. For this transition, not only is the metastable ion at mass 7.36 variable with respect to masses 18 and 44, but the ratio of intensities of ions at mass 18 to those at mass 44 varies by a factor of  $\sim 25$ . In the mass spectrum of DMNA mass 44 is a minor peak,

but in the mass spectrum of dimethylamine, it is the largest peak in the spectrum. This suggests the existence of at least two excitation states of the  $\text{CH}_3\text{NCH}_3^+$  ion. One state is metastable and dissociates to  $\text{NH}_4^+$  and  $\text{C}_2\text{H}_2$ . The other is stable. The ratio in which the two states are formed is a result of the fragmentation process by which the fragment at mass 44 is formed from the parent molecule.

#### Footnotes and References

\* A short summary of work in progress.

1. P. Magee, *New Scientist* 23, 432 (1973).
2. J. Collin, *Bull. Soc. Roy. Sci. Liege* 23, 201 (1954).
3. B. G. Gowenlock, P. P. Jones and J. R. Majer, *Trans. Faraday Soc.* 57, 23 (1961).
4. G. Schroll, R. G. Cooks, P. Klemmensen and S. O. Lawesson, *Ark. Kemi* 28, 413 (1967).

ON THE HOMOGENEITY OF COLUMBIA RIVER  
PLATEAU BASALT AND ITS RELATION  
TO A COASTAL BASALT FLOW

H. R. Bowman, H. Schmincke,\* and A. Hebert

The results of recent chemical analyses on 10 major elements from three eruptive basalts on the Pacific Coast in Washington and Oregon indicate that they are chemically identical to three basalt types erupted over 500 km to the east on the Columbia River Plateau. K/AR dates on two of these related flows<sup>1</sup> differ by at least 3 million years with the coastal member being the younger of the two.

Measurements have been made of the abundances of over 30 trace and major elements using both neutron activation analysis<sup>2</sup> and vacuum x-ray fluorescence analysis<sup>3</sup> on samples from these two related flows. Six samples from the coastal flows (Pack Sack Lookout) were analyzed and the results compared with those obtained from 18 samples of the Pomona flow, it's Columbia River Plateau equivalent. The Pomona flow covers over 10,000 km<sup>2</sup> in the Plateau region<sup>4</sup> and was sampled quite extensively. The purpose of this work was to determine the homogeneity of the Pomona flow in terms of 30 elements and to see if the trace element data confirmed the earlier major element conclusions.

The results of these measurements are shown in Fig. 1 where the abundances for 25 elements are plotted along with the results obtained from limited samples from five other Plateau basalts. The chemical abundances of the six Plateau basalts are represented by the small rectangles in each of the 25 graphs. The basalt flows or sheets are plotted in ascending stratigraphical order going from left to right and are labeled 1-6. This is the general order of their eruption with the Picture Gorge Upper (2) coming later than the Picture Gorge Lower (1). The time span covered in the graphs is of the order of 10 million years. The vertical heights of the rectangles in Fig. 1 are measures of the chemical variability of the flows which include any possible contamination during the eruption. The height of these rectangles in the case of Yakima basalt (3) is a measure of reproducibility since they represent the root-mean-square deviation in six samples of the same material. The Pomona (5) and the Elephant Mountain (6) rectangles demonstrate lateral variations. The Picture Gorge (1, 2) samples were taken vertically, and the Umatilla (4) samples demonstrate local variations only.

The long horizontal bar in each of the graphs demonstrates the range of chemical compositions found in the coastal Pack Sack Lookout basalt.

As can be seen, the Pomona basalt is the only one of the Plateau basalts that correlates for all 25 elements with the coastal basalt. Four of the six Pack Sack Lookout rocks are in excellent agreement with the Pomona results. The most striking feature shown in Fig. 1 is the lack of chemical variation or contamination in the Pomona flow or it's coastal member. The only major contaminant of the Pomona flow is barium wherein 2 of the 18 samples had about twice the barium as the mean of the 14 best samples. The two remaining samples had somewhat less excess barium.

The recurrent patterns in the ascending stratigraphic sequence of the Plateau basalts demonstrates the relatively primitive nature of the Picture Gorge Lower basalt as well as the differences between the six flows. This primitive nature is confirmed by the rare-earth pattern shown in Fig. 2. Rocks with rare-earth pattern similar to chondrites or abyssal-basalts are assumed to be primitive and less differentiated than rocks with continental rare-earth patterns. Two rare-earth patterns of Pacific Ridge basalts<sup>5</sup> (Gorda Ridge basalt) are also shown in Fig. 2. The Pomona and Pack Sack Lookout rare earth patterns have about the same degree of fractionation in the light rare earths and fall intermediately in the range between Lower Picture Gorge and the Umatilla flows.

In conclusion, all of the new chemical data indicate that at least four of the six samples of the Pack Sack Lookout flow on the Pacific Coast of Washington are in excellent agreement with the Plateau derived Pomona flow for over 30 elemental abundances. These two flows must have had a very similar history and very likely a common magma source.

These data also<sup>1</sup> question the validity of the K/AR dates on the Pomona and the Pack Sack Lookout basalts. One might expect to find detectable differences in chemical composition if this magma remained in a magma chamber for over 3 million years before erup-

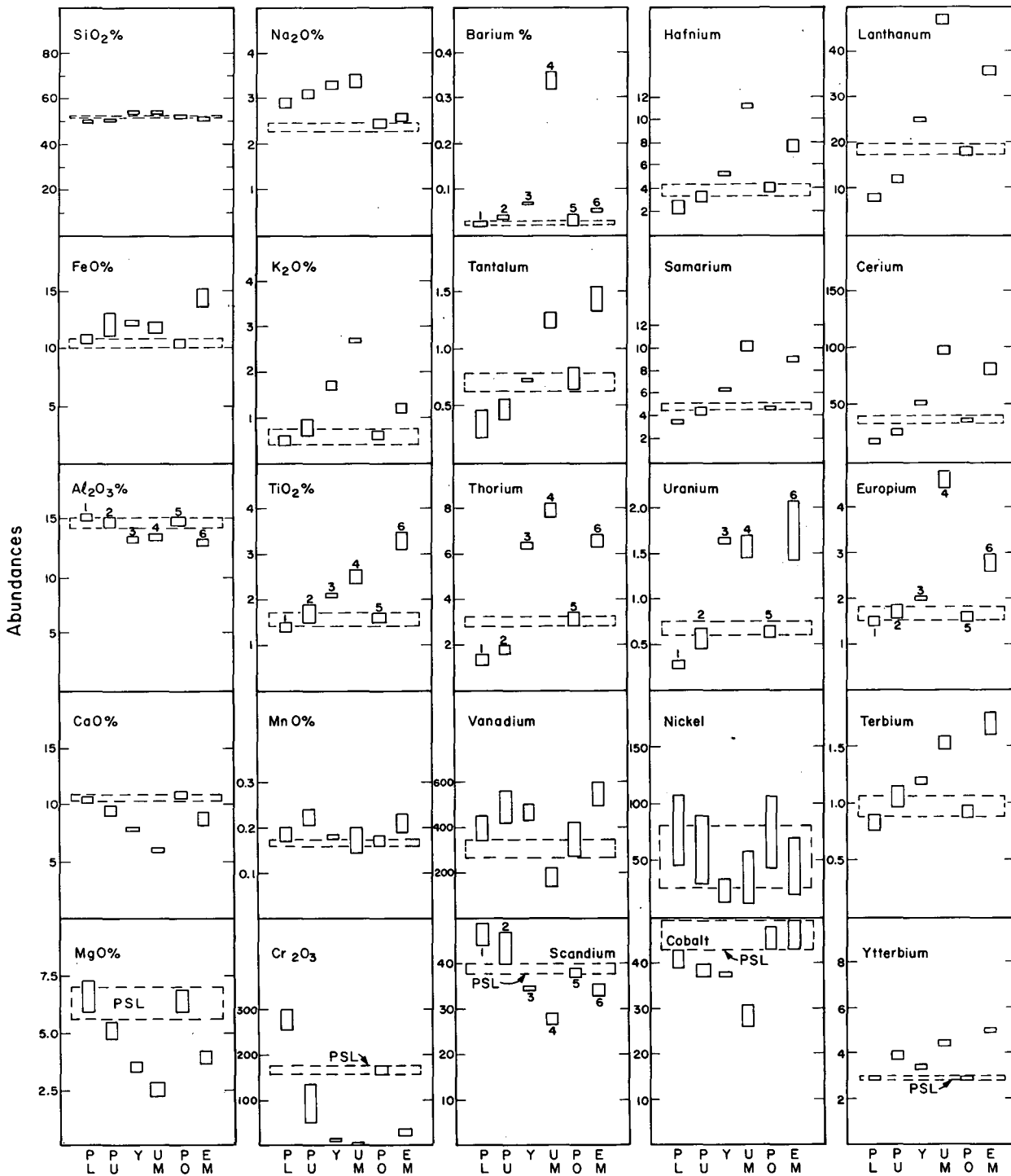


Fig. 1. The chemical compositions of Columbia River Plateau basalt flows (small rectangles): (1) Picture Gorge Lower [10 samples] (2) Picture Gorge Upper [9 samples] (3) Yakima Basalt [6 samples of BCR standard rock] (4) Umatilla [5 samples] (5) Pomona [18 samples] (6) Elephant Mt. [12 samples]. Flows are in ascending stratigraphic order 1-6. Pack Sack Lookout Basalt found on the Pacific Coast is shown as long horizontal rectangle. (XBL 742-2345)



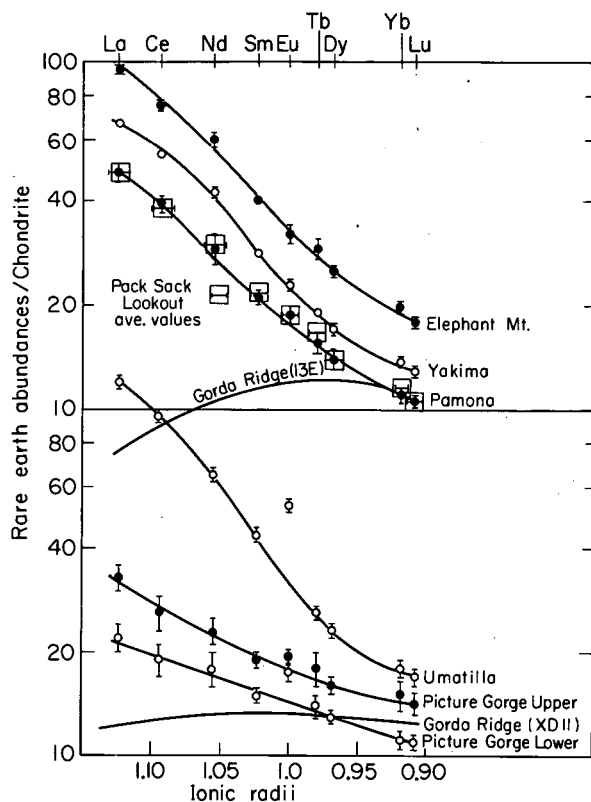


Fig. 2. The rare earth element patterns of Columbia River Plateau Basalts (normalized to chondrites) shown with two samples of Gorda Ridge (Pacific Ridge Basalts). The Pack Sack Lookout values are shown by rectangles.

XBL742-2393

#### DEFINITIVE PROVENIENCE DETERMINATIONS ON MESOAMERICA OBSIDIAN ARTIFACTS

F. Asaro, H. R. Bowman, and F. Stross\*

Much of the previous work dealing with provenience (place of origin) of obsidian artifacts has been done with emission spectroscopy<sup>1</sup> and x-ray fluorescence analysis.<sup>2</sup> Considerable useful work has been accomplished with these techniques but overlapping chemical patterns between sites has introduced some ambiguities. In some cases additional analytical techniques were needed to clearly define sources and artifacts. The present approach (neutron activation analysis)<sup>3</sup> has not only been shown to be definitive in this sense but has demonstrated that in special source areas,<sup>4</sup> precise locations within the source areas can also be determined.

tion a second time along the coast. Further study of the small chemical differences may lead to the means of emplacement. It seems very unlikely that this molten liquid could have travelled either on the surface or below it for hundreds of kilometers without a trace of contamination from the surrounding rocks.

#### Footnotes and References

\*Ruhr-University, Bochum, Germany.

1. P. D. Snavely, *Geol. Soc. of Am. Bul.* **84**, (1973).
2. H. R. Bowman, F. Asaro, and I. Perlman, *J. Geol.* **81**, No. 3 (1973).
3. A. J. Hebert and K. Street, Jr., *Anal. Chem.*, **46**, No. 2, (1974).
4. H. U. Schmincke, *Geol. Soc. of Am. Bul.* **78**, (1967).
5. R. Kay, N. J. Hubbard, and P. W. Gast, *J. Geophysical Res.* **75**, No. 8, (1970).

We have recently examined a number of obsidian artifacts and source areas in Mesoamerica and conclude that similar results can be determined there.

Obsidian source samples were obtained from two highway cuts in the El Chayal deposit at about 22 and 25 km ENE of Guatemala City, from a riverbed at Puente Chetunal somewhat further away from Guatemala City, and from Ixtepeque, also in Guatemala. Table I shows the mean abundances for 24 elements (at 3 locations) and the root-mean-square deviation for each element measured by neutron activation analysis. For one of the sources, Ixte-

Table I. Elemental abundances<sup>a</sup> from neutron activation analyses of obsidian source samples from Guatemala.

	El Chayal (25 km)	Artifact <sup>b</sup>	El Chayal (22-23 km)	Puente Chetunal riverbed	
	12 samples		4 samples	4 samples	4 samples
$\sigma(16)^c$	1.51%		1.57%	2.06%	
$\sigma(24)$	4.02%		3.63%	4.2%	
Ta	0.950 ± .009	0.942	0.973 ± .009	0.930 ± .015	
Hf	3.48 ± .06	3.37	3.44 ± .06	3.51 ± .13	
Eu	0.613 ± .010	0.599	0.579 ± .010	0.485 ± .013	
Th	10.57 ± .13	10.60	10.31 ± .10	11.07 ± .21	
Yb	1.96 ± .03	1.92	2.01 ± .03	1.56 ± .04	
Sc	2.00 ± .04	1.91	2.06 ± .03	2.27 ± .08	
U	4.30 ± .04	4.19	4.73 ± .04	4.30 ± .03	
Sm	3.05 ± .02	3.02	2.93 ± .04	2.46 ± .04	
Mn	618 ± 8	622	603 ± 5	450 ± 7	446 ± 7
Na%	3.09 ± .02	3.03	2.99 ± .04	2.80 ± .03	3.04 ± .06
Ce	47.9 ± .6	46.8	42.4 ± .9	40.7 ± .3	
Al%	7.12 ± .19	6.91	7.09 ± .24	6.95 ± .21	
Ba	946 ± 16	414	896 ± 12	971 ± 19	
La	24.8 ± .5	24.2	22.0 ± .3	22.7 ± .7	
Fe%	0.628 ± .015	0.631	0.747 ± .019	0.75 ± .02	
Cs	7.85 ± .13	7.77	7.43 ± .13	6.4 ± .2	
Dy	2.65 ± .14	2.56	2.57 ± .09	2.12 ± .10	2.28 ± .13
Lu	0.286 ± .018	0.268	0.292 ± .018	0.224 ± .015	
Tb	0.454 ± .025	0.457	0.431 ± .026	0.380 ± .031	
Zn	41 ± 3	43	34 ± 3	31 ± 3	
Rb	163 ± 15	143	171 ± 15	141 ± 11	
K%	3.41 ± .24	3.46	3.09 ± .23	3.44 ± .24	3.61 ± .18
Co	0.31 ± .05	0.25	0.54 ± .05	0.75 ± .06	
Sb	0.70 ± .11	0.68	0.83 ± .10	0.67 ± .06	

<sup>a</sup> Abundances are in ppm or in % if so indicated after the chemical symbol. After the abundance for each element is given the rms deviation for the samples in the group.

<sup>b</sup> Randomly selected artifact from British Honduras.

<sup>c</sup> Best elements.

peque, measurements are shown for only 4 elements and these were determined from a single low power reactor irradiation.

If we assume for each of the sampled locations a Gaussian distribution for elemental abundances, and also adequate sampling, then ~68% of the elemental abundances of an arti-

fact, from one of them, should fall within the root-mean-square deviation ( $1\sigma$ ) of the source material and ~95% of the element should agree within  $2\sigma$ .

For 16 of the elements at El Chayal we have a rms deviation ( $1\sigma$ ) of only 1.51%. Thus this source is very homogeneous and artifacts

must agree with this compositional pattern within 1 or 2% to be assigned this source location. As an example, we will consider a single randomly selected artifact which was analyzed using the same technique. Its composition as seen in Table I agrees very closely with that of the El Chayal source 25 km from Guatemala City and not with that from 22-23 km away. If further source sampling of the El Chayal deposits show variations comparable to the two already measured, we would be able to determine from which area of the deposit artifacts originated, with this technique.

Tests were also made to determine how well one could distinguish between specific sources using a minimum number of irradiations and gamma-ray analyses. Thirty-eight

Table II. Neutron activation analysis of artifacts with a single irradiation and a single  $\gamma$ -ray analysis.

No. of Artifacts in Group	Group I	Group II	Group III
	22	15	1
Na%	$3.01 \pm .02^a$	$3.15 \pm .03^a$	$2.93 \pm .02^b$
Mn	$447 \pm 4$	$629 \pm 5$	$165 \pm 2$
Dy	$2.33 \pm .09$	$2.63 \pm .09$	$3.72 \pm .08$
K%	$3.63 \pm .25$	$3.37 \pm .25$	$4.88 \pm .25$

<sup>a</sup> rms deviations.  
<sup>b</sup> experimental precision.

obsidian artifacts from British Honduras were analyzed for the same four elements as the Ixtepeque sources. The artifacts fell into three obvious chemical groups and they are listed in Table II in that fashion. There is no doubt that if we assume initially that the artifacts had to come from one of the four sites shown in Table I, then Group II came from El Chayal 25 km from Guatemala City, and Group I came from Ixtepeque, but the one sample in Group III came from elsewhere. Thus, if further and more extensive source sampling confirms these results, one could distinguish the given source sites shown in Table I without making a complete neutron activation analysis and thus reduce the cost of artifact sampling. It cannot be stressed too strongly, perhaps, that extensive measurements must be made of all likely source sites before the simpler less expensive measurements can be justified.

#### Footnotes and References

\*Department of Anthropology, University of California, Berkeley.

1. J. R. Can and C. Renfrew, Proc. Prehistoric Soc. 30, 110 (1964).
2. D. P. Stevenson, F. S. Stross, and R. F. Heizer, Archaeometry 13, (1) 17 (1971).
3. I. Perlman and F. Asaro, Archaeometry 11, 21 (1969).
4. H. R. Bowman, F. Asaro, and I. Perlman, Archaeometry 15, 1 (1973).

## ON THE RECONSTRUCTION OF THE NORTH COLOSSUS OF MEMNON

H. R. Bowman, F. Asaro, F. H. Stross and  
R. F. Heizer

Just before the turn of the 3rd century A.D., the Roman emperor, Septimus Severus, reconstructed the upper part of the North Colossus of Memnon, which had been partially destroyed during an earthquake in 27 B.C. Until the present time it has been presumed that only the upper part of the North Statue was reconstructed. The view of the North Statue (from the north) is shown in Fig. 1. The reconstructed portion above the lap can be seen to consist of five layers of stone blocks including the head.

In a previous study, neutron activation analyses were made on a number of samples from the two Colossi of Memnon and the pedestal of the south statue. These are situated across the Nile from modern Luxor in Egypt. It was shown that the two statues and the south pedestal were most likely brought ~430 miles up the Nile from a quarry near Cairo, rather than floated downstream from much closer quarries to the south. Only one measurement was made of a portion of the north pedestal and that was of a loose block.

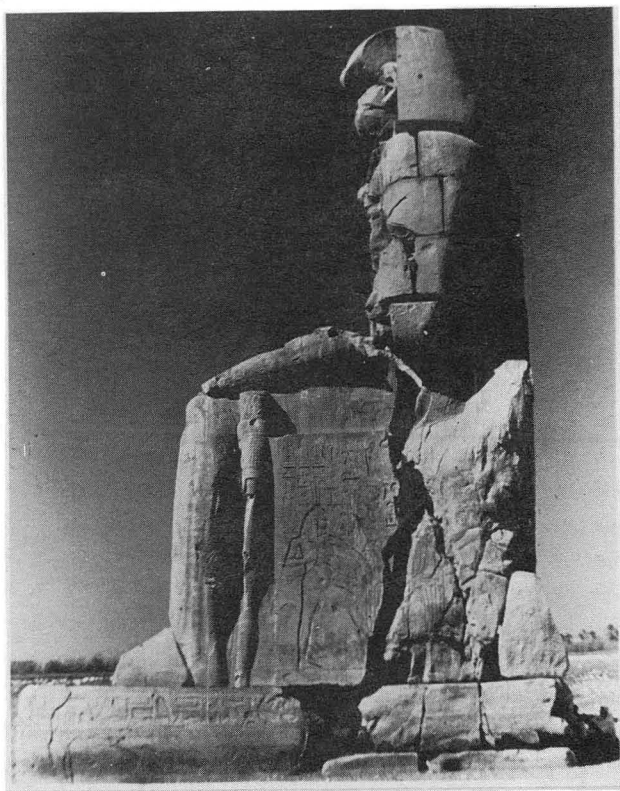


Fig.1. North Colossus of Memnon.

Additional neutron activation studies have now been made on samples from various parts of the pedestal of the north statue.

The abundances of 13 of the best measured and the most distinctive elements in the pedestal samples are shown in Table I. Six other rare-earths were measured, but they simply confirm the pattern indicated by the ones shown. In Column I we show the average values for each element in nine of the rear pedestal blocks. For each element the root-mean-square deviation for all nine blocks is also shown. Column 2 shows the abundance values and precision (10) for the main pedestal block in front. Columns 3-5 show the same data for the three upper reconstruction blocks which were measured and Columns 6-10 show the same data for the southern quarries around Edfu and Aswan. The chemical composition of the main pedestal block in the front part of the north Colossus agrees better with the composition of rocks from the Cairo quarry than with those from the Aswan and Edfu quarries. Further sampling of this block, however, in different areas would be necessary to make a definite assignment by this technique.

The other nine blocks in the rear pedestal had a chemical composition which was very different from the main block, the two Colossi and the quarry samples from Cairo. In addition, the nine blocks as a group were chemical-

Table I. Chemical analyses<sup>1</sup> of pedestal blocks of the North Colossus of Memnon.

	Pedestal blocks		Upper reconstruction blocks			Quarry Sites					Aswan ave.
	Nine rear blocks	Main front block	COLI-609	COLI-610	COLI-18	Edfu		Gebel Simeon		Gebel Osman	
						COLI-423	COLI-17	COLI-149	COLI-157	COLI-301	
U	0.45 ± 0.05	0.49 ± 0.01	0.32 ± 0.01	0.49 ± 0.01	0.33 ± 0.01	0.48 ± 0.01	0.39 ± 0.01	0.38 ± 0.01	0.49 ± 0.01	0.42 ± 0.01	0.43 ± 0.05
La	7.1 ± 1.5	2.3 ± 0.2	5.08 ± 0.17	5.15 ± 0.18	5.73 ± 0.22	8.4 ± 0.2	5.27 ± 0.21	7.4 ± 0.2	8.0 ± 0.2	7.7 ± 0.2	7.7 ± 0.3
Sm	1.04 ± 0.22	0.388 ± 0.004	0.666 ± 0.003	0.833 ± 0.004	0.837 ± 0.005	1.319 ± 0.004	0.730 ± 0.004	0.947 ± 0.004	1.311 ± 0.004	1.034 ± 0.005	1.1 ± 0.2
Eu	0.25 ± 0.04	0.090 ± 0.004	0.159 ± 0.004	0.244 ± 0.005	0.222 ± 0.012	0.235 ± 0.004	0.214 ± 0.001	0.211 ± 0.013	0.308 ± 0.011	0.271 ± 0.014	0.26 ± 0.05
Lu	0.089 ± 0.019	0.041 ± 0.006	0.045 ± 0.005	0.175 ± 0.009	0.077 ± 0.005	0.044 ± 0.005	0.059 ± 0.005	0.076 ± 0.006	0.111 ± 0.007	0.087 ± 0.006	0.09 ± 0.02
Fe%	0.28 ± 0.09	1.06 ± 0.03	0.23 ± 0.01	0.30 ± 0.01	0.10 ± 0.01	0.47 ± 0.01	0.17 ± 0.01	0.30 ± 0.01	0.40 ± 0.01	0.34 ± 0.01	0.35 ± 0.05
Co	3.1 ± 0.8	3.68 ± 0.12	2.20 ± 0.08	3.56 ± 0.11	1.24 ± 0.06	4.65 ± 0.12	2.06 ± 0.08	2.04 ± 0.08	4.53 ± 0.12	3.67 ± 0.10	3.4 ± 1.3
Sc	1.2 ± 0.3	0.63 ± 0.01	0.66 ± 0.01	1.05 ± 0.01	0.98 ± 0.02	0.77 ± 0.01	0.71 ± 0.01	0.98 ± 0.01	1.40 ± 0.02	0.90 ± 0.01	1.1 ± 0.3
Ti%	0.20 ± 0.04	0.033 ± 0.003	0.148 ± 0.003	0.184 ± 0.003	0.174 ± 0.004	0.176 ± 0.003	0.141 ± 0.003	0.213 ± 0.004	0.243 ± 0.004	0.224 ± 0.004	0.23 ± 0.02
Ta	0.26 ± 0.04	0.160 ± 0.002	0.156 ± 0.002	0.211 ± 0.002	0.416 ± 0.003	0.210 ± 0.002	0.193 ± 0.002	0.24 ± 0.02	0.31 ± 0.03	0.301 ± 0.003	0.28 ± 0.04
Hf	4.2 ± 1.0	0.88 ± 0.04	2.24 ± 0.03	5.78 ± 0.08	2.54 ± 0.12	1.51 ± 0.04	2.58 ± 0.11	4.28 ± 0.17	5.38 ± 0.21	3.40 ± 0.14	4.35 ± 0.99
Th	1.03 ± 0.28	0.55 ± 0.04	0.91 ± 0.03	0.93 ± 0.04	0.84 ± 0.04	1.56 ± 0.03	1.05 ± 0.04	1.76 ± 0.04	1.76 ± 0.05	1.14 ± 0.04	1.5 ± 0.4
As	1.9 ± 0.8	0.8 ± 0.6	1.2	1.5	1.1	3.2	1.4	1.0	1.4	2.8	1.7 ± 0.9

<sup>1</sup> Abundances are in parts-per-million except for Fe and Ti which are in percent.

<sup>2</sup> Measurements are from nine pedestal blocks not including the main front block and a loose block on the south side which was not measured.

ly considerably more homogeneous than the samples from either Colossus, the south pedestal or the quarry from Cairo. One of the duplicate samplings of the pedestal blocks gave a much different chemical composition. Further sampling is necessary to determine the cause of this.

The rear pedestal blocks agree best with rock samples from near Aswan. Our quarry sampling from near Edfu, however, has been so limited (two rocks) that we cannot definitely distinguish Edfu from Aswan.

The upper construction blocks are somewhat similar in composition to the rear pedestal blocks but they do not match them as closely as the samples from the Aswan quarries. Again our sampling of only three upper reconstruction blocks was too limited to determine if they had a common origin with the north pedestal rear block.

Petrographic analysis of several of the rear pedestal blocks by Prof. R. Hay of the University of California, Department of Geology and Geophysics indicated that the main block matches quarry samples from near Cairo and a rear pedestal block matched samples from near Edfu.

The new results suggest that the rear of the north pedestal may have been reconstructed as well as the portion of the statue above lap. A similar suggestion arises from visual measurements. Besides the main pedestal block under the front part of the north statue, there are eight others which can be seen under the rear. This contrasts with the pedestal of the south statue which seems to have been constructed to look monolithic and probably consisted of not more than three blocks.

The eight blocks are set in two tiers, the lower tier protrudes some inches above the ground and forms a base on which the upper tier rests. The blocks in the upper tier are very close to 4 ft high and seem to be of about the same size as the blocks in the reconstructed portion above the lap. The angles which the

main and rear pedestal blocks make with the lines caused by the Nile high waters, were estimated from photographs of the north side of the north statue. Whereas the main pedestal block appeared to be tilted at an angle of about 2-3/4 degrees in the east-west direction, the rear blocks were horizontal within about 1/2 degree. These measurements indicate that the rear portion of the pedestal is definitely different in construction than the main pedestal block and was perhaps constructed after the statue had tilted.

The following paragraphs are speculations which suggest new measurements. If further on-site physical measurements demonstrate: (1) that the rear of the north pedestal forms a nearly horizontal base for the statue (2) that the blocks of the upper reconstructed portion are also in horizontal planes, and (3) that the part of the statue in between is tilted by several degrees, then the rear pedestal was very likely constructed after the statue had tilted and at about the same time or before the top portion of the statue was reconstructed.

Further measurements could also establish if the front and rear portions of the north statue are tilted with respect to each other and hence are in two sections which could move independently. All of these measurements together could give an indication of the amount of tilting of the north statue in the last 1800 years and, if it is minimal, alleviate fears of the statue toppling and permit excavations around the base.

## CHEMICAL ANALYSIS OF CERAMIC WARES FROM FUSTAT, EGYPT

H. V. Michel, F. Asaro, and J. D. Frierman\*

Twenty-eight sherds from Fustat, old Cairo, have been analyzed for about 30 chemical elements by neutron activation measurements.<sup>1</sup> Thirteen of the sherds have body composition patterns similar to Egyptian faience. Egyptian faience, according to Lucas,<sup>2</sup> is glazed quartz frit. He says it does not contain clay as does true "faience," which is tin glazed earthenware. The SiO<sub>2</sub> content of the 13 sherds appears to be quite high, as would be expected for faience. The values, which we obtained by differences, subtracting the abundances of the major elements' oxides from 100%, varied between 84-93%. Of these 13 sherds, 10 fall into one of 2 groups of 5 sherds each. Table I shows the composition of the two groups of Egyptian faience. One of the remaining three sherds matches the composition of a

piece of lustre faience of the 9-10th century from Samarra. Two other sherds are each unique in their composition and appearance. The five sherds in the faience group B are all typologically similar, painted underneath the glaze and described by the excavator as Egyptian imitation of 13-14th century A.D. Persian.<sup>3</sup> Two of the sherds in faience group A are kiln wasters, i. e., misfired or otherwise imperfect pots. The wasters would argue for local manufacture of the group A.

Nine of the remaining pottery sherds fall into one of three groups. Table II shows the chemical composition of these three groups and a reference group. Pottery group A consists of four sherds; three lustre ware and one polychrome lustre ware. This group matches

Table I. The chemical composition and standard deviation for each element of two types of Egyptian faience from Fustat.

	A	B
SiO <sub>2</sub> % <sup>b</sup>	86.6 ± 1.5 <sup>a</sup>	88.8 ± 3.3
Ca%	2.68 ± 0.96	4.8 ± 1.6
Al%	2.29 ± 0.25	0.81 ± 0.18
Na%	2.11 ± 0.35	1.09 ± 0.23
K%	0.81 ± 0.18	0.48 ± 0.14
Fe%	1.06 ± 0.10	0.39 ± 0.09
Sc	4.49 ± 0.32	1.91 ± 0.56
Lu	0.12 ± 0.013	0.079 ± 0.013
Ta	0.490 ± 0.074	0.158 ± 0.022
Th	2.83 ± 0.33	1.53 ± 0.41
Hf	2.13 ± 0.55	2.57 ± 0.53
Eu	0.452 ± 0.045	0.239 ± 0.038
Sm	1.94 ± 0.25	1.06 ± 0.18

<sup>a</sup> The two entries for each element in a group are the average abundance and the root mean square deviation. The values are expressed in ppm unless % is indicated after the element symbol.

<sup>b</sup> SiO<sub>2</sub> was obtained by differences, assuming the major elements as oxides.

Table II. Neutron activation analysis abundances<sup>a</sup> of selected elements in three groups of pottery from Fustat and reference group of Samarra ware.

	Pottery Excavated at Fustat			Samarra Ware
	A	B	C	
Al%	6.07 ± 0.12 <sup>a</sup>	9.30 ± 0.30	12.18 ± 0.52 <sup>b</sup>	6.53 ± 0.31
Ca%	13.86 ± 0.32	7.90 ± 1.58	0.98 ± 0.45	13.33 ± 0.90
Mn	950 ± 53	637 ± 53	285 ± 8.5	906 ± 48
Na%	1.413 ± 0.16	0.876 ± 0.11	0.395 ± 0.05	1.659 ± 0.19
U	1.940 ± 0.044	3.15 ± 0.17	3.38 ± 0.11	1.950 ± 0.22
Eu	1.057 ± 0.04	1.443 ± 0.025	2.256 ± 0.037	1.032 ± 0.031
Ba	172 ± 15	338 ± 26	200 ± 7	195 ± 52
Sm	4.041 ± 0.11	6.549 ± 0.104	8.897 ± 0.027	4.123 ± 0.115
La	21.72 ± 1.0	41.07 ± 1.3	55.0 ± 0.40	22.3 ± 1.1
Ti%	0.398 ± 0.028	0.459 ± 0.009	1.037 ± 0.004	0.422 ± 0.062
Lu	0.316 ± 0.017	0.420 ± 0.012	0.516 ± 0.022	0.318 ± 0.018
Co	26.9 ± 1.9	19.14 ± 0.96	15.21 ± 0.41	28.1 ± 1.4
Sc	19.32 ± 0.51	18.26 ± 0.61	27.28 ± 1.23	19.28 ± 0.63
Fe%	5.01 ± 0.12	4.98 ± 0.15	3.93 ± 0.51	4.99 ± 0.17
Ce	47.08 ± 0.90	85.9 ± 2.0	115.5 ± 1.1	47.47 ± 1.7
Cr	260 ± 13	115 ± 6	152 ± 2	280 ± 33
Th	7.125 ± 0.034	14.0 ± 0.48	14.02 ± 0.95	7.0 ± 0.22
Ni	266 ± 13	60 ± 14	55 ± 14	257 ± 19
Hf	3.335 ± 0.058	4.837 ± 0.180	7.420 ± 0.099	3.351 ± 0.147
Ta	0.814 ± 0.018	1.248 ± 0.027	1.736 ± 0.074	0.800 ± 0.032

<sup>a</sup> The two entries for each element in a group are the average abundance and the root mean square deviation. The values are expressed in ppm unless % is indicated after the element symbol.

<sup>b</sup> The two entries for each element in group C are the average abundance and the range.

closely the reference group of pottery called Samarra ware excavated at Sirāf, Iran. Samarra was a center of pottery making for a relatively short time in the 9th century before it was destroyed. Pottery group B contains three sherds whose compositions are somewhat similar to material called "Cypriot Base Ring" and "red polished ware from Rashamra". The third group C consists of two sherds which match the composition of a single sherd previously analyzed from Abkah. Abkah is a site south of the 2nd Cataract on the east bank of the Nile, approximately 600 miles south of Fustat. One of these two Fustat sherds is a waster that would probably not have been exported and thus very likely represents local material.

#### Footnote and References

\* Museum of Ethnic Arts, University of California at Los Angeles, Los Angeles, California.

1. F. Asaro and I. Perlman, *Archaeometry* **11**, 21 (1969).
2. A. Lucas and J. R. Harris, *Ancient Egyptian Materials and Industry*, 4th edition (Edward Arnold Publishers Ltd., London, 1962), p. 156.
3. George T. Scalon, private communication.

#### A LYONS BRANCH OF THE POTTERY-MAKING FIRM OF ATEIUS OF AREZZO

F. Asaro, H. V. Michel, I. Perlman,\* F. Widemann,<sup>†</sup> and M. Picon<sup>‡</sup>

#### INTRODUCTION

##### Romans and the Gallic Market of Ceramics

After the middle of the first century B.C., a new class of ceramics with a red glaze ("terra sigillata"), mostly signed, appeared in Italy.

This pottery came predominantly from the workshops which were producing the black glazed Campanian B,<sup>1</sup> especially those in Arezzo. These new ceramics were soon exported and met with considerable success. This work was quickly imitated in Gaul, and some of the imitations came from the workshops of

Loyasse in Lyons. These imitations, however, were technically very different from their models. In particular, the local potters could not obtain a red glaze comparable to that from the workshops of Arezzo, but only a porous one of low quality. These imitators also distinguished themselves by not signing most of their productions.

The success of their red glazed products probably stimulated the potters of Arezzo to establish branches closer to the new markets which had opened by the Roman conquests in Gaul and on the Rhine. This interpretation is supported by the existence of the large complex of workshops of La Montée de la Muette in Lyons, which did not produce imitations but, and apparently for the first time in Gaul, red pottery which had all the characteristics of those from Arezzo. Furthermore, out of the 14 fragments of moulds which have been discovered in La Muette, two show a distribution of major chemical elements which suggests a provenience from Arezzo.<sup>2</sup>

Among the large firms of Arezzo, Ateius held the attention of scholars largely because of its prominence in the market in Gaul and in the Germanic frontier garrisons.<sup>3-5</sup> Because many sherds with the Ateius signature had been found in Gaul and none in Arezzo, it had been suggested<sup>6, 7</sup> that these potteries may have been locally made. These arguments were revised after the discovery of the Ateius workshop in Arezzo.<sup>8</sup> The possibility still remains, however, that some Ateius pottery was made in Gaul although none has been found in excavations of pottery workshops up to the present time.

Recently a systematic study<sup>9</sup> was made by x-ray fluorescence analysis of the abundances of the major chemical elements of many Italic ceramic imports found in Gaul. Five sherds bearing the Ateius signature had chemical composition patterns or "fingerprints" which were not only distinctly different from that of pottery excavated in Arezzo, but were rather similar to those of pottery excavated in workshops around Lyons.

Although this information by itself was not sufficient to establish Lyons as the site of origin for these sherds, it did suggest that a more detailed investigation of chemical abundances might give definitive answers.

## EXPERIMENTAL TECHNIQUES

### Trace Elements

Besides the major elements found in pottery, there are many which occur only in minute traces, often in just a few parts-per-million (ppm). The abundances of these trace

elements in different clay sources can exhibit large variations that reflect differences in the geochemical history of the clays as well as subsequent alterations in their environment. In addition, some of the practices used in pottery-making can cause changes in chemical composition. Such changes could occur in the processes of levigating clay, which removes coarse particles including some limestone; tempering clay, which introduces organic materials, rock products or old pottery into the clay; and firing calcareous clays at different temperatures, which can result in large variations in the carbonate content.

Although wide differences in trace element abundances can occur in clays from different areas, much of the pottery excavated in a particular site will usually fall into either a single fairly homogeneous chemical group or into a few such groups. Often, some of the pottery in such a group can be shown to be local products by archaeological or other criteria. The chemical abundances of this group then serve as a "fingerprint" to determine if pottery found elsewhere has the same provenience.

### Statistical Criteria for NAA

Neutron activation analysis (NAA) has been shown to be very effective in distinguishing pottery groups and determining provenience by trace (and some major) element analyses. In one such method,<sup>10, 11</sup> that is used in the present work, some 50 elements are looked for in each pottery sample, about 40 are usually observed and the abundances of over 20 of these elements (the ones used to fingerprint the pottery) are measured with an average precision of ~2%.

Some simple statistical criteria<sup>12, 13</sup> have been used for evaluating the chemical abundance data. For a group of pots of similar chemical composition, the fingerprint consists of first, the abundance for each element averaged over all of the pots and second, the root-mean-square deviation ( $\sigma$ ) for each element for the same pots. The root-mean-square deviation for a particular element is obtained by determining the differences between the mean value of the abundance of that element and the values for each of the pots in the group, squaring each of the differences, summing the squares, dividing the sum by the number of pots minus 1 and taking the square root of the quotient. Sixty-eight percent of the pots in the group should have abundances within  $1\sigma$  for each element, 95% should have abundances within  $2\sigma$  for each element and 99.7% should have abundances within  $3\sigma$ . For a pot of unknown provenience to be a member of this "reference" group, on the average 68% of the elements should have abundances within  $1\sigma$  of the group average and 95% within  $2\sigma$ .

For a given pottery group, the smaller the values of  $\sigma$  for the various elements and the larger the number of useful elements included in the analysis, the smaller is the probability of making an erroneous assignment of provenience by this method. In practice, it has been found that if about 20 carefully selected elements are used and the average value for  $\sigma$  of their abundance is 10% or less in the reference group, then the determination of provenience is reliable. The selected elements should be measured with a precision substantially better than 10% and then should vary somewhat randomly with respect to each in the different clay beds, but should not vary erratically in the same pot.

#### Selection of Sherds

The sherds for the NAA were part of the group which had been previously analyzed<sup>9</sup> by x-ray fluorescence (XRF) and were representative of the group in their major element abundances.

Pottery from Arezzo - All twenty three shreds were terra sigillata found in Arezzo which appeared to be rejects from kiln dumps of several workshops.

Pottery from Lyons - As reference sherds from Lyons, we used pieces of broken, mis-baked or deformed pots of terra sigillata from dumps found near the kilns. Twenty-two samples excavated from La Murette and six from Loyasse were used in the present measurements. The coarse pottery was not appropriate as reference material because it was made from a different type of clay that was not calcareous. It has been noted before in studies of pottery from Cyprus<sup>14</sup> and from Lezoux, France<sup>15</sup> that different types of clay were sometimes used to produce different archaeological styles of pottery.

Ateius signed pottery - Four sherds with the Ateius signature (ATE-1-4) were analyzed that had been excavated in Strasbourg and one (DIV-22) that had been excavated in Lyons. None of these sherds, however, came from pottery workshops.

#### Sample Preparations and Measurements

Carbonate measurements - The samples used for XRF measurements were refired in the laboratory at 1000°C before weighing, while those used for NAA were not. The substances removed in the refiring were most likely CO<sub>2</sub> and water. The CO<sub>2</sub> originated either from CaCO<sub>3</sub> (limestone) that was present in the clay before the original firing or was reformed by absorption of CO<sub>2</sub> afterwards. Pottery fired at a low temperature retains its CO<sub>2</sub>, that fired at 1000°C or above loses it and that fired

at temperatures between 900 and 1000°C may lose varying amounts. A comparison between measurements on a sherd by the two techniques which shows the amount of volatile material can indicate if the sherd was well-fired. This will be discussed in more detail later.

In order to determine the CO<sub>2</sub> content of the samples used for NAA measurements, a number of wet chemical analyses were made. The pottery powder was treated with cold 2N HCl and gently heated. The CO<sub>2</sub> released was entrained in a stream of dry nitrogen, scrubbed with sulphuric acid and then dried over anhydrous Mg(ClO<sub>4</sub>)<sub>2</sub>. The CO<sub>2</sub> was then absorbed on ascarite and weighed. The CO<sub>2</sub> measurements were made by Lilly Y. Goda.

NAA measurements - Pottery powder was obtained from a sherd by either first cleaning a surface and then drilling or scraping with sapphire or diamond-tipped tools, or by crushing a cleaned specimen in a mortar and pestle. One hundred mg of the pottery powder was mixed with 50 mg of cellulose binder and pressed into a 1 cm diameter pill.

These pills were irradiated twice in the Triga reactor of the University of California at Berkeley, together with pills of a standard pottery of known composition. The neutron irradiations produce radioactive isotopes in the samples and these emit characteristic gamma rays. The energy of the gamma ray identifies the element, and its intensity, when compared with that of the same gamma ray from the standard pottery, leads to the elemental abundance determination. Two measurements of the gamma ray spectra of each sample were made after a low power irradiation (18 min at  $3 \times 10^{13}$  n/sec-cm<sup>2</sup>).

The gamma ray data were measured with Ge and Ge-Li detector systems coupled to pulse height analyzers that operated in conjunction with automatic sample changers. The spectral data were transferred first to magnetic tapes and then to a computer which calculated the elemental abundances. Further computer analyses of the abundance data were used to help determine the provenience of sherds.

## RESULTS

### Provenience

The abundances measured by NAA for the elements most suitable for provenience determinations are shown in Tables I and II. The average value of the abundance of each element in the group is indicated in the tables together with its root-mean-square deviation. Directly below the group name is shown the number of sherds in the group, and below that is the average value of the root-mean-square deviation.



Table I. NAA abundances<sup>a</sup> of selected elements in pottery from Arezzo and some from Lyons.

Group of sherd	ARE	MML-B	MML-14 <sup>b</sup>	MML-15 <sup>b</sup>	LOY	LOY-3
Qntity. of sherds	23	4			5	
Average $\sigma$	6.5%	5.9%	F = 1.08	F = 1.16	8.6%	
Al%	9.23 ± .55	6.41 ± .23	6.06	6.18	5.37 ± .38	6.76
Ca%	9.5 ± 1.3	18.2 ± 2.4	17.3	15.2	12.7 ± 1.2	9.14
Dy	5.39 ± .21	4.58 ± .31	4.65	4.43	4.04 ± .44	5.31
Mn	1117 ± 41	905 ± 53	862	828	774 ± 89	673
Na%	0.606 ± .027	0.454 ± .014	0.449	0.423	0.507 ± .037	0.687
U	2.70 ± .09	2.61 ± .22	2.60	2.43	2.33 ± .33	3.18
Sm	6.56 ± .20	5.04 ± .05	5.07	5.07	4.69 ± .28	6.10
La	39.4 ± 1.1	29.7 ± .5	29.1	29.6	27.4 ± 1.7	35.0
Ti%	0.477 ± .024	0.270 ± .020	0.236	0.282	0.287 ± .015	0.384
Ta	1.241 ± .039	0.772 ± .018	0.787	0.799	0.785 ± .048	1.133
Co	22.55 ± .86	12.87 ± .19	12.82	12.74	10.27 ± .82	11.84
Sc	19.06 ± .59	11.07 ± .33	10.95	11.33	9.80 ± .69	12.56
Fe%	5.24 ± .19	3.71 ± .06	3.66	3.73	2.96 ± .09	3.20
Yb	2.79 ± .08	2.25 ± .05	2.26	2.29	2.19 ± .11	2.87
Hf	3.95 ± .12	3.06 ± .13	3.30	3.17	4.12 ± .47	6.73
Cs	6.98 ± 1.10	3.68 ± .61	4.32	3.77	5.30 ± .95	8.00
Cr	182 ± 6	79 ± 7	85	70	73 ± 6	85
Th	13.44 ± .47	10.48 ± .13	10.44	10.45	9.70 ± .62	13.26
Eu	1.465 ± .054	1.122 ± .048	1.124	1.145	1.017 ± .059	1.250
Rb	132 ± 16	82 ± 21	81	82	92 ± 19	126 <sup>c</sup>

<sup>a</sup> The two entries for each element in a group are the average abundance and the root-mean-square deviation. The values are expressed in ppm unless % is indicated after the element symbol.

<sup>b</sup> True abundance values are equal to the listed value divided by the enhancement factor, F.

<sup>c</sup> The average Rb counting error for the Loyasse sample was 16 ppm.

tion for the 20 elements expressed as percent of the element abundances.

In the last two columns of Tables II and III are shown the values of one standard deviation for the precision and accuracy of the NAA measurements on sherds of Group MML-A, and these are generally typical of all of the measurements. The precision indicates how well multiple analyses on identical samples should agree if all were made by the same techniques used in the present work. The accuracy contains in addition systematic errors, such as uncertainties in the standard, and should be used for comparison with work done by other techniques or with different standards.

Arezzo pottery — The 23 sherds form a very homogeneous chemical group with an average value of  $\sigma$  for the 20 elements shown in Table I of only 6.5%. This is well below the desirable 10% upper limit discussed previously, and these sherds are thus very suitable as a chemical reference group for assignments of provenience.

The best determined common elements measured by NAA and XRF (Al and Fe) agree very well with each other. Because of the difference in sample preparation involved in the two techniques, the amount of volatile material in the sherds must be very small (~1% or less). The clay from which these pots

Table II. NAA abundances<sup>a</sup> of selected elements in pottery like Group MML-A from La Mulette.

Group of sherd	MML-A	MML-16 <sup>b</sup>	MML-3 <sup>b</sup>	MML-2 <sup>b</sup>	ATE	DIV-22 <sup>b</sup>	Precision <sup>c</sup>	Accuracy <sup>c</sup>
Qty. of sherds	13	F = 0.85	F = 1.08	F = 1.13	4	F = 1.09		
Average $\sigma$	6.4%				3.8%			
Al%	7.38 ± .48	7.16	6.92	7.20	7.32 ± .15	7.15	0.13	0.16
Ca%	10.7 ± 1.6	6.9	12.9	13.0	9.6 ± .6	11.2	0.5	0.5
Dy	5.32 ± .28	5.60	5.19	5.31	5.37 ± .16	5.05	0.14	0.30
Mn	858 ± 82	885	817	840	890 ± 61	855	9	14
Na%	0.363 ± .014	0.365	0.376	0.364	0.391 ± .012	.384	0.007	0.009
U	2.60 ± .13	2.40	2.83	3.08	2.64 ± .10	2.53	0.03	0.23
Sm	6.09 ± .28	6.21	6.02	6.11	6.18 ± .10	6.19	0.03	0.13
La	34.7 ± 1.7	35.6	33.7	34.6	35.8 ± 1.1	35.2	0.5	0.7
Ti%	0.328 ± .021	0.324	0.300	0.293	0.331 ± .014	0.329	0.014	0.020
Ta	0.984 ± .041	0.957	0.966	0.977	0.994 ± .017	1.000	0.007	0.031
Co	14.29 ± .78	14.47	14.78	11.74	14.09 ± .92	12.99	0.19	0.24
Sc	12.62 ± .65	12.77	12.12	12.31	12.78 ± .33	12.54	0.07	0.22
Fe%	3.73 ± .24	3.61	3.62	3.63	3.67 ± .11	3.60	0.04	0.06
Yb	2.70 ± .14	2.76	2.65	2.64	2.80 ± .10	2.73	0.03	0.35
Hf	4.11 ± .22	4.18	4.53	4.47	4.64 ± .12	4.70	0.08	0.31
Cs	6.47 ± .47	6.48	5.65	5.62	6.47 ± .34	6.27	0.17	0.72
Cr	89 ± 9	89	80	85	89 ± 5	84	1.5	5.0
Th	12.09 ± .54	11.73	11.86	11.77	12.14 ± .20	11.92	0.09	0.42
Eu	1.389 ± .072	1.399	1.330	1.390	1.425 ± .021	1.385	0.015	0.041
Rb	125 ± 9	115	146 <sup>d</sup>	114	128 ± 9	119	7	15

<sup>a</sup> The two entries for each element in a group are the average abundance and the root-mean-square deviation. The values are expressed in ppm unless % is indicated after the element symbol.

<sup>b</sup> True abundances are equal to listed values divided by the enhancement factor, F.

<sup>c</sup> Value for one standard deviation.

<sup>d</sup> The precision for this Rb value was 16 ppm rather than 7.

Table III. Abundances<sup>a</sup> of other elements or compounds measured by NAA or wet chemistry.

Group or sherd	ARE	MML-B	MML-14 <sup>b</sup>	MML-15 <sup>b</sup>	LOY	LOY-3		
Number of sherds in group	23	4	F=1.08	F=1.16	5			
Ce	80.8 ±3.0	56.8 ± .9	58.1	59.1	54.0 ±3.6	70.0		
Lu	.402± .017	.317± .022	.345	.350	.328± .021	.397		
Ni	98 ± 15	58 ± 16	48	51	40 ± 11	52		
K%	1.88 ± .31	1.48 ± .32	1.54	1.44	1.39 ± .18	1.42		
Ba	435 ± 36	470 ± 26	496	594	731 ± 198	1217		
As	6.5 ±1.0	27.0 ±3.9	31.3	31.8	25.9 ±10.2	16.9		
Sb	.67 ± .07	1.42 ± .10	1.48	1.33	1.46 ± .40			
Zn	139 ± 7	85± 7	81	88	73 ± 8	91		
CO <sub>2</sub> %				10.2 <sup>(4)</sup>	9.6 ±1.9	3.8		

Group or sherd	MML-A	MML-16 <sup>b</sup>	MML-3 <sup>b</sup>	MML-2 <sup>b</sup>	ATE	DIV-22 <sup>b</sup>	Precision	Accuracy
Number of sherds in group	13	F=0.85	F=1.08	F=1.13	4	F=1.0		
Ce	68.4 ±3.8	68.6	68.9	68.8	70.5 ±1.6	71.0	0.7	3.4
Lu	0.391± .025	.412	0.432	0.425	0.395± .019	0.374	0.017	0.039
Ni	58 ± 15	67	77	46	56± 8	52	9	22
K%	1.82 ± .34	1.67	1.58	1.27	2.19 ± .20	1.73	0.21	0.28
Ba	415 ± 68	371	389	382	490± 105	771	13	24
As	15.1 ±2.0	12.1	15.6	14.6	14.3 ±2.8	12.5	0.7	2.5
Sb	1.25 ± .12	1.09	1.13	1.11	1.20 ± .10	1.52	0.09	0.10
Zn	83 ± 8	80	171	59	87 ± 12	243	5	
CO <sub>2</sub> %	2.0 <sup>d</sup>				0.8 ± .4	4.2	0.3	0.3

<sup>a</sup> The two entries for each element in a group are the average abundance and the root-mean-square deviation. The values are expressed in ppm unless % is indicated after the element symbol.

<sup>b</sup> True abundances are equal to the listed values divided by the enhancement factor, F.

<sup>c</sup> All CO<sub>2</sub> values are true values without any enhancement.

<sup>d</sup> Two values only.

were made very likely contained its Ca predominantly as  $\text{CaCO}_3$  rather than as part of the clay minerals, because the variability in the Ca abundance for the 23 pots is considerably larger (in both measurements) than the variability of the common clay mineral elements. Thus the Arretine sherds were well-fired originally with essentially all of the carbonate destroyed.

Lyons pottery, La Murette - Most of the 22 sherds from La Murette could be divided into two chemical groups which we have designated MML-A, which has 13 sherds, and MML-B which has four sherds. As can be seen from Table I, MML-B is a very homogeneous chemical group with an average  $\sigma$  for 20 elements of only 5.9% and thus is a suitable reference group. The Al and Fe measured by XRF and NAA agree very well with each other, and, for the same reasons as given for the Arezzo pottery, they were well-fired originally.

Two sherds MML-14 and MML-15, would have the same chemical fingerprint as MML-B

if all of their NAA abundances are enhanced by 8 and 16%, respectively. As indicated earlier for a sherd to be a member of the group, ~13 out of 20 elements should have abundances within  $1\sigma$ , ~19 within  $2\sigma$  and approximately all 20 within  $3\sigma$  of the group averages. As shown in Table IV, these two sherds after enhancement agree very well with group MML-B. Comparison of the NAA and XRF data for Al and Fe indicate that the MML-14 and MML-15 samples used for the NAA measurements contained volatile material, to the extent of 8 and 19%, respectively. These values are in good agreement with the enhancement factors used. The presence of carbonate in the MML-15 sample used for NAA was confirmed by wet chemistry which indicated 10.2%  $\text{CO}_2$ . Thus some sherds in group MML-B from Lyons were either not well-fired originally or had picked up  $\text{CO}_2$  since then.

The 13 sherds of MML-A form a homogeneous chemical group with an average  $\sigma$  of 6.4% for the 20 elements shown in Table II. Thus this is a suitable reference group for assign-

Table IV. Statistical comparisons of individual sherds with group averages from neutron activation analysis.

Range of deviation ( $\sigma$ ) expected <sup>a</sup>	Numbers of elements in different ranges of deviation from group average				Reference group	Group Assignment
	0-1 ~13	1-2 ~6	2-3 ~1	3-4 ~0		
ATE-1 <sup>b</sup>	18	2			MML-A	MML-A
ATE-6 <sup>b</sup>	16	3	1			MML-A
ATE-8 <sup>b</sup>	13	7				MML-A
ATE-9 <sup>b</sup>	15	5				MML-A
DIV-22 <sup>c</sup>	17	2	1			MML-A
MML-2 <sup>c</sup>	13	5		2		
MML-3 <sup>c</sup>	13	7				MML-A
MML-16 <sup>c</sup>	16	4	1			MML-A
MML-14 <sup>d</sup>	15	5			MML-B	MML-B
MML-15 <sup>d</sup>	13	6	1			MML-B

<sup>a</sup> Number of elements expected with different ranges of deviations from the group averages for a group member if the abundance distribution is Gaussian.

<sup>b</sup> Abundances reduced by 4% to compensate for 4% average content of volatile material in MML-A.

<sup>c</sup> See Table II for enhancement factors.

<sup>d</sup> See Table I for enhancement factors.

ment of provenience. Comparison between the Fe and Al values measured by XRF and NAA, indicate the NAA samples contain on the average, ~4% volatile material. That at least part of this material was due to carbonate was shown by wet chemistry on two sherds from this group which gave values of 3.0 and 1.3% for the CO<sub>2</sub> content.

One sherd, MML-16, was found to be a member of group MML-A, if its abundances were all reduced by 15% as indicated in Tables II and III. Comparison between XRF and NAA measurements on Fe and Al indicate there was no significant volatile material in MML-16. Thus four of the 15% reduction would be due to the volatile material in group MML-A. Another 5% could be attributed to the lower Ca content of MML-16, which would cause all of the other measured abundances to increase. The variation of Ca abundances in calcareous pottery is often larger than those for other elements because in addition to differences in clay composition, it reflects differences in the potters' techniques for removing limestone.

Another sherd, MML-3 was a member of MML-A if its abundances were enhanced by 8% as shown in Tables II and IV. The Rb abundance differs by over twice the 9 ppm value of  $\sigma$  for MML-A. The counting error on this particular sample, however, was 16 ppm, considerably higher than usual, and that value was therefore substituted for  $\sigma$ . Comparison of XRF and NAA abundance values indicate 14% volatile material in MML-3 and this is in good agreement with the optimum enhancement of 8% needed to make MML-3 agree with MML-A and the 4% average volatile material in MML-A.

The remaining sherd from La Murette, MML-2, agrees somewhat with MML-A if its abundance values are enhanced by 13% as shown in Tables II and IV. However, two elements, U and Co, differ by over 3 $\sigma$ . This may represent some local variation in the MML-A composition. The NAA and XRF values for Fe and Al, which are not very consistent for this sample, indicate about 12% of the sample is volatile material. This value is also not in very good agreement with the 13% enhancement needed to make MML-2 a member of MML-A and the 4% of volatile material in MML-A.

Loyasse - Five of the six sherds from Loyasse form a fairly homogeneous chemical group with an average  $\sigma$  of 8.6% for 20 elements and which is adequate for a chemical reference group. Comparison between XRF and NAA measurements or the Fe and Al in these samples indicate 12% volatile material. This is in good agreement with wet chemical analyses which show an average of 9.6% CO<sub>2</sub> in these five samples as shown in Table III. Thus these samples either retained most of their carbo-

nate after the original firing or absorbed CO<sub>2</sub> afterwards. One sherd from Loyasse, LOY-3, is somewhat different from the other five and probably reflects a local variation.

Ateius - The four signed sherds from Strasbourg have abundances which form an extremely homogeneous group of 20 elements with a  $\sigma$  of 3.8% as can be seen in Table I. If these abundances are reduced by 4%, they are in excellent agreement with group MML-A as shown in Table IV. Comparison between the XRF and NAA measurements for Al and Fe indicate these samples have very little volatile material, and this is confirmed by the results of CO<sub>2</sub> analysis shown in Table III. The 4% reduction is in excellent agreement with the volatile components in MML-A, which are presumed to also be 4%.

One signed sherd, DIV-22, from Lyons has NAA abundances which agree well with MML-A if they are enhanced by 9% as shown in Tables II and IV. Comparison between the XRF and NAA measurements for Fe and Al indicate this sherd has 9% volatile material which is in moderate agreement with the 9% needed to make DIV-22 a member of MML-A and the 4% volatiles in MML-A.

Thus, all five of these signed sherds agree very well in chemical composition with sherds known to have been made in La Murette.

The four sherds from Strasbourg not only may be members of MML-A, but may represent a subgroup as they agree in chemical composition with each other extremely well. DIV-22 and one of the members of MML-A would fit into such a subgroup.

#### Comparison Between the NAA and XRF Measurements

For a number of samples, definite discrepancies were observed between the XRF and NAA measurements, but these could almost all be attributed to differences in the sample preparation procedure. For those sherds with little or no volatile material, the agreements between the XRF and NAA determinations of the same elements were excellent, and the abundance values can be used to determine the differences in the calibrations used in the two measurements.

#### CONCLUSION

Pottery with the Ateius signature has been shown to have the same chemical composition pattern as many pottery rejects found near kilns in the large complex of workshops of Monte de la Murette in Lyons. We believe this indicates definitely that the great pottery-making firm in Arezzo, Ateius, had a branch workshop in Lyons around 10 B.C. This branch

was probably opened with experienced workers and equipment from Arezzo in order to shorten the distance to the new market of the Germanic border legions.

Further measurements of the same type may give information on the extent of the diffusion of pottery from the Lyons workshops into Gaul and Germany and identify additional branch workshops of the firm of Ateius.

#### Footnotes and References

\*Present address: Department of Archaeometry of the Institute of Archaeology at the Hebrew University in Jerusalem.

† Laboratoire de Spectrometrie Nucleaire, Orsay, France.

‡ Laboratoire du Centre d'Etudes Romaines et Gallo-Romaines, Lyon, France.

1. C. Goudineau, *La Ceramique Arétine Lisse*; (de Boccard, Paris, 1968).
2. M. Picon, to be published in *La Revue Archéologique* (1973).
3. J. L. Fiches, *Revue Archéologique du Centre de la France (RAC)* XI, 254 (1972).
4. R. Lombard, *RAC* X, 91 (1971).
5. E. Ettliger, *Rei Cretariae Romanae Fautorum (RCRF) Acta IV* (1962).

6. E. Ritterling, *Mitteil der Alt. Komm. für Westphalen II* (1901), p.142-146.

7. A. Oxé, *Die Halterner Sigillatafunde seit 1925. Bodenaltertümer, Westphalens VI* (1943), p. 15-76.

8. G. Maetzke, *Notizia sulla esplorazione della fornace di C. N. Ateius in Arezzo, RCRF Acta II* (1959), p. 25-27.

9. M. Picon, M. Vichy, and E. Meille, *Composition of the Lezoux, Lyon and Arezzo Samian Ware, Archaeometry* 13, (2) p.191-208 (1971).

10. I. Perlman and F. Asaro, *Science and Archaeology*, R. H. Brill, editors (MIT Press, 1971), p. 182-195.

11. I. Perlman and F. Asaro, UCRL-18734 (1969); *Archaeometry* 11, 21 (1969).

12. F. Asaro and I. Perlman, unpublished data, see Ref. 11.

13. M. Artzy, F. Asaro, and I. Perlman, to be published, *LBL and J. Am. Oriental Soc.* (1/1974).

14. F. Asaro and I. Perlman, *Acts of the International Archaeological Symposium, "The Mycenaean in the Eastern Mediterranean"*, Nicosia, Cyprus, p. 213-224 (1972).

15. H. Vertet, M. Picon, and M. Vichy, *Note sur la composition des céramiques du IV<sup>e</sup> siècle de Lezoux. RAC* (35-36) (1970).

### NEUTRON ACTIVATION, THE WHEEL, AND CYPRIOTE POTTERY FROM AROUND 1600 B.C.

M. Artzy, F. Asaro, and I. Perlman

Until recently Cypriote archaeologists believed that the potters of the Middle Cypriote and Late Cypriote I periods (around 1600 B.C.) did not use the potter's wheel for the production of any of their wares. An effect of this belief was that any wheel-made pottery from this time period found in Cyprus was automatically classed as an import, often from Syria or Palestine.

Neutron activation studies<sup>1</sup> have recently shown, however, that a particular style of wheel-made pottery from this period, Bichrome Ware, considered by archaeologists to be Syro-Palestinian, was instead produced of eastern Cypriote clay. An additional typologi-

cal analysis of the shapes of Palestinian, Syrian, and Cypriote pottery showed the Bichrome Ware to be a variant member of the Cypriote White Painted Ware family.<sup>2</sup>

It seemed worthwhile to extend the neutron activation studies to other styles of wheel-made pottery from this time period, and at the same time to go back and examine a number of the original tomb reports to determine if there was still an archaeological basis for the earlier belief. An examination of Cypriote tomb inventories showed that the wheel-made variety was often more plentiful than its hand-made counterpart. For instance, in Tomb 2 at Enkomi, Dikaios reports eight pieces of Black

Slip Ware, all of which are wheel-made.<sup>3</sup> Plain Ware, which has no decoration and was for common use, was usually made in the area in which it was used. This kind of ware in the Cypriote tomb reports is often exclusively wheel-made. In Enkomi tombs, 35 wheel-made sherds of this ware<sup>4</sup> were found in Tomb 2 and 118 in the large assemblage<sup>5</sup> of Tomb 10. No reference is made to hand-made Plain Ware from these tombs. Thus, it would seem from the tomb reports that there was indeed a great deal of Cypriote pottery being made on a wheel at that early time.

The large quantity of wheel-made vessels already caught the eye of Westholm who said

of the amount of wheel-made pots: "The comparatively large number of foreign wares in this tomb is worthy of notice, especially as most of the classes are represented by several vases".<sup>6</sup> Dikaïos actually states that among the pottery from Enlomi, there are many wares which he considered foreign only because the wheel technique was not used in Cyprus at that time.<sup>7</sup>

Neutron activation measurements were made on wheel-made Plain Ware and Black Slip Ware found in Cyprus as well as hand-made wares of accepted Cypriote origin. In these determinations the abundances of some 40 trace and major elements are measured. From these,

Table I. Data for two groups of hand-made eastern Cypriote pottery and two groups of wheel-made pottery excavated in Cyprus.

	Mla. Handmade <sup>a</sup> (8 pieces) M±σ	Kal. W.P. Handmade <sup>b</sup> (10 pieces) M±σ	Mla. B.S. Wheelmade <sup>c</sup> (13 pieces) M±σ	Enk. Wheelmade <sup>d</sup> (18 pieces) M±σ
Fe%	5.00 ± 0.50	5.68 ± 0.32	4.77 ± 0.17	5.75 ± 0.26
Ta	0.658± 0.066	0.551± 0.030	0.622± 0.030	0.544± 0.034
Sc	20.83 ± 2.56	24.06 ± 1.48	19.87 ± 0.71	24.60 ± 1.04
Co	27.13 ± 2.94	28.27 ± 1.97	28.76 ± 2.16	30.3 ± 2.8
Cs	3.59 ± 0.63	3.8 ± 0.4	4.1 ± 0.3	3.8 ± 0.4
Cr	346 ± 62	313 ± 38	335 ± 65	315 ± 45
Hf	2.97 ± 0.29	2.66 ± 0.15	2.53 ± 0.15	2.53 ± 0.17
Th	6.81 ± 0.78	5.49 ± 0.39	6.88 ± 0.35	5.56 ± 0.31
Ni	229 ± 19	178 ± 15	304 ± 22	204 ± 25
Rb	63 ± 16	54 ± 16	68 ± 6	57 ± 18
La	20.7 ± 1.9	17.9 ± 1.1	19.7 ± 1.7	20.6 ± 1.1
Lu	0.320± 0.019	0.318± 0.015	0.257± 0.015	0.32 ± 0.02
U	2.48 ± 0.77	2.00 ± 0.30	1.45 ± 0.43	2.00 ± 0.45
Ti%	0.454± 0.031	0.466± 0.021	0.376± 0.025	0.46 ± 0.03
Mn	1076 ± 94	1035 ± 106	783 ± 143	1076 ± 62
Na%	1.202± 0.213	1.37 ± 0.24	0.718± 0.100	1.45 ± 0.14
Al%	-- <sup>e</sup>	7.25 ± 0.50	-- <sup>e</sup>	-- <sup>e</sup>
Ca%	9.9 ± 2.6	11.0 ± 1.1	7.8 ± 0.8	8.6 ± 1.5

The numbers for the respective elements are group mean values (M) and the standard deviations (±σ). All are in units of parts-per-million unless designated "(%)".

<sup>a</sup> A group of handmade White Painted and Plain Wares from Milia.

<sup>b</sup> A group of handmade White Painted Ware from Kalopsidha.

<sup>c</sup> A group of wheelmade Black Slip Ware from Milia.

<sup>d</sup> A group of wheelmade Plain Ware from Enkomi.

<sup>e</sup> At the time these were analyzed, aluminum was not measured.

18 of the best measured and most distinctive elements were used to classify the pottery. In Table I are shown the data for two groups of hand-made eastern Cypriote pottery of the period under discussion and two groups of wheel-made pottery which were excavated in Cyprus. For each group, the mean values of the abundances of the 18 elements are tabulated along with the root-mean-square deviations for each element. The four groups comprise eight pieces of Milia hand-made ware, 10 pieces of Kalopsidha White Painted Hand-made Ware, 13 pieces of Milia Black Slip Wheel-made Ware and 18 pieces of Plain Wheel-made Ware. Although we cannot possibly say that the four groups are of exactly the same clay, we can safely assume that they are of similar clays all of which are from eastern Cyprus.

In our study we went further and searched for and selected vessels for neutron activation studies that had been clearly designated archaeologically and typologically. Several likely candidates were found in the basement of the

Cypriote Museum. Following are the results of three such analyses. The first piece (No. A1467) is a complete White Painted tankard, wheel-made and registered in the museum as a 'Syrian import'. We chose this particular tankard, not only because of its distinct family resemblance to the hand-made White Painted Ware, but also its shape and decoration are so reminiscent of the Bichrome Ware. The color of its paint on one side leans heavily toward the color of the Bichrome Ware paint. (The White Painted Ware is painted in a variation of browns while the Bichrome Ware has a brown which leans to blue and a reddish-brown paint.) The second piece (No. RR1748) is a hand-made White Painted krater and of Cypriote origin. We chose this particular piece because of its shape. The third piece (No. RR3066) is a White Painted storage jar, or pithoi, hand-made and, although it was registered as 'imported ware', Åström has since declared it to be Cypriote and incorporated it into his White Painted Ware V group.<sup>8</sup>

Table II. Data from neutron activation studies of clearly designated vessels from the Cypriote Museum.

	MUNC-4 <sup>a</sup>	MUNC-6 <sup>b</sup>	MUNC-7 <sup>c</sup>
Fe%	5.13 ± 0.07	5.08 ± 0.07	4.95 ± 0.07
Ta	0.535 ± 0.005	0.510 ± 0.004	0.517 ± 0.004
Sc	21.97 ± 0.07	22.49 ± 0.08	21.55 ± 0.07
Co	31.06 ± 0.45	28.42 ± 0.44	29.55 ± 0.42
Cs	3.8 ± 0.3	2.9 ± 0.3	4.0 ± 0.3
Cr	312.7 ± 4.5	272.7 ± 4.2	287.5 ± 4.1
Hf	3.02 ± 0.08	2.85 ± 0.08	2.81 ± 0.08
Th	5.44 ± 0.11	4.67 ± 0.13	4.95 ± 0.11
Ni	218 ± 21	170 ± 22	196 ± 19
Rb	61 ± 10	49 ± 11	76 ± 10
La	17.93 ± 0.64	14.42 ± 0.54	17.01 ± 0.56
Lu	0.264 ± 0.016	0.273 ± 0.014	0.284 ± 0.015
U	2.17 ± 0.03	1.61 ± 0.03	3.08 ± 0.03
Ti%	0.433 ± 0.021	0.454 ± 0.017	0.439 ± 0.017
Mn	1106 ± 11	1010 ± 10	1029 ± 8
Na%	1.427 ± 0.016	1.916 ± 0.019	1.194 ± 0.014
Al%	6.42 ± 0.19	6.46 ± 0.12	6.43 ± 0.13
Ca%	10.41 ± 0.64	8.26 ± 0.50	8.60 ± 0.51

<sup>a</sup> A wheelmade White Painted Ware tankard from the Museum in Nicosia.

<sup>b</sup> A handmade White Painted Ware krater from the Museum in Nicosia.

<sup>c</sup> A White Painted Ware storage jar from the Museum in Nicosia.



The neutron activation analysis data are shown in Table II and indicate that the three vessels are products of a very similar clay. This clay is a member of the eastern Cypriote family.

From these results we must conclude that most if not all of the late Middle Cypriote and early Late Cypriote Periods ceramics which were attributed to Syro-Palestine, only because they were made by the wheel and not because of typological differences, are actually composed of Cypriote clays and most likely products of Cypriote potters on the eastern plain of Cyprus.

#### References

1. Michal Artzy, F. Asaro, and I. Perlman, "The Origin of the 'Palestinian' Bichrome Ware", *J. Am. Oriental Soc.* 94, (1974).
2. Michal Artzy, "The Bichrome Ware in its Cypriote Context", *Altes Orient and Altes Testament*, (22) 1973, p. 9-16.
3. P. Dakaios, *Enkomi Excavations 1948-1958 I* (Mainz am Rhein, 1969-1971), p. 345.
4. *Ibid.*, p. 336-347.
5. *Ibid.*, p. 357-394.
6. A. Westholm, "Some Late Bronze Tombs at Milia", *Quarterly of the Dept. of Antiquities in Palestine*, VIII, p. 1-20 (1939).
7. Dakaios, *op. cit.*, p. 226.
8. Paul Åström, *Middle Cypriote Bronze Age* (Lund, 1957), Fig. XVIII:10.

### THE BICHROME WARE KRATER FROM TEL NAGILA

M. Artzy, F. Asaro, and I. Perlman

Neutron activation analyses of pottery fabrics coupled with archaeological stylistic associations have previously strongly suggested<sup>1</sup> that the distinctive so-called "Palestinian" Bichrome Ware of ca. 1600 B.C. had a Cypriote origin instead. This assignment, which has a number of ramifications in Palestinian and Cypriote archaeology, has been accepted by many archaeologists in these fields, although there are some areas of controversy which remain. One of these concerns the origin of Bichrome Ware pottery in the shape of kraters. These vessels are not considered to have been a popular pot in Cyprus around 1600 B.C., whereas they were in Palestine and Syria.

An unusually fine specimen of such a krater,<sup>2</sup> (Fig. 1) on display at the Israel Museum, which has been extensively discussed in several publications has become a focal point of considerable discussion with respect to its origin.

A chemical analysis of the fabric of this particular vessel would show whether it has indeed a Cypriote origin and would help show if kraters are a vessel form which should also be considered as Cypriote.

This krater bears a striking resemblance to other members of the Bichrome Ware assemblage, especially the vessels from Tell el-'Ajjul, although its walls are surprisingly thin for its size, unlike the walls of other Bichrome Ware kraters we sampled. A 100 mg

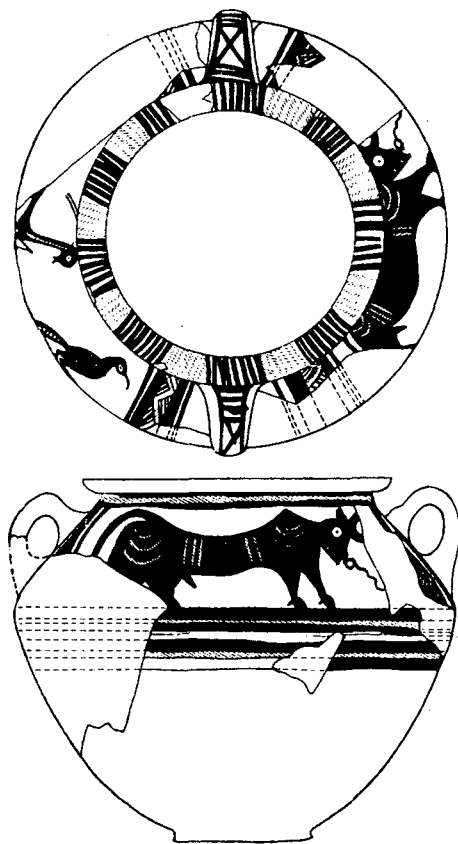


Fig. 1. The Bichrome Ware krater from Tel Nagila. XBL 742-377

sample of pottery was scraped from a cleaned area of the krater and the abundances of some 40 elements were determined by neutron activation analyses. In Table I are shown the abundances for the 18 most distinctive elements that were measured for this pot as well as comparable data for reference groups<sup>1</sup> of Cypriote pottery from Tell el-'Ajjul in Palestine and Milia in Cyprus. The first column represents a group of 36 Bichrome Ware pieces from Tell el-'Ajjul. The second column has the data for the Tel-Nagila Bichrome Ware krater, and the last column represents a group of eight pieces of handmade sherds from Milia-Cyprus which are dated to ca. 1600 B.C.<sup>3</sup>

Table I. Chemical abundances<sup>a</sup> of the Tel-Nagila krater and Cypriote reference groups.

	Aju. Bichr. <sup>b</sup> (36 pieces) <sup>d</sup>	NAGL-1 single sherd	Milia handmade (8 pieces) <sup>d</sup>
Fe%	5.54 ± 0.23	4.76	5.00 ± 0.50
Ta	0.691± 0.034	0.600	0.658± 0.066
Sc	22.08 ± 0.92	19.46	20.83 ± 2.56
Co	30.34 ± 1.78	27.46	27.13 ± 2.94
Cs	4.70 ± 0.50	4.34	3.59 ± 0.63
Cr	351 ± 68	410	346 ± 62
Hf	2.95 ± 0.21	3.00	2.97 ± 0.29
Th	7.05 ± 0.46	6.51	6.81 ± 0.78
Ni	251 ± 21	253	229 ± 19
Rb	95 ± 25	86	63 ± 16
La	21.2 ± 1.2	19.4	20.7 ± 1.9
Lu	0.319± 0.019	0.296	0.320± 0.019
U	2.56 ± 0.92	1.71	2.48 ± 0.77
Ti%	0.420± 0.034	0.355	0.454± 0.031
Mn	973 ± 99	893	1076 ± 94
Na%	1.076± 0.187	0.916	1.202± 0.213
Al%	6.85 ± 0.39	6.48	-- <sup>e</sup>
Ca%	9.8 ± 1.7	9.70	9.9 ± 2.6

<sup>a</sup> All values are in ppm unless % is indicated after the chemical symbol.

<sup>b</sup> Cypriote Bichrome Ware from Tell el-'Ajjul in Israel.

<sup>c</sup> Cypriote handmade pottery from Milia, Cyprus.

<sup>d</sup> The two values for each element are the mean abundance for the group and the root-mean-square deviation.

<sup>e</sup> Al measurements were not being made when these sherds were analyzed.

The Tel-Nagila krater agrees very well in composition with both groups of Cypriote pottery particularly if all of its abundances are enhanced by 10%. General dilution of pottery abundances by water, residual CO<sub>2</sub> as carbonate or by sand are sometimes observed and do not affect the validity of the pottery classification.

Therefore, the Tel-Nagila krater is chemically a member of the same group as the Bichrome Ware which was excavated at Tell el-'Ajjul and the local handmade pottery from eastern Cyprus.

It is possible that clay from Palestine or Syria might accidentally have the same chemical composition as clay from Cyprus, but so far there have been no indications of this in extensive samplings of pottery from Palestine and many sherds from Syria. Hence the Tel-Nagila Bichrome krater is very likely made of eastern Cypriote clay and not of Canaanite (Palestinian) or Syrian clay.

Although decorated pottery does appear in the later part of the Middle Bronze in a Canaanite setting, it is limited in number and the variety of its decoration and its quality. Even Heurtley, who was convinced that the Bichrome Ware was Palestinian in origin, didn't look at the local Canaanite potters for its inspiration. He mentions the imported Cypriote White Painted Ware as the ancestor "... which precipitated a revival of vase painting in Palestine, long overdue".<sup>4</sup> Cyprus had a tradition of painted pottery which extended back to the Neolithic Age.<sup>5</sup>

The question as to where the animal motifs which are very prevalent in the Bichrome Ware came from, has not been answered. Although there are zoomorphic vessels from Cyprus of that period (among them Bichrome and White Painted specimens), there is a conspicuously small number of animal motifs painted on ceramics of the preceding period. The explanation may lie in the contact which existed between the Levant and the island Cyprus. The transmission of the idea of animal motifs could be accomplished with similar ease from Mesopotamia via Syria to Cyprus, as we see it.

We feel that the problem of typology concerned with a Cypriote origin for Bichrome kraters is not unsolvable. The krater shape is a well known one in Syrian and Palestinian corpora, but the krater was also familiar to the Cypriote potters of the White Painted era as may be attested by the kraters from Tomb 10 in Milia,<sup>6</sup> or the White Painted krater No. RR1748 in the Nicosia Museum in Cyprus which was sampled and found it to be of eastern Cypriote origin. We would not want to state at this point that the krater shape didn't originate

in Syria, but for those who do see the Bichrome ware as emanating in Cyprus, the krater is a convenient form to adopt for wheel-construction or was deliberately made for the Syro-Palestinian market, not only in the Bichrome Ware style but in the White Painted Ware style.

#### References

1. Michal Artzy, F. Asaro, and I. Perlman, "The Palestinian Bichrome Ware", *J. Am. Oriental Soc.* 94, 1 (1974).
2. Ruth Amiran and A. Eitan, "A Krater of Bichrome Ware from Tel-Nagila", *Israel Exploration Journal* 14, p. 219-231. See also Ruth Amiran, Ancient Pottery of the Holy Land (Jerusalem, 1969), Ph. 137, PL. 48:10.
3. We chose handmade ware since they are agreed upon to be Cypriote by all archaeologists.
4. W. A. Heurtley, "A Palestinian Vase Painted of the Sixteenth Century B.C.", *Quarterly of the Dept. of Antiquities in Palestine*, VIII, p. 34 (1939).
5. Paul Åström, Middle Cypriote Bronze Age (Lund, 1957), p. 206.
6. A. Westholm, "Some Late Bronze Tombs at Milia", *Quarterly of the Dept. of Antiquities in Palestine*, VIII, p. 1-20, (1939).

### THE LATE BRONZE "PALESTINIAN" BICHROME WARE IN ITS CYPRIOTE CONTEXT

Michal Artzy

Recent work on the Late Bronze Palestinian Bichrome Ware, using neutron activation analysis, has shown that most of the Tell el-'Ajjul Bichrome Ware, as well as the Milia Tomb collection assemblage, was not made in Tell el-'Ajjul, or Megiddo, or, for that matter, in Syria. It became clear that the Bichrome Ware was produced in some quantity on Cyprus, specifically the eastern coast of the island.<sup>1</sup>

It seems highly likely that the Ware was already manufactured in Cyprus during the end of the Middle Cypriote Period and reached the Mainland, in sites such as Tell el-'Ajjul, Lachish (Tell ed-Duweir) and Bethel, in the Stratum preceding the Egyptian destruction which marked the end of the Middle Bronze. It continued to be found in Stratum.IX of Megiddo and reappeared in time in most of the rebuilt cities. For this reason, it became impossible to accept the theory that the indigenous Palestinian Painted pottery of the Late Bronze is the form predecessor of the Bichrome Ware. The appearance of the Bichrome Ware in both the Mainland and Cyprus preceded that of the Palestinian Painted Ware.

The decoration of the Bichrome Ware included, at times, animal motifs, which were thought by some modern archaeologist to be of Hurrian influence.<sup>2</sup> Arguments which put forth the Hurrian origin recognize the Cypriote influence on the Bichrome Ware, but prefer to ignore the implications of that influence, since the transmission of the Cypriote forms would

not have corresponded to the Hurrians' movement and the rise of Mitanni. The reliance of the scholars on the Hurrian migration southward and on the political upheavals caused by the Hyksos' defeat disregards the stratigraphical data of the appearance and reappearance of the Bichrome Ware, which seemed to have been produced regardless of the political situation in the Near East. This suggests the hypothesis that the Bichrome Ware was not produced on the continent but somewhere else. Palestine, itself, had hardly any tradition of expertly painted pottery during its Bronze periods. Cyprus, on the other hand, had a long standing tradition of painted pottery which extended back to the Neolithic Period.<sup>3</sup> Cypriote painted ware of the Middle Bronze Period can easily be shown to be the predecessor of both the form and decoration of the Bichrome Ware assemblage.

The trickle of Middle Cypriote exports to the Levant during the first parts of the Middle Bronze evolved into a developed commerce during the second part of the Middle Bronze Period. There were many factors which may have contributed to the commercial growth and the dominance of the Eastern coast of Cyprus during the end of the Middle Cypriote Period. Turmoils within Palestine during the Egyptian Second Intermediate Period could have forced some inhabitants from the Levant to leave and settle in Eastern Cyprus, thus promoting the trade between the two areas. Cyprus itself may have suffered from internal conflicts, thus

necessitating the new fortified towns which sprang up on the eastern coast at about that time.<sup>4</sup> Still another factor might have been the lull in activity in the Minoan world, which would have caused the eastern ports of Cyprus to grow and sustain a strong trade relationship with the Western ports of the Mediterranean.

The appearance of the Bichrome Ware in Palestine followed that of the White Painted Cypriote Ware. Although most of the White Painted Ware was handmade, there are wheel-made samples which were unearthed not only in Cyprus but also in Palestine. The White Painted Ware in Cyprus is a good example of the changes between the early and later parts of the Middle Cypriote Period. While there is no example of the White Painted II Ware or the White Painted III Ware, which are northern in origin, outside of Cyprus, there are quite a few examples of White Painted V Ware, which is eastern in origin, in sites outside of Cyprus. One example is to be found in Megiddo Tomb 3065, Stratum X.<sup>5</sup>

While Painted I Ware, White Painted II Ware and White Painted III Ware were all found in the northern part of Cyprus. While Painted I was found in Philia, which is situated about 15 kilometers inland from the western coast, 12 from the northern coast. White Painted II and White Painted III were found mainly in the Lapithos on the northern shore. Their origin of form and decoration are still in dispute. Although it has some possible northern influence, it seems highly improbable that it was imported to Cyprus. The three Wares have a slip and are painted. Stewart believes that the affiliation between White Painted I Ware and the Chalcolithic Red on White pottery at Erimi and Ambeliko cannot be overlooked.<sup>6</sup> The decoration on the White Painted II Ware, which opens the Middle Cypriote Period, was usually placed on the upper half of the body and the neck, a practice which was often found in the later forms as well as in the Bichrome Ware. The pigmentation of White Painted III paint ranged from redbrown to black.

The shapes of the White Painted II Wares are varied. I shall try to present them briefly. Special emphasis will be put on the forms which I believe pertain to this study. We already find the bowls, both the shallow, hemispherical ones and the deep bowls: they appear with a knob handle or with a horizontal one (Fig. 1A). We find beaked jugs with globular bodies (Fig. 2A). The amphorae have oval bodies, squat-necked, flat or rounded bases, and two handles starting below the rim and continuing to the shoulder (Figs. 3A, 3B). The askos which we don't find again until the Late Bronze has a basket handle and a spout, and a flat base (Fig. 4A). The White Painted III followed the

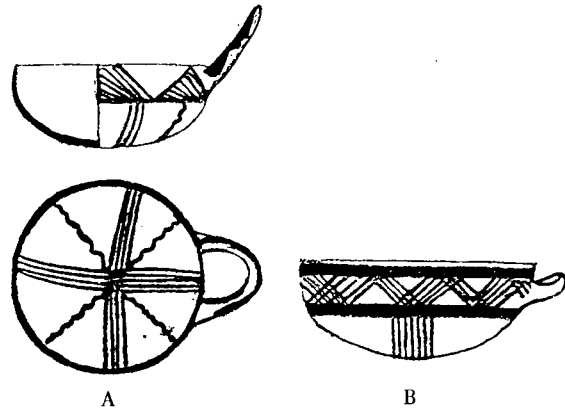


Fig. 1. Bowls (A) White Painted II, (B) Bichrome. XBL 742-378

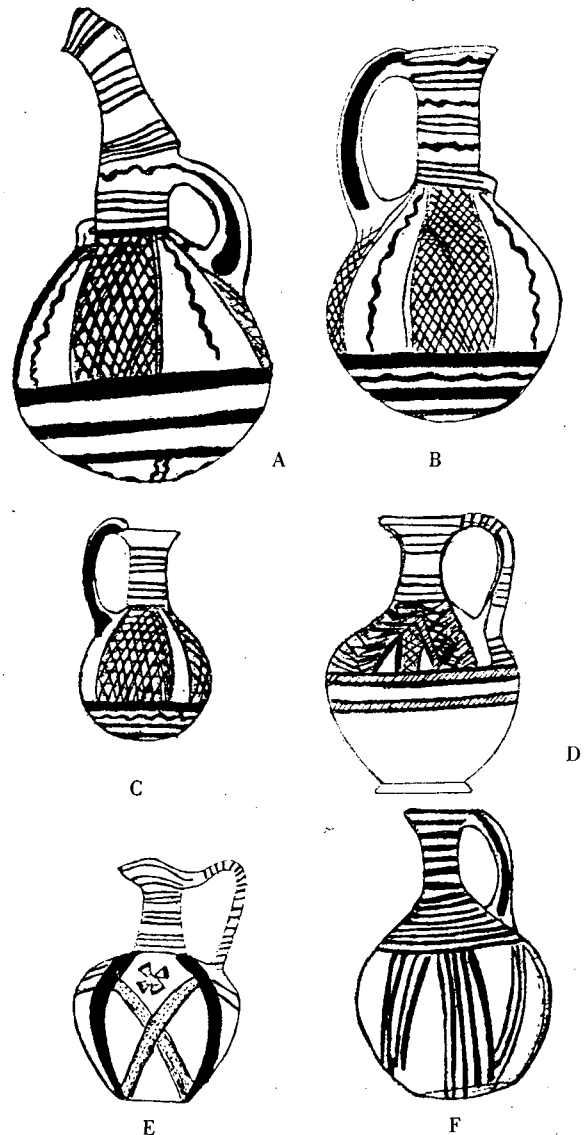


Fig. 2. Jugs (A-C) White Painted II-V, (D-F) Bichrome. XBL 742-381

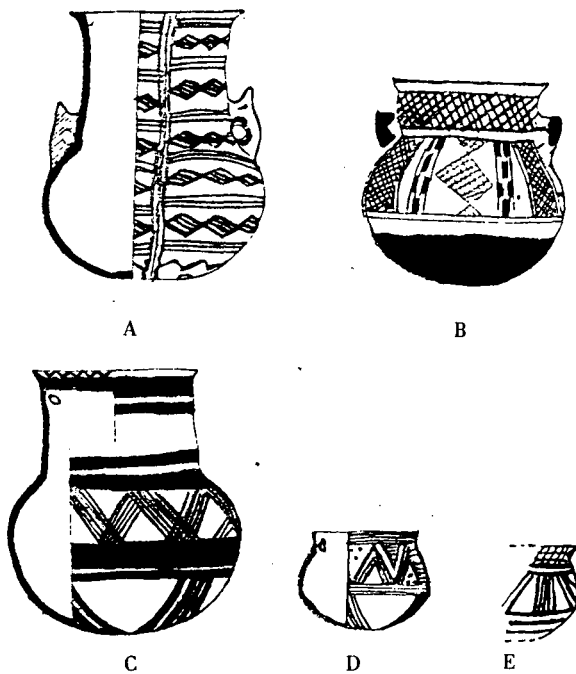


Fig. 3. Amphorae and jars (A-D) White Painted II and V, (E) Bichrome.  
XBL 742-382

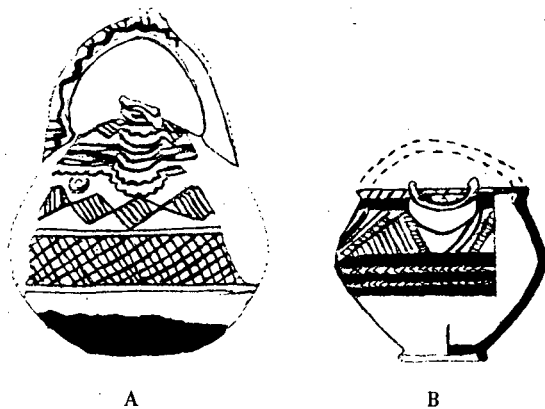


Fig. 4. Askos (A) White Painted II, (B) Bichrome.  
XBL 742-379

steps of the previous White Painted II. There was, however, a new form which is reminiscent of the jug or tankard, as it is called, which became very common in the later stages of the White Painted Ware and the Bichrome Ware (Fig. 5A). It has a globular body, a flat base, slightly carinated rim and shoulder and an almost cylindrical neck; the handle is raised slightly higher than the rim. There may have been a close relationship in forms between the tankards of stage III (Fig. 5A) and the amphorae of stage II (Figs. 3A, 3B).

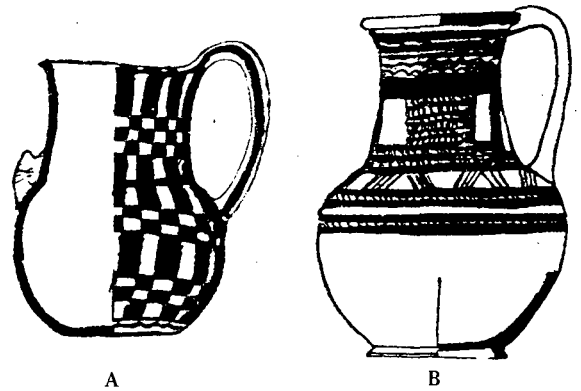


Fig. 5. Tankards (A) White Painted III, (B) (Bichrome)  
XBL 742-380

The next two stages of the White Painted Ware were excavated on Mainland sites. White Painted IV sherds were found both in Megiddo, Strata XII and XI, and at Tell Beit Mirsim, Stratum G. At that juncture we see for the first time the wishbone handles, which are said to have been previously found in Cretan neolithic context.<sup>7</sup> Of the various stages of the White Painted Ware, White Painted V is the most important to our study. It was probably contemporary with the end of the Middle Cypriote Period and the beginning of the Late Cypriote Period. The White Painted V geographic dispersion is impressive, for not only do we find it in Cyprus, but at Ras Shamra, in several tombs at Megiddo, where handmade and wheelmade specimens were found in Tombs 5050 and 5243 of the XI Stratum and Tombs 3046 and 3065, Stratum X, and at Tell el-'Ajjul, where two White Painted V bowls were found. It is usually handmade, although wheelmade specimens do exist; they are said to have been made exclusively in Palestine for the Cypriote market, which with our present knowledge is most unlikely. The tradition of the previous stages continues, although the corpus is augmented by several new forms. The production of both the shallow and the deep bowls is uninterrupted, as is that of the jugs. The tankards become more common during this phase and their necks when compared with previous ones, are wider. The two new shapes are the jars and storage jars. The jars are squat and have an everted rim with or without a widening neck. Below the rim they have a hole on either side which was probably used for suspension. They should probably be considered as descendants of the squat amphorae. The storage jars appear with two vertical handles below the rim.

There is yet another delightful form which appears in the White Painted tradition -- the zoomorphic vessel (Fig. 6A). The earliest

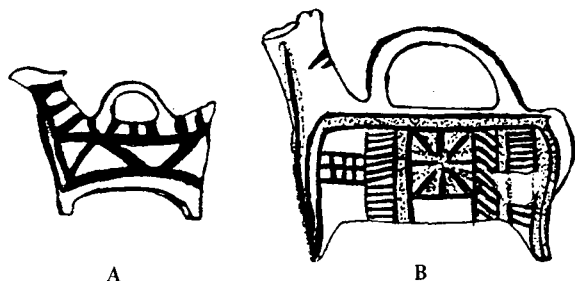


Fig. 6. Zoomorphic vessels (A) White Painted V, (B) Bichrome.

XBL 742-383

example of a zoomorphic White Painted Ware is from the third phase of the tradition. Although ornithomorphics and tripeds appeared in the third and fourth stage, the quadrupedic zoomorphic vessels become the potters' favorite zoomorphic form.

Decorational motifs of the White Painted corpora are also of a special importance to this study. The Ware is usually covered with white, off-white, or orange slips. The paint is brown or reddish-brown; during the end of the fourth phase and the fifth stage, it is black and brown. There is a certain tendency to decorate the vessels profusely on their upper parts in metope decorations as well as geometric motifs and both vertical and horizontal bands. There are also instances where animal motifs were used in decoration; one of them is from Tomb 6 at Ayios Iakovos, depicting three horned quadrupeds placed above one another in diminishing size.<sup>8</sup> There is also a lovely jar of the White Painted IV tradition which depicts two winged birds on one side and on the other side two lady-bug-like creatures engaged in a kissing-like position.<sup>9</sup> Another yet is a bird and a quadruped painted on a wheelmade White Painted jar from Ayia Paraskevi.<sup>10</sup>

In juxtaposing the Bichrome Ware with the White Painted Ware, I would like to show the similarities between the two. The bowls of the Bichrome Ware tradition tend to be of the shallow hemispherical type (Fig. 1B). They are decorated in black and red (Hue 5R 2/1 and Hue 7.5R 3/8 in the Munsell Soil Color Chart) with mostly geometric patterns; the metope idea is common and both horizontal and vertical lines are used. They are, no doubt, Cypriote in tradition, for similar types of bowls in the corpus of the Middle Bronze in Palestine cannot be found. We can, however, trace the shallow bowls back to the Early Cypriote White Painted corpus. It is quite probable that the Cypriote milk bowl of the White Slip I tradition, with its wishbone handle, is of the same common background as that of the Bichrome Ware Bowl.

The Bichrome Ware jugs are globular; they have a flat base, narrow neck and often a beaked mouth (Fig. 2). The beaked mouth is not a popular Palestinian form, at least not during the Middle Bronze; it is, however, a commonly used shape in the Cypriote White Painted Ware corpus. In the Cypriote tradition the beak slowly becomes shorter and levels with the handle and the rim. The decorational motifs of the jugs are often in cross line, which had already become popular in Cyprus in the White Painted V Ware. Among the jugs of the Bichrome Ware there are some which have handles from the base of the neck to the lower part of the shoulder. We already met this particular type among the vessels of the White Painted III Ware. The Palestinian Late Bronze vessel of the similar shape should be considered an imitation of the Bichrome Ware, and its predecessors, therefore, are much the same as those of the White Painted Ware.

The tankard which first appears in the fourth phase of the White Painted Ware has a ring base, although at times the base is so thick that it approaches the form of a flat base (Fig. 5). The handle is extended from the rim to the shoulder; it has a cylindrical neck and a flare-out rim. The decoration is usually executed from the neck, or from the junction of the neck down to the middle of the body. The Late Bronze Palestinian Painted tankard should be looked at as an imitation or a variation of the Bichrome Ware family; it is just as in the case of the jugs, a descendant of the White Painted V Ware tradition in Cyprus.

The next few shapes which I would like to discuss are the askos, the amphora, the storage jar (pithos), and the zoomorphic vessel. The askos was losing its popularity during the Middle of the White Painted tradition (Fig. 4). It seems to have survived only partially into the Late Cypriote Period, and the Bichrome Ware askos from Megiddo Level IX is a bit of a relic for its time.

The storage jar of the Bichrome Ware family is extremely similar in its shape to the jar of the White Painted Ware tradition (Fig. 7). It has a rounded base, flowing rims, and vertical handles below the shoulder. While in Palestine the storage jars were common in both habitats and tombs, in Cyprus they were scarce. This fact further suggests the Cypriote provenance of the Bichrome Ware.

The amphora of the Cypriote Middle Bronze did not survive to the period of the Bichrome Ware en masse (Fig. 3). There are, however, two Bichrome pieces of the squat, short-necked amphorae. One is from Tell el-'Ajjul, OM968; the other from Milia, Tomb 10. It has a squat body, flaring rim, and a hole below the

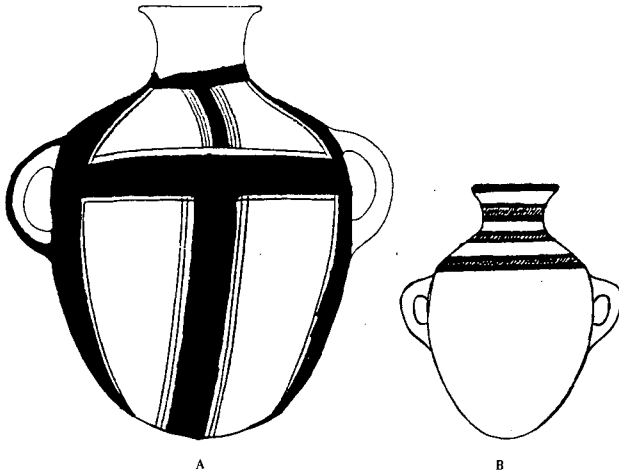


Fig. 7. Storage jars (A) White Painted V,  
(B) Bichrome.

XBL 742-384

rim for suspension. It is very similar to the amphorae of the Cypriote White Painted V tradition.

The similarity between the Bichrome Ware zoomorphic quadruped from Akhera, Cyprus, which was published by Vassos Karageorghis<sup>11</sup>, and the White Painted V Ware quadruped is a continuation of the White Painted Cypriote zoomorphic tradition.

In juxtaposing the 'Palestinian' Late Bronze Tell el-'Ajjul Bichrome Ware and the Cypriote White Painted Ware of the Middle and Late Bronze, it becomes clear that the Bichrome Ware is not Palestinian in its heritage, but Cypriote. The Bichrome Ware was not only the culmination of the White Painted Ware tradition, but was produced by wheel in Cyprus for export to mainland ports. Cyprus at the end of the Middle Bronze and the beginning of the Late Bronze was a major distributor of ceramics. Such pottery as the Basing Ware,

the aesthetically pleasing White Slip Ware and the 'Palestinian' Bichrome Ware was shipped from Cyprus to Anatolia, as well as Syria, Palestine and Egypt.

#### References

1. Michal Artzy, F. Asaro, and I. Perlman, "The Origin of the 'Palestinian' Bichrome Ware," *J. of the Am. Oriental Soc.* Vol. 93, no. 4, pp. 446-462.
2. Claire Epstein, "Palestinian Bichrome Ware," (Leiden: E. J. Brill) 1966, 187. See also K. M. Kenyon, "Archaeology in the Holy Land" (1960), 200.
3. Paul Åström, "The Middle Cypriote Bronze Age" (1957), 206.
4. H. W. Catling, "Cyprus in the Neolithic and Bronze Age Periods," *CAH*, Rev. ed. I and II, 44-45, fasc. 43.
5. J. Shipton, "Notes on the Megiddo Pottery of Strata VI-XX," 20; *Megiddo II*, 170, Plate 41139.
6. J. R. Stewart, "The Early Cypriote Bronze Age," *Swedish Cyprus Expedition*, IV, Part Ia (1962), 254-256.
7. Paul Åström, *op. cit.*, 216.
8. Paul Åström, *ibid.*, 210.
9. Vassos Karageorghis, "Chronique des fouilles et découvertes Archeologique à Chypre en 1967," *Bulletin de Correspondence Hellénique* (1968), 294.
10. J. M. Cook, "Archaeology in Greece, 1948-1949," *Journal of Hellenic Studies* (1950), 14, Fig. 10.
11. Vassos Karageorghis, *Bulletin de Correspondence Hellénique* (1961), Fig. 61.

## DISPERSION OF GASEOUS EMISSIONS FROM A GROUND-LEVEL LINE SOURCE

K. D. Wings, E. A. Grens II, and T. Vermeulen

The spread of vehicular pollutants from along a freeway can be modeled on a family of cross-sectional planes, usually taken perpendicular to the freeway axis. When calculations in such a plane are carried out using a finite-element grid, the emission source can be represented as one, or several, of the two-dimensional grid elements.

Relations between velocity and turbulent transport have been redeveloped<sup>1</sup> from conventional equations for conservation of momentum and of matter. Three elementary cases are considered, in this initial step toward future comprehensive analysis of freeway configurations by a continuity method: parallel flow over a uniform plane; flow over a discontinuity in surface roughness; and, most significant for the freeway problem, flow over a perpendicular barrier attached to a uniform plane.

The velocity profiles used for these respective cases were based, first, on both logarithmic and power-law models; second, on data from Plate;<sup>2</sup> and third, on wind-tunnel data from Nagabhushaniah.<sup>3</sup> In the barrier-flow case, the pressure field was estimated from potential, or inviscid, flow. In all three cases the turbulent transport was characterized by an eddy viscosity for momentum transfer and by an eddy diffusivity for mass transfer, which were set equal and were calculated by the momentum equations.

Concentration profiles were computed in each case for the region downwind from a ground-level emission source. These calculations demonstrate the feasibility of predicting concentration profiles by the continuity method, in configurations for which the velocity and pressure profiles are known or predictable.

To illustrate this approach for the barrier-flow case, the plotted data show input velocities (Fig. 1) and output diffusivities (Fig. 2) and concentration profiles (Fig. 3). The data shown correspond to a barrier height of 1 m, a 10-m-high wind velocity of 5 m/s, a power-law exponent of 1/7, and a source strength of 1.0 m<sup>3</sup> centered at  $x = -0.5$  and  $z = 1.5$ . In these graphs  $x$  is the horizontal

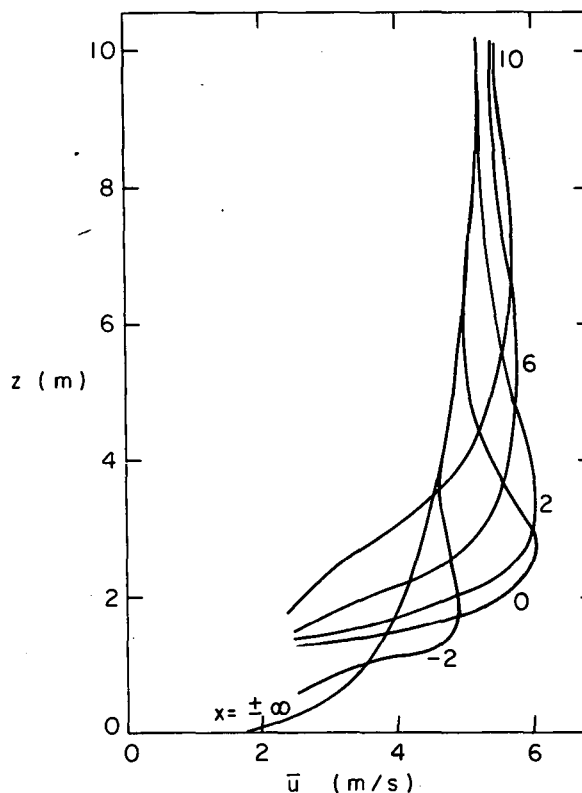


Fig. 1. Velocity profiles for flow over a 1-m-high barrier. (XBL742-2443)

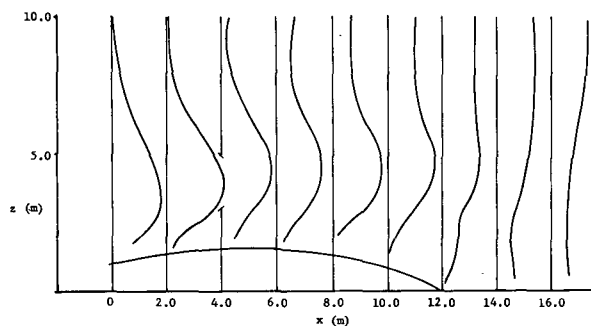
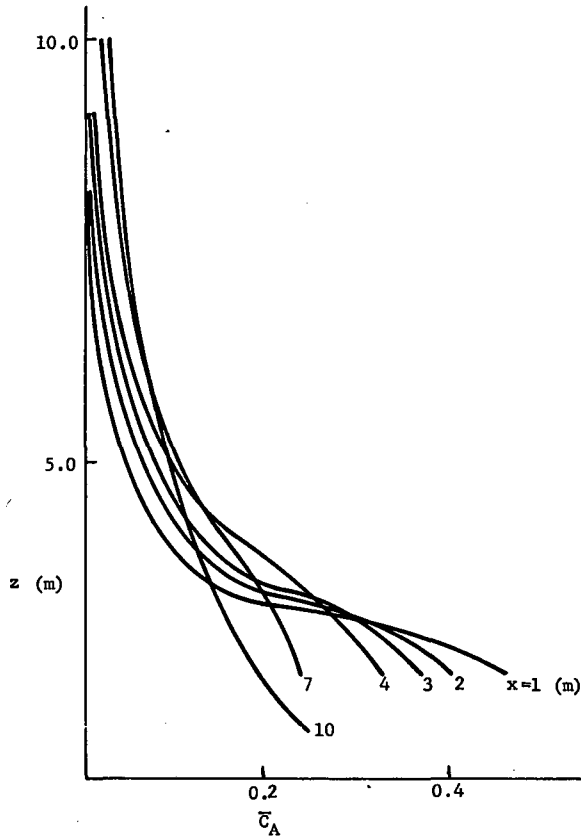


Fig. 2. Eddy-diffusivity function, or effective shear stress:  $\tau$ , or  $(2.5 K/z)^2$ , where  $K$  is eddy diffusivity. Scale unit for  $\tau$  profiles is 4 (m/s)<sup>2</sup>. (XBL-742-420)





distance from the barrier, and  $z$  is the vertical distance from the ground. Results such as these can be generalized by dimensional similarity.

#### References

1. K. D. Wings, E. A. Grens II, and T. Vermeulen, LBL-2444, Nov. 19, 1973.
2. E. J. Plate, Aerodynamic Characteristics of Atmospheric Boundary Layers, report TID-25465, U. S. Atomic Energy Commission, 1971.
3. H. S. Nagabhushaniah, Separation Downstream of a Plate Set Normal to a Plane Boundary, Ph. D. dissertation in civil engineering, Colorado State University, 1962.

Fig. 3. Concentration profiles downstream of emission source. (XBL-742-419)

### NEUTRON ACTIVATION ANALYSIS OF PARTICULATE MATTER IN AIR

H. V. Michel and Frank Asaro

A preliminary study using neutron activation analysis was made of samples containing Pasadena, California, atmospheric particles. The purpose of this study was to determine what modifications are necessary in the techniques developed for pottery analysis<sup>1</sup> so that they can be applied to air pollution studies. The principal changes were in the sample encapsulation procedure and in the flux duration of one of the neutron irradiations.

The samples, which were supplied by the State of Calif., Dept. of Public Health Air and Industrial Hygiene, were made by a four-stage Cascade impactor on a set of Teflon foils and the residual particles collected on a Mitef filter. The largest particles were collected on the stage 1 foil, with the smaller particles collected on the foils from the successive stages. A 1- $\times$ 2.5-cm foil represented a two-hour sampling period. The

mass of material collected at stage 4 varied from 0.05 to 0.24 mg and the final filter contained 0.15 mg. In the process of determining the proper neutron irradiation conditions some of the material on the stage 4 and Mitef samples were lost. Blank samples were run of both Teflon and Mitef. The Mitef sample and blank crumbled upon handling.

The Teflon foils were folded in two (particulate matter inside) and heat-sealed at 550-600° C for 3-5 sec to prevent the loss of particulate matter. These samples were then heat sealed in a secondary 0.001 in. Teflon bag, placed in a graphite capsule, and irradiated in the TRIGA reactor of the Nuclear Engineering Dept., University of California, Berkeley, for 16 min at 500 kW power ( $2 \times 10^{13}$  n/cm<sup>2</sup>/sec). After irradiation, the secondary bag was cut open and each sample placed in a glassine envelope for gamma-ray

Table I. Measured weights (nanograms)

Element	E Stage 1	F Stage 4	G Stage 4	H Mitef	J Teflon blank	K Mitef blank
* Al	37±28	230±150	< 600	5000±1500	440±330	600±370
Mg	275±300	1500±1600	< 3200	10900±5400	1300±800	< 1500
Ca	600±700	< 1900	< 3200	9400±4200	< 1050	2400±1300
V	2.2±1.2	6.0±3.1	14.5±5.9	50±20	< 3	7.4±4.7
Cl	< 120	< 290	260±160	1010±420	< 44	70±50
Br	5.2±3.2	380±28	452±32	2264±80	5.8±3.8	7.4±5.2
Na	11±8	472±24	340±24	4417±147	112±8	83±13
Mn	1.46±.16	19.2±.6	21.4±.5	149±5	1.7±.1	3.06±.30
Sr	7±11	22±25	11±28	123±252	3±7	11±27
K	300±290	900±650	1170±600	7420±3460	600±200	140±310
Ga	< 1.8	< 15	< 10	< 19	< 8	< 5
U	.39±.18	1.0±.2	.78±.25	.60±.48	.23±.09	.22±.20
Sm	.01±.01	.20±.02	.32±.02	1.71±.04	.018±.006	.062±.013
W	5.6±1.1	6.9±1.2	1.2±1.4	< 1.1	< 2.2	< 1.2
Cd	24±17	< 40	< 86	< 162	< 68	< 62
Hg	1.4±.7	< 1.7	< 2.5	< 4	< .8	< .12
As	< 16	< 22	< 27	37±15	< 18	< 17
Ti	127±115	< 400	450±420	< 2350	< 260	< 360
Ta	< 1.2	.9±.6	< 1.7	.87±.48	.23±.12	1.5±.6
Co	11.2±2.0	15.0±2.1	6.2±2.2	8.7±1.3	6.2±.45	1.9±1.1
Sc	1.17±.16	1.09±.17	.86±.24	2.6±.18	.54±.05	.94±.21
Ag	15.8±5.0	< 9.8	< 12.8	< 4.2	.95±.94	< 11
Fe	< 2600	< 4000	3200±1800	6700±1400	550±290	< 3400
Cs	< 1.8	< .7	< 3.0	1.6±.91	< .37	< 2.2
Sb	3.4±2.6	6.9±2.6	26±6	30±3.7	3.7±1.	5.0±2.4
Sn	310±180	< 380	< 620	300±170	< 80	485±190
Ir	< .06	< .07	< .08	< .05	< .02	< .07
Cr	45±18	60±17	26±22	84±17	20±4	23±20
Th	< 2.4	< 1.6	< 3.1	1.8±.8	< .53	< 1.9
Ew	< 1.4	1.4±.7	< 2.2	< 1.4	.15±.1	1.1±.7
Ba	14±6	23±9	< 29	240±110	15±5	< 64
Ni	< 220	< 160	< 200	< 200	59±30	< 110
Rb	104±85	< 180	< 220	75±66	< 27	< 105
Tb	< .7	< .6	.4±.4	< .65	< .14	.58±.36
Hf	< 2.5	< 2.3	< 4	2.6±1.1	< .7	< 3.4
Zn	79±45	300±60	340±66	2100±80	40±10	52±37
Se	< 62	< 84	< 83	41±23	< 20	< 76

\* Some uncertainty in Al value due to unknown Si content of samples.

analysis.

The samples were then wrapped in high-purity Al foil prior to the longer bombardment of 8 h at 1000 kW power ( $4 \times 10^{13}$  n/cm<sup>2</sup>/sec).

Table I shows the detected weights of material in units of  $10^{-9}$  g.

### CHARACTERIZATION OF AEROSOLS IN CALIFORNIA BY X-RAY INDUCED X-RAY FLUORESCENCE ANALYSIS

R. D. Giauque, L. Y. Goda, and N. E. Brown

Elemental analysis of aerosols, coupled with meteorological and particle size distribution data provide information which assists in studying the evaluation of aerosols. From such data the contribution of both man-made and natural sources which yield atmospheric particulate matter, either directly or indirectly through secondary processes may be evaluated.<sup>1,2</sup>

Nondestructive x-ray-induced x-ray fluorescence analysis was employed to determine the elemental concentration in aerosol specimens collected during the California Aerosol Characterization Experiment. The size-segregated aerosol specimens were collected over two-hour intervals on impactor and filter media using multi-stage rotating-drum cascade impactors. Emphasis was placed on characterizing the smaller particles,  $< 1 \mu\text{m}$ , since they (1) degrade visibility and (2) are efficiently trapped in the human respiratory systems. A low-powered molybdenum transmission x-ray tube and a guard-ring semiconductor detector x-ray spectrometer were employed for the analyses. Sensitivities attained using 15 minute counting periods corresponded to less than  $10 \text{ ng/m}^3$  of air sampled for 12 of the 20 elements measured (S through Sr, Pb, Hg).

Figures 1 and 2 illustrate a few of the diurnal patterns established during this study. The aerosol specimens were collected at Fresno and the total and after filters contain particles  $< 20 \mu\text{m}$  and  $< 0.5 \mu\text{m}$ , respectively. The diurnal patterns for K, Ti, Mn, and Fe are very similar for the total filter. These four elements are most likely produced by a mechanical process such as windblown soil dust (large particles) since their concentrations were an order of magnitude lower for the after filter. The Ca was also present almost entirely in the larger particles and

The listed errors are standard deviations, and the limits are equal to two standard deviations, plus the given value for those measurements where the given value is less than 1 standard deviation. An abundance should be three times the standard deviation value to be certain.

is probably from a mixture of soil and cement particles. Approximately 3/4 of the Pb and Br is present in the  $< 0.5\text{-}\mu\text{m}$  range. (This is within the size range of particles which are trapped with a high efficiency in the human respiratory system.)

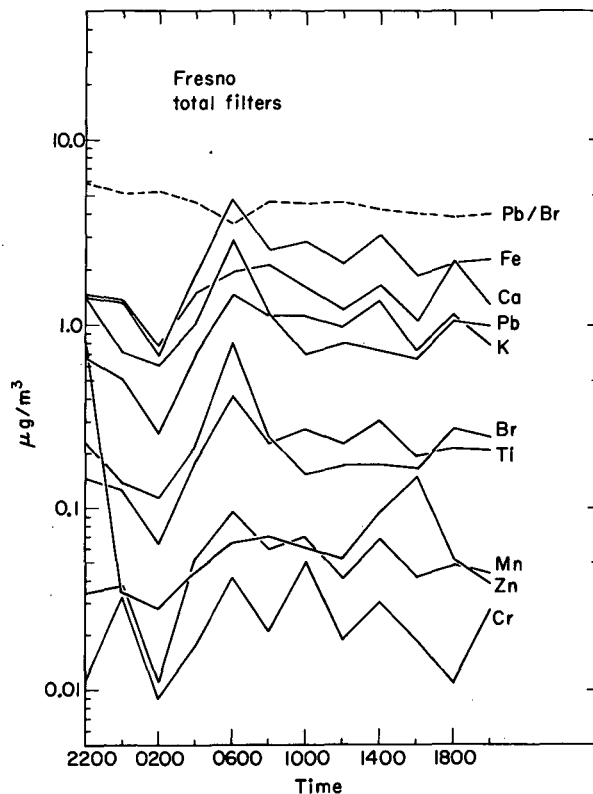


Fig. 1. Diurnal patterns for elements collected on total filters at Fresno on 8/31-9/1. (XBL 735-2929)

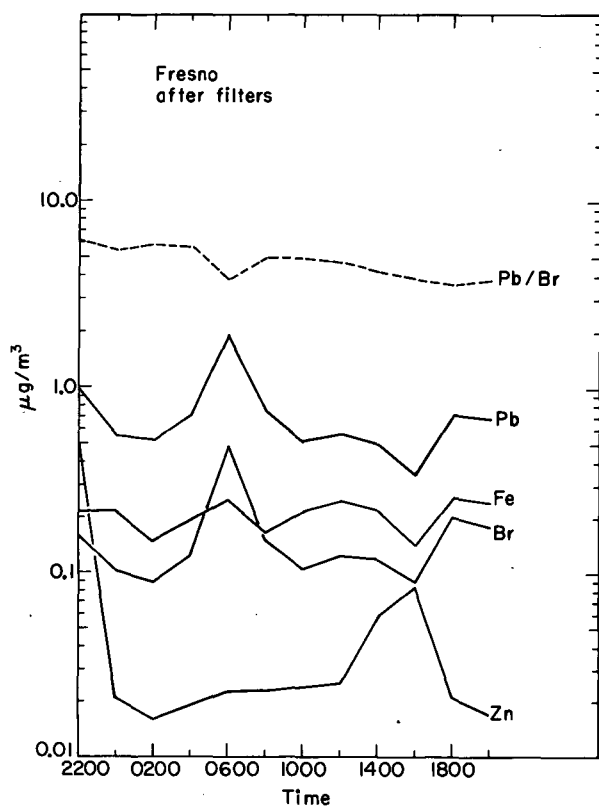


Fig. 2. Diurnal patterns for elements collected on after filters at Fresno on 8/31-9/1. (XBL 735-2928)

The Pb and Br arise from automotive emissions and the Pb/Br ratio indicates the Pb is from an aged aerosol. Over half the Zn was present in the  $<0.5\text{-}\mu\text{m}$  particle size range. Zinc is often thought to be associated with tire dust (larger particles). During these studies, several episodes of high Zn concentrations as illustrated in the Fresno data at 2200 have occurred. The Zn in these cases was predominantly present in the small-particle size range,  $<0.5\text{ }\mu\text{m}$ , and occurred during late evening or early morning hours. The Zn in these cases could be due to combustion sources, possibly from incineration of tires or tin cans.

This data serves to illustrate some of the contributions x-ray fluorescence analysis can make in the study of aerosols. The data has been united with a wealth of other chemical, physical, and meteorological data obtained by other experimenters. The combined data has been used to characterize California aerosols.

#### References

1. G. E. Gordon, W. H. Zoller, E. S. Gladney, and A. G. Jones, "Trace Elements in the Urban Atmosphere," in Nucl. Meth. in Envir. Res., pp. 30-37, Proceed. Amer. Nucl. Soc. Topical Meet., August 1971, Univ. of Missouri.
2. S. K. Friedlander, *Envir. Sci. Tech.* **7**, 235 (1973).

## A SURVEY OF THE OCCURRENCE OF DIMETHYL MERCURY IN THE ATMOSPHERE\*

A. F. Sciamanna and A. S. Newton

It is commonly accepted that methyl mercury compounds, in biological systems, are a product of mercury atoms and ions being acted upon by bacteria to form dimethyl mercury, and this compound is slowly hydrolyzed to  $\text{CH}_3\text{HgX}$  which compound is taken up by animals in the food chain. Sulfhydryl groups in proteins strongly bond the methyl mercury.

To assess the postulate that dimethyl mercury is an intermediate in the transport of mercury in the environment, it is necessary to establish a base line or natural background, if any, of dimethyl mercury in the atmosphere. During certain times of

the year the nearest area for a sampling station of "virgin" ocean air is the California coast from Pt. Reyes to Pt. Arena. At other times it is from Pt. Arena to Cape Mendocino. Power requirements and feasibility limited our consideration to land-based stations for these preliminary studies. It was expected that dimethyl mercury, if present, would have to be concentrated by a factor of  $10^{12}$  from approximately 10-1000 parts in  $10^{15}$  parts of air for our GLC analysis (minimum detectability of 8 picograms Hg).

In GLC, the behavior of dimethyl mercury on porous polymeric beads resembles the behavior of  $\text{C}_5$  to  $\text{C}_6$  hydrocarbons. At room

temperature or lower, these porous polymers have considerable affinity for hydrocarbons. Therefore, utilizing this affinity, 25-mm-i. d. glass tubes containing 50 ml of polymeric beads were used to absorb dimethyl mercury and thereby effect the necessary concentration from air drawn through the sampler with a vacuum pump. After approximately one cubic meter of air was drawn through the sampler, it was returned to the laboratory for analysis. It was placed in a tube furnace in series with a small "u" tube collector (4-min i. d. cooled to 0° C) containing 1 ml of the same polymeric beads. The "u" tube collector was in series upstream of the isothermal analytical GLC column with our microwave-excited argon plasma-mercury detector.<sup>1</sup>

With a 70-ml/min flow of argon through the sampler, the furnace was heated rapidly to 160° C (temperature controlled to  $\pm 2^\circ$  C), held for 80 minutes, and the desorbed dimethyl mercury was collected in the "u" tube collector which was in an ice bath. The collected sample was then flashed out of the collector, with a 175° C liquid-metal bath, directly into the isothermal (153° C) analytical column (2 meters, 4 mm i. d., glass column packed with 50-80 mesh porapak "P"). The dimethyl mercury peak is eluted in approximately 7 minutes from the analytical column under these conditions.

Samples collected outside the laboratory contained various amounts of interstitially

Table I.

(50 cc) Polymer type	0.25- to 25-nanogram dimethyl mercury (% recovery)	Volume of gas before elution of absorbed dimethyl mercury (liters)
50-80 mesh Chromosorb-105	15 - 20	N. D.
80-100 mesh Porapak "P"	98 - 102	350
80-100 Porapak "Q" (Q-1)	44	1060
50-80 mesh Porapak "Q" (Q-2)	63	730
80-100 mesh Porapak "Q" (Q-3) <sup>a</sup>	98.5 - 100	1225
80-100 mesh Porapak "Q" (Q-1) <sup>a</sup>	82.5 - 85	1025
50-80 mesh Porapak "Q" (Q-2) <sup>a</sup>	100	770
50-80 mesh Porapak "R" (R-1) <sup>a</sup>	84.5 - 89	850

<sup>a</sup>Polymer was treated with a liter of a 1:1 solution of concentrated ammonium hydroxide and ethyl alcohol for several days followed by washing with a liter of  $10^{-3}$  M sodium hydroxide in 95% ethyl alcohol, dried, and then GLC conditioned.

Table II.

Site location and date		Picograms dimethyl mercury per cubic meter air	Weight parts Hg per $10^{15}$ parts air (20°C - 760 Torr)
Pt. Reyes 8/8/73	Day	38 ± 8	4
Mt. Tamalpais 8/9/73	Day	> 19	> 2
Bldg. 90, LBL 8/22/73	Day	36	4
	Night	29	3
Bldg. 70, LBL (Rm. 274) 3/12/73	Day & Night	756	91
	Day & Night	> 3.4	> .4

trapped water due to the high humidity conditions which prevailed at the field sampling sites. Therefore, it was necessary to introduce a drying agent before the "u" tube collector. A glass tube 4 mm i. d. containing approximately 2.5 grams of anhydrous magnesium perchlorate was found to quantitatively remove the trapped water and not react with known amounts of dimethyl mercury spiked in the gas and run completely through the system as blanks and for studies of material balance. For example, 98-99% recoveries were obtained when 0.25- to 25-nanogram amounts of dimethyl mercury were injected and 500 to 1000 liters of air or argon passed through the sampler at 11 to 24° C. This water problem in air sampling has been observed<sup>2</sup> but no solution was reported.

The polymeric beads used in the sampler were obtained from two sources. Because certain types of the polymers as received from the manufacturer appear to have an acid component and since dimethyl mercury reacts in an acid media,<sup>1</sup> it was necessary to treat the beads with alkaline-ethyl alcohol solution to neutralize and remove the acid component. These samplers, once chemically treated and conditioned, gave consistently good recoveries of known amounts of added dimethyl mercury as shown in Table I. As can be seen in Table I, Chromosorb-105 was unsatisfactory and did not behave as expected. Porapak "P" behaved as expected, but unfortunately has a relatively low affinity

for dimethyl mercury. Excellent results were obtained with Porapak "Q" after the acid removal treatment. Porapak "R" was intermediate in affinity.

The gas flow meters were calibrated by timing the introduction of gas into an 11.75-liter evacuated container, with atmospheric pressure ( $\pm 5$  Torr) maintained between the sampler and the evacuated container by control with needle valves and zero-centered vac-pressure gauges. Air flows used were commonly 2 to 3 liters per minute in the lab and at the field sites. At least 1000 liters of air was passed through each calibrated sampler at the field sites.

Samples were collected at Pt. Reyes Lighthouse, California (38°N - 123°W) at an elevation of 137 meters above mean sea level and approximately 100 meters onshore. One sample was collected during the day and the other at night on each of two dates in July and August 1973. One sample was collected at Pantoll Camp, Mt. Tamalpais State Park, California (37° 54'N - 122° 36'W) at an elevation of 501 meters above mean sea level. Two samples were collected on the roof of the northwest corner of Building 90, LBL (37° 53'N - 122° 15'W) at an elevation of 244 meters above mean sea level, one sample during the day, the other at night. The results are given in Table II. The results are somewhat lower than expected even in this particular urban area. The results of the Laboratory air are surprisingly higher than expected,

considering the relatively high-flow air ventilation.

#### References

\*A short summary of work in progress.

1. Nuclear Chemistry Annual Report for 1972, LBL 1666, p. 318.

2, J. P. Mievre and M. W. Dietrich, Anal. Chem. 45, 893A (1973).

## DETERMINATION OF LEAD IN ATMOSPHERIC AIR AND IN ALUMINUM BY $^3\text{He}$ -INDUCED NUCLEAR REACTIONS

B. Parsa\* and S. S. Markowitz

Helium-3 activation analysis has been applied to develop a very sensitive means of trace lead analysis. The procedure involves the bombardment of samples with  $^3\text{He}$  particles to induce  $\text{Pb} + ^3\text{He} \rightarrow ^{207}\text{Po}$  reaction on lead isotopes. The 992-keV  $\gamma$ -ray of 5.84-h  $^{207}\text{Po}$  is used as the "signal" for lead determination. Only milligram amounts of sample are required. The excitation function for the production of  $^{207}\text{Po}$  from the reaction of  $^3\text{He}$  with lead of natural isotopic composition is presented. If necessary, destructive analysis may be carried out, and a radiochemical separation procedure to plate polonium onto a silver foil is discussed. The accuracy of the measurement is about 3 to 5% for comparative analyses. For absolute determinations the error is estimated to be 9-12%. Under reasonable irradiation and counting conditions, the detection limit is approximately 50 pg/cm<sup>2</sup>, corresponding to 0.5 ppb in a matrix 100 mg/cm<sup>2</sup> thick.

#### Introduction

Sensitive lead assay by thermal neutron activation techniques is somewhat difficult, because the only long-lived (n,  $\gamma$ ) product practical for analysis is 3.3-h  $^{209}\text{Pb}$ , which has a very low formation cross section, and which decays purely by beta emission. Recent studies utilizing reactor pulsing technique have enabled the detection of up to 0.4  $\mu\text{g}$  of Pb via production and analysis of 0.8-sec  $^{207}\text{mPb}$ .<sup>1,2</sup> Further activation analysis investigations have been carried out to measure lead concentration, with various degrees of success, by fast neutrons<sup>3</sup>, photons<sup>4</sup>, alpha particles<sup>5</sup>, protons, and deuterons<sup>6</sup>. Moreover, lead analysis has been performed by atomic absorption spectroscopy<sup>7</sup> and x-ray fluorescence<sup>8</sup>. Helium-3 induced nuclear reactions may provide an alternatively fruitful method for the determination of lead. Helium-3 activation analysis has been successfully performed in a number of matrices, and its great potential for trace analysis study, especially for light elements, has been observed.<sup>9-12</sup>

In the present work we have investigated the application of the reaction  $\text{Pb} + ^3\text{He} \rightarrow ^{207}\text{Po}$  to the analysis of lead. Recently the decay scheme of  $^{207}\text{Po}$  has been studied very accurately.<sup>13,14</sup> Using the result of the decay-scheme work, the absolute excitation function for production of  $^{207}\text{Po}$  from the reaction of  $^3\text{He}$  with lead of natural isotopic composition has been determined. A number of analyses using the 992-keV  $\gamma$ -ray of  $^{207}\text{Po}$  as "signal" for lead measurement has been carried out.

#### Experimental

Target Preparation. The polonium samples used for measurement were produced by irradiating natural lead with  $^3\text{He}$  ions. The standard targets were made by evaporation of analytical-grade lead metal in vacuum onto 1-in.-diameter and  $\frac{1}{4}$ -mil-thick high-purity aluminum disks. (Republic Foil, Danbury, Conn.) The thickness of the lead deposit was about 2 mg/cm<sup>2</sup> for excitation function determinations. For sample analyses with unknown Pb content, targets were made into 1-in.-diameter foils from the sample sheet. Comparative standards of lead were used for these experiments having thickness of about 100  $\mu\text{g}/\text{cm}^2$ .

Irradiations. Irradiations were performed at the LBL 88-inch cyclotron with  $^3\text{He}$  ions. Ranges in aluminum and lead were determined by means of the known range-energy tables.<sup>15,16</sup> In sample analysis experiments the samples were irradiated together with the comparative standards. Routinely, two or three high-purity Al disks, each of 1.58 mg/cm<sup>2</sup> thickness, separated the sample from the standard. The length of bombardment varied between 30 min. to 1 h, and the average beam current was about 1  $\mu\text{A}$  of  $^3\text{He}$ . Recoiling  $^{207}\text{Po}$  nuclei were caught in the Al backing and in the "upstream" Al cover foil.

Radiochemical Separation. After sample dissolution, a polonium separation with standard plating techniques was carried out.<sup>17</sup> This

was done by adding several drops of methyl red-bromthymol blue-alcohol indicator.<sup>18</sup> Then the solution was neutralized with NaOH pellets to a greenish color. Immediately after the neutralization process, 5 ml conc. HCl was added, and then the sample was diluted with distilled water to a volume of 150 ml in order to make the resulting solution 0.4 N in HCl. The polonium solution was contained in a 250-ml tall-form beaker which was suspended in a boiling water bath. A 1-in.-diameter and 5-mil-thick Ag disk was degreased in trichloroethylene, rinsed in water and introduced to the polonium solution. The heated solution was constantly stirred. In order to minimize any loss of Po, the sides of the beaker and the stirrer were washed down, and the volume of the solution was maintained constant at 150 ml every  $\frac{1}{2}$  h during the plating period.<sup>19</sup> After the Ag disk was exposed for  $1\frac{1}{2}$  h it was removed from the hot solution and rinsed with distilled water. Then the foil was air-dried. Finally it was mounted on an Al sample card for counting.

The average chemical yield was determined with tracer techniques with a stock  $^{210}\text{Po}$  standard solution followed by a gross  $\alpha$  count. Furthermore, the pre- and post-chemistry variations of the 992-keV photopeak of  $^{207}\text{Po}$  produced from lead standards were also used for the chemical yield evaluation. Consequently, in the average, a chemical yield of  $98.4 \pm 1.4\%$  for the metallic targets and a value of  $91.3 \pm 2.5\%$  for the paper specimens were obtained.

**Data Acquisition.** The sources were analyzed by  $\gamma$ -ray spectroscopy with two Ge(Li) detectors, each having an active volume of  $30 \text{ cm}^3$ . In each experiment the activity was followed by measuring the 992-keV photopeak, which is the most intense  $\gamma$ -ray of  $^{207}\text{Po}$ .<sup>13, 14</sup>

## Results and Discussion

**Excitation Function.** The total cross section for the production of  $^{207}\text{Po}$  via  $\text{Pb} + {}^3\text{He}$  reactions was calculated from the 992-keV photopeak intensities. These values were corrected for the detection efficiency and appropriate decay time involved from the end of irradiation. A new  $^{207}\text{Po}$  half-life of  $350.3 \pm 4.1$  min as reported by Parsa and Markowitz<sup>20</sup> was adopted for these calculations. The absolute intensity of the 992-keV  $\gamma$ -ray of  $^{207}\text{Po}$  was calculated to be  $0.59 \pm 0.04$ , based on Astner and Alpsten's decay scheme and their table of transition intensities.<sup>13</sup>

Figure 1 shows the excitation function for the production of  $^{207}\text{Po}$  from the reaction of  ${}^3\text{He}$  with lead of natural isotopic composition. The cross section for this reaction remains fairly constant at an average value of 385 mb

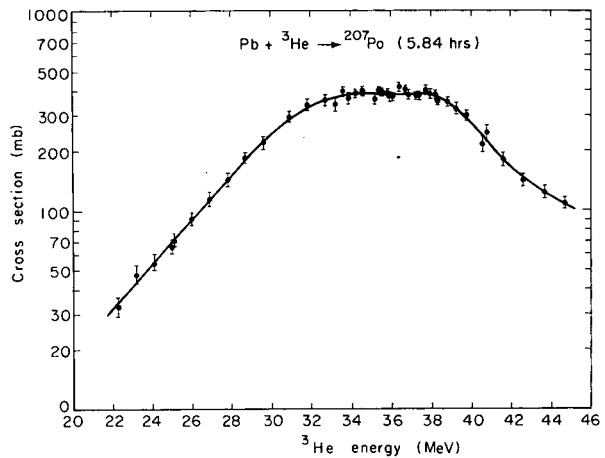


Fig. 1. Excitation function for  $^{207}\text{Po}$  production from  ${}^3\text{He}$ -induced nuclear reactions with natural lead. (XBL735-2953)

within the  ${}^3\text{He}$  energy range of 34 to 38 MeV; the cross section remains above 300 mb from 31 to 40 MeV. This unique characteristic was utilized for the sample analyses so that the samples and the standards could both be irradiated at maximum cross sections for  $^{207}\text{Po}$  production.

**Sample Analyses.** To establish the feasibility of the measurement of lead concentration by this new technique, several analyses were undertaken. In each case a comparative lead standard was placed in the same stack with the "unknown" sample. Subsequently, the same pre- and post-irradiation treatments were applied to them. Then they were counted under identical conditions. In this manner errors in beam current, length of irradiation, decay scheme, and detection efficiency were eliminated. Subsequently, the overall experimental errors were between 3 and 5%. The amount of lead present in the unknown was calculated by comparing the ratio of the 992-keV photopeak areas of the sample to the appropriate lead standard, corrected for radioactive decay.

### 1. Atmospheric Lead Measurements

During the past decade, a series of filter papers were collected weekly from a sampling station in downtown Berkeley by the Safety Service Department of the Lawrence Berkeley Laboratory as part of an environmental survey system.<sup>21</sup> The air was filtered through HV 70 filter paper at an average flow rate of  $4 \pm 0.5 \text{ ft}^3/\text{min}$ . The collected filter papers have been routinely analyzed for lead and bromine content, using the x-ray fluorescence technique.<sup>22, 23</sup> Replicate samples from several filter papers collected at various times during the year 1971



were nondestructively analyzed for lead via  $^3\text{He}$  activation analysis. Table I shows the average lead concentration in the downtown Berkeley atmosphere during those periods. For comparison, the results obtained for the same filter papers by x-ray fluorescence technique are also tabulated.<sup>24</sup> The agreement is good.

Table I. Average atmospheric lead concentration in downtown Berkeley at various times during the year 1971.

Sample collection dates	Lead concentration ( $\mu\text{g}/\text{m}^3$ )	
	This work	X-ray fluorescence work <sup>a</sup>
Feb. 5 to Feb. 12	$6.38 \pm 1.00$	b
May 14 to May 21	$1.50 \pm 0.16$	1.64
Oct. 22 to Oct. 29	$2.10 \pm 0.24$	1.84

<sup>a</sup> Reference 23. The standard deviation in this work is about 10% of the mean value.

<sup>b</sup> X-ray fluorescence analysis was not performed on this sample, but qualitatively it was observed to have comparatively high lead content.<sup>24</sup>

## 2. Measurement of Lead in Aluminum Foils and Filter Papers

The measurement of lead concentration was further extended to the  $\frac{1}{4}$ -mil (1.58 mg/cm<sup>2</sup> thick) Al backing foils used in this study. A few experiments were carried out, and because the lead content was found to be at trace levels, there was an attempt to measure the  $\gamma$ -ray spectrum with a 3×3-inch NaI(Tl) crystal in order to increase the detection efficiency. Figure 2 presents a typical 992-keV  $\gamma$ -ray spectrum of the chemically separated polonium portion; it was obtained by irradiating the  $\frac{1}{4}$ -mil-thick Al foil for 1.5 h with  $^3\text{He}$  particles of about 35 MeV at an average beam current of 3.8  $\mu\text{A}$ . For comparison, the  $\gamma$ -ray spectra were taken with Ge(Li) and NaI(Tl) detectors at similar counting geometries. Although, as expected, the 992-keV peak area in the NaI(Tl)  $\gamma$ -ray spectrum is a factor of 10 times larger than its respective Ge(Li) one, the peak-to-background ratio is only 2:1 in the NaI(Tl) case in comparison with 30:1 for the Ge(Li) detector. Consequently, it is concluded that for this study Ge(Li)  $\gamma$ -ray spectroscopy is far more advantageous, mainly due to its superior resolution. The result of lead analyses in Al foils together with the analyses of "blank" Whatman #41 and

HV 70 filter papers are summarized in Table II. For filter papers the irradiations were limited to the duration of  $\frac{1}{2}$  h and average beam current of 1  $\mu\text{A}$ .

Interferences. By using  $^{207}\text{Po}$  activity, lead analysis via  $^3\text{He}$  activation is basically free from interferences produced by any other element. The only element which could possibly interfere by this technique is Bi. Bismuth, if present, could produce  $^{207}\text{Po}$  via  $^{209}\text{Bi}(^3\text{He}, p^{4n})^{207}\text{Po}$  and  $^{209}\text{Bi}(^3\text{He}, 5n)^{207}\text{At} \xrightarrow{1.81\text{ h}} ^{207}\text{Po}$  reactions; the threshold energy is 25.8

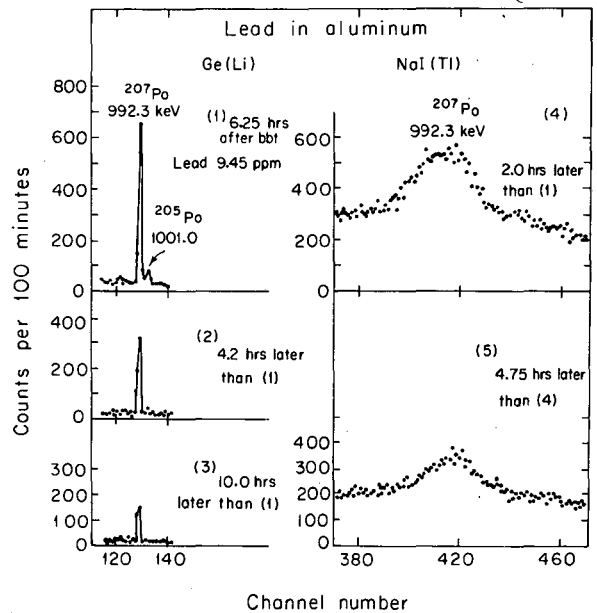


Fig. 2. Comparison of the 992-keV  $\gamma$ -ray spectra of chemically separated Po taken with Ge(Li) and NaI(Tl) detectors at various times. The source was produced by irradiating the  $\frac{1}{4}$ -mil-thick Al foil with  $^3\text{He}$  ions.

(XBL735-2952)

Table II. Lead analysis of various samples.

Sample	Lead content (ppm)
$\frac{1}{4}$ -mil-thick Al (type 1145-H18)	$9.45 \pm 0.52$
Whatman #41 filter paper	$2.11 \pm 0.38$
HV 70 filter paper	$6.46 \pm 0.35$

MeV and 30.8 MeV, respectively. In order to estimate the magnitude of this potential interference, a series of bombardments at different  $^3\text{He}$  energies were carried out; foils of 4-mg/cm<sup>2</sup>-thick metallic Bi evaporated onto thin Al backings were irradiated for 1.5 h at an average beam intensity of  $\sim 1 \mu\text{A}$ . A summary of experimental cross-section data is presented in Table III. The experimental errors are about 10%. The cross section for  $^{207}\text{Po}$  production from Bi +  $^3\text{He}$  reaction at about 35 MeV, the energy region of optimum  $^{207}\text{Po}$  production from the Pb +  $^3\text{He}$  reaction, is 10 times lower than that for Pb +  $^3\text{He}$  reaction. Therefore, at equal concentration of lead and bismuth impurities in a given matrix, at that energy region, only 10% of the  $^{207}\text{Po}$  activity will have been caused by an interfering Bi. However, because the radiochemical procedure in this work does not provide a separation of polonium from astatine, which is also deposited to a large extent on silver foil,<sup>25, 26</sup> the presence of Bi can be determined unambiguously by detection of astatine radioisotopes produced via Bi( $^3\text{He}, \text{xn}$ ) reactions. For example, our Bi +  $^3\text{He}$  reaction studies revealed that 685- and 660-keV photopeak intensities of  $^{208}\text{At}$  produced by  $^{209}\text{Bi}$  ( $^3\text{He}, 4\text{n}$ ) $^{208}\text{At}$  reaction are a factor of  $\sim 10$  times higher than the 992-keV peak intensity. In other words, bismuth – if indeed present – can clearly be determined via the  $^{208}\text{At}$  gamma rays. No other element can produce this nuclide. Alternatively, if the analysis is made on a matrix with high Bi/Pb concentration ratio, the Bi interference can be completely eliminated by bombardments near 25 MeV, which is lower than the threshold energy for production of  $^{207}\text{Po}$  via Bi +  $^3\text{He}$  reactions.

Table III. Cross section for the  $^{209}\text{Bi}(^3\text{He}, 5\text{n} + \text{p}4\text{n})^{207}\text{Po}$  reaction.

Avg. $^3\text{He}$ energy (MeV)	Cross Section (mb)
29.6	16
34.9	38
39.7	303

Estimate of Detection Limit. Under the following conditions: beam current 3.8  $\mu\text{A}$ , length of bombardment 1.5 h, overall detection efficiency 0.5%, we were able to detect Pb concentrations of 45 ng/cm<sup>2</sup> in an Al matrix (Fig. 2). The background constituted only about 1/10 of the total 992-keV peak area; at equal signal-to-background levels, under our

easy conditions, we could detect 4.5 ng/cm<sup>2</sup> lead. Because the beam intensity can be increased by a factor of 10 (or greater, depending on the target matrix), detection coefficients can be easily doubled, length of bombardment increased to at least one  $^{207}\text{Po}$  half-life, and the detection limit can be lowered to about 50 pg/cm<sup>2</sup> lead. If the matrix in which lead is imbedded is 10 to 100 mg/cm<sup>2</sup> thick, the concentration limit of detection would therefore be 5 ppb to 0.5 ppb, respectively.

It should be pointed out that for the analysis of paper, the detection limit is held down to only 1 ppm, under our present target-cooling system.

#### Acknowledgements

The authors wish to thank Mrs. Diana M. Lee for her assistance during this work. One of us (BP) would like to express his gratitude for a Senior Fulbright-Hays grant provided to him throughout this study.

#### Footnote and References

\* Visiting Fulbright-Hays Grantee. Permanent address: Tehran University Nuclear Center, Tehran, Iran.

† Condensed from: Anal. Chem. 46, 186 (1974).

- H. R. Lukens, J. Radioanal. Chem. 1, 349 (1968).
- M. Wiernik and S. Amiel, *ibid.*, 3, 393 (1969).
- P. Meyers, Proc. 2nd Conf., Practical Aspects of Activation Analysis with Charged Particles, Liege, 1967 (Euratom, Brussel, 1968), Vol. I, p. 195.
- E. A. Schweikert and Ph. Albert, Radiochemical Methods of Analysis, Vol. I, 358, IAEA ed. (1965).
- J. C. Cobb, J. Geophys. Res. 69, 1895 (1964).
- E. A. Schweikert, Trans. Am. Nucl. Soc. 13, 58 (1970).
- B. V. L'vov, Atomic Absorption Spectrochemical Analysis (American Elsevier, New York, 1970).
- H. R. Bowman, E. K. Hyde, S. G. Thompson, and R. C. Jared, Science 151, 562 (1966).
- S. S. Markowitz and J. D. Mahoney, Anal. Chem. 34, 329 (1962).
- E. Ricci and R. L. Hahn, *ibid.*, 39, 794 (1967).

11. D. M. Lee, J. F. Lamb, and S. S. Markowitz, ibid., 43, 452 (1971).
12. D. M. Lee and S. S. Markowitz, LBL-682, J. Radioanal. Chem., in press.
13. G. Astner and M. Alpsten, Nucl. Phys. A140, 643 (1970).
14. V. A. Shilin and V. R. Burmistrov, Izvest. Akad. Nauk. SSSR, Ser. Fiz., 35, 1653 (1971).
15. J. F. Lamb (Ph. D. thesis), UCRL-18981 (1969).
16. C. F. Williamson, J. Boujot, and J. Picard, Rapport CEA-R3042 (1966).
17. P. E. Figgins, The Radiochemistry of Polonium, NAS-NS 3039 (January 1961).
18. W. L. Minto, National Nuclear Energy Series, Div. VI, Vol. 3, p. 15, edited by R. M. Fink (McGraw-Hill, New York, 1950).
19. I. Feldman and M. Frisch, Anal. Chem. 28, 2024 (1956).
20. B. Parsa and S. S. Markowitz, LBL-1902, J. Inorg. Nucl. Chem., 36, 000 (1974).
21. H. P. Cantelow, J. S. Peck, A. E. Salo, and P. W. Howe, UCRL-10255 (May 1962).
22. H. R. Bowman, J. G. Conway, and F. Asaro, Envir. Sci. Tech. 6, 558 (1972).
23. L. Y. Goda, J. G. Conway, and H. R. Bowman, LBL-1235 (August 1972).
24. J. G. Conway, private communication.
25. W. Garrison, J. Gile, R. Maxwell, and J. Hamilton, Anal. Chem. 23, 204 (1951).
26. E. H. Appelman, The Radiochemistry of Astatine, NAS-NS 3012 (March 1960).

#### INTERLABORATORY LEAD ANALYSIS OF STANDARDIZED SAMPLES OF SEA WATER

R. G. Clem and D. C. Girvin

The question of whether measurements of lead concentrations in sea water by atomic absorption and anodic stripping voltammetry techniques are as reliable as those determined by isotope dilution is important to researchers in several fields. To provide a background, at a recent International Decade of Ocean Exploration Conference in the United States in May 1972 dealing with Baseline Studies of Pollutants in the Marine Environment, it was found that seven chemical oceanographic laboratories of superior status using atomic absorption or anodic stripping voltammetry techniques could not demonstrate a reliable capability for analyzing lead in tuna fish and could not demonstrate a capability for detecting lead contamination in tuna fish that had actually been grossly contaminated. The general feeling of those attending the meeting was that this type of inaccuracy probably extended to analyses of lead in sea water. It was recommended that a workshop be established to carry out interlaboratory lead analyses of sea water standardized by stable isotope dilution mass spectrometric techniques.

A workshop which was sponsored by the NSF Office for the IDOE was initiated in the

fall of 1972. Two samples of sea water and one sample of distilled water were circulated among nine participating oceanographic laboratories during the next six months. The samples were standardized by stable isotope dilution, using mass spectrometric and clean laboratory techniques in one of the laboratories and were analyzed for lead by either atomic absorption or anodic stripping voltammetry techniques in eight of the other laboratories. In addition to the investigators actually analyzing samples, seven advisors were selected.

The aim of the study was to encourage proper application of rapid and inexpensive analytical techniques such as atomic absorption (and emission) and anodic stripping voltammetry to the analysis of lead in sea water and marine organisms. Ultra-careful isotope dilution analytical techniques for lead cannot be used in the majority of needed applications because it is too slow and expensive.

The results shown in Table I indicate that a dramatic improvement in agreement among the participants was reached during the course of the study. The LBL group was laboratory 4. We found that the determination of lead in sea

Table I.

Participating <sup>a</sup> laboratory	Method <sup>b</sup>	number	Amount(g) per analysis	Analysis date	Applicable standardized value (ng/kg)	Analytical results (ng/kg)	Best value	
1	AS	11/1/72	10	11/20/72	Diss Pb only	14 ± 3	Mean of 8 values	1300
2	AA	11/1/72	500	11/20/72	Diss Pb only	14 ± 3	50, 50	50
3	AA	11/1/72	1220	12/21/72	Diss Pb only	14 ± 3	120, 60	60
4	AS	11/1/72	15	12/2/72	Diss Pb only	14 ± 3	Mean of 3 values	600
5	AA	11/1/72	700	11/25/72	Diss Pb only	14 ± 3	55	55
6	AS	11/1/72	90	12/5/72	Diss Pb only	14 ± 3	200, 180, 460, 450, 120, 180, 170	180
7	AA	11/1/72	500	12/1/72	Diss Pb only	14 ± 3	120	120
8		11/1/72					Did not report	
9	ID	11/1/72	1000	11/20/72	Diss Pb only		Standardized value	14 ± 3
1	AS	4/9/73	75	5/7/73	Diss Pb+Ads Pb	70 ± 4	50, 180, 190, 200	---
2	AA	4/9/73	370	4/30/73	Diss Pb only	38 ± 2	48, 54, 54, 74	60
3	AA	4/9/73	261	5/15/73	Diss Pb only	39 ± 2	63, 61, 57	61
4	AS	4/9/73	15	9/12/73	Diss Pb+Ads Pb	80 ± 4	50, 61, 86, 88	---
5	AA	4/9/73	500	7/3/73	Diss Pb only	45 ± 2	138, 358, 359	---
6	AS	4/9/73	113	5/25/73	Diss Pb+Ads Pb	64 ± 3	95, 89, 87	87
7	PP	4/9/73	600	6/11/73	Diss Pb only	42 ± 2	9, 29	---
8	AA	4/9/73	200	6/4/73	Diss Pb+Ads Pb	80 ± 4	86, 116, 129, 138	134
9	ID	4/9/73	1800	4/11→7/10/73	Diss Pb only		Standardized value	36→45(trend)
9	ID	4/9/73	1800	4/11→7/10/73	Diss Pb+Ads Pb		Standardized value	80→47(trend)

<sup>a</sup>Participating laboratories are anonymous. Numbers do not correspond to alphabetical listing.

<sup>b</sup>AS denotes anodic stripping voltammetry; AA denotes atomic absorption; PP denotes pulse polarography; ID denotes isotope dilution.

water necessitates the use of reagent acids prepared by the non-boiling distillation technique and the use of a clean-air bench fitted with absolute air filters.

It was decided at the meeting that if the lead levels in the next round of samples are lower by a factor of 5 and certainly by a factor of 10 that atomic absorbance would lose any competitive edge it might enjoy at higher lead levels owing to the unfavorable ratio of procedural lead to sample lead. Since a lead extraction is not required prior to the analysis in the LBL approach, our method—*anodic stripping*—should be of great utility at these lower levels.

The conditions used to obtain the results shown in Table I involved the deposition of

mercuric and lead ions in the rotated cell for 30 min from 15 ml of sample prior to the stripping scan. This is contrasted with the procedure used by other participants who used upward to 113 ml of solution and plating times as long as 8 hours.

To remain competitive in the next round of samples, the development of a flowing cell which can accommodate 150 to 1000 ml of sample is necessary. This is under construction at this time. It is anticipated that we will be able to reach a lead sensitivity level of 1 part in  $10^{12}$  within 30 min deposition time.

#### Footnote

\* IDOE workshop held at Pasadena, Calif., Sept. 16-20, 1973.

### A STUDY OF THE EFFECTS OF DREDGING AND SPOILING OPERATION ON THE UPTAKE AND ACCUMULATION OF HEAVY METALS BY BENTHIC ESTUARINE SPECIES\*

V. Anderlini, J. Chapman, A. S. Newton, and R. W. Risebrough

This study, undertaken under a contract with the Corps of Engineers, is designed to determine whether the disruption of accumulated sediments during dredging and spoiling operations results in the release of toxic heavy metals to the adjacent waters with subsequent uptake by the local biota. The site of the study is the Mare Island Channel in which dredging operations were performed in November 1973. The first phase of the project was a field study of the benthic species in the Mare Island Channel, and the collection of samples to establish pre-dredging levels of heavy metals, specifically Ag, Cd, Cu, Hg, and Pb in benthic and intertidal organisms, sediment, and water.

Benthic species were chosen for study because of their intimate association with sediments in which they live and obtain their food. Changes in the sediments should be reflected in changes in the concentrations of heavy metals in the benthic species. Ultimately changes in the benthic species should be reflected in changes in heavy-metal content of species utilized as food by man. Intertidal and fouling organisms are used to compare possible changes in metal concentration in species not associated with sediments, but which are exposed to water adjacent to dredging and spoiling operations.

A pre-survey in late July gave information on the taxonomy, general abundance, and distribution of benthic organism in the Mare Island Channel. These samples were collected with a  $0.05 \text{ m}^2$  Van Veen grab sampler at each of nine stations (Fig. 1. N - inner, 1, and outer, o; S-i and o; D-o; E-i and o; and W-i and o). The species found and identified are shown in Table I.

Samples of sediment, water, and several benthic species were also collected for analysis to establish the approximate levels of heavy metals involved. Biological samples were freeze-dried, powdered, and pressed into pellets for analysis by x-ray fluorescence spectrometry<sup>1</sup> or for mercury by the isotope Zeeman effect atomic absorption apparatus.<sup>2</sup> Representative analyses are shown in Table II.

Because the pre-dredging survey collections showed that samples taken with the Van Veen grab sampler were neither representative nor reproducible, collection techniques were devised in which scuba divers take core samples for population studies, and further use a 16-cm-diameter  $\times$  100-cm-long pipe suction dredge made of PVC to collect samples for metals analysis. Reproducible core samples were taken with PVC pipe cores driven a fixed depth into the sediment. Samples were

Table I. Invertebrate fauna of Mare Island Channel, Solano County, California.\*

Numbers 1-7 are codes; see below.

Annelida		Decapoda	
Oligochaeta		Carides	
Tubificidae 2		<u>Crangon</u> sp.	6
Polychaeta		<u>Palaemon macrodactylus</u>	3
<u>Eteone lighti</u>	2	Brachyura	
<u>Glycinde</u> sp.	2	Cancer sp.	7
<u>Harmothoe imbricata</u>	6	<u>Rhithropanopeus harrisii</u>	3
<u>Heteromastus filiformis</u>	2	Anomura	
<u>Neanthes succinea</u>	1, 2, 3	<u>Upogebia pugettensis</u>	6
<u>Polydora ligni</u>	6		
<u>Pseudopolydora kempfi</u>			
<u>Streblospio benedicti</u>	2	Mollusca	
<u>Tharyx parvus</u>	6	Bivalvia	
		<u>Ischadium demissum</u>	5
		(= <u>Modiolus</u> )	
Arthropoda		<u>Macoma balthica</u>	1, 2
Crustacea		<u>Mya arenaria</u>	2
Ostracoda unidentified sp.	6	<u>Mytilus edulis</u>	3, 4
Cirripedia		<u>Tapes japonica</u>	6
<u>Balanus improvisus</u>		Gastropoda	
Malacostraca		<u>Nassarius obsoletus</u>	7
Cumacea-unidentified sp.			
Chelifera		Chordata	
<u>Tanais vanis</u>	6	Tunicata	
Isopoda		<u>Mogula manhattensis</u>	3
<u>Sphaeroma quoyana</u>	7		
<u>Synidotea laticauda</u>	3		
Amphipoda			
<u>Ampelisca milleri</u>	1, 2		
<u>Ampithoe valida</u>	6		
<u>Corophium acherusicum</u>	2		
<u>Corophium insidiosum</u>	6		
<u>Corophium spinicorne</u>	6		
<u>Corophium</u> sp.	6		
<u>Grandidierella japonica</u>	2		
<u>Melita</u> sp., cf. <u>nitida</u>	7		
<u>Parapleustes pugettensis</u>	7		

## Code:

- 1 = used for metals analysis in benthic survey.  
 2 = used for population analysis in benthic survey.  
 3 = used for metals analysis from fouling survey.  
 4 = used in transplant study.  
 5 = used for intertidal mudflat metals analysis.  
 6 = rare, or biomass of insufficient quantity for consideration.  
 7 = insufficient abundance for metals analysis but not included because of time limitations.

\* Species identified by J. Chapman. Amphipod identification confirmed by J. L. Barnard. Polychaete species will be sent to D. Reish, F. Nicols, and W. Light for confirmation.

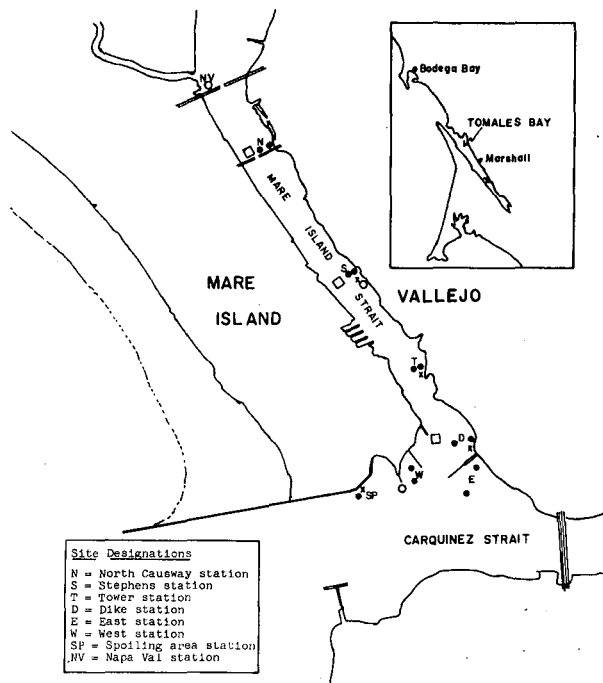


Fig. 1. Collection sites in Mare Island Strait and adjacent waters. (Inset: Tomales Bay.)

- o = Benthic collection sites for heavy metal and biologic samples
- × = Mussel transplant locations
- = Intertidal and fouling organisms collection sites
- = Water collection sites.

(XBL 742-421)

collected at each of 13 stations shown in Fig. 1.

In order to study the effects of metal content of water on the biota, some 1125 bay mussels (*Mytilus edulis*) were transplanted from Tomales Bay (a clean area) to various sites in the Mare Island Channel. These transplanted *M. edulis* have been sampled periodically before, during, and after dredging to observe the rate of growth and equilibration to the new environment. Comparisons are also being made with native *M. edulis* populations at some of the sites.

Water samples collected before, during, and after dredging are being analyzed for lead and cadmium by the anodic stripping method.<sup>3</sup> Two pre-dredging collections of benthic species were made for both biological and metals analysis. These collections were about one month apart. Further benthic collections were made during the dredging, and one post-dredging collection has been made.

Laboratory experiments are also under way to determine the rate of uptake of heavy metals from water and/or sediments by benthic species. Polychaetes, amphipods, and mussels will be tested for uptake of the metals Cu, Cd, Pb, and Hg.

Table II. Representative heavy-element content of sediment, amphipods, clams, and polychaetes from Mare Island Channel.

Element	ppm element in:			
	Sediment	Amphipod, <i>Ampelisca milleri</i>	Clam, <i>Macoma balthica</i>	Polychaete, <i>Neanthes succinea</i>
Cr	200	64	72	118
Mn	700	400	280	430
Fe	43000	8700	7800	17200
Ni	88	26	26	47
Cu	84	52	58	55
Zn	147	73	270	240
Ga	20	5.8	4.7	8.6
Hg	6	8	3	3
As	10	1	6	3
Pb	46	25	16	31
Se	1.8	4.8	4.8	5.8
Br	83	550	150	575
Rb	80	6.9	15	22
Sr	140	1550	89	94

## Footnote and References

\* A short report on work in progress. This study is sponsored by the Corps of Engineers. It is being conducted by LBL in collaboration with the Bodega Bay Institute of Pollution Ecology.

1. R. D. Giaque, F. S. Goulding, J. M. Jaklevic, and R. H. Pehl, *Anal. Chem.* **45**,

671 (1973).

2. T. Hadeishi, *Appl. Phys. Lett.* **21**, 438 (1972).

3. D. Gervin and R. Clem, Conference on Interlaboratory Lead Analyses of Standardized Samples of Sea Water, Sept. 16-20, 1973, Pasadena, Calif. NSF Office for the International Decade of Ocean Exploration.

## ENZYMATIC UTILIZATION OF CELLULOSIC WASTES

G. Mitra and C. R. Wilke

Enzymatic utilization of cellulosic materials has been investigated in recent years as a potential source of reducing sugars.<sup>1-3</sup> On the land area of the earth about  $1.6 \times 10^{10}$  tons of carbon is fixed every year by photosynthesis, out of which about half appears in the form of cellulose. Hydrolysis of one pound of cellulose theoretically yields 1.1 pounds of glucose, which is equivalent to 0.56 pounds of ethyl alcohol. This can be used as liquid fuel, or the hydrolysis products (mainly glucose) can be converted to methane which is a useful source of gaseous fuel.

A process design study earlier initiated in this Laboratory<sup>4</sup> identified the cost of the enzyme (cellulase) production to be crucial in the economic processing of cellulosic materials. In the present phase of the work, enzyme production kinetics was investigated in multiple stirred tanks in series, and an adsorption/wash scheme was devised for effective reuse of the enzyme following hydrolysis.

*Trichoderma viride* QM 9414, a highly productive mutant developed at the U.S. Army Laboratory at Natick, Massachusetts, was grown in a fermentation system for cellulase production. Single-stage stirred-tank runs with 1% glucose yielded a maximum cell productivity of 0.92 mg dry weight/ml $\times$ h at a dilution rate of 0.21/h. Two-stage continuous stirred-tank runs were conducted with cell growth on glucose in the first stage and enzyme induction by cellulose addition in the second stage. Maximum productivity for this mode of operation was determined to be  $27.3 \times 10^{-3}$  filter paper activity/ml $\times$ h for 1% glucose as carbon source and 1% pure cellulose as inducer. Compared to the published results<sup>5</sup> of single-stage stirred-tank operations with 1% pure cellulose this represents an increase in enzyme productivity by a factor of 4.13.

The substrate utilized for hydrolysis was ball-milled newspaper (-100 mesh) with a cellulose content of 61% of its dry weight. Hydrolysis was carried out at a temperature of 50°C and a pH of 4.8 with a 10% suspension of solids. The results obtained with different enzyme activities are shown in Fig. 1. For a residence time of 40 hours an enzyme activity of 2.72 filter paper units resulted in 82% conversion of the cellulose present in the solids.

A detailed description of the current work is reported in the Laboratory report LBL-2334. Economic analysis was carried out for a plant utilizing 885 tons/day of waste paper as substrate. Without assigning any cost to the waste paper the net manufacturing cost of reducing sugar in 5.6% solution was calculated to be 1¢/lb with a fixed capital investment of about \$10,000,000.

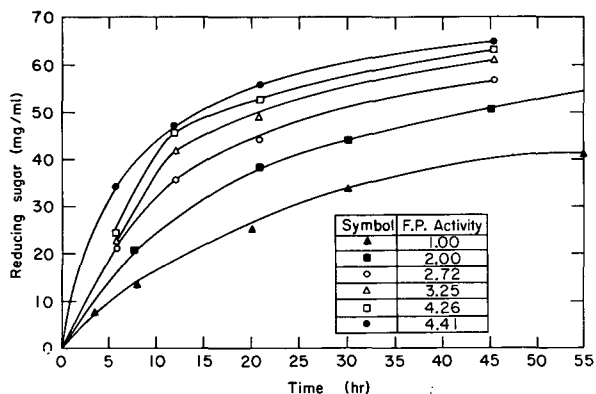


Fig. 1. Hydrolysis of 10% ball-milled (-200 mesh) newsprint. (XBL 7310-4170)



References

1. R. F. Gould, Adv. in Chem. Series 95 (1969).
2. R. G. H. Siu, Microbial Decomposition of Cellulose (Reinhold, New York, 1951).
3. B. Norkrans, Adv. in Appl. Microbiol. 9, 91 (1967).
4. C. R. Wilke, and R. R. Rosenbluth, S. E. R. L. Report No. 70-9, College of Engineering and School of Public Health, University of California, Berkeley, California (1970).
5. M. Mandels, and J. Weber, Adv. in Chem. 95, 391 (1969).

## IV. Instrumentation

## 88-INCH CYCLOTRON OPERATION, DEVELOPMENT, AND STUDIES

J. Bowen, R. Burleigh, D. J. Clark, W. Flood,  
P. E. Frazier, and D. Morris

During 1973 the cyclotron was scheduled for 20 eight-hour shifts per week for experiments in nuclear chemistry and physics, isotope production, and beam development. One shift per week was used for maintenance. The time distribution is shown in Table I. The particle distribution history is shown in Fig. 1. The time occupied by ions heavier than helium increased from 51% in 1972 to 55% in 1973.

More heavy-ion beams were developed with the internal PIG source. As shown in Fig. 1, beams of boron, sulfur, and argon were new in 1973. In addition some beryllium was also accelerated late in the year. The present list of beams that have been run is shown in Table II. Beams of solid materials were produced by mixing in powder of the element or a compound with tantalum powder

Table I. 1973 Time distribution.

Tune up	6%	
Beam optics	4%	
Experiments	57%	
Beam development	9%	
Operating time	76%	(6336 h)
Planned maintenance	17%	
Unplanned maintenance	7%	
Total maintenance	24%	(1968 h)
Total work time	100%	(8304 h)

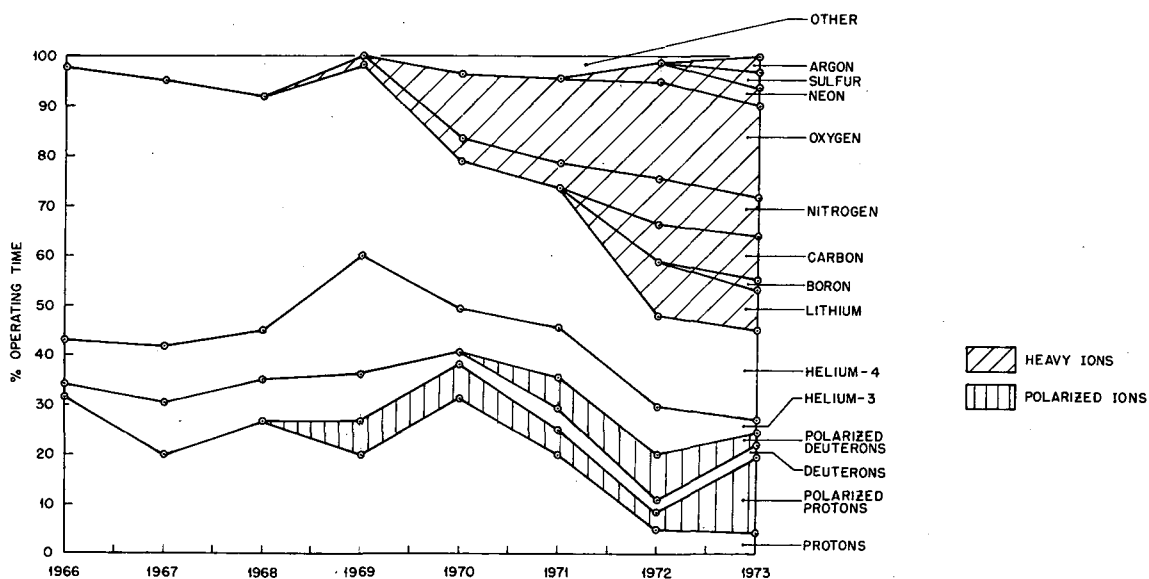


Fig. 1. 88-inch cyclotron particle distribution history. (XBL-741-142)

Table II. 88-inch cyclotron heavy-ion beams—December 1973.

Ion	Energy <sup>a</sup> (MeV)	Harmonic	External beam <sup>b</sup>
${}^6\text{Li}^{2+}$	80, 93	1	1 $\mu\text{A}$
${}^7\text{Li}^{2+}$	37-80	3, 1	1 $\mu\text{A}$
${}^9\text{Be}^{3+}$	120, 140	1	0.2 $\mu\text{A}$
${}^{11}\text{B}^{3+}$	43-115	3, 1	2 $\mu\text{A}$
${}^{12}\text{C}^{3+}$	50-105	3, 1	5 $\mu\text{A}$
${}^{14}\text{N}^{2+}$	34-40	3	1 $\mu\text{A}$
${}^{14}\text{N}^{3+}$	50-90	3, 1	5 $\mu\text{A}$
${}^{14}\text{N}^{4+}$	74-160	3, 1	5 $\mu\text{A}$
${}^{14}\text{N}^{5+}$	250	1	1 $\mu\text{A}$
${}^{14}\text{N}^{6+}$	360	1	$10^3$ part./sec
${}^{16}\text{O}^{3+}$	50-75, 79	3	5 $\mu\text{A}$
${}^{16}\text{O}^{4+}$	85-140	3, 1	5 $\mu\text{A}$
${}^{16}\text{O}^{5+}$	218	1	0.5 $\mu\text{A}$
${}^{20}\text{Ne}^{4+}$	93-107, 112	3	1 $\mu\text{A}$
${}^{20}\text{Ne}^{5+}$	105-150, 175	3, 1	0.5 $\mu\text{A}$
${}^{32}\text{S}^{6+}$	120-150, 158	3	0.1 $\mu\text{A}$
${}^{40}\text{Ar}^{7+}$	130, 171	3	0.3 $\mu\text{A}$
${}^{40}\text{Ar}^{8+}$	170-214, 224	3	0.2 $\mu\text{A}$
${}^{56}\text{Fe}^{10+}$	180-220, 250	3	1 part./sec
${}^{84}\text{Kr}^{12+c}$	207, 240	3	1 part./sec

<sup>a</sup>Energies run. Maximum, if full magnetic field were used, is shown after comma, if higher.

<sup>b</sup>Electrical microamps or particles/sec, total external.

<sup>c</sup>Filament source; other beams used FIG source.

in the cathodes, or by using a sleeve in the anode arc chamber.

Various mechanical improvements were made in 1973. The cooling was improved on the rear rf hinges in the resonator box to prevent burnouts at high rf power levels. A cryogenic pumping system for the cyclotron is well along in the design stage. An ion source shaft guide was installed to provide smoother inser-

tion with the elevator. A second ion source gas valve system was installed for mixing gases and for using toxic gases. A handling device was built for the rf amplifier tube. Faraday cups with electron suppression for accurate beam reading were installed in the vault and caves 3 and 4 for studies of transmission to the spectrometer area. Remote and manual carbon foil holders were installed in the staging line to provide charge change of

heavy-ion beams for dual-beam and ion-separation purposes. Work was done in several areas to comply with the new OSHA safety standards.

Electrical improvements included the installation of a new 12-kV switching system. The new wide-band rf drive system installed in 1972 is running well. The principal maintenance has been the cleaning of the main amplifier tube. A regulated screen power supply is being tested to reduce dee voltage ripple. A new ion source gas control panel was built and installed. A pulsed ion source arc supply is under construction to provide high peak power to the PIG source; this should give higher charge state beams. An energy conservation program was started. The power consumption was reduced 7% in Build-

ing 88 by reducing use of some equipment and lighting.

Studies have been done for two possible future accelerators. One is for a medical cyclotron producing 150-MeV protons; this could be used for cancer therapy in a hospital. The lowest-cost version has a small hill gap and dees in valleys. Its cost is about \$700,000 for design and construction; with the vault included, the total would be \$900,000. Other studies have been done on a cyclotron with a superconducting main coil, which would provide a second stage of acceleration for the 88-inch cyclotron. It would increase the heavy-ion mass range from 50 to about 150 at 8 MeV/A or greater. The cost would be about \$3 million.

### 88-INCH CYCLOTRON ION SOURCE DEVELOPMENT

S. Chintalapudi, D. J. Clark, P. E. Frazier,  
W. R. Holley, D. Morris, and M. Renkas

The external heavy-ion PIG source magnet is being used to test improvements which can be incorporated into the internal PIG source. An internal source is mounted on a short shaft to go into the external magnet which provides a magnetic field of about 6 kG.

Testing is in progress on a version of the PIG source with a filament-heated cathode. This provides a controllable power input to one cathode by adjusting the amount of electron bombardment from the filament. With the present bombardment power of up to 500 watts, the arc power can be varied from 50 watts to several kilowatts. This will be useful in the operation of the internal PIG source to provide low power for light ions and high power for heavy ions. With the present internal PIG source with self-heated cathodes, the arc needs at least a kilowatt to stay on, giving too much beam for light ions. An additional advantage of the filament version is that the impedance of the arc is controllable, to optimize heavy-ion output. Also, less gas is required to run the arc, which may produce higher charge states.

Other developments of the PIG source on the test bench include the construction of a

source with coils around the cathodes to adjust the magnetic field along the bore. Using a higher field at the cathodes creates a mirror field which will tend to confine the ions longer and may give higher charge states. A biased source which can give dc extraction at 10 kV in the cyclotron is ready for testing. This has the advantages of more stable extraction conditions, shorter transit time for harmonic operation, and no back bombardment of the arc chamber as in the normal rf extraction.

Improvements in the polarized ion source are also under way. We have aligned the source components more carefully along the beam axis, and are optimizing the geometry of the dissociator-skimmer region by trying various skimmer and nozzle apertures. These changes have increased the beam from 2 to 4  $\mu\text{A}$ , measured as sextupole on-minus-off near the source. Some planning has been done on increasing the pumping speed on the dissociator. The velocity filter after the source is useful in identifying the ions coming from the ionizer. Its transmission was increased to 60% by using balanced voltages on the plates. Further improvement is planned.

A SIMPLE AND EFFICIENT  $^8\text{Be}$  IDENTIFIER

G. J. Wozniak, N. A. Jelley, and Joseph Cerny

The study of reactions yielding  $^8\text{Be}$  nuclei as exit particles is complicated by the fact that due to its short lifetime ( $\sim 10^{-16}\text{sec}$ ),  $^8\text{Be}$  decays promptly and therefore must be detected indirectly by means of its decay  $\alpha$ -particles. The essential difficulty lies in detecting these two  $\alpha$ -particles with high efficiency and at the same time accurately determining the energy and direction of the original  $^8\text{Be}$  event.

Previous methods of detecting  $^8\text{Be}$  nuclei fall into two general categories: those detecting the  $\alpha$ -particles in coincidence in two separate detectors<sup>1,2</sup> and those using a single counter telescope.<sup>3</sup> For both of these methods good detection efficiency can be obtained if the detectors subtend a large solid angle. However, generally this will be at the expense of the  $^8\text{Be}$  energy resolution, since the uncertainty in the angle of the detected  $^8\text{Be}$  events will be large.

In the  $^8\text{Be}$  identifier described below<sup>4</sup> a position-sensitive detector (PSD) is used to determine the direction of the  $^8\text{Be}$  event, thereby optimizing both the detection efficiency and the energy resolution (see Fig. 1a).  $^8\text{Be}$  events are selectively detected by using a divided collimator in conjunction with the PSD, and a transmission detector is placed in front of the PSD to reduce background (Fig. 1b). Since the center-of-mass breakup energy (92 keV) of the two  $\alpha$ -particles is small compared to typical  $^8\text{Be}$  energies of 45 MeV, the two alphas have, to a first approximation, equal energies [ $\Delta E/(E_1 + E_2) \leq 9\%$ ]. One  $\alpha$ -particle therefore gives a signal  $X_1 E/2$ ; the other,  $X_2 E/2$ . The resultant position signal ( $X$ ) obtained by dividing by the energy gives their average position:

$$X = \frac{(X_1 + X_2)}{2},$$

which establishes the original direction of the  $^8\text{Be}$  (see Fig. 1a).

While good efficiency and energy resolution can be obtained with a large PSD, numerous particle-stable nuclei will also be detected and thus obscure  $^8\text{Be}$  events except when these happen to be the most energetic. To avoid this limitation, the high probability that the angular separation of the two breakup  $\alpha$ -particles is close to the maximum value (i. e.,  $\sim 80\%$  of the breakup  $\alpha$ -particles from 45 MeV  $^8\text{Be}$  events are separated by more than  $4.0^\circ$ , while the maximum angular separation is only  $5.2^\circ$ ) can be exploited to selectively detect  $^8\text{Be}$

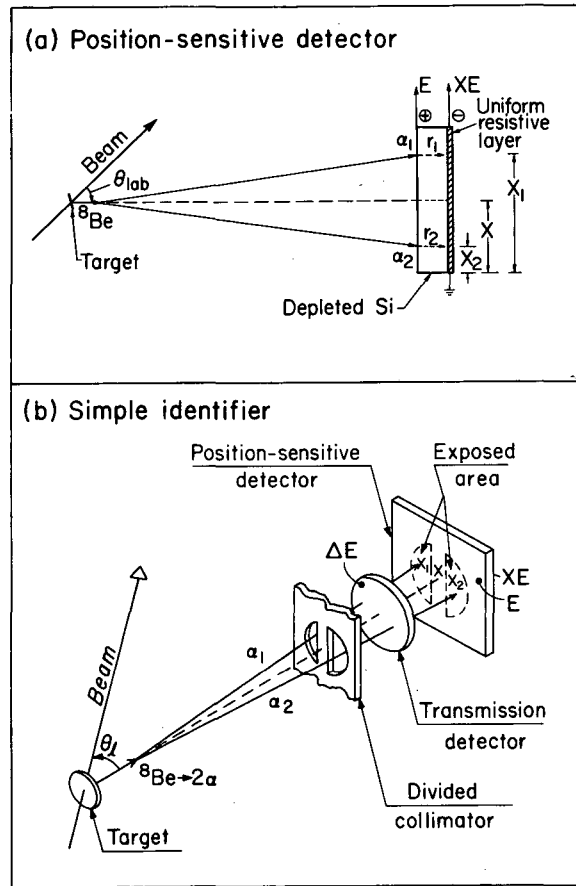


Fig. 1(a). For two similar energy  $\alpha$  particles arriving at the same time, their average position ( $X$ ) as seen by a PSD denotes the laboratory angle at which the parent  $^8\text{Be}$  nucleus was emitted.

(b). The  $^8\text{Be}$  identifier.

(XBL-742-2323)

events while still maintaining a good overall efficiency. Clearly, employing a divided collimator to block out a central strip of the PSD eliminates particle-stable nuclei that are emitted toward the center of the detector, since they are stopped by the post (see Fig. 1b). However, a substantial fraction of the  $^8\text{Be}$  nuclei emitted centrally decay into  $\alpha$ -particles that travel one on either side of the post. These events yield position signals corresponding to the region of the PSD masked by the post, as indicated in Fig. 1b.

Identical position signals may also be generated by the pileup of two particles coming

within the resolution time of the  $^8\text{Be}$  identifier, provided they pass through the divided collimator one on either side of the post. Such pileup events are indistinguishable from  $^8\text{Be}$  events on the basis of position alone. Nearly all of these events are chance coincidences between elastically and inelastically scattered  $\alpha$ -particles, most of which have sufficient energy to traverse the depleted depth of the PSD. However, only a small fraction would be eliminated with a reject detector because most of these events stop in the thick undepleted layer on the back of commercially available position-sensitive detectors. By adding a transmission detector (see Fig. 1b) between the PSD and the divided collimator and performing particle identification (PI) with the  $\Delta E$  and  $E$  signals, one can eliminate most of these pileup events. This is because the approximately equal-energy  $\alpha$ -particles arising from a  $^8\text{Be}$  event identify as a peak in the PI spectrum, while most of the pileup events have PI signals substantially lower in magnitude.

By measuring the detection efficiency for monoenergetic  $^8\text{Be}$  nuclei from the  $^{12}\text{C}(\alpha, ^8\text{Be})^8\text{Be}_{\text{g.s.}}$  reaction with different circular collimators, it can be determined whether the detected  $\alpha$ -particles have the predicted radial distribution across the breakup cone. Figure 2 presents measured efficiency

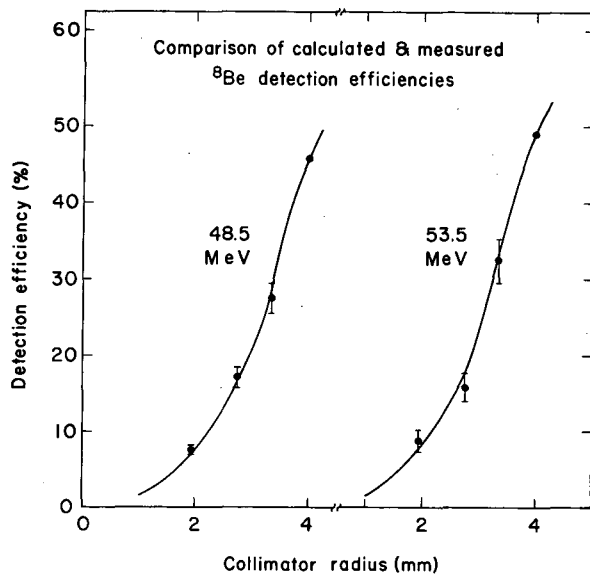


Fig. 2. Determination of the  $\alpha$ - $\alpha$  breakup distribution from the decay of two different energy  $^8\text{Be}$  events. The solid curve is a theoretical calculation of the detection efficiency for circular collimators of varying radius to which the experimental point at  $r = 4\text{ mm}$  is normalized. The error bars shown contain both a statistical and a background subtraction error. (XBL-742-2316)

points versus calculated ones<sup>5</sup> for a series of collimator sizes with a one-degree position gate. Excellent agreement is obtained between the experimental and calculated values at two different  $^8\text{Be}$  energies.

The kinematic focusing of the breakup  $\alpha$ -particles following the decay of an  $\sim 45\text{ MeV}$   $^8\text{Be}$  event causes the  $\alpha$ -particles to be confined to a cone subtending an angle of  $\sim 5.2^\circ$ . To establish this kinematic focusing we used two divided collimators of equal open area having post widths of  $6^\circ$  and  $3^\circ$ , respectively. The wider post blocks out  $^8\text{Be}$  events, as can be seen in Fig. 3a, while the narrower post allows  $^8\text{Be}$  events to be detected (Fig. 3b), confirming the kinematic focusing of the  $\alpha$ -particles.

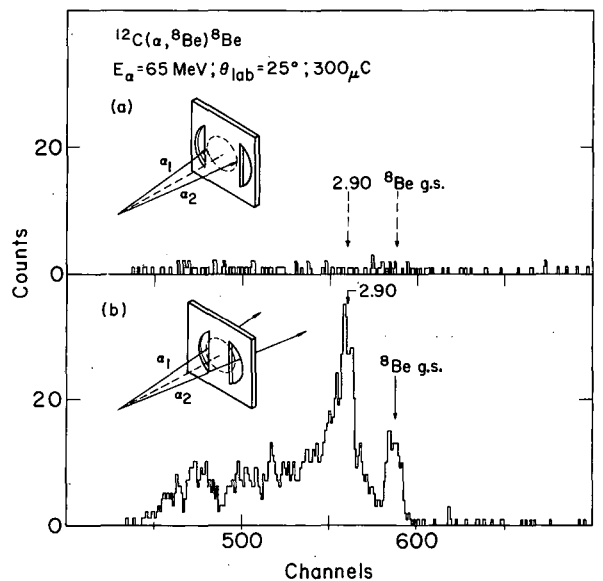


Fig. 3. In a test of the kinematic focusing of the breakup  $\alpha$  particles the above energy spectra were observed from the  $^{12}\text{C}(\alpha, ^8\text{Be})^8\text{Be}$  reaction at  $E(\alpha) = 65\text{ MeV}$  and  $\theta_{\text{lab}} = 25^\circ$  using the collimators (whose size relative to that of the breakup cone is shown) depicted in the respective inserts. (XBL-7311-4591)

The elimination of particle-stable nuclei can be observed in the appropriate position spectrum of Fig. 4a. The upper curve results from placing a circular collimator in front of the PSD, while the lower was generated with a divided collimator of the same dimensions. The counts in the central region of the lower spectrum arise from  $^8\text{Be}$  events and  $\alpha$ - $\alpha$  chance coincidences. In Fig. 4b are shown PI spectra gated by the position gate indicated in Fig. 4a. The upper spectrum in Fig. 4b taken with a circular collimator and

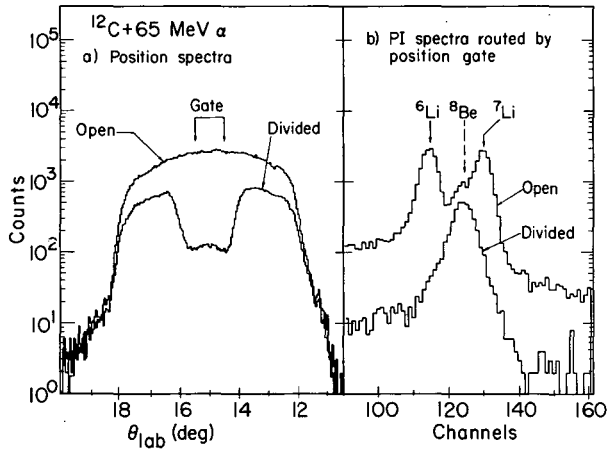


Fig. 4(a). Position spectra taken with an open and a divided circular collimator.  
 (b). Corresponding PI spectra gated by the 1° position gate shown in part (a).

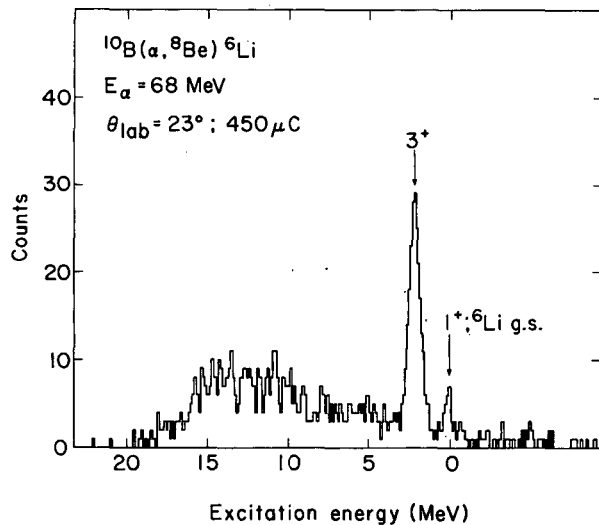


Fig. 5. An energy spectrum of the  $^{10}\text{B}(\alpha, ^8\text{Be})^6\text{Li}$  reaction. (XBL-742-2317)

no post is dominated by the particle-stable nuclei  $^6\text{Li}$  and  $^7\text{Li}$ , while the relatively abundant  $^8\text{Be}$  events are seen as a shoulder on the  $^7\text{Li}$  peak. The lower spectrum taken with the divided collimator, is characterized by the

absence of  $^6\text{Li}$  and  $^7\text{Li}$  events and the lone  $^8\text{Be}$  peak which occurs at the position predicted from range-energy calculations.<sup>3</sup> Background events seen above and below the  $^8\text{Be}$  PI peak correspond to  $\alpha$ - $\alpha$  chance coincident events which are nearly all eliminated from the energy spectrum by setting a PI gate.

In studying the  $(\alpha, ^8\text{Be})$  reaction on light targets, a 190- $\mu$   $\Delta E$  (10-mm diameter) detector and a 300- $\mu$  E(PSD) (10 $\times$ 50 mm) were used. An energy spectrum taken in less than one hour with this simple identifier is shown in Fig. 5. Transitions are seen from the  $^{10}\text{B}(\alpha, ^8\text{Be})^6\text{Li}$  reaction populating the ground and first-excited states of  $^6\text{Li}$  with cross sections of 2  $\mu\text{b}/\text{sr}$  and 17  $\mu\text{b}/\text{sr}$ , respectively, and an experimental resolution of  $\sim 700$  keV. The main contribution to this resolution is the kinematic broadening from the one-degree position gate. The level of counts above the  $^6\text{Li}_{\text{g.s.}}$  is due to  $\alpha$ - $\alpha$  chance-coincident events that fall within the  $^8\text{Be}$  PI gate and is indicative of the low background contribution to spectra that is possible with this simple identifier.

Additional energy spectra taken with the above  $^8\text{Be}$  identifier are discussed in the Nuclear Reactions and Scattering section of this annual report.

#### References

1. R.E. Brown, J.S. Blair, D. Bodansky, N. Cue, and C.D. Kavaloski, *Phys. Rev.* **138**, B1394 (1965).
2. J.G. Cramer, K.A. Eberhard, N.R. Fletcher, E. Mathiak, H.H. Rossner, and A. Weidinger, *Nucl. Instrum. Methods* **111**, 425 (1973) and references therein.
3. G.J. Wozniak, H.L. Harney, K.H. Wilcox, and J. Cerny. *Phys. Rev. Lett.* **28**, 1278 (1972). A. Menchaca-Rocha, *Nucl. Instrum. Methods* **114**, 425 (1974).
4. G.J. Wozniak, N.A. Jelley, and J. Cerny, *Phys. Rev. Lett.* **31**, 607 (1973).

5. Efficiency calculations for both circular and rectangular collimators (with or without a post) were done with the FORTRAN program EFFICR. This program is available from the authors on request.



## SUPERHILAC OPERATIONS

R. M. Main

The debugging of the SuperHILAC system continued, with intermittent operation, during the first three months of the year. During this period the linacs (rf cavities, rf system and control, 10-MW primary power supply, drift tube quadrupoles and their power supplies, vacuum system, etc.) operated with a performance exceeding the original specification and with an overall operational efficiency approaching 90%. Difficulties were experienced in keeping the injectors running smoothly during this period, with the result that the SuperHILAC system efficiency was reduced to 45%.

In October the accelerator was shut down for 3- $\frac{1}{2}$  weeks, during which time modifications and additions were made to the primary power supply and its control, and the amplifier-driver equipment and its control were added to the 8th rf cavity (to increase the maximum energy from 7.2 to 8.5 MeV/A).

Neutron shielding was added to the cave system to provide for a beam dump at the entrance to the Bevalac transport line and the three elements necessary for injection of the HILAC beam into the transport line.

These modifications completed the Phase I of the HILAC portion of the Bevalac project.

Also during this shutdown minor modifications were made to the heavy-ion injector (ADAM), particularly the ion source electronics, the telemetry, and the terminal vacuum equipment. As a result of this work, the system returned to operation (after a period of debugging) with an operating efficiency increased to 70% in December and January.

A realignment of the linac drift tube quadrupoles was also carried out. Precise measurements with the taut pulse wire alignment technique indicated that the original alignment was relatively poor and that the cavities warped and settled subsequent to the alignment. These measurements also indicated that, without vacuum loading and rf heating,

the quadrupoles can be aligned to within 0.001 in rms of the wire-defined axis. The gross misalignments were corrected during the shutdown; precise alignment of the entire system will be carried out later. As a result of this work the problem of tuning through the linacs, particularly the multiple-cavity post-stripper linac, became more tractable.

The system has operated to provide beams of both light (EVE 750-kV injector) and heavy ions (ADAM injector) with a time ratio of about 1:3. The ADAM injector, which has operated at full voltage (2.5 MV) for extended periods, has been restricted in operating to 1.7 MV by internal sparking, the origin of which has not been determined. At present, this restriction is not severe with regard to the research program, and the correction of the problem has been delayed in the interest of continued operation. Beams of carbon, nitrogen, neon, argon, vanadium, iron, and krypton have been accelerated, in intensities ranging from 20  $\mu$ A (particle) for carbon to 0.001  $\mu$ A for vanadium and iron. Krypton has been accelerated with a maximum intensity of 0.5  $\mu$ A.

The design and fabrication of the pulsed magnets and pulsed power supplies, necessary for the Bevalac Phase II program (SuperHILAC time share) continued during the year, with power tests commencing in February 1974. Magnets for the transport of the high-intensity beams into the chemistry cave were also designed and fabricated.

A second shutdown (3-4 weeks) is planned for May 1974 during which time these magnets and power supplies will be installed. After debugging, a limited time-share (single ion) of the beam between the Bevatron and HILAC users will be possible.

During this shutdown the linac quadrupole alignment will be completed, the ADAM high voltage generator will be repaired, and beam monitoring equipment will be installed at numerous points along the accelerator.

## IMPROVEMENTS TO RESISTIVE-WIRE FOCAL PLANE DETECTOR

H. Homeyer,\* J. Mahoney, and B. G. Harvey

Experience with the focal plane detector system<sup>1</sup> that is used in the spectrometer at the 88-inch cyclotron showed that improvement was needed in the identification of heavy-ion nuclear reactions products. In the system previously described, time-of-flight (TOF) of particles through the spectrometer was measured by a plastic scintillator in the focal plane with respect to the cyclotron radio frequency (rf). Time resolution was about 6 nsec, rather marginal for the separation of adjacent masses for heavy ion of mass  $\approx 20$ .

Timing from the cyclotron rf was therefore replaced by a time-zero signal from a thin ( $30\text{--}50\ \mu\text{g}/\text{cm}^2$  for  $^{16}\text{O}$  ions) NE III plastic scintillator foil<sup>2</sup> placed between the target and the entrance slits of the spectrometer. Light flashes from the foil are detected by two RCA 8850 photomultipliers. The foil, mounted on a Lucite frame, is inserted into a bi-conical Lucite light guide as shown in Fig. 1. The summed output of the two photomultipliers is

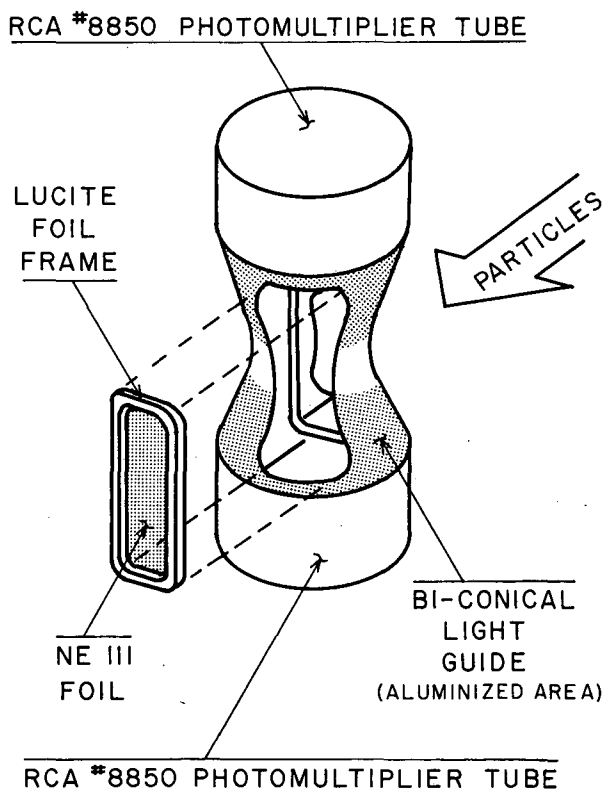


Fig. 1. Thin foil time-zero detector system. (XBL-7310-1270)

independent of the position of the detected particle along the 5-cm vertical dimension of the foil. Since the foil count rate is always much higher than that of the focal plane system, its output, suitably delayed, is used as the stop signal for the time-to-amplitude converter. The foil is highly sensitive to electrons coming from the target. They are removed by a parallel-plate electrostatic deflector 12-cm long with a field of 2 kV/cm.

The efficiency of a foil of  $170\ \mu\text{g}/\text{cm}^2$  was found to be 98% for detection of elastically scattered 86-MeV  $^{11}\text{B}$  ions. For 42-MeV protons, a foil of  $5\ \text{mg}/\text{cm}^2$  was 100% efficient, and probably thicker than necessary. The time resolution of the system is 1.2 nsec (FWHM) with the spectrometer slits opened radially to a width of 2 mm.

In the system previously described, both position and  $dE/dx$  (the energy loss of a particle) were measured in a 1-cm-deep resistive wire proportional counter. The  $dE/dx$  resolution ( $\sim 10\%$  for 104-MeV  $^{16}\text{O}$  at a counter gas pressure of  $1/3$  atm) was limited by energy-loss straggling. The resolution could have been improved by the use of a higher gas pressure to increase the energy loss, but then a thicker entrance window would have been required. This would worsen the position resolution by increasing the multiple scattering, and would limit the lowest detectable energy for heavy ions. The energy loss, and resolution, were therefore increased by installing a 4 cm-deep proportional counter between the position-sensitive counter and the focal plane plastic scintillator. It has the same number of wires—five, 1.5 cm apart—as the front counter. They are 25- $\mu\text{m}$ -diam nickel. The central three wires of the second counter are connected together and ac coupled to an external charge-sensitive preamplifier. The outer two wires, kept at the same potential as the others, serve only as guard wires. The relative gas multiplications of the two counters can be adjusted by applying a separate positive or negative bias to the Ni wires. The counters are operated (for detection of  $^{16}\text{O}$  ions) at gas multiplications of about 100 and 10, respectively.

The energy loss in the second counter is at least four times greater than in the first, and as expected, the  $dE/dx$  resolution is a factor of 2 better: 5% FWHM for 104-MeV  $^{16}\text{O}$  ions. The resolution in atomic number  $z$  is therefore about 2-1/2% (since  $dE/dx \propto Z^2$ ).

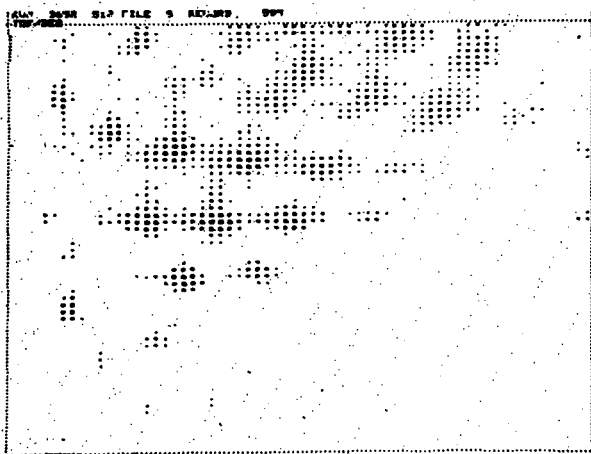


Fig. 2. TOF vs  $(dE/dx)_2$  for 86-MeV  $^{11}\text{B}$  ions on  $^{24}\text{Mg}$  at  $11^\circ$  lab angle. (XBL 744-2896)

The fourfold coincidence requirement (T = 0 foil, position counter,  $dE/dx$  counter, plastic scintillator) greatly reduces the system background count rate. In a study of the reaction  $^{208}\text{Pb}(^{20}\text{Ne}, \alpha)^{224}\text{Th}$ , no  $\alpha$ -parti-

cles were detected in the first 10 MeV of excitation of  $^{224}\text{Th}$ . A single event would have corresponded to a cross section of only 70 nb/msr. The system gave extremely low backgrounds (virtually zero), even for the detection of 42-MeV protons. At the high gas multiplications required in this test, the individual proportional counters were detecting high count rates of neutrons and photons.

In a study of the reaction  $^{24}\text{Mg}(^{11}\text{B}, ^8\text{B})^{27}\text{Mg}$ , a few  $^8\text{B}$  events were detected in the presence of heavy ions ranging from Li to F isotopes. Figure 2 shows a two-dimensional plot of TOF vs  $dE/dx$  in which a very large number of individual nuclear species are clearly resolved.

#### Footnote and References

\*Permanent address: Hahn-Meitner, Institut, Berlin.

1. B.G. Harvey et al., Nucl. Instr. Methods 104, 21 (1972).
2. L. Muga et al., Nucl. Instr. Methods 105, 61 (1972).

### CONSIDERATIONS OF BEAM QUALITY REQUIREMENTS FOR EXPERIMENTS WITH VERY HEAVY IONS\*

J. R. Alonso

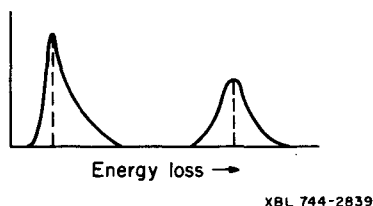
Now that the acceleration of very heavy ions has become a technological reality, experimentalists are beginning to request beams of the highest quality with regard to energy dispersion and emittance. Many experiments require high-quality beams, such as inelastic scattering, resonance, or accurate Q-value measurements. In some instances resolutions of the order of 0.01% have been obtained for experiments with protons, and it is reasonable to ask whether similar resolution figures are attainable with heavy-ion projectiles. The answer is that even if the accelerators could provide beams of such high quality the energy and angular dispersion produced by the target would limit the experimental resolution to many times the above figure. In the following paragraphs we discuss these dispersive effects.

1. Target uniformity. It is very difficult to obtain and maintain better than a few percent overall target thickness variation for thin targets. Since the total energy lost in passing through a target is proportional to the amount of matter the beam traverses, a non-uniformly thick target contributes to a beam energy dispersion that destroys an initially

good resolution. The best thin targets are usually produced by vacuum evaporation, and are subject to nonuniformities on both a macroscopic and a microscopic scale. Macroscopic variations can be controlled by very careful experimental arrangement: proper substrate orientation, large distances between substrate and even, etc. Overall variations can be controlled to about 1 or 2%. However, microscopic variations in the target due, for example, to clustering effects on the surface, are not so easily controlled. Such microscopic variations are probably of no consequence for targets thicker than a few hundred micrograms per square centimeter, but a variation of a few tens of atomic layers represents a large uncertainty in the thickness of a  $50\text{-}\mu\text{g}/\text{cm}^2$  thick film of gold. For example, a surface irregularity of 20 atoms ( $= 10\mu\text{g}/\text{cm}^2$ ) can contribute an energy uncertainty  $\Delta E/E$  of about 0.04% for beams heavier than argon.

2. Energy Straggling. As it traverses the target material a projectile normally undergoes many collisions with electrons in the target. Each collision slightly changes the projectile energy. The statistical nature of

the collision process results in a distribution function for energy loss in the target. Energy straggling is defined to be the full width at half maximum of this distribution function. The shape of the distribution function depends on the total energy lost. The diagram below demonstrates how for low-energy losses the distribution is asymmetric (Landau distribution), but as more energy is lost a symmetric Gaussian shape develops. For intermediate energy losses, Vavilov<sup>1</sup> has given a solution for the distribution functions, tables of which have been compiled by Seltzer and Berger.<sup>2</sup>



Estimates of the energy straggling for various beams through gold targets have been made from the full width at half maximum of these Vavilov distributions. (For details of the calculation, see the Appendix in LBL-1698.)

Figure 1 shows these estimates for energy straggling in terms of  $\Delta E/E$  of 5-MeV/nucleon beams as a function of gold thickness. Normally, targets thinner than  $50 \mu\text{g}/\text{cm}^2$  are not self-supporting, so the dotted lines show the combined effect of straggling through gold deposited on a  $10 \mu\text{g}/\text{cm}^2$  carbon backing.

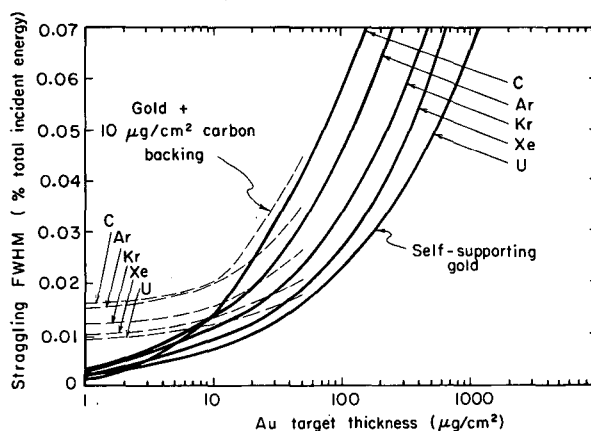


Fig. 1. Energy straggling of heavy-ion beams at 5.0-MeV/A energy through gold targets. Straggling is given in terms of the spread in energy as a percentage of the total incident energy. Dashed lines correspond to thin gold targets mounted on a carbon backing  $10 \mu\text{g}/\text{cm}^2$  thick. (XBL-733-2449)

Figure 1 appears to imply that the heavier ions are less affected by energy straggling, but in terms of actual energy dispersion in keV, heavier ions in fact suffer considerably greater energy spreading. This  $\Delta E$ , however, is a smaller fraction of the total incident energy and therefore  $\Delta E/E$  decreases. It is observed in Fig. 1 that resolutions better than 0.01% are not achievable for a solid target experiment but that straggling effects can be controlled for physically realizable targets if one relaxes the resolution requirement to 0.03%.

Table I. Maximum gold target thickness ( $\mu\text{g}/\text{cm}^2$ ) to keep energy dispersive effects to within 0.03%. (The numbers in columns A and B give the contributions only from the effect named at the top of the column.)

Beam	A Straggling	B Multiple scattering at $\theta_{\text{lab}} = 20^\circ$		Greatest possible thickness, considering both A and B	
		Au	Au + backing	Solid target	Gaseous target
		C	22	3800	3800
Ar	35	340	340	35	45
Kr	80	63	55	30	40
Xe	125	21	15	10	21
U	170	4	-- <sup>a</sup>	--	4

<sup>a</sup> Best possible resolution for solid target is  $5 \times 10^{-4}$ , for zero gold thickness (caused entirely by scattering in carbon backing).

Column 1 of Table I summarizes the maximum thickness of target possible to keep the resolution to 0.03%. For the carbon and argon experiments, the targets are assumed to be mounted on a carbon backing.

3. **Multiple Scattering.** A beam passing through a target experiences angular spreading due to many small-angle Rutherford scattering events. If one large-angle scattering event occurs within the target, the angle of scattering will be uncertain by the contribution of multiple scattering before and after the event of interest. Since the energy loss of the projectile to the recoiling target nucleus (kinematic shift) is a sensitive function of scattering angle, the angular uncertainty caused by multiple scattering will limit the accuracy possible in an experiment. Column 2 of Table I gives the maximum target thickness that keeps kinematic broadening due to multiple scattering to less than  $3 \times 10^{-4}$  of the incident energy. The total mean scattering angle (calculated from the formula derived by Jackson<sup>3</sup>) varies relatively slowly for different beams, from 0.1 mrad/ $(\mu\text{g}/\text{cm}^2)^{1/2}$  for a carbon beam to around 0.2 mrad/ $(\mu\text{g}/\text{cm}^2)^{1/2}$  for a uranium beam; however, kinematic shifts are much more important for heavier beams, so the energy uncertainty becomes more pronounced as the beam charge increases.

Kinematic shifts due to finite acceptance angle can be compensated for by properly designed spectrometers because of the correla-

tion between the total scattering angle and the energy of the particle. Multiple scattering, however, washes out this correlation, so that resolution can only be maintained by reducing the amount of target material.

4. **Beam Heating.** Because of the higher  $(dE/dx)$  values for heavier ions, target heating can be a serious problem. It is important to keep targets at temperatures well below the melting point, since the vapor pressure for most materials becomes substantial near this point and considerable target evaporation can occur. Also, thermal expansion causes sagging and wrinkling, leading to nonuniformities. For the experiments with gold, the temperature should be kept at less than 500°C to preserve an adequate margin of safety. For thick targets conduction cooling is more important than radiation cooling in this temperature range. However, for gold targets thinner than 100  $\mu\text{g}/\text{cm}^2$ , the cross-sectional area available to conduct away the heat is so small that surface radiation is the dominant mode of target cooling.

A useful computer program has been written by J. O. Liljenzin<sup>4</sup> to evaluate the equilibrium temperature at any point of an arbitrarily shaped target for any beam distribution and duty cycle. This program has been utilized to determine the maximum beam current which can be passed through a target to maintain the temperature at 500°C. For these calculations, it is assumed that the target is

Table II. Gold target thicknesses and corresponding maximum beam currents for experiments with best attainable resolutions from 0.01% to 0.07%. (Note that unless otherwise specified the targets are mounted on a 10- $\mu\text{g}/\text{cm}^2$  carbon backing.)

Beam	0.015%		0.03%		0.05%		0.07%	
	Thick- ness ( $\mu\text{g}/\text{cm}^2$ )	Max. beam (pna) <sup>a</sup>	Thick- ness ( $\mu\text{g}/\text{cm}^2$ )	Max. beam (pna)	Thick- ness ( $\mu\text{g}/\text{cm}^2$ )	Max. beam (pna)	Thick- ness ( $\mu\text{g}/\text{cm}^2$ )	Max. beam (pna)
C	0.4	7000	22	4000	65	2400 (1000) <sup>b</sup>	150	1650 (420) <sup>b</sup>
Ar	1.1	1000	35	600	100	320 (100) <sup>b</sup>	220	230 (50) <sup>b</sup>
Kr	1.0	430	30	230	100	130	220	90
Xe	--	--	10	220	45	130	100	75
U	--	--	--	--	6.4 <sup>c</sup>	115 <sup>c</sup>	12	100

<sup>a</sup> Particle nanoamperes.

<sup>b</sup> Beam corresponding to targets without carbon backings. (Note that carbon serves as an efficient radiator when it is not required for target support.)

<sup>c</sup> Figures represent 0.06% resolution for uranium.

0.5 cm diameter with water-cooled edges, the beam is uniformly spread out over the target, and the macroscopic duty cycle is 100%, the beam currents calculated correspond approximately to the maximum peak currents allowed.

The calculated beam currents are summarized in Table II for target thicknesses corresponding to experiments performed at resolutions from 0.015% to 0.07%. Since the radiating surface area is a constant, targets can radiate a constant amount of power and thus for very thin targets, where the total energy loss per beam particle is small, very large beams can be used for the experiment.

As the target thickness is increased, though, the beam currents must be reduced to keep down the total power deposited in the target. Pure gold is a very poor radiator, having only 3% of the theoretical black body efficiency, whereas the efficiency of amorphous carbon approaches 90% of that of a pure black body. Thus for targets deposited on a carbon backing, almost all of the heat is dissipated through the backing. In fact, it is worthwhile even for very thick targets to place a thin layer of carbon on the surface to serve as a heat dissipator.

The numbers in Table II show that the sensitivity of an experiment is limited not only by the thickness of the target which can be employed, but also by the thermal effects of the beam in the target. In particular, as the projectile mass increases, the maximum allowable-beam intensity drops drastically, by a factor of about 20 between carbon and the heavier ions.

Combining the maximum beam currents and greatest target thicknesses, estimates can be made for counting rates in a realistic experiment. These estimates are shown in Fig. 2 for an experiment utilizing a modern particle spectrometer of opening angle  $\sim 2$  milliradians, assuming the cross section of the desired event to be 1 millibarn/steradian. It is seen that experiments become progressively more difficult for the heavier beam. Under the best conditions, experiments with uranium beams will have counting rates about 200 times below the corresponding experiments with carbon beams.

All these considerations indicate that very-high-resolution experiments with heavy-ion beams will be very difficult to perform, so that future directions in heavy-ion experiments will probably have to be in areas where the utmost in resolution is not necessary. Fortunately, high-resolution experiments form a relatively small subset of the new areas opened up for study by heavy ions, so that the restric-

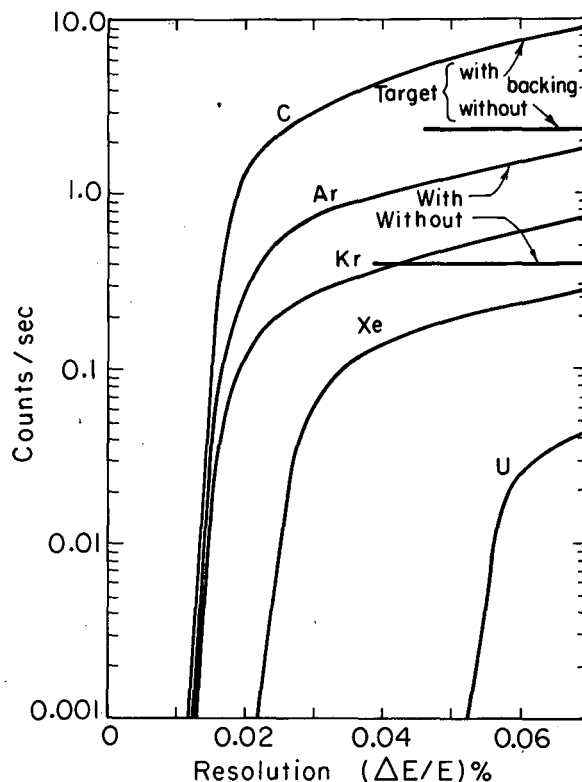


Fig. 2. Sensitivity for heavy-ion experiments, as a function of experimental resolution, given as the counts per second recorded in a spectrometer with a 2 milliradian opening angle ( $d\sigma/d\Omega \approx 1$  mb/sr). The count rates are proportional to the product of the beam currents and target thicknesses given in Table II. All targets are assumed to be mounted on a carbon backing. Count rates for carbon and argon experiments with thick targets without carbon backings are also shown. It is seen that carbon acts as a good heat radiator so that greater beam intensities can be used.

(XBL-734-2727)

tions brought out in this report do not significantly diminish the excitement and promise of heavy-ion physics.

#### Footnote and References

\* This report is a condensation of LBL-1698. Considerations of Beam Quality Requirements for Experiments with Very Heavy Ions, J. R. Alonso and B. G. Harvey, May 1973.

1. P. V. Vavilov, Sov. Phys. -JETP 5, 749 (1957).
2. S. M. Seltzer, M. J. Berger, Chapter 9, in Studies in Penetration of Charged Particles in Matter, NAS-NRC publication 1133 (1964).

3. J. D. Jackson, *Classical Electrodynamics* (Wiley, New York, 1963), p. 458.

4. J. O. Liljenzin, *The Temperature of Thin Foils in Ion Beams*, LBL-1912 (June 1973).

### THE TEMPERATURE OF THIN FOILS IN ION BEAMS\*

J. O. Liljenzin<sup>†</sup>

Thin foils are used in ion beams for stripping of the ions, degradation of beam energy, as vacuum seals, and as beam-transparent targets. Composite materials as well as single elements are used for making such foils.

When the beam passes through the foil it loses part of its energy by interaction with the atoms in the foil. The major part of this

energy is released as heat, which must be removed to prevent the target from melting or evaporating (see Fig. 1). Only in cases where the foil temperature can be kept sufficiently low is it of interest to consider other destructive mechanisms, such as radiation damage, sputtering, etc.

The flow of heat in a piece of solid material

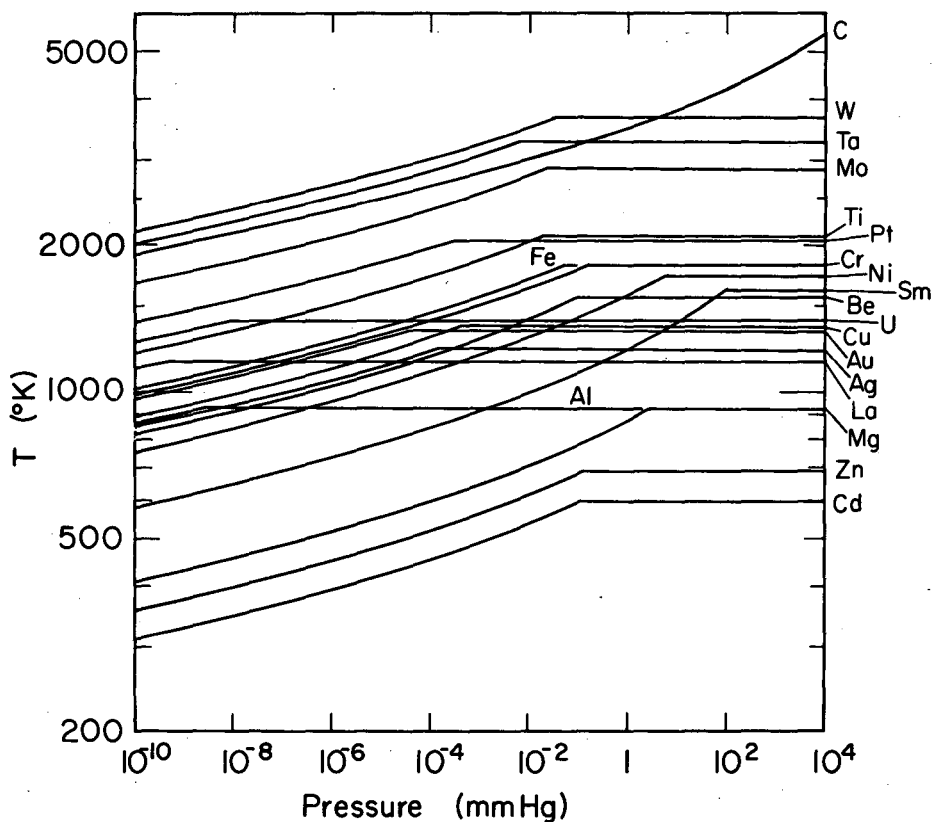


Fig. 1. Temperature limits for material as a function of pressure. At high pressure the limit is set by the melting point and at low pressure by the vapor pressure.

(XBL736-3120)

exchanging heat with its surroundings is described by the following differential equation:

$$dV \left[ \underbrace{\frac{ng\sigma}{dz} (T^4 - T_s^4)}_{\text{heat radiation}} - \underbrace{\frac{d(\lambda \frac{dT}{dx})}{dx} - \frac{d(\lambda \frac{dT}{dy})}{dy} - \frac{d(\lambda \frac{dT}{dz})}{dz}}_{\text{heat conduction}} \right] \quad (1)$$

$$+ \underbrace{\frac{nh}{dz} (T - T_f)}_{\text{heat convection}} \left. \right] = \underbrace{P}_{\text{power input}} - \underbrace{dV \cdot \rho \cdot C_p \cdot \frac{dT}{dt}}_{\text{heat storage}}$$

- $g = G(x,y,z,T)$ ; greyness factor; depends on material, surface structure, and temperature
- $\lambda = L(x,y,z,T)$ ; heat conductivity; depends on material, geometry, and temperature
- $h = H(x,y,x,w,T,T_f)$ ; film coefficient; depends on material, geometry, surface structure, velocity, and temperature
- $p = P(x,y,z,t)$ ; power input; depends on material, geometry, ion, beam energy, beam current, and time
- $\rho C_p = C(x,y,z,T)$ ; storage capacity; depends on material and temperature
- $n = N(x,y,z)$ ; surface count; depends on geometry

$dV = dx \, dy \, dz.$

The first term describes the exchange of heat radiation with the surroundings, the second term describes the flow of heat by conduction, the third term gives the flow of heat by movements in an external medium.

The exchange of heat with the surroundings is balanced by the rate of heat generation and the changes in stored heat. To describe the behavior of physical systems with this equation it is in general necessary to introduce terms which compensate for deviations from the idealized behavior. These terms are normally included in the "constants." These become, then, functions of geometry, space coordinates, time, and temperature. It is then usually not possible to obtain analytical solutions to Eq. (1). The approach can then be along different lines, such as neglect of minor modes of heat transport followed by analytical or numerical solution, or complete numerical evaluation of special cases. Both kinds of approach have been followed in this work. By specializing Eq. (1) to cases of pure radioactive cooling and pure conductive cooling, it was possible to give the solution as monographs, one for each case (see Figs. 2 and 3).

For the second approach a computer program was developed, which uses a three-di-

mensional grid system. For each element of the grid the "constants" in Eq. (1) are represented by different polynomial approximations [see Eq. (2)]. Geometrical descriptions are also given for each grid point. These give the connections to adjacent points and the areas exposed to radiative or conductive heat exchange.

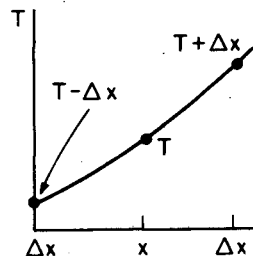
$$-\Delta VL \frac{\Delta^2 T}{\Delta x^2} - \Delta VL \frac{\Delta^2 T}{\Delta y^2} - \Delta VL \frac{\Delta^2 T}{\Delta z^2} = P - \Delta VC \frac{\Delta T}{\Delta t}$$

$$- \Delta V \frac{NG\sigma}{\Delta z} (T^4 - T_s^4) - \frac{NH}{\Delta z} (T - T_f) = Q$$

Assume  $T = a + bx + cx^2$

then  $\frac{\Delta T}{\Delta x} = \frac{T_{\Delta x} - T_{-\Delta x}}{2\Delta x}$

and  $\frac{\Delta^2 T}{\Delta x^2} = \frac{T_{\Delta x} - 2T + T_{-\Delta x}}{(\Delta x)^2}$



XBL 744-2840

$$-\frac{\Delta VL}{\Delta x^2} T_{\Delta x} + \frac{2\Delta VL}{\Delta x^2} T - \frac{\Delta VL}{\Delta x^2} T_{-\Delta x} - \frac{\Delta VL}{\Delta y^2} T_{\Delta y}$$

$$+ \frac{2\Delta VL}{\Delta y^2} T - \frac{\Delta VL}{\Delta y^2} T_{-\Delta y} - \frac{\Delta VL}{\Delta z^2} T_{\Delta z} + \frac{2\Delta VL}{\Delta z^2} T$$

$$- \frac{\Delta VL}{\Delta z^2} T_{-\Delta z} = Q.$$

The absolute value of the underlined terms are together two times larger than any single other term. Hence a Siedel iteration should converge. Compute L, C, etc. for previous value of T. Time dependence can be evaluated by stepping  $\Delta t$  and using the relation  $p = \Phi(t)\Delta t$ .

With this program several cooling methods were studied. The effect of various beam intensity profiles was also investigated. Figure 4 shows a case where a thin foil is hit by a heavy-ion beam with a beam profile given by  $i(r) = k \cdot e^{-(r-F)^2}$ , where  $i$  is the current density and  $r$  is the distance from the center of the foil.

Some general conclusions can be drawn: When a foil is extremely thin with vacuum on both surfaces it is cooled by radiation; then





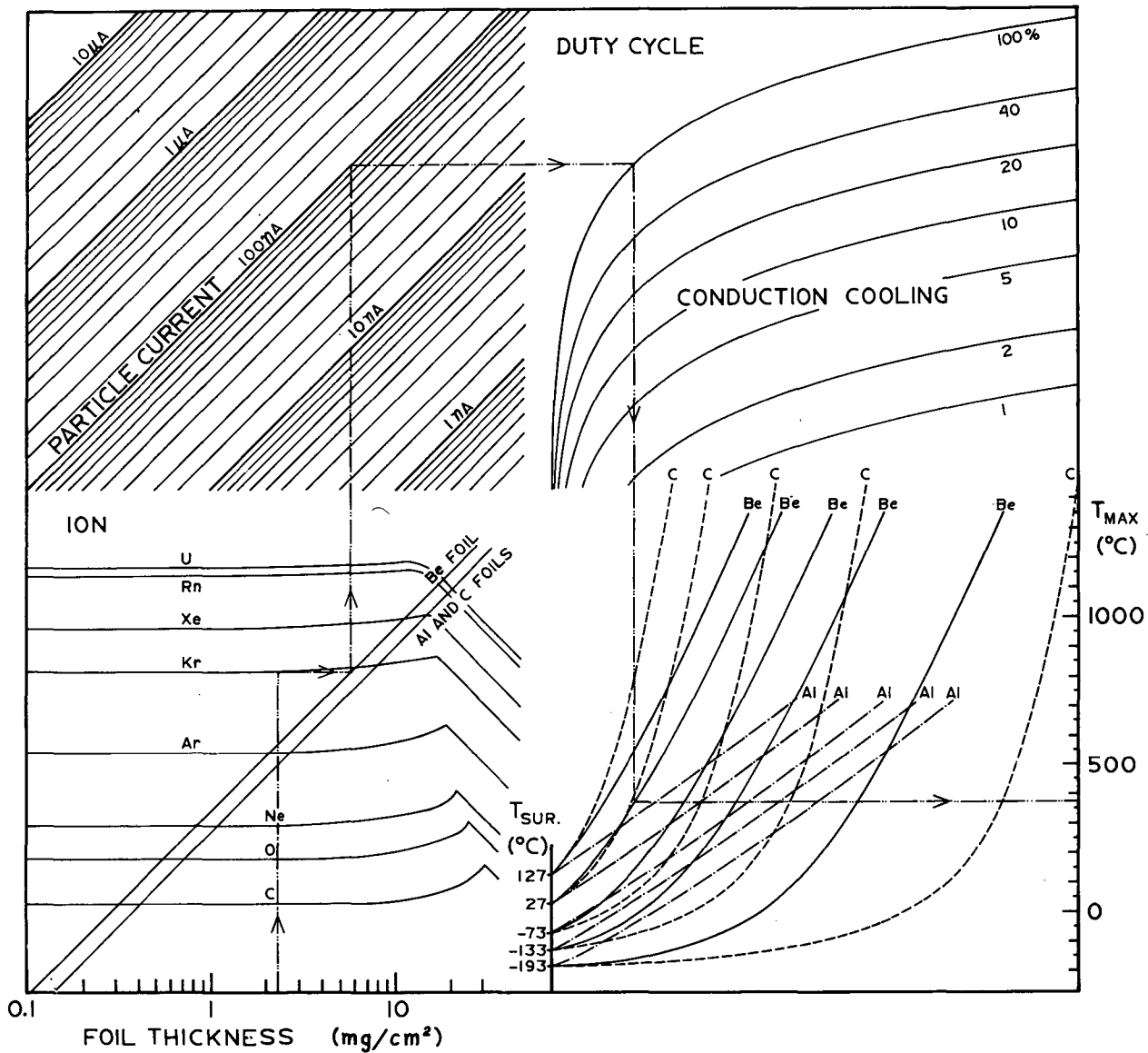


Fig. 3. Nomograph for the evaluation of foil temperatures at 7.5-MeV/amu incident beam energy, uniform beam shape, and pure conduction cooling. A first-order correction for Gaussian beam shape can be made as follows. First obtain the correction factor  $\psi/\alpha$ , then read off the temperature for uniform beam shape, subtract  $T_{\text{sur}}$ , multiply the remainder by  $\psi/\alpha$  and add  $T_{\text{sur}}$  again. The nomograph is constructed for beryllium, aluminum, and carbon foils and consists of four quadrants. In the first quadrant the power per unit thickness and current is evaluated from the foil thickness, ion beam, and foil material. This is converted in the second quadrant to power

per unit thickness by multiplication with the beam current. The third quadrant involves mainly a change of scale from logarithmic to linear but it also corrects for the duty cycle. The curves are to be used for foils where the foil diameter (cm) is smaller than  $\sqrt{0.05 c \lambda / f \rho C_p}$ , where  $c$  is the duty cycle (percent),  $\lambda$  is the heat conductivity (W/cm degree),  $f$  is the beam pulse frequency (Hz),  $\rho$  is the density ( $\text{g}/\text{cm}^3$ ), and  $C_p$  is the heat capacity ( $\text{J}/\text{cm}^3$  degree). In the fourth quadrant the maximum temperature is evaluated from the edge temperature and material.

(XBL735-680)

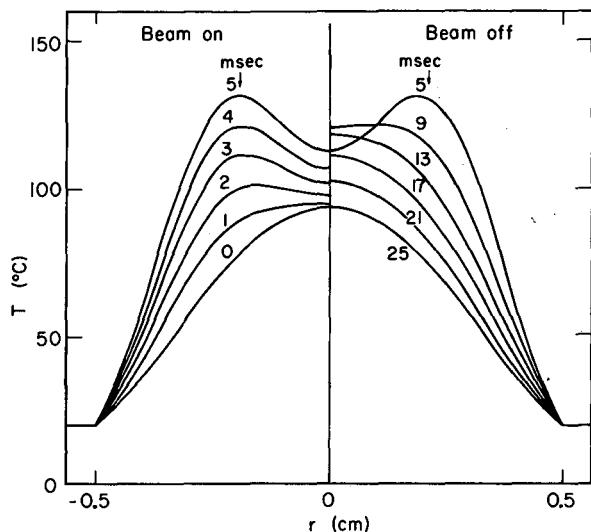


Fig. 4.  $\frac{1}{2}$ -mil, 1-cm-diameter gold foil in a pulsed double-Gaussian beam at a total dissipated power of 4W, a frequency of 40Hz, and a duty cycle of 20%. (XBL736-3119)

#### Acknowledgment

The author is indebted to Prof. G. T. Seaborg, Drs. J. Alonso, A. Ghiorso, J. V. Kratz, and M. Nurmia for encouraging and helpful discussions, and to the Swedish Atomic Research Council for economic support.

#### Footnotes

\* Condensed from LBL-1912.

† Department of Nuclear Chemistry, Chalmers University of Technology, Göteborg, Sweden.

### DEVELOPMENT OF A RECOIL ATOM MASS ANALYZER (RAMA)

R. A. Gough, D. Littlejohn, and J. Cerny

Studies of neutron-deficient nuclei become more and more difficult the further one explores from the line of  $\beta$ -stability. This situation arises due to the lower cross sections for production of nuclei with increasing proton imbalance. The application of presently available experimental techniques to this problem has thus far been frustrated by low yields amidst formidable background problems. We describe here an approach to solving these experimental difficulties and can now report significant progress toward achieving this goal.

Exotic, neutron-deficient nuclei can be produced by light- or heavy-ion bombardment, using the 88-inch cyclotron. These nuclei can be most fruitfully studied by characterizing their decay properties. To do this effectively, one must rapidly separate the activity from the bombardment area and quickly transport it to a background-free environment. This we have done using a He-jet system.<sup>1,2</sup> This technique has worked very well in cases where the identity of the product nucleus can be established by external criteria (e.g., reaction thresholds, cross-bombardments,  $\alpha$ -decay systematics, etc.). For more exotic nuclei however, this is often not possible, and a refinement of experimental technique becomes essential for unambiguous identification. Our present efforts

are directed toward an on-line separation of the new isotopes according to their masses. It is this capability which gives rise to the name of this project: Recoil Atom Mass Analyzer (RAMA).

Figure 1 shows schematically how our He-jet system has been coupled to a hollow-cathode ion source (Ref. 3) which can extract as an ion beam (radioactive) atoms or molecules fed into it. The activity is extracted as (predominantly) singly charged ions which are focused with suitable beam optics and are sent to a magnetic mass separator (yet to be designed). With this set up, it will be possible to produce, transport, and mass-separate a given activity and finally to measure its decay properties all on a time scale of  $\sim 100$  msec. The basic approach described here follows closely the earlier work of Nitschke.<sup>4</sup>

The lower portion of Fig. 1 shows the He-jet target area, which has been described elsewhere.<sup>1,2</sup> Activity recoiling from the target is swept away from the bombardment area by differential pumping of He at a rate of 15-20 Torr-liters/sec through a 5.8-m long capillary tube of  $\sim 1$  mm inside diameter. The capillary tube vents into a vacuum chamber located on the cave roof shielding. This cham-

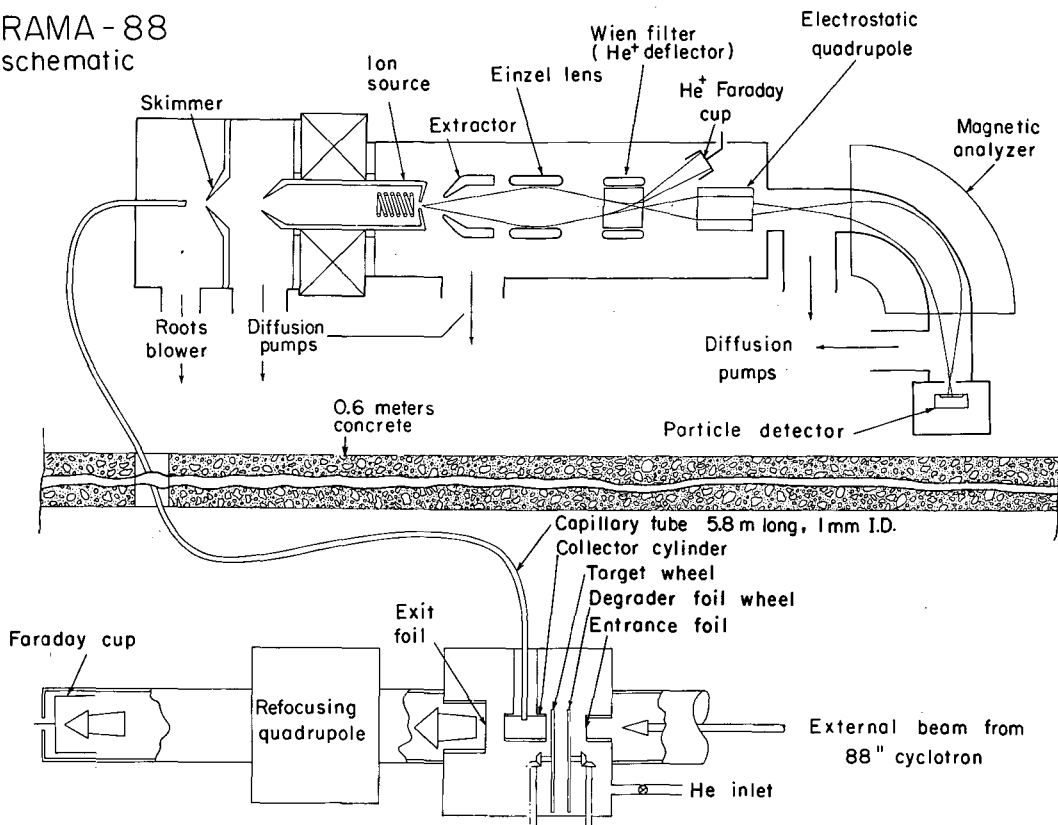
RAMA - 88  
schematic

Fig. 1. An overall schematic of the RAMA system. (XBL735-2949)

ber is maintained at a pressure of  $\sim 50\mu$  by a high-capacity (500 liters/sec of He) Roots blower. The concrete shielding permits personnel to work in the rooftop area during the target irradiations in the cave below.

The capillary tube is directed toward a skimmer element to separate most of the He (which is skimmed off and pumped away) from the heavier radioactivity, most of which passes through the 1-mm-diameter orifice of the skimmer.<sup>5</sup> Using the  $\beta^+$  delayed  $\alpha$ -emitter  $^{20}\text{Na}$ , we have made measurements on either side of the skimmer, which indicate that  $\sim 70\%$  of the activity is confined within a  $2^\circ$  opening cone. This is in good agreement with similar measurements conducted by the UNISOR group at Oak Ridge<sup>6</sup> using  $^{150}\text{Dy}$  activity. The He separation is necessary to obtain proper operating conditions for the ion source.

The ion source is of the early Sidenius hollow-cathode type<sup>3</sup> with some adaptive modifications and is shown in Fig. 2. The upstream end of the filament subtends an angle of  $2^\circ$  at the exit end of the capillary tube. The diameter of the inlet channel is large enough so that most of the activity should drift directly

to the filament region without being intercepted by the walls. Stable operation of the ion source has been achieved by admitting auxiliary support gas for the arc via the annular volume between the anode and cathode contact tubes. This gas bleeds in through the filament coils at the rate of  $\sim 0.1$  Torr-liter/sec. The presence of the auxiliary support gas has two immediate advantages: first it permits independent optimization of the skimming and ion-source parameters, and second, gases other than He can be readily introduced for mass calibrations.

The operating temperature in the filament region has been measured with an optical pyrometer to be  $\sim 2000^\circ\text{C}$ . Once the arc is struck, a plasma is formed in the filament region and extends into the exit hole of the anode cap. Positive ions are extracted from this plasma and are accelerated toward the grounded extraction electrode. A focusing aid is provided by the magnetic field  $\bar{B}$  (see Fig. 2) which is generated by a solenoid coil (not shown) wrapped around the magnetic pole tip. The exact shape of this field and of the electric field created by the extraction voltage can be varied by changing the axial position of the

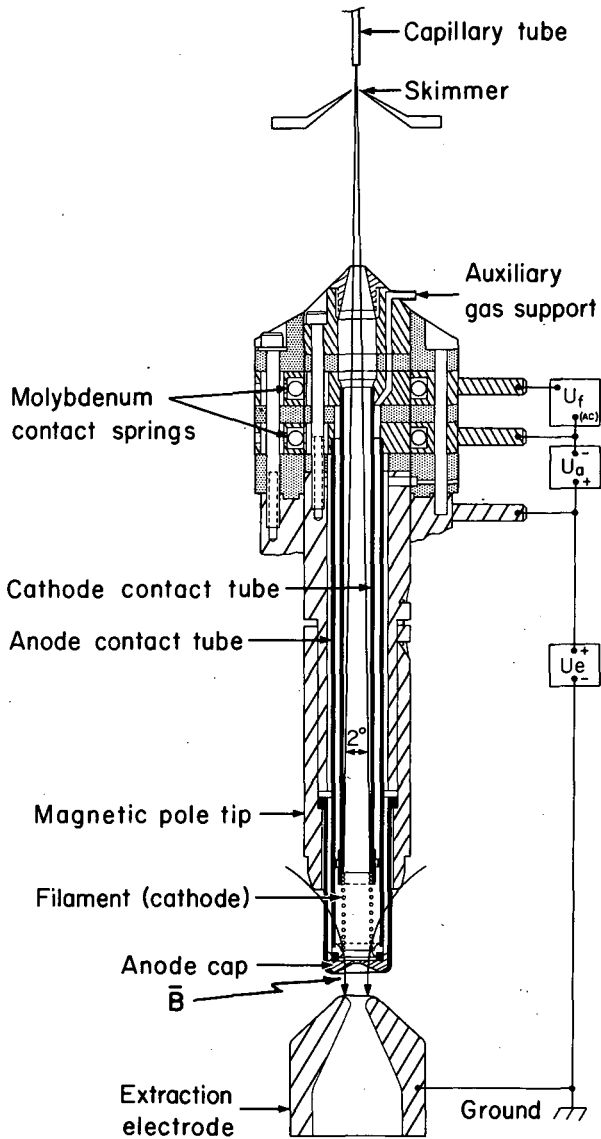


Fig. 2. A cross-sectional view of the heart of the RAMA ion source, showing its relation to the He-jet. (XBL-744-2835)

extraction electrode. We have successfully developed several hundred microamperes of  $\text{He}^+$ ,  $\text{N}^+$ ,  $\text{Ne}^+$ ,  $\text{Ar}^+$ , and  $\text{Xe}^+$  beams under

stable operating conditions. The beam intensities were measured by focusing them into a 2.5-cm-diameter Faraday cup located  $\sim 50$  cm downstream. Typical operating parameters are: extraction voltage  $\equiv U_e = 10$  kV, arc voltage  $\equiv U_a = 300$  V, arc current  $\equiv J_a = 1.5$ - $2.0$  A, filament voltage  $\equiv U_f = 10$  V, and filament current  $\equiv J_f = 20$  A.

The principal component of the extracted beam is formed from the arc support gas. An Einzel lens is employed to focus the beam into a Wien filter which is used to deflect the principal beam component while passing undeflected the "beam" of radioactive ions. This enables us to position a collector foil downstream of the filter and to monitor on-line the ion-source efficiency with a solid-state particle detector. Such a collector foil/monitor system has been constructed. It may also be used to check that activity is going into the ion source, giving assurance that the He-jet is functioning properly.

Tests are presently being conducted to determine and optimize the "on-line efficiency" of the ion source.

#### References

1. R. G. Sextro, R. A. Gough, and J. Cerny, *Phys. Rev. C* **8**, 258 (1973).
2. Nuclear Chemistry Division Annual Report for 1972, LBL-1666, p. 361.
3. G. Sidenious, *First International Conference on Ion Sources*, Saclay, France (1969), p. 401.
4. J. M. Nitschke, in *Proceedings of the International Conference on the Properties of Nuclei Far from the Region of Beta-Stability*, Leysin, Switzerland, 1970 (CERN, Geneva, 1970), Vol. 1, p. 153.
5. J. B. Anderson, R. P. Andres, and J. B. Fenn, *Advan. Chem. Phys.* **10**, 275 (1966).
6. W. D. Schmidt-Ott, private communication.

## F.A.K.E. — A FAST AUTOMATIC KHEMISTRY EXPERIMENT

J. M. Nitschke

With the filling of the 5f shell by lawrencium (element 103) it has been suggested that element 104 (rutherfordium) continues the filling of the 6d shell. This would give it a  $[Rn] 5f^{14} 6d^2 7s^2$  or perhaps  $[Rn] 5f^{14} 6d^1 7s^2 7p^1$  configuration, and would place it in period IV B in which case it should exhibit properties similar to Zr and Hf. The work of Zvara et al.<sup>1</sup> and Silva et al.<sup>2</sup> appears to confirm this.

In order to learn more about the chemistry of Rf we are in the process of investigating the relative chloride complex strength of Zr, Hf, and Rf and the ion association complexes with the charged ammonium group in a quaternary amine Aliquat 336. The Aliquat 336 is absorbed in the stationary phase of a Kel-F column. The calculated ionic radii of Zr, Hf, and Rf

are 0.60, 0.61, and 0.71 Å respectively. In a liquid-liquid phase exchange we expect therefore, Rf to elute before Hf and Zr. The basic chemical reaction can be written symbolically as follows:

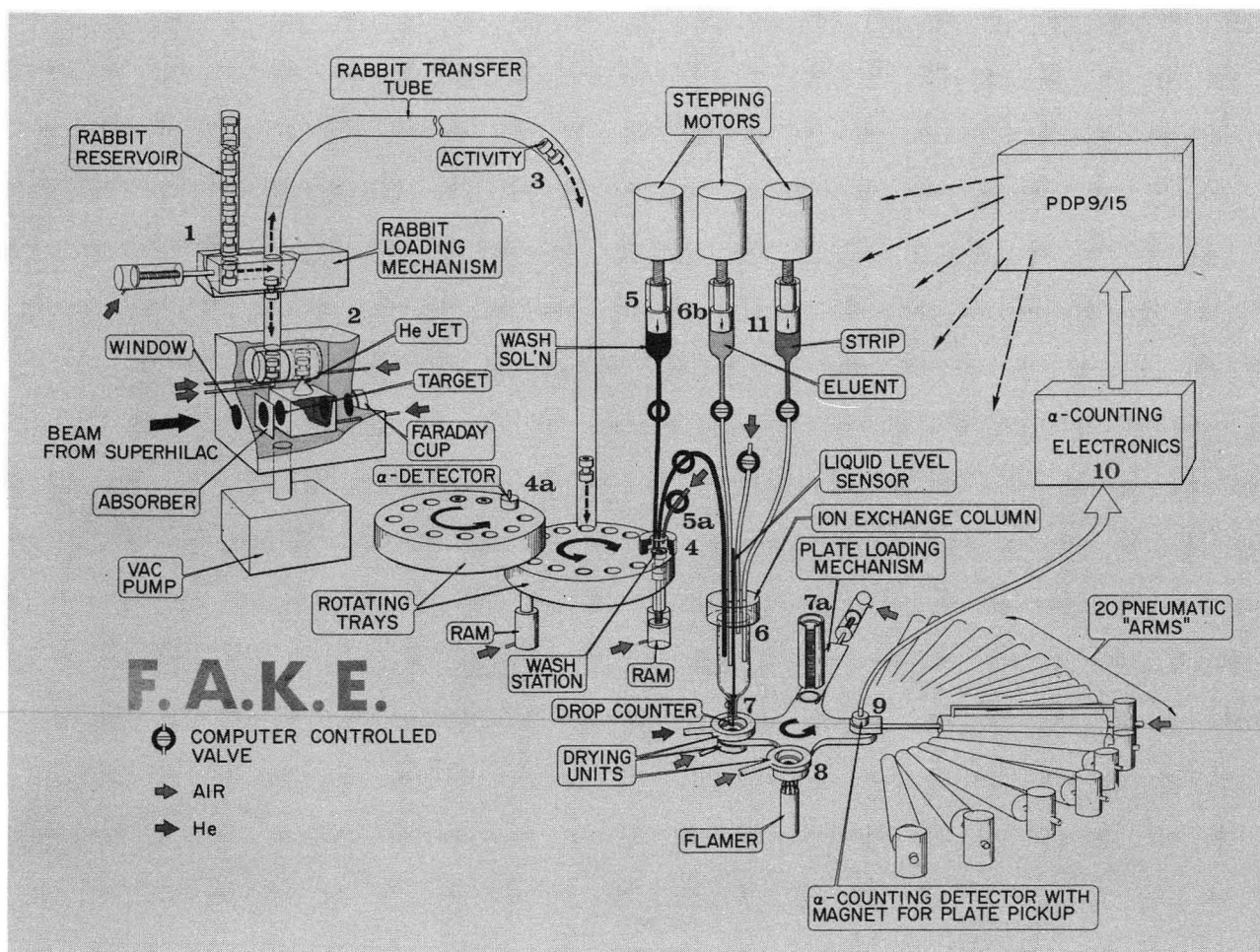
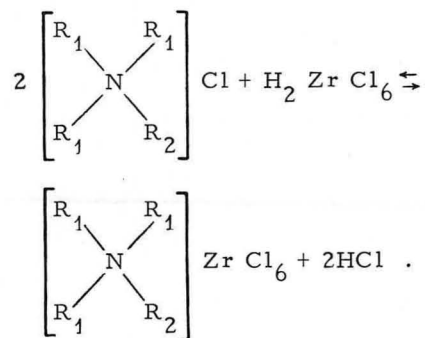


Fig. 1. F.A.K.E. -- fast automatic kHEMistry experiment. (CBB738-4853)

The experimental setup can best be understood by referring to Fig. 1. A thin recoil target of  $800 \mu\text{g}/\text{cm}^2$   $^{248}\text{Cm}$  on a  $\frac{1}{2}$ -mil Be support foil is bombarded at the SuperHILAC with approximately  $3 \mu\text{A}$  of  $^{18}\text{O}^{8+}$  at the optimum energy of 97 MeV to form  $^{261}\text{Rf}$  in a 5n reaction.  $^{261}\text{Rf}$  has the longest half-life of the known Rf isotopes (64 sec) and is therefore the most suitable to perform fast chemical reactions.

The recoils from the target are stopped in approximately one atmosphere of He gas which expands through a small orifice into a vacuum chamber, thereby forming a jet which carries the recoil products with it and deposits them on the "face" of a "rabbit." The rabbits are shot by pressurized air through a 10-m long Tygon tube from the target area into the chemistry apparatus. Here they can move to station 4a for gross  $\alpha$  counting and yield determination, or to station 4 which starts the actual chemistry. Figure 2 shows an  $\alpha$  spectrum that was

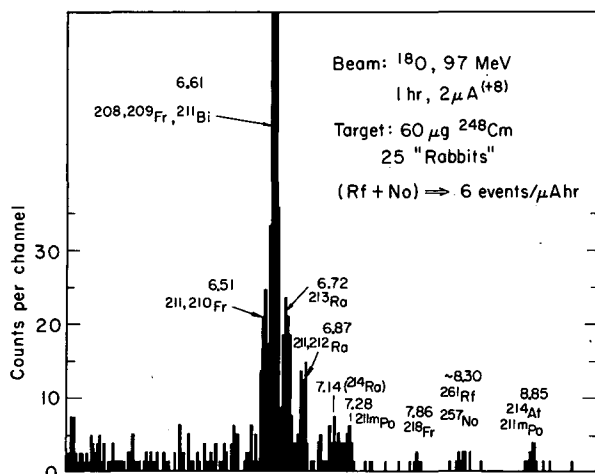


Fig. 2.  $\alpha$  spectrum at station 4a.  
(XBL 738-3815)

obtained at station 4a from 25 rabbits after 1 h of bombardment (target thickness  $200 \mu\text{g}/\text{cm}$ ). Six  $\alpha$  decays of  $^{261}\text{Rf}$  were observed during this time, which corresponds to approximately  $\frac{1}{2}$  Rf atom per rabbit.

At station 4 the activity is washed off in two steps with a total of  $140 \mu\text{l}$  of 11N HCl, transferred to the chromatographic column and pushed through with air pressure. At this HCl-molarity Zr, Hf and Rf stick to the Aliquat 336 forming Cl complexes while the actinides zip through and are collected on a platinum plate (station 7). This plate (and all following plates) are dried (station 7 and 8), flamed (station 8) and counted by one of the 20 surface barrier detectors on movable arms that pick up the plates at station 9. The next step is to add 9.5 N HCl to the column which elutes Rf during the first  $90 \mu$  liters (second plate) and some Rf plus Hf during the second  $90 \mu$  liters (third plate). The third  $90 \mu$  liters (fourth plate) has most of the Hf but no Rf. To monitor the elution position of Hf, occasionally rabbits "doped" with  $^{172}\text{Hf}$  are introduced.

The final step is to "strip" the column with 6 N HCl, and to regenerate it with  $70 \mu$  liters of 11 N HCl.

All parts of the experiment including the beam, target, rabbits, chemistry, and the counting of the  $\alpha$  particles are controlled by a PDP-9 or -15 computer in a "hands-off" mode of operation. Ease of programming and full flexibility are essential for an efficient use of F.A.K.E., therefore all steps of the program can be changed on-line (that is, without recompilation) via teletype commands, and five different  $\alpha$  spectra corresponding to the different chemical fractions can be displayed and plotted.

Provided a working mechanical system exists, entirely new chemical separation schemes can be programmed within a few hours.

#### References

1. I. Zvara, Yu. T. Chburkov, R. Caletka, T. S. Zvarova, M. P. Shaloevskii, and B. V. Shilov, *J. Nucl. Energy* **21**, 601 (1967).
2. R. Silva, J. Harris, M. Nurmia, K. Eskola, and A. Ghiorso, *Inorg. Nucl. Chem. Lett.* **6**, 871 (1970).

#### CALIBRATION OF Si(Li) ELECTRON SPECTROMETERS WITH $^{180\text{m}}\text{Hf}$ , $^{207}\text{Bi}$ , AND $^{210}\text{At}$ <sup>†</sup>

L. J. Jardine and C. M. Lederer

A simple method is presented for calibration of the relative efficiency of a Si(Li) electron spectrometer with the sources  $^{180\text{m}}\text{Hf}$  (5.5 h) and  $^{207}\text{Bi}$  (38 y).

Tables I and II list the relative intensities of conversion electrons associated with the decay of these isotopes. The  $^{180\text{m}}\text{Hf}$  intensities were calculated from the decay scheme,

Table I. Calculated absolute  $\gamma$ -ray and conversion electron intensities in decay of  $^{180m}\text{Hf}$ .

Transition Energy (keV)	Transition Intensity (%)	$\gamma$ -ray Intensity <sup>a</sup> (%)	Assigned Multipolarity	Shell	Electron Energy (keV)	Electron Intensity <sup>a</sup> (%)
93.3	(100)	17.48±0.35	E2	K	28.0	19.23±0.38
				L	83.0	47.9 ±1.0
				M+...	91	15.38±0.31
215.2	(100)	81.4 ±1.6	E2	K	149.9	11.24±0.23
				L	204.7	5.58±0.11
332.3	(100)	94.4 ±1.9	E2	K	267.0	3.97 ±0.08
				L	321.6	1.227±0.025
443.2	(100)	82.5 ±3.3 <sup>b</sup>	E2	K	377.9	1.666±0.067
				L	432.3	0.404±0.016
500.7	(100)	14.5 ±0.6 <sup>b</sup>	E3+3.5% M2	K	435.3	0.593±0.023
				L	490.0	0.227±0.009

<sup>a</sup>The assigned errors assume a ±2% uncertainty in the theoretical conversion coefficients.

<sup>b</sup>The relative  $\gamma$ -ray intensity of these two transitions was measured in the present work.

Table II. Calculated relative conversion electron intensities in decay of  $^{207}\text{Bi}$ .

Transition Energy (keV)	$\gamma$ -ray Intensity <sup>a</sup> (relative)	Assigned Multipolarity	Shell	Electron Energy (keV)	Electron Intensity <sup>b</sup> (relative)
569.7	100	E2	K	481.7	21.7 ±0.9
			L	554.4	6.08 ±0.24
1063.6	75.5 ±2.2	M4	K	975.6	100.0
			L	1048.1	25.3 ±1.0
1770.2	6.95±0.20	M1	K	1682.2	0.344±0.017
			L	1754.4	0.056±0.003

<sup>a</sup>Measured in present work with a Ge(Li)  $\gamma$ -ray spectrometer.

<sup>b</sup>The assigned errors assume a ±2% uncertainty in the theoretical conversion coefficients.

theoretical conversion coefficients, and our new measurement of the  $\gamma$ -ray branching ratio:

$$I_{\gamma}(443.2)/I_{\gamma}(500.7) = 5.70 \pm 0.17$$

The multipolarity of the 500.7-keV transition was taken to be E3+3.5% M2 (Ref. 1) although the L-subshell ratios<sup>2</sup> are only marginally consistent with so large an M2 admixture. The 57.4-keV E1 transition is not used because of uncertainties in its conversion coefficient (which is probably anomalous). The electron intensities for  $^{207}\text{Bi}$  are based on our

new measurement of the relative  $\gamma$ -ray intensities,

$$I_{\gamma}(569.7)/I_{\gamma}(1063.7)/I_{\gamma}(1770.2) = 100/75.5 \pm 2.2/6.95 \pm 0.20$$

and theoretical conversion coefficients for the well-established multipolarity assignments.

A useful secondary standard, with electron lines of somewhat less precisely known relative



intensity, is  $^{210}\text{At}$ . Table III gives the conversion electron intensities, based on recently measured gamma-ray intensities<sup>3</sup> and theoretical conversion coefficients.

Several Si(Li) detectors of different size have been studied with these sources. Figure 1a shows an efficiency curve measured for a 5-mm-thick  $\times$  1 cm-diameter crystal and Fig. 1b for a 3-mm-thick  $\times$  0.5-cm-diameter crystal. We have found, consistent with expectation based on geometric considerations, that

1) "Large area" detectors (radius  $\geq 1.5 \times$  thickness) have a constant efficiency at low energies. The efficiency begins to decrease rapidly as the electron range approaches the detector thickness at the "cutoff" energy.

2) Smaller-area detectors show a gradual decrease in efficiency vs. energy at low energy, followed by a somewhat broader cutoff region. (The response at low energies is more nearly constant if the electron source is collimated so that it strikes only the center of the detector.)

Table III. Calculated relative conversion electron intensities in decay of  $^{210}\text{At}$ .

Transition Energy (keV)	$\gamma$ -ray Intensity <sup>a</sup> (relative)	Assigned Multipolarity	Shell	Electron Energy (keV)	Electron Intensity <sup>b</sup> (relative)
245.3	80.0 $\pm$ 4.0	E2	K	152.2	100.0 $\pm$ 6.0
			L	229.7	92.1 $\pm$ 5.5
1181.4	100	E2	K	1088.3	5.035
			L	1164.8	0.96 $\pm$ 0.05
1436.7	29.2 $\pm$ 1.3	E1	K	1343.6	0.413 $\pm$ 0.021
			L	1420.0	0.063 $\pm$ 0.003
1483.3	46.8 $\pm$ 2.0	E1	K	1390.2	0.62 $\pm$ 0.03
			L	1466.6	0.095 $\pm$ 0.005
1599.5	13.5 $\pm$ 0.6	E1	K	1506.4	0.0118 $\pm$ 0.0006

<sup>a</sup> Measured by Ref. 3.

<sup>b</sup> The assigned errors also include a  $\pm 2\%$  uncertainty in the theoretical conversion coefficients.

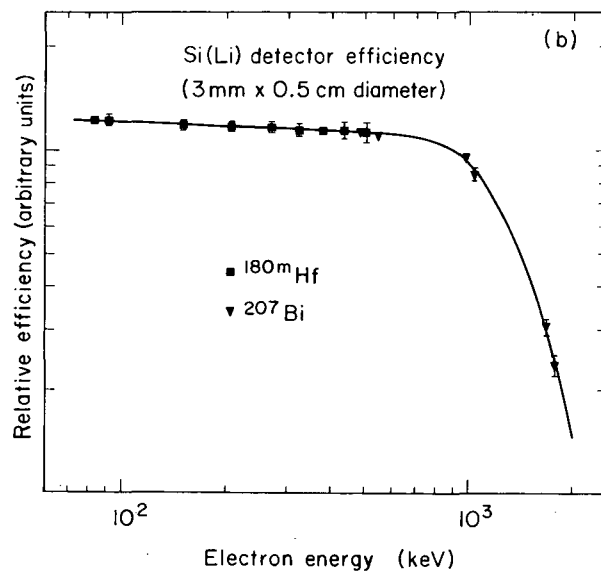
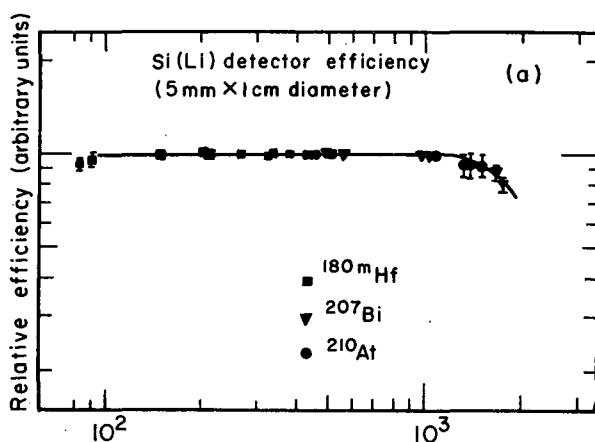


Fig. 1. Relative efficiency curves for  
 (a) 5-mm  $\times$  1-cm-diameter Si(Li) crystal.  
 (b) 3-mm  $\times$  0.5-cm-diameter Si(Li) crystal. (XBL-742-428)

Large-area detectors can thus be conveniently calibrated with  $^{207}\text{Bi}$  and/or  $^{210}\text{At}$ . Small-area detectors require the use of  $^{180\text{m}}\text{Hf}$  also to establish the efficiency function at low energies.

#### Footnotes and References

† Condensed from LBL-205 (submitted to Nucl. Instr. Methods).

1. E. Bodenstedt, H. J. Körner, E. Gerdau, J. Radeloff, C. Günther, and G. Strube, *Z. Physik* **165**, 57 (1964).

2. Jean Gizon and Andrée Gizon, *Comp. Rend.* **264B**, 1607 (1967).

3. L. J. Jardine, S. G. Prussin, and J. M. Hollander, *Nucl. Phys.* **A190**, 261 (1972).

### THE USE OF GLASS FRITS FOR REMOVAL OF RECOILS FROM A CATCHER GAS

J. V. Kratz\*, J. O. Liljenzin,<sup>†</sup> and R. J. Silva<sup>‡</sup>

As a preliminary study related to a future continuous (or semicontinuous) chemical separation of recoil products from heavy ion reactions, experiments have been made to evaluate the separative efficiency of a He-jet system and a glass frit system (see Fig. 1). Such systems can be used to transport the recoil products out of the target chamber; then the recoils can be brought into solution for making chemical separations.

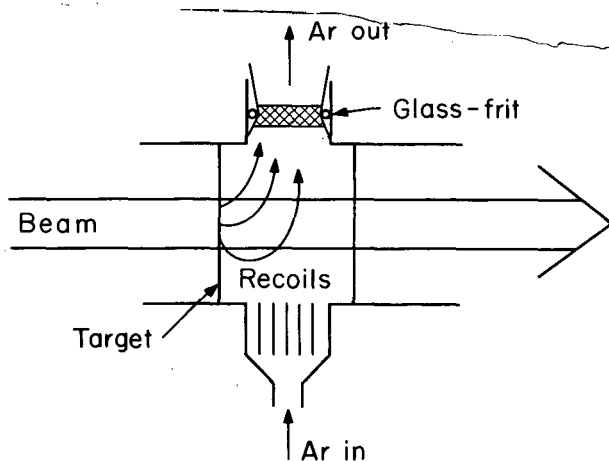


Fig. 1. Schematic diagram of the recoil collection chamber with glass frit. (XBL 744-2836)

A target of  $^{144}\text{Sm}$  was irradiated with 7.2 MeV/amu  $^{12}\text{C}$  ions in the chamber shown in Fig. 1. The recoiling products were stopped in He or Ar gas which streamed through the chamber and left through a jet nozzle or a glass frit. The collected recoils were counted using an  $\alpha$  spectrometer, and the  $\alpha$  activities of 7.2 min  $^{150}\text{Dy}$  were evaluated. The total reaction yield was determined by stopping the recoils in a thick Au foil placed behind the target in vacuum; the  $^{150}\text{Dy}$   $\alpha$  activity was then

counted after chemical separation of a lanthanide fraction. Figure 2 shows some of the experimental results. The curves were calculated by a simple Monte Carlo method. A reaction was assumed somewhere in the target. The angular scattering and range straggling occurring when the recoiling product passed the remaining target layer was estimated from data in the AIP Handbook.<sup>1</sup> This was continued for the gas phase to give the stopping

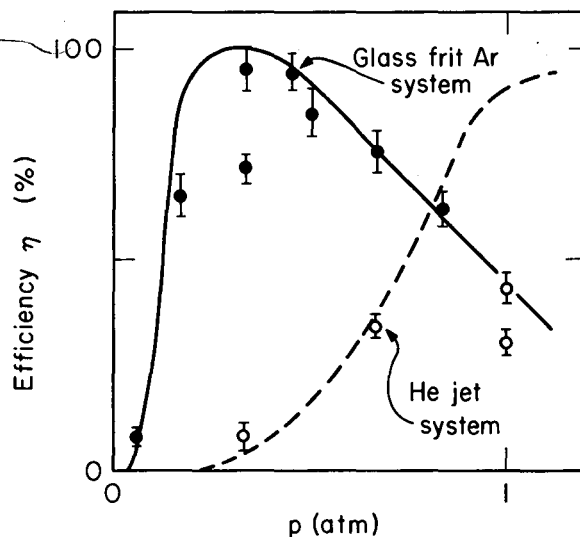


Fig. 2. Measured recoil collection yields for glass frits with Ar gas and an He-jet vs. gas pressure. The curves are calculated by a Monte Carlo method. (XBL 744-2837)

position. If the stopping position was inside the gas stream, the recoil was assumed to be collected; otherwise, if it was stopped on the walls or in the stationary gas layers near target and exit window, it was considered lost.

The geometry used was obtained from measurements of the actual chamber.

It is clear that an optimum pressure exists for a given chamber and recoil mass, charge, and energy. The collection efficiency with the glass-frit Ar system is as good as (or better than) that of the He-jet system. It also has the advantage of a smaller gas pressure. Measurements on the backside of the glass frit or on a second glass frit positioned after the first showed no active products, indicating 100% removal of recoils in the first frit. The recoil products could be dissolved by backwashing the glass-frit with a few drops of 0.1 M HCl/Cl<sub>2</sub>.

A series of glass frits mounted in a rotating disk could thus be used with a future gas target. By circulating the target gas through one of the glass-frits, the reaction products would be removed and the gas compressed and recirculated. The disk with the glass frits could then be rotated stepwise, introducing

new glass frits into the target gas stream and removing the recoil-loaded frits out of the target system and into a dissolver. After removal of the recoil products, the frits could either be dried and reused or replaced by new ones.

#### Footnotes and References

\* On leave from Institut für Kernchemie, Universität Mainz, with a fellowship from Gesellschaft für Schwerionenforschung GSI, Darmstadt, Germany.

† Department of Nuclear Chemistry, Chalmers University of Technology, Göteborg, Sweden.

‡ Oak Ridge National Laboratory, Oak Ridge, Tennessee.

1. The American Institute of Physics Handbook, 3rd ed. (McGraw-Hill, New York, 1972).

### COMPUTER-AIDED ANALYSIS OF $\gamma$ -RAY SPECTRA

I. Binder, M. DiCasa,\* J. V. Kratz,† J. O. Liljenzin,‡ and A. E. Norris§

The  $\gamma$ -ray spectral data obtained from the superheavy-element bombardments discussed elsewhere in this report are evaluated to determine the quantities of nuclides that are formed in these heavy-ion reactions. The procedure that has been developed for these analyses is a set of computer programs written to minimize the limitations of the BKY computer facility for this type of work, while using to advantage information "external" to a given  $\gamma$ -ray spectrum, such as the chemical separations occurring in the preparation of the sample, the rate of decay of a  $\gamma$ -ray peak, and available information about parent-daughter decay relationships and the quantal yields of additional  $\gamma$ -ray lines from the decay of the nuclide under consideration.

Each  $\gamma$ -ray spectrum consists of  $\gamma$  rays from a multitude of nuclides. Many of the nuclides cannot be isolated in pure form, as is necessary for spectrum stripping analysis techniques. Also, it is often not known until after the evaluation of  $\gamma$ -ray spectra which nuclides are formed in the reaction.

The flow diagram to get from the output of a multichannel analyzer to a table containing identified nuclides and their abundances is shown in Fig. 1. It is necessary that the  $\gamma$ -ray

data be taken with a Ge(Li) detector system calibrated for energy and absolute efficiency. Computer code AES1 is used to measure  $\gamma$ -ray peak energies and intensities in a  $\gamma$ -ray spectrum. The data from all the spectra obtained from a sample are combined as the input to code TAU1 for decay rate correlations. The mathematical methods used in these two codes are, on the whole, based on linear algebra techniques commonly used in similar analyses. The purpose of this report is to discuss briefly the TAU2 code, which uses the CDC VISTA system to permit the experimenter to interact with the analysis scheme in the correlation of nuclide decay characteristics with the  $\gamma$ -ray decay data.

Input to the TAU2 program consists of two parts. One is the experimental  $\gamma$ -ray data sorted according to energy and time of measurement. The second part is a  $\gamma$ -ray reference table compiled from various sources.<sup>1-3</sup> The reference table contains information about  $\gamma$ -active nuclides with  $t_{1/2} > 1$  minute,  $\gamma$ -ray energies in the range of  $^{1-3} 50 \text{ keV} \leq E \leq 2 \text{ MeV}$ , and associated relative and absolute  $\gamma$ -ray intensities. The reference table has been broken into subsets consisting of the nuclides that might be present in a given chemical fraction.

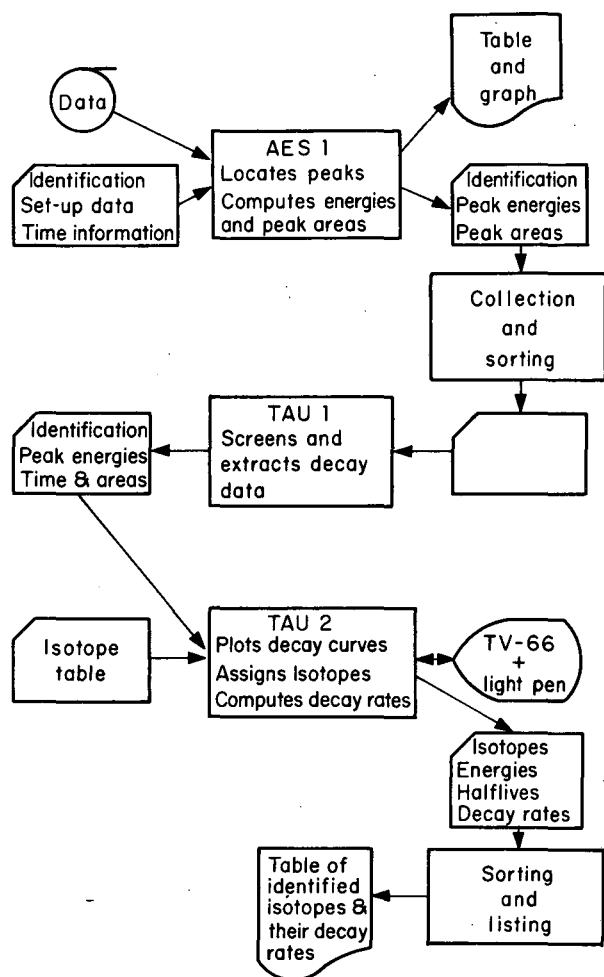


Fig. 1. Flow diagram for the analysis of complex  $\gamma$ -ray spectra. (XBL 744-2838)

In use, the TAU2 code displays on a VISTA console a semi-logarithmic plot of the decay of a  $\gamma$ -ray peak. Simultaneously displayed are a table listing the ten reference  $\gamma$ -ray lines with energies closest to that of the plotted peak and a light-pen command table. The light pen is used to select a particular nuclide from the table. The decay characteristics of the selected nuclide are fitted to the decay data and displayed on the console screen. Provision is made

for light-pen-selected options such as background subtraction, parent-daughter growth and decay, summing of independently decaying activities, and determination of the half-life from decay data for which no suitable nuclide exists in the table.

The output of TAU2 consists of punched cards, each of which contains the  $\gamma$ -ray energy of a data peak, the  $\gamma$ -ray energy of the assigned nuclide, the disintegration rate, and an uncertainty estimate. The final step in the assignment process is to sort the cards according to nuclide identification and to check the result manually for corroboration of the decay characteristics of the identified nuclides.

This set of programs has been extensively used for identification and yield determination of reaction products obtained by bombarding uranium foils with 7.2-MeV/amu Ar and Kr ions. In the case of Ar+U the strongest bombardment gave an output from AES1 of ~35,000 peak areas and energies for the seven separate samples measured over a month's time. These measurements led to a final set of more than 100 nuclides, from 53 elements, where the reaction yields could be determined. The total number of identified nuclides was larger, but the entire set could not be used because of the lack of information about  $\gamma$ -ray yields.

#### Footnotes and References

\* On leave from Instituto di Chimica Generale, University of Pavia, Italy.

† On leave from Institut für Kernchemie, Universität Mainz, with a fellowship from Gesellschaft für Schwerionenforschung GSI, Darmstadt, Germany.

‡ Department of Nuclear Chemistry, Chalmers University of Technology, Göteborg, Sweden.

§ Los Alamos Scientific Laboratory, Los Alamos, New Mexico.

1. C. M. Lederer, J. M. Hollander, I. Perlman, Table of Isotopes, 6th ed. (Wiley, New York).

2. J. Blachot, R. deTourreil, *J. Radioanal. Chem.* 11, 351 (1972).

3. Unpublished data, C. M. Lederer.

## IRATE (INTERACTIVE RETRIEVAL AND TEXT EDITING)

E. Romascan, W. Greiman, C. M. Lederer, and A. Allen

IRATE is a remote console keyboarding system for entry and editing of information. The system is an outgrowth of several earlier prototype systems<sup>1,2</sup> and was motivated by the data input requirements of the Table of Isotopes and Particle Data projects. The current system is designed to handle both running text and structured data.

The hardware architecture of the system is illustrated in Fig. 1. Each console functions as an "expanded font typewriter."

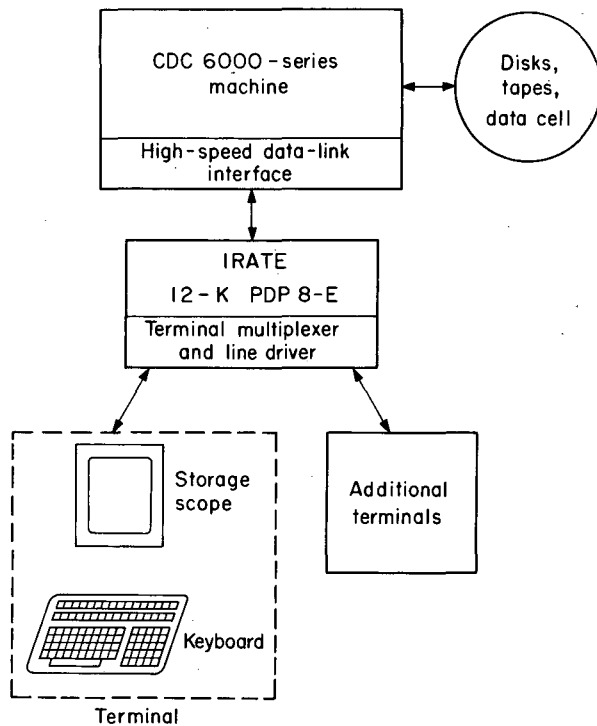


Fig. 1. IRATE system configuration.  
(XBL-744-2834)

Figure 2 shows the keyboard layout for one console. The following are some novel features of the system:

1) It permits easy editing, both when entering data and later, after the data have been entered and proofread. A moving cursor can be positioned anywhere in the text and insertions or deletions performed at the position

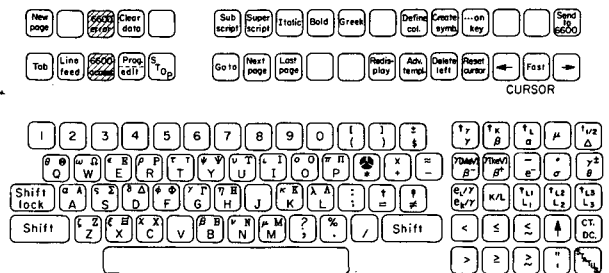


Fig. 2. Layout of the IRATE terminal for the Table of Isotopes project. Special function keys in the top two rows are for

- position control ("Tab", "Line feed", "New Page")
- display control ("Last Page", "Next Page", "Go to" [page number], "Send", and "Redisplay").
- editing (Cursor keys, "Delete left", "Reset cursor", "Clear data")
- retrieval of a specified item ("Go to" [item number X], "Send") (X = f for identifier flags, d for data)
- template control ("Advance Template")
- redefinition of a key ("Create symbol" [keys] "on key" [key])
- column number identification ("Define column")
- fonts ("Subscript", "Superscript", "Italic", "Bold", "Greek"). Foot pedals can also be used for subscript or superscript.

(XBL732-2291)

of the cursor. (Insertions appear at the bottom of the screen and are replaced in the proper part of the text by striking the redisplay key.)

2) Compound symbols, such as  $e_{K/\gamma}$ , can be entered with a single key. In fact, the typist can create such a compound symbol and assign it to a particular key while typing. Frequently used "fonted" characters -- a Greek letter or subscript for example -- can be assigned to a key and then typed without the use of a font key also.

3) "Template" or prompting routines can be used to insure the inclusion of required data identifiers.

4) A true columnar format can be used to enter data directly from published tables. Entries in columnar format, including the TABS and LINE FEEDS themselves, can be edited in the same manner as non-columnar input.

5) Different consoles are attached to separate jobs in the 6000 computer. This permits flexibility in the mode of operation. For example, the presence or absence of a template and its contents, the definition of tabs and/or columns, and special functions, such as title centering, can be different for different consoles.

6) Data can be stored on or retrieved from the data cell or magnetic tapes by the typist.

7) The terminals can also be used as on-line ("RECC") teletypes.

The software includes the PDP-8 program itself, and a group of 6000-routines, under the control of an executive monitor program, that handle the indexing and temporary storage of

blocks of data, and the storage, retrieval, and inventory of the user's data sets. A separate 6000 teletype program permits transfer of data set to and from the chipstore. Development of the PDP-8 software and, to a lesser extent, the 6000 programs, is continuing.

The system has been in use for about 1 year by the Table of Isotopes project, and for a few months by the Particle Data project. It will be used in the near future by Technical Information Division for typing journal articles, and by Math and Computing for documentation.

#### References

1. C. M. Lederer, J. M. Hollander, and L. P. Meissner, UCRL-18530, Oct. 1968.
2. L. P. Meissner, M. L. Clinnick, and R. A. Belshe, UCRL-19390, Feb. 1970.

### FOUR-FUNCTION CALCULATOR USED TO AUTOMATICALLY COMPUTE WAVELENGTH\*

M. Nakamura and G. V. Shalimoff

An inexpensive four-function calculator is being used to calculate on-line the wavelength of spectral lines on photographic plates measured with an optical comparator. We wanted to take advantage of the many features built into low-cost calculators which are readily available. Since the calculator is capable of doing arithmetic operations at millisecond speeds, the wavelength computation is made repetitively in 0.8 sec. The display duration is variable from 0.3 to 3 sec for the operator's convenience.

Although our system already has a semi-automatic card punch system for processing data via a computer, the instantaneous calculation and presentation of wavelengths of spectral lines is of great value. All precise wavelength calculations are made by fitting data to a polynomial equation in a computer program, but it is often desirable to quickly know the wavelength of some spectral line or whether there is a line at some known region. The uniformity of the reciprocal linear dispersion (plate factor in angstroms per mm) of radiation obtained with such instruments is of great practical use and is the basis of the calculation with the device described here.

When measuring wavelengths which increase with distance from left to right, which we call

the normal mode, the wavelength ( $\lambda$ ) is given by the equation

$$\lambda = (d - d_1) PF + \lambda_1,$$

where

$$PF = \text{plate factor} = \frac{\lambda_2 - \lambda_1}{d_2 - d_1},$$

$\lambda_1$  = wavelength of first known spectral line,

$\lambda_2$  = wavelength of second known spectral line,

$d_1$  = digitized screw position of first known spectral line,

$d_2$  = digitized screw position of second known spectral line.

$d$  = digitized screw position of unknown spectral line.

Occasionally we must measure plates where the wavelengths decrease with the distance from left to right. We call this the reverse mode, and when this occurs we use the following equation:

$$-\lambda = (d - d_1) PF - \lambda_1,$$

where the answer in the calculator is given as a negative number. This takes advantage of one of the features built into the calculator and made our job easier in the design of the controller. The negative sign of the result is ignored by the user.

The optical comparator in use at this laboratory has a precisely machined screw which can position a spectrum line of a photographic plate to a precision of one micrometer ( $10^{-6}$  meter). The screw position is digitized via an optical encoder.

A controller has been built which enters the digitized screw position, constants and functions by doing the equivalent of pushing the calculator keys at the appropriate time and in the proper sequence. Thumbwheel switches are used to enter the constants  $d_1$ , PF, and  $\lambda_1$ . Since the calculator is capable of doing chain arithmetic operations following mathematical formulas, the design of the controller to enter the functions and the digital information into the calculator is reasonably straightforward. Minor modifications are made to the calculator to allow interfacing to the controller. The modifications do not impair the normal operation of the calculator.

Although the reciprocal linear dispersion of spectra taken on diffraction grating spectrographs is fairly uniform, there is a gradual change from one end of the plate to the other. For example, a 10-in. spectrum in the first order taken on a 3-meter spectrograph with a grating having 1200 grooves per mm shows a plate factor of 2.769 Å/mm at one end and 2.757 Å/mm at the other end. If an average plate factor for the entire 10-in. plate is used, the

calculated wavelengths will diverge away from the correct value by as much as 0.43 Å at the points farthest from the reference points. Even this kind of accuracy can be useful in initial surveys of plates.

However, of greater interest is this quick calculation of wavelengths within given areas where the plate factor is more accurate for that region. On the same plate described above, over a 30-mm range, the calculated wavelengths are never more than 0.03 Å from their true values, and lines nearest the reference points were calculated to better than 0.01 Å. From the instant calculation of wavelength or from the computed difference of two wavelength calculations, immediate identification of spectral lines is possible.

The instant wavelength calculation is especially useful when one must bootstrap the reference lines in spectra taken in regions where it is not easy to photograph common reference spectra, such as the vacuum ultraviolet regions. Another common application is to identify lines of impurities which are mixed with lines of known elements. A third application is to search for a line of a given wavelength. To do this one simply watches the calculator display for the wavelength as the plate is moved. The controller is set for the shortest display duration so that one can quickly arrive at the wavelength region of interest. Examination of the plate image at that point will indicate if the line of interest is present.

#### Footnote

\* Condensed version of LBL-2331; (in press, Applied Spectroscopy).

## ON-LINE SPARGER FOR VOLTAMMETRIC STUDIES

R. G. Clem and D. H. Anderberg

To do polarographic or voltammetric studies in the negative potential range requires the removal of oxygen. Oxygen is electroactive in this range and thus it interferes with the determination of various substances by increased background or by direct reaction with some of the oxidation or reduction products formed at the electrode. Its removal from sample solutions is essential therefore.

Using conventional means, oxygen is removed or "sparged" from the sample by bubbling an inert gas through the solution. This is a slow process. As a rule of thumb, 1 min of bubbling at a rate compatible with no sam-

ple loss is required for each 1 ml of solution; hence, 15-min sparging is required for 15 ml of solution. In an LBL development<sup>1</sup>—rotating the cell, spinning the sample out into a thin film, and sparging at a high rate—it was possible to sparge 15 ml of sample within 1 to 2 min. While this approach was a time-saving breakthrough for static systems, it was not directly amenable to the voltammetric determination of substances in flowing systems.

The on-line sparger is directly applicable to flowing systems. It consists of a unique self-priming atomizer through which the oxygen-containing sample solution is sparged with

nitrogen or argon. The sample very rapidly exchanges its burden of dissolved oxygen for the inert gas, because the ratio of sample surface to inert gas flow rate is quite favorable.

The solution spray impinges against a dome where it is condensed and led to a drain which exits into the electrochemical cell. The sparge gas exits to the atmosphere through a space provided between the inner impinger dome and a second or outer dome which covers the whole apparatus.

Solution has been sparged of oxygen at a rate

exceeding 60 ml/min and with an inert-gas-use efficiency of 300 ml Ar/ml sample/min—an efficiency some 2 times greater than that obtainable with the rotated cell.

This development was essential for the development of a flowing cell for ASV studies presently under construction.

#### Reference

1. R. G. Clem, G. Litton, and L. D. Ornelas, *Anal. Chem.* **45**, 1305 (1973).

### STYRENE-IMPREGNATED <sup>60</sup>Co-IRRADIATED GRAPHITE ELECTRODE FOR ANODIC STRIPPING ANALYSIS

R. G. Clem and A. F. Sciamanna

The styrene-impregnated, <sup>60</sup>Co-irradiated graphite electrode<sup>1</sup> was developed out of a need for a much longer lived electrode than the wax-impregnated electrodes previously described.<sup>2</sup> Wax electrodes are useable in neutral solutions for as long as 4 to 6 weeks, but fail in acid solutions in only a few days of use. On failure, it appeared that the exposed graphite particles were ejected from the wax matrix. The styrene electrodes, on the other hand, are useable for as long as 6 months in neutral solutions. In acid solution, however, their stability is no better than that of a freshly impregnated wax electrode.

The cause of electrode failure in acid is now thought to be due to the invasion of the graphite itself by acid and acid chloride salts.<sup>1</sup> Lamellar graphite compounds have been long recognized and some have been thoroughly studied.<sup>3</sup> These compounds can be produced by spontaneous reaction; for example, the reaction of graphite with potassium in a NaK solution at room temperature, or by electrolysis—the compound graphite bisulfate is produced in this way. Ternary lamellar compounds with graphite are also possible. All of

these compounds are produced by tunneling between the Van der Waals-held sheets of the graphite crystallites. Efforts using ESCA and an electron microprobe are under way to identify these substances.

It seems likely that if cross-linking between the Van der Waals-held sheets could be effected by particle bombardment, an acid-stable graphite electrode would result. Graphite will be bombarded—probably with protons—to effect radiation damage and used after styrene impregnation to see if this idea is correct.

#### References

1. R. G. Clem and A. F. Sciamanna, LBL-2308, Oct. 1973; to be submitted to *Anal. Chem.*
2. R. G. Clem, G. Litton, and L. D. Ornelas, *Anal. Chem.* **45**, 1305 (1973).
3. G. R. Hennig, *Progress in Inorganic Chemistry* (Interscience, New York, 1959), Vol. 1, pp. 125-201.

### AN INTEGRAL INSTRUMENT FOR ANODIC STRIPPING ANALYSIS

G. W. Kilian and R. G. Clem

The growing concern of people over the pollution of their environment and the consequent need to know the nature and level of the pollutants has created a demand for instruments which can be used to measure the nature and level of the pollutants. Instruments

based on the principles of electrochemistry can be extremely useful for trace element analysis particularly in water. Elements such as Bi, Cu, Sb, Sn, Tl, Cd, In, Zn, and Mn can be detected and measured by using anodic stripping analysis.



A semiautomatic system for anodic stripping analysis, utilizing either a hanging mercury drop or a paraffin-impregnated graphite electrode, has been developed and constructed.

The system as outlined in Fig. 1 permits fast analysis of samples on a routine basis. A rotating cell<sup>1</sup> and a digipotentiostat<sup>2</sup> are integral parts of this system. The system will automatically perform the following steps for anodic stripping analysis after the proper switches and controls are set by the operator. It starts by sparging the sample by rotating the cell at a high rpm; the nitrogen flow is controlled manually. At the end of the selected sparge time the stirring or accumulation mode is performed by reversing the cell's direction of rotation several times per minute. The proper potential for accumulation is applied to the electrodes by the control board. At the end of the accumulate mode there is a momentary pause (five seconds). The cell comes to rest and then the stripping action is started. The potential applied to

the electrodes to produce the stripping is produced in voltage steps by the ramp generator. The digipotentiostat monitors this voltage and maintains the correct current input to the cell to produce the potential at the electrodes. For each specific voltage step applied to the auxiliary electrode and the working electrode, a definite amount of current is fed to the cell. This current directly measures the amount of material that is stripped from the working electrode (paraffin-impregnated graphite). By knowing the potential of the auxiliary electrode in respect to the working electrode, the material being stripped can be identified. The digipotentiostat board digitizes the current and presents a series of pulses to the count-rate meter and to the magnetic tape for storage of the information. The count-rate meter integrates the pulses and presents an analog signal to the small paper recorder, thus the operator has a visual record of results at the time the sample is run.

AUTOMATED POLAROGRAPHY INSTRUMENT  
FOR  
DROPPING MERCURY ELECTRODE OR ANODIC STRIPPING

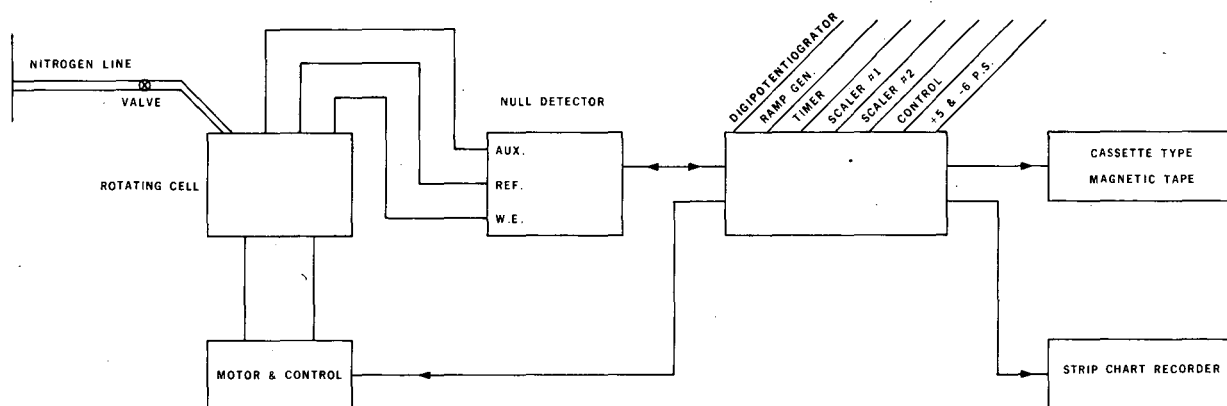


Fig. 1.

(XBL 7310-1302)

References

1. R. G. Clem, G. Litton, and L. D. Ornelas, LBL-679 Rev., Dec. 1972.

2. W. W. Goldworthy and R. G. Clem, A Bipolar Digipotentiostat for Electroanalytical Uses, LBL-282, Dec. 1971.

STUDIES ON THE EXCITATION OF SPECTRA OF  
MULTIPLY-IONIZED ATOMS\*

C. H. H. Van Deurzen† and J. G. Conway

Early methods of producing the spectra of higher states of ionization of atoms have been to use the vacuum spark with a high voltage (~ 30 kV) and low capacitance (~ 0.1 μF). In the last few years the sliding spark has been used to great advantage to produce the spectra up to the seventh stage of ionization. The sliding spark uses a low voltage (~ 1 kV) and higher capacitance (~ 20 μF).

We have studied the effect of variation of the circuit parameters RLC in an electronically switched sliding spark. Figure 1 shows the circuit. We also have the ability of studying the time variation of the line intensity during the light pulse. Figure 2 shows the variation of the relative intensity of various vanadium lines with variation of peak currents at various values of inductance. At low inductance and high current the higher stages of ionization are produced. When the relative intensity is plotted versus 1/L, various peaks in the intensity distribution are observed and these peaks are related to the excitation energy of that given line. The excitation energy is the sum of the ionization potentials and the energy of the transition involved. Figure 3 shows this at the critically damped condition. As one changes to the underdamped condition the curve increases in angle and separation becomes more difficult. As one approaches the overdamped condition the angle decreases and it becomes difficult to obtain higher stages of ionization.

Footnotes

\* Work performed under the auspices of the USAEC and a grant from the National Science Foundation. A more complete description may be found in the thesis by C. H. H. Van Deurzen, Excitation Energies in an Electrically Pulsed Light Emission Source Applied to the Separation of Higher Ionized Atomic States, LBL-1657, May 1973.

† Present address: Physics Dept., Univ. of British Columbia, Vancouver, B.C., Canada.

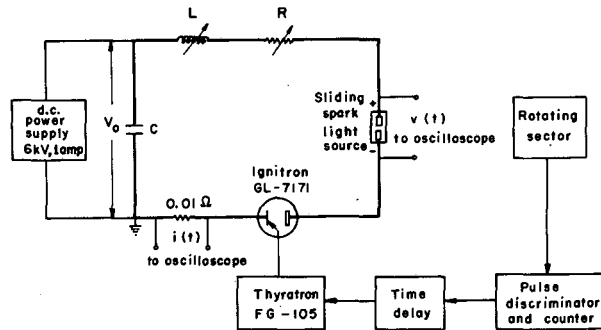


Fig. 1. Schematic of the electrical circuit used to excite spectra of multiply-ionized atoms. (XBL 734-2606)

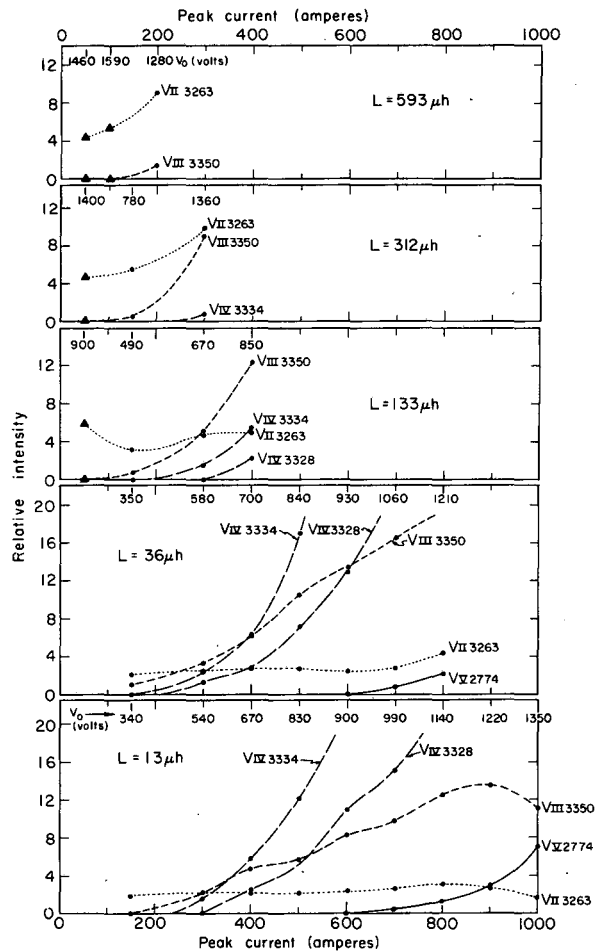


Fig. 2. Relative line intensities of vanadium spectra (V II - V Y) versus peak current. (XBL 734-2594)

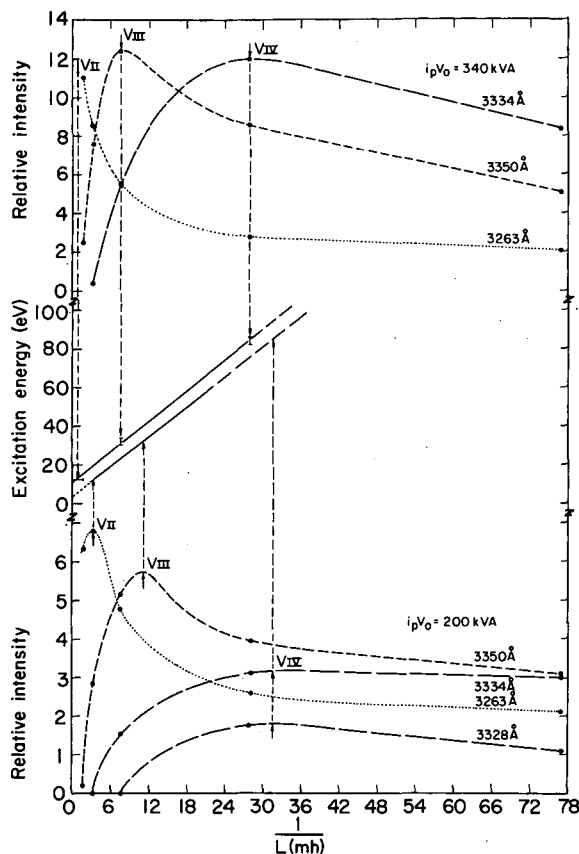


Fig. 3. Relative line intensities and excitation energies versus  $1/L$ . (XBL 734-2599)

### TWO-CHAMBER FURNACE FOR FLAMELESS ATOMIC ABSORPTION SPECTROSCOPY

D. A. Church, T. Hadeishi, L. Leong, R. D. McLaughlin,  
and B. D. Zok

In order to successfully measure trace element concentrations by an atomic absorption (AA) technique, the sample must be reproducibly vaporized and dissociated so that the element of interest can absorb the incident resonance light. Flameless AA measurements are often carried out by placing the sample in a carbon tube, through which the light beam passes. The carbon tube, when heated, serves as a furnace to vaporize and dissociate the sample. With such a furnace, it is generally necessary to carry out drying or ashing steps prior to atomizing the sample, in order to obtain meaningful results. If the sample element to be measured is volatile, or exists in volatile compounds, as do mercury, arsenic, and selenium, these drying and ashing steps

may well lead to loss of this element before the actual measurement.

As a means of circumventing these procedures, we describe a furnace consisting of two heated chambers, which does not suffer from the deficiencies mentioned above. The sample is introduced into the first (combustion) chamber in a holder, along with a stream of carrier gas (Fig. 1). Rapid conductive and radiative heating of the sample holder vaporizes the sample. An oxidizing carrier gas not only assists with the combustion of the sample, reducing smoke and other interferences, but also carries the dissociated constituents reproducibly into the light beam. Following the short residence time in the windowless absorption

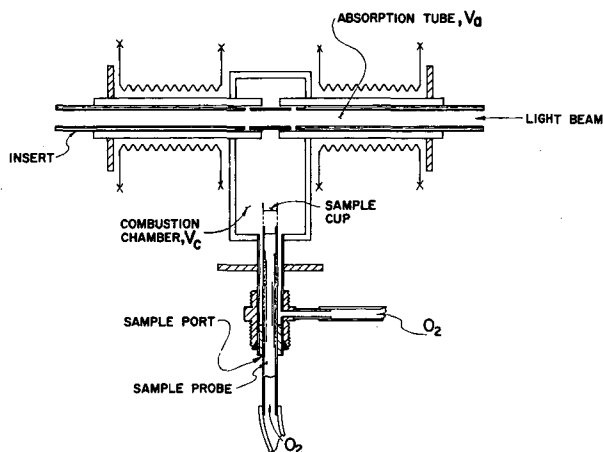


Fig. 1. An example of a two-chamber furnace used in measurements of trace quantities of mercury. The walls of the chamber are made of welded stainless steel. A large ac current is passed through these walls to provide resistive heating in addition to the heating from the heater elements shown. A stop reproducibly positions the sample holder in the furnace. The holder consists of a platinum foil cup supported by four platinum wires welded to a stainless steel tube. The length of the absorption tube is 30 cm, and its diameter is 1.25 cm.

(XBL 736-858)

tube, the sample vapor is vented to the surrounding atmosphere. We have tested such a furnace as a component of the Isotope-shift Zeeman-effect Atomic Absorption (IZAA) spectrometer applied to the measurement of trace quantities of various organic and inorganic compounds of mercury in solid, liquid, and gaseous samples. Such individual measurements can be performed in less than one minute, without chemical preparation of the sample.

Based on simple assumptions, the approximate time dependence of mercury atoms in such a furnace can be predicted. Suppose the sample to contain a number of mercury atoms  $N$ , whether in elemental or molecular form. If the sample is vaporized rapidly compared with the flow rate  $R$  of carrier gas through the system, the liberation of mercury atoms into the combustion chamber can be considered instantaneous. The relatively large impedance to gas flow into the absorption tube aids mixing in the combustion chamber, and time averages the gas spike produced by the sample vaporization. If complete mixing occurs, the rate of increase of atoms in the absorption tube  $N_a$  is

$$dN_a/dt = (NR/V_c) e^{-Rt/V_c}. \quad (1)$$

Again with the assumption of complete mixing, atoms are removed from the absorption tube at the rate

$$dN_a/dt = -(R/V_a)N_a(t). \quad (2)$$

The net density of mercury atoms in the absorption tube, as a function of time  $t$  and initial atom number  $N$ , is

$$N_a(t)/V_a = \frac{N}{(V_c - V_a)} \left( e^{-Rt/V_c} - e^{-Rt/V_a} \right), \quad (3)$$

which has a time dependence in adequate agreement with the signal generally observed. Particularly in the case of insufficiently rapid heating departure from this simple shape are observed when mixtures of compounds with markedly different volatilities are investigated. These effects can be predicted by taking the sample vaporization rate into account. This situation can be eliminated by more rapid sample heating, to drive off all constituents at nearly the same instant.

The solid samples investigated to date include animal and fish muscle, dried and fresh plant leaves and stems, hair, blood, sediments, powdered ceramic, and NBS standard samples. The procedure with solid samples was either to first weigh the sample in a platinum boat which was then placed in the sample holder or to weigh the sample directly in the holder. For a given gas flow rate (typically 400 ml/min) a primary limitation on the weight of solid sample to be run is related to the volume of oxygen available for combustion. When the sample weight approaches a limit proportional to gas flow rate, smoke from the sample begins to be observed. Small increases in sample weight then lead to a large increase in smoke, which eventually attenuates the light beam beyond the capability of the IZAA automatic gain control to function correctly. In practice, we limited sample weight so that no more than 10% of the incident light was obscured by smoke. As Eq. (2) shows, increasing the gas flow rate decreases the dwell time of the atoms in the absorption tube, and hence the signal. Consequently, increases in sensitivity cannot be achieved by increasing both sample weight and gas flow. However, we have found that relatively large sample weights can usually be handled, since smoke is not always a limitation. Sample weights in the 20-30 mg range or higher are routinely run. This relatively high sample weight permits precise control of sample size, and makes it possible

to extend measurements to lower concentrations of mercury. Results of measurements

on calibrated solid samples are presented in Table I.

Table I. Measurements of solid standards, using two slightly different versions of the two-chamber furnace operated near 850°C.

Sample	Sample weight range (mg)	NBS value <sup>a</sup> (ppb)	Number of measurements	Results <sup>b</sup> (ppb)
NBS orchard leaves, SRM 1571	2.9-9.4	155±15	9	154±28
NBS bovine liver SRM 1577	5-10	16±2	9	22.1±6.3
NBS bovine liver SRM 1577	10-12	16±2	9	15.8±5.1
NBS bovine liver SRM 1577	10-20	16±2	8	16.2±3
NBS bovine liver SRM 1577	20-30	16±2	4	13.7±1.4
Seal lion kidney F6	2.2-3.9	1600, <sup>c</sup> 1050 <sup>d</sup>	10	1300±100

<sup>a</sup>Uncertainty is two standard deviations.

<sup>b</sup>Uncertainty is one standard deviations.

<sup>c</sup>Single x-ray fluorescence result (LLL value).

<sup>d</sup>Single cold-vapor AA result (LLL value).

## INSTRUMENTATION FOR AIR POLLUTION MONITORING

C. D. Hollowell and R. D. McLaughlin

In 1971 the Environmental Instrumentation Group of the Lawrence Berkeley Laboratory received an NSF-RANN (National Science Foundation—Research Applied to National Needs) grant to carry out a comprehensive survey of instrumentation for environmental monitoring including monitors of air quality, water quality, radiation, and biomedical samples. The results of the survey are given as descriptions of the physical and operating characteristics of available instruments, critical comparisons among instrumentation methods, and recommendations for development of new instrumentation. The need for such a survey can be appreciated, since over 300 monitors are now commercially available from approximately 100 manufacturers involving over 20 distinctly different principles of operation for the five major gaseous atmospheric pollutants (SO<sub>2</sub>, oxides of nitrogen, oxidants, carbon monoxide, and hydrocarbons).

Tables I, II, and III list the commercially available gaseous pollutant monitors arranged according to their principle of operation. Data concerning the operating characteristics of each of these monitors is contained in Ref. 1. These data include such information as principle of operation, lower detection limit, range of operation, cost and, in some cases, comments from users of the instrument. Discussions of the environmental impact and monitoring methods for these pollutants will be published in the near future.

### Reference

1. Environmental Instrumentation Group, Lawrence Berkeley Laboratory. "Instrumentation for Environmental Monitoring: AIR," LBL-1, Vol. 1, 1972, Tech. Info. Div., LBL, Berkeley, Calif. 94720.

Table I  
Ambient air monitors

	SO <sub>2</sub>	NO <sub>x</sub>	Oxi- dants	CO	HC		SO <sub>2</sub>	NO <sub>x</sub>	Oxi- dants	CO	HC
<b>CONDUCTOMETRIC</b>						<b>GC-FPD</b>					
Calibrated Instruments, Inc.	•					Analytical Instrument Development, Inc.	•				
Casella/London, U.S. distributor, BGI, Inc.	•					Bendix Corp./Process Instruments Div.	•				
CEA Instruments	•					Hewlett Packard Co. Process Analyzers, Inc.	•				
Devco Engineering, Inc.	•					Tracor, Inc.	•				
Intertech Corp.	•					Varian	•				
Kimoto Electric Co., U.S. distributor, Instruments International	•					<b>FID</b>					
Scientific Industries, Inc.	•					Antek Instruments, Inc.					•
Scott Aviation	•					Beckman Instruments, Inc.					•
<b>COLORIMETRIC</b>						Bendix Corp./Process Instruments Division					•
CEA Instruments	•	•				Delphi Industries					•
Enraf-Nonius	•	•	•			Gow-Mac Instrument Co.					•
Kimoto Electric Co., U.S. distributor, Instruments International	•	•	•			Meloy Laboratories, Inc.					•
Precision Scientific Co.						Mine Safety Appliance Co.					•
Scientific Industries, Inc.						Power Designs Pacific, Inc.					•
Technicon Industrial Systems	•	•	•			Process Analyzers, Inc.					•
Wilkens Anderson Co.	•					Scott Aviation					•
Xonics, Inc.	•	•				Scott Research Laboratories, Inc.					•
<b>AMPEROMETRIC (COULOMETRIC)</b>						Teledyne Analytical Instruments					•
Barton ITT	•					Thermo Electron Corp.					•
Beckman Instruments, Inc.	•	•				<b>GC-FID</b>					
Intertech Corp.	•	•				Analytical Instrument Development, Inc.					•
Mast Development Co.	•	•				Beckman Instruments, Inc.					•
Philips Electronic Instruments	•	•	•			Bendix Corp./Process Instruments Division					•
Process Analyzers, Inc.	•					Bryon Instruments, Inc.					•
Welsbach Ozone Systems Corp.			•			Hewlett-Packard Co.					•
<b>PAPER TAPE</b>						<b>NDIR</b>					
Houston Atlas, Inc. (via conversion to H <sub>2</sub> S)	•					Beckman Instruments, Inc.					•
Universal Environmental Instruments Ltd., U.S. distributor, MDA Scientific, Inc.		•				Bendix Corp./Process Instruments Division					•
<b>CATALYTIC OXIDATION</b>						Calibrated Instruments, Inc.					•
Devco Engineering, Inc.						Ecological Instrument Corp.					•
Energetics Science, Inc.						Horiba Instruments, Inc.					•
Matheson Gas Products						Intertech Corp.					•
<b>CHEMICAL SENSING ELECTRODE</b>						Mine Safety Appliance Co.					•
Geomet, Inc.	•	•				<b>FLUORESCENT NDIR</b>					
Orion Research, Inc.	•					Andros Inc.					•
<b>ELECTROCHEMICAL CELL</b>						<b>NONDISPERSIVE UV ABSORPTION</b>					
Dynasciences Corp.	•	•				Canadian Research Institute: U.S. distributor, Sara Scientific Sales Co.					•
EnviroMetrics, Inc.	•	•				Dasibi Corp.					•
Mast Development Co.	•	•				<b>HG SUBSTITUTION UV ABSORPTION</b>					
Theta Sensors, Inc.	•	•				Bacharach Instrument Co.					•
<b>CHEMILUMINESCENCE</b>						<b>DISPERSIVE IR ABSORPTION</b>					
Aerochem Research Laboratories, Inc.		•	•			Wilks Scientific Corp. (IR)					•
Analytical Instrument Development, Inc.						<b>UV FLUORESCENCE</b>					
Beckman Instruments, Inc.		•	•			REM Scientific, Inc.					•
Bendix Corp./Process Instruments Division		•	•			<b>CORRELATION SPECTROSCOPY</b>					
Intertech Corp.		•				Barringer Research Ltd., U.S. distributor, Environmental Measurements Inc.					•
Kimoto Electric Co., U.S. distributor, Instruments International			•			<b>2ND DERIVATIVE SPECTROSCOPY</b>					
LECO Corp.						Spectrometrics/Lear Siegler, Inc.		•	•		•
McMillan Electronics Corp.		•	•			<b>CONDENSATION NUCLEI FORMATION</b>					
Meloy Laboratories, Inc.		•	•			Environment/One Corp.					•
Monitor Labs, Inc.		•	•			<b>BIOLUMINESCENCE</b>					
REM Scientific, Inc.		•	•			RPC Corp.		•			•
Thermo Electron Corp.		•	•								
<b>FPD</b>											
Bendix Corp./Process Instruments Div.	•										
Meloy Laboratories, Inc.	•										

Table II  
 Vehicular emission monitors

	CO	HC	NO <sub>x</sub>		CO	HC	NO <sub>x</sub>
<b>COLORIMETRIC</b>				<b>GC-FID</b>			
Megatech Corp.	•			Beckman Instruments, Inc.	•	•	
<b>CATALYTIC OXIDATION</b>				Byron Instruments, Inc.	•	•	
Bendix Corp./National Environmental Instruments, Inc.	•			Carle Instruments, Inc.	•	•	
Bosch Corp.	•			Hewlett-Packard Co.	•	•	
Matheson Gas Products	•			<b>NDIR</b>			
Mine Safety Appliance Co.	•			Allen Industries	•	•	
Purad Inc.	•	•		Autoscan, Inc.	•	•	
<b>ELECTROCHEMICAL CELLS</b>				Beckman Instruments, Inc.	•	•	•
EnviroMetrics, Inc.	•		•	Bendix Corp./Process Instruments Division	•	•	•
<b>CHEMILUMINESCENCE</b>				Bosch Corp.	•	•	
Aerochem Research Laboratories, Inc.			•	Calibrated Instruments, Inc.	•	•	
Beckman Instruments, Inc.			•	Chrysler Corp.	•	•	
Intertech Corp.			•	Commercial Electronics, Inc.	•	•	
LECO Corp.			•	Ecological Instrument Corp.	•	•	
McMillan Electronics Corp.			•	Horiba Instruments, Inc.	•	•	•
Meloy Laboratories, Inc.			•	Intertech Corp.	•	•	•
REM Scientific, Inc.			•	Marquette Manufacturing Co.	•	•	•
Scott Research Laboratories, Inc.			•	Mine Safety Appliances Co.	•	•	•
Thermo Electron Corp.			•	Peerless Instrument Co.	•	•	•
<b>FID</b>				Peerless Instrument Co., Inc.	•	•	•
Beckman Instruments, Inc.		•		Scott Research Laboratories, Inc.	•	•	•
Delphi Industries		•		Sensors, Inc.	•	•	•
Gow-Mac Instrument Co.		•		Sun Electric Corp.	•	•	•
Heath Survey Consultants, Inc.		•		Triple-A Specialty Co.	•	•	•
Horiba Instruments, Inc.		•		<b>NONDISPERSIVE UV ABSORPTION</b>			
Intertech Corp.		•		Beckman Instruments, Inc.			•
Mine Safety Appliance Co.		•		<b>UV EMISSION</b>			
Scott Research Laboratories, Inc.		•		Detector Electronics Inc.		•	
Thermo Electron Corp.		•		<b>DISPERSIVE IR AND UV ABSORPTION</b>			
				Chrysler Corp. (IR/UV)	•	•	•
				Wilks Scientific Corp. (IR)	•	•	•

Table III  
 Stationary source monitors

	SO <sub>2</sub>	NO <sub>x</sub>	CO	HC		SO <sub>2</sub>	NO <sub>x</sub>	CO	HC
<b>CONDUCTOMETRIC</b>					<b>GC-FID</b>				
Calibrated Instruments, Inc.	•				Beckman Instruments, Inc.			•	•
<b>COLORIMETRIC</b>					Byron Instruments, Inc.			•	•
F & J Scientific		•			Hewlett-Packard Co.			•	•
<b>AMPEROMETRIC (COULOMETRIC)</b>					<b>NDIR</b>				
Barton ITT	•				Barnes Engineering Co.			•	•
<b>PAPER TAPE</b>					Beckman Instruments, Inc.	•	•	•	•
Houston Atlas Inc. (via conversion to H <sub>2</sub> S)	•				Bendix Corp./Process Instruments Div.	•	•	•	•
<b>CATALYTIC OXIDATION</b>					Calibrated Instruments, Inc.	•	•	•	•
Devco Engineering, Inc.			•		Ecological Instrument Corp.	•	•	•	•
Matheson Gas Products			•		Horiba Instruments, Inc.	•	•	•	•
Mine Safety Appliances Co.			•		Infrared Industries	•	•	•	•
<b>CHEMICAL SENSING ELECTRODE</b>					Intertech Corp.	•	•	•	•
Geomet, Inc.	•	•			Leeds & Northrup	•	•	•	•
Orion Research Inc.	•	•			Mine Safety Appliance Co.	•	•	•	•
<b>ELECTROCHEMICAL CELL</b>					Peerless Instrument Co., Inc.	•	•	•	•
Dynasciences Corp.	•	•	•		Scott Research Laboratories, Inc.	•	•	•	•
EnviroMetrics, Inc.	•	•	•		<b>NONDISPERSIVE UV AND VISIBLE ABSORPTION</b>				
Theta Sensors, Inc.	•	•	•		Beckman		•		
<b>CHEMILUMINESCENCE</b>					Canadian Research Institute, U.S. distributor, Sara Scientific Co.	•			
Aerochem Research Laboratories, Inc.			•		E.I. du Pont de Nemours & Co.	•	•		
Beckman Instruments, Inc.			•		Intertech Corp.	•	•		
Bendix Corp./Process Instruments Division			•		Peerless Instrument Co., Inc.	•	•		
Intertech Corp.			•		Teledyne Analytical Instruments	•	•		
LECO Corp.			•		<b>HG SUBSTITUTION UV ABSORPTION</b>				
McMillan Electronics Corp.			•		Barcharach Instrument Co.			•	
REM Scientific, Inc.			•		<b>DISPERSIVE IR AND UV ABSORPTION</b>				
Scott Research Laboratories, Inc.			•		Environmental Data Corp. (IR/UV)	•	•	•	
Thermo Electron Corp.			•		Wilks Scientific Corp. (IR)	•	•	•	
<b>FPD</b>					<b>UV FLUORESCENCE</b>				
Meloy Laboratories, Inc.	•				REM Scientific, Inc.	•			
<b>FID</b>					<b>CORRELATION SPECTROSCOPY</b>				
Beckman Instruments, Inc.			•		Barringer Research Ltd., U.S. distributor, Environmental Measurements Inc.	•			
Mine Safety Appliances Co.			•		CEA Instruments	•			
Process Analyzers, Inc.			•						
Scott Research Laboratories, Inc.			•						
Teledyne Analytical Instruments			•						
Thermo Electron Corp.			•						
Wemco Instrumentation Co.			•						

## V. Thesis Abstracts



## CORE-LEVEL PHOTOELECTRON SPECTROSCOPY OF SMALL MOLECULES

Donald William Davis

(LBL-1900)

Relative core-level binding energies and multiplet splittings in binding energies are measured for a number of gases at low pressures and variable temperatures. These measurements are interpreted with CNDO/2 and INDO/2 wavefunctions.

An analysis of the variation in linewidths of the measured photoelectron spectra is given. The Auger effect is shown to account for some, but not all of the variation in the linewidths. An argument is given for the importance of the Franck-Condon principle in core-level photoionization, particularly in highly fluorinated systems.

The Hellman-Feynman theorem is used to derive a quantitative relation between the two most common theoretical interpretations of core-level chemical shifts. The potential-at-a-nucleus approach is used with CNDO/2 wavefunctions to interpret the measurements made here.

INDO/2 wavefunctions are used to interpret the multiplet splittings observed in a number of core-level photoelectron spectra. Koopmans' theorem is shown to be inapplicable to the interpretation of these multiplet splittings.

## RECOIL TRITIUM REACTIONS WITH CYCLOHEXENE AND METHYLCYCLOHEXENE

Darrell Clark Fee

(LBL-1687)

A study has been made of the reactions of recoil tritium atoms with cyclohexene (at 25°C and 135°C) and with methylcyclohexene (at 135°C). Principle attention was given to unimolecular decomposition processes following T-for-H substitution. T was produced by recoil in the  $^3\text{He}(n, p)\text{T}$  reaction. The neutron irradiations at 25°C were in a specially designed neutron irradiation container in which all samples received the same neutron dose and the temperature was controlled to  $\pm 0.5^\circ\text{C}$ . The tritiated products were analyzed with a specially designed radio-gas-chromatographic system. Peaks were monitored at a constant flow rate in the same detector (a beta proportional counter) and the injection volume was large. A system of four columns used in series gave adequate resolution of more than twenty products from the whole sample. This system was a combination of (1) stop-flow, (2) center-cut, (3) recycle, (4) stepwise temperature programming, and (5) stepwise pressure programming techniques.

The comparative efficiency of  $\text{SO}_2$  and  $\text{O}_2$  as radical scavengers was determined in the T + cyclohexene, T + trans-2-butene, and T + n-butane gas phase system at 25°C.  $\text{O}_2$ , the only scavenger previously in use in T + alkene systems, caused an anomalous increase in the butadiene-t yield from T + cyclohexene reactions. All other tritiated products from cyclohexene and trans-2-butene reactions showed similar scavenging trends. The use of  $\text{SO}_2$  as a scavenger may be advantageous in some alkene systems although  $\text{SO}_2$  fails to remove all thermal contributions to the HT yield in the T + n-butane system.

The anomalous increase in the butadiene-t yield (from T + cyclohexene reactions at 25°C) with  $\text{O}_2$  scavenging was clarified by determining the comparative efficiency of  $\text{H}_2\text{S}$ , butadiene- $\text{d}_6$ ,  $\text{O}_2$ , and  $\text{SO}_2$  as radical scavengers in the T + cyclohexene system at 25°C. Direct tritium substitution of cyclohexene yields cyclohexene-t which may undergo unimolecular decomposition

to produce butadiene-t. In unscavenged samples butadiene-t is selectively depleted by reactions with H atoms produced by radiolysis. Neither SO<sub>2</sub> nor H<sub>2</sub>S is sufficiently reactive with H atoms to protect butadiene-t from such depletion. The "hot" butadiene-t yield can only be determined by means of O<sub>2</sub> or butadiene-d<sub>6</sub> scavenging. All products except butadiene-t exhibit normal behavior with O<sub>2</sub>, SO<sub>2</sub> or H<sub>2</sub>S scavenging.

The pressure dependence (in the 300 to 1500 torr pressure range) of the products of recoil tritium reactions with cyclohexene was determined at 135°C. Both at 135°C and at 25°C roughly 85% of the T + cyclohexene reactions which gave gas phase products resulted from tritium atom abstraction to form HT, addition to form cyclohexyl-t radicals, or T-for-H substitution to form cyclohexene-t. The dependence of product yield on pressure showed that ethylene-t and butadiene-t resulted from the unimolecular decomposition of excited cyclohexene-t (formed by T-for-H substitution). The apparent rate constant of cyclohexene-t unimolecular decomposition was determined as  $5.1 \times 10^6 \text{ sec}^{-1}$ . The *s* parameter in the RRK (for Rice, Ramsperger and Kassel) treatment of the unimolecular decomposition of cyclohexene was determined as *s* = 24. Similarly, the pressure dependence of product yield showed that n-hexene-t, 1-butene-t and methane-t resulted from the unimolecular decomposition of cyclohexyl-t radical (formed by T addition to cyclohexene) with rate constants of  $8 \times 10^3 \text{ sec}^{-1}$ ,  $3 \times 10^4 \text{ sec}^{-1}$ , and  $5 \times 10^2 \text{ sec}^{-1}$ , respectively. The relative rate of abstraction versus addition of radicals in alkenes was determined from the scavenger dependence of the yields of products with a radical precursor.

The reactions of recoil tritium atoms with methylcyclohexene were also studied at 135°C. Roughly 90% of the T + methylcyclohexene reactions which gave gas phase products resulted from tritium atom abstraction to form HT, addition to form methylcyclohexyl-t radicals, or T-for-H substitution to form methylcyclohexene-t. The dependence of product yield on pressure (300 to 1200 torr pressure range) showed that excited 4-methylcyclohexene-t (formed by T-for-H substitution) decomposed unimolecularly to give propylene-t or butadiene-t with a rate constant of  $1 \times 10^7 \text{ sec}^{-1}$  and that similarly excited 3-methylcyclohexene-t decomposed unimolecularly to give ethylene-t or pentadiene-t with a rate constant of  $3 \times 10^6 \text{ sec}^{-1}$ .

A test was made of the RRK-RRKM assumption (*M* reflects the contribution of Marcus) of energy randomization prior to unimolecular decomposition. The rates of unimolecular decomposition of cyclohexene-1-t and cyclohexene-3-t (formed by T-for-methyl substitution reactions of recoil tritium atoms with 1-methylcyclohexene and 3-methylcyclohexene, respectively) were compared. The rates of unimolecular decomposition of cyclohexene-1-t and cyclohexene-3-t were similar. Using the previously determined RRK parameter (*s* = 24) for the unimolecular decomposition of cyclohexene, the average energy of excitation deposited in cyclohexene-t by T-for-methyl substitution reactions with methylcyclohexene was estimated at 6.5 eV for both cyclohexene-1-t and cyclohexene-3-t. For the same energy of excitation, the probability of unimolecular decomposition was independent of the site of energy input.

It was concluded that the RRK-RRKM assumption of energy randomization prior to unimolecular decomposition is valid for the recoil tritium initiated unimolecular decomposition of cyclohexene.

## STRUCTURAL INVESTIGATIONS OF TRANSITION METAL PENTACOORDINATION

Frances Anne Jurnak

(LBL-2335)

The crystal and molecular structures of two salts containing the  $[\text{Ni}(\text{CN})_5]^{3-}$  anion have been determined at -80°C and -10°C from three-dimensional X-ray diffraction data collected by counter methods. Since both distorted trigonal bipyramidal and square pyramidal geometries of the  $[\text{Ni}(\text{CN})_5]^{3-}$  ion exist in the salt  $[\text{Cr}(\text{NH}_2\text{CH}_2\text{CH}_2\text{NH}_2)_3]_2 [\text{Ni}(\text{CN})_5]_2 \cdot 3\text{H}_2\text{O}$ , the

question has remained as to whether the observed geometries correspond to discrete, stable structures or are artifacts of crystal packing forces. The geometry of the  $[\text{Ni}(\text{CN})_5]^{3-}$  anion in both salts reported here can be described as a regular square pyramid in which the apical Ni-C bond distance is considerably longer than the basal Ni-C bonds. In the  $[\text{Cr}(\text{NH}_2\text{CH}_2\text{CH}_2\text{CH}_2\text{NH}_2)_3]^{3+}$  salt, the apical Ni-C distance is 2.140(10) Å and the average basal Ni-C distance is 1.977(9) Å; in the  $[\text{Cr}(\text{NH}_3)_6]^{3+}$  salt, the apical and average basal Ni-C bond distances are 2.101(9) and 1.877(7) Å, respectively. The presence of the same  $[\text{Ni}(\text{CN})_5]^{3-}$  structure in the salts  $[\text{Cr}(\text{NH}_2\text{CH}_2\text{CH}_2\text{CH}_2\text{NH}_2)_3]_2[\text{Ni}(\text{CN})_5]_2 \cdot 3\text{H}_2\text{O}$ ,  $[\text{Cr}(\text{NH}_2\text{CH}_2\text{CH}_2\text{CH}_2\text{NH}_2)_3][\text{Ni}(\text{CN})_5] \cdot 2\text{H}_2\text{O}$  and  $[\text{Cr}(\text{NH}_3)_6][\text{Ni}(\text{CN})_5] \cdot 2\text{H}_2\text{O}$  is cited as evidence for the stereochemical rigidity of the square pyramidal  $[\text{Ni}(\text{CN})_5]^{3-}$  ion, since the crystal packing forces differ substantially in detail from one salt to another.

Tris(1, 3-propanediamine)chromium(III) pentacyanonickelate(II) dihydrate,  $[\text{Cr}(\text{NH}_2\text{CH}_2\text{CH}_2\text{CH}_2\text{NH}_2)_3][\text{Ni}(\text{CN})_5] \cdot 2\text{H}_2\text{O}$ , forms deep red crystals in the orthorhombic space group Pbca with  $a = 23.442(7)$ ,  $b = 13.239(4)$  and  $c = 14.352(6)$  Å at  $-80^\circ\text{C}$ . For eight formula units in the cell the calculated density is  $1.49 \text{ g} \cdot \text{cm}^{-3}$ . For 2356 independent reflections with  $F^2 > \sigma(F^2)$ , full matrix least-squares refinement of positional and anisotropic thermal parameters converged to a final weighted R factor of 5.4%. The second salt,  $[\text{Cr}(\text{NH}_3)_6][\text{Ni}(\text{CN})_5] \cdot 2\text{H}_2\text{O}$ , crystallizes in the orthorhombic space group Pcca with eight formula units in a cell of dimension  $a = 23.102(10)$ ,  $b = 11.592(3)$  and  $c = 11.735(4)$  Å at  $-10^\circ\text{C}$ . The calculated ( $-10^\circ\text{C}$ ) and observed ( $23^\circ\text{C}$ ) densities are 1.61 and  $1.60 \text{ g} \cdot \text{cm}^{-3}$ , respectively. Full matrix least-squares refinement for 1090 independent reflections with  $F^2 > \sigma(F^2)$  converged to  $R = 4.7\%$ . Room and low temperature data sets for  $[\text{Cr}(\text{NH}_2\text{CH}_2\text{CH}_2\text{CH}_2\text{NH}_2)_3][\text{Ni}(\text{CN})_5] \cdot 2\text{H}_2\text{O}$  are compared and the effect of isotropic crystal decomposition on structural information is discussed.

The crystal and molecular structure of the green form of the  $[\text{Co}(\text{CNC}_6\text{H}_5)_5]^{2+}$  cation has been determined at  $23^\circ\text{C}$  from three-dimensional X-ray diffraction data collected by counter methods. The perchlorate salt of the  $[\text{Co}(\text{CNC}_6\text{H}_5)_5]^{2+}$  cation exists in three forms, each with a different color change has been attributed to solvation of the sixth ligand position of the cation or to a stereochemical change in the geometry from  $\text{C}_{4v}$  to  $\text{D}_{3h}$ . The geometry of the green form reported here can be described as a square pyramid in which the average  $\text{C}_{\text{apical}}\text{-Co-C}_{\text{basal}}$  angle has flattened to  $95.0^\circ$  to minimize repulsion with a perchlorate ion below the basal plane of the complex. The perchlorate oxygen and cobalt atoms are separated by 2.594(10) Å. The apical Co-C bond is 1.950(11) Å and is longer than the average basal Co-C bond length of 1.842(6) Å. The effect of a perchlorate ion in the approximate sixth ligand position upon the chemistry of the three color forms of  $[\text{Co}(\text{CNC}_6\text{H}_5)_5]^{2+}$  is discussed.

Pentakis(phenylisocyanide)cobalt(II) perchlorate hemi-1, 2-dichloroethane forms deep green crystals in the monoclinic space group  $\text{P}2_1/\text{c}$  with  $a = 10.336(2)$ ,  $b = 13.939(6)$ ,  $c = 27.143(7)$  Å and  $\beta = 95.589(11)^\circ$ . For four formula units in the cell, the calculated density is  $1.41 \text{ g} \cdot \text{cm}^{-3}$  and agrees satisfactorily with the observed density of  $1.38 \text{ g} \cdot \text{cm}^{-3}$ . For 2358 independent reflections with  $F^2 > 3\sigma(F^2)$ , the full matrix least-squares refinement converged to a final weighted R factor of 11.7%.

A discussion of the unusual conformational features of the  $[\text{Cr}(\text{NH}_2\text{CH}_2\text{CH}_2\text{CH}_2\text{NH}_2)_3]^{3+}$  cation is presented. Only two of the three six-membered rings have the expected chair conformation. The third ring has a conformation analogous to the twist or skew-boat form of cyclohexane. The average Cr-N bond distance is 2.096(3) Å. The average N-Cr-N angle for all rings is  $89.7(3)^\circ$  and the average Cr-N-C angle is  $120.7(4)^\circ$  in the chair and  $116.6(2)^\circ$  in the skew-boat conformers. The dihedral angle between the planes containing the N-C bonds in the skew-boat conformer is  $79.0^\circ$ . A comparison of all structural examples of the chair geometry in 1, 3-propanediamine chelate rings is discussed. A nomenclature for the sixteen possible conformations of tris chelate complexes containing six-membered rings is proposed.

The crystal structure and absolute configuration of a bromoacetyl derivative of vitexin has been determined from three-dimensional X-ray diffraction data collected by counter methods.

Two derivatives of vitexin are found in the unit cell. Seventy percent of the molecules are 6-bromo-5-hydroxy-2'', 3'', 4', 4'', 6'', 7-hexaacetylvitexin. The sugar ring in each derivative is a  $\beta$ -D-glycosyl moiety, attached through C-C bonds to the 8 position of the flavonoid nucleus and is approximately perpendicular to the flavonoid plane.

## TWO-NUCLEON TRANSFER REACTIONS INDUCED BY POLARIZED PROTONS

John Alan Macdonald

(LBL-2320)

$(\vec{p}, t)$  and  $(\vec{p}, {}^3\text{He})$  reactions have been induced by polarized protons of 43.8 MeV on  ${}^{16}\text{O}$ ,  ${}^{15}\text{N}$ ,  ${}^9\text{Be}$ , and  ${}^7\text{Li}$ , and of 49.6 MeV on  ${}^{13}\text{C}$  targets. The  ${}^{208}\text{Pb}(\vec{p}, t)$  transitions at  $E_p = 40$  MeV to four final states in  ${}^{206}\text{Pb}$  have also been observed. Relative differential cross sections and analyzing powers have been measured for over fifty transitions, of which thirty-six have been compared with zero-range DWBA calculations with a spin-orbit potential in the proton channel, and employing wave functions of Cohen and Kurath and of True and Ford. Although generally good results for the differential cross section predictions were obtained, attempts to fit the analyzing powers met with mixed results. In general  $(\vec{p}, t)$  results were fit better than  $(\vec{p}, {}^3\text{He})$ , ground state transitions better than those to excited states, and transitions to analog states better than more complex transitions. These conclusions were not altered by including the effects of spin dependence in the two-body interaction or of spin-orbit coupling in the exit channel. It seems doubtful that the discrepancies can be overcome entirely by finite range calculations, though they should be tried, as should attempts to evaluate the importance of second order effects.

## HIGH-RESOLUTION STUDIES OF BETA-DELAYED PROTON EMISSION IN LIGHT NUCLEI

Richard George Sextro

(LBL-2360)

Identified protons have been observed following beta decay of the precursor nuclei  ${}^{21}\text{Mg}$ ,  ${}^{25}\text{Si}$ ,  ${}^{37}\text{Ca}$ ,  ${}^{40}\text{Sc}$ ,  ${}^{41}\text{Ti}$ , and  ${}^{23}\text{Al}$ . These measurements spanned a proton energy range from 600 keV to 8.5 MeV, and included all significant particle decays of these nuclei. A helium-jet transport system was developed and used with various  $\Delta E$ -E counter telescopes to obtain high-resolution, low-background spectra. These data permitted accurate location of proton unbound levels in the beta-decay daughters, and absolute branching ratios and  $ft$  values for these allowed decays have been determined.

The half-lives of these nuclei have been measured, and all except that for  ${}^{41}\text{Ti}$  are consistent with the previous values. For  ${}^{41}\text{Ti}$ , the half-life is  $80 \pm 2$  msec, which differs from the old value of  $88 \pm 1$  msec. This latter value is thought to have been affected by the presence of  ${}^{37}\text{Ca}$  activity produced in a competing reaction.

The  $ft$  values for  ${}^{21}\text{Mg}$  and  ${}^{25}\text{Si}$  are compared to the neutron decay rates in their respective mirrors. For mass 21,  $(ft)^+ - (ft)^- = 1.10 \pm 0.08$ , while for mass 25 this ratio is  $1.17 \pm 0.04$ . A comparison of predicted and observed beta-decay rates for the superallowed decay to the  $T = 3/2$  state in  ${}^{41}\text{Sc}$  indicates that this level has an isospin impurity of  $\sim 8\%$ .

The observed beta-decay rates in  ${}^{21}\text{Mg}$  and  ${}^{37}\text{Ca}$  are also contrasted with theoretical predictions for decay rates to their respective daughters. The calculated values agree well for  ${}^{21}\text{Mg}$ , while for  ${}^{37}\text{Ca}$  the calculations appear to be limited by the basis space used.

Delayed protons from  $^{23}\text{Al}$ , the first member of the  $A = 4n + 3$  series of  $T_z = 3/2$  nuclei, have been observed, and the half-life of  $^{23}\text{Al}$  has been measured to be  $470 \pm 30$  msec. In addition, delayed protons from  $^{40}\text{Sc}$  were studied in order to ascertain their contribution to the proton spectra obtained from  $^3\text{He}$  bombardment of  $^{40}\text{Ca}$ .

### SYSTEMATICS OF THE $(\alpha, 2\alpha)$ REACTION AT $E_\alpha = 90$ MeV

Joseph Donald Sherman

(LBL-1690)

A coincidence technique has been used to study the  $(\alpha, 2\alpha)$  reaction on a series of nuclei at  $E_\alpha = 90$  MeV. Typically, resolutions of 250-300 keV FWHM have been achieved for the kinematic bands lying in the  $T_3 + T_4$  vs.  $T_3$  kinetic energy plane. Nine targets from  $^{12}\text{C}$  to  $^{66}\text{Zn}$  have been studied. The most complete experimental data were taken on the  $^{12}\text{C}$  and  $^{16}\text{O}$  targets in order to define the angular correlation shape so that a three body reaction theory could be more completely tested. The  $^{12}\text{C}(\alpha, 2\alpha)^8\text{Be}$  and  $^{16}\text{O}(\alpha, 2\alpha)^{12}\text{C}$  reactions included symmetric angle measurements from  $19^\circ$  to  $47^\circ$  in approximate  $4^\circ$  steps; also, an asymmetric angular correlation with one counter fixed at  $42^\circ$  and the other counter ranging from  $25^\circ$  to  $47^\circ$  in  $3^\circ$  steps was taken. Since data were obtained in the energy plane, energy and momentum correlations were also extracted.

The seven remaining targets studied by the  $(\alpha, 2\alpha)$  reaction were  $^{24}\text{Mg}$ ,  $^{26}\text{Mg}$ ,  $^{28}\text{Si}$ ,  $^{30}\text{Si}$ ,  $^{40}\text{Ca}$ , and  $^{66}\text{Zn}$ . Symmetric angular correlations were taken in the  $28^\circ$  to  $47^\circ$  range for these nuclei, typically taking four angular settings for each target. In all cases data were taken at the symmetric quasi-elastic angle. A prominent systematic feature to emerge from this study was the predominance of the ground state transitions. The  $^{40}\text{Ca}(\alpha, 2\alpha)^{36}\text{Ar}$  reaction was the only nucleus to yield excited state cross sections that were comparable to the ground state transition. Another systematic item was that after a rapid fall of cross section from the p-shell nuclei to the sd-shell nuclei, the  $(\alpha, 2\alpha)$  cross sections were found to be nearly constant from the Si isotopes to  $^{66}\text{Zn}$ . The angular correlations for transitions to the ground states of these nuclei are very similar.

A distorted wave impulse approximation (DWIA) calculation was developed; the distortions were described by McCarthy-Pursey wave functions with the focus term set equal to zero. The DWIA was found to fit the angular correlations in shape and magnitude. Systematic features of the energy correlations were also described quite well, although the momentum correlations were fit in shape and magnitude only for  $q \leq 0.5$  (fm) $^{-1}$ . The model was used to extract relative spectroscopic factors from  $^{12}\text{C}$  to  $^{66}\text{Zn}$ , and these results were in good agreement with spectroscopic factors obtained from a DWBA analysis of a systematic ( $^3\text{He}$ ,  $^7\text{Be}$ ) study.

The  $^{16}\text{O}(\alpha, 2\alpha)^{12}\text{C}$  reaction was found to populate the  $^{12}\text{C}$  ground state most strongly, whereas the (d,  $^6\text{Li}$ ) and ( $^3\text{He}$ ,  $^7\text{Be}$ ) reactions have preferentially populated the  $^{12}\text{C}(4.44)$  level. Also, theoretical calculations have shown that the  $\{^{12}\text{C}(4.44)^+\}$  configuration is the principal parent of the  $^{16}\text{O}$  nucleus in an alpha cluster model. Analysis within the plane wave impulse approximation (PWIA) of the  $^{16}\text{O}(\alpha, 2\alpha)^{12}\text{C}$  reaction still indicated that the  $^{12}\text{C}(0.0)$  was receiving most of the  $(\alpha, 2\alpha)$  transition strength. This result indicates that the  $(\alpha, 2\alpha)$  and alpha pickup reactions are probing four particle correlations in different manners, and a careful theoretical analysis of the  $(\alpha, 2\alpha)$  reaction mechanism would be very valuable to nuclear structure studies if these differences were elucidated.

EXCITATION ENERGIES IN AN ELECTRICALLY PULSED LIGHT-EMISSION SOURCE  
 APPLIED TO THE SEPARATION OF HIGHER IONIZED ATOMIC STATES:  
 SPECTRA AND ENERGY LEVELS OF SCANDIUM 2+ AND VANADIUM 4+

Cornelius H. H. Van Deurzen

(LBL-1657)

Spectra of vanadium have been produced in a vacuum sliding spark and their relative line intensities measured as parameters of the electrical circuit were varied. Intensity maxima of the spectral lines are interpreted as representing excitation energies and have been found to depend in a definitive manner on the power delivered to the source and on the duration of the discharge. The differential equation of the circuit is solved for the charge and energy transfer rates from the capacitor to the source, and two functions of the continuous circuit parameter

$$\gamma \equiv \frac{C}{L} \left(\frac{R}{2}\right)^2$$

are defined which greatly assist in interpreting the effect of the circuit parameters on the excitation in the source. With these solutions, the relationship between the excitation in the source and the electrical circuit parameters may be expressed in terms of the inductance, capacitance, the initial voltage on the capacitor, the two known functions one of which is directly associated with the power delivered to the source during a current pulse and the other with the discharge duration, and two constants which in general depend on the source geometry and the electrode sample material.

The circuit parameters were varied to excite and separate spectra of scandium (Sc II and Sc III) by observing total light pulses and spectra of vanadium (V II - V V) by observing both total and time-resolved light pulses. For Sc III, 93 lines are reported in the region 550 Å - 9400 Å which give rise to 23 new levels with an accuracy of about 0.03 cm<sup>-1</sup> and the ionization energy is revised to 199677.37 ± 0.1 cm<sup>-1</sup>. The results for Sc III have been published in J. Opt. Soc. Am. 63, 158 (1973). For V V, 61 lines in the region 480 Å - 8500 Å give rise to 18 new levels and the ionization energy is revised to 526524 ± 5 cm<sup>-1</sup>. The ionization energies have been calculated with a method presented here that allows the use of all the known levels in a series simultaneously. Series formulae are presented which are used to predict some of the newly found levels to within 0.25 cm<sup>-1</sup>. An isoelectronic comparison confirms the inversion of the 3p<sup>6</sup>4f<sup>2</sup>F<sub>5/2</sub><sup>o</sup>, 7/2 levels in V V as being caused by the interaction of these levels with those of the <sup>2</sup>F<sup>o</sup> term in the 3p<sup>5</sup>3d<sup>2</sup> configuration.

GEOMETRY OF SOME METAL HALIDES

Peter Alan Yarnell

(LBL-1973)

Two polarizable ion models are developed to describe the gas phase of metal dihalide molecules. Both models employ electrostatic and repulsive interactions to predict molecular geometries and molecular constants. The first model is applied to the dihalides of the alkaline earths, group II-b metals, transition metals, group IV-a metals, and europium. In addition to the molecular geometry, bending frequencies ( $\nu_2$ ) are derived for most of these molecules. The second or "linear" model is applied to the alkaline earth dihalides; equilibrium internuclear bond lengths ( $\ell$ ), stretching force constants ( $k_1$ ) and stretching frequencies ( $\nu_1$  and  $\nu_3$ ) are determined.

Some of the structural predictions of the polarizable ion model are correlated with experimental data from molecular beam electric deflection spectroscopy. Certain alkaline earth dihalides ( $\text{BaF}_2$ ,  $\text{BaCl}_2$ ,  $\text{SrCl}_2$ ,  $\text{SrBr}_2$ ,  $\text{SrI}_2$ ,  $\text{CaF}_2$ ,  $\text{CaCl}_2$ ,  $\text{MgF}_2$ , and  $\text{MgCl}_2$ ) and lanthanum trifluoride ( $\text{LaF}_3$ ) have been reinvestigated to resolve contradictions in some of the earlier experimental work. Significantly improved sensitivity allows more precise determination of geometry. Also, the gas phase geometries of  $\text{EuCl}_2$ ,  $\text{EuBr}_2$ , and  $\text{EuI}_2$  have been determined using this technique. The correlation between the europium dihalide geometries and analogous alkaline earth dihalides is explored.

## VI. 1973 Publications



## PAPERS PUBLISHED AND LBL REPORTS ISSUED, 1973

- ALBEE, A., (See Heizer, R. F., LBL-1624)
- ALONSO, C. T., (See Rezanka, I., LBL-1223)
- ALONSO, J. R., (Rezanka, I., LBL-1223)
- ALONSO, J., (See Tamura, T., LBL-1689)
- ALONSO, J. R., and B. G. Harvey  
 Considerations of beam quality requirements for experiments with very heavy ions  
 LBL-1698-Rev., May 1973  
 NFP
- ANHOLT, R., and J. O. Rasmussen  
 Theoretical x-ray transition probabilities for high-Z superheavy elements  
 LBL-1947, July 1973  
 Phys. Rev. A 9, 585 (1974)
- ASARO, F., (See Bowman, H. R., LBL-661)
- ASARO, F., (See Perlman, I., LBL-674)
- ASARO, F., (See Browne, E., LBL-1606)
- ASARO, F., (See Heizer, R. F., LBL-1624)
- ASARO, F., (See Widemann, F., LBL-1964)
- ASCUITTO, R. J., and N. K. Glendenning  
 The effect of indirect transitions on two nucleon transfer between heavy ions and their  
 Q-dependence  
 LBL-1645, March 1973  
 Phys. Letters 45B, 85 (1973)
- ASCUITTO, R. J., (See Glendenning, N. K., LBL-1647)
- ASCUITTO, R. J., and N. K. Glendenning  
 On the systematics of the interference between direct and indirect modes in two-nucleon  
 pickup and stripping reactions between heavy-ions  
 LBL-1987, September 1973  
 Phys. Letters 47B, 332 (1973)
- ASCUITTO, R. J., and N. K. Glendenning  
 The sensitivity of the forward cross section in transfer reactions between heavy ions to the  
 edge of the nuclear field  
 LBL-1990, September 1973  
 Phys. Letters 48B, 6 (1974)
- ATCHER, R. W., (See Huizenga, J. R., LBL-2314)
- ATCHER, R. W., (See Huizenga, J. R., LBL-2316)
- BABINET, R., (See Nifenecker, H., LBL-1950)

- BABINET, R. P., (See Moretto, L. G., LBL-2332)
- BACHER, A. D., F. G. Resmini, H. E. Conzett, R. de Swiniarski, H. Meiner, and J. Ernst  
Observation of high-lying levels in  $^8\text{Be}$  from  $\alpha$ - $\alpha$  elastic scattering  
LBL-1228, August 1972  
Phys. Rev. Letters 29, 1331 (1972)
- BACHER, A. D., (See Macdonald, J. A., LBL-2317)
- BACHER, A. D., (See de Swiniarski, R., LBL-2322)
- BACON, F., G. Kaindl, H. -E. Mahnke, and D. A. Shirley  
Nuclear magnetic resonance of oriented  $^{196}\text{Au}$ ,  $^{198}\text{Au}$ , and  $^{200}\text{mAu}$   
LBL-1289, November 1972  
Phys. Rev. C 7, 1654 (1973)
- BACON, F., (See Kaindl, G., LBL-1638)
- BACON, F., (See Kaindl, G., LBL-1684)
- BACON, F., (See Kaindl, G., LBL-1960)
- BAER, H. W., (See Vergados, J. D., LBL-690)
- BAER, W., J. G. Conway, and S. P. Davis  
The crystal spectrum of promethium 3+ in  $\text{LaCl}_3$   
LBL-1642, January 1973  
J. Chem. Phys. 59, 2294 (1973)
- BANNA, M. S., (See Davis, D. W., LBL-1909)
- BANNA, M. S., (See Davis, D. W., LBL-1915)
- BASKIN, C. P., (See Yarkony, D. R., LBL-1969)
- BASKIN, C. P., (See Schwenzer, G. M., LBL-1983)
- BASKIN, C. P., C. F. Bender, C. W. Bauschlicher, Jr., and H. F. Schaefer III  
Reaction pathways for the triplet methylene abstraction  $\text{CH}_2(^3\text{B}_1) + \text{H}_2 \rightarrow \text{CH}_3 + \text{H}$   
LBL-2324, November 1973  
J. Am. Chem. Soc.
- BAUSCHLICHER Jr., C. W., S. V. O'Neil, R. K. Preston, H. F. Schaefer III, and  
C. F. Bender  
Avoided intersection of potential energy surfaces: the  $(\text{H}^+ + \text{H}_2, \text{H} + \text{H}_2^+)$  system  
LBL-1664, March 1973  
J. Chem. Phys. 59, 1286 (1973)
- BAUSCHLICHER Jr., C. W., (See Baskin, C. P., LBL-2324)
- BECCHETTI, F. D., D. G. Kovar, B. G. Harvey, J. Mahoney, B. Mayer, and F. G. Pühlhofer  
Inelastic scattering of  $^{16}\text{O}$  from  $^{208}\text{Pb}$   
LBL-695, July 1972  
Phys. Rev. C 6, 2215 (1972)
- BECCHETTI, F. D., (See Kovar, D. G., LBL-1646)

- BECCHETTI, F. D.  
Inelastic scattering of heavy ions  
LBL-1653, March 1973  
Talk presented at the ANL Heavy Ion Symposium, Physics Division, Tandem Laboratory,  
Argonne National Laboratory, Argonne, Illinois, March 13-21, 1973
- BECCHETTI, F. D., (See Zisman, M. S., LBL-1676)
- BECCHETTI, F. D., D. G. Kovar, B. G. Harvey, D. L. Hendrie, H. Homeyer, J. Mahoney,  
W. von Oertzen, and N. K. Glendenning  
A study of the two proton transfer reactions  $^{208}\text{Pb}(^{12}\text{C}, ^{10}\text{Be})^{210}\text{Po}$  and  $^{208}\text{Pb}(^{16}\text{O}, ^{14}\text{C})^{210}\text{Po}$   
LBL-1972, August 1973  
Phys. Rev. C
- BECCHETTI, F. D., (See DeVries, R. M., LBL-2363)
- BEHKAMI, A. N., (See Huizenga, J. R., LBL-2314)
- BEHKAMI, A. N., (See Huizenga, J. R., LBL-2316)
- BENDER, C. F., (See Liskow, D. H., LBL-696)
- BENDER, C. F., (See O'Neil, S. V., LBL-1200)
- BENDER, C. F., (See Pearson, P. K., LBL-1605)
- BENDER, C. F., (See Bauschlicher Jr., C. W., LBL-1664)
- BENDER, C. F., (See O'Neil, S. V., LBL-1665)
- BENDER, C. F., (See O'Neil, S. V., LBL-1913)
- BENDER, C. F., (See Yarkony, D. R., LBL-1969)
- BENDER, C. F., (See Schwenzler, G. M., LBL-1983)
- BENDER, C. F., (See Liskow, D. H., LBL-2302)
- BENDER, C. F., (See Baskin, C. P., LBL-2324)
- BENNETT-CORNIEA, W., (See Garrison, W., LBL-1269)
- BENSON Jr., D., C. M. Lederer, and E. Cheifetz  
Search for  $\gamma$ -rays emitted in the formation of a fission isomer  
LBL-1216, August 1972  
Nucl. Phys. A201, 445 (1973)
- BENSON Jr., D., (See Stephens, F. S., LBL-1282)
- BERNTHAL, F. M., (See Rezanka, I., LBL-1223)
- BERNTHAL, F. M., (See Massmann, H., LBL-1693)
- BOHLEN, H. G., (See von Oertzen, W., LBL-1622)
- BORYSOWICZ, J., (See Wagner, W. T., LBL-1938)

- BOWMAN, H. R., (See Hebert, A. J., LBL-601)
- BOWMAN, H. R., F. Asaro, and I. Perlman  
On the uniformity of composition in obsidians and evidence for magmatic mixing  
LBL-661, April 1972  
J. Geol. 81, 312 (1973)
- BOWMAN, H., (See Heizer, R. F., LBL-1624)
- BOWMAN, J. D., A. M. Poskanzer, R. G. Korteling, and G. W. Butler  
Discovery of two isotopes,  $^{14}\text{Be}$  and  $^{17}\text{B}$ , at the limits of particle stability  
LBL-1937, June 1973  
Phys. Rev. Letters 31, 614 (1973)
- BOWMAN, J. D., A. M. Poskanzer, R. G. Korteling, and G. W. Butler  
The detection of neutron excess isotopes of low Z elements produced in high energy nuclear reactions  
LBL-1967, September 1973  
Phys. Rev. C
- BRITT, H. C., (See Huizenga, J. R., LBL-2316)
- BROWN, D., (See Edelstein, N., LBL-2348)
- BROWN, N. E., (See Giaque, R. D., LBL-1697)
- BROWNE, E., and F. Asaro  
Nuclear spectroscopy studies on the alpha decay of  $^{235}\text{Np}$  and beta decay of  $^{231}\text{Th}$   
LBL-1606, January 1973  
Phys. Rev. C 7, 2545 (1973)
- BUCHER, J., R. Zuehl, and R. M. Diamond  
Anion and diluent stabilization of tributyl phosphate and tris-ethylhexyl phosphate complexes in the extraction of  $\text{HAuCl}_4$ ,  $\text{HReO}_4$ ,  $\text{HI}$ , and  $\text{HBr}$   
LBL-2342, December 1973  
J. Inorg. Nucl. Chem.
- BUTLER, G. W., (See Bowman, J. D., LBL-1937)
- BUTLER, G. W., (See Bowman, J. D., LBL-1967)
- CAVELL, R. G., S. P. Kowalczyk, L. Ley, R. A. Pollak, B. Mills, D. A. Shirley, and W. Perry  
X-ray photoemission cross-section modulation in diamond, silicon, germanium, methane, silane, and germane  
LBL-1213, November 1972  
Phys. Rev. B 7, 5313 (1973)
- CAVELL, R. G., (See McFeely, F. R., LBL-1989)
- CERNY, J., (See Gough, R. A., LBL-1292)
- CERNY, J., (See Sextro, R. G., LBL-1600)
- CERNY, J., (See Wilcox, K. H., LBL-1644)
- CERNY, J., (See Wozniak, G. J., LBL-1904)

- CERNY, J., (See Macdonald, J. A., LBL-1982)
- CERNY, J., (See Macdonald, J. A., LBL-2317)
- CERNY, J., (See Jelley, N. A., LBL-2329)
- CHADI, D. J., (See Pollak, R. A., LBL-1204)
- CHAPUIS, G., A. Zalkin, and D. H. Templeton  
5-hydroxy-2,3-norbornane dicarboxylic acid  $\gamma$ -lactone  
LBL-1696, May 1973  
Acta Cryst. B29, 2642 (1973)
- CHEIFETZ, E., (See Benson, D., LBL-1216)
- CLEM, R. G., G. Litton, and L. D. Ornelas  
New cell for rapid anodic stripping analysis. User-interactive computer program for  
analysis of anodic stripping data  
LBL-679-Rev., December 1972  
Anal. Chem. 45, 1306 (1973)
- CLEM, R. G.  
Polarography present  
LBL-1295, November 1972  
Industrial Research (magazine, January 1973)
- CLEM, R. G.  
Coulometry present  
LBL-1694, May 1973  
Industrial Research
- COHEN, M. L., (See Pollak, R. A., LBL-1204)
- COHEN, M. L., (See Varea de Alvarez, C., LBL-2330)
- CONWAY, J. G., (See Van Deurzen, C. H., LBL-1217)
- CONWAY, J. G., (See Baer, W., LBL-1642)
- CONWAY, J. G., (See Van Deurzen, C. H. H., LBL-1975)
- CONWAY, J. G., (See Van Deurzen, C. H. H., LBL-1986)
- CONWAY, J. G., (See Worden, E. F., UCRL-74650)
- CONZETT, H. E., (See Bacher, A. D., LBL-1228)
- CONZETT, H. E., (See de Swiniarski, R., LBL-1620)
- CONZETT, H. E., (See Lamontagne, C. R., LBL-1941)
- CRAMER, J. G., (See DeVries, R. M., LBL-2363)
- CRAWLEY, G. M., (See Wagner, W. T., LBL-1938)

- DAVENPORT, I. F., and C. J. King  
Marangoni stabilization of density-driven convection  
LBL-608, January 1972  
Chem. Eng. Sci. Comm. 28, 645 (1972)
- DAVENPORT, I. F., and C. J. King  
Natural convection from time-dependent profiles at a gas-liquid surface  
LBL-1998, October 1973  
Int. J. Heat Mass Transfer 17, 77 (1974)
- DAVENPORT, I. F., and C. J. King  
The onset of natural convection from time-dependent profiles  
LBL-1999, October 1973  
Int. J. Heat Mass Transfer
- DAVIS, D. W.  
Core-level photoelectron spectroscopy of small molecules  
LBL-1900, May 1973  
Ph. D. Thesis
- DAVIS, D. W., M. S. Banna, and D. A. Shirley  
Core-level binding energy shifts in small molecules  
LBL-1909, July 1973  
J. Chem. Phys.
- DAVIS, D. W., R. L. Martin, M. S. Banna, and D. A. Shirley  
Multiplet splitting in 1s hole states of molecules  
LBL-1915, June 1973  
J. Chem. Phys. 59, 4235 (1973)
- DAVIS, D. W., and D. A. Shirley  
The prediction of core-level binding-energy shifts from CNDO molecular orbitals  
LBL-1970, August 1973  
J. Electr. Spectrosc.
- DAVIS, S. P., (See Van Deurzen, C. H., LBL-1217)
- DAVIS, S. P., (See Baer, W., LBL-1642)
- DAVIS, S. P., (See Van Deurzen, C. H. H., LBL-986)
- de SWINIARSKI, R., (See Bacher, A. D., LBL-1228)
- de SWINIARSKI, R., H. E. Conzett, C. R. Lamontagne, B. Frois, and R. J. Slobodrian  
Excitation of the ground-state rotational band in  $^{28}\text{Si}$  by inelastic scattering of 25.25 MeV polarized protons  
LBL-1620, February 1973  
Canadian J. Phys.
- de SWINIARSKI, R., (See Lamontagne, C. R., LBL-1941)
- de SWINIARSKI, R., F. G. Resmini, D. L. Hendrie, and A. D. Bacher  
Study of  $^{16}\text{O}$ ,  $^{20}\text{Ne}$ ,  $^{22}\text{Ne}$ ,  $^{28}\text{Si}$  and  $^{32}\text{S}$  by inelastic scattering of polarized protons  
LBL-2322, October 1973  
Nucl. Phys.

- DeVRIES, R. M., M. S. Zisman, J. G. Cramer, K.-L. Liu, F. D. Becchetti, B. G. Harvey, H. Homeyer, D. G. Kovar, and W. von Oertzen  
 Observation of an anomalous angular distribution in the single nucleon transfer reaction  $^{12}\text{C}(^{14}\text{N}, ^{13}\text{N})^{13}\text{C}$  at 100 MeV  
 LBL-2363, December 1973  
 Phys. Rev. Letters
- DIAMOND, R. M., (See Newton, J. O., LBL-1227)
- DIAMOND, R. M., (See Stephens, F. S., LBL-1282)
- DIAMOND, R. M., (See Leigh, J. R., LBL-1601)
- DIAMOND, R. M., (See Stephens, F. S., LBL-1607)
- DIAMOND, R. M., (See Nakai, K., LBL-1614)
- DIAMOND, R. M., (See Kenjo, T., LBL-1630)
- DIAMOND, R. M., (See Proetel, D., LBL-1939)
- DIAMOND, R. M., (See Gizon, J., LBL-1948)
- DIAMOND, R. M., (See Kienle, P., LBL-1961)
- DIAMOND, R. M., (See Grosse, E., LBL-1962)
- DIAMOND, R. M., (See Kleinheinz, P., LBL-1994)
- DIAMOND, R. M., (See Grosse, E., LBL-1997)
- DIAMOND, R. M., (See Proetel, D., LBL-2309)
- DIAMOND, R. M., (See Bucher, J., LBL-2342)
- DIAMOND, R. M.  
 Lectures on heavy-ion in-beam spectroscopy  
 LBL-2346, December 1973  
 Talk presented at the Institute for Nuclear Studies Summer School, Dogashima, Japan, August 22, 1972
- EDELSTEIN, N., (See Stacy, J. J., LBL-638)
- EDELSTEIN, N., and R. G. Hayes  
 An elementary molecular orbital calculation on  $\text{U}(\text{C}_8\text{H}_8)_2$  and its application to the electronic structures of  $\text{U}(\text{C}_8\text{H}_8)_2$ ,  $\text{Np}(\text{C}_8\text{H}_8)_2$ , and  $\text{Pu}(\text{C}_8\text{H}_8)_2$   
 LBL-650, April 1972  
 J. Am. Chem. Soc. 94, 8688 (1972)
- EDELSTEIN, N., (See Rajnak, K., LBL-1218)
- EDELSTEIN, N., D. Brown, and B. Whittaker  
 Covalency effects on the ligand field splittings of octahedral  $5f^1$  compounds  
 LBL-2348, August 1973  
 Inorg. Chem.
- ERNST, J., (See Bacher, A. D., LBL-1228)

- ESKOLA, K., (See Eskola, P., LBL-2315)
- ESKOLA, P., K. Eskola, M. Nurmi, and A. Ghiorso  
Two new isotopes of einsteinium,  $^{243}\text{Es}$  and  $^{244}\text{Es}$   
LBL-2315, October 1972  
Physica Fennica
- FAIVRE, J.-C., (See Hendrie, D. L., LBL-656)
- FEE, D. C.; and S. S. Markowitz  
Scavenger effects in the recoil tritium reactions of cyclohexene  
LBL-668, May 1972  
J. Inorg. Nucl. Chem. 35, 2153 (1973)
- FEE, D. C., and S. S. Markowitz  
Multicolumn radio-gas chromatographic analysis of recoil tritium reaction products  
LBL-1249, September 1972  
Anal. Chem. 45, 1827 (1973)
- FEE, D. C., and S. S. Markowitz  
Design of a high-temperature neutron irradiation container  
LBL-1264, October 1972  
Nucl. Instr. Methods 109, 445 (1973)
- FEE, D. C.  
Recoil tritium reactions with cyclohexene and methylcyclohexene  
LBL-1687, June 1973  
Ph. D. Thesis
- FEE, D. C., and S. S. Markowitz  
Recoil tritium reactions with cyclohexene and alkenes. Determination of rate parameters  
LBL-1906, June 1973  
J. Phys. Chem. 78, 347 (1974)
- FEE, D. C., and S. S. Markowitz  
Recoil tritium reactions with methylcyclohexene: a test of the assumption of energy  
randomization prior to unimolecular decomposition  
LBL-1910, June 1973  
J. Phys. Chem.
- FEE, D. C., and S. S. Markowitz  
Recoil tritium reactions with alkenes: formation of "polymer-T"  
LBL-1949, July 1973  
J. Inorg. Nucl. Chem.
- FREIESLEBEN, H., (See Huizenga, J. R., LBL-2316)
- FROIS, B., (See de Swiniarski, R., LBL-1620)
- FROIS, B., (See Lamontagne, C. R., LBL-1941)
- GARRISON, W., H. A. Sokol, and W. Bennett-Corniea  
Radiation chemistry of glycylglycine in oxygen-free systems  
LBL-1269, October 1972  
Radiation Res. 53, 376 (1973)
- GATTI, R. C., (See Moretto, L. G., LBL-1966)



GEBAUER, B., (See von Oertzen, W., LBL-1622)

GENEUX, E., (See Hadeishi, T., LBL-1260)

GHIORSO, A., K. Eskola, P. Eskola, and M. Nurmia  
Isomeric states in  $^{250}\text{Fm}$  and  $^{254}\text{No}$   
LBL-1277, October 1972  
Phys. Rev. C 7, 2032 (1973)

GHIORSO, A.

Progress with the superhilac

LBL-1659, March 1973

Particle Accelerator Conference, San Francisco, California, March 5-7, 1973

GHIORSO, A.

The superhilac and the berkeley superheavy element program

LBL-1992, September 1973

Talk presented at the XXIV<sup>th</sup> International Congress of Pure and Applied Chemistry,  
Hamburg, Germany, September 3-8, 1973

GHIORSO, A., (See Eskola, P., LBL-2315)

GIAUQUE, R. D., F. S. Goulding, J. M. Jaklevic, and R. H. Pehl

Trace element determination with semiconductor detector x-ray spectrometers

LBL-647, July 1972

Anal. Chem. 45, 671 (1973)

GIAUQUE, R. D., L. Y. Goda, and N. E. Brown

Characterization of aerosols in california by x-ray induced x-ray fluorescence analysis

LBL-1697, July 1973

Environ. Sci. Technol.

GIZON, A., (See Gizon, J., LBL-1948)

GIZON, J., A. Gizon, M. R. Maier, R. M. Diamond, and F. S. Stephens

Deformed states of neutron-deficient cerium and neodymium nuclei

LBL-1948, July 1973

Nucl. Phys.

GLENDENNING, N. K., (See Schaeffer, R., LBL-689)

GLENDENNING, N. K., (See Ascutto, R. J., LBL-1645)

GLENDENNING, N. K., and R. J. Ascutto

Theoretical study of two nucleon transfer between heavy ions including the effect of  
inelastic processes

LBL-1647, March 1973

Symposium on Heavy-Ion Transfer Reactions, Argonne National Laboratory, Argonne,  
Illinois, March 15-17, 1973

GLENDENNING, N. K., (See Becchetti, F. D., LBL-1972)

GLENDENNING, N. K., (See Ascutto, R. J., LBL-1987)

GLENDENNING, N. K., (See Ascutto, R. J., LBL-1990)

- GO, M. K., and S. S. Markowitz  
Test of the independence postulate in the bohr theory of compound-nucleus decay:  $^{50}\text{Cr}^*$   
system  
LBL-1230, August 1972  
Phys. Rev. C 7, 1464 (1973)
- GODA, L. Y., (See Giauque, R. D., LBL-1697)
- GOUGH, R. A.  
Yrast tables  
LBL-624, February 1972  
NFP
- GOUGH, R. A., R. G. Sextro, and J. Cerny  
On the lowest  $T = 3/2$  state in  $^{41}\text{Sc}$   
LBL-1292, November 1972  
Phys. Letters 43B, 33 (1973)
- GOUGH, R. A., (See Sextro, R. G., LBL-1600)
- GOULD, H., R. Marrus, and R. W. Schmieder  
Lifetime of the  $2^3\text{S}_1$  state of heliumlike argon ( $Z = 18$ ) and heliumlike titanium ( $Z = 22$ )  
LBL-1658-Rev., June 1973  
Phys. Rev. Letters 31, 504 (1973)
- GOULDING, F. S., (See Giauque, R. D., LBL-647)
- GRANT, R. W., (See Varea de Alvarez, C., LBL-2330)
- GROSSE, E. H., (See Kienle, P., LBL-1961)
- GROSSE, E., F. S. Stephens, and R. M. Diamond  
Test of backbending models using odd-A nuclei  
LBL-1962, July 1973  
Phys. Rev. Letters 31, 840 (1973)
- GROSSE, E., F. S. Stephens, and R. M. Diamond  
Backbending in odd-A Ho isotopes  
LBL-1997, October 1973  
Phys. Rev. Letters 32, 74 (1974)
- GRUHN, C. R., (See Petrovich, F., LBL-1651)
- GUTMACHER, R. G., (See Worden, E. F., UCRL-74650)
- HAAS, H., (See Shirley, D. A., LBL-667)
- HAAS, H., and D. A. Shirley  
Nuclear quadrupole interaction studies by perturbed angular correlations  
LBL-1284, October 1972  
J. Chem. Phys. 58, 3339 (1973)
- HADEISHI, T., M. C. Michel, J. Yellin, and E. Geneux  
Improved resolution methods for beam foil spectroscopy  
LBL-1260, February 1973  
Nucl. Instr. Methods 110, 445 (1973)
- HADEISHI, T., (See Yellin, J., LBL-1602)

- HADEISHI, T., (See Yellin, J., LBL-1608)
- HALBACH, K.  
Field correction windings for iron magnets  
UCRL-18969, November 1970  
Nucl. Instr. Methods 107, 515 (1973)
- HALBACH, K.  
Some eddy current effects in solid core magnets  
LBL-1242, September 1972  
Nucl. Instr. Methods 107, 529 (1973)
- HAMMERSTEIN, G. R., R. H. Howell, and F. Petrovich  
Electron and proton inelastic scattering from  $^{40}\text{Ca}$ ,  $^{120}\text{Sn}$ , and  $^{208}\text{Pb}$   
LBL-1626, January 1973  
Nucl. Phys. A213, 45 (1973)
- HAMMERSTEIN, G. R., (See Wagner, W. T., LBL-1938)
- HAND, R. W., W. J. Hunt, and H. F. Schaefer III  
Electronic structure of iron trifluoride  
LBL-1632, February 1973  
J. Am. Chem. Soc. 95, 4517 (1973)
- HARDY, J. C., (See Macdonald, J. A., LBL-2317)
- HARNEY, H. L., (See Robson, D., LBL-1643)
- HARNEY, H. L., (See Wilcox, K. H., LBL-1644)
- HARNEY, H. L., (See Macdonald, J. A., LBL-2317)
- HARVEY, B. G., (See Hendrie, D. L., LBL-656)
- HARVEY, B. G., (See Becchetti, F. D., LBL-695)
- HARVEY, B. G., (See Kovar, D. G., LBL-1646)
- HARVEY, B. G., (See Zisman, M. S., LBL-1676)
- HARVEY, B. G., (See Alonso, J. R., LBL-1698-Rev.)
- HARVEY, B. G., (See Becchetti, F. D., LBL-1972)
- HARVEY, B. G., (See DeVries, R. M., LBL-2363)
- HAUSTEIN, P. E., (See Massmann, H., LBL-1693)
- HAYES, R. G., (See Edelstein, N., LBL-650)
- HEBERT, A. J., H. R. Bowman, and K. Street, Jr.  
A method of rapid thin sample preparation for x-ray fluorescence analysis with  
semiconductor detectors  
LBL-601, February 1973  
NFP

- HEBERT, A. J., and K. Street, Jr.  
Nondispersive soft x-ray fluorescence spectrometer for quantitative analysis of the major elements in rocks and minerals  
LBL-1616-Rev., April 1973  
Anal. Chem. 46, 203 (1974)
- HEIZER, R. F., F. Stross, T. R. Hester, A. Albee, I. Perlman, F. Asaro, and H. Bowman  
The colossi of memnon revisited  
LBL-1624, November 1973  
Science 182, 1219 (1973)
- HENDRIE, D. L., B. G. Harvey, J. R. Meriwether, J. Mahoney, J.-C. Faivre, and D. G. Kovar  
Multipole deformation of  $^{238}\text{U}$   
LBL-656-Rev., April 1972  
Phys. Rev. Letters 30, 571 (1973)
- HENDRIE, D. L., (See Kovar, D. G., LBL-1646)
- HENDRIE, D. L., (See Becchetti, F. D., LBL-1972)
- HENDRIE, D. L.  
Comparison of nuclear and coulomb measurements of nuclear shapes  
LBL-1692, May 1973  
Phys. Rev. Letters 31, 478 (1973)
- HENDRIE, D. L., (See de Swiniarski, R., LBL-2322)
- HESTER, T., (See Heizer, R. F., LBL-1624)
- HEUNEMANN, D., (See Moretto, L. G., LBL-1966)
- HINRICHS, R. A., D. Larson, B. M. Freedom, W. G. Love, and F. Petrovich  
 $^{90}\text{Zr}(p, p')^{90}\text{Zr}$  reaction at 40 MeV  
LBL-1649, July 1973  
Phys. Rev. C 7, 1981 (1973)
- HOLLANDER, F. J., D. H. Templeton, and A. Zalkin  
Investigations of alkaline-earth  $\beta$ -diketone complexes. I. The crystal and molecular structure of bis(dimethylformamido)bis-(1, 3-diphenyl-1, 3-propanedionato)magnesium  
LBL-1266, September 1972  
Acta Cryst. B29, 1289 (1973)
- HOLLANDER, F. J., D. H. Templeton, and A. Zalkin  
Investigations of alkaline-earth  $\beta$ -diketone complexes. II. The crystal and molecular structure of bis-(1, 3-diphenyl-1, 3-propanedionato)calcium hemiethanolate  
LBL-1267, September 1972  
Acta Cryst. B29, 1295 (1973)
- HOLLANDER, F. J., D. H. Templeton, and A. Zalkin  
Investigations of alkaline-earth  $\beta$ -diketone complexes. III. The crystal and molecular structure of bis-(1, 3-diphenyl-1, 3-propanedionato)strontium hemiacetonate  
LBL-1268, September 1972  
Acta Cryst. B29, 1303 (1973)

- HOLLANDER, F. J., D. H. Templeton, and A. Zalkin  
The crystal and molecular structure of 1, 3-diphenyl-1, 3-propanedione enol  
LBL-1273, October 1972  
Acta Cryst. B29, 1552 (1973)
- HOLLANDER, F. J., D. H. Templeton, and A. Zalkin  
Crystal and molecular structure of triphenylmethylphosphonium 1, 1, 1-tricarbonyl-4, 6-dicarba-1-mangana-closo-nonaborate(1-)  
LBL-1661, April 1973  
Inorg. Chem. 12, 2262 (1973)
- HOLLANDER, J. M., (See Lederer, C. M., LBL-1261)
- HOLLANDER, J. M., (See Lederer, C. M., LBL-1262)
- HOMEYER, H., (See Kovar, D. G., LBL-1646)
- HOMEYER, H., (See Becchetti, F. D., LBL-1972)
- HOMEYER, H., (See DeVries, R. M., LBL-2363)
- HOWELL, R. H., (See Hammerstein, G. R., LBL-1626)
- HUIZENGA, J. R., and L. G. Moretto  
Nuclear level densities  
LBL-662, March 1972  
Ann. Rev. Nucl. Sci. 22, 427 (1972)
- HUIZENGA, J. R., A. N. Behkami, J. S. Sventek, and R. W. Atcher  
Comparison of neutron resonance spacings with microscopic theory for spherical nuclei  
LBL-2314, October 1973  
Nucl. Phys.
- HUIZENGA, J. R., A. N. Behkami, R. W. Atcher, J. S. Sventek, H. C. Britt, and  
H. Freiesleben  
Comparison of neutron resonance spacings with microscopic theory for nuclei with static  
deformation  
LBL-2316, October 1973  
Nucl. Phys.
- HULTBERG, S., (See Rezanka, I., LBL-1223)
- HUNT, W. J., (See Pearson, P. K., LBL-1605)
- HUNT, W. J., (See Hand, R. W., LBL-1632)
- HYDE, E. K., (See Korteling, R. G., LBL-663)
- IWATA, S., (See Tamura, T., LBL-1689)
- JAKLEVIC, J. M., (See Giaque, R. D., LBL-647)
- JARED, R. C., H. Nifenecker, and S. G. Thompson  
Measurement of prompt gamma ray lifetimes of fission fragments of  $^{252}\text{Cf}$   
LBL-1963, July 1973  
Third Symposium on the Physics and Chemistry of Fission, Rochester, New York,  
August 13-17, 1973

- JARED, R. C., (See Moretto, L. G., LBL-1966)
- JELLEY, N. A., (See Wilcox, K. H., LBL-1644)
- JELLEY, N. A., (See Wozniak, G. J., LBL-1904)
- JELLEY, N. A., (See Macdonald, J. A., LBL-1982)
- JELLEY, N. A., K. H. Wilcox, R. B. Weisenmiller, G. J. Wozniak, and J. Cerny  
Masses for  $^{43}\text{Ar}$  and the new isotopes  $^{45}\text{Ar}$  and  $^{46}\text{Ar}$   
LBL-2329, December 1973  
Phys. Rev. Letters
- JOANNOPOULOS, J. D., (See Pollak, R. A., LBL-1204)
- JURNAK, F. A.  
Structural investigations of transition metal pentacoordination  
LBL-2335, December 1973  
Ph. D. Thesis
- KAINDL, G., and D. Salomon  
Electronic quadrupole interaction of Ta-181 in hexagonal transition metals  
LBL-641, March 1972  
Phys. Letters 40A, 179 (1972)
- KAINDL, G., and D. Salomon  
High-resolution mössbauer spectroscopy with tantalum-181  
LBL-1210, August 1972  
International Conference on Applications of the Mössbauer Effect, Israel, August 27-31,  
1972. Perspectives in Mössbauer Spectroscopy, ed. by S. G. Cohen and M. Pasternack,  
Plenum Publishing Corporation, New York (1973), p. 195
- KAINDL, G., and D. Salomon  
Hyperfine interaction of  $^{181}\text{Ta}$  in nickel  
LBL-1288, November 1972  
Phys. Letters 42A, 333 (1973)
- KAINDL, G., and D. Salomon  
Effects of temperature on the energy of the 6.2-keV mössbauer gamma rays of  $^{181}\text{Ta}$ .  
LBL-1604, November 1972  
Phys. Rev. Letters 30, 579 (1973)
- KAINDL, G., D. Salomon, and G. Wortmann  
High-resolution study of isomer shifts of the 6.2-keV  $\gamma$  rays of tantalum-181  
LBL-1631, April 1973  
Phys. Rev. B8, 1912 (1973)
- KAINDL, G., F. Bacon, and D. A. Shirley  
Magnetic moment and spin of 6.9-h  $^{93}\text{Mo}^m$   
LBL-1638, February 1973  
Phys. Rev. C 8, 315 (1973)
- KAINDL, G., D. Salomon, and G. Wortmann  
Mössbauer isomer shifts of the 6.2-keV gamma rays of tantalum-181  
LBL-1675, April 1973  
Invited talk presented at the 8<sup>th</sup> Symposium on Mössbauer Effect Methodology, New York,  
New York, January 28, 1973. Mössbauer Effect Methodology 8, 211 (1973), Plenum  
Publishing Corporation, New York

- KAINDL, G., F. Bacon, H. -E. Mahnke, and D. A. Shirley  
Nuclear magnetic resonance on oriented  $^{101}\text{Rh}^m$   
LBL-1684, April 1973  
Phys. Rev. C 8, 3 (1973)
- KAINDL, G., F. Bacon, and A. J. Soinski  
Nuclear quadrupole alignment of  $^{180m}\text{Hf}$  and  $^{175}\text{Hf}$  in hafnium metal  
LBL-1960, June 1973  
Phys. Letters B
- KATARIA, S. K., E. Nardi, and S. G. Thompson  
Simultaneous emission of two light charged particles in spontaneous fission of  $^{252}\text{Cf}$   
LBL-1905, June 1973  
Symposium on the Physics and Chemistry of Fission, University of Rochester, Rochester,  
New York, August 13-17, 1973
- KATARIA, S. K., (See Moretto, L. G., LBL-1942)
- KENJO, T., and R. M. Diamond  
Hydration of the halide ions in certain organic solvents  
LBL-1630, February 1973  
J. Inorg. Nucl. Chem. 36, 183 (1974)
- KIENLE, P., (See Proetel, D., LBL-1939)
- KIENLE, P., M. Kleber, B. Povh, R. M. Diamond, F. S. Stephens, E. Grosse, M. R. Maier, and D. Proetel  
Radiative capture and bremsstrahlung of bound electrons induced by heavy ions  
LBL-1961, June 1973  
Phys. Rev. Letters 31, 1099 (1973)
- KING, C. J., (See Davenport, I. F., LBL-608)
- KING, C. J., (See Davenport, I. F., LBL-660)
- KING, C. J., (See Davenport, I. F., LBL-1998)
- KING, C. J., (See Davenport, I. F., LBL-1999)
- KLEBER, M., (See Kienle, P., LBL-1961)
- KLEINHEINZ, P., (See Nakai, K., LBL-1614)
- KLEINHEINZ, P., (See Stephens, F. S., LBL-1911)
- KLEINHEINZ, P., R. K. Sheline, M. R. Maier, R. M. Diamond, and F. S. Stephens  
Shape coexistence and its cause in  $^{151}\text{Gd}$   
LBL-1994, September 1973  
Phys. Rev. Letters 32, 68 (1974)
- KORTELING, R. G., D. Toren, and E. K. Hyde  
Energy spectra of fragments from silver and uranium bombarded with 5.0-GeV protons  
LBL-663, August 1972  
Phys. Rev. C 7, 1611 (1973)
- KORTELING, R. G., (See Bowman, J. D., LBL-1937)

- KORTELING, R. G., (See Bowman, J. D., LBL-1967)
- KOVAR, D. G., (See Hendrie, D. L., LBL-656)
- KOVAR, D. G., (See Becchetti, F. D., LBL-695)
- KOVAR, D. G., B. G. Harvey, F. D. Becchetti, J. Mahoney, D. L. Hendrie, H. Homeyer, W. von Oertzen, and M. A. Nagarajan  
Evidence for recoil effects in heavy-ion transfer reactions  
LBL-1646, February 1973  
Phys. Rev. Letters 30, 1075 (1973)
- KOVAR, D. G.  
Transfer reactions at high energies on heavy target nuclei  
LBL-1654, March 1973  
NFP
- KOVAR, D. G., (See Zisman, M. S., LBL-1676)
- KOVAR, D. G., (See Becchetti, F. D., LBL-1972)
- KOVAR, D. G., (See DeVries, R. M., LBL-2363)
- KOWALCZYK, S., (See Ley, L., LBL-688)
- KOWALCZYK, S., L. Ley, R. Pollak, and D. A. Shirley  
High-resolution XPS spectra of Ir, Pt, and Au valence bands  
LBL-691, July 1972  
Phys. Letters 41A, 455 (1972)
- KOWALCZYK, S., (See Ley, L., LBL-1203)
- KOWALCZYK, S., (See Pollak, R. A., LBL-1204)
- KOWALCZYK, S., (See Cavell, R. G., LBL-1213)
- KOWALCZYK, S., (See McFeely, R., LBL-1253)
- KOWALCZYK, S. P., L. Ley, R. A. Pollak, F. R. McFeely, and D. A. Shirley  
New multiplet structure in photoemission from  $MnF_2$   
LBL-1275, October 1972  
Phys. Rev. B 7, 4009 (1973)
- KOWALCZYK, S. P., (See Ley, L., LBL-1278-Rev.)
- KOWALCZYK, S. P., R. A. Pollak, F. R. McFeely, L. Ley, and D. A. Shirley  
The  $L_{2,3}M_{45}M_{45}$  Auger spectra of metallic copper and zinc: theory and experiment  
LBL-1641, January 1973  
Phys. Rev. B 8, 2387 (1973)
- KOWALCZYK, S. P., (See Ley, L., LBL-1648)
- KOWALCZYK, S. P., L. Ley, F. R. McFeely, R. A. Pollak, and D. A. Shirley  
X-ray photoemission from sodium lithium  
LBL-1682, April 1973  
Phys. Rev. B 8, 3583 (1973)



- KOWALCZYK, S. P., (See Ley, L., LBL-1688)
- KOWALCZYK S. P., (See McFeely, F. R., LBL-1691)
- KOWALCZYK, S. P., L. Ley, F. R. McFeely, R. A. Pollak, and D. A. Shirley  
The relative effect of extra-atomic relaxation on Auger and ESCA shifts in transition  
metals and salts  
LBL-1916, June 1973  
Phys. Rev. B
- KOWALCZYK, S. P., F. R. McFeely, L. Ley, R. A. Pollak, and D. A. Shirley  
X-ray photoemission studies of the alkali halides  
LBL-1945, November 1973  
Phys. Rev. B
- KOWALCZYK, S. P., (See Pollak, R. A., LBL-1971)
- KOWALCZYK, S. P., (See McFeely, F. R., LBL-1989)
- KOWALCZYK, S. P., (See Ley, L., LBL-2323)
- KOWALCZYK, S. P., (See Varea de Alvarez, C., LBL-2330)
- KRANE, K. S.  
Solid-angle correction factors for "five-sided" coaxial Ge(Li) detectors  
LBL-1621, January 1973  
Nucl. Instr. Methods 109, 401 (1973)
- KRANE, K. S.  
E2/M1 multipole mixing ratios of  $\gamma$  transitions in even-even deformed nuclei  
LBL-1625, January 1973  
Phys. Rev. C 8, 1494 (1973)
- KRANE, K. S.  
Directional correlations of parity and time-reversal non-conserving radiations emitted  
from oriented nuclei  
LBL-1686, April 1973  
NFP
- KRANE, K. S., (See Steyert, W. A., LBL-1981)
- KRANE, K. S., and W. A. Steyert  
Non-alignment of the magnetic hyperfine field of Ir in Fe  
LBL-2337, December 1973  
Phys. Rev. C
- KRAPPE, H. J., and J. R. Nix  
Modified definition of the surface energy in the liquid-drop formula  
LBL-1920, June 1973  
Presented at the Third Symposium on the Physics and Chemistry of Fission, Rochester,  
New York, August 13-17, 1973
- KRIEN, K., R. A. Naumann, J. O. Rasmussen, and I. Rezanka  
High spin states in  $^{155}\text{Dy}$  and  $^{154}\text{Dy}$  from ( $^{12}\text{C}$ , xn,  $\gamma$ ) studies  
LBL-1652, March 1973  
Nucl. Phys. .

- KUO, T. Y. T., (See Petrovich, F., LBL-1651)
- LAMONTAGNE, C. R., (See de Swiniarski, R., LBL-1620)
- LAMONTAGNE, C. R., B. Frois, R. J. Slobodrian, H. E., Conzett, Ch. Leemann, and R. de Swiniarski  
The scattering of polarized protons from Si in the giant resonance region of  $^{29}\text{P}$   
LBL-1941, June 1973  
Phys. Letters
- LARSON, D., (See Hinrichs, R. A., LBL-1649)
- LARSSON, S. E., (See Randrup, J., LBL-1944)
- LEDERER, C. M., (See Benson, D., LBL-1216)
- LEDERER, C. M., and J. M. Hollander  
Development of a computer-based nuclear data compilation - table of isotopes  
LBL-1261, February 1973  
IAEA Symposium on Application of Nuclear Data in Science and Technology, Paris, France,  
March 12-16, 1973
- LEDERER, C. M., and J. M. Hollander  
A survey of nuclear data use in applied fields  
LBL-1262, February 1973  
IAEA Symposium on Application of Nuclear Data in Science and Technology, Paris, France,  
March 12-16, 1973
- LEDERER, C. M.  
LESAGE-level scheme analysis and graphics: user's manual  
LBL-1996, October 1973  
NFP
- LEDERER, C. M.  
Computerized production of a data compilation - table of isotopes  
LBL-2319, October 1973  
Presented at the STC-TID Seminar on Continuing Education in Communication, Lawrence  
Berkeley Laboratory, Berkeley, November 17, 1973
- LEEMANN, Ch., (See Lamontagne, C. R., LBL-1941)
- LEIGH, J. R., K. Nakai, K. H. Maier, F. Pühlhofer, F. S. Stephens, and R. M. Diamond  
Energy-level systematics of odd-mass lanthanum isotopes; a new coupling scheme  
LBL-1601, December 1972  
Nucl. Phys. A213, 1 (1973)
- LEIGH, J. R., (See Nakai, K., LBL-1614)
- LEIGH, J. R., (See Proetel, D., LBL-1939)
- LEY, L., S. Kowalczyk, R. Pollak, and D. A. Shirley  
X-ray photoemission spectra of crystalline and amorphous Si and Ge valence bands  
LBL-688, July 1972  
Phys. Rev. Letters 29, 1088 (1972)
- LEY, L., (See Kowalczyk, S., LBL-691)

- LEY, L., R. Pollak, S. Kowalczyk, and D. A. Shirley  
The onset of relativistic effects in the density of states of the 6s6p elements Tl, Pb, and Bi  
LBL-1203, July 1972  
Phys. Letters 41A, 429 (1972)
- LEY, L., (See Pollak, R. A., LBL-1204)
- LEY, L., (See Cavell, R. G., LBL-1213)
- LEY, L., (See McFeely, R., LBL-1253)
- LEY, L., (See Kowalczyk, S., LBL-1275)
- LEY, L., R. A. Pollak, S. P. Kowalczyk, R. McFeely, and D. A. Shirley  
Evidence for covalent bonding in crystalline and amorphous As, Sb, and Bi from valence-band photoelectron spectra  
LBL-1278-Rev., October 1972  
Phys. Rev. B 8, 641 (1973)
- LEY, L., (See Kowalczyk, S. P., LBL-1641)
- LEY, L., S. P. Kowalczyk, F. R. McFeely, R. A. Pollak, and D. A. Shirley  
X-ray photoemission from zinc: evidence for extra-atomic relaxation via semilocalized excitons  
LBL-1648, February 1973  
Phys. Rev. B 8, 2392 (1973)
- LEY, L., (See Kowalczyk, S. P., LBL-1682)
- LEY, L., R. A. Pollak, F. R. McFeely, S. P. Kowalczyk, and D. A. Shirley  
Total valence-band densities of states of III-V and II-VI compounds from XPS  
LBL-1688, May 1973  
Phys. Rev. B
- LEY, L., (See McFeely, F. R., LBL-1691)
- LEY, L., (See Kowalczyk, S. P., LBL-1916)
- LEY, L., (See Kowalczyk, S. P., LBL-1945)
- LEY, L., (See Pollak, R. A., LBL-1971)
- LEY, L., (See McFeely, F. R., LBL-1989)
- LEY, L., F. R. McFeely, S. P. Kowalczyk, and D. A. Shirley  
Many-body effects in x-ray photoemission from magnesium  
LBL-2323, November 1973  
Phys. Rev. B
- LEY, L., (See Varea de Alvarez, C., LBL-2330)
- LILJENZIN, J. O.  
The temperature of thin foils in ion beams  
LBL-1912, June 1973  
NFP
- LIPES, R. G., (See Wang, W. L., LBL-1988)

- LISKOW, D. H., C. F. Bender, and H. F. Schaefer III  
Some features of the  $\text{CH}_3\text{NC} \rightarrow \text{CH}_3\text{CN}$  potential surface  
LBL-696, July 1972  
J. Chem. Phys. 57, 4509 (1972)
- LISKOW, D. H., C. F. Bender, and H. F. Schaefer III  
Potential energy surfaces related to the ion-molecule reaction  $\text{C}^+ + \text{H}_2$   
LBL-2302, October 1973  
J. Chem. Phys.
- LITTON, G., (See Clem, R. G., LBL-679)
- LIU, K. -L., (See DeVries, R. M., LBL-2363)
- LOUGHEED, R. W., (See Worden, E. F., UCRL-74650)
- LOVE, W. G., (See Hinrichs, R. A., LBL-1649)
- LØVHØIDEN, G., (See Nakai, K., LBL-1614)
- McLAUGHLIN, R. D., (See Stacy, J. J., LBL-638)
- McFEELY, F. R., S. Kowalczyk, L. Ley, R. A. Pollak, and D. A. Shirley  
High-resolution x-ray-photoemission spectra of PbS, PbSe, and PbTe valence bands  
LBL-1253, September 1972  
Phys. Rev. B 7, 5228 (1973)
- McFEELY, F. R., (See Kowalczyk, S., LBL-1275)
- McFEELY, R., (See Ley, L., LBL-1278-Rev.)
- McFEELY, F. R., (See Kowalczyk, S. P., LBL-1641)
- McFEELY, F. R., (See Ley, L., LBL-1648)
- McFEELY, F. R., (See Kowalczyk, S. P., LBL-1682)
- McFEELY, F. R., (See Ley, L., LBL-1688)
- McFEELY, F. R., S. P. Kowalczyk, L. Ley, and D. A. Shirley  
X-ray photoemission study of Gd, Tb and Dy 4f and valence bands  
LBL-1691, June 1973  
Phys. Letters 45A, 227 (1973)
- McFEELY, F. R., (See Kowalczyk, S. P., LBL-1916)
- McFEELY, F. R., (See Kowalczyk, S. P., LBL-1945)
- McFEELY, F. R., (See Pollak, R. A., LBL-1971)
- McFEELY, F. R., S. P. Kowalczyk, L. Ley, R. G. Cavell, R. A. Pollak, and D. A. Shirley  
X-ray photoemission studies of diamond, graphite, and glassy carbon valence bands  
LBL-1989, September 1973  
Phys. Rev. B
- McFEELY, F. R., (See Ley, L., LBL-2323)

McFEELY, F. R., (See Varea de Alvarez, C., LBL-2330)

McMANUS, H., (See Petrovich, F., LBL-1651)

MA, C. W., and J. O. Rasmussen

Exponential dependence of the nuclear moment-of-inertia on pairing correlation and the pairing stretch model for nuclear rotation  
LBL-1677, April 1973  
Phys. Rev.

MA, C. W., (See Rasmussen, J. O., LBL-1908)

MACDONALD, J. A., N. A. Jelley, and J. Cerny

Analyzing powers in  $^{208}\text{Pb}(\bar{p}, t)^{206}\text{Pb}$  transitions  
LBL-1982, September 1973  
Phys. Letters 47B, 237 (1973)

MACDONALD, J. A., J. Cerny, J. C. Hardy, H. L. Harney, A. D. Bacher, and G. R. Plattner

Analyzing powers for two-nucleon transfer reactions in the  $1p$ -shell  
LBL-2317, October 1973  
Phys. Rev. C

MACDONALD, J. A.

Two-nucleon transfer reactions induced by polarized protons  
LBL-2320, October 1973  
Ph. D. Thesis

MAGGIORE, C. J., (See Petrovich, F., LBL-1651)

MAHNKE, H. E., (See Kaindl, G., LBL-1684)

MAHONEY, J., (See Hendrie, D. L., LBL-656)

MAHONEY, J., (See Becchetti, F. D., LBL-695)

MAHONEY, J., (See Kovar, D. G., LBL-1646)

MAHONEY, J., (See Zisman, M. S., LBL-1676)

MAHONEY, J., (See Becchetti, F. D., LBL-1972)

MAIER, K. H., (See Leigh, J. R., LBL-1601)

MAIER, K. H., (See Nakai, K., LBL-1614)

MAIER, M. R., (See Stephens, F. S., LBL-1282)

MAIER, M. R., (See Gizon, J., LBL-1948)

MAIER, M. R., (See Kienle, P., LBL-1961)

MAIER, M. R., (See Kleinheinz, P., LBL-1994)

MARKOWITZ, S. S., (See Fee, D. C., LBL-668)

MARKOWITZ, S. S., (See Go, M. K., LBL-1230)

- MARKOWITZ, S. S., (See Fee, D. C., LBL-1249)
- MARKOWITZ, S. S., (See Fee, D. C., LBL-1264)
- MARKOWITZ, S. S., (See Parsa, B., LBL-1901)
- MARKOWITZ, S. S., (See Parsa, B., LBL-1902)
- MARKOWITZ, S. S., (See Fee, D. C., LBL-1906)
- MARKOWITZ, S. S., (See Fee, D. C., LBL-1910)
- MARKOWITZ, S. S., (See Fee, D. C., LBL-1949)
- MARRUS, R., (See Gould, H., LBL-1658-Rev.)
- MARTIN, R. L., (See Davis, D. W., LBL-1915)
- MARTIN, R. L., and D. A. Shirley  
The relation of core-level binding energy shifts to proton affinity and Lewis basicity  
LBL-2341, December 1973  
J. Am. Chem. Soc.
- MASSMANN, H., J. O. Rasmussen, T. E. Ward, P. E. Haustein, and F. M. Bernthal  
Configuration mixing of two-quasi-particle states in even-even deformed nuclei  
LBL-1693, June 1973  
Nucl. Phys.
- MAYER, B., (See Becchetti, F. D., LBL-695)
- MEHLHORN, R., (See Rajnak, K., LBL-1218)
- MEINER, H., (See Bacher, A. D., LBL-1228)
- MERIWETHER, J. R., (See Hendrie, D. L., LBL-656)
- MICHEL, H. V., (See Perlman, I., LBL-674)
- MICHEL, H. V., (See Widemann, F., LBL-1964)
- MICHEL, M. C., (See Hadeishi, T., LBL-1260)
- MICHEL, M. C., (See Yellin, J., LBL-1602)
- MICHEL, M. C., (See Yellin, J., LBL-1608)
- MÖLLER, P., (See Randrup, J., LBL-1944)
- MORETTO, L. G., (See Huizenga, J. R., LBL-662)
- MORETTO, L. G., (See Nardi, E., LBL-1263)
- MORETTO, L. G.  
Studies on statistically excited shell model nuclei: the dependence of the shell structure and  
of the pairing correlation upon angular momentum  
LBL-1298, November 1972  
Nucl. Phys. A216, 1 (1973)

- MORETTO, L. G.  
Finite temperature calculation of angular velocities and moments of inertia in rotating nuclei  
LBL-1663, March 1973  
Phys. Letters 44B, 494 (1973)
- MORETTO, L. G.  
Fission probabilities in lighter nuclei. A theoretical and experimental investigation of  
the shell and pairing effects in fissioning nuclei  
LBL-1914, July 1973  
Third Symposium on the Physics and Chemistry of Fission, Rochester, New York,  
August 13-17, 1973
- MORETTO, L. G.  
Pairing and spin distribution effects on the yrast line  
LBL-1921, June 1973  
Phys. Letters 46B, 20 (1973)
- MORETTO, L. G., and S. K. Kataria  
Superfluid properties of excited nuclei arising from a  $\delta$ -force residual interaction  
LBL-1942, September 1973  
Lettere al Nuovo Cimento
- MORETTO, L. G., D. Heunemann, R. C. Jared, R. C. Gatti, and S. G. Thompson  
Study of a fission-like environment in reactions with very heavy ions  
LBL-1966, July 1973  
Third Symposium on the Physics and Chemistry of Fission, Rochester, New York,  
August 13-17, 1973
- MYERS, W. D.  
Geometric properties of leptodermous distributions with applications to nuclei  
LBL-1259, October 1972  
Nucl. Phys. A204, 465 (1973)
- MYERS, W. D., and W. J. Swiatecki  
The nuclear droplet model for arbitrary shapes  
LBL-1957, July 1973  
Ann. Phys.
- NAGARAJAN, M. A.  
The effect of recoil on single-nucleon transfer in heavy-ion reactions  
LBL-697, July 1972  
Nucl. Phys. A196, 34 (1972)
- NAGARAJAN, M. A.  
Recoil effects in heavy-ion reactions  
LBL-1629, February 1973  
Nucl. Phys. A209, 485 (1973)
- NAGARAJAN, M. A., (See Kovar, D. G., LBL-1646)
- NAGARAJAN, M. A.  
A three body model for nucleon transfer reactions  
LBL-2300, October 1973  
Nucl. Phys.
- NAKAI, K., (See Leigh, J. R., LBL-1601)

NAKAI, K., P. Kleinheinz, J. R. Leigh, K. H. Maier, F. S. Stephens, R. M. Diamond, and G. Løvghøiden

Prolate deformation in neutron-deficient lanthanum isotopes

LBL-1614, January 1973

Phys. Letters 44B, 443 (1973)

NAKAMURA, M., and G. V. Shalimoff

Four function calculator used to automatically compute wavelength

LBL-2331, December 1973

NFP

NARDI, E., L. G. Moretto, and S. G. Thompson

Calculations of neutron evaporation from  $^{252}\text{Cf}$  fission fragments based on the shell model

LBL-1263, October 1972

Phys. Letters 43B, 259 (1973)

NARDI, E., (See Kataria, S. K., LBL-1905)

NAUMANN, R. A., (See Krien, K., LBL-1652)

NEWTON, A. S., and A. F. Sciamanna

On the metastable dissociation of the  $\text{CH}^+$  ion produced by electron impact

LBL-295, September 1972

J. Chem. Phys. 58, 1292 (1973)

NEWTON, J. O., F. S. Stephens, and R. M. Diamond

Feeding times in  $(\text{HI}, \text{x}\gamma)$  reactions

LBL-1227, December 1972

Nucl. Phys. A210, 19 (1973)

NIFENECKER, H., C. Signarbieux, R. Babinet, and J. Poitou

Neutron and gamma emission in fission

LBL-1950, July 1973

Third Symposium on the Physics and Chemistry of Fission, Rochester, New York,

August 13-17, 1973

NIFENECKER, H., (See Jared, R. C., LBL-1963)

NILSSON, S. G., (See Stephens, F. S., LBL-1607)

NILSSON, S. G., (See Randrup, J., LBL-1944)

NIX, J. R., (See Krappe, H. J., LBL-1920)

NURMIA, M., (See Eskola, P., LBL-2315)

OLOVSSON, I., (See Ruben, H., LBL-1931)

O'NEIL, S. V., P. K. Pearson, H. F. Schaefer III, and C. F. Bender

The  $\text{H} + \text{F}_2 \rightarrow \text{HF} + \text{F}$  reaction. An ab initio potential energy surface

LBL-1200, July 1972

J. Chem. Phys. 58, 1126 (1973)

O'NEIL, S. V., (See Bauschlicher Jr., C. W., LBL-1664)



- O'NEIL, S. V., H. F. Schaefer III, and C. F. Bender  
Barrier height for the exchange reaction  $F + HF \rightarrow FH + F$   
LBL-1665, March 1973  
Proc. Nat. Acad. Sci. 71, 104 (1974)
- O'NEIL, S. V., H. F. Schaefer III, and C. F. Bender  
Geometry of the  $LiO_2$  radical  
LBL-1913, June 1973  
J. Chem. Phys. 59, 3608 (1973)
- O'NEIL, S. V., (See Yarkony, D. R., LBL-1969)
- O'NEIL, S. V., (See Schwenzler, G. M., LBL-1983)
- ORNELAS, D., (See Clem, R. G., LBL-679)
- PARSA, B., and S. S. Markowitz  
Determination of lead in atmospheric air and in aluminum by  $^3He$ -induced nuclear reactions  
LBL-1901, June 1973  
Anal. Chem.
- PARSA, B., and S. S. Markowitz  
The half-life and the  $\alpha$ -decay branching ratio of  $^{207}Po$   
LBL-1902, June 1973  
J. Inorg. Nucl. Chem.
- PEARSON, P. K., (See O'Neil, S. V., LBL-1200)
- PEARSON, P. K., W. J. Hunt, C. F. Bender, and H. F. Schaefer III  
Simplest halogen atom plus alkali dimer potential surface:  $F + Li_2 \rightarrow LiF + Li$   
LBL-1605, December 1972  
J. Chem. Phys. 58, 5358 (1973)
- PEHL, R. H., (See Giaque, R. D., LBL-647)
- PERLMAN, I., (See Bowman, H. R., LBL-661)
- PERLMAN, I., F. Asaro, and H. V. Michel  
Nuclear applications in art and archaeology  
LBL-674, June 1972  
Ann. Rev. Nucl. Sci. 22, 383 (1972)
- PERLMAN, I., (See Heizer, R. F., LBL-1624)
- PERLMAN, I., (See Widemann, F., LBL-1964)
- PETROVICH, F.  
Effective moment operator for magnetic moments and M1 transitions in the Pb region  
LBL-649, August 1972  
Nucl. Phys. A203, 65 (1973)
- PETROVICH, F., (See Hammerstein, G. R., LBL-1626)
- PETROVICH, F., (See Hinrichs, R. A., LBL-1649)

- PETROVICH, F., R. Schaeffer, H. McManus, C. R. Gruhn, T. Y. T. Kuo, B. M. Freedom, and C. J. Maggiore  
Effect of vector and tensor forces in the excitation of  $f_{7/2}-d_{3/2}^{-1}$  states in the  $^{40}\text{Ca}(p, p')^{40}\text{Ca}^*$  reaction  
LBL-1651, February 1973  
Phys. Letters 46B, 141 (1973)
- PETROVICH, F., (See Wagner, W. T., LBL-1938)
- PICON, M., (See Widemann, F., LBL-1964)
- PLATTNER, G. R., (See Macdonald, J. A., LBL-2317)
- POITOU, J., (See Nifenecker, H., LBL-1950)
- POLLAK, R., (See Ley, L., LBL-688)
- POLLAK, R., (See Kowalczyk, S., LBL-691)
- POLLAK, R., (See Ley, L., LBL-1203)
- POLLAK, R. A., L. Ley, S. Kowalczyk, D. A. Shirley, J. D. Joannopoulos, D. J. Chadi, and M. L. Cohen  
X-ray photoemission valence band spectra and theoretical valence band densities of states for Ge, GaAs, and ZnSe  
LBL-1204, July 1972  
Phys. Rev. Letters 29, 1103 (1972)
- POLLAK, R., (See Cavell, R. G., LBL-1213)
- POLLAK, R. A., (See McFeely, R., LBL-1253)
- POLLAK, R. A., (See Kowalczyk, S., LBL-1275)
- POLLAK, R. A., (See Ley, L., LBL-1278-Rev.)
- POLLAK, R. A., (See Kowalczyk, S. P., LBL-1641)
- POLLAK, R. A., (See Ley, L., LBL-1648)
- POLLAK, R. A., (See Kowalczyk, S. P., LBL-1682)
- POLLAK, R. A., (See Ley, L., LBL-1688)
- POLLAK, R. A., (See Kowalczyk, S. P., LBL-1916)
- POLLAK, R. A., (See Kowalczyk, S. P., LBL-1945)
- POLLAK, R. A., L. Ley, F. R. McFeely, S. P. Kowalczyk, and D. A. Shirley  
Characteristic energy loss structure of solids from x-ray photoemission spectra  
LBL-1971, September 1973  
J. Electr. Spectrosc.
- POLLAK, R. A., (See McFeely, F. R., LBL-1989)
- POSKANZER, A. M., (See Bowman, J. D., LBL-1937)

- POSKANZER, A. M., (See Bowman, J. D., LBL-1967)
- POVH, B., (See Kienle, P., LBL-1961)
- PREEDOM, B. M., (See Hinrichs, R. A., LBL-1649)
- PREEDOM, B. M., (See Petrovich, F., LBL-1651)
- PRESTON, R. K., (See Bauschlicher Jr., C. W., LBL-1664)
- PROETEL, D., R. M. Diamond, P. Kienle, J. R. Leigh, K. H. Maier, and F. S. Stephens  
Evidence for strongly deformed shapes in  $^{186}\text{Hg}$   
LBL-1939, June 1973  
Phys. Rev. Letters
- PROETEL, D., (See Kienle, P., LBL-1961)
- PROETEL, D., R. M. Diamond, and F. S. Stephens  
Nuclear deformations in  $^{186}\text{Hg}$  from lifetime measurements  
LBL-2309, October 1973  
Phys. Letters 48B, 102 (1974)
- PÜHLHOFER, F. G., (See Becchetti, F. D., LBL-695)
- PÜHLHOFER, F., (See Leigh, J. R., LBL-1601)
- QUARLES, W. G., D. H. Templeton, and A. Zalkin  
The crystal and molecular structure of melatonin  
LBL-1933, June 1973  
Acta Cryst.
- QUARLES, W. G., D. H. Templeton, and A. Zalkin  
The crystal and molecular structure of 5-methoxytryptamine  
LBL-1934, June 1973  
Acta Cryst.
- RAJNAK, K., R. Mehlhorn, and N. Edelstein  
Calculation of the crystal field splittings of  $\text{Sm}^{3+}$  levels in  $\text{LaCl}_3$  with inclusion of J-mixing  
LBL-1218, August 1972  
J. Chem. Phys. 58, 609 (1973)
- RANDRUP, J.  
A semi-empirical approach to fission inertias and fission half-lives  
LBL-1699, May 1973  
Nucl. Phys.
- RANDRUP, J., C. F. Tsang, P. Möller, S. G. Nilsson, and S. E. Larsson  
Theoretical predictions of fission half-lives of elements with Z between 92 and 106  
LBL-1944, June 1973  
Nucl. Phys.
- RASMUSSEN, J. O., (See Rezanka, I., LBL-1223)
- RASMUSSEN, J. O., (See Krien, K., LBL-1652)
- RASMUSSEN, J. O., (See Ma, C. W., LBL-1677)

- RASMUSSEN, J. O., (See Tamura, T., LBL-1689)
- RASMUSSEN, J. O., (See Massmann, H., LBL-1693)
- RASMUSSEN, J. O., and C. W. Ma  
Number-displacement degrees of freedom in nuclear rotational theory  
LBL-1908, May 1973  
Phys. Rev. Letters 31, 317 (1973).
- RASMUSSEN, J. O., (See Anholt, R., LBL-1947)
- RAY, S., A. Zalkin, and D. H. Templeton  
Crystal structures of the fluosilicate hexahydrates of cobalt, nickel, and zinc  
LBL-1932, June 1973  
Acta Cryst.
- RAY, S., A. Zalkin, and D. H. Templeton  
Crystal structure of copper fluosilicate hexahydrate  
LBL-1935, June 1973  
Acta Cryst.
- RESMINI, F. G., (See Bacher, A. D., LBL-1228)
- RESMINI, F. G., (See de Swiniarski, R., LBL-2322)
- REZANKA, I., J. O. Rasmussen, F. M. Bernthal, C. T. Alonso, J. R. Alonso, S. Hultberg,  
and H. Ryde  
Rotational states in  $^{171}\text{Hf}$   
LBL-1223, August 1972  
Nucl. Phys. A197, 430 (1972)
- REZANKA, I., (See Krien, K., LBL-1652)
- REZANKA, I., (See Tamura, T., LBL-1689)
- RICHTER, A., (See Robson, D., LBL-1643)
- RINNEBERG, H. H., and D. A. Shirley  
Supertransferred hyperfine interaction: perturbed angular correlation of  $^{111m}\text{Cd}$  in  $\text{KNiF}_3$ ,  
 $\text{KCoF}_3$ , and  $\text{RbMnF}_3$   
LBL-1673, April 1973  
Phys. Rev. Letters 30, 1147 (1973)
- ROBINSON, C. W., and C. R. Wilke  
Oxygen absorption in stirred tanks: A correlation for ionic strength effects  
LBL-1943, June 1973  
Biotech. and Bioeng. XV, 755 (1973)
- ROBSON, D., A. Richter, and H. L. Harney  
Consequences of isospin and other conserved quantum numbers for compound-nucleus  
reactions  
LBL-1643, February 1973  
Phys. Rev. C 8, 153 (1973)

RUBEN, H., I. Olovsson, A. Zalkin, and D. H. Templeton  
Sodium chromate tetrahydrate  
LBL-1931, June 1973  
Acta Cryst.

RUBEN, H., A. Zalkin, and D. H. Templeton  
N, N'-bis(2, 2, 6, 6-tetramethylpiperidyl-4) succinic acid diamide dihydrate  
LBL-1936, June 1973  
Acta Cryst.

RYDE, H., (See Rezanka, I., LBL-1223)

SALOMON, D., (See Kaindl, G., LBL-641)

SALOMON, D., (See Kaindl, G., LBL-1210)

SALOMON, D., (See Kaindl, G., LBL-1288)

SALOMON, D., (See Kaindl, G., LBL-1604)

SALOMON, D., (See Kaindl, G., LBL-1631)

SALOMON, D., (See Kaindl, G., LBL-1675)

SALOMON, D., and D. A. Shirley  
Quadrupole coupling at  $^{193}\text{Ir}$  nuclei in iron  
LBL-1956, July 1973  
Phys. Rev. B 9, 29 (1974)

SCHAEFER III, H. F., (See Liskow, D. H., LBL-696)

SCHAEFER III, H. F., (See O'Neil, S. V., LBL-1200)

SCHAEFER III, H. F., (See Pearson, P. K., LBL-1605)

SCHAEFER III, H. F., (See Hand, R. W., LBL-1632)

SCHAEFER III, H. F., (See Bauschlicher Jr., C. W., LBL-1664)

SCHAEFER III, H. F., (See O'Neil, S., LBL-1665)

SCHAEFER III, H. F., (See O'Neil, S. V., LBL-1913)

SCHAEFER III, H. F., (See Yarkony, D. R., LBL-1969)

SCHAEFER III, H. F., (See Schwenzler, G. M., LBL-1983)

SCHAEFER III, H. F., (See Liskow, D. H., LBL-2302)

SCHAEFER III, H. F., (See Baskin, C. P., LBL-2324)

SCHAEFFER, R., and N. K. Glendenning  
Second order effects in the ( $\tau$ , t) reaction  
LBL-689, May 1972  
Nucl. Phys. A207, 321 (1973)

SCHAEFFER, R., (See Petrovich, F., LBL-1651)

- SCHMIEDER, R. W., (See Gould, H., LBL-1658-Rev.)
- SCHMIEDER, R. W.  
Double and triple photon decay of metastable  $^3P_0$  atomic states  
LBL-1946, June 1973  
Phys. Rev. A 7, 1458 (1973)
- SCHWENZER, G. M., S. V. O'Neil, H. F. Schaefer III, C. P. Baskin, and C. F. Bender  
Geometries of the excited electronic states of HCN  
LBL-1983, September 1973  
J. Chem. Phys.
- SCIAMANNA, A. F., (See Newton, A. S., LBL-295)
- SCOTT, D. K.  
Multinucleon transfer reactions  
LBL-1991, August 1973  
Presented at the International Conference on Nuclear Physics, Munich, Germany,  
August 27 - September 1, 1973
- SEABORG, G. T.  
Status report on the transuranium elements  
LBL-2325, September 1973  
Pure and Applied Chemistry
- SEXTRO, R. G., (See Gough, R. A., LBL-1292)
- SEXTRO, R. G., R. A. Gough, and J. Cerny  
 $\beta^+$ -delayed-proton decay of  $^{21}\text{Mg}$   
LBL-1600, February 1973  
Phys. Rev. C 8, 258 (1973)
- SEXTRO, R. G.  
High-resolution studies of beta-delayed proton emission in light nuclei  
LBL-2360, December 1973  
Ph. D. Thesis
- SHAKIN, C. M., (See Wang, W. L., LBL-1995)
- SHALIMOFF, G. V., (See Nakamura, M., LBL-2331)
- SHELINE, R. K., (See Stephens, F. S., LBL-1911)
- SHELINE, R. K., (See Kleinheinz, P., LBL-1994)
- SHERMAN, J. D., (See Zisman, M. S., LBL-1676)
- SHERMAN, J. D.  
Systematics of the  $(\alpha, 2\alpha)$  reaction at  $E_\alpha = 90$  MeV  
LBL-1690, May 1973  
Ph. D. Thesis
- SHIRLEY, D. A.  
ESCA  
LBL-610, January 1972  
Advan. Chem. Phys. 23, 85 (1973)

- SHIRLEY, D. A., and H. Haas  
Perturbed angular correlation of gamma rays  
LBL-667, February 1972  
Ann. Rev. Phys. Chem. 23, 385 (1972)
- SHIRLEY, D. A.  
The effect of atomic and extra-atomic relaxation on atomic binding energies  
LBL-678, June 1972  
Chem. Phys. Letters 16, 220 (1972)
- SHIRLEY, D. A., (See Ley, L., LBL-688)
- SHIRLEY, D. A., (See Kowalczyk, S., LBL-691)
- SHIRLEY, D. A., (See Ley, L., LBL-1203)
- SHIRLEY, D. A., (See Pollak, R. A., LBL-1204)
- SHIRLEY, D. A., (See Cavell, R. G., LBL-1213)
- SHIRLEY, D. A., (See McFeely, R., LBL-1253)
- SHIRLEY, D. A., (See Kowalczyk, S., LBL-1275)
- SHIRLEY, D. A., (See Ley, L., LBL-1278-Rev.)
- SHIRLEY, D. A., (See Haas, H., LBL-1284)
- SHIRLEY, D. A., (See Bacon, F., LBL-1289)
- SHIRLEY, D. A., (See Kaindl, G., LBL-1638)
- SHIRLEY, D. A.  
Theory of KLL Auger energies including static relaxation  
LBL-1640, January 1973  
Phys. Rev. A7, 1520 (1973)
- SHIRLEY, D. A., (See Kowalczyk, S. P., LBL-1641)
- SHIRLEY, D. A., (See Ley, L., LBL-1648)
- SHIRLEY, D. A., (See Rinneberg, H. H., LBL-1673)
- SHIRLEY, D. A., (See Kowalczyk, S. P., LBL-1682)
- SHIRLEY, D. A., (See Kaindl, G., LBL-1684)
- SHIRLEY, D. A., (See Ley, L., LBL-1688)
- SHIRLEY, D. A., (See McFeely, F. R., LBL-1691)
- SHIRLEY, D. A., (See Davis, D. W., LBL-1909)
- SHIRLEY, D. A., (See Davis, D. W., LBL-1915)
- SHIRLEY, D. A., (See Kowalczyk, S. P., LBL-1916)

- SHIRLEY, D. A., (See Kowalczyk, S. P., LBL-1945)
- SHIRLEY, D. A., (See Salomon, D., LBL-1956)
- SHIRLEY, D. A., (See Davis, D. W., LBL-1970)
- SHIRLEY, D. A., (See Pollak, R. A., LBL-1971)
- SHIRLEY, D. A., (See McFeely, F. R., LBL-1989)
- SHIRLEY, D. A.  
Theory of Auger satellite energy shifts  
LBL-1993, October 1973  
Phys. Rev. A
- SHIRLEY, D. A., (See Ley, L., LBL-2323)
- SHIRLEY, D. A., (See Varea de Alvarez, C., LBL-2330)
- SHIRLEY, D. A., (See Martin, R. L., LBL-2341)
- SIGNARBIÉUX, C., (See Nifenecker, H., LBL-1950)
- SIMON, R. S., (See Stephens, F. S., LBL-1911)
- SLOBODRIAN, R. J., (See de Swiniarski, R., LBL-1620)
- SLOBODRIAN, R. J., (See Lamontagne, C. R., LBL-1941)
- SOINSKI, A. J., (See Kaindl, G., LBL-1960)
- SOKOL, H. A., (See Garrison, W., LBL-1269)
- STACY, J. J., N. Edelstein, and R. D. McLaughlin  
Effects of gamma-irradiation on actinide ions in calcium fluoride  
LBL-638, March 1972  
J. Chem. Phys. 57, 4980 (1972)
- STEINBERG, G. M.  
Neutron activation analysis of pottery glazes  
LBL-1907, June 1973  
NFP
- STEPHENS, F. S., (See Newton, J. O., LBL-1227)
- STEPHENS, F. S., R. M. Diamond, D. Benson Jr., and M. R. Maier  
Rotation of moderately-deformed odd-A nuclei  
LBL-1282, October 1972  
Phys. Rev. C 7, 2163 (1973)
- STEPHENS, F. S., (See Leigh, J. R., LBL-1601)
- STEPHENS, F. S., R. M. Diamond, and S. G. Nilsson  
A coupling scheme relevant to high angular momenta and intermediate nuclear deformations  
LBL-1607, January 1973  
Phys. Letters 44B, 429 (1973)



- STEPHENS, F. S., (See Nakai, K., LBL-1614)
- STEPHENS, F. S., P. Kleinheinz, R. K. Sheline, and R. S. Simon  
Backbending and rotation alignment  
LBL-1911, November 1973  
Nucl. Phys.
- STEPHENS, F. S., (See Proetel, D., LBL-1939)
- STEPHENS, F. S., (See Gizon, J., LBL-1948)
- STEPHENS, F. S., (See Kienle, P., LBL-1961)
- STEPHENS, F. S., (See Grosse, E., LBL-1962)
- STEPHENS, F. S.  
Rotation-aligned coupling scheme  
LBL-1968, July 1973  
Presented at the International Conference on Nuclear Physics, Munich, Germany,  
August 27 - September 1, 1973
- STEPHENS, F. S., (See Kleinheinz, P., LBL-1994)
- STEPHENS, F. S., (See Grosse, E., LBL-1997)
- STEPHENS, F. S., (See Proetel, D., LBL-2309)
- STREET Jr., K., (See Hebert, A. J., LBL-601)
- STREET Jr., K., (See Hebert, A. J., LBL-1616-Rev.)
- STEINBERG, G.  
Neutron activation analysis of pottery glazes  
LBL-1907, June 1973  
NFP
- STEYERT, W. A., and K. S. Krane  
Effect of time reversal non-invariance on nuclear  $\gamma$ -decay observables  
LBL-1981, August 1973  
Phys. Rev. Letters
- STEYERT, W. A., (See Krane, K. S., LBL-2337)
- STROSS, F., (See Heizer, R. F., LBL-1624)
- SÜSSMANN, G.  
Description of the nuclear surface by moments  
LBL-1615, June 1973  
Nucl. Phys.
- SVENTEK, J. S., (See Huizenga, J. R., LBL-2314)
- SVENTEK, J. S., (See Huizenga, J. R., LBL-2316)
- SWIATECKI, W. J., (See Myers, W. D., LBL-1957)

- TAMURA, T., I. Rezanka, S. Iwata, J. O. Rasmussen, and J. Alonso  
Levels in  $^{165}\text{Tm}$  excited by decay of 10 min  $^{165}\text{Yb}$  and by the  $^{158}\text{Gd}(^{11}\text{B}, 4n\gamma)$  reactions  
LBL-1689, May 1973  
Phys. Rev.
- TEMPLETON, L. K., D. H. Templeton, and A. Zalkin  
The crystal and molecular structure of 2-(N-nitrosomethylamino)acetamide  
LBL-669, May 1972  
Acta Cryst. B29, 50 (1973)
- TEMPLETON, D. H., (See Templeton, L. K., LBL-669)
- TEMPLETON, D. H., (See Zalkin, A., LBL-1265)
- TEMPLETON, D. H., (See Hollander, F. J., LBL-1266)
- TEMPLETON, D. H., (See Hollander, F. J., LBL-1267)
- TEMPLETON, D. H., (See Hollander, F. J., LBL-1268)
- TEMPLETON, D. H., (See Hollander, F. J., LBL-1273)
- TEMPLETON, D. H., (See Ward, D. L., LBL-1609)
- TEMPLETON, D. H., (See Hollander, F. J., LBL-1661)
- TEMPLETON, D. H., (See Chapuis, G., LBL-1696)
- TEMPLETON, D. H., (See Ruben, H., LBL-1931)
- TEMPLETON, D. H., (See Ray, S., LBL-1932)
- TEMPLETON, D. H., (See Quarles, W. G., LBL-1933)
- TEMPLETON, D. H., (See Quarles, W. G., LBL-1934)
- TEMPLETON, D. H., (See Ray, S., LBL-1935)
- TEMPLETON, D. H., (See Ruben, H., LBL-1936)
- THOMPSON, S. G., (See Nardi, E., LBL-1263)
- THOMPSON, S. G., (See Kataria, S. K., LBL-1905)
- THOMPSON, S. G., (See Jared, R. C., LBL-1963)
- THOMPSON, S. G., (See Moretto, L. G., LBL-1966)
- TOREN, D., (See Korteling, R. G., LBL-663)
- TSANG, C. F., (See Randrup, J., LBL-1944)
- UCHIYAMA, F., (See Wang, W. L., LBL-2313)
- UEKI, T., (See Zalkin, A., LBL-1265)

- VAN DEURZEN, C. H. H., J. G. Conway, and S. P. Davis  
Spectrum and energy levels of doubly ionized scandium (Sc III)  
LBL-1217, August 1972  
J. Opt. Soc. Am. 63, 158 (1973)
- VAN DEURZEN, C. H. H.  
Excitation energies in an electrically pulsed light-emission source applied to the separation  
of higher ionized atomic states: spectra and energy levels of scandium 2+ and vanadium 4+  
LBL-1657, May 1973  
Ph. D. Thesis
- VAN DEURZEN, C. H. H., and J. G. Conway  
Excitation of spectra of multiply-ionized atoms by capacitor discharges  
LBL-1975, August 1973  
Appl. Spectrosc.
- VAN DEURZEN, C. H. H., J. G. Conway, and S. P. Davis  
The spectrum and energy levels of quadrupole ionized vanadium (V  $\text{IV}$ )  
LBL-1986, September 1973  
J. Opt. Soc. Am.
- VAREA de ALVAREZ, C., M. L. Cohen, L. Ley, S. P. Kowalczyk, F. R. McFeely,  
D. A. Shirley, and R. W. Grant  
Electronic density of states and bonding in chalcopyrite-type semiconductors  
LBL-2330, November 1973  
Phys. Rev. Letters
- VERGADOS, J. D., and H. W. Baer  
Importance of momentum dependent terms in radiative pion capture  
LBL-690, July 1972  
Phys. Letters 41B, 560 (1972)
- von OERTZEN, W., H. G. Bohlen, and B. Gebauer  
Enhancement of two-proton transfer in  $N = 82$ . A study of  $1p$ ,  $2p$  and  $(2p + 2n)$  transfer  
reactions induced by  $^{16}\text{O}$  on  $^{140}\text{Ce}$ ,  $^{142}\text{Nd}$  and  $^{144}\text{Sm}$  near the coulomb barrier  
LBL-1622, January 1973  
Nucl. Phys. A207, 91 (1973)
- von OERTZEN, W., (See Kovar, D. G., LBL-1646)
- von OERTZEN, W.  
Some new developments in direct reactions induced by heavy ions  
LBL-1678, April 1973  
Presented at the Minerva Symposium on Physics in Rehovoth, Israel, 2-4 April 1973
- von OERTZEN, W., (See Becchetti, F. D., LBL-1972)
- von OERTZEN, W.  
A study of optical models for the elastic scattering of heavy ions and related transfer  
reactions  
LBL-1985, September 1973  
Nucl. Phys.
- von OERTZEN, W., (See DeVries, R. M., LBL-2363)

- WAGNER, W. T., G. R. Hammerstein, G. M. Crawley, J. Borysowicz, and F. Petrovich  
35 MeV proton inelastic scattering from low-lying states in  $^{207}\text{Pb}$   
LBL-1938, June 1973  
Phys. Rev. Letters
- WANG, W. L., and R. G. Lipcs  
Heavy-ion elastic scattering at high energies  
LBL-1988, August 1973  
Phys. Rev.
- WANG, W. L., and C. M. Shakin  
Angular distribution and polarization of  $^{16}\text{O}(\gamma, n_0)^{15}\text{O}$   
LBL-1995, October 1973  
Phys. Rev. C
- WANG, W. L., and F. Uchiyama  
Differential  $K_L \rightarrow K_S$  regeneration cross section in coherent production model and optical model  
LBL-2313, October 1973  
Nucl. Phys.
- WARD, D. L., D. H. Templeton, and A. Zalkin  
( $\pm$ )-4 $\alpha$ , 8 $\alpha$ , 14 $\beta$ -trimethyl-18-nor-5 $\alpha$ , 13 $\beta$ -androst-9(11)-en-3, 17-dione, a synthetic precursor of fusidic acid  
LBL-1609, December 1972  
Acta Cryst. B29, 2016 (1973)
- WARD, T. E., (See Massmann, H., LBL-1693)
- WEISENMILLER, R. B., (See Wilcox, K. H., LBL-1644)
- WEISENMILLER, R. B., (See Jelley, N. A., LBL-2329)
- WERNAU, C. W., and C. R. Wilke  
New method for evaluation of dissolved oxygen probe response for  $K_L$  determination  
LBL-1209, July 1972  
Bioeng. and Biotech. XV, 571 (1973)
- WHITTAKER, B., (See Edelstein, N., LBL-2348)
- WIDEMANN, F., M. Picon, F. Asaro, H. V. Michel, and I. Perlman  
A Lyons branch of the pottery-making firm of Ateius of Arezzo  
LBL-1964, November 1973  
Archaeometry
- WILCOX, K. H., N. A. Jelley, G. J. Wozniak, R. B. Weisenmiller, H. L. Harney, and J. Cerny  
New spectroscopic measurements via exotic nuclear rearrangement: the reaction  $^{26}\text{Mg}(^7\text{Li}, ^8\text{B})^{25}\text{Ne}$   
LBL-1644, February 1973  
Phys. Rev. Letters 30, 866 (1973)
- WILCOX, K. H., (See Jelley, N. A., LBL-2329)
- WILKE, C. R., (See Wernau, W. C., LBL-1209)
- WILKE, C. R., (See Robinson, C. W., LBL-1943)

- WORDEN, E. F., R. W. Lougheed, R. G. Gutmacher, and J. G. Conway  
Hyperfine structure in the  $^{253}\text{Es}$  emission spectrum, part III; extension of the line list,  
levels of Es I and II, nuclear magnetic dipole and quadrupole moments  
UCRL-74650, March 1973  
J. Opt. Soc. Am.
- WORTMANN, G., (See Kaindl, G., LBL-1631)
- WORTMANN, G., (See Kaindl, G., LBL-1675)
- WOZNIAK, G. J., (See Wilcox, K. H., LBL-1644)
- WOZNIAK, G. J., N. A. Jelley, and J. Cerny  
Feasibility of  $\alpha$ -transfer studies via the  $(\alpha, ^8\text{Be})$  reaction at high energies  
LBL-1904, June 1973  
Phys. Rev. Letters 31, 607 (1973)
- WOZNIAK, G. J., (See Jelley, N. A., LBL-2329)
- YARKONY, D. R., S. V. O'Neil, H. F. Schaefer III, C. P. Baskin, and C. F. Bender  
Interaction potential between two rigid HF molecules  
LBL-1969, August 1973  
J. Chem. Phys.
- YARNELL, P. A.  
Geometry of some metal halides  
LBL-1973, July 1973  
Ph. D. Thesis
- YELLIN, J.  
Optical pumping by forbidden lines  
LBL-293, January 1972  
J. Phys. B
- YELLIN, J., (See Hadeishi, T., LBL-1260)
- YELLIN, J.  
Alignment of some triplet and singlet D states of helium  
LBL-1602, December 1972  
Phys. Rev. Letters 30, 1286 (1973)
- YELLIN, J., T. Hadeishi, and M. C. Michel  
Lifetime and alignment of the  $5^1\text{D}_2$  state of  $^4\text{He}$  by beam-foil level crossing  
LBL-1608, January 1973  
Phys. Rev. Letters 30, 417 (1973)
- ZALKIN, A., (See Templeton, L. K., LBL-669)
- ZALKIN, A., D. H. Templeton, and T. Ueki  
Crystal structure of  $\lambda$ -tris(1,10-phenanthroline)iron(II)bis(antimony(III)d-tartrate)octahydrate  
LBL-1265, September 1972  
Inorg. Chem. 12, 1641 (1973)
- ZALKIN, A., (See Hollander, F. J., LBL-1266)
- ZALKIN, A., (See Hollander, F. J., LBL-1267)

ZALKIN, A., (See Hollander, F. J., LBL-1268)

ZALKIN, A., (See Hollander, F. J., LBL-1273)

ZALKIN, A., (See Ward, D. L., LBL-1609)

ZALKIN, A., (See Hollander, F. J., LBL-1661)

ZALKIN, A., (See Chapuis, G., LBL-1696)

ZALKIN, A., (See Ruben, H., LBL-1931)

ZALKIN, A., (See Ray, S., LBL-1932)

ZALKIN, A., (See Quarles, W. G., LBL-1933)

ZALKIN, A., (See Quarles, W. G., LBL-1934)

ZALKIN, A., (See Ray, S., LBL-1935)

ZALKIN, A., (See Ruben, H., LBL-1936)

ZISMAN, M. S., F. D. Becchetti, B. G. Harvey, D. G. Kovar, J. Mahoney, and J. D. Sherman  
Heavy-ion-induced single-nucleon transfer reactions in the Zr-Mo region  
LBL-1676, April 1973  
Phys. Rev. C 8, 1866 (1973)

ZISMAN, M. S., (See DeVries, R. M., LBL-2363)

ZUEHL, R., (See Bucher, J. J., LBL-2342)

## VII. Author Index

## Author Index

Contributors to This Report

- Abraham, M. M., 247  
Adolphe, C., 331  
Allen, A., 453  
Alonso, C. T., 133  
Alonso, J. R., 10, 150, 435  
Anderberg, D. H., 455  
Anderlini, V., 419  
Anholt, R., 233, 235, 237  
Artzy, M., 396, 399, 401  
Arvieux, F. J., 65, 66, 69  
Asaro, F., 383, 385, 387, 388, 396, 399, 407  
Ascuitto, R. J., 154, 156, 160  
Babinet, R. P., 51, 52, 54, 59, 216  
Bacher, A. D., 111  
Bagus, P. S., 259, 295  
Banna, M. S., 292, 298  
Bartlett, N., 327, 329  
Becchetti, F. D., 81, 86, 87, 94  
Bernthal, F. M., 181  
Bender, C. F., 252  
Binder, I., 61, 451  
Birchall, J., 65, 66, 68, 69, 78  
Blackman, G. L., 257  
Bowen, J., 427  
Bowman, H. R., 381, 383, 385  
Bowman, J. D., 122, 125, 163  
Brown, D. R., 79, 351, 362  
Brown, N. E., 409  
Browne, E., 3  
Burleigh, R., 427  
Butler, G. W., 122  
Cavell, R. G., 275  
Cerny, J., 103, 105, 108, 111, 114, 118, 430, 443  
Chapman, J., 419  
Chapuis, G., 347  
Chatterjee, A., 229  
Chintalapudi, S., 68, 429  
Chu, S. Y., 196  
Church, D. A., 459  
Clark, D. J., 427, 429  
Clem, R. G., 417, 455, 456  
Clements, T., 200  
Cohen, M. L., 286  
Conway, J. G., 239, 458  
Conzett, H. E., 65, 66, 68, 69, 71, 74, 78  
Cramer, J. G., 81  
Dahme, W., 65, 66, 69, 71  
Dairiki, J. M., 3  
Davis, D. W., 244, 292, 295, 298, 467  
Davis, S. P., 239  
de Boer, J., 233  
de Swiniarski, R., 74  
De Vries, R. M., 81  
Diamond, R. M., 18, 20, 22, 24, 26, 27, 29, 31, 227, 233  
DiCasa, M., 451  
Doebler, R. E., 3



- Edelstein, N., 247, 250, 351, 356, 359, 362  
Fee, D. C., 370, 371, 373, 376, 467  
Finch, C. B., 247  
Flood, W., 427  
Frazier, P. E., 427, 429  
Frierman, J. D., 387  
Frois, B., 74  
  
Garrison, W. M., 369  
Gatti, R. C. 37, 51, 52, 57  
Giauque, R. D., 409  
Girvin, D. C., 417  
Gizon, A., 26  
Gizon, J., 26  
  
Glendenning, N. K., 87, 96, 99, 154, 156, 160  
Go, M. K., 33  
Goda, L. Y., 409  
Goldberg, S. Z., 340  
Gough, R. A., 114, 118, 443  
Gould, H., 230  
Grant, R. W., 286  
Greiman, W., 453  
Grens II, E. A., 406  
Grosse, E. H., 18, 20, 24, 26, 227  
Gutbrod, H., 52  
  
Hadeishi, T., 459  
Haeberli, W., 66, 69  
Halpern, I., 79, 80  
Hardy, J. C., 111  
Harmon, C. A., 340  
Harney, H. L., 111  
Harvey, B. G., 81, 84, 86, 87, 94, 96, 99, 100, 101, 102, 434  
Haustein, P. E., 181  
Hayes, R. G., 356  
Hebert, A., 381  
Heizer, R. F., 385  
Hendrie, D. L., 79, 80, 84, 87, 94, 96, 99, 100, 101, 102  
Heunemann, D., 52, 54  
Hollander, F. J., 325, 327  
Hollander, J. M., 3  
Holley, W. R., 429  
Hollowell, C. D., 461  
Homeyer, H., 79, 81, 84, 86, 87, 94, 434  
Hunter, J. C., 52  
  
Iwata, S., 10  
  
Jacob Jr., N. P., 129  
Jardine, L. J., 3, 175, 447  
Jared, R. C., 38, 42, 51, 52, 54, 59  
Jayko, M. E., 229  
Jelley, N. A., 103, 105, 108, 430  
Jurnak, F. A., 468  
  
Kataria, S. K., 45, 54, 211  
Kienle, P., 24, 29, 227  
Kilian, G. W., 456  
Klapisch, R., 126  
Kleber, M., 227  
Kleinheinz, P., 27, 178  
Kolbe, W., 247  
Korteling, R. G., 122  
Kovar, D. G., 71, 81, 84, 86, 87, 94

- Kowalczyk, S. P., 268, 271, 275, 277, 281, 286, 289, 303, 305, 308
- Kratz, J. V., 61, 349, 450, 451
- Kraus, L., 96, 99, 100, 101, 102
- Krien, K., 7
- Lamontagne, C. R., 74, 78
- Larimer, R. M., 65, 66, 68, 69, 71, 78
- Larsson, S. E., 219
- Leary, K., 329
- Lederer, C. M., 3, 447, 453
- Lee, D. M., 34
- Leeman, Ch., 71, 74
- Leigh, J. R., 29
- Leong, L., 459
- Lessard, L., 126
- Levinson, J. L., 51, 52, 54
- Ley, L., 268, 271, 275, 277, 281, 286, 289, 303, 305, 308
- Liljenzin, J. O., 61, 349, 439, 450, 451
- Lipes, R. G., 166
- Liskow, D. H., 259
- Littlejohn, D., 443
- Liu, B., 81, 254, 259
- Ma, C. W., 187, 189, 192, 196, 198
- Macdonald, J. A., 108, 111, 470
- Maguire, C., 86, 96, 99, 100, 101, 102
- Mahoney, J., 81, 84, 86, 87, 94, 96, 99, 100, 101, 102, 434
- Maier, K. H., 29
- Maier, M. R., 26, 27, 227
- Main, R. M., 433
- Markowitz, S. S., 5, 33, 34, 129, 370, 371, 373, 376, 413
- Marrus, R., 230
- Martin, R. L., 298
- Massmann, H., 181, 183
- Mayer, B., 71
- McFeely, F. R., 268, 271, 275, 277, 281, 286, 289, 303, 305, 308
- McLaughlin, R. D., 459, 461
- Mehlhorn, R., 250
- Meyerhof, W. E., 233
- Michel, H. V., 387, 388, 407
- Mitra, G., 422
- Möller, P., 219, 223
- Moretto, L. G., 36, 37, 51, 52, 54, 57, 200, 202, 205, 207, 211, 214, 216
- Morris, D., 427, 429
- Myers, W. D., 131
- Nagarajan, M. A., 153
- Nakamura, M., 454
- Nardi, E., 45
- Naumann, R. A., 7, 42
- Newton, A. S., 378, 410, 419
- Newton, J. O., 22
- Nifenecker, H., 38, 42
- Nilsson, S. G., 219, 223
- Nitschke, J. M., 446
- Norris, A. E., 61, 451
- Olovsson, I., 337
- O'Neil, S. V., 252
- Parsa, B., 5, 413
- Parsons, T. C., 359
- Pearson, P. K., 254, 257
- Perlman, I., 388, 396, 399

- Picon, M., 388  
Plattner, G. R., 111  
Pollak, R. A., 271, 275, 277, 281, 289, 303, 305, 308  
Poskanzer, A. M., 122, 125, 125, 127  
Povh, B., 24, 227  
Proetel, D., 29, 31, 227, 233  
Quarles, W. G., 342, 344  
Rad, F. N., 68  
Ragnarsson, I., 223  
Raich, D. G., 16, 172  
Rajnak, K., 250  
Randrup, J., 137, 141, 143, 219, 223  
Rasmussen, J. O., 7, 10, 16, 150, 172, 175, 181, 183, 187, 189, 192, 196, 235, 237  
Ray, S., 332, 335  
Raymond, K. N., 340  
Rauscher, E. A., 172  
Reisdorf, W., 126  
Renkas, M., 429  
Rezanka, I., 7, 10, 16  
Ribbe, W., 183  
Rigaud, C., 126  
Rinneberg, H. H., 321  
Risebrough, R. W., 419  
Romascan, E., 453  
Rothenberg, S., 252  
Roy, R., 78  
Ruben, H., 337, 338  
Salomon, D., 319  
Savigny, N., 334  
Schaefer III, H. F., 252, 254, 257, 259, 261, 263  
Schmieder, R. W., 230  
Schmincke, H., 381  
Schmitt, R. C., 52, 54  
Schrenk, M., 295  
Sciamanna, A. F., 410, 456  
Scott, D. K., 86, 96, 99, 100, 101, 102  
Seaborg, G. T., 61, 349  
Sextro, R. G., 114, 118, 470  
Shakin, C. M., 170  
Shalimoff, G. V., 454  
Sheline, R. K., 27, 178  
Sherman, J. D., 471  
Shibah-Eldin, A., 3, 175  
Shirley, D. A., 244, 267, 268, 271, 275, 277, 281, 286, 289, 292, 295, 298, 303, 305, 308, 312, 316, 319, 321  
Shirley, V. S., 3  
Simon, R. S., 178  
Silva, R. J., 450  
Slobodrian, R. J., 74, 78  
Soinski, A. J., 172  
Starks, D. F. 358, 359  
Stephens Jr., F. S., 18, 20, 22, 24, 26, 27, 29, 31, 178, 227, 233  
Streitwieser Jr., A., 358, 359  
Stross, F., 383, 385  
Swiatecki, W. J., 131, 143, 163  
Tamura, T., 10  
Templeton, D. H., 325, 327, 329, 331, 332, 335, 337, 338, 340, 342, 344, 347  
Terrien, Y., 96, 99, 100, 101, 102  
Thibault, C., 126

- Thompson, S. G., 37, 38, 42, 45, 51, 52,  
54, 57, 59
- Tjøm, P. O., 233
- Tsang, C. F., 143, 146, 149, 163, 198, 219,  
222, 223
- Uchiyama, F., 168
- Van Deurzen, C. H. H., 239, 458, 472
- Varea de Alvarez, C., 286
- Vermeulen, T., 406
- Viola, V., 127
- von Oertzen, W., 81, 84, 86, 87, 94
- Wahlgren, U., 254, 257
- Wang, W., 166, 168, 170
- Ward, T. E., 181
- Weisenmiller, R. B., 105
- Whalley, M., 3
- Whittaker, B., 351, 362
- Widemann, F., 388
- Wieman, W., 80
- Wilcox, K. H., 105
- Wilhelmy, J. B., 42
- Wilke, C. R., 422
- Winges, K. D., 406
- Wozniak, G. J., 103, 105, 430
- Yagi, K., 96, 99, 100, 101, 102
- Yarkony, D. R., 252
- Yarnell, P. A., 472
- Zalkin, A., 325, 327, 329, 331, 332, 335,  
337, 338, 342, 344, 347
- Zebelman, A. M., 125, 127
- Zisman, M., 80, 81
- Zok, B. D., 459

LEGAL NOTICE

This report was prepared as an account of work sponsored by the United States Government. Neither the United States nor the United States Atomic Energy Commission, nor any of their employees, nor any of their contractors, subcontractors, or their employees, makes any warranty, express or implied, or assumes any legal liability or responsibility for the accuracy, completeness or usefulness of any information, apparatus, product or process disclosed, or represents that its use would not infringe privately owned rights.